8th European Workshop on
Beam Diagnostics and Instrumentation
for Particle Accelerators

DIPAC 2007

NH Laguna Palace

VENICE

Mestre

May 20 - 23, 2007

The biannual DIPAC workshop is the right opportunity for the exchange of the latest advances in the field of beam diagnostics and instrumentation for particle accelerators worldwide.

The scientific programme includes invited and contributed talks, poster sessions and discussion groups.

An industrial exhibition and a visit to ELETTRA and FERMI@elettra are also scheduled.

Photo courtesy of M. Vidmar

Programme Committee

Mario Ferianis (ELETTRA) - Chair
Peter Cameron (BNL)
Peter Forck (GSI)
Eiji Kikutani (KEK)
Alex Lumpkin (APS/ANL)
Andreas Peters (GSI)
Uli Raich (CERN)
Kees Scheidt (ESRF)
Volker Schlott (PSI)
Hermann Schmickler (CERN)
Mario Serio (INFN-LNF)
Tom Shea (SNS/ORNL)
Kay Wittenburg (DESY)

Local Committee

Ilde Weffort - Chair
Ivan Andrian
Laura Badano
Silvano Bassanese
Marlen Bugmann (PSI)
Madeleine Catin (CERN)
Giulia Ciani
Gino D'Eliso
Stefano Deiuri
Raffaele De Monte
Mario Ferianis
Charlie Horak (ORNL)
Isabella Massarotti
Roberto Passuello
Cristiana Roberti
Mojca Skabar
Caterina Tabacco

Deadlines:

abstract submission	March 2, 2007
early registration	March 27, 2007

Hosted by Sincrotrone Trieste
http://www.elettra.trieste.it/dipac07

Preface

The 8th European Workshop on Beam Diagnostics and Instrumentation for Particle Accelerator (DIPAC 2007) was held at the NH Laguna Palace Conference Centre in Venice / Mestre (Italy).

As recently mentioned during an interview by the worldwide known Italian architect, Renzo Piano, the 1st phase of any new design is dialogue: listening, talking and discussing with each other. Dialogue is a well established practice within our Community that is becoming more and more open to other Communities. Therefore, events like DIPAC, while fostering direct communication, are also fundamental ingredients of our everyday work.

There have been three full days of science, technology and exchanges of ideas in a comfortable and stimulating environment, the NH Laguna Palace. The modern and efficient organization of the hosting Conference Center was perfectly matched to the highly trained and skilled staff of the front desk, proceeding office, plenary and poster sessions. As per recent DIPAC tradition, colleagues from other laboratories joined the ELETTRA staff, thus creating a really strong and motivated team.

The Scientific Program included: ten invited talks, nine contributed corals, two poster sessions and four topical discussion sessions.

In the continued tradition of making the DIPAC as much participated as possible, informal discussion sessions (of up to 30 minutes) took place after each oral session, which allowed extended and comprehensive questions & answers time slots. And even the final Q&A time, at the end of the last oral session, was very crowded and ran over on time.

The industrial exhibition ran in parallel to the main scientific program, providing the project teams with the information on the state-of-the-art technological achievements. he number of industrial participants was the highest ever reached in a DIPAC event.

The guided tour of Sincrotrone Trieste was part of the program. Thanks to the professional approach of the ELETTRA staff, it has been possible to illustrate some of the key spots of the laboratory to the many groups (>200 people in total).

The workshop banquet took place at the magnificent Villa Manin di Passariano, located half way between Trieste and Venice. Thanks to the menu and to the jazz live music intermezzo, the dinner has been of the same high standard as the many scientific contributions and as lively as the attendees' participation.

A one-day companion excursion to Murano and Venice has been organized. The boat trip started directly from the Laguna Palace Marina. The visit to one of the most famous glass factory (Archimede Seguso) in Murano and to Palazzo Ducale, the residence of the Venetian Doge, contributed in equal parts to the success of this event.

As previously mentioned, the workshop turned out in a success thanks to the dedicated work of many colleagues. First of all, I would like to thank the Program Committee members who brought in their experience and commitment for the benefit of the whole Community. Secondly, what we have experienced at the Laguna Palace would not have been possible without the contribution of the many friends of the Local Committee. I would like here to mention them individually, starting from Ilde Weffort, our perfect chairwoman, Laura Badano, the Industrial Exhibition manager, Giulia Ciani, Silvano Bassanese and Raffaele Demonte supervisors of all the sessions (plenary and poster's plus visit at Elettra), Ivan Andrian, our JACoW expert and proceeding editor, Stefano Deiuri and Roberto Passuello, respectively WEB site manager and on-site informatic manager. Cristiana Roberti, Caterina Tabacco and Anna Pili were unique in handling all the administrative issues, whereas Isabella Massarotti provided her fundamental support in the local logistic arrangements, Raffaele Demonte and Dirk Noelle, the best event photographers. Marlene Bugmann (PSI), Madeleine Catin (CERN) and Charlie Horak (SNS), our DIPAC angels, shared the front desk and proceeding office efforts. Also, all our Elettra colleagues who guided the many groups during the tour at Sincrotrone.

And, last but not least, I would like to warmly thank Volker Schaa (GSI) and Stefano Krecic whose professional skills and right team spirit, only, made these proceedings possible.

The 9th DIPAC workshop will be held in 2009 and will be hosted by the Paul Scherrer Institute: good luck, Volker!

Mario Ferianis
(Chairman of the DIPAC 2007 Workshop)

Monday, 21 May	
First Oral Session	**MOO1A**
09:00-09:10	M. Ferianis (Sincrotrone Trieste ScpA Elettra) **DIPAC 2007 Welcome Address**
09:10-09:40	E. Bravin (European Organization for Nuclear Research AB Dept) **High Resolution Transverse Profile Measurement**
09:40-10:20	G. Kube (Deutsches Elektronen-Synchrotron) **Review of Synchrotron Radiation based Diagnostics for Transverse Profile Measurements**
10:20-10:50	Discussion
10:50-11:20	**Coffee Break**
Second Oral Session	**MOO2A**
11:20-11:50	V. Malka (Laboratoire d'Optique Appliquée) **Physics and Diagnostics of Laser-Plasma Accelerators**
11:50-12:10	C. Gerth (Deutsches Elektronen - Synchrotron MPY) **Electron Beam Diagnostics for the European X-Ray Free Electron Laser**
12:10-12:30	M. Ferianis (Sincrotrone Trieste ScpA Elettra) **FERMI@elettra Diagnostics**
12:30-12:50	Discussion
12:50-14:00	**Buffet Lunch**
14:00-15:50	**Parallel Sessions**
	J.C. Denard (Chair) **MOD1A** **Commissioning aspects of new machines**
	B. Keil (Chair) **MOD2C** **BPM system: pick-ups and read out electronics**
	J.M. Byrd (Chair) **MOD3B** **Timing and longitudinal diagnostics for IV generation Light Sources**
	K. Wittenburg (Chair) **MOD4D** **Transverse Profile measurements**
15:50-16:20	**Coffee Break**
Third Oral Session	**MOO3A**
16:20-16:40	A. Agari (High Energy Accelerator Research Organization Institute of Particle and Nuclear Studies) **Optical Transition Radiation Monitor for High Intensity Proton Beam at the J-PARC**
16:40-17:00	C.A. Andre (Gesellschaft für Schwerionenforschung mbH, Beam Diagnostics Group) **Beam Induced Fluorescence (BIF) Monitor for Transverse Profile Determination of 5 to 750 MeV/u Heavy Ion Beams**
17:00-17:20	S.G. Arutunian (Yerevan Physics Institute) **First Vibrating Wire Monitor Measurements of a Hard X-ray Undulator Beam at the Advanced Photon Source**
17:20	Discussion

Tuesday, 22 May		
	First Oral Session	**TUO1A**
09:00-09:30	M. Blaskiewicz (Brookhaven National Laboratory Collider-Accelerator Department) **Bunched Beam Stochastic Cooling for RHIC**	
09:30-10:00	R.J. Steinhagen (European Organization for Nuclear Research AB Department) **Feedbacks on Tune and Chromaticity**	
10:00-10:20	F. Epaud (European Synchrotron Radiation Facility) **Beam Diagnostic Features of the ESRF Multibunch Feedback**	
10:20-10:50	**Coffee Break**	
10:50-12:30	**Poster session**	**TUPB**
	Poster session	**TUPC**

Wednesday, 23 May		
	First Oral Session	**WEO1A**
09:00-09:30	A. Winter (Deutsches Elektronen-Synchrotron) **Sub-ps Timing and Synchronization Systems for Longitudinal Electron Bunch Profile Measurements**	
09:30-10:00	J.M. Byrd (Lawrence Berkeley National Laboratory) **Progress in Ultrafast X-ray Streak Cameras**	
10:00-10:20	D. Alesini (Istituto Nazionale di Fisica Nucleare Laboratori Nazionali di Frascati) **Instrumentation for Longitudinal Beam Gymnastics in FELs and in the CLIC test facility 3**	
10:20-10:50	Discussion	
10:50-11:20	**Coffee Break**	
	Second Oral Session	**WEO2A**
11:20-11:40	D.C. Faircloth (Science and Technology Facilites Council Rutherford Appleton Laboratory) **Beam Diagnostics for the Front End Test Stand at RAL**	
11:40-12:00	G. Berden (FOM-Institute for Plasma Physics Rijnhuizen) **Single Shot Longitudinal Bunch Profile Measurements by Temporally Resolved Electro-Optical Detection**	
12:00-12:30	D. Alesini (Istituto Nazionale di Fisica Nucleare Laboratori Nazionali di Frascati) **Advanced Measurements at the SPARC Photoinjector**	
12:30-12:50	Discussion	
12:50-14:00	**Buffet Lunch**	
14:00-16:00	Poster Session	**WEPB**
	Poster Session	**WEPC**
16:00-16:30	**Coffee Break**	
	Third Oral and Closing Session	**WEO3A**
16:30-17:00	D.M. Treyer (Paul Scherrer Institute) **High-Resolution Single-Shot Beam Position Monitors**	
17:00-17:30	A. Peters (Gesellschaft für Schwerionenforschung mbH) **Diagnostic Instrumentation for Medical Accelerator Facilities**	
17:30	M. Ferianis (Sincrotrone Trieste S.C.p.A. ELETTRA) **DIPAC 2007 Closing remarks**	

... water, stones,
colours and
the night-time romantic:
Dirk, you hit them all!

Thank you.

Pictures courtesy of Dirk Noelle.

Contents

Preface **i**
Foreword . . . iii
Program . . . v
. . . water, stones, colours . . . vii
Contents . . . viii
Pictures . . . xii

Proceedings **1**
MOO1A02 – High Resolution Transverse Profile Measurement . . . 1
MOO1A03 – Review of Synchrotron Radiation based Diagnostics for Transverse Profile Measurements . 6
MOO2A01 – Physics And Diagnostics Of Laser-Plasma Accelerators . . . 11
MOO2A02 – Electron Beam Diagnostics for the European X-Ray Free-Electron Laser . . . 17
MOO2A03 – FERMI@elettra Diagnostics . . . 20
MOD1A01 – Digital EBPMs at Diamond: Operational Experience and Integration into a Fast Global Orbit Feedback . . . 24
MOD1A03 – Electron Beam Diagnostics for the ALBA Light Source . . . 27
MOO3A01 – Optical Transition Radiation Monitor for High Intensity Proton Beam at the J-PARC . . . 30
MOO3A02 – Beam Induced Fluorescence (BIF) Monitor for Transverse Profile Determination of 5 to 750 MeV/u Heavy Ion Beams . . . 33
MOO3A03 – First Vibrating Wire Monitor Measurements of a Hard X-ray Undulator Beam at the Advanced Photon Source . . . 36
TUO1A01 – Bunched Beam Stochastic Cooling for RHIC . . . 39
TUO1A02 – Feedbacks on Tune and Chromaticity . . . 43
TUO1A03 – Beam Diagnostic Features of the ESRF Multibunch Feedback . . . 48
TUPB01 – A Fiber Profile Monitor for low Beam Intensities. . . . 51
TUPB02 – Stripline Transversal Filter Techniques For Sub-Picosecond Bunch Timing Measurements . . . 54
TUPB03 – Precision Beam Position Monitor for EUROTeV . . . 57
TUPB04 – BPM detectors upgrade for the ELETTRA Fast Orbit Feedback . . . 60
TUPB05 – A Tagged Photon Source at the Frascati Beam-Test Facility (BTF) . . . 63
TUPB06 – First Tests with the Sis18 Digital BPM System* . . . 66
TUPB07 – Electric -In-Air-X-Ray- Detectors for high Resolution Vertical Beam Position Measurement at the ESRF . . . 69
TUPB08 – Measurement of Vertical Emittance with a system of Six -In-Air-X-Ray- Projection Monitors at the ESRF . . . 72
TUPB09 – Digital Beam Trajectory and Orbit System, for the CERN Proton Synchrotron . . . 75
TUPB10 – Proposed Beam Position and Phase Measurements for the LANSCE Linac . . . 78
TUPB11 – A laserwire beam profile measuring device for the RAL Front End Test Stand . . . 81
TUPB12 – BPMs for the XFEL Cryo module . . . 84
TUPB13 – Design Considerations of a Spectrometer Dipole Magnet for the Photo Injector Test facility at DESY in Zeuthen (PITZ) . . . 87
TUPB14 – Test of a Silicon Photomultiplier for Ionization Profile Monitor Applications . . . 90
TUPB15 – Beam Position Monitors Using a Re-entrant Cavity . . . 93
TUPB16 – Optimization of the Linear-cut Beam Position Monitors Based on Finite Element Methods . . . 96
TUPB17 – Diagnostics for the CTF3 Probe Beam Linac CALIFES . . . 99
TUPB18 – Measurement of Electron Beam Charge in the ESRF Accelerator Complex for Absolute and Injection Efficency Measurements Using an FPGA Based Digital BPM Electronics . . . 102
TUPB19 – Signal Level Calculation for the PETRA-III Beam Position Monitor System . . . 105
TUPB20 – Large Horizontal Aperture BPM and Precision Bunch Arrival Pickup . . . 108
TUPB21 – Experience with Libera Beam Position Monitors at DELTA . . . 111
TUPB22 – Renewal of BPM Electronics of SPring-8 Storage Ring . . . 114
TUPB23 – Design Considerations for Phase Space Tomography Diagnostics at the PITZ Facility . . . 117
TUPB24 – First Results from the LEIR Ionisation Profile Monitors . . . 120
TUPB25 – Beam Profile Measurement with Optical Fiber Sensors at FLASH . . . 123
TUPB26 – Characterisation of the Systematic Effects of the Insertion Devices with Photon Beam Position Monitors . . . 126

TUPB27 – Recent Results from the Electron Beam Profile Monitor at the Swiss Light Source 129
TUPB28 – A Large Scintillating Screen for the LHC Dump Line 132
TUPB29 – Experimental Optimization of the Cathode Laser Temporal Profile 135
TUPB30 – Applications of IEEE-1394 and GigE Vision Digital Camera in the TLS 138
TUPB31 – The Beam Position System of the CERN Neutrino to Gran Sasso Proton Beam Line 141
TUPB32 – An RF Deflector for the Longitudinal and Transverse Beam Phase Space Analysis at PITZ . . 144
TUPC02 – Photo Injector Cathode Laser Beam Intensity and Pointing Position Diagnostics at PITZ 147
TUPC03 – Synchrotron Radiation Monitor for Energy Spectrum Measurements in the Bunch Compressor at FLASH 150
TUPC05 – Screen studies at PITZ 153
TUPC06 – Coherent Radiation Studies For The FERMI@Elettra Relative Bunch Length Diagnostics . . . 156
TUPC07 – Design and Construction of the Multipurpose Dispersive Section at PITZ 159
TUPC08 – Quadrupole Transfer Function for Emittance Measurement 162
TUPC09 – Design of the cavity BPM system for FERMI@elettra 165
TUPC10 – A transverse RF deflecting cavity for the FERMI@elettra project 168
TUPC11 – The Beam Diagnostics System for the FERMI@elettra Photoinjector 171
TUPC12 – FPGA based Frame Grabber for Video Beam Diagnostics 174
TUPC13 – The new Diode BPM system for ELETTRA 177
TUPC16 – Ultimate Resolution of Soleil X-Ray Pinhole Camera 180
TUPC18 – New Type Photocathode for X-Ray Streak Camera of the 10-Fs Resolution 183
TUPC19 – Matlab Code for BPM Button Geometry Computation 186
TUPC20 – The SOLEIL BPM and Orbit Feedback Systems 189
TUPC23 – Design of a Submicron Resolution Cavity BPM for the ILC Main Linac 192
TUPC24 – A Versatile Emittance Meter and Profile Monitor 195
TUPC25 – Design and Calibration of an Emittance Monitor for the PSI XFEL Project 198
TUPC26 – Button Beam Position Monitors for FLASH 201
WEO1A01 – Sub-ps Timing and Synchronization Systems for Longitudinal Electron Bunch Profile Measurements 204
WEO1A02 – Progress in Ultrafast X-ray Streak Cameras 209
WEO1A03 – Instrumentation for Longitudinal Beam Gymnastics in FEL's and in the CLIC test facility 3 . . 215
WEO2A01 – Beam Diagnostics for the Front End Test Stand at RAL 218
WEO2A02 – Single Shot Longitudinal Bunch Profile Measurements by Temporally Resolved Electro-Optical Detection 221
WEO2A03 – Advanced Measurements at the SPARC Photoinjector 224
WEPB01 – Design of an Electron Beam Energy Control Loop Using Transverse Dispersion 229
WEPB02 – Design of an Intra-Bunch-Train Feedback System for the European X-Ray FEL 232
WEPB03 – Femtosecond Yb-Doped Fiber Laser System at 1 um of Wavelength with 100-nm Bandwidth and Variable Pulse Structure for Accelerator Diagnostics 235
WEPB04 – The VEPP-4M Dynamic Aperture Determination Through the Precise Measurement of the Beam Lifetime 238
WEPB05 – Streak Camera Measurements of the SOLEIL Bunch Length 241
WEPB06 – Direct Comparison of the Methods of Beam Energy Spread Determination in the VEPP-4M Collider 244
WEPB07 – Time Domain Diagnostics for the ISAC-II Superconducting Heavy Ion Linac 247
WEPB08 – Noise and drift characterization of critical components for the laser based synchronization system at FLASH 250
WEPB09 – Mechanical Design of the Intensity Measurement Devices for the LHC 253
WEPB12 – Measurement of Bunch Lengthening Effects Using a Streak Camera with Reflective Optics . . 256
WEPB13 – Focusing of Optical Transition and Diffraction Radiation by a Spherical Target 259
WEPB15 – A Sub-50 Femtosecond bunch arrival time monitor system for FLASH 262
WEPB16 – First prototype of an optical cross-correlation based fiber-link stabilization for the FLASH synchronization system 265
WEPB18 – Electron Beam Temperature Measurements at the Fermilab Medium Energy Electron Cooler . 268
WEPB19 – Digital Analysis of Beam Diagnostic Noise 271
WEPB20 – Optical System for Measuring Electron Bunch Length and Longitudinal Phase Space at Pitz: Extension and Methodical Investigations 274

WEPB21 – Kicker Based Tune Measurement for DELTA . . . 277
WEPB22 – Touschek Lifetime Measurement with a Spurious Bunch in UVSOR-II Electron Storage Ring . 280
WEPB23 – Beam Diagnostics Development for the Cryogenic Storage Ring CSR . . . 283
WEPB24 – Machine Protection and Interlock Systems at Synchrotron SOLEIL . . . 286
WEPB25 – Time Domain Measurements at Diamond . . . 289
WEPB26 – Transition Thermal Processes In Vibrating Wire Monitors . . . 292
WEPB28 – First Tests of the Transverse Multibunch Feedback at Diamond . . . 295
WEPB29 – Bunch-by-Bunch Longitudinal Diagnostics at DAFNE by IR Light . . . 298
WEPB30 – Current Status of the SQUID Based Cryogenic Current Comparator for Absolute Measurements of the Dark Current of Superconducting RF Accelerator Cavities . . . 301
WEPB31 – Injector Diagnostics Overview of SPIRAL2 Accelerator . . . 304
WEPC01 – Beam Based Measurements of RF Phase and Amplitude Stability at FLASH . . . 307
WEPC02 – Developments at Elettra of the Electronics for the Bunch-Arrival Monitor . . . 310
WEPC03 – Secondary Electron Emission Beam Loss Monitor for LHC . . . 313
WEPC04 – Transverse Feedback Development at SOLEIL . . . 316
WEPC06 – Single gain radiation tolerant LHC beam loss acquisition card . . . 319
WEPC07 – Injection Diagnostics Using Triggered Bunch-by-Bunch Data Acquisition . . . 322
WEPC08 – Fiberoptics-Based Instrumentation for Storage Ring Beam Diagnostics . . . 325
WEPC09 – Classification of the LHC BLM Ionization Chamber . . . 328
WEPC10 – Tune, Coupling, and Chromaticity Measurement and Feedback During RHIC Run 7 . . . 331
WEPC11 – FERMI@elettra Timing System: Design and Recent Synchronization Achievements . . . 334
WEPC13 – Jitter Reduced Pump-Probe Experiments . . . 337
WEPC14 – Segmented Beam Dump for Time Resolved Spectrometry on a High Current Electron Beam . 340
WEPC16 – Excitation Striplines for SOLEIL Fast Transverse Feedback . . . 343
WEPC17 – Fast Orbit Feeback System Upgrade with New Digital Bpm and Power Supply in the Tls . . . 346
WEPC19 – Toroid Protection System for FLASH . . . 349
WEPC20 – A Real-Time Beam Monitor for Hadrontherapy Applications Based on Thin Foil Secondary Electron Emission and a Back-Thinned Monolithic Pixel Sensor . . . 352
WEPC21 – Diagnostics of the Waveform of Picosecond Electron Bunches Using the Angular Distribution of Coherent Sub-mmTransition and Diffraction Radiation . . . 355
WEPC22 – Synchronization of a 3GHz Repetition Rate Harmonically Mode-Locked Fiber Laser for Optical Timing Applications . . . 358
WEPC23 – Progress of the Diagnostics at the Proscan Beam Lines . . . 361
WEPC24 – A Self Calibrating Real Time Multi-Channel Profile Monitor for the Isis Proton Synchrotron . . 364
WEPC26 – Transverse Bunch-by-Bunch Feedback for the VEPP-4M Electron-Positron Collider . . . 367
WEPC27 – Segmented Foil SEM Grids for High-Intensity Proton Beams at Fermilab . . . 370
WEPC28 – Timing and Synchronization at the LCLS . . . 373
WEO3A01 – Low-Latency High-Resolution Single-Shot Beam Position Monitors . . . 376
WEO3A02 – Diagnostic Instrumentation for Medical Accelerator Facilities . . . 381

Appendices **387**
List of Authors . . . 387
Institutes List . . . 393
Participants List . . . 400
— A — . . . 400
— B — . . . 400
— C — . . . 400
— D — . . . 401
— E — . . . 401
— F — . . . 401
— G — . . . 401
— H — . . . 402
— I — . . . 402
— J — . . . 402
— K — . . . 402
— L — . . . 403
— M — . . . 403

— N — . . . 404
— O — . . . 404
— P — . . . 404
— R — . . . 404
— S — . . . 404
— T — . . . 405
— U — . . . 405
— V — . . . 405
— W — . . . 405
— Z — . . . 406
Sponsors . . . 407
Exhibitors . . . 415

DIPAC 2007
DIPAC 2007

TUPB16
FAIR
PAC 2007
voce

elettra
DIPAC 2007
DIPAC 2007

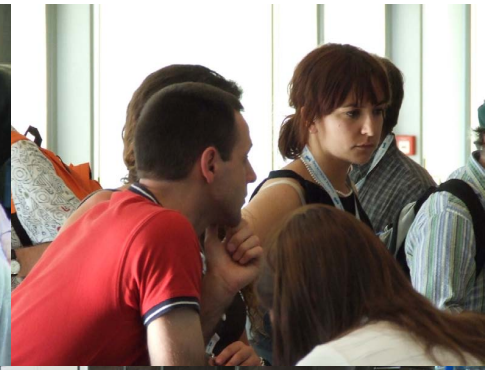

DIPAC 2007
hosted by Sincrotrone Trieste S.C.p.A.
elettra
@elettra
VARIAN
YOKOGAWA

6 Min.
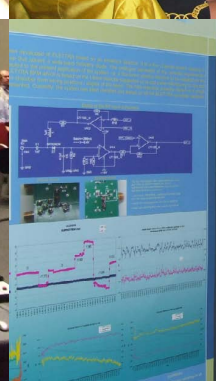

HIGH RESOLUTION TRANSVERSE PROFILE MEASUREMENT

E. Bravin, CERN, Geneva, Switzerland

Abstract

The performance of a particle accelerator is in large part defined by the transverse emittance of the beams. In most cases, like colliders and light sources (Synchrotrons or Free Electron Lasers), the quality of the final product, i.e. luminosity and brilliance, is directly linked to this parameter. For this reason many techniques and devices have been developed over the years for monitoring the transverse distribution of particles along accelerator chains or over machine cycles. Moreover modern designs of accelerators allow smaller size and/or higher current beams. New, more demanding, emittance measurement techniques have to be introduced and existing ones expanded. This presentation will review the different methods and the different instruments developed so far.

WHY HIGH RESOLUTION

There are many reasons why measuring the transverse profiles with high resolution is important, among these are:

- Emittance preservation: particularly important for hadron colliders and linear colliders as there is no synchrotron radiation damping in these machines. Usually particles are accelerated from a source through several linear and circular machines before entering in collision. Emittance blow-up happening at any point in the chain is maintained and amplified. In order to minimize this effect instruments for measuring the emittance at each stage are necessary. Additionally, in the case of circular colliders, the beams are maintained in coasting for several hours, without particular care transverse blow-up would reduce the luminosity. Table 1 presents the emittance budget of the LHC injection system as an example.
- Luminosity maximization: The other important factor in the maximization of the luminosity of a collider is the optimization of the optical functions at the IP. Where possible this is made by directly measuring the beam sizes at the interaction point, otherwise the size has to be calculated using the measured emittances and the calculated/measured optical functions. In the cases where the beam size at the IP can not be directly measured redundant beam profile monitors at different positions in the ring are essential as was for example observed during the LEP operation. Table 2 presents the values of the transverse beam sizes for a relevant sample of different machines.
- Beam loss reduction: another interesting subject in accelerators development is the design of ever more intense "drivers" machine, used to generate very intense particles beams at relatively low energies. This is the case of neutrino factories and neutron spallation sources for example. In these machines even small beam losses, in terms of the fraction of the beam lost, have serious consequences as they can damage the components of the machine or create activation making interventions very difficult. The formation of a halo around the core of the beam is an important process and need to be minimized. For the monitoring of the halo the relevant resolution is more in the measurement of the intensity than on the position.
- Development of new machines: Beside several new accelerators currently being built, LHC, FLASH, LCLS, FERMI etc. there are parallel ongoing studies and developments for the next generation of accelerators. Here beams of smaller and smaller emittances are generated and need to be measured in order to tune the machine and demonstrate the quality of the results.

Table 1: Emittance budget for the LHC injector chain

	E_k [GeV]	ε^* [π μm]	σ [mm]
LINAC	0.0001 – 0.05	~1.0	
BOOSTER	0.05 – 1.4	2.5	0.3 – 6.5
PS	1.4 - 26	3.0	0.3 – 15
SPS	26 - 450	3.5	0.1 – 6
LHC	450 - 7000	3.7	0.1 - 2

Table 2: Beam sizes at the IP for a selection of accelerators

	σ_x [μm]	σ_y [μm]
Tevatron	30	30
LHC	16	16
PEP-II	200	7
SLC	1.5	0.65
ILC	0.6	0.006
CLIC	0.043	0.001

TYPES OF PROFILE MONITORS

Profile monitors can be divided in two families: those for circular machines and those for linear machines and transfer lines.

In the first family there are:

- Fast(er) wire scanners
- Laser wire scanners
- Synchrotron light monitors
- Rest gas ionization

And in the second:

- Slow(er) wire scanners
- Laser wire scanners
- Imaging (scintillators / OTR)
- Wire grids (harps)

The main differences between the two families are dictated by the different beam passage frequencies, in the

order of hundreds of Hertz maximum for the linacs and mega Hertz for circular machines.

WIRE SCANNERS

Wire scanners are among the most used instruments for the measurement of the transverse profiles. The principle is quite simple and consists in scanning a thin wire across the particle beam while measuring the intensity of the interaction between the wire and the beam. Two different detection systems are normally used. The first consists in detecting the flux of secondary high energy particles generated by the interaction of the beam with the nucleus of the wire; this system requires a particle detector downstream of the wire scanner, usually a scintillator-photomultiplier system. The other method is based on the detection of the electric current induced on the wire by the secondary emission of electrons. Both systems provide a signal proportional to the number of particles interacting with the wire, by plotting this signal as function of the wire position the profile is obtained.

Wire scanners can have a linear or a rotative movement, the first is more precise but is limited in speed (max. 1m/s), the second can achieve higher speeds (up to 20m/s)[1] but has a reduced resolution due to accelerations and deformations of the wire and mechanism.

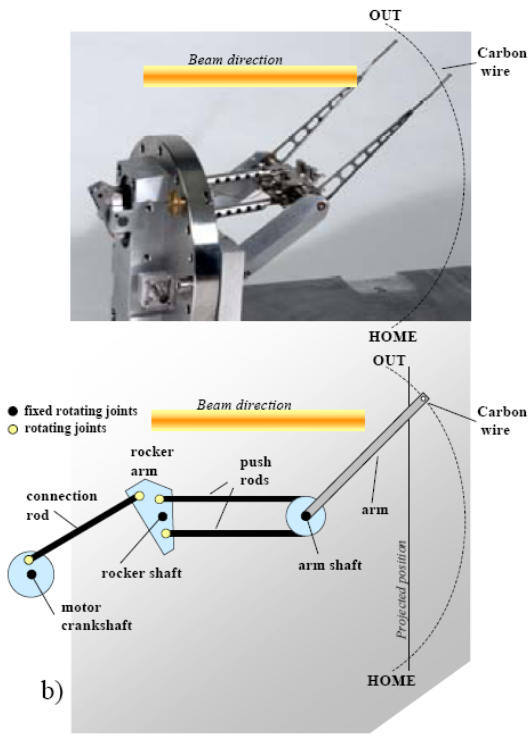

Figure 1: Picture (top) and schematics (bottom) of a rotative wire scanner used in the CERN low energy proton machines. The high current and fast acceleration ramp require fast scans. These devices can achieve 20m/s scanning speed.

Linear scanners are widely used in both linear and circular machines while rotative scanners are normally limited to circular machines.

The high speed may be necessary when a precise snapshot during the acceleration ramp is required or when the beam intensity is high and a slow scanner would get damaged.

In fact one of the most common problem with wire scanners is damage to the wire. Scanning high intensity or high density beams may lead to temperature increase on the wire above the limits and cause its rupture, Fig. 2 depicts a broken carbon filament at SLC. Typically wires are made of carbon fibres or tungsten, although quartz and beryllium wires are also used in special applications. The wire sizes range from a few microns to millimetres.

The resolution of this type of devices is mainly limited by the size of the wire, Eq. 1 shows the relation between the measured profile width, the real beam size and the wire radius. Although it is possible to deconvolute the three factors the final resolution can not be much better than the size of the wire.

$$\sigma_{meas} \cong \sqrt{\sigma^2_{beam} + r^2_{wire}} \qquad (1)$$

Among the best results, in terms of resolution, are those obtained at SLC (SLAC)[2][3] and ATF (KEK)[4] where resolutions of the order of few microns have been achieved. At SLC wire scanners were used extensively all over the machine (about 30 scanners) including the IP where the beam size was smaller than one micron.

Wire scanners are normally used as the reference instrument in the measurement of the transverse beam size and are installed in almost any machine.

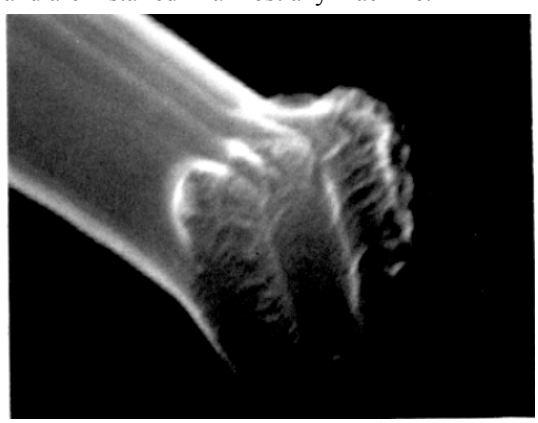

Figure 2: Broken 4μm carbon wire at SLC. It is possible to observe how successive pulses have eroded the wire.

SYNCHROTRON LIGHT

Another important technique for profile monitoring consists in imaging the synchrotron light emitted by the particles. Synchrotron light is radiated by charged particles when their trajectory is modified (curved), typically by a dipole magnet. In most cases the radiation emitted inside, or at the edge, of a lattice bending magnet is used, in this case the characteristics of the radiation are

imposed by the design of the accelerator lattice and may not be optimal for a profile monitor. Undulators or similar devices may be used to obtain a source with specific characteristics, better adapted for profile measurements; this is the case for example of the LHC synchrotron light profile monitors at CERN where dedicated super conducting undulators are used as synchrotron light sources at injection energy (450 GeV)[5].

The intensity of the synchrotron light as well as the spectrum depends heavily on the relativistic factor of the beam, the emission is therefore much more important for light particles like electrons and positrons.

$$\lambda_{cr} \propto \frac{R}{\gamma^3} \qquad P \propto \frac{\gamma^4}{R^2} \tag{2}$$

Eq. 2 show the dependency of the critical wavelength λ_{cr} (emission drops sharply for wavelengths shorter than λ_{cr}) and of the total radiated power P from the relativistic factor γ and the bending radius R. The use of synchrotron light devices for proton machines is limited to high energy accelerators like the Tevatron at FNAL or LHC and SPS at CERN.

In general synchrotron light monitors consist of an in-vacuum "extraction" mirror, a view port, an optical telescope, a set of filters and a camera. Although the principle of these devices is rather simple, they can easily become complicated when the performances are pushed near the limits. In this case refractive optics may be replaced by spherical or parabolic mirrors in order to reduce the aberrations and the overall alignment requires a complicated system[6].

Synchrotron light monitors are passively observing radiation emitted by the beam, for this reason they can be used to continuously monitor the beam profiles during the acceleration or during a store offering a great potential for beam monitoring.

The ultimate resolution of synchrotron light imaging is given by diffraction and is closely dependent on the wavelength of the observed radiation. For this reason shorter wavelength allows better resolutions. At present several devices exists for observing synchrotron light in the x-ray range. The best results so far probably belong to the device developed at KEK-ATF where 3.23keV synchrotron light photons, selected using a monochromator, are focused by mean of a Fresnel Zone Plates microscope on an x-ray camera [7]. The resolution obtained is of the order of 2 microns.

LASER WIRE SCANNERS

In the wire scanners section it has been mentioned how the main limiting factors of these devices are the wire dimension (resolution) and the maximum beam density the wire can stand before being damaged. In order to overcome these limitations it is possible to replace the physical wire with a focused laser beam. In this case the minimum wire size is of the order of the laser wavelength, hundreds of nanometres, and there is no limit on the beam density. The detection is then quite different compared with a traditional wire scanner. The nuclear interactions between the beam and the wire and the secondary emission of surface electrons by the wire are not available. The main observable in case of LWS are inverse Compton scattered photons. In inverse Compton scattering a low energy photon (from the laser) interacts with the high energy particle (from the beam) and creates a high energy photon, usually in the x-ray or γ-ray range. The cross section for this process is however exploitable only for electrons and positrons. Another possible observable for LWS is the photo dissociation of H^- ions; in this case the laser photons are used to neutralize the H^- atoms producing hydrogen atoms and free electrons. The detection can be made by measuring the decrease in the beam current or by detecting the free, low energy, electrons.

Fig. 3 illustrates the schematics of a typical inverse Compton Laser Wire Scanner (LWS) system. The main components are: a high power pulsed laser, a complex system of mirrors and optics to steer and focus the beam, an interaction chamber, a bending magnet to separate the particle beam from the x-ray and the γ detector. In the inverse Compton process a consistent fraction of the energy of the electron is transferred to the photon, this means that the interaction produces degraded electrons on top of the x/γ-ray and these can also be detected, however the high energy photons provide usually a better signal.

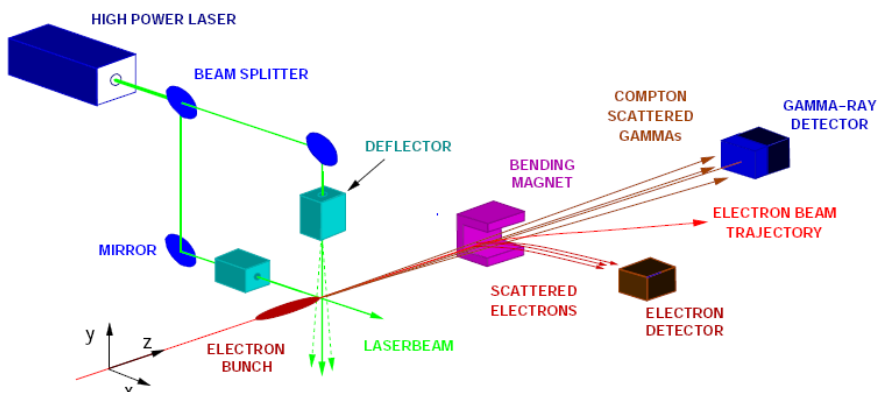

Figure 3: Schematics of a Laser Wire Scanner system

Laser wire scanners of this type have been used in many places: SLC[8], KEK-ATF[9], DESY-PETRA[10] etc. It is worth mentioning that at SLC profiles of about 1μm were measured at the IP. In this case the system was slightly different (see Fig. 4)[8], as the available space for the optics and the scanning mechanism was insufficient, the laser focusing was achieved using lenses and mirrors embedded in the interaction chamber and the electron and positron beams were scanned across the laser beam instead of the other way round.

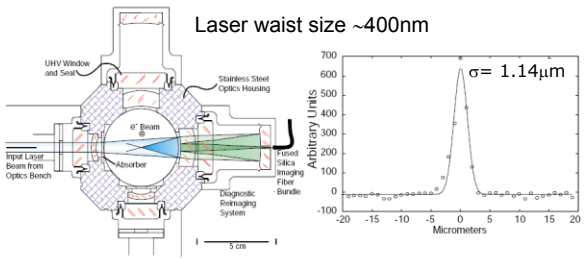

Figure 4: Schematics of the LWS installed on the SLC (left) and measured profile (right).

Another design of LWS was developed at KEK on the ATF damping ring [11]; instead of using a high power pulsed laser, a low power CW laser was used to feed a Fabry-Pérot optical cavity placed across the beam (Fig. 5). The cavity, composed of two high quality spherical mirrors, produces a focused laser beam at its centre with an enhancement of about a factor 1000 of the CW laser power. The waist size is 5.5μm and profiles down to about 7μm could be measured.

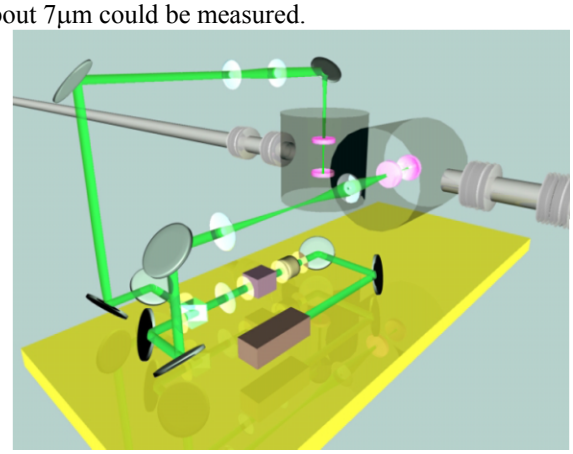

Figure 5: 3D schematics of the LWS system developed at KEK-ATF. The spherical mirrors of the optical cavities are depicted in pink. The green lines represent the laser beam.

A LWS for a H^- beam has been developed and successfully used at SNS [12]. In the superconducting part of the SNS linac traditional wire scanners could not be used due to the risk of contaminating the SC cavities with broken wire filaments. A single laser beam is distributed along the linac with a complicated optics and switches system. Special electron detectors are placed at appropriate locations downstream of the laser wire stations and provide the detection signal.

One important advantage of LWS, on top of those already mentioned, is that it does not perturb the beam in a sensible way. This means that this type of devices can be used for continuous monitoring, something that traditional wire scanners can not do.

One limitation of LWS is that they can not be easily used to measure small flat beams. The length over which the laser can be focused, called Raleigh length, is in fact inversely proportional to the focused beam size. As was shown in Table 2 the electron and positron beams for future linear collider have aspect ratios of up to a factor 100 which will be difficult to measure with LWS systems.

OPTICAL TRANSITION RADIATION

Optical transition radiation (OTR) is emitted when a charged particle crosses the surface between two materials with different dielectric constant. The emission is similar to the bremsstrahlung effect and is due to the sudden annihilation of the image charge induced in the material. If a particle travelling in vacuum crosses a thin foil it will emit twice, once upon entering the foil (backward emission) and once upon exiting the foil (forward emission). In the backward emission the light is emitted in a direction as if the particle was reflected by the foil and converted into photons, the forward emission on the other hand is emitted in the same direction of the particle.

By tilting the foil it is thus very simple to direct the OTR outside of the vacuum chamber and there re-image it on a CCD camera obtaining a picture of the beam that impinged on the foil. Fig. 5 shows the sketch of a typical OTR system.

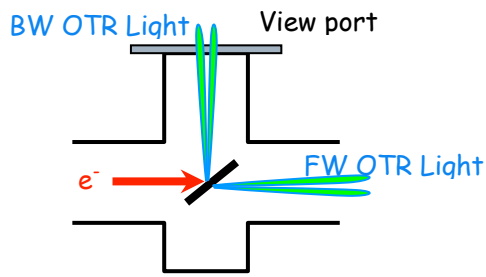

Figure 5: Schematics of the OTR emission mechanism.

In fact OTR based profile monitors are simply imaging systems like those used with scintillating screens. The main advantage of OTR over screens is the perfect linearity (no saturation or long decay times) and the high spatial resolution, basically only limited by diffraction. The spectrum of the BW OTR emission is very large and continuous, up to the plasma frequency of the foils material, covering the whole visible range. By using optical filters to select a narrow bandwidth in the blue or near UV the best resolutions can be achieved. The narrow bandwidth is necessary in order to reduce the effect of the unavoidable chromatic aberrations of the optical system.

OTR light is emitted with a peculiar angular distribution described by a sort of thick walled cone. The semi aperture of the cone is given by the relativistic factor

1/γ. This particular angular distribution means that special care has to be taken in the design of the optical system in order to assure that the vignetting effect does not perturb the measurement.

OTR devices are routinely used in both electron and proton machines anywhere the particles energy is sufficiently high (γ above 20 or so).

Another important aspect of OTR is that any foil, no matter how thin, will emit the same amount of light. This implies that very thin foils can be used inducing little perturbation on the beam itself. In the case of the LHC transfer lines for example 12μm Ti foils are used and several OTR stations can be acquired on the same beam pulse without any noticeable degradation of the beam parameters.

The use of thin foils also allows the observation of the evolution of the beam for several turns after injection in a circular machine. This type of observation is very important for the optimization of the matching of the optical functions of the transfer line and of the ring. Such measurements have been performed in the past in the SPS[13] at CERN and will be used in LHC.

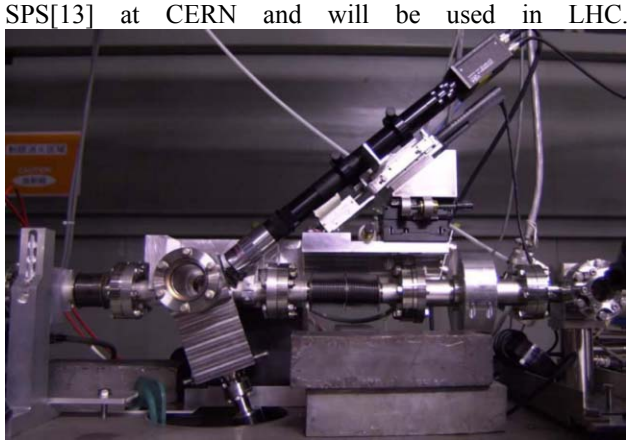

Figure 6: OTR station installed on the ATF extraction line at KEK. The electron beam arrives from the right and impinges on the radiator at an angle of ~10°. The OTR light is then analyzed by a far focus commercial microscope and a CCD camera; the black objects at an angle above the beam pipe.

The highest resolution so far using an OTR system has been achieved at KEK-ATF[14]. By using the system depicted in Fig. 6 beams of about 5μm were measured and the resolution was estimated to be around 2μm. The system is composed of a polished mirror (copper, beryllium and other materials have been tested) tilted 10° with respect to the normal to the beam. The OTR light, at ~20° to the beam, is focused using a commercial far focus microscope onto a CCD camera. During the experiments several radiators have been tested in order to understand the damage limits for the different materials. Fig. 7 Shows images of an electron beam taken on the ATF damping ring at KEK. The two sequences show how the radiator gets damaged in a few seconds when a focalized electron beam impinges upon. This constitutes one of the limitations of this type of detectors. Several materials have been investigated; the results indicate that it will be difficult to develop a monitor for beams with particle densities above few 10^{15} e^-/cm^2.

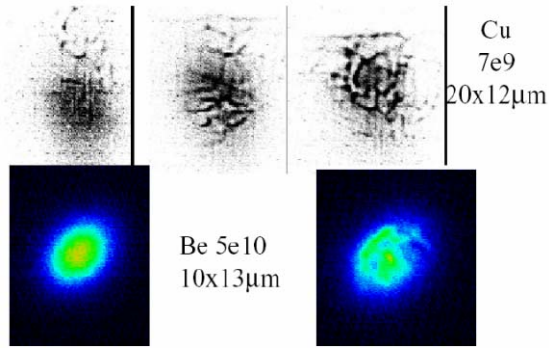

Figure 7: OTR images taken at KEK-ATF and illustrating the damage caused on the OTR radiator by the electron beam.

REFERENCES

[1] S. Burger et al., "The PS Booster Fast Wire Scanner", DIPAC'03, Mainz, DE, May 2003, p. 122
[2] R. fulton et al., SLAC-PUB-4605, April 1988
[3] M. Ross et al., SLAC-PUB-6014, Dec 1992
[4] H. Hayano "Wire Scanners for Small Emittance Beam Measurement in ATF", XX International Linac Conference, Aug 2000, Monterey, CA, USA
[5] O.Brunning et al., CERN-2004-003, June 2004, p367
[6] R.jung et al., "Adaptive optics for the LEP 2 synchrotron light monitors", DIPAC'99, May 1999, Chester, UK
[7] H. Sakai et al., "Measurement of the beam profiles with the improved Fresnel zone plate monitor", EPAC'06, June 2006, Edimburgh, UK
[8] Ross, M.C. et al., "A laser-based beam profile monitor for the SLC/SLD interaction region", BIW'96, May 1996, Argonne, IL, USA New York:AIP Press (1997) pg 281
[9] S.T. Boogert et al., "A laser-wire system at the ATF extraction line", EPAC'06, June 2006, Edimburgh, UK
[10] J. Carter et al., "Beam profile measurements and simulations of the PETRA laser-wire", PAC'05, May 2005, Knoxville, TN, USA
[11] Y. Honda et al., "Measurements of electron beam emittance in the Accelerator Test Facility damping ring operated in multibunch modes", Physical Review Special Topics - Accelerators and Beams, vol. 6, Issue 9
[12] R.Connoly et al., "Laser beam profile monitor development at BNL for SNS", LINAC 2002, Aug 2002, Gyneonju, Korea
[13] R.Jung et al., "The OTR screen betatron matching monitor of the CERN SPS", DIPAC'99, May 1999, Chester, UK
[14] M. Ross et al., SLAC-PUB-9280, July 2002

REVIEW OF SYNCHROTRON RADIATION BASED DIAGNOSTICS FOR TRANSVERSE PROFILE MEASUREMENTS

G. Kube, DESY, Hamburg, Germany

Abstract

The transverse particle beam emittance is a crucial accelerator parameter because it is directly related to the brilliance of a synchrotron light source or the luminosity of a particle beam collider. Therefore a precise online control of the beam profile is highly desirable from which the corresponding emittance can be calculated. Due to its non–destructive nature synchrotron radiation from a bending magnet is a versatile tool for beam profile measurements and is used in nearly every accelerator. There exist a number of different techniques in order to overcome limitations due to resolution broadening effects which can result in theoretical resolutions down to the sub–micron level. In the present article an overview over the methods presently applied in most accelerators will be given, and examples for non–standard profile measurements like e.g. proton synchrotron monitors will be presented.

INTRODUCTION

The production of low–emittance beams is one of the key techniques for electron accelerators and synchrotron light sources. A third–generation light source and future ones require emittances of a few $\mathrm{nm\,rad}$ and even less, and in high–energy physics the linear collider will have such an ultra–low emittance in order to realize the required luminosity. Not only production, also measurement and online control of a low emittance beam is a challenge because the beam profile to be resolved is in the order of a few tens of microns and even less. Therefore sophisticated schemes are necessary to measure the transverse beam emittance with sufficient accuracy, and there exist a number of different techniques in order to overcome limitations due to resolution broadening effects which can result in theoretical resolutions down to the sub–micron level.

Due to its non–destructive nature synchrotron radiation (SR) is a versatile tool for beam profile measurements and is used in nearly every accelerator. While in principle SR from insertion devices or bending magnets can be utilized, in reality most accelerators use bending magnet radiation based profile monitoring because of space limitations. Due to the relativistic energy of the particles the generated light has superior properties [1]:

The process of radiation generation is non–invasive and the radiation spectrum is continuous from infrared up to X-rays. As consequence the photon energy can be freely chosen according to the monitoring problem. Typically the spectrum is characterized by the critical energy $\hbar\omega_c = \frac{3}{2}\hbar c\frac{\gamma^3}{\rho}$ with γ the Lorentz factor and ρ the dipole bending radius. The natural divergence of the radiation is very small with a vertical opening angle of about $1/\gamma$. By choosing the radiation polarization the sensitivity of a profile monitor can be increased depending on the problem under investigation. The radiation properties can be calculated with high accuracy using e.g. numerical near field calculations [2] in order to study resolution broadening effects. Codes like SRW [3] or SPECTRA [4] are freely available allowing computations preserving all phase terms that are necessary for further propagation of the radiation through optical components. In SRW propagation is implemented in the frame of scalar diffraction theory applying the methods of Fourier optics. Finally the single particle radiation pulse is extremely short in the time domain and can even be modified by choosing the appropriate magnet structure which is of particular importance for proton SR diagnostics. All properties mentioned before are of importance for beam diagnostics and are reflected in the different monitor concepts.

PRINCIPLES

SR based transverse emittance diagnostics relies on the measurement of a photon spot size. While the emittance itself is no directly accessible value, beam size or beam divergence can be measured with a monitor system, thus leading to two different monitor concepts. With knowledge of the machine optical parameters, relative energy spread, monitor resolution and radiation properties the emittance can be extracted from the measured light spot. In the case of beam size measurements the simplest case is the direct imaging approach which is widely used for emittance diagnostics. The fundamental limit for such a measurement is given by Heisenberg's uncertainty relation which can be reformulated as $\Delta\sigma = \frac{\lambda}{2\,\Delta\Psi}$ in the specific case. Here $\Delta\sigma$ is the resolution broadening due to diffraction and $\Delta\Psi$ is the opening angle of the emitted photon. While the horizontal emission angle is large due to the particle motion on a curved trajectory in this plane in a bending magnet, the vertical one is small and thus imposing the fundamental resolution limit. For a typical optical wavelength of observation λ = 500 nm and an opening angle $\Delta\Psi$ = 1 mrad, the resolution would amount $\Delta\sigma$ = 250 μm. Considering that the vertical beam size in a modern light source is in the order of a few tens of microns and even less, such a monitor would have a totally diffraction limited resolution. In order to overcome this limit there exist two different concepts. The most straightforward one is imaging at smaller wavelength in the VUV, soft or even hard X–ray region. In this case the discussion about a monitor concept is reduced to the question about the appropriate imaging optics. The second concept is an interferometric approach [5] which is

adapted from the stellar interferometer of Michelson used for the determination of the extent of stars [6]. It is based on the investigation of the spatial coherence properties of the radiation by measuring the blurring of the interferogram which depends on the particle beam size in a double–slit interferometric setup. The fundamental limit of this monitor principle is again Heisenberg's uncertainty relation which can be reformulated for an interferometric measurement as $\Delta n \Delta\Phi \sim 1$, with $\Delta\Phi$ the relative phase difference between the wave trains passing the two individual slits and Δn the number of required photons [7]. As consequence in order to measure the phase difference with high accuracy the intensity must be sufficient.

According to Ref. [8] the concepts for emittance monitoring can be classified in three categories, namely imaging, interference, and projection method. The principle for all methods is the same: the information about the beam spot is encoded onto a spatial resolving detector (CCD camera). The difference is in the way how the emitted wavefront is affected in between, and as consequence the signal from which the emittance will be deduced is either a beam spot, an interferogram, or an angular distribution.

In the following examples for these monitor concepts will be given with the emphasis on small beam size measurements, while a few examples for non–standard profile measurements will be shown at the end.

IMAGING METHODS

The most direct way for emittance diagnostics is the use of VUV or X–ray imaging techniques to obtain high quality radiation focusing, such that the spot size produced by a single particle is much smaller than the size of the beam as a whole (assuming 1:1 imaging). In this range of photon energies focusing optics can be realized either by reflection, diffraction, or refraction. All these principles are used in different emittance monitors and will be shortly described in the following. A comprehensive overview over X–ray focusing techniques can be found for example in Ref. [9].

Reflective Optics: External total reflection can occur when X–ray radiation hits a surface under gracing incidence. The critical angle of external total reflection θ_c can be calculated using Snell's law as $\theta_c = \sqrt{2\,\delta}$ with $\delta \approx 10^{-6}$ the refractive index decrement of the complex index of refraction. Due to the small angle of reflection in the order of $\theta \leq 0.5^\circ$ a simple spherical mirror would suffer from astigmatisms. Thus the most common reflective optics is the Kirkpatrick–Baez setup [10] which consists of a pair of two consecutive cylindrical or elliptical mirrors. An example for a monitor system with such optics is the diagnostic beamline BL 3.1 of the ALS, Berkeley [11]. In this setup the beam spot is imaged onto a scintillator converting the broad X-ray spectrum into a visible image that is viewed by a microscope connected to a video camera. A carbon filter is used to remove synchrotron light with wavelengths longer than 10 nm for to reduce diffraction effects.

Diffractive Optics: The Fresnel zone plate (FZP) has become the most important diffractive optics in X–ray physics, and in the soft X–ray range of the electromagnetic spectrum it is still the best device for microanalysis. The zone plate consists of concentric rings, alternatingly transparent and opaque. The spacing of the rings is chosen such that the penetrating light waves interfere constructively at the focal point, i.e. the parts of the wave front which contribute with opposite sign in phase are absorbed. The width of the outermost zone Δr defines the zone plate resolution $\delta \approx 1.22 \times \Delta r$ and their focal length $f = \frac{4N(\Delta r)^2}{\lambda}$, N is the number of zones and λ the observation wavelength [12]. The latter condition shows that zone plate imaging requires a monochromator because of strong chromatic aberrations.

An example for a beam size monitor using a single zone plate is the X–ray beam imager at SPring–8 [13, 14]. It requires a diagnostic beamline of about 41 m. SR of 8.2 keV from a bending magnet is selected via the (111) reflection of a silicon double crystal monochromator and imaged by the zone plate onto a commercial X–ray zooming tube. The total magnification of the system is 13.7, the spatial resolution 4.1 μm.

The FZP monitor at ATF (KEK) is based on X–ray imaging optics with two FZPs and has the structure of a long–distance microscope [15, 16]. The radiation monochromatization at an energy 3.235 keV is achieved via the (220) reflection of a silicon single crystal monochromator. The 20 times magnified beam image is recorded via a direct incidence, back–thinned illuminated X–ray CCD, thus avoiding resolution broadening in the conversion from X–rays to visible light via a scintillator. The total spatial resolution of this monitor is estimated to 0.7 μm (rms). Using a fast mechanical shutter with opening shutter times ≤ 1 msec it was possible to resolve a vertical beam size of 6.4 μm by removing the effect of an unknown 100 Hz beam oscillation which blurred the vertical size.

A diffractive optics similar to the FZP is the Bragg–Fresnel lens used at ESRF [17] resp. the Bragg–Fresnel multilayer still in use at BESSY-II [18].

Refractive Optics: Refractive X–ray lenses have been considered for a long time as not feasible due to the weak refraction and the relatively strong absorption of X–rays in matter. While the first lenses were fabricated by drilling well aligned holes in aluminium, in the meantime it is possible to produce lenses with rotationally parabolic profile even from beryllium [19]. For a focusing surface this is the optimal shape because it modifies the quadratic terms of the radiation phase essential for focusing without introducing extra aberrations [8]. In order to keep the focal length f at reasonable values N individual lenses are stacked behind each other, resulting in $f = \frac{R}{2N\delta}$ (in thin lens approximation) with the refractive index decrement $\delta \approx 10^{-6}$ and the surface radius of curvature $R \approx 200$ μm [20, 21]. Because of the large number of lenses ($N = 10 \ldots 300$) these devices are called compound refractive lenses (CRLs). Due to the strong dependence of the refractive index decrement

on the photon energy a CRL based profile monitor requires also the use of a monochromator.

So far only one experiment for electron beam imaging using a single refractive lens is published from ESRF [22]. For the new high–brilliance synchrotron light source PETRA III at DESY it is planned to built up a CRL based emittance monitor with 31 beryllium lenses at a photon energy of 20 keV with an estimated monitor resolution of about 1 μm.

Focus–Free (Pinhole) Imaging: While the imaging principles described so far are based on focusing optics, the pinhole optics - without any focusing of the rays at all - is by far the least complicated device. The principle was already known to Aristoteles (384-322 b.C.) and described in his opus "Problemata". The X–ray pinhole camera has the advantage of a simple setup, it is used typically without monochromator and sometimes even outside the vacuum system, is insensitive to heat load, and has a high practical reliability. The drawback of a pinhole based emittance monitor is the limited resolution of ≥ 10 μm.

Pinhole setups are the most common emittance monitors because of the well proven techniques and are used in a widespread number of accelerators as for example at ESRF [23], APS (Argonne) [24], SLS (PSI) [25], and even at the new third generation light sources just put to operation like DIAMOND [26] and SOLEIL [27] and planned ones like ALBA [28] and PETRA III.

The extension of the conventional pinhole monitor with only one aperture is the pinhole array which allows the simultaneous measurement of beam size and vertical beam divergence. Pinhole array monitors are used in the meantime at BESSY II [18], at ALS [29], and at the Australian Light Source [30].

Exploitation of Wave–Optics Features: According to Ref. [8] the use of small radiation wavelengths is not the only approach to improve the resolution for beam size measurements. Another possibility is the exploitation of the wave–optics features of SR, as for example imaging with visible light using the vertical (π) polarization component. The underlying principle is to make use of the on–axis minimum of the π polarized vertical intensity distribution which will be blurred with increasing vertical beam size. From the measured peak-to-valley ratio of the imaged beam spot it is therefore possible to extract the vertical size. This mechanism was applied for the first time at MAX-II [31] and is now used at SLS (PSI), showing good agreement with independent pinhole measurements [25].

INTERFERENCE METHODS

The principle of the interferometric method is based on the investigation of the spatial coherence of SR. In order to quantify the coherence properties usually the first order degree of mutual spatial coherence $\gamma(D)$ is used (c.f. for example Ref. [32]) with D the distance between two wave-front dividing slits, see Fig. 1. The interferometer itself is a wave-front–division-type two-beam interferometer which uses polarized quasimonochromatic radiation. The intensity of the interference pattern measured in the detector plane directly depends on γ [5]:

$$I(y_0) = I_0 \left[\mathrm{sinc}(\frac{2\pi a}{\lambda_0 R})\right]^2 \left[1 + |\gamma| \cos(\frac{2\pi D}{\lambda_0 R} + \varphi)\right] \quad (1)$$

with a the half of the single slit height and D, R as indicated in Fig. 1, λ_0 the wavelength of observation and I_0 the sum of the incoherent intensities from both slits. Under condition of Fraunhofer diffraction (i.e. in far–field limit) the van Cittert–Zernicke theorem [32] relates the degree of coherence γ with the normalized source distribution $f(y)$:

$$\gamma(\nu) = \int \mathrm{d}y f(y) \exp(-i2\pi\nu y) \ , \quad (2)$$

where $\nu = \frac{D}{\lambda_0 R_0}$ denotes the spatial frequency.

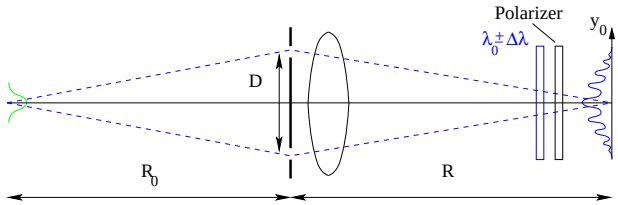

Figure 1: Principle setup for interferometric beam size measurements.

There are two operational modes for the interferometer: in the scanning mode the intensity pattern is recorded for varying slit distance D. From a fit to each individual interferogram Eq.(1) the functional dependency of $\gamma(D)$ can be determined and the beam shape $f(y)$ can be reconstructed by evaluating the Fourier back transform from Eq.(2). If the beam shape $f(y)$ is known to be normal distributed with width σ_y a single measurement for fixed slit distance D_0 is sufficient in order to determine σ_y from the relation

$$\sigma_y = \frac{\lambda_0 R_0}{\pi D_0} \sqrt{\frac{1}{2} \ln \frac{1}{\gamma(D_0)}} \ , \quad (3)$$

while $\gamma(D_0)$ has to be fitted again from the recorded interferogram. The latter mode of operation for fixed slit distance was applied in most interferometric applications. A comprehensive overview concerning the development of the SR interferometer can be found in Ref. [33]

SR interferometers are in use at a widespread number of accelerators as for example the KEK-ATF damping ring [34], ELETTRA [35], and PEP-II [36]. At SPring-8 even a two–dimensional interferometer was realized [37].

As mentioned before the interferometer relies on a precise phase measurement with the prerequisite of sufficient intensity. In order to fulfill this condition at KEK-ATF a 400 nm bandpass filter with large bandwidth of 80 nm was used. It could be demonstrated that for this setup the dominant error results from the dispersion in the refractive optics (lenses), leading to a blurring of the interferogram and

therefore reduced accuracy. As consequence the interferometer was recently improved by using reflective Herschelian optics [38]. With this setup a vertical beam size of 4.73 μm could be resolved while the beam size measured under same conditions with refractive optics amounted 7.2 μm.

PROJECTION METHODS

Projection methods in context with SR from bending magnets for emittance diagnostics are not very common and used mainly at ESRF [39] and ANKA [40]. Due to the horizontal fan from bending magnet radiation only the vertical emittance can be determined.

The principle of this method relies on the fact that only a tiny fraction of very hard X–rays can fully penetrate the dipole crotch absorber and enter in the free air space behind. These X-rays with energies $\geq$ 70 keV at ANKA resp. $\geq$ 150 keV at ESRF are detected by a simple, compact and low–cost device consisting of a $CdWO_4$ scintillator and a standard CCD camera system.

With knowledge of the measured photon spot size $\sigma_{\gamma,y}$, the mean square photon emission angle $\langle\vartheta_\gamma^2\rangle$, the distance between source and image plane L, and the accelerator Twiss parameters at the emission point the emittance can be derived in a similar way to the formalism developed in Ref. [23] as

$$\varepsilon_y = \frac{\sigma_{\gamma,y}^2 - \langle\vartheta_\gamma^2\rangle L^2}{\beta_y + 2\alpha_y L + \gamma_y L^2} \ . \qquad (4)$$

At the ep–collider HERA at DESY the projection method was used mainly for control of the electron beam position and slope at the interaction points of the colliding beam experiments ZEUS and H1. Nevertheless from the measured beam spot also an estimate for the vertical emittance could be derived which was in fair agreement with different online emittance measurements.

NON–STANDARD MEASUREMENTS

In case of proton accelerators the critical wavelength characterizing the SR emission spectrum from a bending magnet is shifted towards the infrared or even millimeter region because of the large proton rest mass. Optical elements are not easily available in these spectral regions and the image resolution would be deteriorated due to an increased contribution from diffraction broadening. In order to overcome these limitations the SR emission spectrum can be extended to higher frequencies if radiation produced in dipole fringe fields or in short magnets is used which contains sufficient intensity to render possible beam profile measurements. In order to understand the increase of intensity at higher frequencies it is helpful to recall the SR field properties in time domain (see for example Ref. [1]) because both quantities are simply related by the square of the absolute value of the Fourier transform.

The typical SR frequency is determined by the length of the radiation pulse seen by an observer. While the duration of the SR electric field produced in the central part of a bending magnet from a 6 GeV electron is in the order of 10^{-2} asec, for a 920 GeV proton it is in the order of fsec (see Fig. 2 left). In order to increase the intensity at higher frequencies a sharp cut–off of the wave train in time domain is necessary as it can be realized by a magnetic fringe field (Fig. 2 center) or a short magnet (Fig. 2 right).

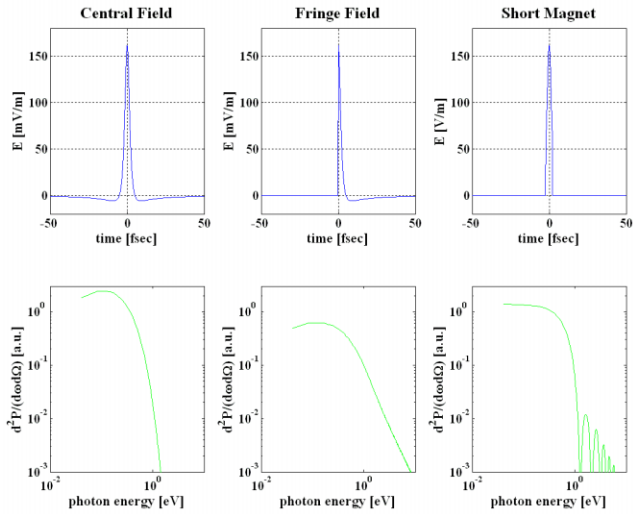

Figure 2: Time dependence of SR electrical field (top) and spectral power (bottom) for central field region (left), fringe field (center), and short magnet (right).

While the SR intensity strongly depends on the proton energy the application of proton beam diagnostics is restricted to only a few accelerators. The first profile monitor based on this principle was realized at the SPS (CERN) [41]. The fringe field between two successive dipole magnets was used for radiation generation. While this monitor worked only at energies above about 350 GeV it was replaced later by an undulator which extended the usable energy range [42]. A similar beam profile monitor has been installed at Tevatron (FNAL) where synchrotron light produced from protons (antiprotons) at the upstream edge of a superconducting magnet is observed [43]. At HERA (DESY) the fringe field of a normal conducting vertical deflecting bending magnet was used to measure the beam size and to perform dynamical studies [44]. For the LHC it is also planned to use this type of monitor for transverse beam diagnostics. In order to optimize the performance over the whole energy range from 450 GeV up to 7 TeV, a superconducting undulator together with a separation dipole will act as radiation source [45].

SR based diagnostics is even not restricted to circular accelerators: at the ESRF the injector complex including two transfer lines utilizes SR profile monitors [46], and in the first bunch compressor of the VUV–FEL FLASH at DESY profile measurements are used to gain information about the energy distribution in a bunch due to the strong dispersion [47].

SUMMARY

This article comprises various techniques presently used mainly at synchrotron light sources for small emittance and profile measurements. Moreover the principles of SR based diagnostics for proton accelerators are summarized and it was shown that the application of SR monitoring is not restricted to circular accelerators.

In addition to emittance diagnostics manifold problems in accelerator physics can be studied with a SR profile monitor. From the huge number of applications only a few will be mentioned as examples: injection mismatch studies [48], turn-by-turn imaging [49], beam halo studies [50], and beam-beam induced beta beating measurements [51].

REFERENCES

[1] A. Hofmann, *The Physics of Synchrotron Radiation*, Cambridge University Press, Cambridge 2004.

[2] O. Chubar, Rev. Sci. Instrum. **66** (1995), 1872.

[3] O. Chubar and P. Elleaume, Proceedings of the EPAC'98, Stockholm, Sweden (1998), 1177.

[4] T. Tanaka and H. Kitamura, J. Synchrotron Rad. **8** (2001), 1221.

[5] T. Mitsuhashi, Proc. of the Joint US–CERN–Japan–Russia School on Particle Accelerators, Montreux, 11-20 May 1998, (World Scientific), pp. 399-427.

[6] A.A. Michelson, Astrophys. J. **51** (1920), 257.

[7] S.G. Lipson, H.S. Lipson, D.S. Tannhauser, *Optical Physics*, Cambridge University Press, Cambridge 1995.

[8] O. Chubar, Proceedings of the EPAC'00, Vienna, Austria (2000), 117.

[9] I. Snigireva and A. Snigirev, J. Environ. Monit. **8** (2006), 33.

[10] P. Kirkpatrick and A.V. Baez, J. Opt. Soc. Am. **38** (1948), 766.

[11] T.R. Renner, H.A. Padmore, and R. Keller, Rev. Sci. Instrum. **67** (1996), 3368.

[12] D.T. Attwood, *Soft X–rays ans extreme ultraviolett radiation principles and applications*, Cambridge University Press, Cambridge 2000.

[13] S. Takano, M. Masaki, and H. Ohkuma, Proc. DIPAC'05, Lyon, France (2005), 241.

[14] S. Takano, M. Masaki, and H. Ohkuma, Nucl. Instrum. Meth. **A 556**, (2006), 357.

[15] H. Sakai et al., Proc. EPAC'06, Edinburgh, Scotland (2006), 2784.

[16] H. Sakai et al., Phys. Rev. ST Accel. Beams **10** (2007), 042801.

[17] Ya. Hartmann et al., Rev. Sci. Instrum. **66** (1995), 1978.

[18] K. Holldack, J. Feikes, and W.B. Peatman, Nucl. Instrum. Meth. **A 467-468**, (2001), 235.

[19] C.G. Schroer et al., *Design and Microfabrication of Novel X–Ray Optics*, ed. D.C. Mancini (Bellingham, WA:SPIE), Proc. SPIE **4783** (2002), 10.

[20] B. Lengeler et al., J. Synchrotron Rad. **6** (1999), 1153.

[21] B. Lengeler et al., J. Phys. D: Applied Phys. **38** (2005), A218.

[22] T. Weitkamp et al., Proceedings of the EPAC'00, Vienna, Austria (2000), 1824.

[23] P. Elleaume et al., J. Synchrotron Rad. **2** (1995), 209.

[24] M. Borland et al., Proceedings of the EPAC'98, Stockholm, Sweden (1998), 1556.

[25] Å. Andersson et al., Proceedings of the EPAC'06, Edinburgh, Scotland (2006), 1223.

[26] C.A. Thomas and G. Rehm, Proc. DIPAC'05, Lyon, France (2005), 93.

[27] J.C. Denard et al., Proc. DIPAC'03, Mainz, Germany (2003), 6.

[28] U. Iriso and F. Pérez, Proceedings of the EPAC'06, Edinburgh, Scotland (2006), 3410.

[29] F. Sannibale et al., Proceedings of the EPAC'04, Lucerne, Switzerland (2004), 2783.

[30] M.J. Boland et al., Proceedings of the EPAC'06, Edinburgh, Scotland (2006), 3263.

[31] Å. Andersson, *Electron beam profile measurements and emittance manipulation at the MAX-laboratory*, Ph.D. thesis, Lund 1997.

[32] M. Born and E. Wolf, *Principles of Optics*, Pergamon Press Ltd., New York, 1980.

[33] T. Mitsuhashi, Proc. of BIW'04, Knoxville, Tennessee, AIP Conf. Proceedings **732** (2004), 3.

[34] H. Hayano et al., Proc. of the PAC'99, New York (1999), 2143.

[35] F. Iazzourene et al., Proceedings of the EPAC'00, Vienna, Austria (2000), 1732.

[36] A.S. Fisher et al., Proc. of the PAC'01, Chicago (2001), 547.

[37] M. Masaki and S. Takano, J. Synchrotron Rad. **10** (2003), 295.

[38] T Naito and T. Mitsuhashi, Phys. Rev. ST Accel. Beams **9** (2006), 122802.

[39] K. Scheidt, Proc. of BIW'06, Batavia, Illinois, AIP Conf. Proceedings **868** (2006), 208.

[40] A.S. Muller et al., Proceedings of the EPAC'06, Edinburgh, Scotland (2006), 1073.

[41] R. Bossart et al., Nucl. Instrum. Meth. **164** (1979), 375.

[42] J. Bosser et al., CERN-SPS/83-5 (1983).

[43] R. Thurman-Keup, Proc. of BIW'06, Batavia, Illinois, AIP Conf. Proceedings **868** (2006), 364.

[44] G. Kube et al., Proc. of BIW'06, Batavia, Illinois, AIP Conf. Proceedings **868** (2006), 374.

[45] L. Ponce, R. Jung, F. Méot, CERN-2004-07 (2004).

[46] K. Scheidt, Proc. DIPAC'05, Lyon, France (2005), 24.

[47] Ch. Gerth, these proceedings.

[48] M.G. Minty and W.L. Spencer, Proc. of the PAC'95, Dallas (1995), 536.

[49] O.I. Meshkov et al., Proc. DIPAC'05, Lyon, France (2005), 42.

[50] T. Mitsuhashi, Proc. DIPAC'05, Lyon, France (2005), 7.

[51] G. Kube and F. Willeke, Proceedings of the EPAC'06, Edinburgh, Scotland (2006), 1046.

PHYSICS AND DIAGNOSTIC OF LASER-PLASMA ACCELERATOR

Victor Malka, Laboratoire d'Optique Appliquée,ENSTA-Ecole Polytechnique, CNRS,
91761 Palaiseau, France

Abstract

The recent and continuing development of powerful laser systems, which can now deliver light pulses containing a few Joules of energy in pulse durations of a few tens of femto seconds, has permitted the emergence of new approaches for generating energetic particle beams. By focusing these laser pulses onto matter, extremely large electric fields can be generated, reaching the TV/m level. Such fields are 10,000 times greater than those produced in the radio-frequency cavities of conventional accelerators. As a result, the distance over which particles extracted from the target can be accelerated GeV energy range is reduced to distances on the order of millimetres. A few years ago, several experiments have shown that laser-plasma accelerators can produce electron beam with maxwellian-like distribution [1], in 2004 high-quality electron beams, with quasi-mono energetic energy distributions at the 100 MeV level [2] and recently in the GeV range using a capillary discharge [3]. These experiments were performed by focusing a single ultra short and ultra intense laser pulse into an under dense plasma. More recently we produced a high quality electron beam using two counter-propagating

Paper not received
(See slides of talk on following pages)

Physics and diagnostics of Laser-Plasma Accelerators

Victor Malka

Laboratoire d'Optique Appliquée,ENSTA-Ecole Polytechnique, CNRS, 91761 Palaiseau, France

DIPAC, Venizia, May 21-23 (2007)

LOA

Collaborators

J. Faure, C. Rechatin, A. Lifschitz, Y. Glinec, A. Norlin,

Laboratoire d'Optique Appliquée,ENSTA-Ecole Polytechnique, CNRS,
91761 Palaiseau, France

E. Lefebvre

Département de Physique Théorique et Appliquée, CEA, DAM Ile-de-France, BP 12, 91680 Bruyères-le-Châtel, France

A. Pukhov

Institut fur Theoretische Physik,1, Heinrich-Heine-Universitat Duesseldorf, 40225 Duesseldorf, Germany

Partially supported by CARE/PHIN FP6 project

LOA

Summary

Part 1 : Laser plasma accelerator : motivation

Part 2 : bubble regime and monoenergetic e-beam

Part 3: Experiment with colliding laser pulses

Part 6 : Conclusion and perspectives

LOA

Classical accelerator limitations

E-field $_{max}$ ≈ few 10 MeV /meter (Breakdown)
R>R_{min} Synchrotron radiation

Courtesy of W. Mori & L. da Silva

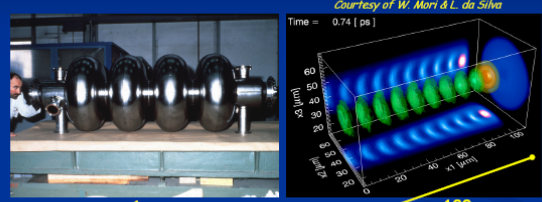

1 m
RF cavity

100 μm
Plasma cavity

LOA

How to excite Relativistic Plasma waves?

The laser wake field

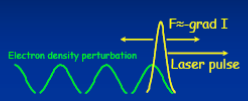

$\tau_{laser} \approx T_p / 2$
=>Short laser pulse

Phase velocity $v_{\phi pw} = v_{gpw}$ => close to c
Analogy with a boat

Are Relativistic Plasma waves efficient ?

$E_z \sim \sqrt{n_e}$

E_z = 0.3 GV/m for 1 % Density Perturbation at 10^{17} cc^{-1}
E_z = 300 GV/m for 100 % Density Perturbation at 10^{19} cc^{-1}

Tajima and Dawson, PRL (1979)

LOA

Summary

Part 1 : Laser plasma accelerator : motivation

Part 2 : bubble regime and monoenergetic e-beam

Part 3: Experiment with colliding laser pulses

Part 4 : Conclusion and perspectives

LOA

Laser plasma injector

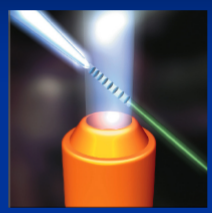

Scheme of principle

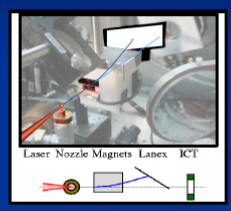

Experimental set up

LOA

Recent results on e-beam : From maxwellian to mono spectra Electron density scan

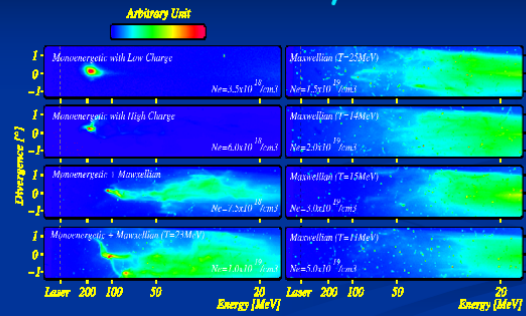

V. Malka, et al., PoP 2005

LOA

Energy distribution improvements: The Bubble regime

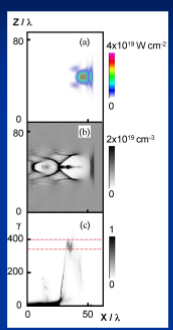

Charge in the peak : 200-300 pC

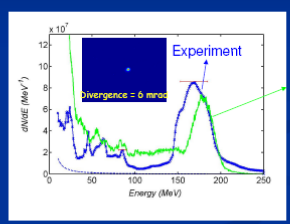

At LOA
J. Faure et al. Nature (2004)

LOA

Direct observation of betatron oscillation

Experimental data :

(i) Accelerating field constant
(ii) Off axis injection (r_0) with $\gamma_0 mc^2$ initial energy
Motion equation :

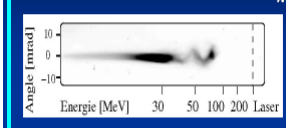

$$\gamma\beta = \frac{eE_z}{mc\omega_0}\,t + \gamma_0\beta_0 \qquad E_m = mc\omega_0/e \qquad \theta_0 = \frac{cp_{x0}}{eE_z}$$

$$\theta_m(t) = -\frac{\theta_0\,(\gamma_0\beta_0)^{1/4}}{\pi\,(\gamma\beta)^{3/4}}\sin\left[\frac{E_z}{E_m}\left(\sqrt{2\gamma\beta} - \sqrt{2\gamma_0\beta_0}\right)\right]$$

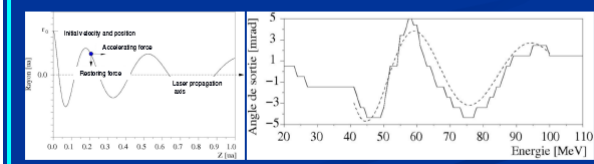

⇒ E_z=150 GV/m, r_0=0.35 µm pour γ_0=10
In agreement with Tsung simulations. Tsung et al. POP (2005)

LOA

Off axis injection due to laser intensity asymetry

Laser asymmetry → Cavity asymmetry → Off axe injection

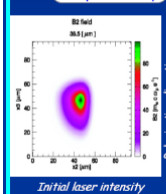

Initial laser intensity profile

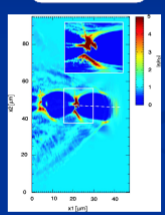

Density profile after 190 um of propagation

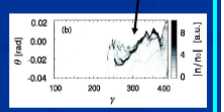

Electron angle versus energy

Parameters : 5 J, 20 fs, Ne=7.7x10¹⁸ cm⁻³, a_0=0.5
1874x248x248 cells = 48x95x95 mm³

In collaboration with GoLP, Lisbon

LOA

En collaboration avec VLPL, Dusseldorf

OTR diagnostics

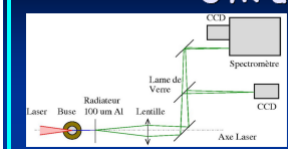

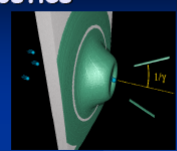

Signal intensity : up to 10⁶ the incoherent level

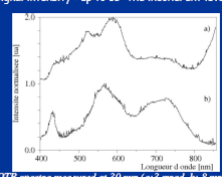

OTR spectra measured at 30 mm (a:3 mrad, b: 8 mrad).

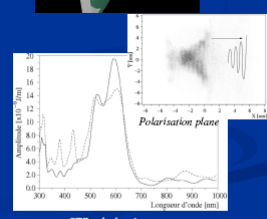

OTR calculated spectra

Glinec et al, this week in PRL

LOA

En collaboration avec VLPL, Dusseldorf

OTR: multibunching

- Two bunches separated by 74 fs >60fs due to lengthening of λ_p.

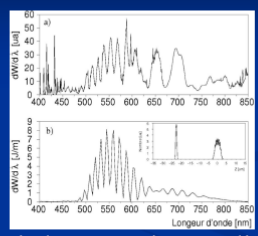

a) Radiator at 1.5 mm : a) experiments. b) Calculated (from the e-distribution in insert)

Glinec *et al*, this week in PRL

LOA

Quasi-monoenergetic beams reported in the litterature

Name	Article	Lab	Energy [MeV]	dE/E [%]	Charge [pC]	Ne [x10^{19}/cm^3]	Intensity [x10^{18} W/cm^2]	τ_c/T_p	Remark
Mangles	Nature (2004)	RAL	73	6	22	20	2,5	1,6	
Geddes	Nature (2004)	L'OASIS	86	2	320	19	11	2,2	Channel
Faure	Nature (2004)	LOA	170	25	500	6	3	0,7	
Hidding	PRL (2006)	JETI	47	9	0,32	40	50	4,6	
Hsieh	PRL (2006)	IAMS	55		336	40		2,6	
Hasokai	PRE (2006)	U. Tokyo	11,5	10	10	80	22	3,0	Preplasma
Miura	APL (2005)	AIST	7	20	432E-6	130	5	5,1	
Hafz	PRE (2006)	KERI	4,3	93	200	28	1	33,4	
Mori	ArXiv (2006)	JAERI	20	24	0,8	50	0.9	4,5	
Mangles	PRL (2006)	Lund LC	150	20		20	5	1,4	

Several groups have obtained quasi monoenergetic e beam but at higher density ($\tau_c > \tau_p$)

LOA

GeV electron beams from a « centimetre-scale » accelerator

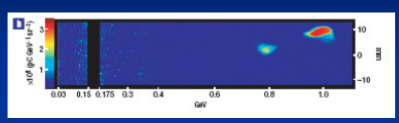

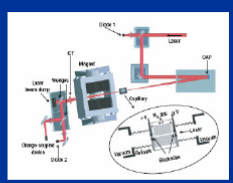

310-µm-diameter channel capillary

P = 40 TW

density 4.3×10^{18} cm^{-3}.

Leemans et al., Nature Physics, september 2006

LOA

Summary

Part 1 : Laser plasma accelerator : motivation

Part 2 : bubble regime and monoenergetic e-beam

Part 3: Experiment with colliding laser pulses

Part 4 : Conclusion and perspectives

LOA

Controlling the injection

Counter-propagating geometry:

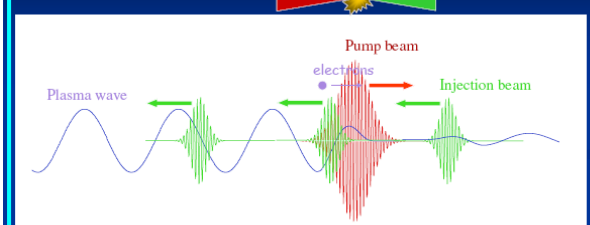

Ponderomotive force of beatwave: $F_p \sim 2a_0a_1/\lambda_0$ (a_0 et a_1 can be "weak")

Boost electrons locally and injects them:

INJECTION IS LOCAL IN FIRST BUCKET

E. Esarey et al, PRL 79, 2682 (1997), G. Fubiani et al. (PRE 2004)

LOA

Experimental set-up

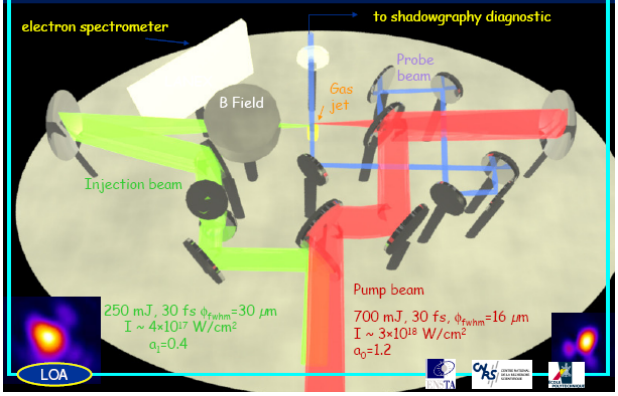

LOA

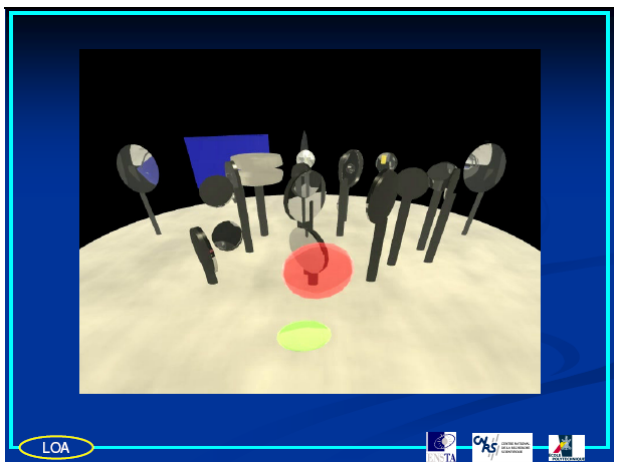
LOA

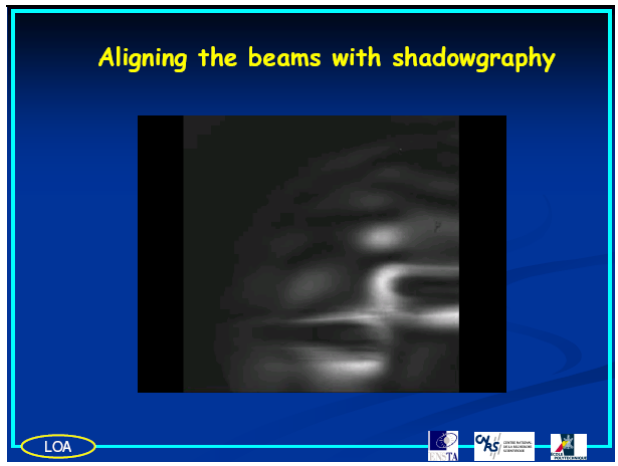
Aligning the beams with shadowgraphy
LOA

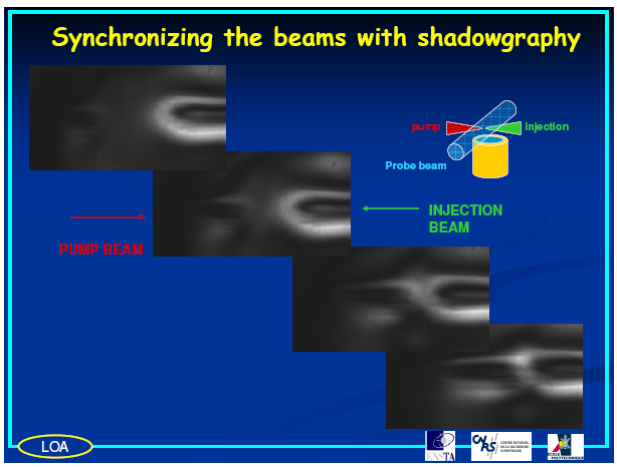
Synchronizing the beams with shadowgraphy
pump
injection
Probe beam
INJECTION BEAM
PUMP BEAM
LOA

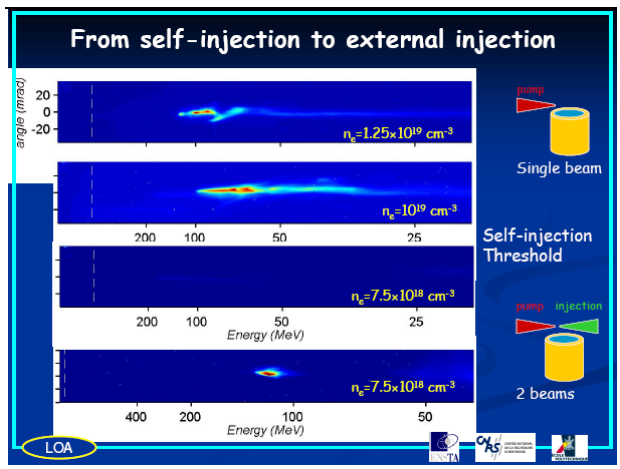
From self-injection to external injection
angle (mrad)
20
0
-20
n_e=1.25x10^{19} cm^{-3}
n_e=10^{19} cm^{-3}
200
100
50
25
n_e=7.5x10^{18} cm^{-3}
Energy (MeV)
n_e=7.5x10^{18} cm^{-3}
400
200
100
50
Energy (MeV)
pump
Single beam
Self-injection Threshold
pump
injection
2 beams
LOA

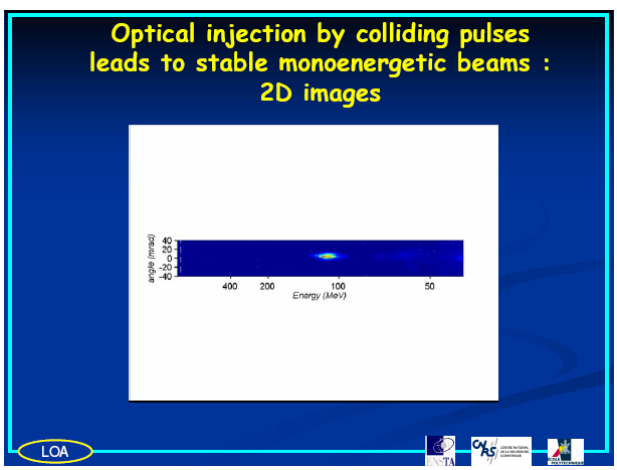
Optical injection by colliding pulses leads to stable monoenergetic beams : 2D images
angle (mrad)
40
20
0
-20
-40
400
200
100
50
Energy (MeV)
LOA

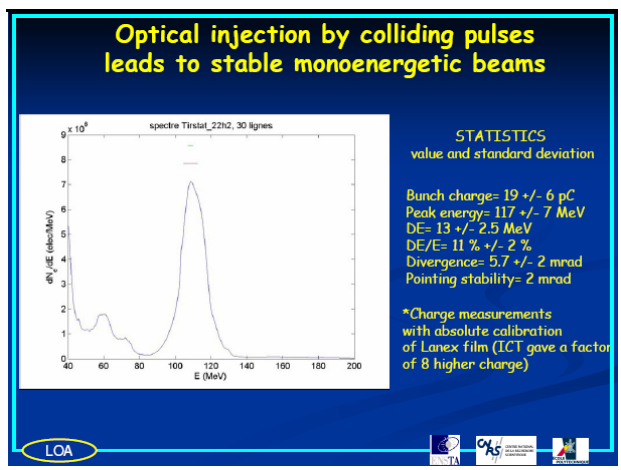
Optical injection by colliding pulses leads to stable monoenergetic beams
spectre Tirstat_22h2, 30 lignes
x 10^8
dN$_e$/dE (elec/MeV)
E (MeV)
STATISTICS
value and standard deviation
Bunch charge= 19 +/- 6 pC
Peak energy= 117 +/- 7 MeV
DE= 13 +/- 2.5 MeV
DE/E= 11 % +/- 2 %
Divergence= 5.7 +/- 2 mrad
Pointing stability= 2 mrad
*Charge measurements with absolute calibration of Lanex film (ICT gave a factor of 8 higher charge)
LOA

Monoenergetic bunch comes from colliding pulses: polarization test

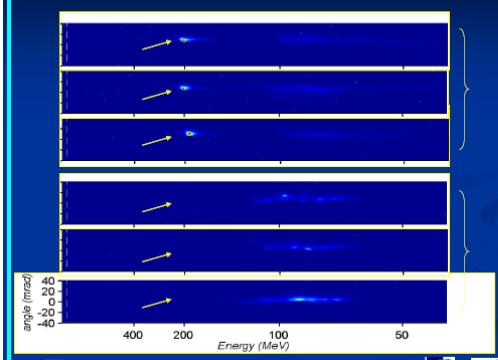

LOA

Controlling the bunch energy by controlling the acceleration length

By changing delay between pulses:
- Change collision point
- Change effective acceleration length
- Tune bunch energy

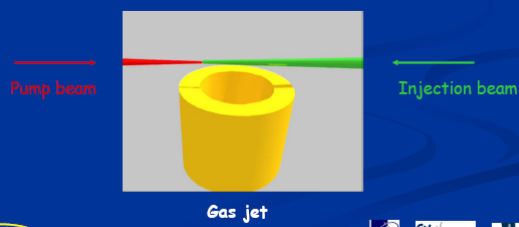

LOA

Tunable monoenergetic bunches

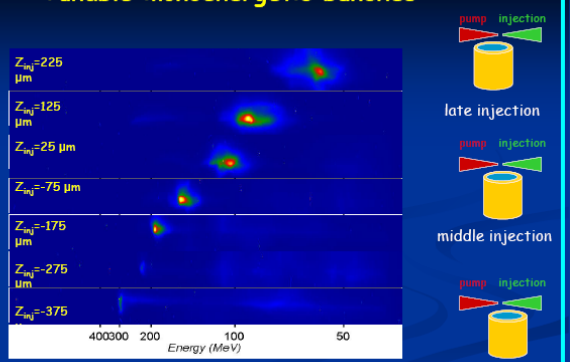

J. Faure et al., Nature december 2006

LOA

Tunable monoenergetic electrons bunches:

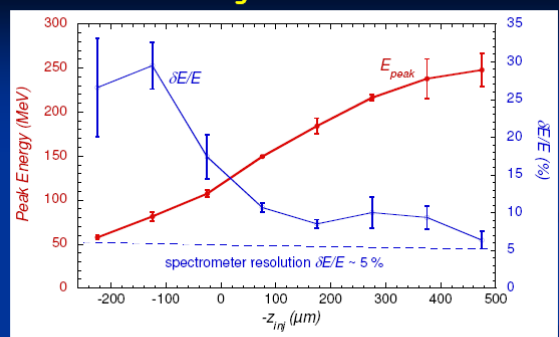

190 MeV gain in 700 µm: E=270 GV/m

LOA

Summary

Part 1 : Laser plasma accelerator : motivation

Part 2 : bubble regime and monoenergetic e-beam

Part 3: Experiment with colliding laser pulses

Part 4 : Conclusion and perspectives

LOA

Conclusions / perspectives

SUMMARY
- Optical injection by colliding pulse: it works !
- Monoenergetic beams trapped in first bucket
- Enhances dramatically stability
- Energy is tunable: 15-300 MeV
- Charge up to 80 pC in monoenergetic bunch
- δE/E down to 5 % (spectrometer resolution), δE ~ 10-20 MeV
- Duration shorter than 10 fs.
- new physics phenomena involved

PERSPECTIVES
- Combine with waveguide: tunable up to few GeV's with δE/E ~ 1 %
- Three laser pulses scheme
- Design future accelerators
- Model the problem for further optimization: higher charge
- Stable source:
  extremely important
  - accelerator development (laser based accelerator design)
  - light source development for XFEL
  - applications (chemistry, radiotherapy, material science)

LOA

ELECTRON BEAM DIAGNOSTICS FOR THE EUROPEAN X-RAY FREE-ELECTRON LASER

Christopher Gerth*
Deutsches Elektronen-Synchrotron DESY, D-22603 Hamburg, Germany

Abstract

To achieve and maintain stable operation of the European X-ray free-electron laser (XFEL) dedicated diagnostic sections are foreseen for the characterization and stabilisation of the electron beam. Especially the measurement and control of the longitudinal phase space during the bunch compression process is very demanding. Non-linear collective effects may degrade the slice emittance or energy spread during the bunch compression process. Moreover, a beam energy jitter transforms into a time jitter in the magnetic chicanes, and the beam arrival time is of particular importance for other synchronised sub-systems, e.g. seed lasers or pump-probe lasers for user experiments. Beam position monitoring with single bunch resolution in the sub-micron range is needed to establish and maintain the overlap of the electron and photon beam in the up to 250m-long undulators. The development status of various new diagnostic devices is discussed, and, where appropriate, experimental results obtained at the Free-electron LASer in Hamburg FLASH are presented.

INTRODUCTION

Future free-electron lasers (FELs) operating in the X-ray regime put tight tolerances on the beam quality of high-brightness electron bunches and their trajectory through the very long undulators. The beam properties vary over a wide range during the passage through a single-pass machine and need to be measured and controlled at various places. For stable long-term operation, they need to be monitored with sufficiently high precision to be able to detect deviations from the nominal values. Moreover, to serve as input signals for feedback systems, the detector systems have to be non-destructive to the electron beam in order to guaranty undisturbed FEL user operation.

As the FEL amplification process is based on exponential gain, the FEL radiation is extremely sensitive to variations of the peak current, transverse emittance and energy spread. Typically, only part of the beam fulfils the required conditions and the diagnostics has to be sensitive to this fraction of the beam. As an example, Fig. 1 shows the longitudinal phase space distribution and the corresponding slice energy width for a non-linear compression scheme as used at FLASH [1]. Since collective effects, such as coherent emission of synchrotron radiation (CSR) and longitudinal space charge (LSC), strongly influence the beam parameters it becomes obvious that projected values are of limited use.

* for the XFEL Team, christopher.gerth@desy.de

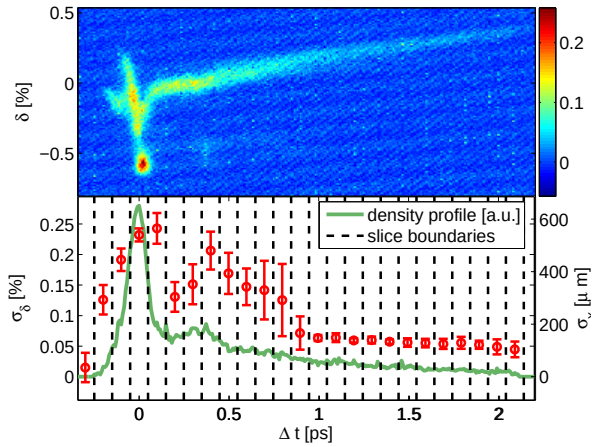

Figure 1: Longitudinal phase space distribution measured at FLASH under SASE conditions (top) and corresponding rms slice energy spread and density profile (bottom).

DIAGNOSTIC SECTIONS

The principle accelerator layout of the European XFEL [2], which will generate laser-like, femtosecond radiation down to the Ångstrom wavelength region, is shown in Fig. 2. In order to achieve high peak currents and ultra-short bunches whilst maintaining small slice energy spreads and emittances the electron beam is accelerated and compressed in several steps mitigating diluting CSR effects in the bunch compressors (BC1 and BC2) and space charge effects at low beam energies. The main beam parameters vary considerably during the compression process and are included in Fig. 2. Dedicated diagnostic sections (denoted as DS) are located in the injector and downstream of the two bunch compressors.

The major objectives of the diagnostic sections are the monitoring and stabilisation of the electron beam parameters with high accuracy and a well-defined matching into the subsequent linac sections. The super-conducting 1.3 GHz linac will be operated at a repetition rate of 10 Hz with 650 μs long bunch trains with 200 ns bunch spacing. Besides feedbacks that compensate for slow drifts, ultra fast detectors that act on a sub-microsecond timescale are required for intra bunch train feedbacks. Consequently, a suite of diagnostic devices for the measurement of the various beam parameters needs to be integrated in the lattice design which in turn should be kept short as the electron bunches need to be accelerated as quickly as possible after bunch compression to reduce LSC effects [3].

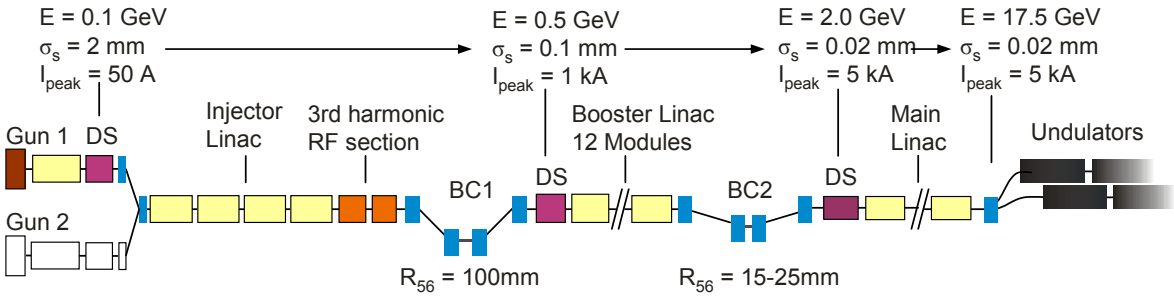

Figure 2: Accelerator layout of the European XFEL (BC: bunch compressor; DS: diagnostic section).

Beam Position Monitoring

The electron trajectory in a single-pass machine is not stabilized due to periodic boundary conditions and needs to be carefully monitored along the full length of the machine. From the injector to the main linac, the required accuracy of the order of a few tens of micrometers can be met by resonant stripline BPMs [4]. Four of these BPMs in combination with fast correction kickers will be used in the diagnostic section of BC1 for an intra bunch train feedback that stabilises actively the beam trajectory.

First start-to-end simulations indicate that a much higher accuracy of a few microns has to be reached in the up to 250 m long undulator sections to ensure stable SASE operation at X-ray wavelengths. C-band cavity BPMs working at 4.4 GHz with sub-micron resolution are being developed in collaboration with PSI, Villingen.

Longitudinal Phase Space

Manipulation of the longitudinal phase space is accomplished in the magnetic bunch compressors in combination with off-crest acceleration in both the injector linac and third-harmonic structures. Extremely challenging is the beam-based measurement and control of this compression process, which has a highly non-linear dependence on the rf settings. The rf amplitude and phase of the fundamental and third-harmonic plus the beam arrival time need to be measured. Different working points result in different tolerances for the phases and amplitudes [5] and it is desirable to find a working point for which one or more parameters are relaxed in order to reduce the number of rf parameters that need to be controlled.

Bunch compression monitors (BCM), which are based on an intensity measurement of the coherent synchrotron radiation emitted by the last dipole of the bunch compressor, can be used as input for fast feedbacks for the low-level rf for phase stabilization. Pyro detectors, which measure the integral radiation power, are used routinely at FLASH to correct the rf phase for slow drifts.

A new bunch arrival time monitor (BAM) has been developed [6] that uses the beam induced signals from button electrodes and modulates the amplitude of an Erbium-doped fibre laser pulse with electro-optical modulators based on $LiNBO_3$. The timing information of the rf pulse is encoded in the amplitude of the laser pulse which is then detected by a fast photo diode. A first test setup has been installed at FLASH and an arrival time difference of two adjacent bunches of the same bunch train has been measured to be 50 fs which gives an upper limit for the resolution of 30 fs for the BAM.

A special BPM with a large horizontal aperture for a flat vacuum chambers [7] has been developed to measure the beam position and size in the dispersive section of the bunch compressors. The BPM consists of a long stripline pickup that is perpendicular to the electron path. The electron bunches induce broadband electrical signals that travel to the opposite ends of the stripline pickup where their arrival times can be measured with an optical technique as used for the BAM. An rf amplitude jitter transforms into a position jitter in first order transport theory via $\Delta x = R_{16}\Delta E/E$. An accuracy better than 30 μm is required to resolve the desired value of the relative beam energy stability of $1\cdot10^{-4}$ for a high beam arrival and peak current stability [5]. An alternative method to record the beam energy is a time-of-flight measurement utilising two BAMs: one upstream and one downstream of the magnetic chicane. To resolve the same relative energy stability an accuracy of better than 10 fs would be required.

Yet another approach to measure the beam energy is the imaging of synchrotron radiation (SR) emitted in the bunch compressor dipoles. To achieve the desired resolution, the wavelength range used for the imaging needs to be optimised for a given beam energy and bend angle. A synchrotron radiation monitor (SRM) [8] that operates in the visible has been installed successfully at FLASH: the SR emitted at the entrance of the third dipole is imaged by a commercial photo-lens and recorded by a gated, intensified CCD camera. Figure 3 shows the bunch-to-bunch energy stability of a single bunch over a period of 120 s: the measured rms energy jitter is $2\cdot10^{-4}$ which includes the resolution of the SRM. By adjusting the timing of the gate, single bunches can be picked out of the bunch train and the energy slope on the bunch train can be measured. This procedure has been used to help adjust the low-level rf [9] and the results are in good agreement with BAM measurements [6].

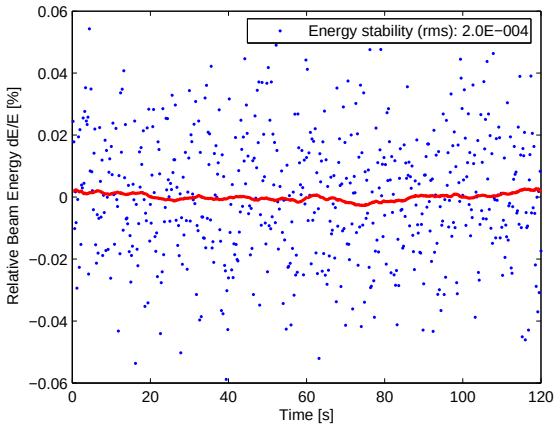

Figure 3: Bunch-to-bunch beam energy jitter measured with a SR monitor in the first bunch compressor at FLASH during SASE operation.

Slice Emittance

The goal is to monitor on-line the slice emittances with an accuracy in the percentage range. A promising solution appears to be a transverse deflecting structure (TDS) in combination with fast kickers that deflect individual bunches in a non-disruptive pulse stealing mode onto multiple off-axis optical transition radiation (OTR) screens. The screens are located in a FODO lattice and measurement of the time-sliced beam width on at least three screens allows the determination of the slice emittance and Twiss parameters (usually referred to as the standard multi-monitor method). The deflected off-axis bunches are then dumped in an absorber upstream of the subsequent accelerating module.

Figure 4 shows the normalised horizontal slice emittance measured with a TDS in combination with a quadrupole scan at FLASH [10]. The measurements were done at on-crest acceleration phases in all modules. The slice emittance varies along the bunch and the mean slice emittance amounts to 2.4 μm. A longitudinal tilt, which is apparent in the image of a bunch during the scan in the upper part of Fig. 4, is the origin of a considerably larger total projected emittance of 3.4 μm.

Slice Energy Spread

A spectrometer magnet followed by a high dispersion section will be located at the end of each diagnostic section and used for slice energy spread measurements in combination with the corresponding TDS. The goal is to resolve the uncorrelated energy spread of the order of several keV utalising an OTR screen. Assuming a resolution of about ~ 10 μm for the optical imaging system a dispersion of 2-3 m is required. Figure 1 shows the slice energy width measured at FLASH under SASE conditions [1].

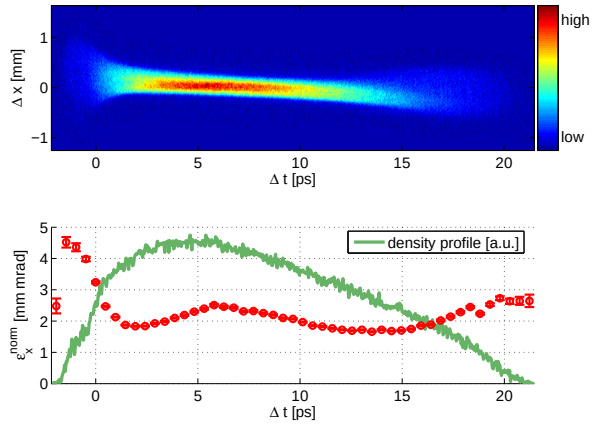

Figure 4: Image of a horizontally streaked bunch during a quadrupole scan (top) and the corresponding slice emittance and density profile (bottom).

CONCLUSIONS

Several diagnostic sections for the monitoring and stabilization of the electron beam are an integral part of the accelerator layout of the European XFEL. A continuous development of new and existing diagnostic techniques is ongoing to meet the demands on accuracy and timing. Not all recent developments could be covered in this conference proceeding and, especially, for an overview on electro-optical methods the reader is referred to Ref. [11].

REFERENCES

[1] M. Röhrs *et al.*, "Investigation of the Longitudinal Electron Bunch Structure at the FLASH Linac with a Transverse Deflecting RF-Structure", FEL2006, Berlin, August 2006.

[2] W. Decking, "Accelerator Layout and Physics of X-Ray Free-Electron Lasers", FEL2005, Stanford, August 2005.

[3] M. Dohlus, "Computational Needs for XFELS", ICAP2006, Chamonix, October 2006.

[4] V. Schlott *et al.*, "Intra Bunch Train Feedback for the European X-FEL", EPAC2006, Edinburgh, June 2006.

[5] M. Dohlus and T. Limberg, "Bunch Compression Stability Dependence on RF parameters", FEL2005, Stanford, August 2005.

[6] F. Löhl *et al.*, "A Sub-50 fs Bunch Arrival Time Monitor System for FLASH", WEPB15, this conference.

[7] K. Hacker *et al.*, "BPM with Large Horizontal Aperture for Use in Dispersive Sections of Magnetic Chicanes", TUPB20, this conference.

[8] Ch. Gerth, "Synchrotron Radiation Monitor for Energy Spectrum Measurements in the Bunch Compressors at FLASH", TUPC03, this conference.

[9] H. Schlarb *et al.*, "Beam Based Measurements of RF Phase and Amplitude Stability at FLASH", WEPC01, this conference.

[10] M. Röhrs *et al.*, to be published.

[11] B. Schmidt, "Overview on Diagnostics for X- and XUV-FEL", FEL2006, Berlin, August 2006.

FERMI@elettra Diagnostics

Mario Ferianis (ELETTRA, Basovizza, Trieste)

Abstract

FERMI@elettra is the fourth generation light source currently under construction at the Sincrotrone Trieste Laboratory. It is a seeded FEL based on the existing 1.0GeV Linac which will be fitted with FEL specific sub-systems like a new photoinjector and two bunch compressors to obtain in front of the undulator chain a stable and high quality beam. Due to the challeging beam parameters, the diagnostics play a key role for the successfull commissioning first, and then for a reliable operation of the new faciltiy. In this paper we give an overview on the FERMI diagnostics operating in the 6-D phase space along with some keynotes on the timing system which is an integral part of the longitudinal diagnostics.

Paper not received
(See slides of talk on following pages)

FERMI@elettra DIAGNOSTICS

Mario Ferianis – Elettra
on behalf of the
Beam Instrumentation Group

20-23 May 2007 DIPAC 2007 - NH Laguna Palace MESTRE

- FERMI@elettra overview
- Diagnostics
- Current activities and achievements

20-23 May 2007 DIPAC 2007 - NH Laguna Palace MESTRE

FERMI@elettra overview

- **FERMI@elettra** is the 4th generation Light Source, currently under construction in Trieste, based on the upgraded Normal Conducting S-band (2998.010 MHz) ELETTRA LINAC.
- Fixed e-beam energy
- single bunch at 50 Hz operation

Spectral range covered by two undulator lines
Seeded Harmonic Generation
FEL 1: 100 – ~40 nm (12-30eV) single stage
Time domain experiments → high stability & intensity
FEL 2: ~40 – 10 nm (30-124eV) two stages
High resolution experiments → frequency domain
Each FEL will *feed two or more* beam lines

- Gap tuning, flexible polarization, Apple Type radiators

Variable photon pulse length (narrow bandwidth operation):
50fs to ~1.0ps

- Need for an excellent timing and Synchronization

20-23 May 2007 DIPAC 2007 - NH Laguna Palace MESTRE

Schematic layout of the accelerator

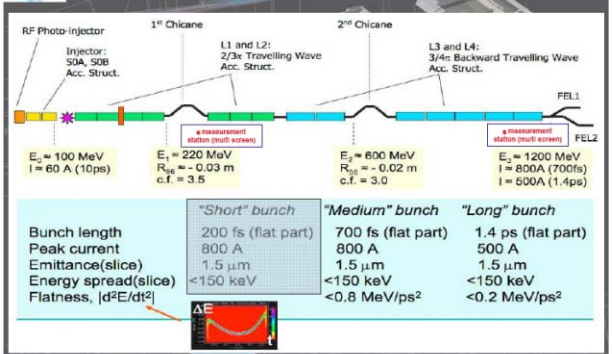

	"Short" bunch	"Medium" bunch	"Long" bunch
Bunch length	200 fs (flat part)	700 fs (flat part)	1.4 ps (flat part)
Peak current	800 A	800 A	500 A
Emittance(slice)	1.5 μm	1.5 μm	1.5 μm
Energy spread(slice)	<150 keV	<150 keV	<150 keV
Flatness, $\|d^2E/dt^2\|$		<0.8 MeV/ps²	<0.2 MeV/ps²

20-23 May 2007 DIPAC 2007 - NH Laguna Palace MESTRE

FERMI@elettra Diagnostics

- accurate photo-injector characterisation:
  emittance, charge profile, energy spread
- seeded FEL scheme: *whole bunch / fresh bunch (core)*
  calls for **slice measurements:**
  longitudinal charge profile,
  emittance,
  energy spread
  transverse and **longitudinal** overlap e- beam/laser
  - high resolution BPM
  - bunch arrival monitors
  - shot-to-shot feedbacks
- **stability of output** FEL radiation
- ***mm* to *sub-mm* bunch length;**
  currently two options:
  medium bunch: LB= 0.21mm (700fs) short FEL pulse
  long bunch: LB= 0.57mm (1.4ps) long FEL pulse

20-23 May 2007 DIPAC 2007 - NH Laguna Palace MESTRE

Photo injector Diagnostics line

ELETTRA- UCLA agreement for a 10 Hz Gun development

beam parameter	beam monitor	type	resolution
charge	current transformer	on-line	1pC
	Faraday cups	interceptive	10 pC
transverse position	stripline BPM	on-line	20 μm
	screens	interceptive	15 – 50 μm
transverse profile	screens	interceptive	15 – 50 μm
longitudinal profile	Cherenkov radiator + streak camera	interceptive	< 300 fs @ 800 nm

20-23 May 2007 TUPC11 / ref. L. Badano DIPAC 2007 - NH Laguna Palace MESTRE

Bunch Compressor Diagnostics

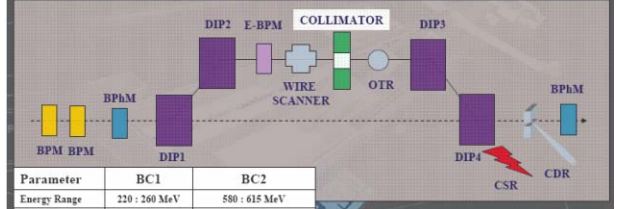

Parameter	BC1	BC2
Energy Range	220 : 260 MeV	580 : 615 MeV
Rel. En. Spread	2.3 : 2.7 %	0.97 : 1.05 %
Beta (β_x)	16 m (z=31 m)	23 m (z=98 m)
Dispersion (D_x)	0.165 : 0.255 m	0.155 : 0.24 m
En. Spread Beam size ±3s	28 : 44 mm	10 : 15 mm
Betatron Beam size ±3s	1.4 mm	2.0 mm
Bunch Length	2.8 psec Medium 5.4 psec Long	0.7 psec Medium 1.4 psec Long

•Synchrotron Rad. •Transition Rad. •Diffraction Rad. •Edge Rad. + Short Bunches → COHERENT RADIATION EMISSION

Intensity ∝N particles Int ∝N² particles

20-23 May 2007 TUPC06 / ref. M. Veronese DIPAC 2007 - NH Laguna Palace MESTRE

RF deflectors

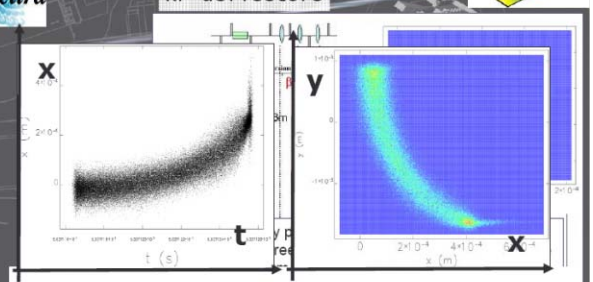

"Banana shape" induced by the Linac horizontal transverse wake field (unsuppressed instability). Bunch head is on the left in "t" coordinate (particle tracking result) and on the top in "y" coordinate (simulation of bunch deflection).

20-23 May 2007 TUPC10 / ref. P.Craievich DIPAC 2007 - NH Laguna Palace MESTRE

Cavity BPM

Two locations: LINAC & FEL

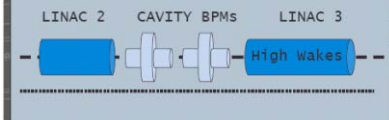

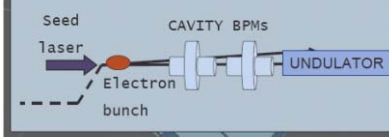

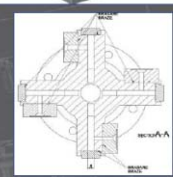

TUPC09/ref. P.Craievich, G.Trovato

20-23 May 2007 DIPAC 2007 - NH Laguna Palace MESTRE

and much more…

-Longitudinal diagnostics: collaboration with DESY on Bunch Arrival Monitor (BAM)

WEPC02 / ref. L.Pavlovic, F.Rossi

- Electro optical sampling (EOS) station

ref. M. Veronese

- Optical Timing developments: collaborations with MIT / DESY, LBNL, CNIT (Pisa)

WEPC22 / ref. Mario Ferianis
WEPC11 / ref. L. Banchi

20-23 May 2007 DIPAC 2007 - NH Laguna Palace MESTRE

Current Activities and achievements

Storage Ring FEL seeding

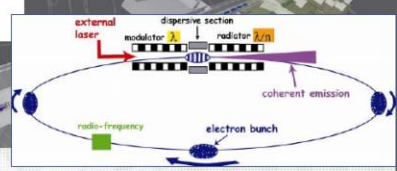

Parameters:

fundamental wavelength of Ti:Sa ~780 nm
(the modulator is tuned at 780nm)
the radiator is tuned at 260nm (3rd harmonic)
spontaneous emission (of second undulator)=260 nm
coherent radiation=260 nm

E. Allaria, M. Coreno, F. Curbis, M. B. Danailov, G. De Ninno, B. Diviacco, E. Karantzoulis, L. Romanzin, C. Spezzani, S. Tileva, M. Trovo'

20-23 May 2007 DIPAC 2007 - NH Laguna Palace MESTRE

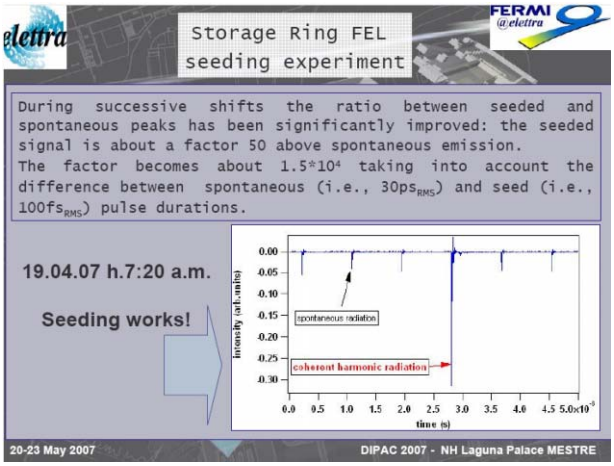
Storage Ring FEL seeding experiment
During successive shifts the ratio between seeded and spontaneous peaks has been significantly improved: the seeded signal is about a factor 50 above spontaneous emission.
The factor becomes about 1.5*10⁴ taking into account the difference between spontaneous (i.e., 30ps$_{RMS}$) and seed (i.e., 100fs$_{RMS}$) pulse durations.
19.04.07 h.7:20 a.m.
Seeding works!
spontaneous radiation
coherent harmonic radiation
intensity (arb. units)
time (s)
20-23 May 2007
DIPAC 2007 - NH Laguna Palace MESTRE

Current Activities and achievements
100Mev & 1.0GeV LINAC test bed for FERMI diagnostics
TUPC11 / ref. L. Badano
M. Veronese
bunch profile and position
transverse emittance (Q- scan)
current/charge
bunch longitudinal profile
bunch length variations (CTR)
energy / energy spread
182 mm
20-23 May 2007
DIPAC 2007 - NH Laguna Palace MESTRE

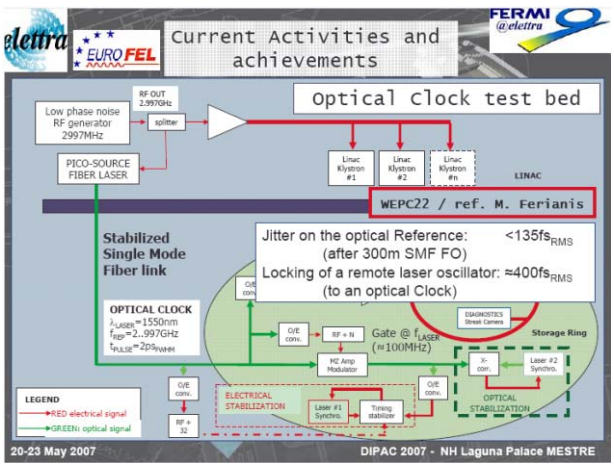
Current Activities and achievements
EURO FEL
Optical Clock test bed
Low phase noise RF generator 2997MHz
PICO-SOURCE FIBER LASER
LINAC
WEPC22 / ref. M. Ferianis
Stabilized Single Mode Fiber link
Jitter on the optical Reference: <135fs$_{RMS}$
(after 300m SMF FO)
Locking of a remote laser oscillator: ≈400fs$_{RMS}$
(to an optical Clock)
OPTICAL CLOCK
Gate @ f$_{LASER}$ (≈100MHz)
Storage Ring
ELECTRICAL STABILIZATION
OPTICAL STABILIZATION
LEGEND
RED electrical signal
GREENi optical signal
20-23 May 2007
DIPAC 2007 - NH Laguna Palace MESTRE

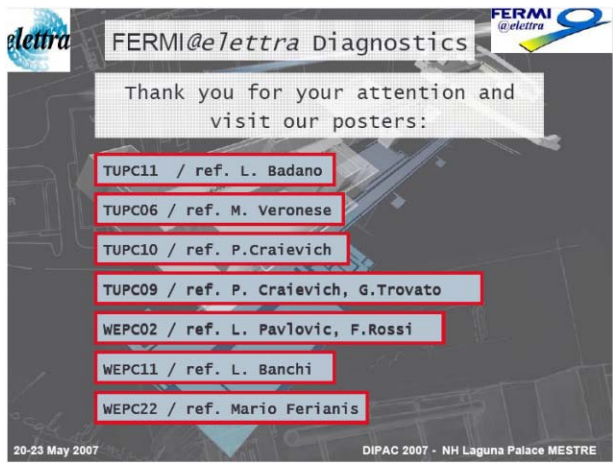
FERMI@elettra Diagnostics
Thank you for your attention and visit our posters:
TUPC11 / ref. L. Badano
TUPC06 / ref. M. Veronese
TUPC10 / ref. P.Craievich
TUPC09 / ref. P. Craievich, G.Trovato
WEPC02 / ref. L. Pavlovic, F.Rossi
WEPC11 / ref. L. Banchi
WEPC22 / ref. Mario Ferianis
20-23 May 2007
DIPAC 2007 - NH Laguna Palace MESTRE

DIGITAL EBPMs AT DIAMOND: OPERATIONAL EXPERIENCE AND INTEGRATION INTO A FAST GLOBAL ORBIT FEEDBACK

G. Rehm, M.G. Abbott, J. Rowland, I.S. Uzun
Diamond Light Source, Oxfordshire, U.K.

Abstract

We present our experience with the Libera Electron Beam Position Monitor (EBPM) during the first months of operation at Diamond. Measurement noise and beam current dependence with beam are compared to earlier lab measurements. Where discrepancies between the performance in the lab and in the application are observed, the causes have been investigated. Furthermore, results of the integration of the EBPMs into a Fast Orbit Feedback (FOFB) system are presented, including measurements of orbit motion spectra with and without FOFB.

INTRODUCTION

Diamond is using 168 Libera EBPMs in its storage ring. These have served most valuable information from first turns during commissioning of the storage ring, to beam based alignment of the BPM readings to quadrupole centres and slow orbit feedback implemented through the EPICS interface and a MatLab based correction routine. The next stage of their integration into Diamonds operation is the FOFB, which has been implemented during the first months of Diamond's operations and has recently been successfully operated for the first time. Prior to and during these tests we discovered some unexpected deviations of key performances when measured on the installed units as compared to lab measurements. It has turned out that many of these deviations from lab measurements were related to the fact that the installed BPM cables running from the button pickups to the EBPM electronics do no provide the four signals with equal phase to the inputs of the electronics.

All data in the following paragraphs refers to Diamond's current operating conditions of 125 mA, 66% fill and all BPM data presented is calculated with scaling factor of 10 mm.

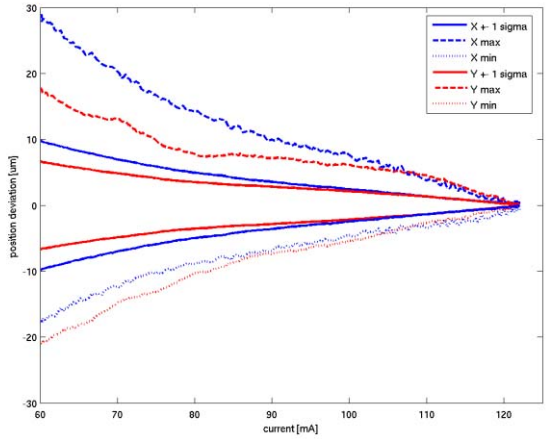

Figure 1: Measured beam current dependence of 48 BPMs in the storage ring

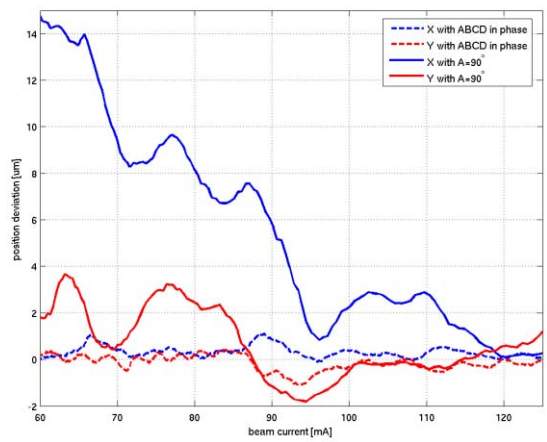

Figure 2: Measured beam current dependence of one BPM in the lab

BEAM CURRENT DEPENDENCE

Beam current dependence (BCD) of the position reading was found to be considerably more than the 1 μm specified and achieved in the lab for the 300-60 mA range. To study this with stored beam, we filled to 125 mA, started recording positions, and then artificially decreased the lifetime to have a decay to 60 mA within a few minutes. This test was done without orbit feedback, but prior stability tests have proven that no position in the orbit would grow to more than a few μm within such a period of time without correction. The deviation of EBPM readings from the value at 125 mA (see figure 1) is thus seen as evidence for the beam current dependence of the position reading. In further lab tests with simulated beam signals, we introduced a phase shift (extra length of cable) for one of the inputs of the EBPM electronics. It was found that for a phase shift of 90° between this one and the other inputs, the influence on performance was largest (see figure 2). We thus conclude, that problems with the installation and termination of BPM cables on site (many cables and connectors had to be replaced) have led to an uncertain phase match on the inputs of the EBPMs and has thus deteriorated the BCD performance. Lowering the BPM internal attenuations seems to improve the situation to some degree (bringing down the deviations from 14 to

symbol	frequency [Hz]	multiples of f_R
f_{RF}	499,654,097	936
f_S	117,440,065	220·$(1-\epsilon)$
f_R	533,818	1
f_{FA}	10,072	$\frac{1}{53}\cdot(1-\epsilon)$
f_{Swi}	13,345	$\frac{1}{40}\cdot(1-\epsilon)$
f_{Swe}	13,345	$\frac{1}{40}$
f_{Sre}	1,668	$\frac{1}{320}$

Table 1: Clock frequencies and decimation ratios of the Diamond Libera EBPM.

4 μm on the one tested unit in the lab), but the only solution currently known to entirely restore the performance would be to precision cut the BPM cables to equal lengths within 4 cm (phase match of 30°) for each set of four.

FAST ACQUISITION DATA

The lab tests also revealed that the fast acquisition (FA) data, which is to be used in the FOFB, showed some strong interference lines appearing in the particularly interesting frequency range up to 100Hz. To understand the origin of these lines, the possible interactions between the different decimations and clocks inside Libera need to be revisited.

Table 1 shows the relevant frequencies in relation to the storage ring revolution frequency f_R. All internal frequencies are derived from the sampling clock f_S which is locked to a multiple of f_R and can be tuned at a small fractional offset $|\epsilon| < 50$ ppm. This tuning is required to avoid harmonics of the input signal (or its revolution frequency sidebands in case of a non-uniform fill) folding back (through the undersampling) to the same intermediate frequency f_{IF} as the signal itself [1]:

$$f_{IF} = |f_{RF} - 4f_S| = (56 - 880\epsilon)f_R \quad (1)$$

$$f_{54} = |54f_{RF} - 230f_S| = (56 + 50600\epsilon)f_R \quad (2)$$

$$f_{56} = |56f_{RF} - 238f_S| = (56 - 52360\epsilon)f_R \quad (3)$$

$$f_{3+4} = |3f_{RF} + 4f_R - 13f_S| = (56 + 2860\epsilon)f_R \quad (4)$$

This calculations show that with $\epsilon = 0$ (no offset) both the 54^{th} and 56^{th} harmonic of the input signal as well as the 4^{th} revolution frequency sideband of the 3^{rd} harmonic fold back to the same intermediate frequency and will cause low frequency noise in the calculated position. This problem can be easily addressed by offset tuning (we typically use $\epsilon = 34$ ppm), which will shift all these frequencies far enough away.

However, this has led to a new problem when automatic switching of the Libera's input multiplexer at f_{Swi} (which is the internal switching frequency derived from the sample clock) is used together with a non uniform fill of the storage ring. As a result of the offset, the switching is no longer synchronous to the fill pattern, it now slowly "walks" through the fill:

$$f_{b1} = 40f_{Swi} - f_R = \epsilon f_R \quad (5)$$

With our typical ϵ this results in beating at f_{b1}=18.2 Hz. Clearly, ϵ cannot be increased enough to move this frequency away from the interesting range. However, locking the switching directly to the externally supplied machine revolution frequency (which was achieved by a change to the FPGA code by Instrumentation Technologies) removed this problem. The switching then happens at f_{Swe} in synchronicity to the machine revolution.

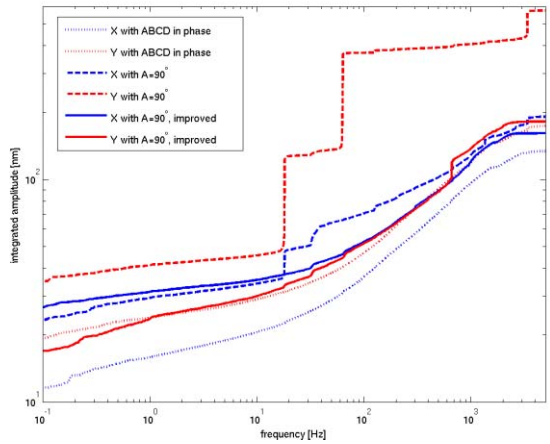

Figure 3: Integrated noise spectra from FA data recorded for 100s measured in the lab

However, when a phase shift between the input signals was introduced, a new interference started to appear (see figure 3). This could be identified as the 6^{th} harmonic of the switch revolution frequency f_{Sre} folding back as a result of the decimation to the FA sampling frequency f_{FA}:

$$f_{b2} = f_{FA} - 6f_{Sre} = \left(\frac{1+\epsilon}{53} - \frac{6}{320}\right) f_R \approx \frac{1}{8480} f_R \quad (6)$$

To suppress $f_{b2} \approx 63$ Hz, the FIR decimation filter and IIR notch filters in the FA chain have been optimised. This is easily done by changing the filter coefficients which are dynamically loaded into the FPGA during runtime. The new FIR filter has been designed to provide sharp notches at precise multiples of $3f_{Sre}$ (see figure 4) and thus almost completely restores the original performance even in the presence of a phase offset on the input (see figure 3).

INTEGRATION INTO FOFB

Using the Multi Gigabit Transceivers (MGBT) on the front of Libera, we have created a fast communication network between all storage ring EBPMs and an additional 26 (one for each cell plus two observers) computation nodes (MVME5550 PowerPC processor boards equipped with PMC modules with MGBT). Position and control data

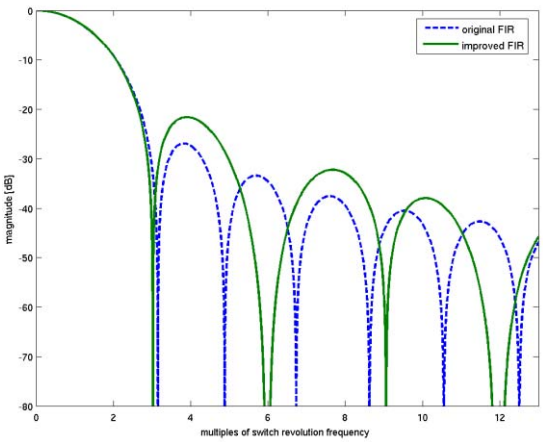

Figure 4: Comparison of original FIR filter and improved FIR with optimised notches

are distributed between all 194 nodes of this network using an in house developed Communication Controller [2].

Position data is exchanged at f_{FA} and all EBPMs are synchronised to output each set of new data at the same time within one machine revolution (1.8μs). The PMC modules issue an interrupt to the CPU 50 μs after the first data packet has been received. By this time, all data packets should have arrived; any missing positions will be marked as invalid. The CPU then converts the position data from fixed point to floating point notation, enabling the use of fast Altivec operations in the matrix multiplication with the inverse response matrix. Each CPU has to multiply with 7 lines of the matrix for each plane to produce correction values for the 7 corrector magnets in each plane per cell. The corrector coils are built into the sextupole magnets and work through a 2 mm stainless steel chamber. The 3 dB bandwidth of the magnet/chamber combination is estimated to be $>$500 Hz, however, the corrector power supplies are currently running with an internal 100 Hz low pass. This low pass currently limits the performance achievable by the feedback loop, whereas the delays in the loop (see table 2) should allow correction to $>$200 Hz.

The FOFB is currently in the commissioning stage and has successfully been running at full rate and with all EBPMs and correctors. The PID loop is currently using only the P and I terms and will require further optimisation. With these preliminary settings, very reasonable suppression could be achieved, in particular for the beam movements around 16 Hz and 25 Hz which have been found to be caused by ground motion (see figure 5). The overall integrated noise in the FA bandwidth (2 kHz) has been reduced in both planes from H/V 4μm/1μm to 1.5μm/0.9μm. More importantly, for frequencies up to 100Hz, the integrated noise has been reduced from 4μm/0.9μm to 1μm/0.4μm.

Already in its present configuration the FOFB is far superior to the slow orbit feedback (SOFB) which operates with one correction per second. While movements of ID gaps or energisation of the multipole wiggler produce small but observable orbit distortions with the SOFB, with the FOFB no orbit movement could be observed in such a case.

reason	delay [μs]
group delay of FIR	148
group delay of 2 IIR (0-500 Hz)	60-71
transport to PMCs	35.5-38.5
time reserved for data to arrive	50
DMA to CPU memory	49
conversion fixed to float	5
matrix multiplication $2 \cdot 7 \cdot 168$	4
PID controller	1
write to power supply controller	3
maximum total	331

Table 2: Delays in the fast feedback loop. Group delays are calculated, all other values are measured.

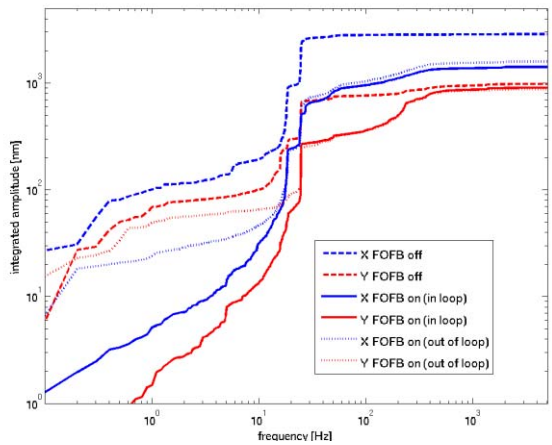

Figure 5: Performance of FOFB during commissioning. Integrated position noise has been measured on the beam with FOFB off and on, both with EBPMs in the feedback loop and out of the feedback loop.

CONCLUSIONS

The Diamond EBPM system has been improved to allow reliable performance in a FOFB. The FOFB has been implemented and tested successfully. Future work with improved PID parameters and possibly increased corrector power supply bandwidth should further improve the performance of the FOFB.

REFERENCES

[1] G. Rehm, M. Abbott, "Performance Verification of the Diamond EBPM electronics", in *Proceedings of DIPAC 2005*

[2] I.S. Uzun, R. Bartolini, G. Rehm, J.A. Dobbing, M.T. Heron, J. Rowland, "Initial Design of the Fast Orbit Feedback System for Diamond Light Source", in *Proceedings of the 10th ICALEPCS 2005*

ELECTRON BEAM DIAGNOSTICS FOR THE ALBA LIGHT SOURCE

U. Iriso*, A. Olmos and F. Pérez
CELLS, P.O. Box 68, 08193 Bellaterra, Spain

Abstract

This paper presents the diagnostics systems that will be used to monitor the electron beam at ALBA, a 3 GeV 3rd generation synchrotron light source. The electron beam is characterized by measuring its transverse position in the beam pipe, beam current, transverse size and longitudinal structure. We provide a complete picture of the systems used to diagnose the electron beam along the ALBA facility, not only in the Storage Ring but also in the injector system (Linac, Booster, and transfer lines).

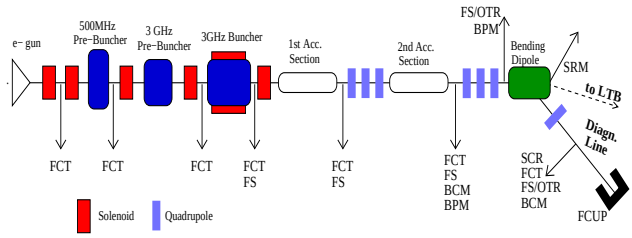

Figure 1: Beam diagnostics components in the Linac.

INTRODUCTION

The ALBA facility consists of a 100 MeV Linac, a Booster that accelerates the beam up to the full energy of 3 GeV, the Storage Ring (SR), and the corresponding transfer lines (Linac To Booster – LTB, and Booster To Storage – BTS). Table 1 lists the main beam parameters for the Linac, Booster (extraction conditions) and SR.

Table 1: Beam parameters in the Linac (single bunch mode), Booster (equilibrium values at 3 GeV) and SR.

	Linac	Booster	SR
energy (GeV)	0.1	3.0	3.0
circumference (m)	...	249.6	268.8
max. current (mA)	5	5	400
bunch spacing (ns)	2 - 128	2	2
rms bunch length (ps)	∼200	60	15
hor. emit. (nm·rad)	150	9.0	4.3
coupling	100 %	10%	1%
dipole field (T)	0.189	0.873	1.42
hor. tune Q_x	...	11.42	18.18
ver. tune Q_y	...	7.38	8.37

We use common instrumentation for light sources thoroughly described in related literature (see for example Ref. [1]). In the following, we describe our choice of the instrumentation that measures the beam parameters listed in Table 1, and thus characterize the beam behaviour along the Linac, Booster, transfer lines and SR.

LINAC

The diagnostics components installed in the ALBA Linac are shown in Fig. 1. The Linac is a turn key system. For the acceptance tests, we shall perform measurements of the beam charge, emittance, energy and energy spread.

Fast Current Transformers (FCT) are installed after each active element. The FCT is a non-interceptive current transformer to measure the beam profile and intensity from the magnetic flux induced in a toroidal core (coil) by a primary winding (the electron beam). As all passive devices, the FCT differentiates the signal, and hence frequencies below a certain threshold are not measured (DC components are lost). These devices are bought *off-the-shelf* from Bergoz and have an upper frequency limit of 2 GHz [2], which is sufficient to measure the beam charge and profile at the Linac exit.

A further crosscheck of the beam charge is performed using the **Beam Charge Monitors (BCM)** [2] and the **Faraday Cup (FCUP)**. The BCMs are *off-the-shelf* units that measure the charge of very fast pulses with high accuracy (resolution is < 1 pC) by means of a capacitively shorted transformer coupled to a fast readout transformer in a common magnetic circuit. The FCUP at the Diagnostics Line is based on the Diamond design [3]. This device is mainly designed as beam stopper, and so it is optimized for charge collection efficiency rather than bandwidth.

The transverse beam spatial distribution is measured using two different screen monitors. The first one includes a movable setup that inserts a **Fluorescent Screens (FS)** in the middle of the vacuum chamber. The screen is made of a fluorescent material (typically YAG:Ce), which produces light upon collision with the electron beam by phosphorence. The second one uses either a FS or an **Optical Transition Radiation (OTR)** monitor (aluminum foil on a polished silicon wafer). While this OTR monitor produces a much lower photon yield, it has the advantage (with respect to the FS) of not saturating because it is a surface effect. This combination of FS and OTR (so abbreviated as **FS/OTR**) is used for the emittance measurements of the Linac Acceptance Tests. At 100 MeV and low currents, the FS provides sufficient photon flux, while for high currents and small beam sizes, we avoid the saturation of the screen using the OTR. The emittance measurements are performed using the well-known technique of the quadrupole scan using the FS/OTR upstream the bending magnet in Fig. 1.

A similar system is thought for the energy and energy

* ubaldo.iriso@cells.es

spread. Both measurements are performed using the bending dipole in Fig. 1 as an energy spectrometer and measuring the beam position and shape with the screen monitor FS/OTR installed in the Diagnostics Line.

BOOSTER

In order to control the injection into the Booster, we locate a FS/OTR downstream the septum to image the beam shape and monitor the beam transport. Furthermore, an FCT allows to control the beam charge that traverses the septum and thus infer the transfer efficiency.

The Booster is equipped with three **Synchrotron Radiation Monitors (SRM)** distributed around the ring. The SRM is a non-destructive method to infer the beam size using the synchrotron radiation produced when the beam traverses a bending magnet. As the FS setups, the light is directed by an optical system of lenses and mirrors towards a CCD camera, where the image is analyzed. This monitor becomes very useful to follow the beam size along the energy ramp, albeit at full energy (3 GeV) the image is affected by diffraction effects and hence a quantitative measurement cannot be provided [4].

The Booster disposes of a **DC Current Transformer (DCCT)**. Similarly to the FCT principle, the DCCT measures the beam intensity based on the magnetic flux induced by the electron beam. However, the DCCT includes a second magnetic modulator that detects the beam DC component using a feedback loop. With the commercially available electronics [2], we expect to achieve sensitivities down to 1 μA/$\sqrt{\text{Hz}}$ (enough for our purposes).

We also instal an **Annular Electrode (AE)**. In this case, an electrode surrounds the inner part of the vacuum chamber, and so when the beam goes through, the electrode detects the complete beam's charge. The advantage of this system is its up to 8 GHz bandwidth [5], permitting bunch length measurements during the energy ramping (yet it is not enough to quantitatively measure the bunch length at top energy).

A total of 44 **Beam Position Monitors (BPM)** are installed around the Booster. The BPM intrinsic resolution is 45.5μm [6] for a beam current of 0.1 mA and a revolution frequency of 1.2 MHz. With 44 horizontal and 28 vertical correctors, simulations show that the orbit correction with this scheme allows an rms residual (at BPMs) below 0.5 mm in both planes [7], and so only 28 BPMs are equipped with the read out electronics.

A proper Booster performance requires the measurement of the betatron tunes. This is carried out using two 50Ω matched **striplines**: the first one excites the beam with an electric kick, the second one is used to obtain the transverse oscillations and thus infer the tune frequency. We have chosen two locations where the phase advance is as close as possible to 90^o in each plane. In an ulterior phase (after the Booster commissioning), and provided that the $\sim$1 mA Booster beam provides enough signal in the button BPMs, any of the 44 BPMs can be used.

Finnally, we have located a FS between the extraction kicker and the extraction septum. This FS is inserted horizontally and is able to intercept the beam orbit at injection (100 MeV) and at extraction (at 3 GeV, when the beam trajectory is kicked towards the BTS).

TRANSFER LINES: LTB AND BTS

The main parameter to care about in the transfer lines is the transmission efficiency. At the LTB, we monitor the beam charge using two BCMs, one installed at the beginning and one at the end of the transfer line. At the BTS, this measurement is performed with two FCTs installed as well at both edges of the BTS.

Both transfer lines dispose of three FS/OTRs, located at the beginning, middle and end of the BTS, which in addition to the SRMs located at the bending dipoles provide beam size and shape information. Together with the button BPMs (4 at each transfer line), this information is used to obtain a proper beam steering along the line and so improve the transfer efficiency.

STORAGE RING

Sections 2 and 3 in the SR are used for beam diagnostics. Figure 2 shows the 3-d sketch of section 2, showing an FS, DCCT, AE, FCT, together with a stripline that will provide the beam excitation for tune measurements. Conceptually identical to the systems installed in the Booster, the main difference is that the DCCT electronics in the SR case dispose of a high resolution module down to 0.5 μA/$\sqrt{\text{Hz}}$ [2] to increase the precision of the beam lifetime measurements.

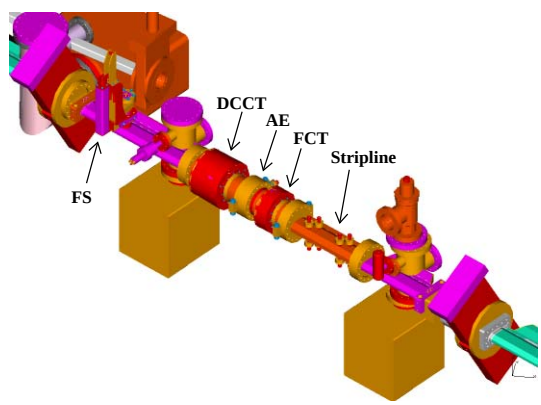

Figure 2: Beam diagnostics components in Sector 2.

Section 3 includes the horizontal and vertical feedback kickers. A feedback kicker consists of two horizontal (or vertical) electrodes of 30 cm length (a bucket length is 60 cm) that are intended to cure possible bunch-by-bunch instabilities using high frequency electric kicks. These kickers will not be installed since day one because their "picky" geometry is in turn a source of beam impedances [8]. We first want to study the SR behaviour

without the kickers and, in case instabilities arise, we will install them to cure these instabilities.

Up to 120 BPMs are installed along the 16 cells of the SR. Furthermore, we dispose of 3 extra BPMs that will be used for bunch-by-bunch feedback and tune measurements. Position data from the BPMS are provided for the slow ($\sim$1 Hz) orbit correction, fast ($\sim$10 kHz) orbit correction, and turn by turn data ($\sim$1 MHz). As an option, data acquisition can be changed upon demand. The intrinsic resolution depends on the bandwidth. At 4 kHz, the SR button provides a resolution of 0.11 μm for currents $\geq$ 10 mA [6].

Similarly to the Booster injection, the SR injection straight disposes of three FS to image the beam and optimize the injection efficiency. Moreover, two **scrapers (SCR)** are installed in this location to get rid of the undesired beam halo particles and protect the Insertion Devices from possible damages produced by mis-steered or off-energy beams. The bending dipoles immediately before and after the injection straight are used as diagnostics front ends. One of them uses the X-ray part of the Synchrotron Radiation to monitor the beam emittance, the second uses the Visible part for quantitative bunch length and bunch purity measurements. They are abbreviated as XSR and VSR, respectively.

X-ray Synchrotron Radiation front end (pinhole)

Because of the low SR emittance and the high energy beam, the beam transverse size is typically in the same range as cameras resolution (around 10μm). The simple principle of a pinhole system is widely used in synchrotron light sources to overcome this limitation. Since imaging using the visible range is diffraction limited, the pinhole system has to use the x-ray part of the spectrum of the synchrotron radiation. This is achieved with the Aluminum vacuum window and the Molybdenum filter. The pinhole system design at ALBA provides a magnification factor of 2, which is enough to avoid the screen resolution limitation. Details about the ALBA pinhole are shown in Ref. [4].

Visible Synchrotron Radiation front end

We have designed a front end that uses the visible part of the synchrotron radiation spectrum produced when the beam traverses a bending dipole [9]. This setup is based on the ESRF design [10]. The key system of this Visible Synchrotron Radiation (VSR) front end is a mirror that is inserted vertically. The mirror is placed in such a way that only the visible part of the spectrum is reflected and sent it to an optical hutch, where the light is analyzed by means of a streak camera. The streak camera uses a double sweep to perform quantitative bunch length measurements (with ps resolution) and allows to characterise longitudinal beam instabilities. The mirror is equipped with three thermocouples to avoid possible heat load damage in the mirror and to control its vertical position. In addition, we foresee the use of an Avalanche PhotoDiode that profits the x-ray part of this radiation (the part that is not reflected by the mirror) for bunch purity measurements in a similar design as [11].

SUMMARY

The diagnostics components that will be installed in the ALBA facility are presented. Using these components, we expect to measure (and hence, control) the beam parameters. Table 2 summaryzes the distribution of this components along the ALBA facility. The acronyms have been listed in the text. Further updates and their location around the facility can be followed at [12].

Table 2: Diagnostics distribution along ALBA. The SRM at the SR refer to the XSR and VSR described in the text.

	LI	LTB	BO	BTS	SR
FCUP	1	1	...	...	...
BCM	1	2	...	...	...
FCT	6	3	1	2	1
DCCT	...	...	1	...	1
FS/OTR	3	3	4	4	6
SRM	...	1	3	2	2*
BPM	1	3	44	4	123
Striplines	...	...	2	...	1
SCR	...	3	...	...	2

ACKNOWLEDGMENTS

We are very grateful for the engineering support from M. Cornelis, E. Al-Dmour and Ll. Ribó. We are also indebted to G. Rehm (DLS), J.-C. Denard (Soleil), V. Schlott (SLS) and K. Scheidt (ESRF).

REFERENCES

[1] J. Bosser (Ed.). *Beam Instrumentation*, CERN-PE-ED, 001-92, 1994.

[2] http://www.bergoz.com

[3] A.F.D. Morgan. *Design of the Faraday Cups in Diamond*, Proc. of DIPAC'05.

[4] U. Iriso and F. Pérez. *Synchrotron Radiation Monitors at ALBA*, Proc. of EPAC'06.

[5] F. Pérez, I. Berkel, E. Huttel, A.S. Müller and M. Pont. *Beam size and bunch length measurements at ANKA*, Proc. of PAC'03.

[6] A. Olmos, T. Günzel and F. Pérez. *BPM design for the ALBA Synchrotron*, Proc. of EPAC06.

[7] G. Benedetti. *Closed orbit correction in the ALBA Booster*, CELLS Tech. Note AAD-BO-BD-AN-0186, 2007.

[8] T. Günzel. *Impedance characterization of the feedback kickers*, CELLS Tech. Note AAD-SR-IZ-FFK-AN-0125, 2006.

[9] U. Iriso. *Visible Synch. Rad. Front End for Beam Diagnostics*, CELLS Tech. Note AAD-FE-DI-AN-0155. 2006.

[10] K. Scheidt. *UV and Visible light diagnostics at the ESRF*, Proc. of EPAC'96.

[11] B. Joly and G.A. Naylor. *A high dynamic range bunch purity tool*, Proc. of DIPAC'01.

[12] http://www.cells.es/Divisions/Accelerators/RF_Diagnostics/Diagnostics/Diagnostics_Scheme/

OPTICAL TRANSITION RADIATION MONITOR FOR HIGH INTENSITY PROTON BEAM AT THE J-PARC

A. Toyoda, K. Agari, M. Ieiri, Y. Katoh, E. Hirose, M. Minakawa, H. Noumi, Y. Sato, Y. Suzuki, H. Takahashi, M. Takasaki, K. Tanaka, Y. Yamanoi, H. Watanabe, Institute of Particle and Nuclear Studies, High Energy Accelerator Research Organization, 1-1, Oho, Tsukuba, Ibaraki, JAPAN.
T. Mitsuhashi, Institute of Materials Structure Science, High Energy Accelerator Research Organization, 1-1, Oho, Tsukuba, Ibaraki, JAPAN.

Abstract

The OTR (Optical Transition Radiation) is a powerful tool to observe 2-dimensional information of beam profile at the high intensity beam line because the OTR intensity only depends on the screen reflectivity so that we can minimize a beam loss. However, it is necessary to overcome large background due to the Cerenkov radiation and low radiation tolerance of camera system. The purpose of the present effort is to achieve small background and good S/N and to prolong the lives of the camera system. This requires that amount of potential Cerenkov radiator be minimized and radiation level at the camera system be suppressed. For this requirement, we design and develop an OTR monitor with the optical system of a Newtonian telescope type. Detail design of the optical system and a result of background measurement performed at one of primary proton beam lines of our old 12 GeV Proton Synchrotron are presented.

INTRODUCTION

For the purpose of improving overall intensity of proton beam in response to a demand from nuclear and particle physics, precise measurement of beam profile is now becoming important. A beam monitor for such high intensity beam line should satisfy the following conditions.

- High resistance for radiation
- Perturbation to the beam by the monitor itself as small as possible

The OTR monitor is a good candidate for this purpose, because the OTR light intensity is only dependent on the reflectivity of the screen, so that we can minimize a thickness of the screen. The OTR also has good features as a profile monitor such as providing 2-dimensional information, directional characteristic leading to a S/N.

The OTR is emitted when a charged particle passes through a boundary between two materials with different dielectric constant. This was first predicted theoretically by Ginzburg and Frank [2], and experimentally measured by Goldsmith and Jelly [3]. Wartski et al. [4] first applied the OTR to the beam diagnosis. After that, the OTR was widely used at electron and proton accelerators for the profile measurement [5] [6].

J-PARC [1] hadron beam line under construction shown in Figure 1 will provide high intensity proton beam whose beam power is 750 kW for experiments of particle and nuclear physics experiments. A 50 GeV proton is slowly extracted into the switch yard and focused on the T1 target to produce secondary particles such as pions, kaons, and so on. The residual proton beams are transported into 750 kW beam dump. The OTR detectors are designed for monitors located just downstream of the extraction point.

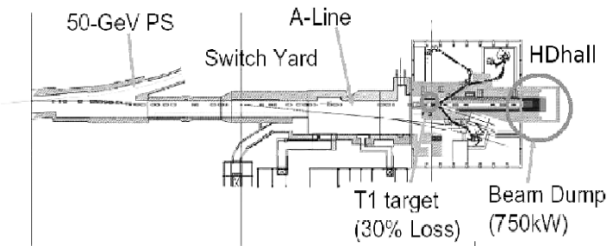

Figure 1: J-PARC hadron beam line

PREVIOUS EXPERIMENTAL RESULT

We need to overcome the following difficulties for development of the OTR monitor at J-PARC.

- A Lorentz gamma factor is small (γ = 32; 30 GeV), so that the directional characteristic is degraded.
- Background level is expected to be large because the OTR monitor will be installed near a loss point.
- An effective OTR intensity decreases due to the time evolution measurement following the standard RS-170 format. A designed beam duration is about 0.7 s.
- At a commissioning stage, we need to measure a profile with a beam intensity less than 10^{12} protons per pulse.

Test experiment with proto-type OTR monitor

To check the OTR light yield and a background shape, we developed a proto-type OTR monitor and performed test experiments at the slow-extraction beam line of the KEK 12-GeV PS (γ = 12.8), whose intensity is 2 x 10^{12} protons per pulse.

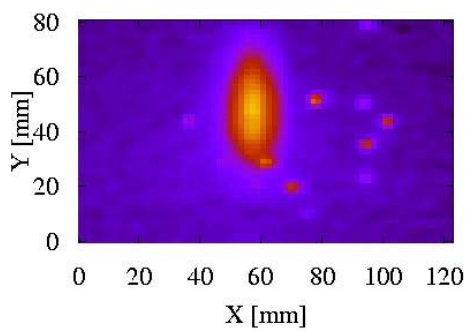

Figure 2: Typical beam image measured by the proto-type OTR monitor

As shown in figure 2, we successfully measured the OTR profile with a beam intensity of down to 4 x 10^{11} protons per pulse. We prepared a SPIC (Segmented Parallel Plate Chamber [7]) profile monitor as a reference, and checked that the OTR monitor performs well as a profile monitor.

Result of the optical fiber system

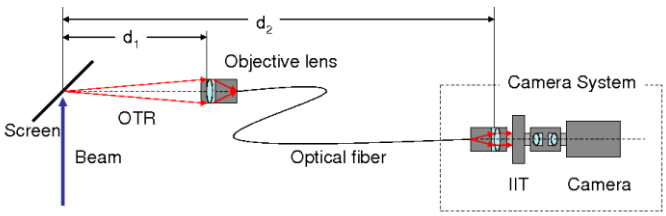

Figure 3: Schematic figure of an OTR monitor with an optical fiber system

Using the above result of the test experiment, we concluded the OTR monitor can be used even on condition of high background and low intensity. However, scattered backgrounds around OTR signal prevents us from getting a clear profile as shown in figure 2, so that we need to refine light detecting system. One of methods to reduce background is to keep a detector as far away as possible. For this purpose, we developed the optical fiber system as shown in figure 3. It is also important that this system leads to reduce radiation level at a position of camera system which has low radiation tolerance.

We performed a test experiment with this optical fiber system in the same way as that with the proto-type OTR monitor and successfully measured a beam profile. However, measured background level is not so low as expected, so that we carefully measured a background level with gradually changing distances of d_1 and d_2 in figure 3. By this research, we found two things as follows.

- Using data set of distance d_2, a background level is confirmed not to depend on the beam loss at a camera position.
- Using data set of distance d_1, a total background sum (BG in arbitrary unit) is described as:

$$BG = 0.114 \times loss + 0.197,$$

where `loss` is a beam loss at an objective lens measured by a loss monitor in unit of nC.

The former result shows direct hit of scattered particles on a camera system is not a main component of the background. The latter result shows some reduction factor exists because a parameter of the order zero is not negligible. One of possible explanations is to assume that a main OTR background comes from a Celenkov radiation produced at an objective lens or an optical window. With putting an objective lens closer to a beam line, a beam loss increases while an effective acceptance of Celenkov radiation decreases.

Thus it is concluded that this method is not effective to reduce an OTR background, but reduces radiation damage to camera system.

OPTICAL SYSTEM

To minimize amount of materials as a Celenkov radiator near a beam line, we developed optical system using a telescope with large solid angle. An optical system using a reflector should satisfy the following conditions.

- Large solid angle to cover the OTR light opening angle. A peek of the opening angle is 31 mrad corresponding to $\gamma = 32$.
- Magnification factor of 8.3. Designed OTR screen target dimension is about 100 mm x 100 mm.
- Keep a camera with low resistance to radiation as far away from the beam line as possible.
- Keep possible background source such as lens and windows as far away from the beam line as possible.
- Suppress an aberration of the system to ensure spatial resolving power of 1 mm or less. This requirement needs to ensure a depth of field to cover an OTR screen enough.
- Minimize cost by reducing number of focusing components.

Considering the above conditions, we determine to use Newtonian telescope type as shown in figure 4. We determine a subject distance to be 5000 mm considering a beam line tunnel size, a depth of field, and radiation level. A diameter of a main reflector is optimized to be 350 mm to cover the OTR light dispersion. To realize the magnification factor of 8.3, a focal length of the main reflector is shortened to be 1000 mm in range of proper aberration. With the help of bright large main reflector, a convergent system is simplified, so that we do not need to use compound lens system which does not have enough radiation tolerance.

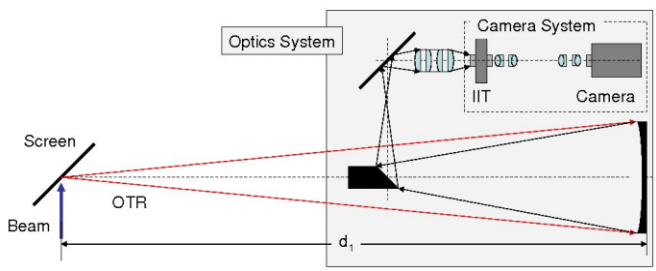

Figure 4: Schematic view of the Newtonian optics system.

OPTICAL PROPERTIES

Figure 5: Newly-developed optical system using a Newtonian reflecting telescope.

We developed optical system based on design works described above sections as shown in figure 5. A light arising at the screen is focused by the main reflector, and lead to a surface of an image intensifier (IIT) whose diameter is 18 mm using four sets of plano-convex lenses. IIT fluorescence is introduced to a camera using a method of a relay lens composed of four sets of achromatic lenses.

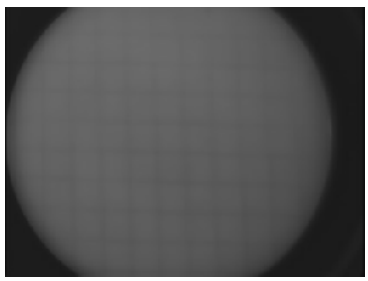

Figure 6: A test target image measured by a CCD camera.

To check optical properties of this system, we prepared an optical test target located at the OTR screen position. A size of the target is 141 x 100 mm which is the same as the real OTR screen, and placed at 45-degree angle. This target is divided into ten by lines of 0.2 mm thickness for both X axis and Y axis. A 2/3" CCD camera is used to measure a test target image.

Figure 6 shows a measured image of this system. There is a little bit distortion, but this is not a problem because it can be corrected by computer software. We successfully measured a target image of about 100 mm x 90 mm area, so that a magnification is enough. We analyze this image to check the optical properties by computer as follows.

Resolution analysis

Sigma (mm)	X direction	Y direction
Centre	1.16 mm	0.94 mm
Left	0.68 mm	1.54 mm
Top	1.26 mm	0.90 mm
Mean	1.03 mm	1.13 mm

Table 1: Resolution analysis result is shown.

Our optics system requires a resolution of about 1 mm for a profile measurement. There is a possibility that a resolution depends on a position in the target due to a lack of a depth of field, so that we evaluated a resolution in three regions such as central, left, and up regions. After that, we projected the image into X and Y axis, and fitted it with a Gaussian function. Table 1 shows a result of this fitting. A resolution width is evaluated by a Gaussian sigma in the unit of mm. There is a little position dependence, but about 1 mm resolution is confirmed to be achieved. A main reason of this resolution deterioration is assumed to come from a low IIT resolution.

Luminance flatness analysis

There is a possibility that a limb darkening disturbs a precise measurement of a beam profile, so that we need to check whether the image has enough good flatness of luminance. To evaluate this, it is necessary to normalize the image by a luminance distribution of the test target, which is not always constant. Figure 7 shows an analysis result of the luminance flatness. A bottom figure shows the ratio of the CCD image to the target luminance distribution is flat enough to measure a profile.

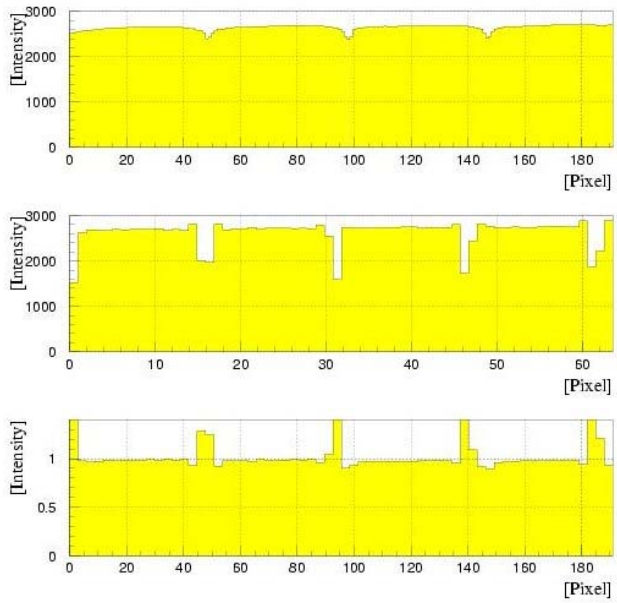

Figure 7: Luminance flatness analysis. Horizontal axis is a y projection of each image in the unit of pixel. Vertical axis is luminance intensity in arbitrary unit. A top figure is for a measured image. A middle one is for a target image captured by a digital camera directly. A bottom one is a division of the top figure by the middle figure.

CONCLUSION

Using the result of the previous test experiments including an OTR background estimation, we successfully developed an OTR monitor applicable to a high radiation and high background circumstance. A detector resolution is estimated to be about 1 mm. Detector luminance flatness is measured to be good enough. It is expected that this monitor can be used from intensity of 4 x 10^{11} protons per cycle. This monitor can be used as a profile monitor located at the extraction point of the J-PARC hadron beam line.

REFERENCES

[1] http://www.j-parc.jp
[2] V.L. Ginzburg and I.M. Frank, JETP 16 (1946) 15.
[3] P. Goldsmith and J.V. Jelly Phil. Mag., 4 (1959) 836.
[4] L. Wartski et al., Appl. Phys., 46 (1975) 3644.
[5] J. Bosser et al., Nucl. Inst. Meth., A238 (1985) 45.
[6] V.E. Scarpine et al., IEEE Trans. Nucl. Sci., 51 (2004) 1529.
[7] K.H. Tanaka et al., KEK preprint 91-2.

BEAM INDUCED FLUORESCENCE (BIF) MONITOR FOR TRANSVERSE PROFILE DETERMINATION OF 5 TO 750 MeV/u HEAVY ION BEAMs *

F. Becker[1†], C. Andre[1], P. Forck[1], D.H.H. Hoffmann[1,2]
[1]Gesellschaft für Schwerionenforschung GSI, Darmstadt, Germany
[2]Technical University Darmstadt, Institut für Kernphysik, Darmstadt, Germany

Abstract

In the frame of the FAIR-project (Facility for Antiproton and Ion Research) at GSI, high intensity beams from protons to Uranium ions with energies ranging from 100 MeV/u to 30 GeV/u are foreseen [1]. Precise beam alignment in transport lines between the synchrotrons and in front of production targets is mandatory. Since the beam energy will be increased from todays 100 Joule to about 10^4 Joule per ion pulse, conventional intercepting beam diagnostics can not be used. For transverse profile determination a non-intercepting Beam Induced Fluorescence (BIF) monitor in residual nitrogen, using an image intensified CCD camera was investigated. The photon yield and background contribution were determined for different ion species, beam energies and N_2 pressures. The spectral response was mapped and associated with the N_2 transitions using narrowband interference filters. Profile distortions were quantified. Additionally, the appropriate layout for different diagnostic tasks is discussed.

THE BIF METHOD

As an alternative to the traditional SEM-Grids, the transverse beam profile in transport lines could be determined by observation of single fluorescence photons emitted by residual gas molecules. The related device is called **B**eam **I**nduced **F**luorescence (**BIF**) Monitor [2] as schematically shown in Fig. 1. When the beam collides with the residual gas molecules, some molecules are ionized remaining with a certain probability in an excited state. In a N_2 dominated residual gas composition, a strong fluorescence in the blue wavelength range 390 nm $< \lambda <$ 470 nm and a lifetime of about 60 ns is generated by a transition band to the

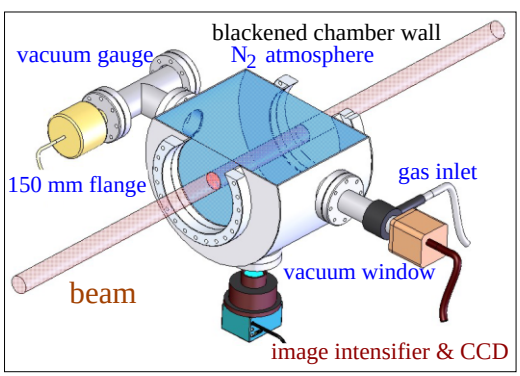

Figure 1: Scheme of a BIF-Monitor.

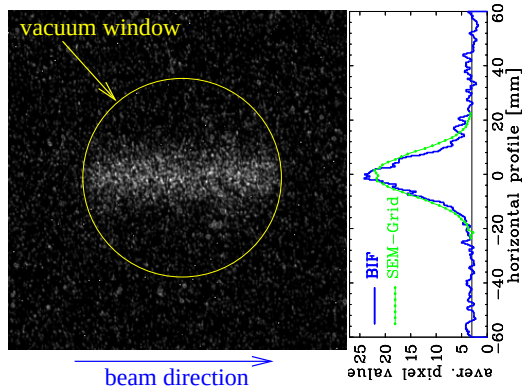

Figure 2: Image from a 1.5 μs long pulse of $2 \cdot 10^9$ Xe^{48+} at 200 MeV/u. The projected horizontal profile is compared to SEM-Grid data. The BIF data were recorded at $1 \cdot 10^{-3}$ mbar and averaged over 20 shots.

N_2^+ electronic ground state ($B^2\Sigma_u^+(v') \rightarrow X^2\Sigma_g^+(v'') + \gamma$, for vibrational levels v) [3]. 'Single-photon counting' was performed using a commercial image intensifier (Company Proxitronic), equipped with a double Micro-Channel Plate (MCP) for up to 10^6-fold photo-electron amplification. The light from the fast P46 phosphor screen with 300 ns decay time is taper-coupled to a digital CCD camera with a fire wire interface (Basler A311f). The device is mounted at a distance of 20 cm from the beam axis. A UV-transmitting quartz-lens with remote-controlled iris and focus and a focal length of 25 mm, leads to a resolution of 180 μm/pixel. In front of the lens a filter wheel equipped with 10 nm narrow band interference filters was installed in order to record spectral resolved beam profiles. The detailed description of the detection setup can be found in [4, 5].

During the last years the BIF method was applied successfully at the GSI heavy ion LINAC for various ion species and energies between 5 and 11.4 MeV/u [4]. In this paper its application for higher energies as extracted from the heavy ion synchrotron SIS18 is described. Beside the signal amplitude, the background contribution is of interest, due to the rising neutron production [6]. In order to cover the full range of aimed nitrogen pressures and beam energies, two different experimental areas were used. One is a LINAC-beamline for low energy (5 to 11.4 MeV/u) and low pressure investigation ($1 \cdot 10^{-6}$ to $1 \cdot 10^{-3}$ mbar). The other location is a high energy beam transport line (HEBT) behind SIS18. The BIF monitor was installed at a distance of 2.1 m from the beam dump and the corresponding part of the vacuum pipe was separated by 50 μm stainless steel vacuum windows to admit gas-pressures up to 1 mbar. This setup has been tested for Xe, Ta, U ions having energies be-

* Work supported by EU, project FP6-CARE-HIPPI
† frank.becker@gsi.de

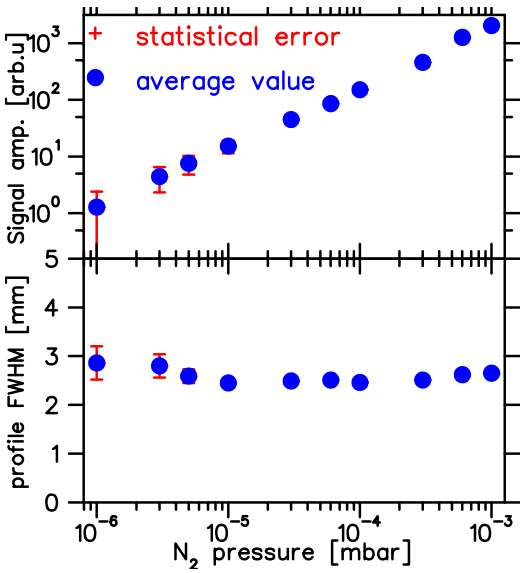

Figure 3: Total signal amplitude and measured profile width shown as a function of vacuum pressure, for a 5.5 ms long pulse of $4 \cdot 10^{10}$ Ni^{6+} at 4.54 MeV/u.

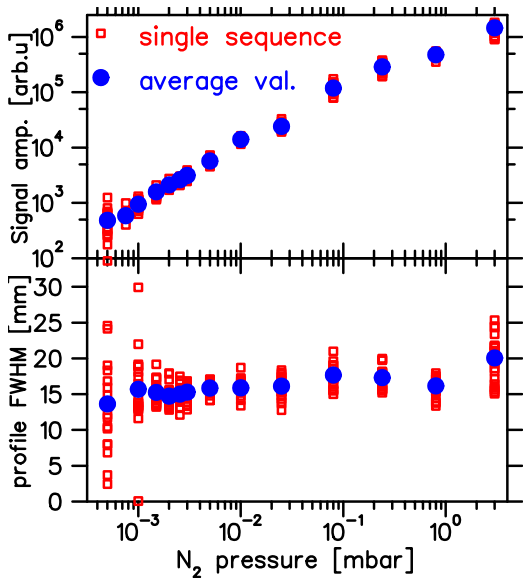

Figure 4: Total signal amplitude and measured profile width shown as a function of vacuum pressure, determined with the beam parameters of Figure 2.

tween 60 and 750 MeV/u in fast and slow extraction-mode. An example of a raw BIF image is shown in Fig. 2: The spots within the area of the vacuum window are created by single optical photons, their projection along the beam axis yield the horizontal profile. The good agreement with SEM-Grid measurements proves the applicability.

SIGNAL DEPENDENCE ON N_2 PRESSURE

The gas pressure acts as a free parameter to match the required photon statistics as the differential energy-loss, given by the Bethe-Bloch formula predicts a linear increase with the N_2 pressure. For a N_2 pressure rise over six orders of magnitude from 10^{-6} mbar to 1 mbar the experimental results confirm the prediction as the photon yield increases linearly, see Fig. 3 and Fig. 4, upper part. The second important result is that over this large pressure range the profile width remains constant within the error bars, see Fig. 3 and Fig. 4, lower part. This was not obvious due to the complex molecular physics involved in the excitation and fluorescence processes [3].

SIGNAL DEPENDENCE ON ENERGY

The BIF method should be applied for ion beam energies from 100 MeV/u up to 10 GeV/u as provided by FAIR. Tests were performed for slowly extracted U^{73+} ions with energies between 60 and 750 MeV/u. The uniformly distributed background was subtracted from the projected signal and the resulting amplitude is plotted in Fig. 5, top. Since the energy loss in matter is described by the Bethe-Bloch formula, parameters of the investigated ions were fitted to it, as shown in relative units in Fig. 5, top. The agreement with the measured signal amplitude is quite good, supporting the proportionality between energy loss and fluorescence yield.

The most critical issue for the BIF method is the background contribution. The background is uniformly distributed on the image and increases as a function of energy as summarized in Fig. 5, middle. The independence on the iris opening and vacuum pressure judges that the background is not caused by optical photons. Also charged particles can be excluded, due to their limited range in the surrounding material of the image intensifier.

Therefore neutrons are the key background-source, which was confirmed by dose measurements and related neutron generation and distribution calculations, see [6, 7]. Since signal to background ratio decreases about two orders of magnitude for the investigated beam energies, Fig. 5, bottom, background reduction has to be achieved by short gating times and an effective neutron shielding. In order to gain space for shielding material surrounding the image intensifier without loosing solid angle, a fiber optics bundle will be used. These commercial systems consist of 1 million optical fibers arranged to perform a 1:1 imaging.

SPECTRAL INVESTIGATION

Nitrogen molecules are excited to vibrational levels corresponding to characteristic line spectra. At low pressures we expected the major contribution by directly excited N_2^+ with its strongest lines at 391.4, 427.8 and 470.9 nm. In this case possible profile distortions might occur due to the displacement of the N_2^+-ion during the decay time of 60 ns [3]. To investigate this excitation process in detail, we mapped beam profiles trough 10 nm narrow band interference filters with central wavelengths λ_0 at 390, 430 and 470 nm and compared their amplitude respectively transition strength and width σ, see Table 1 column 2 to 4. The spectral distribution agrees with former experiments [3]. Moreover the profile width σ remains constant within the

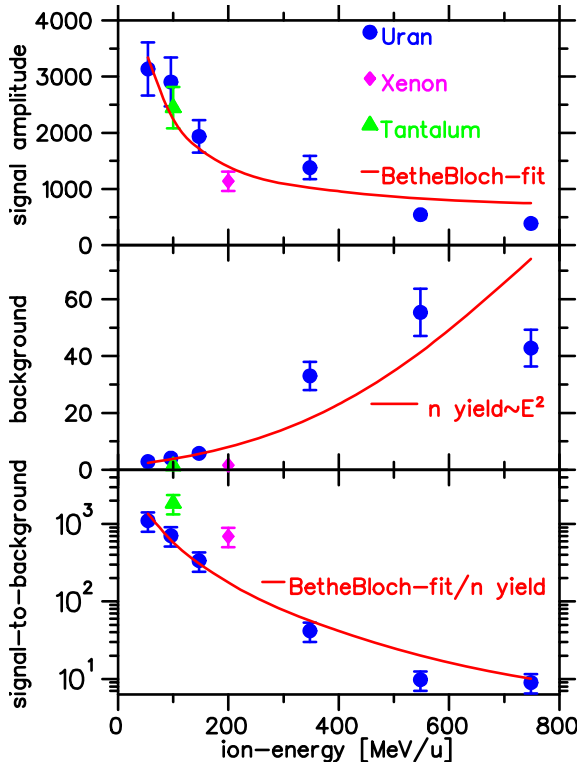

Figure 5: Total signal amplitude (top), background level (middle) and signal-to-background ratio (bottom) as a function of energy for the investigated ions. The amplitude for Xe and Ta were normalized by their charge and mass with respect to U. The background was normalized with respect to the mass only.

error bars for all pressures, beam energies and ion species. All measured beam profiles agree among each other and they are in accordance with standard SEM-grid profiles as exemplary shown in Figure 2.

For pressures $p > 1$ mbar, a 2-step excitation process becomes more important with an expected probability scaling $\propto p^2$. In the first step the ionizing collisions between the beam ions and N_2 cause free electrons. In the second step these electrons can excite N_2 from the ground state to triplet-states leading to fluorescence-light in the near UV ($337\,\text{nm} < \lambda < 358\,\text{nm}$). As the mean free path of electrons at 1 mbar is still about 1 mm, these electrons may travel a certain distance prior to the molecular excitation which leads to an additional profile distortion. We also recorded the strongest line of this 2-step process at $\lambda_0 =$ 337 nm and listed the results in Table 1, last column. As expected the profiles are significantly enlarged but as their contribution is below 1 %, it can be neglected for N_2 pressures below $1 \cdot 10^{-3}$ mbar. This again validates the results for the pressure variation, where the measured profile width does not change up to pressures of 1 mbar, see Fig. 3 and 4. To assure the reliability of measured beam profiles, spectral filters allow to select well known transitions, excluding unwanted 2-step processes. As for the FAIR-project [1] beam intensities will increase by a factor of 10^3 the required pressure bump will decrease by the same factor.

Table 1: Relative transition strength and corresponding profile width σ are given for different pressures and beam-parameter settings, $\delta\sigma \geq 0.5$ pixel.

λ_0 [nm]	390	430	470	337
trans.	N_2^+(0-0)	N_2^+(0-1)	N_2^+(0-2)	N_2 (0-0)
4.54 MeV/u Ni^{6+}, p =1·10^{-5}mbar				
str. [%]	85±12	10±2	4.8±.7	0.1±.01
σ [mm]	1.02(9)	0.91(9)	1.16(9)	1.6(1)
4.54 MeV/u Ni^{6+}, p =1·10^{-3}mbar				
str. [%]	87±13	12±2	1.3±.15	0.2±.02
σ [mm]	1.08(9)	0.99(9)	1.13(9)	1.99(9)
11.46 MeV/u Ni^{6+}, p =1·10^{-3}mbar				
str. [%]	86±13	13±2	1.3±.2	0.2±.02
σ [mm]	1.96(9)	1.95(9)	2.13(9)	2.3(2)
200 MeV/u Au^{64+}, p =5·10^{-2}mbar				
str. [%]	50±8	29±4.5	5±0,8	16±2.5

Even for high energy beam transfer conditions, according Fig. 2, N_2-pressures $\leq 1 \cdot 10^{-6}$ mbar will be sufficient and the N_2 (0-0) contribution can clearly be neglected.

CONCLUSION

The general functionality of BIF had been experimentally proven for the whole energy range from 5 to 750 MeV/u. Profile determination in single pass mode was performed for low energy LINAC conditions and HEBT conditions, even close to a beam dump. Careful investigation concerning signal strength, profile width, background distribution and the contribution of N_2 fluorescence levels have shown the BIF-monitors applicability for all available beam energies, ion species and required gas pressures. Future technical improvements will include chamber-geometry, lens-system, image intensifier, respectively the photo cathode. The major challenge will be the design and development of an effective neutron-shielding using a fiber optics bundle. Further investigation will concentrate on beam profile distortions due to the electrical field of high intensity ion beams. Also correction schemes based on precise modeling will be developed.

REFERENCES

[1] see e.g. P. Spiller et al.,*Proc. EPAC06* and FAIR Baseline Technical Report, Darmstadt, p. 1-39 (2006). http://www.gsi.de/fair/reports/btr.html

[2] see e.g. P. Forck et al., *Proc. DIPAC05*, p. 223, Lyon (2005) and references therein.

[3] R.H. Hughes et al., *Phys. Rev.* **123**, 2084 (1961), L.W. Dotchin et al., *J. Chem. Phys.* **59**, 3960 (1973).

[4] P. Forck, A. Bank, *Proc. EPAC 02*, Paris, p. 1885 (2002) and A. Bank, P. Forck, *Proc. DIPAC 03*, Mainz, p. 137 (2003).

[5] F. Becker, Diploma Thesis, TU Darmstadt (2006).

[6] F. Becker, C. Andre, P.Forck, *Proc. EPAC06*, p. 1013, Edinburgh (2006) and F. Becker, A. Hug, P. Forck, P. Ni, D. Varentsov, *Las. and Part. Beams*, **24**, p. 541-551, Cambridge (2006)

[7] T. Kurosawa et al., *Phys. Rev.* **C 62**, 044615 (2000).

FIRST VIBRATING WIRE MONITOR MEASUREMENTS OF A HARD X-RAY UNDULATOR BEAM AT THE ADVANCED PHOTON SOURCE*

Glenn Decker[1], Suren Arutunian[2], Manvel Mailian[2], Gerd Rosenbaum[3]
[1] Argonne National Laboratory, Argonne, IL 60439 USA
[2] Yerevan Physics Institute, Alikhanian Br. Str. 2, 375036 Yerevan, Armenia
[3] University of Georgia, Athens, GA 30602 USA

Abstract

The first hard x-ray flux measurements with a vibrating wire monitor (VWM) using the acoustic resonance frequencies of two vertically-offset horizontal stainless steel wires as temperature diagnostics were conducted at APS beamline 19-ID. Due to the high sensitivity of this technique, the studies were performed at extremely low power levels using radiation from a 3.3-cm-period permanent magnet hybrid undulator with a 5-mA electron beam at an energy of 7 GeV. The x-ray beam was filtered by transmission through 7 mm of beryllium placed in the photon beam path, assuring that only hard x-rays were detected. The particle beam was scanned through a range of 200 microradians using an asymmetric closed-orbit angle bump, producing two vertical photon beam profiles. The difference between processed wire signals provides a very sensitive measure of photon beam position. Details of the measurements will be given, along with a discussion of the limitations of the method and possible future research directions.

INTRODUCTION

The use of a vibrating wire monitor as a diagnostic for the determination of particle beam transverse profiles was suggested in 1999 [1] and first demonstrated using a 6-nA electron beam at an energy of 20 MeV in 2002 [2]. This work has expanded to measurements of ion beams and halo measurements of proton beams [3]. The VWM has shown sensitivity to temperature changes at the level of 0.001 K, making it well suited to beam halo measurements. In the case of charged particle beams, the electromagnetic interaction between beam and wire requires special care in the interpretation of the data.

At the Advanced Photon Source (APS), a significant effort has been put into the development of ultraviolet (UV) photon beam position monitors (BPMs) for both bending magnet and insertion device (ID) beamlines [4,5]. Use of these monitors has been instrumental in the achievement of sub-microradian-scale long-term pointing stability. Because they are sensitive to UV radiation, however, significant systematic errors caused by stray bending magnet radiation affect the signals for ID photon BPMs.

*Work supported by U.S. Department of Energy, Office of Science, Office of Basic Energy Sciences, under Contract No. DE-AC02-06CH11357, and by Bergoz Instrumentation, Saint Genis Pouilly, France.

To further improve ID beamline stability, an effort to develop beam position monitors that are sensitive only to hard x-rays was initiated in 2005. A spare vacuum vessel at APS beamline 19-ID was instrumented with water-cooled mounting plates, translation stages, and electrical feedthroughs, to test a number of different concepts [6,7]. This vacuum vessel is located approximately 52 meters downstream of an ID source point, allowing low power tests with hard x-ray beams to be conducted with sensitivity to extremely small steering errors, owing to the long lever arm. A rectangular 2.1 x 4.2 mm aperture is located approximately 1 meter upstream of the detector mount.

VWM DESIGN

Shown in Figure 1 is a diagram of the VWM as assembled for the APS experiment. Two horizontally-mounted 3.6-cm-long, 100-micron-diameter stainless steel wires with approximately 1.75-mm vertical separation were stretched across the beam, which passed through a 5-mm-diameter hole. Permanent magnets internal to the device introduce a magnetic field parallel to the beam on one side and antiparallel on the other. With this configuration, an AC flowing along each wire efficiently couples to the wire's second-harmonic acoustic resonance. A simple positive feedback circuit to excite the resonance together with a counting circuit was used to measure the resonance frequency. As the wire temperature changes, this frequency shifts as a consequence of the changing wire tension according to the formula

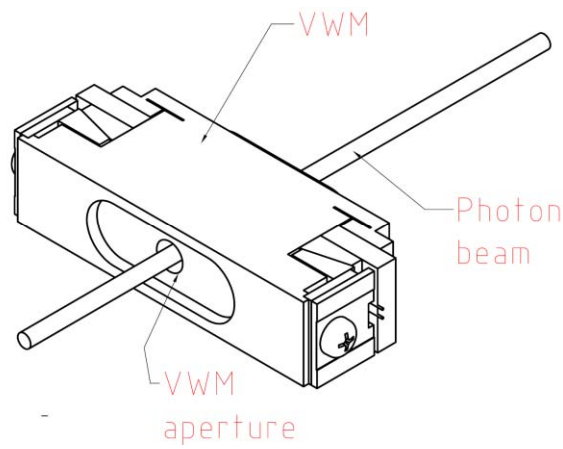

Figure 1. Vibrating wire monitor installed at APS beamline 19-ID.

$$\Delta T_{MAX} = -4\frac{f - f_0}{f_0 E \alpha_S}\sigma_0 \; ; with \;\; \sigma_0 = f_0^2 l^2 \rho \;\; , \qquad (1)$$

where ΔT_{MAX} is the maximum wire temperature assuming a triangular profile along the wire, f_0 is the initial wire resonance frequency, f is the frequency after heating, E is the modulus of elasticity (2e11 Pa for stainless steel), α_S is the thermal expansion coefficient (1.75e-5 K^{-1}), ρ is the density (8e3 kg/m^3), σ_0 is the initial wire stress, and l is the wire length (3.6 cm) [3]. This assumes that the wire support structure is held at fixed temperature. A small water temperature regulation system was used to keep the support temperature stable at the ±0.05 K level. With the detector installed in vacuum, the initial resonance frequencies f_0 of the two wires were approximately 4005 Hz (wire C) and 5149 Hz (wire D), respectively, a result of differing initial wire tension.

EXPERIMENTAL RESULTS

A total of 5 mA of electrons were stored in 12 equally-spaced bunches in the APS storage ring, using a square-response-matrix-orbit-correction algorithm with 80 narrow-band rf BPMs and 80 steering corrector magnets in both the horizontal and vertical planes to control the orbit. The BPMs chosen were mounted at opposite ends of the small-gap ID vacuum chambers, assuring the best resolution and control of the ID source points.

With the ID gap open, i.e., with zero field, UV bending magnet radiation originating from steering correctors located immediately upstream and downstream of the ID propagated down the ID beamline [5] and was detected by the wires as a decrease in frequency of 44 Hz (wire C) and 35 Hz (wire D), respectively. This followed a detailed alignment procedure to assure that both wires were symmetrically placed above and below the accelerator midplane with a clear line of sight to the source. After inserting a 1-mm-thick Beryllium filter upstream of the detector into the beam path, the wire temperatures returned to their closed-shutter values, indicating that only soft UV radiation was present. Using equation (1), the observed frequency shifts correspond to a temperature change of 2.2 K, showing the extreme sensitivity of this detector. The corrector peak field was 1.4 kG; however, they have an extensive fringe field, and this fringe field was the actual source of the observed radiation.

For the insertion device tests, a total of 7 mm of Beryllium was placed in the beam path, both to limit the power striking the wires and to assure that only hard x-rays were being detected. The insertion device used was a standard APS undulator A, capable of producing over 5 kW total power in a beam a few mm high and a couple of cm wide at 52 meters from the source with 100 mA of stored beam current. The field increases approximately exponentially as the ID gap is decreased to a minimum of 11 mm. The wire monitors first detected the beam at a gap of 80 mm, and registered a frequency shift of 1.5 / 2.0 kHz with a gap of 45 mm, which was the smallest used for fear of destroying the wires. Equation (1) indicates that the wire temperatures at this point had risen by somewhere in the range of 90 to 103 K; however the frequencies did not return to their original values when the shutter was closed. This seems to show that the wire properties were changed by exposure to the relatively high flux of hard x-rays. The new "cold" wire frequencies were 4161 Hz and 5223 Hz, somewhat higher than at the start. For the remainder of the measurements, a gap of 60 mm was chosen to give a modest temperature rise of 5.4 K when the photon shutter was opened. It should be noted that the initial alignment using corrector fringe field radiation did a good job of aligning the ID beam between the wires.

Shown in Figure 2 are data collected at a 1-Hz sample rate during a scan of the particle beam's vertical angle under the conditions just described.

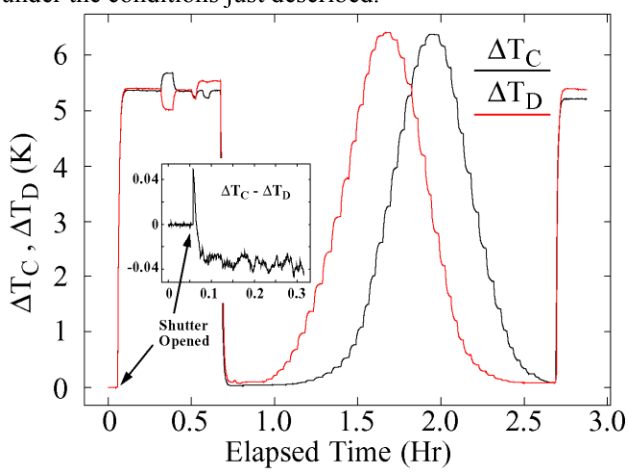

Figure 2. Data collected during vertical angle scan.

The initial frequencies f_0 for the two wires were determined with the shutter closed at the start of the scan. Using these values, the temperature changes ΔT_C and ΔT_D were determined using equation (1), and these values are plotted in Figure 2. After some initial steering tests, the beam was steered downward by 100 microradians (0.6 hours after shutter opening) and then steered upward in 5-microradian steps over the course of the next two hours, after which it was steered back to center. Because the primary mechanisms for cooling are conduction and radiation, it required about 3 minutes for the wire temperatures to achieve steady state following each steering change. During the two hours, the beam current decayed by about 3% from 4.53 to 4.38 mA.

A magnified view of the difference ΔT_C - ΔT_D is shown in the inset of Figure 2. With the shutter closed, the fluctuations fall in the range ±0.001 K, while after opening the shutter with the beam approximately centered, the fluctuations are significantly larger, most likely the result of real beam motion. At the detector location, this ±0.001 K translates into a noise floor near 0.5 microns p-p. Considering the 52 meter distance from the source, this translates into less than 10 nanoradians of p-p angular resolution, which is quite remarkable.

To process the data, it was subdivided into 43 separate files for each step and each segment was fit to a function of the form ΔT = Constant + Factor × exp(-Rate × Time) for each wire. The readbacks from the BPMs straddling the source were averaged for each segment, and an angle was computed from their difference. Multiplying this angle by the 52-meter source-detector distance resulted in an effective beam position value projected to the detector location. Because some segments of the exponential fit were essentially constant, they gave an inaccurate determination of the Rate, so a second pass of fitting was used, with the Rate constrained to equal the average value for all the good segments. A plot of Constant fit value vs. position then gives a good first-cut representation of the x-ray beam profile. The time constant = Rate^{-1} was 30.5 seconds and 30.9 seconds for wires C and D, respectively, using this method. The Constant vs. position data for each wire was then fit to a Gaussian to extract a centroid position and sigma. To extract thermal drift, the sum of the Constants for the two wires was fit to a constrained sum of Gaussians with an additive linear function of time representing the drift, using centroid and sigma values from the previous separate-Gaussian fit. This drift was then subtracted from the original Constant vs. position data, which then was normalized to the average beam current for the data set, producing a second-cut x-ray profile, corrected for thermal drift and beam current decay. The thermal drift amounted to a DC level shift of 0.01 K (relative to time zero of Figure 1) with 0.01 K / hour variation. While the linear thermal drift model is incorrect in detail, this approach at least gives some idea of the scale of the effect and is required prior to beam current normalization to achieve the best accuracy. The results are shown in Figure 3. The plot of ΔT_D was shifted by 1.730 mm in the lower plot, determined from the difference in centroid positions from the Gaussian fits. The wire separation measured later with a microscope was 1.717±.001 mm.

DISCUSSION

The above detailed analysis was conducted with the aim of determining the x-ray beam profile with the best accuracy possible. Insofar as the thermal drift of the two wires track each other and considering that the beam position is related to the temperature difference between the wires, this effect tends to cancel when using this device as a BPM. The observation that the DC baseline on the right-hand side of the profiles falls only to 0.03 K is simply an indication of the inaccuracy of the thermal drift compensation model chosen and does not directly impact the usefulness of this device as a BPM. At the very end of studies the photon shutter was closed, and both wires indicated that the ambient temperature had drifted up by 0.09 K over the 3.5-hour experiment duration. Unfortunately, there was also a difference of 0.008 K between the wires, which would translate directly into a 2-micron position measurement error given the parameters of the experiment. Whether there was a real temperature gradient across the device or a drift in the detection electronics is a subject for further study. Inclusion of additional well-shielded wires to measure local thermal drifts may be a solution.

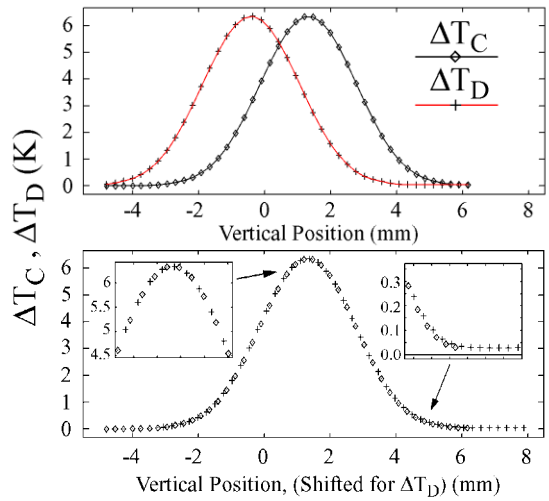

Figure 3. VWM data corrected for thermal drift and beam current decay. The two data sets are offset in the lower panel for direct comparison.

It is clear that the limitations of this device as tested are the slow response time and the power-handling capability. Some of these issues are discussed in a separate paper [8]. Given the extreme sensitivity of this device, one could consider placing it outside of vacuum to detect only very hard x-rays that penetrate the chamber at selected locations [9]. The addition of convective cooling would reduce the response time substantially albeit with reduced sensitivity. This would in addition reduce costs by a large factor. Incorporation of such a device into the design of water-cooled beamline apertures with judicious shielding – a so-called "smart aperture" – is another interesting concept. As a hard x-ray detector, the VWM concept shows a lot of promise due to its very high sensitivity and overall simplicity in both the mechanical design and front-end electronics.

REFERENCES

[1] S. Arutunian, et al., *Phys. Rev. ST Accel. Beams* **2**, 122801 (1999).
[2] S.G. Arutunian, N.M. Dobrovolosk, M.R. Mailian, and I.E. Vasiniuk, *Phys. Rev. ST Accel. Beams* **6**, 042801 (2003).
[3] S.G. Arutunian, M.R. Mailian, Kay Wittenburg, *Nucl. Instrum. Methods A* **572**, 1022-1032 (2007).
[4] G. Decker, O. Singh, PAC '01, Chicago, IL (2001).
[5] G. Decker, O. Singh, *Phys. Rev. ST Accel. Beams* **2**, 112801 (1999).
[6] R. Alkire, G. Rosenbaum, and G. Evans, *J. Synchrotron Rad.* **7**, 61-68 (2000).
[7] G. Decker, G. Rosenbaum, and O. Singh, BIW '06, Batavia, IL, AIP Conf. Proc. 868, 202-207 (2006).
[8] S. Arutunian et al., these proceeedings.
[9] B.K. Scheidt, DIPAC '05, Lyon, France (2005).

BUNCHED BEAM STOCHASTIC COOLING FOR RHIC*

J.M. Brennan+, M.Blaskiewicz, F. Severino,

Brookhaven National Lab 11973, U.S.A.

Abstract

Stochastic cooling is an effective and well-established accelerator technology for improving beam quality. However, stochastic cooling of high frequency bunched beam has always proved problematic. We have built a stochastic cooling system for heavy ions in RHIC that is used on bunched beam. The purpose is to counteract Intra-Beam Scattering and improve integrated luminosity. The chief technical challenge of bunched beam is the strong coherent frequency components in the beam that contaminate the Schottky spectrum. Technical solutions for overcoming this problem are described. Results from commissioning in one ring of RHIC are reported.

INTRODUCTION

Stochastic cooling is an effective and well-established accelerator technology for improving beam quality. However, stochastic cooling of high frequency bunched beam has always proved problematic due to strong coherent components in the Schottky spectra of bunched beam.[1] We have built a stochastic cooling system for RHIC employing specialized techniques to overcome the problem of coherent components. The system works in the 5-8 GHz band and cooling in the longitudinal plane. The kicker of the system is realized in an unusual way by creating the kick voltage with 16 high-Q cavities. Even though the bandwidths of the cavities are much smaller than their separation in frequency the effective bandwidth of the cooling system is sufficiently covered. This follows from the fact the beam bunches are 5 ns long and the separation between cavity frequencies is 200 MHz, that is; the reciprocal of the bunch length.[2] The high-Q cavities greatly reduce the microwave power needed to operate the system. The system was first tested with protons during the FY06 polarized proton run. In the FY07 gold-on-gold run the cooling system was commissioned and proved effective in reducing the beam loss rate and debunching during 5 hour stores.

BUNCHED BEAM COOLING

Coasting beam formulae can be used to calculate cooling rate for bunched beam if the number of particles is replaced by an effective number which is the number that would be in the ring if it were filled at density equal to bunch density. For RHIC this is about 2e12, and implies a cooling time of about one hour for a 5-8 GHz system. This is an adequate cooling rate to counteract Intra-Beam Scattering in RHIC. The key challenge of bunched beam cooling is to overcome the difficulties caused by the coherent components in the Schottky spectra. Figure 1 shows a spectrum with coherent components.

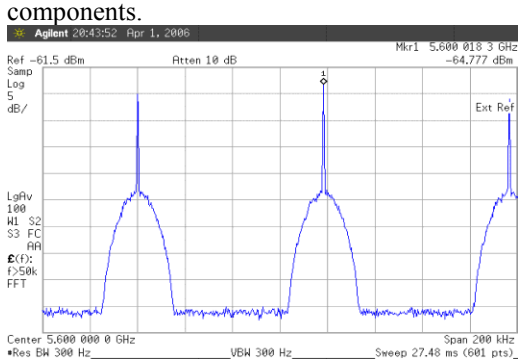

Figure 1 A Schottky spectrum showing coherent components.

Dealing with the Coherent Components

The true significance of the coherent components is not revealed in the frequency domain. However, their existence indicates that large instantaneous voltages are present in the time domain where they may easily overdrive active electronic components such as, low noise amplifiers, causing inter-modulation distortion which defeats the cooling loop. In order to reduce the peak voltages we employ the filter shown in figure 2, which is built from coaxial cables, cut in precise 5.000 ns intervals.

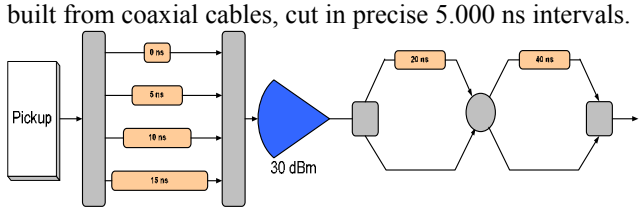

Figure 2 Coax filter used to reduce peak voltages from the pickup before the low noise amplifier and electrical to optical converter.

The filter repeats at reduced voltage the 5 ns beam pulse as shown in figure 3 and creates the frequency response shown in figure 4.

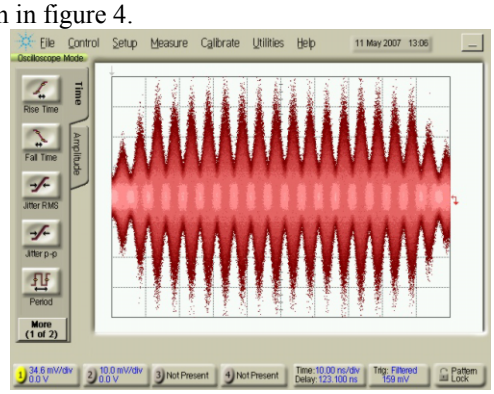

Figure 3, a time domain

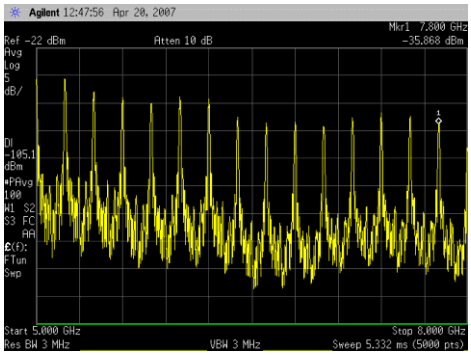

Figure 4 Frequency domain showing 16 lines between 5 to 8 GHz, spaced at 200 MHz.

The signal is sent from the pickup to the kicker via an AM modulated analogue fiber optic link of 6 microsecond length. We have found much better linearity in the link when the source DFB laser is modulated with an external electro-absorption modulator (PHOTONICSystems, inc.) compared to direct modulation of the laser current. Direct modulation causes excessive chirp for large signal, which degrades the signal because of the dispersion in the fiber, SMF28.

The Cooling Filter

For momentum cooling a correlator notch filter is employed to create the correct phase of the kick so as to correct the measured energy fluctuations. The filter essentially differentiates the pickup signal to extract the sign of the energy error from the deviation of the beam signal from the synchronous revolution frequency. The concept is shown schematically in figure 5.

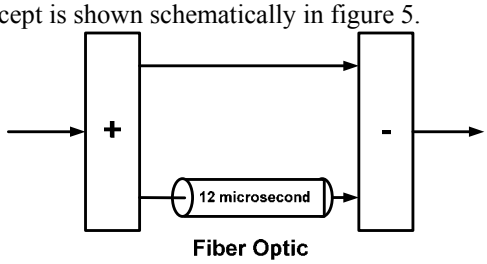

Figure 5. The concept of the notch cooling filter.

The notches it makes at revolution harmonics of the Schottky spectrum are seen in figure 6.

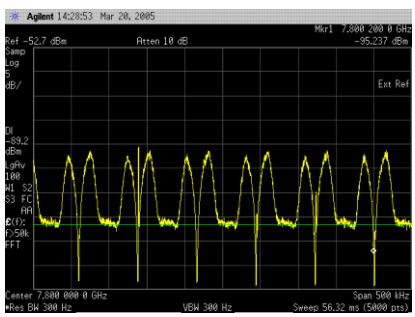

Figure 6. Notches made by the cooling filter.

From the system transfer function shown in figure 7 one sees that the real part (bottom display) changes sign at the revolution frequency (where the notch is). This causes the system to extract energy from the high energy particles and conversely.

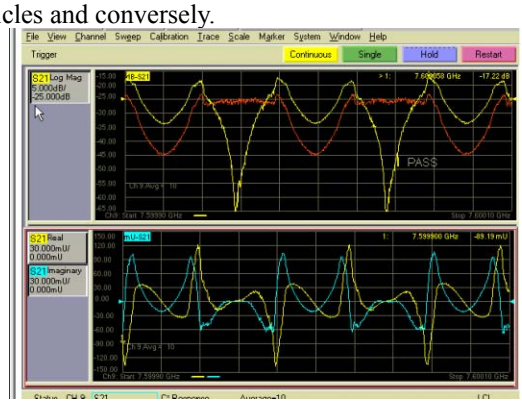

Figure 7. System open loop transfer function, including beam response. The real part is anti-symmetric about the revolution frequency.

Because the delay corresponding to one revolution period is 12.8 microseconds the filter must be realized with a fiber optic cable, in order to have constant frequency response across the 5 to 8 GHz band. The scheme for realizing the cooling filter is shown in figure 8. Matched pairs of photodiodes with >35 dB of CMR assure consistent notch depth across the band with no equalizer.

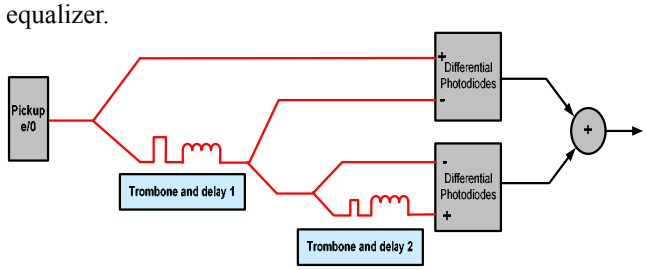

Figure 8 Realization of cooling filter. The four branches synthesize two filters in cascade.

Halo Cooling and the Two-turn Filter

The primary goal of the cooling system is to counteract IBS to prevent beam loss and debunching. This means that the most important particles to cool are those close to the separatrix. These particles have the greatest momentum offsets and are considered in the halo. A two-trun notch filter is used to concentrate the cooling power on the halo particles. The two-turn filter has a wider notch to exclude particles in core of the bunch and also to extend the momentum reach of the stable part of the cooling force. The cooling force from a one-trun filter (red) is compared to that from a two-turn filter in figure 9.

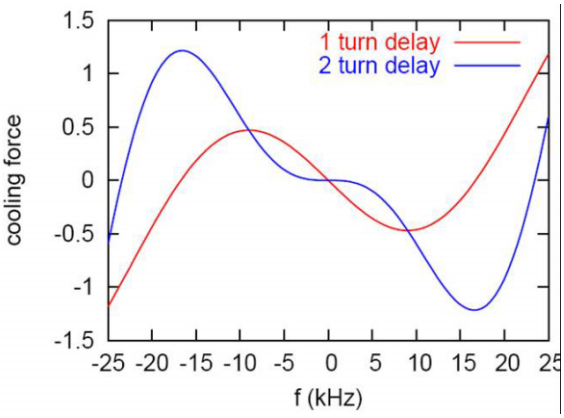

Figure 9 Cooling force for a one-turn(red) and two-turn filter

The two-turn filter is just two one-turn filters in cascade. One can see how the four branches of the filter in figure 8 constitute two filters cascaded filters by expanding the expression for the product of two one-turn filters.

$$S(\omega) = (1 - e^{i\omega T_{rev}})^2$$

$$= 1 - 2e^{i\omega T_{rev}} + e^{i\omega 2T_{rev}}$$

In figure 10 the response of the two-turn filter(red) is compared to that of the one-turn.

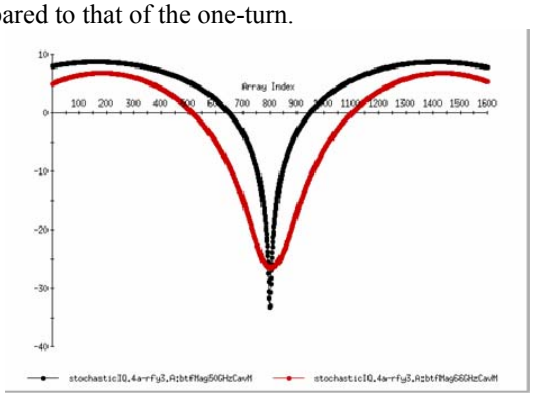

Figure 10 The response of the two-turn filter(red) compared to that of the one turn.

The Kicker Cavities

For optimal cooling of gold ions at 100 GeV/nucleon up to 250 keV must be supplied from the kicker each turn. Although the ion charge is 79 would would require, nevertheless, 3 kV. One could consider a 50 Ohm kicker to cover the 3 GHz span of the system but the required power would then be 90 kW. We synthesize the kick with much less power by employing high-Q cavities to generate the kicks. The cavity frequencies are spaced at 200 MHz intervals in the 5 to 8 GHz band of the system. One can think of these frequencies as a Fourier synthesis of the kick, and because the bunch is 5 ns long the basic harmonic of the series is 200 MHz. The bandwidth of the cavities is chosen to allow filling and emptying the cavities between each bunch. This determines the Q of the cavities and a high shunt impedance is achieved by using a four-cell TM_{010} like structures with R/Q ~ 100 Ohm. A computer model of a typical cavity is shown in figure 11. They have equal two coaxial ports, one for incoupling and one for an external load (located outside the vacuum) which sets the desired loaded Q. They have a 20 mm beam bore hole, which is unacceptablely small for the collider during filling and ramping. They are split on a vertical midplane and opened during filling and ramping and then closed for operation during the store.

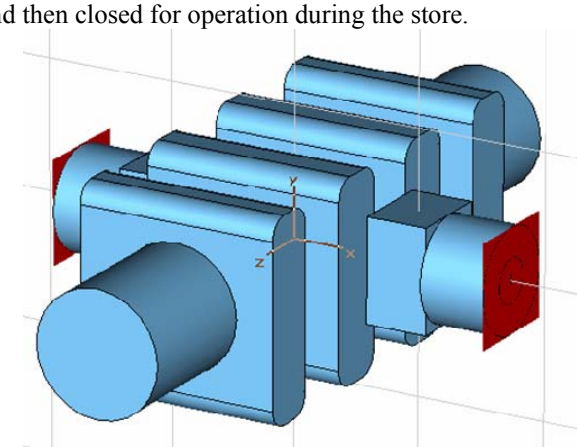

Figure 11 Computer model of a kicker cavity. It has a 20 mm bore and two matched coaxial coupling ports.

The Low-Level System

The low level system resembles a typical rf system with 16 cavities. Each cavity has an IQ modulator and rf power supply (40 Watts). The correct setting of IQs are obtained by measuring the system open loop response function including the beam(Beam Transfer Function). This is done automatically by the network analyzer. Software running in the embedded Window XP PC analyzes the BTF results and calculates settings for the IQs. This is done periodically (about every 15 minutes) during the store to adapt the system gain to cooling beam and to compensate drifts in phase. Phase drifts come about because of heating on the cavities and changes in the long fiber optic cables. The network analyzer also monitors the delays in the notch filters and sends commands to motorized optical trombones. Corrections are typically less than 1 ps in 15 minutes. The operation takes about one minute for a cavity and since the process takes one cavity out of 16 at a time off line, every 15 minutes, it amounts to a negligible degradation of the cooling. Figure 12 shows a typical system response function result.

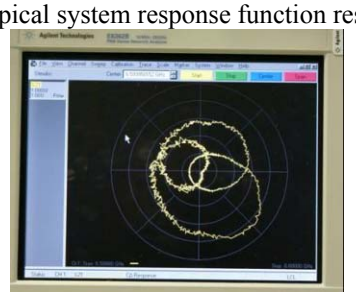

Figure 12 Cooling system response function including BTF and filters.

RESULTS

Tests with Protons

The first system tests were carried out with protons in the polarized proton run at RHIC of FY06. A special low intensity bunch was prepared as an analog to an ion bunch. This was the first successful test of bunched beam stochastic cooling and the results are published elsewhere.[3]

Operational Cooling of Gold Ions

The system was commissioned and made operational in the Yellow ring of RHIC in May FY07. Cooling showed the desired benefit of reducing losses and preventing debunching from the storage buckets. In fact, the losses in the Yellow ring when cooling became operational reached the level of "burn-off" losses. That is the situation when all the particles that are lost are consumed by collisions. Figure 13 shows the stored beam in RHIC for several stores of duration about 5 hours each. In the middle store stochastic cooling was used in the operation mode for the first time. It is clear that the loss rate in the Yellow ring was markedly reduced compared to previous stores and that of the Blue ring.

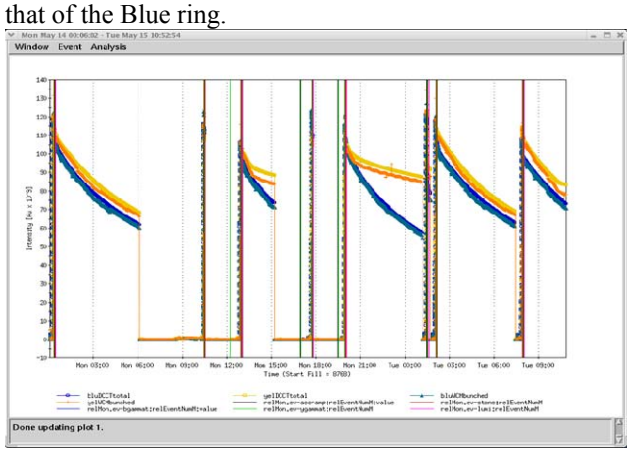

Figure 13 Five stores at RHIC, typically 5 hours. Stochastic cooling was operating for the middle two stores in the Yellow ring

It is apparent that the cooling not only stops losses but also cools the beam to a smaller emittance. In a preliminary test we cooled only half of the bunches in the ring by gating the system at the pickup. In this way we could compare the cooled and un-cooled under the same conditions. Figure 14 shows a scope trace of all the bunches after about 2 hours of cooling. It is clear that the cooled bunches attained higher peak current. Figure 15 compares a detailed view of the bunch profiles. Beam in the satellite 197 buckets is also cooled.

*Work performed under US DOE contract No DE-AC02-98CH1-886.
+ brennan@bnl.gov

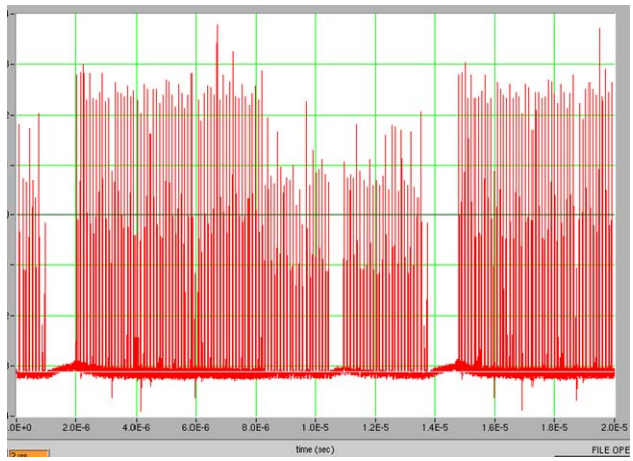

Figure 14 Wall current monitor of all 100 buches. The first 50 were cooled for two hours.

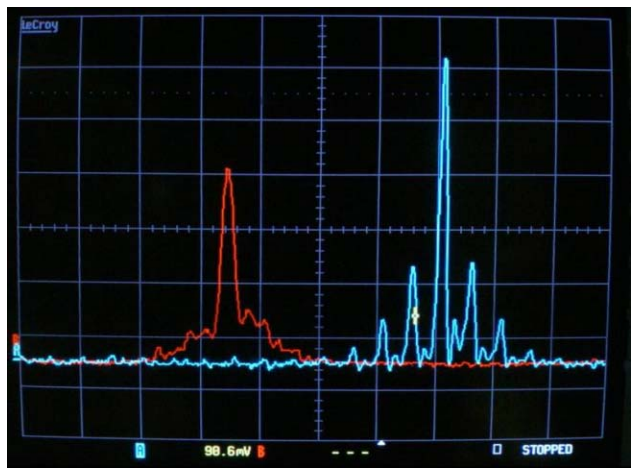

Figure 15 Expanded scale of bunch profiles comparing cooled (blue) and un-cooled bunches.

CONCLUSIONS

Bunched beam stochastic cooling at 100 GeV/nucleon has been achieved at RHIC. A cooling system is operational in the Yellow ring and cools Gold beam to reduce beam losses and reduce the longitudinal phase area of the bunches.

REFERENCES

1.G. Jackson et al, A Test of Bunched Beam Stochastic Cooling in the Tevatron Collider, PAC91, p1759

2. D. Boussard, Schottky Noise and Beam Transfer Function Diagnostics, The Queen's College, Oxford, England, 1985, CERN 87-03 Vol. II

3. M Blaskiewicz, J. M. Brennan and J. Wei, Stochastic Cooling in RHIC, II, EPAC06, Lucerne p2861

FEEDBACKS ON TUNE AND CHROMATICITY

Ralph J. Steinhagen (CERN, Geneva, Switzerland)

Abstract

Feedbacks on tune, coupling and chromaticity are becoming an integral part of safe and reliable accelerator operation. Tight tolerances on beam parameters typically constrain the allowed oscillation amplitudes to the micrometre range, leaving only a small margin for the transverse beam and momentum excitations required for tune and chromaticity measurements. This contribution presents an overview of these beam-based feedback systems, their architecture and design choices involved. It discusses performance limitations due to cross-constraints, non-linearities, the coupling between multiple nested loops, and the interdependence of beam parameters.

INTRODUCTION

The control of orbit and energy became de-facto standard as nearly all modern light sources, lepton and hadron colliders alike deploy at least fast orbit and energy feedbacks that minimise transverse beam movements, spurious dispersion by centreing the beam in the quadrupoles and maintain a stable vertical orbit inside the sextupoles that would otherwise give rise to emittance coupling. A summary and overview of beam stability requirements and stabilisation over a large range of accelerators can be found in [1–3].

Recent improvements in hadron colliders have led to significantly increased stored beam energies which require excellent control of particle losses inside a superconducting machine. Thus, most requirements on key beam parameters in superconducting hadron colliders strongly depend on the capability to control particle losses inside the accelerator. In the case of the LHC, the cleaning system has the tightest constraints on the orbit and requires a stability better than $25\,\mu\mathrm{m}$ during nominal operation at the location of the collimators which leaves only a small margin for beam excitation required for the measurement and control of tune and chromaticity [11].

Automated feedback control systems are usually not limited to the control of orbit and energy but are often complemented by tune, coupling and chromaticity feedbacks, which have become an increasingly important part of operation [4–6,9,10]. As for the orbit, the requirements on tune stability in superconducting hadron colliders is primarily given by the ability to control particle loss and the negligible synchrotron radiation damping. The usually large tune footprint makes it necessary to avoid up to the 12th order resonances [12]. The corresponding stability is usually in the order of $\delta Q \approx 10^{-3}$ and is similar to the one of B-factories as well as ramping synchrotron light sources, although the latter is due to performance rather than machine safety reasons. In addition, these machines have often quite demanding tune working points in the vicinity of the half-integer resonance, as these regions are able to accommodate the usually large footprints as well as mitigate the effect of beam-beam interactions and electron clouds that cause the large footprints in the first place (PEP-II [7]: $q_x = 0.505$ (LER) & $q_x = 0.503$ (HER); KEK-b [8]: $q_x = 0.504$ (LER) & $q_x = 0.510$ (HER)).

The decay and snapback phenomena, a particularity of superconducting magnets causes, in case of the LHC, a large chromaticity drift that if uncorrected is expected to exceed more than 100 units within a few hundred seconds after the start of the ramp [12]. Consequently, to guarantee the stability of multiple particles ensemble, the chromaticity should be controlled within $Q' \approx 2\pm1$. The LHC is thus the first accelerator that, in addition to orbit, energy, tune and coupling, may need to rely on an automated control of chromaticity for safe and reliable machine operation.

FEEDBACK CONTROL DESIGN

In case of low-order beam parameters – orbit, tune, coupling, chromaticity and energy – the effect of individual corrector circuits is, for most accelerators, sufficiently linear and can be cast into matrices. The parameter control in space domain establishes corrector circuit strengths that for steady-state perturbations minimises the residual measured parameter deviation. The control in space domain consists essentially of the inversion of the beam response matrices that relate the corrector circuit strength change to the given bean parameter. Singular-Value-Decomposition (SVD) is one of the most popular and widely used inversion algorithms ([1, 2]). Further information can be found in [3, 13, 14].

Time Domain

A simple loop block diagram consisting of a single-input-single-output (SISO) process $G(s)$ and controller $D(s)$ is shown in Figure 1.

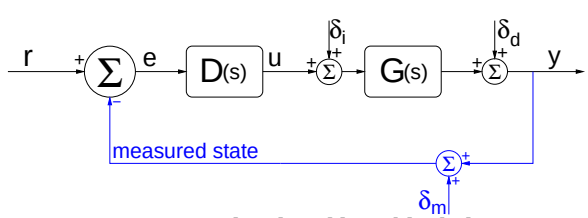

Figure 1: First order closed loop block diagram.

The stability and sensitivity to perturbations and noise is

defined by the following functions

$$T(s) := \frac{y}{r} = \frac{D(s)G(s)}{1+D(s)G(s)} \quad (1)$$

$$S_d(s) := \frac{y}{\delta_d} = \frac{1}{1+D(s)G(s)} \quad (2)$$

$$S_i(s) := \frac{y}{\delta_i} = \frac{G(s)}{1+D(s)G(s)} \quad (3)$$

$$S_u(s) := \frac{u}{\delta_d} = \frac{D(s)}{1+D(s)G(s)} \quad (4)$$

where $T(s)$ is the complementary (nominal) transfer function, $S_d(s)$ the *nominal sensitivity* defining the loop disturbance rejection, $S_i(s)$ the *input-disturbance sensitivity* and $S_u(s)$ the *control sensitivity*. The state variables are indicated in Figure 1. The sensitivity to measurement noise is equal to the nominal transfer function T_0.

Classic feedback designs rely on the discussion of denominator zeros in equation 1 and 2 while keeping constraints such as required bandwidth, minimisation of overshoot, limits on the maximum possible excitation signal and robustness with respect to model and measurement errors. For ideal processes, this yields adequate controller designs but often falls short in providing a simple comprehensive method for estimating and modifying the loop sensitivity (robustness) in the presence of process uncertainties, non-linearities and noise.

This paper focuses on Youla's affine parameterisation method for optimal controllers, which is based on the analytic process inversion, first introduced in [15]. For an open-loop stable process $G(s)$, the nominal closed-loop transfer function is stable if and only if $Q(s)$ is an arbitrary stable proper transfer function and $D(s)$ parameterised as:

$$D(s) = \frac{Q(s)}{1-Q(s)G(s)} \quad (5)$$

The stability of the closed loop system follows immediately out of the above definition if inserted into equations 1 to 4. The sensitivity functions in the $Q(s)$ form are given as:

$$T(s) = Q(s)G(s) \quad (6)$$

$$S_d(s) = 1-Q(s)G(s) \quad (7)$$

$$S_i(s) = (1-Q(s)G(s))G(s) \quad (8)$$

$$S_u(s) = Q(s) \quad (9)$$

Assuming $G(s)$ is stable, the only requirement for closed loop stability is for $Q(s)$ to be stable. The strength of this method is the explicit controller design with respect to required closed loop performance, as visible in equation 6, and required stability (equations 7 to 9). Equations 6 and 7 are complementary and illustrate the intrinsic limiting trade-off of feedbacks that either have a good disturbance rejection or are robust with respect to noise. The ultimate limit is thus defined rather by the bandwidth and noise performance of the corrector circuits and beam measurements than by the feedback loop design itself. Systematic and thorough analysis of involved beam instrumentation and corrector circuits are thus essential for achieving best beam parameter stabilisation.

First Order Example

The design formalism can be demonstrated using a simple first order system $G_0(s) = \frac{K_0}{\tau \cdot s+1}$ with open-loop gain K_0 and time constant τ. A common controller design ansatz is to write $Q(s)$ as

$$Q(s) = F_Q(s) \cdot G_0^i(s) \quad (10)$$

with $F_Q(s)$ a trade-off function and $G_0^i(s)$ the pseudo-inverse of the process. Since G_0 does not contain any instable zeros, the pseudo-inverse equals the inverse and is given by $G_0^i(s) := [G_0(s)]^{-1} = \frac{\tau \cdot s+1}{K_0}$. $Q(s)$. In order for $D(s)$ to be biproper, $F_Q(s)$ must have a degree of one and can be written as:

$$F_Q(s) = \frac{1}{\alpha s+1} \quad (11)$$

Inserting equation 10 into Youla's controller parameterisation equation 5 yields the following controller

$$D(s) = \frac{\tau}{K_0\alpha} + \frac{1}{K_0\alpha s} = K_p + K_i \cdot \frac{1}{s} \quad (12)$$

which shows a a simple PI controller structure with proportional gains K_p and integral gain K_i. Inserting equation 10 into equation 6 yields

$$T_0(s) = F_Q(s) \quad (13)$$

that the closed loop response is essentially determined by the choice of trade-off function $F_Q(s)$ and that the closed loop bandwidth is proportional to the parameter $1/\alpha$. This can be used to tune the closed loop between: high disturbance rejection but high sensitivity to measurement noise (small α) and low noise sensitivity but low disturbance rejection (large α) depending on the operational scenario. The maximum possible closed loop bandwidth is limited by the excitation, as described by equation 9. In case of power converters, for example, the excitation is limited by the maximum available voltage.

Non-linear Feedback Loops

The same method can be extended to open-loop instable and multi-input-multi-output (MIMO) systems [15]. Real life feedbacks may contain significant delays λ (due to e.g. data transmission, data processing etc.) and non-linearities $G_{NL}(s)$, due to e.g. saturation and rate limits of the corrector circuits' power supplies. The modified process can be written, for example as:

$$G(s) = G_0(s) \cdot e^{-\lambda s} G_{NL}(s) \quad (14)$$

Using the same pseudo-inverse $G_0^i(s)$ as for the above example and inserting equation 10 into equation 5 yields

a controller parameterisation $D_{NL}(s)$ including a classic Smith-Predictor and anti-windup paths, discussed in more detail in [16, 17]. Inserting equation 10 including the delay and non-linearities into equation 6 yields the following closed loop transfer function:

$$T(s) = F_Q(s) \cdot e^{-\lambda s} G_{NL}(s) \qquad (15)$$

Similar to the linear case discussed above, the closed loop is essentially defined by the function $F_Q(s)$ that within limits can be chosen arbitrarily based on the required disturbance rejection and robustness during possibly different operational scenarios (gain-scheduling). Further information and a review on Youla's parameterisation can be found in [17, 18].

APPLICATION TO PHASE-LOCKED-LOOP SYSTEM DESIGN

Beam-based feedbacks are ultimately limited by thermal drifts, noise and systematics of involved devices. A systematic and thorough analysis of involved beam instrumentation and corrector circuits is thus mandatory for achieving best beam parameter stabilisation.

The above principles can readily be applied to the design of a Phase-Locked-Loop (PLL) control system that continuously adjusts phase φ and frequency f_e of its reference exciter to match and thus to track changes of the betatron tunes. A classic application of PLL is to modulate the beam momentum using the RF frequency while tracking the tune. The modulation amplitude can be then be used to derive the linear machine chromaticity while the barycentre is a measure of the unperturbed tunes.

The tune resonance is described by a second order harmonic oscillator and thus the tune resonance is found once the the phase between excited and measured oscillation equals $\pi/2$. An exemplary PLL block diagram is shown in Figure 2.

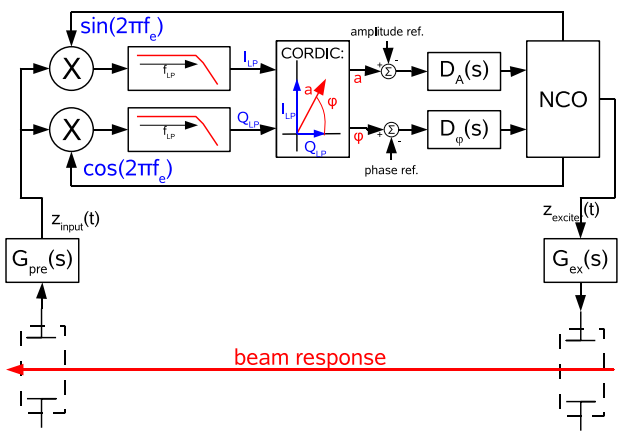

Figure 2: Phase-Locked-Loop Scheme

The system mixes the input with the sine and cosine component of the excitation signal followed by a low-pass filter in order to remove the $2\pi f_e$ frequency component that is created in the process of the mixing. The remaining signals are treated by a rectangular-to-polar (R2P) converter that separates signal phase and amplitude which can further be treated by two independent controller. In comparison to classic analogue phase detectors, this scheme provides a twice as large dynamic range for the phase and a true decoupling from the amplitude which proves to be advantageous in situations when phase and amplitude change at the same time. The actual control input $\Delta\varphi$ is shifted by $pi/2$ to zero in order to obtain a bipolar signal around the tune resonance. Negative phases thus indicate that the excitation frequency is below the tune resonance, and positive phases the opposite. The real implementation requires further compensation for other non-beam related contributions to the measured phase shift such as constant lag due to data processing, cables transmission delays, analogue pre-filters $G_{pre}(s)$ suppressing dominant harmonics (e.g. revolution frequency) and response $G_{ex}(s)$ of the beam exciter itself.

In this representation, the PLL phase control loop dynamics and its design is reduced to a simple first order system with the open loop gain K_0 given by the slope of the phase response at the location of the tune, and the inverse time constant τ by the bandwidth of the low-pass filter. The optimal controller $D_\varphi(s)$ is obtained according to the first order system discussed above.

CROSS-DEPENDABILITY AND CONSTRAINTS

In many accelerators, beam-based feedbacks are usually established and designed one by one. For robust control it is necessary to address possible cross-constraints, cross-talk and coupling between several simultaneous and possibly nested loops already in the design stage.

Betatron-Coupling

In a strict sense, the tune PLL measures eigenmodes rather than the actual tune. In the presence of close tune working points and strong global coupling these eigenmodes may be rotated with respect to the (true) unperturbed tunes. Assuming that the coupling sources are weak and globally distributed, the eigenmodes Q_1 and Q_2 are given by

$$Q_{1,2} = \frac{1}{2}\left(q_x + q_y \pm \sqrt{\Delta^2 + |C^-|^2}\right) \qquad (16)$$

with $\Delta = |q_x - q_y|$ being the unperturbed tune-split and C^- the complex coupling parameter. A direct use of the tune eigenmodes may break any tune feedback loop once the eigenmodes are rotated by $\pi/2$ with respect to the real tune. Thus it was recognised that under above conditions a robust tune feedback loop also requires the control of coupling itself [20]. Further details on this scheme and experimental results can be found in [20].

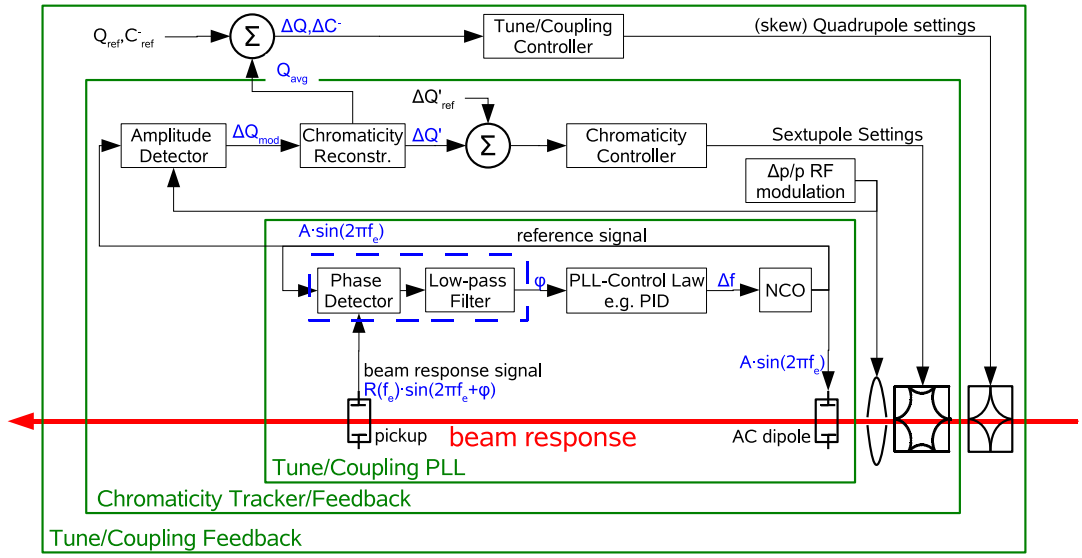

Figure 3: Nested loop scheme required for a coherent control of tune, coupling and chromaticity.

Inter-Loop Dependencies

The LHC, for example, requires a simultaneous control of orbit, tune, coupling, chromaticity and energy. The tightest constraints derives from the LHC collimation system that limits the possible relative momentum modulation, due to aperture constraints and dispersion, to a few $\frac{\Delta p}{p} \approx 10^{-5}$ only. With the requested nominal chromaticity resolution and stability of one unit, the tune changes are minuscule. In order to reflect these constraints in the overall loop design, the following nested control scheme for chromaticity, tune and coupling, shown in Figure 3, is foreseen for the LHC. The tune PLL is the inner-most loop measuring the global tunes and coupling parameters. The loop is first nested within the loop that measures and controls the chromaticity and is then surrounded by the feedback loop controlling the global tunes and coupling. The given hierarchy is based on the fact that the decoupling is obtained by choosing gradually reduced bandwidths for the tune PLL ($f_{bw} \approx 8\,\mathrm{Hz}$), chromaticity ($f_{bw} \approx 1\,\mathrm{Hz}$) and tune feedback ($f_{bw} < 1\,\mathrm{Hz}$). This nesting hierarchy is required particularly to eliminate the cross-talk between tune and chromaticity feedback, as the tune feedback would otherwise minimise the momentum-driven modulation as well as tune modulation and thus compromise the chromaticity measurement.

In addition, cross-talk is introduced between the chromaticity and orbit/energy feedback through the dispersion orbit that is driven by the momentum modulation required by the chromaticity feedback. In order to minimise this cross-dependence, the foreseen LHC orbit feedback filters and separates the dispersion orbit from the measured closed orbit prior to performing any orbit correction.

The required effective correction rate (1 unit per second) and resolution (1 unit) makes the LHC chromaticity feedback one of the most demanding beam-based feedbacks, requires further research and development.

Dependence on Tune Width

As described above, most classic tune PLL implementations assume a constant open loop gain K_0 that depends on the angle of the phase slope at the location of the tune resonance ([4,5,9,10]). Due to varying chromaticity, amplitude detuning, beam-beam, electron cloud, impedance and other effects, the tune width, thus the phase slope and K_0 may change. In this case the optimal controller parameter become functions of, for example, chromaticity itself. Using linear control design only, this cross-dependence implies either a controller design that is optimal for large chromaticities, which becomes sensitive to noise and instable for low values of chromaticity, or a controller design that is optimal for small chromaticities but lags behind the real tune for large values of chromaticity [21][1].

Non-Tune Resonances

Another effect that can break and compromise the proper function of the PLL loop is in the presence of strong resonances other than the tune such as synchrotron sidebands or synchro-betatron resonances. These add π phase advance transitions that due to the phase detector's 2π wrapping property creates several zero phase locations to which the tune PLL can lock onto. Using the Hilbert transform on can show for a minimum-phase system that the PLL essentially locks on the largest peak within the bandwidth. A narrowband excitation signal close to, for example, a synchrotron sideband will thus always cause a lock onto the same resonance. The spurious tune locking can be mitigated by increasing the excitation bandwidth prior to reaching the desired lock condition. This can be done using a chirped excitation and setting the initial PLL working point close to the tune, by adding additional exciter ([10]) or by largely

[1]The effect can be mitigated by stabilising the variation in the first place, which in a way resembles a 'chicken-egg' situation: one needs to stabilise the chromaticity for a stable tune width and thus PLL, while the PLL is needed to measure the chromaticity in the first place.

increasing the closed loop bandwidth to create additional jitter on the excitation frequency. The additional jitter increases the effective sampling range ideally to cover more than one synchrotron resonance. Once the loop is locked, the bandwidth could be reduced in order to improve the tracking stability and to reduce the bleed-through of phase contribution of neighbouring resonances.

LOCKING ON COUPLED BUNCH MODES

A typical cross-dependency is intrinsic to the stability requirements on orbit and tune: though tight constraints on orbit excursion to micrometre level are beneficial to minimise feed-down effects and beam life-time, it also imposes constraints on other feedbacks such as tune and chromaticity, the measurements of which rely on transverse excitations and momentum modulation. For the LHC the tune and coupling PLL operates with transverse excitation levels below $1\ \mu\mathrm{m}$ within the noise level and thus further minimises the cross between PLL and fast transverse damper. However, since the PLL operates within the 'noise floor' of the transverse damper feedback system, it does not benefit from the suppression of coupled bunch modes, which introduce additional resonance lines in the tune spectrum that the PLL can potentially lock onto. This issue is usually addressed by so-called *pilot* or *sacrificial* bunches usually in the beginning of a bunch train, which are excluded by the transverse feedback and explicitly selected for PLL operation.

CONCLUSIONS

Youla's affine parameterisation provides a simple yet powerful design tool for optimal adaptive non-linear control of these feedbacks. Its strength is the explicit controller representation that enables an un-obscured feedback design with respect to closed loop robustness (noise insensitivity) and steering precision.

Feedbacks are commonly deployed as an ensemble and it is thus necessary to reflect this in the early design stage in order to minimise cross-dependences and coupling of multiple simultaneous nested loops and thus cross-talk in between them. Possible decoupling techniques involve orthogonalisation of the feedback parameter space, separation in amplitude or by choosing different bandwidths for each individual feedback loop.

ACKNOWLEDGEMENTS

The author gratefully acknowledges contributions from many colleagues!

REFERENCES

[1] PSI, Proceeding of "3rd International Workshop on Beam Orbit stabilization", 2004, http://iwbs2004.web.psi.ch/

[2] M. Böge, "Achieving Sub-micron Stability in Light Sources", EPAC'04, Lucerne, Switzerland, 2004

[3] R.J. Steinhagen, "Real-Time Feedback on Beam Paramters", APAC'07, Indore, India, 2007

[4] O. Berrig et al., "The Q-Loop: A Function Driven Feedback System for the Betatron Tunes During the LEP Energy Ramp",CERN SL-98-039, 1998

[5] A.Fisher et al., "Tune Feedback in PEP-II",SLAC-PUB-10230, 2003

[6] A. Camiel et. al., "Tune Feedback System at ELETTRA", EPAC'94, London, England, 1994

[7] J. Seemann et al., "Achieving a Luminosity of 1034/cm2/s in the PEP-II B-factory", EPAC'06, Edinburgh, Scotland, 2006

[8] "KEKB 2005 Annual Report", http://www-kekb.kek.jp/Publication/KEK_Annual_Report/AR2006.pdf

[9] P. Cameron et al., "Measuring Chromaticity Along the Ramp Using the PLL Tune-Meter in RHIC", EPAC'02, Paris, 2002

[10] C.Y. Tan, "The Tevatron Tune Tracker PLL", FERMILAB-TM-2275-AD

[11] R. Assmann, "Collimation and Cleaning: Could this limit the LHC Performance?", CERN, Chamonix XII, 2003

[12] S. Fartoukh, O. Brüning, "Field Quality Specification for the LHC Main Dipole Magnets", LHC Project Report 501

[13] G. Golub and C. Reinsch, "Handbook for automatic computation II, Linear Algebra", Springer, NY, 1971

[14] K.G.J. Jacobi, "Über ein leichtes Verfahren, die in der Theorie der Säcularstörungen [..]", Crelle's Journal, 1846, 30 p. 51-94, 97-144

[15] D. C. Youla et al., "Modern Wiener-Hopf Design of Optimal Controllers", IEEE Trans. on Automatic Control,1976, Vol. 21-1,pp. 3-13 & 319-338

[16] O. Smith, "Feedback Control Systems", McGraw-Hill, 1958

[17] Goodwin, Graebe, Salgado, "Control System Design", Prentice Hall, 2000

[18] B. Anderson, "From Youla-Kucera to Identification, Adaptive and Non-linear Control", Automatica, 1998, Vol. 34, No. 12, pp. 1485-1506

[19] M.Gasior, R.Jones, "The principle and first results of betatron tune measurement by direct diode detection", CERN-LHC-Project-Report-853

[20] R. Jones et al., "Towards a Robust Phase Locked Loop Tune Feedback System", DIPAC'05, Lyon, France, 2005

[21] R.J. Steinhagen et al., "Influence of Varying Chromaticity on Robustness of the LHC Tune PLL and its Application for Continuous Chromaticity Measurement.", tbp. at PAC'07, 2007

BEAM DIAGNOSTIC FEATURES OF THE ESRF MULTIBUNCH FEEDBACK

Jean Marc Koch, Graham Naylor, Eric Plouviez, Francis Epaud (ESRF, Grenoble)

Abstract

The ESRF storage ring is now equipped with a set of multibunch feedback systems. The main goal of the implementation of these systems is to prevent longitudinal and transverse instabilities. However, besides this main function, these systems provide a powerful diagnostic to study the longitudinal and transverse beam dynamics and document operation problems.

In this paper we give a short overview of these feedback systems and describe with more details their diagnostic function.

INTRODUCTION

The first motivation of this project was to allow the storage of 300mA with a uniform filling of the buckets of the ESRF ring, instead of the 200mA that we are presently able to store, with the help of a longitudinal feedback. The present limitation is due to the excitation of longitudinal coupled bunch instabilities by higher order modes (HOM) of our RF cavities. We also started in parallel the implementation of a transverse feedback; the additional work to design and implement transverse feedback was moderate; it would allow us to test new machine tunings while studying new modes of operation (16 bunch filling with topping up for instance) or to help stabilise the 300mA current, whose storage was made possible by the longitudinal feedback. It would also be a very powerful diagnostic for transverse studies. Both feedback systems are now meeting our expectation, and allowed us to store, with a uniform filling pattern, 300mA thanks to the longitudinal system and to reduce the horizontal and vertical chromaticity down to zero while storing 200mA thanks to the transverse systems.

LONGITUDINAL FEEDBACK DESIGN

We chose the now classical approach of detecting every turn the variation of the phase of each bunch with respect to its equilibrium phase, to derive from this phase deviation an energy correction to apply to the beam, and to produce this correction using a longitudinal kicker [1].

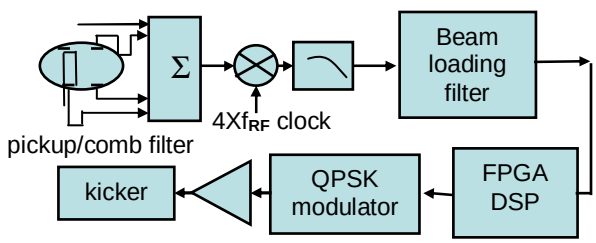

Figure 1: Layout of the ESRF longitudinal feedback .

We paid a lot of attention to achieve the best possible resolution in the phase measurement in order to reduce the maximum required kicker strength.

Kicker Design

Our kicker is a low Q pill box cavity following the deisign used at INFN Frascati[1]. With such a cavity we are able to produce a 600V kick using a 200W RF amplifier. To drive this cavity we are using the QPSK modulator scheme developed for the PEP longitudinal feedback [2]

.

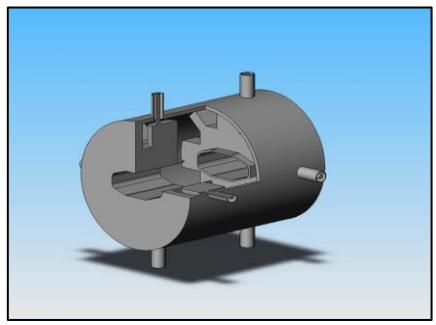

Figure 2: Longitudinal kicker shape.

Signal Processing Principle

We detect the beam signal using a set of 4 capacitive pickups. We combine the pickups signals with cables of different lengths to obtain a comb filter selecting a bandwidth of 352MHz around 1.4GHz (four time our RF frequency of 352.2MHz). We use a RF mixer as a phase detector (see figure 1); the output of the mixer is amplified to match the input range of the 14bit ADC of the FPGA DSP board resulting in the resolution detailed in the table 1.

Table 1: Phase Detection Resolution

Phase detector sensitivity (RF mixer)	≈ 6mV /°
Noise (Z_0 =50Ω, BW =176 MHz, N=6dB)	12µV rms
Phase detector turn by turn resolution δϕ	2 10^{-3}°=4fs
usable range (14 bit ADC, LSB = δϕ)	+/- 32ps

In our storage ring, the ratio between the energy and time amplitude of a longitudinal oscillation is 0.4KeV/fs; so our time resolution of 4fs is equivalent to an energy resolution of 1.6KeV. For each bunch, we derive the correction signal from the error signal by averaging over 9 to 11 turns, followed by a 16 tap FIR; the result is a 2 KHz bandwith bandpass filtering around the synchrotron sideband frequency plus a π/4 phase shift. This phase shift

is equivalent to the derivative needed to turn a phase error signal into an energy kick correction signal [3].

TRANSVERSE FEEDBACK DESIGN

Feedback Layout

There are 2 separate systems for the vertical and horizontal plane. The layout of the transverse feedback is shown in figure 2.

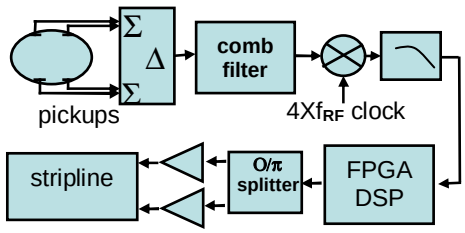

Figure 3: Layout of a transverse feedback system.

The beam signal pickups are 11 mm diameter capacitive electrodes located in high beta H and V locations (36m for both plane). The RF front end detects the position using a synchronous detection of the difference signal of the BPM pick up signals. We perform the detection on the 4th harmonic of the RF frequency in order to increase the sensitivity and to ease the filtering of the 0 to 176 MHz base band signal from the RF clock spurious signal. We use strip line kickers to apply the correction kicks. Each blade of the strip line is fed with a 100W/200MHz BW solid state power amplifier.

Signal Processing Principle

For the transverse feedback we make the same derivative/phase shift approximation as for the longitudinal feedback, but the phase shift between the error and correction signals will also be function of the betatron phase shift between the BPM and the transverse kicker; we use an 8 taps FIR in the vertical plane and a 7 taps FIR in the horizontal plane, without decimation.

Table 1: Transverse Detection Resolution

Feedback parameters	*vertical*	*horizontal*
Measurement range	+/-.4mm	+/-1.5mm
Resolution at 200mA	0.7µm	0.7µm
Kick strength per turn	0.3 10^{-6} rd	0.6 10^{-6} rd
Min. damping time τ_{min}	75µs	300µs
Added noise for $\tau=\tau_{min}$	0.15µm	0.07µm

DIGITAL SIGNAL PROCESSING

DSP Platform

Due to the high resolution requested for the error signal measurement of both longitudinal and transverse systems, we decided to perform this data acquisition without any under sampling ie with a 352.2 MHz sampling and processing rate. Such a processing rate is only achievable if we use a FPGA processor. After considering the different platforms and programming environment potentially adequate for our project, we went for the following solution: we use a special development of the *Libera* bunch signal processor developed by *I-Ttech* for the error signal acquisition, signal processing and correction signal generation. The main feature of this product are: up to 500 Msps ADC and DAC sampling rate with 14bits resolution, *Virtex II pro* FPGA with 64 Mbits of DDRAM for data logging.

Programming Environment

We wanted to be able to reprogram flexibly by our self the details of the feedback algorithm and we could not rely on a dedicated expert in FPGA programming for this project, therefore we specified that the *System Generator* programming environment should be available for the *Libera* platform. *System Generator* is a graphical programming environment developed by *Xilinx* and the *MathWorks* which allow defining and validating a processing algorithm at the bit and sample level using a library of *Matlab/Simulink* models provided by *Xilinx*. The availability of this kind of programming environment is one of the reasons for the relatively short time that was needed for the coding and testing of the feedback algorithms on the FPGA during this project.

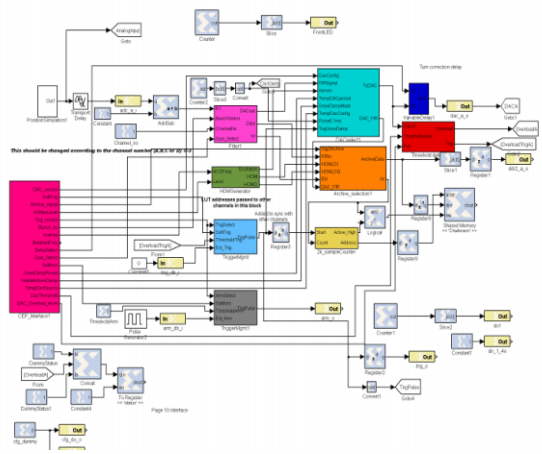

Figure 4: Development of diagnostic facilities on the FPGA using Simulink.

Bunch by bunch feedback algorithms are now relatively standards so it would have been possible to get a totally turn key feedback system without the *System generator* environment. However, it is very convenient to have, in addition to the feedback loop, several diagnostics function which are less standard, such as the open loop analysis tools, grow damp measurement, mode by mode or bunch by bunch tune measurement … These functionalities are more difficult to specify in advance to a subcontractor; downloading and processing the bunch by bunch /turn by turn DDRAM data is also very inefficient except for the purpose of post mortem analysis of unexpected events.

Performing pre processing in the FPGA to reduce the data rate is a good solution, using a DDC algorithm for instance. The availability of the *Simulink/System Generator* environment proved especially powerful in this respect.

Data Handling

A Tango device server has been written to load the main parameters of the data processing such as mode number, tune frequency offset, gain etc., and to download the data buffer generated by the FPGA processing;

Graphical Control Application

A graphical user interface has been developed using *Matlab* in order to test the operation of the feedback and to launch the various diagnostic routines implemented on the FPGA, as well as to perform further post processing. The *Matlab* scripts control the FPGA using the device server commands.

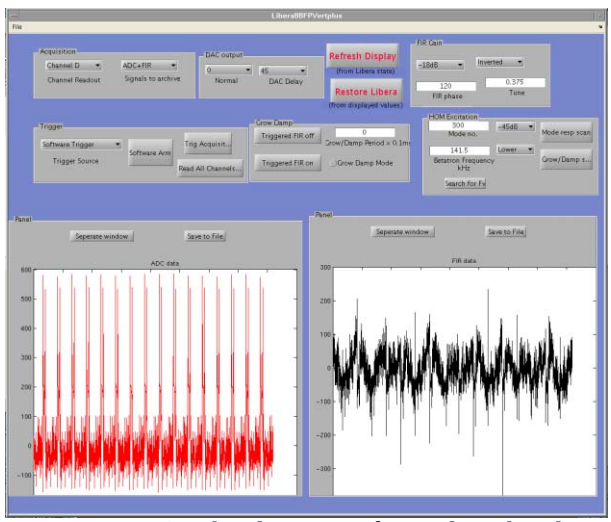

Figure 5: Test Graphical user interface to launch utilities.

Measurement of Open Loop Characteristics

The stability of the feedback loop for all modes is verified by exciting the beam at each mode frequency and measuring the amplitude and phase response of the open loop:

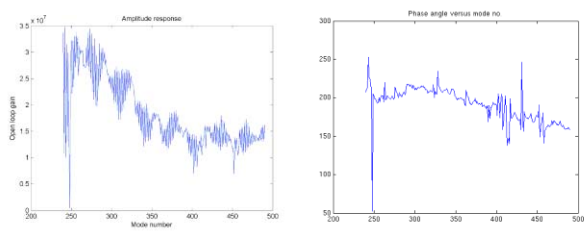

Figure 6: Variation in loop gain (left) and open loop phase response (right) as a function of mode no. (Longitudinal feedback).

Grow Damp Measurements

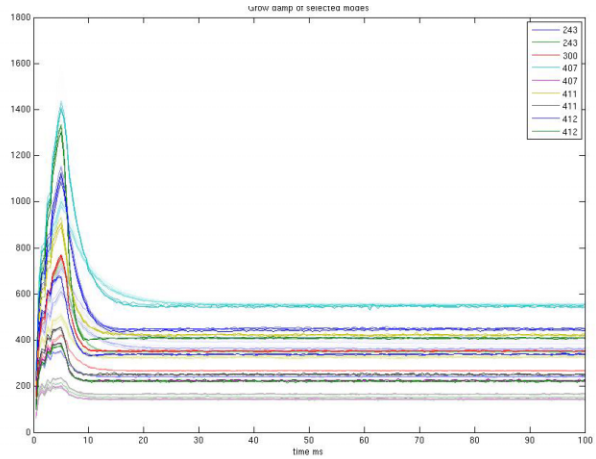

Figure 7: Layout of a transverse feedback system.

The control application is able to configure the feedback operation to couple artificial HOM excitations in the case of longitudinal feedback loop and momentarily open the loop so as to measure the growth rate and damping rate of individual modes.

Future Developments

We are now planning to implement on the transverse system a tune monitor, and some instability interlock functions.

CONCLUSION

The implementation of a bunch by bunch feedback used to be a very challenging task. It is now a well proven technique thanks to the experience gained on feedback systems implemented on many machines during the last 10 years. In addition, thanks to the availability of fast and accurate ADC and DAC, powerful DSP using an FPGA, and a user friendly programming environment, it proved to be a relatively straightforward piece of equipment to design and implement. The diagnostics functions that can be implemented -thanks to the processing power of the FPGA and the ease of programming offered by modern development tools, are also a big asset of our system.

REFERENCES

[1] A. Ghigo et als, “Kickers and power amplifiers for the DAϕNE bunch by bunch longitudinal feedback system ”, EPAC 96, Sitges, June 1996

[2] A. Young, J. Fox, D. Teytelman, VXI based multibunch detector and QPSK modulator for the PEP-II/ALS/DAϕNE longitudinal feedback system, Proc PAC 97,Vancouver, pp2368-2370

[3] E. Plouviez et als, “ Broadband Bunch by Bunch Feedback for the ESRF Using a Single High Resolution and Fast Sampling FPGA DSP”,EPAC 06, Edimburg, June 2006

A FIBER PROFILE MONITOR FOR LOW BEAM INTENSITIES*

G. R. Tassotto†, H. Nguyen, G. Sellberg, D. Schoo, FNAL, Batavia, IL 60510, USA

Abstract

A scintillating Fiber Profile Monitor (FPM) has been prototyped, built and tested for the new low intensity Meson Test (M-Test) beamline at Fermilab. The beamline has the following beam parameters: E = 1-120 GeV, I from a few hundreds to 700,000 particles/spill, the spill length is 4.5 seconds with a cycle time of 1 minute. Segmented Wire Ion Chambers (SWICs) and Proportional Wire Chambers (PWCs) do not display the beam profile accurately below about 10,000 particles.

For the prototype FPM detector a modified SWIC vacuum can was used. An (x, y) array of fibers replaced the chamber containing windows, gas, and AuW wires soldered on a ceramic substrate. The fibers were purchased from Saint Gobain and are of the type BCF-12 MC, 420 nm wavelength. They have a diameter of 0.75 mm and are coated with black EMA for optical isolation. The 64 channel fibers are positioned and then epoxied in a vacuum feed-through "cookie" to match a Burle 64 channel multianode microchannel plate PMT of the type Planacon # 85011-501. The gain of the Planacon PMT is 800,000 at –2400 Volts. Unlike SWICs or PWCs, this device will allow for vacuum continuity. Comparative data with PWCs will be presented.

THE BEAMLINE

Meson Test is a Fixed Target beamline that takes a primary beam of 120 GeV from the Main Injector, through a section of the TeV tunnel and Switchyard before hitting a target station in MT4. Secondary beams of various energies and intensities are then produced and refocused to satisfy experimental requests. Figure 1 shows the location of the Meson Area.

Figure 1. Meson Area

M-Test has recently been re-designed. Various types of secondary beams are now produced. As the energy of the secondary beam is lowered beam scattering increases mainly because of the large amount of material in the beam due to many beamline windows. A fiber profile monitor was developed to allow experimenters to profile secondary beams below the threshold region of SWICs and PWCs.

PWC CHAMBERS

These profile monitors were originally designed and built by Howard Fenker [1] in 1983 and are still in use in a few low intensity, fixed target, secondary beamlines. An X and Y sense plane, made using 10 μm diameter AuW wire is installed between three high voltage cathodes made with 12.5 μm Al foils. A set of 12 μm Al foils complete the assembly. Ar/CO2 at a mix ratio of 80/20% is used as the ionizing gas. Figure 2 shows a PWC layout details.

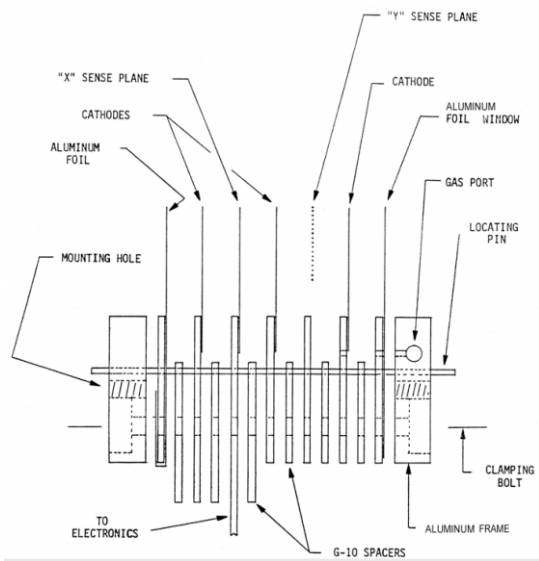

Figure 2. PWC layout

The beamline installation of a PWC requires a vacuum

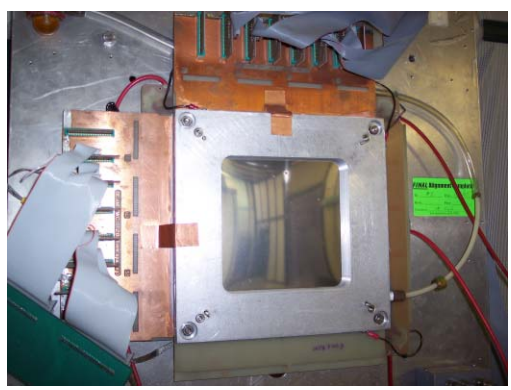

Figure 3. PWC detector

* Operated by Fermi Research Alliance, LLC under Contract No. DE-AC02-07CH11359 with the United States Department of Energy.

† G. R. Tassotto@fnal.gov

break and therefore about 150 μm of Ti per beamline window,. A typical PWC has 60 μm of Al, 2 cm of $ArCO_2$ and 0.05 μm of tungsten corresponding to 0.007 radiation Lengths. This amount of material degrades the beam quality. Figure 3 shows a complete PWC detector.

FIBER PROFILE MONITOR

The Fiber Profile Monitor (FPM) is designed to sample the beam via scintillating fibers in vacuum, thereby minimizing the material seen by the beam. The fibers are mated to a 64 channel multianode microchannel plate PMT (MA-MCP-PMT) via a vacuum "fiber cookie" feed through. This allows all electronics to remain outside the vacuum. The MA-MCP-PMT model is the Burle Planacon # 85011-501 (Planacon PMT).

Two detectors ("MT6WC3" and "MT5FP2") have been built, installed, and tested so far. The MT6WC3 operates in air, while MT5FP2 operates in vacuum.

Fiber Plane Assembly

A set of 32 scintillating fibers having a diameter of 0.75 mm and 2 mm pitch were epoxied on both sides of a ceramic board in an X and Y configuration. Figure 4 shows both fiber planes as they are epoxied on a ceramic board.

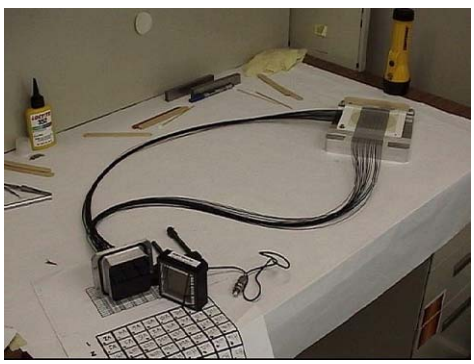

Figure 4. Fiber Plane Assembly

The two sets of fibers were then bundled together, with a heat-sealable Tedlar, to protect the fibers' coating from rubbing against the inside of the vacuum can. The fibers were then bundled and epoxied into a vacuum feed-through "cookie" which has the function to space the fibers evenly over the surface of the epoxy, to match the inputs of the Planacon PMT, and to maintain a vacuum of 10-7 Torr. Figure 5 shows the finishing detail of a cookie

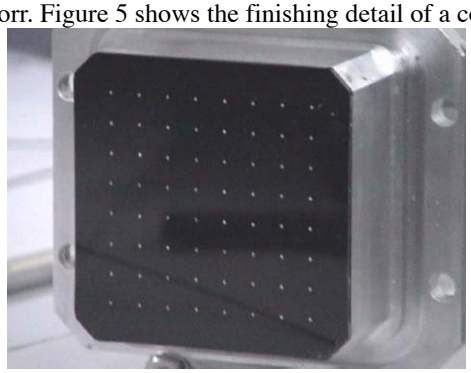

Figure 5. Details of a "Cookie"

Beamline Installation

The fiber plane assembly is then installed in a vacuum can. Figure 6 shows detector MT6WC3 during installation.

A set of flat-to-round cables take the individual signals from the Planacon PMT from the tunnel to the electronics located about 100 m away in a service building.

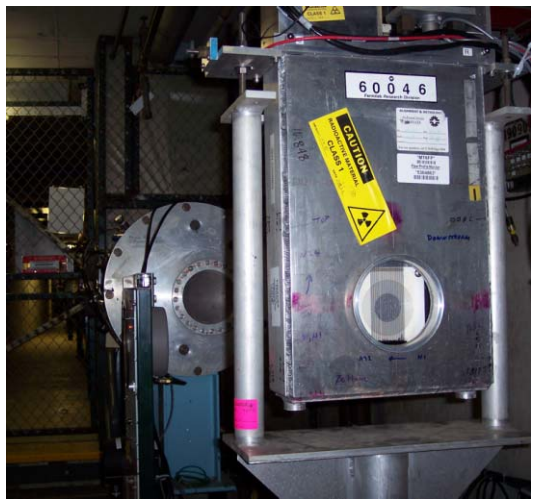

Figure 6. FPM installation

Electronics

Both PWC and FPM use the same readout electronics designed at Fermilab [2]. The readout electronics has a total of 96 integrator channels divided into 48 for horizontal and 48 for vertical. The integration time is programmable from 1 μsec to 6.5 sec. with a dynamic range of 16 bits. The sensitivity is 0.312 mV/ADC count, and the noise is about 0.2% of full scale.

INITIAL RESULTS

We have profiled secondary beams of various energy and intensity and compared them with typical PWC profiles. Figure 7 shows the profile of the first vacuum fiber monitor MT5FP2 (left) as compared with a PWC (right) located about 40.5 m downstream. The secondary beam intensity was about 100,000 particles as displayed by a scintillating counter. The wire spacing of the PWC is 1 mm and that of the FPM is 2 mm. The bias voltages were set to –1800 Volts for the FPM and –2000 for the PWC.

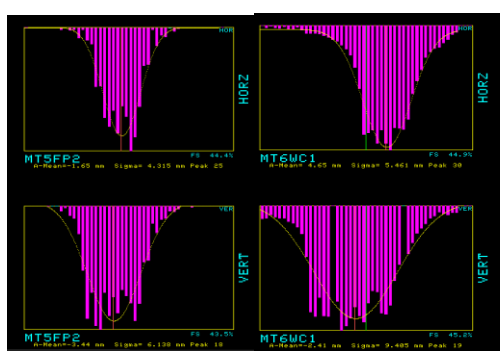

Figure 7. FPM vs. PWC profile

Figure 8 shows the profile of a secondary beam whose intensity was 30,000 particles. The bias voltages were set to –2000 Volts for the FPM and –2200 Volts for the PWC.

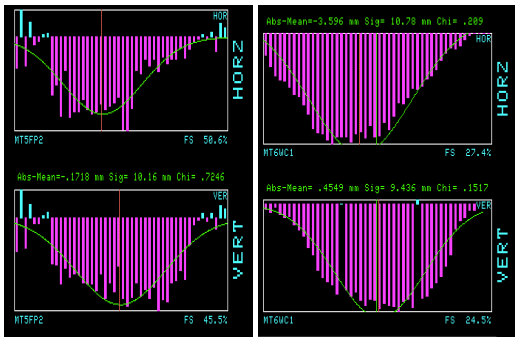

Figure 8. FPM vs. PWC profile

As the beam energy is decrease the profile becomes broader and the noise increases to the point that it did require a background subtraction after the beamline is tuned and the PMT HV was optimized. Figure 9 shows the profiles of about 2000 particles at an energy of 4 GeV. At this level the PWC shows only noise. The bias voltages were set to –2400 Volts for the FPM and –2400 Volts for the PWC.

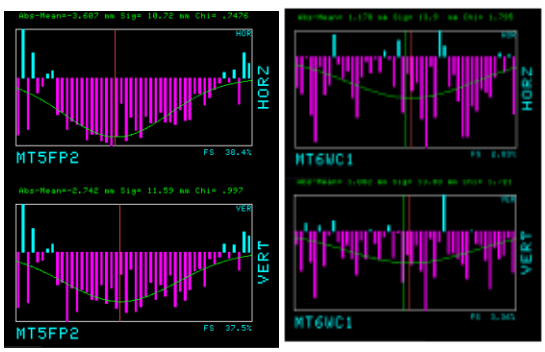

Figure 9. Beam Profiles of 2000 particles

NOISE CONSIDERATIONS

As beam intensity decreased the signal to noise ratio became worse. The PWCs were limited to a maximum of –2500 Volts and did not display any profile at intensities less then about 10,000 particles. We were able to display a profile using the vacuum FPM down to about 2000 particle at a MCP voltage of 2400 Volts and after subtracting the background. The noise was much worse in the case of the FPM in air. For the vacuum FPM, the pedestal background current is approximately 10% of the ADC dynamic range. The source of this is currently unknown and cannot be accounted for by the Planacon PMT dark current. The pedestal time variation is also larger than expected. We also noticed that there was a large amount of unevenness of signal strength due to channel-to-channel gain variation in the Planacon PMT for about the same beam intensity per channel.

CONCLUSION

We have built and tested 2 FPMs and compared their profiles to PWCs. We have also been able to profile beams down to 2000 particles per spill at an energy of 4 Gev. Next we plan to tune the beam down to 1 GeV and make some profile measurements. Before the next FPM installation the plan is to map every MCP channel using a collimated Sr^{90} source. We also are looking at improving the shielding around the detector connectors to minimize sources of electronic noise.

ACKNOWLEDMENTS

We would like to show our appreciation to the many people of various groups that helped with this project: Eileen Hahn - FNAL/PPD/Lab7 Fiber Finish/Thin Film Group, Jim Schellpfeffer - FNAL/PPD/LaB8 CNC router, Mark Rushmann - FNAL/PPD/PAB Vacuum Group, Rick Pierce and Linda Purcell-Taylor - FNAL/AD Instrumentation, and finally Jim Crisp and Martin Hu with FNAL/AD.

REFERENCES

[1] H. Fenker, “A Standard Beam PWC for Fermilab” TM-1179, Feb.1983

[2] W. Kissel, B. Luublynsky, A. Franck, “New SWIC Scanner/Control System”, ICALEPCS “95, Chicago, IL, Oct. 1995

STRIPLINE TRANSVERSAL FILTER TECHNIQUES FOR SUB-PICOSECOND BUNCH TIMING MEASUREMENTS*

John D. Fox, Themis Mastorides and Jiajing Xu
Stanford Linear Accelerator Center, Stanford CA. USA

Abstract

Measurement of time of arrival of a particle bunch is a fundamental beam diagnostic. The PEP-II/ALS/BESSY/PLS longitudinal feedback systems use a planar stripline circuit to convert a 30 ps beam BPM impulse signal into a 4 cycle tone burst at the 6th harmonic of the accelerator RF frequency (2.856 GHz). A phase-detection technique is used to measure the arrival time of these BPM impulses with 200 fs rms single-shot resolution (out of a 330 ps dynamic range). Scaled in frequency, this approach is directly applicable to FEL and other sub-ps regime pulse and timing measurements. The transversal circuit structure is applicable to measurement of microbunches or closely spaced bunches (the PEP-II/ALS/BESSY/PLS examples make independent measurements at 2 ns bunch spacing) and opens up some new diagnostic and control possibilities.

This paper reviews the principles of the technique, and uses data from PEP-II operations to predict the limits of performance of this measurement scheme for arrival phase measurement. These predictions are compared with results in the literature from electro-optic sub-picosecond beam timing and phasing diagnostics.

INTRODUCTION

The longitudinal feedback systems developed to control instabilities in high current factory colliders and light sources must measure the oscillation coordinate of every bunch in order to compute a correction signal. These oscillation displacements are measured relative to a master oscillator. For a 1 cm bunch stabilized to 2% of its' length, the system must sense the time of arrival of the bunch with better than 1 ps resolution and noise.

Instrument techniques to measure bunch longitudinal (time of arrival) coordinates are also of increasing interest for FEL diagnostics, recirculating LINAC applications, and time-resolved photon science experiments.

INSTRUMENT SYSTEM

Signals from a button BPM are processed via a planar stripline circuit band-pass filter which has a $sin(x)/x$ frequency response (figure 1). The output signal is a band-limited tone burst of finite duration (here 4 cycles at 2856 MHz). For multi-bunch applications the finite time response allows an independent measurement 2 ns later of the subsequent bunch (a resonant filter would have to be very low-Q to completely decay in this short interval)[1].

*Work supported by Department of Energy contract DE–AC03–76SF00515

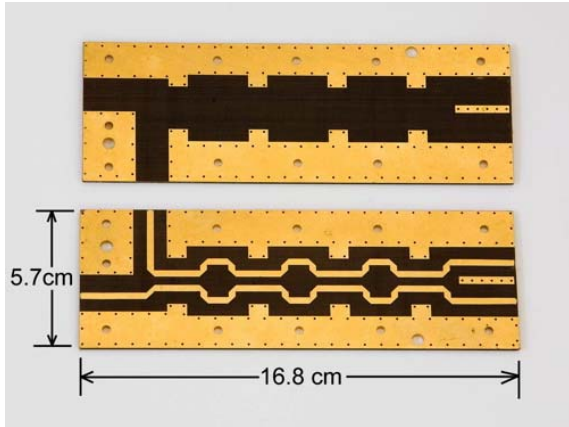

Figure 1: Photo of 4 cycle 2856 Mhz Comb Generator

This tone burst is phase detected against a phase-locked accelerator reference and the baseband phase information is digitized. The wideband processing is implemented with RF gain at the detection frequency and DC-coupled baseband gain after the phase detector. A baseband Bessel low pass filter defines a processing bandwidth (either 400 MHz or 800 MHz) [2]. The baseband detector voltage is of the form:

$V_{out} = kQ_bSin(\phi_{beam} - \phi_{ref}) + V_{offset}$ where k is a system specific gain factor, Q_b the charge in the sensed bucket, and $\phi_{beam} - \phi_{ref}$ is the phase difference of the bunch-derived tone burst and a reference oscillator.

The sensitivity scales directly with detection frequency and signal level (per bunch charge and the processing gain).

BEAM PHASE DETECTOR PERFORMANCE

We use operating feedback systems (ALS, DAΦNE E-, PEP-II LER and HER) to get a sense of the resolution and noise of the beam phase measurement via recordings of of the baseband phase signal [3]. We can then use offline tools to look at rms noise in the signals, and compute power spectra and other diagnostic measurements [4, 5]. The transient record is a two dimensional matrix of ADC samples, for each bucket a sequence of consecutive samples is recorded. The samples/bucket varies from 661 for the PEP-II systems (with 1740 controlled bunches) to 4031 for the DAΦNE systems (with 120 controlled bunches).

As the basic hardware at each installation is identical, we can see the impact of some of the dynamic range and gain selection trade-offs. In Table 1 the noise and beam measurements are computed in rms counts, where the rms

values are first computed along the bunch sample axis (after removing the mean), then the bunch rms values are quadrature weighted along the turn axis resulting in a single weighted rms value.

Table 1: A/D RMS Noise at 4 installations (rms counts)

Parameter	ALS	DAΦNE	HER	LER
Terminated A/D	0.68	0.63	0.63	0.66
Receiver no Beam	0.74	0.96	0.81	0.82
Receiver no beam , no mixer LO			0.75	0.71
Controlled Beam	1.70	4.53	1.97	1.88
I for control study mA	131	890	1740	2700

The baseband channel noise includes contributions from Johnson noise in the pickups and terminations, noise in the RF processing amplifiers, noise mechanisms in the RF mixer, and noise in the baseband stages. There is also contribution from the phase noise of the local reference oscillator. Finally, the system has some spurious signals, some originating in the high-speed logic, which are detectable.

Table 1 shows the noise contribution of the fast sampler and quantizing noise in the A/D with terminated input. The multiple systems are similar, with noise of roughly 0.6 counts averaged over the full recording. This noise can be compared to a perfect quantizer of 0.29 rms counts ($1/\sqrt{12}$). Of greater importance is the measured noise in the systems with no beam, but with the full operating receiver channel. This measurement shows the contributions of the RF and baseband sources within the sampler bandwidth, and the various installations show noise levels in the range of 0.8 to 0.9 counts rms. This base noise floor is the limit we should use in estimating the performance of the measurement. We can understand the relative noise contributions from the baseband and RF signal paths in a measurement of the receiver with the LO power at zero in the mixer. For PEP-II the baseband path contributes roughly 0.1 count rms in quadrature.

Table 1 also shows operating machines with populated bunches. This increased rms level is the fluctuating beam motion plus oscillator phase noise within the sampler bandwidth. Using the calibration factors [1] and typical bucket currents we can estimate the measurement noise floor in RF phase or time units (Table 2).

A power spectrum computed from the beam samples is insightful. Figure 2 presents PEP-II LER data at 2700 mA. The power spectrum shows considerable beam motion at 720 Hz and low frequencies which originate in the RF system klystron power supplies. Harmonics of this excitation are present on the beam from the modulation of the accelerating voltages in the RF cavities. In the narrow band near the 4.3 KHz synchrotron frequency we see that the beam spectral noise power drops to near the receiver noise due to

[1] these are found by modulating the phase reference through 2π at a low frequency and fitting a sinusoid to the response

Table 2: Receiver Noise (rms counts) converted to Beam Phase resolution

Parameter	ALS	DAΦNE	HER	LER
Receiver no Beam	0.74	0.96	0.81	0.82
Current for estimate	400	890	2200	4000
I/bunch (mA)	1.22	9.9	1.3	2.3
C/bunch (C)	8E-10	3.2E-9	9.2E-9	1.6E-8
Calibration (counts/mA/deg@RF)	5.8		18.9	5.36
est. resolution (ps)	0.57		0.20	0.39

the action of the coupled-bunch feedback system. What is happening is that the feedback loop reduces the fluctuations on the beam signal by $1/(1 + loop\ gain)$. The channel has high gain in the DSP filter (maximized at the synchrotron frequency) and the resonant response of the beam further increases the loop gain at the synchrotron frequency.

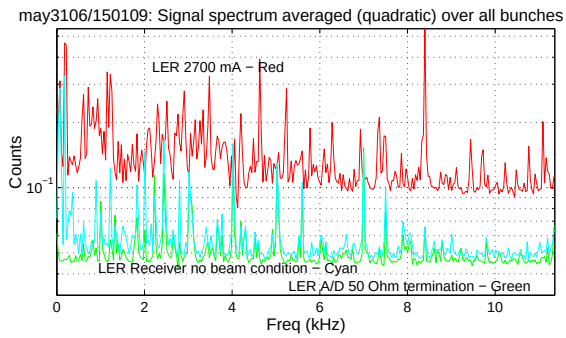

Figure 2: Power Spectrum of beam phase signal, showing noise floors and the controlled beam

It is also possible to compute the amplitude of the beam signals as modal motion, where the motion of the individual bunches are transformed to a modal basis. As seen in figure 3, the data from the HER at 1700 mA is decomposed into even fill basis eigenmodes. This modal amplitude plot shows the motion at the synchrotron frequency, is very small at less than 0.005 degrees per eigenmode, and well below the individual sample noise floor.The largest motion is mode zero from noise in the RF system. Each individual bunch is still moving in a superposition of the contributions of each modal eigenmode.

One observation from this study is that the A/D converter resolution does not dominate this system noise floor, as the noise from the receiver channel is of the same order. If we require better resolution on the instantaneous beam samples we need to improve the receiver noise figure before any improvement from additional resolution in the A/D converter could be significant. [2]

[2] this is also true for the transverse feedback systems studied, as the noise in the transverse motion receiver is also greater than the quantizing noise in the A/D of the feedback channel

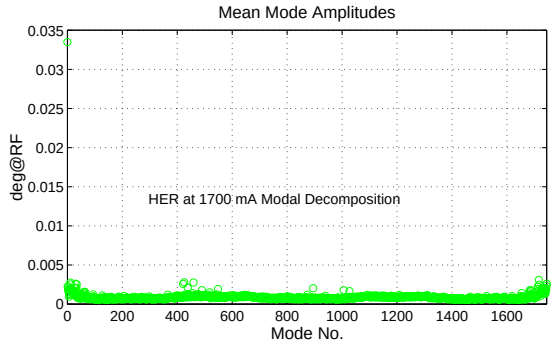

Figure 3: Modal plot of the HER at 1700 mA, showing the controlled noise floor is below 0.005 Degrees at 476 MHz

SUMMARY AND SCALING TO OTHER APPLICATIONS

It is interesting to estimate the limits of this bunch arrival technique. The most direct method to increase the sensitivity is to detect at a higher frequency, with a reduction in measurement range (the phase detector is periodic every 2π). For cm bunched beams there are significant signal components out to 30 GHz and higher. The pick-up electrodes would need clean response at this higher frequency. Similarly, these higher frequencies would likely propagate in a practical vacuum chamber, and if there are resonant structures or HOMs in the vacuum system it may not be feasible to operate at arbitrary detection frequencies. Another factor would be the implementation of the stripline comb generator, and at frequencies above 15 or 20 GHz it likely would have to be fabricated on a sapphire or alumina substrate. It may be helpful to place the comb generator inside the vacuum chamber to reduce the required feedthrough bandwidth.

The systems examined have noise floors which are set by the RF/Baseband receiver processing and have additonal contribution from the wideband samplers. The choice of detection frequency (operating frequency of the phase detector) is independent of this noise floor estimate for systems with similar processing bandwidths (e.g. the thermal noise in a 400 MHz band around 3 GHz would be the same as 400 MHz around 30 GHZ). The noise figure of the RF processing amplifier would not differ significantly. However, the phase noise component of the reference oscillator would likely be worse for similar technical implementation. Additionally, we would expect greater losses in a cable plant which would require increased RF gain.

Table 3 presents a speculative design of 10 and 30 GHz processing channels, with the same scaled noise contribution as from the 3 GHz implementation. Using the 2.2A PEP-II HER design current we estimate the single shot measurement resolution as 200 fs for the implemented system, scaling to 20 fs for the 30 GHz detection frequency . This is comparable to the electro-optic technique described by Loehl, et al in the literature.[6]

One interesting difference between this technique and electro-optical techniques is applicability to bunch train measurements. The comb generator technique allows independent measurements of closely spaced bunches. If a mode-locked laser is used to generate a short sampling pulse, the repetition rate of the laser may be a factor in design, or complexity, of a bunch train diagnostic (Loehl, et al used a 40 MHz sampling rate).

Table 3: Estimated RMS Resolution of 3 Measurement Channels - Scaled from 2200 mA PEP-II HER

Parameter	3 GHz	10 GHz	30 GHz
Channel Noise (rms)	0.8	0.8	0.8
Bunch Charge (C)	1E8	1E8	1E8
Estimated resolution	0.2 ps	0.06 ps	0.02 ps

Both of these techniques are measuring the product of bunch current and time displacement. To make a general channel, which measures both quantities, a quadrature technique could be implemented, with the measurement of sine and cosine components. Subsequent processing would then offer both charge and displacement data.

ACKNOWLEDGEMENTS

We thank Dan Van Winkle for his comments and RF engineering expertise, and the cumulative efforts of Dmitry Teytelman and Shyam Prabhakar in the MATLAB analysis codes. Andrew Young contributed much of the phase detection channel. Allessandro Drago (LNF-INFN) and Greg Stover(LBL) contributed the measurements from DAΦNE and the ALS.

REFERENCES

[1] Briggs, D., et al, "Prompt Bunch by Bunch Synchrotron Oscillation Detection by a Fast Phase Measurement", Proceedings of the IEEE Particle Accelerator Conference, 5/91, 1404-1406.

[2] A. Young, J. Fox, D. Teytelman "VXI based multibunch detector and QPSK modulator for the PEP-II / ALS / DAΦNE longitudinal feedback system." (PAC 97)

[3] J. Fox, et al,"Multi-Bunch Instability Diagnostics via Digital Feedback Systems at PEP-II, DAΦNE, ALS and SPEAR", Proc. IEEE Particle Accelerator Conference, 1999.

[4] D. Teytelman et al, "Accelerator diagnostic techniques using time domain data from a bunch-by-bunch longitudinal feedback system." Presented at 3rd European Workshop on Beam Diagnostics and Instrumentation for Particle Accelerators (DIPAC 97), Frascati, Italy, 12-14 Oct 1997.

[5] D. Teytelman et al, "Beam diagnostics based on time-domain bunch-by-bunch data." Presented at 8th Beam Instrumentation Workshop (BIW 98), Stanford, California, 4-7 May 1998.

[6] F. Loehl, K.E. Hacker, F. Ludwig, H. Schlarb, B. Schmidt A. Winter, '' A Sub 100 fs Electron Bunch Arrival-time Monitor System for FLASH", EPAC 2006 Proceedings pp.2781 - 2783

PRECISION BEAM POSITION MONITOR FOR EUROTEV

I. Podadera, L. Søby, AB department, CERN, Geneva, Switzerland.

Abstract

For future linear colliders (ILC, CLIC) a new Precision Beam Position Monitor (PBPM) has been designed within the framework of EUROTeV. The design goals are a resolution of 100nm and an overall precision of 10μm, in a circular vacuum chamber of 6mm in diameter. The required frequency bandwidth is 100kHz-30MHz. The PBPM is based on an inductive type BPM [2]. Beam positions are derived from the difference between the image currents created by the electron beam into four strip electrodes surrounding the vacuum ceramics insert. In this paper, the design of the PBPM is presented together with first bench measurements, where two micro movers and a rotational stage, installed on a vibration damped table, have been used to characterize the PBPM.

INTRODUCTION

28 European institutes are participating in a Design Study (DS), within the frame work of EUROTeV, for a Linear Collider in the TeV energy range, ILC. Within the same context, the DS will also support, in part, critical R&D for a possible multi-TeV facility i.e CLIC. EUROTeV work package 5 (WP5) contains several different types of monitors, among others Beam Position Monitors (BPM).

The deliverables as defined by EUROTeV are: to design and build a prototype; to report on bench tests and to report on beam tests. The design and construction of the prototype PBPM is reported in [1]. The bench tests have started and preliminary results are reported in this paper. The complete results will be published soon in a EUROTeV report. Beam tests are foreseen for autumn 2007 in the CERN CLIC test facility (CTF3). Table 1 lists the beam parameters of ILC, CLIC and CTF3 at the Combiner Ring (CR) exit.

General Description

The inductive BPM which is based on a design developed for CTF3 [2], has a length of 95 mm (including the bellow) and a external diameter of 68mm and the diameter of the vacuum chamber is 6 mm for this first prototype. A schematic drawing can be seen in Fig. 2.

A ceramic insert forces the image current to pass through the four electrodes placed orthogonally to the horizontal and vertical planes. The position dependant image currents are guided through four current transformers, which transform the currents to voltages in an external resistive load. From these voltages, difference and sum signals are generated in the front end electronics, from which the beam positions are calculated. The sum signal can be used as a true current measurement since all of the image current in the frequency bandwidth of interest pass through the electrodes. A single calibration winding on the current transformers, enables calibration of position and current measurements.

Table 1: Beam Parameters

	CTF3 (CR)	ILC	CLIC
Energy	184 MeV	0.5-1 TeV	0.5-6 TeV
Pulse length	140ns	950us	207ns
Bunch spacing	67ps	300ns	667ps
Bunch length	1.67ps	1ps	0.1ps
Charges/bunch	$1.5 \cdot 10^{10}$	$2 \cdot 10^{10}$	$4 \cdot 10^{9}$
Nb. of bunches	2100	2820	310
$I_{average}$	35A	9.5mA	1.5A

MECHANICAL DESIGN

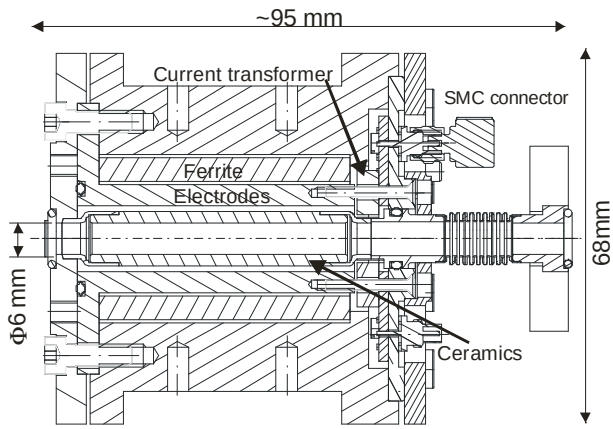

Figure 1: PBPM schematic.

Vacuum Assembly

The 6mm internal diameter vacuum assembly consists of a ceramic tube onto which 2 collars have been brazed. One end is electron beam welded directly into the bottom flange (Fig. 1). On the other end an intermediate piece, a bellow and a rotational DN16 flange are also electron beam welded to the ceramic assembly.

In order to minimize the longitudinal impedance above 100MHz, the inside of the ceramic tube must be coated with a resistive layer (5 Ω/□) [1,3]. At present titanium coating using the sputtering technique is being tested. A precise value of the overall resistance must be obtained, with good uniformity. Coatings inside dummy ceramic tubes could be obtained with the desired accuracy by a magnetron sputtering coating process, adapted to the very small diameter of the pieces. However coating inside the definitive pieces is at present hindered by the presence of the brazed collars which are made of a soft magnetic alloy

which modifies the field lines of the magnetron system. To overcome this problem (without changing the collar material) a modification of the magnetron system has been designed and will soon be tested.

Electrodes

The electrodes are made of copper and they are machined in one single piece. The length of the strip electrodes is 51 mm, the inner diameter is 13mm and they are 3.5mm thick. Three sets of electrodes have been manufactured with electrode apertures of 60º, 70º and 80º, in order to measure the influence of electrode width on the linearity and sensitivity. The image currents are guided through the current transformers with the help of M2 beryllium copper screws, which are screwed into the end of the electrodes.

Current Transformers

Four small current transformers are used to transmit the image currents to the external circuit. VITROVAC cores W650 (6.6 mm of external diameter, 3.5 mm inside and 2 mm thickness) are used. These transformers have a large magnetic permeability ($\mu \approx 50000$) which produces a very good low frequency response. In addition, the small size of the transformers increases the high frequency response due to the capacitive coupling between the windings. A frequency bandwidth of 100Hz-100MHz, i.e. 6 decades, has been obtained, with 30 turns and 50Ω secondary load.

Ferrite

The ferrite which surrounds the electrodes in order to decrease the low frequency cut-off of the sum signal, is a cylindrical piece made by Ceramics Magnetics. The material is C2050 and has a magnetic permeability around 100, constant with the frequency band of the PBPM.

ELECTRONICS

PBPM

To minimize the noise effect and reflections in the PBPM, the four current transformers are mounted on a dedicated PCB installed close to the electrodes. Each current transformer incorporates a single calibration turn and a secondary winding of N=30 turns. The PCB also contains the connections for the beam and calibration signals. Two different low cutoff frequencies can be distinguished, one for the difference signal, $f_{L\Delta}$ and another for the sum signal, $f_{L\Sigma}$ [1].

$$f_{L\Delta} = \frac{1}{2 \cdot \pi \cdot L_{\Delta}} \left(\frac{R_S}{n^2} + R_C \right) \qquad (1)$$

$$f_{L\Sigma} = \frac{1}{2 \cdot \pi \cdot L_{\Sigma}} \left(\frac{R_S}{n^2} + R_C \right) \qquad (2)$$

where L_{Δ} is the inductance of a strip electrode, R_S is the secondary winding load of the transformer and R_C the parasitic connection resistances of the primary loop. The inductance L_{Σ} is calculated with the loops, filled with ferrite, made of the electrodes and the body walls.

Difference Amplifier

The required resolution of the pick-up, 100 nm, is limited by the Common Mode Ratio Rejection (CMRR) and thermal noise of the electronics. The required CMRR for the PBPM in the frequency range 100kHz - 30MHz can be identified as:

$$CMRR \geq 20 \cdot \log\left(\frac{6\text{mm}}{100\text{nm}}\right) = 95\text{dB} \qquad (3)$$

The prototype differential amplifier developed for the PBPM has a CMRR of 80dB in the frequency range of interest. It is very difficult to measure CMRR in this range and especially the phase of the common mode (CM) signal. The part of the CM signal which is in phase (or anti phase) with the difference signal will not limit the resolution but only introduce an electrical offset. CM residuals with 90º phase shift with respect to the difference signal will reduce the amplitude sensitivity to zero in the electrical centre in a range $R \approx d/CMRR$ where d is the internal diameter of the strip electrodes, see figure 2. If a narrow bandwidth acquisition system is used (single frequency), measuring the real part of Δ/Σ eliminates this problem.

A total thermal noise (ΔV_{Noise}), coming from the secondary 50 Ω load and the active difference amplifier, of $3\text{nV}/\sqrt{\text{Hz}} = 16\mu\text{V}$ in a bandwidth of 30 MHz, will be superimposed to the beam pulse induced signals (V_B) and limit the resolution. With sufficient gain the ADC quantisation noise can be ignored and the maximum resolution is given by:

$$\Delta_H / V_{Noise} = k_{XY} \frac{\sqrt{2} \cdot \Delta V_{Noise}}{V_B} \qquad (4)$$

Where k_{xy} are the transverse sensitivities ≈ 8mm. For a CLIC beam current of 1.5A and thus a V_P=2.5V the resolution due to thermal noise would be 72nm. In the case of ILC a Bessel filter is necessary to dilute in time the single 1ps bunch before sampling. After filtering a single bunch will generate a 60ns Gaussian pulse with $V_p \approx 160\,\text{mV}$, which will result in a resolution of 1.1µm. Higher sampling rate and a filter with higher bandwidth will increase the resolution.

TEST BENCH MEASUREMENTS

System Description

To measure the linearity, resolution and long term stability of the PBPM system, two linear micro movers with a resolution of 100nm and a maximum displacement of 25mm have been mounted on a vibration damped table. On top of them a rotational stage is mounted in order to measure the relative offset between the electrical and mechanical centre using a 180º rotation. A Wire

Position System (reference) is attached to the PBPM in order to verify the movement of the motors. Temperature monitoring as well as vibration measurements using a geophone, are also part of the system. A fixed wire is stretched through the PBPM and terminated in 50Ω. The whole setup is screened with a Plexiglas box in order to avoid any wire movements due to air draft. Time domain measurements using a pulse generator and an oscilloscope and frequency domain measurements with a network analyzer have been carried out. In both cases a current of 100mA on the wire is supplied to simulate the beam and results are scaled to CLIC and ILC beam currents. Motor control and acquisition of measurements are done with the help of Labview programs.

Table 3: Frequency Domain Results

Linearity error [±500µm]	1%
Electrical offset	50µm
Sensitivity Δ=Σ (10 MHz, 3mm gap)	11.5mm
Meas. Resol. (100mA, 3kHz BW)	σ_H=28nm, σ_V=52nm
Resolution CLIC	σ_H=180nm, σ_V=350nm
Resolution ILC	σ_H=2.8um, σ_V=5.5µm
Bandwidth Δ	300kHz-80MHz
Bandwidth Σ	5kHz-80MHz

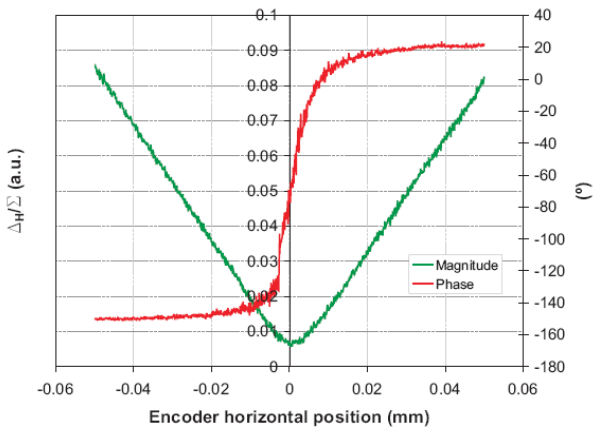

Figure 2: Sensitivity measurement in a ± 50µm range.

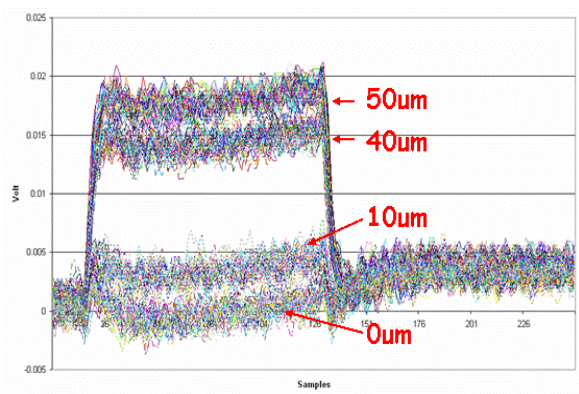

Figure 3: Resolution measurement in time domain.

Frequency Domain Measurements

All of the PBPM characteristics have been measured in frequency domain. For linearity, sensitivity, resolution and electrical offset a single frequency of 10MHz have been used. For the resolution measurements the results are then scaled to a 30MHz bandwidth. The results are resumed in table 3. Fig. 2 shows a ± 50µm sensitivity scan and clearly shows the zero sensitivity of the magnitude around the centre in a range of ± 1µm. In this range the phase could be used to estimate the position.

Resolution in Time Domain

Time domain measurements, using a 200ns 100mA pulse to simulate a CLIC type beam has been done in order to measure the resolution. In figure 3 the PBPM response is seen for 4 different wire positions. The estimated standard deviation of 100 measurements is 2.5µ for a 100mA current, which corresponds to 170nm for the CLIC 1.5A beam. This is in perfect agreement with the network analyser measurements.

CONCLUSION

A high resolution inductive BPM has been designed and preliminary tests have been made using an active damped high resolution test bench. Measurements made with a network analyser using a single frequency have been used to characterise the PBPM. The resolution has been verified in time domain using a pulse generator and an oscilloscope. The measured resolution for CLIC is different for the two planes (180nm/350nm) and is ~ 3-4 times bigger than calculated one. The reason for this is not yet understood. The front end electronics used in the tests had a CMRR of ~80dB and this must be further improved to increase the sensitivity in the centre. The relatively big electrical offset is due to lack of precision in the alignment of the PBPM on the rotational stage. Improvement of this will be studied.

REFERENCES

[1] I. Podadera, L. Søby, Design of a Precision Beam Position Monitor (PBPM) for EUROTeV. EUROTeV-Report-2007-008.

[2] M. Gasior, An inductive pick-up for beam position and current measurement; CERN-AB-2003-053-BDI.

[3] M. Gasior, Limiting high frequency Longitudinal impedance of an inductive pick-up by a thin metallic layer, EPAC'2004, Lucerne, Switzerland.

BPM DETECTORS UPGRADE FOR THE ELETTRA FAST ORBIT FEEDBACK

M. Lonza, L. Battistello, D. Bulfone, R. De Monte, S. Fontanini, V. Forchi', G. Gaio, F. Giacuzzo, R. Marizza, R. Passuello, L. Pivetta, C. Scafuri, Sincrotrone Trieste, Trieste, Italy

Abstract

The project of a fast feedback system to stabilize the closed orbit of the Elettra storage ring is in an advanced stage. All of the existing BPMs have been equipped with new digital detectors in order to provide precise and high rate position measurements to the feedback system. A new beam position interlock system has also been installed to protect the vacuum chamber from synchrotron radiation produced by insertion devices. This paper presents features and performance of the new orbit measurement system and reports some preliminary results of the feedback commissioning.

INTRODUCTION

In the past years of operation at Elettra orbit control has been performed by slow loops correcting every few minutes the orbit at Insertion Device (ID) and bending magnet source points. Two fast local feedback systems based on dedicated low-gap BPMs located at both sides of the IDs in sections 2 and 7 have also been installed and operated during users shifts. In 2005 a new project for the development of a fast global orbit feedback including all of the 96 BPMs and 82 corrector magnets of the storage ring has been started [1]. The original BPM electronics providing orbit position measurements at 200 Hz data rate with *rms* resolution of 2.5 μm has been gradually replaced during 2006 with new digital detectors. The chosen product is Libera Electron manufactured by Instrumentation Technologies [2]. Using the existing rhomboidal BPMs, in the 100-320 mA current range, Libera Electron provides position measurements with *rms* resolution of 0.3 μm at 10 kHz rate and 4 μm in turn-by-turn mode. At slower data rate, i.e. 10 Hz, the achievable *rms* resolution can be as low as a few tens of nm.

BPM DETECTORS UPGRADE

The upgrade of the 96 existing BPM detectors (plus four low-gap BPMs) with Libera Electron has been a gradual process lasted several months and performed during dedicated machine shifts. In order not to disrupt the beamline operations, an empirical offset calibration procedure has been adopted with the objective of reproducing the electron beam position during the users shifts immediately following the upgrade of a group of detectors. The procedure consists in measuring the position of a "reference orbit" with the old detectors, connecting the new detectors and calculating appropriate offsets based on the new position measurements. The offsets are eventually applied to the position readings.

Libera Electron detectors have been integrated in the Elettra control system using an embedded Tango server, running in the internal Single Board Computer (SBC) [3], which is connected to the control system network by means of a 100 Mbit/s Ethernet link. During the upgrade period, Elettra has been operated using a heterogeneous BPM system made of old and new detectors. A server program was arranged to acquire data from all the detectors, merge them together and provide homogeneous closed orbit measurements to the control room client programs. Having finished the upgrade, the new BPM acquisition system, which is completely based on Tango, is able to provide a closed orbit measurement in less than 50 ms.

POSITION INTERLOCK SYSTEM

ID synchrotron radiation generated by a badly centered beam can seriously damage the vacuum chamber. After the upgrade, the position interlock system based on the old BPM detectors had to be replaced. The new protection system relies on the BPMs located at the ends of each of the twelve IDs. It adopts a redundant architecture using both the Libera Electron and a newly developed interlock unit equipped with diode detectors.

Libera Electron features an interlock functionality based on absolute position readings. The interlock output is activated as soon as the x/y beam positions exceed given thresholds. Since the interlock uses the 10 kHz data stream, a low pass filter with programmable cut-off frequency can be included to avoid undesired interlock events due to fast spikes.

The interlock units are based on Schottky diode detectors that process the RF signals from the BPM buttons [4]. Diode detectors have the advantage of having high impedance inputs and can be connected to the same BPM buttons used by Libera Electron without significantly interfering with their operation. The resulting base-band signals are then digitized and processed by a micro-controller that calculates the position error with respect to a reference orbit taken when the ID gap is closed. In case the unit detects a potentially dangerous trajectory, the interlock output is activated.

Libera Electron detectors and interlock units are connected to a dedicated Programmable Logic Controller (PLC). The architecture of the system is depicted in Figure 1. When the program running in the PLC detects that at least one of the Libera Electron or interlock units is in alarm, and if the corresponding ID is closed and the stored current is higher than 20 mA, it dumps the beam by interrupting the RF voltage in the accelerating cavities for

4 ms. The PLC is also connected to the control system through an Ethernet TCP/IP interface.

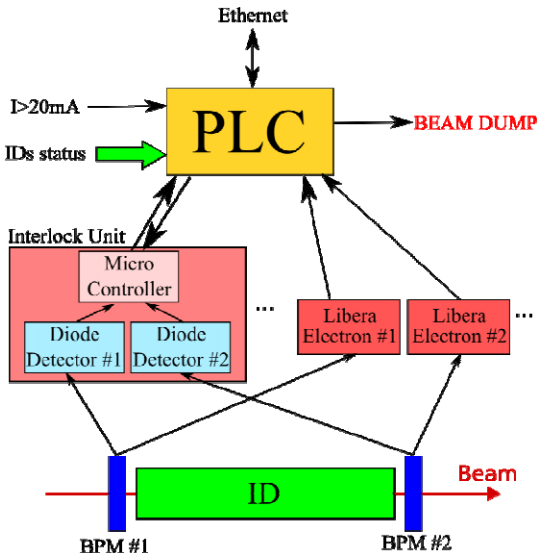

Figure 1: Block diagram of the position interlock system.

BEAM DIAGNOSTIC TOOLS

The global orbit feedback architecture consists of twelve local stations, one for each machine section, and a master station dedicated to global data collection and feedback supervision. The stations are based on VME PowerPC boards running the Linux operating system with real-time extension. The thirteen stations share data by means of reflective memory cards connected by a ring of fibre optics. Each local station collects fast position data at 10 kHz rate from Libera Electron detectors by means of a gigabit Ethernet interface and stores them into the reflective memory. Position errors with respect to a reference orbit are then processed to generate the feedback correction values that are eventually applied to the corrector magnets power supplies via analog links. Each of the twelve stations is in charge of the BPMs and correctors of one machine section. The correction values are also stored in the reflective memory allowing every station to know the whole orbit position and feedback corrections in real-time. A distributed timing system based on VME cards and fibre optics is used to deliver synchronization signals and trigger commands to the local stations.

As a complement to the global orbit feedback a number of diagnostic tools have been developed that take advantage of the fast feedback infrastructure.

Data Recording

A configurable system allows each station to store position and correction data in a number of circular buffers. In the present configuration, each local station stores eight seconds of data at 10 kHz and five days at 1 Hz rate, while the master station stores five seconds of synchronous orbit and correction data at 10 kHz. In the same buffers the status of the feedback components are also recorded to detect and keep track of any anomalous event. By means of the Tango control system, data in the buffers can be downloaded by client programs like graphical panels, machine physics applications and Matlab. Figure 2 is a 3-D plot displaying the amplitude spectrum of each of the 96 BPMs. Spectral components at 23 Hz (quadrupole magnets vibrations) and harmonics of the 50 Hz (from the mains) can be clearly observed.

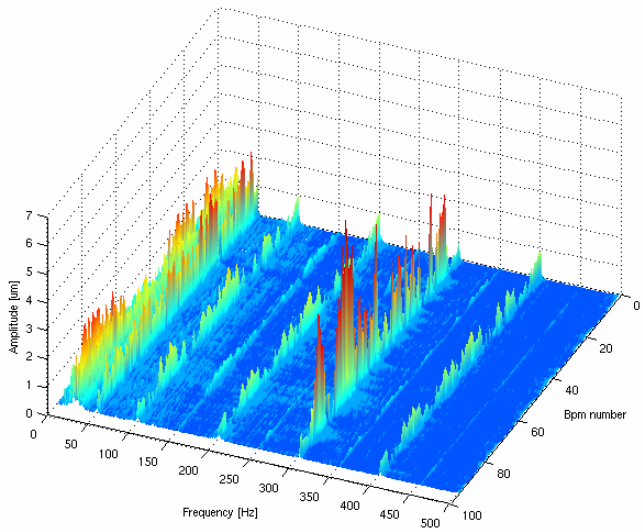

Figure 2: 3-D plot of BPMs amplitude spectra.

Figure 3 shows the control panel of a BPM. Besides the relevant information of the BPM itself, the panel can display horizontal/vertical position data recorded at different rates and plot real-time beam position spectra with 10 Hz refresh rate.

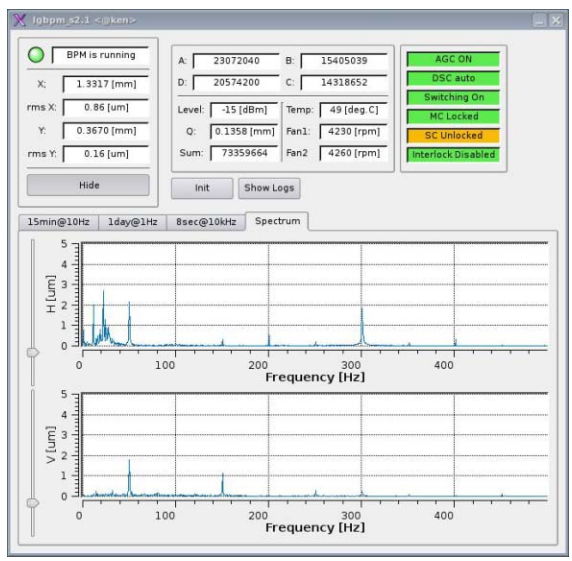

Figure 3: Control room panel of one BPM with real-time position spectra refreshed at 10 Hz rate.

Post Mortem Analysis

The buffering system on the master station implements a mechanism that stops the data acquisition under given conditions, like low BPM sum signal, saturation of the

feedback loop, acquisition errors, etc. One use of this feature is the automatic detection of beam losses and acquisition of post-mortem data from the fast and slow buffers. An example is reported in Figure 4. The system automatically detects a beam loss due to an interruption of the RF voltage in the accelerating cavities by monitoring the sum of the button signals on a given number of BPMs and consequently stops the acquisition. The 3-D plot shows the evolution of the horizontal orbit when the RF voltage is switched off.

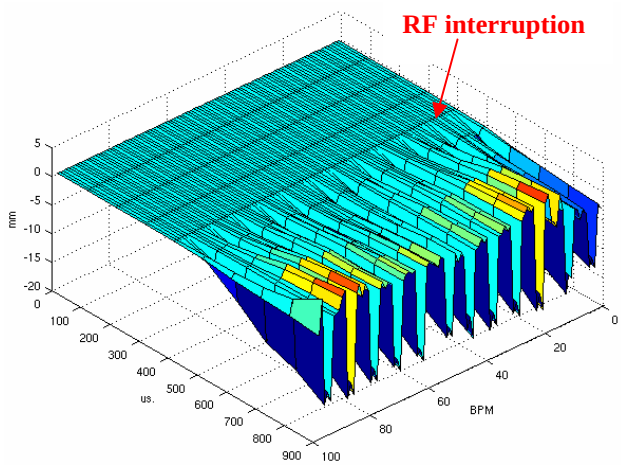

Figure 4: Post mortem data displayed in a 3-D plot: evolution of the horizontal closed orbit after interruption of the RF voltage in the accelerating cavities.

Arbitrary Waveforms Generation

The master station is able to synchronously drive all the corrector magnet power supplies in real-time at 10 kHz using pre-generated waveforms. This feature can be used to characterize the dynamic behaviour of the system by measuring, for example, open/closed loop transfer functions or responses to given excitations. Square and sinusoidal waveforms have been used during the commissioning of the fast feedback to measure the time and frequency domain responses of the corrector magnets.

OPERATIONAL EXPERIENCE

The installation of the new BPM detectors affects many aspects of the day-by-day operations of the storage ring. Slow orbit correction programs benefit from the improved resolution and stability of the beam position measurements and perform more precise orbit corrections. The increased orbit acquisition speed allows performing global orbit corrections in less time, although the maximum repetition rate is still limited by the slow setting of the corrector magnets, which is performed via the power supplies control system interface. The availability of the above mentioned diagnostic tools opens the door to unprecedented opportunities for machine physics studies, investigation of beam noise sources and searching of malfunctioning machine components, with the objective of improving the quality and efficiency of the whole synchrotron light source.

FIRST CLOSED LOOP RESULTS

After the installation of the fast feedback infrastructure, a number of machine shifts have been dedicated to the global feedback commissioning. The feedback loop was successfully closed for the first time using a standard PID regulator and the effects evaluated exploiting the built-in diagnostic features. The PID reduces the noise components up to a frequency of about 100 Hz. The possibility of triggering the post mortem buffers at saturation of the correction values has been a powerful tool for understanding the reasons of unforeseen closed loop instabilities due to software bugs or malfunctioning hardware components. A plot showing the reduction of the horizontal beam position noise at low frequencies (10 Hz data acquisition) when the feedback is activated is shown in Figure 5. The orbit position measurements have been taken from a BPM not included in the feedback loop and specifically used to measure the performance of the feedback.

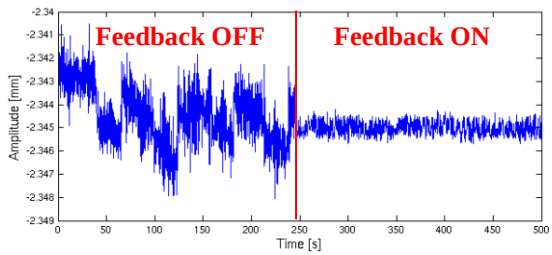

Figure 5: Horizontal beam position measured by a low-gap BPM with feedback off/on.

CURRENT STATUS AND OUTLOOK

The upgrade of the Elettra BPM detectors with digital devices has been completed. The gradual replacement of the existing BPM electronics and the integration of the new devices in the Elettra control system have carried negligible inconvenience to the machine operations and the beam line experiments.

The fast feedback loop has been successfully closed using a PID controller. The commissioning of the feedback will continue with the testing and optimisation of harmonic suppressors, which reduce the periodic components of the noise spectrum as well as with the setting up of the operational procedures for the utilization of the feedback during the users beam time.

REFERENCES

[1] M. Lonza et al., “Status of the ELETTRA Global Orbit Feedback Project”, EPAC’06, Edinburgh, June 2006.
[2] http://www.i-tech.si/
[3] V. Forchi’ et al., “Embedding a Tango Device into a digital BPM”, PCaPAC’06, Newport News, October 2006.
[4] R. De Monte, “The new Diode BPM system for ELETTRA”, these proceedings.

A TAGGED PHOTON SOURCE AT THE FRASCATI BEAM-TEST FACILITY (BTF*)

B. Buonomo†, G. Mazzitelli, F. Murtas, L. Quintieri, INFN-LNF, Frascati (Roma), Italy
P. Valente, INFN-Roma, Roma, Italy
E. Vallazza, INFN-Trieste, Trieste, Italy
L. Foggetta, S. Hasan, A. Mozzanica, M. Prest, Univ. Insubria and INFN-Milano, Como, Italy

Abstract

The DAFNE Beam-Test Facility (BTF), operating at the Frascati National Laboratory of INFN (LNF), provides electron or positron beams with tunable energy from 25 MeV to 750 MeV, while the intensity can be varied from 10^{10}/pulse, down to a single particle per pulse.

Recently a tagged photon source has been designed, built and tested. The photons are produced by bremsstrahlung of electrons, on a pair of x-y silicon micro-strip chambers, placed at the inlet of the last bending magnet of the BTF transfer line. The photons are tagged in energy using the same bending dipole, whose internal walls have been covered by 10 modules of silicon micro-strip detectors. Depending on the energy loss in the photon production, the electrons impinge on a different strip once the dipole current has been set to the nominal value. The correlation between the directions on the electron measured by silicon chambers and the impinging position on the tagging module inside the magnet allows the tagging on the photons. In this paper the configuration of the system is presented with some results obtained during the latest test-beams.

BTF PHOTON TAGGING

The DAFNE BTF can provide electron or positron beams with variable energy (up to 750 MeV) and intensity (down to single particle/pulse) at a maximum repetition rate of 50 Hz [1, 2]. The tipical beam spot size is of the order of σ=2 mm (both in x and y coordinates) and the divergence can be kept as small as 5 mrad. This is crucial for an efficient operation of the photon tagging.

The concept of the tagged photon source is sketched in Fig. 1. The beam-pipe inside the last bending magnet has two sections, the beam can exit from either of the two, according to the magnet settings: from the straight section when the dipole is off, or from the 45° curved section when the field is set to the proper value, given the momentum selected by the upstream dipole+collimators system (with a spread better than 1%).

The beam can be intercepted, before the last bending, by a target, made by two couples of silicon micro-strip detectors, 8.9×8.9 cm^2, 380 μm thick, with a pitch of 228 μm. The two x-y couples of detectors are placed at distance of 15 mm and are inside a aluminum box, movable on a rail system (in and out from the beam-line) and are shown in the left pane of Fig. 2. The point resolution is of about 40 μm, corresponding to an angular resolution of 2 mrad.

When an electron radiates a bremsstrahlung photon by interacting on the silicon chambers (the total thickness corresponds to $\approx$ 1.5% of a radiation length), thus loosing part of its energy, will curve more inside the magnetic field of the bending magnet, thus hitting the beam-pipe in the 45°

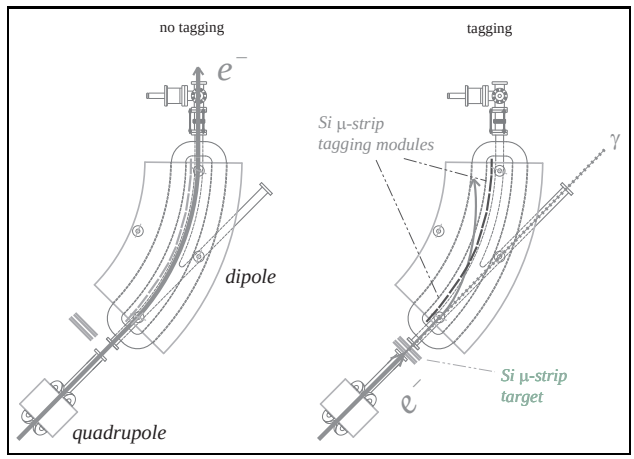

Figure 1: **Left:** layout of the final part of the BTF beamline; the electron beam can exit either from the straight section (bending off), or from the 45° curved section (bending on). **Right:** layout of the photon tagging; the electron irradiates a bremsstrahlung photon on the silicon micro-strip target, and impinges on one of the 10 silicon micro-strip tagging modules outside the wall of the curved section of the beam-pipe.

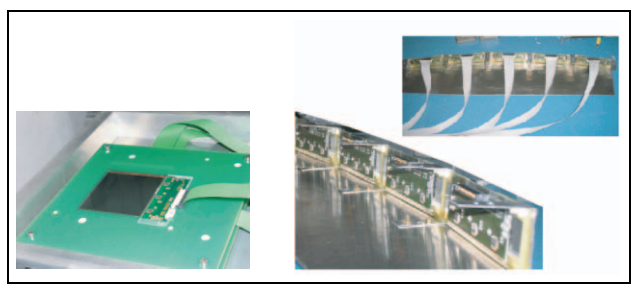

Figure 2: **Left:** silicon micro-strip chambers, acting as active target for bremsstrahlung; **right:** silicon micro-strip tagging modules.

* http://www.lnf.infn.it/acceleratori/btf/
† bruno.buonomo@lnf.infn.it

section. On the external wall of the beam-pipe we have placed two boxes containing 10 modules of silicon micro-strip detectors with an active area of 2 cm heigth, 384 strips each, following the curvature. The strip pitch is of 300 μm in the central region of each module, and 600 μm in the last 3 mm. One supermodule of 5 such detectors is shown in the right pane of Fig. 2.

The 5736 strips of the entire silicon detectors system are read-out by the TAA1 sample-and-hold ASICs (from Ideas, Norway), 128 strips/chip, and multiplexed with a 5 MHz clock by a custom-built VME sequencer. The multiplexed analog signals are then fed to two CAEN sampling ADC VME modules (two channels CAEN V550). All the data acquisition is integrated inside the VME system of the BTF diagnostics.

Further details on the silicon detectors can be found in Ref. [3]. An example online plot of the 4 silicon target planes and of the 10 tagging modules is shown in Fig. 3.

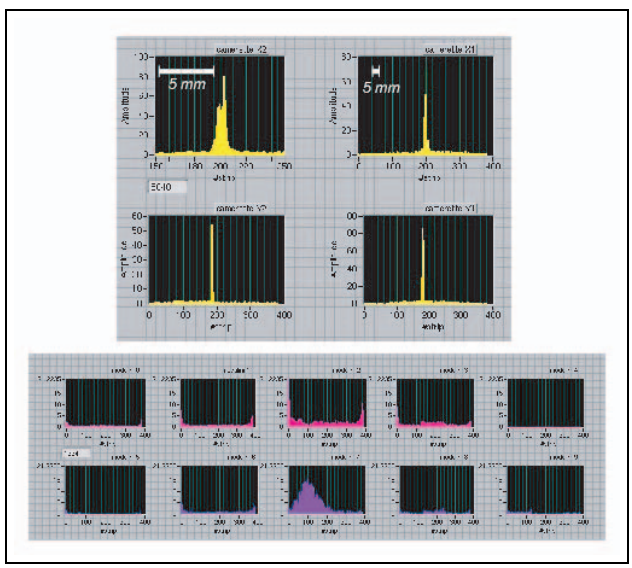

Figure 3: **top:** beam spot on the four silicon micro-strip chambers (x-y views); **bottom:** electron beam on the silicon micro-strip tagging modules (divided in 2 supermodules, 5 detectors each) with magnetic field double with respect to nominal value.

The wall of the aluminum beam-pipe has been thinned to 1 mm in order to reduce the multiple scattering of the electrons before reaching the detectors. Those silicon modules act as tagging system, since from the impact point in the curved section, the bending radius and thus the momentum loss of the electron can be reconstructed, corresponding to the energy of the radiated photon.

The photon will undergo a small ($1/\gamma$) angular deviation from the electron original directions, and thus will exit from the straight beam-line. In order to check the performances of the tagging system, the photon beam has been measured by means of a sodium iodide calorimeter (15 radiation lengths thick). In Fig. 4 the correlation between the photon energy reconstructed from the electon impact point on the tagging modules and the energy measured in the test calorimeter, is shown; the energy of the primary electron beam was of 424 MeV, while he target silicon planes have been used to select single electron tracks on the target itself: a clean linear relationship can be easily seen.

The lower band of events corresponds to reconstructed photons going outside the calorimeter acceptance, essentially due to the beam divergence.

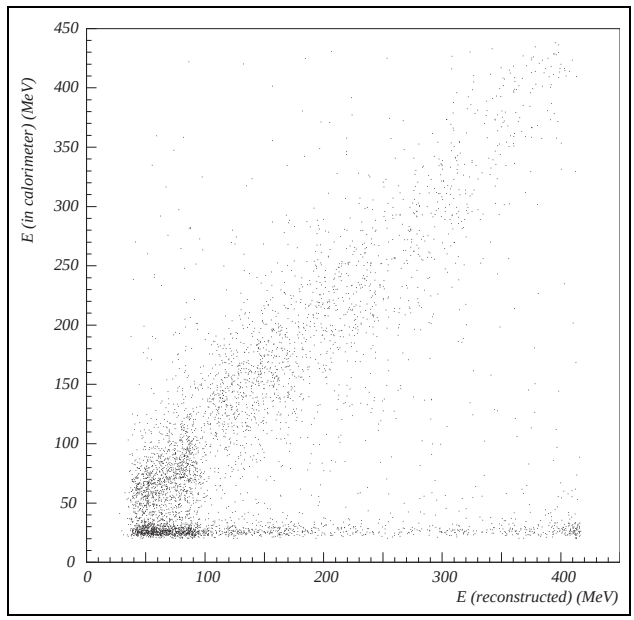

Figure 4: Energy of the photon measured by a calorimeter as a function of the energy reconstructed by the tagging system (energy of primary electrons of 424 MeV).

This has been checked by extrapolating the expected photon position using the reconstructed electron positions and angles in the silicon target planes. The distributions of the x and y (horizontal and vertical) angles of the electron tracks inside the target planes are shown in Fig. 5, while the x and y reconstructed positions are shown in Fig. 6.

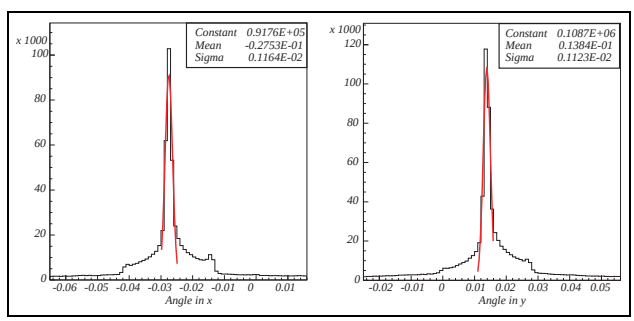

Figure 5: Horizontal and vertical angles of the electron tracks measured inside the target silicon micro-strip planes (energy of incoming electrons of 424 MeV).

In order to estimate the energy resolution of the tagging system, one can use the difference between the estimated (reconstructed) and measured energy in the calorimeter (as

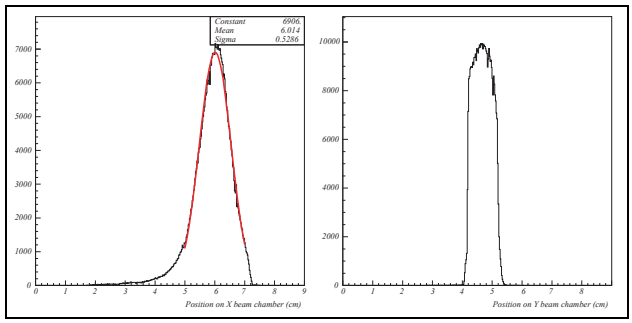

Figure 6: Impact point of the incoming electrons in the horizontal and vertical coordinates measured by the target silicon micro-strip planes (energy of incoming electrons of 424 MeV).

in Fig. 7): the width of the distribution is largely dominated by the intrinsic resolution of the calorimeter (from 6% at maximum energy to about 20% at 100 MeV).

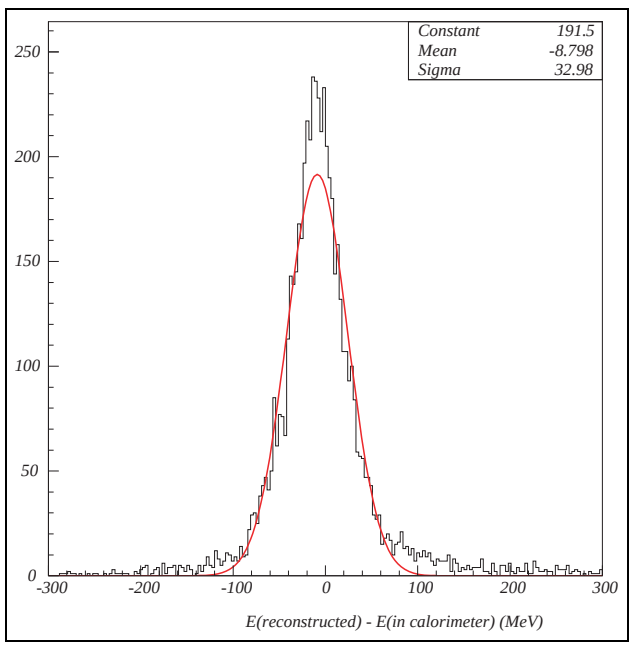

Figure 7: Difference between the photon measured by a test calorimeter and the energy reconstructed by the tagging system (energy of incoming electrons of 424 MeV).

RECENT TESTS AT THE BTF

Recently, a triple-GEM detector [4] has been tested at the BTF, using both electron and photon beams, in order to measure its efficiency for both type of particles. The aim of the project is to realize a couple of segmented detectors, with millimetric spatial accuracy, to be used as a Bhabha detectors for the luminosity measurement of the DAFNE collider (together with a calorimetric measurement of the electron energy).

Photons from radiative Bhabha events and from gas-bremsstrahlung indeed constitute a background for the Bhabha process, so that is crucial to determine the detection efficiency for both photons and electrons.

The triple-GEM has a 3×3 mm^2 pad readout, for a total of 64 pads on a active area 2.4×2.4 cm^2 (over a total area of 10×10 cm^2), read by 4 ASDQ chips and fed to the BTF data acquisition. In Fig. 8 the online distribution of the electron beam spot reconstructed by the 64 pads is shown.

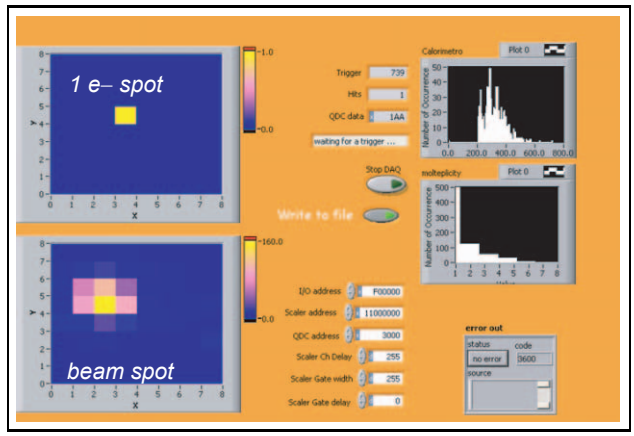

Figure 8: Online panel of the triple-GEM pads readout, showing the beam profile for one electron peak (top) or for the total beam spot (bottom).

The overall detection efficiency measured by this detector has been of 99% with 500 MeV electrons and 1% for photons up to 500 MeV energy; thus showing that this kind of detector is suitable for a precision measurement of the DAFNE luminosity with Bhabha events, with low sensitivity to the radiative Bhabha background.

ACKNOWLEDGEMENTS

We warmly acknowledge the technical staff of DAFNE, in particular: O. Coiro, U. Frasacco, V. Lollo, C. Mencarelli and M. Sperati.

REFERENCES

[1] A. Ghigo, G. Mazzitelli, F. Sannibale, P. Valente and G. Vignola, Nucl. Instrum. Meth. A **515** (2003) 524.

[2] G. Mazzitelli, B. Buonomo, L. Quintieri and P. Valente, Prepared for European Particle Accelerator Conference (EPAC 06), Edinburgh, Scotland, 26-30 Jun 2006

[3] A. Mozzanica et al., Prepared for 9th ICATPP Conference on Astroparticle, Particle, Space Physics, Detectors and Medical Physics Applications, Villa Erba, Como, Italy, 17-21 Oct 2005

[4] M. Alfonsi et al., Nucl. Instrum. Meth. A **535** (2004) 319.

FIRST TESTS WITH THE SIS18 DIGITAL BPM SYSTEM*

Andreas A. Galatis[1,2], K. Lang[1], P. Forck[1], A. Peters[1]
[1]GSI, Beam Diagnostics , Darmstadt, Germany
[2]TUD, Signal Processing Group, Darmstadt, Germany

Abstract

In this paper new approaches for BPM (Beam Position Monitor) measurements are described, which are needed in hadron accelerators with strongly varying beam parameters, such as intensity, accelerating frequency and bunch length. After the data collection and offline evaluation in 2005, first FPGA implementations of algorithms were completed in 2006 and tested at SIS18 and CERN PS. Main aspect of the first tests was the proof of concept in terms of online calculation feasibility. This includes online calculation of the needed integration windows as well as the baseline restoration algorithms. The realization of the hardware and the data handling are discussed. Least squares techniques were used for parametric fitting to gain bunch signal properties which can be used to monitor beam position.

PROBLEM DEFINITION

In most accelerators the exact position determination is crucial information for operation. At the SIS18 the desired resolution is 0.1mm. Compared to most accelerators [1, 2], the SIS18 has some peculiarities a BPM system needs to address, like the large frequency span of the RF from 850kHz to 5Mhz, the high signal dynamic, the injection of unbunched beams as well as the bunch length shortening of over one order of magnitude from some hundreds of ns down to 25ns FWHM [3, 4]. Therefore, novel techniques for beam position calculation which can manage all mentioned difficulties, have to be introduced. The demand of online position calculation introduces an extra challenge. The data is collected by an 125MSa/s-14bit-ADC [5] which is fast enough to overbear the alias boundary, considering the bandwidth of the pick-up units of 50MHz.

INTEGRATION WINDOWS

For the first online tests the algorithm as described in [3] was used. This method implements a filtering scheme which detects the flat regions between two successive bunches. It also includes a short averaging filter to keep the noise reduction algorithm simple in implementation. A length of five taps for the filter proved to be sufficient in most cases. The chosen median filter is easier to implement compared to a moving averaging filter, since it only requires relational operators to be evaluated.

* We acknowledge the support of the European Community-Research Infrastructure Action under the FP6 "Structuring the European Research Area" programme (DIRACsecondary-Beams, contract number 515873).

BASE LINE RESTORING

The method for removing the baseline (BLR) is addressed in [3]. It takes advantage of the known acceleration frequency as well as of the calculated integration windows. With that, two copies of the inverted original signal are used, each shifted by $+$ or $-$ $f_{RF}/2$. The stepwise mean of the those signals is added to the original signal, while the signal outside the previously calculated integration windows is neglected.

FPGA IMPLEMANTATION DETAILS

Using the stated median filter instead of a time averaging filter reduces the latency of calculation and the data overhead inside the FPGA. The median algorithm can be implemented as a parallel working network of comparators and multiplexors, which allows a latency of one clock after the last value arrives. In contrary to that an averaging filter would need one clock cycle for the addition of the last value as well as several clock cycles to produce the needed final division. After the input is flattened using the median filter, the comparison to determine bunch regions is done using parallel working shift registers, which again are optimised for latency minimisation.

The baseline restoration algorithm introduces a delay of half a RF period. The maximal delay is therefore defined by the largest bunch revolution time and is about $1.2\mu s$. For the calculation of the relation between Σ and Δ used in the calculation of the position a pipeline divider is used. The delay introduced by this element depends on the bit width one uses, in this case approximately $0.4\mu s$, leading to a maximum delay for the position calculation of about $1.6\mu s$.

CENTRAL DATA TREATMENT

The delay with which the individual bunch position reaches our central computer is variable. It heavily depends on the packet size one chooses for the ethernet frames, and therefore the number of data that can be sent inside it. It also depends on the used network protocol. These last two points are evaluated at the moment.

Position data of all 12 electronic boxes will be stored in a central point. This central computer has to manage a datastream of about 7MB/s per plane and PU at the maximum RF of about 5MHz. The total gross data will be about 170MB/s. This data has to be positioned correctly in real time and has to be stored. The used hardware for posi-

tion calculation also provides several fast IOs, which can be used as Gigabit Ethernet Ports, to send the data to a central data storage device with the needed speed. Therefore, the system is going to be a server PC, which will build a dedicated Local Area Network (LAN) with the 12 Beam Position Processors and a Gigabit Ethernet Switch as junction. The acquired data can then be sent unidirectional from each PU to the server. Programming and controlling of the Beam Position Processors and data retrieving from the server can then be done over the normal Ethernet network.

FIRST TESTS AT CERN PS AND GSI SIS18

Tests where carried out at the GSI SIS18 in December 2006 using the algorithms in [3]. In parallel to those an implementation with the approach from [6, 7] was running. Both methods revealed problems when the signal strength is very low and the noise floor is relatively high. The approach from [6, 7] failed to syncronise due to the low signal strength, so position data could only be acquired using the GSI approach. The measurements implementing the GSI technique showed a standard deviation of the bunch-by-bunch position of about $0.23mm$.

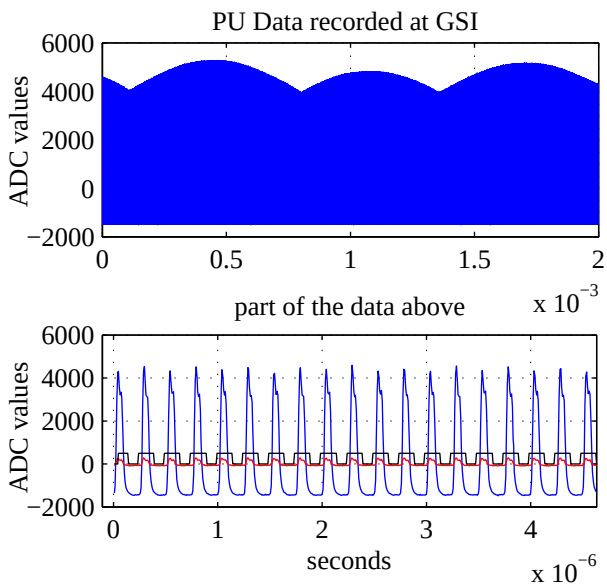

Figure 1: Top curve: complete signal recorder, bottom curve: zoom with sum (blue), difference (red) and window (black) signals

In Figure 1 top curve the complete recording with fluctuations of the peak in the sum signal can be seen. In the bottom curve a zoom into that data with the corresponding difference and the generated gating window – before the BLR – is depictured. In Figure 2 the same signal is shown after the BLR. The first two bunches are cropped due to the initialisation of the BLR algorithm. Figure 3 shows the calculated position of each bunch on $h = 4$ over a span of 2000 turns. The corresponding standard deviation of the position on a bunch-by-bunch basis is as stated

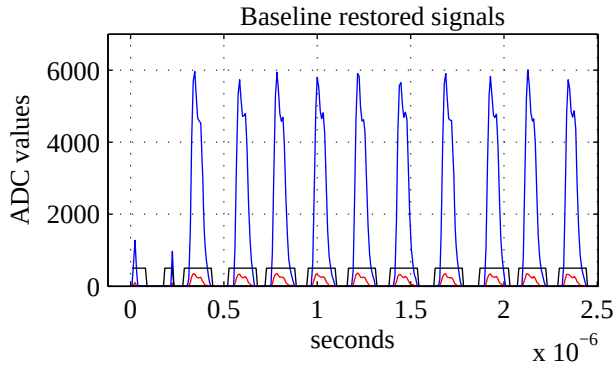

Figure 2: Sum (blue), difference (red) and gating window (black) signals after BLR

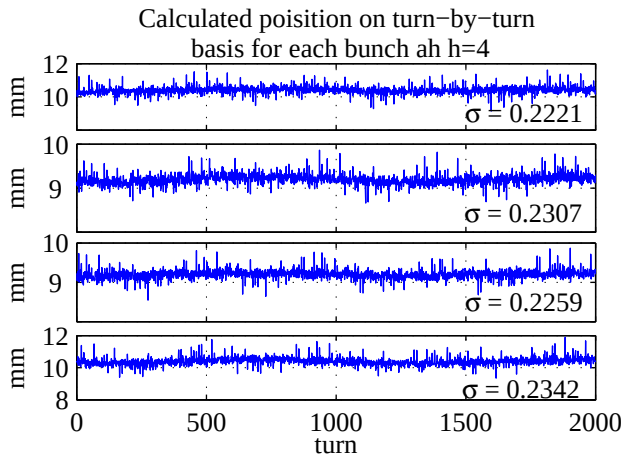

Figure 3: Bunch position on bunch-by-bunch basis on h=4

before about $0.22mm$.

Online tests carried out at the CERN PS using both implementations showed interesting results. While the CERN approach worked faultless, the GSI algorithm performed well in regions with good bunch spacing; a few errors occurring in regions where bunch splitting takes place. Nevertheless this error can be resolved if timing signals indicating a change of the harmonic are provided. The implemented BLR algorithm was not ideally set up for the kind of baseline the PS produces, resulting in a poorly restored signal. The integration window construction worked well except for some initialization faults on the first acquired bunch. This was corrected later off-line. The standard deviation of the acquired bunch-by-bunch position data of both approaches was about $0.27mm$.

LEAST SQUARES APPROACH

Expressing the physical properties of the PU signal by a mathematical model and fitting the acquired data to it, can give new approaches for removing the baseline and create the integration windows.

Parametric Modeling

The following nonlinear equation was used to model the four bunches which are instantaneously inside the acceleration ring:

$$f(n) = \sum_{k=1}^{4} (a_k e^{-\frac{(n-t_k)^2}{\sigma_k^2}} + y_k(n)) + e(n). \quad (1)$$

$$y_k(n) = b_k n + r_k. \quad (2)$$

In Equation 2 b_k is the slope of the baseline, r_k is the constant part of the displacement, $e(n)$ in Equation 1 is the noise term. The parameter vector $\boldsymbol{\theta}_k = [a_k\ b_k\ \sigma_k\ t_k\ r_k]^T$ is introduced, where a_k is the amplitude of the Gauss curve, σ_k its width and t_k its displacement inside the observation window.

Nonlinear Least Squares

The fitting parameters for a set of about 9000 consecutive bunches from a real data set recorded at SIS18 where calculated. Most of the results needed less than 13 iterations to provide stable results. In Figure 4 bottom curve the residuals of the fitting can be seen.

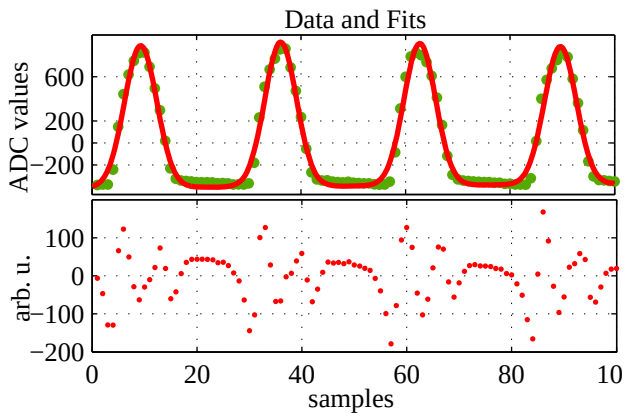

Figure 4: Top curve: original data (dots), fitted data (line), bottom curve: residuals

Results using fitted data

The position calculated from the real data recorded can be seen in Figure 5(a). Comparing the results from real and fitted data as seen in Figure5(a) and (b), gives a measure for the quality of the used model. The difference of both curves, plotted in 5(c), reveals that the inserted error is in the order of 10^{-5}mm with an approximately Gaussian distribution [8].

The implementation of nonlinear least squares (NLS) techniques on a FPGA is difficult, methods minimising the computational cost have to be considered. There are techniques solving the NLS techniques using iterative, minimal cost methods such as the Newton-Raphson (NR) technique. This method uses the previous estimate of θ as well as the Jacobian and the Hessian of the function minimising the NLS error criterion, to calculate the actual θ.

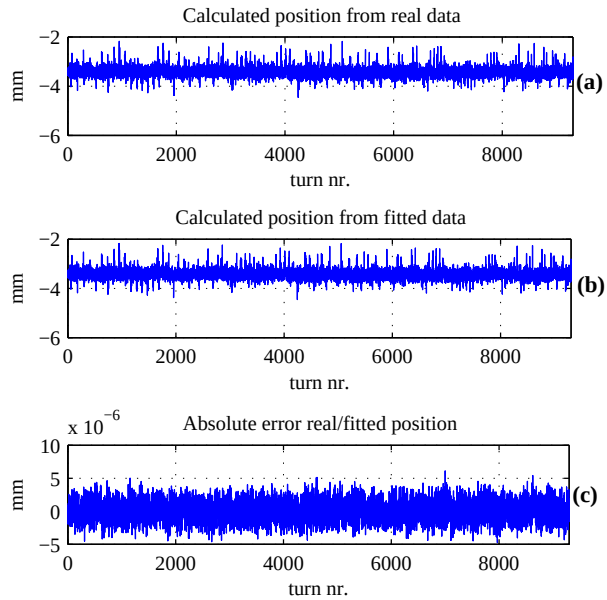

Figure 5: Calculated positions from real (a) and fitted (b) data for the second bunch on turn-by-turn basis, Δ from (a) and (b) in (c)

CONCLUSION

The first online tests using the methods introduced in [3] where successful on both the SIS18 and the CERN PS. The difficulties introduced by bunch gymnastics and varying baselines, can be solved using different approaches and have to be looked into more thoroughly.

The approach implementing the NLS can be used to remove the baseline part of the signal and allow for faster techniques for the integration window generation. More results on that topic are addressed in [8]. The computational complexity can be deducted from the number of multiplications and additions needed in the above update equation. The Hessian and Jacobian matrices have to be calculated at each iteration, nevertheless they are sparse and contain many double entries, reducing the computational cost.

REFERENCES

[1] G. Cancelo et al, "Digital Signal Processing the Tevatron BPM Signals", in Proc. of PAC '05

[2] M. Dehler et al, "New digital BPM System for the Swiss Light Source", in Proc. DIPAC '99

[3] A. Galatis et al, "Digital Techniques in BPM Measurements at GSI-SIS", in Proc. of EPAC '06

[4] A. Galatis et al, "Beam Position Monitor System Development for FAIR", GSI Scientific Report 2005

[5] Instrumentation Technologies, "http://www.i-tech.si"

[6] J. Belleman, "A New Trajectory Measurement System for the CERN Proton Synchrotron", in Proc. DIPAC '05

[7] Grzegorz Kasprowicz et al, "Digital Beam Trajectory and Orbit System, for the CERN PS", in Proc. of DIPAC' 07

[8] A. Galatis et al, "Beam parameter estimation for beam position measurements at the SIS18 accelerator", in Proc. of SSP' 07

ELECTRIC -In-Air-X-Ray- DETECTORS FOR HIGH RESOLUTION VERTICAL BEAM POSITION MEASUREMENT AT THE ESRF

B.K. Scheidt, ESRF, Grenoble, France

Abstract

A simple and in-expensive electric device can detect the tiny fraction of the very hard X-rays that fully penetrate the dipole absorber structure and enter the free air space behind it. This in addition to an already installed, commissioned, and fully independent, system of 6 imaging detectors to measure the emittance [1-3]. It consists of a high-Z metal blade in conjuction with a small In-Air ionization slot that generates a direct strong electric signal allowing for nanometer resolution measurements of vertical beam motion in a spectrum upto 1KHz. The high resolution performance of this detector type is explained by the fact that it touches the heart and centre of the beam whereas other devices have to work on the edges or tails of the beam (X-BPMs) or feel the beam indirectly by wall-current pick-ups (electron-BPMs). The results obtained with prototypes are presented together with the prospects of an installation of 8 units in 2007. The intrinsic advantages of this In-Air detector like costs and simplicity, thanks to a total absence of cooling and UHV requirements, will be emphasized.

X-RAYS TRAVERSING THE ABSORBER

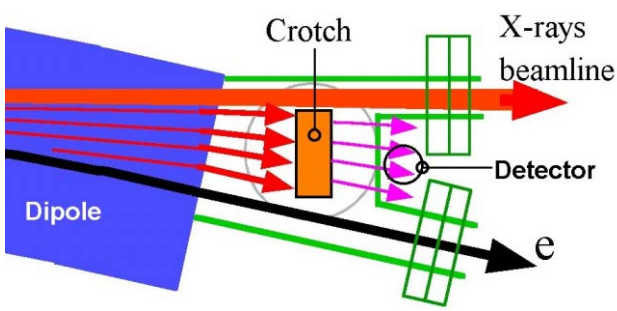

Figure 1: Top-view of detector's position just behind crotch.

A large part of the synchrotron light generated by the Dipole (B=0.86T, E=6GeV) is dissipated directly by an associated crotch absorber (fig.1). However, ~4ppm of this power is not absorbed and traverses the complete structure (of ~35mm Copper and 5mm Steel) to enter the free air behind.

This leakage power (~600uW/mRad hor. angle) is carried by the high energetic photons with a peak at ~170KeV energy and with a total flux of ~2E10 photons in the 100-300KeV range for a 1mrad hor.angle, at 200mA nominal Storage Ring current. These hard X-rays are detected directly by the use of a high-Z blade in combination with a small In-Air ionization volume.

A schematic side-view (fig.2) shows the detector, consisting of 2 parallel plates (or blades) separated by a small distance (typ. 1mm) in air, with the X-ray beam.

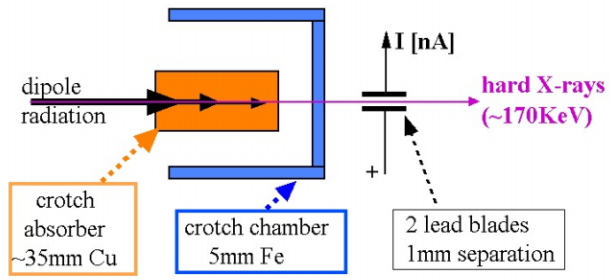

Figure 2: Side-view of the 2-blade electric detector.

One of the blades is connected to a DC bias voltage (typ. 50V), while the other blade is connected via a short coaxial cable to a high impedance electric measurement device (typ. 1Mohm input oscilloscope). The dimensions of the blades are 23x23mm. They are mechanically fixed to an electric isolator that itself is mounted to a miniature mechanical assembly allowing for the angle orientation in 2 planes and a vertical translation. This assembly is a commercial product with 3 DC motors for remote control of these 2 angles and the vertical position of the detector.

It is to be noted that the physical space available between the crotch chamber and the vacuum flanges is very limited and the detector design needs to be very compact and miniaturized so to fit in.

AIR IONIZATION BY X-RAYS HITTING HIGH-Z AT GRAZING INCIDENCE

The correct 2-plane-orientation and vertical position of the blade surface, made of a High-Z metal, with respect to the X-ray beam is crucial. The first alignment aim is to have the beam intercepted by the full area of the blade surface. It is to be noted that the X-ray beam dimensions at this point are horizontally large, i.e. exceeding the 23mm detector width, while vertically very small ~100um.

The sketch in the top part of figure 3 shows the upper blade surface at a small grazing angle (α) with respect to the X-ray beam. With the beam at the vert. position P a maximum of signal is generated. The graph in the lower part of figure 3 shows the signal output when scanning the detector vertically : Another signal is generated with the beam at position Q but of lower amplitude since the beam-surface angle is not optimum in this case.

The interaction of the high energy X-rays with the high-Z material causes, at the surface, a shower generation of secondary particles that themselves cause an ionization of the air molecules in the small volume between the 2 blades. This conductive state together with the applied DC bias voltage now allows for measurement of a small voltage by the 1Mohm instrument. The physics of the X-rays with the high-Z material, the subsequent

particle generation, their exact nature, and their consequence of electric ionization in air are matters outside the scope of this paper and not further described here.

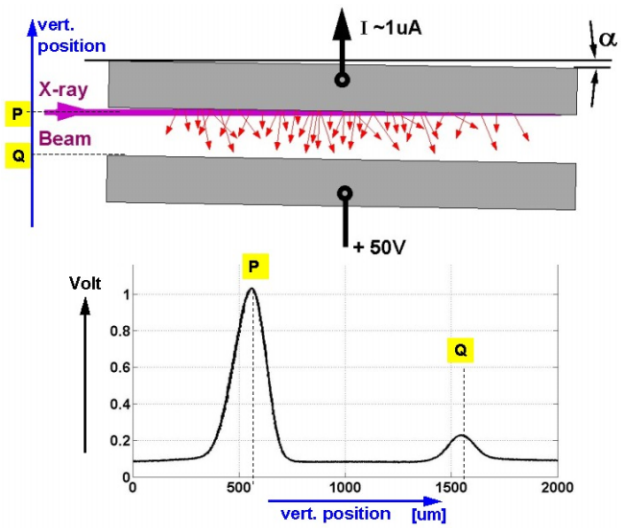

Figure 3: Top : sketch of the blade-surface at grazing incidence with the beam, Bottom: signal output when scanning the detector vertically through the beam.

The blades of a first prototype were both made out of Lead. Later Tungsten and Gold (coating) have been used with the advantage of better surface flatness quality. In a now more finalised version a single 'interceptive' blade made of Nickel with Gold coating is applied, while the 2nd blade (with the bias voltage) is made out of Aluminium.

The signal yield is of roughly equal strength for each of these 3 materials tested : ~1uA for our 23x23mm detector at 200mA beam current. With a distance to the source-point of ~1.8m the hor. acceptance angle is ~13mrad. The X-ray beam power intercepted here is ~8mW, or ~3E11 photons/sec. The 1uA currents amounts to ~6E12 electrons/sec so the actual 'conversion gain' is roughly a factor 20.

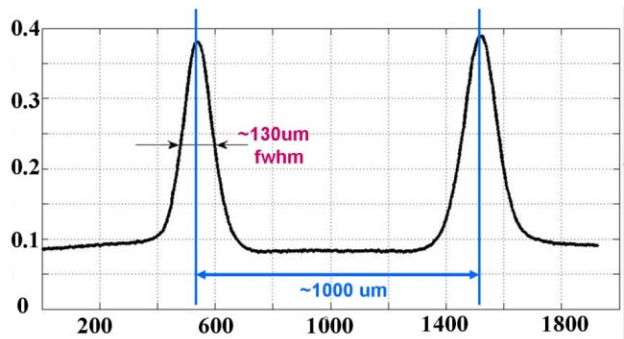

Figure 4: The signal output when scanning the detector position vertically with the blades parallel to the beam.

After installation the initial alignment & angle orientation of the detector is a re-iterative process that consists of scanning the detector vertically through the beam and (time-)recording the signal output, and repeating this at (slightly) varying transverse and longitudinal angles. The signal output in figure 4 shows the case where the blades are parallel to the X-ray beam : the two responses, separated by ~1mm, coming obviously from each of the 2 blades, with the signal strength roughly equal and of minimum width. The optimization of the 2 plane orientation of the blade is done by repeating this scanning/recording so to obtain the best grazing incidence and thus the maximum signal output of one of the blades (the 'interceptive' blade). After that the detector's vertical position is slightly tuned so to be at ~1/2 of this maximum signal, i.e. on the steep slope of the signal. In this way the detector has now become a vertical position monitor with a sensitivity of ~10mV/um without any amplification of the crude detector signal.

RESULTS OF DC AND AC VERTICAL BEAM POSITION MONITORING

The detector positioned on the slope of a ~100um gaussian profile implies a limited range & linearity for use as a beam position monitor. This dislinearity is acceptably small (<10%) for beam displacements of +/- 20um. At the ESRF the schemes of slow & fast Closed Orbit correction & feedback results in an overall beam stability well within that range. The figure 5 shows the DC output (after filtering and amplification by a gain of 50) with the SR beam making a few local displacements of 10um value. The real resolution of the device for DC motion (estimated at <50nm with 1sec measurement time) can simply not be verified with the beam itself that has a residual & uncompressible DC motion above this value.

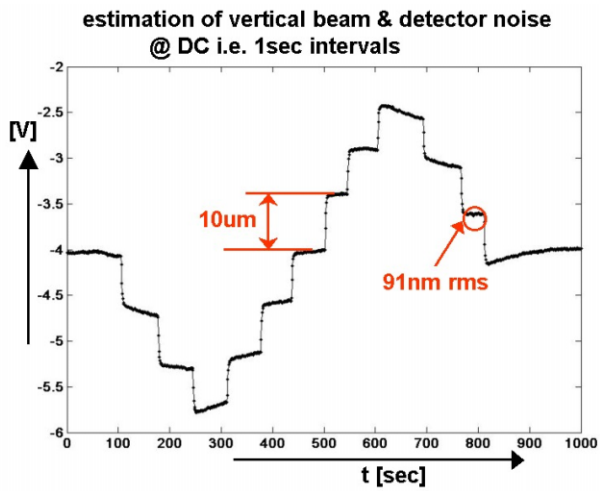

Figure 5: the DC output with the SR beam making a few local vertical displacements of 10um.

The performance in the AC range is shown in time recordings (fig.6) with the Fast Global Feedback going from a switched-off state to the active state [4]. The figure 7 shows the frequency spectrum of the detector with the Global Feedback active, the data was obtained over a 100sec period at 1Khz sampling frequency. Frequency components down to a few nanometer rms amplitude can be resolved.

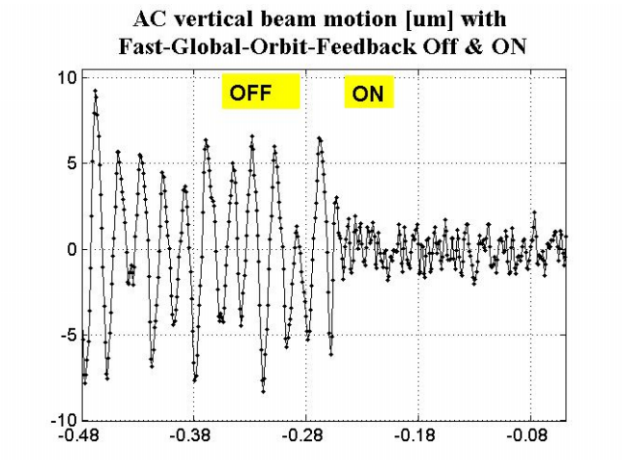

Figure 6: AC time recording of the detector output [um] while switching the ESRF's Fast Orbit Feedback Off-On.

Extensive tests have been carried-out to assess this resolution and to compare that with other diagnostics. The same data-acquisition modules with identical sampling periods & frequency was applied in these cases. Also in certain comparative tests the SR beam was made to oscillate at a known frequency & amplitude with the respective diagnostics scrutinized for their detection resolution. The In-Air blade-monitor, with its source-point in the middle of the dipole, benefits of a high vertical Beta of the ESRF machine lattice at that point (35 or 47m depending on even or odd cell number). It demonstrates a superior resolution to both the fast-electron-BPMs (installed in strait sections, i.e. low vert. Beta) and the classical X-BPM (photo-electric blades in UHV) that suffer from various limitations.

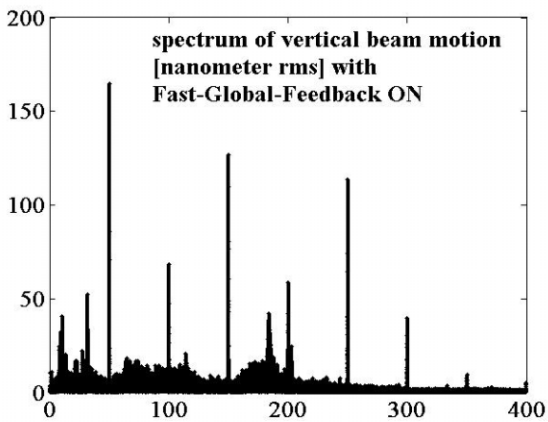

Figure 7: spectrum of vertical beam motion.

The rigidity of the fixation of the detector assembly to the vacuum chamber is crucial to avoid mechanical vibrations in the nanometer region that the detector is potentially capable of resolving. Tests performed with 10min. measurement times show a total absence of unknown lines in the freq. spectrum of the recorded signal.

CONCLUSION AND FUTURE PROSPECTS

It is shown that the small leakage power, carried by the high energetic part of the synchrotron radiation, that traverses absorbers and vacuum chambers and becomes accessible in free air, can be detected efficiently to constitute a very powerful diagnostic of high simplicity.

Although the nature of the dipole radiation imposes that the measurement of electron beam parameters is limited to the vertical plane only, the performance in terms of precision and resolution raises an exciting challenge for this field of detectors. This performance potential combines with the huge advantages of installing, aligning, operating and maintaining these devices in (accessible) free air and at negligible heatload, thereby liberating the designer of major concerns of UHV compatibility and cooling requirements so typical of other diagnostics systems.

The numerous tests performed on the 'blade-monitor', in comparison to other diagnostics for vertical beam motion measurement, have shown that it is of superior performance in terms of resolution. This detector clearly benefits from the fact that it can touch the heart & centre of the beam signal.

The prototype development of the electric blade-monitor itself was finalised in 2006. Appropriate data acquisition modules and associated software and device servers are now under procurement and development so that eight of these devices will be installed and commissioned in 2007 and made available to the accelerator operation for improved survey of vertical beam stability.

The performance and reliability of these detectors will be further evaluated then for deciding on the possibility of integrating them in the Fast Global Orbit Feedback system.

REFERENCES

[1] B.K.Scheidt, "Measurement of Vert. Emittance with a System of 6 In-Air-X-Ray Projection Monitors at the ESRF ", this DIPAC'07 workshop (TUPB08).

[2] B.K.Scheidt, "Detection of Hard X-Rays in Air for Precise Monitoring of Vertical Position & Emittance in the ESRF Dipoles", DIPAC'05, Lyon, 6-8June.

[3] B.K.Scheidt, "In-Air X-Ray Detectors : a New Field of Extremely Simple and Powerful Beam Diagnostics", BIW06 May 2006, Fermilab-fnal.

[4] E.Plouviez, "Upgrade of the Global Feedback of the ESRF Storage Ring", DIPAC'05, Lyon, 6-8June.

MEASUREMENT OF VERTICAL EMITTANCE WITH A SYSTEM OF SIX -In-Air-X-Ray- PROJECTION MONITORS AT THE ESRF

B.K. Scheidt, ESRF, Grenoble, France

Abstract

The ESRF Storage Ring is now equipped with a system of 6 independent imaging monitors that measure the vertical emittance of the electron beam in the middle of the bending magnet through the very hard X-rays that fully traverse the 40mm thick Copper dipole absorbers and enter the free air space behind it. The tiny power that leaks through the absorber, and carried by X-rays of ~170KeV of very narrow vertical divergence, is simply projected onto a scintillator screen at ~1.8m from the source-point and imaged by optics & camera. These inexpensive & compact detectors are fully operated in free air and are easily installed and maintained without any vacuum intervention. They now work reliably and measure routinely the ESRF's vertical emittance with high precision and resolution. Results will be presented together with the underlying principles of the IAX projection detector, and the practical design solutions applied.

X-RAYS TRAVERSING THE ABSORBER

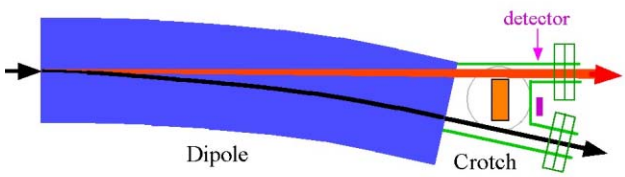

Figure 1: Position of the detector in air just behind crotch.

Only 10% of the synchrotron light generated by the ESRF dipole (B=0.86T, E=6GeV) is accepted for possible passage into an X-ray beamline's front-end. The other 90% are dissipated directly by a crotch absorber (fig.1). However, ~4ppm of this power (i.e. 600uW/mRad hor. angle) is not absorbed and traverses the complete structure (of ~35mm Copper and 5mm Steel) to enter the free air behind.

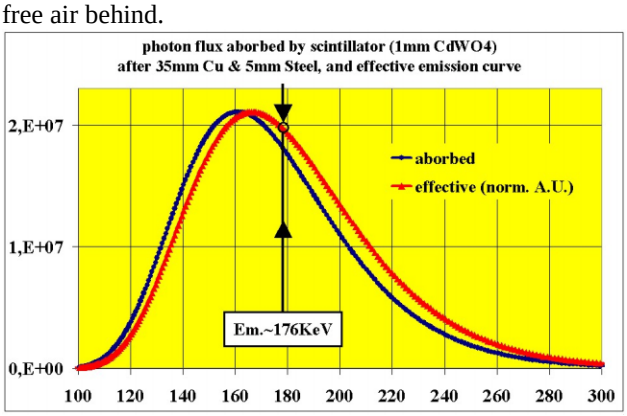

Figure 2: The spectrum (photons per sec. in 0.1%bw & 1mrad hor.angle, at 200mA) absorbed in the scintillator.

This leakage power is carried by the high energetic photons in the 100-300KeV range and can be detected through the use of a high-Z scintillator [1,2]. The fig.2 shows the energy spectrum of the absorbed photons in a 1mm thick CdWO4 scintillator (blue), and the curve of the scintllators' effective emission sensitivity (normalised and in arbitrary units, in red). The median value of the latter lies at ~176KeV. At this energy the photon beam divergence has a nearly perfect gaussian distribution of ~42urad fwhm. This small divergence, in addition to the relative short and precisely known distance of the scintillator to the source-point makes it possible to measure the vertical beamsize of the electron beam [3,4,5].

DETECTO: THE OPTICAL SYSTEM

The fig.3 shows a simplified (side-view) schematic of the IAX detector with : a) the scintillator screen b) an aluminium mirror just behind to deflect the emitted light to c) a lens pair that collects and focuses an image onto d) the CCD matrix of an IEEE-1394 standard camera.

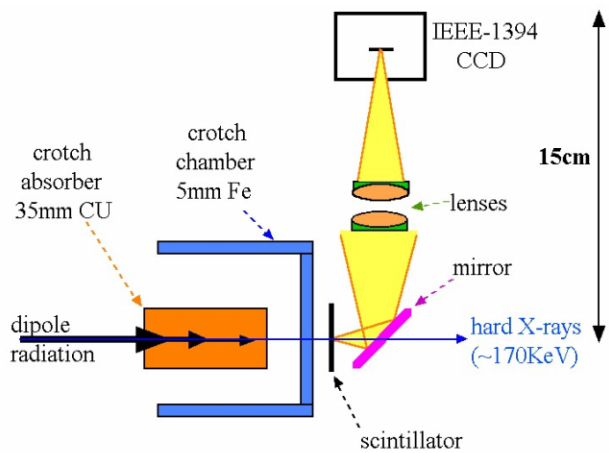

Figure 3: side-view in the vertical plane of the detector.

After going through some test & prototype phases in 2006 in which various optics, cameras, shielding techniques and mechanical assemblies & supports were employed, the detector has now reached a mature and final state that is fully compatible with its performance potential (precision & resolution), the very hostile radiation environment of its location, and the very limited physical space available at this location.

The entire detector is mounted together and adjusted optically in laboratory before installation. All the parts are held by a single aluminium support allowing a rapid and easy (re-)installation.

The optical aperture is 5mm at 60mm distance to the scintillator. The Flea camera of PGR (640x480pixels of 7.4um) which was chosen for its miniature dimensions

and for the ease of operation : gain & exposure control, power-supply and read-out all through a single IEEE-1394 cable [6]. The camera covers a 3.6x2.7mm (hor.-vert.) field at the scintillator with a double achromat system of 60 & 80mm focal length (magn.=1.33).

The lenses & camera are now thoroughly shielded by a Lead tubical structure (machined in a single piece) to avoid damage & degradation by the particles (generated by 13KW of X-ray beam absorbed at a short distance) that scatter around in this area.

CALCULATION OF VERTICAL ELECTRON BEAM SIZE

The X-rays travel 1.78meter before hitting the screen where they project a stripe-line image. In the vertical plane, the relation between the height (h) of the projected image on the screen, and the size of the source-point (i.e. electron beam) can be established in simple and precise terms (see fig.5). Because of the very narrow divergence of the 176KeV photon beam (41.5urad fwhm, and of quasi-gaussian distribution) the projected vertical beam size (h) is only 111um fwhm compared to the vertical electron beam size of 82um fwhm at nominal ESRF emittance of 35pm.rad.

The precision with which the distance (S) and the photon beam divergence (αv) can be determined is such that the absolute precision of the electron beamsize measurement is estimated at better than 2%.

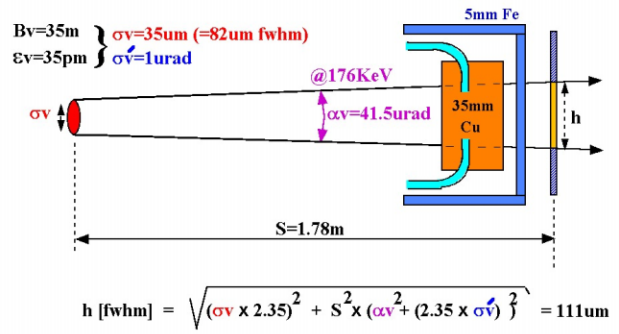

Figure 4: source-point size to projected image size.

DETAILS, IMPROVEMENTS AND TESTS OF THE DETECTOR

The initial problem of camera damage is now totally resolved by a nearly hermetic and (average) 6mm thick Lead shielding. The same Lead tube also holds the 2 achromat lenses that however still suffer from some blackening over time since the inevitable optical aperture for the light signal also lets through particles responsible for this blackening. This achromat blackening was reduced by the application of a 2nd mirror (forming a chicane type of light path inside further Lead shielding), and the application of the CdWO4 (shielding) window just in front of the lenses.

Despite these measures the achromat blackening is not fully avoided and presently still causes a loss of 50% sensitivity after a few months of use. Therefore a set of commercial Quartz lenses (completely immune to blackening) are also being used in some of the 6 individual detectors. However, the intrinsic spatial resolution (or blur) of such optical system would be impaired mainly by the chromatic aberrations and the relatively broad visible emission spectrum of the CdWO4 scintillator. The final image blur would also be worsened by the scintillator's non-negligible (1mm) thickness.

The use of a LuAg:Ce scintillator offered a solution since it has a narrower emission spectrum (~50% less) and is (despite reduced density of 6.7 to 7.9gr/cm3 for CdWO4) even more sensitive (for equal thickness) to the hard X-rays. Using Quartz lenses (50 and 75mm focal length) with 3.5mm optical aperture in combination with a 0.5mm thick LuAg scintillator the system parameters are optimised for spatial resolution & sensitivity.

The blur of the detectors is assessed at ~20um fwhm which is just about acceptable for the typical vertical sizes that we are measuring (i.e. projected beamsize h ~111um). The exact value of the blur is difficult to asses in laboratory only. While the type and thickness of scintillator and the choice of lenses & apertures have an impact on the ultimate value, the main uncertainty comes from the quality of the focussing since the extreme compactness of detector does not allow for a remote control of focus adjustment.

For this reason a simple test-bench was implemented behind an un-used beamport absorber where more space is available then on the real location of the detectors. This test-bench allows to install a fully mounted detector, to expose it to the same energy range of X-rays, and to limit the vertical size of these X-rays by the use of a 5um slit of 3mm thick Tungsten. The profile plot in fig.6 shows the result of such intrinsic spatial detector resolution (red curve) , compared to that of typical result values for beam measurements (black curve).

RESULTS WITH A SYSTEM OF 6 INDEPENDENT DETECTORS

A total of 6 detectors are installed at the up-stream dipoles of the ESRF cells 3, 5, 10, 18, 25 and 26.

Together with the already existing emittance monitors of the X-ray pinhole cameras in cells 9 and 25 [7] the ESRF Storage Ring' vertical emittance is now monitored by 8 independent devices. The corresponding IEEE-1394 cameras are controlled by a set of 5 PCs that run under Linux. A specific Tango device server takes images a rate of 15Hz, and after some selectable range of averaging then calculates the position and fwhm-size (h) of the vertical profile over a selected width of the 'stripy'-like image. The vertical emittance is calculated from h taking into account the (fixed) parameters of distance and photon-beam divergence, and the accelerator's Beta-vert. value at the source-point. The device server provides automatic gain and exposure time control for each camera, and correct background substraction. A panel for read-out & control was created using the Tango application toolkit framework (ATK).

The figures 5a & 5b show images of the 6 IAX detectors plus that of the 2 X-ray pinhole cameras. The first are with small emittance values while the latter are taken with a strong offset current in a skew-quadrupole corrector causing a huge increase of the vert. emittance. Note that the variation of intensity along the hor. axis seen in the IAX images is caused by the water cooling tubes inside the Copper absorber, this has no effect on the measurements in the vertical plane.

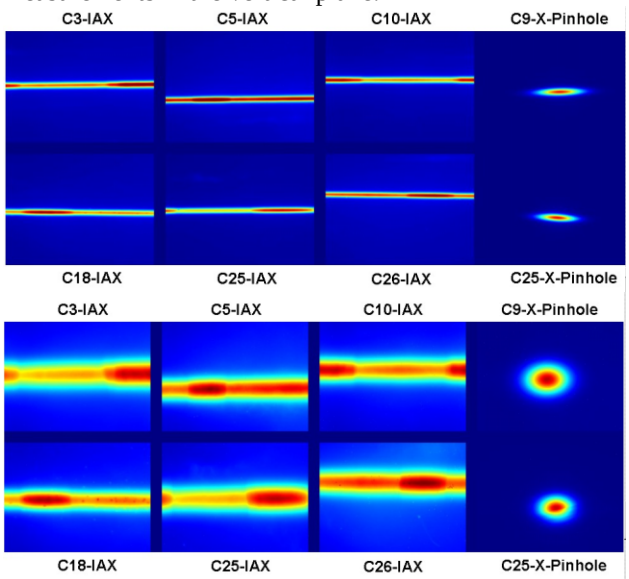

Figure 5a-b: images from the 8 devices under extreme different values of vert. beam emittance (~20 & ~500pm).

The fig.6 shows the vert. profiles of these extremes. It is noted that the scintillator is sensitive to other particles causing a background level in the image. This background level is dependent on the type and thickness of the scintillator, and has been successfully reduced by further detailed Lead shielding around the scintillator itself.

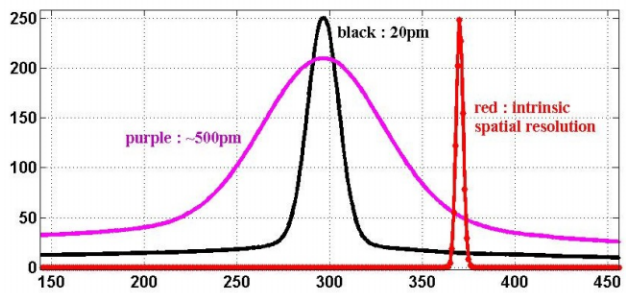

Figure 6: profile plots [A.U. & pixels) of the images shown in Fig. 5, and that of a 5um sized slit of a test set-up (red).

The capacity of the 6 IAX devices to measure very small emittance values (down to ~10pm) is proven. However, their absolute precision at these small values is more difficult to asses, in particular the direct comparison between their absolute result values (and that of the 2 Pinhole devices) is of limited significance because of the variation of the local hor.-vert. beam coupling correction obtained through a large set of local skew-quadrupoles.

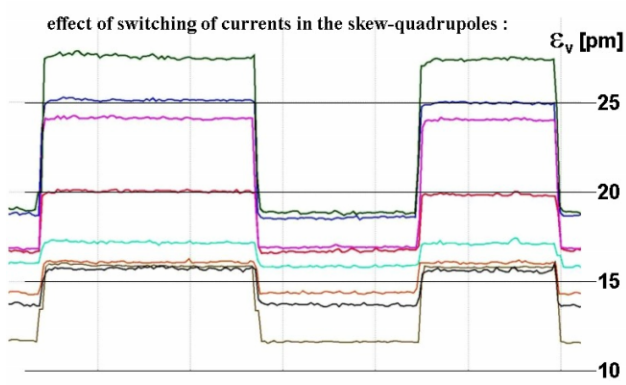

Figure 7: small result values of the 8 devices showing the effect of skew-quad current variation at high resolution.

The resolution (at 1sec measurement time) is estimated at <0.1pm which allows to see tiny effects on the beam of various systems (undulator gap changes, skew-quad correction, vacuum incidents, orbit position control, etc.).

In addition to the beamsize, the vertical beam position of the projected image is also monitored. It provides another tool for surveying the vert. beam position stability around the Storage Ring. The fig.8 shows the excellent correlation of the position results (30sec & 1um /div) of the Cell 25 IAX detector and the X-ray pinhole camera (separated 1.2m in the same dipole).

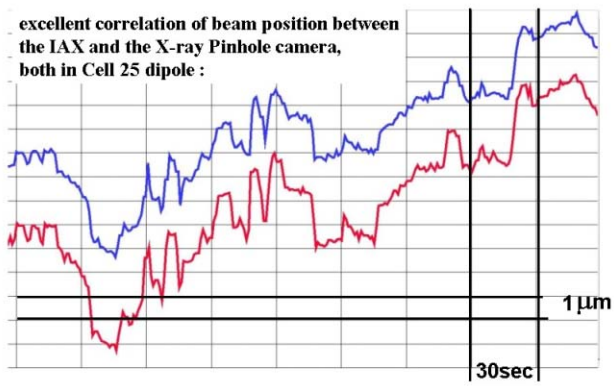

Figure 8: correlation in vert. beam position of 2 devices.

REFERENCES

[1] http://www.detectors.saint-gobain.com/ .
[2] http://www.crytur.cz/ .
[3] B.K.Scheidt, “Detection of Hard X-Rays in Air for Precise Monitoring of Vertical Position & Emittance in the ESRF Dipoles”, DIPAC’05.
[4] A-S.Müller, et al., “Precise Measurements of the Vertical Beam Size in the ANKA Storage Ring with an In-air X-ray ”, EPAC’06.
[5] B.K.Scheidt, “In-Air X-Ray Detectors : a New Field of Extremely Simple and Powerful Beam Diagnostics”, BIW06 May 2006, Fermilab-fnal.
[6] http://www.ptgrey.com/ .
[7] P. Elleaume et al, “Measuring beamsize and ultra-small electron emittance using X-ray pinhole camera”, J. Synchrotron Rad., June 1995-2.

DIGITAL BEAM TRAJECTORY AND ORBIT SYSTEM, FOR THE CERN PROTON SYNCHROTRON

J. Belleman, G. Kasprowicz, U. Raich, CERN, Geneva, Switzerland

Abstract

A new trajectory and orbit measurement system using fast signal sampling and digital signal processing in an FPGA is proposed for the CERN PS. The system uses a constant sampling frequency while the beam revolution frequency changes during acceleration. Synchronization with the beam is accomplished through a numerical PLL algorithm. This algorithm is also capable of treating RF gymnastics like bunch splitting or batch compression with the help of external timing signals. Baseline and position calculation are provided in the FPGA code as well. After having implemented the algorithms in C and MatLab and tested them with data from a test run at the PS, they have now been implemented in the FPGA for online use. Results of measurements on a single beam position monitor in the CERN PS and the SIS-18 at GSI will be presented.

INTRODUCTION

Even though over 50 years old, CERN's Proton Synchrotron (PS) plays a central role in the production of particle beams for all of CERN. Its extremely flexible RF accelerating system manipulates the beam in many different and complicated ways. Several types of beam (see Figure 1) are produced for various users. The PS is equipped with a trajectory measurement system, based on 40 electrostatic pick-ups (PUs), which measures the beam trajectory of any selected particle bunch over two consecutive revolutions anywhere during the acceleration cycle. However, measurements cannot be spaced closer than 5 ms apart and it does not handle bunch splitting and merging operations very gracefully. Also, part of the equipment dates back to 1988 and is in need of replacement.

A new system has been developed that is entirely digital, to be implemented in FPGA logic, and which deals smoothly with any existing and foreseeable beam manipulations (but limited to the regimes where the PUs deliver exploitable signals). It will also be able to provide measurements anywhere during an acceleration cycle without timing restrictions, to several clients simultaneously.

The centre of charge of a bunch is measured by integrating both the sum and the delta signals over the length of a bunch and applying :

$$x = S_x \frac{\Delta_x}{\Sigma}$$

where S_x is a scaling factor to yield a result in mm.

The gate and base line restitution (BLR) timing signals, required for integration are derived from the digitized beam signal using a numerical phase locked loop (PLL).

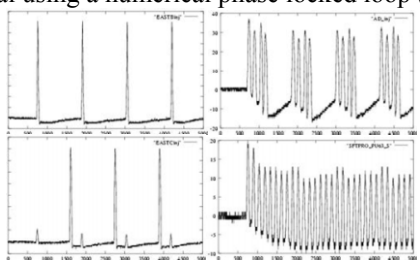

Figure 1: Beams in PS: EASTB, AD, EASTC, SFTPRO [3].

THE PLL ALGORITHM

Referring to Figure 2, a direct digital synthesizer (DDS) block generates a local oscillator (LO) square wave signal, which is then mixed with the PU sum. The product, after low pass filtering, controls the DDS frequency. The filter time constant, pole/zero arrangement and loop gain were chosen as a compromise between loop stability and lock-in time. The PLL ensures a fixed phase relation between the DDS and the beam [2].

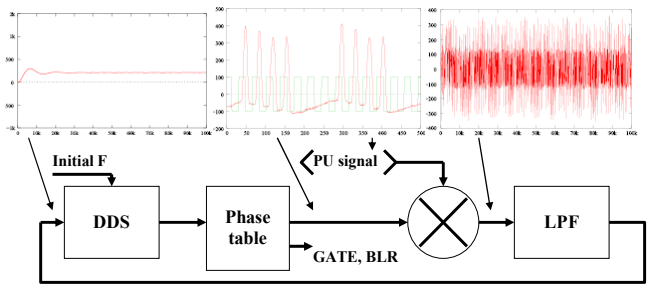

Figure 2: The numerical PLL algorithm principle.

BASELINE RESTORATION AND INTEGRATION

The beam signal originates from an electrostatic shoebox-type pick-up measuring both horizontal and vertical axes in one device. Since the PU does not pass DC, the signal has a baseline droop which needs to be removed before actual processing can be performed. The baseline restoration circuit consists of a filter, which corrects the PU frequency characteristics and a switched DC restorer synchronised by the BLR timing signal. It also protects the digital correction filter against saturation. The baseline correction is applied to the Σ, Δ_x and Δ_y signals. The baseline restoration block output is then integrated numerically over the period specified by the

gating signal. The integration results are stored in a large circular buffer.

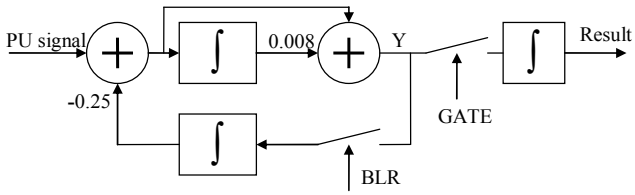

Figure 3 Baseline restorer and integrator.

HARDWARE IMPLEMENTATION

The algorithm is actually independent on the target hardware used. It has been implemented on 2 different hardware platforms, both providing fast 14bit ADCs, big Xilinx Virtex field programmable gate arrays (FPGAs) and fast memory (Figure 5Error! Reference source not found.).

The ADCs and all the processing logic run at a 125MHz clock rate and the FPGA internal data bus is 24 bits wide. Because the beam harmonic number may change during the acceleration cycle, and it varies for different beam types, a phase table was implemented as a double block of RAM in which the integration gate length, baseline removal and local oscillator pulses can be defined separately for each beam type.

The input signal, after baseline restoration, is fed into three numerical integrators which calculate sum and difference components. The integration results are then stored into the 128MB DDRII SDRAM circular buffer. The depth of the buffer allows storing results for more than one full acceleration cycle which takes approximately 2 s. The speed of the SDRAM is not critical, since only the final integration results are stored.

To make navigation over the buffer possible, there is a pointer array, implemented as separate embedded RAM memory, which points to specific events in the SDRAM memory, like harmonic changes, injection triggers and the 1 ms machine reference timing. The information about these events is delivered as external hardware triggers. The results from the buffer are then read out on user request and processed further in software running on a remote machine. There also are diagnostic facilities (Figure 4) that provide remote access to recordings of critical algorithm signals. It has the form of a logical analyser embedded in the main FPGA. Users can set triggers, choose delay times and signals to be recorded. It allows capturing the chosen signals on different time scales. It is controlled by a small program that writes the recordings into text files on the remote machine.

The acquisition and signal processing modules are managed by an embedded ARM-based single board computer (SBC) running the Linux operating system [1].

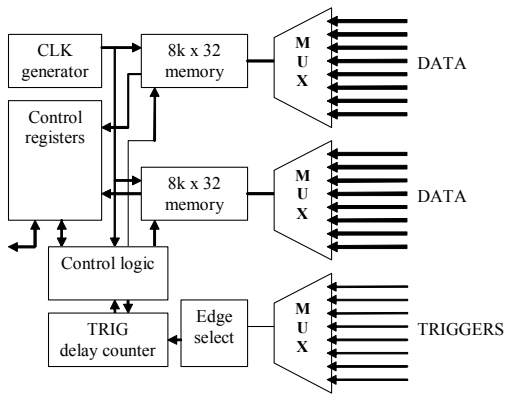

Figure 4: Embedded signal analyser.

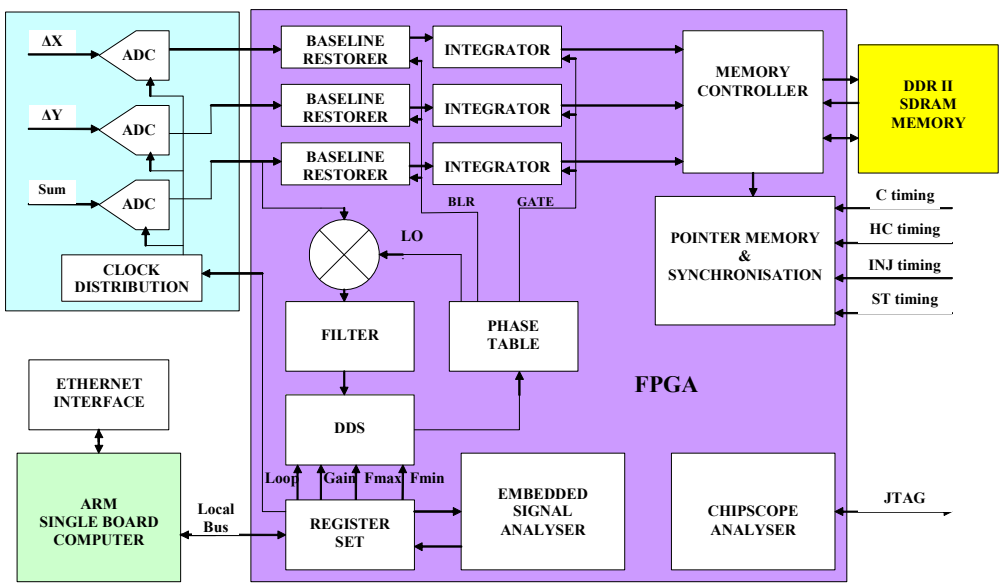

Figure 5: Hardware implementation.

MEASUREMENT RESULTS

Several tests with real signals from a single PU were performed in August 2006 on the CERN PS and in January 2007 on the GSI SIS-18. The results were captured using the embedded logical analyser (Figure 4). Figure 6 shows a raw PU signal (EASTB beam), its baseline corrected version and the gating signal that was generated by the synchronisation algorithm (Figure 2). The gate signal stays locked in phase with the beam pulses.

We also captured the evolution of the reconstructed revolution frequency (DDS frequency register content) during a full acceleration cycle (Figure 7).

It clearly shows that the algorithm stays locked in case of both the PS and SIS-18 accelerator. At the PS the injected beam is already bunched by the preceding PS Booster and the algorithms locks to an external RF system until the beam is injected into the machine. As soon as the beam is circulating in the machine and PU signals are seen, the algorithm switches synchronisation to the PU sum signals.

In case of the SIS-18, the beam is injected from a Linac and is completely unbunched at injection. The RF system bunches the beam shortly before starting acceleration. As soon as the bunch structure appears, the algorithm locks to the beam.

Figure 8 shows the measured sum and horizontal difference integration results, bunch per bunch. The position of the beam is then finally calculated off-line using these results.

The measurement results are rather noisy due to the limited clock frequency used during the preliminary tests (62.5 MHz). The RMS noise of the position measurement is about 0.6 mm, far beyond the target resolution of 0.1 mm. However it was shown, using the offline version of the algorithm on data measured with the full sampling rate, that the target resolution can be reached [1].

Figure 9 shows beam position results with betatron oscillations observed at one of the PUs just after a kicker pulse. An offline FFT allows us to calculate the tune of the accelerator.

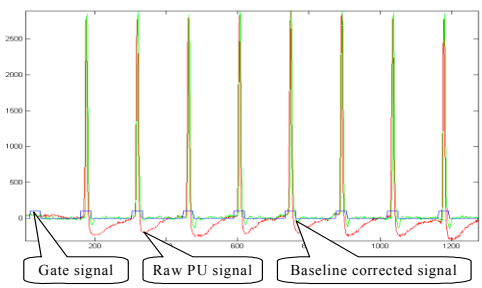

Figure 6: Signals of the PLL algorithm.

CONCLUSION

A prototype digital trajectory measurement system for the CERN PS is being realized. It consists of fast sampling ADCs, big FPGAs and large RAM memories. The FPGAs are used to implement a synchronisation algorithm, baseline correction and numerical integration of sum and difference signals from the electrostatic pickups in the PS.

A first implementation of the algorithms, running in an FPGA, was tested with beam at the CERN PS and the GSI SIS-18. Even though the sampling rate was only half the target frequency of 125 MHz, correct synchronisation with the beam could be demonstrated on both machines. Baseline correction as well as integration procedures worked as expected.

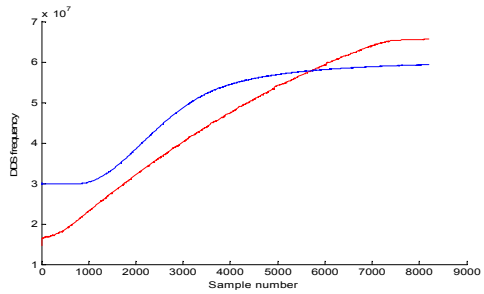

Figure 7: Revolution frequency during acceleration (DDS frequency) PS (blue) and SIS18 (red).

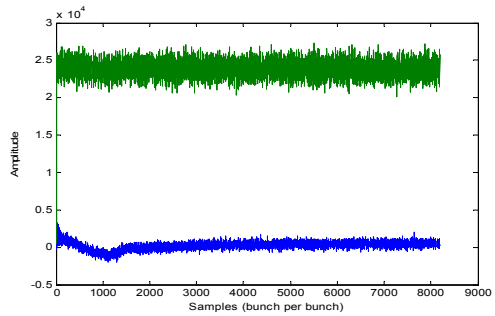

Figure 8: Sum and difference results.

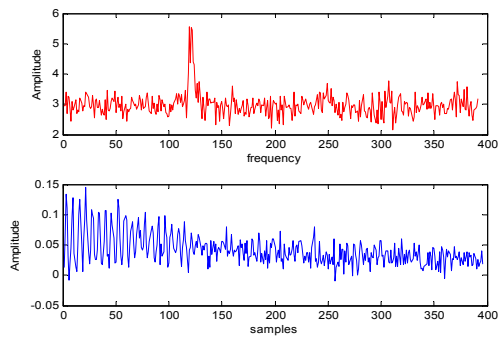

Figure 9: Betatron oscillations and its spectrum.

REFERENCES

[1] J.M. Belleman, "Using a Libera signal processor for acquiring position data from the PS orbit pick-ups", CERN AB-Note-2004-059 BDI, http://documents.cern.ch//archive/electronic/cern/others/ab/ab-note-2004-059.pdf .

[2] J.M. Belleman, "A new trajectory measurement system for the CERN PS", DIPAC2005 slides, http://cern.ch/jeroen/slides/DIPAC05slides.pdf .

[3] Beams in PS, CERN website http://jeroen.web.cern.ch/jeroen/beams.html .

PROPOSED BEAM POSITION AND PHASE MEASUREMENTS FOR THE LANSCE LINAC*

J. D. Gilpatrick#, B. Blind, S. Kurennoy, R. McCrady, J. O'Hara, C. Pillai, J. Power, L. Rybarcyk
LANL, Los Alamos, NM, 87545, U.S.A.

Abstract

There is presently an ongoing effort to develop beam position and phase measurements for the Los Alamos Neutron Science Center (LANSCE) linac associated with an improvement project known as the LANSCE Refurbishment. This non-interceptive measurement's purpose is to provide both measurements of beam phase for determining RF-cavity phase and amplitude set points, and position for determining the 805-MHz linac input beam transverse position and trajectories. The measurement components consist of a four-electrode beam-position and phase monitor (BPPM), a cable plant that transports the 201.25-MHz signals, electronics capable of detecting phase and amplitude signals, and associated software that communicates with a mature LANSCE control system. This paper describes measurement requirements, proposed beam line device, initial concepts for the associated electronics, and some of the issues developing beam measurements for an operational facility.

NEW LINAC BPPM REQUIRED

The LANSCE 805-MHz linac has a series of legacy beam-position monitors (BPMs) that contain four B-dot loops for beam-position measurements and an additional cylindrical-capacitive pickup, known as the "Delta-T loop." The Delta-T loops provide the 201.25-MHz bunched-beam signals to measure the beam's central phase with respect to a reference and determine the time of flight between accelerating cavities. This phase and time-of-flight information allows the LANSCE accelerator operators and operational scientists to set the accelerating modules' RF-fields phase and amplitude. Unfortunately, the B-dot position measurements do not reliably provide beam-position information.

Since there are no dependable non-interceptive beam-position measurements within this 48-module linac, the linac beam steering is corrected using beam-centroid information from slow wire scanners, and loss monitors. These measurement dependencies cause the linac tuning to be slow and eliminate auto-tuning possibilities. Therefore, new BPPM measurement systems are being developed for the 805-MHz linac.

LANSCE BEAM "FLAVOURS"

Once extracted from their independent sources, the 750-keV H^+ and H^- beams are combined in their low-energy transports by temporally multiplexing and injecting them into 16.7-MHz and 201.25-MHz bunching cavities. There they are partially bunched in preparation for their injection into the Drift Tube Linac (DTL), where the beams' 201.25-MHz time structures are maintained while they are being accelerated to 100 MeV. The H^+ beam typically has a 30-Hz Repetition Rate (RR) and a 0.625-ms long "macropulse" resulting in a Duty Factor (DF) of 1.875%. The H^- beam has a more complicated time structure consisting of up to a 40-Hz RR and a 0.625-ms long "macropulse." This "macropulse" is further subdivided or chopped into ~1750 "minipulses" and consists of 300-ns-long beam pulses repeated with a RR of 2.8 MHz, the 72nd sub-harmonic of the 201.25-MHz bunching time structure. Ultimately, the "minipulse" length limits the measurement's ability to acquire valid beam position and phase information.

As both beams emerge from the DTL, they are magnetically separated. The H^- beam's central phase delay is adjusted so that when the two beams are recombined prior to injection into the linac, each beam's central phase matches the proper 805-MHz linac RF bucket. The complicated transport beam line that accomplishes the adjustment of the H^- beam's central phase with minimal disturbance to the beam's transverse characteristics is called the Transition Region (TR). The TR output beams are injected into the 805-MHz side coupled linac that accelerates these beams from 100- to 800-MeV. In the past, both beams were accelerated to 800-MeV but presently only the H^- beam is injected into the linac and accelerated to 800-MeV. A spur beam line located near the beginning of the TR allows the H^+ beam to be transported to the Isotope Production Facility (IPF) beam line. Table 1 describes these conditions commonly called beam "flavours" or types of beams and timing structures that are transported through the linac and associated experimental areas, such as the Proton Storage Ring (PSR), the Proton Radiography (pRAD), or the Ultra Cold Neutron (UCN) areas.

The last row of Table 1 shows a particular beam "flavour" associated with the Weapons Neutron Research (WNR) experimental facility. Presently, each of the beam "flavours" is in its own individual 60-Hz half cycle or 8.3-ms period, except for those beams tuned for WNR. Unlike the other beam "flavours," this particular beam occupies the same "macropulse" period but in opposite 180-deg RF-phase buckets as the IPF beam. This H^- beam has ~2.5X the charge in a single RF bucket and can be separated by multiples of ~1.8 microseconds, the 360th sub-harmonic of 201.25-MHz bunching time structure. Therefore, the BPPM signals will be a combination of the two species drifting through each BPPM bore, resulting in some additional measurement complications.

*Work supported by US Department of Energy.
#gilpatrick@lanl.gov

Table 1: Important LANSCE linac beam "flavours"

Exp. Area	Beam Type	Minipulse		Macropulse		I_{pk}	I_{Avg}
		DF (%)	RR (MHz)	DF (%)	RR (Hz)	(mA)	(μA)
IPF	H+	N/A	N/A	1.875	30	10	200
MTS	H+	N/A	N/A	3.75	60	20	800
UCN	H-	17	5.4	1.875	30	10	60
PSR	H-	84	2.8	2.5	<40	10	200
pRAD	H-	34	5.4	0.3	30	0.3	100
WNR	H-	0.008	5.4	6.25	< 100	~0.7	~5

MEASUREMENT REQUIREMENTS

Table 2 shows the BPPM measurement system's overall requirements, including such parameters as beam position, phase, and bunched beam current.

Table 2: Overall BPPM Measurement Requirements

Parameter	Value
Position Repeatability (mm)	0.1
Position Accuracy (mm)	1
Beam Position Range (±mm)	13
Beam Position Response Time (μs)	2 to 5
Phase Repeatability (201.25-MHz-degrees)	0.25
Phase Accuracy (201.25-MHz-degrees)	N/A
Phase Range (201.25-MHz-degrees)	+/- 180
Beam Phase Response Time (μs)	50 to 100
Current Repeatability (mA)	0.05
Current Accuracy (mA)	N/A
Current Range (mA)	21 to 0.9
Current Response Time (μs)	2 to 5

There are two general goals for the placement of these BPPMs, namely to place a subset of BPPMs so that they provide both position and trajectory angle information, and to place BPPMs in the locations now populated by older and existing Delta-T loops, resulting in 19 locations within the linac.

Operational experience has shown that to minimize the beam losses in the linac, the H^+ or H^- beam is injected into the 805-MHz linac such that established positions are achieved at a number of wire scanner locations. Once injected, the two beams are not steered throughout the rest of the linac. The proposed steering algorithm for placing the beam on the proper trajectory involves beam-position measurements before and after adjustment of upstream horizontal and vertical steerers. The resulting data are used to determine the relevant transfer-matrix elements between steerers and BPPMs, and subsequently, the proper settings of the steerers.

Through a set of simulations, locations in the linac were determined where BPPMs should be placed for the steering algorithm to work under a wide range of beam-optics conditions, such as for linac quadrupole doublets with settings of between 90% and 110% of their historic-average values and linacs with and without acceleration [1]. A single BPPM pair is not sufficient to assure that the beam is on the proper trajectory in all cases. Even for tunes where a particular BPPM pair is acceptable, configurations with three or four BPPMs out-perform a single BPPM pair prior to the 211-MeV beam stop.

Figure 1 shows the results of simulations with rms BPPM measurement errors of between 0.025 mm and 0.15 mm. For each BPPM configuration and rms BPPM error, 10,000 different sets of randomly generated measurement errors were used, and for each set the largest horizontal and vertical beam-centroid excursion after trajectory correction was determined. Then, rms values of the sets of maximum values were computed. Figure 1 shows plots of these horizontal and vertical rms values versus rms BPPM repeatability error, for the linac with acceleration and the historic-average settings of the quadrupoles. In simulating the steering algorithm, the two horizontal and two vertical steerers were adjusted to each cause beam-position changes within the linac of up to 2 mm. For a specific rms BPPM repeatability error, performance improves with larger steerer adjustments. However, in the eventual implementation of the steering algorithm beam losses must be avoided, which limits the acceptable changes in beam position.

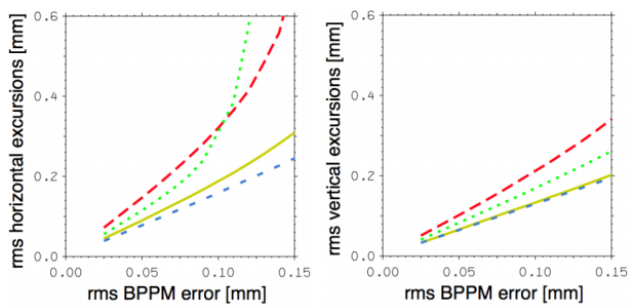

Figure 1. Rms values of the sets of horizontal (left) and vertical (right) maximum excursions as a function of rms BPPM repeatability error, for BPPMs downstream of RF tanks 6 and 7 (**long red dashes**); downstream of RF tanks 6 and 8 (**green dots**); down-stream of RF tanks 6, 7, and 8 (**yellow**); and downstream of RF tanks 7, 8, and 28, and upstream of RF tank 30 (**short blue dashes**).

INSTRUMENTATION COMPONENTS

A different series of RF simulations was performed in order to establish the BPPM mechanical and electrical characteristics [2]. The BPPM measurement systems to be installed will process the beam's fundamental bunching frequency of 201.25 MHz. Since the design's intent is not to detect and measure much higher signal frequencies, the simulations showed that there were two primary designs of interest. One design showed the four electrodes terminated in their characteristic impedance and other design showed its four electrodes shorted to ground. Both of the designs studied operated equally well at the fundamental bunching frequency in the simulations and in the field. Ultimately, the choice between the two

designs was based on reliability and complexity due to the fewest number of SMA coaxial feedthroughs used, resulting in the shorted-electrode design being chosen (see Table 3 for further mechanical design details).

Table 3. Primary Mechanical BPPM Design Details

Mechanical Characteristics	Value
Electrode Characteristic Impedance (Ω)	50
Electrode Inner Radius (mm)	22.16
Electrode Length (mm)	43
Electrode Subtended Angle (degrees)	60
Body Inner Radius (mm)	27.78
Flange-to-Flange distance (mm)	76.2
Simulated Position Sensitivity (dB/mm)	1.26
Analytic Position Sensitivity Estimate (dB/mm)	1.48

To simplify overall requirements, a single mechanical design will be used for the BPPMs throughout the 805-MHz linac. Given this single design, all BPPM electrodes will be as long as possible and will have 60-deg subtended angle. A strong electro-mechanical connection, such as a braze joint, between the feedthrough inner conductor and the electrode will be used. Alignment tooling on the BPPM body will provide a common interface between the BPPM's mapped characterization and its final non-adjustable beam line laser-tracker-measured location. The flanges and vacuum seals are those used throughout the LANSCE facility. Figure 2 shows a BPPM initial concept [3].

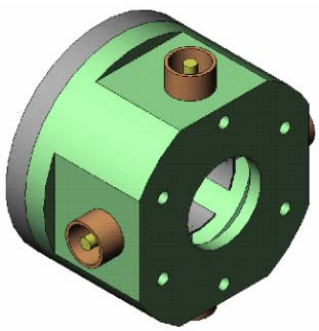

Figure 2. The picture above is a BPPM concept for use in the 805-MHz linac.

From previously discussed studies and other input, including a theoretical analysis of beam position monitors [4,5,6], BPPM signal parameters were estimated (see Table 4). Using these listed parameters, a simulation of In-phase and Quadrature-phase (I/Q) processor channel was performed [7]. This processor channel consists of a 201.25-MHz band pass filter, an amplifier, and a 14-bit Analog-to-Digital Converter (ADC). If the ADCs are clocked at a rate which "undersamples" the fundamental bunching period of the four filtered BPPM-electrode signals such that at least one I- and Q-sample is acquired during a single 60-nanosecond "minipulse", both beam magnitude and phase information may be reconstructed from the acquired samples.

The I/Q simulations showed the beam position measurements can reach their required repeatability by averaging 9 "minipulse" samples and the central beam phase measurements can reach their required repeatability by averaging 10 "minipulse" samples. Within the I/Q simulations, a 35-MHz clock was used to trigger the ADCs and the ADCs external trigger will be required to be synchronous with the linac's reference to within a 0.4-ps rms error.

Table 4. Estimated BPPM Port Signal Parameters

Signal Parameter	100-MeV	800-MeV
Tuning Power $_{0.9\ mA,\ centered}$ (dBm)	-44	-47
Min Power $_{0.9\ mA\ \ offset}$ (dBm)	-56	-59
Max Power $_{21\ mA\ \ offset}$ (dBm)	-6	-10
S:N Ratio $_{0.9\ mA\ \ centered,\ @\ BPPM}$ (dB)	~41	~38
Position Repeatability $_{0.9\ mA\ \ centered}$ (mm)	~0.07	~0.1
Phase Repeatability $_{0.9\ mA,\ centered}$ (deg)	~0.2	~0.3

ACKNOWLEDGEMENTS

The authors would like to acknowledge Don Bruhn, Jerry Davis, Mark Gulley, John Lyles, and Mark Prokop for providing additional information for these proposed beam measurements.

SUMMARY

This paper has described some of the initial issues for developing beam position, phase, and bunched beam current measurements for the LANSCE 805-MHz linac. This report describes the linac operational requirements these BPPM measurements must satisfy. It has also described some of the logic for what locations the new BPPMs will be installed. Finally, this paper described the BPPM mechanical design and some initial simulations of a feasible electronic processor design.

REFERENCES

[1] B. Blind, private communication, February 22, 2007 and April 12, 2007.

[2] S. Kurennoy, "Electromagnetic Modeling of Beam Position and Phase Monitors for LANSCE Linac," to be published at the 2007 Particle Accelerator Conference, Albuquerque, NM, June 25-29, 2007.

[3] J. O'Hara, "LANSCE Prototype Beam Position and Phase Monitor (BPPM) Mechanical Design," to be published at the 2007 Particle Accelerator Conference, Albuquerque, NM, June 25-29, 2007.

[4] J. H. Cupèrus, "Monitoring of Particle Beams at High Frequencies," **NIM**, 145 (1977), pp 219-231.

[5] R. E. Shafer, " Beam Position Monitoring," Beam Instrumentation Workshop 1989, **AIP 212**, pp.27-58.

[6] J. D. Gilpatrick, et al., "Experience with the Ground Test Accelerator Beam Measurement Instrumentation," Beam Instrumentation Workshop of 1993, **AIP 319**, pp. 154-169.

[7] J. Power, "Simulation of a Direct Downconversion BPM Channel with I & Q Data Processing," at LANSCE, March, 2007.

A LASERWIRE BEAM PROFILE MEASURING DEVICE FOR THE RAL FRONT END TEST STAND

D. A. Lee[1], J. K. Pozimski[1+2], C. Gabor[2], P.Savage[1]
[1] Imperial College London, UK, [2] Rutherford Appleton Laboratory, Oxford, UK

Abstract

The Front End Test Stand (FETS) [1] at the Rutherford Appleton Laboratory (RAL) is being developed to demonstrate a chopped H^- beam of 60 mA at 3 MeV with 50 pps and sufficiently high beam quality for future high-power proton accelerators. As such, it requires a suite of diagnostic instruments to provide detailed measurements of the ion beam properties [2]. Due to the high beam brightness and a desire to have online instrumentation while the accelerator is operational, a series of non-intrusive and non-destructive diagnostics based on laser-detachment are being developed.

In this paper, the principle behind the laser-based diagnostic instruments is given and the progress [3] that has been made towards the construction of a laserwire instrument that can measure the beam profile at an arbitrary angle is described. In particular, the results of field distribution and particle tracking simulations are shown and the design of the instrument and the vacuum vessel in which it will be mounted are presented. The software that will be used to reconstruct the 2D transverse beam density distribution from the beam profiles is also described.

INTRODUCTION

The RAL Front End Test Stand will consist of a 60 mA H^- ion source, a magnetic LEBT, a 324 MHz RFQ and a MEBT with a beam chopper at a beam energy of 3 MeV. The length of the macro-pulse will be up to 2ms at a repetition rate of 50Hz (10% duty cycle). The aim is to demonstrate the performance of the ion source and RFQ and to test the high speed chopper [4], which will have a rise time of less than a nanosecond to produce a beam pulse structure suitable for the next generation of high power proton accelerators [5]. The chopper will be placed inside the MEBT [6], which is used to match the ion beam into further linac structures should they be constructed.

From the point of view of beam diagnostics, a device that can make high resolution measurements and withstand the large beam power is desirable. A possibility that meets these requirements is non-destructive laser-based beam diagnostics that has no mechanical parts intercepting the beam.

Such non-intrusive diagnostic devices have other advantages over conventional beam diagnostics. For example, on-line monitoring whilst the accelerator is operational is possible; there is almost no influence on beam parameters like the space charge potential (i.e. there is no production of unwanted secondary particles); their lifetime is greatly increased; and they can offer additional information about the phase space.

LASER-BASED BEAM DIAGNOSTICS

Negative ions can be neutralised by detaching the additional electron with a photon (for H^- ions, the binding energy of the outer electron is ~0.75eV [7, 8]). By using a dipole magnet to separate the different species after neutralisation a variety of beam parameters can be measured.

For the FETS project two diagnostic instruments based on laser detachment are being developed: a device to measure the 6D emittance after the RFQ and MEBT; and a beam profile monitor that will measure the 3D beam density distribution after the ion source. The principle behind the emittance measuring instruments is described in the following subsection before further details about the laserwire beam profiler are given.

The FETS laser-based emittance measurement

A device to measure the emittance of the beam behind the RFQ, before and after the MEBT and chopper, is being developed. It is shown schematically in figure 1.

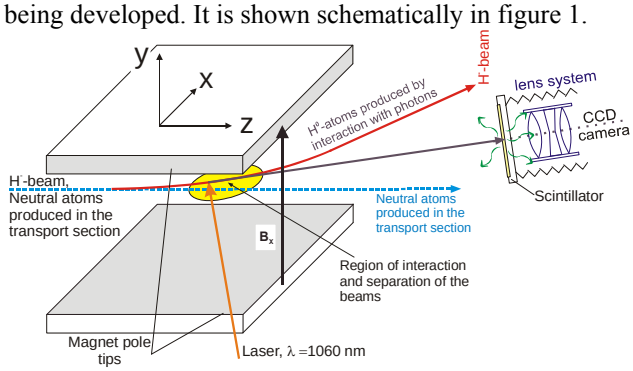

Figure 1: The principle of the photo-detachment emittance measurement. The laser detaches the additional electron of the H^- ions inside a magnetic field and the distribution of the produced neutral H^0 atoms is detected.

A proof-of-principle experiment has been performed at IAP Frankfurt. The focus was on the basic properties of such a device and the interpretation of the transfer function to calculate the emittance. This experiment showed that this method is suitable for the emittance measurement of high brightness ion beams. The experimental results showed that this method gave a good agreement with traditional slit-slit devices while providing additional information about the phase space. See [9, 10] for further details of this experiment.

Typical parameters in the MEBT are foreseen to be a beam radius of 5 mm and a divergence angle of ±25 mrad. To aid the design of the diagnostic dipole magnet, beam envelope calculations have been performed with the aim of reducing particle losses and to check if additional beam optics are required after the MEBT. The current magnet

design has a pole piece separation of 150mm and a reference path length of 500mm. These values have been chosen so that there is enough space for the ion beam and for movable stages to guide the laser beam to and from the ion beam. The predicted performance of the emittance measurement device is an angular resolution of <0.1 mrad with a position resolution, determined by the laser, of approximately 0.5 mm.

The FETS laserwire beam profile monitor

By stepping a laser across the H^- beam and measuring the number of electrons detached a 1D projection of the beam can be measured. The number of electrons can be measured by separating them from the remaining H^- ions and deflecting them into a Faraday cup (see figure 2).

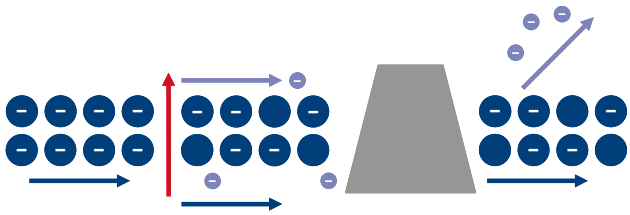

Figure 2: The principle of the laserwire instrument. Electrons (light blue) are detached from the H^- ions by a laser (red) and then the species are separated by a dipole magnet (grey).

Projections of the beam can be taken at several different angles by varying the angle at which the laser passes through the ion beam. These projections can then be used to reconstruct the 2D ion beam density distribution. By using a laser pulse that is shorter than the ion beam pulse duration and delaying the laser pulse relative to the ion beam it will be possible to reconstruct the 3D beam density distribution from several 2D distributions.

Initially the FETS laserwire will use a 500 mW, 671 nm DPSS laser, focussed to a beam diameter of 1.5 mm. This waist gives the narrowest possible parallel laser beam through the ion beam. In each 2 ms pulse the laser will neutralise, at most, 10^{-7} of the total H^- ions giving a peak signal of $\sim 7\times10^7$ electrons.

LASERWIRE COMPONENTS

Vacuum vessel

The FETS laserwire device will be mounted in the first differential pumping vacuum vessel after the ion source. The beamline length, and so space available for the laserwire scanner, is constrained on one side by the need to prevent the ion beam expanding beyond the acceptance of the LEBT and on the other by the need to adequately pump the vessel. A beamline length of ~220 mm has been chosen to enable a CF160 pump port to be used.

The tank will contain mirrors mounted on rotatable and movable stages, to enable projections of the beam at an arbitrary angle to be measured. It will also contain the dipole and detector enclosure. The current design of this vessel is shown in figure 3.

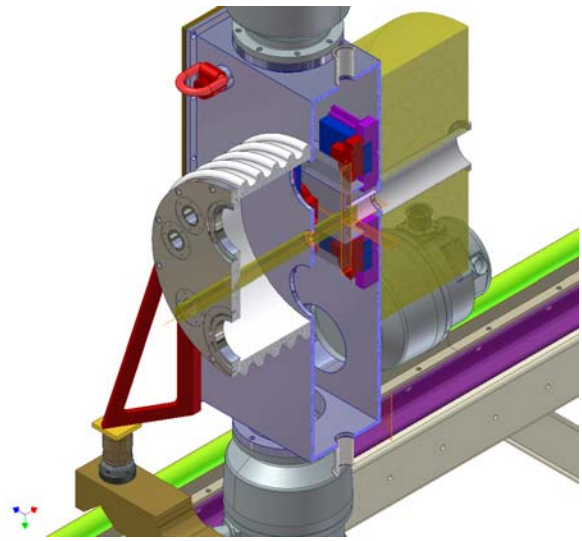

Figure 3: A cut-away of the mechanical design of the laserwire instrument and vacuum vessel. The ion source insulator column is shown to the left, the LEBT to the right.

Dipole enclosure

The FETS ion source will extract an H^- beam at 65 keV. As the momentum transferred from the photons to the detached electrons is negligible the detached electrons are reasonably assumed to be travelling with the same velocity as the H^- ions. At this velocity the magnetic field required to deflect the electrons is comparable to that of the Earth (~2 Gs). To increase the required magnetic field, and so prevent unwanted deflection of the electrons, an additional electrostatic acceleration of 2 kV will be included in the dipole enclosure. This raises the required magnetic field to 23 Gs. The design of the detector (post acceleration, dipole magnet and Faraday cup) is illustrated in figure 4.

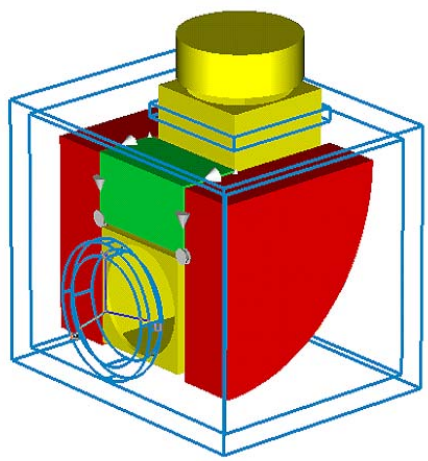

Figure 4: Detector design for the FETS laserwire. Shown in red is the iron yoke and pole pieces, in green are the windings (100 Amp-turns), outlined in blue is the magnetic shielding (at ground), in yellow are the copper accelerating sheath (held at 2 kV) and Faraday cup. The beam aperture is 50 mm and overall length is ~130 mm.

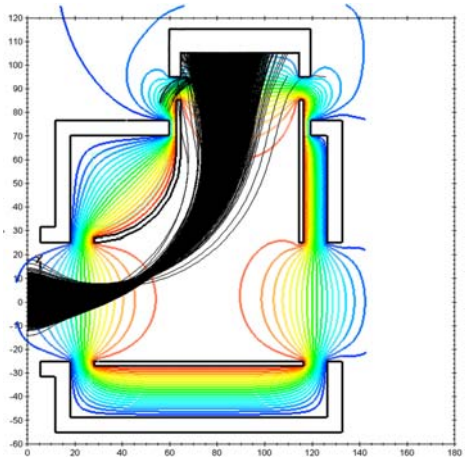

Figure 5: Results of the CST EM STUDIO and GPT simulations. Particle tracks (black) and equipotential lines at 100 V intervals (coloured) are shown through a section of the detector shown in figure 4.

Simulations of the magnet enclosure have been performed using CST EM STUDIO. Particle tracking through the modelled fields was then performed using the General Particle Tracer (GPT) code using preliminary results from the FETS pepperpot device (see [2] for details) for the input distribution. The simulations gave an electron transmission greater than 99% without adversely affecting the H^- beam. A plot is shown in figure 5. The results from these simulations are being used to refine the dipole enclosure design and are being incorporated into the design of the vacuum vessel.

2D BEAM DENSITY DISTRIBUTION RECONSTRUCTION

The Algebraic Reconstruction Technique (ART; see [11]) will be used to reconstruct the 2D beam density distribution. It is an iterative, algebraic approach to image reconstruction, as opposed to an approach that makes use of Fourier Transforms. The ART is preferred to Fourier Transform-based methods for the FETS laserwire due to difficulties in untangling the effects of the laser beam profile on any given projection. It also requires fewer projections (typically 20) to give a good reconstruction.

The ART works by reconstructing the density distribution on a grid, with each pixel within the grid having a density assigned to it. Masks corresponding to the laser's paths through the ion beam, incorporating the laser's beam profile, are constructed. These masks are then cast across the grid and the pixels' values, weighted by the mask's local values, are summed. These summed values are then compared to the measured values from the laserwire device. Any discrepancy between the two values is distributed, according to the weighting of the mask, across the corresponding pixels. The next laser strip is then considered. The algorithm stops when a χ^2 condition is met. Figure 6a shows a 2D profile of the ion beam captured by the pepperpot device. A reconstruction of this image using the ART is shown in figure 6b.

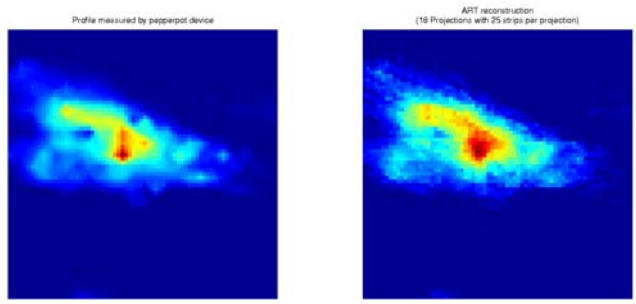

Figure 6a (left): A 2D profile measured by the pepperpot Figure 6b (right): The reconstructed 2D profile from 18 projections, each comprising of 25 strips, after 100,000 iterations.

OUTLOOK

The design of a laserwire beam profile measuring device is progressing well. It is anticipated that it will be installed at RAL this calendar year with results to follow soon after.

A first design of a laser-based emittance measurement shows promising results. The instrument is expected to be available with the RFQ in approximately three years time. First experimental work this summer will concentrate to develop a precise laser guiding system to improve reliability in terms of homogenous transfer function as well as measurement resolution.

REFERENCES

[1] A. P. Letchford et al., "The RAL Front End Test Stand", MOPCH112, EPAC 2006, Edinburgh, UK
[2] S. Jolly, *et al.*, "Beam Diagnostics for the Front End Test Stand at RAL", DIPAC 2007, Venice, Italy
[3] C. Gabor *et al.*, "Laser-based beam diagnostic for the Front End Test Stand (FETS) at RAL", EPAC 2006, Edinburgh, UK
[4] M.A. Clark-Gayther, G. Bellodi, F. Gerick, "A Fast Beam Chopper for the RAL Front End Test Stand", EPAC 2006, Edinburgh, UK
[5] R. Maier, "High power proton linacs, applications and design components", EPAC 2002, Paris, France
[6] C. Plostinar, M.A. Clark-Gayther, C.M. Thomas, "Design progress of the re-bunching RF cavities and hybrid quadrupoles for the RAL Front-End Test Stand (FETS)", LINAC 2006, Knoxville, USA
[7] J. T. Broad and W. P. Reinhardt, Phys. Rev. A 14 (1976), 2159–2173
[8] W. B. Cottingame *et al.*, IEEE Trans. Nucl. Sci., NS-32 (1985), 1871–1873
[9] C. Gabor *et al.*, "Experimental results of a non-destructive emittance measurement device for H^- beams", PAC 2005, Knoxville, USA
[10] C. Gabor *et al.*, "Laser based beam diagnostic for the Front End Test Stand (FETS)", PNNIB 2006, Santa Fe, USA, *to be published in* AIP Conf. Proc.
[11] D. Raparia. *et al.*, "The Algebraic Reconstruction Technique (ART)", PAC 1997, Vancouver, Canada

BPMS FOR THE XFEL CRYO MODULE

D. Nölle, N. Baboi, K. Knaack, D. Lipka, J. Lund-Nielsen, N. Mildner, R. Neumann, M. Siemens, F. Schmidt-Föhre, T. Traber, S. Vilcins , DESY, 22603 Hamburg, Germany

Abstract

The European XFEL is based on superconducting accelerator technology developed in the context of the TESLA collaboration [1]. The accelerator itself consists of cryo modules equipped with 8 acceleration cavities, followed by a quadrupole/steerer package, a BPM and a HOM absorber. This contribution will present the layout of the BPM system for the cryo modules, describing the monitor itself and its integration into the cryo module. Additionally, the electronics concept will be discussed. Finally the results of beam measurements at FLASH using prototypes of the monitor and the electronics will be presented.

INTRODUCTION

The accelerator complex of the European XFEL (Fig.1) at DESY will consist of a superconducting LINAC with a maximum energy of about 20 GeV. It is constructed out of 116 cryo-modules, with only a few warm sections intercepting the cold acceleration chain. The only monitor devices in the cold sections are the BPMs, one in each cryo module. They have to provide position and charge information along the LINAC.

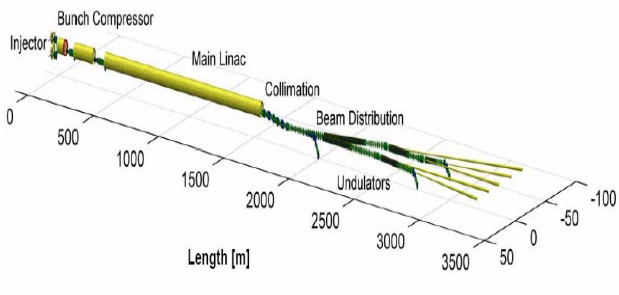

Figure 1: Scheme of the European XFEL.

In contrast to linear collider applications circular beam shapes are appropriate for FEL operation, relaxing the requirements on the XFEL BPMs compared to ILC specs [2]. The requirements on the XFEL module BPMs are listed in table 1.

Two BPM types are currently under investigation: a re-entrant cavity BPM developed by CEA, Saclay in collaboration with DESY, and a button type BPM. The latter is the topic of this paper. The status of the re-entrant cavity BPM is reported also on this DIPAC[3].

Table 1: Requirements of the BPM

Parameter	Value
Charge	0.1 – 1 nC
Bunch Spacing	200 ns (≥, arbitrary pattern)
Position Resolution	< 50 µm (Single Bunch)
Charge Resolution	1 %
Trigger	Internal/External (Gate)
Clock	100 MHz, Sync. To RF Master
Number of Bunches	3250 within 650 µs @ 30 Hz
Length	170 mm
Beam Pipe	78 mm
Align. Tolerance to magnetic Quad. Axis	300 µm, transversal 3 mrad, roll angle
Operation Temp.	4 – 20 °K

INTEGRATION INTO THE XFEL CRYO MODULE

The XFEL cryo module houses 8 TESLA cavities followed by a superconducting magnet block, consisting of a superferric quadrupole and a set of steerers. The BPM is mounted to the vessel of the magnet. Components to follow are a gate valve and the HOM absorber. Fig. 2 shows the layout of the end of the cryo module in detail.

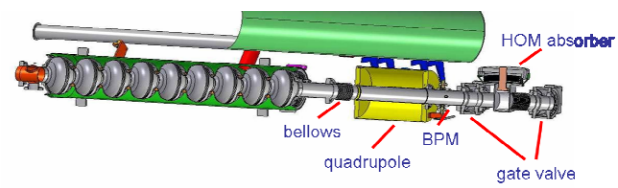

Figure. 2: Layout of the downstream end of the XFEL Cryo module.

In contrast to module BPMs at FLASH [4] (the former TTF), the BPMs are flanged and not welded to the beam pipe. The BPM has a length of 170 mm, with two fixed, (so) called “cavity flanges” on both sides. The beam pipe diameter is 78 mm. The inner beam pipe has to be copper plated. Since the BPM is connected to the liquid He vessel of the quadrupole, the BPM will be at a temperature close to the 4 K level. The vicinity of the superconducting cavities requires a particle free inner volume of the BPM (Cleanroom Class 10). The alignment to the magnetic axis and orientation of the quad has to be better than 300 µm (transverse) and 3 mrad (roll angle). The cables of the BPM have to be a compromise between low cryogenic losses and good RF properties.

BPM MECHANICS

Following the requirements on the mechanics inside the module a prototype pickup monitor has been designed. It is foreseen to mill the BPM out of a single piece of stainless steel, providing optimum tolerances and safety from the vacuum point of view. The alignment to the adjacent quadrupole will be based on field measurements of the quad and the use of dowel pins, included in the mechanical design of the BPM, in order to meet the tolerances mentioned before.

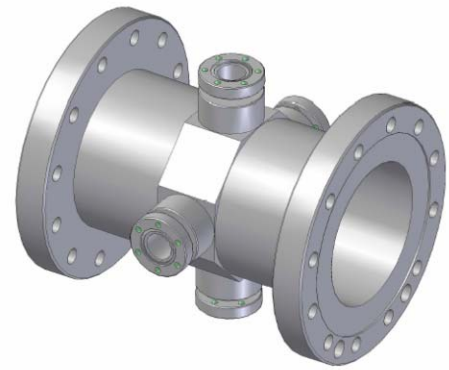

Figure 2: 3D Model of the BPM prototype.

The design of a prototype is shown in Fig. 2. In order to reach the required resolution at the lower charge limit of 0.1 nC, feedthrough geometries with a larger button size of 15 mm are currently under investigation for the final design. Therefore, there will be some changes concerning the mounting of the feedthroughs to the BPM body and concerning the feedthroughs themselves.

The feedthrough will be optimized for RF properties up to about 1.5 GHz. Another requirement is reliable operation in the cryogenic environment. Therefore, extensive tests are foreseen on a prototype series, but also all items of the series production will have to pass a cryogenic test.

Currently the design of a feedthrough is under investigation, starting from the version shown in Fig. 3. Some geometric properties will be optimized for a good compromise of RF and cleaning process.

Different material combinations, like stainless steel, titanium for body and pickup; molybdenum, CuBe or stainless steel for the inner conductor and alumina or glass ceramics for the insulator are currently under investigation. Also different assembly techniques like soldering or force fitting are evaluated. A study looking at the reliability in cryogenic environment with different feedthrough types, which were available at that time, has shown, that as well soldered as force fitted designs are suitable at low temperature [5].

Based on simulations signal amplitudes of 50 V_{pp} are expected for an electron beam of 1 nC passing the center of the button monitor. The RF response is expected to be flat in the frequency regime up to 10 Ghz (Fig. 4).

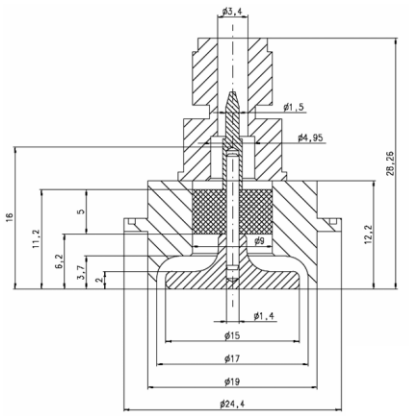

Figure 3: Design study for an XFEL feedthrough.

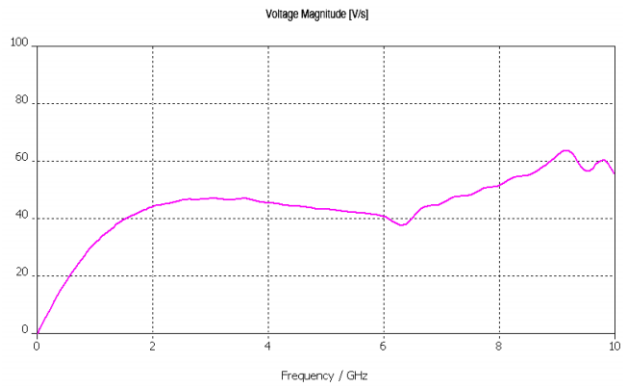

Figure 4: Signal output vs. frequency for a single button and 1 nC charge, simulated with CST particle studio.

ELECTRONICS CONCEPT

As mentioned in Table 1, the bunch to bunch distance in XFEL is as long as 200 ns. Furthermore, the requirement is a single bunch, single pass resolution of 50 µm. These requirements are close to the performance of the electronics type used for the DESY electron rings, typically operating with a bunch spacing of 96 ns [6]. Here the signals of the 4 buttons are added onto a single cable after running through delay lines of certain length. Thus the electronics gets a sequence of 4 pulses for processing. The amplitude of the incoming signals is digitized after peak detection. The influence of the delay lines is taken out by means of calibration. Due to the use of a single electronics channel, one gets good stability properties. XFEL will use a modified and updated version of this scheme. With the given orthogonal geometry of the XFEL BPMs it easy to separate the vertical and the horizontal plane and to process them by separate electronics. Thus there will be one electronic per plane. The electronics will provide both internal as well as external triggering. The external trigger will act more like a gate. The ADC is planned with a speed of 100 MHz, the clock has to be beam synchronized.

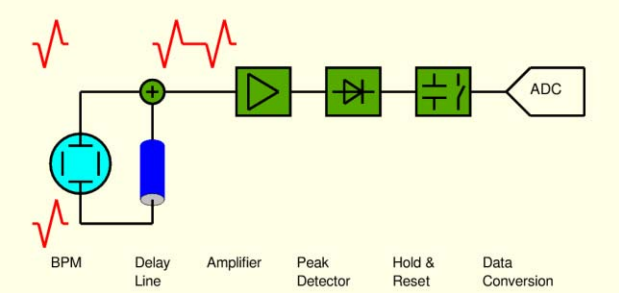

Figure 5: Block diagram of the BPM electronics for the pickup BPMs.

In order to deal with drifts of the delay line network a test and calibration facility will be included in each electronic. It will allow not only help with the commissioning of the system, it allows to send and analyse test pulses before or after each RF pulse of the LINAC, for testing and online calibration.

Since there will be various types of BPMs for XFEL this electronics has to be integrated into an overall framework of a BPM system. Currently this framework is under discussion with the colleges from PSI who plan to collaborate with XFEL on the warm BPM system. It is planned to integrate this electronics, including analogue front end to ADC as a piggy pack board to be mounted on a common processing board. The cold BPM electronics would appear like an ADC unit to the processing board.

Based on the test setups the layout of the PCB for a prototype series is under development, and the boards will be available for testing in summer 07.

BEAM RESULTS AT FLASH

A prototype of this XFEL BPM with adapted flange type (CF) and 8 mm buttons was installed in the FLASH LINAC.

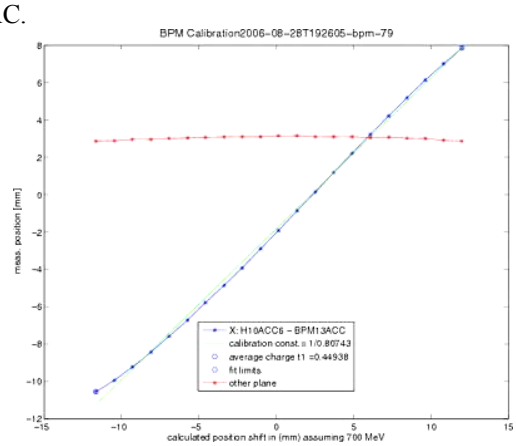

Figure 6: BPM response vs. an upstream corrector magnet at FLASH. The scaling of the x-axis corresponds to a displacement calculated from the kick of the magnet. The y-axis gives the reading of the BPM. The blue curve shows the hor. BPM reading, the red one the response of in the vertical plane. The slope of the fitted line gives the quotient between expected and measured BPM response.

Several studies have been performed with this monitor and different test setups for the electronics. The result of a measurement with this BPM and a first electronics prototype is in Fig. 6.

The BPM was included in resolution measurements using correlation techniques [7]. For different values of the charge in the range of 0.2 to 1 nC the resolution was measured to be better than 30 µm. Dynamic range of ±12 mm was also demonstrated, as well as the required charge resolution of 1%.

CONCLUSION

In this paper the design and first measurements of a prototype for the BPMs in the XFEL cryo modules are presented. With the current design for a button type monitor and an electronics based on the scheme used at HERA, the requirements for European XFEL can be met.

REFERENCES

[1] XFEL Technical Design Report, DESY 2006-97; XFEL.desy.de.
[2] P. Tenenbaum, Beam Instrumentation Callenges at the ILC, Proc. BIW 06, 138.
[3] C. Simon et al, Reentrant Cavity BPM, this proceeding.
[4] V. Ayvazyan et al., First operation of a Free-Electron Laser generating GW powerradiation at 32 nm wavelength, Eur. Phys. J. D37 (2006) 297.
[5] S. Sturm, D. Müller, Diploma Thesis, Hochschule für Angewandte Wissenschaften, Hamburg, 2007, available from:
http://adweb.desy.de/mdi/downloads/diplomarbeit_12_02_07(komplett).pdf.
[6] R. Neumann, private communication.
[7] N. Baboi, Resolution Studies a BPMs at the FLASH Facility at DESY, Proc BIW 06, 227.

DESIGN CONSIDERATIONS OF A SPECTROMETER DIPOLE MAGNET FOR THE PHOTO INJECTOR TEST FACILITY AT DESY IN ZEUTHEN (PITZ)*

J. Rönsch†, J. Rossbach, Hamburg University, 22761 Hamburg, Germany
J. Bähr, S. Khodyachykh, S. Korepanov, M. Krasilnikov, S. Rimjaem,
L. Staykov, F. Stephan, DESY, 15738 Zeuthen, Germany

Abstract

The test and optimization of electron guns at the Photoinjector Test Facility at DESY in Zeuthen (PITZ) demands dedicated diagnostics. The physical specifications of a spectrometer magnet for measurements at a beam momentum range from 15 to 40 MeV/c will be discussed. It will be used for measurements of the momentum distribution, slice emittance and the longitudinal phase space using two different methods. The first method combines the dipole magnet with a RF - transverse deflecting cavity, the second combines it with a Cherenkov radiator whose light is measured by a streak camera. Especially the first method is aiming for a good resolution in order to determine slice momentum spread. The design has to meet the demands of all these techniques for a measurement with high resolution and for bunch trains containing 7200 pulses of 1 nC charge at a repetition rate of 10 Hz. Since there is not enough space for a separate beam dump after the dispersive section the beam has to be transported to the dump of the main beamline.

INTRODUCTION

The main goal of PITZ is to test and to optimize L-Band RF photo injectors for Free-Electron Lasers (FELs) like FLASH and XFEL at DESY in Hamburg and to study the emittance conservation by using a matched booster cavity. The demands on such a photo injector are a small transverse emittances, a charge of about 1 nC, short bunches (of about 20 ps) and the possibility of long bunch trains of 0.8 ms length. Besides the accelerating cavities, the electron beam line (shown in figure 1) consists essentially of diagnostics elements. The physical design considerations of the second spectrometer magnet for measurements after the booster cavity will be discussed in this paper. The second high energetic dispersive arm will be used to measure the following beam parameters:

- the momentum distribution
- slice emittance [1] and
- the longitudinal phase space using:
  - a Cherenkov radiator and a streak camera [2] or
  - the RF-deflector [3].

On the one hand, the measurement of the longitudinal phase space requires to resolve a very small momentum spread of 1 keV/c, but on the other hand the measurement of slice emittance has to be done at a booster phase (off-crest) resulting in a large momentum spread. For the complete analysis and understanding of the system, the ability of the spectrometer to operate in a large range of gun and booster parameters is important. Therefore it is a demanding task to fulfill all the conditions at the same time.

A major design request is to allow the measurement of bunch trains with up to 7200 pulses and a repetition rate of 10 Hz for a long period. This requires a huge beam dump of $(2 \cdot 2 \cdot 2)$ m^3 after the dispersive section, but there is not enough space for a separate dump, so that the beam has to be transported to the dump of the main beamline. For long pulse trains also special diagnostics is needed because a screen would be destroyed.

Since the RF-deflector acts in vertical plane the dipole has to deflect the beam in horizontal direction. The deflecting angle can not be larger than 90^o due to the spatial restrictions, so a 180^o-bend like in the case of the first spectrometer magnet after the booster cavity [1] is excluded.

EQUIPMENT

In order to fulfill the measurement tasks, the following devices have to be included in or before the dispersive section:

- a screen station containing YAG and OTR-screen for the measurement of momentum distribution, slice emittance and longitudinal phase space (with RF-deflector) as well as a Cherenkov radiator for longitudinal phase space measurements (with streak camera);
- a quadrupole magnet and a slit placed about 1 m (focal length of the quadrupole) before the screens for slice emittance measurements;
- a beam position monitor (BPM) with a large aperture, due to the beam dispersion, for the measurement of mean momentum of different bunches in a long pulse train;
- a kicker in vertical direction before the spectrometer in order to analyze a single pulse out of a long pulse train and a corresponding off-axis screen.

SPECTROMETER DESIGN OPTIONS

The position of an electron behind the dipole magnet in dispersion direction can be described by:

* This work has partly been supported by the European Community, contract numbers RII3-CT-2004-506008 and 011935, and by the 'Impuls- und Vernetzungsfonds' of the Helmholtz Association, contract number VH-FZ-005.

† jroensch@ifh.de

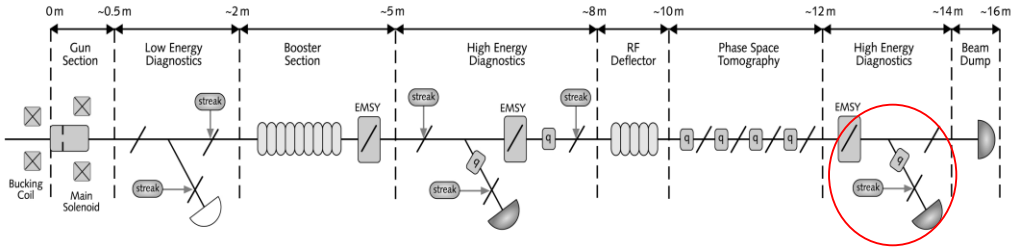

Figure 1: The PITZ2 setup consists of three spectrometer magnets for the analysis of longitudinal beam properties. The last one, the so-called second high-energetic dispersive arm (HEDA2), whose design is discussed in this paper, is marked.

$x_{DA} = R_{11} \cdot x_0 + R_{12} \cdot x'_0 + R_{16} \cdot \frac{\Delta p}{<p>}$, where R_{11}, R_{12} and R_{16} are the matrix elements of the transport-matrix. In order to reach a high resolution momentum measurement the first two summands need to be small. There is a screen station about 1 m upstream the dipole and another one 1 m downstream. An electron with the horizontal position x_0 and the horizontal divergence x'_0 at the point P (see figure 2) will hit these screens S_1 or S_2 at the

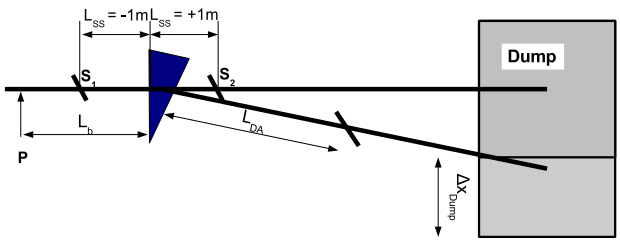

Figure 2: Bending magnet with small deflection angle.

horizontal position $x_S = 1 \cdot x_0 + (L_b + L_{SS}) \cdot x'_0$. If $n \cdot (R_{11} \cdot x_0 + R_{12} \cdot x'_0) = 1 \cdot x_0 + (L_b + L_{SS}) \cdot x'_0$, one can use a quadrupole of the tomography module to focus the beam on the screen S_1 or S_2 to improve the resolution like it was done in case of HEDA1 [1] or apply a deconvolution. So the ratio $\frac{R_{12}}{R_{11}}$ needs to be $\frac{R_{12}}{R_{11}} = L_{SS} = \pm\, 1\ m$ to minimize the influence of transverse beam size and divergence. In the case of using the screen before the dipole ($L_{SS} = -1\ m$) a slit for the measurement with short pulse trains could be provided. The deflecting radius of the dipole magnet should be considerably bigger than the gap of the pole shoes which is expected to be about 50 mm, in order provide a homogeneous field and to minimize fringe fields. The drift length in the dispersive arm L_{DA} has to include the length of the quadrupole magnet and its focal length. All elements have to be placed within a distance of 1.93 m to the main beamline due to safety requirements. On the one hand a large dispersion (R_{16}) improves the momentum resolution, but on the other hand the beam size in the dispersive arm might become too large and the beam will hit the beam tube. The momentum spread times the dispersion (R_{16}) determines the (rms) beam size. Figure 3 shows the momentum spread (rms value) divided by the mean momentum of the particles in the beam. Therefore the dispersion should not be larger than $R_{16} \leq 600$ mm.

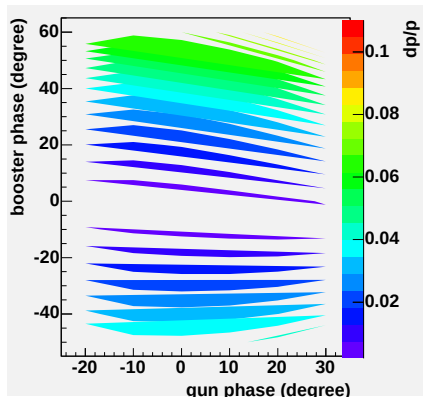

Figure 3: Relative rms momentum spread as a function of gun and booster phase.

Two cases will be considered, to use a small deflection angle, but a large drift length or large deflection angle with a smaller drift.

One Magnet

An easy possibility to transport the beam to the main beam dump is to expand the dump by about a meter in horizontal direction and to use a dipole magnet with a small deflection angle as shown in figure 2. Since the distance between the dipole magnet and the center of the beam dump is about 4.5 m, only a small deflection angle of about 15^o can be used. The main advantage of this scheme is the large drift length in the dispersive section in order to place all the diagnostic devices. For an angle of 15^o the dump has to be enlarged by about Δx_{Dump}=1.2 m in x-direction and the dispersion is about 0.25 to $0.29 \cdot L_{DA}$ for useful values of the deflection radius and pole face rotation. Therefore a drift length (L_{DA}) of about 2 m leads to an useful dispersion. Afterwards a quadrupole magnet can be used to optimize the beam size for the dump.

Two or Four Magnets

To use a larger dispersion angle (30^o - 90^o) a second dipole magnet has to be used to transport the beam to the beam dump of the main beamline (shown in figure 4 at the top). The second dipole needs to have at least the same

Table 1: Different possible dipole magnet settings.

α	r (mm)	L_{DA} (mm)	β_{in}	β_{out}	L_{SS} (mm)	R_{11}	R_{12} (mm)	R_{16} (mm)	$\Delta < p >$	Δp_{rms}	$\Delta\epsilon_{long}$
15^o	500	2000	-14^o	-13.16^o	-1000	-1.94	1940	518.74	$2.4 \cdot 10^{-5}$	$6.5 \cdot 10^{-3}$	0.47
15^o	500	2000	15^o	15.81^o	1000	2.21	2208	553.97	$1.76 \cdot 10^{-5}$	$1.79 \cdot 10^{-2}$	0.47
30^o	500	1000	-13^o	-13.13^o	-1000	-1.00	999	535.74	$8.9 \cdot 10^{-6}$	$1.6 \cdot 10^{-3}$	0.47
30^o	500	1000	18^o	18.63^o	1000	-1.28	1285	612.14	$8.2 \cdot 10^{-6}$	$4.9 \cdot 10^{-3}$	0.49
30^o	400	790.56	13.99^o	16.27^o	1000	1	1000	479	$3.4 \cdot 10^{-6}$	$5.1 \cdot 10^{-3}$	0.47
60^o	300	318.35	0^o	0^o	-1000	-0.42	419	425.69	$5.7 \cdot 10^{-6}$	$4.5 \cdot 10^{-4}$	0.44
60^o	550	908.54	0^o	0^o	-1000	-0.93	930.6	1061.8	$4.9 \cdot 10^{-6}$	$4.7 \cdot 10^{-4}$	0.45
60^o	600	900	30^o	-25.83^o	-1000	-0.59	592.3	861.55	$5.4 \cdot 10^{-6}$	$2.5 \cdot 10^{-4}$	0.44
90^o	500	250	45^o	0^o	-1000	0.5	500	750	$5.4 \cdot 10^{-6}$	$2.5 \cdot 10^{-4}$	0.44
90^o	300	700	45^o	45^o	1000	1	1000	1700	$4.6 \cdot 10^{-6}$	$4.2 \cdot 10^{-4}$	0.44
90^o	700	300	45^o	45^o	1000	1	1000	1300	$4.2 \cdot 10^{-6}$	$7.1 \cdot 10^{-4}$	0.45

deflection angle as the first one in order to deflect the beam parallel to the main beamline or larger to bring it to the center of the main dump. The main disadvantage is that the drift length in the dispersive arm is more limited the larger the deflecting angle becomes. It is needed to couple the current of both dipole magnets to simplify the operation.

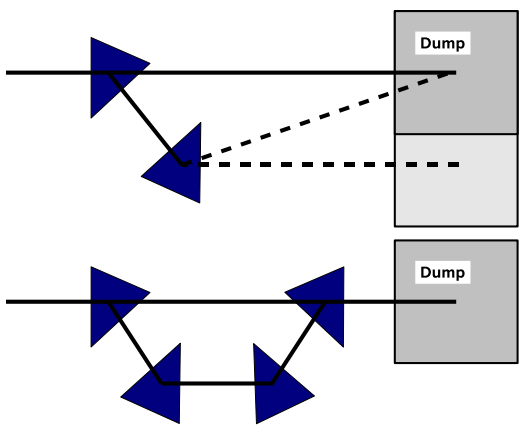

Figure 4: 60^o bending magnet (top) or bunch compressor (bottom).

There is the idea to construct a complete bunch compressor which might be useful in a later setup. The main advantage is that the bunch is brought back to the main beamline before the dump.

COMPARISON OF DIPOLE MAGNETS

Table 1 shows a comparison of different possible deflecting angles and adequate setting for a high resolved momentum measurement.

In the table, α is the deflecting angle, r is the deflecting radius, L_{DA} is the drift length in the dispersive arm, β_{in} and β_{out} are the pole face rotations at the entrance and exit of the dipole magnet. R_{11}, R_{12} and R_{16} determine the momentum resolution of the measurement. $\Delta < p >$ describes the discrepancy of the determination of the mean momentum due to the dipole magnet, Δp_{rms} is the discrepancy of the determination of the momentum spread and $\Delta\epsilon_{long}$ is the discrepancy of the determination of the longitudinal emittance (using the streak camera) due to the dipole magnet. $\Delta\epsilon_{long}$ does not include effects of the Cherenkov radiator or the optics. These rather small discrepancies can be reached only for a proper focussing on one of the concerning screens S_1 or S_2, otherwise the resolution gets much worse.

Non of the setups fulfills all requirements at the same time. Therefore only a compromise has to be found. The setups with the large deflection angles show a rather large dispersion, which limits the range of the possible booster phase and leads to a small drift length in the dispersive arm. This makes measurement of slice emittance difficult. In the case of small deflection angles the resolution gets worse. The determination of mean momentum is very good for all the cases, but there is a strong difference in the resolution of momentum spread.

SUMMARY

Different magnet settings were compared and their advantages and disadvantages were discussed. In general small deflecting angle leads to a worse resolution and for large deflection angle the drift space after the quadrupole magnet is not sufficient to ensure good slice emittance measurements.

REFERENCES

[1] S. Khodyachykh et al., "Design of Multipurpose Dispersive Section at PITZ", FEL'06, Berlin, September 2006.

[2] J. Rönsch et al., "Longitudinal Phase Space Studies at PITZ", FEL'05, SLAC, Stanford, USA, 2005.

[3] S. Korepanov et al., "Design Consideration of the RF Deflector to Optimize the Photo Injector for PITZ", FEL'06, Berlin, September 2006.

TEST OF A SILICON PHOTOMULTIPLIER FOR IONIZATION PROFILE MONITOR APPLICATIONS

D. Liakin, S. Barabin, A.Orlov ITEP, Moscow, Russia
P. Forck, T. Giacomini GSI, Darmstadt, Germany.

Abstract

A samples of SiPM (silicon photomultiplier) has been tested as an elementary light detector for accelerated beam fast profile observation by using it in residual gas ionization profile monitors (IPM). Noise, sensitivity, dynamic range and timing parameter tests of SiPMs were performed. A possible procedure of the data acquisition and following signal reconstruction is discussed. A special attention has been paid to the fine time resolution counting mode with single photon detection. A dedicated signal normalizing and time-to-digit converter design was prototyped and tested. In addition some different modes of operation and optical schemes are discussed in this paper. It is shown that fast optical detectors like SiPMs also could be used for high performance profile measurements with spatial resolution compatible with CCD sensors.

INTRODUCTION

To provide a non-destructive beam profile measurement at modern ion synchrotrons and storage rings an advanced Ionization Profile Monitor (IPM) with improved spatial and time resolution is going to be developed in GSI [1]. Profile observation will be done by residual gas ionization electrons registration. Applied electric and magnetic fields will provide demanded time and spatial resolution. A two-stage MCP with phosphor screen output will be used as a primary signal intensifier. To realise a fast option of IPMs one need a faster detector than currently available CCD devices. As an alternative to a CCD an array of fast avalanche or p-i-n photo diodes was considered as detector in [2] as well as some requirements to operation conditions in analogue mode. A new type of solid state photo detectors named Silicon Photomultiplier (SiPM) shown in Fig.1 provides efficient light utilization.

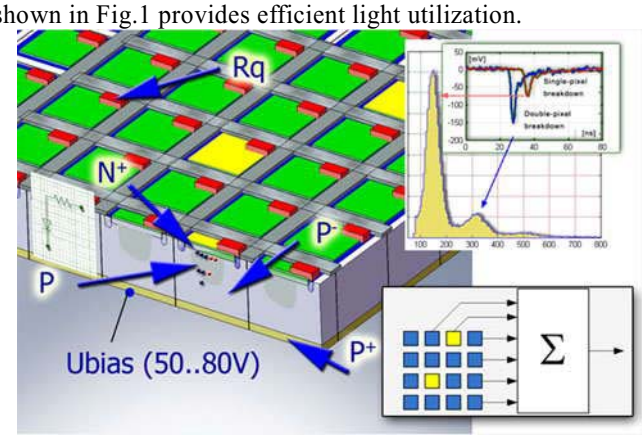

Fig. 1. SiPM is a matrix of avalanche diodes operating in Geiger mode and having common output.

A SiPM [4,5] is a multi-pitch silicon photodiode with a number of micro-cells (typical size of 20–30 μm) joined together on common substrate and working on common load. The operational bias voltage is 10–15% higher than the breakdown voltage, so each SiPM pixel operates in Geiger mode with avalanche current limited by individual polysilicon resistor located on the same substrate, with a gain determined by the charge accumulated within pixel capacitance. Each pixel multiplies the carriers created by photons or thermally by a factor about 10^6, the value close to that of photomultiplier. Actually, each SiPM pixel operates as a binary device, but SiPM upon the whole is an analogue detector, which can measure the light intensity within the dynamic range, determined by a finite number of pixels (~10^3 /mm^2).

SiPM have the following features that approve their use for IPMs: high gain (~10^6), same as in photomultiplier (PMT) but much larger than on Avalanche Photodiodes (APD) (~10^2) with Photon Detection Efficiency (PDE) same as for a PMT (~16%) with respect to the phosphor screen wavelength (350..470nm); photon counting capability; reduced requirements to the noise of the adjacent electronics; small time jitter (δτ 100 ps); short recovery time (~3ns); good temperature and voltage stability (much better than for APD); insensitivity to magnetic field ; low bias voltage (~50V) (comparable to PMT's ~1kV); compactness and robustness; low cost and simplicity of measurement system.

Modes of operation

Linear photocurrent detection

Despite every pixel of the SiPM operating in Geiger mode, an entire device may be used as a linear light detector.

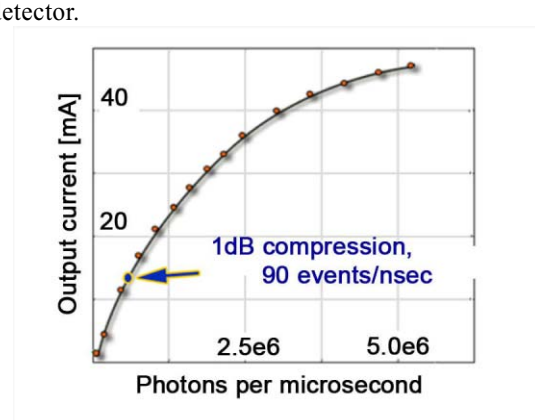

Fig. 2. SiPM's input-output transfer characteristics in analog mode.

Due to the higher internal amplification SiPMs better suited for low noise applications than other types of photodiodes. Fig. 2 shows the conversion curve of the 1000-pitch SiPM. The SiPM features in the linear mode in the frame of IPM applications are discussed more detailed in [3].

Counting mode

The counting mode provides a separate registration of incoming events, keeping the information about time and position of every light spot on the phosphor screen of the IPM. Obviously a higher performance of an adjusted electronics is required than in the case of the photocurrent registration.

The pulse counting operation is natively matches the discrete nature of incoming signals of IPMs. There are also no needs to care about equalising gain coefficients over all channels. No 'imaging quality' of the MCP is required. There are no data losses due to the non-controlled averaging of several pulses.

Reduced quality profile measurements are allowed even with a small amount of events per profile. Fig. 3 shows the confidence interval for the low-statistics and low-resolution case.

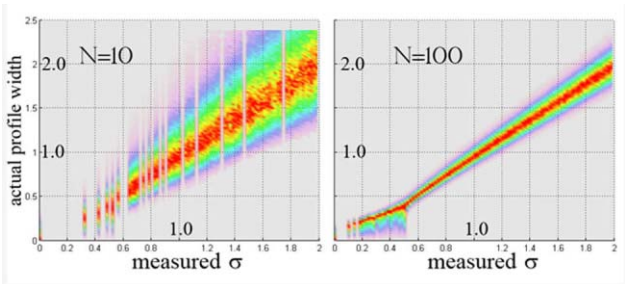

Fig. 3. The confidence intervals for 90% probability for number of samples per profile N equal 10 and 100. For higher σ the interval may be estimated as $1/N^{½}$.

A performance of the counting mode for single-shot measurements is defined by the residual gas pressure. Usually this parameter is not well controlled. This produces certain problems with the dynamic range adjustment. Hopefully for periodic processes the adjustment could be done by the changing of the averaging time.

Encoder mode

The high sensitivity of SiPMs allows using complex optical solutions with relatively high light losses. It is also possible to distribute the light from one event over few detectors obtaining some new possibilities for a profile registration. Using a mapped fiber encoder similar to one shown in fig. 4 allows a higher spatial resolution with a smaller amount of photodetectors. One can use additional bits for error correction to separate the IPM events from the SiPM dark count pulses.

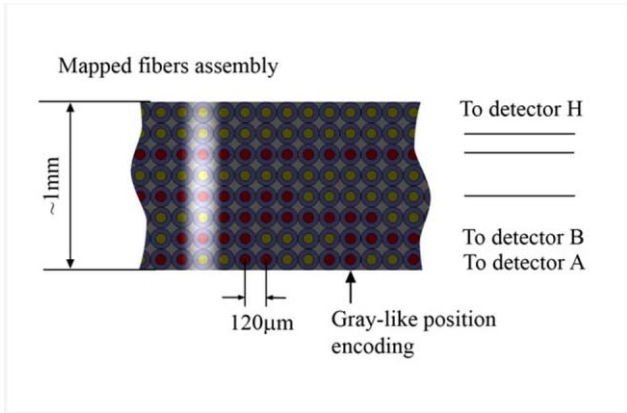

Fig. 4. Spot position encoding by using mapped fibers assembly.

The high sensitivity of the SiPM should be supported by high performance optical system. To simulate complex optical assemblies, an optical system toolbox was designed for MATLAB. It allows to estimate a behaviour of complex optical systems including cylindrical geometry, determine image quality, light losses etc. An example of the simulated system, which has been designed to be used with mapped fiber assembly, is shown on fig. 5. This optical system uses cylindrical lenses due to the principal system non symmetry. Triplet geometry gives freedom to focus the image independently in horizontal plane and defocus it in vertical plane. The simulation shows for the given geometry a light transmitting efficiency from the phosphor to a single fiber about 15e-6 with 20% variation and adjacent channel crosstalk up to 40% in an assumption of a 0.2mm original spot size. This is nearly sufficient for using in a system, equipped with a two-stage MCP and fast E36 phosphor. Due to the limited field of the depth, about 0.5mm, a high resolution encoder must be installed in parallel with phosphor plane of the MCP.

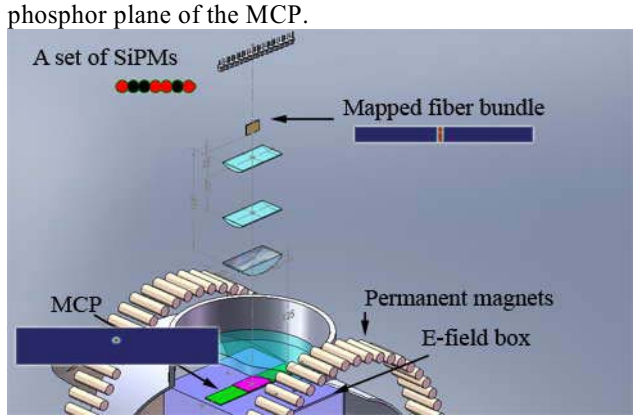

Fig. 5. The simulated optical layout for counting operation with mapped fiber position encoder. The central part of the MCP could be observed with 0.15mm accuracy with 300Mcps performance.

Test layout

A few samples of the SiPM have been tested in the lab. The sensitivity, thermal and temporal gain stability, dark counts rate etc. were measured during the tests. Some

electronic schemes were designed to find the most suitable solution for further IPM applications. The experimental layout is shown in fig. 5. A short light pulse produced by an LED was transmitted via glass fiber to the SiPM holder. This fiber additionally delays the pulse to avoid EMI signals from the pulse generator. Precise intensity regulation in 40 dB range was achieved by changing the distance between the fiber output and the SiPM. The output of SiPM was loaded with 50 Ohm 1GHz amplifier connected to oscilloscope or time-to-digital converter with 20ps LSB resolution.

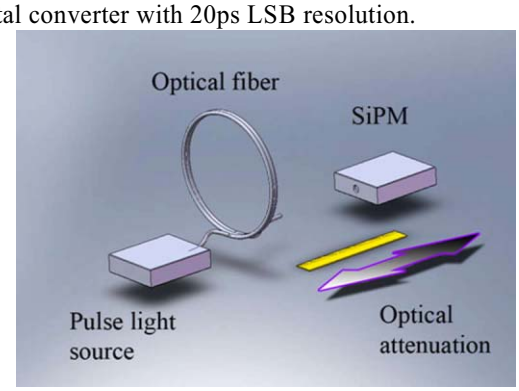

Fig. 6. A testing layout for the silicon photomultiplier's counting mode

A Hamamatsu wideband light receiver was used to control the pulse shape on the light source output. An example of a source signal reconstruction is shown on Fig. 7. To reproduce the form of the original signal the output of SiPM was captured on the screen of a digital oscilloscope in a long exposure mode. Integration of the data gives a good reproduction of the exciting signal with a rising front time of about 30ns. Fig. 7 shows the case of low intensity signal on SiPM input, so one can see single photon events and the dark count noise.

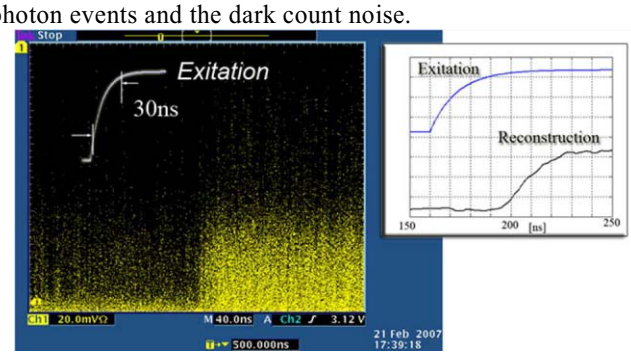

Fig. 7 Reconstruction of the rising front of the periodic excitation signal by averaging the output SiPM pulses.

For pulsed mode of operation our tests showed a time resolution down to 2 ns for periodic signals and this value obviously was not limited by the SiPM properties but by the characteristics of used environment. In the same time a using the SiPM in the counting mode for single-shot measurements without position encoding has no visible advantages in comparing with linear mode of operation.

The dynamic range of the presently available SiPMs in counting mode is limited by a relatively high dark count rate. Some types of SiPMs have up to 250kcps dark count in room temperature conditions. We also have tested SiPMs with different pulse discriminating levels to take off the pulses from single, double or triple-pitch breakdowns. This effectively decreases the dark count rate and gives a possibility to increase the dynamic range of the SiPM into higher intensities. Without that the dark count will hide pulses from phosphors with longer than 100ns decay time.

Conclusion

A SiPM is a well suited light detection device for ionization profile monitors to be used in event counting mode with relatively high count rate. This counting mode could provide 500MHz bandwidth for periodical processes and up to 10 profiles per microsecond with 10% of standard deviation accuracy for single-shot processes (local gas jet is required). To achieve a SiPM performance in single-shot operation a fast nanosecond-range phosphor type is required as well as a high performance multichannel electronic counters with adjustable discrimination level. For low input rate measurements with typical residual gas pressures a cooling down of the SiPM to -20..-40 C^o will be a good option for dark count elimination. Using an optical encoder in combination with a limited amount of SiPMs (or, with same success, in combination with a multichannel photomultiplier) allows reaching sub-millimetre spatial resolution by cost of some performance degradation in transient processes measurements.

REFERENCES

1. P. Forck et al. Advanced residual gas profile monitor for high current synchrotrons and cooler rings, In proc DIPAC03, p.134, Mainz, Germany.
2. D. Liakin et al. Development of a permanent magnet residual gas profile monitor with fast readout. Proc. Of EPAC 2004, p. 2724, Lucerne, Switzerland.
3. S. Barabin et al. Testing the silicon photomultiplier for ionization profile monitor. Proc. EPAC2006, Edinburgh, Scotland.
4. B. Dolgoshein, The advanced study of silicon photomultiplier in International conference on advanced technology and particle physics, Como, Italy, October 2001.
5. SPMMini silicon photomultiplier, SensL, Cork, Ireland, http://www.sensl.com/pdfs/SPMMini_DatasheetV1R3p1.pdf

BEAM POSITION MONITORS USING A RE-ENTRANT CAVITY

C. Simon#, S. Chel, P. Contrepois, P. Girardot, M. Luong, CEA-Saclay, Gif sur Yvette, France
N. Baboi, DESY, Hamburg, Germany
N. Rouvière, CNRS-IN2P3-IPN, Orsay, France

Abstract

Two designs of high resolution beam position monitor, based on a radiofrequency re-entrant cavity, are developed at CEA/Saclay. The first monitor is developed in the framework of the European CARE/SRF program. It is designed to work at cryogenic temperature in a clean environment and get a high resolution with the possibility to perform bunch to bunch measurements. Two prototypes with a large aperture (78 mm) are installed in the Free electron LASer in Hamburg (FLASH), at DESY. The other design with an aperture of 18 mm and a large frequency separation between monopole and dipole modes, as well as a low loop exposure to the electric fields is developed for the Clic Test Facility (CTF3) probe beam CALIFES at CERN. It is operated in single bunch and multi-bunches modes. This paper presents the mechanical and signal processing designs of both systems. Simulation and experimental results will be discussed.

INTRODUCTION

A re-entrant BPM [1] consists of a coaxial cavity arranged around the beam pipe. Passing through the cavity, the beam excites electromagnetic fields (resonant modes), which are coupled by four feedthroughs to the outside. The main radio-frequency modes excited by the beam in the cavity are monopole and dipole modes. The monopole mode signal is proportional to beam intensity and does not depend on the beam position contrary to the dipole mode signal which is proportional to the distance of the beam from the centre axis of the monitor.

Two re-entrant BPMs are installed on the FLASH linac at DESY. The first, operated at cryogenic temperature inside the cryomodule ACC1, in an environment where dust particle contamination has to be avoided, is not discussed here [2]. The second has been qualified with beam in a warm section of the FLASH (TTF) accelerator, achieving 4 µm resolution over a dynamic range of ± 5 mm. Those results are presented in the first part of this paper.

The second part describes the re-entrant BPM designed for the CLIC (Compact LInear Collider) Test Facility (CTF3) probe beam CALIFES [3]. The theoretical performances of this system and the first measurements of the cavity are discussed.

BPM INSTALLED IN THE FLASH LINAC

In the framework of the European CARE/SRF program, the task of CEA/DSM/DAPNIA (Saclay) is the design, the fabrication and the beam test of a BPM in collaboration with DESY. The cold re-entrant BPM prototype installed on the linac outside a cryomodule for tests was designed to achieve a high resolution down to 10 µm and to allow bunch to bunch measurements for the X-Ray Free Electron Laser (X-FEL) and the International Linear Collider (ILC). The monopole and dipole modes are around 1.25 GHz and 1.72 GHz. This BPM has high crosstalk isolation (33 dB) and the quality factors are quite low [4]. Spring 2006, during the maintenance time, the re-entrant BPM was installed in a warm part in the FLASH linac (Fig. 1) at DESY.

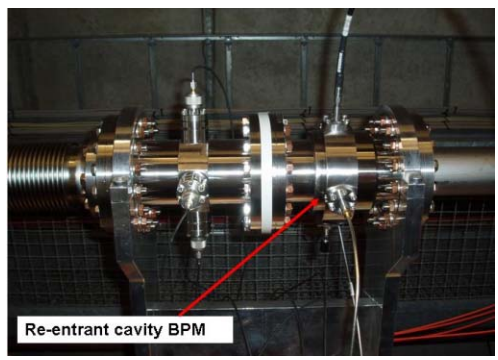

Figure 1: Re-entrant cavity BPM installed in the FLASH linac.

Calibration

After this mounting, the two subsystems, composing the signal processing, were installed and calibrated. The adjustment of phase shifters in the tunnel allows having a high common mode rejection (30 dB at the monopole mode frequency). The gain was modified to improve the resolution and some low pass filters were added on each channel. The new RF signal processing electronics is shown on Fig. 2.

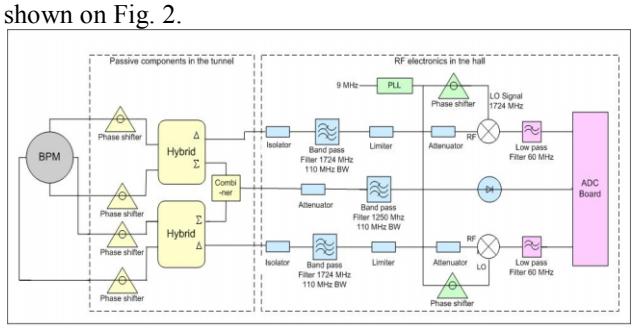

Figure 2: Signal processing electronics.

The synchronous and direct detectors, as well as gain were adjusted to have a linearity range around ± 5 mm.

To carry out the BPM calibration, the vertical and horizontal steerers were used to move the beam. All magnets, between the steerers used and the re-entrant BPM were switched off. The calibration was carried out

#claire.simon@cea.fr

in calculating for each steerer setting, the relative beam position in using a transfer matrix between steerer and BPM. The position measured by the re-entrant BPM vs the calculated position was plotted for the horizontal and vertical steerings (Fig. 3).

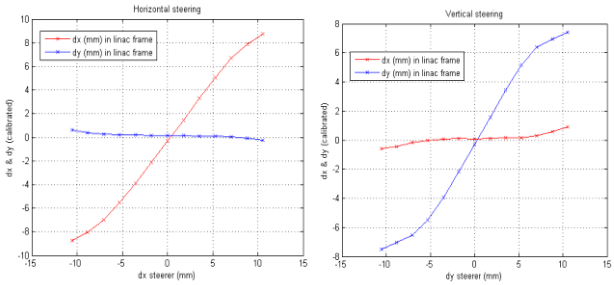

Figure 3: Calibration results in LINAC frame from horizontal (left) and vertical (right) steering.

Figure 3 shows a good linearity in a range ± 5 mm. The BPM resolution has been measured by correlating the reading of the re-entrant BPM in one plane against the readings of all other BPMs in the same plane [5]. In keeping the same dynamic range, the resolution was measured, on the Y channel, around 4 µm and on the X channel around 8 µm limited only by the electromagnetic contamination in the experimental hall. This difference on both channels can be explained by the fact that the bandwidth of the low pass filters is not the same. Those results are quite similar to the theoretical resolution calculated around 3.65 µm with 5 mm beam offset [4]. The noise amplitude on the DOOCs ADC board and on a scope was measured to be about 200 µV peak. The charge of the re-entrant BPM was calibrated thanks to the toroids. The resolution for the charge is around 6.35 pC.

This BPM was designed to have the possibility to do some bunch to bunch measurements. The position of each bunch can be known and read by the re-entrant BPM as shown on Fig. 4.

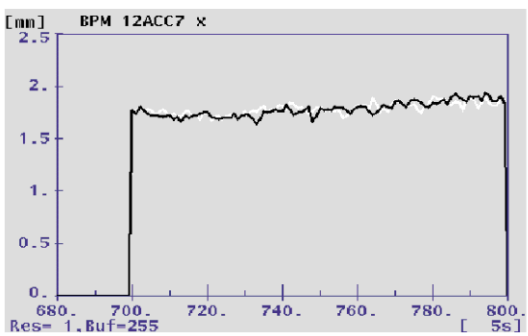

Figure 4: Position of 100 bunches in a macro-pulse read by the re-entrant BPM.

Outlook

In the next studies, the resolution will be improved in adding an amplifier on each channel. As the limitation of the resolution is due to the ADCs noise, to improve the resolution the dynamic range has to be reduced. With a dynamic range around ± 1 mm, the simulated resolution was calculated to be around 0.5 µm.

Improvement of the Mechanical Design

To be installed in an X-FEL cryomodule, the mechanical design has to be improved. The alignment of two pieces composing the cavity has to be precise. A cavity was fabricated to adjust the alignment of two pieces and to validate the copper plating of the beam pipe. With a three-dimensional measurement, the alignment of two pieces was measured with an angle around 0.02°. The copper coating was fabricated with the DESY specifications and its thickness was measured to be around 12.7 µm.

BPM DESIGNED FOR THE CTF3 PROBE BEAM

Coaxial re-entrant cavities [1] have been chosen for the beam orbit measurement - single bunch or 1.5 GHz bunch trains - because of their mechanical simplicity and excellent resolution.

Cavity BPM

A new design, with a large frequency separation between monopole and dipole modes, as well as a low loop exposure to the electric fields, has been developed (Fig. 5).

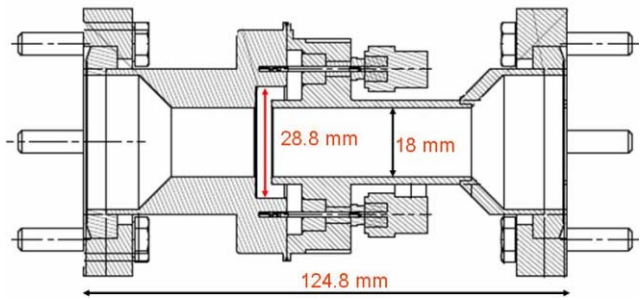

Figure 5: Re-entrant BPM designed for the CTF3 probe beam.

This BPM cavity is fabricated with titanium as compact as possible: 124.8 mm in length and an aperture of 18 mm. Six BPMs will be installed on the CTF3 probe beam CALIFES. The resonant cavity was designed with the software HFSS (Ansoft). The dipole mode frequency has been chosen around 5.997 GHz for a resonant operation with 64 bunches.

Table 1: BPM RF characteristics.

	F (MHz)	**Q_{ext}**	**Longitudinal R/Q (Ω)**	
	Measured in lab.	Measured in lab.	Offset 2 mm	Offset 5 mm
Monopole mode	3976.2	27.09	22.3	22.2
Dipole mode	5964.4	51.49	1.1	7

The RF measurements, presented in Table 1, are an average of the frequencies and external Q measured on the six BPMs. The longitudinal R/Q were computed with the software HFSS. The mechanical dimension Ø 28.8 (fig.5) will be adjusted to have the dipole mode frequency close to the frequency chosen 5.997 GHz.

The standard deviation for the monopole mode frequency is around 5 MHz and for the dipole mode frequency around 8.7 MHz measured on the six BPMs. The cross talk is quite high, it was measured in laboratory better than 28 dB on each BPM.

Electronics

The signal processing uses a single stage downconversion and is shown in Fig. 6. It is composed of standard RF components: hybrid couplers, phase shifters, filters, isolators and I/Q demodulators. The isolation of the hybrids can be adjusted by phase shifters to reject the monopole mode. To reduce the cost, some multiport switches were used to have one signal processing electronics to control six BPMs.

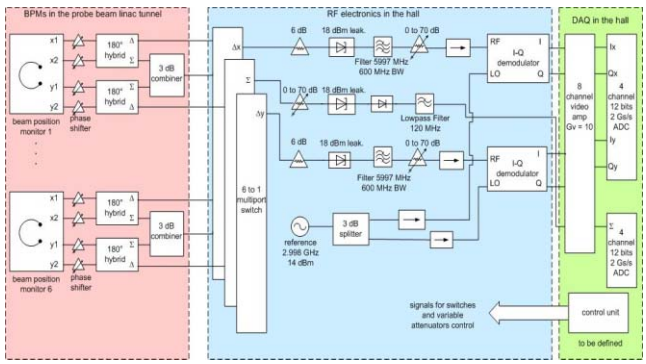

Figure 6: Signal processing electronics.

The control system pilots the switches and variable attenuators.

Theoretical Results

To assess the performance of this system, a model (cavity+signal processing) is elaborated with a Mathcad code based on Fourier transforms [4]. The signal is given by the model (cavity+signal processing) simulation in single bunch mode. The gain was adjusted to get an RF signal level around 0 dBm on the Δ channel with 5 mm beam offset. The position resolution is the rms value related to the minimum position difference that can be statistically resolved. The noise is determined by the thermal noise, the noise from signal processing channel [2] and the noise of ADCs boards. The noise level is about $5 \cdot 10^{-4}$ V. The result gives a resolution around 5 µm with +/- 5 mm of dynamic range.

The damping time of the cavity is around 2.8 ns and the time resolution is around 10 ns in single bunch [2].

This BPM is, also, operated in multi-bunches mode. As the distance between bunches is very short around 667 ps, a new Mathcad model to simulate the re-entrant BPM in multi bunches mode is being developed.

The ADCs boards were chosen to digitize very fast. The model, DC282 developed by Acqiris, has four channels with 10 bits and a sample rate of 8 Gs/s.

CONCLUSION

The re-entrant BPM installed in the FLASH linac has a high linearity in the range of ± 5 mm, and high position resolution below 10 µm (4 µm for the Y channel and 8 µm for the X channel). It has the possibility to do some bunch to bunch measurements and its main features are its operation at cryogenic temperature and its large aperture (78 mm). This BPM appears as a good candidate for being installed in the XFEL and ILC cryomodules.

The BPM designed for the CTF3 probe beam is operated with single bunch and multi bunches. The first simulated results are encouraging. The resolution, in the single bunch mode, was calculated around 5 µm with a dynamic range of ± 5 mm. At the end of this year, the six BPMs and the electronics will be installed at CERN and the first beam tests will start in 2008.

ACKNOWLEDGMENTS

We acknowledge the support of the European Community-Research Infrastructure Activity under the FP6 “Structuring the European Research Area” programme (CARE, contract number RII3-CT-2003-506395).

We thank our colleagues from DESY: the TTF operational team for its support, D. Noelle, N. Mildner, T. Traber, MDI and MVP teams for their help at TTF site and the fruitful discussions on the BPMs. We would like, too, to thank all our colleagues from CEA Saclay and CERN for their work on the CALIFES project.

REFERENCES

[1] R. Bossart, “High precision beam position monitor using a re-entrant coaxial cavity” Processings of LINAC94, KEK, (1994).

[2] C. Simon, et al., “High Resolution BPM for linear collider”, BIW 2006.

[3] A. Mosnier, et al., “The probe beam linac in CFT3”, EPAC 2006.

[4] C. Simon, et al., “High Resolution BPM for linear collider”, EPAC 2006.

[5] N. Baboi, et al., “Resolution Studies at Beam Position Monitors at the FLASH Facility at DESY”, BIW 2006.

OPTIMISATION OF THE LINEAR–CUT BEAM POSITION MONITORS BASED ON FINITE ELEMENT METHODS

P. Kowina, W. Kaufmann, J. Schölles, GSI, Darmstadt, Germany

Abstract

This contribution presents investigations of the Beam Position Monitors (BPMs) for the FAIR project. In the simulations, performed using CST Studio Suite 2006B, the linear-cut BPMs based on a metal coated ceramics were considered as the only solution that meets the required mechanical stability of $\sim 50\mu m$ under cryogenic conditions. The most important BPM features like displacement sensitivity or linearity of position determination were compared for different BPM geometries. In these geometries, based on elliptically shaped ceramic pipe, the vertical and horizontal electrode pairs were either mounted subsequently in series or were spirally shaped and combined alternatively within one unit. It is shown that optimised BPM design with the serial mounted electrodes and separating ring inserted in between the adjacent electrodes has a very high sensitivity and shows much better linearity of the position determination than the design based on spiral–shaped electrodes.

INTRODUCTION

The BPMs that are presented here will be used in superconducting heavy ion synchrotron SIS100 — the main synchrotron in the FAIR accelerator complex [1]. All 84 BPMs will be installed in the cryostats of the quadrupole doublets and will be mechanically fixed to the quadrupole chambers [1, 2]. The cryogenic operation requires a special BPM design that considers e.g. the matching of the thermal contraction of the materials used. For the foreseen bunch frequencies of 0.5 MHz $< f_b <$ 2.7 MHz and bunch lengths ranging from few meters up to several hundreds meters the designed BPM should show a good response in the frequency range from ~ 0.1 MHz to 100 MHz. For such frequencies and bunches much longer than the BPM length a linear–cut BPM is preferred. Its high linearity of the position determination is advantageous for beams that are transversally large and have a complex charge distribution. In order to reach the desired position accuracy of 100 μm [3], the mechanical stability should be in the order of 50 μm. Only the design based on a metal coated Al_2O_3 ceramics gives the required mechanical stability in the cryogenic environment. The aperture of the BPM should be elliptic — matched to the aperture of the proceeding quadrupole chamber to prevents a beam–to–ground impedance jumps. Available total detector length of 400 mm (flange–to–flange) allows to equip each BPM with electrodes for both, horizontal and vertical beam position measurement. The foreseen dynamic range of signal amplitude of over 120 dB [4] requires special electronics [5] and a very careful BPM design. Particularly, the relative distances between electrodes, guard rings and chamber elements have to be large enough to prevent discharges, that may appear for the most intense beams, for which the expected peak voltage of BPM signals reaches 1.8 kV [4].

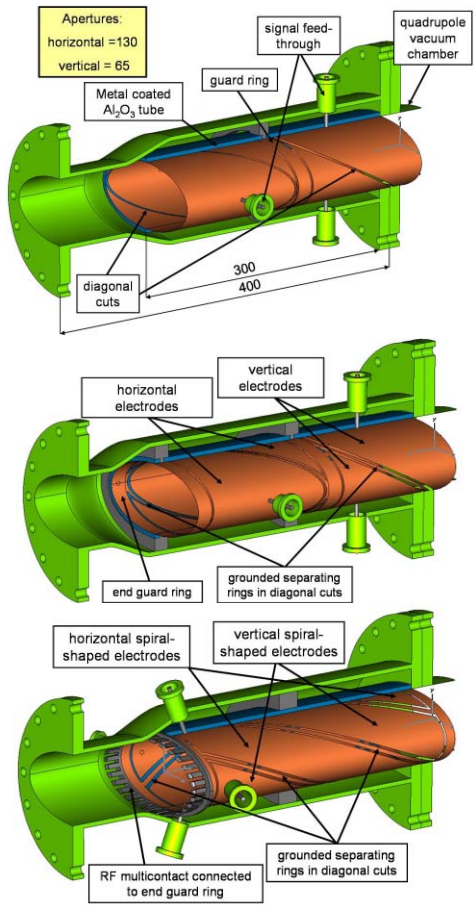

Figure 1: Models of the BPMs compared in the simulations, see description in text.

Two main BPM types were compared: First type considers the geometry shown in Fig. 1 (top and middle) where the vertical and horizontal electrode pairs are mounted subsequently — one pair after the other. The optimisation of this design type, called in this paper *serial BPM* was described precisely in Ref. [4]. It was shown that the improved BPM design with separating ring (Fig. 1 middle) has better linearity of the position determination and higher position sensitivity than the preliminary design shown in Fig. 1 (top). The motivation for further investigations was, that in serial BPM the distance between the point, where the ceramic pipe is fixed to BPM chassis is different for horizontal and vertical signal feed-throughs. Due to this difference, during cooling down from room temperature to liquid helium temperature, the dislocation of the mid-

dle pins in the horizontal signal feed–throughs is twice so high as for vertical ones. To equalise this distance for all feed–throughs the geometry shown in Fig. 1 (bottom) and called *spiral–shaped BPM* was proposed. In this geometry the spiral shaped electrodes cover the full BPM length.

METHODS AND RESULTS

For Finite Element Method simulations CST Studio Suite 2006B was used [6]. All BPM components, i.e. ceramic tube, chassis, feed–throughs etc. were defined using materials with realistic permittivity and conductance. The BPM was treated as a semi–coaxial TEM wave guide with the ion beam approximated by a cylinder of a Perfect Electric Conductor (PEC) [4]. For the simulated BPM models the hexahedral mesh grid was used with about 2×10^6 single mesh cells [7]. A broad–band Gauss shaped signal was used as the excitation signal with the rms width of 5 ns, which covers the frequency band from DC–200 MHz. The electrode outputs were defined as the discrete S-parameter ports with characteristic impedance of $1\mathrm{M}\Omega$. Simulations were performed using the Time Domain Solver [7].

The geometrical design of the investigated BPM was optimised regarding the following criteria:

i) The high *displacement sensitivity* is the measure of BPM signal response $\left(\frac{\Delta U}{\Sigma U}\right)$ to the changes in the beam position and is defined in Ref. [4]. The displacement sensitivity of the BPMs was calculated from the S-parameters expressed in the frequency domain [8]. The position of the simulated beam was swept in the horizontal plane in the range ± 50 mm in 10 mm steps. For each beam position the response of the BPM was analysed for both horizontal and vertical planes. The results are presented in Fig. 2. The displacement sensitivity, as given by the slope of curves in Fig. 2 (top), depends strongly on plate–to–plate coupling.

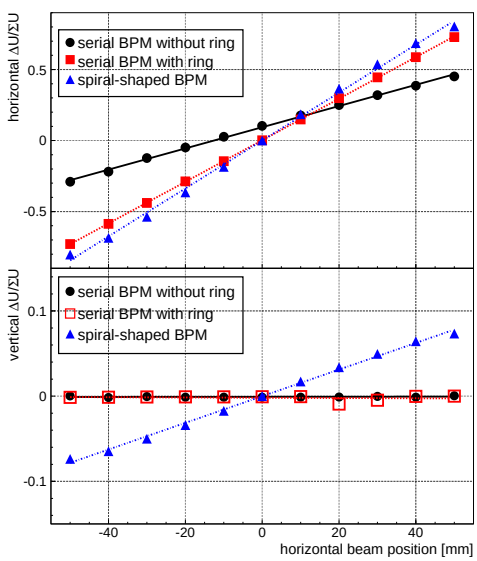

Figure 2: BPM response registered in horizontal (top) and vertical (bottom) plates on the horizontal beam displacement.

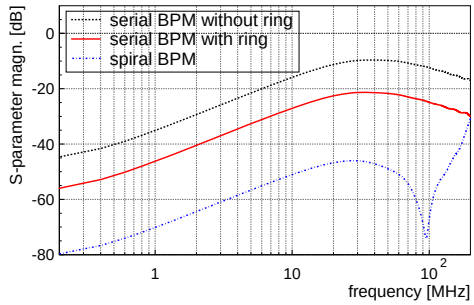

Figure 3: Coupling between two adjacent signal plates obtained in the simulations.

For the ceramic based BPMs large ceramic permittivity ϵ_r=9.6 leads to high coupling capacity that diminishes the difference signal and deteriorates the displacement sensitivity. The methods of investigations of the plate–to–plate coupling are described precisely in Ref. [7]. For the serial BPM the coupling between adjacent plates can be decreased from -9.5 dB to -21 dB by insertion of the separating ring between adjacent plates, see Fig. 3. This increases the displacement sensitivity by a factor of two [4]. In case of the spiral–shaped BPM, the coupling between two plates belonging to the same pair is much weaker than for the serial BPM and is -45 dB. However, it shows a resonant behaviour with a minimum at about 90 MHz [7]. This is the reason for the unhomogenieties in the frequency dependence of the displacement sensitivity for this BPM shown in Fig. 4 (right) and described later on.

ii) *Linearity of the position determination:* The high linearity is typical for the diagonal–cut type BPMs, however, it can be strongly spoiled by unhomogenities of the magnetic and/or electric field caused by e.g. too large distance between subsequent electrodes or by structure discountinities. For the BPM under investigation the maximum deviations from the straight line fit shown in Fig. 2 (top) are smaller than $\pm 2\%$ for the BPM without ring, below $\pm 0.5\%$ for the BPM with ring and $\pm 5\%$ for the spiral–shaped BPM over the whole ± 50 mm displacement range.

iii) The *offset of the electrical centre* of the BPM in respect to its geometrical centre can be reduced from about 13 mm (crossing point with the x-axis of the curve with black circles in Fig. 2 top) to almost zero (curve with the red squares) by an additional massive guard ring installed at the end of the BPM electrodes, see Fig. 1 (middle). It indicates that the geometry of the whole environment (including also the neighbouring guard rings) has to be completely symmetrical for both electrodes belonging to the same electrode pair. This is also valid for the spiral–shaped BPM, where the electrodes have rotation symmetry.

iv) A very careful treatment of the fringe fields is required in order to achieve a maximum *independence of the measurement* in vertical and horizontal directions. Particularly, the length of all guard rings has to be large enough to suppress the fringe fields distortions [9]. For serial BPMs, as it can be seen in Fig. 2 (bottom, circles and squares), the horizontal displacement of the beam has no influence

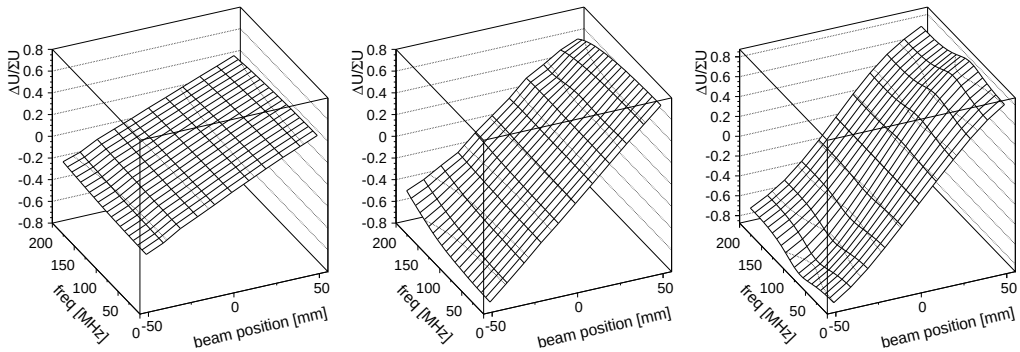

Figure 4: Displacement sensitivity as a function of frequency for the serial BPM without (left) and with (middle) separating ring and for spiral–shaped BPM (right).

on the signal measured in the vertical electrodes. On the contrary, spiral–shaped BPM (triangles) shows a significant horizontal–vertical cross talk due to the increased coupling between the four signal plates. Note that the adjacent plates in the case of the spiral–shaped BPM are the orthogonal plates i.e. electrode pairs: left–top, left–bottom etc.

The displacement sensitivity is often frequency dependent which is especially harmful for bunches with varying longitudinal structure [4, 8]. For those bunches the frequency spectrum varies in time, which effects the beam position estimation. For the serial BPMs, as it can be seen in Fig. 4 (left and middle) the displacement sensitivity is nearly frequency independent, whereas the spiral–shaped BPM shows strong inhomogeneities already at frequency of about 90 MHz, Fig. 4 (right). Projections of slices per-

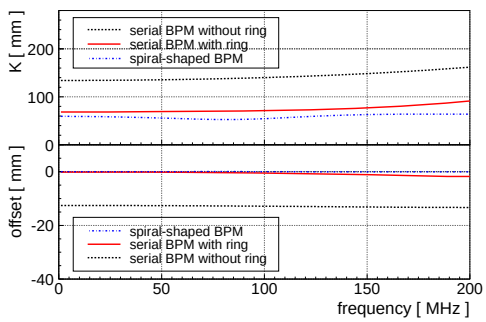

Figure 5: Frequency dependence of *"pickup constant"* K (top) and offset δ of the BPM (bottom) for the horizontal beam displacement.

pendicular to the frequency axis for given frequency (e.g. at typical bunch frequency of 2.5 MHz) lead to the plots in Fig. 2. For each of this slices the *"pickup constant"* K and BPM offset δ can be found [4]. The frequency dependencies of these parameters are shown in Fig. 5. The displacement sensitivity of the BPM with guard ring is a factor of two larger compared to the BPM without ring and is 15% smaller than for the spiral–shaped BPM [1]. The moderate drop of the sensitivity is caused by inductive cross talk between adjacent signal plates which is more pronounced at higher frequencies. Moreover, the offset of the electric centre of the serial BPM without separating ring is about 13 mm whereas the offset for the serial BPM with ring and spiral–shaped BPM is consistent with zero in a frequency range up to 100 MHz.

[1]The smaller the value of K the larger is the BPM response $(\frac{\Delta U}{\Sigma U})$ for the same beam shift (Δx), see Ref. [8].

CONCLUSIONS AND PERSPECTIVES

Simulations showed that the serial BPM with separating ring provides good linearity and high displacement sensitivity. Hence, the separating ring should be always considered in the BPM design as long as a ceramic solution is used. The BPM design based on spiral-shaped electrodes show strong frequency dependence of the displacement sensitivity. Moreover, for this design type the measurements in vertical and horizontal directions are correlated. Therefore, this PBM design is excluded. Since the serial BPM design does not satisfy all mechanical requests, further field/signal simulations will be performed for alternative BPM geometries [10]. First tests of the mechanical features of ceramics in low temperatures showed that the metal coated ceramics can be used under cryogenic conditions. However, further tests are needed for the several metal-ceramic interfaces. The cryogenic tests will be performed in parallel to the dynamic thermal simulation using the new thermal solver of CST-Suite 2006B.

REFERENCES

[1] FAIR – Baseline Technical Report available on: http://www.gsi.de/fair/reports/techrep_e.html

[2] J. Stadlmann et al., *Proc. EPAC06*, Edinburgh (2006) p.214.

[3] A. Galatis et al., *Proc. EPAC06*, Edinburgh (2006) p.1019.

[4] P. Kowina et al., *Proc. EPAC06*, Edinburgh (2006) p.1022.

[5] J. Schölles et al., *Proc. DIPAC05*, Lyon (2005) p.190.

[6] http://www.cst.com

[7] P.Kowina, *Reports of CARE meeting*, Lüneburg (2006), available on: http://adweb.desy.de/mdi/CARE/Lueneburg/ABI-Lueneburg.htm

[8] P. Kowina et al., *Proc. DIPAC05*, Lyon (2005) p.114.

[9] J. H. Cuperus, NIM **145** (1977) p.233-243.

[10] E. Schulte, *Beam Instrumentation*, CERN-PE-ED001-92, Rev. Nov 1994, p.129 and references therein.

DIAGNOSTICS FOR THE CTF3 PROBE BEAM LINAC CALIFES

W. Farabolini, D. Bogard, A. Brabant, A. Curtoni, P. Girardot, F. Gobin, R. Granelli, F. Harrault, C. Lahonde, T. Lerch, M. Luong, A. Mosnier, F. Orsini, F. Peauger, C. Simon, CEA/DAPNIA Saclay, 91191 Gif-sur-Yvette, France

Abstract

CALIFES is the probe beam linac developed by the CEA/DAPNIA and CNRS/LAL in the frame of the CFT3 collaboration at CERN. Its objective is to "mimic" the main beam of CLIC in order to measure the performances of the 12 GHz CLIC accelerating structures.

The requirements on the bunched electron beam in terms of emittance, energy spread and bunch-length are quite stringent and lead to use the most advanced techniques: laser triggered photo-injector, velocity bunching, RF pulse compression...

In order to tune the machine and assess its performances before delivering the beam to the CLIC structure test stand a complete suit of diagnostics is foreseen including charge monitor, beam position and video profile monitors, deflecting cavity, RF pick-up and analysis dipole. All these diagnostics will be interfaced to the CERN control system network. A special effort has been done on the Video Profile Monitors that make use of both scintillation and OTR (Optical Transition Radiation) screens and are fitted with 2 optical magnifications to fulfill field of view and resolution performances (<20μm). Their performances can be checked via an integrated resolution pattern.

SCOPE OF CTF3

CTF3 (CLIC Test Facility 3rd phase) is a collaboration driven by the CERN aimed to demonstrate before 2010 the feasibility of the future multi-TeV linear collider CLIC (Compact Linear Collider). Its scope is to check the two main innovative concepts of this accelerator: the two beams acceleration scheme using 12 GHz RF power and copper structures offering a very high gradient of acceleration (100 MV/m) [1].

The RF power at 12 GHz is generated by decelerating an electron beam (150 MeV – 30 A peak current, 5 Hz repetition frequency) in PETS cavities (Power Extraction and Transfer Structure). This beam, called “drive beam”, is produced in a Linac followed by a delay loop and a combiner ring in order to “densify” the trains of bunches from 1.5 GHz to 12 GHz, and so to increase their intensity (fig. 1)

This RF power feeds accelerating structures that provide a high accelerating gradient to the main beam reaching in the CLIC project the energy of 1.5 TeV after 15 km.

For CTF3, an accelerator called CALIFES (Concept d’Accélérateur Linéaire pour Faisceau d’Electron Sonde) injects this beam, acting here as a probe beam, into the 12 GHz accelerating structures. Its installation in a new building is to be completed by the end of 2007.

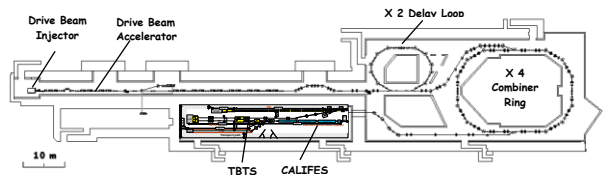

Figure 1: CTF3 Complex at CERN

The TBTS (Two Beam Test Stand) will allow studying the beam quality after high gradient acceleration (emittance, energy spread…) and to test the accelerating structures in operation (breakdown rate, wake-fields…).

PROBE BEAM SPECIFICATIONS

The accelerator CALIFES is built, for cost saving purposes, with 3 former LEP injector linac (LIL) sections at 3 GHz. A laser driven photo-injector delivers trains of short bunches (6 ps) that are velocity compressed in the first section down to 0.75 ps and accelerated up to 200 MeV in the 2 following ones [2].

The stringent beam characteristics detailed in table 1 with their reasons, are checked by a set of diagnostics that allow the tuning of the accelerator (power and phase of the RF, laser pulse power…).

Table 1: CALIFES beam parameters

Parameters		Motivation
Energy	~ 200 MeV	Avoid beam disruption in high RF fields
norm. rms emittance	< 20 π mm.mrad	Fit in 30 GHz structure acceptance
Energy spread	< ± 2%	Measurement resolution
Bunch charge	0.6 nC	~ CLIC parameters
Bunch spacing	0.667 ns	~ CLIC parameters
Number of bunches	1 - 32 - 226	Measure 30 GHz structure transients
rms bunchlength	< 0.75 ps	Acceleration with 30 GHz

The diagnostic suit includes: 6 BPM (beam position monitors) to check the axis of the beam all along the accelerator and tune the steerers, a ICT (Integrated Current Transformer) to measure the bunches train charge just behind the photo-injector, 3 VPM (Video Profile Monitors) to measure the transverse profile of the beam and a RF pick-up for pulse length measurement and tuning of the velocity compression.

Transverse emittance measurement is performed with scanning the gradients of the triplet of quadrupoles associated with transverse profile measurement. Energy spread measurement is performed with a spectrometer

made of an analysis dipole and a VPM, and longitudinal charge distribution measurement is performed with a deflecting cavity tuned at zero crossing (crab cavity) also followed by a VPM.

Most of these diagnostics are grouped in the diagnostic section (fig 2) just before the beam delivery to the TBTS.

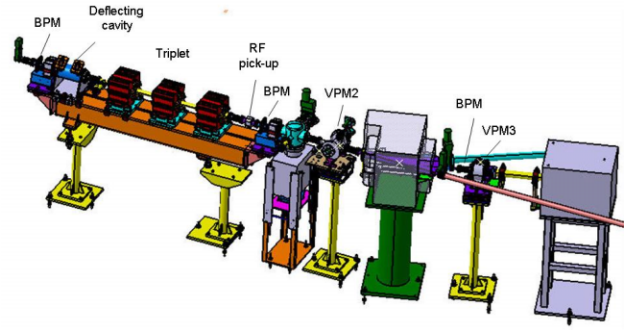

Figure 2: Diagnostics section

BPM

BPM are based on a coaxial re-entrant cavity, with 4 small antennas to pick-up the RF signal. Their low quality factor (Q=52) allow a high bandwidth (115 MHz) and consequently BPM are the only diagnostic providing time resolution along the bunch train. Taking advantage of this capability, a BPM is located just after the analysis dipole to provide data about the mean energy shift due to beam loading. More details on the CALIFES BPM are given at ref. [3]

ICT

Bunches charge delivered by the photocathode depends on its quantum efficiency, likely to evolutes with time and on the laser pulses power. It has to be accurately monitored during the tests and a reference diagnostic (ICT + Integrate-Hold-Reset electronic from BERGOZ) is foreseen just after the photo-injector. For installation ease, a "in flange" ICT model compatible with UHV has been retained. Electronic processing delivers an analog output that is sampled by a digitizer PCB (SIS-3300) to interface with the CERN control network and is driven via TTL signals.

VPM

Most of the beam characteristics measurements (emittance, energy spectrum, charge distribution) rely on the acquisition of beam transverse profile. This is done with a video camera that images a screen, either ceramic based for phosphorescent screen or aluminum for OTR (Optical Transition Radiation) that can be inserted in the electron beam.

Three VPM will be installed in the CALIFES accelerator.

First VPM

The first VPM (fig.3), installed upstream to the compression section, has the function to check the beam delivered by the photo-injector while its energy is about 6 MeV and its transverse size around 1 mm. A ceramic screen (AF995R from Saint-Gobain), is used for its high efficiency (around 600 photons/electron), the relatively large beam size insuring not to damage it. The screen dimensions are 40x40 mm^2, it is inserted at 45° respectively to the beam axis by an air jack. It is viewed through a fused silica viewport perpendicular to the beam axis, reflected by a 50 mm diameter mirror downward to the optical line. The optical line includes a doublet achromatic lens, a motorized diaphragm and a monochrome CCD camera (TELI CS8630HC) with analog output in order to easily interface with the CERN control network. With a CCD chip of 3.6x4.8 mm^2 the desired field of view of 22.3x30 mm^2 is obtained with a magnification of 0.16. Due to the relatively low number of pixels delivered by the frame grabber (312 x 416), the resolution is limited to 217 µm on 3 pixels. The purpose of this VPM being mainly to assess the beam presence, this is considered as acceptable.

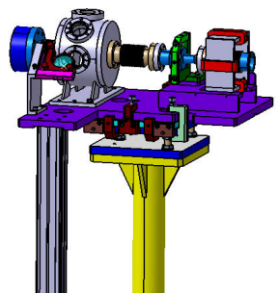

Figure 3: ICT, first VPM and BPM

Second VPM

The second VPM (fig 4), used to measure the transverse and longitudinal beam emittances, is located downstream to the triplet of quadrupoles and the deflecting cavity, after bunch compression and acceleration to 200 MeV.

Due to the low expected transverse emittance (around 10π mm.mrad), the beam size when focused on the screen is only about 50 µm. The density of charge per screen surface unit then exceeds what a phosphorescent screen can withstand. Alternatively, an OTR screen, made of alumina deposited on a silicium slice, offers in this case robustness and a better spatial resolution, while its low efficiency (around 1 photon for 100 electrons at 200 MeV) is no longer a problem. However, for non focused beam the light contrast is insufficient with the OTR screen, and a selectable ceramic screen is also foreseen.

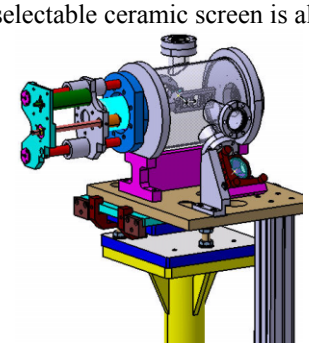

Figure 4: Second VPM

To obtain a sufficient resolution (20 µm desired) a magnification of 1.73 is required, limiting the field of view to 2.1x2.8mm^2. To comply with the field of view requirement of 10x10 mm^2, a second magnification (0.36) is selectable with a resolution limited to 96 µm. These two magnifications are obtained by inserting either a f=200mm or a f=250mm lens by motorized flipper mount (New Focus 8892) in the optical line. Optical performances like aberrations have been computed with Apilux code.

Light attenuation when necessary (long train of bunches) is obtained with a motorized filters wheel, a diaphragm being not able to provide accurate tuning with the narrow lobes of OTR light at 200 MeV.

An optical pattern (line grid) can be inserted at the same place of the screens in order to check the characteristics of the optical line and possibly to correct the distortion by software. Both ceramic and OTR screens and the optical pattern are mounted on a translatable carrier driven by a DC motor through a below. The optical pattern is back lighted via a dedicated viewport and a small mirror.

Due to the relatively high magnification (1.73), the depth of field is limited. Consequently, the angle between the screens and the electron beam has been lowered to 15°, the optical path exiting the tank at 30° to collect the back-OTR lobe through a CF40 fused silica viewport.

Third VPM

The third VPM is used to measure the energy spectrum after the analysis dipole bending the beam at 17.5°. The electron beam being spread a high efficiency phosphorescent screen is required. The screen, whose dimensions are 40x20mm^2, intercepts the beam at 45° and is viewed with a magnification of 0.22. An air jack is used to insert a line grid at the place of the screen for calibration purposes of the optic line. Light intensity is controlled via a motorized diaphragm.

TRANSVERSE EMITTANCE MEASUREMENT

Transverse emittance is computed by scanning quadrupole strength and measuring the corresponding beam size on the second VPM. Should the waist size be too small to be resolved by the optical line and to allow accurate measurement, it is possible to apply an alternative method using various sets of quadrupoles strengths leading to beam sizes (either vertical or horizontal) large enough to minimize measurement errors.

CHARGE LONGITUDINAL DISTRIBUTION MEASUREMENT

A traveling wave deflecting cavity is used at zero crossing for tilting electron bunches [4]. When fed with 3 GHz pulse power of 7 MW, the transversal electric field reaches 1.54 MV/m. The head of a bunch of 0.225 mm (0.75 ps) receives a kick that pitches it of 0.055 mrad and the opposite for the tail. The transverse beam size focused on the second VPM screen is then 200 µm versus 40 µm when the deflecting cavity is off.

RF PICK-UP

For basic operational tuning a non-intercepting measure of bunch length is foreseen that will be calibrated with the deflecting cavity method. It is based on EM field by propagating with the electron bunch [5]. The shorter the bunch length, the wider the generated RF spectrum that is collected by a waveguide and analysed between 30 to 176 GHz. This equipment has been developed by CERN for the drive beam and has to be adapted to the probe been characteristics.

ACKNOWLEDGMENT

The authors are grateful to Dr Thibaut Lefevre and Dr Carsten Welsch from CERN for their continuous support and advice in designing the CALIFES diagnostics.

REFERENCES

[1] H.H. Braun, “Towards a multi TeV Linear Collider; Drive Beam Generation with CTF3”, APAC07 (to be published)

[2] A. Mosnier et al., “The Probe Beam Linac in CTF3”, EPAC 2006, Edinburgh, Scotland

[3] C. Simon, M. Luong, “Beam Position Monitors using a Re-entrant Cavity”, these proceedings

[4] R. Akre, L. Bentson, P. Emma, P. Krejcik, “A Transverse RF Deflecting Structure for Bunch Length and Phase Space Diagnostics”, SLAC-PUB-8864 June 2001.

[5] C. Martinez et al, CLIC note 2000-020R.

.

MEASUREMENT OF ELECTRON BEAM CHARGE IN THE ESRF ACCELERATOR COMPLEX FOR ABSOLUTE AND INJECTION EFFICENCY MEASUREMENTS USING AN FPGA BASED DIGITAL BPM ELECTRONICS

Graham Naylor, Benoit Joly, (ESRF, Grenoble)

Abstract

A Beam Position Monitor (BPM) using Virtex II pro FPGAs ('Libera Electron' from Instrumentation Technologies) has been programmed with an alternative firmware in order to determine the charge by measuring integrated RF amplitude, over an adjusteable time window, of signals from 4 striplines. These striplines are located on the transfer line from the linac to the booster, on the booster ring, on the transfer line from the booster to the storage ring and on the storage ring. By calibrating the RF loss in all the cables, knowing the geometry of the striplines and using the crossbar switching before the 4 RF ADCs of the Libera, the charge/current can be compared in order to determine the efficiency of transfer at various locations during injection. Since the current in the storage ring is known to a high accuracy using a parametric current transformer (from Bergoz Instrumentation), the absolute charge can be determined at all locations.

INTRODUCTION

The transfer efficiency of beam between the various parts of the ESRF accelerator system is currently determined using electronics to integrate the signal from a current transformer in the transfer lines and parametric current transformers to mesure the quasi constant current in the booster and storage rings. The different temporal response of these different systems makes accurate comparative measurements difficult with the variety of time structured modes used at the ESRF. A new method is proposed [1] to measure the beam charge by integration of a beam signal from a stripline taken in a narrow band at the acceleration radio frequency (352.2MHz). Measurements are reported here of such a system using a Libera 'electron' to acquire and filter the signals. The technique also allows the relative RF phase of the beams in the booster and storage rings.

HARDWARE DESIGN

Striplines are located on:

i) The transfer line from the linac to the booster.
ii) The booster
iii) The transfer line from the booster to the storage ring
iv) The storage ring

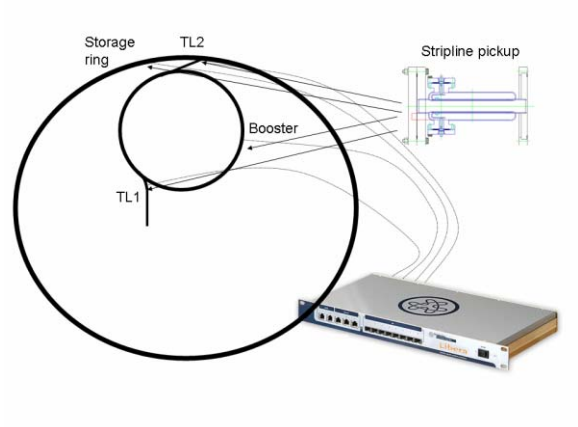

Figure 1: Location of pickups.

The signals from the 4 striplines are connected to the 4 inputs of the libera electron via 1% bandwidth RF filters (centred at 352.2MHz the acceleration frequency). The filter allows 'smearing' of the RF signal over time so as to correctly determine the amplitude with undersampling at 108MHz when in 16 bunch mode where single electron bunches are seperated by 177ns. The smearing of the signal reduces problems due to aliasing. Figure 2 below shows the single bunch currents from the Linac and then in the booster (lower trace), after a 10MHz filter (middle trace) and after a 3.5MHz filter (upper trace).

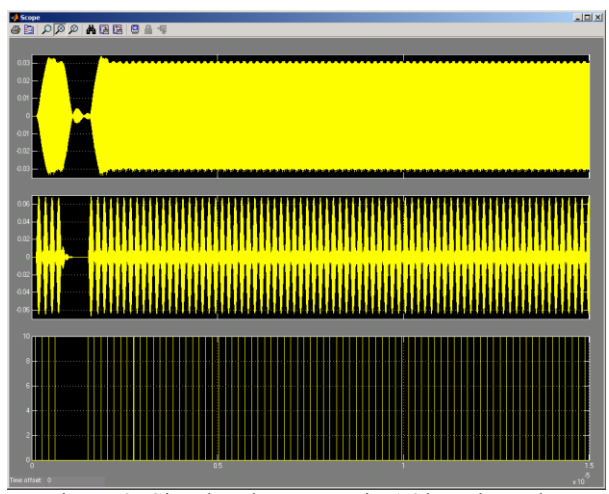

Figure 2: Simulated response in 16 bunch mode.

Libera Electron

The libera electron is a device produced by instrumentation technologies [2]. While its intended purpose is as a BPM electronics, the low noise narrow

band RF front-end with adjusteable gain and 12 bit ADCs make it ideal for the application described here. The ADCs are read using a Virtex II pro FPGA from Xilinx, which is at ease doing the digital signal processing necessary to perform accurate integrated amplitude and phase measurements. It is also designed to be directly connected to an ethernet network allowing a simplified connection to the control system. The alternative FPGA firmware design was prepared using System Generator – a tool provided by Xilinx to integrate DSP functions into their FPGAs within a *Simulink (Matlab)* environment.

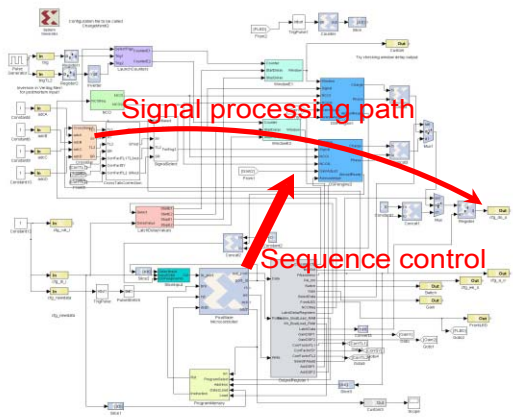

Figure 3: Firmware design in Simulink.

Firmware Design

The input signal is downconverted from the 352.2MHz frequency to an IF of 27MHz due to the undersampling of the input ADC. The image frequencies that would overlap at this frequency due to the undersampling are removed by the SAW RF filters in the front-end of the libera. The IF is mixed with a numerically controlled local oscillator, which is set to within a few kHz of the input signal (ie not locked). The demodulated signal is integrated over a time window of adjusteable delay and duration compared to either a linac trigger pulse or the booster extraction pulse. The sequencing of the integration measurements is controlled by a small 'soft' processor programmed onto the FPGA called a picoblaze. This processor is programmed in assembler and allows the scheduling of many measurements during the injection cycle. Its role is to set up each measurement, choosing a trigger source, timing delays, gain settings, signal source, crossbar setting, RF attenuators etc. The processor is not in the signal processing path, which is performed purely in the logic of the FPGA by two block called DSPeng1 and DSPeng2. The use of 2 'DSPeng' blocks allows 2 measurements to be performed simultaneously, for example to compare the relative phase of the beam in the booster and storage rings. The details of the required measurements are taken from a block RAM on the FPGA which is written to from the control system server.

OPERATION

Control Application

The libera is configured via registers in a shared memory, which is also used to export the results in a buffer. For the purpose of development a graphical application was prepared using *Matlab's* '*Guide*' utility, which allows configuration data to be enterred and details of all the required measurements (eg Transfer line, start and stop delays for integration, trigger pulse to use, numerical gain setting)

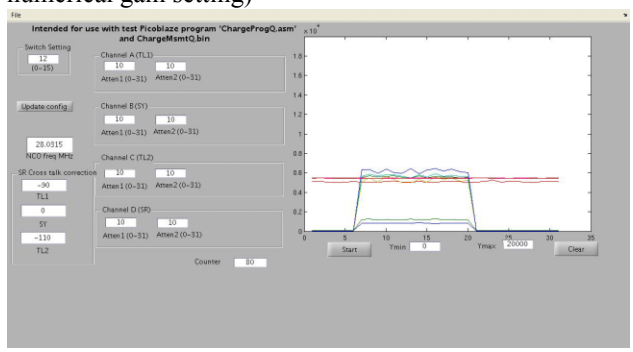

Figure 4: Graphical test application.

Table 1

Trig	Sig	Gain	DSP#	Start/us	Stop/us
0	0	1	0	0,19	2,18
0	1	1	1	2,96	6,94
0	3	2	0	2,96	8,59
0	1	1	1	21,48	25,46
0	3	2	0	21,48	27,11
0	1	1	1	40,00	43,98
0	3	2	0	40,00	45,63
0	1	1	1	9299	9303
0	3	2	0	9299	9304
0	1	1	1	18558	18562
0	3	2	0	18558	18564
0	1	1	1	38836	38840
1	2	1	0	0,19	2,18
1	3	2	1	4,17	9,80
1	3	2	0	18522	18528
1	3	2	1	37041	37046

RESULTS

The measured beam charge at the different stripline locations is shown in figures 5-8 during injections in 16 bunch mode (16 bunches equally seperated in the storage ring turn of 2.8μs).

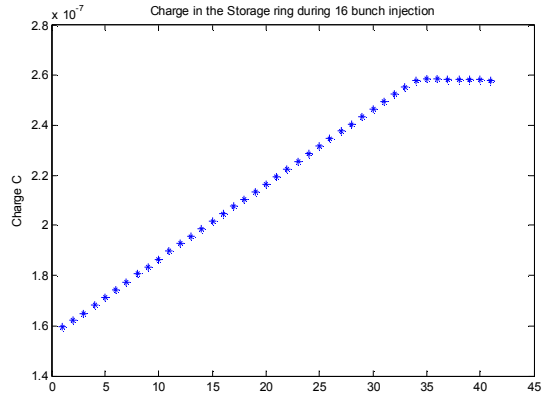

Figure 5: Charge measured in the storage ring (SR).

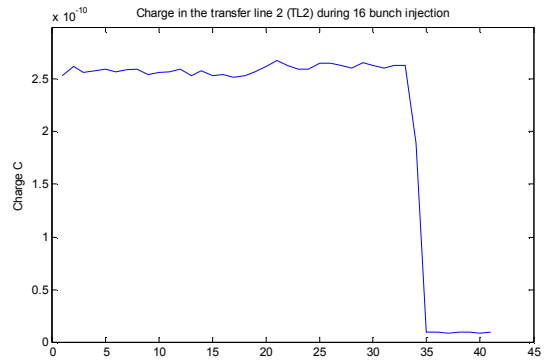

Figure 6: Charge measured in transfer line 2 (TL2).

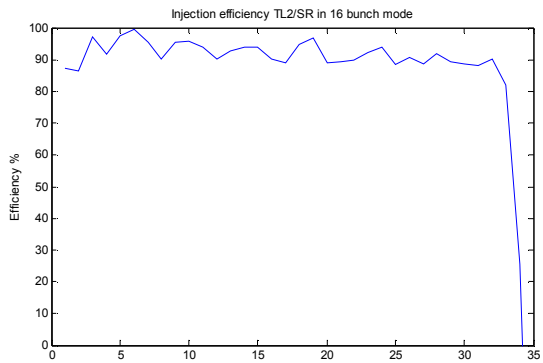

Figure 7: Injection efficiency TL2-SR.

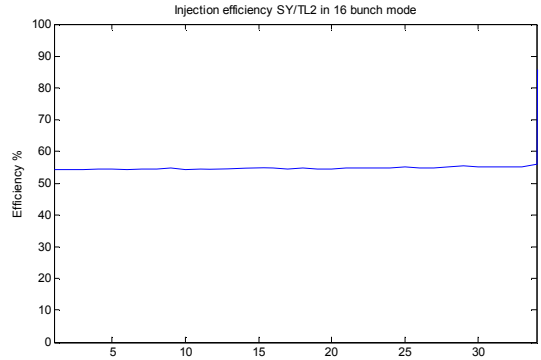

Figure 8: Injection efficiency SY-TL2.

Relative beam phase can also be measured between the booster and storage rings (see figure 9) at different times during the acceleration phase.

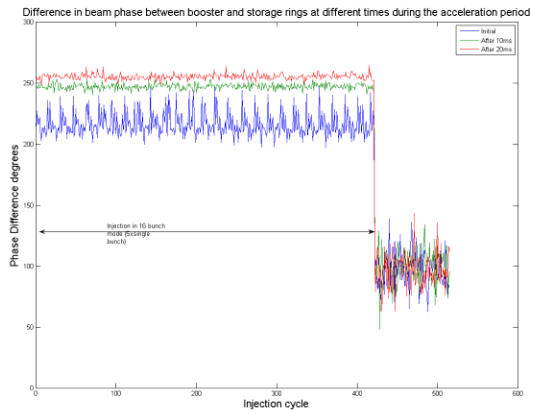

Figure 9: Beam phase difference between booster and storage ring.

CONCLUSION

A system using stripline pickups and a narrow band detection system with signal processing in an FPGA is shown to be an efficient method of measuring beam charge and relative phase. These measurements are of use for optimisation of the injection process.

REFERENCES

[1] G.A. Naylor, B. Joly "Determination of Beam Charge Using Stripline Signals at the RF Frequency by Fast Signal Processing in a FPGA". proceedings DIPAC 2005, Lyon p153

[2] A. Kosicek, "Libera Electron Beam Position Processor", Proceedings of the Particle Accelerator Conference, 2005. Page(s): 4284 - 4286

SIGNAL LEVEL CALCULATION FOR THE PETRA III BEAM POSITION MONITOR SYSTEM

G. Kube, M. Werner, DESY, Hamburg, Germany

Abstract

The new high–brilliance light source PETRA III at DESY requires measurement and control of the closed orbit with a resolution of better than 1 μm (rms). For this purpose it is planned to install about 220 button type beam position monitors (BPMs). To guarantee a good performance of the BPM electronics, the button signals have to meet several criteria in time and frequency domain. Therefore signal levels for different monitor types included for installation have been estimated. In this article the calculation results are summarized together with a comparison of measured monitor signals, and the expected position resolution will be discussed for the detection electronics *Libera*, developed by *Instrumentation Technologies*.

INTRODUCTION

Starting mid of 2007 the PETRA II accelerator at DESY will be converted in a new high-brilliance synchrotron radiation source PETRA III. Therefore nearly 300 meters of the 2.3 km long storage ring have to be rebuilt completely. For measurement and control of the closed orbit about 220 electrostatic beam position monitors (BPMs) are forseen: one BPM per standard FODO cell and additional BPMs at the locations of insertion devices. Due to the unconventional asymmetry in the ring geometry there exist different vacuum sections with varying cross–section. In order to guarantee the required measurement and control of the closed orbit with a resolution of 0.3 μm (rms) at the insertion devices a necessary prerequisite is good performance of the BPMs and their detection electronics, and the button signals have to meet several criteria in time and frequency domain.

In order to study the transient signal behavior for all monitor types included for installation the signal levels have been estimated. The signal modelling follows the method described in Ref. [1] but is generalized such that arbitrary vacuum chamber geometries and beam positions can be taken into account. For this purpose a boundary element method described in Refs. [2, 3, 4] was utilized which is based on a numerical solution of the integral representation for the scalar potential. The calculated monitor signals are compared to measured ones and the expected position resolution will be discussed for the *Libera* detection electronics.

SIGNAL MODELLING IN TIME DOMAIN

The first step is to calculate the image charge induced by the beam as function of time. Assuming an ultra relativistic beam with normal distributed longitudinal beam profile of length σ_b and a circular button with diameter d_B it can be expressed as

$$Q_i(t) = Q_{i0} \int_{-d_B/2}^{+d_B/2} \mathrm{d}z \, \frac{e^{-\frac{(z-ct)^2}{2\sigma_b^2}}}{\sqrt{2\pi}\sigma_b} \sqrt{1-(2z/d_B)^2} \quad (1)$$

with Q_{i0} the induced charge calculated from a two-dimensional electrostatic problem assuming a point charge, which can be derived directly via standard electrostatic methods. For the calculations presented in this paper a boundary element method described in Refs. [2, 3, 4] was used. The dynamics in the signal generating process is described by the integral expression.

From Eq.(1) the image current follows as time derivative from the charge

$$I_i(t) = \frac{\mathrm{d}Q_i}{\mathrm{d}t}. \quad (2)$$

The button voltage in frequency domain is the product of the Fourier transformation $\mathcal{I}_i(\omega)$ of the current Eq.(2) and the impedance seen by this current. The dominant parts of the latter are the impedance of the cable Z_0 shunted by some parasitic button capacitance C_B, i.e. $\mathcal{Z}(\omega) = Z_0 \mid\mid (i\,\omega C_B)^{-1}$. The button voltage in time domain is finally obtained by the inverse Fourier transform

$$U_i(t) = \mathcal{F}^{-1}[\mathcal{U}_i(\omega)] = \mathcal{F}^{-1}[\mathcal{Z}(\omega)\mathcal{I}_i(\omega)]\,. \quad (3)$$

In order to study the transient signal at the input of the detection electronics the frequency response of the connecting coax cable has to be taken into account. According to Refs.[1, 5] for a coax cable with skin effect losses it is given by

$$\mathcal{H}_{coax}(\omega) = e^{-(1+i)\sqrt{\omega/\omega_e}} \quad (4)$$

with ω_e the frequency for which the amplitude is attenuated by a factor of e.

The calculation of the relevant quantities was realized as a MATLAB script with graphical user interface, allowing simplified operation and control of the input parameters. The calculated pickup signal in Fig.1 for a BPM with circular vacuum chamber profile installed in PETRA II agrees well with the signal recorded by an oscilloscope. For the calculation the scope was modelled as first order low pass filter with corresponding bandwidth. Besides the example shown in Fig.1 additional comparisons were performed for the ELETTRA low gap BPM (elliptical chamber profile), and the DIAMOND primary BPM with racetrack resp. arc BPM with octagon profile, all of them showing satisfactory agreement with corresponding fast oscilloscope measurements.

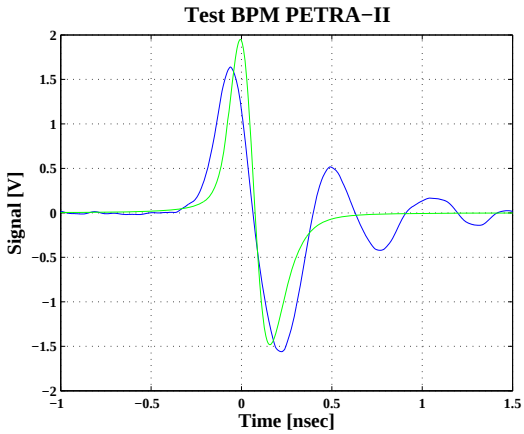

Figure 1: Calculated pickup signal (green line) and measured ones (blue line) for a circular beam pipe BPM (ø120 mm) installed in PETRA II. The beam with 1.1 mA bunch current and (1 σ) bunch length of 14.3 mm was assumed to be centered in the beam pipe. The signal was recorded with a 4 GHz bandwidth scope and 20 dB attenuation. The connection between pickup and scope was performed via a 22 m long 2.6/7.3AF coax cable.

PETRA III MONITOR SIGNALS

It is planned to install BPMs with at least five different vacuum chamber cross sections in PETRA III. The most critical ones shown in Fig. 2 are the low gap monitor and the arc monitor for the new octant where the insertion devices will be installed.

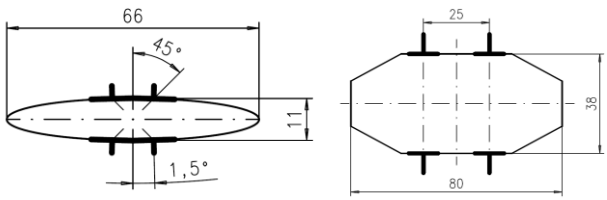

Figure 2: Vacuum chamber cross section of the two monitor types for the new octant: the low gap monitor (left) has an elliptical profile and will be installed close to the insertion devices, the arc monitor has an octagon chamber profile. Both monitors have buttons with diameter ø11 mm.

The subsequent signal analysis is presented for these two BPM types with the beam parameters as follows: beam energy E = 6 GeV, total current I = 100 mA, bunch length σ_z = 40 psec (1 σ). The calculations were performed under the assumption of operation in the time resolved mode, i.e. the fill pattern consists of 40 bunches equally distributed in the machine. This mode corresponds to a bunch charge of 19.2 nCb resp. 1.2×10^{11} particles per bunch. For the other standard operational mode (multibunch mode) with 960 bunches and I = 100 mA the calculated signal levels are reduced by a factor of 24. In order to take into account the influence of the connecting cable between the BPM electronics module and the pickups a 20 m long RFA 3/8”-50 coax cable was considered, resulting in a characteristic frequency f_e = 11.6 GHz.

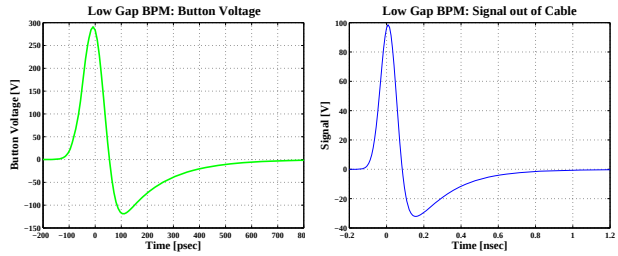

Figure 3: Calculated signals at the button (left) and behind the cable (right) for the low gap BPM, assuming the beam centered onto the monitor axis. The influence of the cable is to smear out the signal and to reduce its amplitude by about a factor of three.

Figs. 3 show the transient signals at the button and behind the cable for the low gap monitors. The signals of the arc monitors are about a factor of three smaller than for the low gap BPMs.

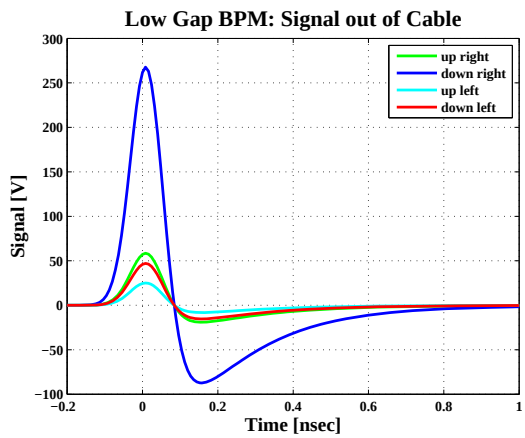

Figure 4: Calculated pickup signal outputs from the cable for the low gap monitor, assuming a beam with 3 mm transverse offset in both planes.

The situation becomes even worse if the beam has an offset with respect to the monitor axis. Fig. 4 shows the transient signals for the low gap BPM behind the cable, assuming 3 mm transverse beam offset in both planes. This is beyond the maximum peak voltage of most BPM electronics and for their non–destructive operation the consequence is that the signal should be attenuated and filtered.

FREQUENCY DOMAIN MODELLING

Signal processing of the BPM electronics is usually performed for only one specific frequency component by special filtering, in the present case it is the signal component at f_0 = 500 MHz. Therefore it is helpful to consider the signal modelling additionally in the frequency domain. The key value in the frequency domain is the transfer impedance $\mathcal{Z}_T(f_0)$ which gives the relation between beam

current $\mathcal{I}$ and the amplitude for the button signal. With the model of a current source working on a cable shunted by the button capacitance and Fourier transform, for short bunches it is

$$\mathcal{Z}_T(f_0) = \frac{\hat{U}(f_0)}{\mathcal{I}} = \frac{2\pi f_0 Z_0}{\sqrt{1+(2\pi f_0 Z_0 C_B)^2}} \frac{d_B^2}{4\,c\,d_{eq}} \quad (5)$$

with $\hat{U}$ the amplitude of $U_i(t) = \hat{U}\cos(2\pi f_0 t)$ to a load of Z_0 connected to the button, and d_{eq} the equivalent bunch to button distance which can be calculated by an electrostatic field solver (e.g. CST studio) by just solving the field distribution in a thin chamber slice with magnetic boundary conditions on either side of the slice.

SIGNAL ATTENUATION

For the following discussion a -7 dBm signal for a centered beam and a peak voltage behind the cable of 400 V for 3 mm beam offset are assumed (e.g. example Fig. 4 including additional safety margin).

To reduce the peak voltage the following solutions are possible: a) insertion of lowpass or bandpass filters between BPM buttons and electronics [6], b) insertion of attenuators between BPM buttons and electronics, or c) use of long cables with enough attenuation.

If attenuators are used to reduce the peak voltage of the signal, the 500 MHz spectral component is reduced as well. For better illustration two theoretical electronics devices will be discussed with maximum allowed peak input voltages of 2 V and 80 V, respectively. The resolution of these devices is assumed to be like in Fig. 5.

For a maximum peak input voltage of U_{max} = 2 V at the BPM electronics, an attenuation of Att = 46 dB is necessary for a peak voltage of 400 V. So the 500 MHz amplitude will be reduced to -53 dBm. Figure 5 shows a resolution of $\approx$ 1.5 μm for a monitor constant K_M = 10 at 1 kHz bandwidth. For U_{max} = 80 V the attenuation can be reduced to Att = 14 dB, resulting in a 500 MHz amplitude of -21dBm. For the same conditions as above the resolution will improve to $\approx$ 0.3 μm. According to the specifications of such attenuators the temperature sensitivity is $<$ 0.0001 dB/(dB °C) and the power sensitivity is $<$ 0.001 dB/(dB W). The temperature sensitivity can be converted directly in a position dependence on the temperature difference of attenuators:

$$\frac{\Delta Pos}{\Delta T} < 5.8 \times 10^{-6} \cdot K_M \cdot \mathrm{Att[dB]}\ . \quad (6)$$

The power sensitivity can be converted in a position dependence on a beam offset O_{Beam}:

$$\frac{\Delta Pos}{O_{Beam}} < P_{att} \cdot 2.3 \times 10^{-4} \cdot \mathrm{Att[dB]}\ . \quad (7)$$

This results in a position change per degree Celsius difference (between the four attenuators) ΔP_T and in a drift ΔPos/mm offset (P_{att} = Power at attenuator $\approx$ Power after cable for centered beam = 0.25 W; low gap BPM with K_M = 5.3 mm):

Table 1: Sensitivity on the attenuator parameters.

U_{max}	Att	ΔP_T	ΔPos
2 V	46 dB	$<$ 1.4 μm / °C	$<$ 2.6 μm / mm
80 V	14 dB	$<$ 0.4 μm / °C	$<$ 0.8 μm / mm

SUMMARY

In the present paper the BPM monitor planned to use in the new arc of PETRA III is discussed in view of signal levels and sensitivity. It was shown that the huge signal levels require additional attenuation and estimations were presented to demonstrate the attenuator influence on the accuracy for position measurement.

ACKNOWLEDGEMENTS

The authors acknowledge I. Krouptchenkov for performing the measurement at PETRA II, K. Wittenburg for discussions and support in preparing the manuscript, G. Rehm (DIAMOND) and E. Lonza (ELETTRA) for providing information about their monitor signal levels, E. Plouviez (ESRF) for information about the filtering, and Instrumentation Technologies for the information about the *Libera* electronics.

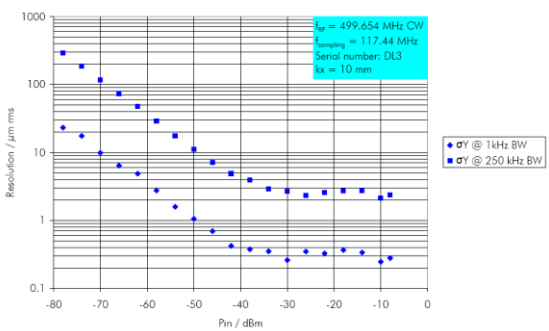

Figure 5: Resolution of the "LIBERA Electron" beam processor at two different bandwidths. Picture taken from Ref. [7].

REFERENCES

[1] S.R. Smith, in Proceedings of BIW'96, Argonne, Illinois, AIP Conf. Proceedings **390** (1997), 50.

[2] T. Shintake et al., Nucl. Instr. Meth. **A 254** (1987) 146.

[3] A. Stella, DAΦNE Technical Note **CD-10** (1997).

[4] G. Kube, *Sensitivity Estimation for the PETRA-III Beam Position Monitors based on a Boundary Element Method*, DESY Technical Note **07-01** (2007).

[5] R.L. Wigington, N.S. Nahman, in Proc. IRE **45** (1957), 166.

[6] E. Plouviez, private communication.

[7] A. Kosicek, in Proceedings of PAC'05, Knoxville, Tennessee (2005), 4284.

LARGE HORIZONTAL APERTURE BPM AND PRECISION BUNCH ARRIVAL PICKUP

K. Hacker, F. Loehl, H. Schlarb DESY, Hamburg, Germany

Abstract

The large horizontal aperture chicane BPM and the precision bunch arrival monitor at FLASH will be important tools to stabilize the arrival-time of the beam at the end of the linac. The pickups for these monitors will be paired with front-ends that sample the zero-crossing of the beam transient through the use of electro-optical modulators and sub-picosecond-long laser pulses delivered by the master-laser oscillator. The design of pickups for this front-end requires the consideration of the beam transient shape as well as the amplitude. Simulations and oscilloscope traces from pickups that use or will use the EOM based phase measurement and the expected limitations and benefits of each pickup are presented. In particular, the design for a 5 μm resolution BPM with a 10 cm horizontal aperture is demonstrated in terms of its capability to measure the beam energy and its sensitivity to the shape and orientation of the beam.

INTRODUCTION

A bunch arrival-time stability of 30 fs (~10 μm at v=c) is desired for pump-probe experiments and is mandatory for laser-based electron beam manipulation at FLASH and the XFEL [1]. With the accelerating LLRF goal energy stability of 10^{-4} at FLASH, the transverse position jitter in the dispersive section of the first chicane becomes 34.5 μm and results in a longitudinal position jitter of 18 μm. A monitor for a feedback system should be able to measure the beam energy by a factor of three better than the desired energy stability of $5*10^{-5}$ and this means that the resolution for a beam position measurement in the chicane must be better than 6 μm and a longitudinal time-of-flight path-length measurement should resolve 3 μm.

A longitudinal time-of-flight energy measurement can be made with two bunch arrival monitors (BAMs): one before and one after a chicane, but a chicane BPM energy measurement has an advantage given by the ratio of the R_{16} to the R_{56} terms. In the case of the first bunch compressor for the XFEL, this advantage in the required sensitivity of the monitor is a factor of six.

The chicane BPM used together with the BAM can distinguish the energy jitter that results from injector timing changes from the energy jitter caused by acceleration RF phase and amplitude changes. The chicane BPM used together with a bunch length monitor can distinguish the RF amplitude jitter from the RF phase jitter. BPMs that reside before and after the chicane can be used to remove orbit jitter from the chicane BPM's energy measurement.

The pickup transients from these chicane BPMs and BAMs will be paired with the sub-picosecond pulses from the master laser oscillator (MLO) from the timing and synchronization system in an electro-optical modulator (EOM) in order to sample the zero crossing of the beam transient, giving a phase measurement with an accuracy of 5-50 fs, depending on the pickup and cables used [2, 3]. Temperature dependent cable drifts are removed by installing the EOM front-end in the tunnel [4].

In this paper, a ring-shaped BAM, a button-style BAM, and a perpendicularly mounted stripline chicane BPM are analyzed with Microwave Studio simulations and measured oscilloscope traces with regard to their suitability for the EOM phase measurement technique. Measurements of the beam energy with the 10 cm wide chicane BPM pickup and an oscilloscope are analyzed with respect to their sensitivity to beam shape and orientation changes.

EOM PHASE MEASUREMENT

The EOM phase measurement [2, 3] utilizes a short optical pulse (< 1 ps) from a master laser oscillator that is locked to the 1.3 GHz reference of the machine. The light pulse travels via fiber optics through an EOM which encodes the amplitude information of an RF pulse into the laser pulse energy. Essentially, the laser pulse samples the beam transient. The modulated laser pulse is then detected with a fast photo diode and read out by a 108 MHz, 16bit ADC that is clocked with the laser pulse at twice the repetition rate of the laser.

Since changes in the RF pulse arrival-time produce a change in laser intensity, the measurement is limited by the steepness of the beam transient slope and the precision of the laser amplitude detection. Slope changes can distort the measurement, so a feedback is used to maintain the measurement at the zero-crossing. For a particular 30 fs resolution measurement, the slope at the zero crossing was 250 mV/ps and the single-shot noise with which the laser pulse intensity was detected was 0.3% [2]. This particular measurement was done with a 10 m cable attached to the pickup, and much higher resolution is, of course, possible with in-tunnel measurements.

For the first in-tunnel tests, the EOM setup will be duplicated several times for use with two BAMs and a chicane BPM. Fiber-optic links have been sent to several key points in the tunnel in order to transport the signals without the effects of RF cable drifts and attenuation [4]. The commissioning of these front-ends will occur in September 2007.

PICKUP DESIGN

Beam pickups for the EOM phase measurement must produce a steep transient slope for maximum resolution. They must also have a minimum of ringing so that the transient of a bunch that comes earlier is not detected.

This requires the high bandwidth and voltage that are produced by short bunches, pickups with a large area exposed to the beam, and good impedance matching. Bunches that are longer than ~25 ps (RMS) will have reduced resolution because the slope of the transient becomes less steep (e.g. 50% for 25 ps).

BAM

A ring shaped pickup was originally available for the BAM prototype measurements; however, it had a critical flaw [6]. The spectral response has a notch at 5 GHz, corresponding to a quarter-length of the ring circumference, implying that the beam does not couple strongly to the second harmonic of the ring. A strong position dependence of the zero-crossing is therefore seen through a beat between the fundamental and third harmonics of the ring. This position dependence of the phase can be partially removed if the signals from both sides of the ring are combined.

Another consideration of BAM pickup design is the ratio between the amplitude of the transient and the slope of the transient. An optimal pickup would produce a large slope and small amplitude. Large amplitude is undesirable because it must be limited or attenuated in order to protect the EOM from damage. Attenuators reduce the signal slope and limiters have AM-PM conversion behaviour. The ring-shaped pickup produced a slope of 1 V/ps and a peak-to-peak voltage of 130 V when measured in the tunnel with an 8GHz bandwidth oscilloscope, but the EOM can only tolerate ~10 V.

The most obvious alternative to a ring is a button pickup. A Microwave Studio and oscilloscope based comparison between the button pickups in the FLASH linac yielded that, although many button pickups designed with attention to impedance matching would be adequate for an EOM phase measurement, an optimal pickup would have no "button" at all; it would consist of a simple coaxial cylinder with one end open to the beam and the other end connected to a vacuum feedthrough of the same inner and outer diameters. A type-N feedthrough was chosen for the final design because of its large diameter, enabling the pickup to achieve the same signal slope as the ring-shaped monitor, but less than half of the peak-to-peak voltage. To remove the position dependent amplitude changes, the signals from opposing buttons are combined.

Chicane BPM

The chicane BPM design utilizes a cylindrical pickup within a cylindrically shaped vacuum chamber channel that lies over and perpendicular to the path of the electron beam (see Fig. 1) [3]. When the electron beam travels beneath this pickup, short electrical pulses travel to opposite ends. The arrival-times of the pulses are then measured with the EOM technique and used to determine the position of the electron beam. They have been installed in both the 1st and 2nd bunch compressor chicanes at FLASH with respective horizontal ranges of 10 and 20 cm.

In Fig. 1, the perpendicularly mounted stripline is depicted in 3-D as well as in cross-section.

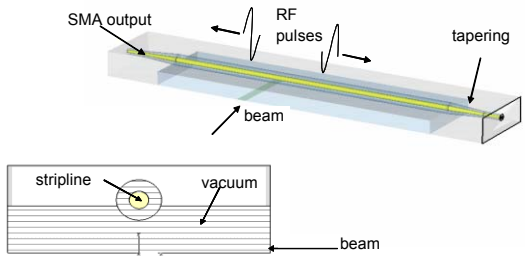

Figure 1: Perpendicularly-mounted stripline BPM pickup.

In the 3-D depiction, only the upper-half of the BPM is shown, since the lower-half is identical. The beam is represented by a thick line underneath the stripline. The central piece of the stripline is tapered on both ends from a 3 mm diameter to an SMA sized connector pin. The vacuum feedthroughs to SMA connectors are at the ends of the stripline.

A simpler design that utilizes a type N feedthrough and does not require tapering was not possible for the first installation because the vacuum chamber height is only 8 mm. This would, however, be a good option for the XFEL where the vacuum chamber height will be 40 mm.

In a Microwave Studio simulation, a 50 GHz bandwidth (FWHM) Gaussian pulse was applied to the monopole mode of a waveguide port in order to simulate the electron beam. The output signals of the SMA connector ports were scaled according to a 1 nC electron bunch charge and low-pass filtered to 8 GHz to match the bandwidth of the oscilloscope measurement (Fig. 2).

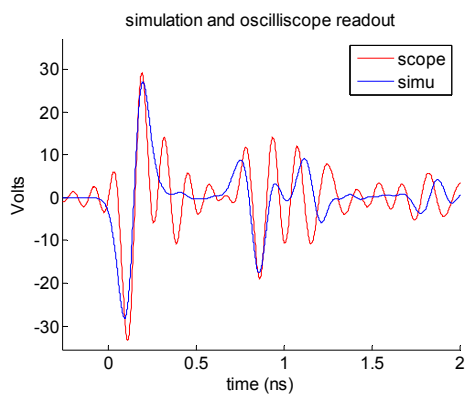

Figure 4: Simulated and measured stripline output. The ringing in the measured signal is an oscilloscope artefact. The echo with 0.6 ns delay is caused by a ceramic support at the opposite end of the stripline.

Good agreement is observed between the measured and simulated signals, except for the ringing seen on the oscilloscope signal. This ringing starts before the arrival of the electron beam and is observed only for in-tunnel

measurements. It is observed for different types of pickups measured in the tunnel. If the higher frequencies are attenuated through the use of a long cable before the oscilloscope, the ringing is gone. The oscilloscope is not designed for signals with a bandwidth of much more than 8 GHz and in simulation the spectral response of the monitor is strong up to 50GHz, yielding a short >300 V peak-to-peak pulse.

The oscilloscope was attatched to either end of the stripline and used to measure the beam energy in the chicane (Fig. 5). The pickup operates as expected over the entire 10 cm aperture and the measurement was only limited by the maximum amplitude of the accelerating module on one end and by the chamber width on the other..The position resolution with the oscilloscope with an intrinsic trigger jitter of 0.5 ps rms was only 150 um, but 5 um is the expected resolution with the EOM front end.

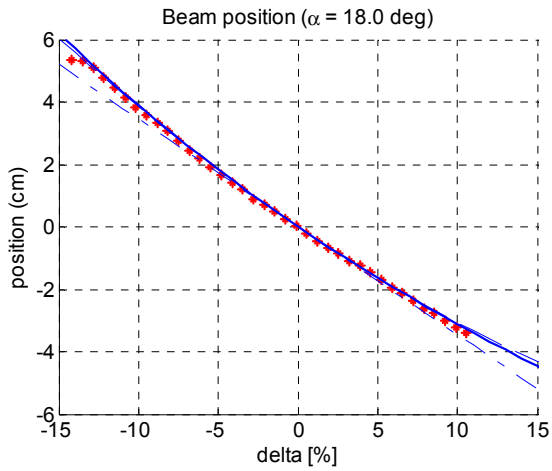

Figure 5: Calculated and measured beam position. The measurement points are shown in red and the calculated positions using R16, T166, and R1666 for the bunch compressor are shown in blue.

The pickup also responds as expected to changes in beam width (Fig. 6) and transverse tilt (Fig. 7). If the nominal beam width (4 mm FWHM) changes by a factor of 2, the slope at the zero crossing will change by less than 10%. A 200 um position measurement error is predicted by simulation and measured for a 4 mm (FWHM) wide beam tilted by 5 degrees. This means that the signals from the top and bottom pickups must be combined to remove this effect.

An error that cannot be removed would be caused by a longitudinally (XZ) tilted beam with a significant charge distribution asymmetry. In simulation, a 4 mm (FWHM) wide asymmetric Gaussian beam with the center-of-charge shifted horizontally by 1 mm relative to the peak will cause the BPM to show a 170 um absolute position error if the beam is tilted by 0.2 rad in the XZ plane. This kind of tilt would be expected for off-crest operation. As long as the beam distribution or orientation does not change dramatically, it does not have any influence on the BPM's functionality in an energy feedback.

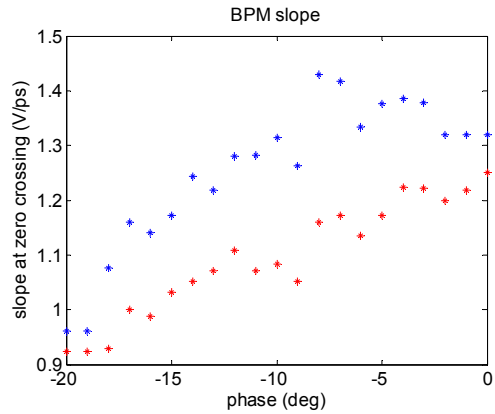

Figure 6: The slope of the transient at the zero crossing depends weakly on the beam width. The two different sets of points represent data from the left and right output of the monitor. The beam width was changed by varying the accelerator phase from nominal by ±10°.

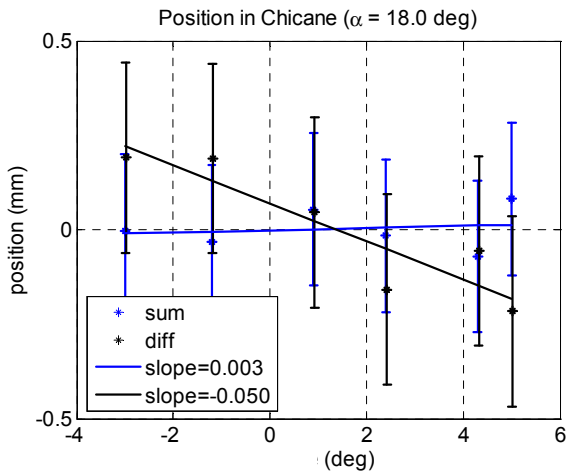

Figure 7: A transverse tilt of the electron beam would cause a measurable error unless the signals from the top and bottom pickups are combined.

SUMMARY

- EOM technique makes high resolution phase measurements possible.
- Optimal pickups for the EOM technique must maximize the slope and minimize amplitude, ringing, and transient distortions.
- Pickups perform as expected in tests with beam.

REFERENCES

[1] X-FEL Technical Design Report Sect. 4.8 2006.
[2] F. Loehl et. al., "Beam Arrival-time Monitor", EPAC'06, Edinburgh, June 2006.
[3] F. Loehl et. al., This conference WEPB15.
[4] F. Loehl et. al., This conference WEPB16.
[5] K. Hacker et. al., "BPM with Large Horizontal Aperture", EPAC'06, Edinburgh, June 2006.
[6] K. Hacker et. al., "Beam Pickup Designs Suited for an Optical Sampling Technique", FEL'06, Berlin, June 2006.

EXPERIENCE WITH LIBERA BEAM POSITION MONITORS AT DELTA

P. Hartmann*, J. Fürsch, D. Schirmer, T. Weis, K. Wille
Zentrum für Synchrotronstrahlung DELTA, Universität Dortmund, D-44221 Dortmund

Abstract

Libera beam position monitor electronics have been installed at the electron storage ring Delta in order to extend the capabilities of the BPM system to turn-by-turn orbit measurements. This report covers the integration of Liberas into the beam diagnostics infrastructure at DELTA and its control system EPICS. Prior to their application in user runs the devices have undergone characterization measurements in a BPM teststand and during machine runs for accelerator physics. The results of these measurements are compared to measurements with DELTA's standard BPM electronics. The necessary clock and trigger signals are provided by a low-cost signal distribution device developed at DELTA.

INTRODUCTION

The storage ring Delta as well as the booster BoDo are equipped with analog beam position monitor (BPM) electronics[1] which have been working reliably without any problems for roughly ten years. They have proven to be excellent tools for beam orbit measurement up to a maximum bandwidth of 10 kHz.

The advent of off-the-shelf turn-by-turn (TBT) BPM electronics[2] offer the opportunity to acquire TBT orbit data in parallel to 'slow' orbit measurement. Turn-by-turn orbit data open up a new window in beam diagnostics at DELTA. Optics parameters, for example tune and chromaticity, can now be monitored with high temporal resolution. Turn-by-turn data, taken within a fraction of a millisecond, can be obtained during user shifts often even without any beam distortion [1], and not only during dedicated machine shifts.

This report describes the extension of our BPM testbed to incorporate Libera BPMs and the creation of the infrastructure in the Delta storage ring in order to use all features of Libera. First measurements are presented.

BPM TESTBED

Prior to installation in the ring, new BPM electronics and new firmware versions have to be tested. For this purpose we have set up a BPM testbed (see fig. 1).

The signal from an RF generator running at 499.82 MHz is split by high bandwidth power dividers and is fed into the inputs of a MX-BPM and a Libera. The RF generator can be pulsed in order to simulate a variety of filling patterns. In addition a Clock Splitter and a trigger generator was installed. On the Liberas we currently use firmware version 1.21 together with the DIAMOND EPICS driver version 0.63. The output signals of both BPMs can be monitored from any PC in the control system.

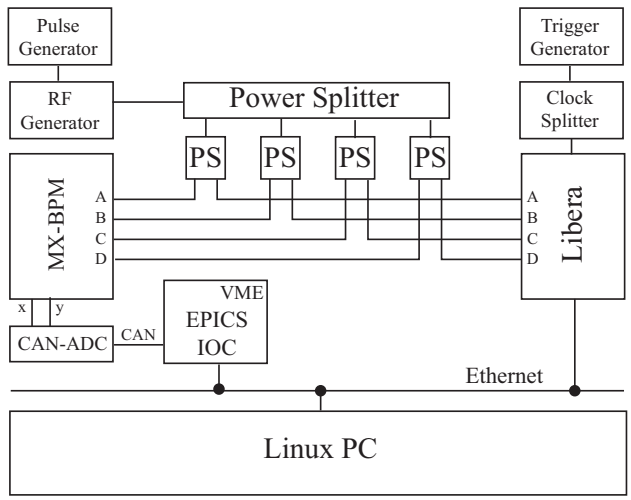

Figure 1: Setup of the BPM testbed.

The Digital Signal Conditioning (DSC) feature of the Liberas, intended to compensate for slow amplifier drifts of the four signal paths of the analog frontend of the Liberas, generates a signal distortion on the turn by turn data which renders TBT measurements unusable. Slow beam orbit measurements, on the other hand, need DSC in order to give reasonable results. Thus a parallel operation of fast and slow data taking is, for the moment, not possible.

The EPICS driver does not support the Automatic Gain Control (AGC) feature of the Libera BPMs thus we do gain switching with a set of EPICS records.

A comparison of the 'slow acquisition' data of the analog and the digital BPM electronics resulted in only small differences at beam currents above 2 mA. Only the vertical component of the slow acquisition data from the Libera shows a deviation in the 10 μm range below 2 mA beam current corresponding to -55 dBm input power. Lowering the beam current to less than 0.8 mA, deviations of more than 100 μm were observed (see fig. 2). The impact on the ring installation is low, since the Delta orbit correction stops operating at its lower beam current limit of 1 mA.

RING INSTALLATION

The installation of Liberas requires an infrastructure for the distribution of a variety of signals, if all features the

* hartmann@delta.uni-dortmund.de
[1] Bergoz MX-BPM
[2] I-Tech Libera electron

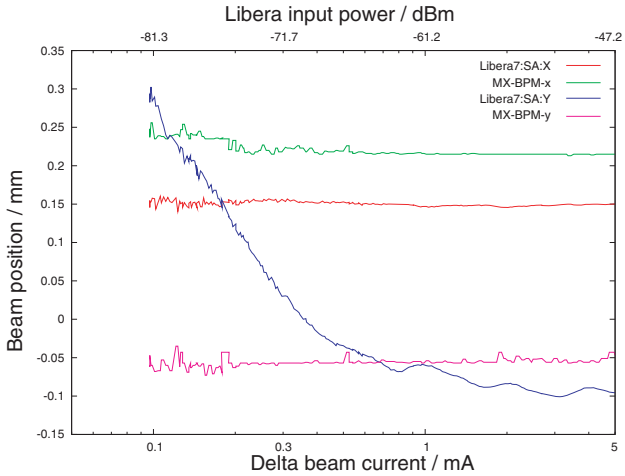

Figure 2: Beam position versus beam current of orbit signals from different BPM electronics.

Liberas provide shall be used. Figure 3 depicts the signal generation and the two-stage distribution network. The first stage (Clock Distributor) resides in a rack on the outside of the ring, accessible during machine runs. Signals will be transported by optical fibers to the inside of the ring where the second stage (Clock Splitter) transforms the optical signals into differential electrical signals required by the Liberas. Clock Splitters were developed at DELTA based

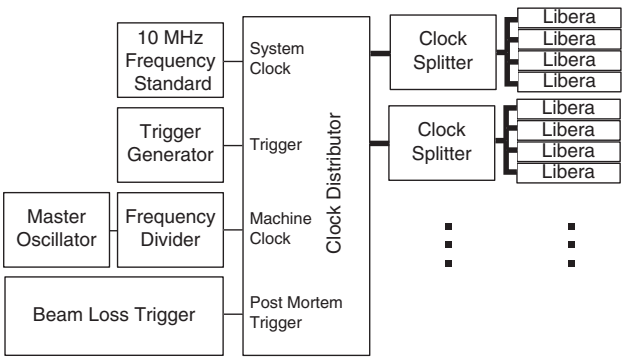

Figure 3: Infrastructure needed by the Libera BPM electronics. All devices except the central Clock Distributor are installed up to now.

on a design provided by the beam diagnostics group of the DIAMOND Light Source. Since at DELTA BPMs are organized in groups of four and signal distribution is planned to be done with optical fibers, a commerially available solution was not an option.
The DELTA Clock Splitter processes four inputs for System Clock, Machine Clock, Trigger and Post Mortem Trigger and has one backward path for the Interlock signal. Parallel to optical fiber inputs, BNC connectors for TTL level signals are available.

Seven Liberas have been installed in the Delta storage ring up to now. The four mostly used ones are connected to BPM13 - BPM16 (see fig. 4). BPM14 and BPM15 are connected to the pickups via power splitters. BPM13 and BPM16 are connected directly to the pickups. Only BPM14 has the “free run” option of the EPICS driver enabled which is necessary for tune measurement [1].

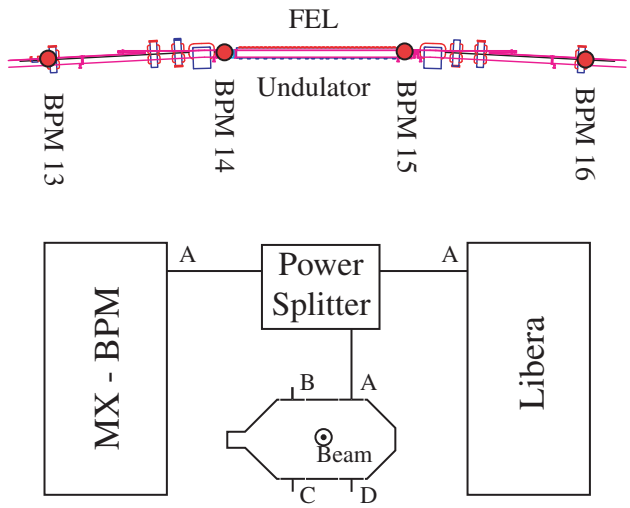

Figure 4: Position of four of the seven Liberas currently installed in the ring. BPM 14 and 15 are connected to the pickups via four power splitters (only one is shown).

Operating two BPM electronics in parallel on a power divider is not unproblematic as can be seen in fig. 5. Sudden orbit steps were observed on the Libera TBT data having a repetition rate of about 8 kHz. They are attributed to reflections the MX-BPM generates on the RF inputs due to unadapted impedances of the multiplexer. The problem is known to the manufacturer and may be suppressed to negligible level. These orbit steps average out in slow acquisition data. For BPM 14 and 15 MX-BPMs with very low reflections have been chosen.

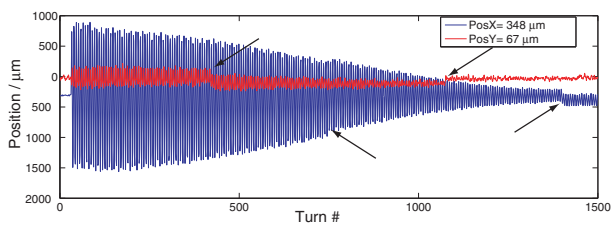

Figure 5: Steps in the turn by turn orbit measurements at 8 kHz repetition rate are attributed to reflections from the MX-BPMs that propagate back through the power splitter.

Phase space measurement

Besides the measurement of the tune the measurement of the phase space on two successive BPMs is quickly set

up, in case the transfer matrix between them is known. The transfer matrix between BPM14 and 15 is that of a simple drift space. The beam was excited using one of the injection kickers. The kick takes place only in the horizontal

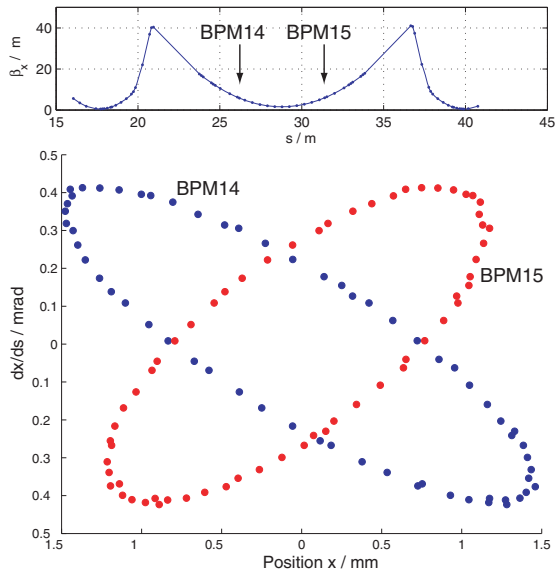

Figure 6: Horizontal beta function from the optics model and measured horizontal phase space at BPM14 and BPM15.

plane and only due to coupling betatron oscillations can be observed in the vertical plane, too (see fig. 5). Plotting the difference of the offsets from the equilibrium orbit divided by the distance between the BPMs versus the offset itself, a phase space ellipse shows up (see fig. 6). A fit to the measured ellipse allows the deduction of the twiss parameters which may serve as a verification for the machine model.

Analyzing beam loss

The experiment in figure 7 was set up to check the post mortem trigger capability of the Liberas. Turn-by-turn data

Figure 7: Setup for analyzing beam loss 'post mortem'. The beam loss trigger is generated from the differential output of a Parametric Current Transformer (PCT) used for beam current measurement.

are stored in a 16.000 turn ring buffer. Whenever a post mortem trigger occurs, writing to the buffer is stopped. The buffered data can then be analyzed in order to check for reasons of beam loss. We have generated the beam loss trigger from the differential output of the Parametric Current Transformer (PCT) used for beam current measurement. Although this signal is delayed it is still fast enough to detect 'instantaneous' beam loss caused for example by a kicker (see fig. 8). Beam loss due to RF trips have, presumably due to their low lossrate, not been identified up to now.

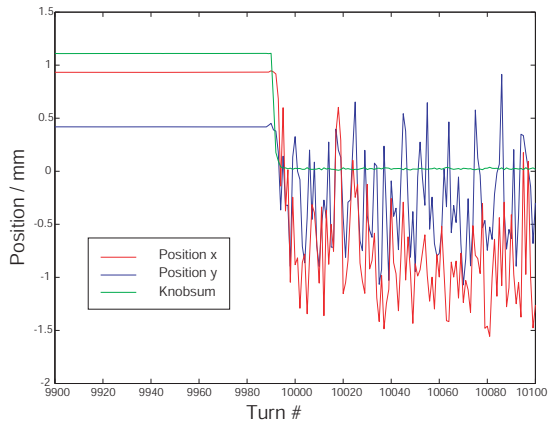

Figure 8: Beamloss within five turns generated by a pulse of one of the injection kickers. These events are extremely rare and can identified and distinguished from RF trips by the analysis of post mortem BPM data.

CONCLUSION

Within the last year we have, after carefully testing the Libera beam position monitor electronics, installed seven devices in the Delta storage ring. A comparison with the available MX-BPMs in the BPM testbed gave the following results: At beam currents above 2 mA the 'slow acquisition' data from Liberas is of roughly the same quality as the data from the MX-BPMs. At lower beam currents Liberas show a slight deviation in measuremets of the vertical component. We have shown in first measurements that TBT orbit data of high quality may serve amongst others as input for machine modelling. The advantage of having this turn-by-turn data justifies under all circumstances the installation of at least a limited number of Libera electronics at suitable positions in the Delta ring.

ACKNOWLEDGEMENTS

We thank the Electronics Lab for developments and the beam diagnostics group of the DIAMOND Light Source for support with hardware and software.

REFERENCES

[1] P. Hartmann et al.,Kicker Based Tune Measurement for DELTA, These proceedings.

[2] http://www.i-tech.si, see also Libera workshop 2006

[3] http://sourceforge.net/projects/libera-epics

RENEWAL OF BPM ELECTRONICS OF SPRING-8 STORAGE RING

S. Sasaki, T. Fujita, M. Shoji, T. Takashima,
JASRI/SPring-8, Kouto1-1-1, Sayo, Hyogo 679-5198, Japan.

Abstract

The signal processing electronics of the SPring-8 Storage Ring beam position monitors (BPM) were replaced during the summer shutdown period of the year 2006. Since then, the new electronics have been put into operation for user experiment runs. The purpose of the renewal was to upgrade the performance of the position measurement system, i.e. the position resolution, the speed of the measurement, etc. The position resolution of them in the real operation condition was estimated by using the stored beam, in the following way. The closed orbit distortions (COD) were repeatedly measured with the interval of four seconds in order to obtain the square mean (SM) and their square root, i.e. root mean square (RMS) of differences between two consecutive measurements. The obtained SM values included the intrinsic resolution of the position measurement system and the effect of the beam motion. The effect of the beam motion was separated from the obtained SM data in order to estimate the intrinsic resolution. For the separation, the influence of the beam motion was assumed to be proportional to the betatron function values at the BPM locations. As a result, the intrinsic resolution was estimated to be better than 0.1 μm.

INTRODUCTION

The signal processing electronics circuits for the beam position monitors (BPM) of the SPring-8 storage ring were renewed during the summer shutdown period of the year 2006. All 24 sets of the circuits covering the whole ring were replaced on this occasion. From September 2006, they were put into operation and included in the periodic orbit correction loop. The purpose of the replacement was to improve the performance of the beam position measurements: faster measurements, better position resolution.

The SPring-8 storage ring works as a third generation synchrotron radiation light source with the horizontal emittance of $3x10^{-9}$ m rad. To extract the highest performance as a light source with such a small emittance, the orbit stabilization is one of the most important issues to be achieved. The BPM are one of the key components to stabilize the beam. The BPM are necessary to monitor the stability of the beam orbit, even if they were not included in the feedback loop to stabilize the beam [1].

The electronics that were used until before the summer of 2006 achieved the resolution in the sub-micron range, however, the measurement speed was rather slow; over 20 seconds were necessary to obtain the COD data of the whole ring. A faster system with better position resolution had been desired.

The performance goal of the new electronics was set to sub-micron position resolution with 1-kHz bandwidth for the 100-mA stored current. The basic performance was confirmed by bench tests using the prototype circuits and the signal generator (SG) for the signal source [2].

For the next step, we evaluated the position resolution of the BPM system with the production version of the electronics using the actual beams. We report on the position resolution evaluated by using the beam in the actual operation condition of the storage ring.

ELECTRONICS CONFIGURATION

The electronics employed a multiplexing method to reduce the effect of characteristics difference of the circuits. The detection frequency was chosen as the same frequency of the radio frequency (RF) acceleration frequency of the storage ring: 508.58 MHz. The signals pass through the band pass filters that select the detection frequency after the selection by the multiplexer. They are fed into the RF amplifiers and mixed down to 250-kHz intermediate frequency (IF) signals.

The IF signals are sampled by 16-bit 2-MSPS ADC with the record length of 2048 for each electrode, which corresponds 1.024 ms duration of the sampling. Because of this time duration for sampling, the basic effective bandwidth is 1 kHz.

The sampled data are sent to DSP board made as a VME module in which the signal amplitudes are calculated from the sampled data. The calculated amplitudes are converted to the beam position data in the DSP and sent to the work stations in the central control system through the network.

One set of the electronics circuits has four signal passes and every pass covers three BPM. Since one BPM is composed of four electrodes, one signal pass switches 12 times to complete one measurement cycle.

Switching twelve times completes the measurement of the COD of the whole ring, because all the 24 sets of the circuits and all four passes in each set of electronics process the signals in parallel,

Typically, it takes 15 ms to complete one measurement cycle inside the DSP; 12 times 1-ms sampling plus some overhead.

Longer time is necessary to make measurements by the workstation in the control system, typically more than 1 s, because of the data transfer through the network, the access time to the database through database management system to store the data, and the processing time of the workstation including the disk I/O and GUI on the display.

EVALUATION OF THE POSITION RESOLUTION

The basic characteristics of the circuits were measured and evaluated by using the prototypes [2]. This time, as

the first and the most important step, we performed the estimation of the position resolution with the actual operation condition of the storage ring.

Method of Estimating the Position Resolution

In actual condition we adopt the averaging the position data in the DSP by 100 times, which took 3-s measurement time composed of 1.5 s in the DSP averaging and the process overhead of about 1.5 s through the network and database access. This averaging makes the effective bandwidth 10 Hz.

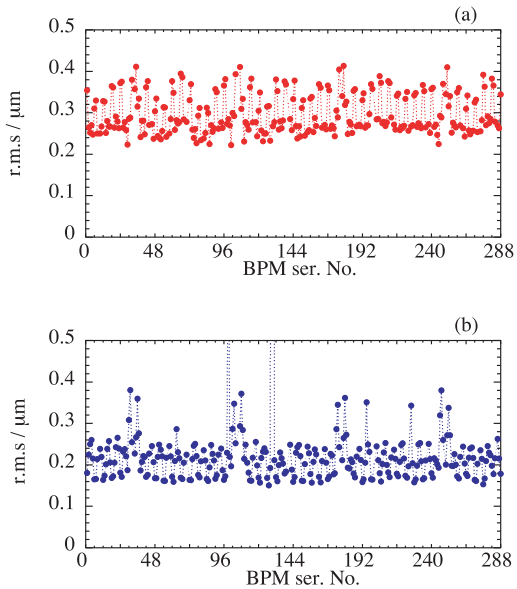

Figure 1: RMS values vs. BPM serial numbers. Lines just connect the points. (a):Horizontal, (b):Vertical direction. In the vertical direction, 2 points are out of the scale; they are 0.8 μm at serial No. 99 and 1.9 μm at serial No. 130.

To estimate the position resolution, the closed orbit distortion (COD) data were measured repeatedly every four seconds.

The differences between two successive measurements were calculated for every BPM, and the square mean(SM) values and their square root, i.e. root mean square (RMS) values of the differences were obtained to estimate the reproducibility of the measurements.

These obtained values included both the resolution of the measurement system and the effect of the beam motion during the two consecutive measurement interval.

In Fig. 1 the obtained RMS values are plotted against the BPM serial number. A distinctive pattern is observed in Fig. 1.

Since the storage ring has four-fold symmetry in its lattice structure, the data were parallel translated by multiples of quadrant of the ring and over plotted. The results are shown in Fig. 2. The points well coincide barring some exception points.

The pattern resembles the betatron function patterns; the square root of the betatron function values are also plotted in Fig. 2.

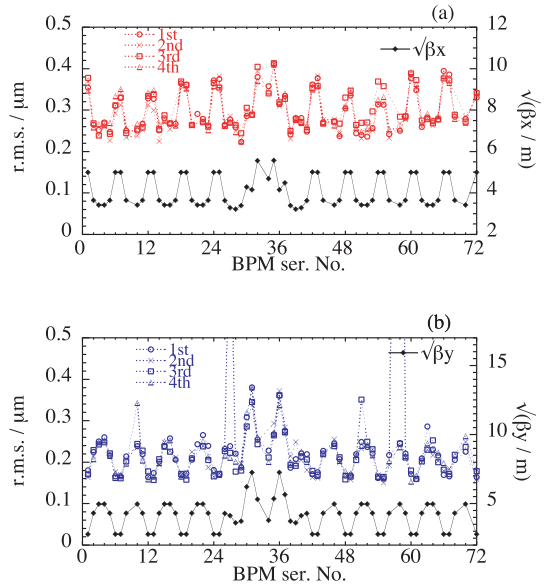

Figure 2: RMS values vs. BPM serial numbers for the left vertical axis. Square root of the betatron function values at the BPM locations are also plotted in black marks and lines for the right vertical axis. The points are translated by multiple of quadrant of the storage ring. (a): Horizontal, (b):Vertical direction. Open circle: first quadrant, cross: second quadrant, square: third quadrant, and triangle: fourth quadrant.

Separation of the Effect of Beam Motion

We considered that the effect of the beam motion in SM values was proportional to the betatron function values at BPM locations. Therefore, a following model can be postulated. In the model, the SM values are composed of the intrinsic resolution of the measurement system and the effect of the beam motion which is proportional to the betatron function; i.e.

$$SM_i = v_0 + A\beta_i \,, \qquad (1)$$

where SM_i is the SM value of the i-th BPM, β_i is the betatron function value at the i-th BPM location, v_0 is the variance of the measurement repeatability of the system, and A is the proportional constant.

We plotted SM as a function of betatron function values in Fig. 3. According to the model, a regression analysis was done with the fitting parameters of A and v_0 for the data in Fig. 3. For the fitting, the data those show exceptionally large SM values were excluded.

The obtained fitting parameters are shown in Table 1.

Taking the square root of the obtained parameter v_0, the intrinsic resolution was evaluated to be 0.13 μm for the horizontal and 0.10 μm for the vertical directions.

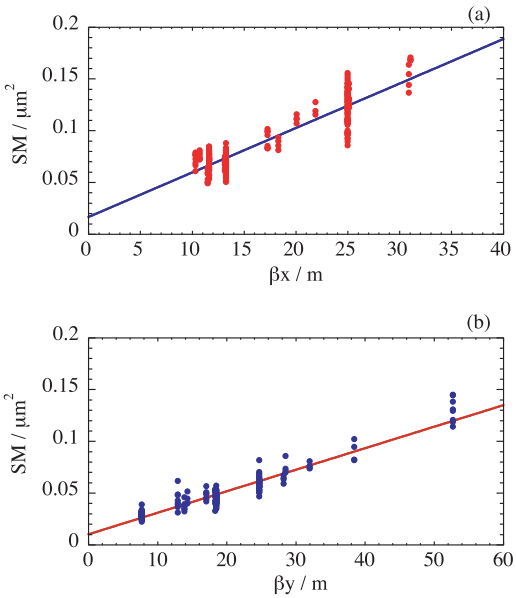

Figure 3: SM values vs. betatron function values at the corresponding BPM locations. The betatron function values are calculated ones with the lattice parameters of the optics for the operation condition. (a):Horizontal, (b):Vertical directions. The lines are the fitted ones with the equation (1). The parameters obtained by the fit are listed in Table 1.

Table 1: The Parameters Obtained by the Fit.

	$v_0(\mu m^2)$	$A(\mu m^2/m)$
horizontal	0.0166±0.0023	0.00430±0.00012
vertical	0.0101±0.0008	0.00208±0.00004

Discussion

The obtained resolution values are worse by three to seven times as the values obtained by the prototype and the SG, which were 0.02 μm for horizontal and 0.03 μm for vertical directions.

The reason for this discrepancy is unclear.

A possible explanation is that the influence of the beam motion was not fully eliminated from the data by this kind of procedure. The resolution values obtained with the actual operation condition of the storage ring beams show that the horizontal resolution is worse than the vertical one by 1.3 times. On the contrary, the data obtained with SG as a signal source show that the vertical resolution is worse than the horizontal one by about 1.5 times. This ratio of 1.5 corresponds to the ratio of the sensitivity coefficients which are determined by the geometrical configuration of the electrodes in the cross sectional shape of the vacuum chamber.

If the resolution is determined by the signal to noise ratio (S/N) of the circuits and the sensitivity coefficients, the ratio of the resolution obtained with the beam should be much closer to the ratio of the sensitivity.

This suggests that the obtained resolution values using the actual beams still include the effect of the beam motion, and the intrinsic resolution determined by the circuit performance itself would be much better than the values estimated by the procedure taken this time.

Further investigation, including the study of the influence of the multiplexing [3], etc., should be done for clarifying the reason of the discrepancy between the bench test data and the actual beam data.

SUMMARY

The electronics for SPring-8 storage ring BPM were renewed during the 2006 summer shutdown and put into operation.

The position resolution of the BPM system was estimated using actual beam, and found to be better than 0.1 μm with the effective bandwidth of 10 Hz.

ACKNOWLEDGMENT

We express our appreciation to the members of operation and beam diagnostics group of SPring-8 accelerator division, Dr. M. Takao and Dr. K. Soutome for their contribution to the process to put the electronics into operation during the tuning period after the 2006 summer shutdown. We appreciate the members of control group of SPring-8 accelerator division, Dr. T. Fukui and Dr. T. Masuda for their contribution to develop the ADC and the DSP board. We also thank to the staff members of accelerator division to help taking the data.

REFERENCES

[1] H. Tanaka, "Stabilization of Stored Beam in the SPring-8 Storage Ring", Proc. of the NANOBEAM 2005, the 36th ICFA Advanced Beam Dynamics Workshop, Uji Campus, Kyoto University, 2005, p-12.

[2] S. Sasaki, T. Fujita, M. Shoji, T. Takashima, “Upgrade of BPM Electronics for the SPring-8 Storage Ring”, Beam Instrumentation Workshop 2006, Batavia, Illinois, U.S.A., 1 - 4 May 2006, p. 463, AIP conference proceedings 868.

[3] Till Straumann, “Dynamic X-Y Crosstalk / Aliasing Errors of Multiplexing BPMs”, Proceedings DIPAC 2003, Mainz, Germany, 5-7 May 2003, p.181.

DESIGN CONSIDERATIONS FOR PHASE SPACE TOMOGRAPHY DIAGNOSTICS AT THE PITZ FACILITY*

G. Asova†, S. Khodyachykh, M. Krasilnikov, F. Stephan, DESY, 15738 Zeuthen, Germany
K. Floettmann, DESY, 22761 Hamburg, Germany
D.J. Holder, B. Muratori, ASTeC, STFC Daresbury Laboratory, Warrington, UK

Abstract

A major goal of the Photo Injector Test Facility at DESY in Zeuthen (PITZ) is to build and to optimise high brightness electron sources for SASE FELs where the detailed knowledge of the phase-space distribution of the electron beam is very important.

The current upgrade of the PITZ facility includes a diagnostic section suitable for transverse phase space tomography and multiscreen emittance measurements. The designed module should be capable of operation over a range of beam momenta between 15 and 40 MV/c. It mainly consists of four observation screens with three FODO cells in between them. An upstream section of a number of quadrupoles is used to match the electron beam Twiss parameters to the tomography section.

The design considerations of the tomography section and results from numerical simulations will be presented in this contribution.

INTRODUCTION

The Photo Injector Test Facility at DESY in Zeuthen (PITZ) will be upgraded to operate with higher beam energies in early 2008. The upgrade also implies extended diagnostics, including a tomography section for detailed analysis of the transverse phase-space density distribution of the electron beam. At a later stage the tomography module will be equipped with an RF deflecting cavity to study the transverse distributions and measure emittance of longitudinal slices for selected electron bunches [1].

The tomography module will consist of three FODO cells and four diagnostic stations for beam size measurements. It has previously been shown that 45° phase advance between the cells delivers the smallest emittance measurement errors using four screens [2]. Since the beam in general does not have the necessary size and slope on the first screen, a matching section is necessary. Both the tomography and the matching sections have been designed in a collaboration between STFC Daresbury Laboratory and DESY. Preceding iterations of the design can be found in [3].

In this paper some major aspects concerning the design of the tomography module are reviewed as follows: The first section justifies the choice of the physical layout; this is followed by general considerations of the matching section and then two different examples of matching are given, confronted with an ideal case where no space charge forces are acting on the beam (zero current). Phase space reconstruction from ASTRA-simulated [4] distributions provides the final results.

DESIGN LAYOUT OF THE TOMOGRAPHY SETUP

The proposed tomography setup is shown schematically in Fig. 1. It consists of a number of matching quadrupoles, which will be discussed later, and the three identical symmetric FODO cells at the end. In a previous design iteration a quadrupole effective length of 0.06 m was assumed but, due to stringent space restrictions, shorter quadrupoles with an effective length of 0.04 m and a physical one of 0.062 m have been chosen now. Geometrically the minimum drift allowed between two adjacent quadupoles is 0.26 m but the drifts between the quadrupoles in the first two cells and the one between the quadrupoles in an identical cell upstream, used for matching, have to accommodate kicker magnets for extraction of a single bunch from the bunch train. From the point of view of motion stability, the quadrupole effective length allows the use of any drift for which $|\cos\mu = \frac{T_{11}+T_{22}}{2}| \leq 1$, where T is the transport matrix from screen to screen and μ is the phase advance, up to a maximum 0.46 m. Thus, a cell length of 0.76 m was chosen. As it can be seen from Fig. 2, for the ideal case of zero current phase advance, the maximum RMS size excursion does not exceed 0.15 mm for a normalised emittance of 0.99 mm·mrad and beam energy of 32 MeV and on a screen the Twiss parameters are $\beta_{x,y} = 0.99$ m, $\alpha_{x,y} = \mp 1.12$.

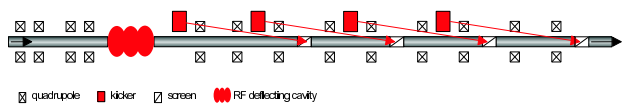

Figure 1: Tomography and matching setup (not to scale). Two more upstream quadrupoles are not shown.

Numerical simulations excluding particles' self-repulsion, for quadrupoles with effective lengths of 0.06 m, show smaller β-mismatch [1] on the screens in

*This work has partially been supported by the European Community, contracts RII3-CT-2004-506008 and 011935 (EUROFEL), and by'Impuls- und Vernetzungsfonds' of the Helmholtz Association, contract VH-FZ-005.

† galina.asova@desy.de

[1] $\Delta\beta[\%] = \frac{\beta_{designed}-\beta_{measured}}{\beta_{designed}} \cdot 100$

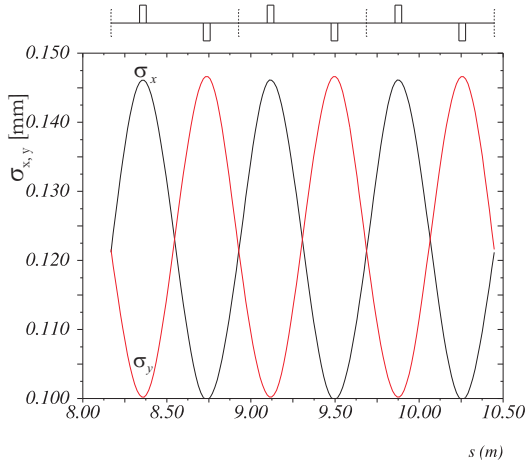

Figure 2: RMS beam size inside the FODO lattice for a beam with zero current. The abscissa coordinates are shifted with respect to the entrance of the matching section so that $s = 0$ corresponds to the beginning of the drift space in front of the first matching quadrupole.

comparison to the case of 0.04 m effective length. The mismatch increases when decreasing the energy which clearly shows that the space charge term dominates over the emittance term in the equations of motion. For beam momentum of 32 MeV/c the space charge term is 10 times the emittance one and decreasing the energy to 15 MeV leads to 50 times bigger space charge term. Thus, the matching procedure should be based on the equations of motion including space charge and emittance terms.

MATCHING OF THE ELECTRON BEAM TO THE TOMOGRAPHY SECTION

Matching of space charge-dominated beams implies minimisation of a 'cost function' which takes into account the beam size X(z), Y(z) and slope X′(z), Y′(z) and generalised perveance[2], including the kinetic energy and the beam peak current as a ratio between the bunch charge and length.

Initially five quadrupoles used for matching were assumed but they are not sufficient with the effective length we are planning to use. There is a possibility to include up to a further four magnets, located in an upstream straight section. Two independent approaches and setups were evaluated in order to obtain a matched beam on the first screen in the presence of self repulsive forces.

Initially ASTRA was used to track the electron beam along the full setup shown in Fig. 1 - seven matching quadrupoles, excluding the self-field repulsion. This would represent the ideal solution to be achieved. Including the space charge afterwards gives an idea of what the beam size mismatch is and where the effects have strongest influence.

[2] $K = \frac{I_{peak}}{I_{Alfven}} \cdot \frac{2}{(\beta\gamma)^3}$

The defined cost function is

$$\Delta^2 = (\delta X'_w - \delta X'_{wo})^2 + (\delta Y'_w - \delta Y'_{wo})^2 + (\sigma_{x,w} - \sigma_{x,wo})^2 + (\sigma_{y,w} - \sigma_{y,wo})^2,$$

where w denotes simulation with space charge included, wo - with space charge forces switched off, and

$$\delta U' = \frac{\sigma_{U,z_{start}} - \sigma_{U,z_{end}}}{z_{end} - z_{start}},$$

with U being either X or Y for both w and wo, z_{start} and z_{end} refer to the beginning and the end of the drifts surrounding the quadrupoles taken into account. The cost function has to be minimised in a number of iterations where the strength of each magnet for zero current is corrected with a predefined value

$$\delta k = \frac{L}{L_{eff}} \cdot \frac{K}{R^2},$$

where L is the overall length the space charge forces are acting on, L_{eff} is the quadrupole effective length, K is the perveance and R is beam radius. δk can be changed in each successive iteration to a value where the value of Δ is smaller. This iterative procedure has to include not less than two quadrupoles at a time. The process is rather time consuming since it requires evaluation of the results but in this way the mismatch was decreased down five times inside the FODO lattice, while without correction no periodic solution was obtained. An example of the results inside the FODO lattice is shown in Fig. 3 The beam was

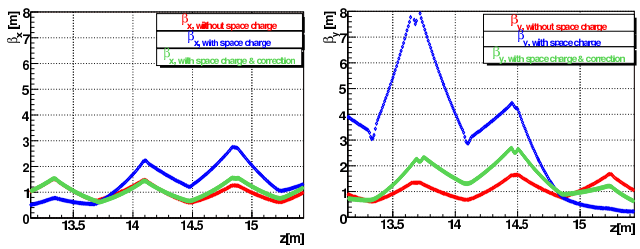

Figure 3: β_x (left) and β_y (right) along the tomography section.

also matched with the help of TRACE-3D [5] for the same layout of quadrupoles. The agreement in the resulting mismatch between the two methods is rather good. In both cases the periodicity in one of the transverse planes is better than in the other.

This can be seen as well using a different matching setup - excluding the first magnet from the previous case and including one more upstream. The result is shown in Fig. 4 - here the periodic solution for one plane was very good, while for the other it was not found. Inverting the polarity swaps the results for the two planes. Since the tomographic reconstruction requires recording (x, y) projections for both planes, the reconstruction error will depend strongly on the mismatch for either of the transverse planes if they are coupled.

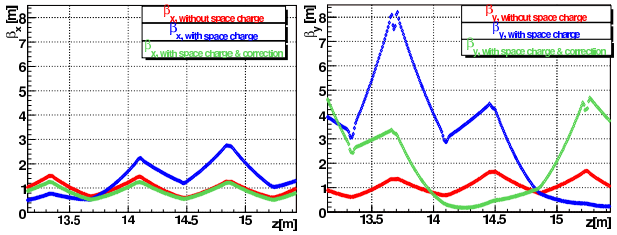

Figure 4: β_x (left) and β_y (right) along the tomography section. Inverting the quadrupoles' gradients along the tomography and matching sections delivers the same periodic solution for β_y.

PHASE SPACE RECONSTRUCTION FROM NUMERICAL DATA

Electron beam distributions have been numerically generated (using ASTRA), matched and tracked along both sections for the two matching setups described here. The four (x, y) on-screen distributions obtained are used as an input for the adopted Maximum ENTropy (MENT) [6] reconstruction algorithm. Results from (x, y) reconstruction onto (y, y') with the first setup, where the beam matching is worse in this same plane (see Fig. 3), are presented in Fig. 5. Fig. 6 shows results from the second setup, again in the plane with stronger mismatch (see Fig. 4).

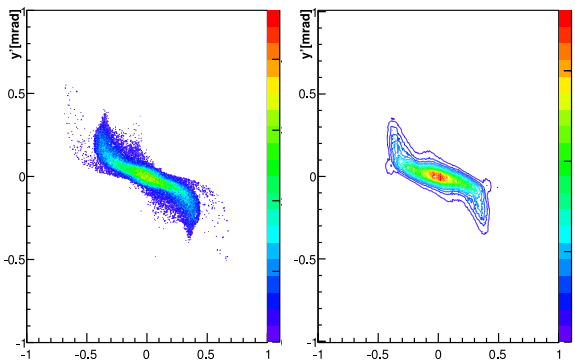

Figure 5: Original (left) and reconstructed (right) phase space in (y, y') plane.

Visually there is a good agreement with respect to the slope of the ellipses, but this is not the case for the size when there is a strong mismatch. The disagreement between the reconstructed and the ASTRA-generated distributions in terms of emittance, RMS size and the covariance are summarised in Table 1.

CONCLUSIONS

The present work reviews some basic considerations concerning a tomography diagnostics setup at the PITZ facility, particularly with regard to space charge effects. It has been shown that a space charge-dominated beam can be successfully matched (if done separately in both planes) but work still has to be done in order to easily obtain this result in both planes simultaneously. Reconstruction results for two different matching cases have been presented with good agreement in terms of phase space RMS radius, slope and covariance between the simulated and reconstructed distributions when the beam size mismatch is minimised.

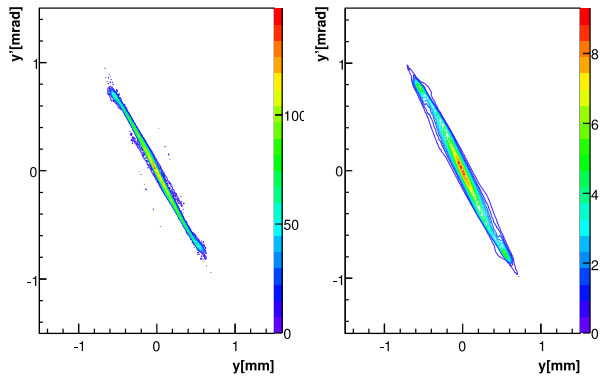

Figure 6: Original (left) and reconstructed (right) phase space in (y, y') plane.

Table 1: Disagreement between the ASTRA-simulated and the reconstructed result (matching case 1, 2 referred to with subscripts).

	Original	**Reconstructed**	**Disagreement [%]**
$\sigma_{y,1}$	0.26	0.24	7.7
$\sigma_{yy',1}$	-0.03	-0.03	-
$\varepsilon_{y,N,1}$	1.21	1.18	2.6
$\sigma_{y,2}$	0.3	0.3	-
$\sigma_{yy',2}$	-0.12	-0.13	8.3
$\varepsilon_{y,N,2}$	1.24	1.48	19

REFERENCES

[1] S. Korepanov at al., "RF Deflector for the Longitudinal and Transverse Beam Phase Space Analysis at PITZ", these proceedings

[2] G. Asova et al., "Phase space tomography diagnostics at the PITZ facility", proceedings of ICAP 2006, Chamonix, France

[3] D.J. Holder et al., "A phase space tomography diagnostic for PITZ", proceedings of EPAC 2006, Edinburgh, UK.

[4] ASTRA: A Space Charge Tracking Algorithm, http://www.desy.de/˜mpyflo/.

[5] PBO Lab 2.0, Gillespie Associates, Inc., 2001

[6] J.J. Scheins, "Tomographic Reconstruction of Tranverse and Longitudinal Phase Space Distribution using Maximum Entropy Algorithm", TESLA Report 2004-08

FIRST RESULTS FROM THE LEIR IONISATION PROFILE MONITORS

C. Bal, V. Prieto, R. Sautier, G. Tranquille, CERN, Geneva, Switzerland

Abstract

The role of the Low Energy Ion Ring, LEIR, is to transform long pulses of lead ions from the Linac 3 to short dense bunches for transfer to the LHC. This is accomplished by the accumulation of up to 4 Linac pulses by electron cooling. In order to non-destructively monitor the cooling performance and determine the accumulated beam characteristics, two prototype ionisation profile monitors have been built and were tested during the LEIR commissioning runs with O^{4+} and Pb^{54+} ions in 2006.

In this paper we present the results obtained with the prototype monitors, the problems encountered and describe the modifications made for the final design. The modified monitors have been installed on the LEIR machine and are waiting for the next ion run planned in August.

INTRODUCTION

The LHC program foresees lead-lead collisions in the spring of 2008 with luminosity up to 10^{27} $cm^{-2}s^{-1}$. The Low Energy Ion Ring (LEIR) has undergone a major upgrade [1] in order to prepare these dense bunches of lead ions by the transformation of ion beam pulses from the Linac 3 into short high-brightness bunches using multi-turn injection, cooling and accumulation.

Electron cooling [2] plays an essential role in producing the required beam brightness by rapidly cooling down the newly injected beam and then dragging it to the stack. The cooling performance can be measured by various diagnostics such as Schottky scans or scrapers [3] [4]. For the non-destructive measurement of the circulating beam emittance, ionisation profile monitors (IPM) are widely used. In such devices an electrostatic field accelerates the ionisation products from the beam-residual gas interaction towards a micro-channel plate (MCP). Either the electrons or the ions can be used for beam profile detection and when these particles reach the MCP, secondary electrons are produced, amplified and accelerated on to a readout device.

A major challenge for the new devices was their integration into the LEIR ultra high vacuum environment, requiring a bakeout of the apparatus at 300ºC, and where the choice of materials is critical in order to ensure that the average vacuum level in the ring (2×10^{-12} torr) is not perturbed by the operation of the monitors. Another constraint was the physical space allocated to the monitors, forcing us to make compromises with respect to the detector dimensions and also to pay careful attention to the readout.

DETECTOR DESIGN

The detectors (see Fig. 1) are essentially of the same design for the horizontal and the vertical profile measurements, differing only in their physical dimensions and the resolution of the readout. The two electrodes creating the electric field are made of 316LN stainless steel and are separated from each other by two 1 cm thick aluminium oxide (AL_2O_3) blocks. The top electrode has a rectangular area corresponding to the size (80 mm x 30 mm) of the MCP cut away in its centre.

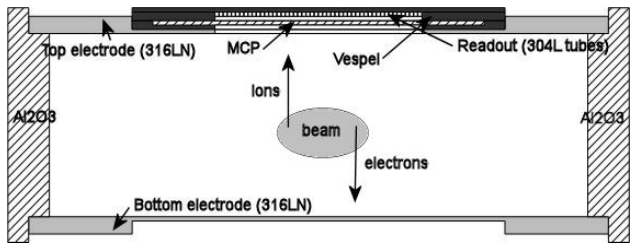

Figure 1: Drawing of the horizontal IPM.

The MCP is supported in a Vespel sandwich on top of which is placed the signal readout. The readout (see Fig. 2) consists of up to 80 AISI 304 stainless steel tubes of 0.8 mm diameter placed on a grooved Vespel plate. The total thickness of the MCP support and the readout is 4 mm. A thin kapton wire is pinched to the end of each tube and carries the charge deposited on the readout to UHV flange mounted sub-D connectors. The air-side connection to the readout electronics is made by a flat ribbon cable. In the horizontal plane, due to a limitation on the number of sub-D connectors that could be mounted on the vacuum flange, we were only able to use 50 tubes which were spaced by 1.5 mm. This ensured that the profile of the newly injected ion beam could be measured. The vertical measurement has 80 readout channels with a spacing of 1 mm. The charges collected by each readout channel are integrated by means of R-C electronics.

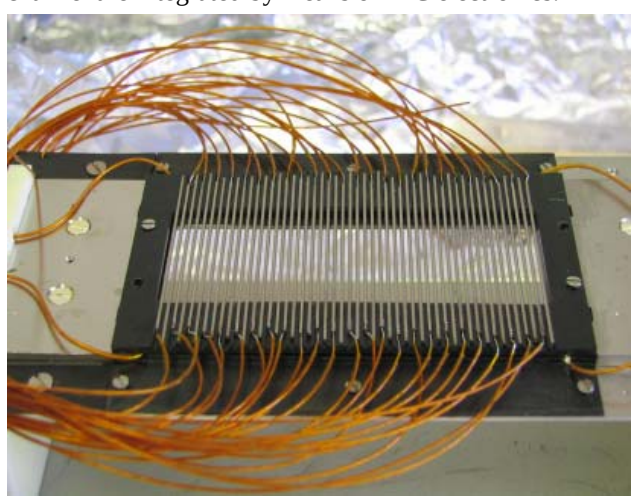

Figure 2: The horizontal readout.

CONTROL AND DATA ACQUISITION

The control and data acquisition of the IPMs is handled by the ADwinPro system. The ADwin hardware consists

of a dedicated real-time processor, fast analogue and digital inputs and outputs and an ethernet link to the local area network. Low priority tasks perform the control of the 8 high voltage power supplies needed to polarise the electrodes and the MCPs. An externally triggered high priority application takes care of acquiring the 130 data channels with the necessary time resolution. Typically, horizontal and vertical profiles are acquired every 20 ms. An example of an acquisition cycle is shown in figure 3.

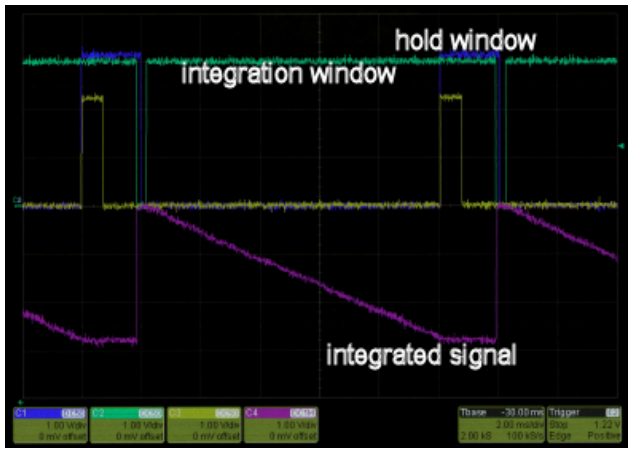

Figure 3: Acquisition cycle for the RC integrators.

The R-C integrator chips are controlled by two Agilent 33220A waveform generators providing the integration and hold windows. When the signal for the integration window (green trace) is high, the circuit starts the integration of all the channels. After the desired integration time has elapsed, a hold window (blue trace) is generated and the analogue to digital conversion of the signals is made via 14 bit ADC modules of the ADwin system. The total time needed to acquire all 130 channels of the horizontal and vertical monitors is 770 µs.

Figure 4: IPM acquisition application.

The acquired data is stored in the local memory of the ADwin system and can be transferred to any data analysis program on any computer on the local area network. In our case we used an application written in TestPoint running on a windows based PC. TestPoint is a tool for creating custom test, measurement, and data acquisition applications and includes features for controlling external hardware, creating user interfaces, processing and displaying data, creating report files, and exchanging information with other Windows programs. The interface panel for the TestPoint IPM application is shown in figure 4. The application provides the means to visualise the individual profiles and to store all the data to file for post analysis.

A more detailed analysis of the cooled beam profiles can be made using a dedicated data analysis package called FlexPro (see Fig. 5). Using this package we can display the data in a variety of ways enabling us to extract all the necessary information concerning the cooling/stacking process and the characteristics of the ion beam before its transfer to the next accelerator in the LHC ion injector chain.

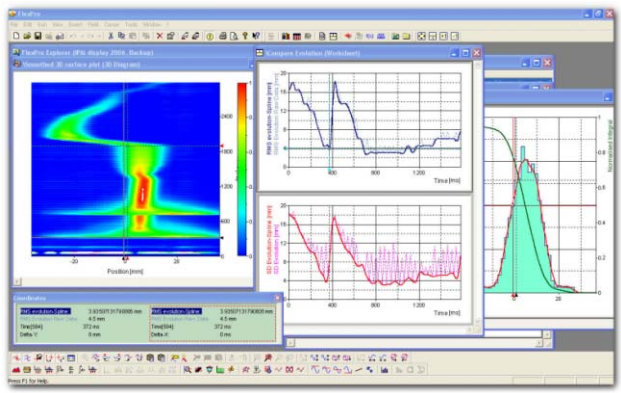

Figure 5: FlexPro data analysis interface.

RESULTS

Test with O^{4+} Ions

The first tests of the IPMs were made at the end of 2005 during the LEIR commissioning run with oxygen ions. Clear signals from the rest gas ionisation were seen but an error in the cabling of the readout made the reconstruction of the beam profile laborious. By the time this cabling error had been resolved, we started to experience high voltage problems in the vicinity of the MCP and readout. As a consequence many of the integrator inputs were damaged and we were obliged to modify the readout electronics boards with a diode protection for each input channel.

Profile measurements with Pb^{54+} Ions

Before the start of the lead ion run it was decided to open the vacuum sector where the IPMs are installed in order to try to understand the origins of the high voltage problems. Investigation of the vertical monitor showed traces of direct beam impact on the readout and the kapton wires and some damage of the MCP was observed on the horizontal monitor. Out of precaution, this MCP was exchanged and gold plated collimators were welded onto the vacuum chamber at the entrance to the vertical IPM in order to protect the monitor against any impact from the ion beam.

Unfortunately the situation did not improve during this run and we still experienced numerous high voltage breakdowns. It became clear that the plate resistance

between the faces was slowly deteriorating because of these ongoing HT problems. This obliged us to decrease the voltage across the MCP, thus lowering the gain of the system. When the monitors were removed from the machine in December 2006 for modifications, the two MCPs were found to be damaged at many points.

Despite these problems we were still able to make many beam profile measurements which confirmed the excellent performance of the electron cooler. The evolution of the beam size (see Fig. 6) as seen by the IPMs gave invaluable information for the setting up and optimisation of the accumulation process. Detailed studies of the electron cooler (cooling times & lifetimes, equilibrium emittances etc.) were also possible with the individual profile acquisition time as short as 10 ms when the highest MCP gain was used.

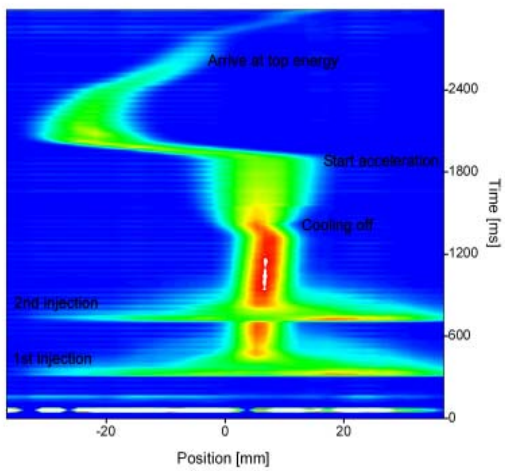

Figure 6: Evolution of the horizontal ion beam size during the whole LEIR cycle.

CONCLUSION AND OUTLOOK

The ionisation profile monitor has proved to be an invaluable tool for the commissioning of the low energy ion accumulator ring at CERN. Despite a problem with the high voltage insulation between the readout channels and the MCP, we were still able to make fast (<<20ms) acquisitions of the beam profiles needed for the fine tuning of the cooling/accumulation process. This was mainly due to the excellent signal level coming from the rest gas ionisation by the lead ions and collected on the readout.

From the experience gained with the prototype monitors we have made a number of modifications to the design in order to overcome the high voltage problems that we encountered during the LEIR commissioning. The main modifications are:

- The use of a softer grade Vespel such that degassing grooves can be etched onto the plates that hold the MCP and the readout. This should help to avoid a build up of molecules in the volume around the MCP which can lead to high voltage breakdown.
- The high voltage on the MCP faces is better distributed by using a thin beryllium-copper frame around the whole MCP (see Fig. 7). On the prototypes, the HT contact was made only along one edge.
- Separation of the HT and readout wires. The four HT wires are grouped together and pass below the electrode opposite to the readout. The connections to the top electrode and MCP are made as far away from the readout as possible (see Fig. 7).
- The ADwin control and acquisition system has been connected to the computer technical network and the software modified for remote operations from the CCC.

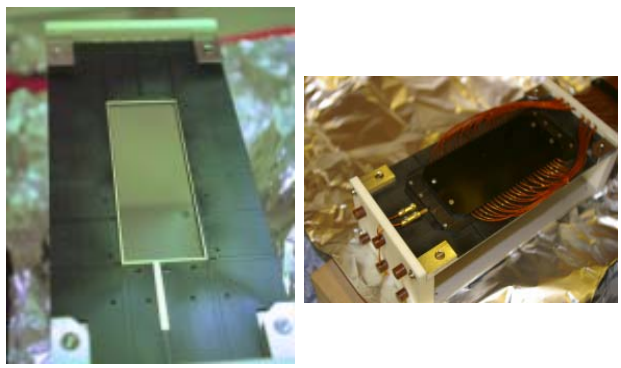

Figure 7: New Vespel plate design (left) with degassing grooves. The beryllium-copper frame used to evenly distribute the high voltage on the MCP face is also visible. On the right, the MCP high voltage connections

The new monitors were designed and built in the second half of 2006 and have been installed in the LEIR ring during the annual shutdown. Prior to the installation of the vertical monitor, a bakeout was made of this detector in its vacuum tank in the laboratory to check the quality of the vacuum when the MCP is polarised. The test showed that the vacuum quality is not at all affected by this monitor and no high voltage breakdowns were experienced, even with the MCP running at its maximum gain i.e. a voltage difference of 1.6 kV across the faces.

The commissioning of the definite detectors will take place during the next ion run planned to start in August this year.

REFERENCES

[1] P. Belochitskii et al., “LEIR Commissioning”, EPAC’06, Edinburgh, June 2006, p. 1876.
[2] A. Bubley, V. Parkhomchuk, V. Prieto, R. Sautier and G. Tranquille, “LEIR Electron Cooler Status”, EPAC’06, Edinburgh, June 2006, p. 1651.
[3] C. Bal et al., “LEIR Beam Instrumentation”, DIPAC’05, Lyon, June 2005, p. 258.
[4] J. Tan and G. Tranquille, “Beam Diagnostics with Schottky Noise in LEIR”, EPAC’06, Edinburgh, June 2006, p. 1214.

BEAM PROFILE MEASUREMENT WITH OPTICAL FIBER SENSORS AT FLASH

W. Goettmann [2], M. Körfer [1], F. Wulf [2]
[1] Deutsches Elektronen Synchrotron DESY, Hamburg, Germany
[2] Hahn-Meitner-Institut Berlin, Germany

Abstract

The system is intended to determine the beam profile at the DESY-FLASH undulator section as well as measuring beam losses with high spatial resolution. The measurement setup is based on wire scanners, optical fibers which are symmetrically mounted around the beam line over the full length (30 m) of the undulator section, a signal conditioning unit and a data acquisition system. The optical fibers are used as beam loss sensors, and depending on the software configuration, the setup is working either as a beam loss position monitor [1] or as a beam profile measuring system.

INTRODUCTION

Modern linear accelerators for Free Electron Laser operation (FEL) require highly sophisticated techniques to monitor the beam profile, beam tails or HALO and beam losses.

This paper describes a system developed for the free electron laser facility FLASH at DESY, Hamburg (Germany) [2]. The permanent magnets of the undulators are radiation sensitive components and must be protected. Continuous control of the radiation exposure at the undulators not only protects the permanent magnets from degradation but also verifies the efficiency of the collimators in front of the undulator section. During accelerator commissioning as well as routine operation the real time response of the beam loss monitor system enable the operators to a direct adjustment of machine parameters. Complementing the established beam diagnostic systems, the time resolved measurement provides information about the spatial distribution of particle losses.

Beam profile measurement can be achieved by using the existing beam loss position measurement system (BLPM), upgraded with hardware modules to enregister the current wire scanner position and using extended software.

CHERENKOV RADIATION

Cherenkov light is generated when the speed of a charged particle exceeds that of light in a dielectric medium through which it passes [3-4]. The threshold velocity v_{thr} for the generation of Cherenkov light is a function of the refractive index n of the medium given by $v_{thr}=c/n(\lambda)$ depending on the wavelength λ. For a refractive index of 1.5 the threshold of the kinetic energy for an electron to cause Cherenkov light is 175 keV. The light is emitted in a cone in forward direction with an opening angle depending on the energy of the particle. The number of photons that are emitted per unit wavelength and per unit length is proportional to $1/\lambda^2$. The light is emitted predominantly in the ultra violet region. The Cherenkov light is produced instantaneously while the particle passes through the medium in contrast to other luminescence effects where characteristic time constants increase the response time.

Cherenkov light inside the optical fiber as a result of beam losses e.g. caused by wire scanner operation, allows the measurement of the spatial distribution of the scattered beam and furthermore the determination of beam profile.

OPTICAL FIBERS

The detection system needs a radiation resistant optical fiber extending the working periods without relevant changes of fiber properties. The most radiation resistant commercial fibers for visible light and light of shorter wavelength are multi-mode step-index fibers with pure silica core of high OH-content. To increase the signal to noise ratio the fiber was shielded by black Nylon buffer against ambient light, which results in a total fiber diameter of about 800 μm. The light output of the sensor fiber increase linear with the diameter, but a larger diameter reduces the bandwidth and limits thus the local resolution. The spectrum of the output light depends strongly on the spectral attenuation of the fiber. According with theoretical predictions the maximum intensity was measured in the wavelength range around 550 nm, after travelling through a fiber length of 35 m.

EXPERIMENTAL SETUP

The optical fibers are installed in the undulator section of FLASH. This part of the accelerator consists of a 30 m long undulator, comprising six single permanent magnet segments. These units are separated by a wire scanner system combined with a quadrupole doublet and vacuum pumps. As yet, the wire scanners [5] are used for measuring the transversal beam profile, in conjunction with standard scintillation sensors.

The new beam profile measurement system consists of the following components: 4 optical fiber sensors, each of them with a length of 40 m, which are installed in equidistant radial arrangement along the FLASH undulator section in narrow slots very close to the beam line. The optical fibers are both, sensor as well as guiding medium to lead the generated Cherenkov light pulses to the photomultiplier tubes (PMT). The analog output signals of

the PMT are conditioned and amplified using a Signal Conditioning Unit (SCU) which is installed near the undulator section in the tunnel. The SCU is connected via a RF-cable to the data control and monitoring unit outside the tunnel (fig. 1).

To accomplish beam profile measurement it is necessary to obtain precise information about the wire scanner position, while passing the beam. This is realized by counting the pulses which are steering the WS stepper motor, preconditioned that the WS start position is well defined; further information see [5].

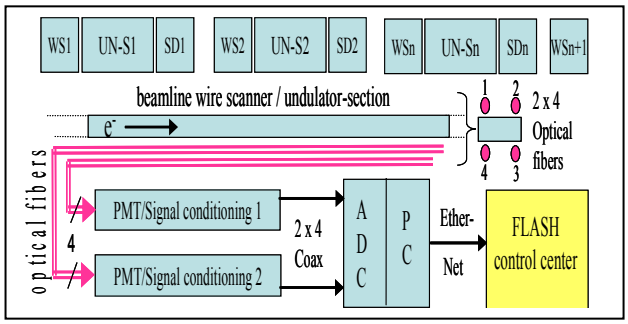

Figure 1: Schematic outline of the beam profile / beam loss position monitoring system. In the upper position are shown the undulator segments (UN-S1), the wire scanners (WS1) and the scintillation detectors.

The implemented photomultipliers (PMT) are tested, to obtain the gain characteristic of each device. Thus enables to set the gain control voltage of each individual PMT in the way that the PMT output signals are directly comparable. Remote PMT gain control is done by means of Ethernet controlled DACs, which are installed inside the signal conditioning units. Dedicated software was developed to use this measurement system either in BLPM mode or in beam profile measurement mode. The software written in LabVIEW enables the monitoring of the current beam losses, shown in the left section of the control panel (fig. 2). At the right side the beam profile is displayed. All relevant parameters, e.g. scan size, number of samples, used wire scanner, PMT gain, are tuneable on the fly.

BEAM PROFILE MEASUREMENT

Two measurement systems, each with four fibers sensors are synchronously used; one is working with high PMT gain and the other system with predefined lower gain. The high gain set up is used to measure the beam tail or beam HALO. To protect the PMTs against very high levels of input signal (Cherenkov radiation), the PMT gain is reduced to prefixed values if the incoming light exceeds a specified level. The second system is working with an appropriate lower PMT sensitivity, to show the results in a continuous graph (fig. 3,4).

Figure 2: LabVIEW control panel of the beam profile measurement system.

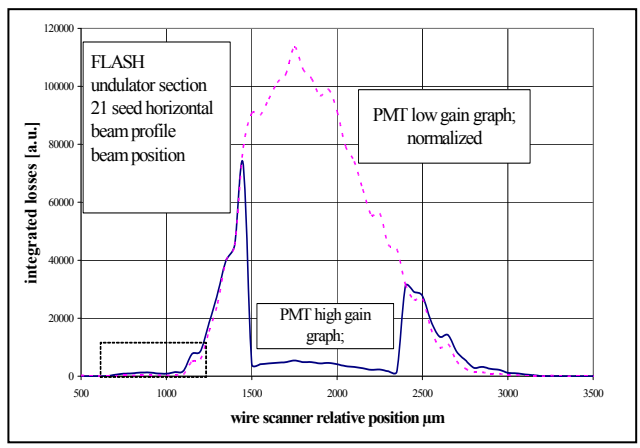

Figure 3: Beam profile measured with two independent measurement systems, with different gain, showing the beam position and beam size.

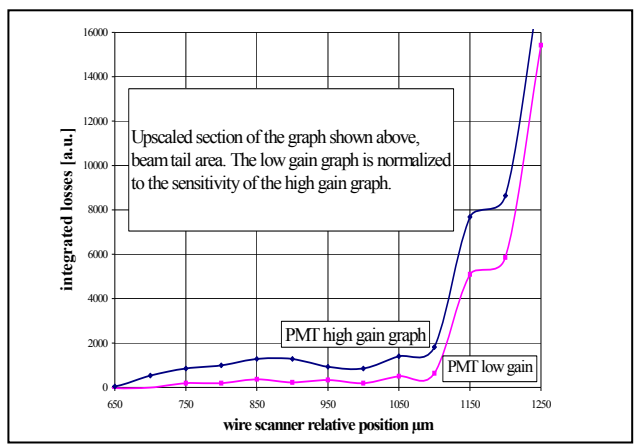

Figure 4: Expanded section of a beam tail in figure 3. The beam profile was generated with the wire scanner 21 Seed horizontal.

A measuring cycle starts, when the used wire scanner reaches a predefined position. The measuring interval (e.g. 100 µm) is defined by a prefixed number of micro steps of the wire scanner. At each interval increment, the generated Cherenkov light in the fiber sensors - which is proportional to the intensity of bremsstrahlung - is measured. As an improvement, the loss shower is not only measured at a singular location but over the entire length of the undulator section. Accomplishing an x-y-scan leads to a two dimensional profile of the beam. The synchronisation with the beam trigger allows the characterization of each bunch. The data are visualized in real time and stored in a log file for extended evaluation. The high sensitivity of the system allows an accurate monitoring of the beam profile as well as beam tails or HALO measurement.

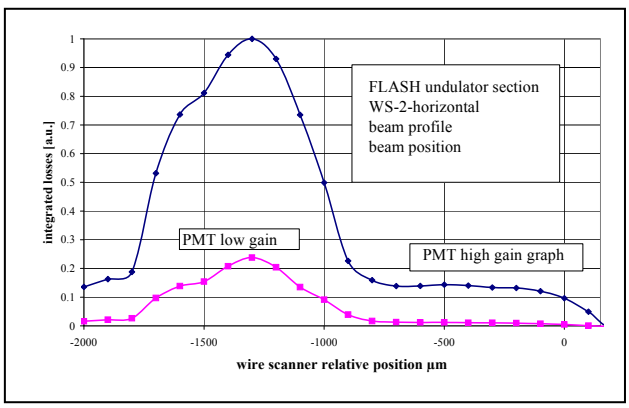

Figure 5: Beam profile measurement with very low light intensities, thus the high gain section is not shutting down the sensitivity. On the right side an extended beam tail profile was obtained.

At FLASH, the standard wire scanner is positioned upstream of the szintillation target. The distance between scanner and scintillation target is about 4.75 m. Due to geometrical constraints the scintillators are partially shielded by the undulator block. This decreases their geometric acceptance angle.

The existing BLPM system with optical fibers allows as well the reconstruction of the transverse beam profile. The loss traces generated at successive wire positions are measured and recorded. In detail :

Time of flight in the beam line, light travel time in the optical fibers and the undulator length of 30 m results in a measuring time (data aquisition time) of about 240 ns. Reaching a prefixed position of the wire scanner and started by the system trigger, with adequate post/pre-trigger timing, all PMT output signals are digitized , with a sample rate of 1 ns. The result is a group of four data files, representing the loss signals in each optical fiber. Integrating the values of each file in the group and summing up these data, provides one data point of the beam profile graph, with respect to one distinct wire scanner position. This happens synchronuously for the high gain PMT system and the low gain system, and continues until the wire scanner leaves the predifined measuring area.

The result represents the radiation response (bremsstrahlung) for a predefined number of successive wire scanner positions and allows a more precise determination of beam profiles, especially of the weak signals generated by the tail of the beam. The reconstructed transverse beam profile generated with the BLPM system is shown in figure 3 and 5. The results are in good agreement with the measured beam profiles of the standard measurement system used in the undulators.

CONCLUSION

A real time monitor system measuring the spatial distribution of electron losses at FLASH undulators was presented. This system was used as a beam loss position monitor system [1] and in addition as a beam profile measurement system. The system has been operated successfully during the FLASH commissioning and routine operation runs. The advantages of the presented beam profile measurement with fiber sensors are as follows:

- accurate monitoring of the beam profile as well as beam tails or HALO
- Obtaining of beam losses over the entire length of the undulators
- Real time verification of mismatch active components e.g. RF, collimators, magnets

REFERENCES

[1] Goettmann W. ; Wulf F. ; Körfer M. ; Kuhnhenn J.: Beam Loss Position Monitor using Cerenkov radiation in optical fibers. 7th DIPAC 2005 : Lyon, France, 6 - 8 June, 2005. , 2005, p. 295-297.

[2] http://flash.desy.de/ .

[3] G. Anzivino et al, Quartz fibre calorimetry – Monte Carlo simulation, Nucl. Inst. Meth. A357 (1995) 380-385.

[4] B.L.Pruett et al, Gamma-Ray to Cerenkov-Light Conversion Efficiency for Pure-Silica-Core Optical Fibers, SPIE Proceedings 506 (1984) 10-16.

[5] N. von Bargen et al, TESLA Report 2002-08 Prototype of a wire scanner for TTF II.

CHARACTERISATION OF THE SYSTEMATIC EFFECTS OF THE INSERTION DEVICES WITH PHOTON BEAM POSITION MONITORS

E. van Garderen, J. Krempaský , M. Böge, J. Chrin , V. Schlott, T. Schmidt, A. Streun
Paul Scherrer Institut, Switzerland

Abstract

The X-ray photo-emission monitors at the Swiss Light Source (SLS) are used for beam-position diagnostics and beam stabilization down to the sub-micron level. The main systematic change of the photon beam-position is induced by varying insertion device (ID) settings, such as photon energy, harmonic-selection or light polarization. An ID beam-position correction scheme is based on digital beam-position monitors (DBPM) located inside the storage ring, combined with analogue Bergoz BPMs, located inside the ID straight section, and analogue photon monitors (XBPMs), in beam line front-ends. The use of XBPMs in this correction scheme will be demonstrated. Moreover, in order to achieve sub-micron photon-beam stability while changing the ID parameters with XBPM-readouts requires precise XBPM alignment and characterization for each ID-setting [1-2]. We present an account of the design and performance of the XBPMs as used for characterizing systematic effects of the **U19**, and the more challenging elliptical undulator **UE44** [3], a newly designed fixed-gap APPLE II undulator recently installed at the advanced resonant spectroscopy beam line [4].

INTRODUCTION

The Swiss Light Source is a third-generation synchrotron radiation facility, which is in operation since mid-2001. The undulators at the SLS are working in the soft x-ray regime. By varying ID-settings such as energy and polarization of light, the angular power distribution of the synchrotron radiation changes. A blade monitor must be designed in order to provide optimal position response to different ID-settings [5]. We describe this briefly in the next section whereby the effects of light polarization of the **UE44** and a gap change of **U19** will be demonstrated.

The XBPM position response, given by simple signal asymmetry detection in the horizontal and vertical plane, is made by means of low-current asymmetry detectors. A graphical user interface in Fig. 1 illustrates the blade readouts *B1, B2, B3* and *B4* for a gap of 6 mm for **U19**. The horizontal and vertical positions are seen to be well aligned with the nominal beam axis. However, differences in the absolute value of the readouts (about 12%) introduce errors in the exact determination of the beam position. These errors, determined by differences in blade resistance, impose limitations on the readout accuracy based on simple asymmetry calculation (e.g. *(B1+B2-B3-B4)/(B1+B2+B3+B4)* for horizontal asymmetry). For this reason the XBPM asymmetry readouts need to be calibrated. A calibration based on machine bumps is proposed below, whereby the systematic effect due to the changing in the light polarization of the **UE44** will be demonstrated.

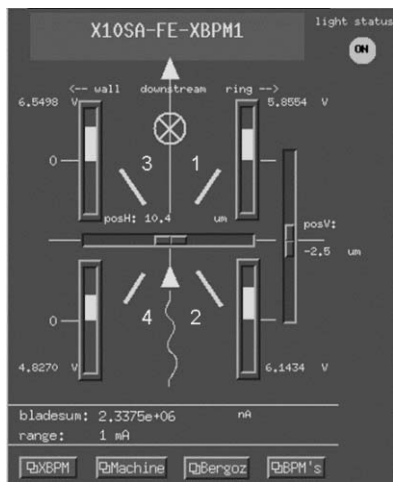

Figure 1: XBPM centered at the nominal beam axis of the U19 undulator (gap 6 mm). The horizontal (*posH*=10.4 μm) and vertical XBPM position (*posV*=-2.5 μm) are calculated from signal asymmetries. The signal level (V) of each blade is displayed with vertical bars.

XBPM DESIGN FOR UE44

The total power distribution (TPD) of **UE44**, weighted by a detector response function of XBPM tungsten blades, is shown in Fig. 2 for linear vertical and circular polarizations [6]. A horizontal magnetic field in the electron beam induces wiggled motion in the vertical direction, which is responsible for the vertically elongated TPD. Applying the peak fields of 0.64 T in *x* and *y* direction the helical motion of the electron beam causes a “donut” shaped power

distribution, as shown in Fig. 2. The determination of the theoretical TPDs is important for the XBPM blade design.

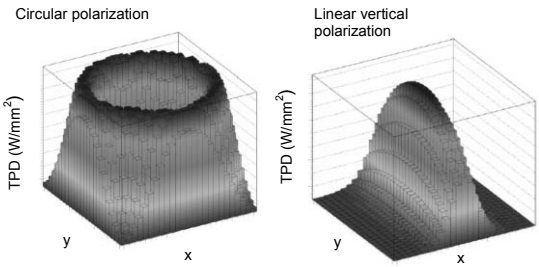

Figure 2: (color) TPD of the **UE44** for circular polarizations (maximum 1E-9 W/mm^2) and linear vertical (maximum 0.25E-8 W/mm^2) [6]. The *x* and *y* scales are ±6 mm. To reflect these TPDs, the horizontal (vertical) gap between the XBPM blades has been set to 5.2 (5.0) mm, respectively.

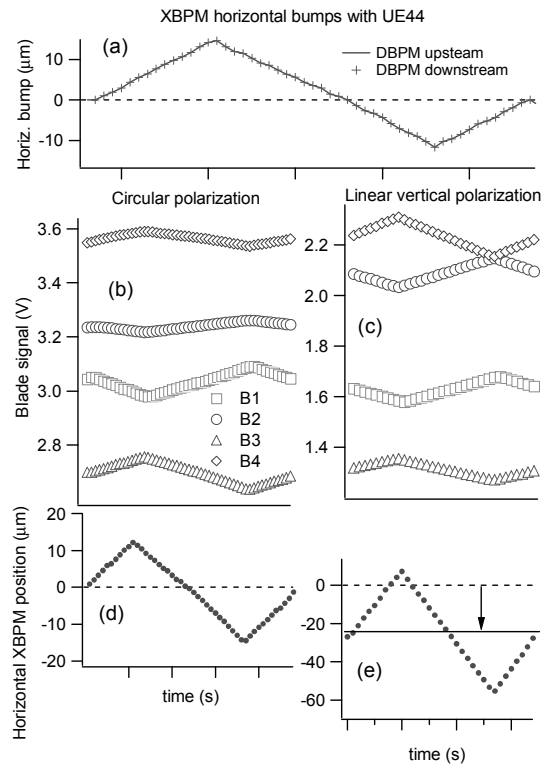

Figure 3: (color inline) XBPM response to symmetrical horizontal machine bump (a) and switching the **UE44** from circular (b,d) to planar (c,e) mode. (time scale: 50 s).The shift in the horizontal photon beam excursion between the two modes is denoted by the arrow (e). The spatial assignments of XBPM blades *B1, B2, B3, B4* is shown in Fig. 1.

XBPM CALIBRATION WITH MACHINE BUMPS

The most direct XBPM calibration is made by means of machine bumps, which are routinely performed at SLS during fast-orbit feedback (FOFB) [7] machine operation. The XBPM response to symmetrical horizontal machine bump displacements (±15 µm) with FOFB is shown in Fig. 3. A time-dependency of a symmetrical horizontal bump, controlled with upsteam and downstream DBPMs of the **UE44** straight section, is shown in Fig. 3a. Since the XBPM has been aligned in circular mode, the beam nominal axis for this polarization is set to zero (Fig. 3d). In planar mode, the signal asymmetries change when compared to the circular mode. The response of the blade *B2* is an upward shift, while the other blades retain their signal level with respect to Fig. 3b. According to the blade layout in Fig. 1, this signal asymmetry change indicates a downwards-right shift in the photon beam. In the horizontal plane, this shift is well observed: the beam position is now centered 25 µm away with respect to the circular mode. The downward photon beam shift is reflected by enhanced peak-to-peak response of the blade *B4*, which is also observed on vertical symmetric and/or asymmetric bumps (not shown). The factor 2 better sensitivity in vertical mode shown in Fig. 3e is given by the TPD 2σ ratio between linear and circular mode [6].

The different signal levels relate to differences in the Ohmic resistance of the blades and could in principle be removed by introducing calibration factors (gains) for each individual blade. However, the ~25 µm shift in the horizontal photon beam centre, indicated in Fig. 3e, reflects a *systematic* shift in the horizontal beam position upon ID light polarization change. In the following, we show the influence of **U19** undulator on the photon beam.

XBPM IN INSERTION DEVICE FEED FORWARD CORRECTION SCHEME

Correction of insertion device (ID) induced orbit distortions at the SLS are performed by means of feed forward schemes (IDFF) [8] down to the micron level. The remaining orbit fluctuations are suppressed by XBPM feedbacks which are an integral part of the fast orbit feedback system (FOFB) [9]. Although the correction feedback is based on the *relative* variation of the photon-beam position, the best XBPM readout sensitivity is observed while the monitor is placed on the nominal photon-beam axis. Since all undulator XBPMs have motorized stages, it is possible to adjust their horizontal and vertical positions on-line during machine operation in order to restore the horizontal and/or vertical asymmetries for a given ID-setting. As an example, Fig. 4a shows the **U19** XBPM aligned to

the nominal photon beam axis at gap 8.5 mm. Upon a gap change, and without IDFF, a horizontal beam position excursion of the order of ~150 μm is evident. An active IDFF removes this beam position excursion. It must be emphasized, that in order to obtain an IDFF performance with XBPM as shown in Fig. 4a, the XBPM must be: (i) well aligned to the undulator nominal axis; (ii) calibrated with horizontal (vertical) machine bumps for each gap. The calibration constants are derived separately for horizontal and vertical components (Fig. 4b).

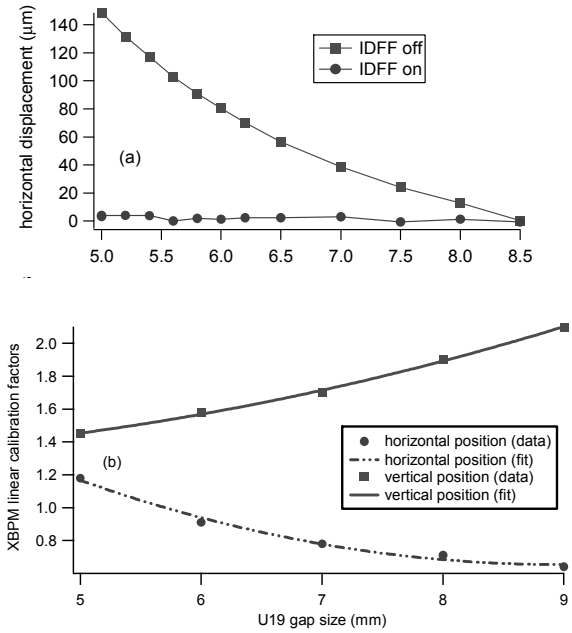

Figure 4: (color inline) (a) Systematic horizontal excursion of the **U19** undulator photon beam position upon gap change. The horizontal excursion of ~150 μm (■) is suppressed owing to an active IDFF (●). (b) Horizontal (data: dots, fit: dashed line) and vertical (squares and full line, respectively) XBPM-readout calibration factors.

The significant change in the calibration factors in both horizontal and vertical directions (~100%) during the ID-gap change shown in Fig. 4 should be noted. It has to be emphasized, that the bending magnet radiation gives a factor 100 less signal compared with the total photon flux. This can be easily checked with a *bladesum* signal *B1+B2+B3+B4* measured at a fully opened gap. Such undulator/bending magnet signal-to-noise ratio is achieved through optimized spatial placement of the XBPM blades [6].

CONCLUSIONS

In summary, well designed, aligned and calibrated XBPMs are capable of accounting for the systematic photon beam position distortions induced by ID-settings variations. The orbit distortion is created by kicks at entry and exit of the ID, due to typical edge field behaviour. Two different undulator types, where light polarization and gap was changed, have been studied. In general, each ID-setting requires an XBPM calibration. XBPM calibrations based on machine bumps across the undulator straight sections are fully automatized in EPICS and are made during dedicated machine shifts at SLS. The chosen method for compensating the systematic effects of the IDs are IDFF correction tables which include the XBPM readout.

ACKNOWLEDGMENTS

We would like to thank K. Holldack (BESSY) for useful discussions. We also acknowledge the technical support from Q. Chen and R. Wullschlaeger during the installation of the XBPMs into the front-ends.

REFERENCES

[1] K. Holldack et al., *Review of Emittance and Stability Monitoring Using Synchrotron Radiation Monitors*, DIPAC 2001
[2] J. Krempasky et al., *The Use of Photon Monitors at the SLS*, EPAC 2004
[3] http://sls.web.psi.ch/view.php/beamlines/address
[4] T. Schmidt et al., Insertion device activities, PSI scientific report, Vol VII, 2004
[5] J. Krempaský et al., *Insertion device photon beam studies with X-ray monitors*, proceedings EPAC 2004
[6] K. Holldack, *SLS-UE44: On the Design of Front-End Monitors,* private communications
[7] T. Schilcher et al., *Commissioning and Operation of the SLS Fast Orbit Feedback*, EPAC 2004
[8] T. Schmidt, J. Chrin, A. Streun, D. Zimoch, *Feed Forward Corrections for Insertion Devices at the SLS,* PSI Scientific Report 2003, Vol. VI, 2003.
[9] M. Böge et al., *Correction of insertion device induced orbit distortion at the SLS*, PAC 2005

RECENT RESULTS FROM THE ELECTRON BEAM PROFILE MONITOR AT THE SWISS LIGHT SOURCE

Å. Andersson, A. Lüdeke, M. Rohrer, V. Schlott, A. Streun, PSI, Villigen, Switzerland
Oleg Chubar, SOLEIL, Gif-sur-Yvette, France

Abstract

Two different methods of beam profile measurements using a) visible-to-UV range synchrotron radiation and b) X-ray synchrotron radiation have been realized in a single diagnostics beam line at the Swiss Light Source (SLS). In the visible-to-UV case the vertically polarized synchrotron radiation renders an image heavily influenced by inherent emission and diffraction effects of synchrotron radiation. This nevertheless turns out to be an advantageous influence when determining rms beam profiles below 10 μm. However, high-precision wave-optics based calculations of the synchrotron light characteristics need to be performed (SRW-code) to ensure correct interpretation of the measured profiles. The visible-to-UV branch has a few built-in features allowing numerous cross-checks of the SRW-model. Surprisingly, wave-optics based calculations are also applicable, and required, for the X-ray pinhole camera setup. We briefly discuss the advantage of applying two different measuring techniques at the same source point. In total, for standard user operation at the SLS, the beam line has helped to establish a vertical emittance below 10 pmrad.

INTRODUCTION

For emittance measurements on a synchrotron radiation (SR) source, an image formation method is most often used. Thus, the emittance determination relies on a beam *size* measurement, and knowledge of the machine functions. A successful measurement of the beam size needs a) a good optic scheme resulting in a near distortion-free image and b) a model for SR emission and propagation through the optics to find the relation between image and actual beam size. At SLS we have realized two optics schemes which observe (almost) the same point within a bending magnet. One such scheme is the well know pinhole camera using SR X-rays (ex. [1]). The other uses focused vertically polarized visible-to-UV SR, a technique developed at MAX-lab [2].

The model we use to describe the two optics schemes is based on a near-field calculation, using the retarded potentials, of the SR electromagnetic fields at the first optical element. Preserving all phase information, the fields are then propagated, through pinhole/lens and other apertures, within the frame of scalar diffraction theory. Finally the intensity distribution is calculated in the image plane. This distribution, resulting from a single relativistic electron, is termed the "filament-beam-spread-function" (FBSF). It is the equivalent to point-spread-functions in the case of virtual point sources. Convoluting the FBSF with a Gaussian distribution (or any assumed electron distribution) gives the measured image profile. The SRW-code [3], used for our calculations, is based on this model. In the case of focused vertically polarised light the FBSF - in the vertical direction - is a two-peaked distribution with a zero minima in the centre (for 2-dim. visualisation please see [4]). For an increasing vertical beam size this minimum becomes shallower, allowing for a sensitive beam size determination. A vertically thin absorber blocks the intense mid-part of SR in our optical scheme. It is included in the modelling, but only marginally affects the FBSF. In the pinhole camera case, the result is a FBSF with a slightly smaller width than the one given from the approximate approach of 'adding in square' contributions from Fraunhofer diffraction and geometrical blurring due to the finite pinhole size.

THE DIAGNOSTIC BEAMLINE

The source point of the beam line is the centre of the middle bending magnet in the SLS triple bend achromat lattice (see Table 1 for machine parameters). The X-ray branch uses only 0.8 mrad_H, while the visible branch, immediately next to it, has a clearance of 7.0 mrad_H x 8.8 mrad_V. The water cooled pinhole array, fabricated from a 150μm thick Tungsten sheet with 15μm diameter holes, is located 4.022 m from the source point (sp). The light escaping these holes carries negligible power and is released through a 250μm thick Aluminium window.

In the visible branch the light is twice directed through 90° angles to achieve parallelism with the X-rays at a separation of 0.35m. The first mirror is made of SiC, a material which has a very advantageous ratio of thermal conductivity and expansion. This helps in low current measurements for moderate heat loads (a few tens of Watts). However it is stressed that for higher currents a "thin absorber" has been inserted before the mirror, while obstructing only the mid ±0.45 mrad_V of the SR. This takes away almost all the 400 Watt heat load on the mirror at full current, avoiding mirror deformation. The second mirror is a movable aluminized fused silica (FS) mirror. A FS spherical lens (5.076m from sp) is positioned between the two mirrors. These three optical components are chosen with λ/20 surface accuracy. One vertically, and two horizontally movable blocking blades are situated near the lens to vary the acceptance angles. The visible-to-UV light is brought out of vacuum only at the end of the beam line (~9m from sp), through a FS window.

Monochromating Molybdenum filters and phosphor (P43) for the X-ray branch, grey filters, bandpass (BP) filters, a polarizer for the visible branch and the two Firewire, "Pointgrey Flea", CCD cameras (pixel size 4.65 μm) are placed on an optical table at the end of the beam line. The visible branch camera can be remotely moved longitudinally when different BP filters are used, since the

lens' focal length is wavelength dependant; the X-ray branch camera has a zoom and focus adjustable lens system. The magnification of the two optical schemes are 0.840/0.854 (at 364/403 nm) and 1.276 (to phosphor).

Table 1: Some SLS parameters

Energy	2.4 GeV
Dipole field	1.4 T
Nat. Energy Spread	0.086%
β_x ; β_y ; η_x (at obs.point)	0.45 m;14.3 m;29 mm
Nom. Hor. Emittance FEMTO-wiggler [5] open/closed	5.5/7.3 nmrad
$\sigma_{xtheory}$ (at obs.point)	56/62 µm

MEASUREMENTS

Fig. 1 shows the beam size application displaying the visible branch. Data is updated at a rate of approx. 1 Hz. The scales are in pixel units, while the X_sig and Y_sig values presented are the derived electron beam rms values, σ_{ex} and σ_{ez} . σ_{ez} is derived from the summation of the pixel intensities within the red lines. The valley-to-peak intensity ratio (blue lines) is then converted by a pre-SRW-calculated table to σ_{ez} . σ_{ex} is arrived at after integrating over the whole image spot, determining the FWHM value, and again converting by help of pre-SRW-calculations to σ_{ex} . A similar window can be opened for the X-ray branch.

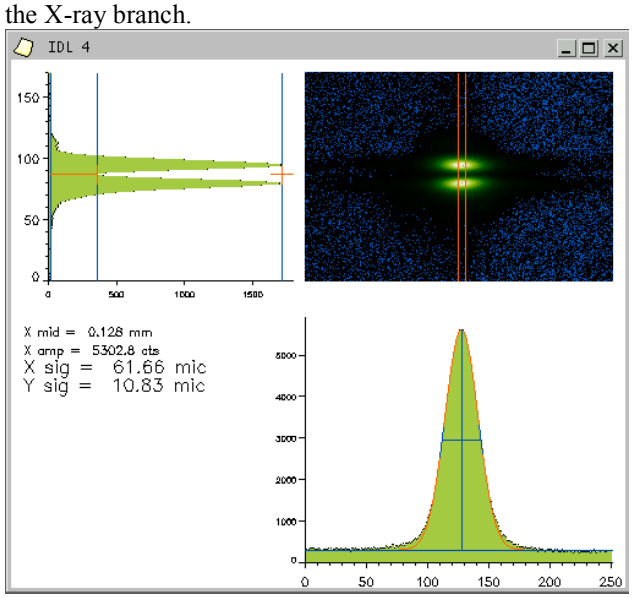

Figure 1: Image from the visible-to-UV branch. Vertically polarized at 403 nm. Machine conditions (M.c's): 350 mA, user top-up mode, FEMTO (F)-wiggler closed.

Vis-to-UV Branch

Even though it is more challenging to determine the vertical beam size, it is also of great interest to verify that the model predictions also agree with measurements in the horizontal case, where usually the beam size is much larger. To explore this we measured horizontal image profiles - still with the setup for vertically polarized light - for different horizontal apertures set by the blocking blades at the lens position.

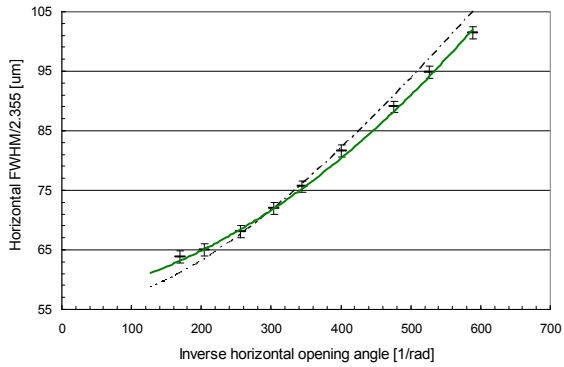

Figure 2: Measured (marks) and predicted (solid line) FWHM/2.355-values at 403 nm. M.c's: 350 mA, user top-up mode, F-wiggler open.

Fig. 2 shows the results, where we have plotted measured and predicted FWHM/2.355 of the images, against the inverse accepted horizontal SR opening angle. The solid line is the prediction from SRW, which is a convolution of a σ_{ex} = 55.6 µm Gaussian electron beam shape and the calculated FBSF for the different opening angles. We have also indicated (dashed line) the result given from simply adding in square the electron beam width and a $(\sin x/x)^2$ width resulting from the simplified assumption of treating the filament beam as a far away point source (Fraunhofer diffraction case). Discrepancies for small hor. acceptance angles originate only from the simplified 'adding in square' method instead of performing a pure convolution. Hence, a Fraunhofer approach is valid in this acceptance region. For large acceptance angles the deviation is additionally due to the more complicated phase relations of the SR electric field emission over the arc, compared to a virtual point source, making the Fraunhofer approach invalid.

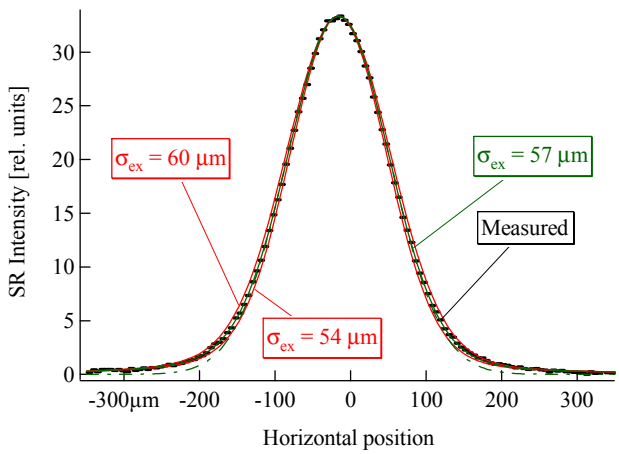

Figure 3: Measured (marks) and predicted (solid lines) horizontal profile at 364 nm, 3.9 mrad_H. M.c's: 350 mA in user top-up mode, F-wiggler open.

Fig. 3 shows an example of an entire horizontal image profile. The lines are profile predictions calculated from the SRW model by convoluting the FBSF with a Gaussian electron beam and afterwards integrating over the entire image, as done with the on-line monitor. Of particular

note is the good agreement in the tails, which clearly deviates from a Gaussian shape (dashed line).

As an example of the vertical beam size measurement performed with vertically polarized light we present a profile (Fig. 4) obtained at 350 mA circulating current. SLS was for several weeks operated in standard user mode with these beam properties. This mode, with carefully tuned sqew quadrupole settings, gave the smallest vertical rms beam size, $\sigma_{ez} = (7.5 \pm 0.5)$ µm at the monitor. This corresponds to a vertical emittance of, $\varepsilon_z = (3.9 \pm 0.7)$ pmrad, the smallest so far reached at SLS. Again, the SRW model predicts very well the profile - peak widths correspond to valley depth. However, the example shows that we start to reach the limit resolution of the method. The slightly raised intensity levels in the tails most probably originate from one or several non-ideal optics element. Such a contribution in the intensity valley can therefore not be excluded. The estimated vert. beam size is hence an upper estimation of the real size.

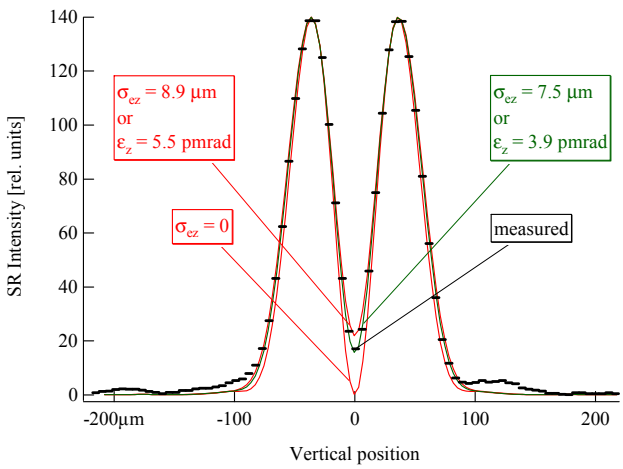

Figure 4: Measured (marks) and predicted (solid lines) vertical profile at 364 nm, 3.9 mrad_H. M.c's: 350 mA in user top-up mode, F-wiggler open, tuned sqew quads.

To circumvent this problem one could either block a major part of the central SR, or detect at shorter wavelengths. Both methods bring the peaks of the FBSF closer together, making the valley to peak intensity ratio more prone to smaller beam sizes. We prefer the latter method, since it preserves the possibility to cross-check the optics quality from the tails behaviour. In the former case, one is essentially moving towards a pure interferometric [6] method, where tails and possible beam rotations are being obscured by a growing fringe pattern.

In order to cross-check the model predictions, in a fashion similar to that for the horizontal case, the vertically blocking blade is used, making the SR contribution to the image asymmetric. No contradictions have so far been made evident.

X-Ray Branch

The X-ray branch has also been modelled by the SRW code for monochromatic 16 keV SR, giving a FBSF of 9 µm FWHM/2.355, in both directions (converted to 1:1 imaging). The vertical spot size FWHM/2.355 obtained for the above mentioned SLS conditions was 13.7 µm. De-convolution gives σ_{ez} = 10 µm. This is however not necessarily in contradiction to the visible branch result, since chromatic effects and phosphor related effects are excluded. Phosphor thickness and phosphor grain size contributes to the final image to as yet unquantified extent. In the near future we will install pinholes of different sizes in order to systematically compare measured profiles with the model predictions, as done in the visible branch. An advantage of the X-ray branch is that small beam rotations can be quantified. A drawback, compared to the visible branch, is the over-all light yield, which is between 10^3 and 10^4 times lower, preventing us from making fast and/or low current measurements.

Combined Measurements

Even though the X-ray branch does not yet reach the same resolution as the visible branch, it serves as a perfect complement in order to verify tiny (< 0.5 µm) beam size changes during machine operation. If seen on both monitors, one can most often exclude measurement artefacts, as the cause of change. In this way it has been possible to search, and find, the cause of several tiny beam size alterations.

CONCLUSION

A method utilizing vertically polarised visible-to-UV SR has been implemented to determine the vertical beam size at SLS. For the so far best tuned sqew quadrupole setting found, at 350 mA top-up mode, the upper limit of the rms beam size at the monitor was determined to be σ_{ez} = (7.5 ± 0.5) µm. This corresponds to a vertical emittance of, $\varepsilon_z = (3.9 \pm 0.7)$ pmrad including possible vertical beta function errors. An X-ray pinhole camera setup measures at the same source point σ_{ez} = 10 µm. In this case, possible chromatic and phosphor related effects have to be further explored to determine their error contribution. The two monitors have served to provide important feedback to machine operators regarding the electron beam size, and have helped to establish a vertical emittance of less than 10 pmrad, for standard user operation at the SLS.

REFERENCES

[1] P. Elleaume et.al., J. Synchrotron Rad.(1995)2, p.209
[2] Å. Andersson, Ph.D. thesis work (1997), ISBN 91-628-2686-7, and Å. Andersson, M. Eriksson, O. Chubar, EPAC'96, p. 1689.
[3] O. Chubar, P. Elleaume, EPAC'98, p. 1177.
[4] O. Chubar, P. Elleaume, A. Snigerev, Nucl. Instr. And Meth. A 435 (1999), p. 495.
[5] A. Streun et. al, "Sub-picosecond X-ray Source FEMTO at SLS", EPAC'06, p. 3427.
[6] T. Mitsuhashi, PAC'97, p. 766.

A LARGE SCINTILLATING SCREEN FOR THE LHC DUMP LINE

T. Lefèvre, C. Bal, E. Bravin, S. Burger, B. Goddard, S. Hutchins, T. Renaglia,
CERN, Geneva, Switzerland

Abstract

The 7 TeV proton beam from the LHC ring is ejected through a long transfer line to beam dump blocks, approximately 100m downstream of the ejection septa, a series of dilution kicker magnets provide a sweeping deflection spreading the extracted beam over a 40 cm diameter area on the face of the beam dump cores. During normal operation, the quality of each dump event must be recorded and verified. The so-called "Post-Mortem" dataset will include information from the beam dumping system (logic signals, kicker pulses…) as well as from the beam diagnostics along the extraction lines. For this purpose, profile monitors in front of the dump blocks must be permanently available during machine operation.

With more than 10^{14} protons stored in LHC, the energy deposited in the screen becomes an issue and thermal-resistant materials have to be considered.

In this paper, the design of this quite unusual device is presented. The different technical options considered for the choice of the screen material are discussed first. The complete layout of the installation is then described with a special emphasis on the mechanical design, the screen assembly and the choice of the radiation-hard camera used to observe the screen.

INTRODUCTION

The LHC beam dumping system [1] is designed to make a fast extraction of the circulating beams from each ring of the collider with minimal losses. The particles are then transported to an external dump blocks, which are located in caverns at the end of a 650 m long vacuum line. A system of horizontal and vertical dilution kickers in these lines will be used to sweep the beams in an "e" shaped form on the surface of the dump, as an undiluted full energy and intensity beam can damage the dump block. For the case of a normal beam dump, the 2808 proton bunches are swept over a path length of about 110cm at the entrance window of the dump. The beta-functions at this location are about 4.6 km in each plane, such that the beam spot is circular, with σ of 6.0mm at 450GeV and 1.5mm at 7TeV.

The trace produced by the dilution kickers (see Figure 1) must be monitored using an imaging system, named the BTVDD (Beam TV Dump Detector). As part of the post-mortem analysis, the corresponding image would be stored and checked to ensure that the dilution system functioned correctly for each beam dump. High resolution for this device is not critical since accurate knowledge of the beam size is not important. A precision on the beam position and size around 1-2 mm r.m.s. is required with a reproducibility of about 0.5 mm.

For high energy particles, beam imaging systems are usually relying on the use of Optical Transition Radiation (OTR) screens [2] or on luminescent screens.

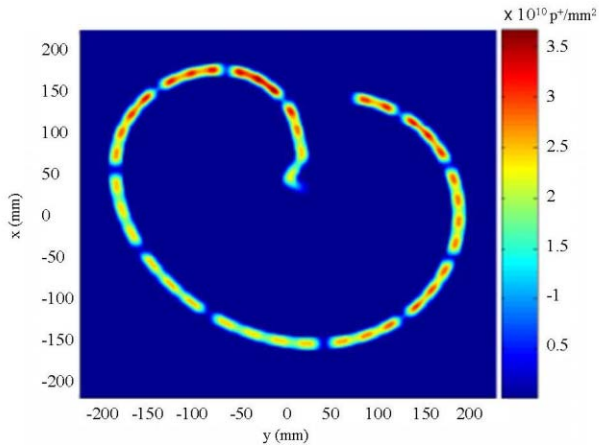

Figure 1: Protons density on the screen for a nominal sweep and 450GeV protons

Optical Transition Radiators provide a very reliable source with a total number of photons per proton in the wavelength range $[\lambda_a, \lambda_b]$ given by:

$$N_{OTR} = \frac{2\alpha R}{\pi}\left[\left(\beta + 1/\beta\right)\cdot \ln\left(\frac{1+\beta}{1-\beta}\right) - 2\right]\ln\left(\frac{\lambda_b}{\lambda_a}\right)$$

with α the fine structure constant, β the proton velocity, γ the relativistic factor and R the optical reflectivity of the screen. Moreover the OTR photons are emitted in a $1/\gamma$ aperture cone centred on the specular reflection of the beam trajectory with respect to the perpendicular of the screen surface. In consequence, only a small part of the OTR would be recuperated from particles away from the central axis. In addition, thermal resistant radiators, like carbon, have low reflectivity (27%), limiting by the same amount the light intensity produced.

Several decades of research on ceramic phosphors at CERN [3] and at other laboratories has led to the almost exclusive use of doped alumina ceramic screens, i.e., $Al_2O_3:Cr^{3+}$, for accelerator beam observation. Alumina (type AF995 [4]) is doped with 0.5% chrome sesquioxide and at room temperature two principal lines of luminescence at 692.9 and 694.3 nm are generated with a decay time of 3.4ms [5]. These screens are also compatible with ultrahigh vacuum systems, they exhibit good response linearity, and their radiation resistance is high. For example, in tests made at CERN, screens have withstood integrated relativistic proton fluxes of up to 10^{20} protons/cm^2.

A comparison between a carbon OTR screen and chromium doped alumina is presented in Table 1. From these values the use of OTR would be limited to the

observation of well centered beams with relatively small sizes. The photon yield mentioned for alumina is expressed in photon per MeV of deposited energy. The number of photons generated is much greater than from an OTR screen, but since luminescence is isotropic, only a small fraction can be recuperated by the optical system. For high energy particles, alumina has shown sensitivities starting for 10^7-10^8 protons [6] when observed with a normal CCD camera. Even if the melting point for alumina is 2000°C, one should not use it with temperature higher than 1650°C.

Table 1: OTR and luminescent screen parameters

Screen	OTR Carbon	$Al_2O_3:Cr^{3+}$
Density (g/cm^3)	1.7	3.96
Specific heat (J/gK)	0.7-2.4	1.09
Melting point (°C)	3527	2000
Light directivity	0.07mrad	isotropic
Photons yield	10^{-2} (ph/p$^+$)	10^4 (ph/MeV)

The use of a thermal resistant luminescent alumina screen was considered for the BTVDD a few years ago in a preliminary study [7].

THERMAL ANALYSIS

Failures of the dilution kickers will result in higher particle densities which may damage the screen. The most dangerous are the total failure of all the dilution kickers in one plane, e.g. Fig. 2, or a total dilution failure, in which the full beam impacts in the center of the screen in a small spot.

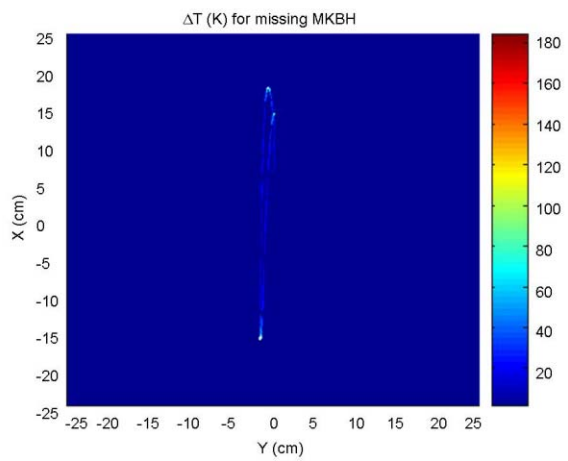

Figure 2: Spatial distribution of the temperature increase for a failure of all horizontal dilution kickers

Simulations have been performed using the Monte-Carlo code Fluka [8] in order to evaluate the energy deposition inside the screen. From these values, the local temperature increase of the screen has been calculated for the various load cases, which are reported in Table 2. The rates of the different failure modes expected per year [9] are indicated as well.

Carbon would survive any beam conditions and the temperature increase for alumina would be close to the acceptable limit for the case of a total failure. The energy deposition for 450GeV and 7TeV protons only differs by a few % but since the beam size is 4 times smaller for the highest beam energy, the maximum temperature increase will drop down by a factor 16 for 450GeV protons.

Table 2: Maximum temperature increase for different load cases for 7TeV protons together with expected occurrence rate

Load case	ΔTp (°C)		Rate (y^{-1})
	Carbon	$Al_2O_3:Cr^{3+}$	
One bunch	1	1.6	-
Nominal	15	22	400
No MKBH	116	191	0.008
No MKBV	166	241	0.005
No MKB	891	1150	4.2×10^{-5}

TECHNICAL CONSIDERATIONS

To observe the full dilution, the screen has to cover an area of 60cm in diameter, which is quite unusual in accelerators. Due to some limitations in the fabrication process of the ceramic, it was not possible to produce a screen in one piece. The screen is therefore made of 4 quadrants, which are machined in a way such that a 5cm diameter central area is left open to avoid damage in the case of non diluted beam (see Figure 3).

The central part of the screen is covered by a 5cm large, 35cm long, rectangular screen. Two options are envisaged for the choice of this second screen. During the commissioning period, either a single bunch or a reduced beam charge is used and AF995 Alumina is required because of its high photon yield. However, as previously mentioned, this screen will not stand a total dilution failure, so this would be replaced by an OTR carbon foil capable of surviving the highest charge densities. The observation angle and the screen tilt angle are chosen so that these two options can be implemented just by changing the central part of the screen.

The optical system consists of a set of optical density filters for the control of the light intensity and a camera located at a distance of 1.2m from the screen. The required magnification of 0.015 is obtained by a fused silica 12.5mm focal length camera lens. Compared to the design done in [7] with a set of 4 lenses, the present design provides a much better optical spatial resolution, with lower aberrations. The simplicity of the system, avoiding any precise optical alignment makes it easily and rapidly maintainable.

The spatial resolution of ceramic screen is limited by the combination of three characteristics [10]: finite thickness of the screen, limited opacity of the screen material, and light scattering inside the screen. The beam creates a line of light emitter points inside the screen. The light coming from these points is not strongly attenuated, while it is scattered before it reaches the screen surface.

As a consequence, a blurring of the spot on the screen occurs and degrades the spatial resolution. In order to minimize this effect the screen should be as thin as possible, and the angle between the screen and the beam trajectory should be close to 90°. For mechanical reasons a 3mm thick screen is preferred and 80° tilt angle screen is chosen. The observation angle is then set to 20°. The resolution of the screen would be better than 1mm.

The radiation dose received by the camera has been estimated using Fluka and corresponds to 270krad for a year of nominal operation. The simulations are done for 7TeV protons and only consider the shower corresponding to the beam hitting the screen. In reality, the radiation dose would be higher because of beam losses and interactions between protons and rest gas atoms upstream of the BTVDD. A radiation resistant camera was selected (SIRA APS250) and tested [11], it will withstand up to 10Mrad. It should be noted that possibly due to the lower fill factor of the sensors, these radiation resistant Charge Injection Detector (CID) cameras present a factor 10 less sensitivity compared to a normal CCD camera.

OVERALL SYSTEM

The overall system is described in Figure 3. The 2m long 60cm diameter vacuum chamber is directly welded to the beam tube at both ends. It is installed at a distance of 30m upstream of the vacuum window [12]. Even if the tunnel is large, the beam line is installed to one side in order to leave most of the place free for transport vehicles. The 4 quadrants screen support is mounted on a vertical flange and due to its weight needs some dedicated equipment to be manipulated securely. The central screen support is on the 6cm diameter flange which can be quickly connected. This is an important feature of the design to ensure an easy and quick maintenance since the central part of the screen is the most likely to be often damaged and replaced.

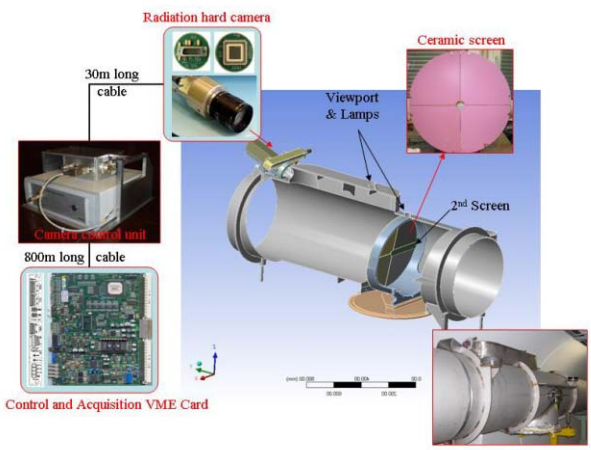

Figure 3: Overview of the BTVDD imaging system

The camera is composed of two parts, a radiation resistant sensor and its control unit which is more sensitive to radiation damage. Therefore the control unit is installed 25m upstream of the BTVDD tank and surrounded by iron and concrete blocks for shielding. The control of the camera, the control of two lamps used for calibration and the control of the filter wheel are done using a CERN standard VME card [13], which is located in a technical gallery at a distance of 800m from the BTVDD. This card is also equipped with a frame grabber for image acquisition. The trigger signal (1µs, 12V), provided by the firing system of the extraction kicker, is interfaced via a dedicated PCB to match the TTL trigger required by the frame grabber.

The choice of the optical density filter must be set automatically in accordance with the total beam charge circulating in the machine.

CONCLUSIONS AND PERSPECTIVES

The design and the construction of the large imaging screen for the LHC dump line have been done. It relies on the use of high sensitivity and thermal resistant chromium doped alumina. Fluka simulations have been performed to estimate energy deposition in screen and the corresponding temperature increase for the different beam dumping scenarios. The overall system has been designed to guarantee a simple maintenance and to survive in high radiation zone.

REFERENCES

[1] O.Bruning et al., LHC Design Report Volume III, *http://ab-div.web.cern.ch/ab-div/Publications/LHCDesignReport.html*
[2] L. Wartski *et al*, J. Appl. Phys. 46, 3644 (1975)
[3] C. D. Johnson, "The Development and Use of Alumina Ceramic Fluorescent Screens", CERN/PS/90-42
[4] AF995R from Saint Gobain Céramiques Avancées Desmarquest : *http://www.ndfc.saint-gobain.com*
[5] K.J MacCarthy *et al*, "Characterization of the Response of Chromium-doped Alumina Screens in the Vacuum Ultraviolet Using Synchrotron Radiation", J. Appl. Phys. 92, 6541 (2002)
[6] R. Jung *et al*, "Single Pass Optical Monitoring", DIPAC 2003, Mainz, Germany, pp.10
[7] A. Variola and L. Bruno, "Proposal for the LHC Beam Dump Upstream Monitor", LHC project Note 241, (2000)
[8] A.Fasso *et al.*, "FLUKA: Status and Prospective for Hadronic Applications", Monte Carlo 2000 Conference, Lisbon, pp.955
[9] R. Filippini and J Uythoven, "Dependability Analysis of a Safety Critical System ", CERN-Thesis-2006-054
[10] B.K. Scheidt, "Upgrade of the ESRF Fluorescent Screen Monitors", DIPAC 2003, Mainz, Germany, pp.125
[11] S.Hutchins *et al*, "Radiation Tests on Solid state cameras for Instrumentation" DIPAC 2005, Lyon, France, pp.315
[12] A. Presland *et al*, "A Large Diameter Entrance Window for the LHC Beam Dump Line", PAC 2005, Knoxville, Tennessee, pp.1698
[13] S. Burger *et al*, "A New TV Beam Observation System for CERN', DIPAC 2005, Lyon, France, pp.214

EXPERIMENTAL OPTIMIZATION OF THE CATHODE LASER TEMPORAL PROFILE*

M. Krasilnikov#, J. Bähr, M. Hänel, F. Stephan, DESY, Zeuthen, Germany
I. Will, MBI, Berlin, Germany

Abstract

Producing a flat-top temporal intensity profile for the cathode laser pulse is a key issue for the XFEL photo injector. The photo injector test facility at DESY in Zeuthen (PITZ) serves as a test bench for FEL photo injectors. The PITZ cathode laser contains a pulse shaper to produce flat-top temporal pulse profiles. Based on birefringent filters the pulse shaper includes four degrees of freedom to achieve a pulse profile with parameters closer to the required XFEL photo injector specifications (20 ps FWHM, 2 ps rise/fall time). A procedure for experimental temporal laser profile optimization is presented in this paper. The laser profile is measured using a streak camera. The five parameters - pulse length (FWHM), rise and fall time as well as flat-top modulation period and depth which are obtained from a flat-top fit of the measured profile - are used in the profile evaluation. Using results of beam dynamics simulations for various cathode laser profiles a single value of the goal function – the expected emittance growth due to measured imperfections of the profile - can be obtained. The procedure of the goal function minimization has been implemented and tested at PITZ.

INTRODUCTION

A projected normalized beam emittance of ~0.9 mm mrad from the photo injector is the key requirement to fulfill the XFEL specifications [1]. In order to achieve such a challenging performance of the electron source a cathode laser with temporal flat-top profile having 20 ps FWHM and ≤ 2 ps rise and fall time has to be used.

A pulse shaper based on the birefringent filter is currently in use at PITZ to produce a flat-top cathode laser temporal profile. The laser temporal distribution deviates from the goal flat-top (20 ps FWHM, 2 ps rise/fall time) profile. The main reason for this is the limited fluorescence bandwidth of the amplifying medium (Neodymium-doped Yttrium-Lithium Fluoride, Nd:YLF) used in the laser system.

In order to study the impact of the laser temporal profile imperfections onto the quality of the electron beam in the photo injector corresponding beam dynamics simulations have been performed. A procedure for the evaluation of the experimentally obtained laser shape has been developed based on results of beam dynamics simulations. An algorithm for the pulse shaper optimization is proposed.

* Work is partially supported by the European Community, contract numbers RII3-CT-2004-506008 and 011935, and by the "Impuls- und Vernetzungsfonds of the Helmholtz Association, contract number VH-FZ-005.
#mikhail.krasilnikov@desy.de

LASER PULSE SHAPER AT PITZ

The laser system and the temporal pulse shaper [2] operated at PITZ were developed at the Max-Born-Institute (MBI) in Berlin. The laser produces pulse trains up to 800 µs length with a single pulse separation of 1 µs and a pulse train repetition rate of up to 10 Hz.

An IR Gaussian laser pulse (wavelength 1047 nm) is generated by the mode locked pulse train oscillator (PTO) [3], followed by the pulse shaper and six stages of diode pumped Nd:YLF amplifiers. Two nonlinear crystals are used to convert the IR laser pulse into its fourth harmonics (UV, wavelength 262 nm). A pulse shaper based on birefringent filters is currently in use at PITZ, its schematics is shown in Fig.1.

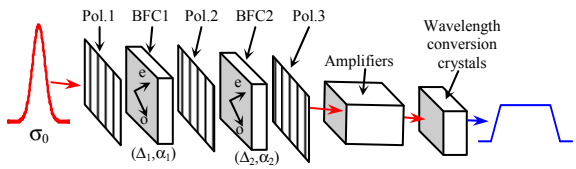

Figure 1: Schematics of pulse shaping elements.

The pulse shaper is composed of a stack of birefringent crystals (BFC1, BFC2) interspersed with polarizers (Pol.1,2,3). High birefringence of the crystals provides a phase shift between ordinary and extraordinary waves $\Delta = 2\pi(n_e(\lambda) - n_o(\lambda))d/\lambda$, where n_o and n_e are the refractive indices for ordinary and extraordinary waves in the crystal of thickness d, $\lambda = 1047nm$ is the laser wavelength. σ_o is the rms pulse duration of the initial Gaussian pulse. By adjusting the orientation of the crystals (α_1, α_2) and tuning the phase shifts (Δ_1, Δ_2) a temporal profile of the output pulse close to a flat-top can be achieved. The limited fluorescence bandwidth of the used laser medium Nd:YLF significantly modifies the pulse shape during the amplification process and restricts the rise and fall time of the output pulse to 4…5 ps. In addition, modulations in the flat-top area of the output pulse arise. Streak-camera measurements [4] show a typical modulation depth of ~10-20%. These modulations can be reduced at the cost of increased rise and fall time. The effects of the amplifier and wavelength conversion stages are significant and need to be studied in more detail. Electron beam dynamics simulations have been involved in order to find a proper compromise between modulation depth and rise/fall time of the laser pulse.

BEAM DYNAMICS SIMULATIONS

ASTRA [5] beam dynamics simulations have been performed in order to establish a figure of merit for experimentally obtained cathode laser temporal profiles. Four main factors have been considered: pulse length (FWHM), rise/fall time, frequency and depth of the flat-top modulation.

The optimized setup of the XFEL photo injector [1] has been used to simulate the influence of the cathode laser temporal profile imperfections. The nominal flat-top distribution with 20 ps FWHM and 2 ps rise/fall time has been considered as the baseline for the comparison. A homogeneous transverse cathode laser profile with rms size of 0.4 mm has been used for the simulations. Electron bunch properties at the distance z = 15 m from the photo cathode are simulated by ASTRA, the beam is generated by a 1.5-cell L-band RF gun with 60 MV/m at the photo cathode and accelerated by the first module (8 TESLA cavities) up to an energy of ~150 MeV. The projected normalized beam emittance as a function of rise/fall time is shown in Fig.2a. The dependence of the transverse and longitudinal emittance is shown in Fig.2b as a function of the pulse length (FWHM). The transverse projected emittance is lower for longer laser pulses due to reduced transverse space charge effect, especially during emission from the photo cathode. The drawback is the increased longitudinal emittance, which is a consequence not only of the increased bunch length but also a result of the increased contribution of the longitudinal nonlinearity of the RF field.

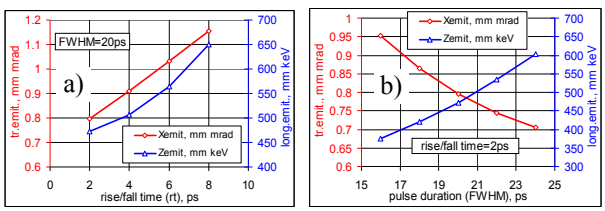

Figure 2: The beam projected transverse normalized emittance and longitudinal emittance at z=15 m. a) vs. rise/fall time of the photo cathode laser pulse; b) vs. photo cathode pulse duration (FWHM of the flat-top).

The impact of the flat-top modulation is illustrated in Fig.3, where the transverse and longitudinal emittance is shown as a function of modulation depth m for various modulation periods $T_n = 18ps/(n+0.5)$ (n=1, 2, 3, 8). Typical intensity distributions used to simulate the flat-top modulation are shown in Fig.4a. It should be noticed that these modulation frequencies are lower than those which can be critical in bunch compression schemes (which are out of the scope of this work).

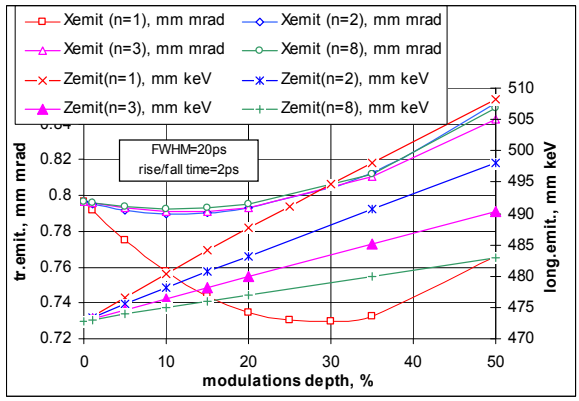

Figure 3: Simulated projected normalized transverse and longitudinal emittance vs. flat-top modulation depth m for various modulation frequencies (n is the number of the modulation half-wavelength on the flat-top).

For higher modulation frequency (n ≥ 2) a shallow minimum of the emittance for ~10% modulation depth is caused by the modification of the space charge force due to the modulation of the electron longitudinal phase space. On the other hand the laser intensity modulation results in a modulation of the longitudinal phase space of the electron beam and, therefore, in the longitudinal emittance growth.

A goal function for the experimental cathode laser profile optimization can be modelled now by a combination of imperfection factors: rise (*rt*) and fall time (*ft*), pulse length (*FWHM*) and modulation parameters (*n* and *m*):

$$\Phi = \sqrt{\Phi_{rt}(rt)\Phi_{rt}(ft)} \cdot \Phi_l(FWHM) \cdot \Phi_{\mathrm{mod}}(n,m). \quad (1)$$

Based on simulation results these factors can be approximated as expected transverse emittance growth due to the corresponding laser shape imperfection:

$$\Phi_{rt}(x) = 1 + 0.008 \cdot (x-2)$$

$$\Phi_l(x) = \begin{cases} 1 - 0.039 \cdot (x-20) + 0.003 \cdot (x-20)^2, \text{ if } x < 20 \\ 1 + 0.061 \cdot (x-20) + 0.002 \cdot (x-20)^2, \text{ if } x > 20 \end{cases} \quad (2)$$

$$\Phi_{\mathrm{mod}}(n,m) = \begin{cases} 1 - 0.059 \cdot m + 0.0001 \cdot m^2, \text{ if n} = 1 \\ 1 - 0.0011 \cdot m + 0.00005 \cdot m^2, \text{ if n} > 2 \end{cases}$$

In order to keep the minimum of the Φ_l at FWHM=20 ps, a relative longitudinal emittance growth has been used for FWHM > 20 ps.

MEASUREMENTS OF THE TEMPORAL LASER PROFILE AT PITZ

The temporal profile of the cathode laser is measured by use of a streak-camera [4] at PITZ. In order to evaluate the measured profile, a flat-top fit procedure (Fig.4b) has been developed. It yields the parameters of the flat-top laser profile (*rt,ft,FWHM,n,m*), which when being applied in (2), delivers a single value of the goal function (1). The physical meaning of this value is the expected emittance growth due to imperfections of the measured laser temporal profile.

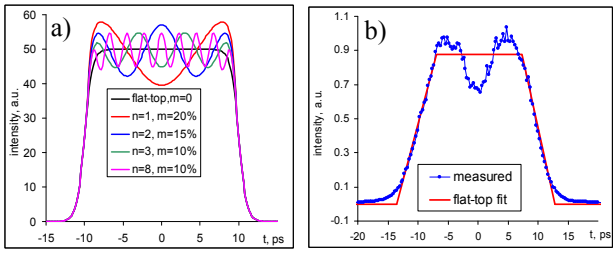

Figure 4: Cathode laser temporal profiles: a) used in beam dynamics simulations; b) measured at PITZ with a streak camera.

OPTIMIZATION OF THE TEMPORAL LASER PROFILE

Four pulse shaper parameters are available at PITZ for the tuning of the cathode laser temporal profile: rotation angles of both birefringent crystals (α_1, α_2) and their temperatures (T_1, T_2), by means of those one can vary the effective thickness (Δ_1 , Δ_2) and, therefore, the corresponding phase shifts.

In order to illustrate the complexity of the optimization procedure a contour plot of the measured goal function (1) vs. rotation angles (α_1, α_2) (for fixed temperatures (T_1, T_2)) is shown in Fig.5.

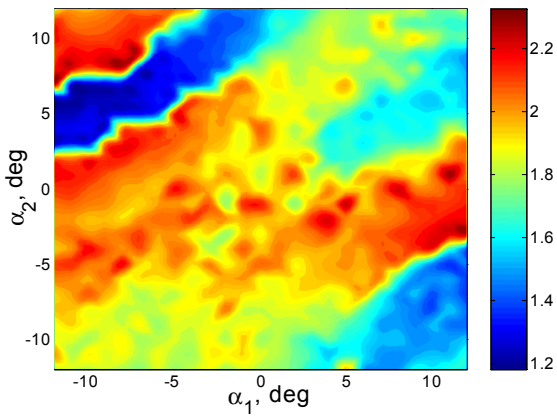

Figure 5: Contour plot o the goal function, based on measured cathode laser temporal profiles vs. rotation angles of birefringent crystals while their temperatures (phase shifts) being kept constant.

It can be clearly seen that even in the 2-dimensional cross section of the 4-dimensional parameter space there are several local minima. This makes the procedure of the laser temporal profile optimization rather sensitive to the initial parameter set. A staged strategy for the laser temporal profile optimization has been chosen: the goal function has been minimized by the simplex method [6] in the 4-parameter space (α_1, α_2 , T_1, T_2), but the initial simplex has been randomly seeded. The area of the parameter search has been smoothly restricted (to the physical parameter ranges) by applying corresponding penalty functions. At each step of the optimization three laser profile measurements have been performed in order to avoid random fluctuations. The optimization procedure and results of two trials are shown in Fig.6.

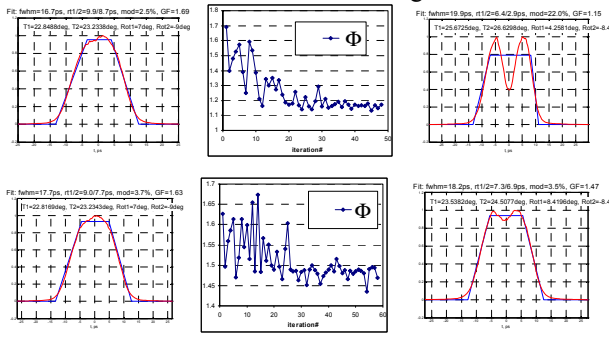

Figure 6: Optimization of the cathode laser temporal profile: left plots - initial measured distributions (the best from the randomly seeded series); middle plots – goal function evolution vs. optimization step, right plots – final measured distributions of the laser intensity.

One can see that the final profile in the upper row has comparatively short rise/fall time, but the modulation of the flat-top is rather large. In contrary, the second row represents the optimization results with small modulation at the price of increased rise/fall time.

CONCLUSIONS

A procedure for the optimization of the photo cathode laser temporal profile has been developed. It is based on the tuning of 4 parameters of a pulse shaper, based on birefringent filters. The flat-top profile evaluation is based on beam dynamics simulations for the beam emittance of the electron beam in a photo injector. The optimization is complicated by complexity of the goal function relief, which makes the search strongly dependent on the initial parameter set of the pulse shaper.

REFERENCES

[1] The European XFEL Technical Design Report, DESY 2006, July 2006, http://xfel.desy.de/tdr/index_eng.html
[2] I. Will, Generation of flat-top picosecond pulses by means of a two-stage birefringent filter, to be published in NIM A.
[3] I. Will, G. Koss, I. Templin, The upgraded photo cathode laser of the TESLA Test Facility, NIM A 541 (2005), pp. 467-477.
[4] Hamamatsu Photonics, http://www.hamamatsu.com.
[5] ASTRA, http://www.desy.de/~mpyflo/.
[6] J.A. Nelder and R. Mead, Computer Journal, 1965, vol 7, pp 308-313.

APPLICATIONS OF IEEE-1394 AND GigE VISION DIGITAL CAMERA IN THE TLS

C. Y. Wu, C. H. Kuo, Jenny Chen, S. Y. Hsu, Demi Lee, P.C. Chiu, K. T. Hsu
NSRRC, Hsinchu 30076, Taiwan

Abstract

Digital cameras comply with IEEE-1394 and GigE Vision standard are applied for beam diagnostic applications at NSRRC. These cameras provide low distortion for image transmission over long distance and flexible camera parameters adjustment with remote interface. These digital interfaces include of FireWire and gigabit Ethernet. The wide bandwidth bus can reduce latency time and timing jitter effectively and provides high quality image transportation. It also provides lossless compressed image with high update rate. Experiences accompany with both kinds of cameras will be summarized. System integration with control system and applications will also include in the report.

INTRODUCTION

Imaging applications in the accelerator community are often utilized to measure beam profile and interference fringes. The beam profile may convert form fluorescence, various optical diagnostics (SR, OTR, DR, etc.). A fluorescence screen/OTR and a synchrotron light source radiation monitor are mostly employed to measures beam profile and beam size of the accelerator system in order to optimize performance, check routine operation and study various beam physics. These tools are beneficial to characterize and analyze properties of electron beam. For example, the beam emittance is calculated from the measured beam size.

Digital cameras were adopted to enhance functionality of accelerator diagnostics [1-4]. The major upgrades of data acquisition and analysis have been implemented. The main goals are to increase the signal transmission quality, the dynamic range, the linearity of the profile monitor, and the superior supports for data analysis.

Using a fully digital camera has two major advantages compared to analogue CCD camera. First, the A/D conversion is performed closer to the CCD/CMOS sensor and therefore minimizes electronic noise. Once the digitized signal is immune to noise, we can implement long haul (10 m ~ 10^3 m) applications in the accelerator diagnostics. Various long hops solution is supported by the IEEE1394A/B interface. Noise immunity and isolation are provided by this solution that must be favourable in the accelerator environment. Second, unlike analogue camera systems, digital systems do not suffer from pixel jitter. Each captured pixel value corresponds to a well-defined pixel on the CCD/CMOS chip. The IEEE1394 interface is a hot swappable and self-configuring high performance serial bus interface that is capable of 400 Mbit/sec data transmission and will be enhanced to 3.2 Gbit/s for the next generation products. The interface supports asynchronous (guaranteed delivery) and isochronous (guaranteed bandwidth and latency) data transfers. By applying digital IEEE1394 camera system, we are able to eliminate the frame-grabber stage of processing and directly transfer data at maximum rates of 400 MB/sec. IEEE1394 general purposed CMOS cameras (Prosilica CV640, 659 x 494 4.65 μm square pixels) were chosen for screen monitor application. There is no frame grabber or additional power supply required. Frame rates of up to 30 fps can be achieved adequately in the full frame.

The GigE Vision standard from the Advanced Imaging Association (AIA) is a new interface standard for the latest vision of cameras with high performance. GigE Vision combined features of high data rates (required for uncompressed video or imaging applications), ubiquitous computer interface hardware, low cost cabling, and widespread popularity makes Gigabit Ethernet an attractive interface option for accelerator applications. The GigE Vision standard including of both the hardware interface standard (Gigabit Ethernet) and the communications protocols, can be utilized for controlling and communication of cameras. The GigE Vision camera control registers are based on a command structure called GenICam which is administered through the European Machine Vision Association (EMVA). GenICam seeks to establish a common camera control interface so that the third party software can communicate with the cameras from various manufacturers without customization. GenICam is incorporated as a part of the GigE Vision standard. GigE Vision is analogous to FireWire's DCAM (IIDC) and beneficial to facilitate system integration and thus reduce costs.

APPLICATIONS OF IEEE-1394 AND GigE VISION CAMERA AT TLS

FireWire camera was adopted for synchrotron radiation at the booster synchrotron and the storage ring very successful since 2003 [1]. Qimaging QICAM 12 bits camera was selected to capture synchrotron radiation profile. Parameters of the camera are completely programmable so that this is very useful to accommodate with various beam conditions and effectively increase reliability.

FireWire CMOS camera was adopted for the transport line screen monitor since 2004 [2] as shown in Fig. 1,2 and 3. Functionality is satisfactory while the only problem is less reliability near the injection kicker of the storage ring. The problem might be caused from bad grounding of the kickers and the cameras which might be hanged due to the noise induced by the long IEEE-1394 cable. After

the kicker grounding improved and the camera with IEEE-1394B fibre interface replaced, the reliability is increased drastically.

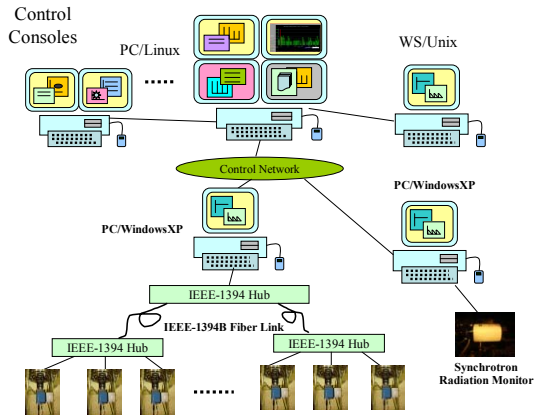

Figure 1: Topology of the IEEE-1394 camera installation.

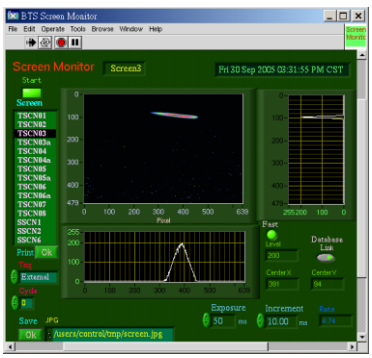

Figure 2: The VI for transport line screen monitors operation.

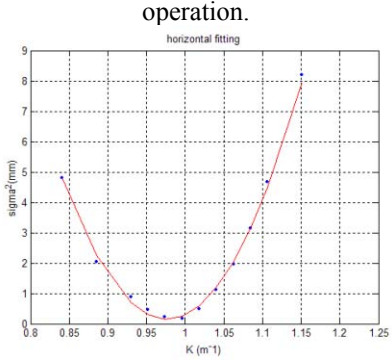

Figure 3: Example of transverse beam emittance measurements at transport line by using quadrupole scan method. Fitted emittance is ε_x = 238 nm-rad.

The new GigE camera interface is also applied for preliminary evaluation. Set up of the experiment is shown in Fig. 4. Figure 5 shown a typical profile measurement result. Emittance is measured by the quadrupole scan method in the exit of the 50 MeV linaer accelerator. The beam profile as a function of one nearest quadrupole strength was measured as shown in Figure 6. The profile image is captured and analyzed by using Matlab scripts. Emittance will be immediately adjusted and reduced from the machine parameter by the measured data. Performance and reliability of the GigE Vision camera is evaluated. Since the camera is installed near the klystron modulator, the camera is occasionally hanged during klystron power off. A remote power reset will be applied as a solution of this problem.

Figure 4: A GigE Vision camera installed at exit of 50 MeV linaer accelerator for test.

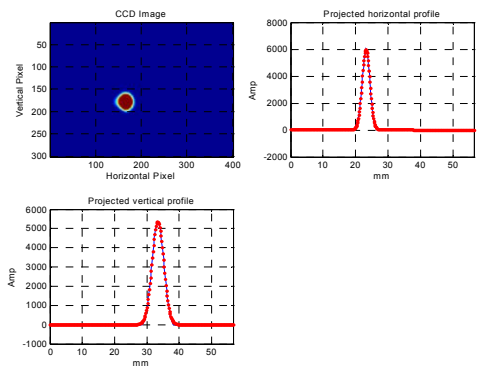

Figure 5: Profile measured by the GigE Vision camera.

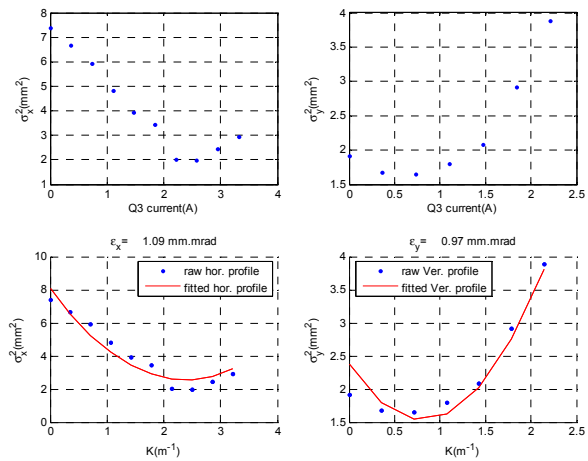

Figure 6: Measured horizontal and vertical emittance of the 50 MeV lianc by quadrupole scan method. The fitted normized emittance is ε_x = 1.09 mm-mrad and $\boldsymbol{\varepsilon_y}$ = 0.97 mm-mrad in the horizontal and vertical respectively.

EXPERIENCES OF IEEE-1394 AND GbE VISION CAMERA FOR BEAM DIAGNOSTIC APPLICATION

Both of IEEE-1394 cameras and GigE Vision cameras were tested and applied for several diagnostics for the TLS. Some of the experience is summarized in the following paragraphs.

Control System Integration

To simplify the control system integration, a PC/ running Windows/XP was adopted for FireWire camera server as well as GigE Vision camera. There are few drivers supporting both kinds of interface. The standard DCAM camera driver with LabVIEW and other COTS softwares are supported for FireWire camera. The GigE standard camera driver is being developing now. We use non-standard windows XP/Linux camera driver in this report. User interface was written by LabVIEW. The user interface was developed by LabVIEW and Matlab to support various experiments and remote controls.

Cabling

Maximum copper cable length in the FireWire is around 10 meters with full speed. Hub is essential to extend the length of links. For long haul transmission, IEEE-1394B fibre link can be used. This fibre link is also useful for hostile EMI environment near the kickers. The connection for GigE Vision camera can be CAT5e or CAT6 Ethernet cables with RJ-45 connectors up to 100 meters. Gigabit Ethernet provides high performance camera interface to convey control and image data up to 100 meters long using inexpensive CAT5e or CAT6 cabling. Such long cable lengths are not generally possible with other kinds of interface. For the hostile EMI environment, this kind of connection sometimes will deteriorate the camera reliability. Remote power reset is still essential for these cases.

Operation Performance

Performance of the IEEE-1394 and GigE Vision camera seems not bad. Exposure condition can be controlled remotely and as a consequence, it is very helpful for diagnostic applications with various beam conditions. Image quality is good and irrelevant to the distance of links.

Reliability and Measure

Reliability of FireWire camera and GigE Vision camera seems no big difference. The FireWire primary problem is resulted from the rigidity of the connectors and power supply problem between several layers hub. At the initial stage, the unreliability is mainly come from the bugs of the device driver. After problem solved, the reliability seems not bad. However, there is a micro-controller inside. If unintentional high field noise due to a fault of the grounding of kickers causes camera hanging, it is no way to recovery without power reset [3]. To remedy this disadvantage, a remote power on/off control was implemented.

Radiation Damage

The FireWire cameras have been operated over two years, there are no severe damages observed. Similarly, the GigE Vision cameras have been operated over 6 months, no observable radiation damage was observed. So, the radiation damage is similar with the analogue camera.

SUMMARY

FireWire camera and GigE Vision cameras are tested at TLS for several diagnostic applications. Their setup allowed images to be transmitted digitally, removing the request from cumbersome frame grabbers and coax switches. Furthermore, the simplicity of triggered acquisition made this mode be a standard rather than a special case. Both FireWire cameras and GigE Vision cameras with the TLS control system allow seamless integration with control room displays and are easy to access image for various machine studies. Experiences gain form these experiments and image quality are excellent. Varying exposure time is very helpful to increase the dynamic range. The only shortage is less reliable than the analogy camera. This can be modified by the aid of reset power reset. Both kinds of interfaces will be suitable for the newly proposed in the 3 GeV Taiwan Photon Source.

REFERENCES

[1] C. H. Kuo, et al., “The Profile Measurement of Synchrotron Radiation Monitor in NSRRC”, 9th ICALEPCS Int. Conf. on Accelerator & Large Expt. Physics Control Systems, Gyeongju, Korea, 13 - 17 Oct 2003, 563 (2003).

[2] C. H. Kuo, et al., “Automatic Beam profile Measurement for the Beam Transport Line”, 10th ICALEPCS Int. Conf. on Accelerator & Large Expt. Physics Control Systems, Geneva, 10 - 14 Oct 2005, PO2.011-2 (2005).

[3] Thomas, C. A. and Rehm, G. DIAMOND Storage Ring Optical and X-ray Diagnostics. In Proc. BIW 2004, Knoxville, Tennessee, 2004.

[4] L. Catani, et al., “A Large Distributed Digital Camera System for Accelerator Beam Diagnostics”, Rev. Sci. Instrum. 76, 073303 (2005).

THE BEAM POSITION SYSTEM OF THE CERN NEUTRINO TO GRAND SASSO PROTON BEAM LINE

T. Bogey, R. Jones, CERN, Geneva, Switzerland

Abstract

The CERN Neutrino to Gran Sasso (CNGS) experiment uses 400GeV protons extracted from the SPS, which travel along 825 meters of beam line before reaching the CNGS target. This beam line is equipped with 23 BPMs capable of measuring both the horizontal and vertical position of the beam. The final BPM is linked to the target station and due to radiation constraints has been designed to work in air.

This contribution will give an overview of the BPMs used in the transfer line. It will also provide a detailed explanation of their logarithmic amplifier based acquisition electronics, which consists of an auto-triggered sequencer controlling an integrator, the A/D conversion and the Manchester encoded transmission of the digital data to the surface. At the surface the digital data is acquired using the Digital Acquisition Board (DAB) developed by TRIUMF (Canada) for the LHC BPM system.

Results from both laboratory measurements and beam measurements during the 2006 CNGS run will also be presented.

INTRODUCTION

The primary protons beam is extracted from the CERN-SPS with a fast kicker system in two batches of 10.5 µs each, with 50 ms time between the two extractions and travel along the TT40/41 transfer line before reaching the CNGS target. This beam line is equipped with 4 large aperture stripline pick-ups (BPK), 18 button electrode pick-ups (BPG) and one target station stripline pick-up (BPKG). All these monitors are capable of measuring both the horizontal and vertical position of the beam.

The beam position for all of these monitors is obtained using an auto-triggered logarithmic amplifier based acquisition system.

BPM REQUIREMENTS

Table 1: CNGS BPMs requirements

Source	rms uncertainty	Tolerance
BPM (global accuracy)	0.25 mm	± 0.5 mm
Alignment	0.20 mm	± 0.4 mm
Total	0.32 mm	± 0.6 mm
Intensity Range $1x10^{12}$ to $3.5x10^{13}$		

The specification for the CNGS BPM system is described in [1] and summarised in Table 1. The 2 last monitors in the line and the target monitor have tighter constraints, requiring a resolution of less than 0.1mm and an absolute precision of ±0.2mm. This comes from the fact that these monitors are used to centre and keep the beam on the 5mm diameter target rods.

The electronics were therefore designed to comply with the tighter constraints given by these last 3 monitors.

BEAM POSITION MONITORS

Beam Line Position Monitors

The first part of the CNGS extraction line from the CERN-SPS (TT40) is shared between the beams extracted to LHC and those destined for the CNGS target. Since the structure of the beam is different for LHC and CNGS the already developed LHC electronics could not be re-used for CNGS, so requiring additional pick-ups. In order to minimise cost, four existing 33cm long stripline pick-ups were modified as shown in Figure 1, to produce two shorted 11cm shorted stripline pick-ups. This allowed the LHC electronics to be connected to the upstream port and the CNGS electronics to the downstream port.

For the main part of the line (TT41) it was decided to use the same button electrode pick-ups as had already been used in the two 3km SPS to LHC transfer lines. These are 60mm diameter pick-ups using recuperated LEP buttons.

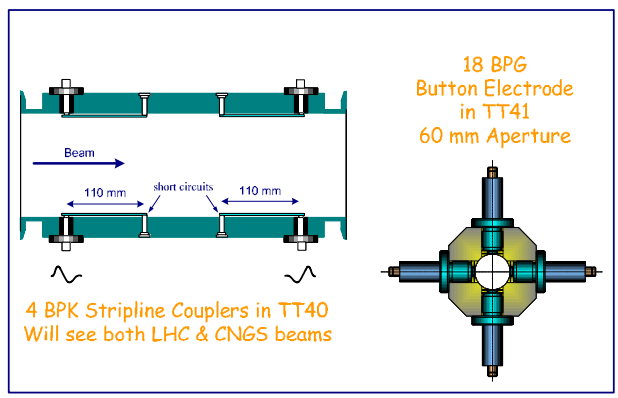

Figure 1: TT40 BPK & TT41 BPG.

Target Station Monitor

The last monitor of the proton line (see Figure 2) is linked to the target station where radiation levels are expected to exceed $5x10^6$ Gy per year. This makes access to this zone impossible, so requiring a simple and robust design. This, along with the fact that it was difficult to obtain vacuum windows capable of withstanding the beam power at this location, led to the proposal to use a stripline pick-up working in air. Tests in both the CERN-PS Booster and the CERN-SPS have shown that such an

electromagnetic monitor is much less susceptible to the effect of air ionisation than an electrostatic button monitor.

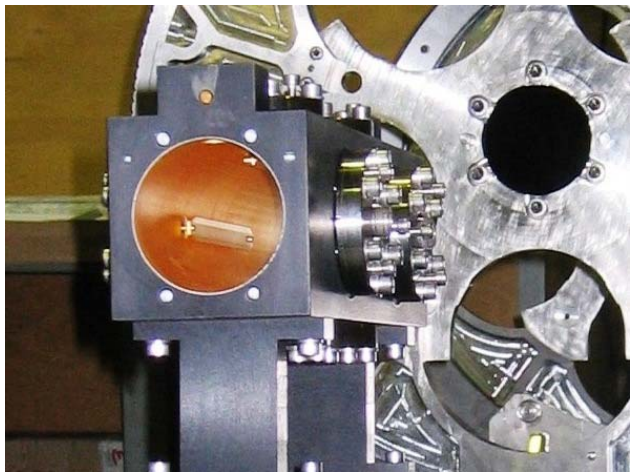

Figure 2: BPKG Target Station Monitor.

Due to the high radiation environment special care had to be taken have taken for this construction. The pick-up body and electrodes were made of an aluminium alloy to lower the remnant radiation. A 30µm gold layer was deposited on the inner surface to maintain a good conductivity while withstanding the effects of radiation. For the outer surface a black penetrating oxide layer treatment was chosen to give thermal stability while withstanding radiation effects.

All 8 ports of the target station monitor were connected to a patch panel outside the target shielding using 3m semi-rigid silicon dioxide cables. The connection of the four downstream ports allows calibration signals to be injected directly into the pick-up, something which is important to study any radiation induced effects.

THE CNGS BPM ELECRONIC SYSTEM

The decision was taken to use logarithmic processing for the CNGS BPM electronics. This was motivated by four main reasons:

- The possibility of basing the system on an existing design used to measure similar beams in the PS to SPS transfer line [2].
- Its low cabling cost as only 1 coaxial cable is required per pick-up.
- Its inherent large dynamic range without requiring gain switching.
- The possibility of auto-triggering the system, making the system much more robust against external timing issues.

The Logarithmic Amplifier Concept

The signal from each electrode is filtered, compressed by a logarithmic amplifier and applied to a differential amplifier [2]. The position response for such a system is given by:

$$\textbf{Position} = [\log(A/B)] = [\log(A) - \log(B)] = (V_{out})$$

Where A and B are the inputs and V_{out} is the voltage after the differential amplifier. This can be shown to give a near linear response close to the pick-up centre, becoming non-linear as the position moves further away from the centre (see figure 4).

The Front-End Design

A schematic of the front-end is shown in Figure 3. It is based on an Analog Devices Limiting-Logarithmic Amplifier (AD8306) and a CERN designed fast switchable slope integrator.

The incoming signals are first split, with one part used for the autotrigger detection and the other filtered using a 200MHz bandpass filter (the frequency corresponding to the 200MHZ frequency structure of the beam). The filtered signals pass though the logarithmic amplifiers and are either combined using differential amplifiers to give a position dependent signal or summed to give an intensity dependent signal. These three signals (horizontal & vertical position and total intensity), are then integrated before being converted into digital signals using a four

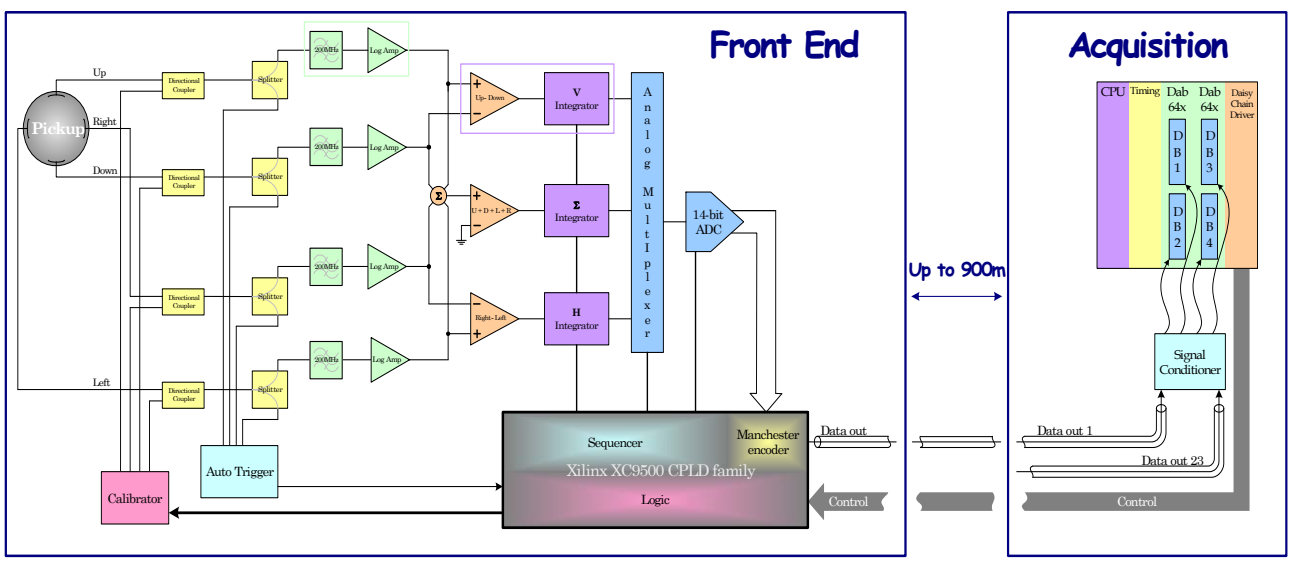

Figure 3: Front End electronics

channel simultaneous sampling 14-Bit ADC (AD7865).

An In-System Programmable CPLD (Xilinx XC95144) is used for the control of the card and contains the following modules:

- Auto trigger conditioner
- Integrator gate & reset generator
- ADC timing conversion sequence controller
- Manchester encoder
- Calibration trigger generator
- General control

The resulting digital data is Manchester encoded and serially transmitted from the front-end to the surface via a coaxial cable link.

The Digital Acquisition System

The digital acquisition system was based around the standard LHC BPM digital VME64x acquisition card (DAB64x), developed by TRIUMF, Canada [3]. Each of these cards is equipped with two mezzanine cards, with each mezzanine card capable of processing the data from six front-ends. Each mezzanine card performs the Manchester decoding of the data from up to six front-ends, and uses a Xilinx FPGA to take care of the timing and to convert the data it into the correct format for the DAB64x.

In the final CNGS configuration, two DAB64x cards, each with two mezzanines process the data from the 23 CNGS pick-ups.

RESULTS

Laboratory Results

Figure 4 shows the effect of combing logarithmic amplifier electronics with an electrostatic button pick-up. It can be seen that in this case the non-linearities are of opposite sign, leading to a resultant function which is linear to better than 1% over much of the aperture.

This was confirmed in a test-bench set-up using the final electronics, where an antenna was displaced along one axis in a replica of the CNGS button pick-up (Figure 5). It can be seen that without applying any linearisation function the position error stays below 1% over one third of the aperture.

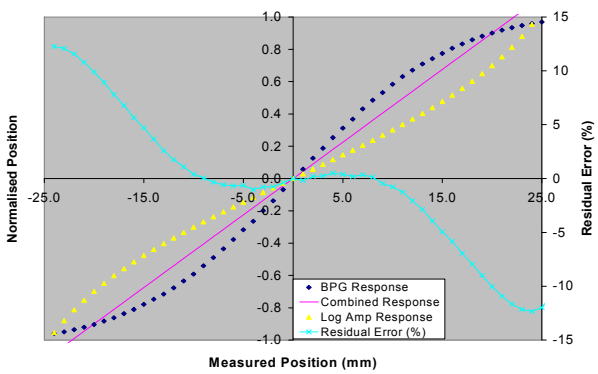

Figure 4: Combining a Button Pick-Up with a LogAmp Acquisition System.

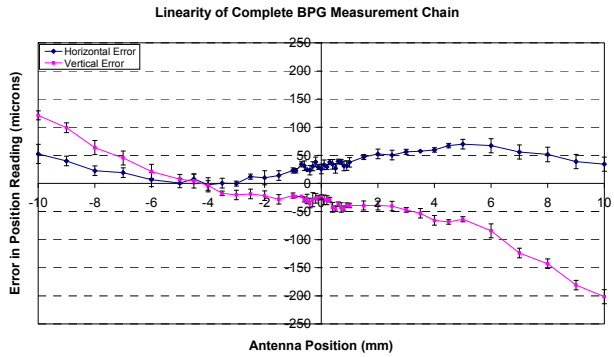

Figure 5: Laboratory Results of BPM System.

First results with Beam

Figure 6 shows the performance of the target station monitor that was used to align the beam on the target. It can be seen that in the vertical plane the measured rms stability of 15 µm is close to the noise level of the electronic system (1 ADC bit ~ 7 µm). In the horizontal plane, however, the performance is dominated by beam stability, mainly coming from the non-reproducibility of the horizontal SPS extraction kicker.

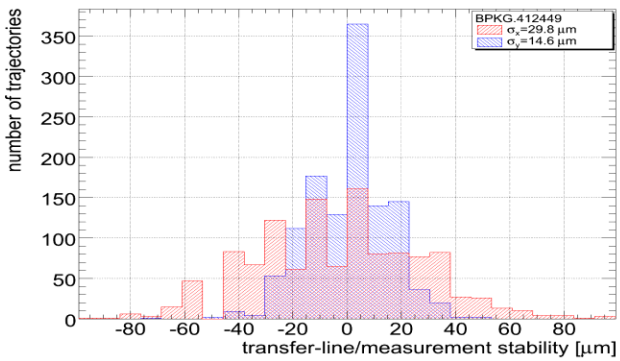

Figure 6: Stability of the target station BPM reading.

CONCLUSIONS

The logarithmic amplifier based CNGS beam position measurement system was successfully commissioned during the 2006 CERN-SPS run. A global accuracy for nominal beams of better than 250 µm over ± 10mm was achieved with a resolution at the 20 µm level [4].

REFERENCES

[1] J-P. Koutchouk, Beam Measurements for the CNGS Beam Line, CERN EDMS No. 376330.

[2] H. Schmickler, G. Vismara, A logarithmic processor for beam position measuements applied to a transfert line at CERN, DIPAC2001 PM10

[3] VME64x Digital Acquisition Board for the LHC trajectory and closed orbit system, LHC-BP-ES-0002, CERN EDMS No. 410295.

[4] T. Bogey et al, Operational Experience with the CNGS beam position monitoring system, NBI2006 http://proj-cngs.web.cern.ch/proj-cngs/Publications/Publications.htm

AN RF DEFLECTOR FOR THE LONGITUDINAL AND TRANSVERSE BEAM PHASE SPACE ANALYSIS AT PITZ*

S.Korepanov#, M.Krasilnikov, F.Stephan,DESY-Zeuthen, Germany,
D.Alesini, L.Ficcadenti, INFN/LNF, Italy

Abstract

A detailed characterization of the longitudinal and transverse phase space of the electron beam provided by the Photo Injector Test Facility at DESY in Zeuthen (PITZ) is required to optimize electron beam for Free-Electron Laser (FEL) applications. By means of a RF deflector the transverse slice emittance and the longitudinal phase space can be analysed. The analysis of the prospect diagnostics shows the possibility to achieve a time resolution of about 0.5 ps, and a longitudinal momentum resolution of 10^{-4}. The influence of the deflector on the longitudinal beam phase space is analysed.

INTRODUCTION

The main research goal of PITZ is the development of electron sources with minimized transverse emittance [1].

At PITZ2 the application of an RF deflector is planned. The deflector position is about 9 m from the gun. The next 3.5 m of space are taken by a tomography module, see Fig.1. At about 15.5 m a spectrometer based on a dipole magnet is positioned. The RF deflector in combination with the tomography module gives possibility to analyse the transverse emittance of longitudinal slices. Using the RF deflector and a dispersive arm the longitudinal beam phase space can be completely reconstructed.

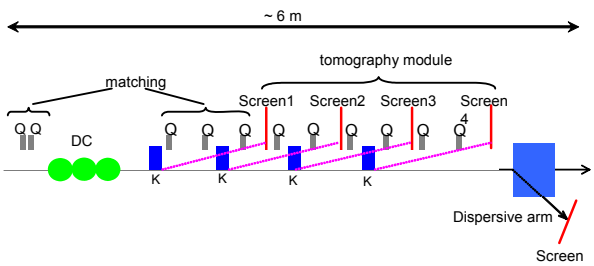

Figure 1: Prospect diagnostic for the beam phase space analysis.

We expect the following beam parameters at PITZ2: bunch length 23 ps, transverse size at the point of the deflecting cavity 3…5 mm (0.7-1.2 mm RMS), slice emittance - about 0.7pi mm mrad, longitudinal momentum 32 MeV/c. The diagnostics components have to provide a time resolution down to 0.5 ps (40 slices), an emittance measurement precision <10% and a precision of the longitudinal momentum spread measurements for 0.5 ps slices of about 1.4 keV/c.

RF DEFLECTOR

A travelling wave structure was chosen for the RF deflector. It has small field filling time. That permits to analyse single bunch without distortion others. In Fig. 2 you see the general view of the cavity. It has two couplers: input and output, and two pump port on the opposite side for symmetry reasons that reduce the nouniformity of the field distribution in the coupler cells.

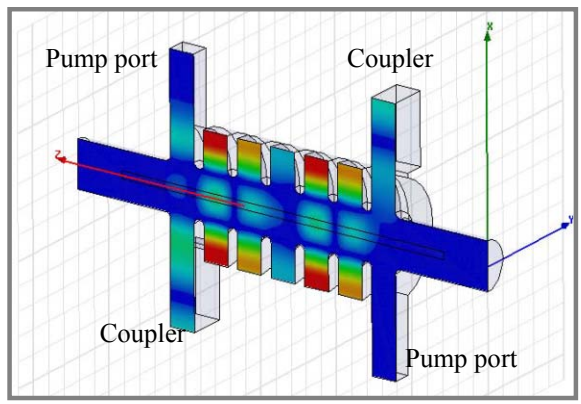

Figure 2: RF deflector based on travelling wave.

The RF deflector has to provide a deflecting voltage up to 1.8 MV and should cause minimal distortion of the beam phase space in the measurement directions. In this paper we compare two travelling wave structures operating at 1.3 GHz and 3.0 GHz frequencies. In table 1 you can find the RF power needed for the diagnostics.

Table 1: RF power and corresponding deflecting voltage needed for both kind of diagnostics

	1.3 GHz	3.0 GHz
Longitudinal phase space measurements	1.7 MW (0.8 MV)	0.35 MW (0.35 MV)
Slice emittance measurement, resolution 0.5 ps	9.1 MW (1.8 MV)	1.7 MW (0.8 MV)

BEAM LONGITUDINAL MOMENTUM DISTORTION IN THE RF DEFLECTOR

The correct using of the RF deflector requires a negligibly small influence from the RF fields on the measured parameters (transverse slice emittance (X direction), longitudinal phase space (Z direction)). Let us analyse the longitudinal momentum distortion.

Linear Longitudinal Momentum Distortion

The transport matrix of an ideal RF deflecting cavity looks like:

$$\begin{pmatrix} y \\ y' \\ z \\ dp_z \end{pmatrix} = \begin{pmatrix} 1 & 0 & 0 & 0 \\ 0 & 1 & a & 0 \\ 0 & 0 & 1 & 0 \\ a & 0 & 0 & 1 \end{pmatrix} \cdot \begin{pmatrix} y_0 \\ y_0' \\ z_0 \\ dp_{z0} \end{pmatrix} \quad (1)$$

dp_z – energy spread in relative units.

From Panofsky-Wenzel theorem we can find the relation between the transverse deflecting voltage and the longitudinal electrical field gradient in the RF deflector:

$$V_y = i\frac{c}{\omega}\int \nabla_y E_z e^{i\frac{\omega}{c}z}\,dz \quad (2)$$

where ω is the RF frequency, c - the velocity of light, y - the deflecting direction, z - the longitudinal position in the deflector, E_z - the longitudinal electric field, V_y - the integrated transverse deflecting voltage and the integration is performed over the deflector length.

Using the Panofsky-Wenzel theorem we can find the change of the energy for a single particle after passing the deflector:

$$dp_z = \frac{dE}{E} = \frac{\omega}{c}\cdot\frac{V_{y\max}}{E/e}\cdot y_0 \quad (3)$$

where V_{ymax} is amplitude value of the deflecting voltage, E – particle energy.

Let's look at the couple of deflector and a screen, Fig.3.

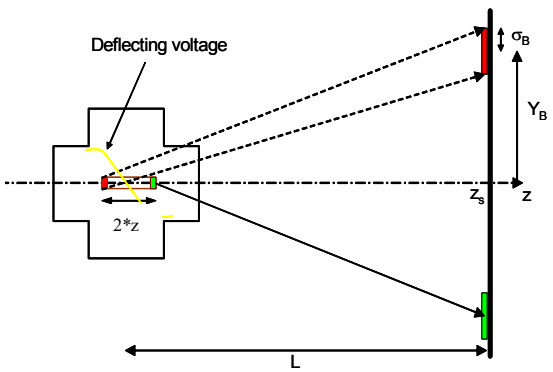

Figure 3: The principal of the RF deflector work.

The vertical beam size is:

$$y_B = \frac{2\cdot\pi\cdot f\cdot L\cdot z_0\cdot V_{y\max}}{c\cdot E/e} \quad (5)$$

The number of slices which we can resolve is described by the formula:

$$N_{slices} = \frac{y_B}{y_0} = \frac{2\cdot\pi\cdot f\cdot L\cdot z_0\cdot V_{y\max}}{y_0\cdot c\cdot E/e} \quad (6)$$

From the last expression we can derive V_{ymax} and put it in formula (3). Finally we have following expression for energy spread:

$$dp_z = \frac{dE}{E} = \frac{N_{slices}\cdot y_0^2}{L\cdot z_0} \quad (7)$$

So we have shown that the energy spread doesn't depend on the RF frequency and beam energy. Let us continue the linear analysis for a 1.3 GHz deflector.

For PITZ two cases of RF cavity operation are presented, see Table 1. They require to different distances L from the deflector to a screen. For longitudinal phase space analysis in the dispersive section L~6m. The second case is transverse slice emittance measurements in the tomography module and L_{min} ~ 2.5m. At PITZ we want to use the maximum possible screen size in vertical direction – about 30 mm. That means that the beam size at the output of the deflector (L_deflector~1m) is already different from the entrance. For the case of longitudinal phase space diagnostic the maximum vertical beam size at the end of the deflector is about 1.2 mm, for the case of transverse slice emittance measurements – up to 7.5 mm. For the outermost slice we have a maximum momentum distortion according to Fig. 4.

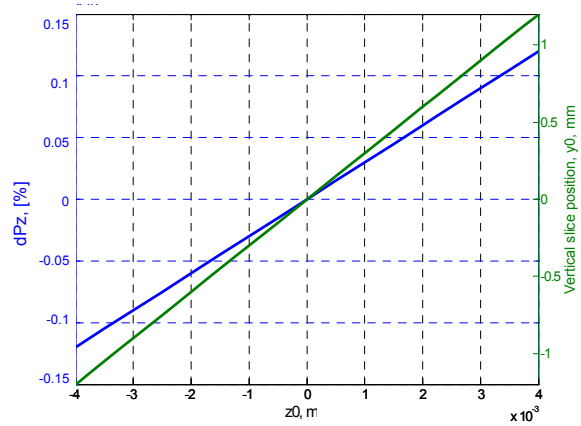

Figure 4: Momentum distortion for different slice positions along the bunch (blue line), Vertical slice position (green line). Longitudinal phase space analysis diagnostic.

For the case of longitudinal phase space diagnostic the distortion of the longitudinal energy is maximum for the first and the last slices, ***dP_z(linear)~1.2*10^{-3}*** (for Prf=1.7MW). For the transverse slice emittance measurements we can show that the momentum distortion in relative units ***dP_z(linear) ~ 27*10^{-3}*** (for Prf=9.1MW) for the first and the last slices.

For measurements of the longitudinal phase space using the RF deflector and the dipole magnet we can unfold the original momentum distribution from the one introduced by the RF deflector. The energy spread of the single bunch can be described by:

$$\sigma_E^{'2} = \sigma_E^2 + \left[\frac{\omega}{c}V_{y\max}\cos(\omega t)\right]^2\sigma_y^2 = \sigma_E^2 + \Delta\sigma_{defl}^2 \quad (8)$$

where σ_E is the slice energy spread before the deflector and σ_y is the average rms transverse slice dimension in the deflector. The last equation is strictly valid if the y and E plane of each slice are uncorrelated. The slice energy spread then can be "reconstructed" knowing the deflecting voltage, the frequency of operation and the average transverse beam dimension (σ_y) in the deflector:

$$\sigma_E = \sqrt{\sigma_E^{'2} - \left[\frac{\omega}{c}V_{y\max}\cos(\omega t)\right]^2\sigma_y^2} \quad (9)$$

Nonlinearity of the Electro-Magnetic Fields in the RF Deflector

According the linear theory ([2]) the *Ez* component of the electrical field along the axis X for fixed Y and Z coordinates is constant. We have made numerical calculations of the real electro-magnetic field distribution in the RF deflector for the two different frequencies 1.3 GHz and 3.0 GHz starting with the cavities geometry and using the CST MicroWave Studio software. We were comparing the E_z distributions along the axis X at fixed Y position. In the Fig.5 the relative values $E_z(x,y=1mm,z)/E_z(x=0mm,y=1mm,z)$ for two different TW structures are shown. The black lines show the region of the bunch.

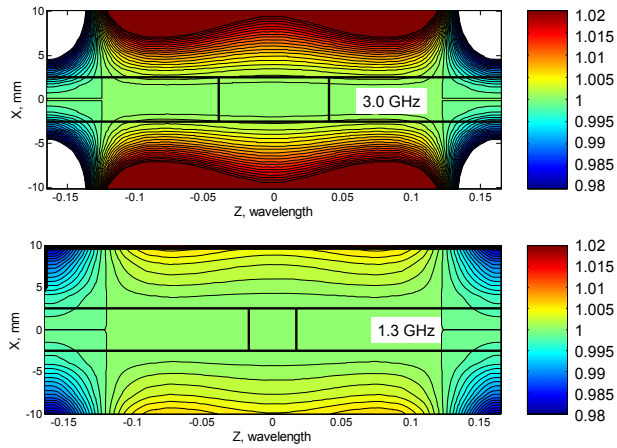

Figure 5: Relative values of E_z.

One can see that in the case of the 3.0 GHz TW structure the deviation of E_z from constant is up to several percents. For the 1.3 GHz structure this deviation is smaller – smaller then one percent.

This effect of not constant Ez dependence vs X can not be taken into account during the longitudinal phase space measurements (see previous paragraph). The final result of the momentum distortion due to this nonlinear effect we can estimate:

$$dE / E_{final} = dE / E + dE / E \cdot \delta \qquad (10)$$

where $\frac{dE}{E} = \frac{N_{slices} \cdot y_0^2}{L \cdot z_0}$ - linear momentum distortion for the off axis particles (in Y direction), δ - coefficient corresponding to the nonuniformity of *Uz* in X direction, *Uz* = ∫*Ez(x,y)dl* – integral along the slice trajectory in the cavity.

To estimate the value of δ we can use the distributions of the dEz (look at the Fig. 5). The beam size in X direction is about 3-5 mm (full size). For the 3.0GHz cavity nonuniformity of Ez is about 1%, so we can estimate $\delta \sim 0.02$. For the 1.3 GHz cavity δ is less than *0.005*.

Let us make the estimations of the momentum distortion for 1.3 GHz and 3.0 GHz structures for the longitudinal phase space diagnostic (large distance deflector-screen ~6m , vertical beam size on the exit of the cavity *y0*=1.2 mm, longitudinal half bunch length *z0* = 4 mm):

$$dp_z(nonlinear_x) = /1.3GHz/ = \frac{N_{slices} \cdot y_0^2}{L \cdot z_0} \cdot \delta_{1.3GHz} = \frac{20 \cdot (1.2 \cdot 10^{-3})^2}{6 \cdot 4 \cdot 10^{-3}} \cdot 0.005 = 0.6 \cdot 10^{-5}$$

$$dp_z(nonlinear_x) = /3.0GHz/ = \frac{N_{slices} \cdot y_0^2}{L \cdot z_0} \cdot \delta_{3.0GHz} = \frac{20 \cdot (1.2 \cdot 10^{-3})^2}{6 \cdot 4 \cdot 10^{-3}} \cdot 0.01 = 1.2 \cdot 10^{-5}$$

Another nonlinear effect comes from the finite length of the bunch. In Fig.6 the accelerating voltage along the bunch is shown in relative units.

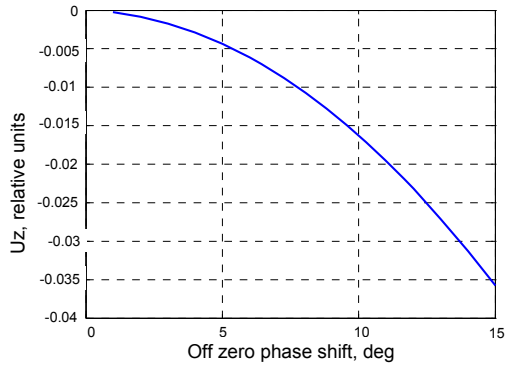

Figure 6: *Uz* vs off phase.

For different slices along the bunch we have different RF phases. The difference of *Uz* between the center and the edge of the bunch is about 3.5 % for 3GHz structure and ~0.5 % for 1.3 GHz cavity. That gives the maximum momentum distortion for the first and last slices:

$$dp_z(longitudinal) = /3.0GHz/ = dp_z(linear) \cdot 0.035 = 3.6 \cdot 10^{-5}$$

$$dp_z(longitudinal) = /1.3GHz/ = dp_z(linear) \cdot 0.005 = 0.6 \cdot 10^{-5}$$

The sum of both processes (transverse nonlinear *Ez* distribution and longitudinal nonlinear *Ez* distribution) is:

$$dp_z(sum) = /3.0GHz/ = \sqrt{dp_z(nolinear_x)^2 + dp_z(longitudinal)^2} = 3.8 \cdot 10^{-5}$$

$$dp_z(sum) = /1.3GHz/ = \sqrt{dp_z(nolinear_x)^2 + dp_z(longitudinal)^2} = 0.85 \cdot 10^{-5}$$

DISCUSSION

The study of 1.3 GHz and 3.0 GHz cavities for phase space diagnostics at PITZ shows that longitudinal distortions in the RF structures are not expected from linear theory. But nonlinear E_z distribution in the cavity due to the real geometry of the TW structures will cause longitudinal distortions.

The analysis shows that a distortion of a single slice in a 1.3GHz structure sums up to dpz~$0.85 \cdot 10^{-5}$ and for a 3.0GHz structure yields dpz~$3.8 \cdot 10^{-5}$. $4*10^{-5}$ corresponds to the value of the original momentum spread in a slice (0.5ps) and the minimum non-correlated momentum spread is ~$2*10^{-5}$ in relative units. The distortion from the 3 GHz cavity would be of the same order resulting in worse resolution during longitudinal phase space measurements.

REFERENCES

[1] F.Stephan, D.Kraemer, I.Will and A.Novokhatski, Proc. FEL2k, Durham, USA, August 2000.

[2] O.H. Alternmueller et. al. "Investigation of traveling-wave separators for the Standford Two-Mile Linear Accelerator" SLAC-PUB-17, 1963.

PHOTO INJECTOR CATHODE LASER BEAM INTENSITY AND POINTING STABILITY DIAGNOSTICS.*

Y. Ivanisenko†, G. Asova, J. Bähr, S. Korepanov, M. Krasilnikov,
B. Petrosyan, F. Stephan, DESY, Zeuthen, D 15738, Germany
O. Kalekin, Physikalisches Institut der Universität Erlangen - Nürnberg, Erlangen, Germany

Abstract

A photo cathode laser with unique parameters is used at the Photo Injector Test facility at DESY in Zeuthen, PITZ [1, 2]. It is capable of producing laser pulse trains consisting of up to 800 pulses with a separation of 1 μs where each laser pulse has a flat-top temporal profile. The knowledge of the laser stability is very important for the emittance measurements procedure. Therefore, a system for monitoring the laser beam intensity and pointing position stability was created at PITZ. It is capable of measuring the laser spot position and pulse intensity for each of the laser pulses in the train using a quadrant diode and a photomultiplier tube, respectively. Taking into account the laser beam spot transverse intensity distribution measured by a CCD camera allows to study the position of the laser spot on the photo cathode with a resolution of 8.3 um. Laser intensity measurements can be done for a wide dynamical range of intensities due to the tuneable photo multiplier tube gain. The first experiments with the new system show very small laser spot position jitter on the cathode surface of about 20 μm and laser intensity fluctuations of about 14 %.

INTRODUCTION

PITZ is a test facility for photoinjectors designed for FEL operation. The PITZ group develops the measurement methods and the equipment for the injector characterization.

PITZ operates at 10 Hz repetition rate, and in each cycle the injector can produce up to 800 electron bunches with an emission frequency of 1 MHz. The generation is based on electron photoemission from a Cs2Te cathode impinged by laser light of 262 nm wavelength. Formation of a flat-top laser pulse of about 18 ps length is the initial process [2]. Then the laser light is transmitted from the laser table to the tunnel through a 22 m optical beam line [3] and enters the vacuum through the input window. It is directed to the cathode by a mirror.

* This work has partly been supported by the European Community, contract number RII3-CT-2004-506008 and 011935, and by the 'Impuls- und Vernetzungsfonds' of the Helmholtz Association, contract number VH-FZ-005

† yevgeniy.ivanisenko@desy.de

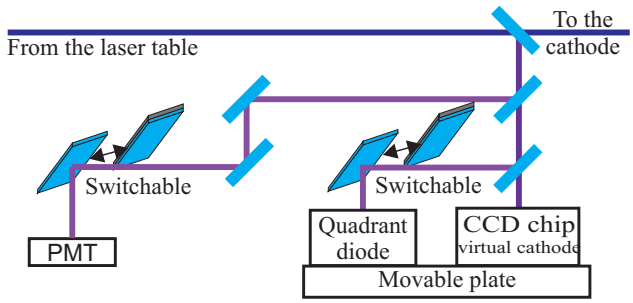

Figure 1: Optical scheme of the laser beam stability diagnostics

DIAGNOSTICS SYSTEM

On the path of the laser beam there is a beam splitter, which directs 2% of the light to the laser beam diagnostics system.

Before the entrance to the laser beam diagnostics there is a beam limiting aperture, which makes the laser spot size fixed at the cathode. The transverse displacement of the laser beam before the aperture will result in the laser beam center of gravity movement, if the intensity profile is non-homogeneous along the displacement direction. This change is detected then by the quadrant diode - one should observe a repartition of the quadrant diode signals.

The measurement system scheme is shown in Fig. 1. The quartz beam divider plates are inserted before the detectors in order to match the input intensity range and the linear response range of the devices. A CCD matrix chip is situated in such a way, that the optical path length for the laser radiation is the same as the path to the photocathode. The camera is used for the transverse laser beam profile measurements. The quadrant diode is used for the laser beam pointing position monitoring - the software analyzes the transverse profile from the CCD together with the quadrant diode signals and calculates the laser beam position. Photomultiplier (PM) is used for the laser beam intensity measurements.

INTENSITY MEASUREMENTS

The structure of the pulse train defines that the response time should be much less than 1 μs, and there is a 10^4 dynamical range to cover. The PM module H6780 (Hamamatsu) with integrated high-voltage converter was chosen.

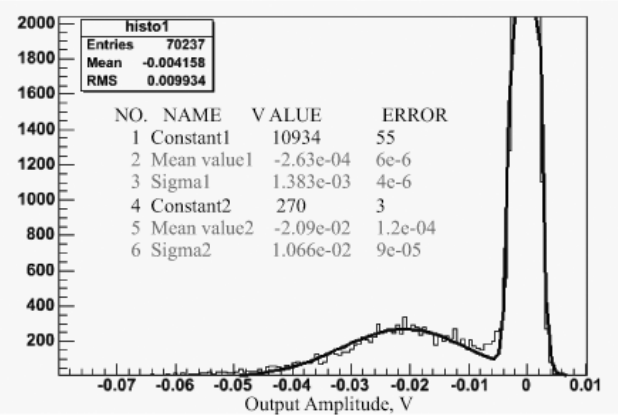

Figure 2: Single photoelectron spectrum

This PM module has a bialkali type cathode with quantum efficiency of 0.8 % at 260 nm and an effective area diameter of 8 mm.

Another UV-sensitive type H6780-03 has a quantum efficiency $\approx$ 4.5%. The gain of the PM can be regulated externally in the range from 100 to 10^6. Maximum linear output current is 100 μA. The photocathode saturation current is 0.1 μA for the bialkali. If the gain is less then 10^3 the linear output is limited by the cathode current, otherwise by the space charge forces in the dynode system during the multiplication.

To analyze the PM response function and noise level a single photoelectron measurement was done. Result of the analysis is shown in Fig. 2. For the PM gain 10^6 the mean response signal is $\approx 21mV$ and the standard deviation is 10 mV.

POINTING POSITION MEASUREMENTS

There is a charge coupled discrete elements detector which is used for the transverse laser beam intensity distribution measurements. It is not fast enough, to satisfy the demands for a parallel to facility operation measurement of the transverse distribution of the individual micropulses in a bunch train.

The idea of a hybrid detector was proposed for the first time and the equipment was developed for PITZ. The laser beam intensity distribution is measured by a CCD matrix. From the distribution it is possible to find a relation between the geometric center and the gravity center of the laser beam, which is also measured by the quadrant diode. Applying this method there is no demand on the laser beam transverse profile cylindric symmetry. The cathode laser beam at PITZ should have a flat-top, radius transverse intensity distribution, which in some cases can be distorted enough in practice (Fig. 3).

For the measurements in our case the PIN quadrant photodiode S4349 (Hamamatsu) was chosen. The response time is $\approx$ 100 ns. The QD has 40% quantum efficiency at 262 nm. Four signals are transmitted to the electronics, they are integrated, digitized and stored on the hard drive. The sensitive area is a square with 3 mm side length. The gap between the quadrants is 0.1 mm. The separating gaps of the CCD matrix are parallel or perpendicular to the gap lines, which divides the quadrant photodiode in four parts.

For the position measurements it is important to have symmetry of the four channels of the quadrant diode. If the condition is not matched at the level of the equipment then it can be corrected by the analyzing software. To check this a test was made for identity of the quads and their electronic circuits. The integrator channels after the test and the recalibration (is done in the analysis software) are found to be within an accuracy of 1%.

Test of the full QD readout showed the same accuracy as the previous test, what means if differences exist they are much smaller than the value of 1%.

The linear response of the quadrants are limited by the electronic interference at the low intensities and by the saturation at the high intensities. That is why it was decided to make a switchable quartz to mirror reflector before the quadrant diode. The mirror reflects ten times more light than the quartz plate does.

Each quadrant integrates the light signal over its surface. The same is done in the software for the four parts of the spatial intensity distribution, which is divided by the virtual gap cross. The cross can be moved with the resolution of 8.3 μm - the dimension of the square pixel of the CCD. The quadrant diode signals are simulated by the software and compared with the normalized real ones. The position of the cross relatively to the intensity distribution corresponds to the minimal discrepancy between the real and simulated values, defined as:

$$X = \frac{S_1 + S_2}{S_1 + S_2 + S_3 + S_4} \quad (1)$$

$$Y = \frac{S_1 + S_4}{S_1 + S_2 + S_3 + S_4} \quad (2)$$

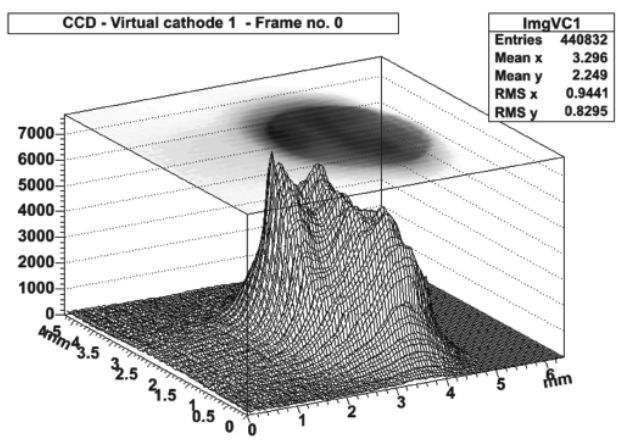

Figure 3: One special example of the laser beam transverse intensity distribution

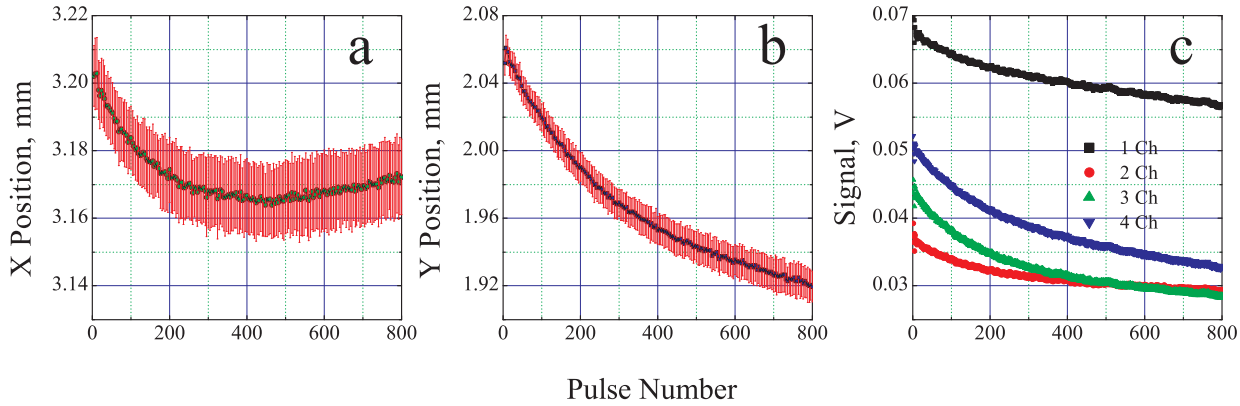

Figure 4: Averaged over 300 trains pulse positions (800 pulses train): a - along the X axis; b - along the Y axis; c - the quadrant diode signals

where X and Y are independent and define the position on the surface. S_i - is a signal from the i^{th} quadrant. Quadrants are numbered clockwise.

RESULTS

The sample of the laser intensity measured for 800 micropulses train averaged over 300 samples is shown in Fig. 5. The intensity jitter amounts 14% (red bars). Furthermore the decreasing about 20% of the laser intensity during the train exists. The accuracy of the measurements depends on the laser intensity level and for the work regime is about 1 %.

The pointing position measurements results are presented in Fig. 4. Each microbunch position in the 800 pulse train is averaged over 300 trains. Standard deviation of a laser beam micropulse position equals to 18 μm for the measurement. The observed position change (drift) during the train (Fig.4 a and b) it is thought to be connected to the laser elements heating - the drift corresponds to the pointing angle deviation inside the laser system of about 10^{-5} rad.

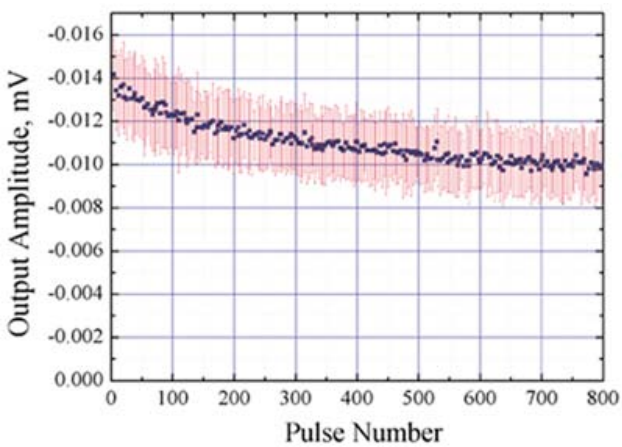

Figure 5: Laser beam intensity measurements. Averaged over 300 trains pulse intensities

CONCLUSIONS

The laser beam intensity and pointing stability diagnostics have been developed at PITZ. They allow to analyze the laser beam microbunches with arbitrary transverse intensity distribution. The laser microbunches emission frequency is up to 1 MHz. The accuracy of the pointing position measurements is 8.3 μm.

The next step is the implementation of the diagnostics in the PITZ control and measuring complex to make these diagnostics routine.

REFERENCES

[1] A. Oppelt et al., Status of the PITZ Facility Upgrade, *LINAC Conference*, MOP020, USA, Knoxville (TN), August $21^{th} - 25^{th}$, 2006.

[2] I. Will, G. Koss, I. Templin, The upgraded photocathode laser of the Tesla Facility, *Nucl. Instr. and Meth.* 541(2005) pp. 467-477

[3] J. Bähr, , Upgrate of the laser beam-line at PITZ, *FEL conference*, MOPP034, Standford, USA, 21-26 August, 2005.

[4] E.H. Bellamy, I. Chirikov-Zorin, S. Tokar and et al., Absolute Calibration and Monitoring of a Spectrometric Channel Using a Photomultiplier, *Nucl. Instr. and Meth.* A339(1994), pp. 468-476.

SYNCHROTRON RADIATION MONITOR FOR ENERGY SPECTRUM MEASUREMENTS IN THE BUNCH COMPRESSOR AT FLASH

Christopher Gerth*
Deutsches Elektronen-Synchrotron DESY, D-22603 Hamburg, Germany

Abstract

Longitudinal bunch compression in magnetic chicanes is used at the Free-electron LASer in Hamburg FLASH for the generation of ultra-short electron bunches. A Synchrotron Radiation monitor (SRM) has been installed behind the third dipole of the first bunch compressor to measure the energy and energy profile of the dispersed bunches. An intensified CCD camera records the emitted SR in the visible and enables one to select single bunches out of a bunch train. The performance of the system has been tested for different accelerator settings. The setup serves as a test bed for the European X-ray Free Electron Laser.

INTRODUCTION

The imaging of Synchrotron Radiation (SR) emitted in bending magnets and wigglers has been utilised successfully for many years in electron and proton storage rings for beam position, beam size and emittance measurements [1]. In short wavelength free-electron lasers (FELs), longitudinal bunch compression is used to produce ultra-short electron bunches with high peak currents. A common scheme for bunch compression, which is foreseen in most of the proposed FEL facilities, is based on off-crest acceleration in combination with magnetic chicanes. These magnetic chicanes are excellent candidates for the imaging of SR in the linear accelerator that drives the FEL.

A synchrotron radiation monitor (SRM) has been installed in the dispersive section of the first bunch compressor BC2 at FLASH. A sketch of the FLASH injector is shown in the top layer of Fig. 1. The rf photo-cathode gun is directly followed by the super-conducting 1.3GHz accelerating module ACC1 which accelerates the electrons to a beam energy of typically 130 MeV. A quadrupole triplet focuses the electron beam into the 4-dipole chicane BC2 and produces a beam waist between the third and fourth dipole.

The large horizontal aperture of the flat vacuum chamber (200 mm $\times$ 8 mm cross section) allows one to operate BC2 at bend angles in the range 15° - 21°. The lower part of Fig. 1 depicts the geometry of BC2 and beam trajectories for bend angles of 16°, 18° and 20°. For optimum bunch compression, the module ACC1 is operated at about 9° off-crest acceleration. The inset of Fig. 1 shows the top view of a particle distribution at the entrance of the third dipole, modelled with the particle tracking codes ASTRA and elegant for 9° off-crest acceleration. The horizontal beam widths is completely dominated by the horizontal dispersion which is about 300 to 390 mm for bend angles in the range 16° - 20° [2]. The tail with higher beam energy takes an inner trajectory and catches up with the head. The imaging of the transverse beam distribution reveals information on the longitudinal energy distribution, t-y correlated beam tilts and the transverse beam size and position as is reported in this paper. The spectral distribution emitted by a single particle with an energy of 130 MeV has been calculated with Schwinger's equation and is shown for 3 bend angles in Fig. 2.

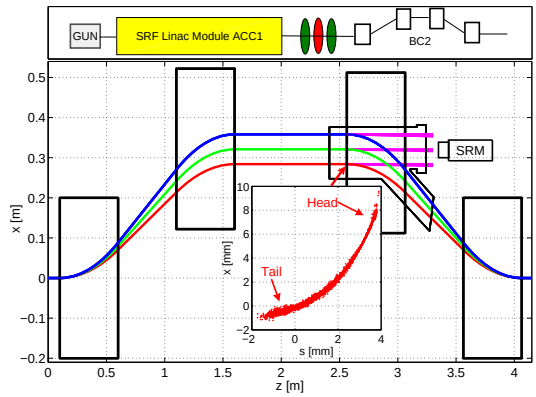

Figure 1: Top: Sketch of the FLASH injector. Bottom: Geometry of BC2 and beam trajectories for bend angles of 16°, 18° and 20°. Inset: Top view of particle distribution at 9° off-crest acceleration in module ACC1 (simulation).

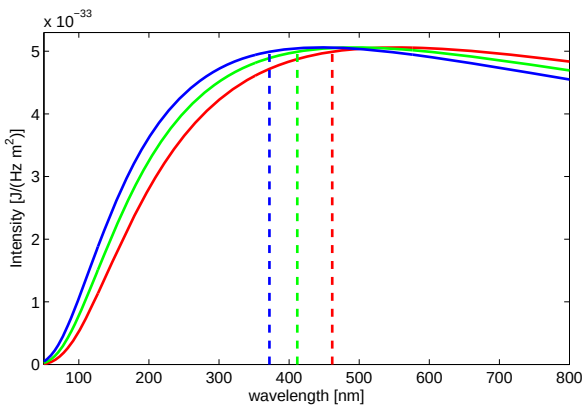

Figure 2: Spectral distribution of the SR calculated with Schwinger's equation for bend angles of 16°, 18° and 20° in BC2. Dashed lines indicate the corresponding critical wavelengths.

* christopher.gerth@desy.de

SR MONITOR SETUP

A new vacuum chamber with a special SR port was installed at the third dipole of BC2 in October 2006. The port houses a flat, Ag-coated laser mirror (Linos, 20 mm $\times$ 30 mm), which deflects the SR emitted at the entrance of the third dipole downwards by 90°. The SR is then imaged by a commercial lens (Sigma, f = 180 mm) and recorded by a gated, intensified CCD camera (PCO, dicam pro) which are located in the accelerator tunnel at a distance of about 1.25 m to the source point. The imaged source size is 10 cm $\times$ 8.2 cm which gives a pixel resolution of 80 μm per pixel. Both the deflecting mirror and the camera system are mounted on movers which can be moved perpendicular to the linac axis to be able to adjust to the electron beam trajectory for different bend angles. The lens is also equipped with a stepper motor to be able to change the lens focus remotely. Figure 3 shows the measured vertical (rms) beam size versus the lens focus. By adjusting the gate and delay of the camera timing, single bunches can be recorded out of a bunch train.

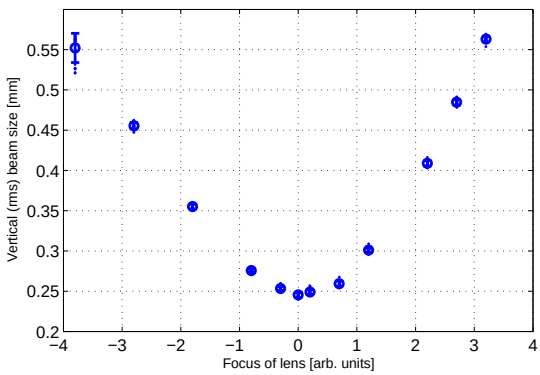

Figure 3: Measured rms beam size vs. lens focus.

A BG39 filter (Schott) in front of the lens was used to cut off wavelengths above 600 nm. The diffraction-limited resolution can be estimated by $0.61(\lambda/\theta)$ for a round aperture, where θ is the half opening angle of the SR. In addition, the depth of field and finite arc length from which the SR is emitted determine the total resolution [3]. The aperture of the lens should be adopted to the opening angle of the SR: A smaller aperture would increase the diffraction and, on the other hand, a larger aperture degrades the resolution due to an increase of the depth of field and finite arc that is imaged. The total resolution has been calculated for 3 f-numbers (5.6, 8, and 11) of the lens and are shown in Fig. 4. The vertical (rms) beam size was measured for these settings. The real beam size can be estimated from particle tracking simulations and beam optics to be 230 ± 20 μm. This value was subtracted quadratically from the measured beam sizes and the result is included in Fig. 4 and in good agreement with the analytical estimates. All measurements presented in the remainder were carried out with a focus and f-number that gave the best resolution of $\sim 90\mu$m.

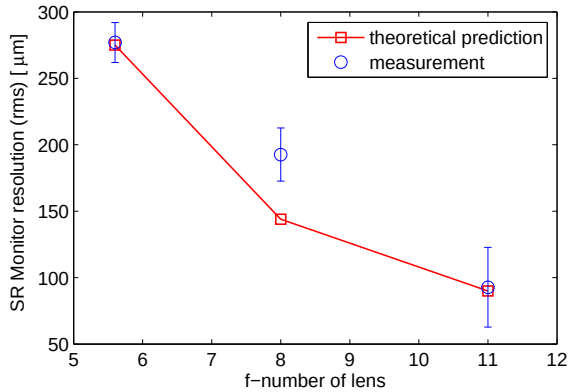

Figure 4: Resolution of SR monitor (for further explanation see text).

Energy Calibration

An energy scale can be established by scanning the dipole current - all dipoles are driven by one power supply - and recording the horizontal beam position. The result of such a scan is shown in Fig. 5 and the linear fit gives a calibration constant of 35.1 pixel/% relative energy deviation.

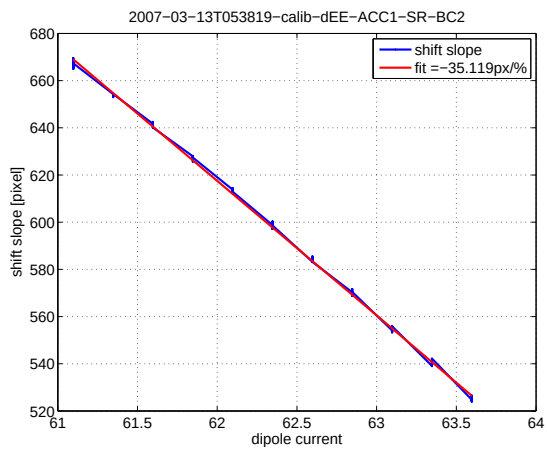

Figure 5: Energy calibration of SR monitor.

Module ACC1 Phase Scan

The left part of Fig. 6 shows the transverse beam distributions measured for 2°, 4°, 6° and 8° off-crest acceleration in module ACC1. The corresponding horizontal beam profiles for which the x axis has been converted to an energy axis are shown in the right part of Fig. 6. As can be seen, the profile first develops a tail towards smaller beam energies until it becomes more symmetric again and starts to shift completely to smaller beam energies. At 8° off-crest phase, which is well within the range for FEL SASE operation, the peak-to-peak energy spread is about 3%. For stable SASE operation it is important to measure and control the rms energy stability to an accuracy better than 10^{-4} which is about 1/300 of the full energy spread.

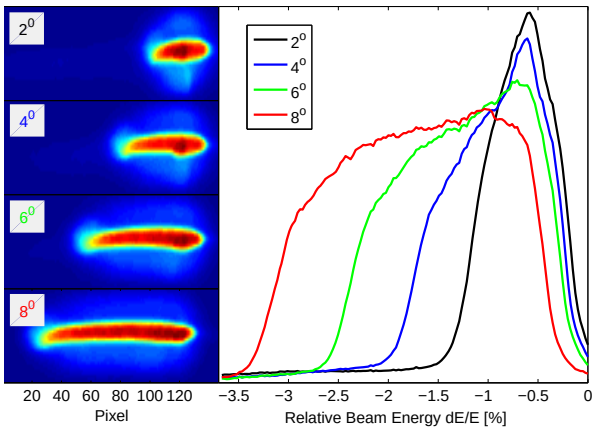

Figure 6: Transverse beam distributions and profiles for 4 off-crest acceleration phases of module ACC1.

JITTER MEASUREMENTS

An energy jitter transforms into a horizontal position jitter via $\Delta x = R_{16}\Delta E/E$ (1st-order transport theory). A relative energy jitter of less than $1\cdot10^{-4}$, which corresponds to a beam position jitter of about 30 μm, is desirable for an operation with a high beam arrival and peak current stability. Figure 7 shows the bunch-to-bunch energy and position stability recorded for the first bunch in a bunch train over a period of 120 s: the measured rms energy jitter is $2\cdot10^{-4}$ and the rms vertical centroid jitter is 10 μm.

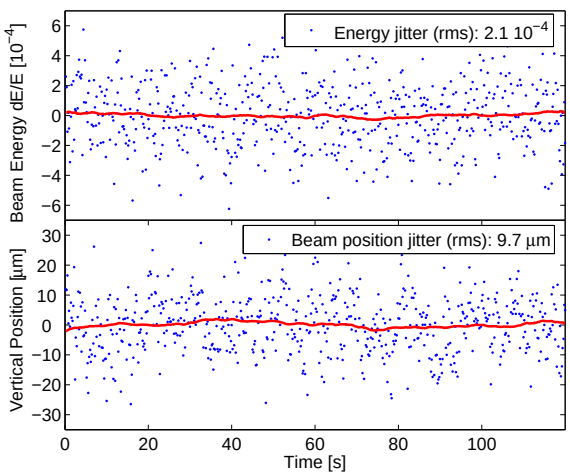

Figure 7: Single-bunch beam energy jitter measured during a SASE run at 9° off-crest acceleration in module ACC1.

By scanning the camera's trigger delay, the energy slope on the bunch train can be measured. This procedure has been used to crosscheck the intra-bunch train energy feedback of the low-level rf [4]. An energy jitter transforms also into a time jitter by $\Delta t = \Delta E/E \cdot R_{56}/c$ which can be calculated from the measured energy jitter $\Delta E/E$ and the knowledge of the longitudinal dispersion R_{56} [2]. A measurement synchronised with an electro-optical tempo-

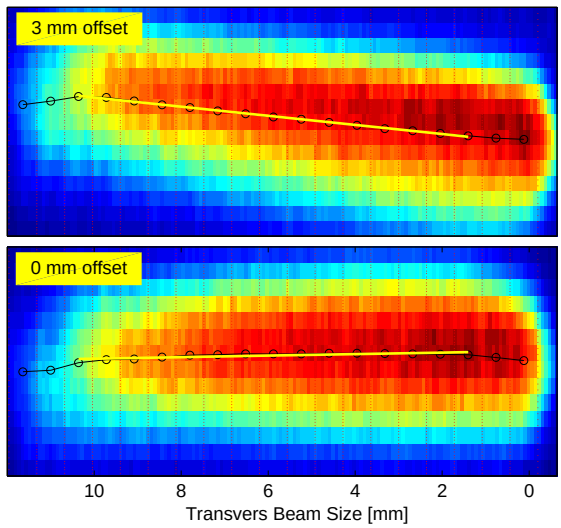

Figure 8: A vertical beam tilt is induced by an offset in the beam trajectory in module ACC1.

ral decoding experiment located upstream of the FEL undulators has indicated that the main contribution of the timing jitter arises in BC2 [5].

TILT MEASUREMENTS

Upstream of the first bunch compressor, where the electron bunches are rather long, careful steering through the accelerating module is important to avoid longitudinal tilts of the beam due to wakefields, coupler kicks or dispersion generated in the cavities. In a test measurement, corrector magnets were used to generate an offset of 3 mm at the exit of module ACC1. As the electron beam is streaked out horizontally in BC2 due to dispersion, a longitudinal t-y correlation transforms into a transverse x-y correlation. The transverse beam distributions for the cases with and without an offset are compared in Fig. 8. The horizontal beam distribution was cut into 19 slices and the mean vertical beam position has been calculated (black dots). A linear fit (solid yellow line) was used to calculate a beam tilt of about 30 mrad.

REFERENCES

[1] G. Kube, "Review of Synchrotron Radiation based Diagnostics for Transverse Profile Measurements", MOO1A03, this conference.

[2] P. Castro, "Beam trajectory calculations in the bunch compressors of TTF2 ", DESY Technical Note 03-01, April 2003.

[3] A. Hofmann and F. Méot, "Optical Resolution of Beam Cross-Section Measurements by Means of Synchrotron Radiation", Nucl. Instr. and Meth. **203**, 1982, 483-493.

[4] H. Schlarb *et al.*, "Beam Based Measurements of RF Phase and Amplitude Stability at FLASH", WEPC01, this conference.

[5] A. Azima *et al.*, to be published in Phys. Rev. ST-AB.

SCREEN STUDIES AT PITZ*

R.Spesyvtsev†, J.Bähr, S.Khodyachykh, L.Staykov, DESY, 15738 Zeuthen, Germany

Abstract

The Photo Injector Test facility at DESY in Zeuthen (PITZ) has been built to test and to optimize electron sources that fulfill the requirements of SASE FEL's such as FLASH and XFEL. Basic properties of the electron beam such as momentum, momentum spread, transverse emittance etc. are determined using measurement of the beam size on YAG or OTR screens. Detailed knowledge of the uncertainties and systematic errors associated with these measurements are important to understand the underlying beam physics. The screen stations consist of a screen setup, an optical transmission line to a CCD camera, and the video data acquisition system. In this paper we make a detailed description of the screen based beam size measurement systems that we use at PITZ and discuss the systematic uncertainties associated with each single element of a system.

INTRODUCTION

The goal of PITZ is to provide electron beam capable for SASE FEL operation. Major requirement for such a source is the lowest transverse emittance for bunch charge of 1 nC. The main components of PITZ [1] are a photo cathode UV laser, a Cs_2Te equipped L-band RF gun, space charge compensation solenoids and a booster cavity for conservation of the small beam emittance. Extensive simulation studies have shown that the projected normalized transverse emittance as small as 1 mm.mrad can be achieved with the current PITZ setup, and even smaller values are expected after the foreseen upgrade with a Cut Disk Structure (CDS) type booster cavity [2], improved laser shaping and high gradient in the gun .

The beam emittance is a product of the beam RMS size and divergence when the correlation between them is negligible. In order to compare emittance of beams with different energies normalization with the relativistic factor $\beta\gamma$ is applied. In PITZ the transverse emittance is measured with the Emittance Measurement SYstem (EMSY) [3] which consists of single slit masks for measurement of divergence and YAG or OTR screens for beam and beamlet size measurements. The momentum is measured using a dipole magnet and a YAG screen. Other types of diagnostics at PITZ are Faraday Cups (FC's) and Integrated Current Transformers (ICT's) for charge monitoring and measurement, and longitudinal phase space diagnostics [4].

Such a small emittance pose stringent requirements for the beam diagnostics with accent on the beam size measurement. The aim is a measurement uncertainty below $10\,\%$. The expected range for the RMS beam sizes is from about 2.5 down to $0.2\ mm$ and as small as 50 μm for the beamlets.

METHODS

At PITZ mainly screens are used for measurements of beam size, but in cases of high beam power wire scanners are foreseen in order to avoid radiation or heat damage to the screens. Each screen is combined with an optical transmission line - consisting of mirrors and lenses, and CCD camera and signal transmission line for storage and visualization of the images.

YAG screen

The Yttrium Aluminum Garnet (YAG) scintillator is widely used for the measurements of transverse beamsize, possible drawbacks are saturation[1] at high beam power, multiple scattering of the electrons etc.. At PITZ two different configurations for the YAG screens are used:

- The screen (typically YAG coated Al or Si plates) is placed with 45° incidence angle to the beam. A mirror placed outside the beam pipe directs the light to the CCD camera. The main contribution to the uncertainty in this case is the depth of field associated with the screen mounting with respect to the optical plane. Those are typically used in the low energy part of PITZ.

- The screen is mounted with normal incidence angle to the beam. There the scintillation layer of YAG powder is coated on the back side[2] of a Si wafer, a mirror placed next to the screen directs the light out of the vacuum chamber where an additional mirror redirects the light to the CCD camera. Since the electrons must pass through the matter (thickness about 0.275 mm Si and a YAG layer of about 5 - 20 μm), they are subject of multiple scattering which contributes to the measurement uncertainty.

OTR screen

At PITZ the Optical Transition Radiation (OTR) screens are mounted with 45° incidence angle, typical characteristics of OTR's are high spatial resolution, narrow angular

* This work has partly been supported by the European Community, Contract Number RII3-CT-2004-506008, and by the 'Impuls- und Vernetzungsfonds' of the Helmholtz Association, contract number VH-FZ-005.

† corresponding author e-mail: spesroma@googlemail.com

[1] It was shown that at PITZ the saturation contribution is negligible [5]

[2] with respect to the electron beam

distribution of the emitted light that implies high light collection, no saturation effects are expected. Drawback is lower light output with respect to the YAG screen and the depth of field problem associated with the 45° geometry.

Optical system

The optical system includes a system of mirrors and an optical lens. Typical aperture of optical system at PITZ is 0.05 rad with a distance between the center of the screen and the image plane of about 0.5 m. The optical resolution of the system depends on the magnification and is found in the range 20 $mm^{-1} \div 50$ mm^{-1} for the magnification range 0.1 - 1.

CCD camera

An important element of a screen station is the CCD camera. Main features of a CCD camera are spatial resolution - defined from the total number of pixels over the size of the projected area in mm, and the digital resolution of the CCD chip defined by the Analog to Digital signal Conversion (ADC) associated with the camera. The CCD chip used at PITZ has dimensions 782x582 pixels with pixel size of 8.3 μm and 8-bit analog to digital converter, placed after a long analog line (40 - 60 m). Major upgrade of the transverse beam measurements diagnostics will be the foreseen installation of new 12 bit digital cameras.

MULTIPLE SCATTERING

To simulate the passage of electrons through the material of the screen in normal incidence angle case, the simulation package GEANT4 [6] was used. Gauss function was taken as initial particle distribution and simulations were done for two different initial RMS sizes of the beam σ = 0.1 mm and σ = 0.5 mm, 1e6 particles were used. The deviation $\delta\sigma = \sigma_s - \sigma$ of the image size σ_s from the original electron beam RMS size σ is shown in fig. 1 as a function of the screen (Si) thickness. This difference gives a systematic uncertainty in the order of 5 % for beam size of 0.1 mm and screen thickness of 0.275 mm. It was shown [5] that above 10 MeV the point spread function does not depend on the energy.

OPTICAL RESOLUTION

The response of any real optical system to a point source is a spot with a finite size. The degradation of the beam image due to the finite optical resolution $f_{deg}(x)$ can be estimated from a convolution of the distribution of the point spread function $g(x)$ and the initial distribution $f(x)$.

$$f_{deg}(x) = \int_{-\infty}^{\infty} f(y-x)g(y)dy. \qquad (1)$$

As a response function $g(x)$ we use the Gauss distribution. The description of the optical resolution of optical systems

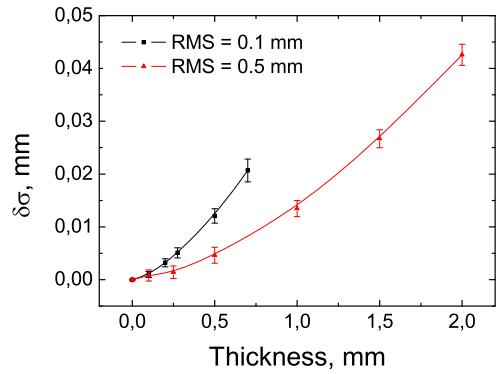

Figure 1: GEANT4 simulations of RMS beam size deviation due to the multiple scattering as a function of the screen thickness. Electron energy is 13 MeV.

is made with the so called Modulation Transfer Function (MTF) formalism.

$$z(\omega) = \int_{-\infty}^{\infty} g(x)e^{-i\omega x}dx, \qquad (2)$$

where ω is called spatial frequency. The optical resolution ω_0 is often defined as a solution of the Eq. (2) when $z(\omega_0) = 0.1$. In fig.2 the difference $\delta\sigma/\sigma = (\sigma_{deg} - \sigma)/\sigma$ between the RMS sizes of the functions $f_{deg}(x)$ and $f(x)$ related to the initial beam size is shown as a function of the initial beam size for two common resolutions used at PITZ.

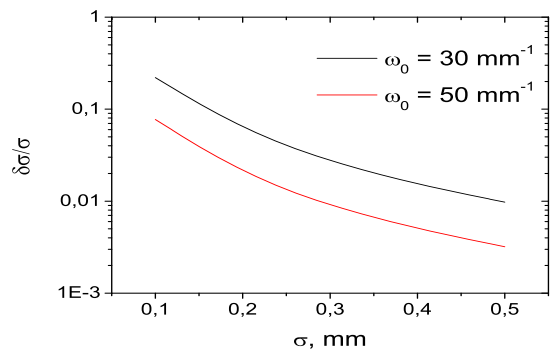

Figure 2: Influence of the optical resolution on the measured beam RMS size.

DEPTH OF FOCUS

The finite thickness of the scintillation layer or the angle (45°) between the screen and the image plane of the optical system are implying different optical paths between different parts of the image on the screen and the image on the CCD chip. This results in an additional uncertainty of the

measured beam size. A point source situated at a distance d from the image plane results in a spot with radius:

$$R = d \cdot \tan\alpha \tag{3}$$

here α is the light cone, in case of YAG screen this is the optical aperture of the system ($\sim$0.05 rad), for OTR it scales inversely proportional to the relativistic momentum $\alpha = 1/\gamma$. Numerical integration was applied on initial Gauss distribution with 0.1 and 0.5 mm RMS sizes. The results are shown in fig. 3. Because the convergence for $R < 0.2\,mm$ is bad, the result is fitted with 4-th order polynom to estimate the values for smaller R. It is visible, that to keep the uncertainty in the desired range one should restrict $R \leq 0.1\,mm$. In the case of YAG d must be kept

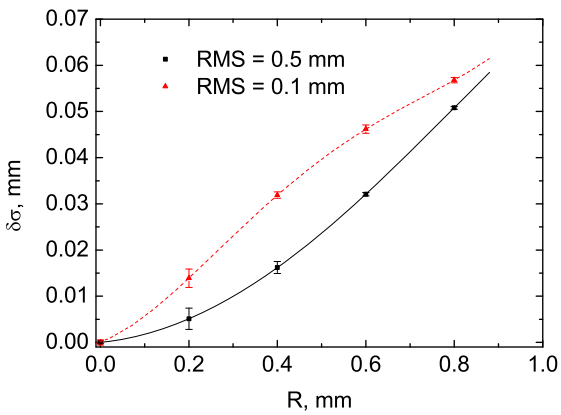

Figure 3: $\delta\sigma/\sigma$ as a function of the depth of focus.

below 2 mm in order to have uncertainty smaller than 10 %. For electrons with energy of 15 MeV the light cone from the OTR is 0.03 rad, this allows us to use depth of field values up to $\pm 3.3\,mm$. These restrictions allow us to use screens with 45° incidence angle.

CCD CAMERA

The main contribution to the uncertainty of the beamsize measurements with a CCD camera is the transformation of the image due to the discrete digital sampling of the amplitude signal from the chip. This effect becomes important when measuring beams with large halos. We can simulate a beam with halo by mixing two Gauss distributions with different weight and RMS size. In fig. 4 the projection of two Gauss distributions with a ratio between the weights of $1/10$ and two different ratios between the RMS sizes. The corresponding RMS sizes are $\sigma_{1/4} = 0.2\,mm$ and $\sigma_{1/16} = 0.1\,mm$. The resulting deviation from the initial RMS size is more than 10 % for the 8 bit case and less than 1 % for the other two.

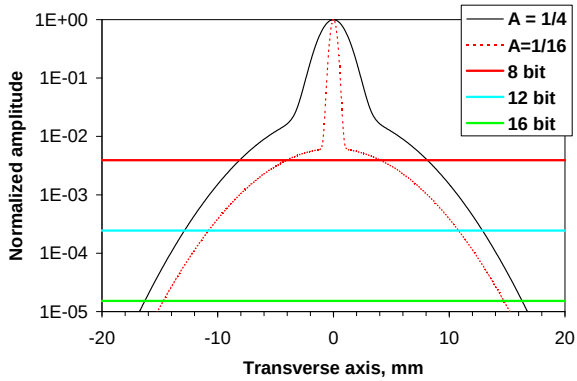

Figure 4: Projections of two mixed Gauss distributions together with the discrimination levels of 8, 12 and 16 bit.

CONCLUSIONS

We presented a detailed assessment of the systematic uncertainty associated with each of the above described components of the screen stations used at PITZ. Most critical parts of the screen station are the spatial resolution of the optical system and the digital resolution of the CCD camera. Still the interactions between effects from different components of the system are to be investigated.

ACKNOWLEDGMENTS

The authors would like to acknowledge the contribution from colleagues at DESY, namely S.Schreiber and K.Honkavaara from Hamburg and S.Weisse from Zeuthen.

REFERENCES

[1] A. Oppelt et al., “Status of the PITZ Facility Upgrade”, LINAC’06, Knoxville, USA, 2006.

[2] V. V. Paramonov et al., “DESGIGN PARAMETERS OF THE NORMAL CONDUCTING BOOSTER CAVITY FOR THE PITZ-2 TEST STAND, LINAC 2004, Lübeck, Germany, 2004.

[3] L. Staykov et al., “Commissioning of a New Emittance Measurement System at PITZ”, FEL’06, Berlin, Germany, 2006.

[4] J. Roensch et al., “Measurement of the longitudinal phase space at the photo injector test facility at DESY in Zeuthen (PITZ)”, DIPAC’05, Lyon, France, 2005.

[5] R. Spesyvtsev, “Transverse Beam Size Measurement Systems at Photo Injector Test Facility in Zeuthen”, Diploma thesis, DESY/Karazin Kharkiv National University, 2006.

[6] GEANT collaboration, CERN/LHCC 98-44, GEANT4: “An Object Oriented Toolkit for Simulation in HEP”; see also website: http//wwwinfo.cern.ch/asd/geant4/geant4.html

COHERENT RADIATION STUDIES FOR THE FERMI@ELETTRA RELATIVE BUNCH LENGTH DIAGNOSTICS

S. Di Mitri, M. Ferianis, M. Veronese*, Sincrotrone Trieste, Trieste, Italy

Abstract

Bunch compressors are key components of the seeded FEL FERMI@Elettra. Assuring their stable operation requires multiple non-destructive diagnostics to provide error signals to the feedback systems. Both the energy and the peak current of the electron bunch have to be stabilized by the feedback systems. The peak current stabilization implies charge and bunch length stabilization. The latter will be achieved by a redundant diagnostics based on Coherent Synchrotron Radiation (CSR) and Coherent Diffraction Radiation (CDR). In this paper we describe a study of Coherent Radiation emission downstream bunch compressors as the source of a relative bunch length measurement. The study evaluates the most critical parameters in the design of such a diagnostic using numerical integration to calculate the spectral angular properties of the radiation for both CSR and CDR.

COHERENT RADIATION EMISSION.

An introduction to the main concepts related to the coherent radiation emission can be found in ref.[1]. The spectral angular intensity distribution of a N-electrons bunch is related to the spectral angular distribution of a single electron as shown in eq.1.

$$\frac{d^2I}{d\nu d\Omega} = \left[N + N\left(N-1\right)\left|F(\rho)\right|^2\right]\frac{d^2I}{d\nu d\Omega}_{1e-} \qquad (1)$$

Where $F(\rho)$ is the Fourier transform of the longitudinal normalized bunch distribution $\rho(t)$. The total N-electron spectral angular distribution is the sum of the incoherent term ($\propto N$) and a coherent term ($\propto N^2$). The frequency behavior of the coherent contribution depends on the square of the Fourier Transform of $\rho(t)$. As the bunch gets shorter, the F($\rho(t)$) becomes spectrally broader and the emitted power increases. To evaluate the emission properties (spectral distribution and intensity) we have computed the coherent spectral angular distribution in two steps. In the first we have calculated F($\rho(t)$), by means of the FFT of the bunch profile derived from Elegant simulations at the exit of the bunch compressors (or by a rectangular approximation of it). In the second we have used a numerical code to calculate the single electron spectral-angular distribution. This approach has been used for CSR and CDR.

* marco.veronese@elettra.trieste.it

Table 1: Parameters used in the calculation.

Parameter	BC1	BC2
Energy [MeV]	220	600
Dipole length [m]	0.5	0.5
Dipole field [T]	0.1(M, L)	0.2(M) 0.32(L)
Dipoles distance [m]	2.5	2.5
Detector size [mm]	30x30	30x30
Charge [nC]	0.8(M) 1(L)	0.8(M) 1(L)
Bunch length [ps]	2.8(M) 5.4(L)	0.7(M) 1.8(L)

COHERENT SYNCHROTRON RADIATION

The calculation of the 1-electron spectral angular distribution of synchrotron radiation has been performed using a Matlab code written by O.Grimm (DESY) which performs a single electron tracking through an arbitrary magnetic field. The code is based on the Liénard Wiechert potentials:

$$\vec{E} = \frac{e}{4\pi\epsilon_0}\left\{\frac{(\vec{n}-\vec{\beta})}{\gamma^2(1-\vec{n}\vec{\beta})^3R^2} + \frac{\vec{n}\times((\vec{n}-\vec{\beta})\times\vec{\beta})}{c(1-\vec{n}\vec{\beta})^3R}\right\} \qquad (2)$$

Where $\vec{n}$ is the vector from the initial position to the observation point, R is the distance between the initial position and the observation point, while $\vec{\beta}$ is the vector velocity divided by c (the speed of light) and $\vec{\beta}' = d\vec{\beta}/dt$ is the acceleration, finally γ is the Lorentz factor. The first term of eq. 2 is known as velocity term and the second as acceleration term. In our case both terms have to be considered together with the finite size of the magnets (see [2]).

The spectral angular distribution is calculated as the sum of the different contribution of the Fourier transforms of the electric field along the particle trajectory:

$$\frac{d^2I}{d\nu d\Omega}_{1el.} = 2\epsilon_0 c\left[\left|F_x^2\right| + \left|F_y^2\right| + \left|F_z^2\right|\right] \qquad (3)$$

Where the F_k are the sums over j (the particle tracking step) of the phase components:

$$F_k = \sum_j \frac{1}{2\pi i}E_{j-1}(\vec{r}_{ret})e^{-2\pi i\nu t_{j-1}}(1-e^{-2\pi i\nu\Delta t}) \qquad (4)$$

The parameters used in the simulation are listed in Table 1, where (M) and (L) mean respectively $Medium$ and $Long$ bunches. In the simulation we have considered not only the emission from the fourth dipole of the chicane but also from the third dipole and accounted for the shielding (low

frequency cut-off) due to the vacuum chambers walls using the mirror charges approach (see e.g. [3]) for perfectly conducting planes.

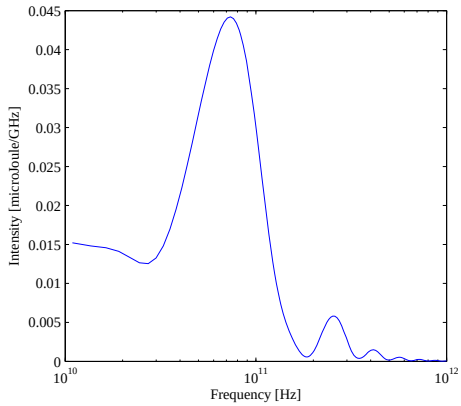

Figure 1: CSR spectral distribution for BC1 *Medium Bunch*.

Fig.1 shows the spectral distribution obtained for BC1 *Long Bunch* integrating over the detector. The detector corresponds to an area of 30x30mm whose origin is centered transversally 25mm away from the electron beam trajectory and is placed 150mm downstream the exit of the 4^{th} dipole of BC1. The intensity distribution at the detector is shown in Fig. 2.

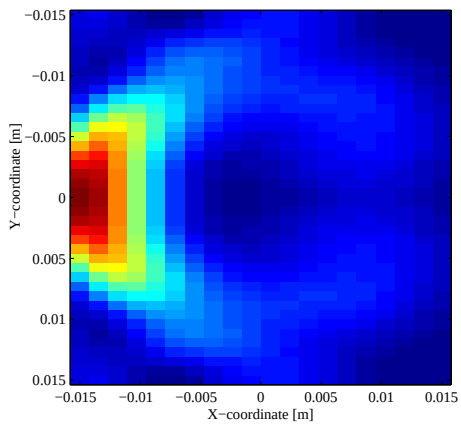

Figure 2: BC1 *long bunch* intensity distribution at the detector.

The calculated values of energy per pulse for BC1 and BC2 in the *Medium* and *Long* cases are summarized in Table 2. The first frequency range is the one of the calculation, the second accounts for the limited pyroelectric detectors spectral sensitivity. The emitted energy increases the shorter are the bunches. For BC2 we can expect a higher CSR intensity than for BC1.
Other approaches to the problem are possible as done in [4] for the BC1 of LCSL where the CSR has been studied via an integral formulation.

Table 2: CSR emitted energy per bunch.

Range	**BC1-M**	**BC1-L**	**BC2-M**	**BC2-L**
0.01-1 THz	11 μJ	4.1 μJ	66 μJ	27 μJ
0.15-1 THz	1.5 μJ	0.3 μJ	46 μJ	8 μJ

COHERENT DIFFRACTION RADIATION

To calculate the spectral angular distribution of CDR in near field we have used a numerical approach to the analytical treatment described in [5] (see also [6]).
For FERMI *Medium bunch*, and *Long bunch*, both the large target size approximation ($a >> \gamma\lambda$) and the far field approximation ($D >> \gamma^2\lambda$) are violated. Here a is the radius of the emitter screen, D is the distance between the detector and the screen planes, λ is the wavelength of the emitted radiation and γ is the Lorentz factor. As an example we can take BC1 *long* bunch ($\lambda = 3mm$ and $\gamma = 430$) then the first condition is satisfied for $a > 1.3m$ and the second for $D > 600m$. The diffraction radiation emission spectral angular distribution has be calculated evaluating numerically:

$$\frac{d^2I}{d\nu d\Omega} = \frac{4e^2k^4}{(2\pi)^2\epsilon_0\beta^4\gamma^2c} \times \left| \int_b^a K_1\left(\frac{k\rho}{\beta\gamma}\right) e^{\left(\frac{ik\rho^2}{2D/cos\theta}\right)} J_1(k\rho sin\theta)\rho d\rho \right|^2 \quad (5)$$

This expression is the diffraction radiation equivalent of expression for transition radiation in ref. [5]. Here b is the hole radius, ρ is the distance from the screen center to a point on the screen in cylindrical coordinate and θ is the angle between the center of the screen and the point of observation P on the detector plane. Equation 5 gives, in the limit of $b \to 0$, the transition radiation expression in near field, moreover in the limits of $a, D \to \infty$ it gives to the Ginzburg-Frank formula.
We have first investigated the effect of near field. Fig. 4 shows the Coherent Transition Radiation (CTR) spectrum at BC2 for the *medium bunch* as a function of the distance D between the plane of the transition radiation screen and the plane of observation. The change from the far-field regime to the near field regime is shown as a suppression of intensity as the distance D decreases. Even though the far field condition in this case would state $D >> 3947$ m at 100 GHz, the expected intensity suppression in near field, becomes noticeable approximately for $D < 1$ m.

From all figures is is clear there is a relevant benefit in using the largest possible angular acceptance and screen radius. The screen radius used in the calculation is 60mm and the

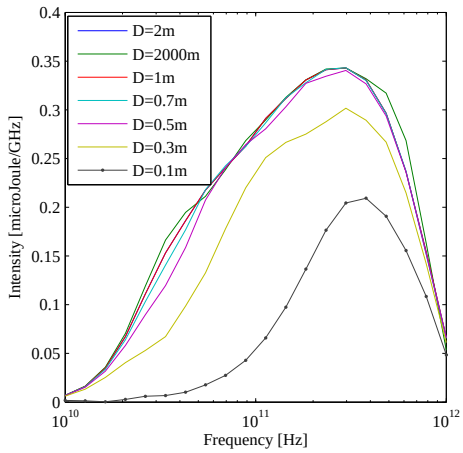

Figure 3: CTR for BC2 *Medium Bunch* as a function of distance D with angular acceptance of 0.1rad and 0.2rad

angular acceptance is 0.1 rad (0.2 rad calculation are plotted for comparison).

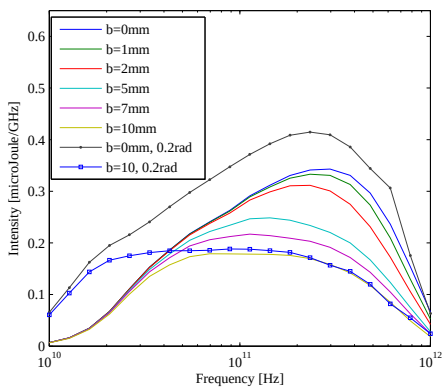

Figure 4: CDR for BC2 *Medium Bunch* as a function of the hole radius b of angular acceptance of 0.1rad and 0.2rad

The choice of the hole radius for a CDR emitter is important and should be done as a compromise between CDR intensity output and beam dynamics requirements in terms of wakefields induced by the screen. A hole radius of the order of 5-10 mm should radiate with sufficient intensity without giving major contributions to the wakefields budgets since the iris of the RF accelerating structures of FERMI are of the same order of magnitude and the total number of irises is about one thousand.

In particular for BC1 *Long bunch* (see Fig. 5) the hole radius b does not impact too much the integrated intensity for 0.1rad of angular acceptance in the range from 0 to 10mm, moreover when increasing to 0.2rad the angular acceptance of the system, we immediately gain spectral intensity below 70 GHz. The situation is different for BC2 *Medium* in Fig. 4 where the effect of the hole radius size is more pronounced while the use of larger angular acceptance is less

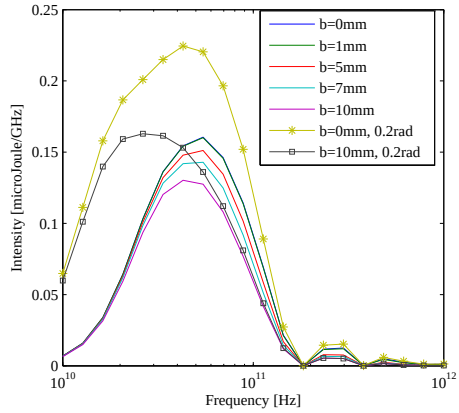

Figure 5: CDR for BC1 *Long Bunch* as a function of hole radius b of angular acceptance of 0.1rad and 0.2rad.

important than in the case of BC1 *Long*. The CDR emitted intensity in terms of energy/bunch obtained by integration of the espctral distribution are reported in Table 3.

Table 3: CDR emitted energy per bunch, a=60mm, D=1m.

Bunch	**b=0mm 0.1rad**	**b=5mm 0.1rad**	**b=10mm 0.1rad**	**b=10mm 0.2rad**
BC1-L	17 μJ	14 μJ	11 μJ	14 μJ
BC2-M	233 μJ	146 μJ	105 μJ	110 μJ

CONCLUSIONS

We have studied the properties of both CSR and CDR radiation sources for the application to the relative bunch length measurement system of FERMI@Elettra. Both sources are capable to provide μJoule level energy pulses and are suitable for the foreseen application. A detailed knowledge of the influence of the main parameters on the coherent radiation emission is important to guarantee the needed performances of this diagnostics.

ACKNOWLEDGMENT

The authors would like to thank O. Grimm for providing his Matlab code and E. Chiadroni for useful discussions.

REFERENCES

[1] O. Grimm, pg.1040, Proc. FEL Conf. 2006 (2006)
[2] E.L. Saldin *etal.*, NIM-A, pg 373, v. 398 (1997)
[3] M. Dholus and T. Limberg, NIM-A, pg 278, v. 407 (1998)
[4] G. Stupakov *etal.* pg.728, Proc. FEL Conf. 2006 (2006)
[5] S. Casalbuoni *etal.* TESLA Report 2005-15 (2005)
[6] M.Castellano *etal.*, NIM-A pg. 297, v. 435 (1999)

DESIGN AND CONSTRUCTION OF THE MULTIPURPOSE DISPERSIVE SECTION AT PITZ*

Sergiy Khodyachykh†, Juergen W. Bähr, Mikhail Krasilnikov, Anne Oppelt‡, Sakhorn Rimjaem, Roman Spesyvtsev, Lazar Staykov, Frank Stephan (DESY, Zeuthen, Germany), Terence Garvey‡(LAL, Orsay, France), Juliane Rönsch (Universität HH, Hamburg, Germany)

Abstract

For the characterization of RF photo-electron guns a full set of beam parameters has to be measured. For this purpose a new high energy dispersive arm (HEDA1) will be used at the Photo Injector Test Facility at DESY in Zeuthen (PITZ) in addition to the existing beam diagnostics. This multipurpose device is designed [1] for an electron energy range up to 40 MeV and will be put into operation in autumn 2007. It combines the functionality of (i) an electron spectrometer, (ii) a device for the characterization of the longitudinal phase space, and (iii) a transverse slice emittance measuring system. HEDA1 consists of a 180 degree dipole magnet followed by a slit, a quadrupole magnet, and two screen stations. One of the screen stations will be equipped with an optical read-out for a streak camera. We report about the detailed design of individual components and the construction progress.

INTRODUCTION

The test facility PITZ was built in Zeuthen in collaboration with international partners with the goal to develop and to optimize high brightness electron sources suitable for SASE FEL operation.

The PITZ facility is an electron accelerator which consists of a 1.5 cell L-band RF gun with its photo-cathode laser system, followed by a low energy diagnostics section, a normal-conducting booster cavity and a high energy diagnostics section. For the detailed description of the PITZ layout we refer to [2, 3]. In parallel to beam operation we are permanently extending the diagnostic section in order to enable more detailed studies of the beam properties. The beam line which has a present length of about 13 meters will be extended up to about 21 meters towards the middle of 2008. Several additional diagnostic components will be added to the present setup. Together with the deflecting cavity [4], the phase space tomography module [5] and the second high-energy dispersive arm (HEDA2) [6], HEDA1 will extend the existing diagnostics system of the PITZ facility. The dispersive section is designed to combine the functionality of (i) an electron spectrometer, (ii) a device for characterization of the longitudinal phase space, and (iii) a transverse slice emittance measuring system. The details of the physical design of HEDA1 were discussed in our earlier paper [1], whereas in the present paper we concentrate on some aspects of the technical implementation of the multi-purpose high energy dispersive arm.

SETUP

The layout of the dispersive section HEDA1 is schematically shown in Fig 1. The heart of the dispersive section is a 180° dipole magnet having the bending radius of 300 mm. Main parameters of the dipole magnet are summarized in Table 1.

Table 1: Parameters of the dipole magnet.

Bending radius	300	mm
Maximum magnetic field	0.46	T
Homogeneous area	$\pm$ 40	mm
Field accuracy ΔB/B	$7 \cdot 10^{-4}$	
Electrical power	4857	W
Maximum current	160	A
Current density in the conductor	7.1	A/mm^2
Total weight	650	kg
Cooling type	Water	

The bending radius has been chosen as a compromise between the ability of the spectrometer to operate within the large range of gun and booster parameters, having at the same time good momentum resolution on the one hand and space restrictions on the other hand.

The dipole magnet (Fig. 2) has been designed, manufactured, and magnetic field map was measured[1]. After its delivery to PITZ, the acceptance tests for water cooling and electric power have been performed at PITZ. For an operating condition at 160A, a maximum magnetic field of 0.46 T has been achieved with a temperature rise of $\leq$13°C at an operating water pressure of 5 bar, a pressure drop of 3.2 bar and a water flow rate of 5.2 l/min. The magnetic field measurements were carried out and are in a good agreement with the results provided by the manufacturer. The results of the magnetic field measurements versus applied current are shown in Fig. 3.

Being deflected in vertical plane, the electron beam enters the dispersive arm which goes back below the main beam line. The dispersive arm includes a pumping port combined with a removable slit mask, a quadrupole magnet Q_1, two screen stations, a pumping port and a beam dump.

* This work has partly been supported by the European Community, contracts RII3-CT-2004-506008 and 011935, and by the 'Impuls- und Vernetzungsfonds' of the Helmholtz Association, contract VH-FZ-005.

† sergiy.khodyachykh@desy.de

‡ Presently at Paul Scherrer Institut, 5232 Villigen PSI, Switzerland.

[1] By SIGMAPHI, France

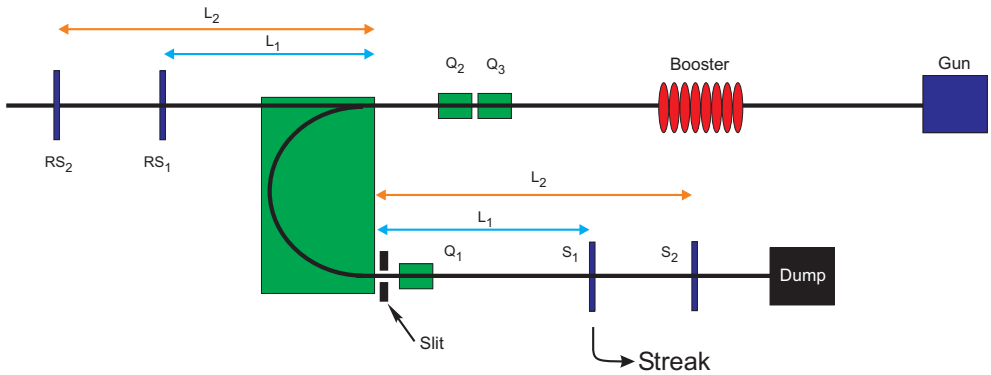

Figure 1: Simplified layout of PITZ with the first high energy dispersive section.

Figure 2: View of the dipole magnet.

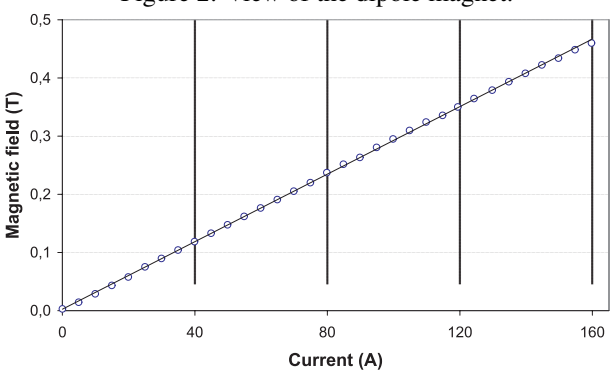

Figure 3: Magnetic field measurements versus applied current.

The functionality of HEDA1 can be enhanced with a setup that allows to measure the transverse emittance of the electron beam at different longitudinal positions along the bunch. The so-called slice emittance is providing better understanding of the physics of a photoinjector, particularly the emittance compensation and conservation principles. Using proper phasing of the booster cavity one can obtain linear correlation between the momentum and longitudinal distribution of the electrons in the bunch. A slit at the dipole exit selects the necessary slice from the energy chirped beam. This slice is scanned with the quadrupole magnet Q_1 focusing in a plane orthogonal to the dispersion plane and the beam distribution is observed on screen S_2. The slit mask for the slice emittance measurements is made from a 3 mm thick tungsten with a slit opening of 30 mm ± 1 mm. The possibility to exchange a slit mask by one with a smaller opening is foreseen. The slit is oriented perpendicularly to the bending plane with the accuracy of better than $\pm 1^\circ$. The tilt of the slit with respect to the reference trajectory around the horizontal axis should be less than $\pm 4^\circ$.

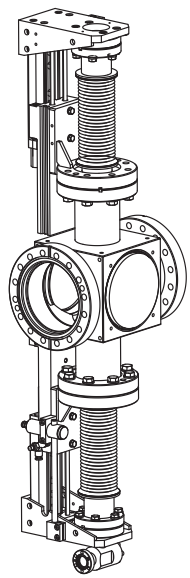

Figure 4: Simplified technical drawing of the screen station.

The quadrupole magnet Q_1 has parameters which are listed in Table 2. It is followed by a drift space and two screen stations. Since the dispersive arm is only 600 mm below the main beamline and due to the need of a long drift space after the quadrupole magnet exit for slice emittance measurements, two screen stations will be included in HEDA1. Each screen station has two actuators and two

Table 2: Parameters of the quadrupole magnet used for slice emittance measurements.

Maximum gradient	2.0	T/m
Bore diameter	80	mm
Number of Amper turns	1328	At
Gradient accuracy ΔG/G	$5 \cdot 10^{-4}$	
Total weight	80	kg
Cooling type	Air	

view ports (see Fig. 4). The drifts from the middle of the quadrupole magnet Q_1 to the first and to the second screen stations are equal to 690 mm and 1237 mm, respectively. The first screen station S_1 contains a YAG screen which will be used for momentum measurements in general and a Cherenkov radiator (Silica aerogel, n=1.05) which is used for measurements of the longitudinal phase space. The design considerations of the aerogel chamber and optical system for the measurement of the longitudinal phase space are described in details in [7]. The second screen station S_2 contains a YAG and an optical transition radiation (OTR) screen. The YAG screen will be used for slice emittance measurements. The OTR will be used for momentum measurements with a higher number of pulses and a small momentum spread in order to prevent the burning of the YAG layer. An additional streak readout for the full cone of the OTR could be of interest especially for higher energies since the emission angle is rather small then. This is not realized in the present design but can be easily extended.

After exit from a 180° dipole magnet the electron beam size stays almost constant. Thus, the maximum screen size is defined by the inner diameter of the quadrupole magnet and is equal to 80 mm. So the size of all YAG and OTR screens was chosen with 80 mm x 60 mm, which corresponds to the ratio of CCD camera chip size. The aerogel, however, has only a size of 80mm x 18mm which is limited by the opening of the streak camera slit in non-dispersion direction. For measuring the bunch charge an integrating current transformer (ICT) is foreseen between the two screen stations. The dispersive section will be end at a beam dump.

The main advantage of the spectrometer based on a 180° dipole magnet is the simplicity to reconstruct the momentum distribution [1]. One uses the reference screen RS_i in the straight section and measures the contribution from the transverse beam size and divergence, which can be deconvoluted with the spectrum measured on the corresponding screen S_i to obtain the pure momentum distribution. This deconvolution is simple and straight forward if the distances L_1 (L_2) from the entrance of the dipole magnet to the measuring S_1 (S_2) and the reference RS_1 (RS_2) screens are equal. For this reason reference screen stations RS_1 and RS_2 are placed downstream to the dipole magnet in the main beam line. Additional components which contribute to the measurements at HEDA1 are two quadrupole magnets Q_2 and Q_3 locating in front of the dipole magnet entrance. By focusing the beam on the screen RS_i with the help of these quadrupole magnets one controls the resolution of the momentum measurement on the corresponding screen S_i. The quadrupole magnets Q_2 and Q_3 will also be used as a part of the matching section for the phase space tomography diagnostics [5]. A numerical example of the momentum measurements is shown in Fig. 5. The original momentum distribution obtained with ASTRA [8] (black) is compared with the reconstructed one after the tracking through the dipole magnet using the measured field distribution (red).

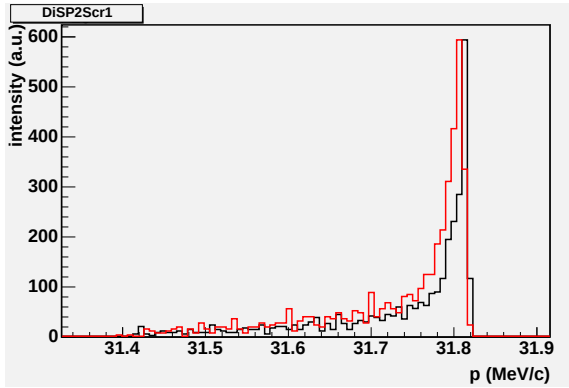

Figure 5: Original momentum distribution obtained with ASTRA (black) and the reconstructed after the tracking through the dipole magnet using the real field distribution (red).

The high energy dispersive arm HEDA1 will be installed at PITZ during the shut down of summer 2007 and will enable measurements of beam momentum, longitudinal phase space, and transverse slice emittance.

REFERENCES

[1] S. Khodyachykh et al., Design of Multipurpose Dispersive Section at PITZ, Proceedings of FEL 2006, Berlin, Germany, 2006.

[2] S. Khodyachykh et al., New Beam Diagnostic developments at the Photo-Injector Test Facility PITZ, to be published in Proceedings of PAC 2007, Albuquerque, USA, 2007.

[3] A. Oppelt et al., Status of the PITZ Facility Upgrade, Proceedings of LINAC 2006, Knoxwille, TN, USA, 2006.

[4] S. Korepanov et al., Design Consideration of the RF Deflector to optimize the Photo Injector PITZ, Proceedings of FEL 2006, Berlin, Germany, 2006.

[5] G. Asova et al., Design Considerations for Phase Space Tomography Diagnostics at the PITZ Facility, Proceedings of DIPAC 07, Venice, Italy, 2007.

[6] J. Rönsch et al., Design Considerations of a Spectrometer Dipole Magnet for the Photo Injector Test Facility PITZ, Proceedings of DIPAC 07, Venice, Italy, 2007.

[7] J.Bähr, J.Rönsch, Optical system for measurement of electron bunch length and longitudinal phase space at PITZ: extension and methodical investigations, Proceedings of DIPAC 07, Venice, Italy, 2007.

[8] K. Floetmann, A Space Charge Tracking Algorithm, http://www.desy.de/~mpyflo/

QUADRUPOLE TRANSFER FUNCTION FOR EMITTANCE MEASUREMENT*

Peter Cameron, BNL, Upton, NY 11973, USA
Marek Gasior, CERN, Geneva, Switzerland
Andreas Jansson, Cheng-Yang Tan, FNAL, Batavia, IL 60510, USA

Abstract

Historically the use of the quadrupole moment measurement has been impeded by the requirement for large dynamic range, as well as measurement sensitivity to beam position. We investigate the use of the transfer function technique [1-3] in combination with the sensitivity and 160dB revolution line rejection of the direct diode detection analog front end [4] to open the possibility of an emittance diagnostic that may be implemented without operational complication, quasi-parasitic to the operation of existing tune measurement systems. Such a diagnostic would be particularly useful as an emittance monitor during acceleration ramp development in machines like RHIC and the LHC.

INTRODUCTION

QMMs (Quadrupole mode monitors) have historically been used in two different ways. In linacs and transfer lines, several pick-ups may be used to provide a single shot measurement of emittance and Twiss parameters [5]. Although this kind of measurement is also possible in a ring [6,7], in circular accelerators QMMs have primarily been used to measure injection matching, by detecting a frequency component due to beam envelope oscillation at twice the betatron frequency. Both methods have some caveats. In both cases, the quadrupole signal must be measured in the presence of a much stronger sum signal. This problem may be solved by purpose-built magnetic pick-ups [6,7]. Additionally, the quadrupole signal depends on beam position. For the single-shot measurement, this means that the position must be measured and its contribution subtracted before the emittance can be calculated. The injection matching measurement is not sensitive to a DC offset of the beam, since the mismatch signal is separated by frequency. However, any significant beam position oscillation will generate a signal at twice the betatron frequency that may be mistaken for a beam size oscillation.

The approach we describe here offers the possibility of eliminating the classical problems affecting emittance measurement using QMMs. The key to the approach is the Quadrupole Transfer Function (QTF). The QTF shifts the signal from the revolution frequency to approximately twice the betatron frequency. This removes the DC position dependence, just as in the case of injection mismatch measurement, and opens the possibility of using the sensitivity and dynamic range of the Direct Diode Detection Analog Front End (3D AFE).

PICKUP AND BEAM PARAMETERS

For the purpose of presenting quantitative estimates of signal levels in the LHC, one possible set of pickup and beam parameters has been selected. These parameters are shown in Table 1, and are used in the calculations in the following section. It is assumed that pickups similar to existing pickups can at some point be installed in available space in the region of large beta functions adjacent to the 4 o'clock IP.

parameter	symbol	value
electrode radius [cm]	b	3
electrode length [cm]	L	60
subtended angle [deg]	ϕ_0	70
stripline impedance [ohms]	Z	50
Lorentz factor	γ	7461
bunch charge [q]	N	$1x10^{11}$
number of bunches	N_b	1
rms bunch length [nsec]	σ	0.25
emittance [mm-mrad]	$\varepsilon_x = \varepsilon_y$	4
Hor beta function [m]	β_x	400
Vert beta function [m]	β_y	200
Hor rms beam size [mm]	σ_x	0.46
Vert rms beam size [mm]	σ_y	0.33

Table 1. Pickup and Beam Parameters

The pickup parameters and beta functions shown here are representative of such an installation. The selected beam parameters represent something close to 'worst case', a single bunch at store, where beam size and quadrupole signal are minimized.

BEAM SIGNALS

Given the pickup and beam parameters in Table 1, one can calculate the response of the various modes of the pickup (sum, difference, quadrupole,…) as the beam position and shape changes [8,9]. Signal powers for the various modes as a function of beam offset are plotted in Figure 1. Also shown for purpose of comparison is the spectral power density (per Hz) of the room temperature thermal noise floor.

The sum mode (ie the sum of the power from striplines on opposite sides of the beam) power is ~+9dBm, or a little less than 10mW. To first order sum mode power is not a function of beam position. In frequency domain this power appears at the revolution line.

Power appears in the difference mode (the difference in power from striplines on opposite sides of the beam) when the beam is not centered. If the there is no coherent

dipoles excitation, all of this power appear at the revolution line.

Power appears in the quadrupole mode (the difference in sum mode power from the horizontal and vertical planes) if there is beam offset OR an asymmetric beam ($\sigma_x \neq \sigma_y$). If there is no coherent quadrupole or dipole excitation, all the power in the quadrupole mode will appear at the revolution line.

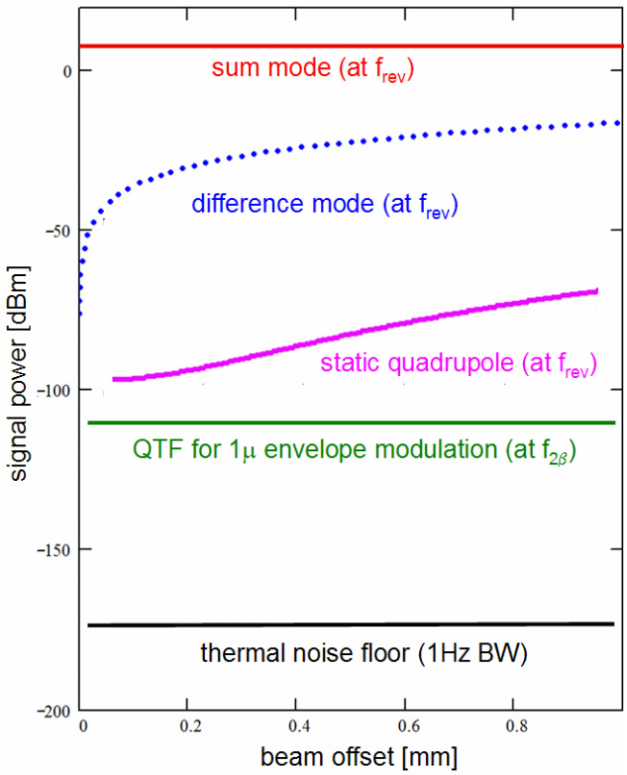

Figure 1. Signal power from the pickup modes as a function of beam position

With the QTF approach, the beam is excited at the quadrupole resonance. Even though a quadrupole kicker may act as a dipole if the beam is offset, the excitation frequency is far for the dipole resonance, so very little coherent dipole oscillation results. Therefore, all signal components except those coming from beam size modulation appear at the revolution line, and can be filtered, giving a measurement of the envelope modulation response which is *separated from interfering sum, difference, and position-dependent quadrupole signals* in the frequency domain.

Kicker power requirements for the 1μ envelope modulation shown in Figure 1 may be estimated by considering the ratio of beam rms radius to kicker radius. This suggests that the kicker field at rms beam radius must be ~x10 that of the BBQ kicker, and the kicker power would then need to be ~x100 that of the BBQ kicker. For the LHC at full energy, this possibly is a formidable requirement. It might be considered to use a resonant kicker in this application.

MEASUREMENT METHOD

When measuring the usual (dipole) transfer function, one excites coherent beam position oscillations using angular kicks from a dipole magnet, and measures the beam position response. The amplitude response

$$F(f) = \frac{\sqrt{\beta_k \cdot \beta_p} \cdot \Delta\theta}{\Delta x}$$

is proportional to the local density of particles with natural oscillation frequencies close to the driving frequency.

In the case of a quadrupole transfer function, one excites fluctuations in the lattice beta function using quadrupole kicks. However, what is measured is not the lattice function directly, but the beam size. The beam size is a function of both the beta function and the beam emittance. This is what opens the possibility to measure emittance with a quadrupole transfer function.

When making a QTF measurement, the observable is actually variations in the square of the beam size. If the beam envelope is being modulated by a quadrupole of integrated strength $\Delta k \cdot l$ at frequency f, the resulting response can be written

$$\Delta(\sigma^2) = G(f) \cdot \beta_k \cdot \beta_p \cdot \varepsilon \cdot \Delta k \cdot l$$

where G(f) represents the frequency dependence of the quadrupole resonance response, and the beta functions are at the kicker and pickup locations. If one assumes that the resonance response G(f) does not depend on emittance (ie no detuning with amplitude) and that there is no incoherent tune shift (due for instance to space charge), it is not unreasonable to postulate that

F(f) is proportional to G(2f)

which is just another way of saying that the same particles that contribute to the dipole response at f contribute to the quadrupole response at 2f.

Then, by measuring the ratio of the quadrupole transfer function at f and the quadrupole transfer function at 2f, one can obtain a relative measure of emittance.

A POSSIBLE SYSTEM ARCHITECTURE

One possible system block diagram is shown in Figure 2. The outer loop (black) is the conventional Baseband Tune measurement system (BBQ), as employed in RHIC [10] and in development for the LHC [11]. It permits continuous measurement of tune, coupling, and chromaticity. In RHIC, feedback loops have been closed (red) for real-time control of tune and coupling during beam acceleration.

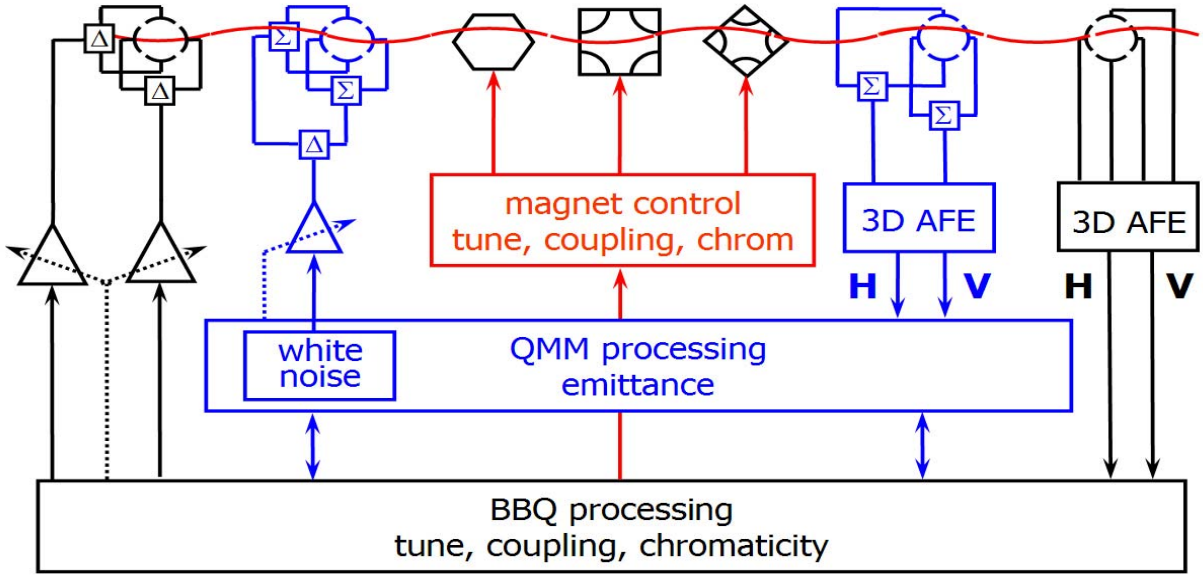

Figure 2. A Possible System Block Diagram

The QMM loop (blue) is shown nestled within the BBQ. In this configuration, it is straightforward to excite the quadrupole resonance with a quadrupole kicker at exactly twice the betatron frequency (the betatron frequency is tracked by the BBQ), to scale the QMM excitation to the BBQ excitation, and to normalize the QMM signal to the BBQ signal, which provides a relative emittance calibration. If the location in frequency domain of the quadrupole resonance relative to the betatron resonance remained constant through the ramp, this would probably be the optimal configuration. However, space charge incoherent tune shift causes this to be untrue, and will be discussed further in a later section.

Space Charge and Noise Excitation

In the LHC, the injection and store incoherent tune shifts due to space charge are estimated to be ~10^{-3} and 10^{-5} respectively. It is not yet clear how this shift of the quadrupole mode frequency away from twice the betatron frequency might affect the data quality of the simple approach of exciting the quadrupole resonance at precisely twice the betatron frequency. Machine nonlinearities causing detuning with amplitude may cause similar problems. As an alternative, the quadrupole mode might be excited with white noise, and the 3dB power of the resonance response measured to extract beam size information. Continuous white noise excitation of the betatron resonance during acceleration ramps has been successfully employed in RHIC, for the purpose of observing tunes, coupling, chromaticity and non-linear tune spread. These results suggest that a similar approach may be successful for the quadrupole mode.

CONCLUSION

We have presented a new approach to the application of the quadrupole monitor to emittance measurement. It has the potential to overcome some of the obstacles that have prevented the quadrupole monitor from being more widely used in accelerators. Studies are planned in both RHIC and LHC to validate the method.

REFERENCES

[1] M. Chanel, EPAC 1996, Barcelona
[2] W. Guo and S.Y. Lee, Phys. Rev. E, 65, 066505, 2002.
[3] S. Sakanaka et al, PAC 2003, Portland.
[4] M. Gasior and R. Jones, CERN-LHC Project Report 853, 2005, available at http://documents.cern.ch/cgi-bin/setlink?base=preprint&categ=cern&id=lhcproj-2005-853
[5] R.H. Miller et al, "Non-Invasive Emittance Monitor", PAC 1983, Batavia, IL.
[6] A. Jansson, "The Magnetic Quadrupole Pickups in the CERN PS", BIW 2002, Brookhaven.
[7] A. Jansson, PhD thesis, 2001, available at http://doc.cern.ch/archive/electronic/cern/preprints/ps/ps-2001-014.pdf
[8] R. Shafer, "Beam Position Monitoring", BIW 1989, Brookhaven.
[9] P. Cameron, "QMM for Emittance Measurement in RHIC", C-AD AP 277, available at http://www.agsrhichome.bnl.gov/AP/ap_notes/cad_ap_index.html
[10] P. Cameron et al, PRST-AB 9, 122801, Dec. 2006
[11] see http://www.agsrhichome.bnl.gov/LARP/061024_TF_FDR/index.html for further information

DESIGN OF THE CAVITY BPM SYSTEM FOR FERMI@ELETTRA

P. Craievich*, C. Bontoiu, M. Ferianis and G. Trovato, Sincrotrone Trieste, ELETTRA, Trieste, Italy
M. Poggi, Laboratori Nazionali di Legnaro, INFN, Italy
V. Smaluk, The Budker Institute of Nuclear Physics SB RAS, Novosibirsk, Russia

Abstract

The cavity Beam Position Monitor (BPM) is a fundamental beam diagnostic instrument for a seeded FEL, like FERMI@elettra. It allows the measurement of the electron beam trajectory non-destructively, on a shot-by shot basis and with sub-micron resolution. The high resolution the cavity BPM is providing relies on the excitation of the dipole mode that is originated when the bunch passes off axis in the cavity. In this paper we present the prototype of the cavity BPM developed for the FERMI@elettra facility. Furthermore, the design of the prototype electronics for the acquisition and the processing of the signals from the BPM cavities is presented. The adopted scheme consists of a down converter from the C-band to an intermediate frequency followed by an IQ demodulator to generate the base-band signal which is proportional to the transverse beam position. The performed simulation session is presented as well which we run before building the hardware for bench tests.

INTRODUCTION

The FERMI@Elettra FEL project requires an accurate measurement of the transverse beam position throughout all the machine. In order to provide the required single shot resolution for the position measurement cavity BPMs have been adopted. They are a resonant pill-box cavity where the information on beam position is encoded in the amplitude and phase variations of the dipole mode (TM_{110}) with beam transverse position [1, 2]. A scaling from X-band to C-band of cavity BPM was performed in [3]. Here we present the prototype of the cavity BPM developed and the design of the electronics for the acquisition and the processing of the signals from the BPM and reference cavities. Since wakefields budget is an important issue for FEL machine, longitudinal and transverse wake potentials have been calculated using the GdfidL code [4]. The comparisons between analytical and numerical results are presented here.

CAVITY BPM PROTOTYPE

Figure 1 shows a 3-D view of the cavity BPM as mechanically designed [5]. The prototype is actually fitted with two cavities: one for the position measurement and a second one for the generation of the reference signal for the demodulator. The signal from waveguide is coupled out by means of a coaxial feedthroughs antenna. In the cold test a optimization of the antenna coupling is foreseen. Table 1 shows RF parameters of the BPM and reference cavity prototype. Since the electronics require an overlapping between the BPM and reference resonant frequencies, the requirement on the cavity frequencies becomes stringent. Besides it is important to maintain the cavity simmetry to minimize the monopole mode leakage and $x - y$ coupling. Thus, the required machining tolerance was fixed to $\pm 10 \mu m$ for cavities, waveguides and their relative positioning.

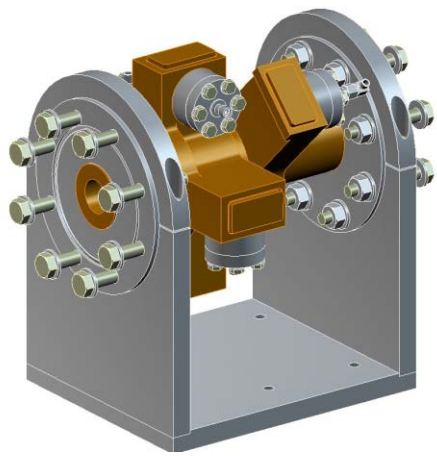

Figure 1: A 3-D view of the cavity BPM prototype.

Table 1: RF parameters for BPM and reference cavities. Charge $1nC$, *offset $1\mu m$ and **on axis, voltage normalized to $R = 50\Omega$ and $T = 0s$.

cavity BPM	**ref. cavity**
Mode TM_{110}	Mode TM_{010}
$f_{110} = 6479MHz$	$f_{010} = 6475MHz$
$Q_0 = 8400$	$Q_0 = 7250$
$Q_{ext} = 10500$	$Q_{ext} = 36800$
$k_{110} = 8.3V/nC/mm^2$	$k_{010} = 1410V/nC$
$\partial f/\partial r = -2.3MHz/10\mu m$	$\partial f/\partial r = -3.7MHz/10\mu m$
$V^*_{ext} = 1.27mV$	$V^{**}_{ext} = 8.85V$

CAVITY BPM ELECTRONICS

In general a cavity BPM provides two independent signals, one for each x and y axis. As known from the theory when the beam passes off axis through a resonant cavity dipole mode is excited and its outputs can be modeled by a

* paolo.craievich@elettra.trieste.it

damped sinusoidal signal:

$$m_x(t) = V_{110,x}e^{-\alpha_{110}t}sin(\omega_{110}t + \varphi_{110,x}) \quad (1)$$

$$m_y(t) = V_{110,y}e^{-\alpha_{110}t}sin(\omega_{110}t + \varphi_{110,y}) \quad (2)$$

where $\alpha_{110} = \pi f_{110}/Q$ is the attenuation constant, f_{110} and Q are the 6.5 GHz resonant frequency and loaded quality factor of the cavity, respectively. $\varphi_{110,x}$ and $\varphi_{110,y}$ are the phases of the signal, which may assume only $-\frac{\pi}{2}$ or $\frac{\pi}{2}$ values, depending on the beam position with respect to the axis considered. V_{110} is the amplitude of the signal which is linearly dependent on the transverse position of the beam. Figure 2 shows the simulated output from the BPM when we assume a duration of the RF signal of approximately $2.5\mu s$ and a load $Q = 10000$ for the cavity. Furthermore

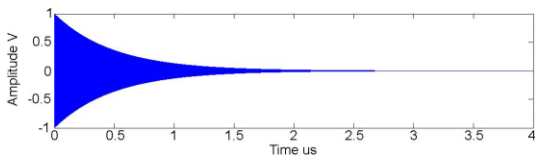

Figure 2: Simulated signal from cavity [6].

a reference resonant cavity, at the same frequency of the dipole mode, is adopted to desensitize the system from the timing jitter of the beam. In this cavity the beam excites the monopole mode TM_{010} and the output signal can be written by:

$$r(t) = V_{010}e^{-\alpha_{010}t}\sin(\omega_{010}t + \varphi_{010}) \quad (3)$$

where $\alpha_{010} = \pi f_{010}/Q$ is the attenuation constant, f_{010} and Q are the resonant frequency and loaded quality factor of the cavity, respectively. φ_{010} is the phase and V_{010} is the amplitude of the signal which is in a first approximation independent on the transverse position of the beam.
In order to get a deeper understanding of the electronics, a bench test characterization, shown in figure 3, is currently in progress. In this block diagram the receiver is a single-stage three-channel heterodyne receiver. The RF signals from the two cavities are attenuated and filtered by means of low band pass or pass band filters. Then the signals are down-converted from the C-band frequency of 6.5 GHz to the intermediate frequency (IF) in the range from 30 to 40 MHz by means of mixers. As an example figure 4 shows a typical output from the receiver. The local oscillators (LO) are all synchronized and phase locked with the global timing of the LINAC [7]. Furthermore the LO, used to down-convert signals from the measurement cavity, is locked for working at 6.46-6.47 GHz, while the LO of the reference chain is tunable in the range of 6.46-6.54 GHz. By doing so any possible mismatch between the frequency of the reference cavity and the frequency of the measurement cavity due to mechanical tolerances is compensated. The outputs from the receivers after filtering are given by:

$$m_{IF,x} = A_x e^{-\alpha_{110}t}\sin(\omega_{110,IF}t + \varphi_{110,x}) \quad (4)$$

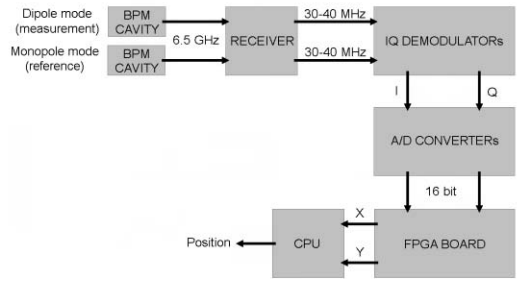

Figure 3: Architecture for test bench BPM electronics

$$m_{IF,y} = A_y e^{-\alpha_{110}t}\sin(\omega_{110,IF}t + \varphi_{110,y}) \quad (5)$$

$$r_{IF} = Be^{-\alpha 010t}\sin(\omega_{010,IF}t + \varphi_{010}) \quad (6)$$

where the amplitudes A_x, A_y are proportional to amplitudes $V_{110,x}$, $V_{110,y}$ repectively and the amplitude B is proportional to amplitude V_{010}. In our test bench system the

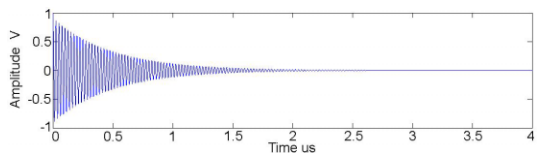

Figure 4: Simulated output from receiver [6].

IF signals are demodulated by two analog I-Q demodulators, one for each axis, providing two signals in baseband, shown in figure 5, one in-phase (I) and in one quadrature (Q):

$$I_x = C_x e^{-\alpha t}\sin(\varphi_{110,x} - \varphi_{010}) \quad (7)$$

$$Q_x = C_x e^{-\alpha t}\cos(\varphi_{110,x} - \varphi_{010}) \quad (8)$$

$$I_y = C_y e^{-\alpha t}\sin(\varphi_{110,y} - \varphi_{010}) \quad (9)$$

$$Q_y = C_y e^{-\alpha t}\cos(\varphi_{110,y} - \varphi_{010}) \quad (10)$$

where $\alpha = \alpha_{110} + \alpha_{010}$, the amplitude C_x is proportional to the amplitudes A_x and the amplitude C_y is proportional to the amplitude A_y.
In principle the beam displacement, from the axis considered, can be calculated by

$$s = \sqrt{I^2 + Q^2} \quad (11)$$

and the phase information is given by:

$$\vartheta = \arctan\left(\frac{I}{Q}\right) \quad (12)$$

Figure 6 show a more detailed block diagram for the receiver and I-Q demodulators. Finally the I-Q signals are digitalized by two A/D converters. Such A/D converters, indicated in figure 3, have a resolution of 16 bit and a sampling rate of 130 MSPS. The reference clocks are synchronized with the Linac timing reference. For the final version of the electronics, shown in figure 7, the A/D conversion is performed after the receiver and the I-Q demodulation

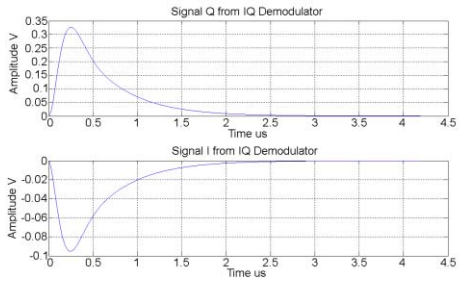

Figure 5: I-Q components [6].

is implemented digitally. This solution has the advantage of minimizing the typical errors of the I/Q detector, such as gain matching, DC offset, quadrature phase errors and carrier leakage.

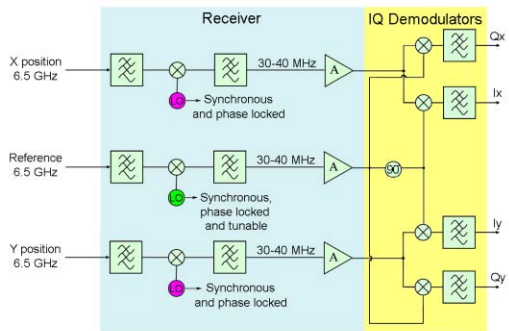

Figure 6: Receiver and I-Q demodulators block diagrams [8].

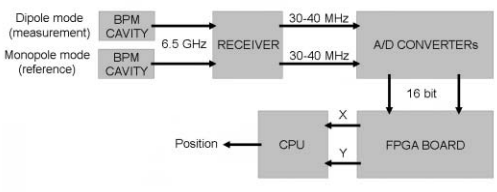

Figure 7: Block Diagram of final version.

CAVITY BPM WAKEFIELD BUDEGET

Longitudinal and transverse wake potentials of the reference and BPM cavities have been calculated using the GdfidL code [4]. For the BPM geometry, the minimal mesh size limited by the computer power is $0.25mm$. To obtain reliable results of the GdfidL calculation, the mesh size should be at least 5 times less than the bunch length. Thus the calculations were performed for a RMS bunch length of $5mm$ and $2mm$. Figures 8and 9 show a comparison between numerical and analytical longitudinal and transverse wake potentials, respectively. The analytical wake potentials are been obtained by means of the convolutions between longitudinal charge distribution and the wake functions given in [9]. It is worthwhile to note that the waveguides have an influence in the wakes calculation. This point is handled in the reference [10].

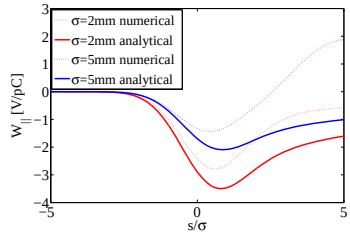

Figure 8: Comparison between numerical and analytical longitudinal wake potentials.

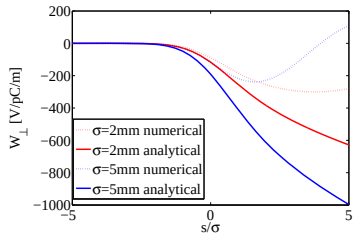

Figure 9: Comparison between numerical and analytical transverse wake potentials.

CONCLUSION

In this paper the prototype of the cavity BPM developed for the FERMI@elettra facility has been presented. To meet the stringent requirements on RF parameters the machining tolerance was fixed to $\pm 10\mu m$ for cavities, waveguides and their relative positioning. Furthermore, the design of the prototype electronics for the acquisition and the processing of the signals from the BPM cavities is also presented. The adopted scheme consists of a down converter from the C-band to an intermediate frequency followed by an IQ demodulator to generate the base-band signal which is proportional to the transverse beam position. Preliminary longitudinal and transverse wakefield estimations have been performed. As a results, it seems likely that the waveguides on the BPM have an influence in the calculation.

REFERENCES

[1] V. Balakin et al., PAC 1999, New York, 1999.
[2] R. Johnson et al., BIW 2002, Upton, NY, May 2002.
[3] P. Craievich et al., FEL 2006, Germany, Aug 2006.
[4] W. Bruns, http://www.gdfidl.de.
[5] Cinel Strumenti Scientifici, http://www.cinel.com.
[6] Matlab Simulation, http://www.mathworks.com.
[7] D. Treyer, private communication, http://www.psi.ch.
[8] R. Lill et al., FEL 2006, Germany, Aug 2006.
[9] K. Bane and M. Sands, SLAC-PUB-4441, Nov1987.
[10] P. Craievich et al., to be published.

A TRANSVERSE RF DEFLECTING CAVITY FOR THE FERMI@ELETTRA PROJECT

P. Craievich*, S. Di Mitri, M. Ferianis and M. Veronese, Sincrotrone Trieste, ELETTRA, Trieste, Italy
M. Petronio, Università degli Studi di Trieste, Trieste, Italy
D. Alesini, Laboratori Nazionali di Frascati, INFN, Italy

Abstract

The layout of FERMI@Elettra includes a high energy transfer line (TL) which brings the accelerated electron bunch to the FEL undulator chains. The TL optics has been designed according to several space constraints and with the purpose of including diagnostics for the complete characterization of the electron bunch just before the FEL process starts. Basing on such optics, this paper reports the study of the electron bunch deflection at nominal energy of 1.2 GeV for the measurement of the bunch length, of the transverse slice emittance and of the slice energy spread, coupled to a downstream dipole. The effect of the cavity on the electron beam was simulated by tracking code and the specification on the deflecting voltage was thus confirmed. Furthermore the RF design and electromagnetic simulations are also presented here.

INTRODUCTION

The layout of FERMI@Elettra includes a high energy transfer line (TL) designed according to several space constraints and with the purpose of including diagnostics for the complete characterization of the electron bunch just before the FEL process starts [1]. Using such optics as a base, this note reports the study of the electron bunch deflection at approximately 1.2 GeV for the measurement of the bunch length and of the transverse slice emittance. The well-known formulas contained in [2, 3, 4] concerning the dynamics of the bunch deflection as function of the RF deflector parameters and of the optical Twiss parameters are here used. Perturbations to the ideal case due to in the finite transverse emittance is also considered. Then, some of the basic formulas have been manipulated in to evaluate the measurement resolution, which depends on the transverse finite emittance and on the screen resolution. Specification for the high energy RF deflector in FERMI is given. The analytical predictions are verified by the particle tracking [5]. Furthermore tracking section also includes some considerations about the single bunch beam break up (BBU) instability acting in the main Linac. In the last section RF design and structure parameters for the deflector are addressed.

* paolo.craievich@elettra.trieste.it

OPTICS

It is supposed here that the RF deflector alternately operates in both transverse planes to allow the measurement of the horizontal and vertical transverse slice emittance. In addition, this allows the BBU instability to be observed in both planes ([6] and references therein). The RF deflector is placed in a drift section 2.5 m long and it is followed by a (multi) 5-screen emittance measurement section. The quadrupole magnets in between the five OTR screens are separated by $\pi/4$ phase advance in both planes. The betatron phase advance over the cavity length is small, thus the phase advance in the cavity is approximated by its average value ($\beta_D = 18m$ and $\beta_S = 4.5m$ are beta function at the deflector and at the screens, respectively). Since the efficiency of the bunch deflection at the chosen observation point depends on $sin(\Delta\psi_{D,S})$ (see next section), a null vertical deflection occurs at $\Delta\psi_{D,4} = 180deg$ (OTR4), the maximum deflection is at $\Delta\psi_{D,2} = 78deg$ (OTR2) and a poorly deflection occurs at $\Delta\psi_{D,1} = 25deg$ (OTR1) both in the vertical plane. The parameters concerning the Medium Length Bunch option (MLB) [7] used are: bunch charge $0.8nC$, average energy of $1.14GeV$, total normalized emittance of $2\mu mrad$ and RMS bunch length of $90\mu m$.

BASICS

In the approximation of pencil beam (null transverse emittance, $\sigma_{y,0} = 0$), the RMS beam size at the screen location when $\varphi_{RF} = 0$ (the centroid remains on the axis trajectory) is:

$$\sigma_{y,S} = \frac{eV_\perp}{E}\sigma_z \left[\frac{\omega_{RF}}{c}\right] \sqrt{\beta_D \beta_S}\sin(\Delta\psi_{DS}) \qquad (1)$$

where $V_\perp$ is the total transverse voltage of the deflecting structure and σ_z is the bunch length before the action of the deflection.

Finite Transverse Emittance

If the finite transverse emittance of the bunch is taken into account, then the RMS beam size at the screen after the deflection is estimated by the quadratic summation of the RMS non-deflected particle transverse size distribution and of the RMS beam size in the pencil beam approximation:

$$\sigma_{y,S,\epsilon} = \sqrt{\frac{\epsilon_N \beta_S}{\gamma} + \left[\frac{eV_\perp}{E}\sigma_z \frac{\omega_{RF}}{c} R_{34}\right]^2} \qquad (2)$$

RESOLUTION

Resolution from beam finite emittance

Eq. 2 describes the increase of the beam size measured at the screen in the presence of a finite transverse emittance. This perturbation is negligible if $\sigma_{y,S} >> \sigma_{y,0}$. If it is $\sigma_{y,S} = \kappa\sigma_{y,0}$ then:

$$\sigma_{y,S,\varepsilon}(\kappa) = \sqrt{\sigma_{y,0}^2 + \sigma_{y,S}^2} = \frac{\sqrt{1+\kappa^2}}{\kappa}\sigma_{y,S} \qquad (3)$$

and the relative error on the beam size is:

$$\frac{|\sigma_{y,S,\varepsilon} - \sigma_{y,S}|}{\sigma_{y,S}} = \frac{\Delta\sigma_{y,S}}{\sigma_{y,S}}(\kappa) = \left|\frac{\sqrt{1+\kappa^2}}{\kappa} - 1\right| \qquad (4)$$

Notice that the measurement of the horizontal slice emittance is not affected by a vertical enlargement of the beam size at the screen as the horizontal width of the beam spot is only of interest. Eq. (2) shows that if $V_\perp$ is sufficiently large, the bunch RF deflection satisfies the approximation of pencil beam. Once κ has been fixed accordingly to the relative error given by eq. (3) and eq. (4), then the minimum peak voltage of the RF deflector (when $\varphi_{RF} = 0$) providing such an error is given by:

$$V_{\perp,\min} = \kappa\frac{E}{e}\frac{1}{\sigma_z}\sqrt{\frac{\varepsilon_N}{\gamma\beta_D}}\left(\frac{c}{\omega_{RF}}\right)\frac{1}{|\sin(\Delta\psi_{DS})|} \qquad (5)$$

with ϵ_N the total normalized emittance of the non-deflected bunch. Figure 1(left) plots eq. (5) with varying κ.

As an example, an RMS intrinsic relative error on the bunch length measurement $\Delta\sigma_z/\sigma_z$ of about 3% is guaranteed by the error parameter $\kappa = 4$ (in absence of other perturbations to the deflection). The minimum RF deflector peak voltage $V_{\perp,MIN}$ required by this specification is something less than $6MV$ (see figure 1 (left)).

Maximum peak voltage specification

The measurement of the transverse slice emittance requires short portions of the bunch length to be resolved at the screen after the bunch is deflected. That is, the resolution of the measurement system has to provide the necessary sensitivity to the intensity contrast. Then, the CCD camera detecting the screen will be able to distinguish density clusters. The OTR screen resolution is estimated to be $10\mu m$ RMS, while in this handling we have not taken in account the CCD pixel size. Figure 1 (right) shows the measured beam size as a function of $V_\perp$ according to eq. (2) (worse phase advance of the OTR1 screen for the bunch vertical deflection). The deflected RMS beam size at the screen for $V_\perp = 20MV$ is $380\mu m$.

A first estimate of the minimum slice length detectable as a function of the deflecting voltage can be obtained by using the following simple approach. A portion of the longitudinal density distribution of the electron bunch is modeled by two identical Gaussians with different centers at a given distance Δx; the sigma of the Gaussians is the instrumental RMS resolution. This is sketched in figure 2 (left). Then, the intensity contrast is defined by: $IC = (A-B)/A$ (see figure 2 (left)). Thus, by fixing the specified intensity contrast, a minimum distance between the density peaks is determined; this can be taken in turn as the minimum detectable slice length. The intensity contrast as a function of centers distance Δx can be plotted for different screen resolutions (see figure 2 (right)). Assuming $10\mu m$ RMS resolution of the screen, a contrast of 70% allows for the detection of about a $40\mu m$ slice length. This correspond to 30 slice in the MLB if we consider the approximation of a uniform bunch current distribution and taking a peak voltage of $18MV$. According to figure 1 (right), the RMS beam spot size at the OTR1 screen is about $350\mu m$.

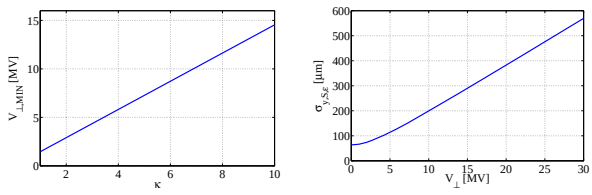

Figure 1: Left: Minimum deflecting voltage as a function of the error parameter κ. It has been assumed a beam size measurement at the OTR2 screen location. Right: The measured beam size at the OTR1 screen location as a function of the deflector peak voltage $V_\perp$. The curve represents the less efficient vertical deflection over the available screens.

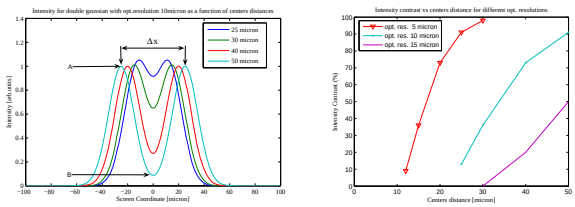

Figure 2: Left: Intensity contrast for a double Gaussian particle distribution as a function of the centers distance. Right: Intensity contrast vs. distance between the centers of the double Gaussian particle distribution for three RMS resolution of the OTR screen.

PARTICLE TRACKING

The vertical deflection has been applied to the MLB option. Particle distributions of the deflected bunch observed at the OTR2 screen are shown in figure 3. The beam spot size obtained is about $3mm$ in height. The on-axis bunch deflection has been performed with a peak voltage $V_\perp = 20MV$ and it is observed at the OTR2 screen location. This can be compared with the analytical result where a $20MV$ peak voltage provides an RMS beam spot size on the OTR2 screen of about $840\mu m$. This correspond to a $\sqrt{12}\cdot 840\mu m = 2.9mm$ full width of the image for an ideally uniform particle distribution, namely a good agreement between theory and particle tracking.

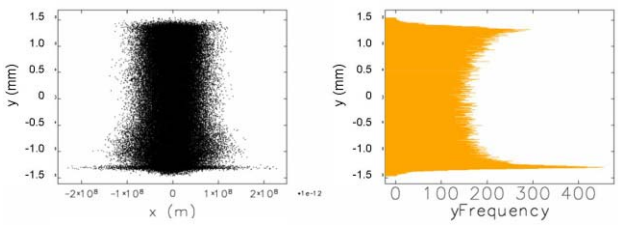

Figure 3: Particle distribution of the deflected bunch observed at the OTR2 screen. On the top left, particles in the x-y plane; the vertical extension contains information on the bunch length. The other plot shows the particle distributions in the vertical plane.

Single bunch beam beak-up instability

The geometric wake fields in the accelerating structures upstream of the RF deflector [8] induce a BBU instability in both the transverse planes; as a result, the bunch tail is laterally displaced with respect to the head in the plane of action of the wake field and the bunch assumes a typical "banana shape" [6]. If the bunch distortion is in the horizontal plane, then the vertical deflection will show it in the x-y plane of the screen. In such a way the BBU instability in the main Linac can be checked and compensated locally by means of trajectory management. Figure 4 shows the "banana shape" at the OTR2 location induced by the horizontal transverse wake field in the Linac. No special wakefield compensation is implemented. Notice that in the previous figure 3 the local trajectory bumps have been implemented in the simulation.

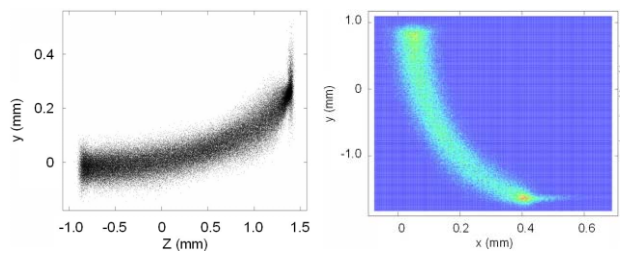

Figure 4: "Banana shape" induced by the Linac horizontal transverse wake field. Before (left) and after (right) the vertical deflection of the bunch.

RF DEFLECTOR DESIGN

The RF design and the choice between different options was done taking in account the following constrains:

- the required deflecting voltage $V_\perp = 18MV$;
- the working RF frequency $f_{RF} = 2998MHz$;
- filling time $t_f \leq 3\mu s$;
- the available space of about $2m$
- the available RF power $P_{RF} = 15MW$;

The required deflecting voltage $V_\perp = 18MV$ is normally achieved by travelling wave (TW) structure. The optimization of the RF structure is extensively handled in the reference [9]. Table 1 lists the main RF and structure parameters of the deflector which has a phase advance for cell of $2\pi/3$. Geometric parameters are iris radius a, iris thickness t, period L and cavity radius b while RF parameters are quality factor Q, normalized group velocity $\beta_g = v_g/c$, attenuation constant α, $r_\perp/Q = (v_g/\omega_{RF})(F_\perp/e)^2/P_{RF}$ and $r_\perp = (F_\perp/e)^2/(dP/dz)$. Let us note that the group velocity is negative which means that the mode in the deflector is a backward wave. Thus the RF power will be fed in at the coupler at the downstream end of the structure. The connection between RF power and transverse deflecting voltage for the deflector $2m$ long was calculated in [9] and is given by:

$$V_\perp = 0.941\sqrt{r_\perp P_{RF}} \qquad (6)$$

Table 1: Main RF and structure parameters of the transverse deflector.

L	$33.33\ [mm]$	β_g	-0.0157
b	$59.33\ [mm]$	α	$0.1480\ [m^{-1}]$
a	$12.50\ [mm]$	$r_\perp/Q$	$2074\ [\Omega/m]$
t	$8\ [mm]$	$r_\perp$	$28\ [M\Omega/m]$
f_{RF}	$2.998\ [GHz]$	t_f	$0.425\ [\mu s@2m]$
$Mode$	$2\pi/3$	P_{RF}	$15\ [MW]$
Q	13500	$V_\perp$	$19.3\ [MV@2m]$

CONCLUSION

In this paper the study of the electron bunch deflection at around $1.2GeV$ for the measurement of the bunch length and of the transverse slice emittance is performed. Some of the basic formulas have been manipulated to evaluate the measurement resolution in the presence of a transverse finite emittance and on the screen resolution at the observation point. As a conclusion, a peak voltage of $18MV$ for the RF deflector is completely satisfactory for the bunch length measurement. The same specification allows for a resolution of 30 slices over the MLB with an intensity contrast of about 70% The analytical predictions have been verified by the particle tracking.

REFERENCES

[1] A. Zholents et al., FERMI Note ST/F-TN 07/01 (2007).

[2] P. Craievich et al., FERMI Note ST/F-TN 07/09 (2007).

[3] P. Emma, J. Frisch and P. Krejcik, LCLS Technical Note LCLS-TN-00-12 (2000).

[4] D.Alesini, "RF deflector-based sub-ps beam diagnostics: application to FELs, advanced accelerators and FERMI project", talk held at the Elettra Laboratory, 2006.

[5] M. Borland, APS LS-287, ICAP, Darmstadt, (2000).

[6] P. Craievich and S. Di Mitri, EPAC, Scotland (UK) 2006.

[7] A. Zholents et al., FERMI Note ST/F-TN-06/15, July 2006.

[8] P. Craievich, T. Weiland and I. Zagorodnov, NIM A, 558, 58 (2006).

[9] M. Petronio,Thesis of degree, Università degli Studi di Trieste, April, 2007.

THE BEAM DIAGNOSTICS SYSTEM FOR THE FERMI@ELETTRA PHOTOINJECTOR

L. Badano*, M. Ferianis, M. Trovò, M. Veronese, Sincrotrone Trieste, Trieste, Italy

Abstract

The quality of the photoinjector high brightness electron beam plays a crucial role for the performance of the seeded FERMI@elettra FEL. Optimization of the gun is possible with an extensive characterization of the 5 MeV electron beam longitudinal and transverse phase space. The photoinjector diagnostics system includes interceptive instrumentation as YAG:Ce screens for transverse position and profile measurements and Faraday cups for the absolute beam charge measurements. A Cherenkov radiator coupled to a streak camera provides an accurate reconstruction of the longitudinal profile and a slit/pepper pot followed by a screen is foreseen for the transverse emittance measurement. Information on beam transverse position and charge is obtained non-disruptively with respectively stripline BPMs and a current transformer. A dispersive beamline is also foreseen for the beam energy, energy spread and longitudinal phase space measurements. The diagnostics system performances and design principles are presented.

INTRODUCTION

Beam instrumentation has been designed to extensively characterize the low energy, high brilliance photoinjector beam in both transverse and longitudinal planes [1]. The nominal beam parameters in the FERMI photoinjector are summarized in Table 1.

Table 1: Photoinjector main beam parameters

Beam energy	5 MeV
Beam correlated energy spread	100 keV
Bunch charge	0.3 - 1 nC
Bunch length (FWHM)	10 ps
Bunch repetition rate	10 - 50 Hz
Min bunch transverse size @1 nC ($\pm 2\sigma$)	2.7 mm

During commissioning the bunch charge will be lowered down to 50 pC for thermal emittance measurements. The scintillation screens position versus horizontal beam envelope and projected emittance is represented in Fig. 1.

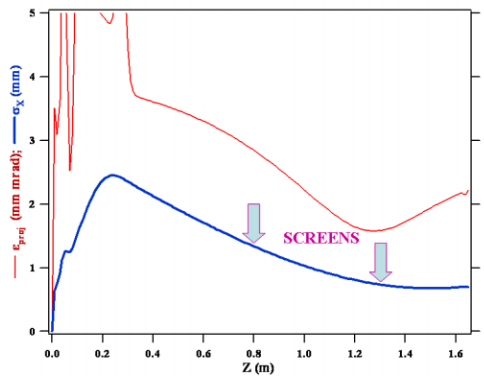

Figure 1: Screen position versus horizontal beam envelope and projected emittance behaviour as a function of the distance from the photocathode.

FERMI PHOTOINJECTOR BEAM DIAGNOSTICS SYSTEM

Beam charge measurement

Beam charge measurements provide information on possible drifts of the photocathode quantum efficiency and help to adjust the laser settings, in particular the correct phase between the laser and RF gun.

The beam charge will be measured non-destructively with a commercial, in-flange, high resolution current transformer [2]; a 60.4 mm internal diameter model is foreseen for the passage of the photocathode laser beam. An interceptive absolute beam charge measurement will be performed with a Faraday cup. Faraday cups including secondary electrons suppression allows 1 pC resolution, while the ICT performs a 1 pC shot-to-shot rms noise.

Transverse plane measurements

The photoinjector BPMs are matched stripline BPMs; electrodes are 150 mm long and signal detection is based on commercial, 500 MHz electronics. The strips are fixed to and aligned with respect to flanges which are, in turn, fixed to the BPM body. For locations where longitudinal space is an issue, resonant striplines [3, 4] less bulky than matched ones, are being considered; their dedicated electronics needs further developing.

Scintillation screens are the preferred solution to measure the electron beam transverse profile at low energy because of their higher photon yield compared to OTR screens. 100 μm thick Yttrium-Aluminium Garnet Cerium doped (YAG:Ce) screens ensure a spatial resolution better than 10 μm, compatible with the limit of the CCD

* laura.badano@elettra.trieste.it

pixel/sensor size and of the optical setup.

At low energies, where the beam dynamics is strongly dominated by space charge effects, accurate emittance measurements are performed using either a 2D pepper-pot device or a 1D slit array. Tungsten single or multi-slit convert the space charge dominated incoming beam into several emittance dominated beamlets which then drift to a detection scintillation screen. Evaluation of the rms emittance only depends on the slit mask geometry, the beamlets size and the intensity distribution on the screen [5], the resolution being mainly limited by jitters of the beam transverse position or profile.

Longitudinal plane measurements

The electron beam longitudinal current distribution and the bunch length are measured using an Cherenkov emitter (Silica aerogel with refractive index of about 1.008) coupled to a streak camera that performs a 200 ps resolution [6].

A magnetic spectrometer is a crucial diagnostics element for establishing the proper RF gun tune and overall performance. The dispersive beamline provides information on the beam energy, energy spread and longitudinal phase space [7]. The expected rms energy spread varies in the range 100 - 300 keV depending on the phase between the laser pulse and the gun peak field. The spectrometer design goal is to measure it with 1 % resolution.

FERMI PHOTOINJECTOR DIAGNOSTICS LINES LAYOUT

One of the crucial aspect in the design of the beam diagnostics system for the FERMI photoinjector is the very tight longitudinal space (less than 1 m from the solenoid exit to the entrance of the first accelerating session). In Fig. 2 the foreseen layout is schematically shown as a function of the distance from the photocathode.

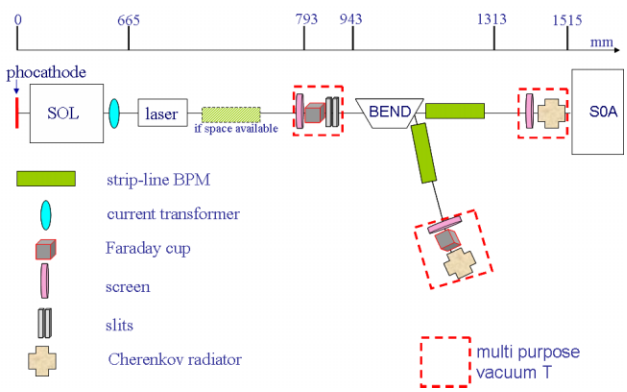

Figure 2: Schematic layout of the beam diagnostics system as a function of the distance from the photocathode.

In Fig. 3 the beam diagnostics system is integrated with the other photoinjector components. Just after the solenoid is a vacuum van followed by the current transformer for the non-destructive beam charge measurement.

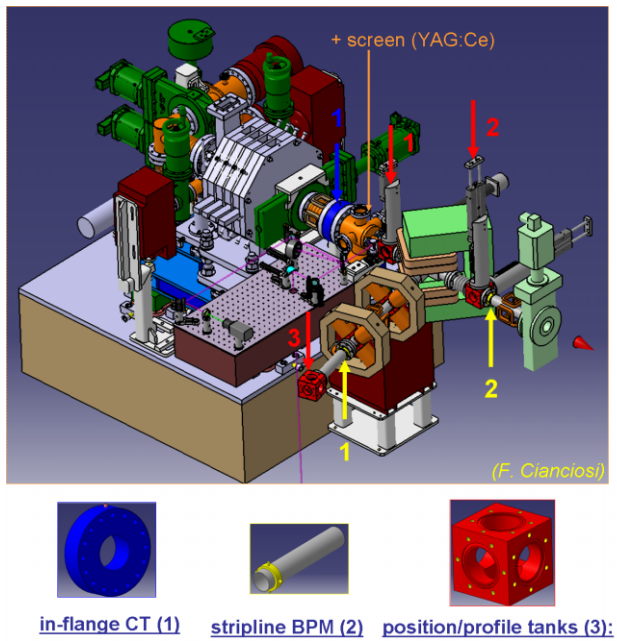

Figure 3: Photoinjector lines layout with instrumentation mechanical details.

The path of the photocathode laser beam inside the photoinjector vacuum chamber is represented in Fig. 4.

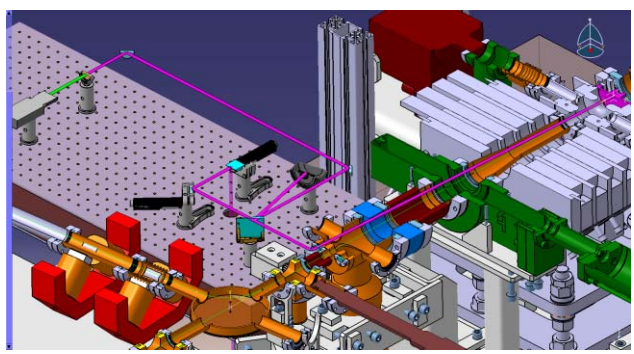

Figure 4: Photoinjector lines layout - cut view with laser beam path.

A first YAG:Ce screen, controlled by a stepper motor, will be placed in the tank for the photocathode laser beam entrance to adjust the beam centering and measure the dark current with the gun on and the laser off. A first beam position monitor (BPM) will provide non-interceptive information on the beam position if the available longitudinal space is sufficient. A second tank will host a YAG:Ce screen, a movable Faraday cup and the horizontal and vertical slits to be used for the emittance measurement with the second screen in the straight line.

A second BPM measures the beam position in the straight line after the spectrometer, followed by the screen for the emittance measurement; the tank will be equipped

also with a Cherenkov detector for the beam longitudinal profile measurement.

Finally, the dispersive beam line will be equipped with a BPM and a tank that hosts a screen, a Cherenkov detector and a Faraday cup. These monitors provides the beam intensity, position and profile and allow the reconstruction of the longitudinal phase space.

BEAM DIAGNOSTICS PROTOTYPE TESTS AT THE 1.0 GEV LINAC

Two diagnostics station have been installed on the 1.0 GeV LINAC to test FERMI diagnostics prototypes on the currently available beam. The station at 100 MeV, shown in Fig. 5, consists of an integrating current transformer and a tank equipped with an optical radiation transition screen (OTR) and two different scintillation screens: Chromox, traditionally used at the laboratory and a YAG:Ce screen for a better spatial resolution. The station at 1 GeV consists of a wideband longitudinal pickup (BAM) and a tank with the an OTR and two scintillation screens as above, as shown in Fig. 6.

Aim of the tests is to provide information on the main beam parameters as bunch profile and position, transverse emittance, charge and beam longitudinal structure.

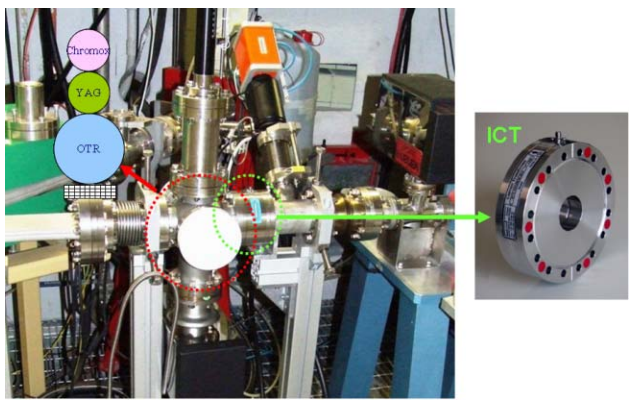

Figure 5: The FERMI beam diagnostics station prototype in the LINAC @ 100 MeV with a schematic representation of the screens/calibration grid geometry and a detailed view of the in-flange ICT.

The integrating current transformer, as shown in Fig. 5, is embedded in conflat flanges for direct mounting on the beam pipe and longitudinal space saving.

Screens are coupled to digital CCD (Basler A321f [8]) with remote controllable gain/shutter time to avoid saturation in a large dynamic range. It is foreseen to establish a remote control for the lens diaphragm and focus and to use telecentric lenses to increase the spatial resolution of the detection system. CCDs are shielded with lead bricks because of their low radiation hardness.

The two screen stations are equipped with an illumination system and a 10 mm long, 1 mm pitch grid in both vertical and horizontal planes for calibration.

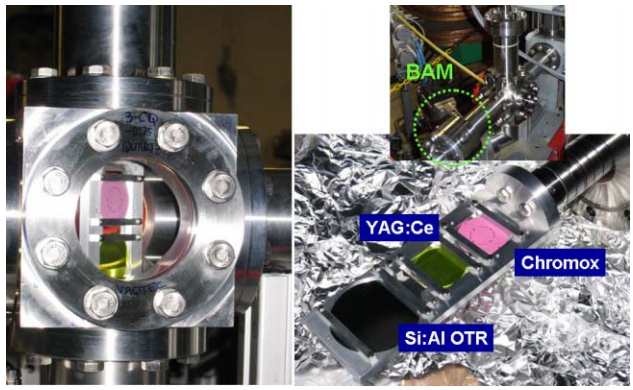

Figure 6: The FERMI beam diagnostics station prototype in the LINAC @ 1 GeV with a detailed view of the screens mounted on the support and of the in-flange BAM.

CONCLUSIONS

An overview of the beam diagnostics and instrumentation system for the complete characterization of the FERMI photoinjector low energy high brilliance beam is presented. Two FERMI diagnostics prototypes ready to be used in the ELETTRA 1 GeV LINAC for beam charge, longitudinal structure and transverse plane measurements are also described.

REFERENCES

[1] Conceptual Design Report (CDR) for the FERMI@Elettra project, http://www.elettra.trieste.it/FERMI, January 2007.

[2] In-flange integrating current transformer, model: ICT-CF6”60.4-40-UHV-05:1, CF100, 60.4 mm ID.

[3] M. Dehler, DIPAC 2005, 208 (2005).

[4] V. Schlott et al., EPAC 2006, 3017 (2006).

[5] M. Zhang, Fermilab-TM-1988 (1996).

[6] http://jp.hamamatsu.com/resources/products/sys/pdf/eng/e_fesca.pdf.

[7] J. Rönsch et al., DIPAC 2005, 66 (2005).

[8] http://www.baslerweb.com/downloads/11678/Basler_A312f_EMVA_Standard_1288.pdf

FPGA BASED FRAME GRABBER FOR VIDEO BEAM DIAGNOSTICS

I. Krouptchenkov, K.Wittenburg, DESY, Hamburg, Germany

Abstract

TV-based accelerator diagnostics are widely used for machine operation and beam diagnostics. It is planned to renew the video memory modules of the TV monitor data acquisition systems for the injection and transfer lines at DESY. New FPGA based Frame Grabber (FG) modules were developed within this project. The modules are required to be able to work with different analog signal formats, to capture video frames on trigger and to provide live mode operation. The main feature of this FG is the possibility of reprogramming. This allows us to optimize its functionality, for example to operate with non-standard or corrupted video signals. This has proved especially useful for grabbing images from CCD-cameras suffering from radiation damage.

INTRODUCTION

Beam diagnostic systems based on TV image acquisition are widely used at accelerators for tuning of transfer lines and for studying physical properties of the beam [1]. Beam monitoring using TV-cameras has a long history and this method is still popular today. These systems have a wide distribution due to their unsophisticated structure, low price because commercially available components can be used, and their relative simplicity in maintenance.

The hardware of a system consists of a movable scintillator or OTR screen, lens, a commercially available TV-camera, and a frame grabber. One example at DESY is the video beam diagnostics for the injection and transfer lines for the electron synchrotron DESY-2. A block diagram of the readout scheme is shown in Figure 1.

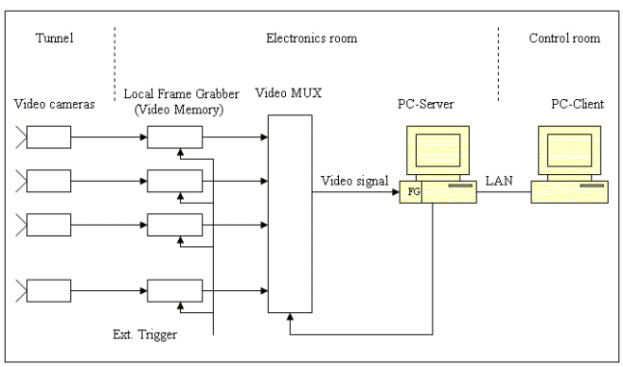

Figure 1: Block diagram of the readout scheme.

Images of the beam from the movable thin luminescence screens are read out by CCD video cameras. Radiation hard cameras are used in highly irradiated areas. The output signals of the cameras are digitized by local frame grabbers after an external trigger. The frame grabbers are triggered at the transfer or injection of electrons or protons. The two TV-half-frames are stored until the next trigger; the local FG therefore operates as a video memory. The output of the FG is an analogue TV signal of the stored half-frames.

The number of FG modules in a system varies from 1 (e.g. a synchrotron light monitor) up to 24 (e.g. a proton transfer line). The output signals of the local FG are connected to a video multiplexer which is controlled by a server in the control system.

The analogue FG output can be viewed in the control room using a TV or a PC with integrated frame grabber. For improved functionality, we now use a control system PC with integrated grabber [2] to grab the images, perform analysis, and to distribute the digitized images over the control system [3], [4]. In this way digitized and stored images of the beam from all screens can be displayed and analyzed off-line using client programs (see Fig. 2).

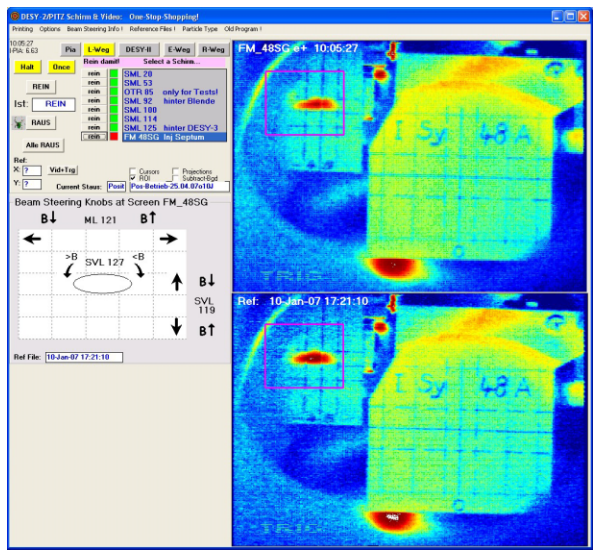

Figure 2: Image of the beam displayed using a transport line video client program. Upper image: live picture; lower image: reference picture; left side: control of the video equipment of the transfer lines.

The beam position as well as size and emittance can be measured from the screen images. This helps to improve injection efficiency, emittance preservation and beam optics matching.

It was decided to replace the more than 10 years old video memory modules [5] which were becoming difficult to maintain. Beam instrumentation has special demands compared to those of the consumer TV data acquisition market. There should be the possibility to treat the output analogue signal of the video camera before final digitization. It was not possible to find a commercial frame grabber with this feature. Another reason for the in-house development follows from the layout of the readout

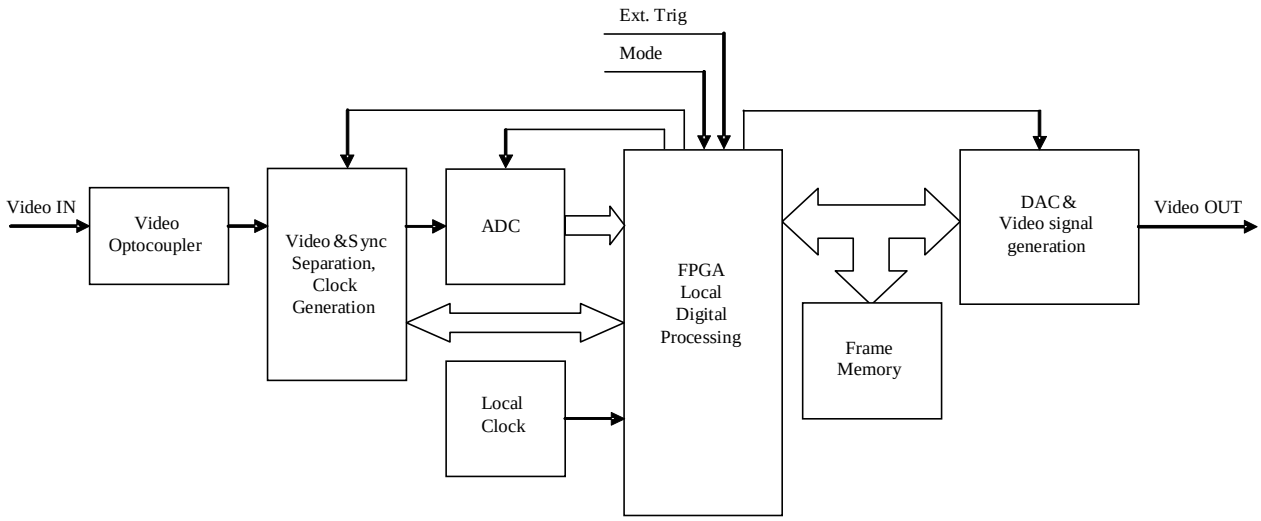

Figure 3: Block scheme of frame grabber.

schemes. In some locations we have up to 24 local FG, in others only one module is needed. Commercially available frame grabbers are mainly performed in PCI-standard. There is little sense in using either a group of PCs in the first case or a dedicated PC in the second case, only as a video memory. Therefore it was decided to develop a module which can operate either stand-alone, or as part of a multi-channel system.

DESCRIPTION

Figure 3 shows a block scheme of the frame grabber. The input video coupler can be used in order to avoid the possible large potential difference between the grounds of the FG and the video camera. An external trigger starts the TV data acquisition. Line and field synchronization signals from the sync-separator are used to start line and frame recording. A phase locked loop circuit synchronizes the digitization clock of the Analog to Digital Converter (ADC) with the incoming video signal. This means that a consistent number of samples are taken on each video line and more importantly that the samples are taken in a precise vertical line on the raster. This is essential for further digital processing. The 12-bit ADC converts the video signal to a digital representation at 13.5MHz sample rate. The data from the ADC is fed to a Field Programmable Gate Array (FPGA) for digital filtering. The result is stored in two 256kB high speed static memories. One or both fields of the input video signal can be recorded. Stored data is transformed to the output composite video signal by means of Digital to Analog Converter (DAC). A video line driver is used to drive the output signal. The stored picture is present on the output of the FG until the next external trigger signal is received. The FPGA controls the local digital signal processing.

Additional feature of the FG are:

- Ability to sense the standard of the input video signal,
- Automatic Gain Control,
- No signal detection,
- "Live" mode of operation,
- Status information (e.g. "No Input Signal") is integrated into the output video signal.

The module of FG is built on a compact 3U Eurocard format. In addition two types of enclosures for the FG were developed. The first type has one slot for a power supply and one for a frame grabber plus two additional slots for test and extra purposes. The second type has 17 free slots for FG modules in addition to the power supply. The boxes are based on a 19" enclosure. Two corresponding types of backplanes were developed as well. The pin assignments of the backplanes were chosen to be as close as possible to the VME-standard.

INITIAL EXPERIENCE

The main feature of the developed FG is the possibility for reprogramming. This is very important feature because the signals from the video cameras do not always meet TV-standards. Video cameras are generally located in high radiation environments. After a long period of operation, degradation of the output signal of cameras can be observed, even with extra shielding against the radiation. What we have found is that industrial frame grabbers are not always able to grab such degraded signals; they are designed for clean, standard input video signals. In such a case it would be necessary to replace the camera which is a costly and time consuming solution. The designed FG module is able to grab images with partially corrupted signal. Thus it allows us to extend the useful lifetime of the video cameras.

Figure 4 shows the composite video signal from the camera SY48a located in one of the transfer lines. One can see that the total period of one video line is 63μsec; this period in the PAL TV-standard is 64μsec. Some commercial FGs have difficulties to grab such a signal. In

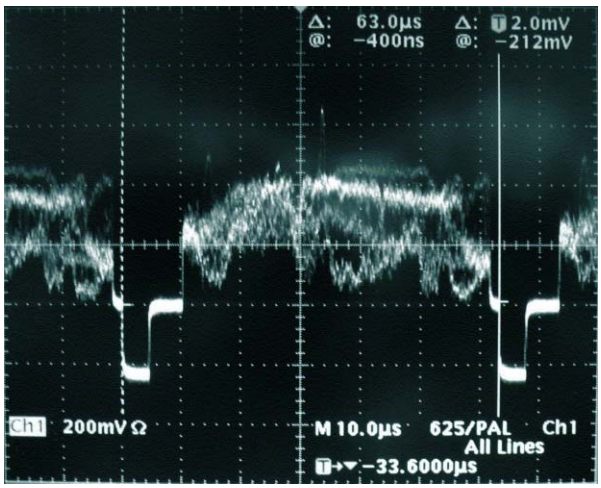

Figure 4: Degraded composite video signal.

one extreme case, for a camera in operation the total period of one line was only 61.16µsec. The developed FG was able to grab this signal. Thanks to the possibility to reprogram the FPGA it was possible to process this signal and convert it into the standard PAL format.

Another adverse factor is noise. Often the processing electronics are located hundreds of meters away from the TV-camera because of the radiation environment. This means that the incoming video signal can be noisy. In such a case additional digital filtering inside the FPGA helps to achieve a useful video picture.

SUMMARY

Commercial available frame grabbers do not always satisfy the requirements of accelerator beam instrumentation. The new FPGA based frame grabber module can be used as a video memory in TV image acquisition systems for electron and proton transfer lines and first turn analysis in storage rings.

Due to their reprogramming ability it is possible to operate the frame grabbers with noisy or corrupted video signals. This allows us to postpone the replacement of video cameras located in radiation environments.

ACKNOWLEDGEMENTS

The authors wish to express their gratitude to Mark Lomperski for his interest and help during commissioning. We would like to thank our colleagues from IHEP (Protvino, Russia) for the manufacturing of the printed circuit boards for the modules and backplanes.

REFERENCES

[1] J.A. Clarke, “A review of optical diagnostics techniques for beam profile measurements”, 4th European Particle Accelerator Conference (EPAC94), London, England, 1994.

[2] DALSA-CORECO PC-Vision PCI card.

[3] F. Solodovnik, T. Limberg, K. Wittenburg, “Analysis of the Proton Beam in the DESY Transport Lines by Video Readout”, 4th European Workshop DIPAC99, Frascati, Italy, 1999.

[4] S. Weisse, GrabServ2 – A Program to Acquire Images from Cameras“, DESY Internal Note, 2003.

[5] M. Werner, “Digitalizierung und Aufbreitung eines Kamera Signales”, Diplom Thesis RWTH-Aachen, 1984

.

THE NEW DIODE BPM SYSTEM FOR ELETTRA

R. De Monte, Sincrotrone Trieste SCpA, Trieste, Italy

Abstract

A new Beam Position Monitor system has been developed at ELETTRA based on an envelope detector. It is a four channel system reading in parallel the four voltages from a button pick-up that adopts a wide-band Schottky diode. The analogue bandwidth of the currently implemented detector is less than 1 kHz which has been adapted to the present application of the system, i.e. a fast beam position interlock to be installed on the ELETTRA storage ring.

The upgrade of the ELETTRA BPM which is based on the Libera detector suggested us to add some redundancy on the fast position interlock in order to protect the vacuum chamber from wrong positions / angles of the beam. The data collection scheme, based on a single board computer for each straight section, is presented. Currently, the system has been installed and tested on all the ELETTRA undulator sections; the first running experience is here presented.

THE HARDWARE

The main purpose of the system is the real time acquisition and comparison of two BPM readings, the ones upstream and downstream the ID straight, to prevent the overheating of the Elettra front ends vacuum chamber due to wrong beam trajectories. It is running in parallel with the close orbit BPM detector (Libera).

.

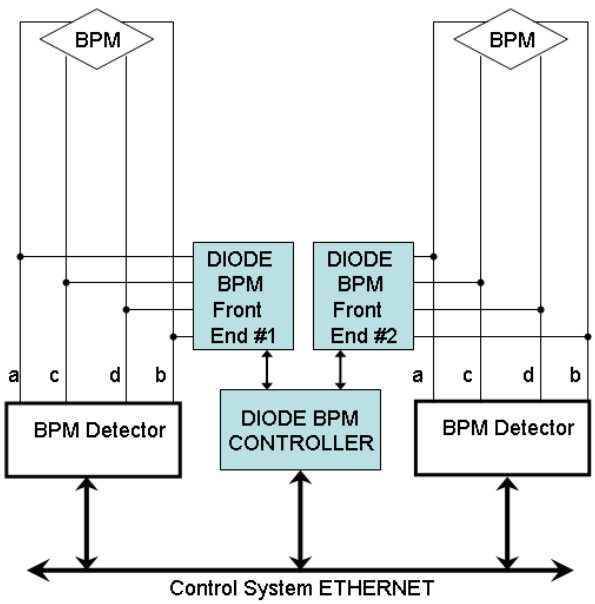

The Front End electronics is closed to main signal cables. It is connected with a 'T' connector to maintain the insertion loss as low as possible. The total signal loss for the BPM detector when the DIODE BPM Front End is connected is 5% of the total signal. The wide-band Schottky diode used in the front end is few millimetres away from the connector to keep RF reflections at a minimum level.

The Front End board

The Front End simplified schematics is shown in the figure above and represent one of the four channels of one Front End Board.

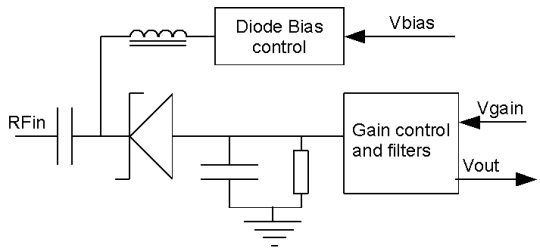

"Vgain" is software controlled using a single 12 bit DAC fitted to the DiodeBPM controller, common for the four channels. 'Vbias' is software managed using a 4 channel 16bit high precision DAC available on the Front End board. All the signal conditioning is performed by ultra low noise operational amplifiers to keep the total noise as low as possible.

The frequency range of these inputs goes from 100MHz to 800MHz. The upper bandwidth is limited by the cable capacitance whose length has been kept at a minimum to reach optimum performances. On the Elettra installation, the mean values of the rectified signal are listed in table 1.

mA	15m cable	25m cable
300	700 mV	450 mV
200	480 mV	300 mV
100	200 mV	130 mV
75	140 mV	80 mV

table1

The two front ends are linked to the Diode Bpm Controller via two flat cables. The RC filters after the diodes assures a flat response up to 1KHz. The subsequent filters, have a cut-off frequency of 300Hz; these low values are used to avoid any interference with an RF multiplexer present on the BPM detector connected on the same cables that in our case are 8 KHz of Libera Detectors.

The Controller board

The simplified block diagram of the Controller is shown on the figure above:

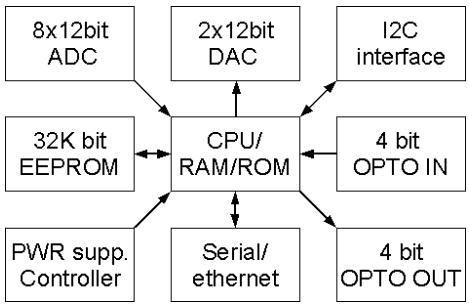

The CPU is an Analog Devices 80C51-compatible ADuC812 microcontroller. It runs at 11MHz without operating system. The communication with the Elettra Control System Network is granted by a Lantronix serial to Ethernet adapter, "transparent" towards the CPU serial port. There are also 4 bits of opto-coupled inputs and 4 bits of opto-coupled outputs. In Elettra implementation these I/O are connected with a PLC that is super visioning the undulator status and the Elettra machine current. One of these opto-coupled outputs is linked to the 'Beam Kill' signal. The 32kbit EEPROM is used to store calibration data concerning the two associated Front Ends. The I2C bus is used to communicate with the remote quadruple 16 bit DACS that resides on the Front End and that provide very accurate biasing for the Schottky diodes.

THE SOFTWARE

The CPU is an 8 bit single chip microcontroller @11MHz. It has 128KB RAM and 128KBFLASH ROM. The software is written in 'C' language. The software is structured in a way to be very deterministic. In fact all of the main tasks are done in an InterruptServiceRoutine (ISR) waked up by a timer. The commands received by the CPU via the serial/Ethernet link are processed at very low priority, and is not possible that any command stop the acquisition.

The main software tasks are: 8 ADC reading, automatic gain control, position computation using offsets and lookup table coefficients, limits and in undulator beam trajectory computation. All of the calculi are in integer, so internally the algorithms perform some multiplications and divisions by 1000 for precision purposes.

ADC reading

An internal timer is programmed to start acquisition of the eight 12 bit ADC's at 10Hz. After the acquisition starts, four values for every channel are stored and used to make a mean to increase the signal/noise margin. When the mean is computed, the other tasks in the ISR routine are executed.

Automatic Gain Control

When the mean data from ADC are available, the Automatic Gain Control routine is executed to check the levels. The routine maintain the ADC values at 85% of the ADC capability -+ 5%, driving the two DACS, one for each Front End. The routine compute also a correction factor for the absolute signal values used to compute the position. The formula used is:

*delta_agc = (ActDAC – DefltDAC) * DAC_gain*

where ActDAC is the actual applied DAC value, DefltDAC is the DAC value to read 0 with no signals and DAC_gain is a number derived from the operational amplifiers gain that is in our case is 3.7. As result, we will have the four electrodes values that are in range 0-8000 from a zero signal to full signal accepted by the system (1500mV).

Calibration factors and lookup table

The Schottky diodes have no linear response with signals. For that reason, a laboratory calibration is made to linearize the response of the diodes versus the signal input. From this calibration, performed putting a known source, a lookup table is obtained. This is a graphical representation of one of them:

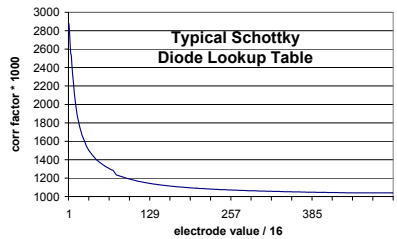

The values are stored in the EEPROM and are common for 4 electrodes of every Front End.

Other calibration factors calculated in laboratory and stored in the EEPROM are:

- The 4 values of the 16bit DAC to maintain every Schottky diode with a same bias current that correspond at 500mV in the rectified point.
- The AGC DAC value to read 0 with no input signal
- The four little offsets to read 0 on every electrode (Za,Zb,Zc,and Zd). This value is subtracted to any ADC read value: the values are in example -7 -21 -30 -15 and are generated by little differences in gain control and filters block.
- The four multiplication factors to read the same value on the four channels at full signal input MFa,MFb,MFc,and MFd.

Position Computation

The position routine applies all of the calibration coefficients, and applies different correction factors every 16 units according the Lookup Table. To compute the X and Y position the standard formula for rhomboidal BPM is used:

$$X = X_COEFF\frac{(Va+Vd)-(Vb+Vc)}{Va+Vb+Vc+Vd}$$

$$Y = Y_COEFF\frac{(Va+Vb)-(Vc+Vd)}{Va+Vb+Vc+Vd}$$

$$\text{Where: } Vx = (\text{VmeanADC - delta_agc - Zx}) * \text{MFx}$$

The position is computed synchronously and a circular buffer with the last 200 values is saved, ready to be read by control system as all other operating parameters.

An additional task is also performed once the position is computed: an orbit trajectory is calculated in order to protect the vacuum chamber and if the position is considered dangerous, a signal is generated on one of the opto-coupled outputs to dump the beam.

THE RESULTS

Actually 12 DIODE BPM SYSTEM is installed and is operating in the Elettra Storage Ring.

The on field performances with 50-400mA machine current, 20mm vacuum chamber, a stable beam are:

RMS uncertainty : max 40µm min 15µm

8-hour stability : max 50µm

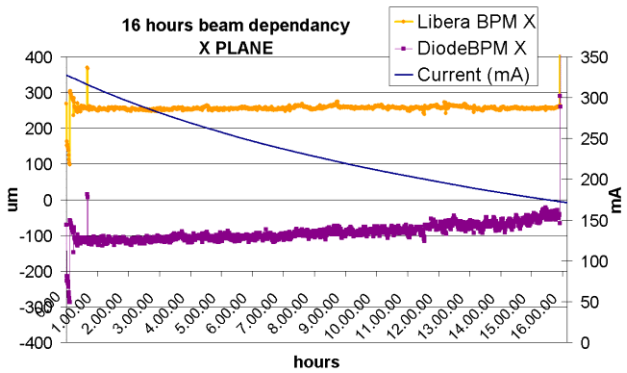

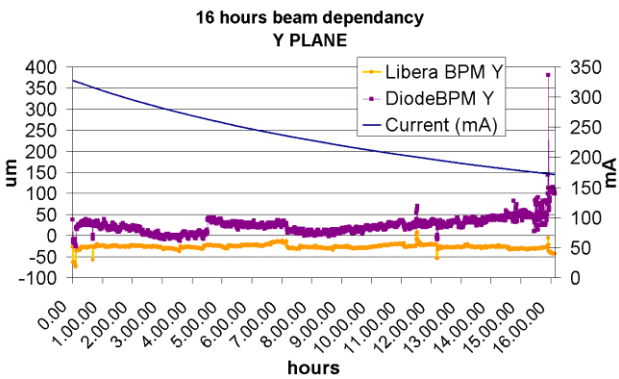

On the Y plane graph is possible to observe a local orbit correction software effects.

THE CORRECTIONS

The big disadvantage of the direct diode detection is the wider bandwidth. That gives the position computation affected by higher modes instability of the machine. This happens because the four input stages react slightly differently one to each other at different frequencies, due to mechanical/component tolerances. A good solution has been found and consists to:

- use diodes, capacitors, resistors of the input stage from the same series/lot/production
- mount the input stage with very low on soldering
- clean very carefully from every soldering residual

With these tricks we reach a maximum of 5% of position reading mismatches for an 'in centre' beam from 400 to 800MHz. The effects are visible in the acquired on field graphs above:

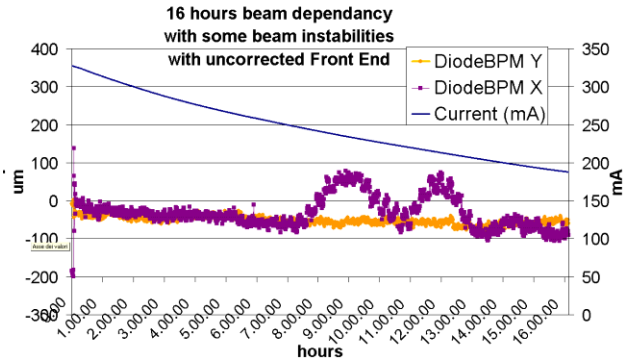

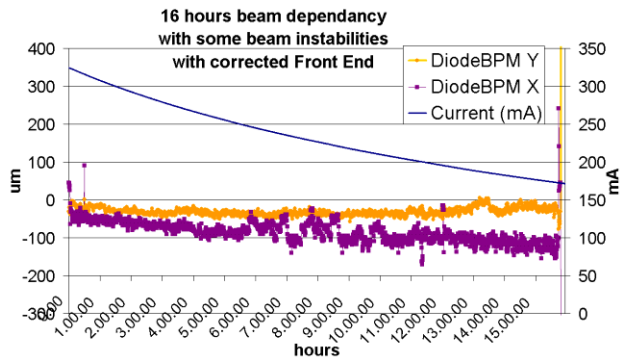

CONCLUSIONS

The system is installed and operating on all Elettra's BPM that are around the undulators. It has detected some wrong orbit values and it has generated the appropriate Beam Dump signal to prevent vacuum chamber damages. During the system's commissioning few spurious beam dump has been generated due to electronic lacks.

ACKNOWLEDGEMENTS

We would like to thank V. Forchì and M. Lonza for their help throughout the on field installation of the system, integrating it into the Elettra's Control System.

REFERENCES

[1] M. Lonza et al.: "BPM detectors upgrade for the ELETTRA Fast Orbit Feedback", DIPAC2007

[2] M. Gasior, R. Jones,"High sensitivity tune measurement by direct diode detection", DIPAC'05

ULTIMATE RESOLUTION OF SOLEIL X-RAY PINHOLE CAMERA

M.-A. Tordeux*, L. Cassinari, O. Chubar, J.-C. Denard, D. Pédeau, B. Pottin.

SOLEIL, Saint-Aubin - BP48, 91192 Gif-sur-Yvette, France.

Abstract

During the SOLEIL Storage Ring commissioning, the beam emittances have been measured with an X-ray pinhole camera. As a result of the excellent alignment of the ring magnets, the vertical beam size is smaller than expected. It prompted an effort for improving the initial resolution of the instrument. Selecting the harder X-ray part of the radiation spectrum seems the key element leading to better resolutions. However it requires a more sensitive CCD camera. Recently, the machine has been tuned up to a very low coupling (~1‰) and the usual quadratic addition of the individual resolutions (pinhole geometry, diffraction, CCD) did not fit the measurements. A better analysis using the "Synchrotron Radiation Wavefront" (SRW) code shows that the actual resolution limit due to the pinhole itself is twice better than expected and as a consequence, resolutions in the 4 µm range are achievable even for medium energy machines like SOLEIL.

INTRODUCTION

A pinhole camera, based on the ESRF design [1] is installed at a location with a low dispersion value of 1.8 cm. The rms beam sizes at that place are theoretically 40.5 µm in the horizontal plane and 23.8 µm in the vertical plane for 1% coupling. Beam size measurements show a 3.7 nm.rad horizontal emittance (as expected) and a machine coupling below 0.5%. For monitoring the coupling down to 0.1 % we need to accurately measure an 8 µm beam size, which requires a resolution in the 5 µm range. This paper reports on the evaluation of the ultimate resolution the present instrument can achieve.

At a fixed wavelength, there is an optimum pinhole size that can be evaluated with Fraunhofer diffraction formula. By inserting a tapered piece of copper in the photon beam path, we can select a higher part of the spectrum at the cost of the photon count on the CCD camera. The radiation spectrum that creates the visible photons arriving on the CCD can be computed. Then, the Point Spread Function (PSF) of the geometric and the diffraction contributions of the pinhole, can be added quadratically in order to evaluate the optimum pinhole size and the resolution. However, the optimum resolution occurs in a region where the Fraunhofer diffraction formula is not really valid. A better way consists in simulating the propagation of the actual X-ray wave front from its source up to the scintillator, this is done with the SRW code [2].

MONITOR DESCRIPTION

The instrument set-up is shown in figure 1. The X-ray beam comes out of a bending magnet from a source point 3.8° downstream of the magnet entrance. The photon beam exits the Storage Ring vacuum through a cooled aluminum slit-window assembly machined out of an aluminium-stainless steel flange. The 1 mm wide slot has a 0.22 mrad horizontal aperture. It limits the radiation power that exits the window to 17 W at most. A tapered copper block acts as a filter-attenuator. Its thickness along the beam path can be set from 0 up to about 15 mm. The pinhole, like that of the ESRF [1], is made of tungsten plates and one can choose between 3x3=9 rectangular holes of different horizontal and vertical sizes. The pinhole assembly is remotely moveable with four degrees of freedom. It is located 4.36 m from the source point. A transparent cadmium tungstate (CdWO4) scintillator is located 5.7 m downstream of the pinhole. The photo electric absorption of the X-ray energy in the crystal is converted in visible light emitted omnidirectionally along the X-ray path. This scintillator has been the ESRF choice. More recently after testing different materials DIAMOND adopted it too. The imaging system with two CCD cameras is protected by a thick lead wall. One camera has a field wide enough to see the whole scintillator (8x10 mm); the other with an optic of better quality and greater magnification measures accurately the beam sizes. The Al window, the pinhole assembly and the camera housing are aligned on the 3.8º direction of the synchrotron radiation fan.

An image analyser calculates the beam size several times per second.

MONITOR RESOLUTION

Simplified theoretical model

From the geometry shown in figure 1, a point source of light illuminating a rectangular hole at a distance d, will project a rectangular spot of light on the scintillator. The size of that spot is a (D+d)/d, where "a" is the hole width and D its distance to the scintillator. The camera geometric magnification is D/d, and the corresponding Full Width Half Maximum (FWHM) of the point spread function (PSF) at the source is:

$$Wg_{FWHM} = a\,(D+d)/D \qquad (1)$$

This formula shows the PSF improving with smaller holes. This is true as long as the effect of diffraction is negligible, for $a >> 2\sqrt{(\lambda d)}$.

For very small holes the PSF is dominated by the diffraction. Its FWHM width is:

$$Wdiff_{FWHM} = 1.10\ 10^{-6}\ d/(a*E) \qquad (2)$$

where E is the photon energy in eV; the other dimensions are in meter.

*marie-agnes.tordeux@synchrotron-soleil.fr

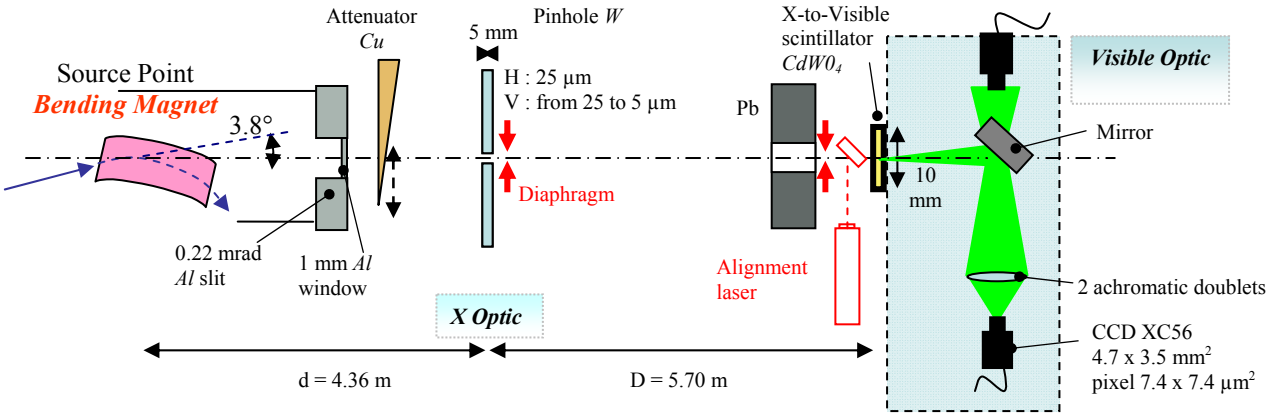

Figure 1: Pinhole Camera set-up

There are several reasons to express the PSF width in terms of the FWHM instead of the usual standard deviation of a gaussian fit to the actual function: i) the full width at half maximum is well defined and does not depend on the type of fit performed, ii) the FWHM value can be retrieved from the SRW data output, and iii) the experimental results can also be expressed in this way, without any approximation problem.

For the sake of simplicity, we can add quadratically the geometric and the diffraction widths of the pinhole PSFs. It is an approximation since the operation is valid only for gaussian distributions. Let's mention that the complete PSF also includes the scintillator and the CCD camera PSFs. The scintillator is transparent and there should be no significant secondary scattering of the visible photons inside the crystal as long it does not darken with time. The resolution of the CCD camera has been carefully measured; it amounts to 3.7 µm. It can be made negligible by increasing the optical magnification. Then, we are left with the geometric and the diffraction PSFs for our search of the ultimate resolution.

Effective X-ray spectrum

For calculating the PSF width we need the effective radiation spectrum that yields the visible photons collected on the CCD. The spectrum is that of the photon beam, attenuated by the 1 mm of the aluminum window, 6 m of air, the filter-attenuator in copper, and the scintillator conversion efficiency. The CdWO4 conversion efficiency is proportional to its X-ray photo-absorption [3]. The NIST web site [4] provides the data needed for all these materials.

The filtering applied to the synchrotron radiation for several copper thicknesses and the intensity of the visible light on the CCD expected for these thicknesses, are shown in figure 2a and 2b. To each spectrum corresponds a mean energy that can be applied to formula (2). The result of the quadratic combination of formula 1 and 2 for several thicknesses of copper is shown in figure 3.

The exposition time of the XC56 Sony camera can be controlled up to 0.5 second. With an optical magnification of 2.6 and an f# of about 10, such a camera enabled to measure beam sizes at 200 mA with up to 3 mm of copper. Figure 3 predicts the FWHM resolution would get down to 14.6 µm (~6.25 µm rms) with a 6 µm optimum pinhole size for that thickness.

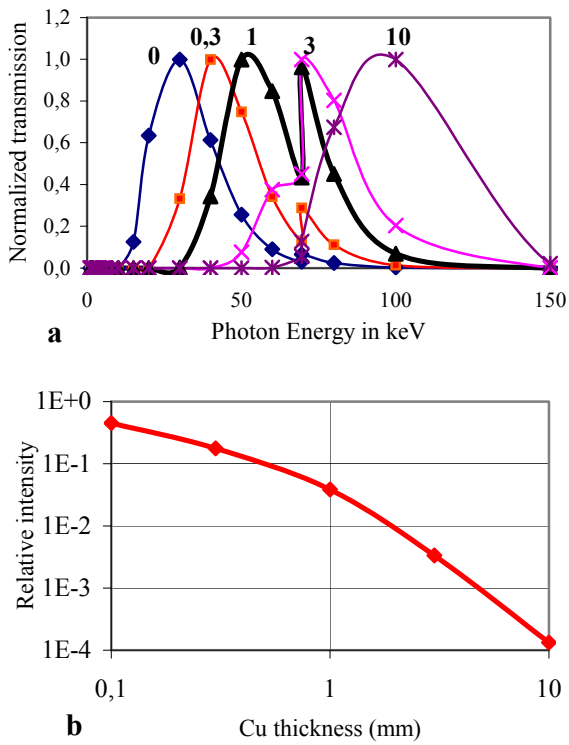

Figure 2: a) Normalized transmission spectra for several copper thicknesses (in mm). b) Relative intensity of the visible light collected on the CCD versus copper thickness. No copper is the reference.

Actual beam size measurements

After optimizing the machine coupling and with 20 mA in the Storage Ring, the vertical spot size on the scintillator was measured at 26 µm FWHM with a 10 µm hole and 0.3 mm of copper. Taking into account the instrument geometric magnification of 1.31, it translates into a 19.8 µm FWHM beam size. It is quite surprising since with that copper thickness, figure 3 (second curve

from the bottom) predicts that same value for the 10 µm pinhole resolution alone.

A problem arises when we want to fit narrow vertical beam profiles to a gaussian distribution: the base is wide, only the top half resembles a gaussian. Actually, the relevant information is contained in the top half of the beam profile. The image analyzer fits the top half after bringing the base to the background level, away from the beam spot. The FWHM of the gaussian fit and that of the vertical beam profile are near equal. Then, we consider the rms width of a beam profile or the resolution of a PSF is that of the gaussian.

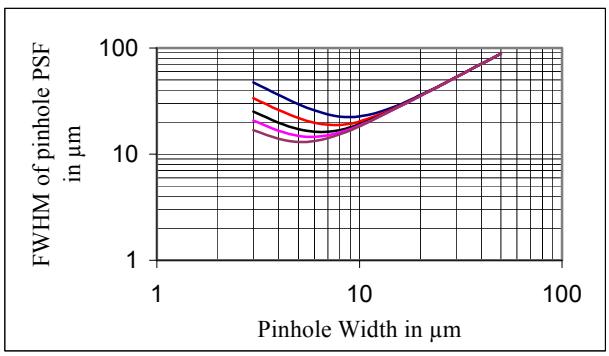

Figure 3: FWHM of pinhole PSF via the quadratic addition of the geometry and diffraction contributions. The five mean energies of fig.2a spectra have been used for the computation.

Simulation with the SRW code

SRW [2] is a wave optics simulation code that can take the actual wave front of the light emitted by a filament like source in the bending magnet and propagate it through the hole, up to the scintillator. With the proper spectrum as an input, SRW can calculate the PSF on the scintillator (fig. 4). The FWHM of the PSF versus the pinhole size is shown in fig.5. One can observe that its minima are about twice smaller than previously anticipated. They all occur with pinhole widths comprised between 10 and 15 µm instead of the 6 to 10 µm expected range. If we neglect the instrument resolution, the 19.8 µm FWHM previously measured corresponds to a 4.7 pm.rad vertical emittance and to a coupling less than 0.13 %. A camera ten times more sensitive should allow increasing the visible optic magnification by a factor of 3 which would make the CCD resolution negligible (1.3 µm rms). Then, a 3.5 µm rms global resolution is achievable.

Looking at the graph shown in fig. 4, one can see that the gauss-like criterion applies to the black curve which is the most interesting one since it features the minimum width. Then we can interchangeably use the rms or FWHM values linked by the relation:

$$W_{rms} = W_{FWHM} / 2.355 \qquad (3)$$

CONCLUSION

The experience confirms the results of the SRW computation code. SOLEIL X-Ray pinhole camera equipped with a simple CCD camera already achieves a resolution in the 5 µm rms range and a machine coupling less than 0.13 % has been measured. A more sensitive camera is on order. It should bring the instrument performance to 3.5 µm which is much better than has ever been expected.

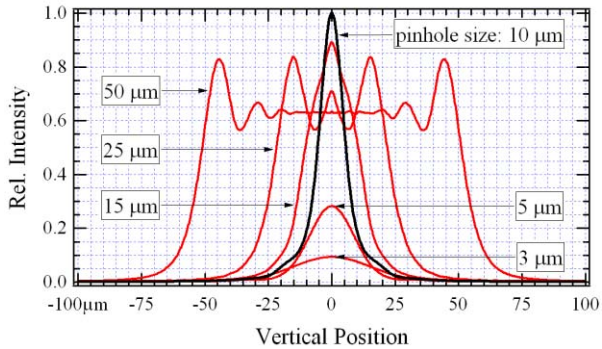

Figure 4: PSF on the scintillator from SRW for several hole sizes with 1 mm of copper.

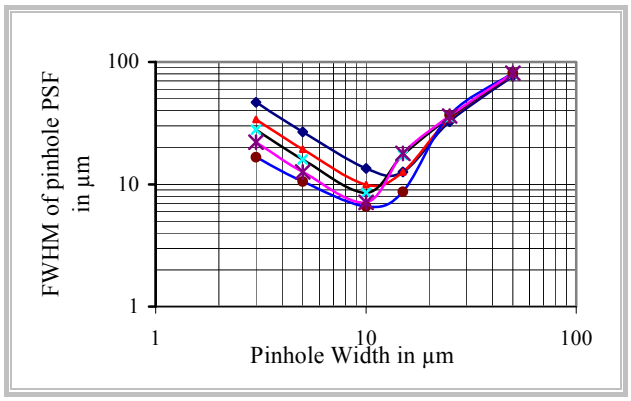

Figure 5: FWHM of pinhole PSFs obtained with SRW. The five curves correspond to the five spectra of fig.2a

ACKNOWLEDGEMENTS

We would like to thank P. Elleaume from the ESRF, C. Thomas from Diamond, Kadda Medjoubi from the SOLEIL detectors group, for very fruitful discussions.

REFERENCES

[1] P. Elleaume et al., J. Synchrotron Rad. (1995). **2**, 209-214

[2] O. Chubar and P. Elleaume, "Accurate and Efficient Computation of Synchrotron Radiation in the Near Field Region" EPAC98, THP01G, pp.1177-1179.

[3] C. Thomas, BIW2004; Diamond internal report.

[4] NIST physics reference data http://physics.nist.gov/PhysRefData/Xcom/Text/XCOM.html and http://physics.nist.gov/PhysRefData/XrayMassCoef/ComTab/air.html.

NEW TYPE PHOTOCATHODE FOR X-RAY STREAK CAMERA OF THE 10-FS RESOLUTION

A.M. Tron#, LPI, Moscow, Russia
T. Gorlov, MEPhI, Moscow, Russia

Abstract

High current streak camera with new principle of operation allowing to get resolution of the order of 10 fs in the frequency range both of visible light and x-ray is described. One of the key units of the camera is photocathode of spherical configuration with its surface radius of 10…100 micrometers. For creating the photocathode new technologies, developed and realized, are described. The results of the photocathode fabrication and investigations of its main features are presented and discussed.

INTRODUCTION

Longitudinal profile monitoring of short electron bunches or x-ray pulses with temporal resolution of the order of 10 fs and less is playing an increasingly critical role at present that is dealt with creation, first of all, of the x-ray FEL, based on the SASE FEL concept [1, 2].

All well-known methods for short electron bunch length and shape monitoring with resolution in femtosecond range may be divided onto two groups. One of them bases on measurement of bunch radiation spectrum in frequency range of coherent radiation with further retrieving of the bunch shape assuming that the spectrum, emitted by a single electron in specific terms of device, is known exactly, - that is not so [3] and that can be extend to any type coherent bunch radiation. The coherent technique can be considered more as a technique for indication of changes in the bunch length or shape.

The second and more reliable method is the method based on registration of the bunch radiation intensity in the frequency range of incoherent radiation by means of technique like a streak camera.

A conventional streak camera is a reliable tool for recording the bunch radiation, but its resolution in the range of visible light does not exceed 300…200 fs [4], and in the range of soft x-ray the streak camera is the only tool, but its resolution here is near 1 ps [5].

Hence, at present we need the measuring technique exceeding the reached temporal resolution by a factor of 10^2 at least for the mentioned x-ray pulse measurement.

In the paper x-ray streak camera realizing new principles of operation [6, 7] is considered.

The results of investigating a space-charge and photocathode surface roughness effects on the new type camera resolution have been carried out early and published in papers [8, 9].

The key unit of the camera is a principal new photocathode of spherical configuration, technology fabrication of which is presented in the paper.

#atron@sci.lebedev.ru

NEW PRINCIPLES IN STREAK CAMERA OPERATION

New principles consist in the following: transformation of the time of photoelectron escapement from photocathode into its energy is carried out at the moment of the escapement and for the shortest time.

By combining the electrostatic accelerating field and rf-field, modulating electron on its longitudinal momentum, and taking the radius of the photocathode surface rather small (100…20 μm) one can enhance and localize the field near the surface of emitter so that the time of effective interaction between photoelectron and these fields will be about 1 ps. In the case many effects cannot develop, and the resolution can reach 10 fs and much less.

CAMERATRON - NEW GENERATION PHOTOELECTRON CAMERA WITH THE LIMITING TEMPORAL RESOLUTION

By reserving the name “streak camera” for a conventional photoelectron camera with transverse swiping photoelectron beam it could be reasonable to call the new camera, emphasizing its principal distinctions, shortly as “cameratron” where time transformation is occurred at a photocathode surface by using a longitudinal modulation and the photocathode surface with a small radius of its curvature.

In Figure 1 a possible scheme of cameratron is shown, where the photoelectrons, modulated in energy in the gap, are analysed with a spectrometer. The rf-gap is a capacity gap of a quarter wave coaxial resonator with its internal conductor ending by needle with a tip in the form sphere, covered by a photocathode material.

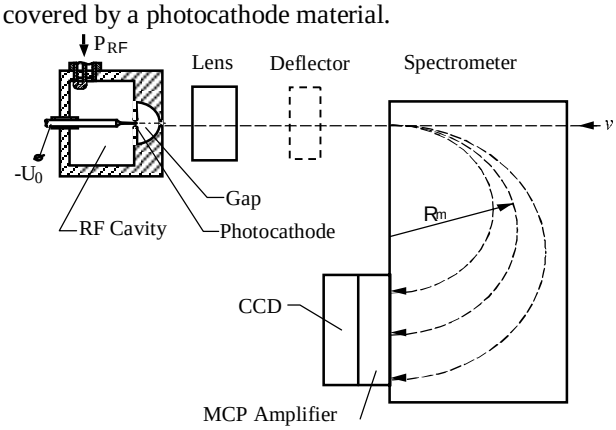

Figure 1: Scheme of cameratron with longitudinal modulation of photoelectrons in spherical gap.

For recording the longitudinal bunch charge distribution within the bunch train and without them superimposing the deflector, in the scheme, is installed, that deflects the bunch distribution from bunch to bunch during the train in the direction perpendicular to plane of the picture.

As to chromatic aberration of the lens and deflector, shown in the camera scheme, it should be noted that the resolved line of the camera (corresponding to its temporal resolution nearly 10 fs) equaled to about 0.01% in particle momentum and total relative spread in the photoelectron bunch after the modulating gap is less than 1%, so that the aberration will be negligible.

Rf-power for the camera resonator can be supplied from appropriate rf-system of an accelerator, so that, in the case, there is no, in fact, a time jitter, and electronic part will be more simple in comparison with corresponding part of a conventional streak camera.

In Figure 2 the scheme of the spherical gap more in detail is presented, where the diaphragm radius and its thickness are r_d = 1 mm and h_d = 1…2 mm, the external and internal conductors of resonator - r_{in} = 1.6 mm and r_{ex} = 19 mm at the frequency 3 GHz, r_a= 1 mm, l_n= 5 mm.

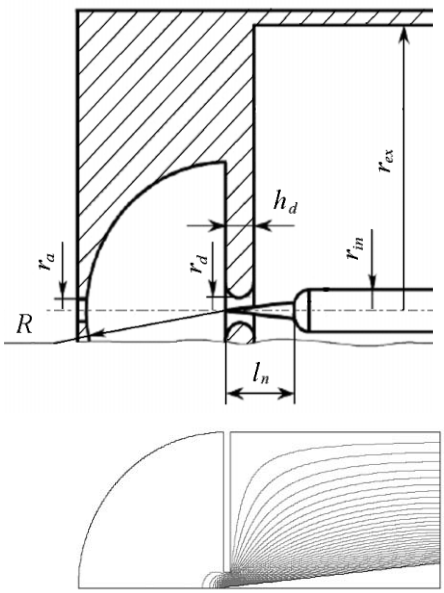

Figure 2: Layout of quarter wave coaxial resonator with its capacity gap forming itself the modulating gap of the camera, below which equipotentials in the gap with the outside line relative level of 0.025 are shown.

The photocathode radius was taken R_0 = (50±5) μm; the electrostatic voltage on the gap - U_0 = -4 kV. The amplitude of the modulating field at the 3 GHz frequency is U = 10kV.

Space charge effect in the camera has been investigated in detail with self-consistent bunch dynamics simulation by representing the bunch as an assembly of charge rings in the paper [8]. More in detail of cameratron, its characteristics one can find also in paper [7].

PHOTOCATHODE

The photocathode surface roughness is main parameter that strong impacts on the camera resolution. This effect is rather importent also for bunch emittance formation in photogun. The first time and in detail, with high accuracy the effect has been investigated in paper [9].

Requirements

By means of statistical tests the temporal resolution of the camera, taking into account an angular distribution as a cosine-cube type and initial energy distribution for the gold photocathode, illuminated by x-ray, taken from the paper [10], has been determined for the photocathode surface roughness with its rms slope of 0.3 and 0.1, (definition of which is presented in the paper [9]). The resolution of the camera gap have been defined as ratio of a twice standard of electron distribution in the r-component of the electron momentum at the exit of the camera gap to the derivative of outlet momentum of the electron with respect to its time of start.

In Figure 3 the dependences of temporal resolution for the x-ray camera on the rms height surface roughness are presented.

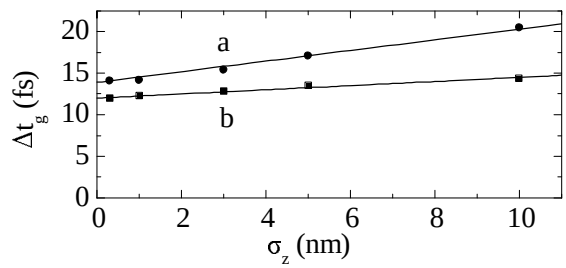

Figure 3: Dependences of x-ray camera resolution on rms height of the gold photocathode surface roughness for two rms slopes of it: $\sigma_{tg\alpha}$ = 0.3 (**a**), $\sigma_{tg\alpha}$ = 0.1 (**b**).

Hence, for getting temporal resolution not worse 20 fs, the rms height of roughness must not exceed 10 nm.

Technology

The technology of metallic photocathode fabrication consists of the following steps.

1. Shaping photocathode holder with semi-angle of taper within 3°…5° by electrochemical etching.

2. Spherical shaping the tip of the holder (see Fig. 5) by means of its heating in an electric discharge causing melting and roll-up into a ball by surface tension [10]. Scheme of the bench for spherical photocathode fabrication is presented in Fig. 4, where for preventing an oxidation of the photocathode during the melting a shielding gas is used. The developed and created spark generator for discharge ignition, photo of which is presented in Fig. 4, generates a rectangle pulse with controllable parameters of its duration and current. This technique allows to form high accuracy sphere of a required radius with accuracy 1 μm.

3. The electrochemical gold plating of spherical part of the photocatode with the 1 μm layer.

4. Scaling down the surface roughness by pulsed melting the gold layer using spark generator and subsequent heating in vacuum during 3 hours at 900° C that one can see in Fig. 6.

5. Combined chemical and electrochemical polishing the photocathode surface. This polishing allows to get a rms height roughness, compared with a noise of AFM.

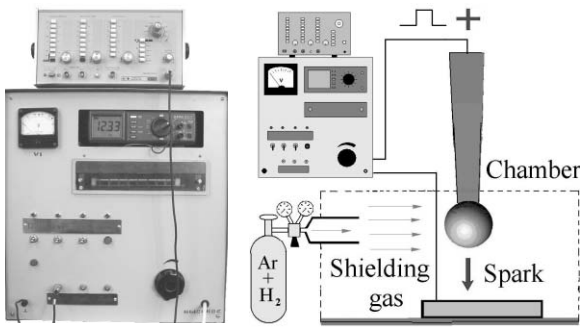

Figure 4: Photo of the spark generator (left) and scheme of the bench for spherical photocathode fabrication and for pulsed melting of gold plating.

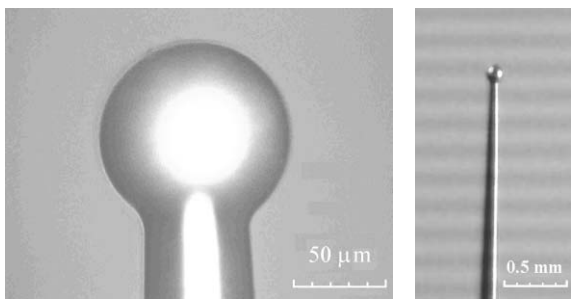

Figure 5: Gold-plated photocathode with the 50-μm radius before polishing (left) and conical steely holder of the spherical photocathode before its gold plating.

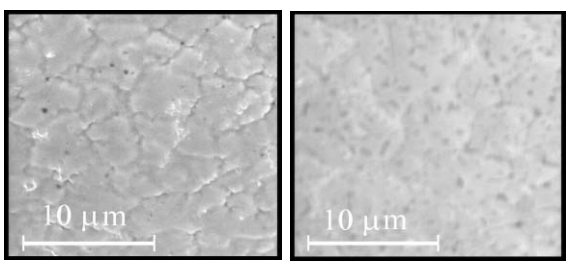

Figure 6: Gold-plated photocathode surface after its pulsed melting (left) and the same surface after subsequent heating in vacuum during 3 hours at temperature 900° C.

All listed steps of technology for the photocathode production allow to get the desired result: the rms height of the surface roughness was less than 10 nm.

CONCLUSION

From our consideration one can conclude:

the considered camera for x-ray pulse or electron bunch radiation photochronography, so named cameratron that is based on new principles of operation, allows to carry out measurement with temporal resolution of 10 fs at radiation registration in the range from the visible light to x-ray with practically the same high temporal resolution;

the considered camera is a high current camera allowing to operate in the regime single shoot or for measuring the bunch train, from bunch to bunch without superimposing the bunch distributions;

the mentioned high temporal resolution can be reached at rather low static voltages on photocathode (not more than 4 kV), small pulsed RF-power feeding (100 W at 3GHz), and all device, outlined in Fig. 1, can be placed on the sheet of format A4;

for getting temporal resolution not worse 20 fs, at registering pulses both of visible light and x-ray radiation, the rms height of roughness must not exceed 10 nm;

the key unit of the camera is principal new photocathode of spherical configuration, technology for its production has been proposed, developed and realized that is outlined in corresponding section of the paper.

The photocathodes similar to the considered allow to create a high current photogun of new scheme of implementation with the limiting high brightness of electron beam that will be published in the nearest time.

REFERENCES

[1] R. Brinkmann, "The European XFEL Project", *Proc. of the FEL 2006 Conf.*, Berlin, August 2006, p. 24.

[2] Linac Coherent Light Source (LCLS) Conceptual Design Report, SLAC-R-593 (2002).

[3] A.M. Tron, "Limitations at Short Bunch Length Monitoring", *Proc. of the PAC99 Conf.*, New York, USA. 1999. p. 2190.

[4] M.Ya. Schelev, *Physics – Uspekhi* **43**, 9 (2000) 931.

[5] Z. Chang et al., *Proc. of SPIE* **2869** (1998) 971.

[6] A.M. Tron, "New principles in Photochronography of Femtosecond Resolution", *Proc. of SPIE* **4948** (2003) 141.

[7] A.M. Tron, I.G. Merinov, "Method of Bunch Radiation Photochronography with 10 Femtosecond and Less Resolution", *Proc. of the PAHBEB2005 Conf.*, Erice, Italy, Octorber 2005. http://www.physics.ucla.edu/PAHBEB2005/talks/10_oct_2005/wg_2/a_tron.pdf

[8] A.M. Tron, I.G. Merinov, T. Gorlov. "New Generation Streak Camera Design and Investigation". *Proc. of EPAC 2006*, Edinburgh, June 2006, p. 1175.

[9] A.M. Tron, T. Gorlov, "Photocathode Roughness Impact on Photogun Beam Characteristics". *Proc. of EPAC 2006*, Edinburgh, June 2006, p. 121.

[10] B.L. Henke, J.A. Smith, J. Appl. Phys. 48 (1977) 1852.

[11] S.S. Sripada, I.M. Cohen, P.S. Ayyaswamy, ASME J. Heat Transfer, Vol. 125 (2003) 661.

MATLAB CODE FOR BPM BUTTON GEOMETRY COMPUTATION

A. Olmos, F. Pérez , ALBA-CELLS, Cerdanyola, Barcelona, Spain
G. Rehm, Diamond Light Source, Oxfordshire, U.K.

Abstract

Third generation Synchrotron Light Sources with vertical beam sizes down to few microns require beam resolutions on the submicron level. Study of different Beam Position Monitors (BPM) geometries has been done to reach such tight requirements. The used Matlab Graphical User Interface (GUI) is based on the simulation of a charged particle inside a selectable vacuum chamber type, computing the induced signal that it produces on the button feedthroughs. Needed parameters for the computation are the button electrode dimensions, vacuum chamber profile, electron beam current and measurement bandwidth. Output results from the GUI are the induced power on the feedthroughs, BPM sensitivity and intrinsic resolution of the analyzed geometry. As sensitivity and resolution are BPM geometry dependent terms, the Matlab GUI turned out to be an easy and fast way for first step geometry analysis.

INTRODUCTION

The idea of developing a software tool to study BPM geometries arose at the design phase of the buttons feedthrough for the ALBA machine. Non clear understanding of the best way to face the buttons design turned out to be a good excuse to spend some time developing a tool for quick analysis of different setups. Matlab mathematical software was chosen to implement a GUI based on analytical calculations from DAFNE [1,2].

WHAT FOR?

The purpose of the developed GUI is the comparison between different button feedthrough designs to determine which one better matches the accelerator requirements. As ALBA storage ring is injected from a LINAC + Booster system, two different types of vacuum chambers were thought to be analyzed. A round setup for the injector chambers and an octagonal setup for the storage ring ones. The GUI and the code behind it can be easily adapted to cope with other vacuum chamber types and geometries.

Obtained calculations for a fixed BPM geometry and different buttons designs are:

- Feedthroughs capacitance
- Non-linear BPM response
- BPM sensitivity
- Induced power on a 50Ω load
- BPM intrinsic resolution vs. beam current
- BPM intrinsic resolution vs. measurement bandwidth

understanding the intrinsic resolution as the resolution at the buttons level, not taking into account any processing electronics.

HOW TO?

Vacuum chamber

The main body of the GUI is showed in Figure 2. First thing to be done is to define the vacuum chamber geometry, quite easy for a Booster type chamber (only chamber radius is needed), but a bit more tricky for storage ring types vessels. Figure 1 shows a sketch of the dimensions required for each case.

Round type chamber are assumed to have a 45º buttons geometry, while the distance between buttons can be specified for the octagonal chamber case.

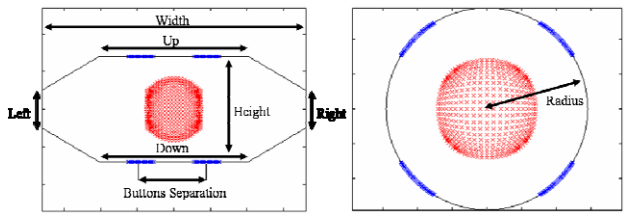

Figure 1: Vacuum chambers definition

Button feedthroughs

Code simulates the feedthroughs as round electrodes buttons type. The GUI can analyze either a single button design or make a comparison between three different buttons dimensions. Buttons are defined as:

- Electrode **diameter**
- Electrode **thickness**
- **Gap** between the electrode edge and the button shell

The button feedthrough capacitance (C_b) is obtained from these parameters and, for a specific beam current I, the average induced power is approached as

$$\langle P_0(\omega)\rangle = \frac{1}{2}|I|^2 R_0 \phi^2 \left(\frac{w_1}{w_2}\right)^2 \frac{(\omega/w_1)^2}{1+(\omega/w_1)^2} \qquad \begin{matrix} w_1 = 1/R_0 C_b \\ w_2 = c/2r \end{matrix} \quad (1)$$

where R_0 stands for a load impedance of *50Ω*, ϕ is the coverage factor that depends on the BPM-button geometry and r is the button radius [2].

Study parameters

Detected beam signal depends on the BPM placement in the machine and therefore two different **beam current raster** can be selected. Low current thresholds are meant for BPMs installed in boosters, LINACs and transfer paths (10μA-10mA) while higher beam currents are thought for storage ring BPMs (1mA-1A).

To perform the computations, a charged particle is moved vertical and horizontally inside a ±10mm range. Broadly known *Delta over Sum* approach is used for the calculation of the position detection and BPM sensitivity.

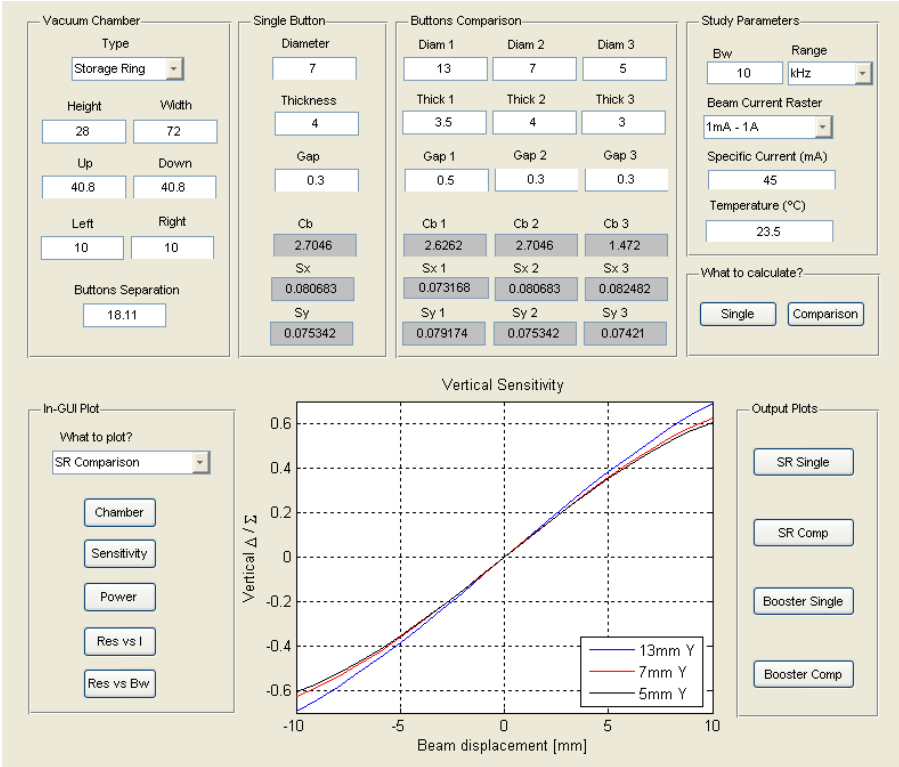

Figure 2: Matlab GUI main window. Comparison study of 3 button design is showed

The intrinsic resolution is inversely proportional to the noise level (only thermal noise considered. See equation 2). Measurement bandwidth (**Bw**) and **temperature** determine the thermal noise (N_{th}).

$$\sigma_{\text{int}} = \frac{b}{2\sqrt{2}} \frac{1}{\sqrt{SNR}} \qquad b = button\ to\ beam\ [mm] \qquad SNR = P_0 / N_{th} \tag{2}$$

Specific Current parameter defines a fix beam current at which the intrinsic resolution function of the measurement bandwidth is calculated.

Once the vacuum chamber geometry, buttons dimensions and study parameters are set, the computation can be performed.

OUTPUT INFORMATION

Two different types of calculations can be done: **Single** or **Comparison**. First one just computes the setup defined by the vacuum geometry and the button design set in the single button fields. Comparison study generates data evaluating all types of button designs.

First obtained information are the capacitance values of the button designs (C_b) and the sensitivity parameters of the BPM geometry S_x and S_y (K_x=1/S_x, K_y=1/S_y). For a comparison study of feedthroughs, even having the same BPM geometry, changed buttons diameters present different sensitivities.

In-GUI plots

Main GUI calculations are showed to the user as plots. All studies presented in the previous sections are computed at the same time and can be plotted in the central GUI graph by setting the "What to plot?" controls (see Figure 3).

Chamber button generates a sketch of the BPM setup (as the ones showed in Figure 1) and illustrates the non-linear behaviour of the BPM. Red spots on the figure show the BPM sensitivity map (a square shape is ideally expected).

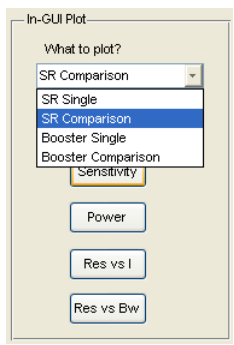

Figure 3: Selection of study to plot

The **sensitivity** plot shows the delta over sum curves function of the displaced beam, also known as calibration curves (see plot in Figure 2).

Induced power function of the beam current is showed in the central graph if **power** button is triggered. Beam current axis limits depend on the chosen thresholds in the *beam current raster* control. Figure 4 illustrates an example for a booster BPM (chamber radius 15.5mm, button diameter 14.3mm).

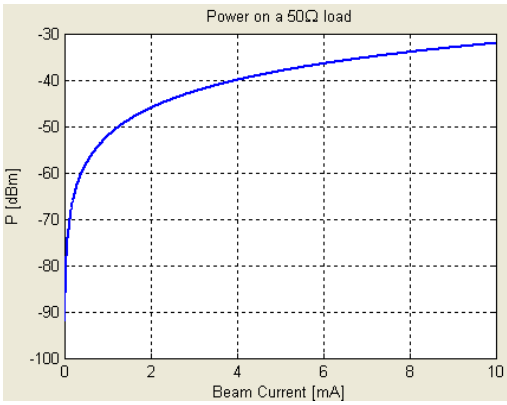

Figure 4: Induced power in a booster BPM

As can be figured out from equations 1 and 2, the intrinsic resolution of a BPM setup depends on the current of the passing beam and on the bandwidth used for measuring that beam (among other things). Therefore, two different intrinsic resolution plots are obtained. One function of the beam current, based on the analysis of the resolution on a fixed measurement bandwidth, defined by the *Bw* and *Range* controls. Second intrinsic resolution plot is measurement bandwidth dependent and is defined on a fixed beam current. Figures 5 and 6 show examples of these plots.

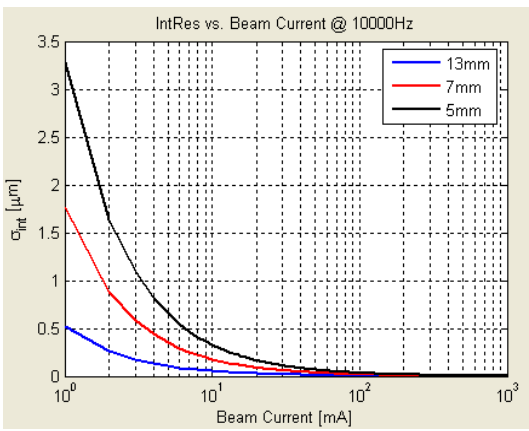

Figure 5: Intrinsic resolution vs. beam current at 10kHz measurement bandwidth

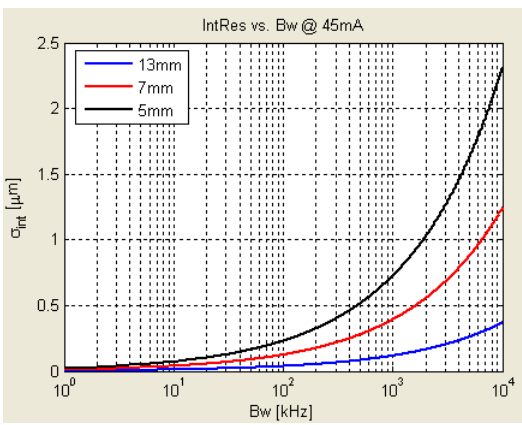

Figure 6: Intrinsic resolution vs. measurement bandwidth for a 45mA beam current

Output Plots

The control buttons grouped in the *Output Plots* box create an all-in-one independent figure that includes the obtained calculations after the computation (see Figure 7). Each different type of study (so called storage ring single, storage ring comparison, booster single and booster comparison) has its own control. These new windows give an overview of the BPM and feedthroughs behaviour.

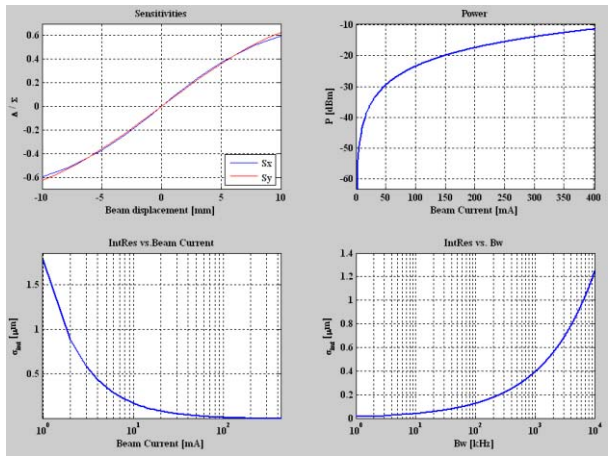

Figure 7: All-in-one output plots for the ALBA storage ring BPMs (Bw=10kHz, Specific current=45mA)

CONCLUSIONS

BPM systems main parameters are the geometry sensitivity and the resolution of position measurement, which usually have an inverse relation. Developed Matlab GUI is a useful simulation tool to look for the compromise between these parameters and help to choose the right button – BPM geometry. The results for ALBA storage ring BPM, calculated with the GUI, are showed in Figure 7 and Table 1.

Table 1: ALBA storage ring BPMs characteristics

Buttons Diameter [mm]	7
Buttons Thickness [mm]	4
Buttons Gap [mm]	0.3
Capacitance [pF]	2.7
Sx [mm^{-1}]	0.080
Sy [mm^{-1}]	0.075

REFERENCES

[1] A. Stella, “Analysis of the DAFNE Beam Position Monitor with a Boundary Element Method”, INFN-LNF, Accelerator Division, Frascati, December 1997

[2] F. Marcellini, M. Serio, M. Zobov, “DAFNE Broad-Band Button Electrodes”, INFN-LNF, Accelerator Division, Frascati, January 1996

THE SOLEIL BPM AND ORBIT FEEDBACK SYSTEMS

N. Hubert, L. Cassinari, J-C. Denard, N. Leclercq, A. Nadji, L. Nadolski, D. Pédeau;
Synchrotron SOLEIL, Gif-sur-Yvette, FRANCE

Abstract

SOLEIL is a third generation light source built in France, near Paris. Its BPM system is important for machine physics studies and for delivering stable beams to the users. A beam stable to 1/10th of the dimensions requires submicron stability in the vertical plane. The monitors anchored either to the girders or to the ground, are fixed points of the vacuum chamber. The electronics design was driven by combined efforts through active communication between accelerator laboratories (SOLEIL at first, later joined by DIAMOND) and Instrumentation Technologies. The result is the "Libera Electron" beam position processor. This paper reports on the performance of this new electronics installed on SOLEIL Storage Ring. It combines a 0.2µm rms resolution and micron level stability for beam delivery with accurate turn-by-turn measurements (3µm resolution at 0.8MHz) for machine commissioning and beam physics studies. It also features position interlock, tune measurement, and post-mortem capabilities. A Slow Orbit Feedback for correcting low frequency drifts (0 to 0.1Hz) is currently in operation. The Fast Orbit Feedback to be implemented soon will suppress higher frequency perturbations up to 100Hz.

INTRODUCTION

SOLEIL is a third generation light source built near Paris (France). It is designed for delivering to users very bright and stable photon beams. Its Beam Position Monitoring (BPM) system is based on a new digital electronics, the "Libera Electron", manufactured by Instrumentation Technologies. 146 BPMs equip the machine (first transfer line: 1, booster: 22, second transfer line: 3, storage ring: 120, tune monitors: 2). This paper reports on the SOLEIL BPM system, its commissioning and its use in the orbit feedback systems.

BPM BLOCKS AND CABLES

All 120 BPMs of the Storage Ring have the same vacuum chamber cross section (25x84mm). They include a bellow and a mechanical reference that is used for calibration, for survey, and for support. They have been manufactured at RIAL Vacuum (Italy), with electrodes and vacuum feedthroughs built by Saint Gobain (France). The horizontal separation of the button electrodes (Ø=10mm) is 16mm. It allows for a calibration factor of 11.2mm, identical in both planes. During the feedthrough design, a special attention was paid to their contribution to the vacuum chamber impedance, as well as to the heating power deposited by the beam on the button. The final design provides a good 50Ω matching up to 10GHz. A water cooling circuit stabilizes the BPM block temperature to 21±0.1°C.

The arc BPM fixtures are bolted to the magnet girders (Fig. 1). The straight sections BPM have a bellow on each side. They stand upon steel columns, directly anchored to the tunnel concrete slab.

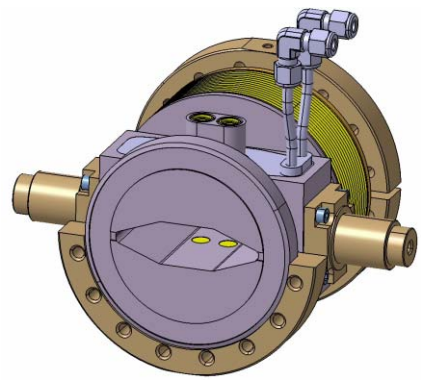

Figure 1: Arc BPM with bellow and cooling.

At several stages of the fabrication process, the proper insulation of the electrodes, and their capacitance matching, has been checked in order to minimize sensitivity differences between the four buttons of each BPM block.

The electrical offsets of the blocks have been measured with respect to their mechanical center and entered into a database for automatic correction (maximum electrical offset ≈ 600µm).

The blocks have been surveyed, and the survey offsets entered in the database for correcting the measured position (maximum survey offsets ≈ 500µm).

Because of their poor accessibility, we do not plan to disconnect the cables, even during vacuum chamber bake-outs. Therefore, 10cm long semi-rigid PEEK-insulated cables have been placed between the SMA feedthroughs and the long cables that take the signal to the processor. The four long cables of each BPM are enclosed in a shielded sheath and matched in length. Depending on the distance between the BPM block and its electronics, a different type of cable is used: either CNT195 22m long, or CNT240 33m long. The 352MHz signals get the same 5 dB attenuation in both cases.

BPM ELECTRONICS

Libera Modules

In 2002, SOLEIL initiated a new electronics concept of switched-electrode electronics with a small company. The result is the 'Libera Electron' digital electronics, manufactured by Instrumentation Technologies. It is composed of two main boards:

- An analog board with 4 multiplexed RF channels (automatic switching).

• A digital board with a powerful FPGA and fast inputs/outputs connections (Rocket I/O)

Libera Data Flow

Libera modules have five different kinds of data flows in order to meet several requirements.
The following data flows are available to the control system:

• ADC data is a 16ksample buffer at the sampling rate of the converters: around 109MHz.

• Turn-by-turn data at revolution frequency: 846kHz for the storage ring; 1.9MHz for the booster. This kind of data (buffer up to 100ksamples) was extensively used during the commissioning and now allows monitoring of the booster and its transfer lines, machine physics studies (the resolution is 3µm on the storage ring) and tune measurements.

• Turn-by-turn data decimated by 64. The decimation factor has been chosen in order to visualize a complete booster ramp in one 16ksample buffer.

• Slow Acquisition Data is a continuous flow of data at 10Hz that gives the mean position of the stored beam. The system accommodates large current variations and different bunch patterns; it provides a good accuracy and a very good resolution (0.2µm rms) for the slow orbit feedback.

• Fast Acquisition Data is a 10kHz continuous data flow available inside the FPGA for fast orbit feedback processing.

RF Channel Crosstalk

The accurate measurement and correction of the machine coupling relies on the BPM readings. A crosstalk measurement campaign has been carried out. It has been done with a generator, a horizontal beam displacement was simulated with an attenuator and its effect measured in the vertical plane. The average crosstalk value is -1.77% with a standard deviation of 2.5% (Fig. 2). Our first approach will be to apply a correction factor on each Libera. Another option would be to replace the Libera RF board.

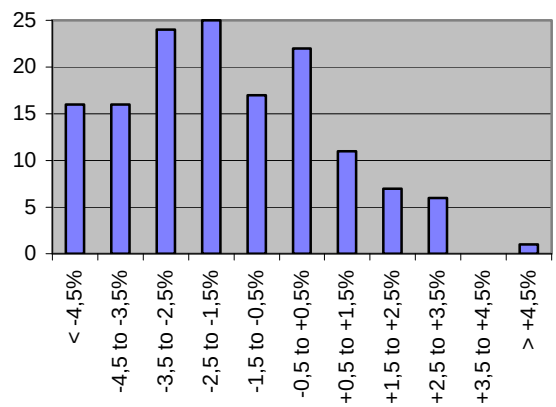

Figure 2: Crosstalk measurement (.Z/.X in %).

Other Functionalities

On top of the position measurement, the Libera modules have the following functionalities:

• Position Interlock: When the beam goes outside a predefined position range, the BPM electronics provides a low latency interlock signal used for killing the beam and prevent any damage to the machine [1].

• Post-Mortem: After a trigger is applied to a dedicated input, the Libera stores in a 16 ksample buffer the turn-by-turn measurements preceding the trigger.

CONTROL COMMAND

As the very first Libera user, SOLEIL has been deeply involved in the early stages of its Control System Programming Interface (CSPI) design. While the SOLEIL control system is based on TANGO [2], it has been decided to provide a generic and flexible interface in order to ease the integration of the Libera into any control system. This generic approach provides a way to factorize the common software components and allows any Libera user to benefit from features additions and bug fixes. We also suggested designing the CSPI so that one can choose between embedded or external runtime strategies. The CSPI abstracts the communication link and a simple recompilation is now enough to switch to "Libera embedded" or "external host" running of control system agent representing the Libera module.

The SOLEIL software architecture maps the physical deployment of the BPMs on the facility. Thanks to the object oriented nature of TANGO, each BPM module is exposed as an instance of the dedicated device-server. Through its attributes and commands, the latter provides the user with an exhaustive access to the Libera configuration parameters and data sources.

For both the booster and the storage ring, a so called "logical" TANGO device collects the beam position on each Libera device and makes the beam orbit available to the control system clients.

COMMISSIONING PROCESS

The BPM electronics was still under development when the machine commissioning started. Libera functionalities and data flows became available step by step. The first one was the turn-by-turn data. It facilitated the beam injection and the correction of the first turns and allowed online tune measurement. After the beam was stored, we received and commissioned the Slow Acquisition data flow. The position interlock functionality has been used later, in order to protect the machine for stored currents exceeding 20mA. The Automatic Gain Control automatically adjusts the attenuation at the input of the Libera to accommodate the whole current range from 0 to 500mA: it works up to 1Hz injection rate.

The system resulting from a new design, we encountered many inherent remaining bugs. All new functionalities were tested in the lab previously to being deployed on the machine. But the main difficulty was to detect and reproduce on a few modules in the lab sporadic events that could occur on one of the 120 BPMs on the machine. Nevertheless, we could always trust Instrumentation Technologies to quickly find solutions to the problems.

ORBIT FEEDBACKS

Slow Orbit Feedback

The slow orbit feedback (SOFB) has been put into operation since January 2007. The correction scheme relies on 120 BPMs and 56 corrector magnets in both planes. Theses correctors are secondary coils located in the sextupole magnets. Corrector power supplies use 20 bit DACs both for readback and setpoint values. Maximum corrector strengths are 0.9 and 0.7mrad.

The SOFB is implemented as a global feedback using the SVD algorithm: currently 56 and 32 singular values are used respectively in the horizontal and vertical planes. The RF frequency is an extra horizontal corrector coping with global circumference variation.

The system is implemented in the control-room as a Matlab programme. It runs at a 0.2Hz rate with 80% single step gains.

First results are very encouraging. Without SOFB, the orbit shift is a few tens of µm after several hours. Turning it on, orbit excursions reduce down to a few µm. Figure 3 is an example of position/angle stability during a 15 hour shift for a given beamline.

To get this performance for all beamlines and in a steady way some fine tuning of our system is still needed.

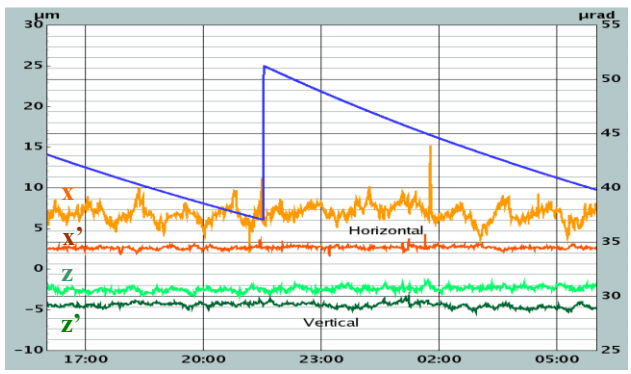

Figure 3: Angle (µrad) and position (µm) stability in both planes for a medium straight section. The blue curve exhibits the beam current for a 15 hour shift.

Fast Orbit Feedback

The fast orbit feedback (FOFB) is a global feedback under development. Its purpose is to correct orbit distortions up to 100Hz. The use of a frequency deadband between SOFB and FOFB will be implemented as a first step. The final aim is to be able to have a FOFB bandwidth starting from DC following a philosophy close to the ALS's one [3].

The FOFB uses up to 120 BPMs and 48 dedicated air coil correctors providing 20µrad maximum strength in both planes. These latter are installed around the upstream and downstream bellows of each of the 24 straight sections.

The SVD correction processing is distributed all around the storage ring, as embedded in the Libera FPGA. The Liberas of the 48 BPMs adjacent to the straight sections calculate the correction for their nearby correctors using the position data of the 120 BPMs. Then the Libera directly drives the magnet power-supply using a dedicated 10kHz serial RS485 link.

The bandwidth of the subsystem, (power supply + corrector + chamber), has been recently measured on the beam. The cut-off frequency at -3dB level is 2.4kHz in vertical and 3kHz in the horizontal plane (Fig. 4).

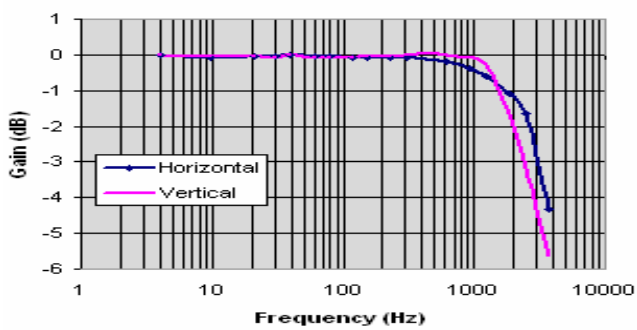

Figure 4: Bandwidth of the power supply + corrector + vacuum chamber + beam, measured on a BPM.

All BPM data are transmitted to each Libera used in the FOFB thanks to Diamond 'Communication Controller' [4] through a 2.12Gbits/s private network. The overall system latency (from position processing to power supply) is expected to be about 300µs.

CONCLUSION

A lot of effort as been put into the design of the Libera by Soleil and Instrumentation Technologies teams. It resulted in a BPM system quickly put in operation on the first days of commissioning. Even after several months of increased functionality, there are still a few improvements to bring. The SOFB is in commissioning phase and gives already promising results. The FOFB is under development, and we expect to close the loop this year.

ACKNOWLEDGEMENTS

We would like to thank all the Instrumentation Technology staff involved in the Libera project. We are also grateful to I. Uzun from Diamond Light source for his collaboration in the fast feedback project. We also thank J-M. Filhol that believed from the start that this ambitious BPM system would end up satisfying Soleil needs.

REFERENCES

[1] Y-M. Abiven, "Machine Protection System for Soleil Storage Ring", DIPAC'07, Trieste, May 2007.

[2] TANGO collaboration web site: http://www.tango-controls.org

[3] C. Steier et al. "Operational Experience Integrated slow and fast Orbit Feedbacks ath the ALS", EPAC'04, Lucerne, July 2004.

[4] G. Rehm, "Digital EBPMs at Diamond: Operational Experience and Integration into a fast Orbit Feedback", DIPAC'07, Trieste, May 2007.

DESIGN OF A SUBMICRON RESOLUTION CAVITY BPM FOR THE ILC MAIN LINAC

A. Lunin, G. Romanov, N. Solyak, M. Wendt, FNAL, U.S.A.*

Abstract

A 500 GeV center-of-mass International Linear Collider (ILC), currently under R&D development, is foreseen as next generation High-Energy Physics (HEP) instrument. High resolution Beam Position Monitors (BPMs) are necessary for preservation of the low emittance beam, i.e. to steer the beam along an optimal trajectory through the Main Linacs of the ILC. We present the cavity BPM developed at Fermilab within ILC collaboration. This monitor will be operated at cryogenic temperature and rigidly attached to the quad magnet. The same cylindrical cavity is used to obtain the signals from both dipole and monopole modes excited by beam. Such a scheme makes the BPM more compact for placing it inside the magnet space and simplifying the signal processing. The ceramic windows are brazed inside coupling slots for vacuum isolation and easy cavity cleaning. In order to measure a single bunch trajectory within 300 ns timescale we use resonant coupling to lower cavity Q-factor. We will present a BPM detailed numerical study and analyze its tolerance requirements for submicron resolution.

INTRODUCTION

The proposed International Linear Collider [1] requires a very precise control of the beam parameters by using high resolution beam instruments. Simulations quantify the need of BPMs with < 1 μm resolution in the Main Linacs and other areas of the ILC, to preserve the low vertical beam emittance by correction of non-linear field effects. A cold L-Band cavity BPM is being developed at Fermilab in order to meet these requirements. The design is based on TM_{110} dipole selective mode coupling [2,3]. Since BPM will be installed to the superconductive quad magnet we are limited in available space and have to follow certain cryogenic technology rules such as material ultra-cleaning. Therefore we implemented two novel features to BPM design. The first one is utilization of four vacuum tight coupling slots with brazed ceramic windows and the second one is the conception of one common cavity as both monopole and dipole signal source. The ceramic windows separate closed waveguides from the main BPM cavity and relax the problem of ultra cleaning while using a common cavity allows to save double longitudinal space. In this paper we also propose the symmetrical signal processing scheme. The main idea is to tune monopole and dipole modes frequencies in such a way as to make the reference frequency exactly in middle between them. This ensured that the down-converter electronics for dipole and monopole mode signals can be made almost identical. Finally we will present the detail numerical analysis of mechanical tolerance requirements to reach submicron resolution using such a cavity BPM.

*This work was supported by Fermi National Accelerator Laboratory, operated by Fermi Research Alliance, LLC under contract No. DE-AC02-07CH11359 with the United States Department of Energy.

CAVITY BPM DESIGN

The proposed microwave BPM consists of the simple circular cavity exited in the TM_{110} mode by an off-axis beam. General view of BPM model is shown in Fig. 1.

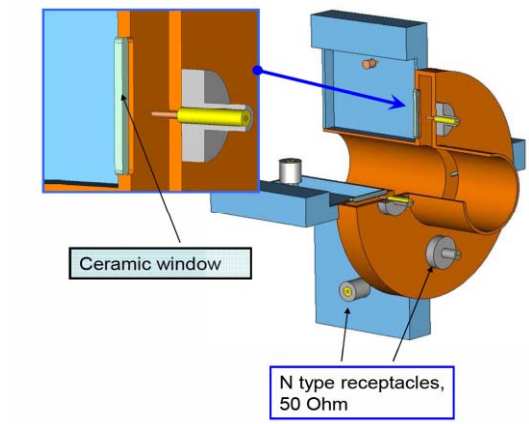

Figure 1: FNAL L-Band Cavity BPM.

The cavity is loaded with coupling ports. Four ceramic windows utilize magnetic coupling with dipole modes and extract beam position signals in two orthogonal planes. Another four N-type coaxial vacuum feedthrough are connected to two hybrids in pairs and provide monopole signal to measure a bunch charge.

Table 1. Main BPM Parameters

Monopole mode frequency , *f010* GHz	1.120
Dipole mode frequency, *f110* GHz	1.470
Loaded *Q* (both monopole and dipole)	~500
Beam pipe radius, mm	39
Cavity Radius, mm	113
Cavity Length, mm	15
Waveguide, mm	120x25
Ceramic window (Al_2O_3, ε=*9.4*), mm	50x5x3
Dipole mode sensitivity, V/nQ/mm	0.24
Monopole mode sensitivity, V/nQ	6
BPM resolution, μm	<1
BPM dynamic range, mm	±1

The copper material was chosen for cavity production to minimize possible cryolosses. Ceramic window is brazed in a special designed nonrigid ring slot with narrow walls to compensate ceramic temperature

deformations due to a different expansion coefficient compare to the copper. The main design parameters of BPM are given in the Table 1.

In order to increase dipole mode coupling while keeping the same sizes of ceramic window we approached the idea of resonant coupling. The waveguide to coaxial transition forms itself low-Q resonator with resonance frequency close to the dipole mode. It helps to increase the overall coupling coefficient by factor of 10. The result of HFSS simulation is shown in Fig. 2.

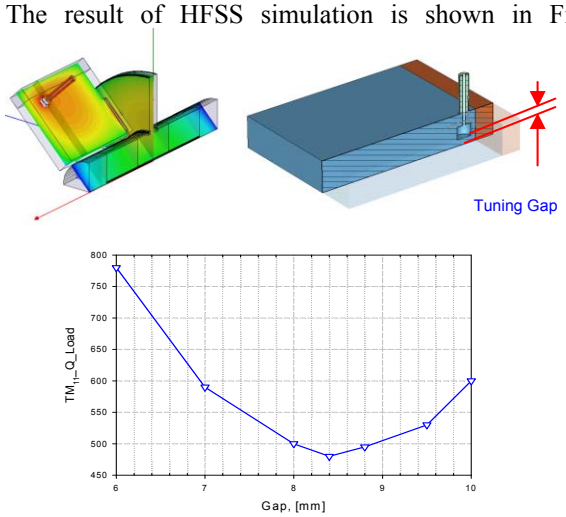

Figure 2: Tuning of resonant dipole mode coupling to coaxial pickup.

The short end of the waveguide is filled with alumina ceramic material as well. This solution gives us more radial space to fit BPM inside cryomodule.

Figure 3: Dipole mode distortion by coupling slots vs radius.

The coupling slots perturb the theoretical field distribution. That breaks the dipole mode cosine azimuth dependence and causes the pseudo-quadrupole components occurrence. We compare two signals rotated to $\pi/4$ in respect to each other. The result is illustrated in Fig. 3. The error is less than 10^{-3} up to 5mm of a beam offset.

PROCESSING OF SYMMETRIC CAVITY BPM SIGNALS

The major part of the processing of the dipole (TM_{110}) and monopole (TM_{010}) mode signals of the cavity BPM will handled in the digital domain. An ATCA-standard based digitizer board, utilizing 16x 500 MS/s ADCs (12-bit) and 16x 1200 MS/s DACs (14-bit), is currently under development. It processes the analog signals from DC to 200 MHz, and extends the frequency range to > 1GHz by applying undersampling techniques.

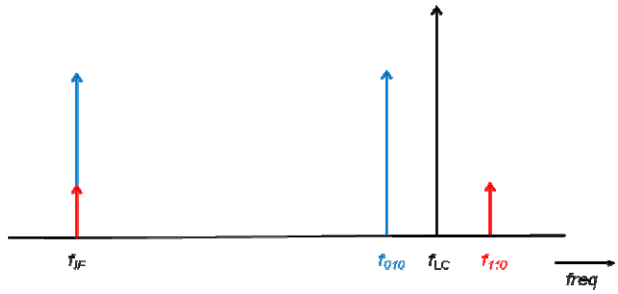

Fig. 4: Symmetric down-conversion of dipole and monopole-mode signals.

Some minimum signal processing however has to be still accomplished in the analog domain. The effective digitizer resolution is mainly limited by clock jitter, so a digital direct down-conversion (DDC) of the cavity signals is not applicable. Therefore analog down-mixing of the dipole (f_{110}) and monopole (f_{010}) mode to an intermediate frequency (f_{IF}) is required. The signal processing is simplified by designing the cavity dimensions such that $f_{IF} = f_{110} - f_{LO} = f_{LO} - f_{010}$

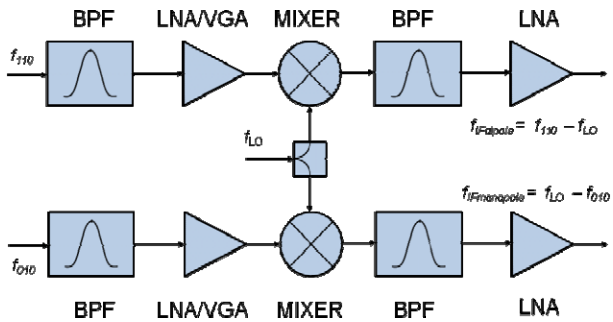

Fig. 5: Analog downconversion of symmetric dipole- and monopole mode signals.

The local oscillator reference frequency f_{LO} is located arithmetically between dipole and monopole mode frequencies (see Fig. 4). Now the down-converter electronics for dipole- and monopole mode signals can be made almost identical (Fig. 5), except a lower gain is required for the monopole mode signal. The LO signal, as well as the ADC clock are derived and locked to the accelerator f_{RF}. The IF signals are digitally down-converted to baseband, both for their inphase (I) and quadrature (Q) components. In further stages the magnitude and phase are computed to normalize the dipole mode signal to the bunch intensity (monopole mode signal), which gives the wanted beam position. The computed phase of the dipole mode signal provides the sign information for the beam displacement data.

TOLERANCE

Fabrication errors may cause the significant degradation of BPM measurement accuracy. Important reasons are resonant frequencies shift, monopole mode

leakage to the pickup port and orthogonality violation between two polarizations of dipole mode. The cavity frequencies shift has an influence on further signal processing because we are locked to accelerator RF frequency as the reference. The monopole mode coupling results the blind spot near BPM electrical center and therefore limits BPM resolution. The dipole modes nonorthogonality induce cross coupling between *x-y* pickup ports. While the symmetrical loaded *x-y* coupling can be removed numerically, the general unpredictable reflections from electronics and feedthroughs may also deteriorate the BPM dynamic range.

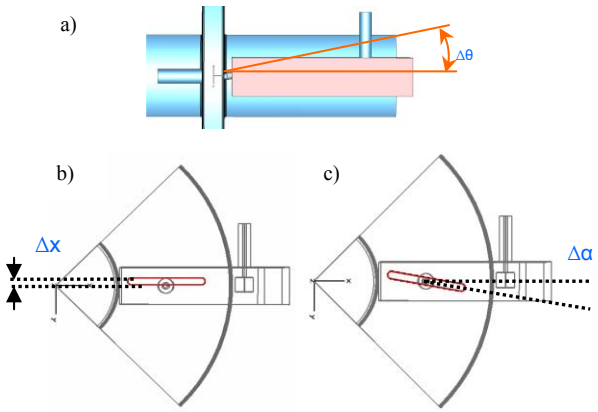

Figure 6: Three cases of slot misalignments: a) tilt, b) shift, c) rotation.

We take into account three possible misalignments as shown in Fig. 6 and calculate their influence on BPM resolution.

Frequency Tuning

The calculated central frequency *(f110+f010)/2* sensitivity versus cavity radius is about 0.011 MHz/μm. We believe that mechanical tolerances 10 μm together with low cavity loaded Q-factor allows us to eliminate the additional frequency tuning tools and simplify final BPM construction.

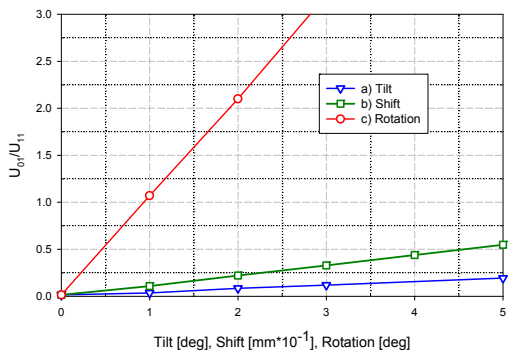

Figure 7: Monopole mode output signals normalized to dipole signal at 1 μm beam offset.

Monopole to Dipole Mode Coupling

Misalignments result in non-zero projections of the magnetic or electric field components of the TE_{10} mode in the coupling slot, produces monopole mode coupling to the waveguide. For the comparison we normalized the output monopole signal to the dipole one at 1 μm beam offset taking into account electronics passband and frequency discrimination. The results are summarized in Fig.7. The monopole mode coupling is most sensitive to the slot rotation misalignment which has to be bellow 1 degree to get the submicron BPM resolution.

Dipole Modes Orthogonality

Waveguide to coaxial transition brakes coupling symmetry and hence the dipole modes orthogonality. The slot misalignments particularly enhance this effect. We calculated the *x-y* ports cross coupling for the cases b) and c) (see Fig.6) and presented results in Fig.8 and 9.

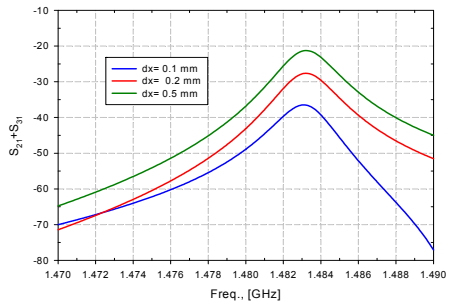

Figure 8: Dipole modes *x-y* cross coupling, case b).

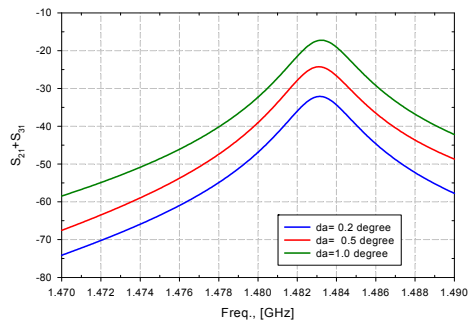

Figure 9: Dipole modes *x-y* cross coupling, case c)

Assuming possible signal reflections from the electronics of order of -30 dB one can choose maximum *x-y* cross coupling bellow -30 dB to get the ±1 mm total BPM dynamic range with submicron resolution.

CONCLUSION

We designed the prototype of cold cavity BPM for ILC project. New approaches such as the common dipole-monopole cavity and ceramic vacuum windows allow us to meet the ILC BPM requirements. Submicron resolution can be achieved with acceptable mechanical tolerances.

REFERENCES

[1] International Linear Collider Reference Design Report 2007, (http://media.linearcollider.org/rdr_draft_v1.pdf)
[2] V. Balakin, *et al*, "Beam Position Monitor With Nanometer Resolution For Linear Collider," Proc of PAC1999
[3] Zenghai Li, *et all*,."Cavity BPM with Dipole-Mode-Selective Coupler ", PAC, 2003, Portland

A VERSATILE EMITTANCE METER AND PROFILE MONITOR*

H.R. Kremers*, J.P.M. Beijers, S. Brandenburg, KVI, Groningen, the Netherlands

Abstract

An emittance meter has been developed to measure the full 4D phase space distribution for low energy ion beams. The instrument will be installed at different locations, where the expected shape of the phase space distribution is highly variable. To cope with these different conditions the instrument combines the pepperpot and scanning techniques. The phase space distribution is imaged on a CCD-camera using a MCP + phosphor screen combination.

In the first commissioning experiments the single ion response of the instrument has been measured and emittance measurements have been performed.

INTRODUCTION

Superconducting ECR ion sources [1] operate at fields of several Tesla, while the total extracted beam intensity is in the range 10-100 mA. Consequently, the magnetic fringe field through which the beam is extracted from the source and space charge effects will cause correlations and higher order effects to be much more important than they already are in present sources.

The intensities of highly charged heavy ion beams required for experiments at intermediate and high energy accelerators can only be met if the beams extracted from these sources can be properly matched to the acceptance of the accelerators. Consequently, detailed knowledge of the full 4D phase space distribution of the beams is essential. Therefore a 4D emittance meter has been developed in the framework of the ECR ion source development at KVI and the EU-supported ISIBHI-collaboration [2]. In order to handle widely varying shapes of the phase space distribution we use a hybrid technique consisting of a linear array of small holes in one direction and scanning in the perpendicular direction.

In this paper the details of the design and first results, focussing on the single ion response and the resolution of the instrument will be described.

EMITTANCEMETER DESIGN

The instrument should be capable to measure 4D phase space distributions with in one plane a maximal divergence of $\pm$ 50 mrad and a narrow width and in the other plane a maximal beam width of 40 mm and a small divergence. To meet these conflicting requirements a hybrid solution has been adopted, in which a linear pepperpot is used for the plane with small divergence and scanning for the other plane. In this way an acceptable accuracy is achieved for both planes. A schematic view of the instrument, indicating the main components, is shown in Fig. 1.

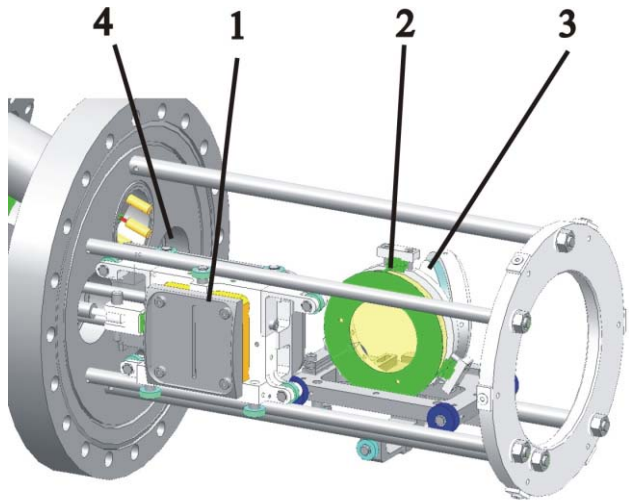

Figure 1: Layout of the emittance meter: 1) pepper plate, 2) multi channel plate, 3) mirror, 4) view port to CCD camera.

The pepperpot plate (Fig 1: 1) should be able to absorb 150 W of beam power and is therefore mounted on a water-cooled block. The pepperpot plate is a 25 µm tantalum foil with a row of 20 holes of Ø 20 µm, machined by laser cutting, with a pitch of 2 mm. By changing the geometry of the hole pattern the instrument can be adapted to the expected phase space distribution.

The position sensitive detector (Fig. 1: 2) is mounted 53.8 mm downstream of the pepper plate and consists of two multi-channel plates (MCP) in chevron configuration and a phosphor screen both with an effective diameter of 41.5 mm, purchased from El-Mul. The MCP has a maximum gain of up to 5×10^7 and is capable of detecting individual ions. The decay time of the light emission of from the phosphor screen is 1.2 ms. The 2D light-intensity distribution from the phosphor screen is imaged with a mirror (Ø 50 mm) (Fig.1: 3) and a lens system (PENTAX C2514M) onto a CCD camera mounted outside the vacuum (Fig.1: 4). The whole system is bakeable and suitable to operate in a 10^{-9} mbar vacuum.

The optical transmission from the phosphor screen to the CCD was found to have a slight position dependence, which is easily corrected by incorporating a digital filter in the analysis software. The SONY XCL-U1000 CCD camera has 1600 × 1200 pixels of 4.4 × 4.4 µm and is capable of taking 15 frames per second. The shutter time can be varied from 0.07 to 10^{-4} s.

The MCP, phosphor screen and mirror are mounted on a table which can be moved in and out of the beam. The pepperpot plate is also moved through the beam by a servo-controlled translation mechanism. The positioning accuracy of this mechanism is better than 10 µm, the minimum displacement is 10 µm.

COMMISIONING EXPERIMENTS

The initial commissioning of the emittance meter has been performed at the injection beam line of the AGOR facility at KVI using heavy-ion beams produced with the KVI-AECR ion source [3]. First measurements of the single-ion response of the emittance meter are presented, followed by an initial measurement of the (partial) emittance.

Single-Ion Response

The single-ion response of the MCP + phosphor screen determines the ultimate angular resolution that can be reached, independent of the geometrical dimensions and the imaging system. The single-ion response has been determined using a very low-intensity, defocused beam of O^{7+} ions impinging on a 1 mm diaphragm placed in front of the MCP. The light from the phosphor screen is focused onto the CCD camera with a single lens with magnification M = 0.28. The CCD shutter time was set at a value of 35 ms. The ion flux incident on the MCP was determined by measuring the MCP count rate. Rates down to 100 s^{-1} were easily produced.

Figure 2 shows a CCD image of an 84 keV O^{7+} beam at a count rate of 400 s^{-1}. Individual ion impacts can easily be distinguished. This is shown more clearly in Fig. 3 where an intensity distribution is plotted of six ions hitting the MCP along the vertical line indicated in Fig. 2. As can be seen the single-ion responses can easily be fitted with Gaussians, whose positions are determined with a standard deviation of 2 pixels. The 3σ accuracy of the impact location of an ion hitting the MCP corresponds to a spatial uncertainty of ~100 µm on the phosphor screen. The spatial binning of the imaging optics is 44 µm, which thus is not a limiting factor for the intrinsic spatial resolution. The corresponding angular resolution is 1.9 mrad.

It should be pointed out that the sampling, i.e. 2 mm in the one direction and the step size used in the other direction determines the resolving power of the spatial intensity distribution in the beam.

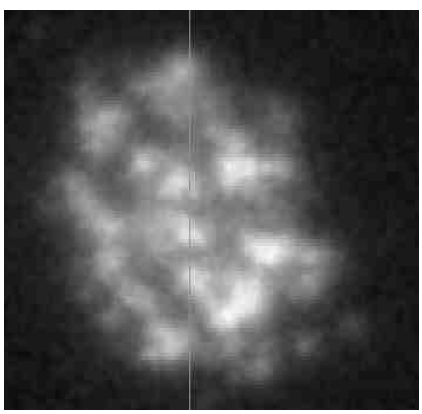

Figure 2: CCD image of 87 keV O^{7+} ions at a MCP count rate of 400 s^{-1}.

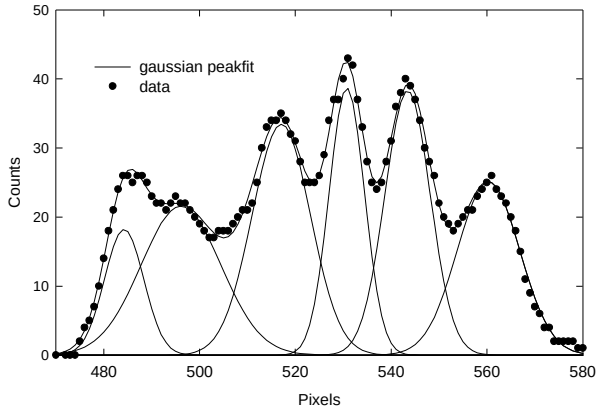

Figure 3: Intensity distribution along the vertical line indicated in Fig. 2.

First Emittance Measurements

Emittance measurements were made with an 84 keV Ne^{7+} beam of 6 µA. The individual beamlets exiting from Ø 20 µm holes have an intensity in the order of 10 pA. Figure 4 shows the image of the transmitted beamlets on the phosphor screen as read out by a LabVIEW application together with the location of the holes. The individual beamlets are clearly separated. The image clearly shows a correlation between Y and X', which can not be detected with Allison-type scanners.

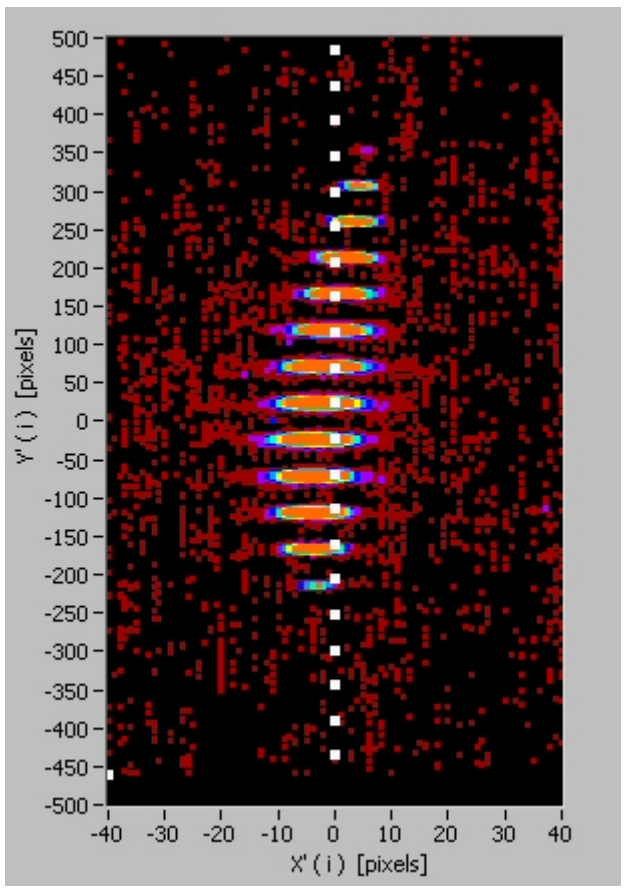

Figure 4: 2D Profile of a 12 kV O+7 beam.

The magnification of the optical system was determined by imaging the pepperpot plate, located at the position of the phosphor screen, onto the CCD camera. The measured value (M = 0.1) is in very good agreement with the manufacturer specifications.

The projection of the phase space distribution on the Y-Y' plane is constructed by associating a range of horizontal rows with each hole and summing over each row (≡ integration over X') and summing over the images for different horizontal positions of the pepperpot plate (≡ integration over X). The CCD noise is eliminated by neglecting pixels with a collected charge below a preset value. In Fig. 5 the Y-Y' distribution for a single image (at X = 0) and a single column centred at X' = 0 for the image of Fig. 4 is displayed.

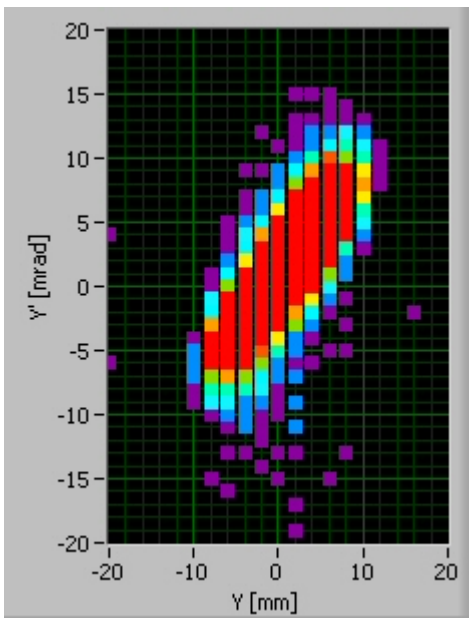

Figure 5: Y-Y' distribution for X=0; X'=0 of the image shown in Fig. 4.

CONCLUSIONS AND OUTLOOK

An emittance measuring device aiming at determining the full 4D phase space distribution of low energy ion beams has been designed and constructed. First measurements have shown that the angular resolution of the instrument is dominated by the single ion response and amounts to 1.9 mrad, in agreement with the design objectives. The spatial resolution in both X and Y is determined by the sampling pitch. By exchanging the pepperpot plate the instrument can be easily adapted to varying experimental conditions.

The algorithm to extract the data needed to construct the Y and Y' intensity distributions has been successfully tested. The analysis software to extract the full 4D phase space distribution from the data and to determine the various dimensions and correlations is presently under development.

To complete the calibration measurements of the relative area of the holes in the pepperpot plate and the position dependence of the light yield of the phosphor screen still have to be performed. Furthermore the measured transmission of the imaging system has to be verified against simulations also taking into account polarization effects.

Furthermore, the behaviour at high beam intensities (e.g. sputtering of the pepperpot plate, degradation of the MCP and phosphor screen performance) requires further investigation.

REFERENCES

[1] D. Leitner *et al.*, Nucl. Instr. Meth. B **235**(2005)486
L.T. Sun *et al.*, Nucl. Instr. Meth. B **235**(2005)524
S. Gammino, Rev. Sci. Instr. **72**(2001)4090
P.A. Zavodsky *et al.*, Nucl. Instr. Meth. B **241**(2005)959.
[2] G. Ciavola et al., Rev Sci. Instrum. **77**, 03A303 (2006).
[3] H.R. Kremers, J.P.M. Beijers and S. Brandenburg, Rev. Sci. Instrum. 77, 03A311 (2006).

ACKNOWLEDGEMENTS

This work has been performed as part of the research programme of the "Stichting voor Fundamenteel Onderzoek der Materie" (FOM), with support of the "Nederlandse Organisatie voor Wetenschappelijk Onderzoek" (NWO).

It has been supported by the Rijks Universiteit Groningen (R*u*G), the Gesellschaft für Schwerionen-forschung mbH and the European Commission through the EURONS-I3 (European Commission Contract No. 506065).

DESIGN AND CALIBRATION OF AN EMITTANCE MONITOR FOR THE PSI XFEL PROJECT

Volker Schlott, Åke Andersson, Miroslaw Dach, Simon Leemann, Martin Rohrer, Andreas Streun,
Paul Scherrer Institute, CH-5232 Villigen, Switzerland

Abstract

The Paul Scherrer Institute (PSI) intends to realize a compact X-ray Free Electron Laser (XFEL) based on the development of a high brightness, high current electron source. Field emitter arrays (FEA) in combination with high gradient acceleration promise a substantial reduction of transverse emittances by up to one order of magnitude compared to existing electron sources for XFELs. The acceleration concept and the main beam parameters will be demonstrated in a 250 MeV injector LINAC project. A flexible, high resolution emittance meter based on the pepperpot measurement technique has thus been designed to characterize this low emittance beam. The realization of this monitor and the calibration procedure will be presented.

THE LOW EMITTANCE GUN PROJECT AND THE ROAD TO THE PSI XFEL

A feasibility study to explore the options for an economic Free Electron Laser (FEL) facility in the hard X-ray regime with a target wavelength of 1 Å has been initiated at PSI [1]. Since the FEL radiation wavelength depends only linearly on the electron beam emittance, while it scales quadratically with beam energy, the main focus of activities in the present phase of the PSI XFEL project is directed towards the generation of a low emittance electron beam. In this context, a novel electron source – the so called low emittance gun (LEG) – is under development. It should provide sufficient peak current and up to one order of magnitude higher transverse brightness compared as to state-of-the-art RF photo-cathode guns. The LEG Test Facility starts operation with a conventional photo-cathode laser gun and concentrates during its first phase on the investigation of high gradient pulsed diode acceleration (up to 1 MV/m over 200 ns) [2] followed by a combined fundamental and 3rd harmonic RF cavity [3]. Particle tracking indicates that the combination of DC and RF acceleration provides emittance preservation and sufficient linearization of the longitudinal phase space, which eases bunch compression in order to reach the peak currents required for the XFEL project. A diagnostics section has been designed to allow the full characterization of the electron beam with its main focus on the determination and optimization of transverse emittances and energy spread as critical beam parameters. In parallel to the demonstration of this novel acceleration concept, PSI investigates the properties of laser-induced field emission from single ZrC tips [4] and gated Mo field emitter arrays [4] as possible cathode materials promising normalized beam emittances as low as 0.05 mm mrad [5].

There are two test facilities to be realized at PSI until the end of the year 2010 and before starting with the actual XFEL facility. The LEG test stand is presently being set-up for demonstrating the performance of the novel high brightness electron source. The validity of the acceleration concept (including ballistic and magnetic bunch compression) shall be demonstrated in the 250 MeV XFEL injector test facility. More information on the PSI XFEL Project and its new developments including a full set of beam parameters can be found in [6].

THE LEG TEST FACILITY

A mechanical drawing and the schematic overview of the LEG test facility is shown in the upper part of figure 1. For the expected range of beam currents (0.1 - 5.5 A), the smallest transverse emittances will be reached over a length of 0.5 m. The corresponding beam envelopes are shown in the lower part of figure 1.

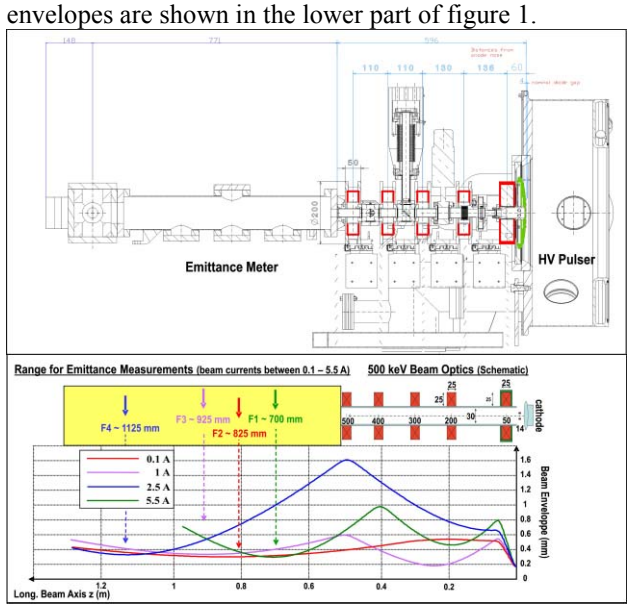

Figure 1: Mechanical drawing of 1st phase of LEG test facility (upper part). Optics simulations for expected beam current range showing beam envelopes at locations of smallest transverse emittances (lower part). The measuring rage of the emittance monitor is indicated in yellow.

The electron beam will be generated by a commercial Nd:VAN laser (Duettino from TimeBandwidth company) providing 20 µJ pulse energy at 266 nm (frequency tripled) and up to 10 Hz repetition rate at pulse widths

between 15 and 40 ps (FWHM). With a copper cathode (QE ~ 10^{-5}), beam charges of only 40 pC will be accelerated by the high voltage (500 kV) pulser. An upgrade of the laser system for generating the PSI XFEL design current of 5.5 A (200 pC beam charge) is foreseen for the next phase of the facility when the two frequency (fundamental and 3rd harmonic) RF cavity will also be installed, providing acceleration up to 4 MeV.

In the 1st phase of the LEG test facility the high gradient pulsed diode acceleration will be tested. In case of an optimized gun geometry and accelerating gradients of > 250 MV/m, normalized transverse emittances as low as 50 nmrad and beam sizes in the order of 0.7 mm (FWHM) are predicted by beam dynamics simulations using Homdyn [7] and the particle-in-cell code CAPONE [8]. Linear space charge forces can be compensated over a wide range of beam currents (0.1 – 5.5 A) by using a total of 5 solenoid magnets.

DESIGN CRITERIA FOR THE LEG EMITTANCE MONITOR

As indicated in the previous paragraph, the LEG test facility will be operated in different phases over a wide range of beam currents and beam energies, requiring the highest possible flexibility from the beam diagnostics devices. For the 500 keV and 1 MeV cases (beam optics shown in the lower part of figure 1) the emittance monitor needs to cover a measuring range of at least 0.5 m length. At the same time, it should be as compact as possible, since further use in the 250 MeV XFEL injector test facility might be required for cathode material studies.

The well known "pepperpot" measurement appears most suited for determining the transverse emittance of a space charge dominated, low energy electron beam. While an exhaustive elaboration of the measurement principle is given in [9], only a short and simplistic explanation of the technique is given in the following using the notation indicated in figure 2.

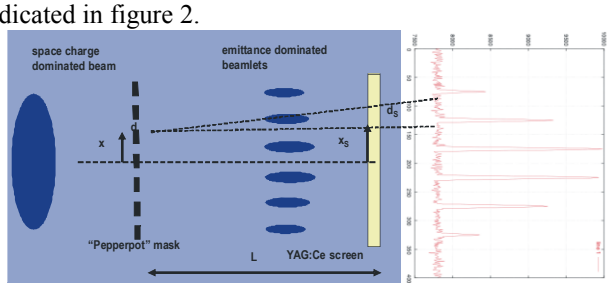

Figure 2: Illustration of "pepperpot" measuring principle.

A space charge dominated beam is converted in a set of emittance dominated beamlets after passing the "pepperpot" holes. The beamlets are visualized on a screen, which is placed at a distance L behind the "peppepot" mask. The corresponding beam profiles on the screen provide information of the angular beam distribution at the location of the "peppepot". A broadening of the beamlets is a measure of the uncorrelated beam divergence, while the beamlet position with respect to the centre of gravity is a measure for the correlated beam divergence. The RMS beam emittance can be determined by considering the second moments of the average values of x and x' to

$$\varepsilon_{RMS} = 4 \cdot \sqrt{\langle x^2 \rangle \langle x'^2 \rangle - \langle xx' \rangle^2} ,$$

where <x> is the RMS distance of the optical / central axis to the "pepperpot" holes and <x'> is the RMS slope of the particles' paths with respect to the optical / central axis, given by $(x_S - x)/L$.

"Pepperpot Mask" and Scintillation Screen

A tungsten "pepperpot" mask of 5 mm diameter, with 150 µm hole spacing and 20 µm hole diameter has been fabricated by laser beam machining. The mask thickness of 0.5 mm stops electrons with energies up to 4 MeV and should thus provide sufficient background suppression. A photograph of the "peperpot" mask is shown in the inlet of figure 3. YAG:Ce and LuAG:Ce (Lutetium Aluminium Garnet) have been selected as scintillation materials to visualize the electron beamlets, which are passing through the "pepperpot" holes. Both, YAG and LuAG are high density materials allowing the production of very thin freestanding screens. Their predominant emission in the green spectral range (535 – 550 nm) is well matched to the maximum sensitivity of CCD cameras. For least scattering of electrons in the material and highest spatial resolution, screen thicknesses of 50 µm at 5 mm diameter have been chosen.

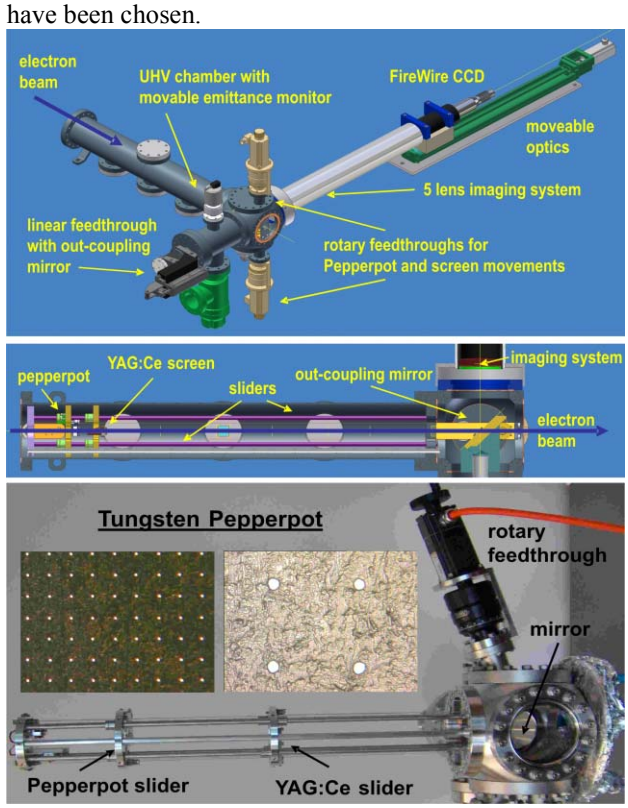

Figure 3: Schematic drawing of emittance monitor and imaging system (top), cross section of UHV part showing the sliders for the "pepperpot" and scintillation screen (middle), photograph of the emittance monitor (without UHV chamber) and "pepperpot mask" (bottom)

Mechanics and Imaging System

Both, "pepperpot" mask and scintillation screen are mounted on stainless steel sliders inside of a 900 mm long DN100CF UHV chamber. Cable winches, which are driven by a pair of rotary feedthroughs and deflection rollers at back end of the monitor, allow travel of the sliders along the entire length of the UHV chamber. In this way, "pepperpot" and scintillation screen can be moved at any location along the emittance monitor and the distance between both can be freely selected depending on the divergence of the electron beam. "Pepperpot" mask and scintillation screen can both be moved out of the beam, when reaching a "parking position" at the front end of the UHV chamber. An out-coupling mirror (90 mm in diameter, λ/20 planarity) at the back end of the monitor deflects the transmitted light from the scintillation screen under an angle of 90° out of the UHV chamber. An objective consisting of 5 lenses with 100 mm diameter and a focal length of 800 mm images the beamlets onto a 12bit IEEE1394 (FireWire) B/W CCD camera (Flea by Point Grey Research company) with 4.65 µm x 4.65 µm pixel size and 1024 by 768 pixels. This 1:1 imaging system has a theoretical resolution of 100 lp/mm at 550 nm wavelength (10% bandwidth). Objective and CCD camera are mounted on a motorized linear stage in order to keep the focal distance of 800 mm between scintillation screen and image plane.

CALIBRATION OF THE OPTICAL SYSTEM – POINT SPREAD FUNCTION

Since the optical system dominates the ultimate resolution of the emittance measurement, the so called "Point Spread Function" (PSF) was experimentally determined. The PSF is defined as the 2-dimensional intensity distribution in the image plane, produced by a point source in the source plane. It therefore includes all possible diluting contributions – namely diffraction effects, optical aberrations as well as CCD pixel resolution, readout noise, vibrations and others. A schematic overview of the experimental set-up is shown in figure 4.

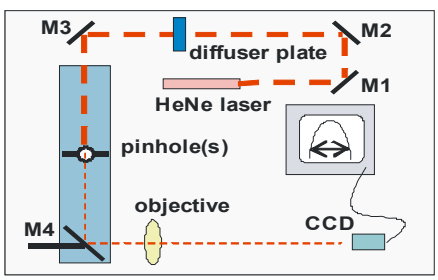

Figure 4: Schematic overview of the measuring set-up for determining the PSF of the emittance monitor.

Pinholes of different diameters (5 µm to 50 µm) were illuminated from the back side by a HeNe laser. The collimated laser beam passed a diffuser plate and the light intensity was reduced by a set of neutral density filters in order to prevent saturation of the CCD camera. The imaging system of the emittance monitor was focused on the pinhole plane and the image sizes were analyzed by fitting the 2-dimensional beam distributions.

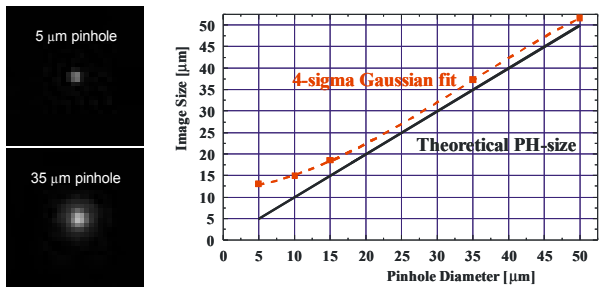

Figure 5: Pinhole images (left side) and measured PSF of the emittance monitor's imaging system (right side)

Figure 5 shows the relation between the known pinhole diameters (still 10% uncertainty might be considered) and the measured image sizes. Since the recorded 2-dimensional beam distribution does not resample the rectangular pinhole shape and changes with increasing pinhole diameter, the 4-sigma value of a Gaussian fit (95% of the data points) was taken as the image size. The image size threshold, which indicates the PSF of the optical system, was extrapolated to 11.8 µm, a value, which agrees very well with the theoretical resolution of the imaging system, which was calculated to 100 lp/mm using ray tracing. A similar online calibration option for the emittance monitor imaging system will be installed in the LEG test facility in order to cross check its resolution in case of electron beam emittance measurements.

REFERENCES

[1] K. Li et al., "*Low Emittance XFEL Development*", Proc. FEL 2005, Palo Alto, USA, 483

[2] C. Gough, M. Paraliev, "*Pulsed Power Techniques fort the Low Emittance Gun (LEG)*", see web-page: http://leg.web.psi.ch/public/publications/Gough-yr03.pdf

[3] J.-Y. Raguin et al., "*A Two-Frequency RF Cavity for the PSI Low Emittance Gun*", Proc. FEL 2005, Palo Alto, USA, 324

[4] R. Ganter et al., "Nanoseconds Field Emitted Currents from ZrC Needles and Field Emitter Arrays", J.Vac.Sci.Tech. B24 (2006) 974

[5] M. Dehler, "Design and Modeling of Field Emitter Arrays for a High Brilliance Electron Source", Proc. 9th ICAP'2006, Chamonix, France, 114

[6] See PSI FEL web-page: http://fel.web.psi.ch/

[7] M. Ferrario, Homdyn on ASTeC collaboration portal: https://projects.astec.ac.uk/Plone/Codes/spacecharge/homdyn/

[8] A. Candel, „ Simulation of Electron Source for Next Generation X-Ray Free Electron Laser", PhD-thesis, Diss ETH Nr. 16181, ETH-Zürich 2005

[9] K.T. McDonald, D.P. Russel,"Methods of Emittance Measurement", Proc. Joint US-CERN Acc. School on Observation, Diagnostics and Correction in Particle Beams, Oct. 20-26 1988, Capri, Italy

BUTTON BEAM POSITION MONITORS FOR FLASH

J. Lund-Nielsen*, N. Baboi, DESY, Hamburg, Germany; W. Riesch, DESY, Zeuthen, Germany

Abstract

FLASH accelerates electron bunches to up to 750 MeV for producing intense, coherent, very short pulses of radiation in special undulators. Various types of BPMs are installed in the linac: cavity and re-entrant-cavity BPMs in the accelerating cryo-modules and button and stripline BPMs in the room-temperature sections. The undulator section is one of the most critical areas of the linac in terms of beam position, therefore here the requirements on the BPMs are tightest. Due to the limited space, button BPMs were mounted here. The electronics is based on the AM/PM principle. In the past couple of years these BPMs were commissioned and intensively studied. A few modifications have been made in the electronics, in order to deal with the small signals and the very high frequencies of the ultra-short bunches. The studies and changes on the electronics are presented in this paper.

INTRODUCTION

FLASH (Free Electron Laser in Hamburg) [1] is a user facility for an intense coherent ultra short radiation, as well as a test facility for the European XFEL (X-Ray Free Electron Laser) and the ILC (International Linear Collider). Electron bunches are compressed and accelerated to up to 750 MeV#, before passing about 30 m of undulators where the radiation is produced.

Since the intensity and stability of the radiation depends critically on the beam position, several tens of beam position monitors (BPM) of various kinds are installed in the linac. Cavity and re-entrant cavity monitors are mounted at the end of each of the 5 accelerator modules. Stripline BPMs are found in most of the room temperature sections. They provide large signals, allowing for a good resolution. In the undulator section, as well as in a few other locations, button monitors are installed due to space restrictions. The characterization studies made on the button BPMs in the diagnostics sections between individual undulators and some modifications that have been made on the electronics are presented in this paper.

BUTTON BPMS

Four antennas mounted transversely and symmetrically in the beam pipe form a button BPM. There are two main types of button BPMs installed in FLASH. One has discs ("buttons") on the tip of the antennas and is used in areas with 34 mm cross-sections or larger. In the undulator section, the chamber has 9 mm diameter, so that solely thin antennas, 1.6 mm in diameter, are used (Fig. 1).

Inside the undulators similar antennas are mounted from the sides (up-left, up-right, down-left and down-right) and the signals from all four antennas have to be combined in order to get the horizontal and vertical beam position. These BPMs are not discussed in this paper, but the electronics is the same as for the other button BPMs.

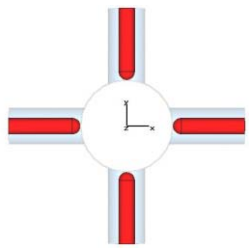

Figure 1: Button BPM in the undulator diagnostic station.

The undulator area is the most critical area from point of view of beam position and stability, therefore the monitors in this area have to be very precise.

BPM Electronics

The electronics of the FLASH button BPMs works on the AM/PM (amplitude modulation / phase modulation) normalization principle [2]. Changes in the beam position determine a change – modulation – in the signals amplitude at the BPMs pickups. The electronics converts this amplitude modulation (AM) into a phase modulation (PM). The zero crossing of the two signals is compared and in this way the charge dependency is eliminated and the resulting pulse depends only on the beam position.

Fig. 2 shows the schematics of the electronic-boards in their present form. The signal from each pickup passes a pulse forming Gauss filter (cut-off 150 MHz) and then a 1 GHz low pass filter (SHF LP), which cuts the very high frequency components of the FLASH bunches. The signal is then pre-amplified by 40 dB by the dual low noise amplifier (LNA), which has a negligible drift between the two channels. The hybrid and the dual comparator transform the difference in amplitudes into a phase difference, which is then analyzed by the time comparator. The length of the resulting pulses is proportional to the beam offset. Four identical pulses are generated here, which are again LP filtered to obtain an averaging effect, before being amplified and DC-shifted by an operational amplifier. The peak of the pulse is then sampled using an external trigger, and then frozen for 1 μs (the typical bunch spacing) by a Track&Hold amplifier. The delay of the external trigger as well as various internal parameters, such as the offset and hysteresis of the dual comparator, the offset of the operational amplifier, can be adjusted remotely by means of a I2C bus. This was important since many electronics boards are installed in the accelerator tunnel.

MODIFICATION OF THE ELECTRONICS

After the initial commissioning of the undulator BPMs at FLASH, it was found that the position reading was very

* jorgen.lund-nielsen@desy.de

about 1 GeV will be reached after the shutdown in summer 2007.

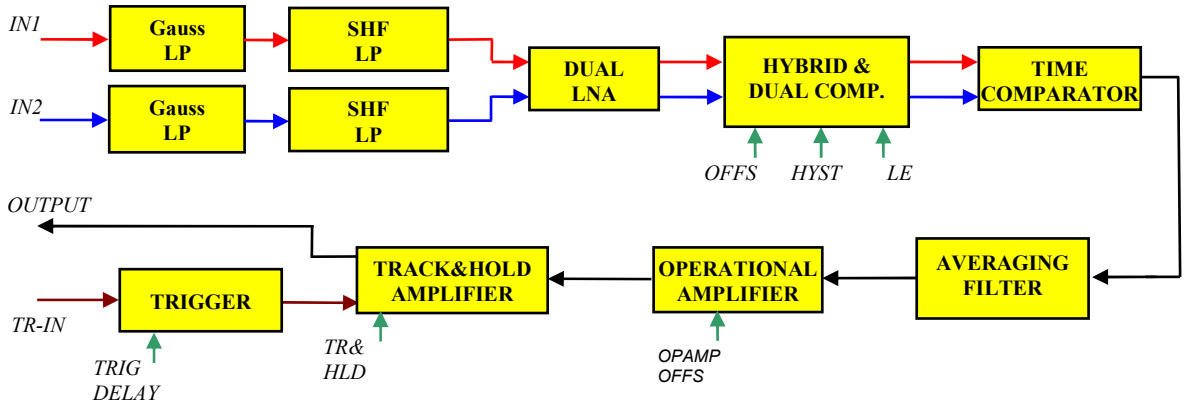

Figure 2: Principle of the FLASH button BPM electronics.

unstable, especially at low beam charge below 1 nC. Below 0.4 nC the electronics stopped responding. Also non-linearities were observed. These problems have been investigated and a few changes in the electronics proved to improve their performance.

Signal Amplitude

Investigations showed that the signal at the input of the AM/PM converter hybrid was too weak. On one hand the signal delivered by the pickups is much smaller than at TTF1, where similar BPMs were used, due to the lower charge. On the other hand, the upper cut-off frequency of the Gauss-LPF in conjunction with the lower cut-off frequency of the monitor, results in a very small signal amplitude. This is shown in Fig. 3. The dotted line represents the transfer function of the BPM pickup, normalized to 0 dB, as obtained from a simulation with Microwave Studio [3]. A wire has been used in the center of the beam pipe with a radius of 300 µm [4]. A measurement made on a similar BPM at TTF1, shows a resembling result [5]. The continuous curve in Fig. 3 is a measurement of the transfer function of a Gauss LP filter. At the frequency of the pickup signal, around 300 MHz, roughly 20 dB are lost in the filter. In order to compensate for this, an additional amplifier was installed.

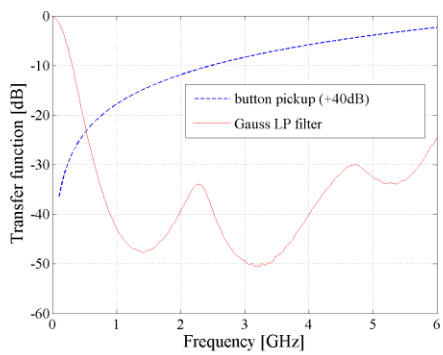

Figure 3: Transfer function of the BPM pickup (simulated) and of the Gauss LP filter (measured).

Charge Dependent Non-Linearity

The additional amplifier cured the susceptibility to the low bunch charge. However the reading was still somewhat unstable and showed some charge dependent non-linearity, which was not noticed on the bench. The electronic itself showed a certain non-linearity on the bench, but this was, repeatable from unit to unit and it was not bunch charge dependent. More on this topic is presented in the next sub-section.

We have found that strong very high frequency signals passed the Gaussian LPF. These frequencies are generated by the very short bunches. Fig. 4 shows the measured transfer function of a Gauss LPF up to 20 GHz. It can be seen that at about 8 to 10 GHz the signal is damped only by about 10 dB. These high frequencies were above the cut-off of the dual LNA and drove it into saturation. The amount of distorted - wanted signal - and the additional fraction of ultra high frequencies that pass the amplifier lead the fast comparators to misbehave, hence to unstable and non-linear response of the electronics.

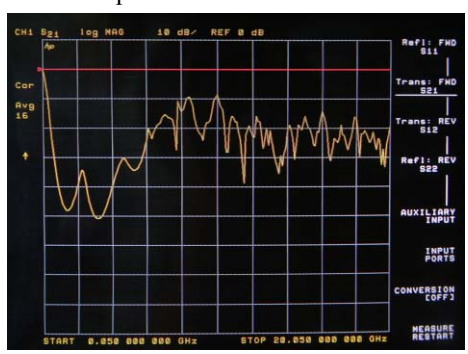

Figure 4: Measurement of the transfer function of the Gauss filter.

An additional LPF (SHF LP in Fig. 2), which has a specified 40 dB minimum attenuation from the cut-off at 1 GHz up to 20 GHz, cured the saturation effects and also the odd non-linearities. Fig. 5 shows a measurement of the Gauss LPF followed by a SHF LPF.

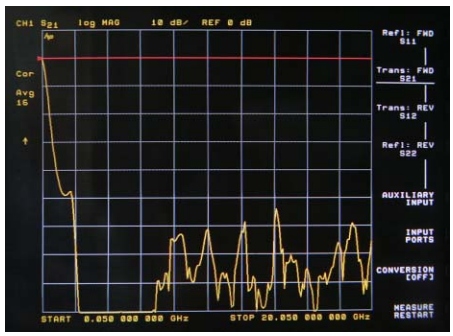

Figure 5: Measurement of the transfer function of the Gauss filter followed by a SHF LP filter.

Fig. 6 presents a measurement of the beam signal from a BPM pickup at FLASH after the Gauss filter. The bunch charge was about 1 nC. The distorted signal is cleaned by the addition of the SHF filter, as the measurement in Fig. 7 shows.

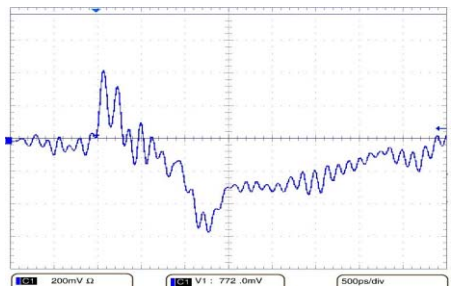

Figure 6: Measurement of the beam signal at FLASH after passing the Gauss LP filter and the (inverting) LNA.

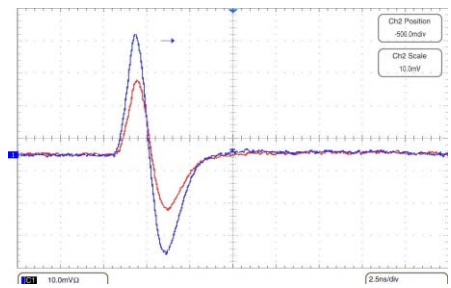

Figure 7: Measurement of the beam signal at FLASH after passing the Gauss and the SHF LP filters and the (inverting) LNA.

Further Non-Linearity

One source of non-linearity of the electronics, proved to be a reflection at the LP-averaging filter, back to the prior electronic and then back to the filter again, all inside of the measurement time. This disturbs the pulse-width modulated signals, more or less dependent on the actual pulse width. The cure was a bit "brute force" by inserting a delay line, so that the reflections fall out of the measurement time slot. Other methods (additional back-termination and a matching network) are rejected due to the resulting loss in signal amplitude, which would require extra amplification again.

Another source of nonlinearity was found in the operational amplifier, which had slew rate limitations. Here the cure was swapping some components and low pass filtering in front of the amplifier.

Trigger Jitter

The remaining unstable reading of the electronic, which was not present at the bench, was investigated and some causes were found. The averaged signal of the PWM was frozen with a track-and-hold circuit due to the FWHM of the signal is about 3-4 ns long and has to be hold constant for the external, relatively slow ADC.

An external trigger is used. Unfortunately this trigger was found out to have too much jitter and was also drifting over time, so that the sampling point was uncertain, leading to an unstable measurement. Careful centering of the moment of freezing lowers the amount of noise. When the trigger is riding near the rising or falling edge, the BPM noise gets worse.

To cure the timing problem, an additional electronic is under investigation [6]. This electronic resynchronizes the timing with a very clean and stable 81 MHz signal, delivered from the master oscillator. Measurements with a prototype showed an improvement in the trigger jitter by up to a factor of ten. During the shutdown in summer 2007 all BPM crates will be equipped with this trigger conditioner. On the other hand a program has been written that automatically sets the trigger on the signal peak.

During the measurements of the resynchronization electronics, another jitter source was found: The trigger distribution boards, used in all crates, are inverting the trigger signal, which was not expected. So the electronics triggered on the wrong edge, which was found to be not as stable as the designated edge. A patch, correcting the distribution boards will be done during this shut down.

SUMMARY AND CONCLUSIONS

Intensive studies with beam and on the test bench have lead to several changes in the electronics of the button BPMs at FLASH. The noise and the linearity have been improved. In this way the specifications of the BPMs have been largely met. The resolution determined with a correlation method [7] is around 10 µm rms. Other characteristics of the BPMs are to be studied in the future, as for example the long-term drift.

ACKNOWLEDGEMENTS

We thank our colleagues from MDI and other DESY groups for the contribution and the fruitful discussions.

REFERENCES

[1] V. Ayvazyan et al., Eur. Phys. J. D37, 297 (2006); W. Ackermann et al., Nat. Phot. 1, to be publ. (2007)
[2] M. Wendt, DIPAC 2001, Grenoble, France.
[3] http://www.cst.com
[4] F. Marcellini et al., Nucl.Instr.Meth. A402 (1998) 27.
[5] R. Lorenz et al., PAC97, Vancouver, B.C., Canada.
[6] Axel Winter, Private Communication.
[7] N. Baboi et al., BIW06, Batavia, IL, U.S.A.

SUB-PS TIMING AND SYNCHRONIZATION SYSTEMS FOR LONGITUDINAL ELECTRON BUNCH PROFILE MEASUREMENTS

Axel Winter, Universität Hamburg, Hamburg, Germany

Abstract

Precise timing and synchronization systems have become an increasingly important topic for next generation light sources. Particularly free electron lasers can emit X-ray pulses with pulse durations down to the few-tens of femtoseconds level. In order to utilize this potential temporal resolution for pump-probe experiments, a precise synchronization of the experimental laser to the X-ray pulse and stabilization of the electron beam arrival time at the undulators are mandatory. This requires a timing and synchronization system which can supply ultra-stable phase references over long distances, thus enabling the temporal stabilization of the electron beam to a sub-100 fs level. Furthermore, a precise timing and synchronization system renders possible extremely accurate measurements of the longitudinal electron bunch profile. This talk will give an overview of the status of existing sub-ps timing and synchronization systems and of systems currently under construction.

INTRODUCTION

One of the key challenges for the linac-based FEL sources such as the European XFEL or FERMI at Elettra is to implement a timing stabilization and distribution system that allows the full exploitation of the ultra-short x-ray pulse for pump-probe experiments. The important factor at the end of the day is the temporal jitter and drift between the FEL pulse and the experimental laser used for the pump-probe experiments. The current effort evolving around optical timing and synchronization systems is to distribute signals to various end stations along the machine with varying distances ranging from around 100 meters to several kilometers with a stability of around 10 fs. This however, will eventually lead to a sub-100 fs arrival time stability of the electron bunch with respect to the main machine reference. With future development, another factor of two improvement seems feasible, however 10 fs arrival time stability of the electron bunch does not seem within reach in the next few years. A way to circumvent this problem is a seeded machine, for instance using high harmonic generation (HHG). Here, a femtosecond laser pulse is used to generate light at a particular harmonic of the optical frequency which modulates the electron bunch energy. This energy modulation is converted into a density modulation in a dispersive section and this part of the electron bunch emits radiation in a second undulator. This puts the load on the synchronization between seed laser and experimental laser. The electron bunch arrival time however still needs to be reasonably stable to guarantee overlap with the ultra-short seed laser pulse.

In the following sections, an overview of the present development of optical synchronization systems, which are key components for a sub-100 fs electron bunch arrival time stability, followed by a description of measurement techniques and possibilities making use of the optical synchronization systems will be given.

OPTICAL SYNCHRONIZATION SYSTEMS

A comment needs to be made regarding jitter and drift. Whenever a 10-fs stabilization is mentioned, this refers to the relative jitter between different components in the linear accelerator. Since all machine systems are synchronized to a common reference (usually done with a Phase-locked-loop), they follow this reference up to the PLL bandwidth. Hence only the relative jitter between the subsystems is important up to this bandwidth, which is usually in the 1 to 10 kHz range. The absolute phase noise is usually significantly higher. For faster fluctuations, which cannot be corrected by the PLL, the intrinsic absolute timing jitter becomes important. It is therefore reasonable to identify two different frequency regimes; one for frequencies above 1 kHz where the absolute phase noise is important and a second one for slower fluctuations where the relative phase noise compared to the common machine reference is relevant.

So why is a new approach for the synchronization system needed in next generation light sources?

Traditional coaxial cable based systems can deliver very stable signals from microwave oscillators over short timescales. For long distances however, the attenuation of cables for high-frequency signals is substantial. To compensate, high-power amplifiers are needed, which introduce additional jitter and drifts. RF cables are also susceptible to drifts caused by temperature fluctuations along the machine. Even if extremely stable RF cables are used, they still exhibit a temperature coefficient of 0.5 ppm/deg C. This can easily amount to several picoseconds per degree C for a kilometer-long facility. Optical fibers exhibit an even larger temperature coefficient (5 ppm/deg

C), but can be actively stabilized. These stabilized links can deliver signals to remote locations with femtosecond stability over long timescales. If one only takes the signal transmission capabilities into account, the cost/benefit ratio of optical synchronization systems vs. cable based systems becomes debatable. With passive stabilization techniques employed, RF cables can also deliver signals with low drift performance over short distances. However, as soon as length scales are in excess on a few hundred meters, the optical synchronization systems are clearly advantageous.

The main feature which makes optical synchronization systems unique, is the possibility to optically phase-lock different laser systems with an actively stabilized fiber-link used to transport the reference signal. This has been demonstrated with a stability of sub-10 fs over short and long timescales. This is a significant advantage compared to the traditional locking of lasers to a microwave reference, which has been demonstrated to a 60 fs level [5]

At present, there are two different schemes to employ a synchronization system based on the distribution of laser radiation in development. One approach, being investigated at Berkeley National Lab (LBL), is based on the interferometric stabilization of optical fiber and will be called frequency domain approach in this paper. The second option, suggested by MIT [6] and presently developed by a collaboration between DESY, MIT and Trieste, distributes femtosecond laser pulses and makes use of the timing information contained in the repetition rate of the laser pulses. It will be called time-domain approach.

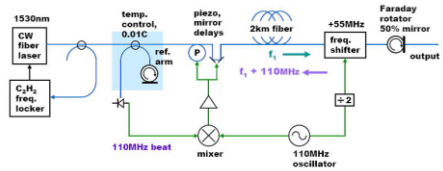

Figure 1: Schematic setup of the setup of the frequency domain stabilization scheme.[7]

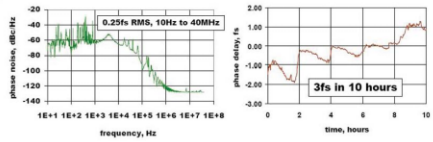

Figure 2: left: Jitter Power spectral density (250 as rms); right: drift over several hours (3 fs).[7]

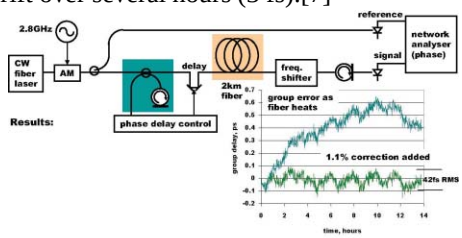

Figure 3: Measurement setup and results of group vs. phase velocity drifts.[10]

Frequency Domain Approach

A schematic of the stabilization setup is depicted in figure 1. A continuous-wave single-frequency erbium-doped fiber laser at a wavelength of 1550 nm is sent down the fiber link. As this scheme relies on a sufficiently long coherence length of the fiber laser used, it is stabilized to an acelty-lence resonance, which results in 10^{-9} frequency stability. At the end of the link, the optical frequency is upshifted by 55 MHz using an acousto-optic modulator and a portion of the light is reflected back and passes the modulator again for a total upshift of 110 MHz. A microwave signal at 110 MHz is obtained at the start of the link by a heterodyne beat between reflected and original signal. This is compared to the microwave signal used to upshift the optical radiation in a phase detector. This resulting dc error signal is fed via a Controller to a piezo-based fiber stretcher which closes the stabilization loop. Results for an out-of-loop measurement, where a link of 2 km length is compared to a 1 meter long link. The stability obtained is 250 as rms for short term fluctuations (10 Hz ... 40 MHz) and drifts amount to 3 fs over 10 hours (see figure 2). It must be noted, that only the phase velocity of the light propagating down the fiber is stabilized. However, any signals being transmitted travel at the group velocity. The proposed scheme to bring RF signals to the end stations is to amplitude modulate the cw light with the frequency of choice using an electro-optic modulator. The temperature coefficient of group velocity and phase velocity differ on the order of 10^{-2}. That means for a total correction applied to the piezo-stretcher of say 100 ps (which is a typical value for a km-long link over the course of one day), the transmitted RF signal will have drifted by 1 ps. At present, a 1.1% fixed correction is applied to the phase velocity error signal. This brings the error down to around 40 fs rms over the course of several hours. A schematic of the measurement setup and results are shown in figure 3. This work is ongoing and improvements are to be expected. It will remain to be seen if a long-term stability on the order of 10 fs rms can be achieved. Remote lasers can be phase locked by stabilizing two cw lasers operating at slightly different wavelengths to two different lines of the frequency comb of a mode-locked laser. This phase information is transmitted over the stabilized link and a slave laser is locked to these two incoming signals using a PLL. Here, the scheme does not suffer the problems of group velocity vs. phase velocity, since the only phase information of the cw signals propagating down the link is relevant. Further details regarding the stabilization scheme can be found in references [7, 8, 9].

Time Domain Approach

The centerpiece of the stabilization approach using ultra-short optical pulses is a passively mode-locked erbium-doped fiber laser. It not only supplies the pulses to stabilize the transmission lines using optical cross correlation, but the timing information is also encoded in the precise repetition rate of the oscillator. The intrinsic low phase noise of the fiber laser at frequencies above 1 kHz is combined with the low close-in phase noise of commercially available microwave oscillators using a PLL. Hence an optical frequency source is derived which combines the benefits of both microwave oscillators and lasers.

Mode-locked fiber lasers are a natural choice to realize an optical master oscillator, because of the ease of coupling to the fiber distribution system, their excellent long-term stability, and the well-developed and mature component base available at the optical communications wavelength of 1550 nm. Recently, their technical capabilities have also improved significantly [11, 12]. Yb-doped and Er-doped fiber lasers offer stable and practical platforms for short pulse generation, at $1\mu\mathrm{m}$ and $1.5\mu\mathrm{m}$, respectively. Fiber lasers can generate pulses from picosecond down to 35 fs in duration by simultaneous phase coherent lasing of multiple longitudinal modes spaced in frequency by the pulse repetition rate of the laser. During photodetection, these optical modes beat in the photodetector and generate all harmonics of the repetition rate within the bandwidth of the photodetector. A detailed description of the mode of operation of these lasers can be found in reference [13].

One of the most important features of these lasers is the low phase noise in the frequency range above 1 kHz. As mentioned above, this range cannot be compensated easily with a PLL, so the intrinsic noise performance is a key issue. At present, erbium-doped fiber lasers in both the soliton and stretched-pulse mode of operation are under consideration. A phase noise measurement for both laser types is shown in figure 4. I can be seen that the performance differences in the regime above 1 kHz are small so both lasers are potential candidates. The noise floor of the soliton laser is slightly lower, as the measurements are limited by the electrical power level in the filtered harmonic of the laser repetition rate after photodetection. Since the total output power of the photodiode is constant, there is more power in each spectral line of the higher repetition rate laser.

The stabilization of the optical links is done using optical cross correlation. A schematic of the stabilization scheme is depicted in figure 5. As a testbed, a 400 m long dispersion compensated fiber link is used, which is installed in a hall at DESY. A Faraday rotator mirror reflects part of the light intensity back at the end of the link. The returning pulses are combined with the pulses coming directly out of the laser in a balanced cross correlator (see lower right of figure 5). Two light pulses with orthogonal

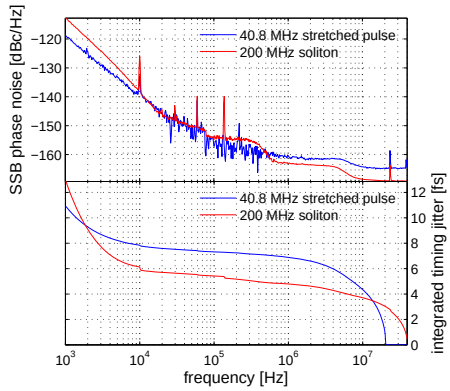

Figure 4: Phase noise comparision between a 40.8 MHz stretched-pulse laser and a 200 MHz soliton laser. Top: single-sideband phase noise measured at the harmonics at 980 MHz (stretched-pulse) and 1.2 GHz (soliton), respectively. Bottom: integrated timing jitter starting integration at 20.4MHz (stretched-pulse) and 40 MHz (soliton)[14].

polarization pass through a type-II PPKTP crystal. Inside the crystal the two polarizations experience a different group delay. With a dichroic mirror the second harmonic generated in the crystal is sent to a first detector, while the fundamental is back-reflected, passing the crystal a second time. The second harmonic is separated by a second dichroic mirror and directed to a second detector. Using the difference signal of the two detectors, amplitude fluctuations of the incoming pulses can be suppressed by a large amount. Changes are corrected by a DSP based feedback system which drives a piezo stretcher inside the link. The bandwidth of the feedback loop is around 1 kHz. Larger timing changes are corrected by a motorized optical delay line. Results are shown in figure 6. The jitter over a timescale of 12 hours is (7.5 ± 1.8) fs rms with a timing drift of 25 fs. The red line indicates changes with a time constant of 100 s. The timing jitter faster than 100 s is (4.4 ± 1.1) fs. Further details can be found in reference [14].

The RF reconversion can be done in two different ways. The first possibility is using a regular photodiode, combined with a bandpass filter for frequency selection. This leads to results shown in figure 4, but suffers from changes of detected phase with temperature and the limited noise floor. The second option is locking a microwave oscillator to the optical pulse train using for instance a sagnac-type interferometer. Details regarding this method can be found in reference [15].

BEAM DIAGNOSTICS USING OPTICAL SYNCHRONIZATION SYSTEMS

The prime benefit of an optical synchronization system is the possibility to lock lasers to the optical reference with femtosecond precision using for instance optical

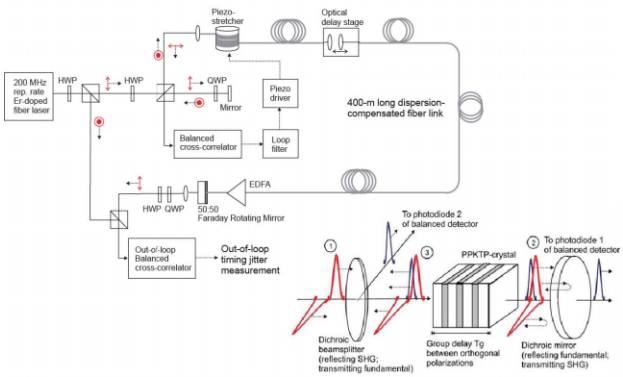

Figure 5: Experimental setup of the fiber link stabilization. lower right: Principle of the balanced optical cross-correlator [14].

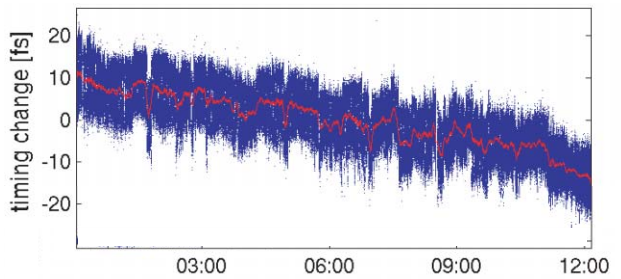

Figure 6: Out of loop drift measurement of a 400 m long fiberlink [14].

cross correlation techniques. So in prinpical any beam diagnostic system using lasers will benefit. For brevity, three examples will be treated in this paper. One is the so-called beam arrival monitor (BAM) [16], making use of the optical pulse train directly by converting the arrival time of the electron bunch into an amplitude modulation. The second example, which at a later stage will use the optical pulse train as a seed for a Ti:sapphire based amplifier system, is the Optical Replica Synthesizer [18]. Third, a brief description of electro-optical techniques will be given.

The Bunch Arrival Monitor

Laser pulses from a fiber link output are fed to an electro-optical modulator (EOM), where the laser amplitude is modulated by a fast transient of a beam pick-up signal. This way, the arrival time fluctuations of the electron bunch are transferred into an amplitude modulation of the laser pulses. These amplitude changes are now detected by a photo-detector and recorded by a fast ADC. The principal of the detection is illustrated in figure 7. Results from a test setup using a fiber laser at a repetition rate of 40.8 MHz synchronized to the machine RF with a conventional PLL are shown in figure 8. The arrival time measured at the end of the machine with the bunch arrival monitor is compared to the average energy deviation measured using

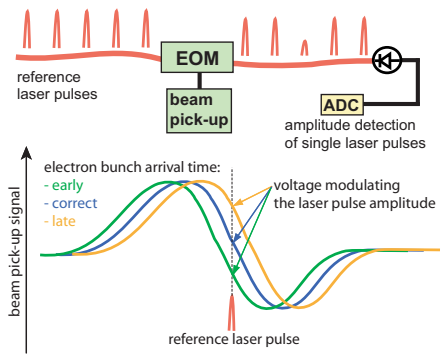

Figure 7: Principle of the arrival time detection. [16].

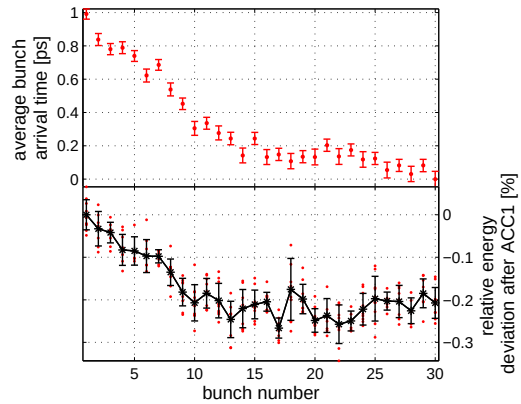

Figure 8: Comparison of the average bunch arrival time over the bunch train at the end of the machine with the average beam energy after the first accelerating module [16].

a synchrotron radiation monitor. in the first bunch compressor. The large energy slope visible in the first part of the bunch train is transformed into arrival time differences inside the magnetic chicanes. More details can be found in reference [16, 17].

The Optical Replica Synthesizer

Here, an amplified Ti:sapphire beam of sub-1 mJ energy is used to intensity modulate the electron bunch in an undulator. The intensity modulation is transferred into a density modulation in a chicane. This density modulation will radiate in a second undulator and emit an optical pulse at the laser wavelength onto which the electron bunch structure has been imprinted. The system is presently being set up at FLASH, for further details see reference [18]. The optical pulse length required is on the order of ps. Hence frequency doubled Er-doped fiber laser pulses can be used to seed the Ti:sapphire amplifier. This system is a natural candidate to be seeded by pulses coming from the output of a fiber link.

Electro-optical experiments

There are various electro-optical techniques under development at the moment ranging from spectral and tem-

poral decoding [19] to spatial decoding [20], each having different laser requirements. The best resolution currently observed is 118 fs FWHM for the temporal decoding technique. Here, the time structure of the electric field of the electron bunch is encoded onto the intensity profile of a chirped laser pulse. In the electro-optic crystal the polarization of the stretched laser pulse is rotated such, that it is slightly elliptical. The ellipticity is proportional to the electric field of the electron bunch. A polarizer turns the elliptical polarization into an intensity modulation, which is then sampled by the gate pulse in a single-shot cross-correlator, using a second harmonic crystal (BBO). Further details may be found in references [19, 21].
Commonly used in all those techniques are Ti:sapphire lasers, either just the oscillator or paired with an amplifier. The oscillators can be synchronized to an optical synchronization system using cross-correlators. This would mean an improvement in terms of jitter from ~ 60 fs to the few-fs level and thus be very attractive.

CONCLUSION AND OUTLOOK

Optical synchronization systems will play a major role in order to meet the stringent stability requirements for next generation light sources, such as the European XFEL. An overview about the potential sources of jitter and ways to circumvent them has been given in this paper. Furthermore, an overview about the two concepts for optical synchronization systems that have been proposed and an update on their present state of development has been given. There are also various beam diagnostic systems that rely directly or indirectly on the optical synchronization system of which three examples were described.
Without the help and contributions of many people this review would not have been possible. I would like to thank R. Willcox, H. Schlarb, F. Loehl, F. Ö. Ilday, G. Angelova, L. Banchi, M. Ferianis, J. Mueller, B. Lorbeer, J. Byrd, J. Phillips for providing data and helpful discussions.

REFERENCES

[1] V. Ayvazyan et. al., "First Operation of a free-electron laser generating GW power radiation at 32 nm wavelength," European Physical Journal D **92**(2), 297-303 (2006).

[2] C. Brochetta et. al., "FERMI@ELETTRA A Seeded Harmonic Cascade FEL For EUV And Soft X-RAYS," Proceedings of the FEL 2005 conference, Stanford, CA USA, p. 682-685.

[3] M. Altarelli et. al., "The European X-Ray Free Electron Laser - Technical Design Report," available at: http://xfel.desy.de/tdr/index_eng.html

[4] H. Schlarb, C. Gerth, W. Koprek, F. Loehl, E. Vogel, "Beam Based Measurements of RF Phase and Amplitude Stability at FLASH," WEPC01, this conference.

[5] A. Winter, E.-A. Knabbe, S. Simrock, B. Steffen, N. Ignachin, A. Simonov, S. Sytov, "Femtosecond synchronisation of ultrashort pulse lasers to a microwave RF clock," Proceedings of the PAC 2005, Knoxville TN.

[6] J. W. Kim et. al., "Large scale timing distribution and RF-synchronization for FEL facilities," FEL Conference 2004, Trieste, Italy, 2004.

[7] R. Willcox, J. W. Staples, "Synchronizing Lasers over Fiber by Transmitting Continuous Waves," Proceedings of CLEO 2007, Baltimore, MD USA.

[8] J. M. Byrd, L. Doolittle, A. Ratti, J. W. Staples, R. Wilcox, "Timing Distribution in Accelerators via Stabilized Optical Fiber Links," Proceedings of the LINAC 2006 conference, Knoxville, TN USA p. 577-579.

[9] J. W. Staples and R. Willcox, "Fiber Transmission Stabilization by Optical Heterodyne Techniques and Synchronization of Mode-locked Lasers using two Spectral Lines," Proceedings of the FEL 2005 conference, Stanford, CA, USA p. 686-688.

[10] R. Willcox, private communication

[11] F. Ö. Ilday, J. R. Buckley, H. Lim, and F. W. Wise, "Generation of 50-fs, 5-nJ pulses at 1.03 μm from a wave-breaking-free fiber laser," Opt. Lett. **28**, 1365-1367 (2003).

[12] F. Ö. Ilday, J. R. Buckley, W. G. Clark, F. W. Wise, "Self-similar evolution of parabolic pulses in a laser," Phys. Rev. Lett. **92**, 3902 (2004).

[13] A. Winter et. al., "High-precision Laser Master Oscillators for Optical Timing Distribution Systems in Future Light Sources," EPAC Conference 2006, Edinburgh, UK, 2006.

[14] F. Loehl, H. Schlarb, J. Chen, F. X. Kaertner, J-W. Kim, "First prototype of an optical cross-correlation based fiber-link stabilization for the FLASH synchronization system," WEPB016, this conference.

[15] J-W. Kim, F.X. Kaertner, F. Ludwig, "Balanced optical-microwave phase detectors for optoelectronic phase-locked loops", Opt. Lett. **31**, 3659-3661 (2006).

[16] F. Loehl, K. E. Hacker, H. Schlarb, "A Sub-50 Femtosecond bunch arrival time monitor system for FLASH," WEPB015, this conference.

[17] F. Loehl et. al., "A sub-100 fs electron bunch arrival-time monitor system for FLASH," EPAC Conference 2006, Edinburgh, UK, 2006.

[18] P. van der Meulen et. al., "Technical Aspects Of The Integration Of The Optical Replica Synthesizer For The Diagnostics Of Ultra-short Bunches In FLASH At DESY," FEL Conference 2006, Berlin, Germany, 2006.

[19] G. Berden et. al., "Single Shot Longitudinal Bunch Profile Measurements at FLASH using Electro-Optic Techniques," proceedings of the EPAC 2006 conference, Edinburgh, UK.

[20] A. Azima, S. Duesterer, J. Feldhaus, P. Radcliffe, H. Redlin, H. Schlarb, "Jitter Reduced Pump-Probe Experiments," this conference, ID WEPC13.

[21] J. P. Phillips et. al., "Single Shot Longitudinal Bunch Profile Measurements by Temporally Resolved Electro-Optical Detection," invited oral WEO2A02, this conference.

Progress in ultrafast x-ray streak cameras at Berkeley Lab

John Byrd (LBNL, Berkeley, California)

Abstract

Streak cameras remain one of the tools for study of ultrafast phenomena. We present progress on modeling of x-ray streak cameras with application to measurement of ultrafast phenomena. Our approach is based on treating the streak camera as a photocathode gun and applying modeling tools for beam optics and electromagnetic fields. We use these models to compare with experimental results from a streak camera developed at the Advanced Light Source. We also show how this model can be used to explore several ideas for achieving sub-100 fsec resolution.

Paper not received
(See slides of talk on following pages)

Progress in ultrafast x-ray streak cameras at Berkeley Lab

John Byrd
23 May 2007

Overview

- Introduction to x-ray streak cameras
- Applications of X-ray SC
- ALS SC R&D program
- Start-to-end SC model
- Future improvements

People

H. Padmore, J. Feng, T. Young, A. Scholl , J. Nasiatka, A. Comin, A. Bartelt - ESG / ALS
W. Wan - Accelerator Physics Group / ALS
J. Byrd, J. Qiang, G. Huang – Center for Beam Physics / AFRD
R. Falcone (UCB/ALS)
K. Opachich (USD) / ESG, M. Greaves (UCB) / ESG

- Joint effort between beamline and accelerator scientists
- Combined expertise of accelerator tools and detectors
- Light source environment ideal for "mixing the gene pool"

Streaking: a brief history

The first recorded incident of streaking by a college student in the United States occurred in 1804 at then Washington College (now Washington and Lee University) when senior George William Crump was arrested for running nude through Lexington, Virginia, where the university is located. Crump was suspended for the academic session, and would later go on to become a U.S. Congressman and Ambassador to Chile.

ALS X-ray streak camera

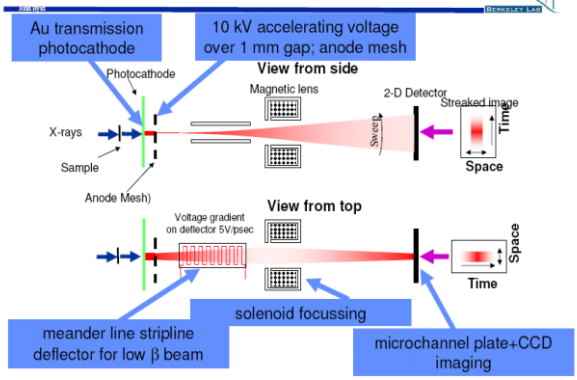

ALS x-ray streak camera

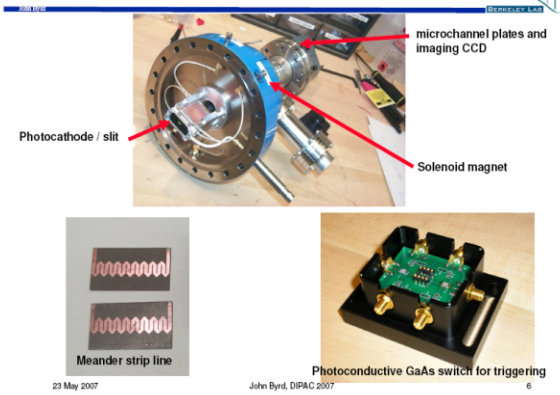

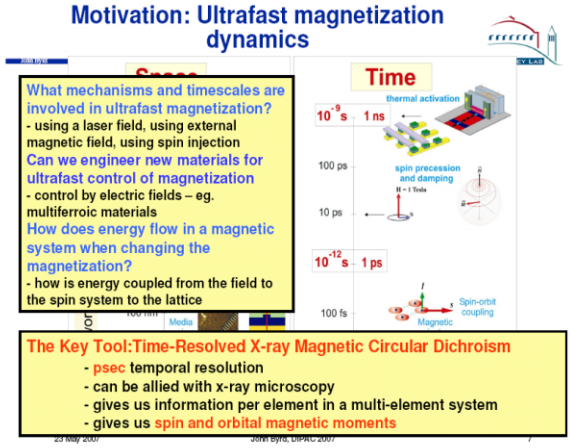
Motivation: Ultrafast magnetization dynamics
Time
What mechanisms and timescales are involved in ultrafast magnetization?
- using a laser field, using external magnetic field, using spin injection
Can we engineer new materials for ultrafast control of magnetization
- control by electric fields – eg. multiferroic materials
How does energy flow in a magnetic system when changing the magnetization?
- how is energy coupled from the field to the spin system to the lattice
thermal activation
spin precession and damping
Spin-orbit coupling
Magnetic
The Key Tool:Time-Resolved X-ray Magnetic Circular Dichroism
- psec temporal resolution
- can be allied with x-ray microscopy
- gives us information per element in a multi-element system
- gives us spin and orbital magnetic moments

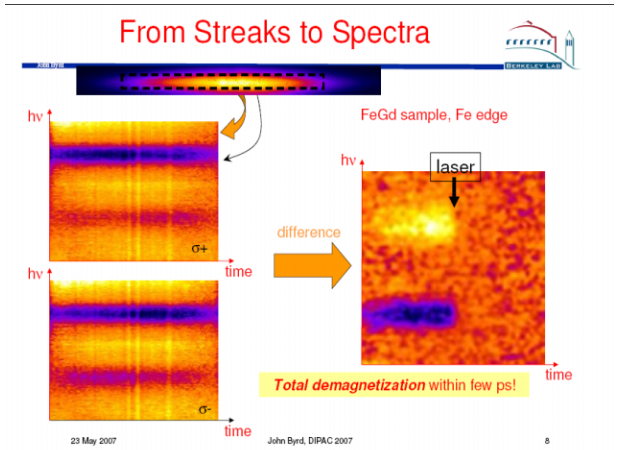
From Streaks to Spectra
FeGd sample, Fe edge
hv
laser
difference
time
Total demagnetization within few ps!
23 May 2007
John Byrd, DIPAC 2007
8

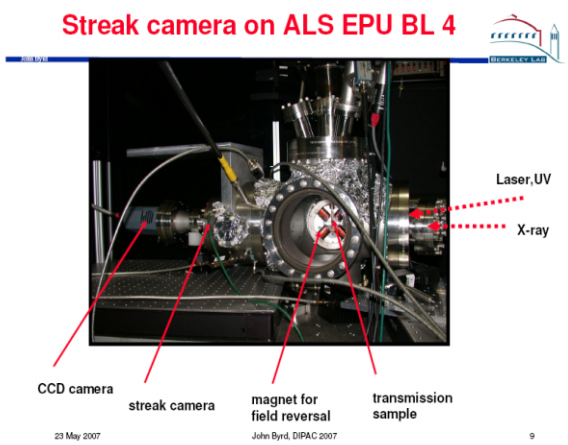
Streak camera on ALS EPU BL 4
Laser,UV
X-ray
CCD camera
streak camera
magnet for field reversal
transmission sample
23 May 2007
John Byrd, DIPAC 2007
9

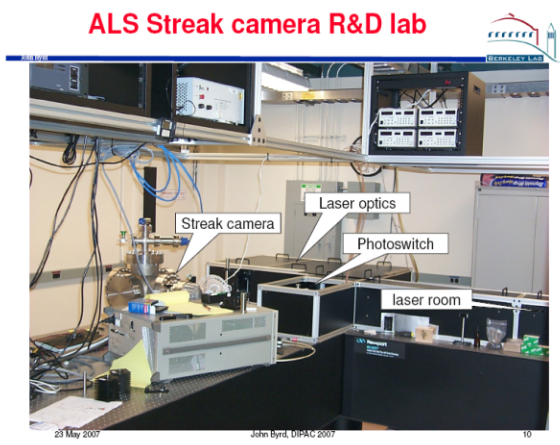
ALS Streak camera R&D lab
Streak camera
Laser optics
Photoswitch
laser room
23 May 2007
John Byrd, DIPAC 2007
10

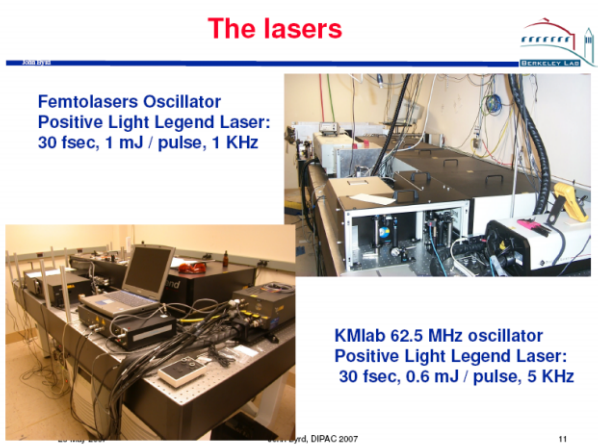
The lasers
Femtolasers Oscillator
Positive Light Legend Laser:
30 fsec, 1 mJ / pulse, 1 KHz
KMlab 62.5 MHz oscillator
Positive Light Legend Laser:
30 fsec, 0.6 mJ / pulse, 5 KHz
John Byrd, DIPAC 2007
11

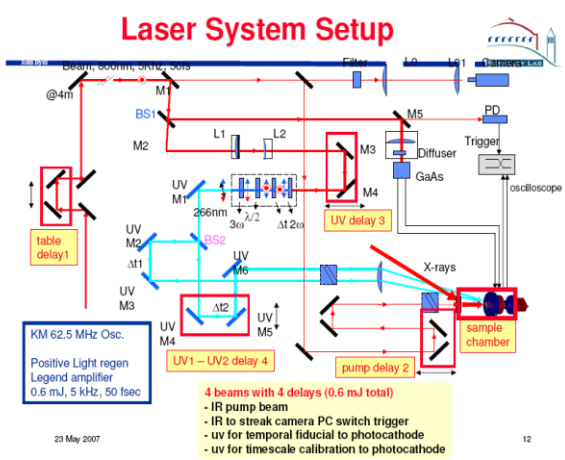
Laser System Setup
@4m
M1
BS1
M2
L1
L2
M3
M5
PD
Trigger
Diffuser
GaAs
oscilloscope
M4
UV M1
266nm
3ω
λ/2
Δt 2ω
UV delay 3
table delay1
UV M2
BS2
Δt1
UV M6
X-rays
UV M3
Δt2
UV M5
UV M4
sample chamber
KM 62.5 MHz Osc.
Positive Light regen Legend amplifier
0.6 mJ, 5 kHz, 50 fsec
UV1 – UV2 delay 4
pump delay 2
4 beams with 4 delays (0.6 mJ total)
- IR pump beam
- IR to streak camera PC switch trigger
- uv for temporal fiducial to photocathode
- uv for timescale calibration to photocathode
23 May 2007
12

Why are we involved?

- Streak cameras are DC photoguns
  - —fundamental limitations of streak cameras similar to those of RF PC guns
  - —interesting beam dynamics
- Still room for improvement
  - —ultimate resolution limited by time response of photocathode
  - —standard accelerator modeling tools highly relevant: magnetic optics, RF and microwave design, space charge dynamics. Detector groups typically do not have access or expertise to these tools.
  - —common design approach is to daisy-chain approximations
- **Direct collaboration with beamline users**
- Lots of fun!

Streak camera issues

- **Ballistic expansion from energy spread at photocathode**
  - **—reduced by higher voltage accelerating gaps**
  - **—space charge increases energy spread**
- **Maximize streak speed (slope of angular deflection)**
  - **—transmission of fast pulse**
  - **—effective beam voltage**
  - **—synchronization of deflection pulse with source**
- **High resolution imaging of electron beam**
  - **—avoid aberrations from solenoid**
  - **—minimize chromatic effects**
  - **—efficiently detect electrons**

Build a start-to-end model of camera to guide design.

End-to-End Streak Camera Model

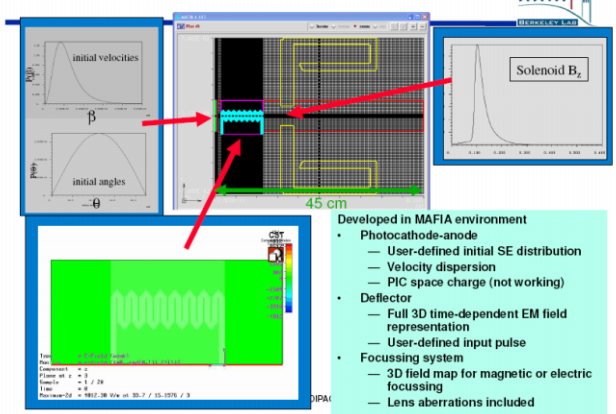

Developed in MAFIA environment
- Photocathode-anode
  - — User-defined initial SE distribution
  - — Velocity dispersion
  - — PIC space charge (not working)
- Deflector
  - — Full 3D time-dependent EM field representation
  - — User-defined input pulse
- Focussing system
  - — 3D field map for magnetic or electric focussing
  - — Lens aberrations included

Meander Stripline Temporal Response

Streak camera resolution is proportional to time gradient of vertical deflection. How fast can we deflect the beam?

ALS SC design incorporated meander line stripline to match kick pulse with beam velocity, increasing efficiency

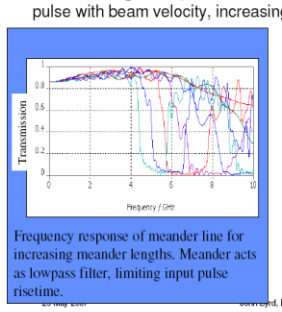

Frequency response of meander line for increasing meander lengths. Meander acts as lowpass filter, limiting input pulse risetime.

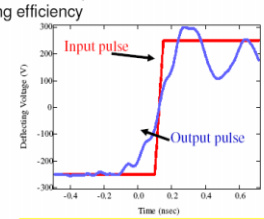

Effective slope reduced for sub-100 psec risetime input pulse. Linearity is also compromised. Solution calls for broader bandwidth structure or resonant cavity.

Meander Stripline Deflector Modeling

- **Full 3-D EM fields and particle tracking allows detailed simulation of beam dynamics in the deflector**
- **Simulation result indicated significant beam energy spread and pulse length increase within deflector**
- **Investigation uncovered relatively strong time-dependent E_z at each meander (off axis).**
- **Meander line is much more complicated than initially conceived.**

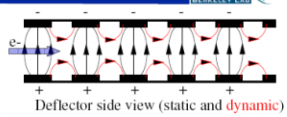

Deflector side view (static and dynamic)

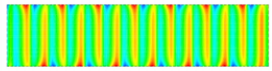

MAFIA off-axis E_z profile (top view)

Deflector design options:
- larger gap meander
- dielectric-loaded stripline
- resonant cavity

Start-to-end SC Simulation

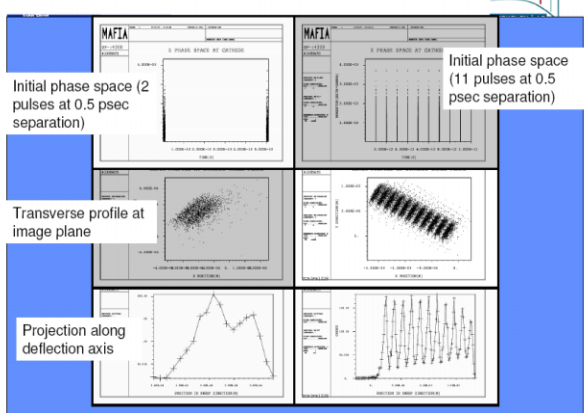

Experimental Results

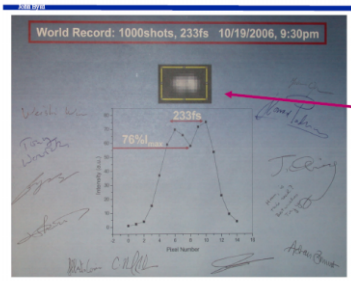

CCD Image with 1000 shots

Submitted to App. Phys. Lett.

World record resolution for SC.
Low trigger jitter
SC model points the way to better results!

23 May 2007 John Byrd, DIPAC 2007 19

Future directions

- Photocathode
  - —understand physics of secondary electrons angular and energy spread; engineered PC?
- Ballistic expansion
  - —higher extraction voltage
  - —RF extraction
  - —time-of-flight correction optics
- Sweep speed
  - —engineered photoswitch
  - —RF deflector (I.e. synchroscan)
- Detection and imaging
  - —take advantage of high rep rate x-ray source (~500 MHz)
  - —RF deflector synchronized with MO for accumulation (I.e. synchroscan) fast image readout
  - —higher resolution CCDs

23 May 2007 John Byrd, DIPAC 2007 20

Trigger Jitter

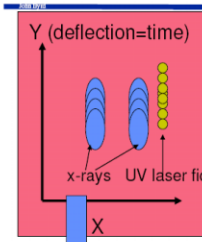

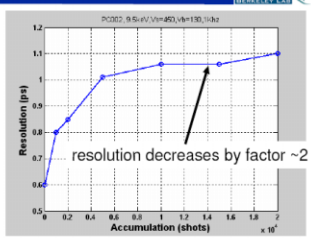

No jitter allows accumulation of images and more signal integrated between CCD readouts
•Improve time response of photoswitch
•Improve laser/ring synchronization
•Use resonant deflection (I.e. synchroscan)

23 May 2007

UV pulse temporal fiducialization

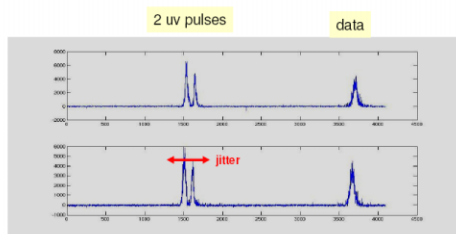

- find centroid of uv pulse(s)
- shift data to keep at constant detector position

- camera readout at sweep frequency (5 KHz)
- using c-plates + cmos camera + FPGA compressor + video processor

Time dispersion in cathode - anode

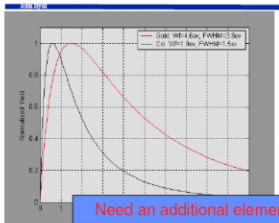

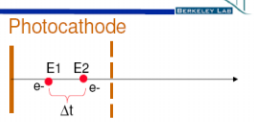

Photocathode has negative time dispersion
Au,Wf=4.6ev, FWHM=3.8ev, 10kV/mm field, ~600fs

Need an additional element to produce positive energy dependent time of flight

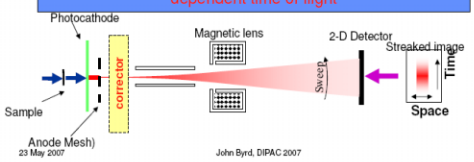

23 May 2007 John Byrd, DIPAC 2007 23

Jannamagi corrector: SPIE 5194 (2003)

- anode cathode: negative energy dependent time of flight dispersion
  - ie. low energy electrons take the longest time
- corrector gives positive energy dependent time of flight dispersion
  - low energy electrons take the shortest path and therefore take the shortest time

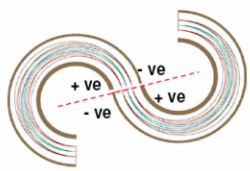

Double Cylindrical TOF corrector

- symmetric 256 degree system need for field aberration cancellation
- fringe fields between halves mess up the imaging properties

23 May 2007 John Byrd, DIPAC 2007 24

Chromatic time of flight correction

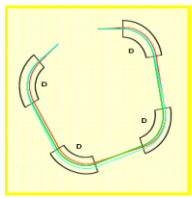

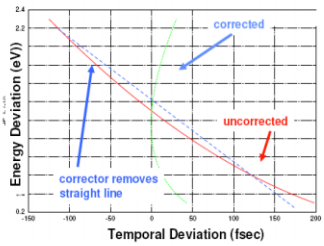

- 4 dipoles can be arranged to be double focusing, achromatic, zero angular time of flight dispersion and with defined dT/dE for correction
- < 50 fsec resolution from initial simulation!

Full simulation: Gold Photocathode Temporal Response

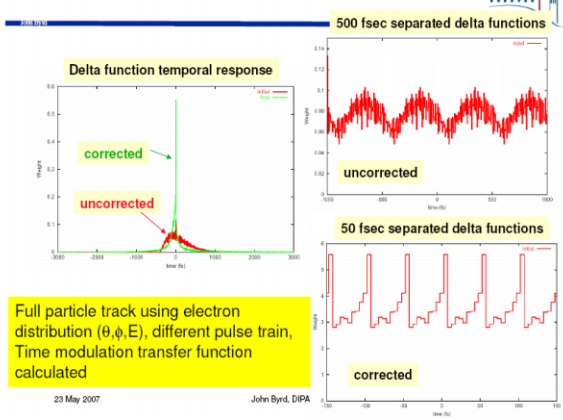

Full particle track using electron distribution (θ,ϕ,E), different pulse train, Time modulation transfer function calculated

23 May 2007 John Byrd, DIPA

Application to FELs

- Timing information is critical for next gen FELs
- Most timing diagnostics operate on e-beam
- Diagnostics needed for arrival time of x-ray pulse
- However…
  - —resolution of best existing cameras does not appear suited for short pulses produced by FEL
- However…
  - —timing information does not need to resolve pulse structure but simply pulse centroid

23 May 2007 John Byrd, DIPAC 2007 27

Centroid Determination: Optical Microscopy

SCIENCE VOL 300 27 JUNE 2003

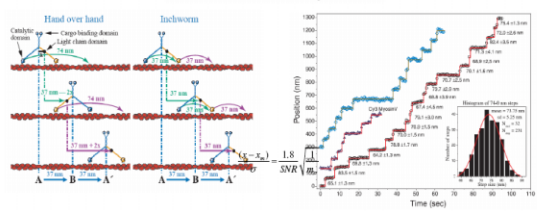

Myosin V Walks Hand-Over-Hand: Single Fluorophore Imaging with 1.5-nm Localization

$$\frac{(x - x_m)}{\sigma} = \frac{1.8}{SNR\sqrt{m_\sigma}}$$

SNR - signal to noise ratio
σ - 1 sigma of gaussian
M - # of pixels / 1 sigma

Shot noise limited

- 1e4 electrons, 4 pixels / 1 sigma
- error 1% of 1 sigma

23 May 2007 John Byrd, DIPAC 2007 28

Space Charge Limited Resolution

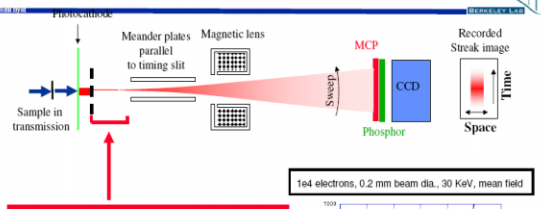

space charge limit set by anode to deflector transit

-potential energy transfer to longitudinal velocity

- correlated energy spread

- solution high energy, short transit to deflector

-using accelerator modeling codes to optimize effect: Astra, Parmela, Impact

-Trying to incorporate Barnes-Hut model into s2e model

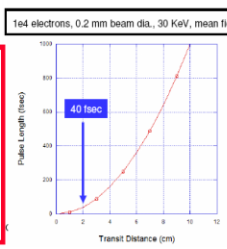

Summary

- *X-ray streak cameras very useful for studying psec phenomena*
  - *—relevant for sub-psec studies for storage rings*
  - *—potential as x-ray timing diagnostic for FELs with <100 fsec centroid resolution*
- *ALS x-ray streak camera development*
  - *—ALS streak camera demonstrated 230 fsec resolution*
  - *—start-to-end model of camera shows good agreement with measurements*
  - *—indicates limitations on performance*
- *possible improvements*
  - *—higher extraction gradients; RF acceleration?*
  - *—faster, stronger deflection; RF deflection!*
  - *—better synchronization (storage rings) for image accumulation*

23 May 2007 John Byrd, DIPAC 2007 30

INSTRUMENTATION FOR LONGITUDINAL BEAM GYMNASTICS IN FEL'S AND AT THE CLIC TEST FACILITY 3

T. Lefèvre, H.H. Braun, E. Bravin, S. Burger, R. Corsini, S. Döbert,
L. Søby, F. Tecker, P. Urschütz, C.P. Welsch, CERN, Geneva, Switzerland
D. Alesini, C. Biscari, B. Buonomo, O. Coiro, A. Ghigo,
F. Marcellini, B. Preger, INFN Frascati, Roma, Italy
A. Dabrowski, M. Velasco, Northwestern University, Illinois, USA
P. Craievich, M. Ferianis, M. Veronese, Sincrotrone, Trieste, Italy
A. Ferrari, Uppsala University, Sweden

Abstract

Built at CERN by an international collaboration, the CLIC Test Facility 3 (CTF3) aims at demonstrating the feasibility of a high luminosity 3 TeV e^+-e^- collider by the year 2010. One of the main issues to be demonstrated is the generation of a high average current (30 A) high frequency (12 GHz) bunched beam by means of RF manipulation. At the same time, Free Electron Lasers (FEL) are developed in several places all over the world with the aim of providing high brilliance photon sources. These machines rely on the production of high peak current electron bunches. The required performances put high demands on the diagnostic equipment and innovative longitudinal monitors have been developed during the past years. This paper gives an overview of the longitudinal instrumentation developed at ELETTRA and CTF3, where a special effort was made in order to implement at the same time non-intercepting devices for online monitoring, and destructive diagnostics which have the advantage of providing more detailed information.

INTRODUCTION

The single-pass seeded FEL project FERMI at ELETTRA [1] will be a user facility providing high-quality photons in the EUV to soft X-ray range. With a peak brightness more than ten orders of magnitude greater than 3rd generation sources, full transverse coherence, a choice of pulse lengths of the order of 1 ps or less, variable polarization and energy tunability, the FERMI source will provide a powerful tool for scientific investigation.

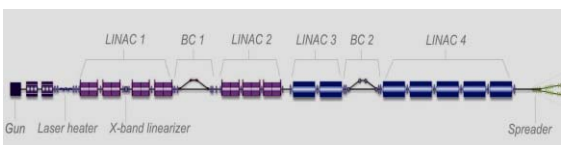

Figure 1: Overview of FERMI at ELETTRA

Figure 1 shows the layout of the facility. The accelerator starts with a photo-injector followed by two short linac sections providing acceleration up to 100 MeV. The main linear accelerator will alternatively time compress or accelerate the electron bunches. Two magnetic chicanes will be installed along the linac at beam energies of 220 and 600 MeV and will provide a total longitudinal compression factor of 10. The resulting bunch length will be as short as 200 fs RMS with a peak current of 800 A. After the second bunch chicane, the beam will be further accelerated up to 1.2 GeV before being sent to the undulators.

In parallel, in the framework of the Compact Linear Collider (CLIC) project [2], a test facility named CTF3 [3] is constructed at CERN by an international collaboration. It shall demonstrate by 2010 the key technological challenges for the construction of a high luminosity 3 TeV e^+-e^- collider. The generation of the CLIC RF power source is one of them, which relies on the production of a high average current (30 A) high frequency (12 GHz) bunched beam as depicted in Figure 2.

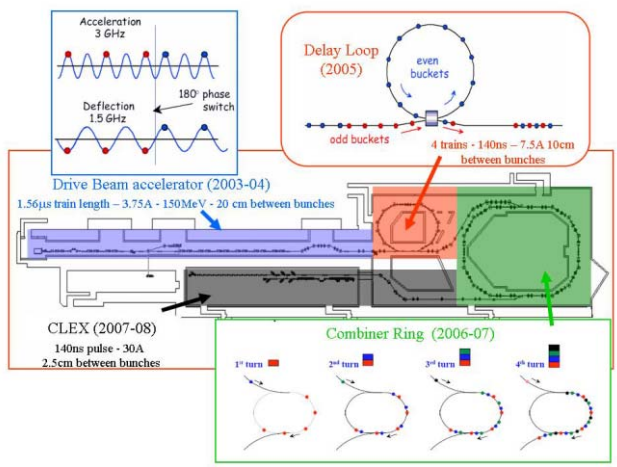

Figure 2: Overview of the CTF3 complex

In the present scheme, a long train of bunches with a bunch spacing of 20 cm is converted into an eight times shorter train with a 2.5 cm bunch spacing. The complex starts with a 3 GHz linac (twice the bunch frequency) that produces a pulsed electron beam with a present maximum energy of 150 MeV. Moreover, the macro pulse consists of alternated sequences of even and odd buckets with a duration of 140 ns each. The difference in phase between the trains is one RF wavelength, i.e. the phase of the RF is changed by 180º every 140 ns. The linac is connected to the Delay Loop (DL) [4] where a 1.5 GHz RF deflector deviates the odd bunch sequences to the left inside the Delay Loop and the even ones to the right. The DL length corresponds to a time of flight of 140 ns so that after one turn the odd sequence will be recombined with the

incoming even sequence to fill the interleaved empty buckets. At the exit of the DL, the beam is composed of four consecutive bunch trains, each of them having a 7.5 A average current and 10 cm bunch spacing. The electrons are then injected into the Combiner Ring (CR) by a 3 GHz RF deflector [5]. After the 4th turn, the bunch trains are combined into a single one with a current of 30 A and a 2.5 cm distance between the bunches. The beam is finally extracted and sent to the CLIC experimental area (CLEX) where it produces high peak power at 12 GHz passing through the CLIC decelerating structures.

BUNCH LENGTH MONITORS

High peak current electron beams are crucial for the performance of single pass FELs. This demands high quality bunch compressors and high resolution longitudinal beam diagnostics. In a similar way, the bunch length needs to be controlled precisely in the CTF3 complex. In the linac the bunches must remain short to keep the energy spread as low as possible, but need to be stretched before the rings to minimize emittance dilution due to coherent synchrotron radiation.

Streak cameras combined with Optical Transition Radiation (OTR) or Synchrotron Radiation (SR) have been used for decades for bunch length measurements [6]. State of the art streak tubes allow measurements with time resolutions down to 200 fs [7]. These measurements are complemented by other techniques that have proven their ability to measure sub-ps bunch lengths.

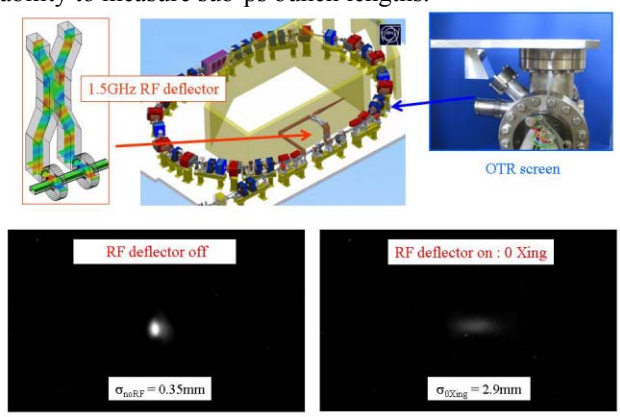

Figure 3: RF deflector measurement at CTF3

One of the most promising alternative techniques is based on the use of RF deflecting cavities. As the bunch is passing through the cavity, it experiences a time dependent deflection which converts time into spatial information. By measuring the beam size at a downstream location, the longitudinal profile can be extracted. The time resolution depends on the deflecting power available, the beam optics at the location of both the deflector and the beam profile monitor, and finally on the spatial resolution of this monitor [8]. With this method time resolutions of 10 fs have already been obtained [9].

An example of a bunch length measurement made at CTF3 is presented in Figure 3. The deflection is done using the 1.5 GHz standing wave cavity installed in the DL [10]. The beam is then imaged by an OTR screen and the bunch length is measured by switching on and off the RF power in the deflector. A bunch length of 6.7 ps was measured in this case.

Two RF deflectors will also be implemented at FERMI, one located after the first magnetic chicane and the second at the end of the linac. For the latter, a sophisticated set-up is foreseen to fully characterize the beam before the FEL. With two cavities providing deflection in X and Y planes, the system will measure not only the bunch length but also the slice emittance monitored by five different OTR screens. Moreover, downstream of the deflectors, a dipole followed by an additional OTR screen will be installed to measure the slice energy spread. A complete design of the system, including particle tracking simulations with the ELEGANT code is presented in [11].

NON-INTERCEPTIVE MONITORS

In FEL's, the need for peak current stabilization implies the development of non-destructive bunch length monitors. The aim is to provide reliable input signals for RF phase and amplitude feedback systems. The technique considered for this application is based on the fact that electron bunches start to radiate coherently for wavelengths which are longer than the bunch length. Therefore, by analyzing the corresponding frequency spectrum, the bunch length can be determined. Pyroelectric detectors are being developed and will be implemented in the magnetic chicane to detect coherent synchrotron radiation (CSR) and coherent diffraction radiation (CDR) as depicted in Figure 4. CSR is emitted from the last dipole of the chicane and CDR is emitted from a slit located just downstream of the chicane. For electron bunches with ps and sub-ps duration the coherent emission is in the mm/sub-mm wavelength range. The design of the system developed for FERMI is presented in [12].

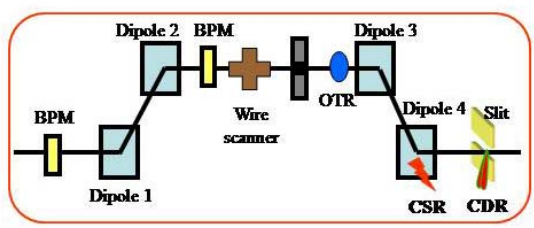

Figure 4: Magnetic chicane monitors at FERMI

The development of non-intercepting bunch length monitors is pursued also at CTF3, in particular through the use of an RF pick-up. Using a series of down-converting mixing stages and filters, the detector analyzes the power spectrum of the electromagnetic field picked-up by a single waveguide. In the present set-up, the signal amplitude and phase are measured simultaneously in four different frequency bands: 26.5-40 GHz, 45-69 GHz, 75-90 GHz and 157-170 GHz. Each signal is then digitized using ADCs with a bandwidth of 2 GHz. The system is

capable of performing single shot bunch length measurements with a 300 fs time resolution. The pick-up is installed close to the RF deflector and used for cross-calibrations. Detailed results of the recent commissioning of the detector are presented in [13].

BUNCH TRAIN COMBINATION

The bunch frequency multiplication performed at CTF3 is an innovative and flexible way of producing high frequency bunched beams. It relies on the performance of the phase coding inserted in the 1.5 GHz Sub-Harmonic Bunching System (SHBS) and on the accuracy of the bunch combination in the rings using RF deflector injection.

Successfully operated since 2006, the details and the results on the SHBS can be found in [14]. In order to control the bunch interleaving, the beam time-of-flight in the ring must be precisely equal to an integer number of RF deflector periods. This is performed with a wiggler, installed in the DL, which tunes the path length of the electrons accordingly.

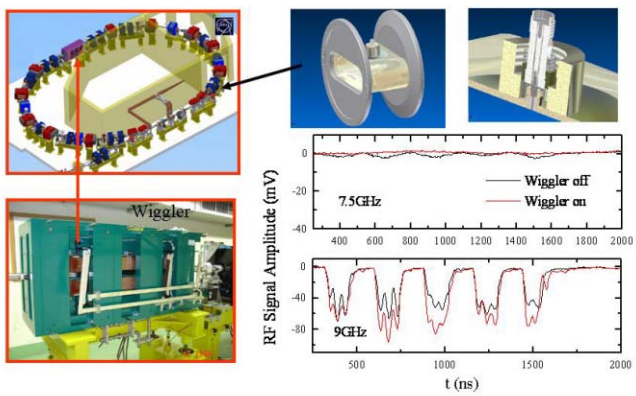

Figure 5: Bunch train combination in the Delay Loop

The bunch train combination is observed using an OTR screen located downstream the DL that is coupled to a streak camera [6] via a long optical line. For the same purpose, a non-intercepting monitor, called phase monitor, was installed close to the OTR screen for comparison and calibration. The detector is an RF antenna as shown in Figure 5, which was already tested several years ago at a previous test facility [15]. It measures the amplitude of the electromagnetic field at harmonic frequencies of 1.5 and 3 GHz. In the present design, the signal from the antenna is split into two, bandpass filtered at 7.5 and 9 GHz and finally measured by Schottky diodes. As a consequence of the bunch frequency multiplication, the signal at 7.5 GHz should disappear and the one at 9 GHz should double. As shown in Figure 5, the signal of the pick-up can be used to accurately tune the combination using different settings of the wiggler field.

CONCLUSIONS AND PERSPECTIVES

The longitudinal gymnastics performed for FELs and for the linear collider study at CTF3 present a number of similarities and rely on the development of high-quality beam diagnostic elements.

Measuring short bunches has been investigated in much detail during the past years and very sophisticated methods are now available, providing time resolutions in the sub-ps regime. To ensure the stable operation of these accelerators, a special effort has been carried out to develop simple and reliable non-intercepting devices capable of providing input signals for feedback stabilization systems.

REFERENCES

[1] E. Allaria *et al*, "FERMI@ELETTRA: A Seeded FEL Facility for EUV and Soft X-rays", Proceeding of FEL 2006, Berlin, Gemany, pp.166

[2] H.H. Braun *et al*, "Updated CLIC parameters 2005", CLIC note 627, (2005)

[3] G. Geschonke, "Status of the CLIC Test Facility 3 (CTF3)", Proceeding of LINAC 2006, Knoxville, Tennessee, USA, pp.11

[4] R. Corsini *et al*, "Commissioning Status of the CTF3 Delay Loop", Proceeding of EPAC 2006, Edinburgh, UK, pp.771

[5] C. Biscari *et al*, "CTF3: Design of Driving Beam Combiner Ring", Proceeding of EPAC 2000, Vienna, Austria, pp.450

[6] C. Welsch *et al*, "Longitudinal Beam Profile Measurements at CTF3 Using a Streak Camera", Journal of Instrumentation, 1, (2006), P09002

[7] Model FESCA 200 from Hamamatsu

[8] C. Welsch, E. Bravin and T. Lefevre, "Investigations of OTR Screen Surfaces and Shapes", Proceeding of EPAC 2006, Edinburgh, UK, pp.1220

[9] P. Emma *et al*, "A Transverse RF Deflecting Structure for Bunch Length and Phase Space Diagnostics", LCLS-TN-00-12, (2000)

[10] A. Ghigo *et al*, "Commissioning and First Measurements on the CTF3 Chicane", Proceeding of PAC 2005, Knoxville, Tennessee, USA, pp.785

[11] P. Craievich *et al*, "A Transverse RF Deflecting Cavity for the FERMI@ELETTRA Project", These proceeding

[12] M. Veronese *et al*, "The Diagnostics of the FERMI@ELETTRA Bunch Compressors", Proceeding of FEL 2006, Berlin, Germany, pp.629

[13] A. Dabrowski *et al*, "Non Destructive Single Shot Bunch Length Measurements at CTF3", To be published at PAC 2007, Albuquerque, New Mexico, USA

[14] P. Urschütz *et al*, "Beam dynamics and First Operation of the Sub-Harmonic Bunching System in the CTF3 Injector", Proceeding of EPAC 2006, Edinburgh, UK, pp. 795

[15] R. Corsini et al, "Experimental Results on Electron Beam Combination and Bunch Frequency Multiplication", Phys. Rev. STAB 7, 04101, (2004)

BEAM DIAGNOSTICS FOR THE FRONT END TEST STAND AT RAL

S. Jolly, D. Lee, J. Pozimski, P. Savage (Imperial College, London, UK)
D. Faircloth, C. Gabor (STFC/RAL, Chilton, Didcot, Oxon, UK)

Abstract

The Front End Test Stand (FETS) at the Rutherford Appleton Laboratory (RAL) is intended to demonstrate the production of a 60 mA, 2 ms, 50 pps chopped beam required for future high power proton accelerators. A number of different diagnostic systems are currently under development to provide precise measurements of the H^- ion beam produced by the FETS ion source. A pepperpot emittance measurement system, which is also capable of high resolution transverse beam density measurements, has been designed for use on the ion source development rig. This system is capable of sub-microsecond time-resolved measurements at a range of positions along the beam axis. Details are given of the current design, with recent emittance and beam profile measurements presented.

INTRODUCTION

As part of the ongoing development of future high power proton accelerators (HPPA's) and to contribute to the UK design effort on the neutrino factory, the Front End Test Stand (FETS) is being constructed at the Rutherford Appleton Laboratory (RAL) in the UK. The aim of FETS is to demonstrate the production of a 60 mA, 2 ms, 50 pps chopped beam; a detailed description of the project is given in [1]. To provide the necessary low emittance, high current H^- ion beam for FETS, an ion source development program is currently under way. The aim is to increase the extracted beam current from 35 mA to 70 mA and to increase the pulse length from 250 μs to 2 ms over the current ISIS H^- ion source at RAL, with an *rms* emittance of 0.3 π mm mrad (for more details of the ion source, see [2]).

As part of the development program, and to provide necessary information for FETS beam dynamics simulations, high quality correlated emittance and beam profile measurements are required [3]. Two types of beam profile and emittance measurement are being developed, based on photo detachment by laser. These will provide non-invasive measurements of both the longitudinal and transverse profile of the beam: more details are given in [4]. In addition, a pepperpot device has been developed to provide correlated 4-D emittance measurements. Previous measurements made with a slit-slit emittance scanner had a number of shortcomings: 1) measurements in the horizontal and vertical planes must be made independently, with no information on x-y correlation or 2-D beam profile; 2) the distance (z) from the ion source extraction was too large and fixed leading to a very large beam diameter; and 3) the slit length is too small, rejecting the outer part of the beam and resulting in an artificially low emittance measurement.

THE FETS PEPPERPOT

The purpose of the FETS pepperpot emittance measurement system is to provide correlated 4-D emittance information and high resolution beam profile measurements at a range of positions along the beam axis of the ion source. The current Mk.II FETS pepperpot is a significant improvement over the previous Mk.I system described in [3]. The principle is identical: an intercepting screen splits the beam into beamlets, which are allowed to drift and are imaged by a scintillator screen; however, many parts of the current system are significant upgrades.

Mechanical Assembly

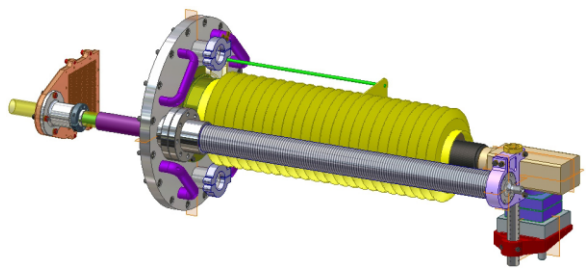

Figure 1: 3-D model of the pepperpot assembly; intercepting head is at the far left, camera and support is on the right.

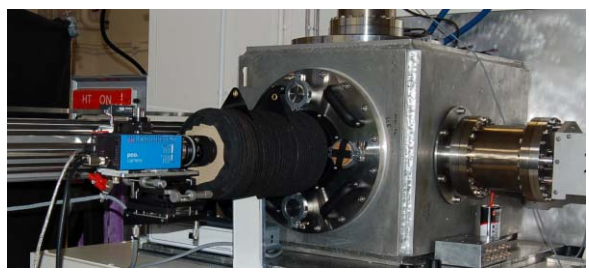

Figure 2: The FETS pepperpot, mounted to the ion source development rig. The existing emittance scanners are mounted to the top and right of the tank.

A 3-D model of the Mk.II pepperpot assembly is shown in Fig. 1. The pepperpot assembly consists of 3 main elements: an intercepting head, a high speed CCD camera and a main support structure. The head consists of a tungsten intercepting screen sandwiched between two copper plates. The intercepting screen is a 100 μm thick tungsten foil with a square array of 41×41 holes, each 50 μm in diameter, on a 3 mm pitch [5], giving a total imaging area of 120×120 mm^2. Laser drilling produces tolerances of less

than 10 μm in both hole size and absolute position. The front and back support plates are copper with an identical hole array to the intercepting screen, but with 2 mm diameter holes, and are 2 mm and 10 mm thick respectively. The front plate absorbs a significant fraction of the incident beam and the back plate provides the 10 mm drift length and prevents the beamlets from overlapping; both provide improved cooling to the tungsten screen. Mounted to the back of the rear copper plate is a single $152\times152\times6.4$ mm pure quartz scintillator plate. A second, interchangeable head is also used for high-resolution profile measurements: mounted into a copper frame, the entire surface of the quartz plate intercepts the beam, without the tungsten mesh and copper support plates.

The scintillation light from the quartz plate is imaged with a PCO 2000 high speed camera with a 2048×2048 pixel, 14-bit monochrome sensor and a Nikon 105 mm f/2.8 macro-lens; this interfaces with a PC via a high-speed Firewire connection. The camera is mounted on a system of Newport linear and tip-tilt stages that provide full 6-D position adjustment . The camera-to-screen distance is currently fixed at 1100 mm providing a resolution of 70 μm per pixel and an angular resolution of 7 mrad. The entire camera and head assemblies are mounted at either end of a linear shift mechanism, with a 700 mm stroke, mounted on a CF64 flange with a CF35 travelling flange. 38 mm bore stainless steel edge-welded bellows with an internal support tube keep the head and travelling assembly under permanent vacuum. A side mounted DC motor and controller with a linear digital vernier provide precise control over the longitudinal position of the assembly.

The central support rod passes through a rotatable CF64 flange of a 400 mm stainless steel vacuum flange, which is mounted to the rear of the ion source development rig vacuum tank and is shown in Fig. 2 (*cf.* Fig. 2 in [2]). A central 160 mm ISO-K observation window allows the camera to view the scintillator screen. A neoprene-coated nylon camera bellow, 200 mm in diameter and mounted between the observation window and the camera lens, ensures the light path to the camera remains light tight. Three additional KF40 ports on the main vacuum flange allow illumination of the copper head with an external light source and provide access for additional instruments. Cooling of the pepperpot head is provided by a cold finger that passes through the main flange via the inside of the travel mechanism bellows. Two concentric stainless steel tubes allow water to pass down the central volume and back through the outer volume. The head is clamped to the cold finger and is cooled by conduction.

Calibration

During data taking, accurate calibration data is crucial in converting the pepperpot images into emittance data. 3 pieces of information are needed for calibration: the centre of the pepperpot mesh, the relative rotation of the tungsten mesh with respect to the camera, and the spot-to-spot spacing, in pixels, of the mesh. This information is obtained from 4 lines, forming a $9\,\text{mm}\times9\,\text{mm}$ square around the central hole, marked on the surface of the rear copper plate facing the camera. The 4 corners of this square provide all the necessary calibration information, allowing the position of each hole in the tungsten mesh to be precisely reconstructed within the data analysis software.

Data Analysis Procedure

Data is recorded from the camera direct to a multi-image TIFF file and analysed with Matlab. Emittance data is derived from the x' and y' angles from the beam axis of each beamlet produced by the pepperpot plate. This is calculated by measuring the difference between the position of the light spot produced by the beamlet on the scintillator (see Fig. 3a) and the predicted position of a beamlet with zero divergence *ie.* parallel to the beam axis. The predicted hole positions are generated from the calibration data and compared to the data image. The weighted centre of each light spot is used to calculate a rough emittance distribution; real emittance values are produced by calculating x' and y' values for every single pixel with an intensity above a cut threshold. Summing up the total pixel intensity for each spot provides the beam intensity information.

RESULTS

To illustrate the performance of the device, 2 sets of data were recorded using the pepperpot setup: 1) variation in z-position of the pepperpot head, from 0 mm to 300 mm in 100 mm steps, for constant extract voltage (13 kV) and beam current (34 mA); and 2) ion source extract voltages of 6 kV, 9 kV, 13 kV and 17 kV at a constant z-position of 0 mm. The position of the pepperpot head was measured some 57 mm downstream of the ion source exit plane; 300 mm is therefore approximately the same z-position as the slit-slit scanners. For all measurements the platform voltage (and therefore the beam energy) was held constant at 35 kV.

Results for a single measurement are shown in Fig. 3: the raw spot image in Fig. 3a is used to reconstruct both the intensity profile shown in Fig. 3b and the emittance. Quiver plots for dataset 1 are shown in Fig. 4: arrows indicate the mean beam divergence for each spot, overlaid with contours of beam intensity. The behaviour of the beam is broadly as one would expect, with a steady expansion in beam size along the beam axis; the corresponding emittance (indicated by the arrows) shows no obvious nonlinearities. The measured beam properties are summarised in Table 1. The steady increase in emittance for increasing z-position may indicate space charge effects: the level of space charge compensation will be investigated with future simulations. The flat top and bottom of the beam profile are the likely result of unwanted collimation occurring upstream of the ion source exit. Variation in extract voltage (Fig. 5) shows a distinct change in beam shape, density distribution and emittance. The change in beam shape

and emittance may be partly a result of the upstream collimation; however, other factors will also contribute. The change in extract potential will cause a change in the shape of the field within the extract region, and affect the shape of the discharge plasma. An increase in extract potential also requires a corresponding increase in the 90° sector magnet current, changing not only the bending field but also the focussing effect of the fringe fields. In addition, an increase in extract potential requires a corresponding decrease in the post-acceleration voltage to keep the total acceleration potential constant at 35 kV: transverse focussing from the fringe fields within the post-acceleration gap will change accordingly.

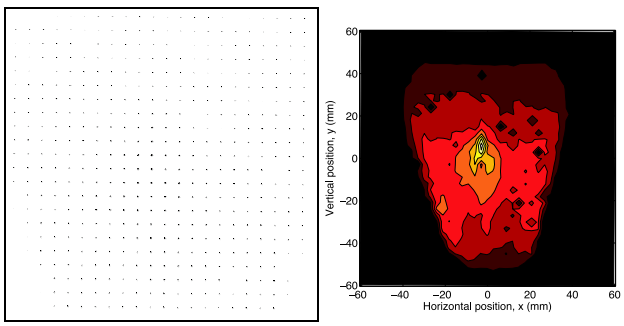

(a) Raw image (b) Beam profile

Figure 3: Enhanced section ($60\times60\,\mathrm{mm}^2$) of a raw data image, and the extracted 2-D density distribution, at 300 mm with 13 kV extract (*cf.* Fig. 4d).

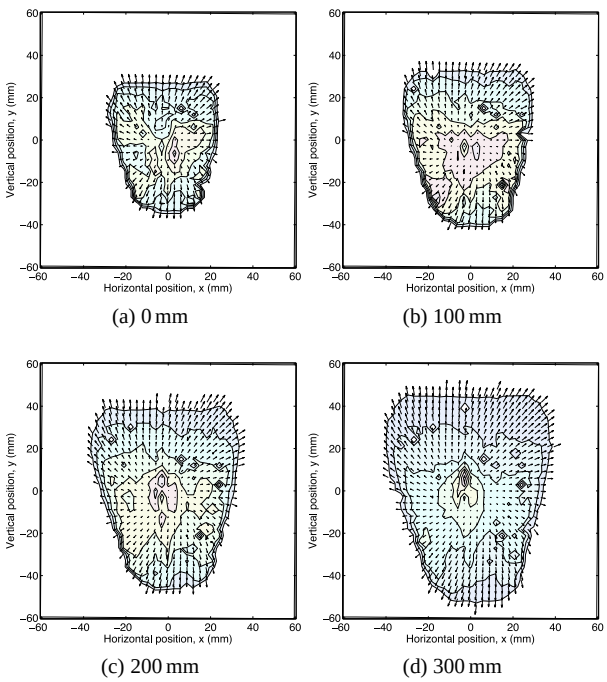

(a) 0 mm (b) 100 mm

(c) 200 mm (d) 300 mm

Figure 4: Variation in z-position with 13 kV extract.

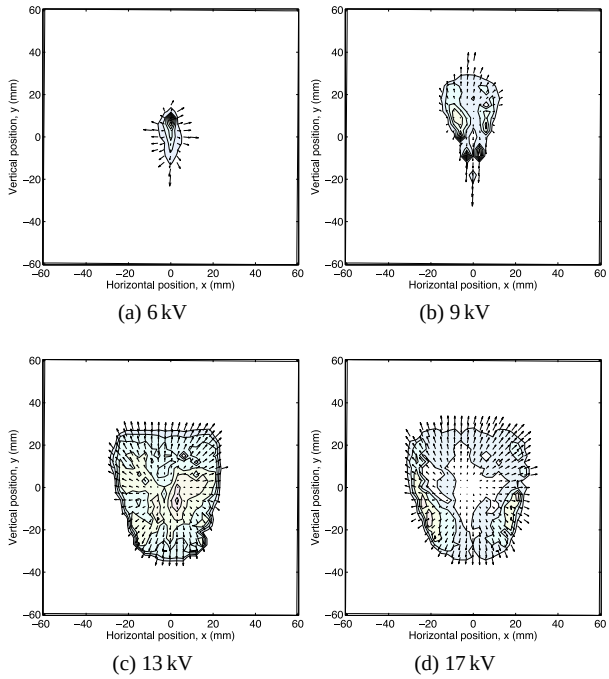

(a) 6 kV (b) 9 kV

(c) 13 kV (d) 17 kV

Figure 5: Variation in extract voltage at 0 mm: (a) shows strong asymmetric divergence in both planes; (b) shows mostly vertical expansion; (c) is nearly symmetric and slightly collimated and (d) is highly collimated.

Extract (kV)	Z (mm)	Beam size		ϵ (π mm mrad)	
		x (mm)	y (mm)	$\epsilon_{x,rms}$	$\epsilon_{y,rms}$
±1	±0.1	±3		$\pm5\,\%$	
6	0	18	33	0.25	0.77
9	0	27	63	0.74	1.14
13	0	51	60	1.36	1.47
13	100	57	72	1.65	1.78
13	200	69	87	1.82	1.96
13	300	78	102	1.90	2.04
17	0	57	63	2.02	1.92

Table 1: Beam properties for pepperpot measurements.

CONCLUSIONS

The advantage of the pepperpot method in the measurement of correlated emittance data has been clearly demonstrated. More detailed measurements are required to investigate the effects detailed above and to provide input data for beam dynamics simulations.

REFERENCES

[1] A.P. Letchford *et al.*, MOPCH112, EPAC 2006, p. 303.

[2] J.W.G. Thomason *et al.*, TUPLT141, EPAC 2004, p. 1458.

[3] S. Jolly *et al.*, TUPLS090, EPAC 2006, p. 1714.

[4] D. Lee *et al.*, TUPB11, these proceedings.

[5] Laser- und Medizin-Technologie GmbH, Berlin.

SINGLE SHOT LONGITUDINAL BUNCH PROFILE MEASUREMENTS BY TEMPORALLY RESOLVED ELECTRO-OPTICAL DETECTION

P.J. Phillips, W.A. Gillespie, Dundee University, Dundee, UK
B. Steffen, E-A. Knabbe, B. Schmidt, P. Schmüser, DESY, Hamburg, Germany
S.P. Jamison, ASTEC, Daresbury Laboratory, STFC, UK
G. Berden, A.F.G. van der Meer, FELIX / FOM Insitute 'Rijnhuizen', Nieuwegein, NL
A. M. MacLeod, Abertay University, Dundee, UK

Abstract

For the high gain operation of a SASE FEL, extremely short electron bunches are essential to generate sufficiently high peak currents. At the superconducting linac of FLASH at DESY, we have installed an electro-optic measurement system to probe the time structure of the electric field of single ~100 fs electron bunches. In this technique, the field induced birefringence in an electro-optic crystal is encoded on a chirped picosecond laser pulse. The longitudinal electric field profile of the electron bunch is then obtained from the encoded optical pulse by a single shot cross correlation with a 35 fs laser pulse using a second harmonic crystal (temporal decoding). An electro-optical signal exhibiting a feature with 118 fs FWHM was observed, and this is close to the limit of resolution due to the material properties of the particular electro-optic crystal used. The measured electro-optic signals are compared to bunch shapes simultaneously measured with a transverse deflecting cavity.

INTRODUCTION

Precise measurements of the longitudinal temporal profile of extremely short electron bunches are essential for a detailed understanding of the lasing and operating principles of a SASE FEL [1]. At FLASH (DESY), several monitors for the longitudinal profile of the compressed beam are located within a few meters of each other: the LOLA transverse deflecting RF structure [2], and the single shot electro-optic detection monitor [3] measuring the Coulomb field of the bunches as described in this paper.

MEASUREMENT SETUP

The temporal decoding method for single shot electro-optic detection of the electric field of electron bunches [4] is schematically depicted in Fig. 1. The time structure of the electric field of the electron bunch is encoded onto a chirped laser pulse. In the electro-optic crystal the stretched laser pulse acquires an elliptic polarization with an ellipticity which is proportional to the electric field of the electron bunch and encodes its temporal structure. The analyser, A, turns the elliptical polarization into an intensity modulation, which is then sampled by the gate pulse in a single-shot cross-correlator, using a second harmonic BBO crystal.

The femtosecond laser consists of a Ti:Sa oscillator, which is synchronised to the rf of the accelerator, and a Ti:Sa amplifier, which delivers pulses of 35 fs duration at a central wavelength of 792 nm with an energy of 1 mJ. A full description of the electro-optical temporal decoding has been given elsewhere [3,4,5]. The laser pulse is transported 20m to an optical table near the beam pipe where it is injected into the beam pipe and through an electro-optic crystal. It is then coupled out of the pipe and into the temporal decoding setup comprising the polarisers, electro-optic crystal and cross-correlator shown in figure 1.

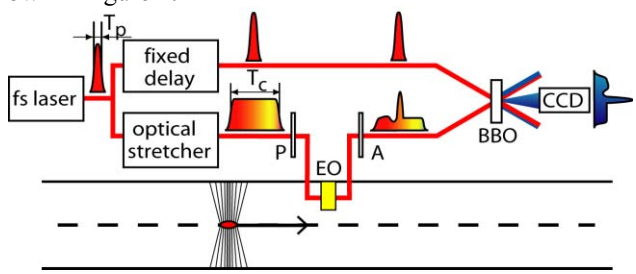

Figure 1: The single-shot technique for measuring the longitudinal electric field profile of electron bunches using electro-optic encoding and temporal decoding. P and A are polarizers, BBO is the second-harmonic crystal of the cross-correlator and the signal is recorded by the CCD.

There are four main factors which influence the accuracy of temporal decoding measurements: the material properties of the electro-optic crystal, the energy of the electron beam, the geometry of the electro-optic interaction and the geometry of the cross correlator.

The Coulomb field of the electron bunch behaves as a single cycle terahertz pulse which, for maximum time resolution and electro-optic signal strength, must propagate through the electro-optic crystal with the same group velocity as the laser pulse. This condition is evidently not met when the signal has significant components near a phonon resonance of the electro-optic crystal, where the refractive index changes rapidly with frequency. We have, in the past, used ZnTe, which has a phonon resonance around 5.3 THz, as an electro-optic crystal. In the experiments described here we use GaP as the electro-optic crystal: the higher resonance frequency of 11 THz should give a corresponding improvement in time resolution. We note that the details of the phonon resonances strongly depend on the material quality and manufacturing parameters. Figure 2 shows theoretical calculations made on both ZnTe and GaP [5].

The electric field of a charge moving at relativistic fields is compressed in the longitudinal direction and has an opening angle of $2/\gamma$ [5]. This small opening angle leads to a slight temporal broadening of the electric field pulse at a finite distance, which results in a reduction of the high frequency parts of electric field at the electro-optic crystal.

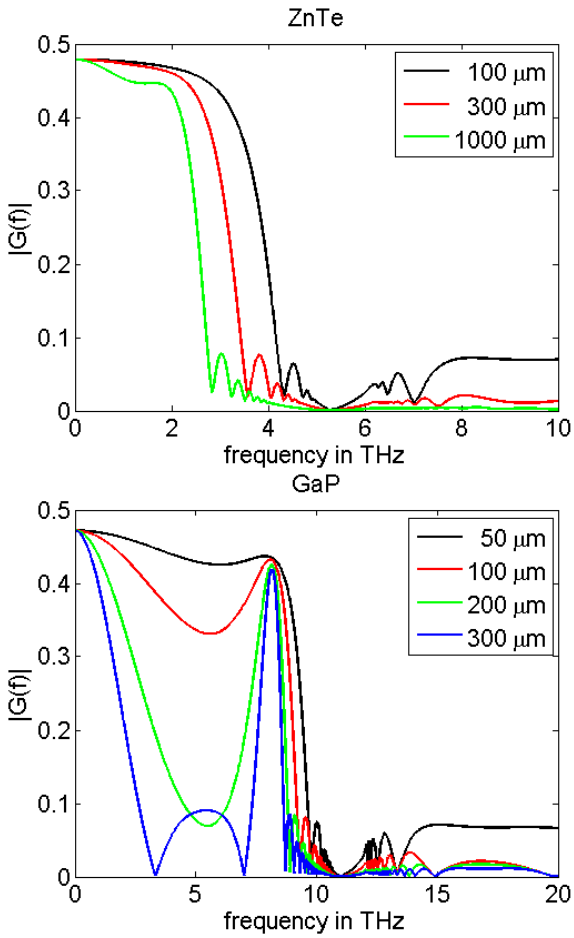

Figure 2: Electro-Optic response function for ZnTe (upper) and for GaP (lower) for different thickness of crystal.

While the THz pulse travels perpendicular to the surface through the crystal, the laser beam is inclined by a small angle. The right hand part of the laser arrives earlier at the crystal surface then the left hand part. Therefore the phase retardation resulting from the interaction of the THz pulse laser field is not distributed perpendicular to the direction of travel of the laser but tilted by the small angle. This effect is leads to a broadening of the electro optical signal (approximately a Gaussian convolution of 35 fs).

An upper limit for the time resolution of the cross-correlator was experimentally determined to be better then 50 fs (rms), including in the response of the BBO crystal, the imaging optics and the length of the gate pulse.

In these experiments we also compared the electro-optic detection with results from a Transverse Deflecting Cavity (TDC), which currently produces the highest resolution of all the longitudinal diagnostics at FLASH. The TDC streaks the longitudinal phase space of the bunch transversely without producing any mean deflection, and is preceded by a kicker that adds an additional mean deflection, so that a single bunch can be deflected onto an off-axis OTR screen. A number of electro-optic temporal decoding traces have been taken in parallel with longitudinal bunch profile measurements with high temporal resolution using TDC. Owing to space constraints, the electro-optic experiment had to be mounted downstream of the TDC. Although it was not possible to measure using both techniques simultaneously, we were able to use the electro-optic detector to measure the bunch immediately preceding or immediately following the bunch deflected by the TDC.

RESULTS AND DISCUSSION

The data is obtained directly from the CCD camera in real time and is displayed in the format as shown in Figure 3. The camera image, which is in false colour representation, clearly shows a reflection from the electro-optic crystal. The lower panel shows the electro-optic signal obtained after binning, background subtraction, and normalisation of the image. Using a 100mm thick GaP crystal in the temporal decoding setup of Figure 1, a pulse of 118 fs FWHM in a 12 ps measurement window was observed. The leading edge of the electron bunch is on the left. The small peak around 8.5 ps is due to the reflection of the THz field in the electro-optic crystal.

Simultaneous TDC and the electro-optic measurements, not presented here, show a good correlation between the shapes of the electron bunch profiles.

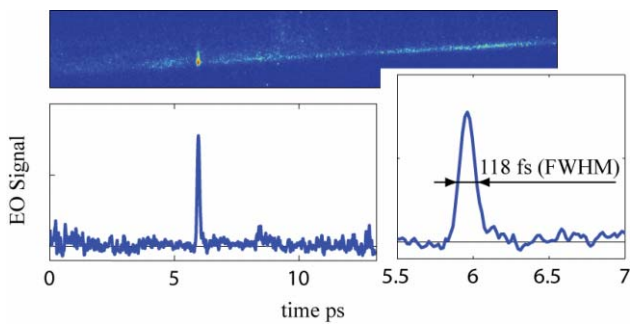

Figure 3: A typical measurement from temporal decoding showing the camera image and a binned image. The insert displays an exploded view of the peak.

The CCD camera which captures the images in the electro-optic experiment is part of the FLASH control system. This makes it possible to tune the accelerator

while observing the electron bunch shape. Electro-optic measurements have been performed during the SASE output. These measurements did not adversely influence the SASE process.

CONCLUSION

Electro-optic detection of single electron bunches with a FWHM of 118 fs has been observed. The response of the electro-optic material, GaP in our case, is the dominant temporal limitation in these measurements. Simultaneous TDC and electro-optic measurements show a good agreement in the shapes of the electron bunch profile. The non-invasive property of the electro-optic measurement allowed it to be used as a diagnostic tool during SASE operation.

We are currently designing a robust version of the electro-optic diagnostic with a reduced footprint, a better temporal resolution and increased measurement stability. Such a setup will be installed at FLASH and at the Energy Recovery Linac Prototype (ERLP) at Daresbury laboratory. Furthermore, the setup will be readily transportable to other laboratories.

REFERENCES

[1] B. Schmidt, “Overview on diagnostics for X- and XUV-FEL”, Proceedings of the 28th International Free Electron Laser Conference (FEL 2006), Berlin, Germany 2006, p. 761.

[2] M. Huning, A. Bolzmann, H. Schlarb, J. Frisch, D. McCormick, M. Ross, T. Smith, J. Rossbach, “Observation of femtosecond bunch length using a transverse deflecting structure”, Proceedings of the 27th International Free Electron Laser Conference (FEL 2005), Stanford, USA 2005, p. 538.

[3] G. Berden, A.F.G. van der Meer, S.P. Jamison, B. Steffen, E.-A. Knabbe, B. Schmidt, P. Schmüser, A.M. MacLeod, P.J Phillips, W.A. Gillespie, ”Single shot longitudinal bunch profile measurements at FLASH using electro-optic techniques” EPAC, 2006, Edinburgh, Scotland, p. 1055.

[4] G. Berden, S.P. Jamison, A.M. MacLeod, W.A. Gillespie, B. Redlich, and A.F.G. van der Meer, “Electro-optic technique with improved Time resolution for real-time, non-destructive, single-shot measurements of femtosecond electron bunch profiles”, Phys. Rev. Lett., 93,114802 (2004).

[5] S. Casalbuoni, H. Schlarb, B. Schmidt, P. Schmüser, B. Steffen, A. Winter “Numerical studies on the Electro-Optic sampling of Relativistic Electron Bunches”, TESLA Report 2005-0, DESY.

ADVANCED MEASUREMENTS AT THE SPARC PHOTOINJECTOR*

A.Cianchi[a†], D.Alesini[b],A.Bacci[c], M.Bellaveglia[b],R. Boni[b], M.Boscolo[b], M.Castellano[b], L.Catani[a], E.Chiadroni[b], S.Cialdi[c], A.Clozza[b], A. Cook[f],L. Cultrera[b], G.Di Pirro[b], A.Drago[b], M. Dunning[f], A. Esposito[b], D. Filippetto[b], M. Ferrario[b], P. Frigola[f], V. Fusco[b], A. Gallo[b], G. Gatti[b], A. Ghigo[b], L. Giannessi[d],M. Incurvati[b],C. Ligi[b], M.Migliorati[e], A.Mostacci[e], P.Musumeci[f], E.Pace[b],L.Palumbo[e],L.Pellegrino[b], M.Petrarca[g], M.Quattromini[d], R.Ricci[b], C.Ronsivalle[d], J.Rosenzweig[f],A.R.Rossi[c], C.Sanelli[b], L.Serafini[c], M.Serio[b], F.Sgamma[b], B.Spataro[b], F.Tazzioli[b], S.Tomassini[b],C.Vaccarezza[b],M.Vescovi[b],C.Vicario[b]

[a]INFN-Roma "Tor Vergata", via della Ricerca Scientifica, 1 - 00133 Rome, Italy
[b]INFN-LNF, via E. Fermi, 40 - 00044 Frascati, Rome, Italy
[c]INFN-Milano, Via Celoria 16, 20133 Milan, Italy, [d]ENEA, via E. Fermi, 00044 Frascati, Rome, Italy
[e]Università di Roma "La Sapienza", Dip. Energetica, via A. Scarpa, 14 - 00161, Rome, Italy
[f]UCLA - Dept. of Physics and Astronomy, 405 Hilgard Avenue, Los Angeles, California 90095, USA
[g]INFN-Roma I, p.le A. Moro 5, 00185 Roma, Italy

Abstract

The goal of the first stage of the SPARC commissioning was the optimization of the RF-gun settings that best match the design working point. This entailed detailed study of the emittance compensation process providing the optimal value of emittance at the end of the linac. For this purpose an innovative beam diagnostic, the emittance-meter [1], consisting of a movable emittance measurement system, was conceived and built. More than a simple improvement over conventional, though non-trivial, beam diagnostic tools this device defines a new strategy for the characterization of new high performance photo-injectors. The emittance meter allows measurements at different locations along the beamline of the evolution of important beam parameters both in longitudinal and in the transverse phase spaces. These parameters, which include such as beam sizes, energy spread and rms transverse emittances, are measured in a region where the space-charge effects dominate the electron dynamics. The quality and the quantity of the data allowed a clear reconstruction of the phase space evolution. We report also the first experimental observation of the double emittance minima effect up on which the optimized matching with the SPARC linac is based.

INTRODUCTION

The SPARC [2] project is an R&D photo-injector directed towards production of high brightness electron beam that is able to drive a SASE-FEL experiment. The 150 MeV SPARC photo-injector consists of a 1.6 cell RF gun operated at S-band (2.856 GHz, of the BNL/UCLA/SLAC type) and high-peak field on the cathode incorporated metallic photo-cathode of 120 MV/m [3], generating a 5.6 MeV, 100A (1 nC, 10 ps) beam.

The beam is then focused and matched into 2 SLAC-type accelerating sections, which boost its energy to 150-200 MeV. SPARC is also the prototype of the recently approved SPARX project that foresees the construction of a new high brightness electron linac for producing SASE-FEL radiation with wavelengths in the range of 10-1.5 nm.

The first phase of the SPARC Project has been dedicated to the complete characterization of the beam parameters, at different distances from the photocathode, to find the injector settings optimizing emittance compensation and to make code validation.

The possibility of measure beam parameters at different *z* position (being *z* the longitudinal distance from the cathode) was considered fundamental to allow a complete reconstruction of the evolution of these parameters and to make extensive studies on the beam dynamics.

EMITTANCE-METER

To make measurement in different z positions, a dedicated movable emittance measurement device (emittance-meter) was used. This device allowed measurement of beam parameters in the range from about *z*=1000 mm to *z*=2100 mm.

The technique of measuring the beam emittance and the phase space, in both the horizontal and vertical planes, makes use of a double system of horizontal and vertical slit masks [4].

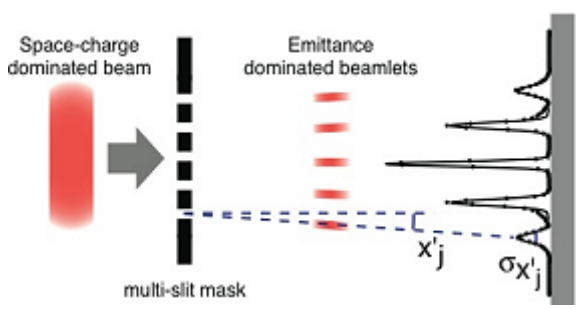

Figure 1: technique

* partially supported by the EU Commission in the FP6 program, Contract No. 011935 EUROFEL-DS1
† cianchi@roma2.infn.it

Selecting an array of beamlets by means of an intercepting multi-slit mask, alternatively creating one beamlet using a single slit moving transverse over the beam spot, reduces the space charge dominated incoming beam into emittance-dominated beamlets that drift up to an intercepting screen(see Fig. 1). If the screen response is linear, the intensity of beamlets spots on the screen are directly proportional to the number of particles in the beamlets which hit the screen. The emittance can be retrieved calculating the second momentum of the beam as reported in [5]. The slits mask must stop, or largely degrade, the intercepted components of the beam , while avoiding excessive slit-scattering effects. A 2 mm thick tungsten is used for the mask.

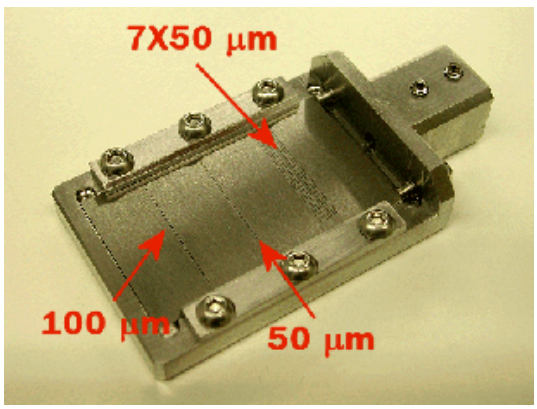

Figure 2: Mask layout

Along the beam trajectory spanned by the emittance meter the beam changes from converging to diverging as it undergoes a space-charge dominated waist. For this reason some flexibility was built into the diagnostic, by using different inter-slit spacing for different conditions.

To this end each mask consists of a slit array(7 slits, 50 μm width spaced of 500 μm, 2 mm thick) and two single slits, 50 and 100 μm width(see Fig. 2). The slits are fabricated by electro-chemical etching, which provides, in comparison to mechanical machining, higher precision and improved smoothness of the slit edges. Each individual slit was machined as a component of 0.5 mm height and later assembled into the frame. This configuration allows the geometry of the slit mask to be changed by simply reorganizing the component pieces.

The multi-slit mask was used for single shot measurements, when the beam size was large enough for an adequate beam sampling by the slit array. Alternatively, a single slit was moved across the beam spot in a multi-shot measurement. In this case the accuracy of transverse sampling can be freely chosen adjusting the step between the different positions of the slit. Typical values of the sampling distance between the slit positions ranges from 110 μm to 380 μm Between nine and thirteen beamlets are collected in the single slit scans. No relevant differences were found between results obtained using single or multislits techniques in cases where comparison was possible. Because the accuracy of the phase space reconstruction is much better with single slit and it further gives also the flexibility of changing the relative distance between the beamlets, it was usually employed.

Linear actuators with stepper motors were used to move the slits masks into the beamline. A differential encoder and a reference end switch guarantees reproducibility and accuracy of the movement to better than 2 μm, as required for single-slit multi-shots measurements.

The beamlets emerging from the slit-mask are measured by means of a downstream Ce:YAG radiator. Because beam size and divergence depend on the device's longitudinal position, the slit to screen distance must be properly adjusted in order to optimize the accuracy of the beamlet profiles measurement. A bellow is therefore placed (see Fig. 3) in between the slit mask and the screen, allowing their relative distance to be changed from 22 to 42 cm, to optimize the drift in order to accomodate several scenarios (converging beam, diverging beam, single or multi-slits).

Radiation emitted in the forward direction from the Ce:YAG crystal is collected by a 45 degrees mirror just downstream of the radiator, and attached to the same screen holder. The back face of the transparent crystal radiator is observed, thus minimizing degradation of the spatial resolution due to the depth of field of the optics. The small thickness of the crystal (100 μm) prevents appreciable blurring effect, due to bulk emission, as well as significant multiple scattering. A calibration grid, with 2 mm wire spacing, is also machined to the same frame holder of the YAG crystal, allowing in situ calibration.

Images are acquired using digital CCD cameras (Basler 311f) equipped with simple 105mm "macro" type objectives from SIGMA. The magnification used of about 0.66 gives a calibration near to 15 μm per pixel and a field of view of the screen around 9.6 X 7.2 mm.

Such cameras offer the advantage that the signal is digitalized directly by on-board electronics so that there is no need for a frame grabber and the output signal, being digital, is less sensitive to environmental noise. The IEEE1394 (Firewire) link allows simpler cabling topology because it carries both pixel readouts and commands to the camera. The Firewire cable from every CCD is connected to a front end industrial PC inside the accelerator tunnel running windows XP.

LabVIEW^{TM} software was used for DAQ and control because of its simplicity in accomodating hardware connections, data acquisition and manipulation. There are drivers available for Firewire interface using LabVIEW^{TM} only under Windows XP. The data are collected by the industrial PC and sent to a central server that is the basis of the SPARC control system [6].

The overall system is similar to the optical diagnostic system that we've realized at FLASH [7], with the extension of the connection topology to all devices in the tunnel hall. The camera system applications software and the configuration files are made available to the camera controllers from a shared network disk hosted by the central server.

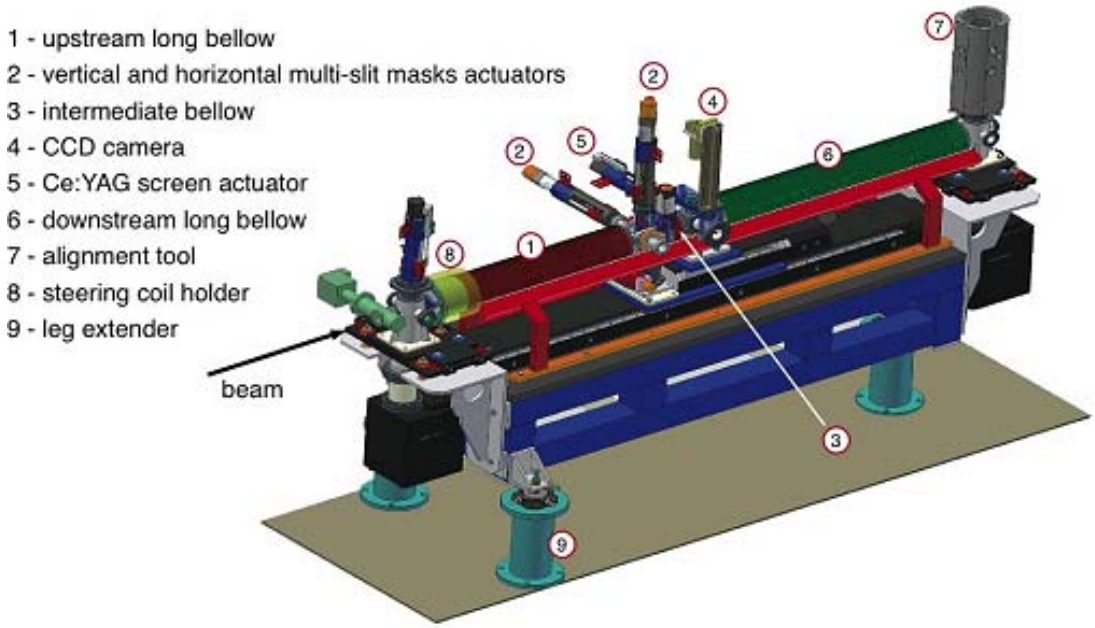

Figure 3: 3D drawings of the emittance meter

This simplifies greatly the installation and maintenance of all hardware devices.

The emittance-meter is followed by a magnetic spectrometer which measures the beam energy and energy spread. The charge is measured by means of ICT placed in the spectrometer area.

The influence on the beam quality of the 1.5 m long bellow has been investigated [8]. Wake field perturbations due to the corrugated structure, especially when beam is not well-aligned on-axis, were studied using HOMDYN code and the wake fields were computed with the diffractive model of Bane and Sands [9]. In the worst case of 1 mm misalignment the contribution of the wakes to the emittance degradation is practically negligible.

RESULTS

In the early runs of SPARC the laser illuminated the photocathode through the 72 degrees view port built in the gun. The results of this run has been already reported in [10] and will not be discussed here. To decrease the laser energy lost in the light transport, and to improve the laser spot transverse uniformity, a simpler scheme using quasi-normal incidence on the photocathode has been adopted.

Beam envelope

The measure of the beam envelope is central finding the position of the beam waist, comparing it to the expected position, and benchmarking the field strength of the solenoid.

The emittance meter allows meaurements of the beam envelope at different z positions by simply moving from one position to other, collecting images and averaging over several shots.

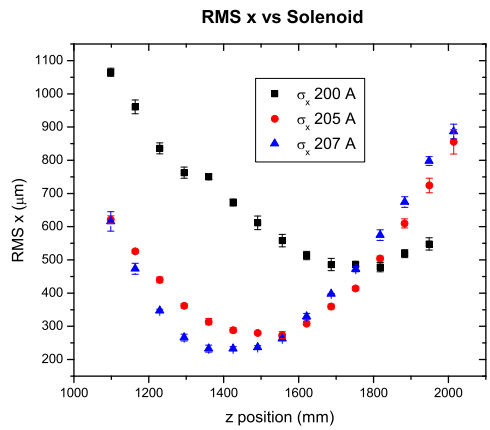

Figure 4: Several rms beam size measurements with different solenoid field

The envelope measurement is a critical input for benchmarking simulations because it provides additional information on the beam dynamics that aid in the reconstruction of the beam evolution.

Emittance

The measurement of the emittance evolution along the photoinjector was the main goal of the diagnostic. Several runs were dedicated to comparison of the dynamics of the beam under different conditions: moving the injection phase, changing the solenoid strength, and varying the longitudinal profile of the laser. Fig. 5 shows a measurement with a flat top longitudinal beam profile, 9 ps FWHM,

with rise time of about 2.5 ps and nominal current of 92A. The solid line is the result of a PARMELA [11] simulation using actual beam parameters, such as laser pulse length, beam size, launch phase and so on.

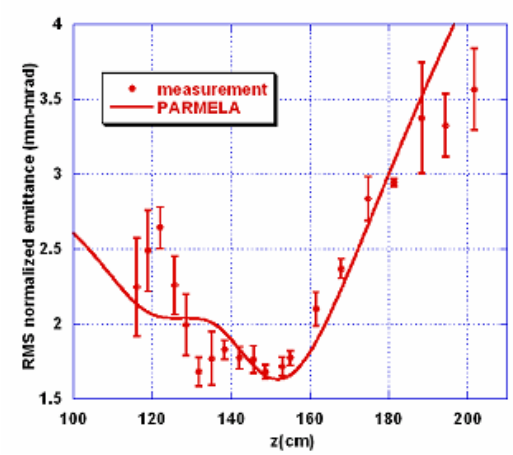

Figure 5: Emittance evolution of high brightness beam. The solid line is a PARMELA simulation

The agreement between the measurements and the simulation is very good. It must be stressed that these are the first experiments ever performed in which the beam emittance evolution in z was measured. Until now, the only possibility was to measure the emittance and the beam size at a fixed position in z. By variation of the beam parameters it was possible to move the solid line in Fig. 5 over the position where the measurements were done. Unfortunately this approach has the disadvantage that the curve doesn't move rigidly, so a certain number of assumption must be made in order to interpret the data and benchmark the experiment with the simulation. With the emittance meter there is a direct measurement of the emittance evolution, and no assumptions are required. Fig. 6 shows the comparison between a flat top longitudinal pulse with 85A current 8.5 ps length, 2.5 ps rise time, and a gaussian beam with the same FWHM length.

The emittance oscillation observed in simulation of the photoinjector is a notable feature of the Ferrario working point [12], the most common emittance compensation design now employed in photoinjectors worldwide. This effect is quite small and is enhanced both by fast laser rise time and high energy spread. We have obtained a direct evidence of this type of double minimum oscillation working with very small laser rise time ($\cong$ 1.5 ps) and moving the phase toward the crest of the RF, even if the minimum achievable value of the emittance is larger in this case.

Phase space

The technique used to measure the emittance allows the phase space sampling. Using a large number of samples (13 moving the single slit over the beam) it's possible to reconstruct the beam transverse phase space and follow its evolution, as shown in Fig. 8.

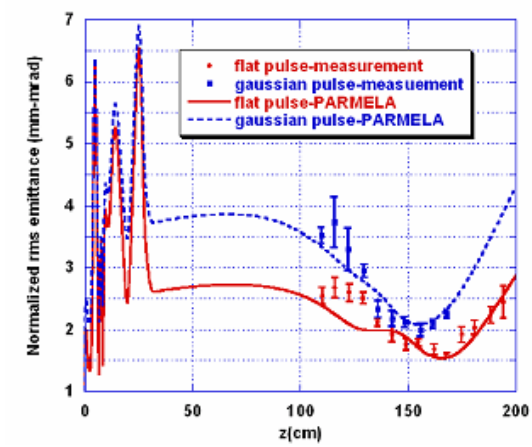

Figure 6: Comparison between the emittance vs z of two different beams: longitudinal flat top with rise time of 2 ps and gaussian profile with the same FWHM of 8.5 ps.

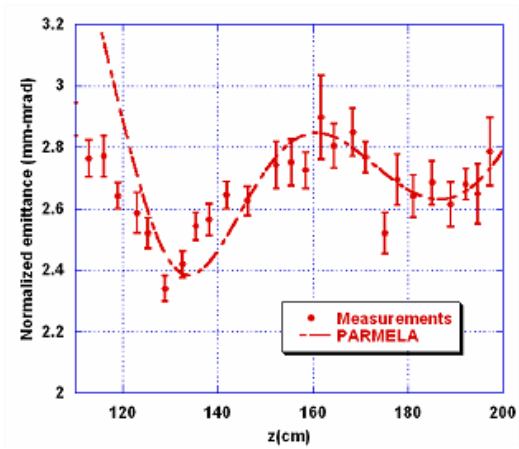

Figure 7: The first direct evidence of a double minimum oscillation of the emittance in a photoinjector

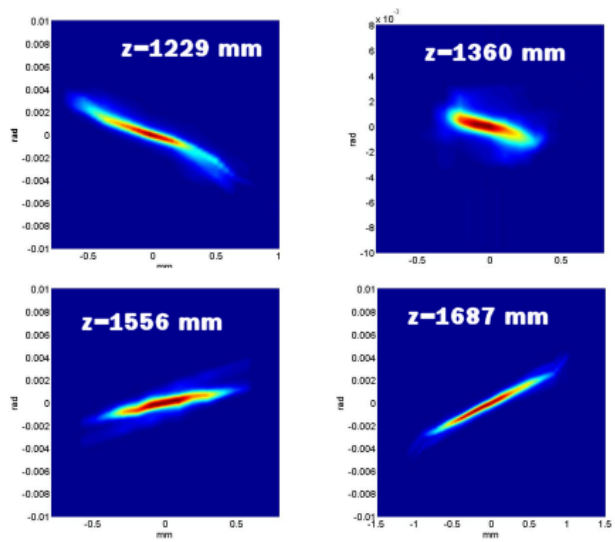

Figure 8: Reconstructed phase space for different z position

In addition to being a visual aid in understanding the beam dynamics, the phase space contains valuable information. A new algorithm has been developed to calculate the value of the emittance using the phase space data. The agreement with a traditional algorithm starting from the beamlets images [13] is excellent [14].

Energy spread

After the tungsten mask the emerging beamlets are not longer space charge dominated. The contribution of the space charge to the energy spread is also frozen.

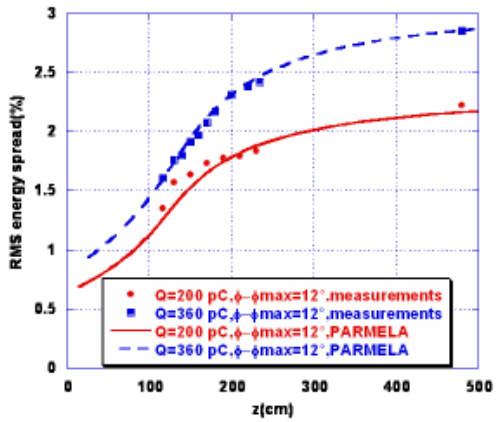

Figure 9: Energy spread vs z for two different bunch current

In Fig. 9 a measure of the energy spread obtained by collimating the beam with one slit at different z positions for two different current, along with the preditions of PARMELA simulations. Because in the fit model there is no contribution from the long emittance meter bellows, it was possible to confirm that the effect of the bellows is negligible. Also this gives information on the longitudinal phase space of the beam.

CONCLUSIONS

The SPARC emittance meter gives the possibility of measuring the beam parameters at different distances from the cathode, giving information on the transverse and longitudinal phase spaces. Improvement in the laser parameters, changes in the solenoids field, and modifications in the solenoid alignment can be easily and quickly checked. Also the possibility of having several measurements along the beam line gives a better understanding of the dynamics and a more direct comparison with the simulations. The agreement between the measurement and the simulations is excellent, due to the large number of the samples taken, as well as to the cross check provided by the envelope measurement. The high sampling rate of the phase space also allows running tools directly on it to evaluate the value of the emittance.

Finally, we note that the measurement of the double minimum in the emittance oscillation provides a direct validation of the theory behind the choice of the Ferrario's working point.

Acknowledgment

The authors wish to thank all SPARC collaboration scientists and engineers who contributed to the design and commissioning of the emittance meter. Special thanks to V. Lollo for his contribution to the system mechanical design, engineering, and bench testing, F. Anelli and S. Fioravanti for their work on motor controllers. Also thanks to A. Battisti, L. Antonio and S. Stabioli

This work has been partially supported by the EU Commission in the sixth framework program, Contract No. 011935 EUROFEL-DS1.

REFERENCES

[1] L. Catani et al."'Design and characterization of a movable emittance meter for low-energy electron beams"',Review of Scientific Instruments 77, 093301 2006

[2] D. Alesini et al., Nucl. Instr. & Meth. In Phys. Res. A 507 (2003) 345-349C

[3] J.B. Rosenzweig, A.M. Cook, M.P. Dunning, P. Frigola, G. Travish, C. Sanelli, F. Tazzioli, D.T. Palmer,'RF and magnetic measurements on the SPARC photoinjector and solenoid at UCLA', Proceedings of the PAC 2005,Knoxville (USA), pag 2624 - 2626

[4] S.G. Anderson, J.B. Rosenzweig, G. P. Le Sage, J.K. Crane, Space-charge effects in high brightness electron beam emittance measurements, Phys. Rev. ST Accel Beams 5, 014201 (2001)

[5] Claude Lejeune and Jean Aubert, Adv. Electron. Electron Phys., Suppl. 13A, 159 (1980).

[6] M. Bellaveglia et. al "'SPARC control system"' Proceedings of PCAPAC2005, Hayama,Japan

[7] L. Catani, A. Cianchi, G. Di Pirro,K. Honkavaara "A large distributed digital camera system for accelerator beam diagnostics",Review of Scientific Instruments 76, 073303 (2005)

[8] V. Fusco et al., "Wake Fields Effects in the Photoinjector of the SPARC Project", Proceedings of EPAC2004, Lucerne, Switzerland pag.405

[9] K. Bane, M. Sands, SLAC-Pub-4441

[10] A. Cianchi et al.,"Characteriztion of the SPARC Photo-injector movable emittance meter",Procceding of EPAC2006,Edinburgh, Scotland (2006), pag 3523

[11] L. M. Young, PARMELA, Los Alamos National Laboratory report LA-UR-96-1835

[12] M. Ferrario, J. E. Clendenin, D. T. Palmer, J. B. Rosenzweig, L. Serafini,"Homdyn study for the LCLS RF photoinjector",SLAC-PUB 8400

[13] D. Filippeto et al "Robust alghoritm for slit emittance measurement", SPARC-note to pe published

[14] A.Cianchi et al. "Accurate emittance calculation from phase space analysis", SPARC-note to be published

DESIGN OF AN ELECTRON BEAM ENERGY CONTROL LOOP USING TRANSVERSE DISPERSION

M. Justus, U. Lehnert, P. Michel, Research Centre Dresden-Rossendorf, Germany
P. Evtushenko, Jefferson Lab, Newport News, Virginia, USA

Abstract

Stability in mean electron beam energy is of highest interest for a number of experiments performed at the ELBE accelerator. Energy drifts affect parameters of the generated Bremsstrahlung spectra, X-rays or infrared light, as well as the beam trajectory at the production targets or through the FEL waveguide, respectively.

In practise, we observe a slow drifting of the effective accelerating field during the first hours after a machine power-up or after switching to different nominal beam energies. Initially, this effect was compensated manually. A first order automation solution has been developed that corrects the resulting energy drift continuously, using a non-intrusive beam position monitor placed in a transversely dispersive part of the beam guide.

This paper describes the beam line setup and the simplified dynamic model of the control loop derived from it. Calculation of controller parameters using standard a standard method is shown. The user interface of the control system and working conditions for the loop are explained. Operational performance and conclusions towards improvements close this contribution.

ENERGY DRIFT OF THE ELBE ACCELERATOR

In fig. 1 the observable drift in fed forward and reflected RF power and thus in beam energy is shown exemplarily. A second order delay behaviour was found to fit the data best using time constants of 30 min and 25 min. The usual method to compensate for this was to adjust the RF gradient value of the last accelerating module ten-minute-wise, until the thermal drift behaviour settles. To indicate a change in energy, a λ/4 strip line beam position monitor (BPM, [1]) placed in a dispersive part of the beam guide, was observed. Intuitively, the first order solution is to perform this correction automatically by a continuous control loop.

THE CONTROL LOOP

System identification

In fig. 2, the elements building the control loop are displayed exemplarily for the Bremsstrahlung beam line of ELBE, where photo activation experiments are most sensitive to the beam energy. The transfer function F_S of the controlled system is the product of:

- the TESLA cavity with a length of 1000 mm

$$F_C = \frac{\partial E_{El}\,/_{MeV}}{\partial G_C\,/_{(MV/m)}} = \cos\varphi\,, \qquad (1a)$$

- the bending magnet

$$F_D = \frac{\partial x_1}{\partial E_{El}} = \frac{D_D}{E_{nom}}\,, \qquad (1b)$$

- the drift space

$$F_{Dr} = \frac{\partial x_2}{\partial x_1} = 1 + \frac{D'_D}{D_D}\cdot L_{Dr}\,, \qquad (1c)$$

- the beam position monitor

$$F_{BPM} = \frac{\partial x_2^*}{\partial x_2} = \frac{1}{1 + pT_\Sigma}\,, \qquad (1d)$$

- a low pass filter in the PLC algorithm

$$F_F = \frac{1}{1 + pT_F} \quad \text{with } T_F = 30s\,. \qquad (1e)$$

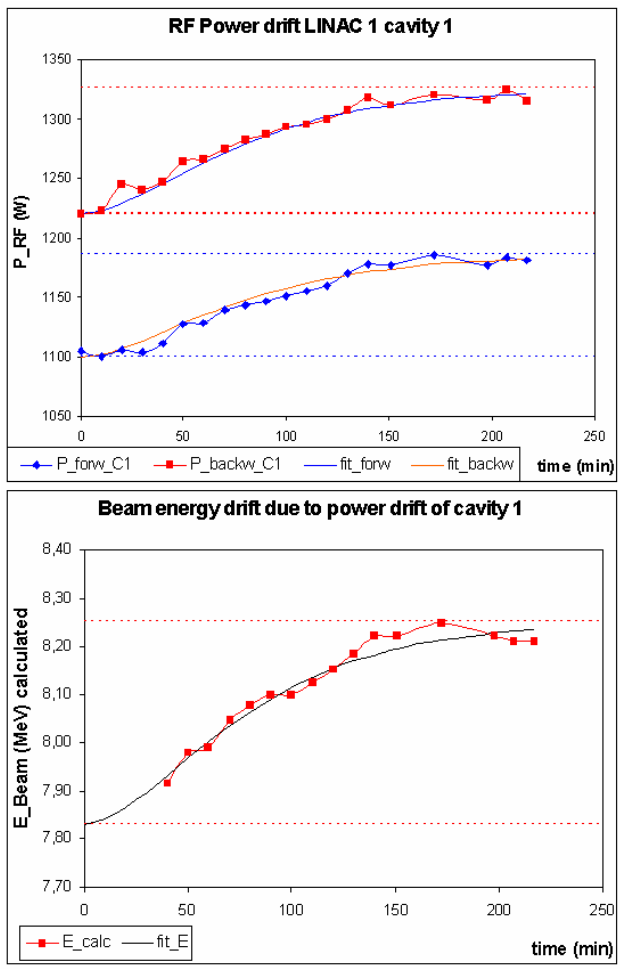

Figure 1a: RF power and mean beam energy drift after start up of the accelerator. (G_{C1} = 10 MV/m, $G_{C2} \approx 0$, E_{nom} = 8 MeV)

Have a look at fig. 3 for the corresponding control loop model. The notations used above are:

φ	RF phase
G_C	RF gradient
x_1, x_2	transverse displacement (horizontal)
D_D	dispersion
E_{nom}	nominal beam energy
D'_D/D_D	horizontal momentum (angul. notation)
L_{Dr}	length of drift space
T_F	filter time constant

Equation (1a) implies the transit time factor of cavity 2 to be unity. The dispersion is a geometric attribute of the dipole and is not derived here in detail. This may be studied with appropriate literature on particle beam optics [i.e. 3, 4]. The delay time T_Σ in equation (1d) is the so called "accumulated delay time" [5], representing all response times of the BPM RF signal transmission, data acquisition and transfer of the BPM results to the PLC (programmable logic control). It was found experimentally to be ≈ 0.3 s. The filter is designed as to eliminate higher frequency parts of the BPM signal, which are small deviations of beam deflection and energy, as well as measurement noise. They may result from local charging up effects in the injector section or RF system modulations and are not handled by this control loop.

Controller Design

Using general rules of structural design for linear control loops [5] a PI controller is used that compensates for the large delay time T_F of the system:

$$F_R = \frac{1+pT_F}{pT_I} = P + \frac{1}{pT_I} \qquad (2)$$

For the resulting second order control loop, the necessary damping D can be calculated by selecting a certain overshoot h_+ that has to be inserted as a percentage:

$$D = \frac{1}{\sqrt{1+\left(\pi/(\ln h_+)\right)^2}} \qquad (3)$$

The open loop transfer function $F_0(j\omega)$ in frequency domain is calculated by developing $F_0=F_R*F_S$ towards

$$F_0(j\omega) = \frac{V_S}{j\omega_0 T_I (1+j\omega T_\Sigma)} \qquad (4a)$$

Equating with

$$F_0(j\omega) = \frac{\omega_0^2}{(j\omega)^2 + 2D\omega_0 \cdot j\omega} \qquad (4b)$$

and using

$$\omega_0 = \frac{1}{2DT_\Sigma} \text{ and } T_I = \frac{V_S}{\omega_0^2 T_\Sigma}, \qquad (5)$$

one can calculate the integration time and the gain of the controller. Here, ω_0 is the eigen frequency of the open loop. This generalized derivation for the controller parameters has been used to meet any ratio of T_F and T_Σ, i.e. if the filter time is modified or one faces data transmission delays other than expected.

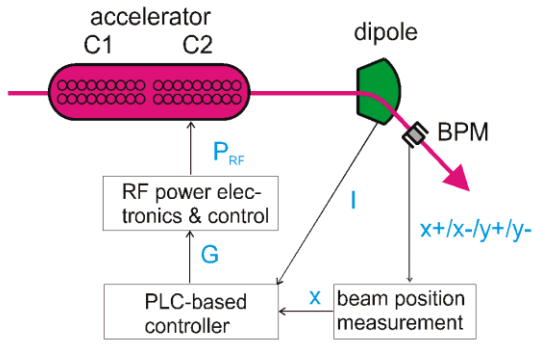

Figure 2: Scheme of the energy stabilization system. (C1, C2: Tesla cavities)

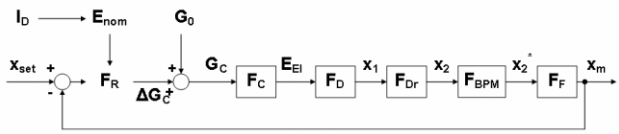

Figure 3: Control loop scheme.

SOFTWARE IMPLEMENTATION

ELBE is run using commercial PLC and visualization technology by Siemens [2]. For implementation into this environment, a standard function block for de facto continuous PI(D) control is used. In every iteration step (period of 500 ms), the required controller parameters are calculated according to the above standing rules from machine parameters. The filter is a simple discrete delay element using the backwards differentiation method with a period of 50 ms. The controller is adaptive in terms of the dependence of the system gain from the nominal energy, which is calculated from the current set value I_D and the design value $(\Delta I/\Delta E)_D$ of the dipole for the nominal deflection radius:

$$E_{nom} = \frac{I_D + I_0}{(\Delta I/\Delta E)_D} \qquad (6)$$

Further, a user interface was created for the operating personnel, allowing full control of the loop parameters. The operator can check whether the running conditions are fulfilled (beam is on, the appropriate beam line is selected, a minimum macro bunch length and current are given and pre-alignment has been done). These are switch-off conditions as well, triggering appropriate error messages. When the controller is activated, the actual gradient set value is stored as controller output offset, controller parameters are initialized, and the input due value is set to zero or to the actual BPM reading, respectively. The direct input options for all beam line elements determining beam current, energy or trajectory are restricted.

VERIFICATION

Fig. 4 shows the operation of the control loop over a timescale of 5 hours in the nuclear physics beam line. Over the first 30 minutes of the plot, the machine was set up manually. One can see that from the moment of switching on, the BPM reading stays on a constant base line (curve BPM-X). The remaining higher frequent part of the signal is in the order of +/- 25 µm, corresponding to a value for $\partial E/E_{nom}$ = $2.4 \cdot 10^{-4}$, if this was pure energy modulation. The gradient set value decreases slowly, reflecting thus partly the exponential drift behaviour of the cavities depicted before (curve GRAD_C2).

To check the step responses of the loop, the parameters were varied in different ways (see fig. 5). Attention was paid here on minimizing the overshoot of the gradient set value, which has not been discussed so far. As a result, optimum P values were found be off the calculated values by a factors of 2 to 3. The reason for that is first seen in adding up of errors in the system identification and in beam misalignment (i.e. off-center passing of a quadrupole, yielding unknown deflections). Further, a couple of assumptions had been made, like zero horizontal displacement and momentum of the beam when entering the dipole, as well as on crest operation of the cavity and the experimentally obtained delay time.

CONCLUSION AND LOOK-OUT

Drawing a line, we can state that the method is working properly and as expected and is definitely an upgrade in beam quality and operability for long term experiments requiring higher mean energy stability. Looking at the reproducibility of any aimed time behaviour, there have to be improvements in the future, although the robustness of the loop is fitting our needs. One could develop a more detailed model of the system, containing the disturbing element, but measures taken will be rather a self tuning algorithm for the controller, combined with active horizontal position control and high resolution field measurement, being thus an absolute energy measurement. The necessary technologies are partly already applied at ELBE (NMR measurement). In case of FEL operation, users are rather interested in the infrared wavelength than in the energy, so the intention is to use continuous spectrometry as input for the control loop instead of dispersion.

Figure 5: Optimizing the controller.
(due value with added step function)

REFERENCES

[1] P. Evtushenko "Electron Beam Diagnostics at the Radiation Source ELBE", 10th Beam Instrumentation Workshop, Brookhaven National Laboratory, Upton, NY, May 6 - 9, 2002

[2] SIMATIC Automation Systems, Siemens AG, Munich http://www.siemens.com/simatic

[3] K. Wille "Physik der Teilchenbeschleuniger und Synchrotronstrahlungsquellen", B.G. Teubner, Stuttgart, 1996

[4] J. Rossbach, P. Schmüser „Basic course on accelerator optics", Proceedings of the CAS 5th General accelerator physics course, CAS 94-01 Vol.1, Geneva, 1994

[5] H. Lutz, W. Wendt "Taschenbuch der Regelungstechnik", Verlag Harri Deutsch, Frankfurt a. M., 2002

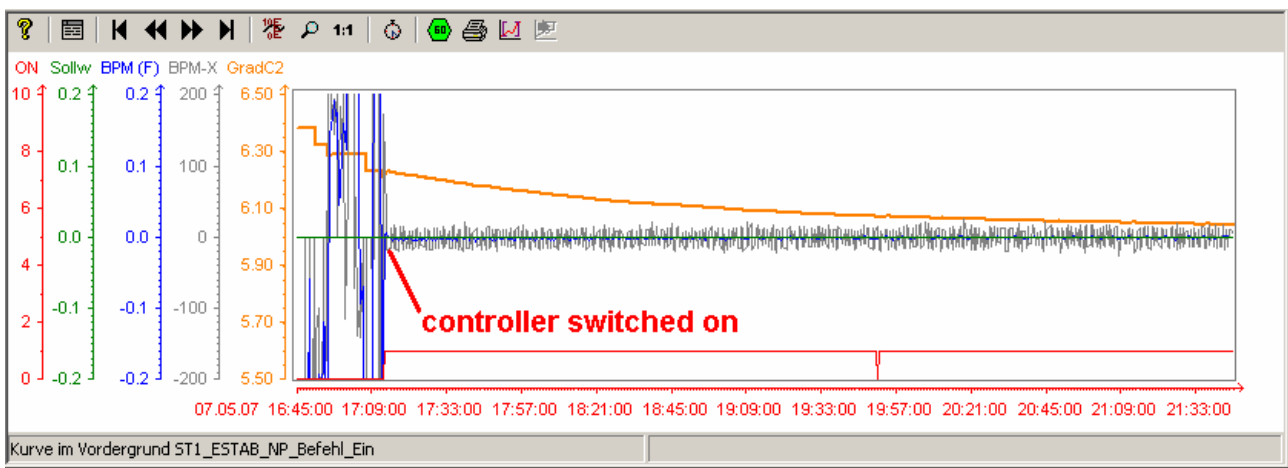

Figure 4: Operation of the energy control loop at E_{nom} = 14.5MeV, G_{C1} = 10 MV/m, I_{Beam} = 450µA in cw mode.
("ON": controller on state, "Sollw": BPM due value, "BPM(F)": BPM reading filtered with 30 sec,
"BPM-X": BPM reading, "GRAD_C2": gradient set value for cavity 2 (controller output).

DESIGN OF AN INTRA-BUNCH-TRAIN FEEDBACK SYSTEM FOR THE EUROPEAN X-RAY FEL

B. Keil, G. Behrmann, M. Dehler, R. Kramert, G. Marinkovic, P. Pollet, M. Roggli, M. Rohrer, T. Schilcher, V. Schlott, D. Treyer, PSI, Villigen, Switzerland*
J. Lund-Nielsen, D. Noelle, M. Siemens, S. Vilcins, DESY, Hamburg, Germany

Abstract

After joining the preparatory phase of the European X-ray FEL project, the Paul Scherrer Institute agreed in taking over responsibility for electron beam stabilization by developing a fast intra-bunch-train feedback (IBFB) system, which will be tested in its prototype version at the FLASH linac of the collaboration partner DESY. The proposed IBFB topology consists of two beam position monitors ("upstream BPMs") followed by two kicker magnets for each transverse plane and two more BPMs ("downstream BPMs"). By measuring the position of each bunch at the upstream BPMs and applying suitable transverse kicks individually to the following bunches, the architecture of the FPGA-based digital IBFB electronics (with a latency preferably below the bunch spacing of 200 ns and 1000 ns for the XFEL and FLASH) allows to damp beam motions up to hundreds of kHz. In addition to the FPGA-based feedback, DSPs enable adaptive feed-forward correction of repetitive beam motions as well as feedback parameter optimization using the downstream BPMs. This paper gives an overview of the architecture and status of the IBFB subsystems being developed, like stripline BPMs, digital electronics, and kicker magnets.

INTRODUCTION

In order to guarantee the stable SASE operation of the European X-ray FEL (XFEL) at its 1 Å target wavelength, the 1 nC 20 GeV electron beam of the XFEL main linac requires a transverse RMS position stability in the order of 10% of the ~30 µm beam size σ in the undulators [1]. In contrast to other proposed linac-based FELs that use single bunches with repetition rates in the order of 100 Hz, the XFEL will have bunch trains of up to 3250 bunches and 200 ns bunch spacing at 10 Hz repetition rate.

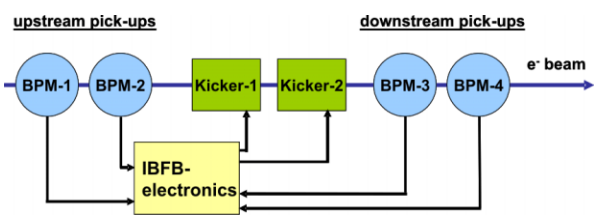

Figure 1: Proposed IBFB Topology.

When installed behind the main linac, the measurement and correction the of transverse position in both planes on a bunch-by-bunch basis would allow the proposed IBFB system [2] to damp harmful beam position perturbations up to frequencies of some 100 kHz that may originate from noise sources like cooling water and helium flow, ground motions, power supply jitter, switching magnets, RF transients and jitter, photo-cathode laser jitter and related beam current variations as well as long range wakefields. Table 1 contains a summary of the IBFB specifications for the prototype system to be tested at FLASH as well as for the final system for the XFEL. The following sections give summaries of the design and status of the different IBFB subsystems.

Table 1: Transverse IBFB Specifications

Transv. IBFB Specifications	**FLASH**	**XFEL**
bunch-by-bunch stability - at location of IBFB - along undulators	< σ/10 5 - 15 µm < 5 µm	< σ/10 3 - 10 µm < 3 µm
max. beam position offset - at location of the pick-ups	< 10 · σ < 1.5 mm	< 10 · σ < 1 mm
bunch-by-bunch resolution	≤ 2 µm	≤ 1 µm
system latency	< 1000 ns	< 200 ns

RESONANT STRIPLINE BPM

The IBFB needs a BPM pickup that generates a signal which is short compared to the desired IBFB latency of about 200 ns, and that is also large enough to be safely above the electronics noise level limits for the desired resolution of 1-2 µm. Therefore a novel resonant stripline pickup was developed in a collaboration of PSI (concept [4] and electromagnetic design) and DESY (mechanical construction and UHV/dust-free compliant production). So far one pickup was installed at the DESY flash facility and three in the SLS booster that has a bunch charge and repetition rate similar to FLASH (up to 1 nC, 1 µs) but provides more space, which allowed to install three pickups in a single straight section for beam-based noise correlation measurements.

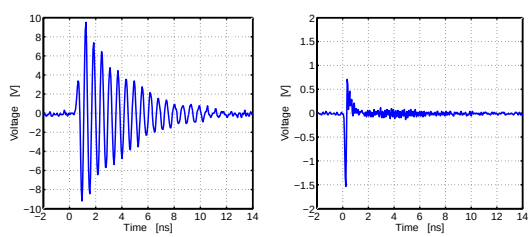

Figure 2: Comparison of beam induced signal at resonant stripline pick-up (left) and button pickup (right).

*Work supported by Swiss State Secretariat for Education and Research SER

Fig. 2 shows the low-pass filtered signal of a resonant stripline pickup at the SLS booster for ~0.5 nC bunch charge. Compared to typical button and non-resonant stripline pickups, the usable signal level and energy content is much larger, with only ~10 ns decay time.

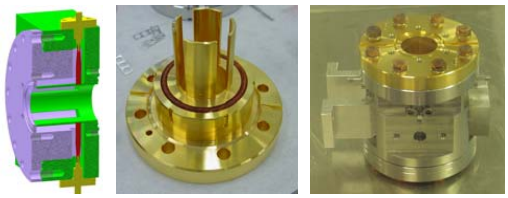

Figure 3: Resonant Stripline BPM Pickup.

Measurements with a BPM test bench consisting of 2D motorized stages and a 50 ohms matched inner conductor built at PSI as well as measurements performed at DESY allowed to identify and optimize critical points of the design. Following the original prototype, a refined version has been built, which will be used for the IBFB prototype system. The frequencies of monopole (1.615 GHz), dipole (1.653 GHz) and quadrupole (1.677 GHz) modes as well as internal and external Q factors obtained from measurements for the optimized design are in good agreement with theoretical predictions.

CAVITY BPM

In addition to the resonant stripline that will be used as "workhorse" BPM for first tests of the IBFB at FLASH, a cavity BPM was designed and built at PSI [2] in collaboration with a company in order to study the feasibility of ultra-high resolution BPMs for the final XFEL IBFB. The BPM consists of a 4.3896 GHz monopole cavity to be used as a beam current reference and a 4.3875 GHz dipole cavity where the TM11 mode couples to external waveguides where it is extracted using capacitively coupled SMA feedthroughs for position measurement while the TM01 mode coupling is suppressed. The dipole cavity was recently delivered to PSI and is ready for tests on the BPM test bench.

RF FRONT-END

Fig. 4 shows the proposed architecture of the RF front-end (RFFE) for the resonant stripline BPM for one transverse plane. The signals of opposite pickup electrodes are filtered, and a 180° hybrid separates the monopole mode signal (Σ) that is proportional to the beam current from the dipole mode signal (Δ) that is proportional to the beam position times the current. The resulting signals pass variable gain amplifiers and are then mixed down to DC using tunable PLLs that use a machine reference clock to synthesize the desired frequencies. The mixed signals are filtered, and the resulting pulses of about 15 ns length are available at the RFFE outputs for digitization. In order to achieve optimal separation of strong monopole and weak dipole mode (-75 dBc for 1 µm), amplitude and phase tuners in front of the hybrid will be periodically adjusted during the time in between two bunch trains using a sinusoidal pilot signal that is coupled into the complete signal chain. See Ref. [2] for further details. So far most parts of the modular RFFE design have been fabricated. At present different input filter designs for the RFFE are being characterized and compared to simulations, with signals of the three pickups recently installed in the SLS booster allowing to find an optimal compromise between monopole signal suppression, filter latency, insensitivity to component tolerances, and effort for calibration and tuning.

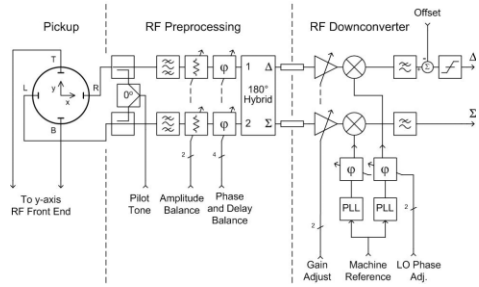

Figure 4: Proposed BPM RF front end (x-axis only).

DIGITAL ELECTRONICS AND CORRECTION ALGORITHM

Fig. 5 shows the architecture of the PSI DSP Carrier (PDC) board, a VME/VXS board that is being developed at PSI to serve as data processing back-end for the IBFB. The PDC is based on the PSI "VPC" board [3], but uses two high-performance TS201 "TigerSHARC" DSPs instead of one low-cost DSP, four Virtex-4 instead of two Virtex-2 Pro FPGAs, 100 times more RAM, multi-gigabit LVDS mezzanine connectors instead of PMC connectors, and the VXS standard for multi-gigabit communication between PDCs via the VME/VXS crate backplane. For the IBFB the PDC will be equipped with two mezzanine modules that are being developed. Each contains four 12-bit 500 Msps ADCs with 4.5 samples latency that are used to digitize the ~15ns long Σ and Δ pulses of two RFFEs, and two 14-bit DACs with max. 1 Gsps sample rate and 18 samples latency to drive the kicker magnet amplifiers.

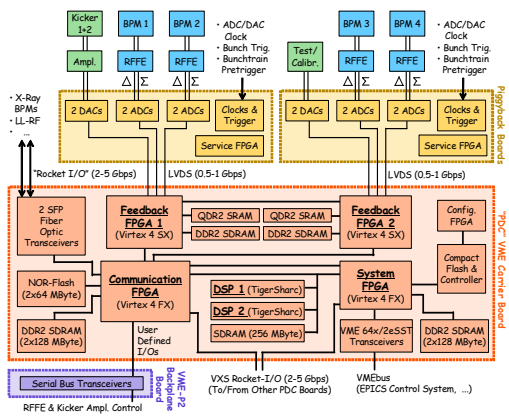

Figure 5: IBFB digital signal processing hardware architecture: PDC board with ADC/DAC mezzanines.

ADCs and DACs of each mezzanine are connected to Virtex-4 SX "Feedback" FPGAs on the PDC (one FPGA per mezzanine). These FPGAs calculate the beam positions and kick amplitudes using an FIR-based

feedback algorithm that predicts the kick necessary to correct the position of bunch no. N from the positions of bunches N-1, N-2, N-3 etc. Only the upstream BPM data is used to predict these kicks (using a beam optics model), since the maximum latency allowed for the electronics using the upstream BPMs is 200 ns minus the *difference* of cable delays and electron flight time from BPM1 to kicker 2 (see Fig. 1), while the latency budget when using the downstream BPMs would be 200 ns minus the *sum* of the cable delay BPM4-kicker1 and flight time kicker1-BPM4 (since the cable signal and electrons travel in opposite directions). However, the downstream BPM data will be used to check and automatically correct and optimize the model used for the calculation of the kicks.

In addition to a bunch-by-bunch feedback, the two TS201 DSPs on the PDC board will perform an adaptive feed-forward algorithm to correct beam motions that are the same from bunch train to bunch train. The DSPs will calculate lookup tables for beam positions to be subtracted and kicks to be added by the Feedback FPGA (see Fig. 6) for each bunch, so that the actual feedback algorithm just needs to correct non-repetitive beam motions that are different from bunch train to bunch train.

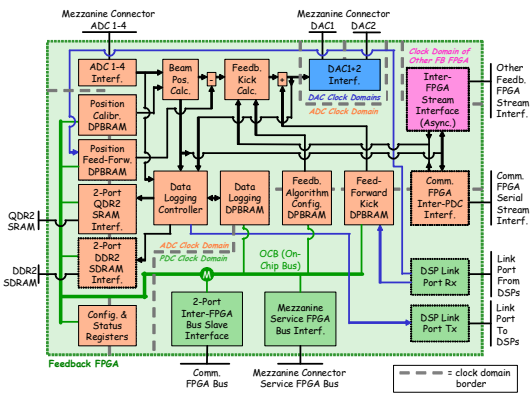

Figure 6: Firmware architecture of the Virtex4-SX "Feedback" FPGA on the PDC board.

The PDC board can be used in two possible configurations: a) one PDC handles all four RFFEs and two kickers for one plane, another PDC handles the other plane, or b) one PDC handles all RFFEs of the upstream BPMs and all kickers for both planes, and another PDC handles the downstream BPMs for both planes. Data exchange between two PDCs or between PDCs and other accelerator subsystems is possible using multi-gigabit links on the PDC front-panel (SFP) or on the VME/VXS backplane. Since these links have latencies in the order of 100-300 ns (depending on baud rate and protocol used), the above mentioned configuration a) will only be used if the coupling between both planes is so small that it does not have to be accounted for on a bunch-by-bunch basis (e.g. by rotating hor./vert. position vectors), since the position data cannot be transmitted from one PDC to the other fast enough (for the XFEL). Configuration b) allows to use the data of both planes of all upstream BPMs to calculate the kicks for each of the four kickers by using low-latency links between the two Feedback FPGAs on the same PDC, at the expense of longer latency for the downstream BPM data transfer via gigabit links.

The PDC schematics, mechanical design and PCB component placement is finished and the layout (~22 layers) is in progress. First prototype tests of PDC and mezzanine are scheduled for autumn 2007. Apart from the IBFB, the PDC could also be used e.g. for multibunch feedbacks or global orbit feedbacks in storage rings.

KICKER DESIGN

The beam position corrections for the IBFB will be applied by two kicker magnets for each plane. Fig. 7 shows a stripline kicker designed at PSI that will be built until end 2007 and installed for tests of the IBFB at FLASH in 2008. The stripline shape matches the beam pipe diameter of 34 mm. Fig. 8 a) shows the computed S parameters of the structure. The kicker bandwidth (green curve, x=50 MHz/div., y=10dB/div., scale=-70...0 dB) exceeds the desired value of 50 MHz. Reflections (red curve) are below -25 dB, which is excellent. In Fig. 8 b), we see the deflecting electrical field in the stripline center vs. frequency (x=100 MHz/div., y=200V/div., scale=0...800V). The resulting correction kick is expected to be 16 µrad at 1 GeV using 25 kW input power per port.

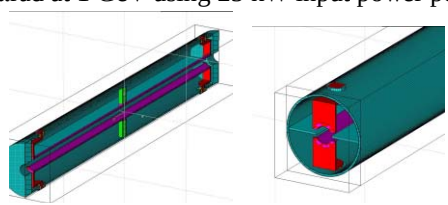

Figure 7: 3D views of vertical IBFB stripline kicker.

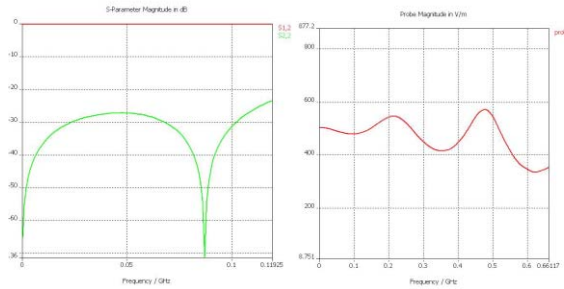

Figure 8: a) Simulated S-parameters (left side) and b) transverse electrical field strength of IBFB stripline kicker (right side).

REFERENCES

[1] W. Decking, X-FEL Project Team, private comm.
[2] V. Schlott et al., "Intra Bunch Train Feedback System for the European X-FEL", Proc. EPAC´06, Edinburgh, Scotland, June 2006, p. 3017.
[3] B. Keil et al., "The PSI VPC Board - First Applications of a Common Digital Back-End for Electron and Proton Beam Instrumentation at PSI", Proc. DIPAC´05, Lyon, France, June 2005, p. 140.
[4] M. Dehler, "Resonant Stripline BPM for Ultra Low Current Measurement", Proc. DIPAC´05, Lyon, France, June 2005, p. 284.

FEMTOSECOND Yb-DOPED FIBER LASER SYSTEM AT 1 μm OF WAVELENGTH WITH 100-nm BANDWIDTH AND VARIABLE PULSE STRUCTURE FOR ACCELERATOR DIAGNOSTICS

Axel Winter, Universität Hamburg, Hamburg, Germany,
F. Ömer Ilday, Bilkent University, Ankara, Turkey
B. Steffen, DESY Hamburg, Germany

Abstract

Laser-based diagnostic systems play an increasingly important role in accelerator diagnostics in, for instance, electron bunch length measurements. To date, the laser system of choice for electro-optic experiments has been the Ti:sapphire laser, providing several nanojoules of pulse energies at fixed a repetition rate, which is not well suited to the bunch structure of accelerator facilities such as FLASH. Limited long-term stability and operability of Ti:sapphire systems are significant drawbacks for a continuously running measurement system requiring minimal maintenance and maximum uptime. We propose fiber lasers as a promising alternative with significant advantages. Gating of the pulse train to match the bunch profile is simple with fiber-coupled modulators, in contrast to bulk modulators needed for Ti:sapphire lasers. An in-line fiber amplifier can boost the power, such that a constant pulse energy is maintained regardless of the chosen pulse pattern. Significantly, these lasers offer excellent robustness at a fraction of the cost of a Ti:sapphire laser and occupy a fraction of the optical table space.

INTRODUCTION

There is much progress and scientific excitement on new light sources, which will provide higher brightness and shorter temporal structures, with promise for broad impact in a large number of disciplines, from condensed matter physics and nanotechnology, to materials science and biology. Among the emerging key requirements, is to determine the electron bunch length and temporal structure for free electron laser based machines, such as FLASH to ensure best possible lasing performance. Various optical techniques based on electro-optic effects have been implemented and these methods have delivered promising results as non-invasive means to characterize the electron bunch structure [1, 2].

However, none of these diagnostic methods have yet evolved into a routine tool. One of the leading reasons is the complexity, limited robustness and flexibility of the laser systems in use. Most commonly, the laser of choice is the Ti:sapphire laser. Although these laser oscillators offer the best performance in some aspects (such as the pulse duration and spectral bandwidth), they have significant shortcomings in other aspects of significance for these applications. The repetition rate is fixed and most commonly set to a value between 70 and 120 MHz, with pulse energies of ~ 5 nJ. If more energy is required, an amplified Ti:sapphire system has to be used, which in turn is limited to a kHz-level repetition rate. Such a laser system is a vastly more complicated tool and occupies nearly an entire optical table. In terms of the repetition rate, neither the laser oscillator nor the amplified system are particularly suited for free-electron laser or synchrotron based light sources: A superconducting machine such as FLASH, requires a repetition rate of 1 MHz if every pulse in the bunch is to be sampled. The bunch pattern typically consists of hundreds of pulses with 1 MHz spacing, with the overall pattern being repeated at 1-5 Hz. Gating of the pulse train of a Ti:sapphire laser is possible with electro-optic modulators, but these modulators are lossy, require high voltages to operate and need to be precisely aligned with respect to the laser beam to maintain a contrast ratio of ~ 25 dB. Subsequent amplification, to restore the pulse energy, requires the addition of an amplifier, which is a major modification of the experimental setup.

Mode-locked fiber laser systems present a promising alternative, as the pulse pattern can be engineered to match the machine requirements through gating and subsequent amplification. Even plain laboratory-constructed fiber lasers without professional packaging have been shown to work without interruption for several months and longer. Rapid progress has been made with Yb-fiber laser oscillators operating at 1 μm in the past few years. A new mode-locking regime exploiting self-similar pulse propagation has been demonstrated [3] and these lasers now routinely generate sub-100 fs pulses with over 5 nJ of energy at repetition rates of 30-60 MHz [4]. A suitable harmonic of the repetition rate of the oscillator can be locked to an external reference by modulating a piezo-driven fiber stretcher, which is part of the cavity. Thus, the pulse train produced by the oscillator is synchronized to the facility clock. The pulse train can be gated to produce any desired pattern, thereby matching the electron bunch structure exactly. Both fiber-couped acousto-optic modulators (AOM) and electro-optic modulators (EOM) are available at this wavelength, therefore gating is simple to implement. The on/off contrast ratio for a fiber-coupled AOM is extremely high (at least 50 dB) and in practice limited by the driving electronics. Fiber-coupled EOMs offer the convenience of requiring less than 5 V for switching and the contrast can be as high as 35 dB. Following pulse gating, the re-

duced optical power can be boosted with an in-line fiber amplifier. Small signal gain for a single pas through a fiber amplifier is as high as 30-40 dB, an extraordinarily high value in comparison to typical solid-state laser gain media. Pump light is provided by telecom-grade singlemode fiber-coupled diode lasers, which are low-cost and extremely compact. Thus, subsequent amplification is practical and easy to implement, in sharp contrast to Ti:sapphire amplifiers. In other words, if so desired, the individual pulse energy can be kept the same value, regardless of the particular bunch pattern. Using in-core pumping, up to 1 W of power can easily be generated (corresponding to several 1μJ at 1 MHz repetition rate). Higher power levels (several watts) can also be implemented with double-clad gain fibers and multimode pump diodes. In practice, the biggest challenge is the limitation to peak power and pulse energy set by the strong nonlinear effects that occur in fibers. In this regards, boosting the individual pulse energy up to 100 nJ is relatively easily achieved with a design that optimizes the nonlinear and dispersive effects. This level of pulse energy is sufficient for several of the diagnostic techniques. At the higher end, pulse energies as high as 100μJ have been obtained from fiber amplifiers.

Mode-locking of a fiber laser is initiated by a mechanism (a saturable absorber) providing lower loss (hence, higher net gain) for a pulse than for continuous wave (cw) radiation, leading to pulse formation from intra-cavity noise once the laser reaches a certain intracavity power. Once the pulses are shortened, the laser dynamics are dominated by an interplay of group velocity dispersion (different frequencies have different speeds) and Kerr nonlinearity (the refractive index depends on intensity), leading to the formation of soliton-like pulses, which intrinsically balance dispersion and nonlinearity [5]. As the gain has finite bandwidth, the generated pulses need to be stabilized by the saturable absorber. Thus, at the simplest possible level, short-pulse laser dynamics can be described by four processes: laser gain, saturable absorption, Kerr nonlinearity, and dispersion. In fiber lasers, the fiber assumes multiple roles, providing nonlinear and dispersive effects that dictate the soliton-like pulse shaping mechanism. The Yb-doped fiber segments form the gain medium, pumped conveniently by low-cost, fiber-coupled, 980-nm diode lasers.

MODE-LOCKED YTTERBIUM FIBER LASERS

Our experimental setup is compact, occupying a 30cmx45cm optical board, including the pump lasers, and thus able to fit into a small case (see figure 2). A unidirectional ring cavity (Figure 1) is chosen for self-starting operation. We use a 60 cm-long, highly doped Yb fiber (N.A., 0.12; core diameter, 6 μm). The Yb fiber is pumped at 980 nm by a laser diode with a maximum power of 500 mW coupled into single-mode fiber. The pump light is delivered to the gain fiber by a wavelength-division multiplexing coupler. A pair of diffraction gratings compensate for the normal group velocity dispersion (GVD) of the fiber. Mode-locked operation is initiated and stabilized by nonlinear polarization rotation, which is implemented with in-line polarization controllers (alternatively, bulk waveplates can be used). Following the gratings, the pulse is coupled back into fiber, where it traverses approximately 2 m of single-mode fiber, which is wrapped around a piezo material, acting as a fiber stretcher, before reaching the Yb-fiber, completing the cavity loop. The total lengths of the fiber and free-space sections of the cavity are adjusted such that the repetition rate (54 MHz) is an exact sub-harmonic (24^{th}) of the reference frequency (1300 MHz) for the FLASH facility. The output is taken directly from the polarization ejection port, placed immediately after the fiber section and prior to the gratings. A schematic of the laser is shown in Figure 1.

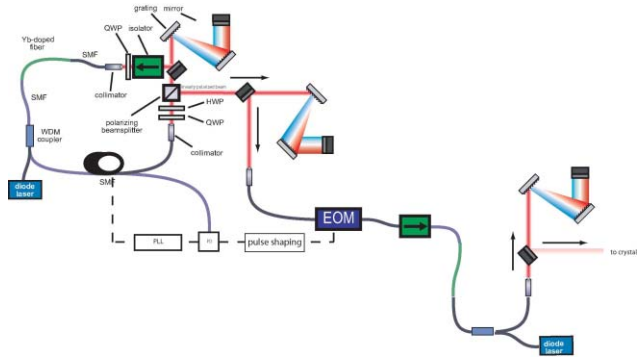

Figure 1: Schematic of the Yb-doped fiber laser setup.

Figure 2: Photograph of the laser and external dechirping gratings in its transportation case.

The laser generates positively chirped pulses, which are dechirped with a grating pair external to the cavity. The positive chirp is intentionally overcompensated and the pulses are coupled into the fiber amplifier with a negative chirp. The amount of this negative chirp is adjusted such that the pulses are chirp-free, maximizing their peak power, at a point within the fiber amplifier, where the power is highest. This way, the dominant nonlinear effect, self-phase modulation, is maximized, resulting in broadening of the pulse spectrum. The spectrum of the pulses after the amplifier have a full-width at half-maximum of ~ 100 nm. The spectral flatness shown in figure 3 is satisfac-

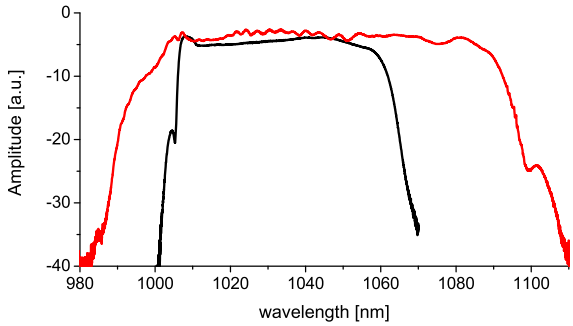

Figure 3: Optical spectrum obtained directly out of the laser (black) and after amplification and spectral broadening (red).

tory, which can be improved further with proper control of higher-order dispersion.

ELECTRO-OPTICAL EXPERIMENTS AT 1 μM WAVELENGTH - SIMULATIONS

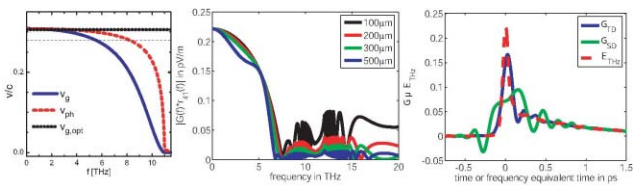

Figure 4: left: group velocity of optical radiation at 1 μm (dotted line) and 800 nm (dashed line) and group and phase velocity at THz frequencies for GaP middle: crystal response function for GaP including group velocity mismatch and frequency dependence of the electro-optic coefficient r_{41} right: Simulated ideal signal expected for a 70 fs long, 0.5 nC electron bunch passing the crystal in 4 mm distance (red); signal expected with temporal decoding(blue) and spectral decoding (green).

It is also important to consider the interaction of the laser pulses with the THz radiation obtained from the electron bunch. In this regards, a Yb-fiber laser system operating at 1μm of central wavelength is advantegous over Ti:sapphire lasers at 800 nm of central wavelength. The limiting factors in terms of resolution and signal-to-noise ratio in electro-optic experiments are the phonon resonances of the crystals used and the phase matching between THz radiation and the laser pulse. This limits the allowable crystal thickness and hence the signal-to-noise ratio. The group velocity of the pulse at 1 μm wavelength is almost exactly equal to the group velocity of radiation up to 7 THz, which is the point at which resonance effects start to play a significant role (left panel of figure 4). A simulated transfer function of the crystal is numerally obtained (middle panel of figure 4. We conclude that a crystal thickness up to 500 μm can be tolerated without significant degradation of the crystal response. This is about a factor of five more than that is possible for 800 nm, hence a similar level of improvement can be expected for the signal-to-noise performance, assuming otherwise equal conditions. The right panel of figure 4 shows the expected signal for a 70 fs long, 0.5 nC charge electron bunch passing the crystal at a distance of 4 mm. The expected signal using the temporal decoding measurement scheme is shown in blue with a duration of 138 fs, whereas the signal to be expected from a spectral decoding measurement is shown in green in the same figure. This assumes a laser pulse with 100 nm bandwidth chirped to 2 ps. For details regarding the measurement techniques, see [1, 6].

CONCLUSIONS

We propose fiber lasers as an attractive alternative laser system for non-invasive electron beam diagnostics. The fiber laser approach offers significant advantages over the traditional choice of Ti:sapphire lasers. Fiber lasers are very compact in size, cost significant less and have better long-term stability and operatability. In addition, the ability to generate a pulse train that matches the bunch profile exact, in a way that it can be electronically reconfigured, while maintaining a nearly fixed individual energy appear to be significant advantages. Experimentally, we have constructed a ytterbium-doped fiber laser with a configurable pulse pattern (using a fiber-coupled electro-optic modulator), implementing an intra-cavity fiber stretcher for locking a harmonic of the repetition to the facility. The laser generates nearly 100-fs pulses, which are amplified and spectrally broadened such that the spectral bandwidth is 100 nm and 350-mW of average power (limited by available pump power), corresponding to a pulse energy of ~ 6.5 nJ. This combination of parameters makes this laser nearly ideal for electro-optic measurements of all bunches within a FLASH macropulse. Simulations indicate that the wavelength of 1 μm is excellently suited to electro-optic experiments, in terms of phase matching with the THz radiation.

REFERENCES

[1] G. Berden et. al., "Single Shot Longitudinal Bunch Profile Measurements at FLASH using Electro-Optic Techniques," proceedings of the EPAC 2006 conference, Edinburgh, UK.

[2] A. Azima, et. al., "Jitter Reduced Pump-Probe Experiments," this conference, ID WEPC13.

[3] F. O. Ilday, J. R. Buckley, W. G. Clark, F. W. Wise, "Self-similar evolution of parabolic pulses in a laser," Phys. Rev. Lett. **92**, 3902-3905 (2004).

[4] J. R. Buckley, F. W. Wise, F. O. Ilday, and T. Sosnowski, "Femtosecond fiber lasers with pulse energies above 10 nJ,"to be published in Optics Letters.

[5] H. A. Haus, "Mode-locking of lasers," IEEE J. Sel. Top. Quantum Electron. **6**, 1173-1185 (2000).

[6] J. P. Phillips et. al., "Single Shot Longitudinal Bunch Profile Measurements by Temporally Resolved Electro-Optical Detection," invited oral WEO2A02, this conference.

THE VEPP-4M DYNAMIC APERTURE DETERMINATION THROUGH THE PRECISE MEASUREMENT OF THE BEAM LIFETIME

A.N. Zhuravlev #, S.A. Glukhov, V.F Gurko, A.D. Khilchenko, V.A. Kiselev, A.N. Kvashnin, E.B.Levichev, O.I. Meshkov, P.A. Piminov, V.V. Smaluk, P.V. Zubarev, BINP, Novosibirsk, Russia.

Abstract

To determine experimentally the particle stable area in the electron-positron collider VEPP-4M we measure the beam lifetime with high accuracy as a function of moving aperture. The measurement is performed by a photodiode installed in the collider diagnostic beam line. The experimental setup and the measurement results are described. Comparison with the tracking simulation is presented.

INTRODUCTION

Measurement of the dynamic aperture (DA) is one of the interesting experimental problems on the accelerator complex VEPP-4M [1]. Usually dynamic aperture is estimated from the results of simulation; we made an attempt to measure the dynamic aperture by three different methods and to compare methods between themselves. Also, the dependence of the dynamic aperture on chromaticity was received and was compared with the results of the simulation.

EXPERIMENTS

Method of artificial limitation of the aperture

For experimental measurement of the dynamic aperture we determined the beam lifetime as a function of artificially limited geometrical aperture (GA) [2]. If the artificially limited geometrical aperture is larger than the dynamic aperture the lifetime remains constant. As soon as geometrical limitation appears in the field of the dynamic aperture - we see the reduction of the beam lifetime. Let us consider this inflection point as the dynamic aperture.

The limitation of the vertical and the radial apertures was carried out using scrapers 1,2 (Fig.1) operated by a computer. The beam lifetime was measured from the intensity of synchrotron radiation (SR) extracted from the bending magnet (Fig.1). The SR intensity, proportional to a number of particles in a bunch, was measured using the HAMAMATSU S2387-33R photodiode. The signal from the photodiode was digitized by a 16-digit ADC. The relative accuracy of the beam current measurements was $3 \cdot 10^{-4}$.

The measurements of the aperture were performed with the beam current of I_b < 1mA to limit the influence of collective effects. The dependence of lifetime on the beam current was also taken into account.

Zhuravlev@inp.nsk.su

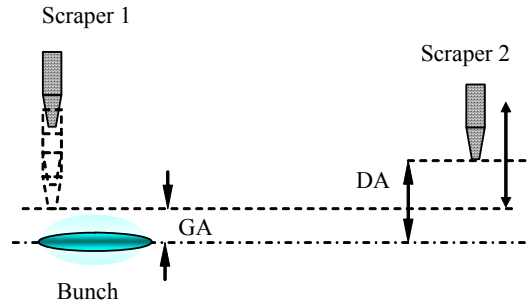

Figure 1: GA – geometrical aperture depended on the transverse coordinate of Scraper 1.
DA – dynamical aperture, measured with dependence of the beam lifetime on transverse coordinate of Scraper 2.
Case of GA<DA is shown.

To test the validity of the method we artificially limited the radial aperture by scraper 1 (Fig.1) and tried to see this restriction with scraper 2. The dependence of the beam lifetime on the position of scraper 2 with the restriction of geometrical aperture (GA) by scraper 1 is presented in Fig.2.

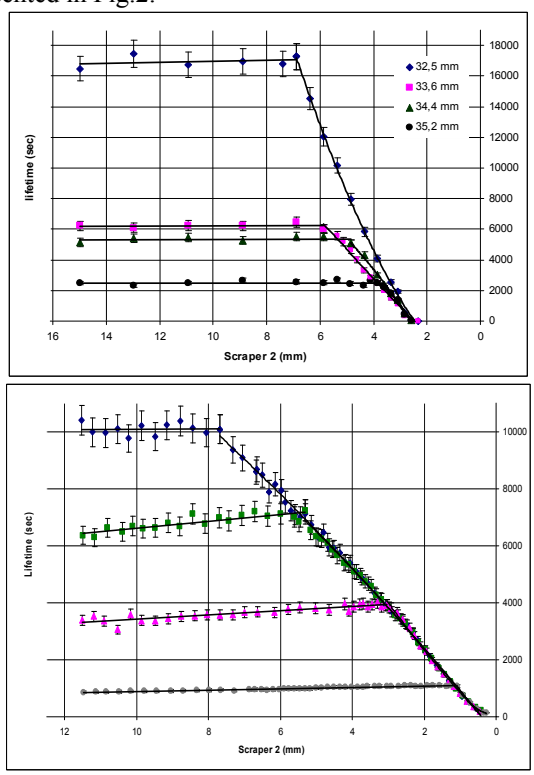

Figure 2: The beam lifetime dependence on horizontal (top) and vertical (bottom) positions of scraper 2 at different insertion depth of scraper 1.

The dependence of the radial aperture, determined with the scraper 2 on various positions of scraper 1 is presented in Fig.3.

A linear character of the dependence of the aperture on the insertion depth of scraper 1 gives us the basis to consider the method as valid.

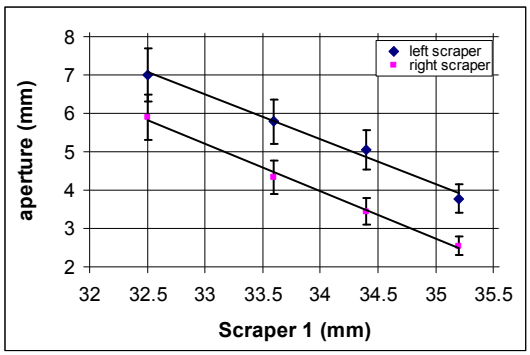

Figure 3: Dependence of the aperture measured by scraper 2 on the insertion depth of scraper 1.

The dependence of the dynamic aperture on the chromaticity

To decrease the dynamic aperture we increased the chromaticity $C_{x,y}$ using sextupole final focus lenses which mainly influence the vertical dynamical aperture.

The measurement of the dynamic aperture was carried out applying the method described above.

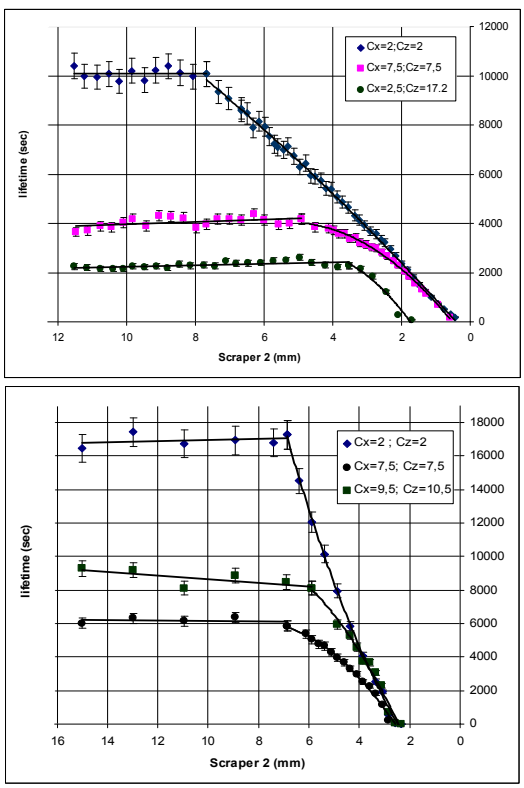

Figure 4: The vertical (top) and horizontal (bottom) aperture with different chromaticity values Cx, Cz.

The results of the measurement with different chromaticity values are shown in Fig.4; Fig.5. presents the results of the simulation and experimental points.

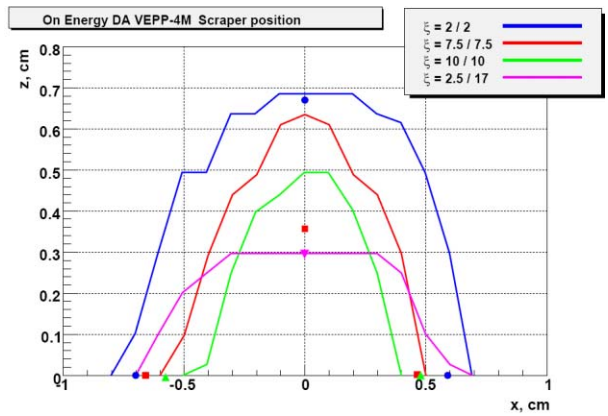

Figure 5: The results of simulation with experimental points.

Measurement of DA with the dependence of the beam lifetime on accelerating voltage

In these experiments we determined Tousheck beam lifetime τ_T as a function of the accelerating voltage [3].

$$\tau_T = \frac{\mathrm{N}}{\dot{N}_T} \propto \frac{\delta p_{\max}{}^2}{\sqrt{U_{rf}}},$$

$$\dot{N}_T \propto \frac{N^2}{\sigma_x \sigma_y \sigma_z \delta p_{\max}}, \qquad \sigma_z \propto \frac{1}{\nu_s} \propto \frac{1}{\sqrt{U_{rf}}},$$

where $\dot{N}_T$ - Tousheck beam losses, N - the amount of beam particles, $\sigma_x, \sigma_y, \sigma_z$ - the beam dimensions.

The maximal allowed deviation of beam particle energy $\delta P_{\max}$ in accelerator is limited by RF separatrix width or by the dynamic aperture.

$$\delta p_{\max} = \sqrt{\frac{2}{\pi q}\frac{eU_{rf}}{E}\frac{1}{\alpha - 1/\gamma^2}\left(\cos\varphi_s - \frac{\pi - 2\varphi_s}{2}\sin\varphi_s\right)} \quad (1)$$

where E- beam energy, q – multiplicity of harmonic, α – compaction factor, φ_s – equilibrium phase.

The increase of the RF accelerating voltage results in the increase of the maximal allowed beam energy deviation and, correspondingly, of the beam lifetime (1). A particle with a non-equilibrium energy has a horizontal deviation due to dispersion. If this deviation reaches the dynamic aperture, a particle is lost. Thus, the beam lifetime dependence on the accelerating voltage should have the maximum connected with the reaching the

maximal allowed energy deviation determined by the dynamic aperture.

The dependence of the maximal allowed energy deviation of a particle on the horizontal dynamic aperture A_x is determined by the following expression [4]:

$$\delta p^*_{\max} \approx \frac{A_x}{\overline{\eta_x}} \qquad (2)$$

where $\overline{\eta_x}$ - the average ring dispersion value.

As one can see from Fig.6, the maximal beam lifetime occurs at $U_{RF} = 480$ kV.

The horizontal dynamic aperture value A_x= 6.2 mm one is determined from (1), (2) at E=1855 MeV, $\overline{\eta_x} = 1.011264$, α=0.0168, φ_s=175.3°, q=222.

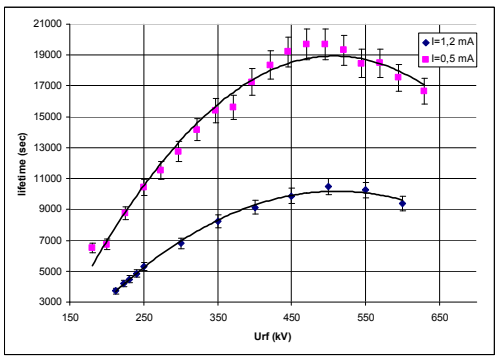

Figure 6: The dependence of the beam lifetime on accelerating voltage.

It should be noted that the position of the maximum does not depend on the beam current because RF separatrix width depends only on the accelerating voltage in working range of the beam current.

DA measurement by the fast kick

A detailed description of the measurement technique can be found in [5]. The dynamic aperture was measured by the coherent beam motion excitation by fast electromagnet kickers. The beam displacement and intensity were measured by the single-turn BMP system.

For low kick amplitudes the BPM does not indicate the intensity reduction because all particles move inside the stable area. But with the kick strength increasing a beam loss appears and for large kick the bulk of the beam is cut off by the DA boundary in a rather short time (~ tens of revolutions) as it is shown in Fig.7.

To distinguish the beam lost at the dynamic or the mechanic aperture we arranged an artificial limitation of the geometrical aperture by insertion of the scraper blade inside the vacuum chamber. The difference is clearly seen from the Fig.7. Outside the dynamic aperture the particle trajectories are exponentially unstable and it takes ~ tens of turns to lose the particles while in the case of geometrical limitation for our betatron tunes (~0.5) two revolutions are quite enough.

Considering the beam loss process turn-by-turn it is possible to determine the border of the DA with good accuracy. For VEPP-4M the vertical aperture has been measured by this method and it is equal to A_z= 6.9 mm.

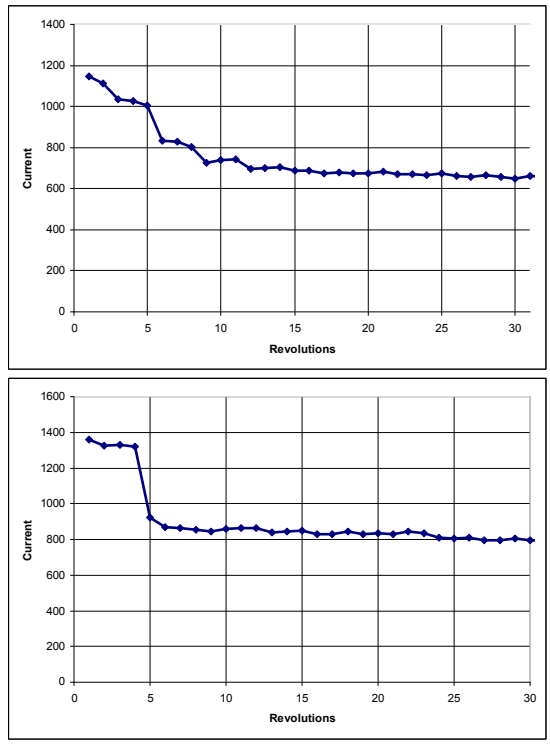

Figure 7: Beam loss at the dynamic (top) and mechanic (bottom) apertures.

CONCLUSION

The horizontal aperture of VEPP-4M was measured by a precise determination of the beam lifetime. In the case of limitation of the beam lifetime by the scraper blade the aperture A_x = 6.45 mm was found while the dependence of the DA on the accelerating voltage amplitude gives A_x = 6.2 mm. Both values seem quite consistent.

As for the vertical aperture, the scraper limitation method (A_z = 6.7 mm) was compared with the fast kick method (A_z=6.9 mm); and, again, both results are rather close to each other.

REFERENCES

[1] V. Smaluk, Status of the VEPP-4M collider. XX RUPAC, Novosibirsk, 2006.

[2] B. Simon, P. Kuske. The dynamic aperture of BESSY. 2nd Advanced ICFA Beam Dynamics Workshop, 1988.

[3] A.A.Valishev, Ph.D. thesis. BINP, Novosibirsk, in Russian.

[4] S.A. Nikitin, A.B. Temnykh. Study of intra-beam scattering effect at CESR and VEPP-4M storage rings at 1.8 GeV energy. Budker INP 2004-56.

[5] V. Kiselev, E. Levichev, V. Sajaev, V. Smaluk. Dynamic aperture study at the VEPP-4M storage ring. Proc. of the 1997 Particle Accelerator Conference, Vancouver, 1997.

STREAK CAMERA MEASUREMENTS OF THE SOLEIL BUNCH LENGTH

M. Labat, M.E. Couprie, L. Cassinari, D. Pedeau, R. Nagaoka, SOLEIL, Saint-Aubin, France

Abstract

A double sweep streak camera (C5680, Hamamatsu) has been installed on the French third generation light source SOLEIL. The visible radiation of the diagnostics beam-line is used to study the longitudinal profile of the stored electron bunches. Measurements of single-bunch length as a function of various machine parameters such as RF cavity voltage and frequency, and beam current with a few picoseconds resolution are reported, and interpreted in terms of vacuum chamber impedance and beam stability.

INTRODUCTION

The third generation French light source SOLEIL has been recently inaugurated, and the machine commissioning with all the chambers of the insertion devices (except the invacuum devices) has been achieved. Among the 24 experimental beam lines foreseen, 9 are already opened. Synchrotron Radiation from infrared to hard x-rays ($>$ 8 keV) provided by bending magnets, undulators (U20, HU80 and HU256) and wigglers, is delivered for various type of experiments: micro-imaging, tomography, infrared to X-ray spectroscopy, electronic and magnetic studies [1]. The electrons are stored at an energy of 2.75 GeV, with an horizontal emittance of 3.74 nm.rad. Up to 300 mA can be stored presently in multibunch mode and 20 mA in single bunch mode. A Streak Camera has been installed in September 2006, for the study of the longitudinal profile of the electron beam either in stable or evolutive regimes.

STREAK CAMERA COMMISSIONING

Passing through a bending magnet, the 2.75 GeV electron beam emits light from visible to x-ray. The upper part of the radiation, in the visible range, is collected by an under vacuum aluminum flat mirror with a nickel coating. Using a periscope and a pair of mirrors, the beam is transported to the diagnostic hutch. The last four mirrors are all glass made, with an aluminum coating. On the diagnostic hutch optical table, a glass cube splits the beam in two lines, one sent to an imaging system for transverse size measurements [2] and the other to the entrance pinhole of the Streak Camera. A photocathode converts the light pulse into an electronic pulse, with similar longitudinal distribution.

A fast sweep, i.e. high frequency electric field, is applied at the ouput of the photocathode to deviate the electronic pulse in the vertical direction, allowing longitudinal projection of the distribution on a phosphore screen imaged by a CCD camera. Because the electronic of the device can't follow the 352 MHz RF frequency, the fast sweep is triggered at one fourth of this frequency, i.e. 88 MHz using a divider. A delay line (Hamamatsu C1097) is then used to adjust (with 0.5 ns steps) the timing position of the bunch on the fast "sweeping" sinusoid. Within one fast sweep period, four successive bunches are deflected (two with positive and two with negative fields). Four vertical scales are available, corresponding to four different sweeping ramps. Scale 1 enables a sweep of 149 ps, 2 of 694 ps, 3 of 1293 ps, and 4 of 1883 ps (widest possible scan with a 88 MHz sweep frequency). A second slow sweep, i.e. lower frequency electric field is simultaneously applied in the horizontal direction. The bunch profiles are juxtaposed (starting from left) according to their arrival time, allowing to follow their evolution. The slow sweep (as well as the CCD camera) are triggered by the storage ring master clock at 846 kHz. The time delay in between slow sweep and camera acquisition can be adjusted with a Stanford, DG535. The horizontal scales range from 100 ns to 1 s.

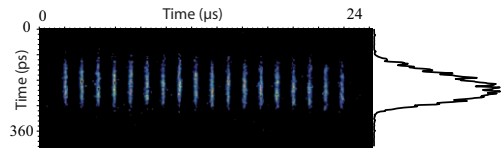

Figure 1: Evolution in time of the longitudnial bunch profil. Streak Camera measurement. V_{RF}= 2 MV. Horizontal scale: 20 μs, Vertical scale: 800 ps. Single bunch mode. I=12.6 mA. Data of 15/12/2006.

The images recorded by the CCD camera are further analyzed to provide the desired information on the longitudinal distribution of the electron beam using momenta calculations. A typical image is given in Figure 1.

The resolution of the Streak Camera depends on the spatial resolution and the vertical scale: $Res_T = \frac{Spot\ size(pixels)}{Total\ Number\ of\ pixels} \times Vertical\ scale(ps)$. The spatial resolution is measured using the FOCUS mode (see Figure 2), i.e. without sweep. With an entrance hole of 30 μm (resp. 100 μm), the spot size is 8.7 mm FWHM (resp. 16.3 mm FWHM), corresponding to 5 pixels (resp. 9 pixels). Since the expected resolution is higher with 30 μm, its use became systematic. Highest resolution of 1.5 ps is reached with scale 1 and 30 μm entrance hole. But scale 2 is mostly usually used, suiting better to the length to be measured at SOLEIL: in this case, the resolution is 6.8 ps.

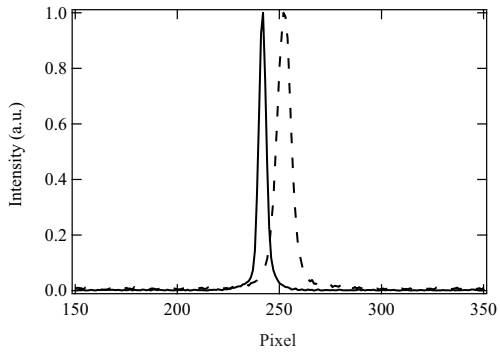

Figure 2: Streak Camera spatial resolution measurement. Vertical line profile of the Streak Camera image of the bunch radiation in the FOCUS mode. Entrance hole diameter: 30 μm (Continuous line), and 100 μm (Dashed line).

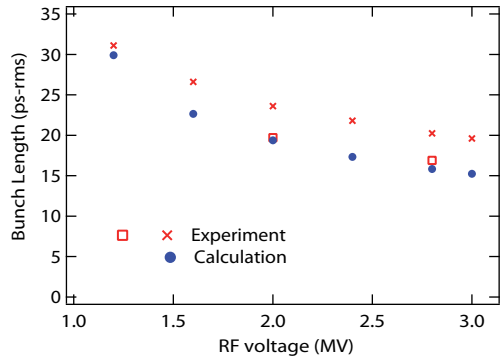

Figure 3: Bunch length at zero current as a function of the RF voltage. Experimental values in (□) multibunch mode (28 bunches, average over 5 ms), (×) Single bunch mode (average over 100 ms). (•) Calculated values using Equation (1).

BUNCH LENGTH MEASUREMENT AT ZERO CURRENT

The bunch length has been measured at very low current (below 0.2 mA) in two different operating modes: single bunch and multibunch (with 28 bunches injected). According to theory [3], the expected bunch length in a storage ring at zero current σ_{e0} is defined as:

$$\sigma_{e0} = \frac{\alpha}{2\pi f_S}\sigma_\gamma, \qquad (1)$$

with α the momentum compaction factor, f_S the synchrotron frequency which depends on the RF voltage, and σ_γ the natural energy spread. A single bunch tracking code [4] provides estimation of the bunch length at zero current using relation 1.

The theoretical and experimental results are presented Figure 3. The measured bunch length in single bunch mode is higher by 1.5 to 4.5 ps than the value given by (1), and the smaller the RF voltage, the smaller the discrepancy. At 1.2 MV, it is only 1.5 ps. The measured bunch length at zero current with 28 bunches stored leads to shorter values, and therefore closer to the value given by (1): the discrepancy remains below 1.6 ps at 2 and 2.8 MV. The difference observed between single bunch and 28 bunches modes may be partially due to the fact that distinct horizontal scales were used: 5 ms for 28 bunches operation and 100 ms for single bunch operation. The difference observed between theory and experiment could also be explained by the measurement conditions: no measurements were performed below 0.11 mA.

BUNCH LENGTHENING

Bunch lengthening at SOLEIL is studied as a function of the beam current, for different RF voltage values. As illustrated in Figure 4, the bunch length increases with the current, and the higher the RF voltage, the shorter the bunch length. In addition, because of the vacuum chamber impedance, the longitudinal profile becomes more asymetrical at high current. A pinhole camera enables simultaneous measurement of the energy spread. It is found constant on this range of current. The lengthening may mainly be due to impedance effects.

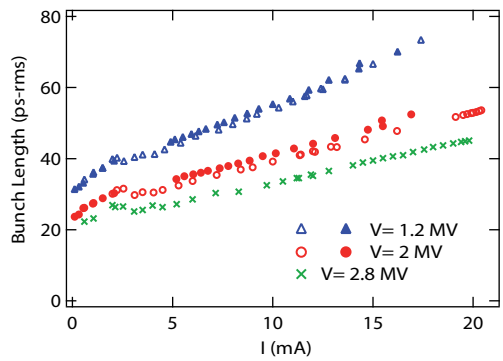

Figure 4: Bunch length measured versus current. (○,△,×) before (February 2007), and (•,▲) after (April 2007) installation of an additionnal insertion device: U20. Single bunch mode. Streak Camera measurement.

Figure 4 presents two series of bunch length values versus current with 1.2 and 2 MV, which are found in very good agreement. In between the two measurements (February and April 2007), an additionnal in vacuum insertion device, an U20, was installed with its chamber without effect on the bunch lengthening. Such results validates the use of RF fingers for impedance matching at the entrance and output of the undulator.

The lengthening is simulated using the tracking code (see Figure 5). At non zero current, the simulation uses an impedance evaluated taking into acount the elements along the ring such as BPMs, the dimension of the vacuum chamber as well as its main discontinuities and inside rugosity. The influence of the NEG deposition on the wall of aluminium vacuum chambers is not yet considered. The experimental lengthening with respect to the zero current

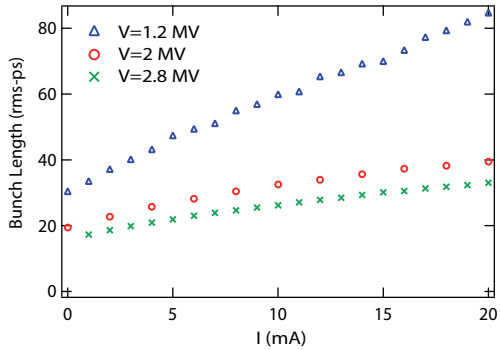

Figure 5: Bunch length calculated versus current using the tracking code.

value between 0 and 20 mA is found in good agreement with the simulation. At 1.2 MV (resp. 2 and 2.8 MV) the simulated lengthening is 155 % (resp. 104 and 92 %) and 114 % (resp. 103 and 100 %) experimentally. The relative enhancements are similar. In addition, both experiment and simulation agree on the following behaviour: the higher the RF voltage, the slower the lengthening. Finally, operation at 1.2 MV clearly leads to larger enhancement. A dramatic reduction of the lifetime was simultaneously observed: the dynamic acceptance limit was reached.

The remaining discrepancies may be due to some imperfections in the modeling of the impedance in the tracking code. Further investigations for impedance measurement are foreseen.

LONGITUDINAL BEAM STABILITY

Figure 6 shows a high level of longitudinal stability in the multibunch (1/4) mode. It results from SOLEIL choice of adopting superconducting cavities (two within one cryomodule). Such technique supresses the excitation of the beam by Higher Order Modes (HOM).

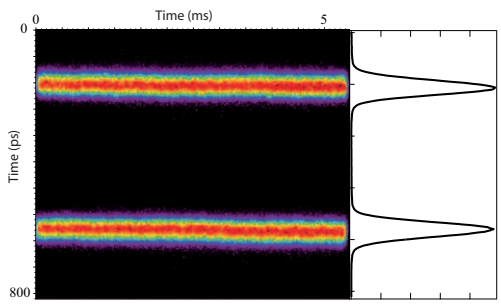

Figure 6: Illustration of the longitudinal stability of the beam in mutlibunch (one fourth of the RF buckets are filled) mode. Streak camera image and associated vertical profile. I=65mA. Data from 09/2006.

Nevertheless, longitudinal beam instabilities can be obtained with external excitation of the beam. In the example presented in Figure 7, longitudinal oscillations with a period of 1.2 ms are observed. Those instabilities result from a sudden change of the RF voltage: from 2 to 1.5 MV. Similar oscillations were observed simultaneously on the BPMs.

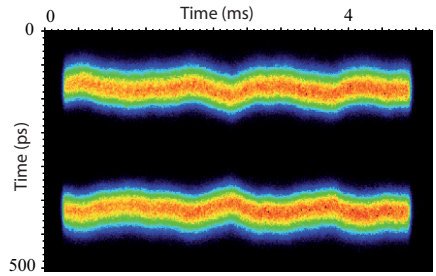

Figure 7: Evolution in time of the longitudinal bunch profil. V_{RF}= 1.5 MV. Multibunch mode with 28 bunches. I=156 mA. Streak Camera measurement. Horizontal scale: 5 ms, Vertical scale: 800 ps. Data of 04/10/2006.

CONCLUSION

The SOLEIL Streak Camera enables electron beam longitudinal studies. The first issue was bunch length measurement under various parameters such as current and RF voltage. It provides an evaluation of the light pulse duration delivered to the users, with a precision below 6.8 ps, whatever the operating mode (single or multibunch). The device also allows dynamical studies and validated the longitudinal stability of the beam thanks to the superconducting cavities. Finally, further studies are undergoing to investigate the ring impedance via phase shift measurements. Those might help refining the impedance model by confirming that the NEG deposition does not influence its real part.

ACKNOWLEDGMENTS

The authors would like to thank J. Roux (Hamamatsu France) and J.C. Denard for their support.

REFERENCES

[1] J.M. Filhol and al., Proccedings of the EPAC'06 Conference, 2723 (2006).

[2] L. Cassinari, D. Pedeau, J.C. Denard, presented at this conference: ID1202.

[3] M. Sands, The Physics of Electron Storage Rings. An introduction (1971).

[4] R. Nagaoka et al., to be submitted at PAC'07.

DIRECT COMPARISON OF THE METHODS OF BEAM ENERGY SPREAD DETERMINATION IN THE VEPP-4M COLLIDER

#O. I. Meshkov, V.V. Zhilich, A. N. Zhuravlev, V. A. Kiselev, N. Yu. Muchnoi, V.V. Smaluk,
S. V. Sinyatkin, BINP SB RAS, Novosibirsk, Russia

Abstract

The VEPP-4M electron-positron collider is now operating with the KEDR detector for the experiment of precise measurement of tau-lepton mass [1]. The nearest experimental program of the accelerator also includes a scan of the energy area below J/ψ meson to search narrow resonances. The monitoring of beam energy spread is important to know the energy spread contribution into the total systematic error.

In this report we discuss the application of several diagnostics for beam energy spread measurement. The data obtained with Compton Back-Scattering (CBS) technique [2] are compared with the value of the spread derived from the betatron motion of the beam [3]. The measurements by all the methods were done at the same accelerator run, i.e. the different diagnostics can be compared directly. The value of the energy spread was determined for a set of collider operating modes, covering the energy area from 1200 MeV up to 1855 MeV……..

INTRODUCTION

Value of beam energy spread σ_E is directly included into accuracy of the mass measurement. Knowledge of exact value of the beam energy spread enables us to reduce significantly a systematical error in the experiment of $c-\tau$ lepton mass measurement. It is also an essential supplement to precision measurement of average beam energy.

The measurement of τ lepton mass with accuracy of ± 100 keV requires determination of beam energy spread with accuracy of ± 10%. In this case, the impact of energy spread on the systematical error of the τ lepton mass determination doesn't exceed ± 25 keV. Clear understanding of the effects of the parameters influencing the beam spread and the ability to control this value are important tasks for our experiments.

Compton Back-Scattering (CBS) is used at the VEPP-4M collider for permanent control of the electron beam energy during the run [2]. This diagnostics is able to measure the beam energy every 8-10 minutes with an accuracy of $\Delta\varepsilon = \pm 60$ кэВ.Period of the measurement is determined by the flow of the registered gamma quantum. Spectrum of scattered Compton quanta also contains information about the beam energy spread.

For a long time, spectrum processing method, as well as spectrum calibration, has been refined via comparison between the CBS data and the results of energy measurement by resonance depolarization technique [1]. Value of the beam energy spread averaged over a set of the collider runs is in a satisfactory agreement with a width of ψ' resonance determined by KEDR [4]. At the same time the successive measurements during the collider run do have a significant spread. This fact prompts us to compare the measurements from different diagnostics to elicit possible errors of the CBS method.

Correction of the systematical errors will allow us to control permanently the beam energy spread during the collider run. This is important for the future experiments at VEPP-4M in search of narrow resonances inside 0.9 – 1.5 GeV area. Perhaps, it will also cause the improvement of the accuracy in the beam energy measurement.

At the experiments, described above, beam energy of VEPP-4M (Fig. 1) was changed from 1100 GeV to 1855 GeV. The energy spread of the beam can be increased with the 3-pole snakes established in the experimental area (Fig.1). Snakes were applied only during the beam energy spread measurements described below.

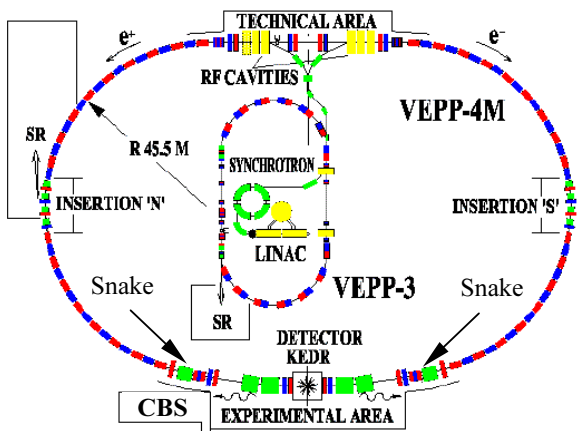

Figure 1. VEPP-4M general layout

APPLIED METHODS FOR BEAM ENERGY SPREAD MEASUREMENT

Compton Back - Scattering (I)

The VEPP-4M collider has a system of Compton Back-Scattering for permanent measurement of the average beam energy and the energy spread. [2], Fig.1.

When the monochromatic laser radiation with the photon energy w_0 interacts with the contrary relativistic electron beam with average particle energy E_0, the scattered photons with maximal energy $W_{\max}$ form a narrow edge in the spectrum. The value of $W_{\max}$ is strictly coupled with the average energy of the beam

#O.I.Meshkov@inp.nsk.su

electrons by a simple relation: $W_{\max} \approx 4w_0 \cdot (E/m_e c^2)^2$. The width of the edge is mostly determined by the resolution of the photons detector and the energy spread of the electron beam. Thus, direct measurement of the energy spectrum of scattered photons allows us to measure both the electron beam average energy and the energy spread.

Chromaticity dependence of envelope of betatron oscillations (II)

It was shown [3] that envelope $A(t)$ of free coherent betatron oscillations excited by a kick with an amplitude $b >> \sigma_y$ b is described as

$$A(t) \propto \exp\left(-\frac{t^2}{2\tau^2}\right) \cdot \exp\left(-\left(\frac{\partial\omega_y}{\partial E}\frac{\sigma_E}{\omega_s}\right)^2 \cdot (1-\cos(\omega_s t))\right)$$

$$\text{where } \tau = \left(2\frac{\partial\omega_y}{\partial a^2} b \cdot \sigma_y\right)^{-1}. \qquad (1)$$

Experimentally, the energy spread was determined comparing the measured beam betatron motion with the theoretical curve $A(t)$.

Bunch length dependence of energy spread (III)

The r.m.s of a bunch length σ_z is directly proportional to the r.m.s. of the energy spread:

$$\sigma_z = R\alpha \frac{\omega_s}{\omega_0}\frac{\sigma_E}{E_0} \qquad (2),$$

where R – the average radius of the ring, α - momentum compaction factor, E_0 - beam energy [4].

The φ-dissector [5] is used at VEPP-4M to measure the beam length σ_z. This device has a temporal resolution of about 30 ps (≈ 1 cm).

EXPERIMENTAL RESULTS

Measurements of the beam energy spread were carried out during two runs of VEPP-4M.

During the first run the collider energy was changed from 1855 MeV down to 1100 MeV with a step of about 100 MeV. Within the energy area of 1300 – 1855 MeV the measurements were performed by the three mentioned diagnostics together. The beam current was about $I_b \approx 80$ – 100 mkA to neglect the collective effects. During the second run the accelerator energy was set to 1855 MeV and the snake current was varied from 0 up to 2000 A..

Spectra of the Compton Back-Scattering are shown in Fig. 2. The steepening of the spectrum edge with the beam energy spread increase can be easily seen.

For betatron frequency measurement we have applied an optical diagnostics based on the Multi-Anode Photomultiplier Tube R5900U-00-L16 HAMAMASU (MAPMT) [6]. To increase an accuracy, the digital filter was applied to the measured data. For envelope analysis, the oscillation is calculated by the inverse Fourier transform of spectrum of measured betatron oscillations, but only $\nu_y \pm m\nu_s$ harmonics are taken into account.

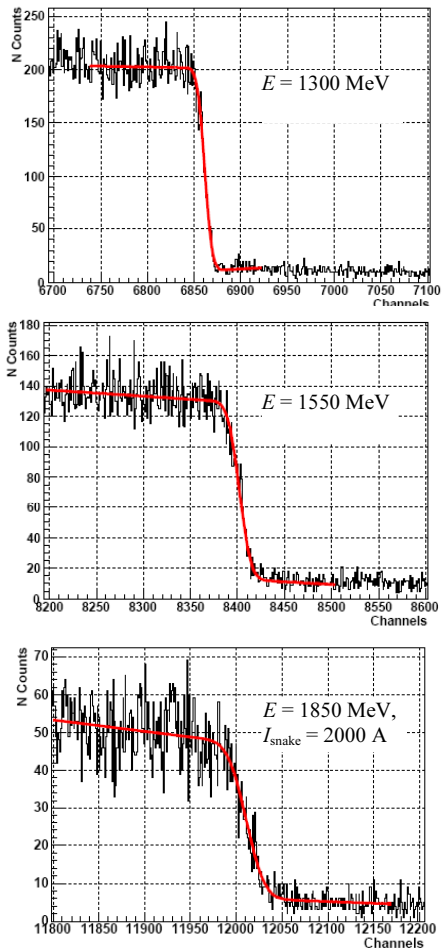

Figure 2: Compton Back-Scattering spectra for various values of the beam energy spread. Channel number is proportional to the γ-quantum energy.

The envelope of the derived betatron motion $En(t)$ was compared with (1). Energy spread δ_E was used as a fitting parameter. An example of filtered experimental envelope in comparison with theoretical curve $A(t)$ for 3 different values of energy spread σ_E is presented in Fig. 3.

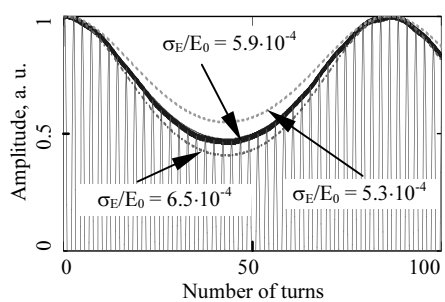

Figure 3: Measured betatron oscillation envelope in comparison with theoretical one.

The results of the measurements of beam energy spread are presented in Fig. 4.

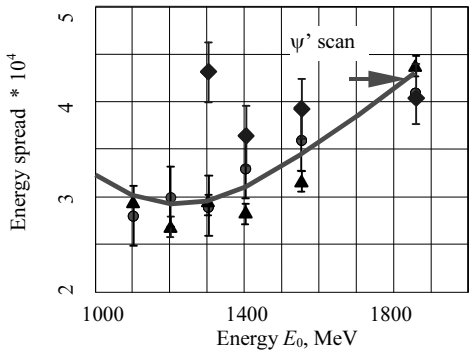

Figure 4: Variation of the beam energy spread depending on the beam energy.
◆ - CBS data; ▲ - method (*III*) data; ● - method (*II*) data; ▬ - simulation results. An arrow shows the data of KEDR.

Fig. 5. represents the variation of the beam energy spread with the snake current increase.

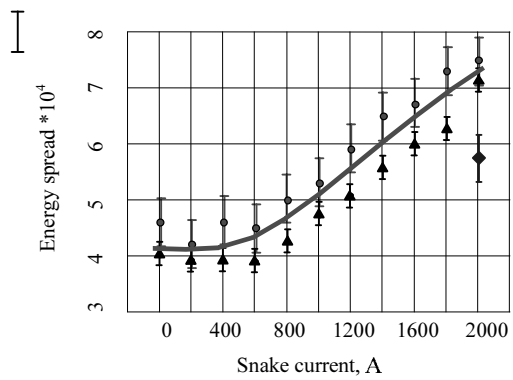

Figure 5: The beam energy spread depending on the snake current. E_0 = 1855 MeV, the same symbols.

DISCUSSION

Determination of the beam energy spread by the measurement of a beam length been applied for a long time, therefore the data of this diagnostics look reliable.

Measurement accuracy of the described experiments is determined by the inherent noise of the dissector, which was rather high. The reasons of it are the small beam current and the reduced transparency of output window of vacuum chamber darkened under SR-influence during a 5-year run. Each point in Fig. 5 was obtained as a result of averaging out of 512 beam profiles registered by the dissector.

The main source for errors during derivation of the beam energy spread from an envelope of betatron oscillations (method *II*) is a noise of the Fourier spectrum. It influences the accuracy of the envelope restoration with the inverse Fourier transform.

The systematical discrepancy between (*II*) and (*III*) during the measurement of the beam energy spread depending on the snake current may be related to that.

An accuracy of the method (*II*) can be estimated as 10 percent (Fig. 3). The level of modulation depth of about 0.5 is necessary for a reliable reconstruction of the envelope. It creates some experimental inconveniences as it requires the increase of a vertical chromaticity up to $C_y \approx 13-18$, that exceeds significantly the nominal value.

Spectra of Compton Back-Scattering were got parallel with the measurements of two other diagnostics (Fig.6). In spite of an obvious sensitivity of CBS to the beam energy spread (Fig. 2), we have to recognize the discrepancy between the CBS data and the measurements of (*II*) and (*III*). This difference may be connected with the solid angle in which the CBS detector collects the scattered gamma quanta. Possibly, the "tails" of the scattered photons do not reach the detector that leads to distortion of the spectrum edge.

However, this hypothesis requires further investigation; and we plan to continue the experiments on comparison of the data of different methods for the beam energy spread measurement.

CONCLUSION

Experiments on the beam energy spread have been carried out at the VEPP-4M collider using three different diagnostics.

All three diagnostics have been used simultaneously during the same accelerator run.

The results of the measurements are in a satisfactory agreement, but further experiments to elicit the nature of systematical errors of CBS are necessary.

REFERENCES

[1] KEDR collaboration. New precision determination of τ lepton mass. Proceed. of RUPAC 2006, Novosibirsk, Russia.

[2] N. Muchnoi, S. Nikitin, V. Zhilich. Fast and Precise Beam Energy Monitor Based on the Compton Backscattering at the VEPP-4M Collider. Proceed. of EPAC 2006, Edinburg, Scotland, TUPCH074

[3] V. V. Danilov, I. N. Nesterenko, E. A. Perevedentsev. Measurement of betatron coherent tune shifts and collective damping rates in BEP storage ring with the optical technique.// *Int. J. Mod. Phys. A,* Proc. Suppl. 2A (1993) 230-233.

[4] J. Le Duff. Single and multiple Touschek effects. // *CAS, Fifth Advanced Accelerator Physics Course*, CERN 95-06, Geneva, 1995, pp. 573-586

[5] Coppens J., Luijckx G., Zinin E. Commissioning of a bunch length monitor at AmPS // Proceedings of the EPAC 96, Barcelona, 10 - 14 June 1996. Vol. 2. 1704 - 1706.

[6] A.V. Bogomyagkov et al. New beam profile monitor for the electron-positron collider tuning. Rev. of Sci. Inst., be published.

TIME DOMAIN DIAGNOSTICS FOR THE ISAC-II SUPERCONDUCTING HEAVY ION LINAC

V.A.Verzilov, R.E.Laxdal, M.Marchetto, W.R.Rawnsley
TRIUMF, 4004 Wesbrook Mall, Vancouver, Canada

Abstract

The medium beta section of the ISAC-II superconducting linac has 20 bulk niobium quarter wave resonators and adds up to 20 MeV of energy to the 1.5MeV/u and A/q≤ 6 ion beam injected from the ISAC-I accelerators A standard array of ISAC diagnostics were installed to commission and tune the transport beam line and linac optics. In addition two new devices were developed: a silicon detector measuring beam particles scattered from a gold foil and time-of-flight (TOF) monitors based on micro-channel plates. These are used both to tune the linac and characterize the accelerated beams in the longitudinal phase space. The TOF monitors reach a time resolution of < 100 ps, energy resolution of 0.1% and a dynamic range spanning seven orders of magnitudes.

INTRODUCTION

The ISAC accelerators produce stable and radioactive ion beams with A/q ≤ 6 and an energy of up to 1.5 MeV/u. An upgrade of the facility with an aim to further increase the final beam energy started in 2000. The first phase of the upgrade, the medium beta section of the ISAC-II superconducting linac, was completed in 2006 by commissioning started in April 2006 [1] and the first radioactive beam delivered to the experiment in January 2007. The linac comprises twenty bulk niobium quarter wave resonators grouped in five cryomodules. Operated at an average accelerating gradient in excess of 6 MV/m in an 18cm gap the medium beta section adds 20 MeV of energy to the injected beam. The linac is connected to the ISAC facility with a 25 m long S-bend achromatic transport line consisting of a transverse focusing structures and a 35 MHz rf buncher to match the input linac optics. Following the linac the beam is transported via a 27 m long straight FODO transport line to the experimental areas. Both transport lines and linac are equipped with standard diagnostics equipment: faraday cups, slits and wire scanners. In addition, two new time domain devices were added: a scattered particle monitor and time-of-flight monitors.

MONITOR DESIGN

The scattered particle and TOF monitors are intended primarily for beam energy and timing measurements delivering, however, different levels of accuracy. In both monitors, intrinsically intended for single particle detection, signal attenuation is achieved in different ways to make measurements possible with nA beams. The monitor design is similar to one developed at ANL [2].

Scattered Particle Monitor

As the monitor name suggests the beam particles are scattered in it from a thin, 40 nm, gold foil towards a Canberra, 50 mm^2 ion implanted, silicon detector with an improved time response placed at 30 degrees with respect to the incoming beam. The detector location is fixed but the scattering foil is mounted on a pneumatically driven actuator and retracts into a collar to protect it during pumping and venting. With this foil thickness and an angular acceptance of the detector of ~7°, the monitor can operate with beam currents from ~100 pA up to a few nA. Depending on the beam energy the count rate from the monitor varies from a few tens to a few hundred counts/sec. The design also incorporates a shutter to protect the silicon detector from a direct beam impact when the beam is tuned. An alpha source is available on the same shutter for test and calibration purposes. The monitor aims to provide beam energy and timing measurements with accuracies of 1-3% and ~200 ps, respectively.

The monitor has been operated for nearly one year with only small signs of radiation damage.

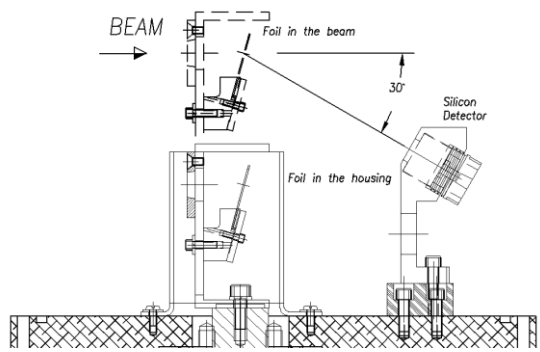

Figure 1: A sketch of the scattered particle monitor.

Time-of-Flight Monitors

The ISAC-II TOF monitors are designed for measurements of the beam velocity with an accuracy of better than 0.1% for v/c of 0.03 to 0.2. The system consists of three identical secondary electron emission (SEE) monitors spaced apart by 3 and 9 m. In each SEE monitor the beam strikes a 50 μm diameter tungsten wire stretched on the axis of a grounded metal cylinder and generates secondary electrons. The secondary electrons are accelerated in a radial electrostatic field when a potential of a few kV is applied to the wire. A small fraction of them, ~4%, passes through an 11 mm aperture in the cylinder and is detected by a fast micro-channel plate (MCP) Hamamatsu F4655-12. The metal cylinder is

mounted on a pneumatic actuator and can be retracted from the beam. The MCP is mounted in the housing with a protection mesh of 500 lines per inch on the input aperture. It should be noted that a strong field emission was observed from a fresh tungsten wire at a voltage larger than 800V. Extended conditioning was required to bring the HV up to higher values.

Each SEE monitor detects the time when the beam passes through. Measuring the beam transit time between the monitors, the ion velocity and, thus, the beam energy can be computed.

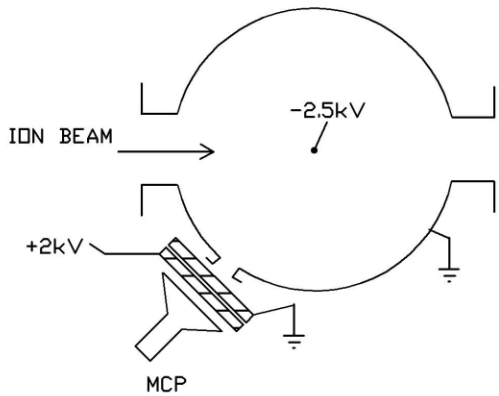

Figure 2: A time-of-flight monitor schematic view. Secondary electrons are extracted by the beam from a wire, accelerated in the electrostatic field and detected by a microchannel plate.

To get the desired resolution at the high energy end of the range, the monitors should be separated by a substantial distance of ~10 m. This introduces an element of ambiguity in the data analysis since the beam transit time between the monitors is significantly longer than the bunch separation of 85 ns. Generally, signals in different TOF monitors are generated by different bunches and the beam transit time is measured with an uncertainty of an integer number of bunch periods. To determine that integer an energy estimate with accuracy of better than 10% is required which is provided by the scattered particle monitor or determined from the accelerating fields in the cavities.

The performance of the system was initially estimated by means of computer simulations. They confirmed that a time resolution in the range of 50 to 70 ps can be achieved. The monitors typically intercept less than 5% of the beam and, thus, can be considered nearly non-intercepting. The monitors are capable of operating with beam intensities from ~10 nA down to 1 fA, thus spanning seven orders of magnitude with a little adjustment of the MCP bias.

The monitors were tested in the lab with a short pulse UV laser. The laser beam was split in two and sent simultaneously to a fast UV silicon photodiode and to a FTM monitor. The pulse shape of the photodiode signal was measured with a 6 GHz Tektronix TDS820 sampling scope. It was in a very good agreement with the FTM time spectra. Both measured a pulse width of ~500 ps.

The low loss phase stable signal cables for the FTM monitors were cut to have equal electrical lengths of within a few tens of ps. The overall signal transit time variation for the different FTM monitors was measured to be less than 100 ps. Later in 2007 it is planned to equip the TOF monitors with a calibration UV laser that will make possible periodic corrections of electronic and other drifts in the system.

Data Acquisition and Processing

The data acquisition system is built on the basis of commercial NIM and VME modules. Signals from the silicon detector, following a charge preamplifier, are sent for pulse height and timing analysis. In the later case they are discriminated and compared by a TDC with a reference 11.8 MHz bunch repetition frequency. Signals from TOF monitors are amplified and sent to low jitter CFDs. The CFD outputs are connected to a 25 ps resolution multihit TDC operating in trigger mode and a logical OR unit generating a common trigger for all three monitors. The TDC calculates the deviation of TOF signals w.r.t. the same 11.8 MHz reference. The modules are controlled by a VME CPU running Linux.

The same CPU provides the interface to the EPICS based ISAC control system. The fast data acquisition is performed by a set of applications communicating with the EPICS soft IO channel by means of a run-time database resident in a segment of the OS supported shared memory. The on-line data processing is done by a number of Matlab applications run on a remote host. Peak fitting, peak position and widths, energy computations and automatic phase scanning of the RF cavities is done in this way. The system is highly automated and transparent to the users.

MEASUREMENT RESULTS

During the linac commissioning the scattered particle and TOF monitors were used both to tune the linac and to characterize the accelerated beams in the longitudinal phase space.

Six different beams from ^{4}He to ^{40}Ca with A/q ratios of 2, 4 and 5.5 were successfully accelerated. Beams from ISAC at two different reference energies were delivered and coasted through the linac to calibrate the scattered particle monitor. The energy losses in the foil and detector window and energy transfer occurring in the scattering from the gold foil vary with the ion mass and charge and require monitor calibration for every ion species being accelerated. This rather time demanding procedure limits the use of the monitor for absolute energy measurements. It proved very useful for the phasing of the buncher and cavities, however.

Following the S-bend buncher, each linac cavity was turned on starting from the upstream end. The cavities were phased by measuring the beam energy for four different phases and fitting the data to a cosine profile to find 0°. After that all cavities were set to a synchronous phase of -25° for acceleration.

Using the monitor we were able to observe components a "cocktail" beam of $^{20}Ne^{5+}$ and $^{40}Ca^{10+}$ accelerated at the same time. Both ions have the same velocity and A/q and would be indistinguishable by the ISAC PRAGUE magnetic energy spectrometer and by the TOF monitors.

Currently, there is no bunching cavity present downstream of the linac, however, it was possible to use one of the linac cavities to focus the beam in time or energy. Thus, by using the second cavity of the fifth cryomodule we could bunch the beam accelerated in the first two cryomodules The scattered particle monitor conveniently allows us to observe the energy and time spectra at the same time (Fig.3). The smallest beam energy and time spreads observed with the monitor were 0.5% and 0.6ns (FWHM), respectively. Both values are very close to and possibly limited by the monitor resolution.

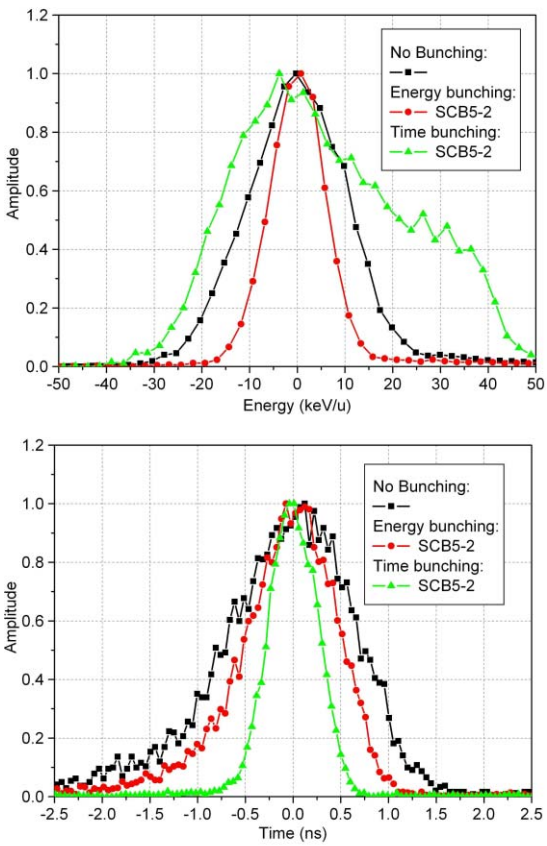

Figure 3: The beam energy (upper) and time (lower) distributions of a beam bunched in energy or in time compared to the non bunched beam at the location of the scattered particle monitor.

Accurate energy measurements were done with the TOF monitors. At the moment of commissioning two of three TOF monitors were in operation. The accuracy of the monitors was initially evaluated by comparing the TOF data with the measurement of the PRAGUE magnet when the beam was brought through the linac without acceleration. An agreement of better than 0.1% was observed in this case. Care, however, must be taken to center the beam on the TOF monitors since they are sensitive to ionization of the residual gas by the beam.

The measured energy for three accelerated beams versus the number of cavities in operation is shown in the Fig.4. Final energies of 10.8, 6.8 and 5.5 Mev/u were reached for beams with A/q values of 2, 4, and 5.5, respectively. The accelerating gradient calculated from these measurements had a very good consistency for all three beams. The average gradient in each case was 7.2 MeV/m corresponding to an average voltage gain of 1.3 MeV/cavity.

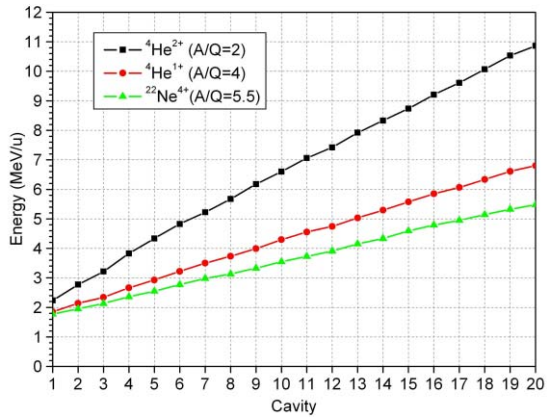

Figure 4: The full beam energy as a function of the number of cavities turned on for three different accelerated ions. Synchronous phase is -25°.

An attempt to determine the beam longitudinal emittance was undertaken taking advantage of three time domain devices available after the linac. The parameters of the beam ellipse in the longitudinal phase space can be calculated on the basis of measuring the time spread at three different locations along the transfer line where no acceleration fields are present. Using this method with a $^{20}Ne^{5+}$ beam a 1σ longitudinal emittance between 0.8 and 1.2 keV/u ns was obtained which can be compared with the theoretical value of 1.5 keV/u ns obtained from computer simulations.

CONCLUSION

Two new devices: scattered particle monitor and TOF monitors add to the ISAC-II superconducting linac time domain diagnostics. Both devices were successfully used in the linac commissioning for cavity phasing and energy measurements, energy and time spread and longitudinal emittance measurements.

REFERENCES

[1] R.E.Laxdal, et al., "Commissioning of the ISAC-II superconducting linac at TRIUMF", EPAC'06, Edinburgh, June, 2006, p. 1556.

[2] P.K. Den Hartog et al., "The beam bunching and transport system of the Argon positive ion injector", PAC'89, Chicago, IL, March 1989, p. 545.

NOISE AND DRIFT CHARACTERIZATION OF CRITICAL COMPONENENTS FOR THE LASER BASED SYNCHRONIZATION SYSTEM AT FLASH

Bastian Lorbeer, Jost Müller (TUHH / DESY, Hamburg, Germany)*
Frank Ludwig, Florian Loehl, Holger Schlarb, Axel Winter (DESY, Hamburg, Germany)

Abstract

At FLASH, a new synchronization system based on distributing streams of short laser pulses through optical fibers will be installed and commissioned in 2007. At several end stations, a low drift- and low noise conversion of the optical signal into RF signals is needed. In this paper, we present the influence of photodiodes on the phase stability of the optical pulse streams and investigate the drift performance of the photo-detection scheme for the extraction of the RF signal.

INTRODUCTION

A novel optical synchronisation system based on the generation and distribution of laser pulses in the Free Electron LASer facility in Hamburg (FLASH) at DESY is currently under development [1] and a candidate to overcome the short and long term stability limits given by a conventional RF distribution system [2].

The tight synchronisation requirements at distant tap points for experiments performed with the coherent FEL radiation can be met by locking a Fiber Master Laser to a microwave Master Oscillator (M.O.) and distributing the optical pulse train via fiber links inside the facility [3]. The distributed optical pulses are converted into RF signals using photodiodes. The optical pulse train with a repetition rate of $f_{\text{rep}} = 54\,\text{MHz}$ is generated with an erbium-doped mode-locked stretched pulse laser [4]. Here we investigate the phase noise and phase drift limitations given by the components used for the extraction of the RF signal.

GENERATION OF RF SIGNAL

The optical pulse train generated in an erbium-doped mode locked stretched pulse fiber laser is fed to a photodiode that generates an electrical pulse train with a repetition rate $f_{\text{rep}} = 40.625\,\text{MHz}$ given by the laser. A fourier transform of the electrical pulse train will lead to fourier components equally spaced at the repetition frequency of the pulses. We extract the 32^{nd} harmonic of the pulse train at $1.3\,\text{GHz}$ with a bandpass filter and amplify the signal using a low noise amplifier with a gain of approximately $G = 30\,\text{dB}$. We designate this method as the direct conversion scheme for extracting the RF signal out of the pulse train. The measurement principle is sketched in figure 1.

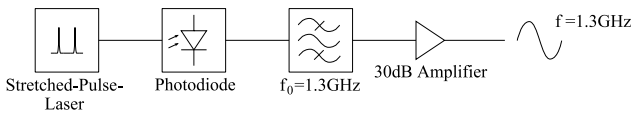

Figure 1: Direct conversion scheme for extracting 1.3 GHz

PHASE NOISE AND INTEGRATED TIMING JITTER

After the extraction of the RF signal from the optical pulse train with the method described above we measure its single sideband phase noise spectral density. We integrate the phase noise in a bandwidth from $f_1 = 1\,\text{kHz}$ to $f_2 = 20\,\text{MHz}$ and obtain the integrated timing jitter by

$$\Delta T_{\text{rms}} = \frac{1}{2\pi f_0}\sqrt{\int_{f_1}^{f_2} S_\phi(f)df}[s]_{\text{rms}} \qquad (1)$$

where $S_\phi(f)$ is two times the measured single sideband phase noise $\mathscr{L}(f)$ [5].

Integrated timing jitter of direct conversion

Experiments have shown, however, that for obtaining a suitable integrated timing jitter performance and enough power for the distribution of pulses in the fiber link an Erbium-Doped Fiber Amplifier (EDFA) between the laser source and $10\,\text{GHz}$ bandwidth photodiodes are inevitable. The measurement setup includes a signal source analyzer to measure the single sideband phase noise of the detection chain. A minimum of phase noise obtained during our investigation is shown in figure 2.

The integrated timing jitter for the direct conversion scheme in a bandwidth from $f_1 = 1\,\text{kHz}$ to $f_2 = 20\,\text{MHz}$ amounts to $\Delta T_{\text{rms}} = 9\,\text{fs}$.

Phase noise contribution of photodiodes

The phase noise limitation of the detection chain photodiode, bandpass filter and low noise amplifier has been experimentally observed to mainly originate in an AM[1] to PM[2] conversion process in the photodiodes. We compared four $10\,\text{GHz}$ photodiodes in their AM to PM characteristics with the setup in figure 3. For approximately $5\,\text{mW}$ of optical power, the diodes are not saturated and show a significantly higher AM to PM contribution (see figure 4) than for higher optical powers. The conversion coefficients

* bastian.lorbeer@desy.de, jost.mueller@desy.de

[1] Amplitude Modulation
[2] Phase Modulation

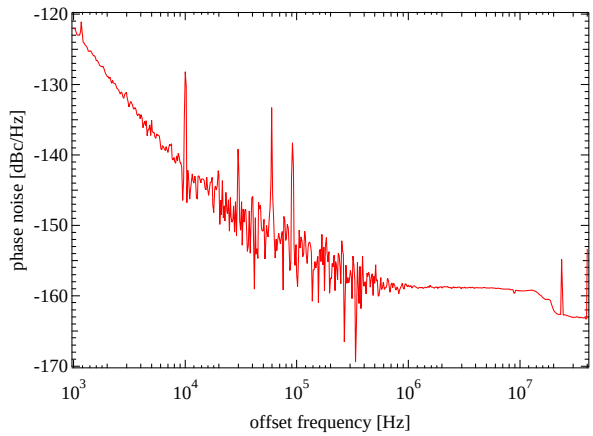

Figure 2: Measured phase noise, integrated timing jitter in a bandwidth from $f_1 = 1$ kHz to $f_2 = 20$ MHz amounts to $\Delta T_{\mathrm{rms}} = 9$ fs

are estimated as a linear fit for power fluctuations between 10 mW and 20 mW. They are summarized in table 1.

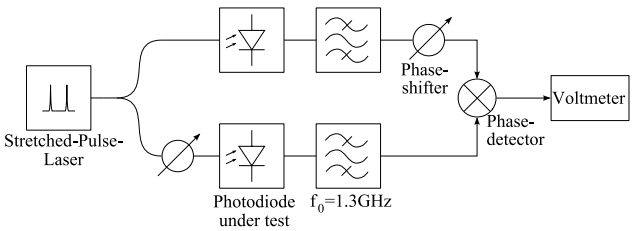

Figure 3: Setup to examine AM to PM conversion of photodiodes

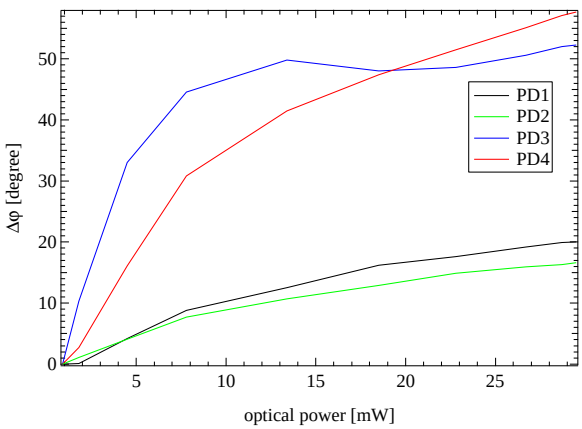

Figure 4: AM to PM characteristics of photodiodes

These photodiodes are investigated concerning their integrated timing jitter performance with a variation of the optical input power, as shown in setup 5. Figure 6 reveals this measurement for photodiode PD3 for different pump powers of the EDFA. The integrated timing jitter dependence of the EDFA gain is neglectible compared to the photodiodes but has a minimum value for an optical power of approximately 12.5 mW showing consistency with a minimum for the AM to PM conversion coefficient for the same optical power (see figure 4). The RF power for the extracted 1.3 GHz signal varies as the integrated timing jitter causes a change of the power in the sidebands.

Photodiode	$\frac{\Delta\phi}{\Delta P_{\mathrm{opt}}}\left[\frac{^\circ}{\mathbf{mW}}\right]$	$\frac{\Delta T}{\Delta P_{\mathrm{opt}}}\left[\frac{\mathbf{ps}}{\mathbf{mW}}\right]$
PD1	1.6	3.4
PD2	0..0.9	0..1.9
PD3	0.7	1.5
PD4	0.5	1.1

Table 1: AM/PM conversion coefficients

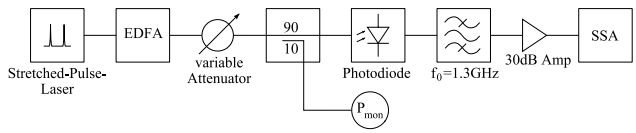

Figure 5: Photodiode phase noise measurement setup with variation of optical power

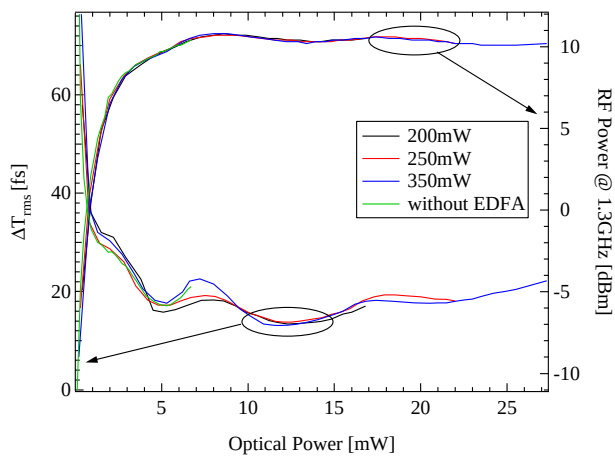

Figure 6: Integrated timing jitter and RF power of photodiode PD3 vs. optical power for different EDFA pump-powers at 980nm

PHASE DRIFT PERFORMANCE OF PHOTODIODES

For the determination of the phase drift contribution of the photodiodes in the direct conversion detection process described above, we make defined temperature steps on a photodiode and observe its temperature dependent characteristics in comparison to a reference photodiode which is stabilized in temperature (figure 7). The phase difference of the amplified 1.3 GHz signals is measured with a phase detector and recorded with a high resolution data logger. The recorded voltage fluctuations ΔV are converted to phase fluctuations $\Delta\phi$ by the conversion gain K_ϕ of the phase detector

$$\Delta\phi = \frac{\Delta V}{K_\phi} \tag{2}$$

and then related to the period T_0 of the carrier with frequency $f_0 = 1.3\,\mathrm{GHz}$[3].

$$\Delta T = \frac{\Delta\phi}{360^\circ}\, T_0 \tag{3}$$

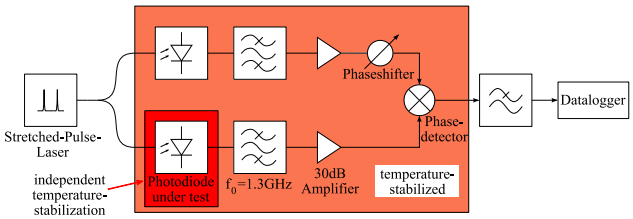

Figure 7: Setup for drift determination of 10 GHz bandwidth photodiodes

To minimize the influence of the temperature dependent characteristics of all devices on the overall phase drifts, everything but the photodiode under test has been mounted on an aluminum plate that is kept at a constant temperature of around $36°C$ with a temperature stability of $0.1°C$ indicated by the outer red box in figure 7. Our measurement limit of the setup when stabilizing all components in temperature is in the range of $50\,\mathrm{fs_{pp}}$ and is shown in figure 8.

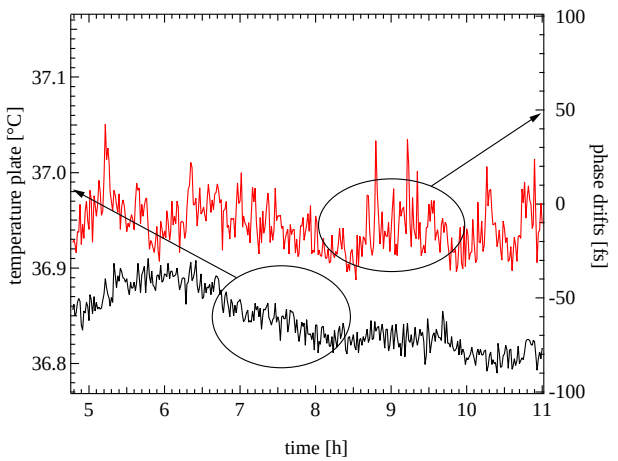

Figure 8: Measurement limit for phase drift characterization of photodiodes

With an independent temperature stabilization (inner red box in figure 7), we provide temperature steps on the photodiode under test and extract the temperature dependent phase drift coefficients in $\left[\frac{\mathrm{fs}}{°\mathrm{C}}\right]$ for each temperature step. The temperature coefficients for the measurement shown in figure 9 vary between 128 $\frac{\mathrm{fs}}{°\mathrm{C}}$ and 224 $\frac{\mathrm{fs}}{°\mathrm{C}}$.

[3] T_0 is the period of the carrier with a frequency of f_0

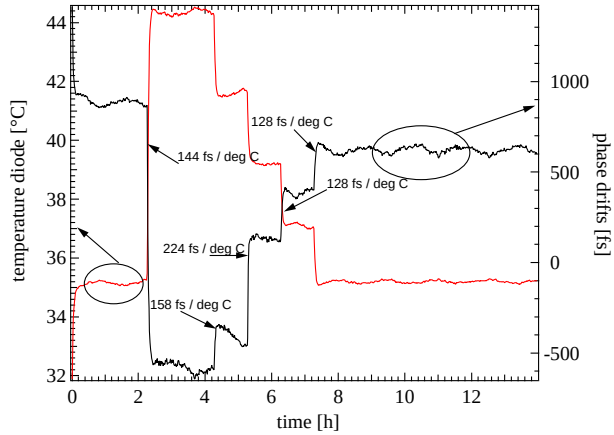

Figure 9: Phase drift dependence of photodiode

OUTLOOK

We have shown that the direct conversion scheme is limited by the performance of the photodiodes. This limitation is 10 fs for the integrated timing jitter and 150 $\frac{\mathrm{fs}}{°\mathrm{C}}$ for the phase drifts. The phase noise contributions of this detection method have been shown to originate in an AM to PM conversion process that either could be overcome with amplitude stabilization of the optical pulses or an alternative conversion method independent from amplitude fluctuations [6]. The noise contribution of the EDFA is significantly lower than the phase noise limitations given by our measurement methods and should be figured out with optical measurement methods.

A high degree of correlation between the photodiode temperature and the phase drifts is observable. However, repetitive phase drift measurements show a big variance of the temperature dependent phase change. A miniaturization and improved temperature stabilization for the extraction of the RF signal to overcome the RF phase drifts due to temperature changes in the detection chain is currently in preparation.

REFERENCES

[1] J. Kim et. al., "An integrated femtosecond timing distribution system for XFEL's", EPAC 2006, Edinburgh, UK, 2006

[2] K. Czuba et. al., "Master Oscillator Design For The VUV - FEL Project", MIKON conference 2006

[3] F. Loehl et. al., "First prototype of an optical cross-correlation based fiber-link stabilization for the FLASH synchronization system," this Conference, Venice, Italy, 2007

[4] A. Winter et. al., "High-precision laser master oscillators for optical timing distribution systems in future light sources", EPAC 2006, Edinburgh, UK, 2006

[5] M. Thumm et. al., "Hochfrequenzmesstechnik. Verfahren und Meßsysteme", B.G. Teubner Stuttgart, September 1998, ISBN 3519163608

[6] J. Kim et. al., "Balanced optical-microwave phase detectors for optoelectronic phase-locked loops", Optics Letters, December 2006, Vol.31, No.24

MECHANICAL DESIGN OF THE INTENSITY MEASUREMENT DEVICES FOR THE LHC

D. Belohrad*, P. Odier, S. Thoulet, S. Longo
CERN, CH-1211 Geneva 23, Switzerland

Abstract

The intensity measurement for the LHC ring is provided by eight current transformers (2×DCCT, 2×FBCT per beam). The measurement resolution of $1\mu A_{rms}$ at 1s average for the DCCTs and $\pm 10^9$p in 25ns for the FBCTs is required. Such constraints call for low noise electronics and a compact magnetically shielded mechanical design. Correct integration of these devices into the vacuum system also requires the vacuum chambers equipped with the non-evaporable getter (NEG) film. The NEG is activated by heating the vacuum chamber to $200\,^{\circ}$C and more. Such temperatures affect the structure of the magnetic materials, which form the base part of the intensity measurement devices, and degrade their performace. A cooling circuit is needed. Due to the mechanical constraints, the cooling circuit, as well as heating element must form an integral part of the design. The aim of this paper is to present the solutions to these problems and discuss the mechanical construction of the DCCTs and FBCTs currently being installed in the LHC.

INSTALLATION OVERVIEW

The intensity measurement for the LHC ring is provided by eight current transformers. There are two DC current transformers (DCCT) and two fast current transformers (FBCT) installed on each vacuum chamber of the circulating beam. In addition, two supplementary FBCTs are installed on each beam dump transfer line. While the FBCTs for the dump and circulating beam are the same, the installation of the dump transformers differs from the installation of the ring transformers. The difference is given by the lack of the NEG coating and water cooling circuitry for the dump transformers.

The transformers for the ring measurements are installed in the LHC IP4, at the right side, approximately 160 metres away from the central point. The installation (fig. 2) consists of a 12 metres long girder which is used in common by the DCCTs and FBCTs. The monitors are fixed on the support in four sections. Adjacent sections are connected via a standard 80/84mm vacuum chamber. Each section is composed of two monitors of the same type and their vacuum chambers, installed symmetrically around the fixed point flange. The fixed point flange assures longitudinal fixation of the two vacuum chambers. In order to suppress mechanical forces acting on the ceramics and originating from baking and alignment, bellows are installed at both extremities of each section. Reduction of the impedance mismatch is achieved by RF fingers installed at the interior of each bellow.

Such setup of the monitors has several advantages. Having common design of the support, fixed flanges and the vacuum chambers reduces design complexity and cost. The proximity of the DCCTs and FBCTs gives us the possibility of cross-calibrating the two equipments. It also allows the arbitration of the intensity values sent to the machine protection system. By connecting each monitor from the section into a different VME crate one can improve the availability of the measurement while keeping the cost reduced.

THE VACUUM CHAMBER

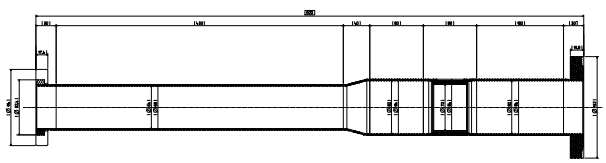

Figure 1: Common vacuum chamber for the DCCTs and FBCTs. Long parts are made of OFS copper, brazed parts are made of OFE copper electron welded to the OFS parts. There are 4 brazing parts: two at the extremities of the ceramics and one per each flange.

Due to the presence of the NEG coating and need for its activation, both measuring systems must be equipped by cooling circuitry protecting the transformer cores against excessive temperatures during bake-out. This, together with the requirements for the compact size lead to the design of the vacuum chamber having a partially reduced diameter, as seen on the figure 1. The reduction from standard diameter of 80/84mm to 64/68mm introduces a minimal risk with respect to the increase of the radiation and permits us to install a heatsink and heating element over the reduced diameter, still keeping the internal diameter of the toroidal transformer minimal with respect to the standard vacuum chamber diameter. The conical section between the standard and reduced diameter eliminates sudden longitudinal impedance changes. The slope of the section is 11°. Such a vacuum chamber configuration is satisfactory for the DCCTs which can operate with the ceramics outside of the measurement device. However, the FBCTs need to be installed over the ceramics gap during the measurement in order to assure the shortest possible RF path for the wall image current. This requires that the FBCTs are installed over the cooling tank during bake-out, and moved to the measurement position once baking is finished. Due to this

* david.belohrad@cern.ch

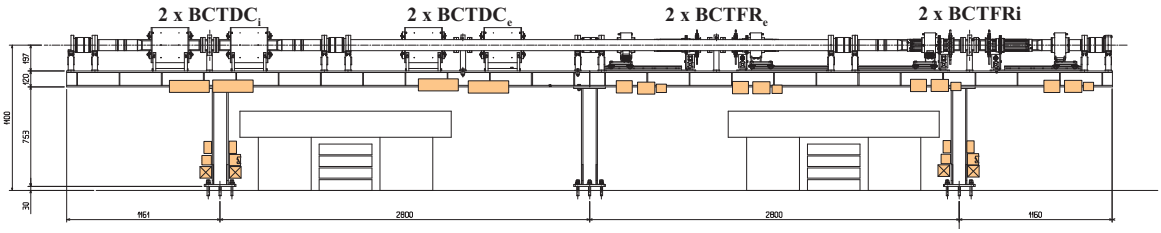

Figure 2: Installation of the intensity measurement devices in the LHC ring. There are four sections of the transformers, each section contains two transformers connected by fixed flange.

fact any mechanical obstacles, preventing the FBCTs from moving must be avoided.

The vacuum chamber is made of OFS copper. This eliminates the need for diffusion of supplementary copper layer at the interior of standard INOX vacuum chamber. The connection of the ceramics to the INOX vacuum chamber was replaced by brazing of the vacuum chamber directly to the ceramics by using OFE copper collars . The ceramics (WESGO Ceramics, type AL300) is metallised by 25μm MoMn at the brazing places. The diffusion of the resistive layer (TiO_2) on the interior of the ceramics was necessary in order to avoid the deposit of the charges, and to dump resonances caused by the volume of the FBCT outer shell. For the DCCTs the nominal resistance of 10kΩ was chosen. The resistance of 25Ω for the FBCTs was found to be optimal with respect to ringing of the FBCT output signal. Results of the measurements are depicted at figure 3.

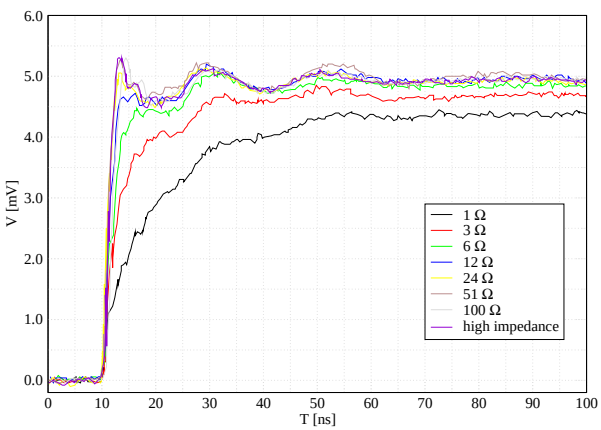

Figure 3: Time-domain measurement of the FBCT output signal for different resistive load on ceramic gap.

DC CURRENT TRANSFORMERS

The principal layout of the DCCT is shown at figure 4. The device is permanently installed over the cooling tank (pos. 1). Physically the cooling tank is built of two copper halve-cylinders to which the cooling pipe is brazed. These cylinders form 2 separate water circuits per DCCT. The internal section of the cooling pipe is 4mm^2, which permits water flow of more than 2l/min. By experiments it

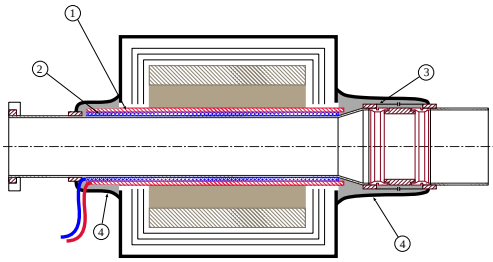

Figure 4: The sketch of the DCCT transformer.

was found that the flow of 1l/min is satisfactory to keep the temperature in the inner parts of the DCCT shell well below 40°C when using 200°C baking temperature. The baking layer and corresponding isolation is permanently fixed on the vacuum chamber (pos. 2) as well. In order to ensure correct conditions during the bakeout temperature and water-flow detectors are installed and connected to the interlock of the heating system.

The internal diameter of the DCCT is 114mm. It permits to keep the mechanical parts of the DCCT isolated from the vacuum chamber and cooling elements, and also allows to dismantle the vacuum chamber and DCCT separately. This is assured by usage of demountable flanges at reduced diameter side of the vacuum chamber. The transformer cores are custom built, by using Nanophy magnetic material from Mecagis-Imphy, installed into provided fiber glass supporting rings.

The magnetic protection of the transformer cores is formed by three Mu-metal layers. In order to increase the magnetic permeability of the material after machining the layers were temperature treated [1]. This is needed due to the loss of permeability during machining disrupting the alignment of the material's grain. The Mu-metal was annealed at 1080°C during 1 hour under vacuum and let to be naturally cooled down. The physical protection of the DCCTs is realized by a thick Armco layer serving as external housing. It serves also to prevent the Mu-metal shielding against the saturation in case of high magnetic field perturbation. The Armco material was temperature treated at 980°C during 1 hour in vacuum. Temperature controlled cool-down of 100°C per hour was necessary. Sand blasting and cadmium coating followed the thermal treatment in order to protect the Armco housing against rust. A cadmium

layer thickness of 20μm was chosen.

The RF component of the wall image current passes through the DCCT via a series of capacitors placed around the ceramic gap (position 3 at figure 4). The LF component passes via the Armco shielding connected to the vacuum pipe by copper braids (4). The modulation frequency of 200Hz was chosen in order to ensure the compatibility with previous installation. The value of the by-pass capacitor can be up to 1μF.

FAST CURRENT TRANSFORMERS

The demand of placement of the FBCTs over the cooling tank during baking results in complex mechanical design shown at figure 5. The monitor itself (pos. 1) is fixed by rolling wheels to the HEPCO rail (2). The connection assures smooth and easy realignment of the transformer when moving from one position to the other one. It is also used to fine adjust the vertical alignment of the device with respect to the beam. During the bakeout the transformer is placed

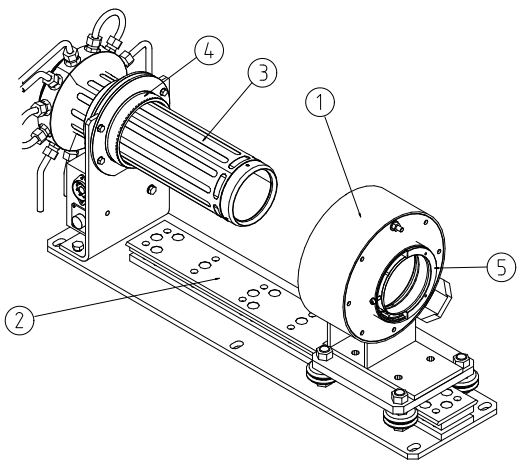

Figure 5: Mechanical design of the FBCTs used for the measurement in the LHC rings.

over the cooling tank (3) and pushed to the switch contact (4) realized by the flange made of fiber glass equipped with RF contacts. The RF contacts are connected to the bakeout interlock system and do not permit baking when the transformer is not correctly placed on the cooling tank. The cooler is composed of three independent parts, allowing water flow of more than 4l/min per part. It is connected via water flow meters into the LHC general water distribution system.

During the measurement the transformer is fixed by four half-collars (5) to the vacuum chamber. In addition to the mechanical fixation they serve also as the RF signal path between the vacuum chamber and external shielding of the transformer. To assure good electrical contact the collars are made of copper covered by a 10μm thick silver layer. The collars are mounted between the vacuum chamber and the transformer shell by using RF contacts. At the place of the connection the vacuum chamber is treated with silver painting. As in the case of DCCTs, the outer shell of the FBCTs is made of Armco, however instead of cadmium treatment the shell was galvanically silvered. The thickness of the silver layer is 10μm.

The monitor itself is composed of two independent transformer cores covering different frequency ranges. The sketch of arrangement is shown on the figure 6. The high-frequency core (1) is 1:40 turns low-droop Bergoz transformer, covering the frequency range from 400Hz to $\approx$1GHz. The low-freqency core (2) is made from Vitroperm 500F and equipped with 120 turns. Its low-frequency cut-off of 22Hz provides us with additional information which will be used in the recovery of the DC component of the measured beam signal. Mechanical fixation of the two cores is provided by a 5mm thick fiber glass layer (3) on which the calibration turn circuit (4) is fixed . The calibration circuit is realized by a set of resistances and microstripes distributing the calibration current equally into 8 parallel calibration turns, appearing at the input as a 50Ω single calibration turn. To ensure good impedance characteristics the calibration circuit is made of 0.3mm thick RF material Neltec NY9220.

The electronic part of FBCTs is inserted into the Mu-metal shell (5) protecting the transformers against external low-frequency magnetic fields. The annealing process was applied as in the case of DCCTs. The entire construction is placed into the Armco housing and centered by system of a 3mm thick printed circuit boards (6). The centering boards are copper plated at both sides and electrically connected to the Armco housing. Position (7) in the figure 6 shows the placement of the RF half-collars already mentioned.

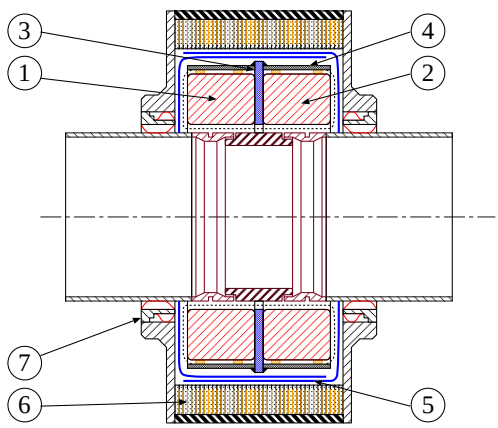

Figure 6: The sketch of the FBCT monitor for the LHC

REFERENCES

[1] P. Odier, “Proposal for three Beam Current Transformers for CNAO”, AB-Note-2004-067, CERN, Swizerland, September 2004.

MEASUREMENT OF BUNCH LENGTHENING EFFECTS USING A STREAK CAMERA WITH REFLECTIVE OPTICS

T. Obina* and T. Mitsuhashi
Photon Factory, High Energy Accelerator Research Institute (KEK), 305-0801 Japan.

Abstract

For precise measurements of the bunch length, the incident optics of a streak camera should be free from optical path differences induced by chromatic effects. A reflective optics system was designed and installed on a camera: its performance was compared with the original refractive optics. Since reflective optics can employ white light of the synchrotron radiation, bunch length measurements at very low beam currents can be performed. We measured the bunch length as a function of the beam current and estimated the longitudinal coupling impedance of the PF-Ring.

INTRODUCTION

A streak camera is a powerful tool for the instantaneous measurement of the bunch length. It converts the temporal structure of the input light into a spatial distribution. For the bunch length measurement using synchrotron radiation (SR), visible SR is focused to form an image of the beam profile on the entrance slit of the streak camera. The optical relay system transfers the image of the slit onto the photocathode of the streak tube. The built-in optical relay system comprises a compound lens system. Usually, streak cameras are used in the laser applications, where quasi-monochromatic incident light is used. Normally, a monochrometer, such as the band-pass filter, is used for bunch length measurements in order to reduce dispersion effects (e.g., chromatic aberrations.) in the lens system. However, the band-pass filter will reduce the intensity of the incident SR by more than 1/10. This loss in the incident intensity often introduces difficulty in measuring the bunch length for very low currents. To avoid this loss in the incident intensity, we designed and installed an optical relay system with reflective optics with no dispersion effects such as chromatic aberrations. In addition, Newtonian objective optics is employed to form the first image of the beam profile onto the entrance slit. By using these reflective-optics systems, we can measure the bunch length down to 0.1 mA. The results of the bunch length measurement are described in this paper. Bunch lengthening in the PF-ring is also discussed.

REFLECTIVE OPTICS

Streak Camera with Offner-type Relay System

We used a Hamamatsu model C5680-01 streak camera equipped with a dual sweep unit. The streak camera converts the temporal information of the SR into two-dimensional spatial information on a CCD. Fast scan is performed along the vertical direction on the screen with the highest resolution of 2ps. By using the dual time-base unit, a slow scan is performed along the horizontal direction; the bunch shape in successive revolutions can be measured.

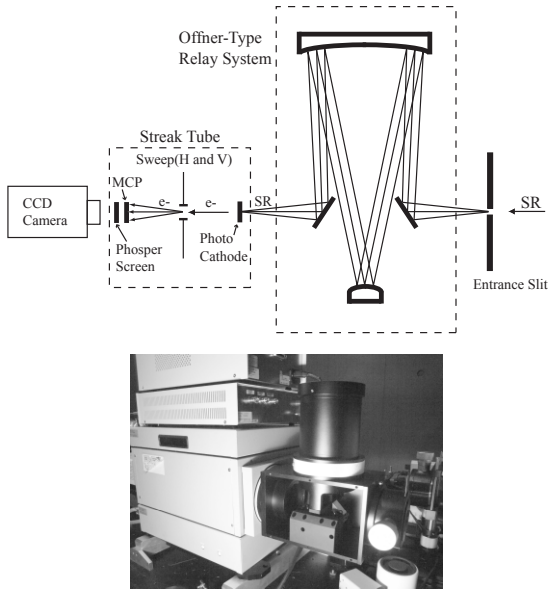

Figure 1: Schematic drawing (top) and a photo (bottom) of the Offner's relay system installed in the streak camera. (The figure is not to scale)

In front of the streak tube, an optical relay system is employed to form an image of the entrance slit onto the photocathode of the streak tube. Conventional streak cameras use lens systems with refractive optics, which induce certain dispersive effects (e.g., optical path differences (OPD)) in the bunch length measurement. On the other hand, reflective optics is free from dispersive effects because the light does not pass through the inside of glass material. The Offner's relay system, comprising two nearly concentric spherical mirrors, yields images with one-to-one magnification at a high resolution and low distortion [1, 2]. We designed and constructed an Offner-type relay system for the streak camera, as shown in Fig.1. A photograph of the system is also shown in this figure.

Effect of Incident Optics

The dispersion effects were compared by replacing the incident optics of the streak camera. Monochrometers such as band-pass filters were not used in the measurement. Figure 2 shows the bunch lengths measured by using reflective optics and refractive optics. Both these measurements were performed by storing a single bunch in the ring. The symbol in the figure denotes the average

*takashi.obina@kek.jp

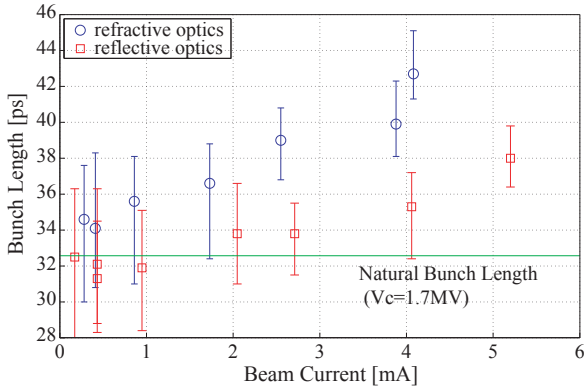

Figure 2: Bunch length difference with refractive optics and reflective optics. At low beam currents, the bunch length is close to its natural value obtained in the reflective optics measurement.

value of the bunch length, and the error bar shows the minimum and maximum in several measurements. The natural bunch length is also shown in the figure. It is evident that the refractive optics exhibits a systematically larger bunch length as compared to reflective optics. With regard to the reflective optics, the measurement shows a good agreement with the calculated natural bunch length. For small beam currents, the intensity of the SR is also weak. As a band-pass filter decrease the intensity more than 1/10, the measurement for small beam currents became difficult. Reflective optics does not need a monochrometer and hence the precise measurement at very low beam currents becomes possible.

BUNCH LENGTHENING MEASUREMENT

Optical Layout

The optical layout of the bunch lengthening measurement is shown in Fig.3. To avoid the heat load because of the hard X-ray components of SR, a water-cooled mirror made of beryllium (Be) reflects the visible

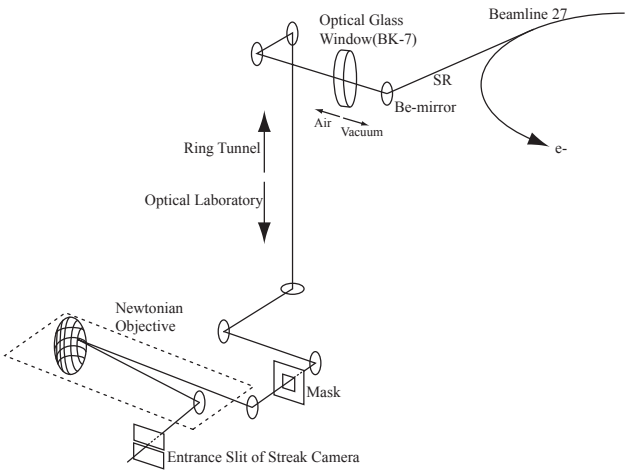

Figure 3: Optical layout of the bunch length measurement. The optical laboratory is located at the underground level of the storage ring.

light components of the SR. The light is extracted to the atmosphere pressure environment through a 20mm-thick quartz window and fed to the optical laboratory underneath the storage ring tunnel. The distance from the source point to the optical bench is approximately 8m, and the optical path is surrounded by pipes and boxes in order to avoid path fluctuations caused by air turbulence.

Usually, a converging lens is used to form a focus image of the beam profile on the entrance slit of the streak camera. The Newtonian objective, indicated as the dotted box in Fig.3, is used to avoid the dispersion effect of lens glass. The focal length of the parabolic mirror is 800 mm. The Newtonian objective system is used to create a focusing image directly on the entrance slit of the streak camera.

The bunch lengths at several cavity voltages were measured and the results are shown in Fig. 4. The beam currents were selected to be around 0.7 mA to avoid the bunch lengthening. The red line in the figure shows the theoretical calculation of the natural bunch lengths, which is in good agreement with the measured vaule.

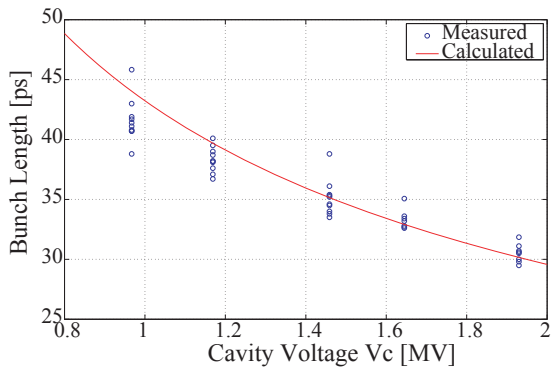

Figure 4: Bunch length as a function of cavity voltage at a beam current of 0.7mA. The solid line represents the calculated natural bunch length.

Potential Well Bunch Lengthening

In the low beam current region, the streak camera image exhibits a Gaussian distribution in the longitudinal z direction. Along with an increase in the beam current, the bunch shape became asymmetric: it can be characterized as[3],

$$I(z) = I_0 + I_1 \exp\left\{-\frac{1}{2}\left(\frac{z-\bar{z}}{[1+\mathrm{sgn}(z-\bar{z})A]\sigma}\right)^2\right\},$$

where I_0 and I_1 denote the pedestal and peak of the distribution, respectively. The term $[1+\mathrm{sgn}(z-\bar{z})A]$ is the asymmetric factor that characterizes the bunch shape, σ is the root-mean-square bunch length and $\bar{z}$ is the mean. The bunch length as a function of the beam current is shown in Fig.5. The bunch shape had tails longer than the heads, and the asymmetry factor A in the above mentioned equation increased with the beam current. This is caused by potential well distortion induced by the resistive impedance.

The potential well effect caused by the beam duct is estimated using simple model in ref. [4, 5], and the fitted

result is shown as the solid line in Fig.5. Although the model is simple, the fitted result is not bad because the calculated natural bunch length in the PF-Ring is 22 mm in the FWHM, which is not too short as compared to the aperture of the vacuum duct. The typical size of the duct is 38 mm in height and 90 mm in width[6].

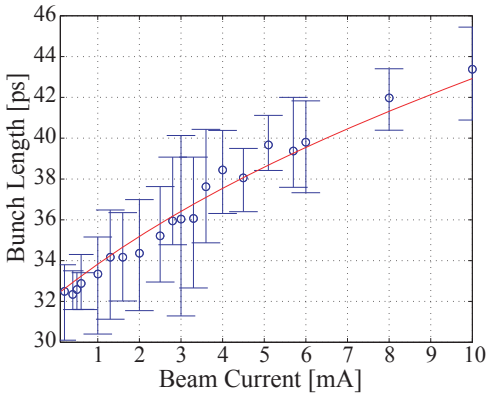

Figure 5: Bunch length at low beam currents. The solid line shows the fitted result with the potential-well distortion model.

Microwave Instability

In the high beam current region, namely, above the threshold current of microwave instability, the bunch shape starts to deviate from neither the Gaussian nor the asymmetric Gaussian shape. At the same time, the bunch shape became unstable and the change in the bunch length became large. We used the FWHM bunch length and calculated the standard deviation divided by the factor 2.355. Although this factor has no meaning when the bunch shape is not like the Gaussian distribution, we use this value as a rough estimation of the bunch length.

When the longitudinal broadband impedance exhibits frequency dependence with the form $Z(\omega) \propto \omega^a$, Chao-Gareyte scaling law holds above the threshold, which states that the bunch length is proportional to the power of the scaling parameter ξ as[7,8]

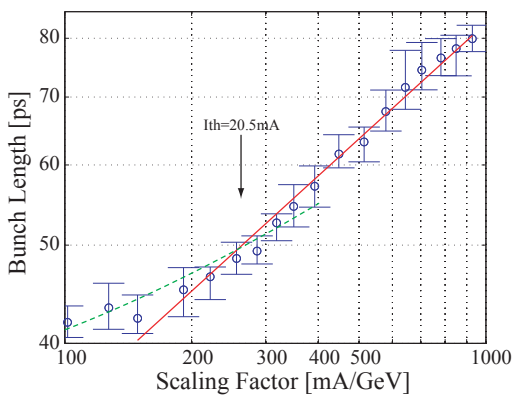

Figure 6: Bunch length above the threshold. The solid line and dotted lines denote the calculation using the scaling law and potential well distortion model, respectively.

$$\sigma \propto \xi^{1/(2+a)} = \left(\frac{\alpha I_b}{E \nu_{s0}^2} \right)^{1/(2+a)},$$

where I_b denotes the beam current, α the momentum compaction factor, E the beam energy, ν_{s0} unperturbed synchrotron tune, respectively. The result of fitting is shown with solid line in Fig.6, and the parameter a is determined to be 0.64.

Impedance Estimation

From the potential well model and scaling estimation, the threshold current of the microwave instability was determined to be 20.5 mA. The corresponding coupling impedance was to be approximately 0.5 Ω [5,9].

In 2005, the PF carried out major upgrade. The project aimed to introduce four new straight sections for short-gap undulators, and to enlarge the length of the existing straight sections[10]. Before the upgrade, the threshold current for microwave instability was 12 mA, and corresponding impedance was approximately 1.1 Ω. Threshold current has been improved because the old vacuum components such as unshielded bellows and small cavity-like structure in vacuum flanges have been renewed. We also plan to measure a change in energy spread to compare to this result.

CONCLUSION AND FUTURE PLAN

Incident optics with reflective optics was designed and installed for the streak camera. It is confirmed that dispersion effects induce a systematic error in ordinal refractive optics with white light. Reflective optics can use white light and is effective for measurements in small beam current. This incident optics is already used in the streak camera of KEK B-Factory and PF-AR.

The longitudinal coupling impedance of each vacuum component can be estimated from calculation using MAFIA or some computer codes: this estimation is in progress. The threshold of the microwave instability was estimated from the bunch length measurement, and the preliminary estimation of the longitudinal impedance was performed. Another Be-mirror will be installed in beamline 21 of the PF-ring. Measurement of the energy spread using two optical monitors will be done in 2007.

REFERENCES

[1] T. Mitsuhashi and M. Tadano, PAC'03, (2003) 2506
[2] L. Mertz, "Excursions in Astronomical Optics", 1996, Springer.
[3] O. Holtzapple, et al., Phys. Rev. ST Accel. Beams, **3**, 034401 (2000) .
[4] B. Zotter, CERN/ISR-TH/78-16 (1978).
[5] T. Nakamura, et al., PAC'91, (1991) 440 .
[6] T. Obina, et al, DIPAC 2005, (2005) 196.
[7] K. Bane, et al, SLAC-PUB-8846 (2001).
[8] A. Chao and J. Gareyte, Particle Accel., **25**(1990)229.
[9] A. Hofmann and J. Maidment, LEP note 168(1979).
[10] T. Honda et al., PAC2005, (2005)2678.

FOCUSING OF OPTICAL TRANSITION AND DIFFRACTION RADIATION BY A SPHERICAL TARGET

L.G. Sukhikh*, G.A. Naumenko, and A.P. Potylitsyn
Tomsk Polytechnic University, Tomsk, Russia
J. Urakawa and A.S. Aryshev
KEK, Tsukuba, Japan
S. Boogert and P.V. Karataev
John Adams Institute at Royal Holloway, University of London, Egham, UK

Abstract

For the first time the focusing effect of optical transition and diffraction radiation generated by electrons with the energy of 1.28 GeV has been observed experimentally. A comparison of angular distribution of detected radiation was made for flat and spherical targets. It was shown, that application of such targets allows increasing the spectral-angular density in the focus of the sphere without any additional optical devices.

INTRODUCTION

Transition (TR) and diffraction (DR) radiation are widely used for an electron beam diagnostics. In the experiment [1] the authors have demonstrated the measurements of the transverse size of an electron beam via optical TR (OTR) imaging technique with the resolution of order of 2 μm. In the experiment [2], the transverse beam size was measured using optical DR (ODR) with the accuracy of order of 14 μm. But the advantage of the ODR technique is related to a possibility to perform an almost noninvasive beam diagnostics. Besides it is also possible to measure longitudinal beam size using coherent TR or DR. Authors of the paper [3] have focused coherent TR generated by a bunch with length of ~1mm onto an electro-optic crystal (EOC) using an external optical device. Under CTR field EOC characteristics were changed. It allowed to measure the bunch duration by monitoring the polarization variation of a stable laser. Sensitivity of the Electro-optic technique might be improved by increasing the CTR photon density on the EOC.

Recently we proposed to use focused coherent diffraction radiation (CDR) for soft x-ray generation via inverse Thompson scattering process [4].

In applications mentioned above there is one serious problem – so called "pre-wave zone effect", which becomes significant when the distance between target and detector is shorter than $\gamma^2\lambda$ [5], where γ is the charged particle Lorentz-factor and λ is the DR wavelength. Because of this effect the angular distributions of TR and DR become broader and the spectral-angular radiation density decreases. Those two facts seriously complicate the use of TR and DR for different applications.

The electro-magnetic field of an ultra-relativistic particle can be considered as a set of plane waves (in other words the behavior of the virtual photons of the particle field is similar to the behavior of real photons). That is why some of the present paper authors proposed [6,7] to use paraboloidal targets for TR (DR) generation in order to focus TR (DR) on a detector.

* Leonidus_ii@mai.ru

EXPERIMENTAL SETUP

In order to verify this approach we carried out an experiment at KEK-ATF (Accelerator Test Facility). The experimental setup is shown in Figure. 1. It has been installed in the diagnostics section of the KEK-ATF extraction line [8]. The extracted beam parameters in the vicinity of the target chamber during the experiment are listed up in Table 1.

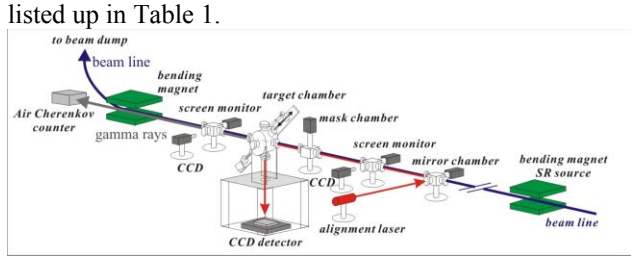

Figure.1 Experimental setup

Table 1. Beam parameters at the target chamber

Energy	1.28 GeV (γ=2500)
Bunch population	$0.9 \cdot 10^{10}$
Bunch repetition	1.56 Hz
Vertical beam size	σ_y=29.35±1.1 μm
Horizontal beam size	σ_x <150 μm

The target chamber has a very precise target stage actuator with linear movement accuracy better than 0.5 μm. The target chamber allows to install two targets. A 10μm thick tungsten wire was also installed in the target chamber, and the vertical beam size mentioned in the Table 1 has been measured using this wire. There was no possibility to measure the horizontal beam size in the target chamber directly. In the Table 1 the horizontal beam size was predicted by the SAD code [9].

The targets are very important parts of the experiment. Even a small deformation of target may cause a significant distortion of the ODR distribution. A flat target was a 300 μm thick gold-coated silicon wafer of 7×9 mm dimensions [2]. Instead of a paraboloidal target we used a spherical one. It is well-known that if the radiation spot dimension on the sphere surface is much smaller than its radius, the sphere can be approximated by a paraboloid. The spherical target was an aluminized

glass segment with transverse dimension of 15×7.5 mm and 500 mm focus. Roughness of the target surfaces was less than 150 nm. Both targets were mounted in the target chamber with 45 deg to the beam trajectory. The targets installed allowed both OTR and ODR measurements. That is why the position of the target with respect to the electron beam is important. Measuring OTR one must be sure that there is no edge effect. Measuring ODR one should precisely know the impact-parameter (the shortest distance between the target edge and the electron trajectory). An air Cherenkov counter was used to measure the bremsstrahlung photons generated when the electron beam interacted with the target. The dependence of the detector response versus target position (see Figure. 2) allowed us to define the impact-parameter [8]. The air cherenkov signal dependence for single electron has a form shown by the dashed line in Figure.2. The point where this linear fit crossed abscissa is assumed to be the point of zero impact-parameter. Because of nearly Gaussian distribution of the electrons in vertical direction at the point of zero impact parameter half of the beam interacted with the target directly. The solid curve in the Figure.2 shows single electron dependence convoluted with Gaussian distribution (σ_v= 29 μm).

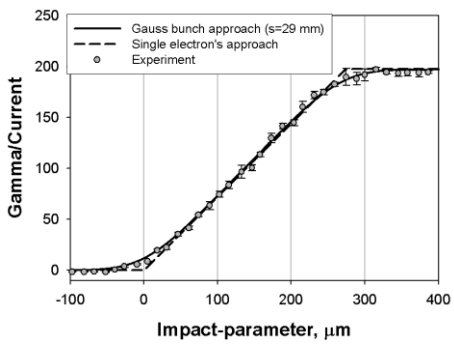

Figure 2. The dependence of air Cherenkov counter signal vs. impact-parameter (points); single electron approach (dashed line); Gauss bunch approach (solid line)

The optical system consisted of a polarizer, optical filter and highly sensitive cooled CCD-camera (Alta E4000). The main parameters of the CCD are listed-up in Table 2.

Table 2. CCD-camera characteristics

CCD	Kodak KAI-4020M
Pixel size (micron /γ^{-1})	7.4×7.4 / 0.04×0.04
Imaging area (mm / pixels)	15.15×15.15 / 2048×2048
Quantum efficiency Peak (500 nm)	55%

The high quantum efficiency of the CCD-camera along with high bunch population allowed to carry out single-shot measurements.

The detector was installed at a distance of L=440 mm, which corresponds to 0.14 $\gamma^2\lambda$ (extreme pre-wave zone) for $\lambda = 500$ nm. A laser system consisting of a laser focusing system, a vacuum mirror, and two screen monitors was used for optical system alignment. The accuracy of this system was better than 0.4 mrad [8].

The ATF extraction line contains many different magnetic devices, which may lead to appearance of synchrotron radiation (SR) background. To avoid the SR contribution a mask has been installed half a meter upstream of the target to cut the SR off. The mask itself was a ceramic plate with a 1×2 mm hole in the center of it [10-11].

EXPERIMENTAL RESULTS

The OTR angular distributions of the vertical polarization component without optical filters from the both targets were measured. The theory predicted that for the experimental conditions OTR distribution from the spherical target would be almost two times narrower than from the flat one (the focusing effect). The measured distributions of OTR vertical polarization components of both targets are shown in Figure.3.

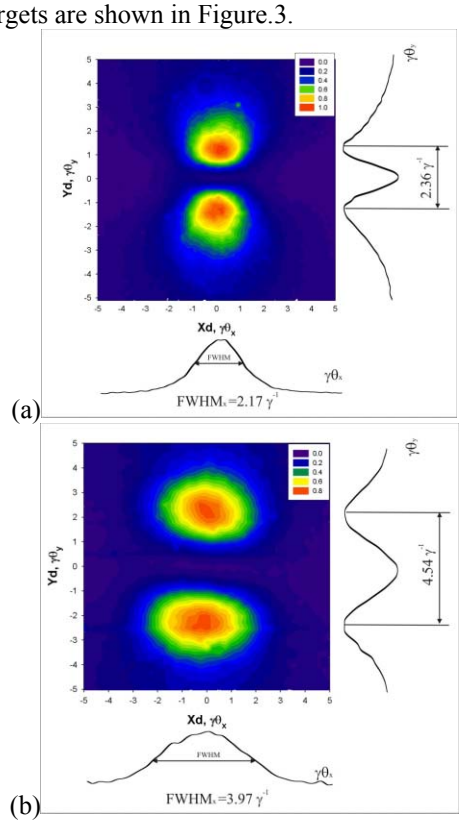

Figure 3. (a) Three-dimensional distribution of the OTR vertical polarization component from the spherical target. (b) – the same from the flat target. Solid lines represent the projections.

Two-dimensional OTR distributions along the vertical (Yd) direction (for Xd=0) are shown in the Figure 4 by the gray circles for the spherical target, and for the flat target – by the open squares. The theoretical predictions for the spherical target are shown in the Figure 4 by a solid line and for the flat target – by a dashed line. The estimations were made for wavelength λ=550 nm.

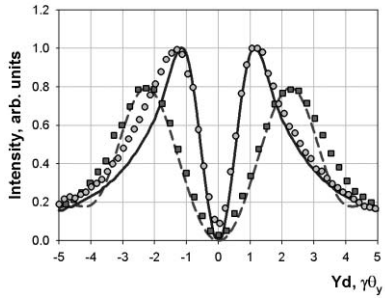

Figure.4. The two-dimensional distributions along Yd direction (for Xd=0) measured from the spherical target (gray circles) and from the flat one (dark gray squares), and calculated distributions: the spherical target – solid line, the flat target – dashed line.

From the Figure.4 one can see that OTR angular distribution from the spherical target is narrower than from the flat one. The interpeak distance of OTR distribution from the spherical target is 2.36 γ^{-1}, and from the flat target – 4.54 γ^{-1}. The angular distribution from the spherical target in the pre-wave zone is very similar to the far-field zone distribution with well-known inter-peak distance of 2 γ^{-1} [7,8].

(a) (b)

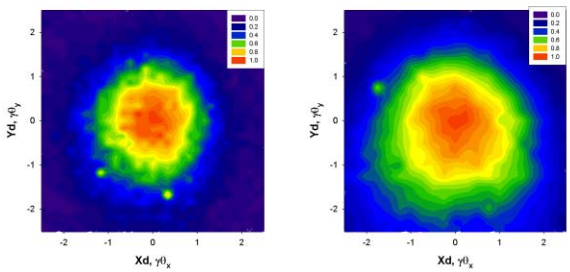

Figure 5. (a) Three-dimensional distribution of the ODR vertical component from the spherical target. (b) – the same from the flat target. Impact-parameter h = 45 μm. Distributions were normalized on maximum

The ODR angular distributions of the vertical polarization component without optical filters from both targets have also been measured. Three-dimensional distributions of the ODR vertical component from the spherical target and from the flat one for impact-parameter h = 45 μm are shown in Figure 5.

The main characteristic of the ODR is the dependence of the distribution width (FWHM) in horizontal direction ($\gamma\theta_x$) vs. impact-parameter [8]. This dependence is shown in Figure 6. The FWHM decreases as the impact parameter increases. The lines represent the theoretical prediction. It is clear that the experiment is in good agreement with the theory.

From the Figure 6 one can see that ODR distribution from the spherical target is narrower than from the flat one. The theoretical predictions and the experimental results are in good agreement. A little disagreement might be explained by the influence of the vertical beam size which was not taken into account in the theoretical model and by the influence of joint action of CCD-detector spectral efficiency and Fresnel reflection coefficients of the target materials.

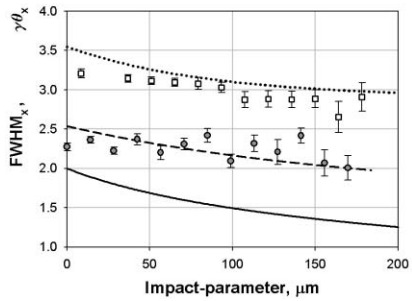

Figure 6. ODR FWHM vs. impact-parameter. Gray circles – the spherical target experiment, open squares – the flat target experiment. Solid line – far-field zone approach, dashed line – spherical target theoretical predictions, dotted line – flat target theoretical predictions. The estimations were made for wavelength λ=550 nm.

CONCLUSION

Finally we can say that during this proof-of-principle experiment the OTR and ODR focusing by the spherical target was clearly observed. The received experimental distributions are in good agreement with the theoretical predictions. One may expect that coherent TR and coherent DR may be focused too. Received results allow to hope that the spherical target application will be widely adopted in different beam diagnostics tools. For instance, using the focusing of CDR by a concave target electro-optic diagnostics becomes noninvasive and more sensitive due to placement of EOC at the minimal possible distance in the extreme pre-wave zone. Moreover it might simplify the performance of the method.

REFERENCES

1. M. Ross, S. Anderson, J. Frisch, et al., SLAC-PUB-9280 (July 2002).
2. P.Karataev, S. Araki, R. Hamatsu et al., PRL, 93, 244802 (2004)
3. A. Winter, et al., in: Proceedings of EPAC 2004, Lucerne, Switzerland, 2004, p.253
4. A.P. Potylitsyn, L.G. Sukhikh, A.S. Kostousov, J. Urakawa, A. Aryshev, S. Boogert, P.V.Karataev, http://rupac2006.inp.nsk.su/ready/mono07.pdf
5. V.A. Verzilov, Phys. Lett. A 273 (2000) 135.
6. A.P. Potylitsyn, R.O. Rezaev, NIMB **252** (2006) 44.
7. P.V. Karataev, Phys. Lett. A **345** (2005) 428-438
8. T.Muto, S. Araki, R. Hamatsu, et al., PRL 90, 10 (2003) 104801.
9. SAD, Strategic Accelerator Design, http://acc-physics.kek.jp/SAD/sad.html
10. P. Karataev, PhD thesis, Tokyo Metropolitan University, 2004
11. P.Karataev, et al., European Part. Accel. Conf., July 5-9, 2004, Lucerne, Switzerland, p. 2643

A SUB-50 FEMTOSECOND BUNCH ARRIVAL TIME MONITOR SYSTEM FOR FLASH

F. Loehl, K. Hacker, H. Schlarb, DESY, Hamburg, Germany

Abstract

A bunch arrival time monitor using the future laser based synchronization system at FLASH has been developed. The signal of a beam pick-up with several GHz bandwidth is sampled by a sub-ps laser pulse using a broadband electro-optical modulator. Bunch arrival time deviations are converted into amplitude modulations of the sampling laser pulses which are then detected by a photo-detector. A resolution of 30 fs could be reached with the capability towards sub-10 fs level. In this paper we describe the design of the optical system and present recent results.

INTRODUCTION

The operation of ultra-violet and X-ray free electron lasers like FLASH (Free electron LASer in Hamburg) or the planned European XFEL requires an arrival-time stability on the order of several tens of femtoseconds between the X-ray pulses and laser pulses of external probe lasers, to be able to take full advantage of the fs-short X-ray pulses in pump-probe experiments.

A fs-stable synchronization system and monitor systems for the bunch arrival time with resolutions on the order of 10 fs are needed to establish a high level of stability. To distinguish accelerating gradient changes upstream of the dispersive sections from timing changes of the photo-injector laser, precise monitor systems for the beam energy in the dispersive sections are needed in addition.

Long-term, femtosecond-stable synchronization cannot be achieved by conventional coaxial distribution systems. At FLASH and the XFEL an optical synchronization system, developed in collaboration with MIT (see [1]), will be used. The system uses a mode-locked Erbium doped fiber laser as an optical master oscillator. It is locked to a microwave RF oscillator. For the FLASH synchronization system, two diffent types of fiber lasers are under investigation: one operates in the stretched-pulse regime at a repetition rate of 54 MHz [2], and the other one is a soliton laser with a repetition rate of 216 MHz [3]. The light pulses generated by these lasers are distributed to the remote locations via actively length-stabilized, dispersion compensated fiber links ([4], [5]). There, the light pulses are converted either into RF signals, used to synchronize external lasers by optical cross-correlation or seeding, or used to drive optodiagnostic devices such as the bunch arrival time monitors (BAMs) presented here.

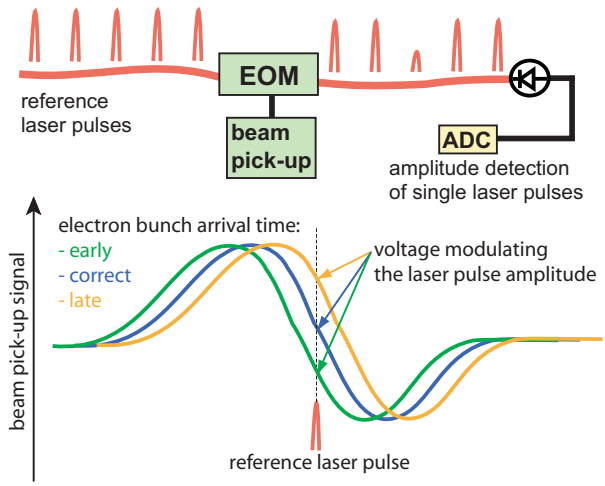

Figure 1: Principle of the arrival time detection. Reference laser pulses traverse an electro-optical modulator which is driven by the signal of a beam pick-up (top). Arrival time changes of the electron beam cause different modulation voltages at the laser pulse arrival time (bottom), leading to laser amplitude changes that are detected by a photo detector.

MEASUREMENT SETUP

The system of the bunch arrival time monitor is described in [6], the principle of the arrival time detection is shown in Fig. 1. Reference laser pulses are fed into an electro-optical modulator (EOM) where the laser amplitude is modulated by the fast transient of a beam pick-up signal. The laser amplitude changes, which are a measure of the bunch arrival time, are detected by a photo-detector and recorded by a fast ADC. By using laser pulses from actively stabilized fiber-links and installing the EOM directly next to the beam pick-up to reduce cable-drifts, the realization of an almost drift-free arrival time detection with respect to the master laser will be become feasable.

The performance of the BAM system, was evaluated using the pulses from a 40.625 MHz stretched-pulse laser as a reference. The laser was phase-locked to the accelerator RF and, by using a vector-modulator, the laser pulses could be shifted in time. In [6] we found a strong electron-orbit dependence of the ring electrode used as a beam pick-up. This could be used to determine the beam position with high resolution from the difference signal of two arrival time measurements. With a special beam pick-up this method will be used for beam position measurements inside the mag-

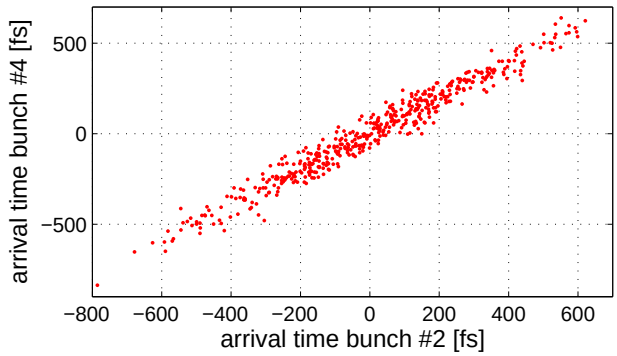

Figure 2: Correlation between the measured bunch arrival time of two bunches inside the same bunch train for 500 bunch trains. From the arrival time difference a single bunch resolution around 30 fs can be estimated.

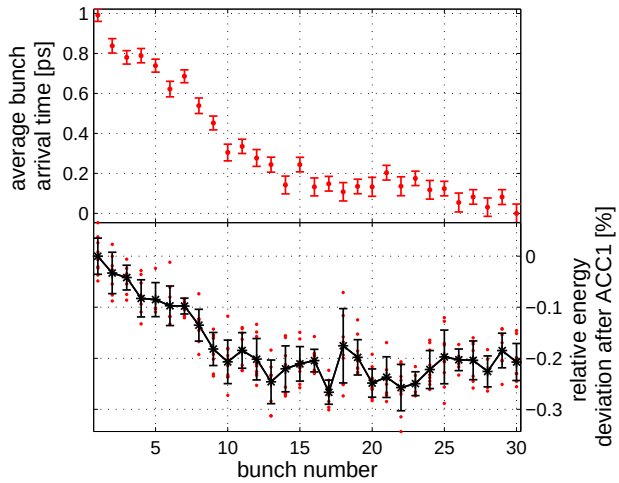

Figure 3: Comparison of the average bunch arrival time over the bunch train at the end of the machine with the average beam energy after the first accelerating module ACC1.

netic chicanes of FLASH [7]. Since the orbit dependence complicates the arrival time measurement, a new pick-up design [7] with a smaller orbit dependence, based on buttons, will be used for FLASH.

All measurements presented here have been carried out with the ring electrode. In order to reduce the orbit dependence, two outputs on opposite sides of the pick-up were combined, resulting in an orbit dependence smaller than $200\,\mathrm{fs}/\,\mathrm{mm}$. This could be corrected by beam position monitor readings.

The resolution of the system is limited by two sources: the accuracy with which the amplitude of the single laser pulses can be detected and the beam pick-up signal slope. The signal slope defines the degree of laser amplitude modulation for a given timing change. Since in the test setup the EOM was connected to the beam pick-up by a $30\,\mathrm{m}$ long cable, high frequency components of the pick-up signal were damped out, resulting in a voltage slope around $0.25\,\mathrm{V}/\,\mathrm{ps}$. This gives a time-to-optical amplitude conversion factor of around $60-80\,\mathrm{fs}$ / (% laser amplitude modulation) in the optical setup. Being able to read out the laser amplitude with an accuracy of about 0.3% gives a resolution of $20-25\,\mathrm{fs}$ for this set-up. The amplitude read-out was mainly limited by ADC clock-jitter, and with a better ADC 0.08% detection accuracy could be reached in a laboratory setup. Measurements of the beam pick-up signal with a fast oscilloscope installed directly in the tunnel gave a voltage slope of around $1\,\mathrm{V}/\,\mathrm{ps}$ for the ring-electrode and also for the new button design. We are, therefore, optimistic that a monitor resolution below $10\,\mathrm{fs}$ is feasable with the setup installed directly in the tunnel.

MEASUREMENTS

An upper limit of the resolution achieved with the monitor system can be estimated using the special time structure of the superconducting FLASH linac. With a repetition rate of $5\,\mathrm{Hz}$, trains of up to 800 bunches with $1\,\mu\mathrm{s}$ spacing are produced. Due to the short bunch spacing, fluctuations of the accelerating fields experienced by adjacent bunches are small. The correlation of the arrival time of two bunches in the bunch train for many different shots gives an upper resolution limit, since amplitude changes of the accelerating fields are experienced by both bunches. The limiting factor is only the shot-to-shot change of the amplitude slope of the accelerating fields.

Figure 2 shows the correlation between the arrival time of two bunches inside the bunch train for 500 shots. The jitter of the arrival time difference is around $40\,\mathrm{fs}$ over 100 and $50\,\mathrm{fs}$ over 500 shots. The resolution of a single bunch measurement is smaller by a factor of $1/\sqrt{2}$ leading to around $30\,\mathrm{fs}$ single bunch accuracy. This confirms the resolution estimated before.

Figure 3 shows a comparison between the average arrival-time measured by the BAM system at the end of the machine and the average energy deviation measured with a synchrotron radiation monitor [8] in the first bunch compressor. A large energy slope in the first part of the bunch train is visible. This is transformed inside the magnetic chicanes into arrival time differences. The arrival time change Δt is related to beam energy changes $\delta E/E$ by

$$\Delta t = \frac{R_{56}}{c_0}\frac{\delta E}{E}, \qquad (1)$$

where the momentum compaction factor $R_{56} = 180\,\mathrm{mm}$ for FLASH giving an arrival time change of $6\,\mathrm{ps}$ per % energy change. This is in good agreement with the measurements of the BAM.

This measurement shows the high potential for using the BAM or other devices that use this optical front end in beam based feedback systems. Being able to measure the arrival time over the entire bunch train together with the ease of the data acquisition makes the system ideally suited for fast intra bunch-train feedbacks.

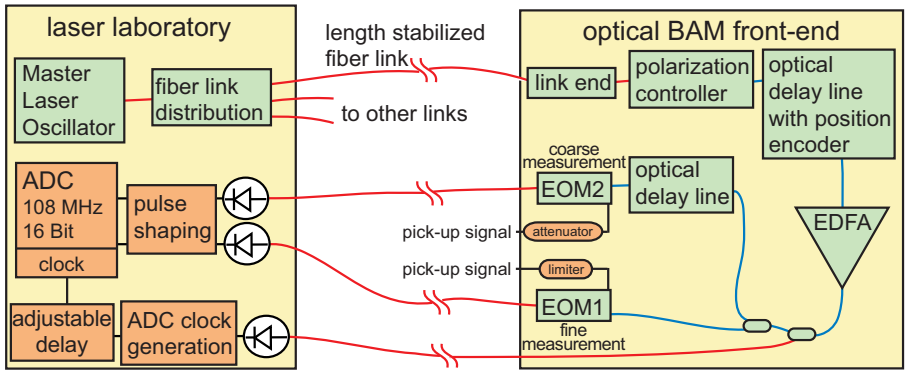

Figure 4: Schematic design of the BAM system for FLASH.

DESIGN OF THE SYSTEM FOR FLASH

Figure 4 shows a schematic of the BAM design for FLASH. Optical front-ends installed directly next to the beam pick-ups will be used. The reference laser pulses from the master laser oscillator are supplied by actively length-stabilized fiber-links. Since the fiber-links do not use polarization maintaining fibers, a polarization feedback will be applied. It is not yet decided, whether the polarization adjustment will be done inside the fiber-link or at the exit. An optical delay line (ODL) will be used to adjust the timing of the reference laser pulses such that the pick-up signal is sampled at the zero-crossing in order to reduce the dependence on the signal amplitude. With a feedback on the ODL position, this timing adjustment will be stabilized. Since the timing of the reference laser pulses is changed by the ODL, a precise position readout of the ODL is required. We use absolute position encoders with a resolution of $3\,\mu\mathrm{m}$ over a $100\,\mathrm{mm}$ range. The bunch arrival time is determined from the combination of ODL position and laser amplitude modulation. Having an ODL installed, the dynamic range of the arrival time detection is limited only by the length of the ODL, which corresponds to a maximum timing change of $330\,\mathrm{ps}$ in our case. Without the ODL, the dynamic range is in the order of $1\,\mathrm{ps}$ and fast changes of machine parameters could be a problem. A second EOM is, therefore, foreseen which is modulated by a strongly attenuated pick-up signal. This gives a low resolution measurement with a dynamic range of several picoseconds which can be used to adjust the ODL in case the high resolution measurement is out of range. The timing adjustment between the two EOMs can be done using either accurate fiber- and cable lengths or a second delay line.

The modulated laser pulses are sent back to the laser laboratory where the master laser is also located. This has the advantage that changes in the readout system can be made without accessing the accelerator tunnel. With photo detectors, a pulse shaping unit, which in the easiest case is just a low pass filter, and a fast ADC, the amplitudes of the laser pulses are measured. The ADC is clocked with $108\,\mathrm{MHz}$; this is twice the repetition rate of the $54\,\mathrm{MHz}$ master laser. With a proper timing adjustment, the laser pulses and the base line of the photo detector signal can be sampled, allowing for offset-free amplitude detection. The ADC clock is generated directly out of the laser pulses that sample the pick-up signal. This makes sure that the sampling position remains the same when the ODL position is changed. To simplify the ADC sampling time adjustment, a clock-delay module will be used [9]. In case a $216\,\mathrm{MHz}$ laser will be used, either faster ADCs are needed, or the baseline and the laser amplitude have to be sampled by different ADC channels. In the latter case drifts of the ADC channels could become an error source.

SUMMARY AND OUTLOOK

A monitor system to measure the arrival time of fast electrical transients with fs-resolution has been developed. A resolution below $30\,\mathrm{fs}$ could be reached with the capability towards sub-$10\,\mathrm{fs}$ level. The system will be installed at FLASH for measurements of the bunch arrival time and for precise measurements of the beam position inside the magnetic chicanes.

REFERENCES

[1] J. W. Kim et. al., "Large scale timing distribution and RF-synchronization for FEL facilities," FEL Conference 2004, Trieste, Italy, 2004.

[2] A. Winter et. al., "High-precision Laser Master Oscillators for Optical Timing Distribution Systems in Future Light Sources," EPAC Conference 2006, Edinburgh, UK, 2006.

[3] J. Chen et. al., Opt. Lett. **32**, 1566-1568 (2007)

[4] F. Loehl et. al., this Conference WEPB16.

[5] J. Kim et. al., Opt. Lett. **32**, 1044-1046 (2007)

[6] F. Loehl et. al., "A sub-100 fs electron bunch arrival-time monitor system for FLASH," EPAC Conference 2006, Edinburgh, UK, 2006.

[7] K. Hacker et. al., this Conference TUPB20.

[8] C. Gerth, this Conference TUPC03.

[9] L. Pavlovic et al., this Conference WEPC02.

FIRST PROTOTYPE OF AN OPTICAL CROSS-CORRELATION BASED FIBER-LINK STABILIZATION FOR THE FLASH SYNCHRONIZATION SYSTEM

F. Loehl, H. Schlarb, DESY, Hamburg, Germany
Jeff Chen, Franz Xaver Kaertner, Jung-Won Kim, MIT, Cambridge, Massachusetts

Abstract

A drift free synchronization distribution system with femtosecond accuracy is of great interest for free-electron-lasers such as FLASH or the European XFEL. Stability at that level can be reached by distributing laser pulses from a mode-locked erbium-doped fiber laser master oscillator over actively optical-length stabilized fiber-links. In this paper we present a prototype of a fiber-link stabilization system based on balanced optical cross-correlation. The optical cross-correlation offers drift-free timing jitter detection. With this approach we were able to reduce the timing jitter added by a 400 m long fiber-link installed in a noisy accelerator environment to below 10 fs (rms) over 12 hours.

INTRODUCTION

The operation of ultra-violet and X-ray free electron lasers like FLASH (Free electron LASer in Hamburg) or the planned European XFEL requires synchronization of various devices in the accelerator to better than 10 fs. The most critical devices are the photo-injector laser, the RF gun, the accelerating modules in front of the bunch compressors, and pump-probe and seed lasers for user experiments. These locations are separated by 400 m for FLASH and by 3.5 km for the XFEL.

The high accuracy of synchronization required over these large distances cannot be achieved by conventional coaxial RF distribution systems. At FLASH and for the XFEL an optical synchronization, developed in collaboration with MIT (see [1]), will be used. The system uses a mode-locked Erbium doped fiber laser which is locked to a microwave RF master oscillator. Two diffent kinds of fiber lasers are under investigation, one operating in the stretched-pulse regime at a repetition rate of 54 MHz [2], the other one is a soliton laser operating at 216 MHz [3]. The light pulses generated by these lasers are distributed to the remote locations via actively length-stabilized, dispersion compensated fiber-links. There, the light pulses are either converted into RF signals which are needed in the accelerating cavities, they are used to synchronize external lasers by optical cross-correlation or seeding, or they are directly used for opto-diagnostic devices ([4], [5]).

INVESTIGATED FIBER LASERS

For the prototype of the fiber-link stabilization a 200 MHz soliton laser was used. The higher repetition rate compared to a 54 MHz stretched-pulse laser has several advantages: The maximum pulse energy which can be transmitted through the fiber-links is limited by nonlinearities and the higher repetition rate allows for four times more average power inside a link with the same pulse energy and, consequently, the same amount of non-linear behaviour. Since the pulse spacing is reduced by a factor of four, timing adjustments to overlap the laser pulses with other signals are much easier. The soliton lasers we use generate optical pulses with a Fourier limited pulse duration of around 130 – 160 fs. The stretched-pulse lasers generate a much broader optical spectrum which complicates dispersion compensation of the fiber-links. Limiting the wavelength spectrum by an aperture in a dispersive section is possible but leads to a loss of optical energy. The effect of the optical spectrum shape on the system performance must still be investigated.

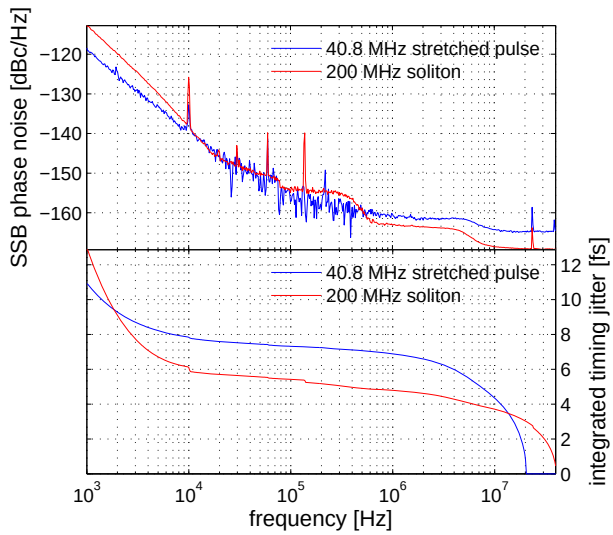

Figure 1: Phase noise comparision between a 40.8 MHz stretched-pulse laser and a 200 MHz soliton laser. Top: single-sideband phase noise measured at the harmonics at 980 MHz (stretched-pulse) and 1.2 GHz (soliton), respectively. Bottom: integrated timing jitter starting integration at 20.4 MHz (stretched-pulse) and 40 MHz (soliton). The measurements for the stretched-pulse laser are from [2].

On the other hand, single laser pulse detection, which is used for several electron beam diagnostic devices ([4], [5]) as well as RF phase detection with the fundamental laser repetition rate used as an intermediate frequency, is more complicated at higher repetition rates because it requires faster ADCs or an optical gating unit.

The distribution scheme relies on low phase noise for

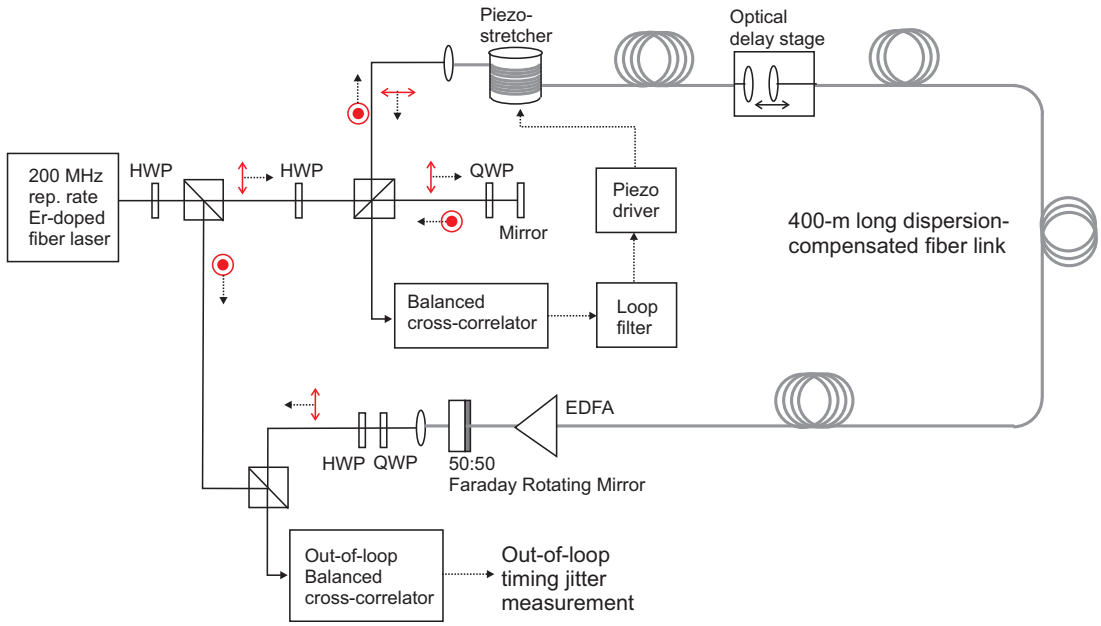

Figure 2: Experimental setup for the fiberlink stabilization.

frequencies above the link roundtrip frequency. This frequency is on the order of 250 kHz for the maximum link length of 400 m at FLASH and 25 kHz for the 4 km long links for the XFEL. Both fiber-laser types have very low integrated phase noise above these frequencies. Figure 1 shows the single sideband phase noise and the integrated timing jitter of a 40.8 MHz stretched-pulse laser and of a 200 MHz soliton laser. The measurement is done by evaluating the phase stability of high harmonics of the repetition rate, filtered out from the signal of a fast photo detector. At high offset-frequencies the detection scheme is limited by the photo detection process [6]. Due to the higher repetition rate of the soliton laser, the intensity is distributed to fewer frequency components giving this laser type clear advantages in this frequency range. In the frequency range from $1 - 10$ kHz the soliton laser is less stable than the stretched-pulse one. With a 10 kHz fast phase-lock loop to a microwave oscillator, however, this could be overcome.

MEASUREMENT SETUP

A schematic of the experimental setup, similar to the laboratory setup used in [7], is shown in Fig. 2. The laser pulses are coupled into a 400 m long, dispersion compensated fiber-link. In order to test the influence of a noisy enviroment, the fiber is installed around the circumference of an accelerator hall. At the end of the link, part of the light intensity is back-reflected using a Faraday rotator mirror. The returning pulses are combined with the pulses coming directly out of the laser. Inside a balanced optical cross-correlator (see Fig. 3) the overlap between the two signals is measured. Changes are corrected by a DSP based feedback system which drives a piezo stretcher inside the link. The bandwidth of the feedback loop is around 1 kHz.

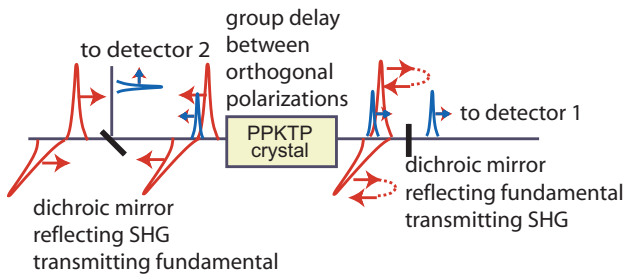

Figure 3: Principle of the balanced optical cross-correlator. Two light pulses with orthogonal polarization pass through a type-II PPKTP crystal. Inside the crystal the two polarizations experience a different group delay. With a dichroic mirror the second harmonic generated in the crystal is sent to a first detector, while the fundamental is back-reflected, passing the crystal a second time. The second harmonic is separated by a second dichroic mirror and directed to a second detector. Using the difference signal of the two detectors, amplitude fluctuations of the incoming pulses can be suppressed by a large amount.

Larger timing changes are corrected by a motorized optical delay line (ODL). To evaluate the timing stability of the fiber-link, a second optical cross-correlator is used in which the pulses out of the link are overlapped with pulses coming directly from the laser.

MEASUREMENT RESULTS

Figure 4 shows the response of the out-of-loop cross-correlator as a function of the delay between the two pulses. The link stability has been measured at the zero-crossing

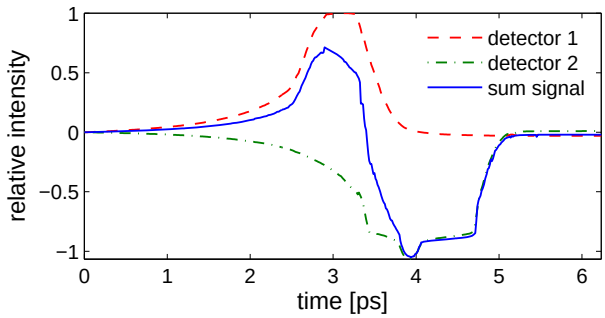

Figure 4: Response of the balanced out of loop optical cross-correlator. The signals of the two detectors (dashed traces) are combined digitally giving the sum signal (solid trace). The link timing jitter measurement is performed at the zero crossing of the sum signal.

of the balanced detector signal. This has the advantage that amplitude fluctuations are suppressed. Having a motorized optical delay stage installed inside the link, the limitations of a too small adjustment range of the piezo stretcher to keep the lock closed over hours [7] could be overcome. With this we were able to close the feedback loop over days.

Figure 5 shows the timing stability of the fiber-link over 12 hours. The rms timing jitter is (7.5 ± 1.8) fs at a measurement bandwidth of 200 kHz. Timing changes with a time constant below 100 s are (4.4 ± 1.1) fs, the timing drift over 12 hours is 25 fs. It is surprising that the link length has to be corrected by as much as $1 - 3$ ps on a timescale of 10 seconds. Furthermore we found a correlation between changes of the piezo displacement and the link timing. This, together with the small timing drift visible in Fig. 5 could be caused by two sources: Since the polarization at the end of the link is not stabilized, polarization changes (e.g. due to the piezo-stretcher or temperature drifts) inside the link cause changes of the amplitude entering the balanced detector. A non-perfect balancing would lead to an error in the arrival time detection. A second reason could be polarization mode dispersion inside the fiberlink. Since this would be an ultimate limitation when using standard single mode fiber instead of polarization maintaining fiber, we plan to repeat the measurement having a polariation feedback installed at the end of the link.

Another polarization related effect we found is caused by Erbium-doped fiber amplifiers. In several Erbium-doped fiber amplifiers, built with different kinds of fibers, we found a wavelength dependent polarization rotation which is independent of the pump power and, therefore, most probably not caused by self-phase modulation. Further investigations on this topic have to be performed.

SUMMARY AND OUTLOOK

We demonstrated the proper performance of a fiber-link stabilization system based on optical cross-correlation. The

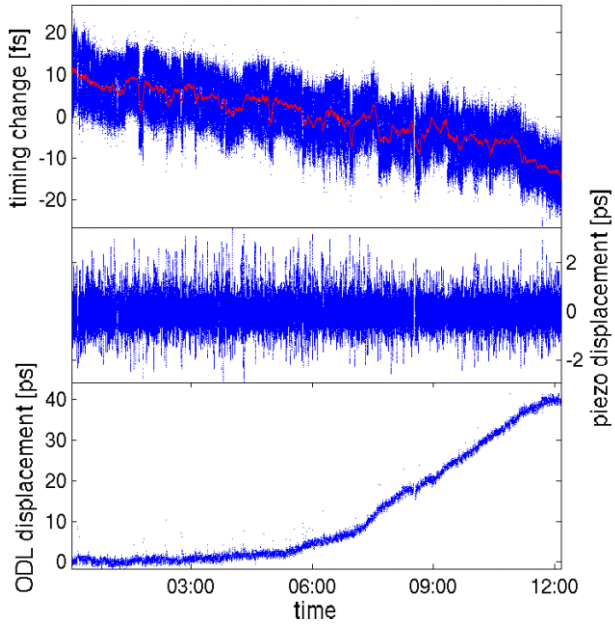

Figure 5: Out of loop drift measurement of a 400 m long fiberlink. Top: end of link timing change (blue). Over 12 hours the rms jitter is (7.5 ± 1.8) fs with a timing drift of 25 fs. The red line indicates changes with a time constant of 100 s. The timing jitter faster than 100 s is (4.4 ± 1.1) fs. Middle: piezo stretcher displacement. Bottom: Displacement of optical delay line (ODL).

fiber was installed in a noisy envirement and we achived an rms link timing stability below 10 fs over 12 hours. Next steps involve further investigation of polarization effects inside the link and the installation of first prototypes of the system inside the FLASH linac.

ACKNOWLEDGEMENT

We would like to thank Jörg Thomas for the support of the stepper motor control and Gevorg Petrosyan for his help with the DSP regulation.

REFERENCES

[1] J. W. Kim et. al., "Large scale timing distribution and RF-synchronization for FEL facilities," FEL Conference 2004, Trieste, Italy, 2004.

[2] A. Winter et. al., "High-precision Laser Master Oscillators for Optical Timing Distribution Systems in Future Light Sources," EPAC Conference 2006, Edinburgh, UK, 2006.

[3] J. Chen et. al., Opt. Lett. **32**, 1566-1568 (2007)

[4] F. Loehl et. al., "A Sub-50 fs Bunch Arrival Time Monitor System for FLASH," this Conference, Venice, Italy, 2007.

[5] K. Hacker et. al., this Conference TUPB20.

[6] J. Mueller et. al., this Conference WEPB08.

[7] J. Kim et. al., Opt. Lett. **32**, 1044-1046 (2007)

ELECTRON BEAM TEMPERATURE MEASUREMENTS AT THE FERMILAB MEDIUM ENERGY ELECTRON COOLER*

A. Warner#, K. Carlson, L. Prost, M. Sutherland FNAL, Batavia, IL 60510, U.S.A.
G. Kazakevich, BINP, 630090 Novosibirsk, Russia

Abstract

The Fermilab Recycler ring employs an electron cooler to store and cool 8.9-GeV anti-protons. The cooler is based on an electrostatic accelerator (Pelletron) working in an energy-recovery regime [1]. Several techniques for determining the characteristics of the beam dynamics have been investigated. Beam temperature measurements using optical transition radiation (OTR) [2],[3], in conjunction with a Pepper-pot have been made at several settings of the upstream optics of the machine. Without temperature the pepper-pot hole images would have sharp boundaries. A finite temperature makes these boundaries broader. Thus, comparison of the ratios of the hole image boundaries and intensities is a measure of the beam temperature. In this paper we report the results so far obtained using this technique.

INTRODUCTION

Electron cooling of the anti-protons in the Recycler requires that a monochromatic (cold) electron beam be transported to a common 20 meter long cooling section to interact with the stored anti-protons. The cooling efficiency strongly depends on the effective angle between these electrons and the anti-protons. Hence, to have optimal cooling, the electron rms angle should be as small as possible. Several sources including the source temperature contribute to the total rms angle. As a result, optimization of the cooling process places an upper limit on the contribution to the total angle due to beam temperature. A significant effort was made to determine this contribution by analyzing images of the electron beam taken with optical transition radiation monitors in conjunction with a pepper-pot scraper. The main parameters of the cooler are summarized in table 1.

Table 1: Electron Cooler Main Parameters

Parameter	Symbol	Value	Unit
Electron kinetic energy	E_b	4.34	MeV
Beam current	I_b	0.1-0.5	A
High voltage ripple, rms	δU	250	V
CS length	L	20	m
Solenoid field in CS	B_{cs}	105	G
Beam radius in CS	R_b	3-4.5	mm

EXPERIMENTAL SET-UP

The Recycler Electron cooler is equipped with a so-called pepper-pot (PP), installed downstream of the acceleration tube right above the first bending magnet as shown in Figure 1. The PP is a copper plate with 475 equally spaced (0.81 mm center-to center), 0.27 mm-diameter round holes which have been designed to form a square grid pattern. The density of holes is sufficient to cover the smallest beam diameter of ~ 5 mm at the PP location by 5 holes. When inserted and used with a 2-μs pulsed electron beam the PP blocks the beam allowing only beamlets (small beams) to pass through the holes. These beamlets can vary in number from a few to several dozen depending on the focusing and the beam current. The beamlets that pass through are observed on a down stream OTR monitor and CCD camera system.

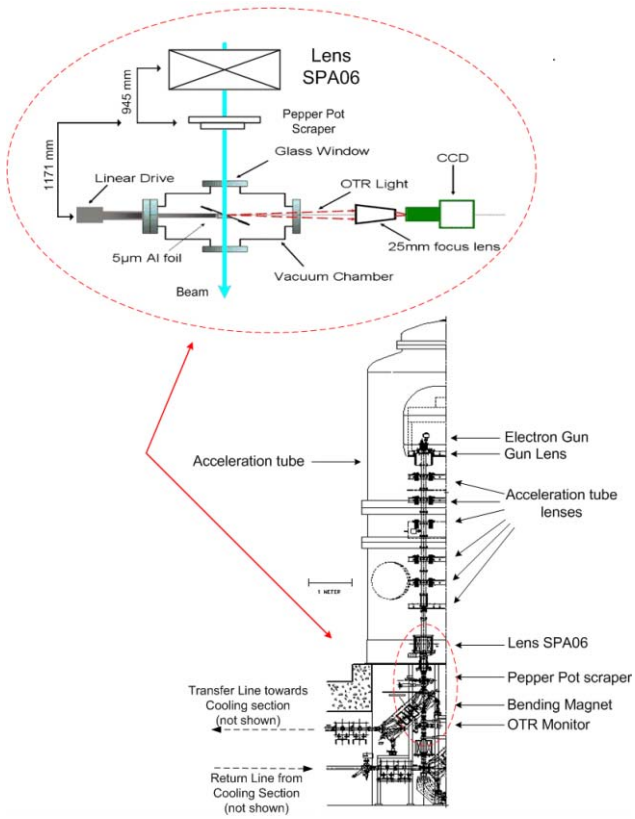

Figure 1: Layout of experimental set-up.

The transition radiation screen is a 5μm, 2-inch diameter aluminum foil tensioned onto a ring frame. Such thin foils were used to reduce the background signal due to beam scattering and bremsstrahlung radiation. The response of the monitors as a function of the beam current shows good linearity over the practical range of the cooler (Figure 2) and the light output is very uniform over the surface of the monitor. A linear motor drive inserts the OTR screen in the beam path with an accuracy of 0.1 mm and the screen is at an angle of 38.9 degrees with respect

*Operated by Fermi Research Alliance, LLC under Contract No. DE-AC02-07CH11359 with the United States Department of Energy.
#warner@fnal.gov

to the beam direction. This corresponds to the angle $\theta \approx 1/\beta\gamma$ [4], where the intensity of the light is at a maximum.

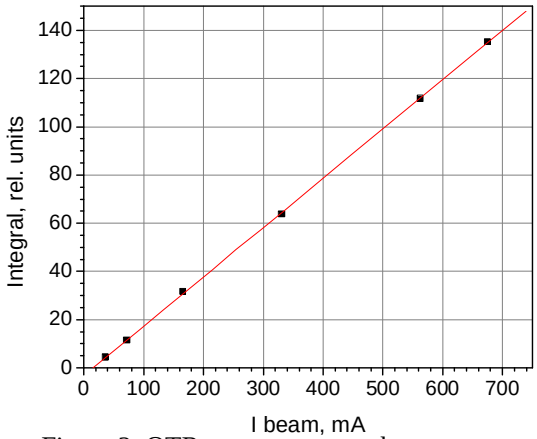

Figure 2: OTR response versus beam current.

Principle of Measurement

In the ideal case of a linear axially symmetric distribution of the electron angles, the hole pattern produced by the beamlets at the OTR should be undistorted and therefore image analysis would allow one to measure both quadrupole and non-linear aberrations in the beam angles. In other words a beam without temperature would have sharp boundaries; however, due to finite temperature these boundaries are broadened. Thus comparison of the widths of the hole images with that of the scraper is a measure of the beam temperature. Likewise comparison of the imaged intensity from the PP is also a measure of the temperature. Due to temperature, the image intensity of a beamlet on the OTR screen can be represented as $\propto \exp(-r^2/(2\sigma^2))$, where r is the distance from the image center, and the width σ depends on the thermal emittance and optical functions [5]. If the beam is round at the scraper and there are no optical elements between the scraper and the OTR detector, the width of the point image is given by:

$$\sigma = \frac{p_T a_g}{p a_o} l \qquad (1)$$

Where p is the total momentum, $p_T = \sqrt{m_e T}$ is the transverse momentum due to thermal motion, a_g is the cathode radius, a_0 is the beam radius at the scraper and l is the distance between the scraper and the OTR detector. Equation (1) can be rewritten in term of the ratio of the intensities [5] as:

$$\frac{I_i}{I_0} = \frac{\rho^2}{\sigma^2} = \frac{\rho^2}{2\theta_T^2 l^2} \qquad (2)$$

Where I_i is the intensity of a beamlet at position (x_i, y_i), I_0 is the intensity of the full beam, θ_T is the transverse momentum due to thermal motion and ρ is the PP hole radius. To prevent loss of image brightness the PP holes has to be wide enough, such that the radius of the hole be much larger than the hole depth.

Data Acquisition

The optical monitor system uses digital CCD cameras connected via IEEE 1394 (fire-wire) standards to computers; the images are first converted to optical signals in order to transport the data over longer distances. At the interface to the computer the signal is converted back to 1394 standard input. A LabView™ based application program that was designed using commercially developed image analysis tools is used to process the data. The system incorporates image digitization, image display, as well as image analysis and system calibration in a real-time module. The gain and other attributes of the camera are controlled via this interface as well.

Data Analysis

First, linear (convolution) filters are applied to the images in order to remove unwanted background due to x-rays. Then, the images are scaled to reflect real world coordinates and corrected for angular errors and aberrations due to tilts or camera misalignment. The correction to the beam image shape due to the angle of the OTR foil (38.9°) is ~ 20 pixels/mm horizontally and ~ 16 pixels/mm vertically. The CCDs chosen are square pixel CCDs so that there is no need to convert the aspect ratio during the processing. Measurements of the beam centers, the rms beam size and the ratio of the intensity of the images are determined using the image analysis tools.

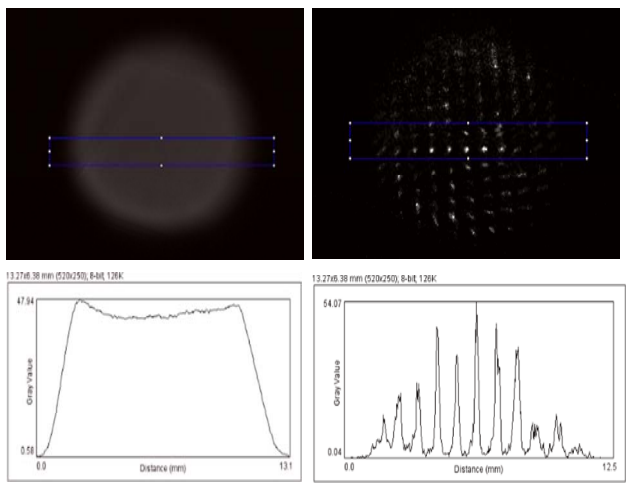

Figure 3: Top left: OTR image, Top right: PP image Bottom left: ROI integral, Bottom right: ROI PP image.

Figure 3 shows a processed data set where the beam (top left) and the corresponding PP image (top right) are measured and the relative grey scale intensities are used to determine θ_T from equation (2). The data shown was taken

for fixed optics upstream of the OTR monitor and for a pulsed beam current of ~ 900 mA. The integral over a specified region of interest (ROI) is also shown in Figure 3 (bottom left and bottom right) for the beam and its PP image. The current emitted during a pulse is controlled by varying the pulse voltage of the gun control electrode; to compensate for pulser and optics variations during the rise of the pulse, data from 1μs beam pulses are subtracted from 2 μs beam pulses, such that only the flat-top-equivalent image remains. The shape of the pulse-signal is shown in Figure 4. The PP data shown was scaled by a multiplicative factor to enhance the image of the beamlets for data processing. The scaling factors were taken care of when the ratios of the image intensities were determined.

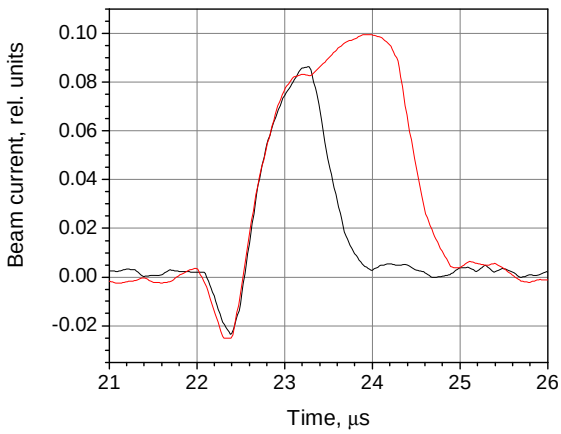

Figure 4: Pulse signal shape at 1 μs and 2 μs.

RESULTS

The results of the measurements are summarized in Table 2. Using Eq. (1) and (2), we find that thermal angles are ~71 μrad ≈ ≃ 0.45 eV. As mentioned previously several sources contribute independently to the total rms angle, including imperfections of the magnetic field (< 100 μrad), perturbations from external fields (~ 40 μrad), and envelope oscillations (estimated at ~ 120 μrad) [6]. These angles are added in quadrature.

Table2: Measurement Results

Parameter	Symbol	Value	Unit
PP to OTR distance	l	1171	mm
Cathode radius	a_g	3.8	mm
Beam radius	a_o	5.7	mm
Total momentum	p	4.8	MeV/c
Thermal angle	θ_T	71	μrad
Thermal momentum	P_T	504	eV
Beam Temperature	T	0.45	eV

ACKNOWLEDGEMENTS

The authors are thankful to A. Burov and A. Shemyakin for their useful discussions and for the analytical work that was done in the design of the pepper-pot scraper. We also wish to acknowledge Charles Schmidt for his participation in the data collection and R. Kellett for his technical assistance during the hardware installation.

SUMMARY

The measured thermal angle is within the tolerance of the design goal and the total rms angle meets the goal of < 0.2 mrad. The resultant electron beam quality achieved lead to successful cooling up to 400 × 10^{10} antiprotons.

Table 2: Summary of electron angles in the cooling section

Component	Design μrad	Present estimation μrad	Diagnostics
Temperature	90	70	OTR + PP
Aberrations	90	50 ≤30 (@ 1 mm)	Simulated BPMs
Envelope scalloping	100	120	Movable orifices
Dipole motion caused by magnetic field imperfections	100	40	Magnetic measurements + BPMs
Beam motion	50	40	BPMs
Drift velocity	20	20	Calculated
Total	**200**	**160**	

REFERENCES

[1] S. Nagaitsev et al, Phys. Rev. Lett. 96, 044801 (2006).

[2] L. Wartski et al, "Interference phenomenon in optical transition radiation and its application to particle beam diagnostics and multiple-scattering measurements," J. Appl. Phys., vol. 46, no. 8, pp. 3644-3653, 1975.

[3] V. L. Ginzburg and I. M. Frank, "Radiation from a uniformly moving electron passing from one medium to another,." J. Exp. Theoret. Phys., Vol. 16, no. 15, pp. 15-26, 1946.

[4] A. Warner et al, "Beam profile diagnostics for the Fermilab Medium Energy Electron Cooler. " IEEE Trans. Nucl. Sci,V. 52, no. 5, 2005.

[5] A. Burov and A. Shemyakin, "Pepper-pot Scraper Parameters and Data Processing ," Fermilab-TM-2258, July 2004.

[6] A. Burov *et al.*, AIP Conf. Proc. Vol. 821 (2006) 139.

DIGITAL ANALYSIS OF BEAM DIAGNOSTIC NOISE

P. A. Duperrex, G. Gamma, B. Keil, U. Müller, PSI-Villigen, Switzerland

Abstract

A digital coherence analysis has been performed to analyze the origin of the noise observed on several beam diagnostics. By correlating different channels from the same electronics or from different monitors, the instrumental or physical origin of the noise can be deduced.

INTRODUCTION

This paper presents some results about the origin of the noise observed using different diagnostics systems either on Proscan, a 250Mev proton accelerator medical facility, or on the 590 MeV proton accelerator. The origin of the noise is always a question that arises when interpreting the experimental data. Is it simply a noise from the measurement system (instrumental noise) of does it really reflect some physical fluctuations of the parameter that is being measured ("physical" noise)? Coherence analysis using digital signal processing has been used to address this issue.

Coherence analysis [1] compares the spectral content of two signals and indicates how well the signal frequency components are correlated. It is a function of the power spectral density ($P_{xx}(f)$ and $P_{yy}(f)$) of x and y and the cross power spectral density ($P_{xy}(f)$) of x and y and is defined as: $C_{xy}(f) = \frac{|P_{xy}(f)|^2}{P_{xx}(f)P_{yy}(f)}$. For the results presented here, the coherence has been computed with MATLAB applying the Welch method with 50% overlap.

NOISE ANALYSIS FOR CURRENT MEASUREMENTS

Logarithmic amplifier electronics (LogIVs) [2] is extensively used to measure the current signals from beam current monitors or harp monitors [3, 4] for PROSCAN.

VME LogIV-32 instrumental noise

A 32-channel VME LogIV electronic board has been developed for the harp monitors. The possible cross-talk between channels has been investigated by using a 150pA test source as input for all 32 channels and by calculating the coherence spectra of the sampled data. The sampling frequency was 5kHz and the spectral resolution was 9.8Hz. Altogether 496 spectra have been computed. The coherence spectra between most of the channels indicate no statistically significant cross-talk (see Fig. 1 the coherence spectrum between Ch.1 and Ch2). However, the coherence exhibited values above 0.5 over the whole frequency range for a few cases (see Fig.2). The cross-talk could be traced back to the capacitive line coupling between the log amplifier voltage output and the current input of a nearby log amplifier for some specific channels.

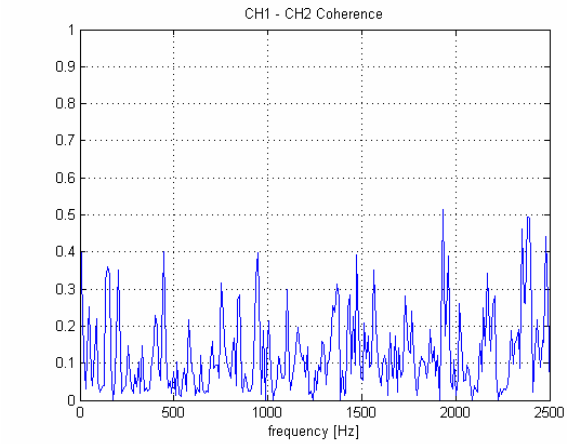

Figure 1: Typical coherence spectrum between VME LogIV-32 channels, in this case, Ch.1 & 2.

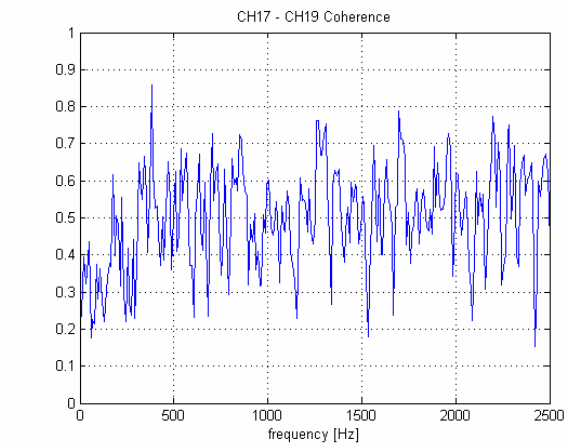

Figure 2: Evidence of cross-talk between channel 17 & 19

As a result of this capacitive coupling, the noise of a few channels increases at very low current measurements (<1nA) though the DC value is not affected. For larger current (>1nA) the coupling is negligible.

Beam noise

PROSCAN beam current measurements (see Fig.3) exhibit significant noise level (50% is not unusual). The coherence analysis has been applied to exclude any instrumental origin and to possibly identify the origin of the observed noise. 2 VME LogIV-4x4 boards were used for the beam current monitors MMAC1 & MMAC3

whereas a CAMAC LogIV-16 was used for the harp measurements. The analogue outputs of the electronics have been sampled at a frequency of 100kHz; the use of a datalogger allowed us to record more than 131'000 samples (up to 512000 samples have been recorded for some cases) leading to spectral resolution better than 13Hz.

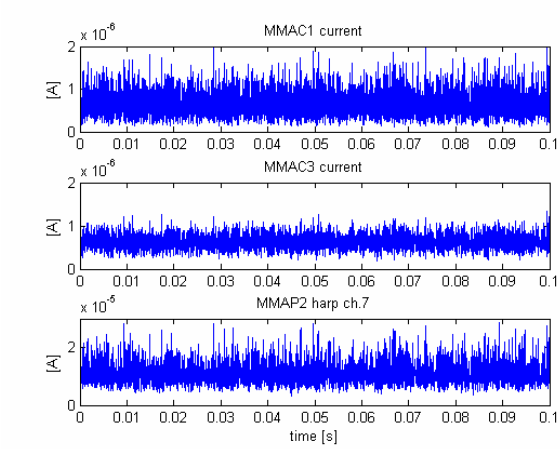

Figure 3: PROSCAN beam signals

The coherence spectrum between the two beam current monitor signals (Fig.4) exhibits an excellent correlation for frequencies up to 40kHz. Excellent correlation is also observed between beam current monitors and harp signals (Fig.5).

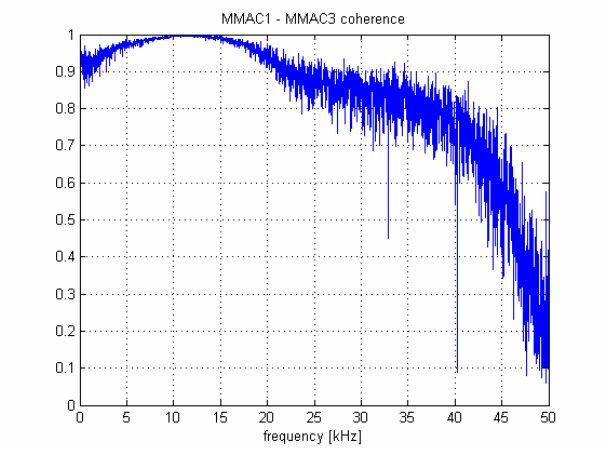

Figure 4: Coherence spectrum of beam currents

Since the signals have been measured using different electronics boards (2 VME and 1 CAMAC) the correlated noise cannot be attributed to the used electronics. The current monitor fluctuations reflect beam intensity fluctuations whereas harp signals are in addition sensitive to beam position variations. This implies that the observed noise is due to beam intensity fluctuations the most probable noise source being the ion source itself.

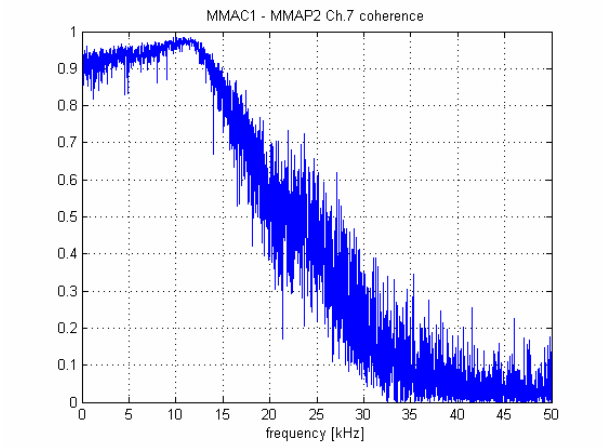

Figure 5: Coherence spectrum between a beam current and a harp monitor signal.

BEAM POSITION MONITOR NOISE

The beam position monitor (BPM) systems [2] are based on digital receiver technology and use the signals from 4 pick-up coils. The RF 2nd harmonic (101.26MHz) signals (beam signals) are directly frequency down-converted (no analogue LO), and the online measurement of individual channel overall gain using 101.31 MHz pilot signals. The beam position is deduced from the difference over the sum of the normalised signals: $\Delta x \propto \frac{S_n^+ - S_n^-}{S_n^+ + S_n^-}$ with $S_n^{+(-)} = \frac{S_{beam}^{+(-)}}{S_{pilot}^{+(-)}}$ the normalized sensor + or -.signal.

Some preliminary results have been obtained as far as the noise analysis from BPM signal is concerned. The MXS3 BPM has been used for these measurements at a beam current of 1.97 mA. The effective sampling frequency was 1kHz. The beam and pilot signals are well correlated for the horizontal direction (Fig.6). Similar results have been obtained in the vertical direction. However no correlation has been observed between horizontal and vertical signals.

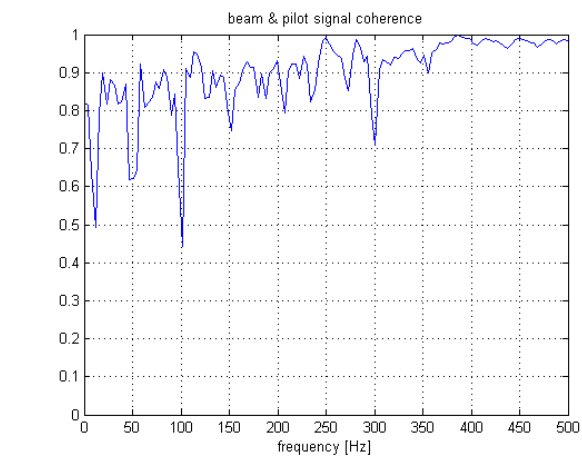

Figure 6: Beam & pilot signal coherence spectrum.

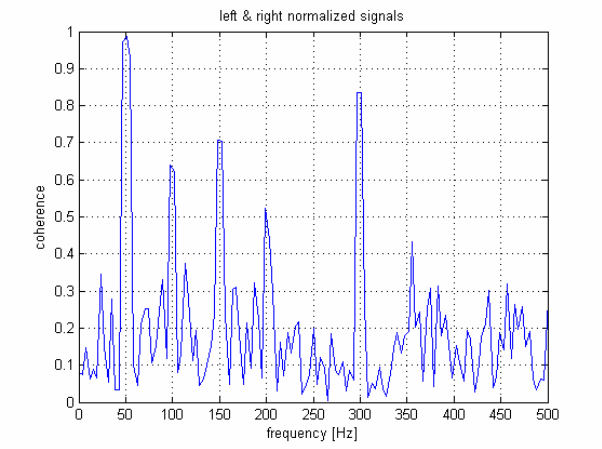

Figure 7: Normalized signal coherence spectrum.

This suggests that the observed beam or pilot signal noise is of instrumental origin, most probably generated by the RF preamplifiers. It is interesting to notice that the normalized signals exhibit some correlation only for the 50Hz harmonics (Fig.7). The interpretation of the normalized signal coherence spectra is more difficult. Indeed, the power spectrum of a normalized signal is the result of the convolution of two spectra. It can be shown with some simulations that the raw data coherence may be lost with the signal normalization. The observed instrumental noise is expected to be removed with the second version of the RF preamplifier which is being presently developed.

REFERENCES

[1] J. S. Bendat, A. G. Piersol, "Engineering Applications of Correlation and Spectral Analysis", John Wiley & Sons, p.72.

[2] P.A. Duperrex, U. Frei, G. Gamma, U. Müller and L. Rezzonico, "Latest Diagnostics Electronics Development for the PROSCAN Proton accelerator", in Beam Instrumentation Workshop-2004, Knoxville, Tennesee, AIP Conference Proceeding vol. 732, pp.268-275.

[3] R. Dölling, "Ionisation Chambers and Second Emission Monitors at the PROSCAN Beam Lines" in Beam Instrumentation Workshop-2006, Batavia, AIP Conference Proceeding vol. 868, pp.271-280.

[4] R. Dölling, "Progress of the Diagnostics at the Proscan Beam Lines" this conference.

OPTICAL SYSTEM FOR MEASURING ELECTRON BUNCH LENGTH AND LONGITUDINAL PHASE SPACE AT PITZ: EXTENSION AND METHODICAL INVESTIGATIONS *

J.Bähr[1], H.Lüdecke, DESY, Zeuthen,Germany
J.Rönsch,University of Hamburg, Germany

Abstract
A complex optical system for measuring the electron bunch length and the longitudinal phase space using a streak camera is installed at PITZ. This system will be extended by two new branches in 2007. The physics design of the chambers containing the radiators and of the optical system is presented. The results of optical calculations of the whole system will be given. Results of methodical investigations will be shown as well, especially concerning transversal optical resolution and time dispersion.

INTRODUCTION

The Photo Injector Test facility at Zeuthen PITZ [1] is a dedicated facility for the developing rf guns for FELs as FLASH or the European XFEL at DESY. The experimental setup consists of a 1.5-cell L-band rf gun with a Cs_2Te cathode. The photocathode laser is capable to generate pulse trains up to 0.8ms length with a pulse to pulse separation of 1 μs. Besides diagnostics elements the gun is followed by a booster cavity which accelerates the electrons up to about 13 MeV. This booster will be exchanged in 2008 by a newly developed one. Then a beam energy of about 28 MeV will be reached. The whole electron beam line which is still under further development consists essentially of diagnostics elements. Besides several systems used for the analysis of the transverse phase space, which is crucial for the optimum running of any SASE-FEL, an extended system for the measurement and analysis of the longitudinal phase space is installed.

The longitudinal phase space [2] and the beam momentum are measured by screen chambers being part of magnet spectrometers whereas the electron bunch length is measured by use of screen stations in the main beam-line all containing special radiators. In both cases a streak camera for the detection of light created mainly by Cherenkov radiators is used. The typical bunch length in the gun is currently about 20 ps. The rise and fall time of the laser pulse creating the electrons of the bunch is about 7 ps later 2 ps. These numbers give the order of magnitude for the temporal resolution needed to be reached by the optical system including the streak camera, which is a device C5680 of Hamamatsu [3] with a resolution of about 2 ps FWHM.

*Work is partly supported by the European Community, contract numbers RII3-CT-2004-506008 and 011935, and by the "Impuls- und Vernetzungsfonds of the Helmholtz Association, contract number VH-FZ-005.
[1]juergen.baehr@desy.de

DESCRIPTION AND EXTENSION OF THE EXISTING OPTICAL SYSTEM

A specially developed optical system [4] transmitting the Cherenkov light [5] from the radiator in the e-beam to the streak camera about 27 m apart from the electron beam line is used at PITZ. Up to now three readout chambers are installed: DISP.scr1 (1) [2] in the low momentum spectrometer and LOW.scr3 (2). A further screen station HIGH1.scr2 (3) is mounted in PITZ just behind the booster cavity for measuring the bunch length and longitudinal bunch profile in the high energy section. Furthermore, a magnet spectrometer for the momentum measurement behind the booster cavity [6] is under development containing screen stations, one with optical readout (DISP2.scr1 (4)) for the streak camera. It will be installed in September 2007. The optical system for this spectrometer is essentially developed and described here.

The optical system is consisting of several branches of input optics, a commonly used optical transport system and a de-magnifying (matching) system. The system is modular and can easily be extended.

Two basic types of radiators are in use to convert the temporal electron bunch shape into that of a visible light pulse: Cherenkov radiators and radiators based on Optical Transition Radiation (OTR). Silica aerogel of different refractive indeces and a quartz plate are used as Cherenkov detectors. Up to now Silica aerogel is mostly used in the range of electron energy available up to now at PITZ (5-13 MeV) because of the higher amount of emitted light compared to OTR, see Fig. 1a.

Two types of optical schemes are used in the light collection systems. In the case that the bunch length is to be measured at a screen station in the main beam line, the so called "full cone"-approach is applied. All Cherenkov light is collected by the high aperture input optics. This method is not applicable in the case of rather extended input light distributions like momentum spectra. It is excluded in principle to transport light of an extended object field by a very high input aperture without remarkable light losses for off-axis object points. Therefore only a small fraction out of the Cherenkov cone of about one or two degrees is used. This scheme is called "partial cone". The light distribution of the momentum spectrum has to be imaged with appropriate spatial resolution onto the entrance slit of the streak camera which has dimensions about 0.05 mm x 6 mm. Therefore, for each screen station a suitable overall magnification has to be realized. In Tab.1 the radiators and related

optical input schemes are shown for all screen stations in use or under development.

Tab1: Screen stations, their physical tasks, radiators, optical input schemes, OTR: optical transition radiation, YAG: Yttrium-Aluminium garnet, F: full cone, P: partial cone

Port	Physical task	Radiator	F/P
1	TV (momentum)	YAG	
	Long. phase space	Aerogel, n = 1.05, quartz	P
	Long. Phase space	OTR	F
2	Bunch length	Aerogel n=1.03, OTR	F
	TV,Beam size	YAG	
	Bunch length, test of partial cone	Quartz	P
3	TV, beam size	YAG, OTR	
	Bunch length	Aerogel n=1.008, OTR	F
4	TV: momentum	YAG	
	Long. Phase space	Aerogel n=1.05	P
5	TV(slice emittance)	YAG	
	TV:momentum, long.phase space possible	OTR	F

Further demands to the optical imaging are a high light collection and transmission efficiency and a minimum time dispersion of the light passing the optical transport line. Generally, achromatic lenses of large focal length forming telescopes with 4-F geometry are used for the imaging over large distances. These lenses have usually a low aperture. Therefore the aperture of the light coming from the light collection system has to be matched to the lenses by magnification. The matching system at the end of the beam line de-magnifies the intermediated images so that the final image fits to the slit dimensions and a maximum of light is passing through the slit of the streak camera. The system is optimized to have minimum of light losses and minimum of optical elements. An image rotating box [9] using switch-able mirrors is used to turn the image of the low energy momentum spectrum by 60 degrees to fit to the streak camera slit orientation.

Port (2) is used for the bunch length measurement [7] in the low energy section. The mostly used configuration is aerogel n=1.03 and will be 1.008 in future (to match the foreseen higher momentum after the gun) and full cone optics.

DESIGN OF TWO NEW RADIATOR CHAMBERS AND RELATED OPTICS

The screen station (3) allows the determination of the longitudinal distribution in the high energy section just behind the booster cavity. It contains an OTR screen and an aerogel radiator with refractive index n = 1.008 and a thickness of 9 mm for bunch length measurements. The full light cone has to be transported. Further screens are installed to measure the transverse distribution by a CCD camera. A detailed description of the design considerations of radiators in screen station (3) can be found in [8].

The High Energy Dispersive Arm HEDA1 (port (4), (5)) is used for momentum and longitudinal phase space measurements [9] in the high energy section of PITZ and includes two screen stations. The first one (4) contains a Silica aerogel radiator (n=1.05, 80mm x 20mm x 5mm) for streak readout. The "partial cone" optical input scheme is used because of the dimensions of the spectrum. The thickness of the aerogel of 5 mm leads to a contribution of about 0.6 ps to the temporal resolution for a momentum of 15 MeV/c. Fig. 1a and Fig.1b show the number of photons and the temporal resolution vs. beam momentum.

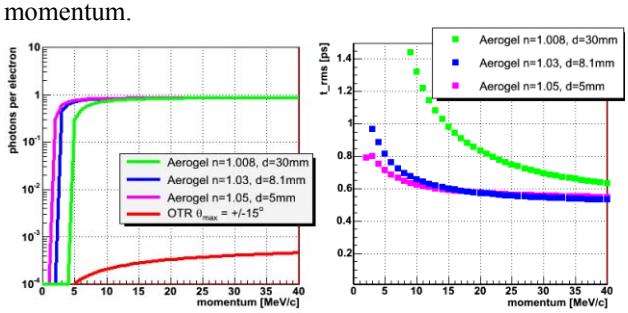

Fig.1a: Number of photons produced by different aerogels and OTR vs. beam momentum, Fig. 1b: Temporal resolution of different Silica aerogels vs. beam momentum

All the suggested aerogel solutions produce about the same number of photons at about 30 MeV/c, but for n =1.05 the resolution in the range from 5 to 15 MeV/c is at minimum compared to the other options and the number of photons for lower energies is higher.

The second screen station (5) in HEDA1 contains an OTR-screen and will initially be used for TV readout. Streak optics can be added later easily. For about 30 to 40 MeV/c the emission angle of an OTR radiator is rather small, so the full cone can be measured.

CHARACTERIZATION OF THE WHOLE OPTICAL SYSTEM

Several quantitative characteristics are used to describe the whole system:

- collection efficiency ε(coll)
- transmission efficiency ε(Tr)
- Modulation Transfer Function (MTF)
- spatial resolution R
- time dispersion Δt

The design of the optical system for "full cone" is such that the collection efficiency is about 100%, while in case of "partial cone" it is <1%. All subsystems are designed such that the transmission efficiency is maximized and any vignetting is avoided. For example the transmission efficiency at screen 3) for a beam of 2 mm diameter is 98% for a central ray and 85% for a ray with 1.4 mm off-set. The other characteristics will be used to compare measurements and simulations shown in Tab. 2.

Tab.2: Results of measurements and simulations of the optical systems of four branches: R: spatial resolution, ΔT: time dispersion, F: full cone, P: partial cone, M: magnification

No. port	R/ Lp/mm	R/Lp/mm at λ/nm	ΔT/ ps	ΔT/ ps	M
	Meas.	Calcul.	Meas.	Calcul.	
1	3 ‡	>9 (550)	68	58	0,2
2	12§**	170 (550) 20 at (400-700)	73	52	1,6
3	15	9	-	45	1.4
4	-	20	-	40	0.07

The measured time dispersion is larger than the calculated one. This can be explained with facts like dispersion in air, that lenses in reality are mostly thicker than their values in the catalogues and misalignment of optical elements. The values of spatial resolution are mostly better than the design values.

For screen station 1 the calculated Modulation Transfer Function MTF is shown in Fig. 2. The figure shows the high transverse spatial resolution of at least 8 Lp/mm.

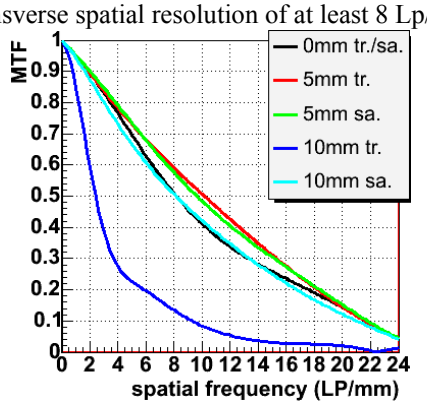

Fig 2: MTF for screen (1), different conditions for the range of 545-555 nm, offset from optical axis in mm, sa: sagittal, tr: transversal

REFLECTIVE OPTICS

The goal of the design of the optical system is to reach a temporal resolution of the whole system which is comparable to the temporal resolution of the streak camera, i.e. about 2 ps. As earlier measurements have shown [5], the temporal resolution of the system is about 60 ps caused by dispersion in the lenses. It is necessary to restrict the spectral bandwidth essentially to reach the wanted time resolution. This results of course in a large loss of light. To improve the situation significantly, refractive elements (lenses) must be exchanged by reflective elements (mirrors) because these do not cause any dispersion. We consider the use of aspheric mirrors to avoid, beside a large chromatic aberration also spherical aberration at the same time. A simple ansatz was tested experimentally and by simulation as a first step for an improved system. It is based on telescopes formed by mirrors in 4-F configurations see Fig. 3. The mirrors are aspheric on-axis with rather high aperture. Also a system consisting of two telescopes of such mirrors was investigated. The spatial resolution was measured to 30 Lp/mm for a scheme of four parabolic mirrors (two 4-F schemes, magnification = 1, f1 = f2 = 660 mm, f3 = f4 = 1500 mm, overall length about 12 m).

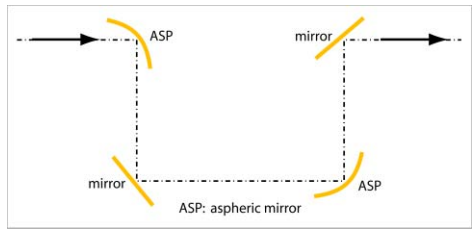

Fig.3: Scheme of a telescope formed by aspheric mirrors (ASP)

CONCLUSION

The optical system for the measurement of bunch length and longitudinal phase space by streak camera has been described and evaluated. In 2007 it will be extended by two new branches. The transverse resolution, the time dispersion and further characteristics are measured and simulated. Most of theses are better than the design goals. The basic problem of the time dispersion caused by use of lenses is going to be solved by aspheric mirrors.

REFERENCES

[1] F.Stephan et al., Photo Injector Test Facility and Construction at DESY, FEL 2000, Durham.

[2] J.Rönsch et al., Longitudinal Phase Space Studies at PITZ, FEL '05, SLAC, Stanford, USA, 2005.

[3] Hamamatsu Photonics, Hamamatsu city, Japan

[4] J.Bähr et al., Optical Transmission Line for Streak Camera Measurements at PITZ, DIPAC '03, Mainz, Germany 2003

[5] J.Bähr et al., Measurement of the longitudinal phase space at the Photo Injector Test Facility at DESY Zeuthen DIPAC '03, Mainz, Germany 2003.

[6] S.Khodyachykh et al., Design and Construction of the Multipurpose Dispersive Section at PITZ, DIPAC'07, Venice,Italia.

[7] J.Bähr et al., Measurement of the Longitudinal Phase Space at the Photo Injector Test Facility at DESY Zeuthen, FEL '03, Tsukuba, Japan.

[8] J.Rönsch et al., Investigations of the Longitudinal Beam Properties at the Photo Injector Test Facility in Zeuthen, FEL'06, Berlin, Germany.

[9] J.Rönsch, Measurement of the Longitudinal Phase Space at the Photo Injector Test Facility at DESY in Zeuthen (PITZ), DIPAC'05, Lyon, France, 2005

‡ resolution measurements limited by pixel size of used CCD camera

§ resolution measurements limited by pixel size of used CCD camera

** without first lens f = 80mm

KICKER BASED TUNE MEASUREMENT FOR DELTA

P. Hartmann*, J. Fürsch, R. Wagner[1], T. Weis, K. Wille
Zentrum für Synchrotronstrahlung DELTA, Universität Dortmund, D-44221 Dortmund
[1] Fachbereich Physik, Bergische Universität Wuppertal, D-42097 Wuppertal

Abstract

We have set up a tune measurement for the electron storage ring Delta based on broadband beam excitation with a kicker magnet and measurement of the relaxation betatron oscillations turn-by-turn. By averaging over several kicks the kick amplitude may be as low as 1 μrad in standard user runs, leading to negligible beam distortion. Signal to noise ratios in excess of 10 are reliably achieved down to 200 μA beam current using a maximum kicker amplitude of 30 μrad. The measurement can be repeated 10 times per second. The precision of the frequency estimate is as low as 10^{-5}. A simple tune feedback algorithm based on this measurement compensates for tune shifts due to vacuum chamber movement and orbit movement in sextupoles.

INTRODUCTION

A precise, reliable and fast measurement of the tune is an essential prerequisite for the stable operation of a storage ring. Fast tune measurements in an electron machine require an excitation of the beam prior to the tune detection. After exciting the beam the tune is inferred from side bands of the revolution harmonics in the spectrum of a difference signal of two adjacent beam pickups.

The most simple beam excitation would be a broadband constant beam shaker excitation with white noise covering the whole spectrum up to half the revolution frequency. All frequencies in the desired bandwidth are excited with equal strength and at all times. Betatron resonances can be seen immediately as peaks in the frequency spectrum.

The total perturbation applied to the beam by the excitation shaker, though, is inacceptable for synchrotron light users. It can be lowered either by constraining the bandwidth of the beam excitation around a center frequency and scanning this frequency over the desired bandwidth (frequency scan method) or by constraining the time, the broadband excitation signal is applied to the beam (kicker excitation method).

Although DELTA is equipped with a frequency scan method tune measurement [1] which is an excellent tool for peak evaluation done by the human eye, we have tried for quite a while to implement an automated tune stabilization mechanism based on this measurement without great success. Mainly the sudden appearance of noise signals kept us from providing a reliable enough automated measurement for tune stabilization [2].

The advent of fully digital off-the-shelf turn-by-turn (TBT) beam position monitor electronics [3] allow an increase in precision and a decrease in measurement time compared to the frequency scan method setup.

EXPERIMENTAL SETUP

The experimental setup for the kick-method (see fig. 1) is relatively simple compared to the frequency scan setup while the cost is comparable. Although not at an optimal

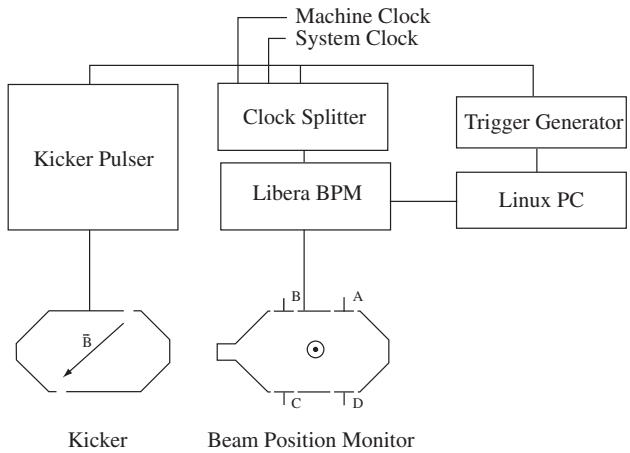

Figure 1: Setup overview.

ninety degrees, the phase advance between the kicker magnet and the chosen BPM is such that a moderate kick in the diagonal plane generates well measurable betatron oscillation amplitudes at the BPM position in the horizontal and the vertical plane. The measured amplitudes may still be increased by at least a factor of two by choosing a better suited BPM head which is currently not equipped with a Libera monitor. A large beta function at the BPM enhances the measurement of the betatron oscillation. Due to dephasing the collective beam oscillations are damped after about 1000 turns to less than one half of their original amplitude.

The maximum measurement repetition rate is limited to about 12 to 15 s^{-1} by the processor load of the Libera device. We do not exceed 10 s^{-1} which generates a load of about 55 %.

Beam excitation kicker

The kick is applied to the beam by the DELTA diagnostic kicker magnet [4]. The kicker magnet is driven by a typical halfwave pulser (see fig. 2), employing an IXYS Power MOSFET as the switch. A charging voltage U_{ch} of 300 V results in a peak current of 100 A, measured with a current transformer CT. A trigger pulse of 1.2 μs generates a FWHM pulse width of 250 ns which is determined

* hartmann@delta.uni-dortmund.de

by the cable/kicker impedance together with the capacitor C_2. Following MAFIA simulations [4] 100 A pulse current generate a kick of 30 μrad at the full beam energy of 1485 MeV in the horizontal as well as in the vertical plane. The pulse repetition rate of the kicker is limited by the charging resistor R_{ch} to about 100 Hz.

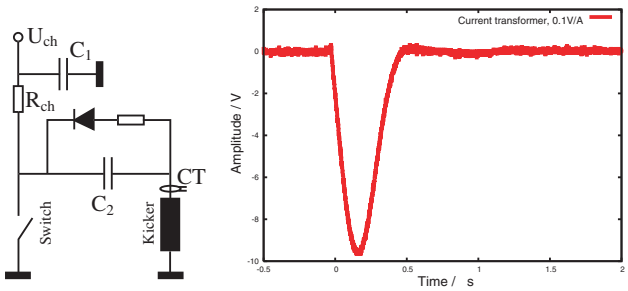

Figure 2: Schematic view of a typical half-wave pulser and pulse trace measured with a current transformer CT. As the switch we use an IXYS Power MOSFET.

Libera beam position monitor

An I-Tech Libera beam position monitor provides the turn-by-turn measurement data of the beam orbit. Currently we use firmware version 1.21 on the Liberas with the DIAMOND EPICS driver [5] version 0.63. This version of the firmware does not allow to switch off the Digital Signal Conditioning (DSC) without having large orbit jumps. DSC generates noise on the turn-by-turn data which renders the measurement unusable for tune measurement. Therefore, this Libera is for now not used for slow orbit detection and is dedicated solely to tune measurement. Subsequent versions of the firmware will allow to switch off DSC without orbit jumps [3] and thus the BPM will in the future be used for slow orbit correction in parallel to tune measurement.

Unfortunately, the Libera internal automatic gain switching (AGC) is not supported by the DIAMOND EPICS driver. AGC is thus done with a set of two EPICS records. An improved version of the Libera internal AGC is planned to be used with future firmware versions. Triggering the Libera with 10 Hz with the 'Free Run' option of the EPICS driver switched ON leads to a processor load of abut 55 %. Trigger rates in excess of 10 Hz are possible but are currently not used. The driver puts 2048 TBT points, starting at the trigger event, into a waveform record. This record is then further processed by an EPICS client application on a Linux PC.

Peak detection and evaluation

Peak detection and evaluation is done in several stages with a multithreaded algorithm on a PC.

At first, 1024 points of the TBT data starting at the trigger event are fourier transformed using the FFTW software

(a)

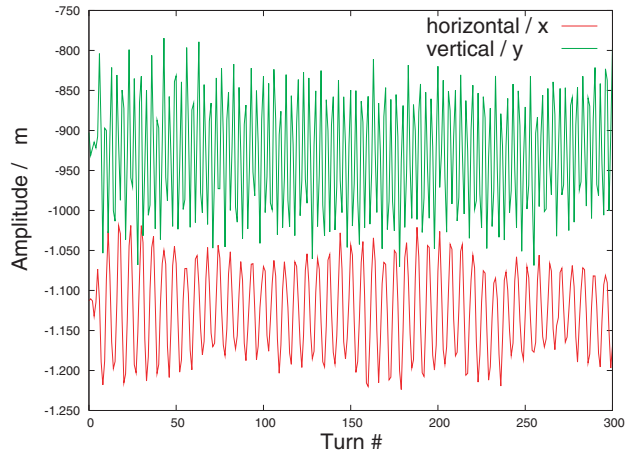

(b)

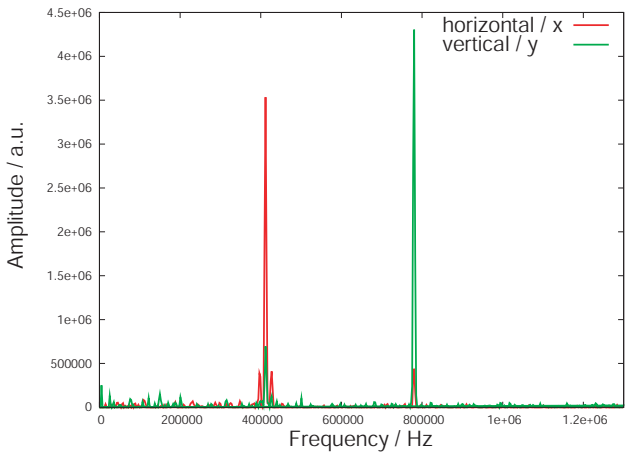

Figure 3: (a) Beam response in the horizontal (red) and vertical (green) plane measured after applying a kick of 30μrad to a beam of 80 mA beam current.
(b) FFT-Spectrum of 1024 data points. The modulation in fig. (a) of the horizontal signal and the sidelobes on the spectrum in fig. (b) are due to an uncorrected horizontal chromaticity.

package [6]. From the resulting spectrum, connected areas with amplitudes in excess of the average plus 5 sigma are considered a peak. Peaks are added to a list containing their amplitude and frequency. Under normal circumstances, the list contains 1-2 elements after searching the whole spectrum. Due to coupling the vertical betatron frequency is, with low amplitude, visibel in the horizontal plane and vice versa, even at some distance from the coupling resonance. At low beam current the list may contain additional noise peaks.

The identification of the proper peak, especially at low beam current, is based on several criteria that contribute with different weights to the final choice. Peak height is the most important criteria, while being in a region of in-

terest and the distance from the former 'good' peak is also considered.

The most helpful strategy with noisy power spectra is the employment of previous knowledge. Based on the fact that, due to dephasing, the betatron amplitude decays within 1000 turns, we generate two power spectra each from 1024 data points, one starting at turn 0 the other starting at turn 1024. By substracting the two spectra point by point, noise peaks with constant amplitude cancel out while damped oscillations are enhanced.

The precision of the FFT method is limited to plus or minus half a spectrum bin, which is in our case $\pm$2.5 kHz or $2 \cdot 10^{-3}$. A signal to noise ratio (SNR) between 10 and 15 is easily achieved on a per kick basis down to a beam current of 4 mA. Further reduction of the beam current requires several kicks for a successful measurement. Since the phase of the betatron amplitude between kicks is constant, the turn by turn data points of consequent kicks can be added to increase the SNR. Applying this method, tunes can reliably measured down to a beam current of 0.2 mA. On the other hand this method can also be applied at high currents during user runs in order to further decrease the beam perturbation. Averaging over a maximum of 20 kicks at 120 mA beam current allows to decrease the kick amplitude down to 1 μrad or 10V charging voltage respectively.

An experiment with the X-ray absorption beamline BL8 at DELTA has been carried out in order to check for beam distortion. The temporal resolution was determined by the ion chambers filter rise times to between 3 and 10 ms. The spatial resolution was set by the entrance slit of the beamline to about 15 % of the FWHM of the vertical photon beam size. At maximum kick amplitude beam distortion was clearly seen on the ion chamber signal. Lowering the kick amplitude led to a decrease in the distortion amplitude to negligible level. Filter settings for typical beamline operation average out beam distortion with this repetition frequency anyway.

Once the FFT evaluation is done, the data, frequency and amplitude of the tune peak is fed into a thread which fits a sinewave to the measurement data using a Marquardt-Levenberg algorithm implemented by the free software package LEVMAR [7]. While the precision of a frequency measurement using a fourier transform increases linearly with the number of data points, the precision of the ML algorithm increases proportional to it's fourth power. Using amplitude, frequency and phase as the fit parameters and fitting to noisy data with side frequency peaks this precision however can not be reached. Nevertheless, an increase in precision of two orders of magnitude to better than $2 \cdot 10^{-5}$ is routinely achieved fitting to 512 data points. Even though the starting points of frequency and amplitude for the fit are known to better than 1 %, runs with test data have shown that the best strategy for archieving a good fit is to run the algorithm with a set of three phases between 0 and π and three frequencies in the middle and at the edges of the power spectrum bin. After running those 9 fits in a row the parameter set providing the least quadratic deviation from the data points is taken as the result.

CONCLUSION

We have set up a tune measurement based on the kick method which is more reliable, more than twice as fast and has a two orders of magnitude higher precision than the previously applied frequency scan method. Based on this setup a PID based tune feedback algorithm is implemented that helps beam operators in setting up the machine during machine startups. The high precision achieved allows to set up an online-chromaticity measurement based on a frequency modulation of the main oscillator with very low amplitude.

For the last six months this method is regularly applied as the standard tune measurement method at the Delta storage ring. We have tested it at 1485 MeV and at 550 MeV beam energy, with multibunch filling patterns as well as in single bunch operation. A further increase in reliability may be done using a BPM position more optimized for phase advances and betafunctions.

ACKNOWLEDGEMENTS

We thank the Electronics Lab for developments and P. Kuske from BESSY for helpful hints.

REFERENCES

[1] K. Dunkel et al., Status of the DELTA Betatron-Tune-Monitor System, Proc 1997 DIPAC, Frascati, Italy.

[2] A. Kwiatkowski, Diploma thesis, Univ. Dortmund, 2003

[3] http://www.i-tech.si, see also Libera workshop 2006

[4] G. Blokesch et al., A slotted-pipe kicker for high-current storage rings, Nucl Instr. Meth. A 338, 151
see also U. Scholz, Diploma thesis, Univ. Dortmund, 1994

[5] http://sourceforge.net/projects/libera-epics

[6] http://www.fftw.org

[7] http://www.ics.forth.gr/∼lourakis/levmar/

TOUSCHEK LIFETIME MEASUREMENT WITH A SPURIOUS BUNCH IN UVSOR-II ELECTRON STORAGE RING

A. Mochihashi, M. Katoh, M. Shimada, Institute for Molecular Science, Okazaki 444-8585, Japan
M. Hosaka, Y. Takashima, Nagoya University, Chikusa, Nagoya 464-8603, Japan
Y. Hori, High Energy Accelerator Research Organization (KEK), Tsukuba 305-0801, Japan

Abstract

We have developed a method to measure the Touschek beam lifetime of an electron storage ring using spurious bunches in single-bunch operation by measuring changes in the single-bunch impurity over time. To measure a spurious bunch and the main bunch simultaneously, we use a photon counting method with sufficient dynamic range and response time. We demonstrate the method by measuring the Touschek beam lifetime in the UVSOR-II electron storage ring. We find that the Touschek beam lifetime dominates the total beam lifetime in UVSOR-II in the usual vacuum condition. The beam lifetime measurement in the multibunch condition indicates that the Touschek lifetime still dominates even in the multibunch operation in which the beam current is 12 times larger than that of the single-bunch condition.

BEAM LIFETIME IN ELECTRON STORAGE RING

In typical electron storage rings, such as synchrotron radiation (SR) light sources, the beam lifetime τ is mainly determined by two processes; one is the Touschek lifetime [1, 2] which comes from scattering between electrons in the same electron bunch, and the other is the beam–gas scattering lifetime which comes from scattering between electrons in the beam and residual gas molecules in the beam ducts. In case the quantum lifetime can be neglected, the total beam lifetime τ can thus be expressed as $1/\tau = 1/\tau_T + 1/\tau_g$, where τ_T is the Touschek lifetime and τ_g is the beam–gas scattering lifetime. The Touschek lifetime τ_T can be written as [2, 3]

$$\frac{1}{\tau_T} = \frac{r_c^2 c N_b}{8\pi\sigma_x\sigma_y\sigma_l}\frac{\lambda^3}{\gamma^2}D, \qquad (1)$$

where r_c is the classical electron radius, c is the speed of light, N_b is the number of electrons in a bunch, σ_x, σ_y and σ_l are the standard values of the Gaussian bunch width, height and length, λ^{-1} is the momentum acceptance and γ is the Lorentz factor of the electron beam. D is the function [3] which gives dependence of τ_T on the momentum acceptance of the storage ring. For beam diagnostics, the Touschek lifetime is useful for measuring the basic parameters of the electron beam.

The beam lifetime τ consists of the Touschek lifetime and the beam–gas scattering lifetime; however, it is difficult to measure the two beam lifetimes separately because both depend on the beam current. The Touschek lifetime depends directly on the beam current; on the other hand, the beam–gas lifetime depends on the vacuum pressure, which depends on the beam current.

At the SuperACO SR facility [4] the Touschek lifetime was measured by storing two bunches with different bunch charges simultaneously and measuring their decay rates. The Touschek lifetime could then be analyzed by comparing the decay rate of each bunch, even though the vacuum conditions could change during the measurement, because both bunches experience the same vacuum conditions. The 'two unequal bunches' method of SuperACO is very effective for measuring the Touschek lifetime if it is assumed that the bunch volume does not change with the bunch charge, namely, the Touschek lifetime is inversely proportional to the number of electrons in the bunch. However, the assumption is not valid for electron storage rings in general because of perturbation of the bunch volume.

The need for the assumption can be avoided by preparing two bunches with extremely different bunch charges. If the Touschek lifetime of the weaker bunch of the two is very long compared with that of the more intense bunch, it is possible to measure the Touschek lifetime of the intense bunch without making any assumption about the dependence of the Touschek lifetime on the bunch charge. However, it is difficult to make two bunches that have extremely different bunch charges when the bunch charge of the intense bunch is small.

Spurious bunches in single-bunch operation in electron storage rings have extremely small charge compared with the main bunch charge regardless of the size of the main bunch charge, and can be generated automatically[5, 6]. Therefore, spurious bunches can be a useful probe for measuring the Touschek lifetime. Even though a spurious bunch can grow continuously during a measurement, it is possible to cancel the effects of the growth and measure the Touschek lifetime of the main bunch precisely using only the intensity of the main and spurious bunches, without requiring calculated beam or storage ring parameters.

THEORY

We consider the change with time in the number of electrons in a main bunch N_0 in single-bunch operation. We assume electron loss by the Touschek effect and beam–gas scattering, such that the change in N_0 with time is written as

$$\frac{dN_0}{dt} = -\frac{N_0}{\tau_T(N_0)} - \frac{N_0}{\tau_g}, \qquad (2)$$

where the first term in the right-hand side represents the decay rate of the electrons from the Touschek effect and the second term represents that from beam–gas scattering.

We consider next the change in the number of electrons as a function of time in the RF bucket immediately following the main bucket. The number of electrons in the next bucket, N_1, also decreases due to Touschek and beam–gas scattering; however, some electrons expelled from the main bucket by Touschek scattering can enter the next bucket[6]. The change in N_1 with time is written as

$$\frac{dN_1}{dt} = N_0 C_0 - \frac{N_1}{\tau_T(N_1)} - \frac{N_1}{\tau_g}, \tag{3}$$

where the first term on the right-hand side represents the growth of the spurious bunch due to electrons transferred from the main bucket. The parameter C_0 represents growth of the single-bunch impurity in a unit time. The second and third terms represent the decay rates of the spurious bunch due to the Touschek effect and beam–gas scattering.

We now consider the single-bunch impurity defined as the ratio of the charge of the first spurious bunch to that of the main bunch. From Eqs. (2) and (3), the change in the single-bunch impurity with time is written as

$$\frac{d}{dt}\left(\frac{N_1}{N_0}\right) \approx C_0 + \frac{1}{\tau_T(N_0)}\frac{N_1}{N_0}, \tag{4}$$

where the approximation is valid when $1/\tau_T(N_1) \ll 1/\tau_T(N_0)$. If the growth of the single-bunch impurity in one Touschek lifetime period can be neglected compared with the single-bunch impurity, namely, if $N_1/N_0 \gg C_0\tau_T$, then the Touschek lifetime τ_T can simply be written as

$$\frac{1}{\tau_T(N_0)} = \frac{d}{dt}\log\left(\frac{N_1}{N_0}\right). \tag{5}$$

If the approximation $N_1/N_0 \gg C_0\tau_T$ is not valid, it is still possible to measure the Touschek lifetime by repeating the measurement with a different spurious bunch charge with the same main bunch charge. For spurious bunch charges N_1 and N_1^* ($N_1 > N_1^*$) and main bunch charge N_0, from Eq. (4), $\tau_T\,(N_0)$ can also be written simply as

$$\frac{1}{\tau_T(N_0)} = \frac{d}{dt}\log\left(\frac{N_1 - N_1^*}{N_0}\right). \tag{6}$$

We note that both Eqs. (5) and (6) can be written with only N_0, N_1 and N_1^*, which can be determined from measurement such as photon counting method [6, 7] ; the equations contain no calculated beam parameters or storage ring parameters.

OBSERVATION

To observe both the main bunch and a spurious bunch simultaneously, we used a photon counting method [6, 7] with a dynamic range greater than 10^5. To separate the signals from individual bunches, we used a microchannel plate-photomultiplier tube (MCP-PMT, Hamamatsu R2809U) with good time resolution (rise time of 150 ps and transit time spread of 55 ps). Fig. 1 shows a typical change with time in the intensity of the main and spurious bunches, measured by photon counting in single-bunch condition in UVSOR-II electron storage ring [7]. By measuring the change in the single-bunch impurity with time we can analyze the Touschek beam lifetime with Eq.(5) or (6); in case of the UVSOR-II we used Eq.(6) because of the condition of the approximation. Fig. 2 shows the Touschek lifetime from Eq.(6) and the total beam lifetime with different skew quadrupole magnet conditions. The Touschek lifetime from Eq.(6) is almost equal to the total beam lifetime even in larger skew quadrupole current. Even though the Touschek scattering effect decreased and the Touschek lifetime increased because of the skew quadrupole field, the lifetime was still dominated by the

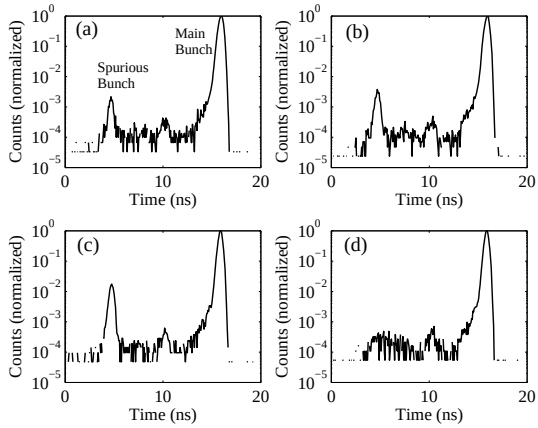

Figure 1: Change in temporal structure with time in single-bunch operation. Temporal structure (a)just after injection (total current 63.7mA), (b) after 10min(48.0mA), (c) after 87min (15.2mA), and (d) temporal structure without spurious bunches.

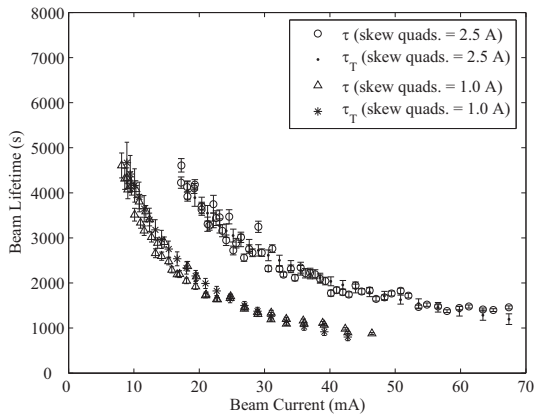

Figure 2: Touschek and total beam lifetimes for two skew quadrupole conditions. The dots/stars and circles/triangles correspond to the analyzed Touschek lifetime and the total beam lifetime, respectively, when the skew quadrupoles were set at 2.5/1.0 A.

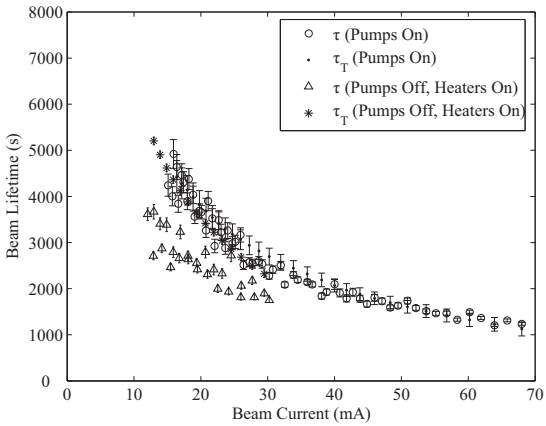

Figure 3: Touschek and total beam lifetimes for the same skew quadrupole condition (2.5 A) but different vacuum conditions. The dots and circles correspond to the Touschek lifetime and the total beam lifetime, respectively, under normal vacuum conditions (the same as for Fig. 2). The stars and triangles correspond to the Touschek and the total beam lifetimes, respectively, with all the SIPs and DIPs turned off and the baking heaters turned on.

Touschek effect. To make a situation where the Touschek lifetime and the beam–gas scattering lifetime are comparable, we tried to decrease the beam–gas scattering lifetime drastically. We turned off all the SIPs and DIPs in the storage ring and partly raised the temperature of the beam ducts with heaters, which are usually used for bake-out evacuation of the beam ducts. The vacuum pressure measured using the vacuum gauges increased from 2×10^{-8} Pa to 1×10^{-6} Pa. We injected and stored a single bunch under this condition and measured the beam lifetime. The Touschek and total beam lifetimes are shown in Fig. 3. In this experiment, we could only measure the beam lifetime below a beam current of 30 mA. As seen in the figure, the total beam lifetime clearly decreased compared with that under the normal vacuum condition. On the other hand, the Touschek lifetime kept the same value as that under the normal vacuum condition. This clearly demonstrates that we can measure the Touschek lifetime and the beam–gas scattering lifetime separately using this method.

We have estimated the vacuum pressure of the beam orbit using a model [7] of scattering between residual gas atoms and high energy electrons in the beam. From the estimation of the scattering cross section which leads the beam loss, we assume CO gas contributes to the beam–gas scattering lifetime in the UVSOR-II [7]. From the beam–gas scattering lifetime in poor vacuum condition in Fig. 3, the averaged CO pressure is estimated to be $1.12 \times 10^{-6} \pm 2.03 \times 10^{-7}$ Pa, which is close to the pressure measured using the vacuum gauges.

BEAM LIFETIME IN MULTIBUNCH OPERATION

We measured the beam lifetime in multibunch (successive 12 bunches + successive 4 vacant buckets) and single-bunch condition with the same operating mode; the same RF voltage and optical functions. Fig. 4 shows the $I\tau$ product in the multibunch and the single-bunch condition. The beam lifetime in the multibunch condition is slightly larger than that of the single-bunch condition. As discussed in the previous section, in the single-bunch condition the Touschek lifetime dominates the beam lifetime in the UVSOR-II. The result in Fig. 4 then indicates that even in the multibunch condition in which the total beam current is 12 times larger than that in the single-bunch condition the Touschek lifetime still dominates the beam lifetime. Small difference between the multibunch and the single-bunch may come from perturbation of the bunch volume due to wake field. Precise measurement of the Touschek lifetime in the multibunch condition is the next subject.

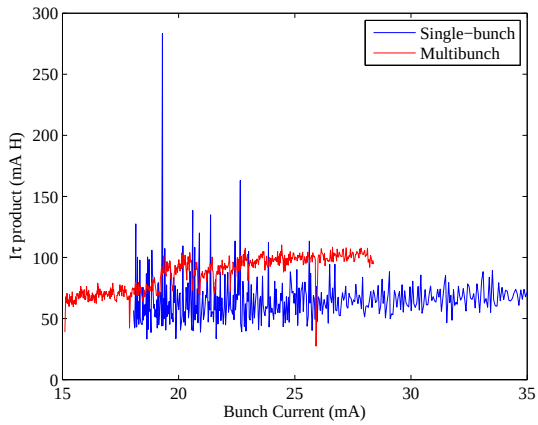

Figure 4: $I\tau$ product in multibunch and single-bunch operation in the same condition. The multibunch operation has 12 bunches; the total beam current is 12 times larger than the bunch current.

REFERENCES

[1] C. Bernardini et al., Phys. Rev. Lett. **10** (1963) 407.

[2] H. Bruck, *Accélérateurs Circulaires de Particules*, (Presses Universitaires de France, 1966), 303.

[3] H. Wiedemann, *Particle Accelerator Physics II*, 2nd edition (Springer-Verlag, Berlin, 1999), 329.

[4] J. C. Besson et. al., Commissioning of SuperACO, ORSAY Report RT-88-01, 34.

[5] T. Kasuga, H. Yonehara, M. Hasumoto and T. Kinoshita, Jpn. J. Appl. Phys. **28** (1989) 541.

[6] T. Obina, T. Kasuga, M. Tobiyama, T. Katsura, K. Tamura, Nucl. Instrum. Methods Phys. Res. A **354** (1995) 204.

[7] A. Mochihashi, M. Katoh, M. Hosaka, Y. Takashima, Y. Hori, Nucl. Instrum. Methods Phys. Res. A **572** (2007) 1033.

BEAM DIAGNOSTICS DEVELOPMENT FOR THE CRYOGENIC STORAGE RING CSR

T. Sieber, H. Fadil, M. Grieser, R. von Hahn, A. Wolf
Max Planck Institut für Kernphysik, 69117 Heidelberg, Germany

Abstract

A cryogenic storage ring (CSR) is under construction at the MPI-K Heidelberg. It consists of electrostatic elements and has a circumference of ~35 m. The CSR shall be used for storage of rotationally non-excited molecules and highly charged ions, therefore extremely low temperatures (<4K) and gas pressures (10^{-15} mbar) are required. The ring shall also be operational at room temperature and bakeable to at least 300°C. The maximum energy of singly charged ions is 300 keV, the intensities will be in the range 1 nA – 1 µA. For the mass range, A<100 is taken as reasonable design value, in later stages of CSR operation experiments with heavier ions are foreseen.

Due to the exceptional boundary conditions we are working on new or further developments for most of the diagnostics devices. For example our RGMs have to produce their own local pressure bumps. The MCPs have to work at temperatures around 4 K. The beam position pickups shall be operated in resonant mode for increased sensitivity. Our beam profiler will use secondary electrons from a stopper plate, which allows beam imaging in the intensity range 10^2 to 10^{12} pps. For intensity measurements a SQUID CCC system is under discussion.

INTRODUCTION

The planned experimental programme of the CSR [1] covers a wide range of ion species, energies and intensities. Low charge states, low velocities and low intensities put - besides temperature and XHV - strong demands on the beam diagnostics system. Table 1 shows some basic parameters of the CSR at one glance.

Table 1: Parameters of the CSR.

Type	Electrostatic
Circumference	35.2 m
Operation temperature	2 - 300 K
Vacuum pressure	1×10^{-15} mbar
Mass range	1 – 100 amu
Energy range (1^+ ions)	20 – 300 keV
Intensity range	1 nA – 1 µA
Revolution Frequency	5 -220 kHz

A possible layout of the CSR beam diagnostics system is shown in Figure 1. Molecules, highly charged ions and neutral beams are injected in three corners of the ring, which requires in the following straight sections a device for measurement of beam position and size during the injection procedure. For this measurement a multi channel plate (MCP) based low intensity beam profiler (see below) will be used.

To measure the profile and position of the circulating beam, a Residual Gas Monitor has to be adapted to XHV conditions. To get count rates around 1 kHz on the MCP, the pressure has to be increased locally to 10^{-12} mbar (at < 4 K). MCP operation at these low temperatures is not well tested, but recent results at MPI-K and Manne-Siegbahn Laboratory look promising [2].

The beam intensity is planned to be measured with a SQUID based Cryogenic Current Comparator (CCC) like described in [3]. The resolution of these devices has currently reached ~100 pA/Hz$^{1/2}$, which would be sufficient for our application. However, extensive R&D is necessary to make the CCC bakeable, to optimise the magnetic shielding and to make the SQUID itself demountable.

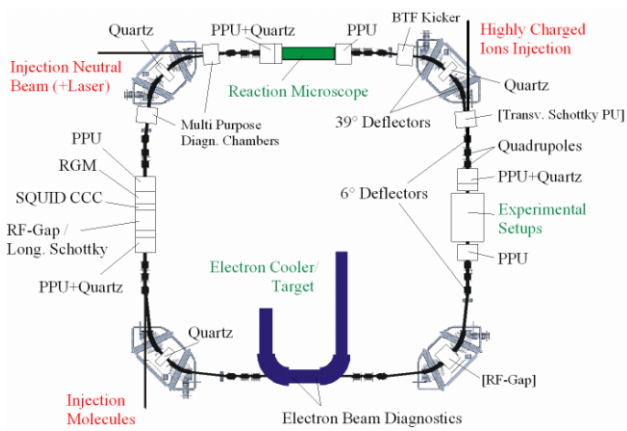

Figure 1: Layout of the CSR beam diagnostics system

At the entrance and at the exit of each straight section there will be Beam Position Monitor pickups for closed orbit measurement. Like proposed for single particle measurements in ion traps, we are looking into the possibility to operate the capacitive pickups in a resonant circuit with high shunt impedance to increase pickup sensitivity.

The diagnostics of the electron beam size and position is done with a wire scanner placed inside the HTS solenoid of the electron cooler. Since this scanner works also as a scraper for the ion beam, it will allow precise measurements of the relative positions of electron and ion beam.

THE LOW INTENSITY BEAM PROFILER

Numerous tests with have been performed to find an appropriate scintillator material for our first turn diagnostics. We found that in the given energy and mass range the damage caused by sputtering was too heavy for all the materials we checked [4]. Comparable to measurements at LEIR and Linac3 [5] we measured a drastical decrease of luminosity after some hours of irradiation. For that reason (and moreover because of the limited sensitivity and intensity range of any scintillator material) we replaced the scintillator by a metal plate for production of secondary electrons, which are - after passing an acceleration grid - detected on an MCP / phosphor screen combination to produce an image of the beam (see Fig. 2). This device has been well tested in the REX-ISOLDE diagnostics system [6]. It requires three additional HV feedthroughs into the CSR cold chamber, but has the advantage of high sensitivity and large detection range (10^2 – 10^{12} particles per second).

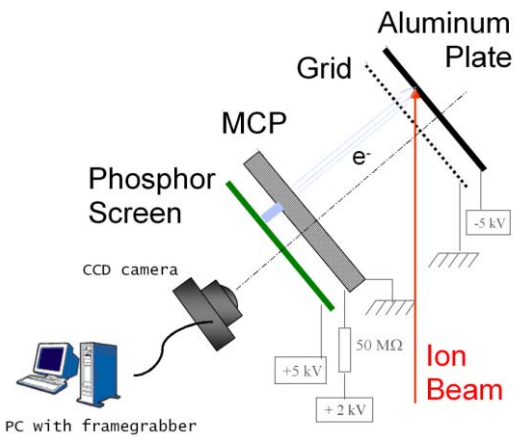

Figure 2: Low intensity beam profiler.

For the injection beamline of the CSR prototype, which is currently under construction, we have built a diagnostic box, housing the device shown in Fig. 2. Figure 3 shows the mechanical layout of this box.

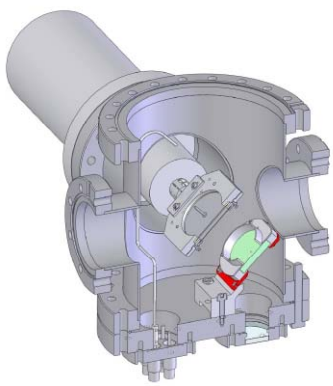

Figure 3: Diagnostic Box with beam profiler.

For control of the voltages of acceleration grid, MCP and phosphor screen, a control program has been developed, which shows the beam (optionally in combination with a beam profile) in artificial colours and is equipped with some reasonable functions, like avoiding movement of components under high voltage and slow changing of MCP and phosphor screen voltages. Figure 4 shows a screenshot of the program, during measurement of a 20 keV, 1 nA H_2^+ beam at the CSR prototype injection beamline. The beam in the picture has a diameter of about 15 mm. In the background, the shape (blue oval) of the 40 mm phosphor screen can be seen.

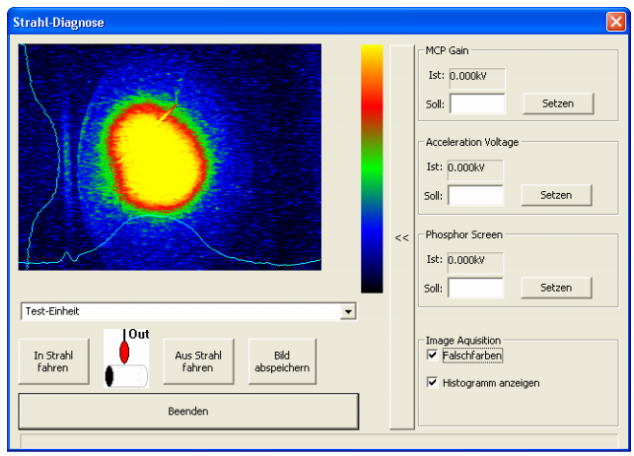

Figure 4: Control program for profile measurement.

Our further developments foresee to optimise the beam profiler mainly with respect to electron production efficiency, transmission of the grid and imaging properties (in dependance on geometry and acceleration voltage). The device could also be very interesting for the CSR experimental setups, as a single particle detector.

BEAM POSITION MONITORS

In the CSR a stored beam of 1 nA, 300 keV, A = 3 ions induces at a pickup capacity of 80pF and high input impedance (1 MΩ) of the head amplifier a voltage signal of about 340 nV. With a scaling factor of 200 mm one can calculate the differential signal for a beam displacement of 0.5 mm to 870 pV. Even with ultra low noise amplifiers (voltage noise: 0.5 nV/Hz$^{1/2}$) like developed for the CERN AD closed orbit measurement system and additional bandwidth reduction, it is extremely difficult to separate these weak signals from the background noise.
For that reason we are investigating the possibility to build the CSR capacitive pickups as part of a high Q resonant circuit and benefit from the narrow bandwidth and high shuntimpedance of such a system. With a given capacity of the pickups of 80 pF, the required inductance to reach the bunch (and revolution) frequency of the CSR is 10 mH. Using 3B7 and 3H1 Ferrox Cube P-Cores and regular copper wires, we reached Q-values of around 150 and (by adding a capacitive diode) managed to tune the system in a frequency range from 60 kHz to 250 kHz

(whereby the Q values went down to 70 - 30 because of losses in the diode). Since we expected mechanical problems and changing of the μ_r during the cooling process we finally decided not to use ferrites and go for cooled air-core coils with n ≈ 1000.

To first demonstrate the feasibility of the concept at an existing machine, using a real ion beam instead of a coaxial wire, we started with coils with n = 50 to reach the bunch frequency of the Heidelberg TSR (TestSpeicherRing) of 3 MHz. With a 80 pF vacuum capacitor (simulating the pickups) we achieved Q values of >500 with coils made of normal copper wire, turned on a Teflon tube and cooled down to 78K. For the frequency tuning we consider (so far) an antiquated mechanical variable capacitor as the best solution. We tested a 10 - 260 pF capacitor at our setup, tuning the frequency from 1.5 to 3.5 MHz and managed to have a Q of 200 - 230 at room temperature! However, at n = 700, the resonant circuit still suffers from high C of the coil and parasitic resonances, so for low frequencies a lot of optimisation work is still necessary.

BEAM PROFILE MEASUREMENT

At a vacuum pressure of 1×10^{-15} mbar, the count rate for residual gas ionisation by a 300 keV, 1 µA Proton beam is calculated with $R = \sigma\, n\, v\, \eta\, N$ to 10 Hz. Here σ is the ionisation cross section, taken from [7], n is the residual gas density, v is the beam velocity, η is the ratio of effective detector length to ring circumference and N is the number of stored ions. A count rate of 10 Hz is slightly above the MCP noise and does not allow for reasonable beam profile measurements. Since it is not acceptable to extend the integration time (electron cooling times: 1 – 10 s), we consider the possibility of increasing the pressure to at least 10^{-12} mbar in a short, well defined section of the ring. At the moment we discuss two possible solutions for the production of this pressure bump. Either we will heat one or several components of the RGM with a laser, or install a gas inlet. Laser heating is the more practicable solution, but does not allow to define the gas species (for example noble gas to avoid charge exchange).

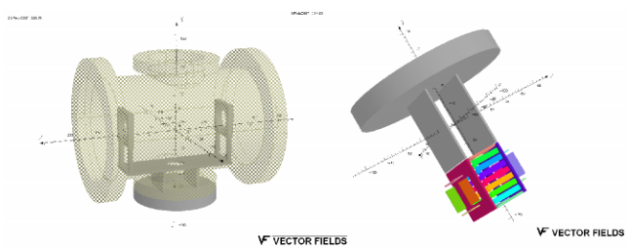

Figure 5: Ion trap test chamber with BPM pickups (left). The laser light comes from below, the RGM (right) will be mounted from above.

Both alternatives will be tested in the CSR prototype, which is in an advanced state of construction and is in principle a short section of the CSR cryostat, housing an electrostatic ion trap. TOSCA© calculations have been performed to fix the geometry of a small 5 x 5 cm RGM, mounted on a CF100 flange, which shall be installed inside the test chamber of the ion trap. The required electrode voltages are comparatively small due to the low temperature. We calculated reasonable ion trajectories and imaging for voltages of ±50 V.

ELECTRON BEAM DIAGNOSTICS

To have an accurate beam diagnostics for the adjustment of the electron cooler beam to the ion beam, we accepted two 20 mm interruptions of the cooler solenoid, 300 mm from the entrance and exit of the 1.84 m high temperature superconducting coil. At these positions wire scanners for the electron beam, which shall (in connection with the PPUs or the SQUID CCC) also work as scrapers for the ion beam, will be inserted into the cold chamber. The construction of the CSR electron cooler is currently starting.

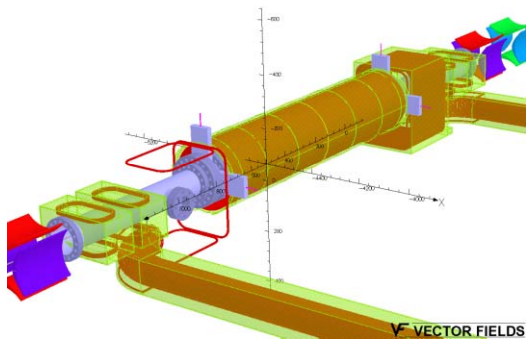

Figure 6: Mechanical layout of the CSR electron cooler with the electron beam diagnostics. The ion beam circulates through the thick beam tube (solenoid). The electron beam comes perpendicular through the thinner, U-shaped tube. The x,y wire scanner/scraper is located at the entrance and exit of the solenoid.

REFERENCES

[1] A. Wolf et al., The Heidelberg CSR: Low-Energy Ion Beams in a Cryogenic Electrostatic Storage Ring, Proc. COOL05, Galena, USA (2005), p. 473

[2] K. U. Kühnel (MPI-K, HD) private communication

[3] A. Peters et al., A Cryogenic Current Comparator for Nondestructive Beam Intensity Measurements, Proc. EPAC94, London, UK (1994), p. 290

[4] T. Sieber et al., A Beam Diagnostics System for the Heidelberg Cryogenic Storage Ring CSR

[5] T. Lefèvre et al., Scintillating Screens Study for LEIR/LHC Heavy Ion Beams, Proc. DIPAC05, Lyon, France (2005), p. 57

[6] P. Van den Bergh et al., The REX-ISOLDE Beam Diagnostics System, CAARI, Denton, USA (2000), AIP conf. proc. P. 235

[7] D.S.F. Crothers, J. F. McCann, Ionisation of Atoms by Ion Impact, J. Phys. B,: At. Mol. Phys. 16 (1983) p. 3229

MACHINE PROTECTION AND INTERLOCK SYSTEMS AT SYNCHROTRON SOLEIL

YM. Abiven, F. Dohou, P. Rommeluère, Synchrotron Soleil, Saint Aubin, France
Synchrotron Soleil, Saint Aubin, France

Abstract

SOLEIL is a third generation Synchrotron radiation source located in France near Paris, having the classical accelerator structure consisting of a Linac pre-accelerator, a Booster accelerator and a Storage Ring, which are connected by two transfer lines[1]. Since January, the Storage Ring delivers photon beam to 9 beamlines.

In order to protect the very sensitive and essential equipment during machine operation, (vacuum chambers, vacuum valves, mirrors, etc.) an interlock system has been implemented. This system is based on industrial and autonomous PLC (Programmable Logic Controller). This paper describes each level of the interlock chain from the diagnostics and vacuum sensors and processes, up to the backbone of the interlock system which stops the RF system.

INTERLOCK SYSTEM DESCRIPTION

Principle and organisation

The interlock system collects the critical defaults from diagnostics and vacuum subsystems to switch off the RF system which kills the beam in the storage ring and/or disables injections.

At Soleil, the interlock chain consists of two levels.

The first one is composed of local processes developed by the Vacuum and Diagnostics groups in each of the 16 cells around the storage ring. At this level, signals are picked up from sensors and processed by PLCs. This process actuates locally and supplies the default signals to the interlock system.

The second level is the interlock system itself which is developed and implemented by the ECA group (the Electronic group). This system reads the critical signals from subsystems and stops the RF power or inhibits pulsed elements. The system reacts in less than 1ms.

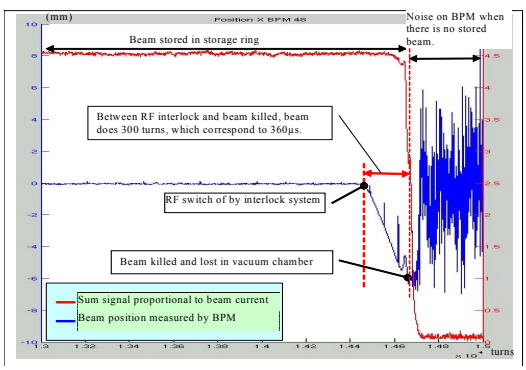

Figure 1: this graph shows the loss of beam when the interlock system switches off the RF power.

Processed signals

About 100 critical signals are picked up around the storage ring to protect vacuum chambers and mirrors. These signals are the following:

- Beam position default signal generated when the stored beam current is above a current threshold (20mA).
- MRSV default signal. MRSV is the optical system allowing observing visible synchrotron radiation.
- Instability default signal, detecting beam blow-up.
- Vacuum security signals from front-ends, straight-sections and arcs all around the storage ring

These signals are exchanged between PLCs of the interlock system and PLCs of the diagnostics and vacuum subsystems.

They respect positive logic to ensure security policy. Signals are 24V for high level when there is no default and 0V for low level which signifies default. This logic insures that the system works correctly in case of local power supply shut down or sheared cable by stopping the RF system.

Architecture of the interlock system

The interlock system is based on PLC technology (Siemens [2] S7-300), with 17 modules distributed around the accelerators. They are linked together to the Master PLC by the Profibus network. Moreover, the Master PLC is connected to supervision via Ethernet. Each distributed module embeds a boolean processor (FM352-5) which ensures a quick reaction (less than 1ms) and is autonomous from the control system. In order to improve system reliability, the signal stopping the RF is cabled with redundancy as shown in figure 2.

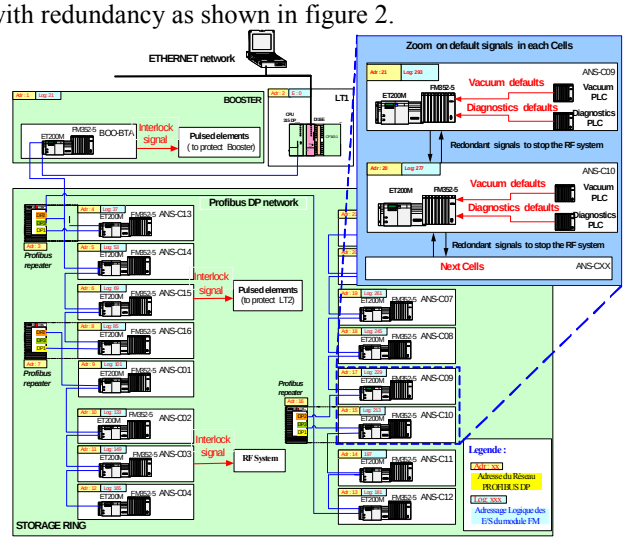

Figure 2 : Interlock system architecture.

On the Booster and the transfer line linked to the storage ring, the interlock system is used to protect vacuum valves. In this case the interlock inhibits the pulsed elements to avoid beam injection when a vacuum default is detected. This action does not have any impact on the stored beam in the storage ring.

DIAGNOSTICS DEFAULTS ON THE STORAGE RING

Diagnostics defaults are mandatory to avoid overheating any component inside the vacuum chamber.

Beam position interlock

The position of the beam is detected by 120 Beam Position Monitor (BPM) and measured by Libera modules which are the acquisition and processing electronic device by I-tech [3]. BPM and Libera modules are distributed around the storage ring within the 16 cells. Position default is generated by each Libera module when the beam position is out of range. In each cell, seven or eight position default signals are multiplexed by a dedicated diagnostics PLC to generate the faulty signal. The response time between the input and the output of this PLC is lower than 75µs. Presently, this position interlock is enabled on only 32 BPM.

MRSV interlock

The MRSV system uses a mirror located inside the storage ring which allows visible synchrotron radiation to be observed. MRSV default protects the mirror from overheating to prevent surface deformation.

The mirror, fixed on a motorised blade, surfs on the X-Ray part of the photon beam. Close to the mirror thermocouple sensors measure temperature (See description in Figure3). In order to protect the mirror a feedback is implemented to move the mirror as fast as temperature increase. Moreover, if the MRSV is not well extracted and if the temperature exceeds a given threshold, a default signal is sent through the interlock system to kill the beam. Process to read the thermocouple and generate default signal is done by diagnostics PLC.

Instability interlock

An instability default system is installed to protect from beam blow-up the storage ring equipment which are not cooled. The system is made of a 5mm slit equipped with 6 thermocouples, 3 on each blade of the slit. In operation, the photon beam goes through the slit (See the description in Figure3). The temperature on the blades of the slit is measured by a PLC. Instability default signal is sent out to the interlock system when the temperature goes beyond a given threshold.

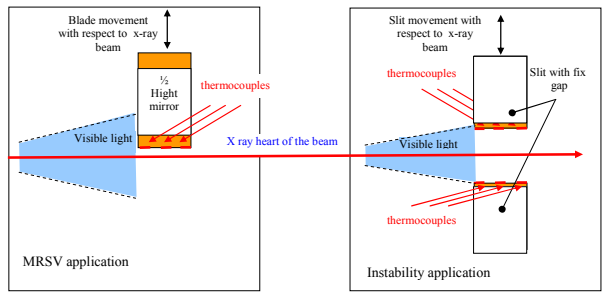

Figure 3 Description of the MRSV and the instability applications.

Current interlock

The Current Default System measures the stored beam current in the storage ring and generates 4 alarms according to the beam intensity. Among these alarms, Alarm2 is used in the interlock system to enable the position default.

The generated alarms are listed below:

- Alarm1: stops Linac injection when maximum intensity is reached.
- Alarm2: enables position interlock when the current is higher than 20 mA.
- Alarm3: enables top-up when the operationnal current is reached in the storage ring (not yet implemented).
- Alarm4: enables instability interlock when the current is stored.

The sensor used to read the current is a DCCT (Direct Current Current Transformer) associated with its electronic device by BERGOZ [4] which converts the current into an analog tension (0-10V). Alarm levels are configured in a PAXD0010 module by RedLion [5]. This module reads the current measure by means of the DCCT electronic devices and activates relays according to the programmed level. For redundancy two independent systems are installed on the storage ring.

STORAGE RING VACUUM INTERLOCKS

Stopping the RF system is mandatory to protect some vacuum devices, either to avoid that the electron beam hits the valves when closed or in order to avoid overheating of the vacuum chambers, of the ring absorbers or of the beamline front-ends.

Signals and detectors used

Signals which are continuously monitored are:

- Ion pump currents, since they are representative of the pressure. Thanks to the number of ion pumps on the machine (more than 350) and their right repartition, a map of pressure levels can be achieved.
- Pirani gauge pressure (through their controllers) when pressure is too high for ion pump to operate.
- Temperatures from K and J-type thermocouples.
- Cooling water flowing by flow meters.

- Valve states through open position switches
- High vacuum triggers (in front-ends only)
- Temperatures of mirrors for infrared beamlines

Cold- and Hot-cathode gauges are also present at SOLEIL but are not used on the interlock chain.

Security is ensured by one vacuum PLC per arc (16 on the storage ring, 6 on the booster) or per straight section (24) or per front end (12 in 2007). To achieve maximum detection speed, analog or digital signals acquired by dedicated measurement cards in the PLC are preferred to remote measurement modules via the Profibus link. For a few devices (such as the ion pump controllers), digital outputs of the controller are used to detect the alarm state. Profibus information which is slow, is employed as a confirmation of the alarm.

Security rules

RF interlock is generated when:

- The signal of at least one security device is incoherent or above the alarm value.
- At least one security device is off or out of service
- At least one arc gate valve is closed

Each device can be excluded from the security chain by an authorized person or an expert.

Performances

PLC cycle time ensures a signal detection and RF interlock generation between 30 and 50 ms. This time is faster than the movement of a normal cell gate valve which receives the interlock at the same time. This response time allows normal RF shutdown before the gate valve hits the electron beam.
There is one exception for front-end fast closing valves. These valves may hit the beam when closing because of their special driving method (they receive the closing command not only from the PLC but also from a faster dedicated electronic box associated with a special gauge acting as a trigger) and their short closing time (10ms). Closure of these valves is not supposed to happen frequently (only in case of accidental incoming air rush from the beam lines). If this occurs, the damaged fast valve may have to be changed.

INTEGRATION IN THE CONTROL SYSTEM

Hardware integration

Interlock system and subsystems are based on Siemens PLCs S7-300 family products, which are standard hardware components of SOLEIL Control Systems. Surrounding the booster and the 354 meters of the storage ring, 87 PLCs configurations are installed with 50 for vacuum security, 19 for diagnostics subsystem security and 18 for the interlock system.

Supervision applications

Interlock system and subsystems are linked to the TANGO [6] Control System by Ethernet. Communication between PLCs and Software devices has been developed by the ICA group (the Software control group). Above the TANGO devices, a GlobalSCREEN [7] application provides a graphical interface of the system to the end user. As shown in figure 4, the application allows operators to configure alarm values and to acknowledge the system. Moreover, states of the systems, default state, first cells in fault and beam intensity are graphically presented in this interface. This presentation of information quickly gives the state of the system to the machine operator.

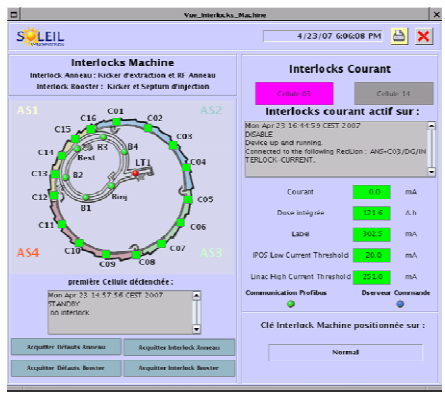

Figure 4 : Interlock Supervision application

CONCLUSION

Nowadays, the interlock system has been fully commissioned and is operational. It reacts as expected and allows accelerators to work safely with 300mA (500mA) beam in the storage ring. Currently, all diagnostics default applications are installed. For vacuum defaults, 12 other front-ends will gradually be installed in the next years and integrated into the interlock system.

REFERENCES

[1] J.M. FILHOL, Overview of the status of the SOLEIL project, EPAC 2006.
[2] Siemens PLC supplier, www.siemens.com
[3] I-tech Liberas supplier, www.i-tech.si
[4] BERGOZ manufacturer, www.bergoz.com
[5] RedLion, www.redlion.net
[6]The TANGO framework, http://www.tango-controls.org/
[7] GlobalSCREEN software is edited by Ordinal Technologies, http://www.ordinal.fr/

TIME DOMAIN MEASUREMENTS AT DIAMOND

C.A. Thomas, G. Rehm
Diamond Light Source, Oxfordshire, U.K.

Abstract

We present a set of four complementary measurements of the synchrotron visible light to characterise the stored electron beam at Diamond in the time domain. The electron bunch profiles and its evolution are measured with picosecond accuracy using a dual sweep streak camera. The beam dynamics are also given by a fast photodiode connected to a fast oscilloscope. The fill pattern is measured using a time correlated single photon counting system which has a high dynamic range for bunch purity measurement, and a fast averaging card which gives the fill structure with high accuracy within a short integration time. We describe our set of instruments, discuss their performance and show first results from measurements at Diamond.

INTRODUCTION

Diamond is the UK third generation synchrotron light source and has been commissioned in 2006 [1]. During this period many diagnostics for the electron beam have been developed and successfully integrated in the diagnostic control system. This includes a set of diagnostics related to characterising the time domain properties of the stored electron bunches using synchrotron light. To measure the electron beam longitudinal profile and dynamics we use a dual sweep streak camera, a fast 25 GHz bandwidth diode, a photon counting system, and a fast averaging card. These four systems produce a complete picture of the time-domain behaviour of the stored electrons. They all use the visible light from a bending magnet for which the beam line is described in [2]

In this paper we firstly present in detail these four measurements. The streak camera measures the single bunch profile in a single shot. The fast diode gives a complementary picture of the streak camera in the frequency domain. To measure the electron beam fill pattern a single photon counting system is used, and the complementary measurement is performed using a fast averaging card. We will then compare all these measurements in a second section before giving some concluding remarks.

TIME DOMAIN MEASUREMENTS

The dual sweep streak camera

The dual sweep streak camera (SC) from Optronis converts the time structure of a photon pulse into a linear deflection along one axis of a charged coupled device (CCD). Detailed descriptions of SCs can be found in [3, 4, 5]. Our choice for the streak camera was determined by the resolution of the fast axis of the camera (2 ps), the ability to use a synchroscan sweep at 250 MHz, half the RF cavity frequency (the same frequency would be ideal), and the second sweep covering the entire range sweeping across from several bunches to many thousands of storage ring revolution (1.3 ns to 65 ms). We have been performing beam longitudinal measurements at Diamond with the SC from the early days of commissioning. We have been measuring bunch profiles as short as 16 ps as predicted by the energy spread measurements, the RF cavity voltage readout, and the momentum compaction factor. We expect to measure shorter bunch profile with the installation of our second RF cavity which will bring the voltage to 3.3 MV instead of 2 MV for the latest measurements. In addition, operation with a very small momentum compaction factor should produce electron bunches of 1 ps r.m.s, which will put the SC to its limit.

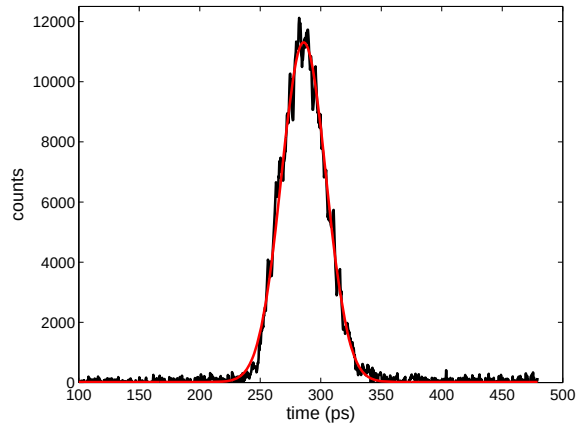

Figure 1: Single bunch profile calculated from SC image. The current is 0.1 mA and the r.m.s bunch length is 16 ps.

Resolution of the SC As the SC produces images, the resolution is given by the FWHM of the point spread function. In our case the smallest point spread function is 5.5 pixels FWHM. On the fast axis, the best resolution for the fastest sweep is 0.139 ps/pixel, which makes 0.7 ps FWHM spot size, and the resolution of the streak camera is specified to resolve two pulses spaced by 2 ps. On the slow sweep axis, this resolution varies between 50 ps (9.2 ps/pixel) to 0.38 ms (0.0695 ms/pixel). The detection level of the camera is very low. At Diamond, measurements of single bunch with 0.1 mA (187 pc) current can be done in a single sweep. This corresponds to visible light pulses of 10 mW peak power. Figure 1 shows such a measure-

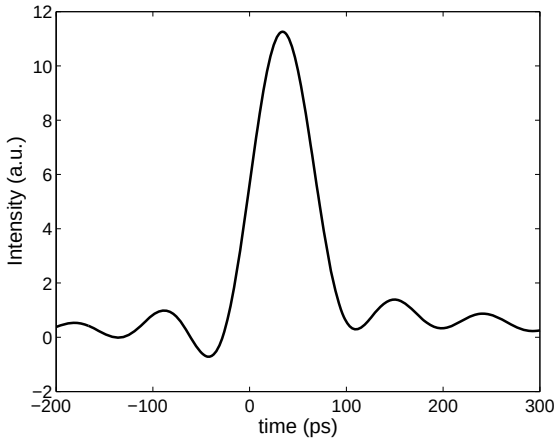

Figure 2: Diode 1481-S-50 response measured with a 10 GHz real time oscilloscope. The input pulse is a 33 ps FWHM laser pulse at 638 nm.

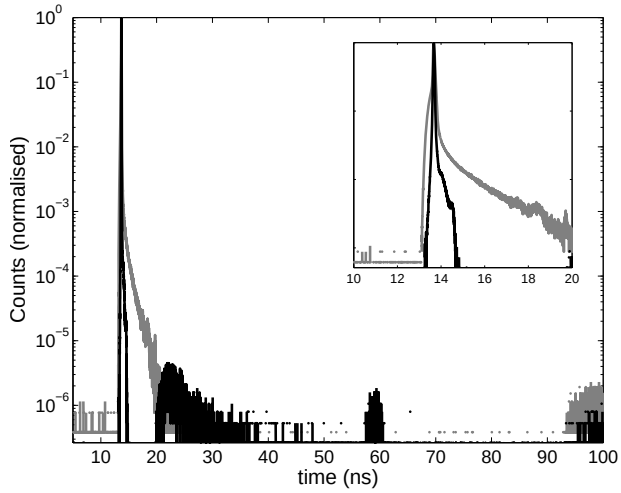

Figure 3: TCSPC IRF with the MCP-PMT (dark line) and with the id-100-20 (gray line).

ment.

For Diamond, the SC is used to measure accurately the bunch profile with a r.m.s length expected to be as short as 10 ps and at low current (typically 0.1 mA). In addition the slow sweep unit permits to measure a train of pulses and study their longitudinal dynamic, from bunch-by-bunch to 35000 turns.

The fast diode

Beam longitudinal dynamics can be studied as well in the frequency domain. For that we use a 25 GHz Bandwidth diode (1481-S-50 from New Focus) either connected to a 10 GHz bandwidth oscilloscope or to a 27 GHz bandwidth spectrum analyser. The resolution of the system in the time domain is shown in figure 2. In this measurement, the FWHM is 67 ps which determined by the bandwidth of the oscilloscope. However, analysing the output of the fast diode on the 27 GHz bandwidth spectrum analyser will allow to investigate longitudinal characteristics by Fourier transform the synchrotron light signal, which covers most of the observable phenomena in the electron beam dynamics. As this fast diode has a sensitivity of only 10 V/W and the peak power of the synchrotron radiation in the visible beam line 18 μW/mA for a 2/3 fill, the detection level is estimated to be ≈ 100 mA stored beam.

The TCSPC system

In order to measure the beam fill pattern and the single bunch purity, we use a Time Correlated Single Photon Counting system. It is composed of a fast single photon detector, in our case we use either the MCP-PMT RU380-50 from Hamamatsu or the id100-20 from id-Quantique. To count the photons detected, we use the PicoHarp300 from PicoQuant as a stand alone TCSPC module. Figure 3 shows the instrument response functions (IRF) of the two detectors. It shows the limitations for bunch purity measurements. The MCP-PCT has a very clean signal, rising and decaying by more than 7 orders of magnitude in less than 2 ns. However, the MCP-PMT has a probability of 10^{-5} to emit a signal from a detected photon with 9 ns and 45 ns delays [4]. With such a behaviour, the MCP-PMT is the better of the two detectors for bunch purity measurement with single bunch fill pattern, but in an hybrid fill pattern, having 2/3 of the buckets filled and one isolated bunch in the gap, the delayed pulses limit the dynamic resolution to 10^3. In contrast, the diode has a comparatively long trailing edge, which has decayed 5 orders of magnitude 2 ns after the main pulse. Therefore the diode limits the dynamic resolution to 10^5 for a bunch purity measurement with single bunch fill. Nevertheless, this allows to measure a hybrid beam fill pattern with 5 orders of dynamic resolution. The minimum power detectable by this system is very low, we can detect as little as 1 pC stored in a bunch. However, in order to achieve a rate of 1 Count per revolution ($533 \cdot 10^3$ counts/s), the average flux needs to be of the order of several nW.

The fast averaging system

The fill pattern of the electron beam is also measured with a 1 GHz bandwidth diode coupled to a fast averaging card (AP200 from Acqiris). This card has a 2 GS/s sampler (clocked at externally supplied quadrupled RF frequency) and facilitates realtime averaging. We can thus produce an average of measurements over 20000 turns consisting of 3744 samples (4 samples per 936 buckets) at an update rate of 13 Hz. This results in a fast measurement of the fill pattern with better than 0.5% resolution on the charge per bucket. Figure 4 compares measurement of the 2/3 fill pattern at 83 mA stored current, with the picoharp300 and the

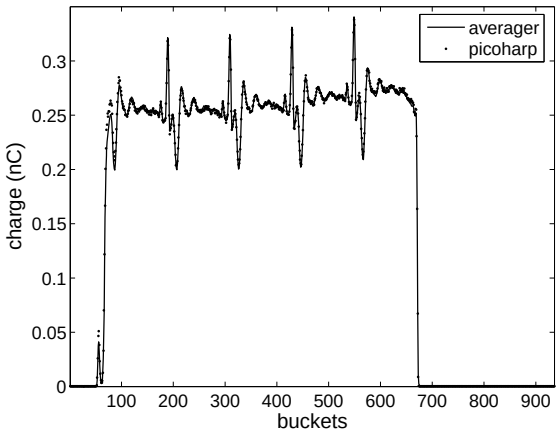

Figure 4: Measurement of the fill pattern with the picoharp300 and the fast averaging card. The traces are normalised using the total stored charge (156 nC). The agreement between the two traces is better than 1 %. The noise floor is ≈ 0.5 % from the averager and it is ≈ 0.005 % in the picoharp300 measurement.

AP200. The agreement between the two measurements is very good. We note the noise floor of the averaging card is about 0.5%. It isn't shown in the figure as it has been removed due to the normalisation of the recorded trace. We intend to use this system for top-up operation with fill pattern feedback allowing a re-assessment of the fill pattern after each injector shot at 5 Hz.

CONCLUDING REMARKS

With this set of 4 measurements, we are able to characterise the longitudinal profile of the stored electron beam. The SC is able to measure real time single pulse profile, with 2 ps resolution. It is able as well to follow the dynamics of the stored bunches from individual bunches to 35000 turns. As a complementary measurement we can use a fast photodiode which to give temporal information on a real time oscilloscope or frequency domain information on a broadband spectrum analyser. The fill pattern is measured with two complementary systems, one is a TCSPC measurement, and the other is averaging a sampled trace. The TCSPC is by far the most accurate, but needs time for acquisition, whereas the averaging system can measure the fill pattern within fractions of a second and reasonable resolution. In addition, single bunch purity can be measured with better than 6 orders of magnitude using the TCSPC system. Table 1 summarises the performance of each of these four measurement systems. A number of future improvements is possible. Firstly, the use of a fast repetitive sampling scope with considerably larger bandwidth (instead of the 10 GHz realtime scope). Secondly, the use of a broadband, low noise amplifier after the fast photo diode should lower the detection limit. Finally, for the TSCPC system, a detector with the same fast decay like the MCP-PMT, but without the observed delayed pulses would be ideal.

REFERENCES

[1] R.P. Walker. Overview of the Status of the Diamond Project. In *Proceedings of EPAC, (Edinburgh)*, pages 2718–2722, June 2006.

[2] C. A. Thomas, G. Rehm, H. L. Owen, N. G. Wyles, S. W. Botchway, V. Schlott, and M. Wahl. Bunch purity measurement for Diamond. *Nuclear Instruments and Methods in Physics Research A*, 566:762–766, October 2006.

[3] K. Scheidt. Review of streak cameras for accelerators: features, applications and results. In *Proceedings of EPAC, (Vienna)*, page 182, June 2000.

[4] C. A. Thomas and G. Rehm. DIAMOND Storage Ring Optical and X-Ray Diagnostics. In T. Shea and R. C. I. Silbey, editors, *American Institute of Physics Conference Series*, pages 182–189, November 2004.

[5] C. A. Thomas and G. Rehm. Diamond Optical Diagnostics: First Streak Camera Measurements. In *Proceedings of EPAC, (Edinburgh)*, pages 1112–1114, June 2006.

Table 1: Comparison of the system performances

	Streak camera	Fast diode	Photon Counting	Fast Averager
Single shot	yes	yes	no	yes
IRF (FWHM) (ps)	2	17	40	1000
temporal quantisation (ps)	0.139/pixel	25 [a]	4 [b]	500
shortest measurement time	1 sweep	1 sweep	-	1 turn
typical measurement time	1 sweep	< 1 ms	5 s	20000 turns
Dynamic range (bits)	16	8	16 [c]	8 [d]
Detectable charge (pC)	200	30	<1	2

[a] with 40Gs/s 10 GHz bandwidth oscilloscope

[b] to cover the full turn of 1,872 ns with the 65536 bins, a 32 ps quantisation has to be selected

[c] the TCSPC system has 16 bits bin depth in hardware. Further counting can be realised in software.

[d] the sampler has 8 bit resolution, averaging over n acquisitions increases the resolution by $\ln(\sqrt{n})/\ln 2$

TRANSITION THERMAL PROCESSES IN VIBRATING WIRE MONITORS*

Arutunian S.G.[1], Decker G.[2], Mailian M.R.[1], Rosenbaum G.[3]
[1] Yerevan Physics Institute, Armenia
[2] Argonne National Laboratory, Argonne, IL 60439 USA
[3] University of Georgia, Athens, GA 30602 USA

Abstract

Dynamic characteristics of vibrating wire monitors (VWM) strongly depend on the media where the wire oscillates, and also on the geometry and materials of the wire and VWM housing. On the basis of a one-dimensional model of heat transfer along the wire, the time characteristics of transition processes of thermal equilibrium profiles are defined for wires of different materials and geometry. To decrease the response time of the VWM, a new scheme of measurement with constant mean temperature is suggested. In addition to the flux of particles/radiation deposited on the wire, the additional DC current maintains a constant wire oscillation frequency. The value of DC current serves as measure of particles/radiation flux.

INTRODUCTION

The first measurements of a hard X-ray undulator beam at the APS with a Vibrating Wire Monitor (VWM) [1] showed that the VWM is well-suited to neutral beams such as x-rays. Here we discuss the dynamic characteristics of the VWM depending on wire and housing materials. The measurements of convection heat sink parameters in air and hydrogen at different pressures are done. A new modification of the VWM with Tungsten wires and enlarged aperture is presented.

VWM DYNAMIC CHARACTERISTICS

In case of permanent photon flux falling on the wire, the equilibrium temperature profile along the wire is determined by the balance between the heat deposited on the wire and heat dissipation occurring in three ways: thermal conductivity along the wire, heat radiation and convective heatsink (in gas media). A change in mean wire temperature results in a change of wire strain, which is registered by measurement of the wire's natural oscillation frequency.

The temperature distribution $T(t,z)$ along the wire is determined by the heat conductivity equation:

$$c\rho\frac{\partial T}{\partial t}=\frac{\partial}{\partial z}\left(\lambda\frac{\partial T}{\partial z}\right)+q-R-A. \qquad (1)$$

Here c is the coefficient of heat capacity, ρ is the density, and λ is the coefficient of heat conductivity of the wire material, σ is the Stefan-Boltzman constant, q is the density of the deposited heat from all sources, $R=2\varepsilon\sigma(T^4-T_0^4)/r_w$ - heat sink by radiation, ε – emissivity factor, $A=2\alpha_{conv}(T-T_0)/r_w$ - heat sink by convection with factor α_{conv}, r_w. – wire radius. T_0 - housing temperature. The power flux deposited on the wire is set $P=P_0\exp\left(-z^2/2\sigma_z^2\right)$, where σ_z is the width of the bunch. In this case $q=2A(z)P/\pi r_w$ ($A(z)$ is equal 1 in VWM aperture and 0 elsewhere). If through the wire passes current a I_0 a term $I_0^2\Omega/\pi^2 r_w^4$ must be added to the q (Ω is the wire resistivity).

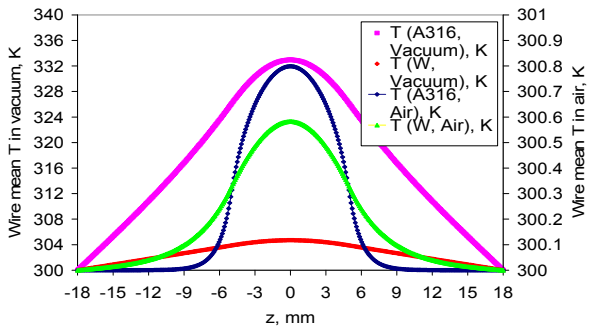

Fig. 1. Temperature profile along the wire for Stainless Steel and Tungsten in vacuum and air.

Results of calculations are presented in Fig. 1 (profiles for Stainless Steel and Tungsten in vacuum and air with heat sink factor α = 380 W/m/K, σ_z = 5 mm, P_0 = 1 mW/mm^2, VWM aperture 5 mm). It is seen that without convective heat dissipation the profiles are almost triangular. The largest overheating is revealed for Stainless Steel in vacuum.

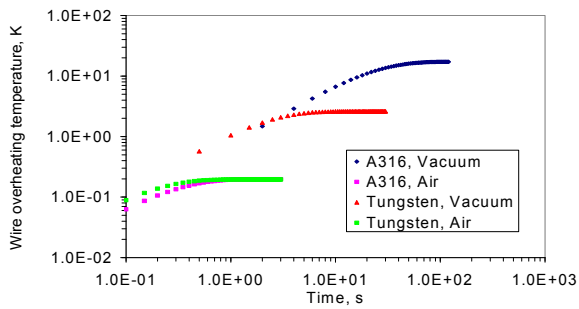

Fig. 2. Dynamic characteristics of temperature profile stabilization. Temperature in the center of the wire is presented.

* Work supported by U.S. Department of Energy, Office of Science, Office of Basic Energy Sciences, under Contract No. DE-AC02-06CH11357, and by Bergoz Instrumentation, Saint Genis Pouilly, France.

Fig. 2. represents the graphs of temperature dynamics in the wire center. For Stainless Steel in vacuum, due to a small coefficient of thermal conductivity (16.3 W/m/K) the temperature stabilization time is a few minutes (with accuracy of about 0.001 ^{0}C).

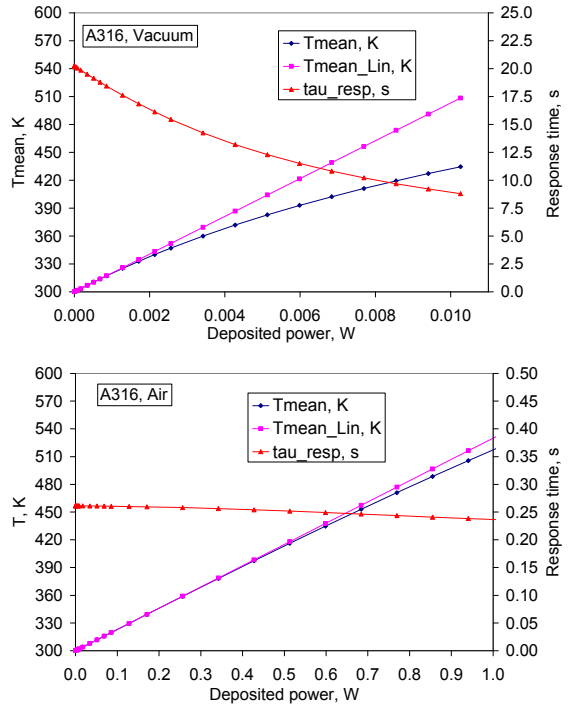

Fig. 3. Parameters of VWM with Stainless Steel wire in air and vacuum.

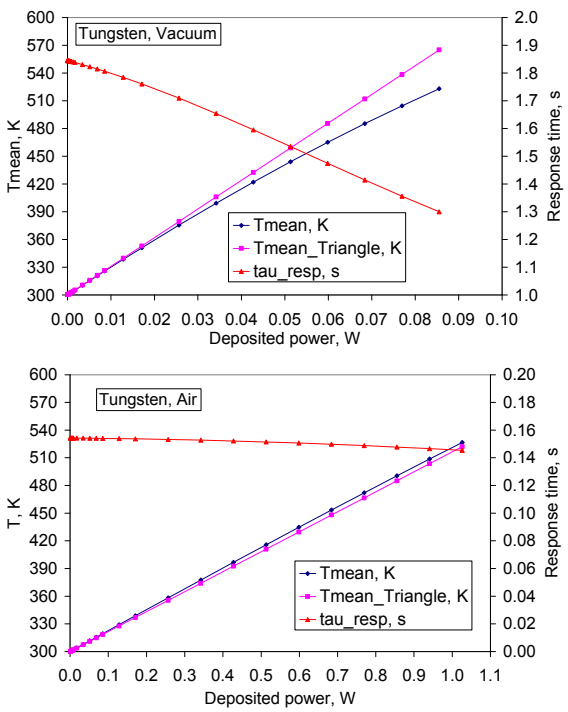

Fig. 4. Parameters of VWM with Tungsten wire in air and vacuum.

For practical applications it is important to determine dependence of wire mean temperature on the deposited power and dependence of the wire oscillation frequency on its temperature. The temperature profiles of Stainless Steel and Tungsten wires are calculated for different levels of power deposited on the wire. Results for Stainless Steel are presented in Fig. 3 and for Tungsten in Fig. 4.

For comparison, the graphs of linear dependence are calculated for a triangular model of temperature and linear approximation of radiation heatsink. A difference from linear dependence occurs owing to the fact that heat radiation is proportional to the fourth power of temperature, so that the portion of thermal loss due to radiation increases at high temperatures.

Summary characteristics of Stainless Steel (A316) and Tungsten wires are presented in Table 1.

Table 1

Material	A316 Vacuum	A316 Air	Tungsten Vacuum	Tungsten Air
$\Delta T_{mean}/\Delta Q$, K/mW	19.4	0.23	3.0	0.23
$\Delta F/\Delta T_{mean}$, Hz/K at F_0 = 4200 Hz	40.2	40.2	8.8	8.8
$\Delta F/\Delta Q$, Hz/mW	779.6	9.3	26.4	2.0
response time, s	20.2	0.26	1.8	0.15

We present useful formulas for the calculation of wire maximal overheat temperature ΔT_{MAX} and response time τ assuming a trianglular profile at room temperature.

$$\Delta T_{MAX} = \frac{q}{\pi d^2 l(\lambda / l^2 + 2\sigma_{SB} T_0^3 + \alpha_{conv} / 2d)} \quad (2)$$

$$\tau = \frac{\rho c}{8(\lambda / l^2 + 2\sigma_{SB} T_0^3 + \alpha_{conv} / 2d)} \quad (3)$$

Fig. 5. VWM with tungsten wires and enlarged aperture.

In Fig. 5 a new modification of VWM with two Tungsten wires and enlarged 8 mm aperture is presented.

The housing is made from AlN ceramic with a high value of thermal conductivity. This modification has a shorter response time and can be used both in vacuum and air. In the APS experiment [1], a VWM with two Stainless Steel wires and a 5 mm aperture was used.

CONSTANT TEMPERATURE VWM

Response of the VWM can be accelerated if instead of a "cold" wire a preheated wire is used. Such preheating can be done with an additional DC current [2]. As the photon beam heating varies, the DC current can be varied in order to maintain a constant frequency. This current is then used as a measure of photon beam heating. Note that such a procedure is used in so-called Constant Temperature Anemometers, see e.g. [3].

Let the Stainless Steel wire be heated by a current I = 20 mA (wire overheating is 19.1702 K). In this case, if the photon beam deposits P_0=0.7 mW/mm^2 onto the wire, the DC current I = 12.2033 mA results in the same mean wire temperature (see Fig. 6).

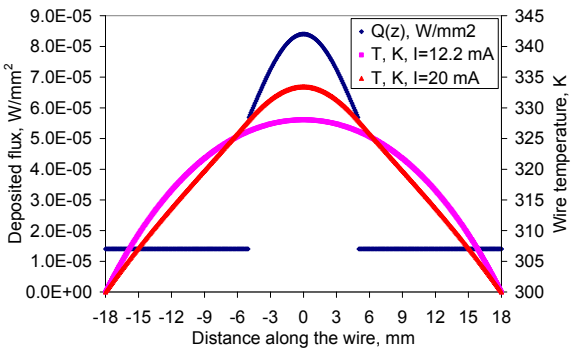

Fig. 6. Deposited power $Q(z)$ (DC current 12.2 mA and photon flux with P_0=0.7 mW/mm^2) and temperature profiles at DC currents 20 mA and 12.2 mA with photon flux.

In Fig. 7 we present the wire mean temperature dynamics from preheated state (DC current 20 mA) to the step photon flux 0.7 mW/mm^2 and DC current 12.2 mA (blue diamands). To compare we also present the dynamics from step photon flux 1.116207 mW/mm^2 that leads to the same temperature increment 19.1702 K. As one can see the same level of temperature close to the final increament is reached faster for preheated wire. E.g. the level 19.100 K is reached at 42th second for preheated wire and at 102th second for cold wire.

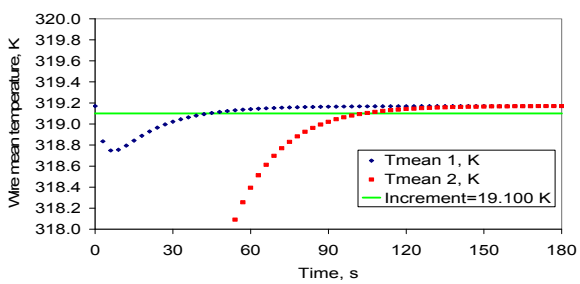

Fig. 7. Dynamics of wire mean temperature from preheated state (Tmean 1) and from cold state (Tmean 2).

CONVECTION FACTOR FOR VWM

Measurements of the convection factor for vibrating wires were performed at different pressures for air and hydrogen. This factor is determined by the properties of the heat sink surface, its location, the temperatures of the surface and surrounding media, and its consistency (see, e.g. [4]). For a vibrating wire the relative motion of the wire with respect to the media must also be taken into account. Experimental results are shown in Fig. 8.

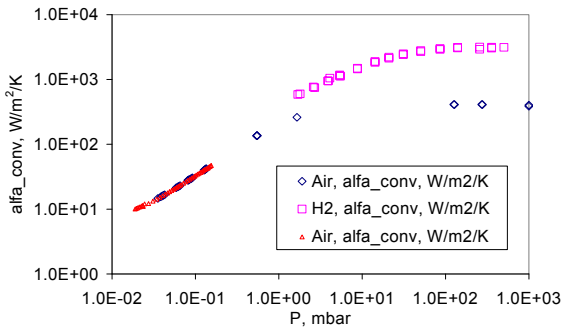

Fig. 8. Summary of convection factors for vibrating wires in air and hydrogen at different pressures.

The convective factor decreases sharply as the pressure is reduced below 1 mbar for air, and 10 mbar for hydrogen.. For hydrogen at normal pressure, this parameter is nearly an order magnitude larger than for air.

DISCUSSION

The response time of the VWM can be decreased in vacuum by using wires with a high thermal conductivity. Additional reductions in response time can be achieved by using the VWM in a gas media. As a consequence, however, the sensitivity of the VWM is decreased. Some decreasing of response time can be done also by constant temperature method. New modifications of the VWM with enlarged aperture and an AlN ceramic housing allows for more stable thermal conditions. This type of VWM can be further improved by using four wires. (two horizontal and two vertical).

REFERENCES

[1] G. Decker, S. Arutunian, M. Mailian, G. Rosenbaum. “First Vibrating Wire Monitor Measurements of a Hard X-ray Undulator Beam at the Advanced Photon Source”, these proceedings.

[2] Arutunian S.G., Dobrovolski N.M., Mailian M.R., Sinenko I.G., Vasiniuk I.E. “Vibrating wire for beam profile scanning.” Phys. Rev. ST Accel. and Beams, **2**, 122801 (1999).

[3] http://www.aoe.vt.edu/~simpson/aoe4154/hotwirelab.pdf.

[4] A.V. Yegorov. “Calculation of Power and Parameters of Electric Furnaces in Ferrous Metallurgy.” Moscow, 1990.

FIRST TESTS OF THE TRANSVERSE MULTIBUNCH FEEDBACK AT DIAMOND.

A. F. D. Morgan, G. Rehm, I. Uzun, Diamond Light Source, Oxfordshire, UK

Abstract

This paper describes the design and initial tests of the transverse multibunch feedback system under development at Diamond. The system is designed to damp instabilities up to 200 MHz in both the vertical and horizontal planes. This will lead to an increase of effective instability thresholds which will permit a reduction of chromaticity and thus should improve dynamic aperture and lifetime.

OVERVIEW

The Transverse multibunch feedback system (TMBF) is used to damp down instabilities below 200 MHz. It operates on a per bunch basis and is intended to be used in parallel with the global orbit feedback system. Figure 1

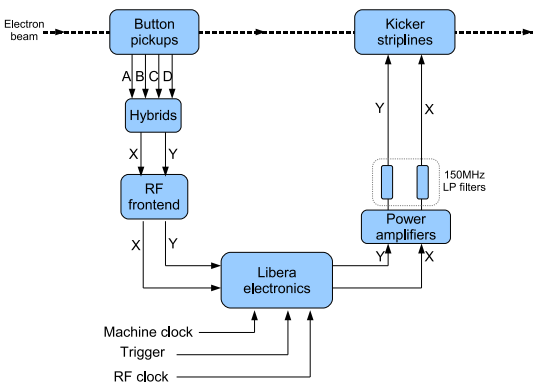

Figure 1: Current TMBF schematic

shows the system level structure of the TMBF system. The position of each bunch is picked up by a set of four button pickups. The resulting signals are then passed through a set of hybrid combiners to generate the X and Y position signals. These signals are passed into the RF frontend where the signal is filtered and amplified to the correct level for the electronics. The electronics calculate the motion of each bunch and the resulting correction required to damp any instabilities. This information is passed to a power amplifier which, through some low pass filters, drive two sets of kicker striplines (one in X and one in Y) to apply the corrections to the beam.

DETAILS

The button pickups are capacitive pickups of the same type as are used in the EBPM system. The basic geometry is shown in figure 2.

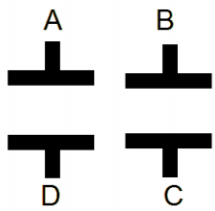

Figure 2: Button pickup geometry

The hybrid system comprises four hybrid combiners in the configuration shown in figure 3. The hybrids are located close to the beam pipe and are connected to the buttons with well defined lengths of semi-ridged cable, in order to maintain the relative phases of the signals. This arrangement means that the phase dependent conversions are done as soon as possible and eliminates the need to maintain the exact phase relationships over the 30 m of cable from tunnel to instrumentation area.

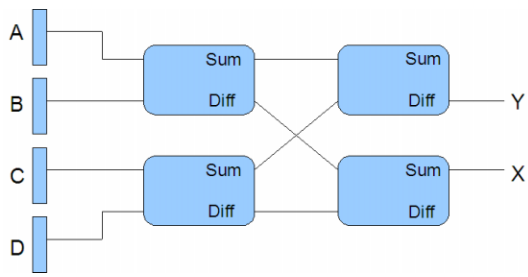

Figure 3: Pickup hybrid configuration

The RF frontend is an in house development inspired by an existing ESRF design [1]. Its job is to clean up the incoming signals to a quality suitable to go into the electronics. It first passes the X (Y) signal through a band pass filter to select the 4^{th} harmonic (The 4^{th} harmonic is used as it has the most power in it). This is then amplified and mixed with the frequency quadrupled machine RF signal to bring the signal back to baseband. It is then passed through a 200 MHz low pass filter to remove any residual high frequency signal generated by the mixing process. Finally it is passed through a last amplification stage to output the correct signal level for the electronics.

For the electronics we selected the Libera Bunch-by-Bunch processor platform developed by Instrumentation Technologies for the digital signal processing and correction signal generation. A block diagram of Libera electronics is shown in figure 4.

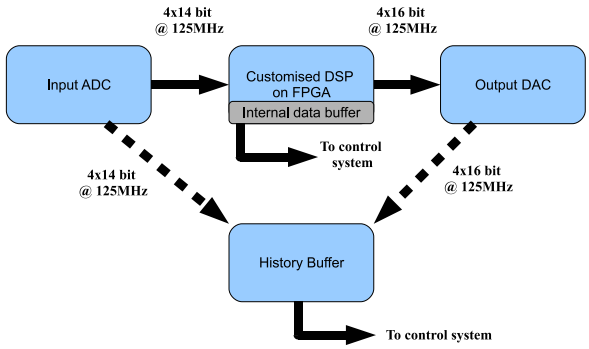

Figure 4: Libera electronics schematic

The X (Y) position data provided by the RF frontend is sampled by the Libera analog module which consists of four ADC channels. Each ADC is clocked at 125 MHz ($\frac{f_{RF}}{4}$) and the channels have phase shifts of $0°$, $90°$, $180°$ and $270°$. This interleaving effect allows the 4 ADCs to act as 1 ADC clocked at RF frequency, thus allowing every bunch to be measured individually.

Data from the four ADCs is processed in the customised DSP block implemented on a VirtexII Pro FPGA. The FPGA design is based on an ESRF design [2]. It consists of four identical FIR filtering channels for parallel processing of the four ADC channels. Each channel (n) processes bunch numbers n, n+4, n+8, . where n=1,2,3,4 is the channel number. The FIR filters are sinusoidal in shape with no windowing and have 8-taps for the vertical plane and 9-taps for the horizontal plane. The design also has a 16K-sample internal data buffer for mode scan response analysis to allow us to find the loop delay of the system, and grow damp scan analysis to allow us to calculate the damping time of the system.

The correction signal (Z) for each bunch, every turn, is calculated from the input error signal of an FIR band pass filter centered around the tune frequency, then a $-(G \times Z)$ correction kick is applied to each bunch every turn (G being gain of the FIR feedback term).

Finally, the output data goes to a fast DAC for analog output and then to the power amplifier.

Additionally, there is a history buffer which is used to store data for off-line analysis. Either data from the input ADC or the output DAC can be stored. Both the history buffer and the internal data buffer can be accessed from the control system, allowing us to troubleshoot problems much more efficiently [3].

The power amplifiers take the analog output signal from the electronics and drive the striplines to apply the correction. The striplines are of the SLS 500 MHz resonant type [4]. Currently only one of each pair of striplines is excited. The 150 MHz low pass filters are to protect the amplifier from beam induced signal coming back from the striplines. These are a temporary measure until the final 300 MHz filters are available.

The loop delay of the system has to be such that the correction is applied an integer number of turns after the pickup (to ensure the correct bunch is addressed) and the signal must be $180°$ out of phase with the motion to achieve damping. In our setup the nominal delay between pickup and correction is 9 turns in the horizontal plane and 8 turns in the vertical plane. The phase of the analog output can adjusted by tuning the FIR filter coefficients. The phase can be tuned from $-\pi$ to π. The correct loop delay was achieved in two stages. The delay in the FPGA can be adjusted in 8 ns steps from 0 to revolution period. So the initial delay was corrected to within 8 ns in this fashion. The fine tuning was done by adjusting the cable lengths between the components. In the horizontal plane the actual delay has been adjusted to within 0.1 ns. of the nominal.

INITIAL RESULTS

The system for the horizontal plane has been tested by setting the horizontal chromaticity to zero and applying the feedback. As can be seen in figure 5 the TMBF system is generally effective at damping down the horizontal instabilities.

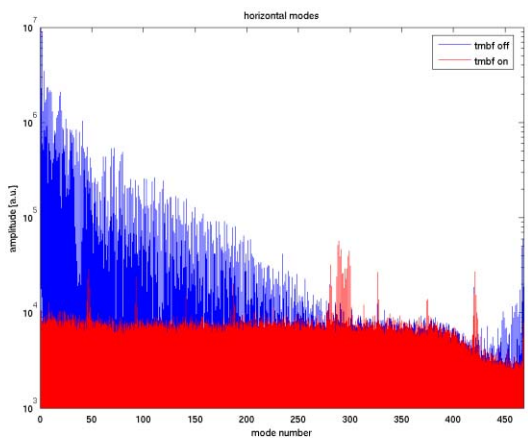

Figure 5: Amplitudes of the modes of horizontal beam motion with and without feedback

The enhancement around mode number 300 is thought to be due to the roll off (and related phase shift) of the 150 MHz low pass filter between the amplifier and the kicker striplines. The further reduction after mode 400 is due to the 200 MHz low pass filter in the RF front end.

A first damping time measurement was done by exciting a mode 10 for 350 turns, then turning on the feedback and waiting for the amplitude of oscillation to drop to $\frac{1}{e}$. Figure 6 show the effect of increasing the strength of the feedback correction. The damping time for the system is about 700 turns and we are currently limited by the accuracy of our loop delay. However, we hope to improve this as the commissioning of the system continues.

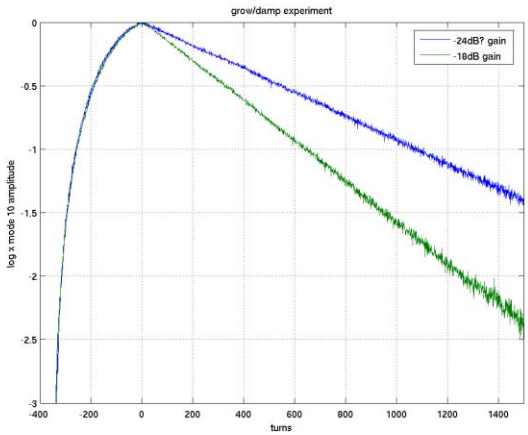

Figure 6: Damping time of mode 10 for two correction strengths

Figure 7 shows the effect of the feedback on the oscillations within the bunch train. Our initial results show an overall reduction in the amplitude of the instabilities at zero horizontal chromaticity, however, the feedback system also seems to drive an oscillation at 62 MHz, corresponding to an oscillating period of 8 bunches which needs further investigation.

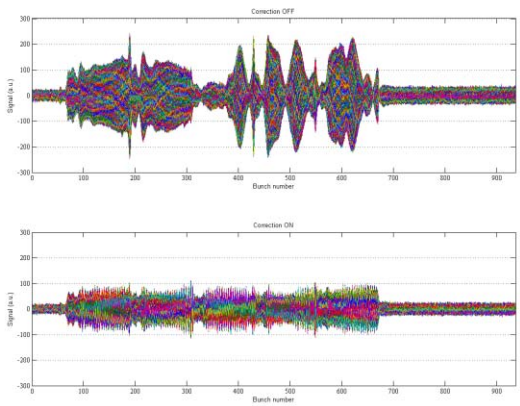

Figure 7: Amplitudes of motion of individual bunches with and without feedback

FUTURE DEVELOPMENTS

We are planning to pass the correction signal through some hybrids to allow the kickers to be driven in a differential mode, which results in a more uniform field and lower power demands on the amplifier. The hybrids will also offer the amplifier some additional protection as only out of phase signals will be routed back to the amplifier (the rest being passed to a termination on the 4^{th} port).

It is also intended to replace the 150 MHz low pass filter with a 300 MHz low pass filter to allow correction of the higher frequency modes and to remove the enhancement around mode 300. Figure 8 shows the final system design.

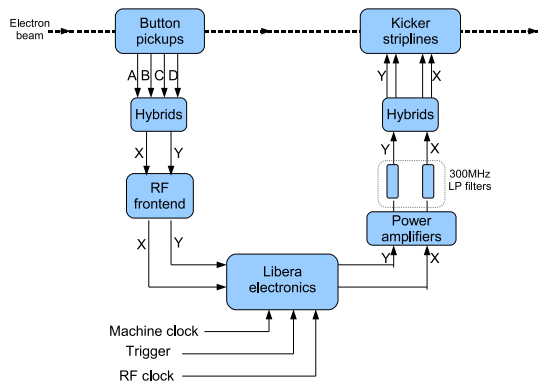

Figure 8: Final TMBF schematic

CONCLUSION

The TMBF system has been tested in the horizontal plane and proven its ability to correct horizontal instabilities with chromaticity set to zero. The initial results are encouraging, however, further commissioning is required to optimise the correction and to bring the vertical system up to the same standard.

By combining existing designs into a full system we have been able to very rapidly develop and implement a very competent TMBF system.

REFERENCES

[1] Private communications with E. Plouviez

[2] E. Plouviez, P. Arnoux, F. Epaud, J. Jacob, J-M. Koch, N. Michel, G. A. Naylor, J-L. Revol, V. Serriere, D. Vial Broadband Bunch by Bunch Feedback for the ESRF using a Single High Resolution and Fast Sampling FPGA DSP. Proceedings of EPAC 2006

[3] G. A. Naylor, Beam Diagnostic Features of the ESRF Multibunch Feedback Systems (This conference)

[4] M. Dehler, V. Schlott, D. Bulfone, M. Lonza, R. Ursic, Current status of the ELETTRA/SLS transverse multibunch feedback. Proceedings of EPAC 2000

BUNCH-BY-BUNCH LONGITUDINAL DIAGNOSTICS AT DAΦNE BY IR LIGHT

A. Bocci[1,2], A. Drago[1], A. Marcelli[1], A. Clozza[1], R. Sorchetti[1], A. Grilli[1], M. Cestelli Guidi[1], E. Pace[2], M. Piccinini[1,3] A. Raco[1], and J.Piotrowski[4]
[1]Laboratori Nazionali di Frascati - INFN, Via E. Fermi 40, 00044 Frascati (Roma), Italy
[2]Università degli Studi di Firenze, Dipartimento di Astronomia e Scienza dello Spazio, L.go E. Fermi 2, 50125 Firenze, Italy
[3]Università Roma Tre, Dipartimento di Scienze Geologiche, L.go S. Leonardo Murialdo, 1 – 00146 Roma, Italy
[4]VIGO SYSTEM SA, 3 Swietlikow Str., 01-389 Warsaw, Poland.

Abstract

Compact uncooled HgCdTe semiconductor detectors optimized in the mid-IR range have been used to record time resolved single bunch synchrotron radiation (SR) emissions from the DAΦNE electron ring [1]. These IR devices allow a low cost bunch-by-bunch longitudinal diagnostics. Indeed, these detectors make possible to record a train of a few ns long bunches per turn. To the purpose of diagnostic a comparison with the light signals coming from the positron ring appears stimulating but at DAΦNE only two SR beamlines are operational on the electron ring. The lack of apertures in the shielding wall offers no easy alternatives for the emission from the e^+ ring. To solve the problem, a compact SR port has been designed and is going to be implemented at DAΦNE where a HV chamber and remotely controlled mirrors will focus the positron light on IR detectors.

The source characteristics have been simulated and the optical setup with the complete acquisition system will be described. After the installation and tests, a real time comparison between data collected with the two beams will be possible improving accelerator diagnostics and as a major tool to increase the stored currents in the e^+ ring and possibly the collider luminosity.

INTRODUCTION

Particle accelerator diagnostics in the IR region has never been considered because visible light devices are much more popular easy to use and characterized by a large bandwidth (e.g. Si photodiodes, InGaAs Shottky photodiodes [2, 3] and also streak cameras). Moreover, many X-ray based synchrotron light monitors exist and they are preferred because of their spatial resolution, a characteristic extremely important to measure low and very low emittance beams and to obtain high resolution times (e.g., a few ps times) [4]. This is easier in particular for high energy accelerators while DAΦNE is a low energy collider working at 0.51 GeV and loosing 9.7 keV per turn for radiation damping.

The devices that we will describe in the next, acquire signals in the mid-IR, are vacuum compatible and work at room temperature without cooling. They represent the result of an important synergy that shares expertises from three quite different researches areas: astronomy, industrial semiconductor research and particle accelerator diagnostics.

DESCRIPTION OF THE APPARATUS

The technology of IR detectors in the near and mid IR range based on photovoltaic devices, e.g., those fabricated on HgCdTe semiconductors and cooled at liquid nitrogen temperatures, is essentially limited to response times of a few ns. However, new uncooled mid-IR devices exhibit sub-ns response time and may be used with success for the detection of intense IR sources such as SR storage rings.

Figure 1 – Photo of the IR photoconductive device.

Uncooled and compact photoconductive (see Figure 1), photovoltaic or photoelectromagnetic IR devices, all working at ambient temperature, realized with HgCdTe semiconductors (see Figure 2) and optimized in the mid-IR range with sub-ns response times, are available for fast detection of the intense and brilliant IR SR emissions [5].

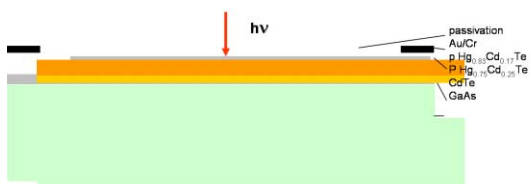

Figure 2 – Schematic cross section of an uncooled IR $Hg_{1-x}Cd_xTe$ photodetector.

MEASUREMENTS ON THE ELECTRON BEAM

Since 2001 SINBAD (Synchrotron Infrared Beamline At DAΦNE) an IR SR beamline is operational at DAΦNE [6]. The IR beam is extracted by a bending magnet located in the external arc section of the electron ring. Time resolved measurements of the synchrotron light emitted by the e^- bunches have been already carried out at SINBAD to monitor the longitudinal bunch length of the accumulated bunches [7,8]. Measurements with different single-element uncooled detectors have been performed detecting the pulsed structure of the IR light emission. The emission of the 106 bunches was measured by using uncooled photoconductive and photovoltaic detectors. The detectors have been placed at the focus of the last mirror at the entrance of the interferometer of the SINBAD beamline monitoring the pulsed structure of the DAΦNE emission (see Figure 3).

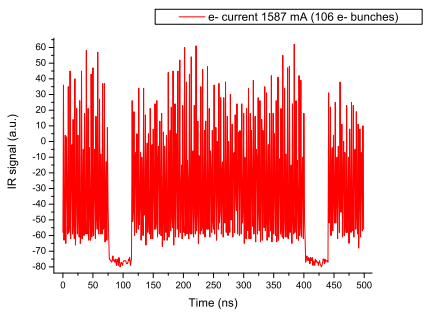

Figure 3: The DAΦNE electron bunches structure as detected by a fast IR uncooled device.

The IR emission of single bunches were measured by using a single element uncooled photoconductive detector. The device is a high-speed device operating at RT and optimized at 10.6 μm, typically a HgCdTe heterostructure fabricated on GaAs substrate that is buffered with CdTe or CdZnTe [9] (Figure 2). This device is front-side illuminated and as a consequence the absorption of radiation at any wavelength occurs only in the narrow energy gap absorbing layer.

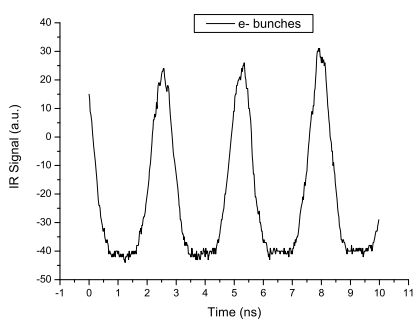

Figure 4: IR signal of three adjacent electron bunches.

The detector was biased by a current of about 20 mA through a bias tee. The output was amplified by a voltage amplifier (gain ~ 40 dB, bandwidth of 2.5 GHz) and acquired by a scope with a bandwidth of 6 GHz. The average rise time and fall time of the signal emitted by a single-electron bunch are about 560 ps and 600 ps respectively (Figure 4).

Measurements in multibunch and single bunch configuration have been carried out at DAΦNE with a photoconductive IR detector (see Figure 1). In multibunch mode, the electron synchrotron frequency has been measured as well the longitudinal feedback correct behaviour showed in Figure 5.

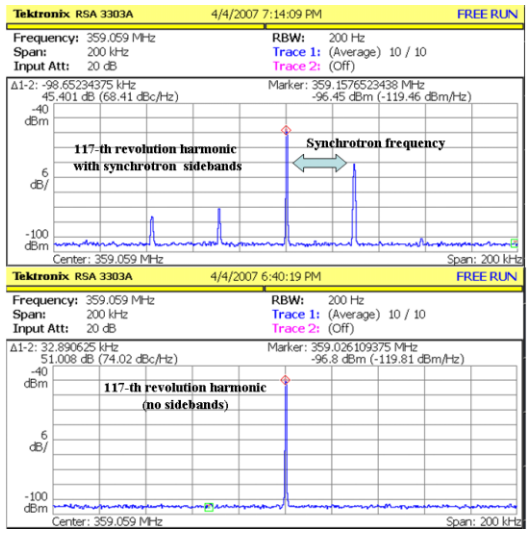

Figure 5: Upper panel: 106 bunches with 734 mA e^- beam current and longitudinal feedback **off**. Lower panel: 106 bunches with 1227 mA e^- beam current with longitudinal feedback **on**.

In a single bunch mode different currents have been stored, from ~3 mA to ~18 mA. For each electron current value, a signal has been measured with a single element uncooled photoconductive detector (Figure 6).

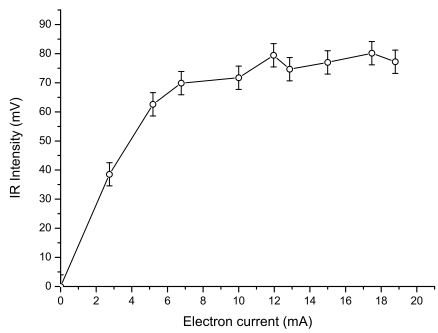

Figure 6: IR signal vs. the electron current.

The intensity of the bunch signal has been plotted vs. the electron currents in Figure 6. The detector is suitable for this experiments because also from this preliminary

data is evident that the output signal collected by the experimental apparatus, e.g., detector and amplifier, was saturated when the electron current of a single bunch was about 8 mA (Figure 6).

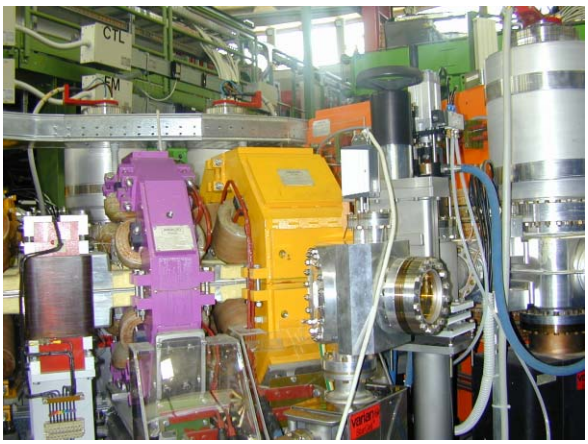

Figure 7: Photo of the exit port recently installed at one of the bending magnet of the DAΦNE positron ring.

SIGNAL ACQUISITION FOR THE POSITRON BEAM

To the purpose in the future to measure bunch by bunch both the electron and positron signals with dedicated photoconductive or photovoltaic uncooled IR detectors, a new experiment, 3+L (*Time Resolved Positron Light Emission*), funded by the Istituto Nazionale di Fisica Nucleare, is going to be installed at the exit of a bending magnet at DAΦNE. A photo of the compact Al made HV chamber containing a gold coated mirror and the ZnSe IR window recently installed on one of the bending magnet of the positron ring is visible in Figure 7. After the window the IR beam will be focussed towards the detector by a set of mirrors working in air and remotely controlled.

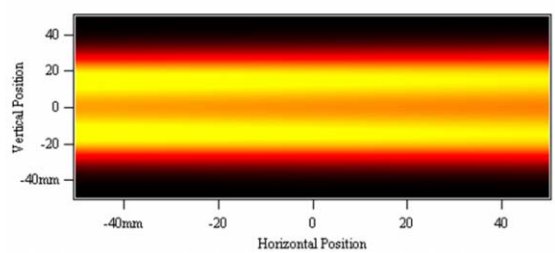

Figure 8: Simulation of the intensity distribution of the DAΦNE bending magnet IR emission at the wavelength of 10 μm.

To design the optical system we performed simulations of the IR source at the wavelength of 10μm (Figure 8). The vertical and horizontal intensity distribution of the IR synchrotron radiation source simulated at 20 cm from the ZnSe window with the SRW software package [10] is showed in Figure 9.

CONCLUSIONS

Beam diagnostics is really a key aspect of the future advancement of accelerator and represents one of the major issues of the next generation storage rings and FEL's. As a consequence, this really simple and fast diagnostics tool has already demonstrated powerful capabilities to perform bunch-by-bunch longitudinal measurements. New IR devices are available and they promise to increase the detection performances to the sub-ns time domain [11]. As a consequence an accurate real time comparison of the longitudinal characteristics of e^- and e^+ beams at DAΦNE where the typical bunch lengths are hundreds of ps appears then possible. When the 3+L installations will be tested a comparison between data collected from the two SR exit ports will be possible improving accelerator diagnostics in order to increase both the stored current in the e^+ ring and the collider luminosity.

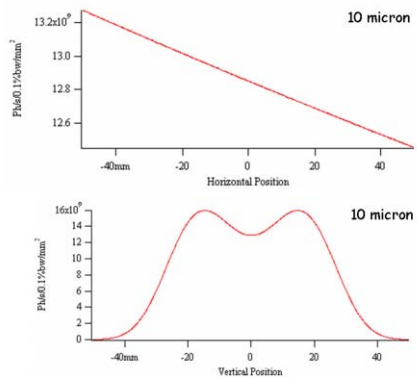

Figure 9: Vertical and horizontal intensity distributions of the IR source simulated at 20 cm from the window.

REFERENCES

[1] A. Drago, *et al.*, Proceedings PAC2003, Portland, Oregon, 2003.
[2] Y. Yamamoto *et al.*, Nucl. Instr. Meth. Phys. Res. A 533 (2004) 505.
[3] J.A. Clarke, Proceedings of EPAC, London, 1994, 1682.
[4] L. Vos, in: EPAC '97, Stockholm, 1998, p. 1626.
[5] J. Piotrowski, Opto-Electron. Rev. 12 (2004) 111.
[6] M. Cestelli Guidi *et al.*, J. Opt. Soc. Am. A 22 (2005) 2810.
[7] A. Bocci *et al.*, Nucl. Instr. Meth. Phys. Res. A., http://dx.doi.org/10.1016/j.nima.2007.05.081, in press.
[8] A. Bocci *et al.*, Proceeding of the 9th International Conference on Synchrotron Radiation Instrumentation, Daegu, 2006, AIP Proceedings.
[9] J. Piotrowski and A. Rogalski, Inf. Phys. Techn. 46 (2004) 115.
[10] O. Chubar and P. Elleaume, Proceedings EPAC98 1998, p.1177-1179.
[11] J. Piotrowski and A. Piotrowski, Proc. SPIE 5957 (2005) 117.

CURRENT STATUS OF THE SQUID BASED CRYOGENIC CURRENT COMPARATOR FOR ABSOLUTE MEASUREMENTS OF THE DARK CURRENT OF SUPERCONDUCTING RF ACCELERATOR CAVITIES

W. Vodel, R. Neubert, S. Nietzsche, F. Schiller University Jena, Germany
K. Knaack, K. Wittenburg, DESY Hamburg, Germany
A. Peters, HIT Heidelberg, Germany

Abstract

This paper presents a new system to measure very low currents in an accelerator environment, using a Cryogenic Current Comparator (CCC). In principle a CCC is a conventional current transformer using the high performance SQUID technology to sense the magnetic fields caused by the beam current. Since the system is sensitive on a pA level, it is an optimum device to detect dark currents of superconducting cavities. The system presented here is designed for the test facilities of the superconducting accelerator modules for the European XFEL at the Deutsches Elektronen-Synchrotron (DESY) in Hamburg. Measurements in a quiet environment showed that an intrinsic noise level of the CCC of 40 pA/√Hz could be achieved.

INTRODUCTION

Due to the development of the TESLA technology [1] superconducting cavities have increasingly high cavity gradients. In addition to the quality factor Q, an important criterion for good performance is a low rate of field emission. The so-called dark current consists of particles emitted by field emission, which are captured by the accelerating fields of the cavity. Since this current can be emitted at arbitrary locations in the accelerator, dark current does not fit in energy, and thus gets lost in focussing elements close to its origin. This results in additional cryogenic loss and activation of components. Therefore, dark current is often the parameter that puts practical limits on the cavity performance.

A further increase in the gradients is technically possible by developing the preparation procedures. In order to do this, or to guarantee a given performance during a larger production series, field emission or dark current has to be controlled during the fabrication process. The device presented here provides the necessary resolution and bandwidth to measure on the pA level. The CCC device takes advantage of the existing cryogenic environment; thus the requirement for cryogenic temperatures is not an additional complication.

The linear accelerator technology, based on superconducting L-band (1.3 GHz) cavities, is currently under study at DESY [1]. The XFEL will be equipped with a total of 116 superconducting acceleration modules each containing 8 “nine cell cavities”. A gradient of 23.4 MV/m is required for a so-called superstructure arrangement of couples of 9-cell cavities. Higher gradients up to the physical limit at 50 MV/m are desired. The dark current, due to emission of electrons in these high gradient fields, is an unwanted particle source.

The apparatus presented here senses dark currents in the nA range. It is based on the cryogenic current comparator (CCC) principle, which includes a highly sensitive LTS SQUID system as magnetic field sensor. Furthermore, the setup contains a Faraday cup and will be housed in the cryostat of the CHECHIA cavity test stand and mounted at a temperature of 1.8 K.

REQUIREMENTS FOR DARK CURRENT MEASUREMENT APPARATUS

Electrons can leave the niobium cavity material if the force of an applied external electric field is higher than the bounding forces inside the crystal structure. The highest field gradients occur at corners, spikes or other discontinuities, due to imperfections of the cavity shape. Another potential field emitter is due to any kind of imperfection on the crystal matter, such as grain boundaries, inclusion of "foreign" contaminants (micro particles of e.g. In, Fe, Cr, Si, Cu) and material inhomogeneity. At these imperfections the bounding forces are reduced and electrons are emitted under the applied high electromagnetic fields [2]. The inner surfaces of the superconducting cavities undergo a series of special treatments to minimize these effects. A reliable, absolute measurement of the dark current allows the comparison of different processing methods and a quality control in the future mass-production.

The XFEL will be operated in a pulse mode with up to 10 Hz repetition rate. The 1.3 GHz r.f. pulse duration is 650 µs flat top. During this time the dark current is present and has to be measured. Therefore a bandwidth of 10 kHz for the dark current instrument is sufficient. As field emission is a statistical process, the electrons leave the cavity at both ends of the beam pipe. Thus, half of the dark current exits at each side, and it has to be measured at one side only. With the 1.3 GHz r.f. applied, we expect that the dark current will have a strong amplitude modulation at this frequency. This frequency has to be carefully rejected from the instrument electronics to insure its proper operation and to avoid a malfunction of the SQUID. This was done by the use of careful r.f. shielding, appropriate filtering of all leads feeding to the SQUID input coil, and the low pass characteristic of the transformer used.

The use of a cryogenic current comparator as dark current sensor has some important advantages:

- measurement of the absolute value of the dark current,
- independence of the electron trajectories,

- accurate absolute calibration with an additional wire loop,
- extremely high resolution.

The required working temperature of 4.2 K (boiling temperature of LHe) for the apparatus is already provided by the CHECHIA test stand for cooling the niobium cavities. In order to enable the CCC to measure the magnetic field of the dark current only, effective shielding against external magnetic fields has to be realized.

THE CRYOGENIC CURRENT COMPARATOR (CCC)

In principle, the CCC comprises three main components:
- the superconducting pick-up coil,
- the highly effective superconducting shield, and
- the high performance LTS-SQUID system.

The CCC, first developed by Harvey in 1972 [3], is a non-destructive method to compare two currents with high precision using a meander shaped flux transducer. Thus only the magnetic field component, which is proportional to the current in the wires, will be sensed by the pick-up coil. All other field components are strongly suppressed. In our apparatus the signal current induced in the pick-up coil is fed into the input coil of an LTS d.c. SQUID.

The design of the CCC for measurements of dark currents has been realized by collaboration between DESY Hamburg, Jena University, and GSI Darmstadt. The prototype apparatus will be placed in the CHECHIA cavity test stand and operated at a temperature of 4.2 K.

Pickup Coil

A single turn pick-up coil is formed as a superconducting niobium toroid with a slot around the circumference. It contains a Vitrovac 6025-F core (Vacuumschmelze GmbH, Hanau, Germany) providing a high permeability

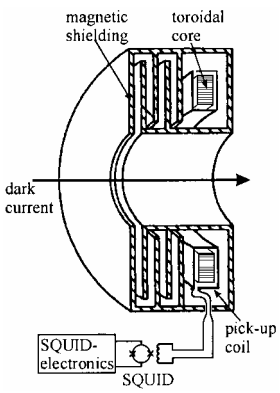

Fig. 1. Simplified schematic view of the magnetic shielding, the toroidal pick-up coil, and the SQUID.

of about 30,000 at liquid helium temperatures [4]. According to our experience 6025-F cores give the lowest noise level in comparison to other materials tested. The material inhomogeneity of the core is averaged by complete encapsulation of a toroidal niobium coil.

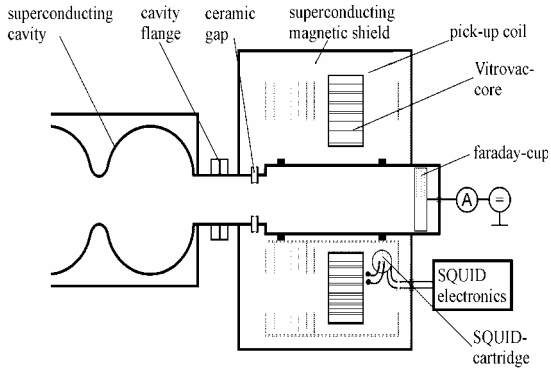

Fig. 2. Schematic view of the CHECHIA's CCC.

Superconductive Shields

The resolution of the CCC is reduced if the toroidal pick-up coil operates in presence of external disturbing magnetic fields. In practice, external fields are unavoidable, therefore an extremely effective shielding has to be applied. A circular meander ("ring cavities") shielding structure (see Fig. 1) allows to pass only the azimuthally magnetic field component of the dark current, while the non-azimuthal field components are strongly attenuated.

SQUID Measurement System

The key component of the CCC is a high performance DC SQUID system developed and manufactured at Jena University. The system makes use of the sensor UJ 111 [5].

The SQUID electronics consists of the low noise preamplifier and the SQUID control and detector unit.

For an optimal choice of bias and flux modulation point, a white flux spectral density of 2×10^{-6} $\Phi_0/\sqrt{\text{Hz}}$ for the SQUID system was found. This flux noise corresponds to an equivalent current noise through the input coil of 0.9 pA/√Hz, an effective energy factor of 543×h (h: Planck's constant), and an energy resolution of 3.6×10^{-31} J/Hz. Using optimum electric and magnetic screening of the sensor the 1/f noise knee was found below 0.1 Hz even in a normal laboratory environment [5].

In a DC coupled feedback loop, the field of the dark current to be measured is compensated at the SQUID by an external magnetic field generated from the attached electronics. Due to the superconductivity of all leads in the input circuitry (pick-up coil, transformer, SQUID input coil) the CCC is able to detect even DC currents. For an optimum coupling between the 1-turn toroidal pick-up coil (40 µH) and the SQUID a matching transformer is necessary. The overall current sensitivity of the CCC was calculated to 175 nA/Φ_0. Using a modulation frequency of 307 kHz the measurement system provides an over-all bandwidth of 20 kHz (signal level 1 Φ_0) or 70 kHz (signal level 0.1 Φ_0), respectively. Thus, it will be possible to characterize the pulse shape of the dark current beam (300 µs rise time, 950 µs flattop, 300 µs fall time, 10 Hz repetition rate) which is dominated by the r.f. structure applied to the cavities.

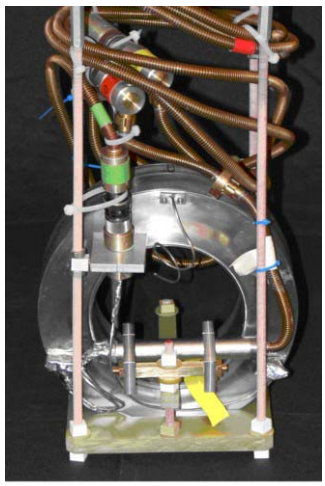

Fig. 3. Nb pick-up coil prepared for preliminary tests at 4.2 K in a liquid helium wide-neck cryostat.

Faraday Cup

Because the energy of dark current electrons is relatively small at CHECHIA, the design includes a Faraday cup to provide a second measurement system for comparison. We installed the Faraday cup at the end of the cavity vacuum chamber. The readout electronics will measure the current to ground.

The simplified scheme of the main components of the CHECHIA's CCC is shown in Fig. 2. Later configurations for complete module tests in the test stand will not allow simple Faraday cups because of the much higher energies (some 100 MeV) of the dark current.

RESULTS AND OUTLOOK

Test measurements of the completed pick-up coil with the special cabling and feed-throughs at 4.2 K were successfully carried out in a wide-neck cryostat at the low temperature laboratory of Jena University (see Fig. 3). A current generator was used as a signal source to simulate the expected dark electron beam pulses. By supplying the calibration coil with a calibrated current pulse the current sensitivity of the CCC was found to be 200 nA/Φ_0, which is in a rather good agreement with the design value of 175 nA/Φ_0.

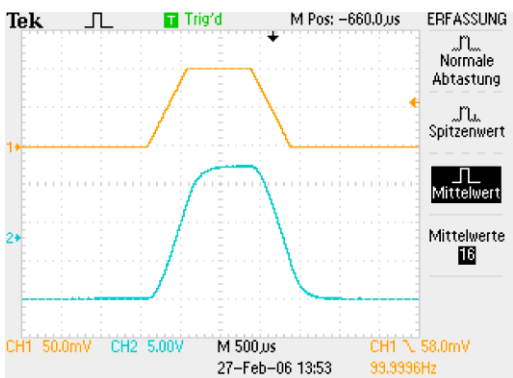

Fig. 4. Simulated beam pulse (upper curve, 300 µs rise time, 950 µs flattop, 300 µs fall time) and SQUID output signal (lower curve).

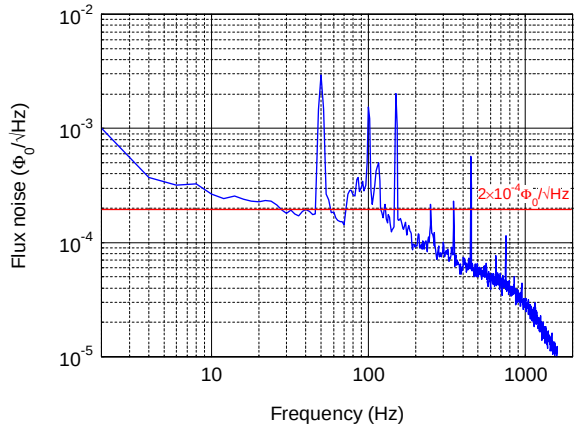

Fig. 5. Noise spectrum of the CCC within a bandwidth from 1 Hz to 1600 Hz. Low pass filter: 1 kHz.

Fig. 4 shows of plot of the simulated beam signal generated by a programmable current generator with the amplitude of 340 nA. The response signal of the SQUID system was 1.7 Φ_0 corresponding with a current sensitivity of 200 nA/Φ_0.

The spectral flux noise density of the system in the frequency range between 1 and 1600 Hz was measured using a HP spectrum analyzer in the laboratory at Jena University and a level of 2×10^{-4} $\Phi_0/\sqrt{\text{Hz}}$ was observed (see Fig. 5). For these measurements a low pass filter with a cut-off frequency of 1 kHz was used. This flux noise level corresponds to a noise limited current resolution of the system of 40 pA/√Hz which is significantly better than required.

As a result of the rough measurement conditions at DESY a noise limited current resolution of the CCC of 500 pA/√Hz was achieved. This is primarily a result of the external electrical disturbances and mechanical vibrations caused by numerous machines and other equipment of the test facility.

Long-term measurements of the output voltage of the CCC to detect flux drifts, caused for instance by temperature drifts of the core material (Vitrovac 6025-F), showed a sufficient small drift of $< 2 \times 10^{-5}$ Φ_0/s.

The complete CCC is now ready for use and the final commissioning of the apparatus in the CHECHIA test stand is planned within the next months.

REFERENCES

[1] R. Brinkmann; TESLA Technical Design Report.
[2] G. R. Werner, et al.; Proc. of the Part. Acc. Conf. PAC 2001, pp. 1071-73.
[3] I. K. Harvey, Rev. Sci. Instrum., vol. 43, p. 1626, 1972
[4] Datasheet "Toroidal strip-wound cores of VITROVAC 6025 F" and private communication from Vacuumschmelze Hanau, Germany
[5] W. Vodel, K. Mäkiniemi, "An ultra low noise SQUID system for biomagnetic research", Meas. Science and Technology Vol 3, No 2, pp. 1155-1160, Dec. 1999

INJECTOR DIAGNOSTICS OVERVIEW OF SPIRAL2 ACCELERATOR

C. Jamet, T. André, C. Doutressoulles, B. Ducoudret, W. Le Coz, J.L. Vignet (GANIL, Caen),
P. Ausset (IPN, Orsay), C. Olivetto (IPHC, Strasbourg)
GANIL, BP 55027, 14076 Caen Cedex 5, France

Abstract

The SPIRAL2 project is based on a multi-beam driver in order to allow both ISOL and low-energy in-flight techniques to produce Radioactive Ion beams (RIB). A superconducting light/heavy-ion linac capable of accelerating 5 mA deuterons up to 40 MeV and 1 mA ions up to 14.5 MeV/u is used to bombard both thick and thin targets. These beams could be used for the production of intense RIB by several reaction mechanisms (fusion, fission, transfer, etc.). The post acceleration of RIB in the SPIRAL2 project is assured by the existing CIME cyclotron. SPIRAL2 beams, both before and after acceleration, can be used in the present experimental area of GANIL.

The construction phase of SPIRAL2 is being started since the 1st of July 2005. An injector design overview is presented with diagnostics used to tune and qualify beams.

SPIRAL2 DESCRIPTION

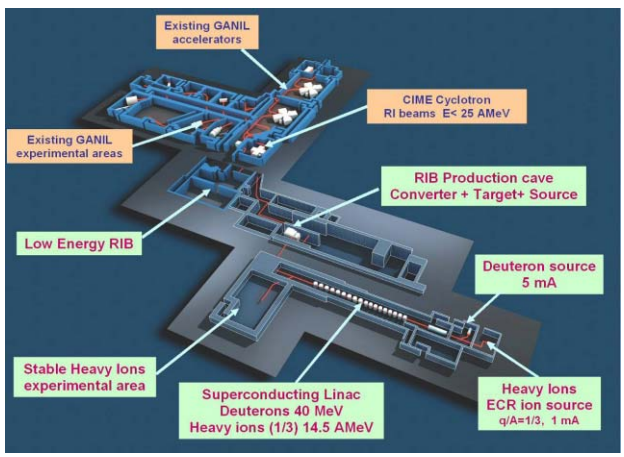

The SPIRAL 2 facility is based on a high-power, superconducting driver LINAC, which will deliver a high-intensity, 40 MeV deuteron beam as well as a variety of heavy-ion beams with mass-to-charge ratio equal to 3 and energy up to 14.5 MeV/u. The driver accelerator will send stable beams in a new experimental area and in a cave for the production of Radioactive Ion Beam (RIB). The commissioning of the driver should start in 2011 at GANIL.

Using a carbon converter, fast neutrons from the break-up of the 5 mA of deuterons impinging on a uranium carbide target will induce a rate of up to 10^{14} fissions/s.

The extracted RIB will subsequently be accelerated to energies of up to 20 MeV/nucl. (Typically 6-7 MeV/nucl. for fission fragments) by the existing CIME cyclotron.

ACCELERATOR

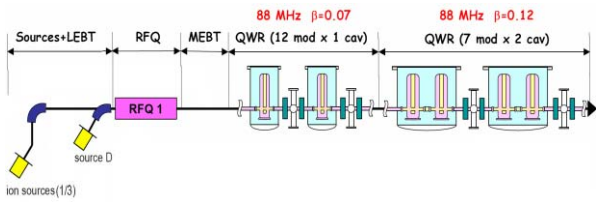

The accelerator is composed by an injector, a superconducting linac and a high energy line. In the injector part, we found a deuteron/proton line, an ion line (LEBT), a RFQ and a MEBT. Two kinds of superconductivity cavity are used for the Linac (β=0.07, β=0.12). In a first time, the injector will be built at the Saclay Laboratory (near Paris). First beams are scheduled in the middle of 2009.

INJECTOR

Low Energy Beam Transport (LEBT)

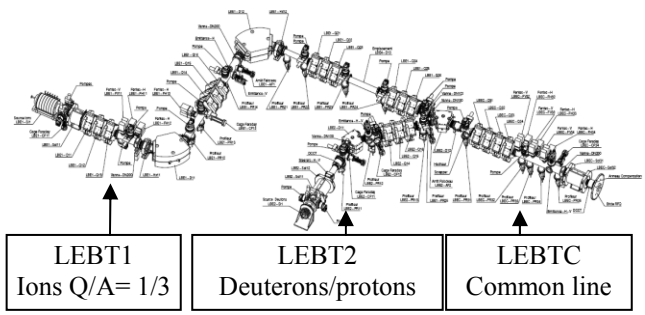

Diagnostics used on the LEBT are:

- 16 Beam profile monitors
- 3 Emittancemeters (H and V)
- 2 DCCT
- 5 Faraday cups

Medium Energy Beam Transport (MEBT)

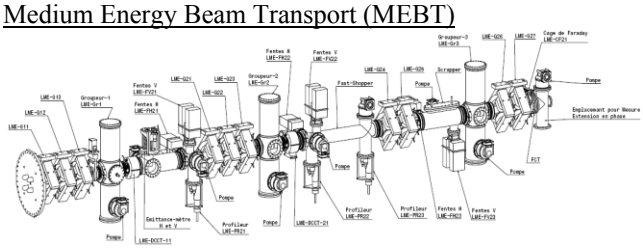

Diagnostics used on the MEBT are:

- 3 Beam profile monitors
- 1 Emittancemeter (H and V)
- 1 DCCT
- 1 Faraday cup
- 1 FCT (Fast current transformer)
- 1 bunch length measurement

INJECTOR TEST BENCH

During the commissioning of the RFQ and the MEBT, an Injector Test Bench (BTI) will be used to qualify the beam at the output of the RFQ.

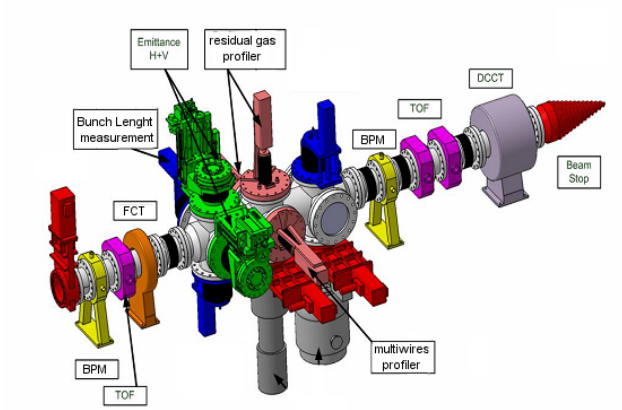

Diagnostics used on the BTI are:

- 2 Beam profiler monitors (SEM and gas residual)
- 1 Emittancemeter
- 1 DCCT
- 1 Faraday cup
- 1 FCT (Fast current transformer)
- 1 bunch length measurement
- Time of flight measurement Pick-up
- Beam Position Monitor

INJECTOR BEAM CARACTERISTICS

Maximum values

	Intensity	Energy	Power
LEBT1 (ions)	1 mA	20 keV/A	60 W
LEBT2 (deuterons)	5 mA	40 keV	200 W
MEBT	5 mA	750 keV/A	7.5 kW

In LEBT, diagnostics should support a power density of 2 $kw.cm^{-2}$.

FARADAY CUP

Faraday cups will measure with a good precision beam currents and efficiencies in lines.
Imax: 10 mA
Maximum Beam size: 80 mm
LME Maximum Power: 7,5kW
Accuracy: $\sim 10^{-3}$
Materials: cupper for ions, nickel for deuterons

Temperature simulation

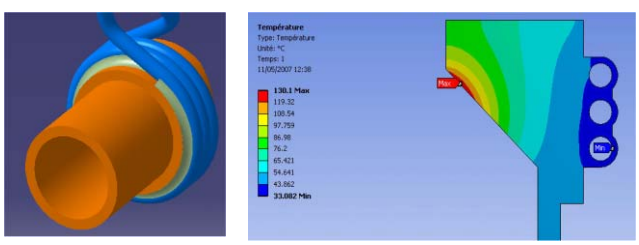

DC CURRENT TRANSFORMER

New PCT of Bergoz has been chosen to measure beam current. The NPCT works on the principle of the zero-flux DC current transformer.
NPCT-175
Full scale range: +/-20mA
High resolution model: $< 1\mu A / \sqrt{Hz}$

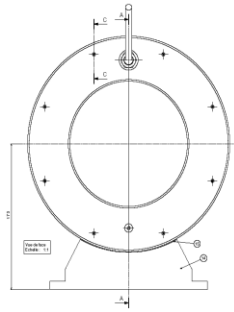

Magnetic shielding is composed by three materials (ARMCO and mumetal separated by aluminium).

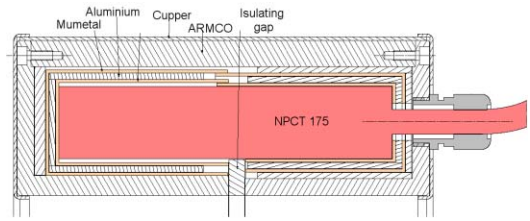

EMITTANCEMETER

Each emittancemeter consist of two Allison scanners, in the horizontal and vertical plane.

Principle of an Allison emittancemeter

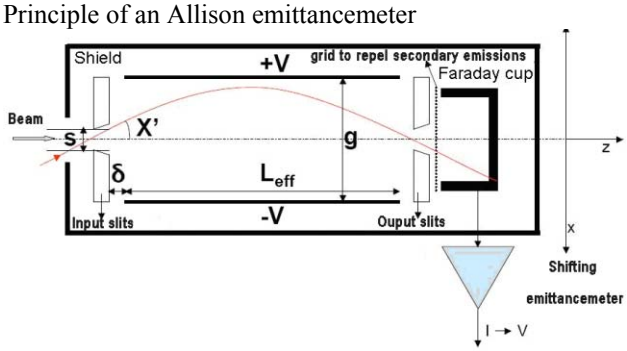

With an energy q.U, an ion (charge q) enters with an angle x', is deviated by a voltage V and goes through output slits. The equation of V is given by:

$$V = 2.U.x'.(g/Leff)$$

For each position of the emittancemeter, a voltage is applied to measure a maximum current on the Faraday cup.
Maximum beam diameter capability: 80 mm
Maximum Voltage: 1.5kV

BEAM PROFILE MONITOR

Secondary-emission monitors (SEM)

Monitors are composed by a horizontal and vertical grid of 47 gold tungsten wires of 150 µm. These wires are welded on alumina board to obtain a maximum out gazing rate of 1.10^{-8} Pa.m^3.s^{-1} (after a baking at 150 °C). Two kinds of grid can be installed, in function of the maximum size needed to be measured: 47 wires spaced of 1 mm for maximum beam size of 30 mm and 47 wires spaced of 3 different steps (1, 2, 3 mm) for maximum beam size of 80 mm. In order to resist to the beam power, a maximum rate of 5 ms/s will be applied on the beam.

The total mechanical precision of this diagnostic will be 0.2 mm.

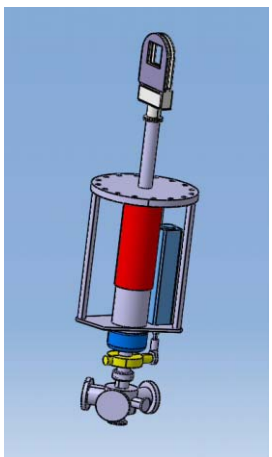

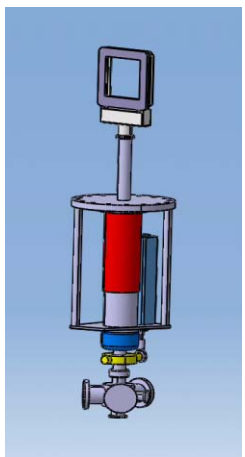

BUNCH LENGTH MEASUREMENT

FAST CURRENT TRANSFORMER (FCT)

FCT will be used for bunch length visualizations.
Characteristics:
FCT-0122-20:1 of Bergoz
Pulse response: 150ps
Upper cut-off frequency: 1.6 GHz
In flange CT: ID = 96 mm OD = 225 mm

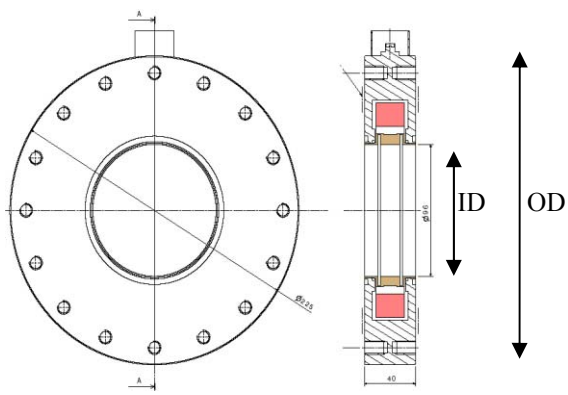

The beam phase extension in the MEBT is estimated to 40° (σ = 6°). That gives a bunch length total of about 1.3ns.

COAXIAL FARADAY CUP

An interceptive diagnostic like a coaxial Faraday cup will be used to measure bunch lengths. The bandwidth should be upper than 2 GHz to have a fast rise time (< 200 ps.).

TIME OF FLIGHT MEASUREMENT

The beam energy will be calculated from the time of flight measurement.

The non-relativist relation gives $E = \frac{1}{2}mv^2 = \frac{m}{2}.(\frac{L}{T})^2$

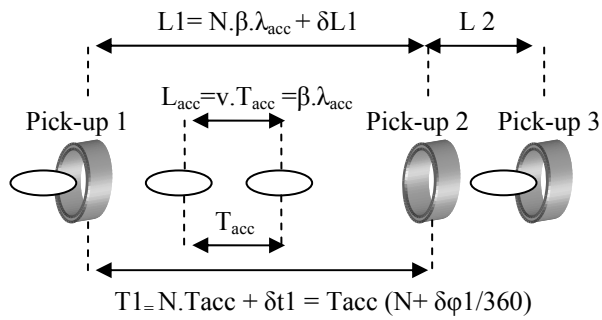

The third pick-up is used to determine the number N of bunches between pick-up 1 and pick-up 2.

Energy E (MeV/u)	0.75
Velocity β=v/c	0.04
Frequency F_{acc} (MHz)	88.05
Wavelength λ_{acc} (m)	3.4
Length L_{acc} (mm)	136
Length L1(m)	1.5
Diameter (mm)	80

Phase of pick-up signals will be measured to deduce time of flight and energy.

The energy accuracy depends of the length and the phase measurement accuracy.

$$\left|\frac{\Delta E}{E}\right| = 2.\left|\frac{\Delta L}{L}\right| + 2.\left|\frac{\Delta\rho}{360.N + \Delta\rho}\right|$$

REFERENCES

[1] T. Junquera & al, The high intensity superconducting Linac for the SPIRAL2 project at Ganil, Proceedings of LINAC06, Knoxville, Tennessee USA
[3] P. Bertrand, JL Biarrotte and D. Uriot, Beam dynamics studies for the Spiral2 project, Proceedings of EPAC06, Edinburgh (UK) 2006.
4] M.H. Moscatello & A. Mosnier, "Design of the high Intensity exotic beams Spiral 2 project", PAC'05, Knoxville, TN, USA.
[5] "The SPIRAL2 project APD report", January 2005.

BEAM BASED MEASUREMENTS OF RF PHASE AND AMPLITUDE STABILITY AT FLASH

H. Schlarb, Ch. Gerth, W. Koprek, F. Loehl, E. Vogel
DESY, D-22607 Hamburg, Germany

Abstract

Beam based measurements of the phase and amplitude stability of the photo-cathode laser, the RF gun and superconducting acceleration modules are key tools for understanding and controlling these critical acceleration sub-systems. The measurements are used to identify the sources of instabilities, to determine response functions, and to optimize RF feedback parameters and algorithms. In this paper, an overview of the measurement techniques, together with some important results on the RF and laser stability currently achieved at FLASH.

INTRODUCTION

One of the most challenging tasks for the operation of high gain single pass FELs is the precision control and stabilization of the longitudinal electron bunch profile and its arrival at the FEL undulator. The acceleration RF fields prior to the bunch compression sections are sources for slow drifts and fast fluctuations. The large bunch compression factor (30-100) required to achieve peak currents in the kA range cause large bunch length variations from small changes in energy chirp rate and cause unacceptable arrival time jitter due to energy fluctuations. The RF stability is, therefore, key for successful user operation of FELs.

At FLASH and the future XFEL, the RF amplitude and phase must be controlled to about 10^{-4} and 0.01° to reduce peak current variation to the % level and to stabilize bunch arrival times to within the rms bunch duration (e.g. XFEL 60 fs). The bunch train is accelerated in superconducting TESLA-like modules operated with millisecond long RF pulses and repetition rates in the Hz range. Electron bunch trains with a frequency of MHz are accelerated during the RF flat-top. The RF pulses are controlled through the 1.3 GHz preamplifier input signal via a digital feedback system that calculates the RF vector-sum from the individual cavity pickup signals.

The complex low-level RF field regulation is fraught with difficult to identify systematic errors caused by electronics, electromagnetic noise, calibration errors, and faulty hardware. It is, therefore, of importance to develop beam based measurements that allow for validation and optimization of the RF field regulation.

RF GUN PHASE STABILITY

In the FLASH RF photo-injector, the electron beam is produced by impinging a 10 ps FWHM UV laser pulse onto a photo-cathode in the 1.5 cell L-band cavity. Laser injection phase into the cavity is at about ϕ =-38° from the RF zero-crossing. Time-of-flight effects of the non-relativistic electron bunch exiting the cathode cause a variation of the beam arrival at the following acceleration module, ACC1. The arrival-time at ACC1 changes by approximately 1 ps per 1° phase change of the RF gun. In the case of a linear energy chirp rate of 0.14%/ps impressed on the bunch by $\phi_{acc1} = 10°$ off-crest acceleration in ACC1, the energy deviation already amounts to 0.14%/ϕ_{gun}. It then becomes nearly impossible to distinguish between energy variations caused by RF gun induced arrival time changes and the energy changes from ACC1 amplitude fluctuation.

To measure the gun phase stability, a current transformer (toroid) for bunch charge measurements is used. First, the gun phasing is performed by scanning the RF cavity over 360° while recording the bunch charge. The result of a scan is shown in Fig. 1. If the field gradient at the photo-cathode is decelerating when the laser pulse impinges on the photo-cathode, then no electrons exit the gun ($\phi > 0$). When the RF phase is close to the zero-crossing, half of the emitted electrons are accelerated ($\phi \approx -10°$). Operation of the gun phase close to the zero-crossing makes the charge-phase dependency strongest and provides a direct measurement of the relative phase stability between the laser and the gun cavity. With a slew rate of typically 0.05 nC/deg, marked as a red line in Fig. 1, and a single shot toroid resolution of 2-3 pC, the phase jitter can be determined bunch-by-bunch with a precision of 0.05° (100 fs) [1].

Figure 2(a) shows the gun-laser phase jitter derived from the charge measurement as recorded for a period of 12 min. The rms fluctuations from macropulse to macropulse with a repetition rate of 5 Hz amount to only 0.06°. N = 30 bunches separated by 25 μs have been used. The macropulse measurement is not limited by the toroid

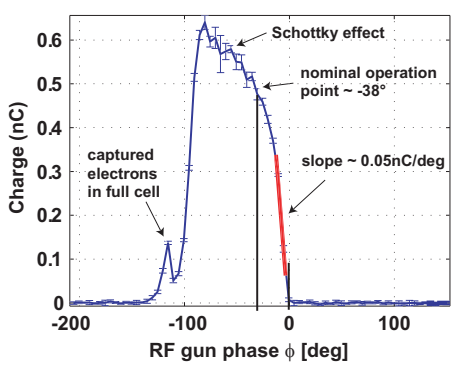

Figure 1: Charge measured by a toroid versus RF gun phase. Scans are performed for phasing the RF cavity. The nominal operation point is -38° from the point when the first electrons are detected.

resolution because the electronic noise readout limitation is reduced by $1/\sqrt{N}$.

The field regulation without a probe is particularly difficult because small variations of gun body temperature cause cavity detuning with a rate of 25 kHz/K. Thus, even for a constant forward power phase into the RF gun, the cavity acceleration phase changes by 35 °/K (Q≈20000). The gun is, therefore, carefully water cooled with a temperature feedback sensor mounted in the cavity iris. The achieved temperature stability of $\pm 0.02°$ is, however, still insufficient and results in peak-to-peak phase variations of $\pm 0.7°$. This variation can be determined from the reflected power phase shown on Fig. 2(b) and used to regulate the forward power [2]. As seen, in Fig. 2, the large variations of the reflected power phase do not correlate with the beam-based measurement of the cavity phase measured, therefore the combination of adaptive feed forward and feedback algorithms used was properly adjusted (see [1] otherwise). The remaining macro-pulse jitter of 0.064 ° (137 fs) is induced by the photocathode laser arrival time jitter.

Figure 2(c) shows the gun-laser phase across macro-pulses containing 30 bunches spaced by 25 μs. The unexpectedly large phase slope of 4.3 °/ms is in contradiction to previous results. By varying the start time of the gun RF and different laser parameters, the dominant part of the slope source could be traced back to the amplifier for the

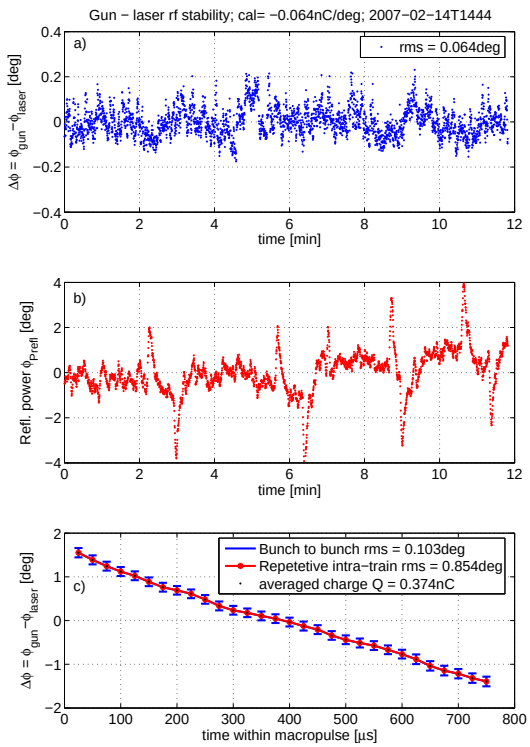

Figure 2: (a) Jitter between gun phase and laser determined from charge measurement (0.06 nC/deg) from macro-pulse to macro-pulse (5 Hz). (b) Variation of the reflected power phase with a directional coupler. c) Variation of the phase across the macro-pulse with 30 bunches spaced by 25 μs.

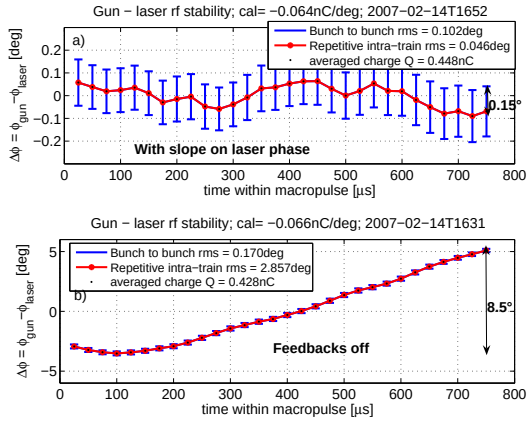

Figure 3: (a) Phase stability gun-laser when a phase slope is introduced to laser oscillator EOM. (b) All feedback algorithm for the gun are switched off.

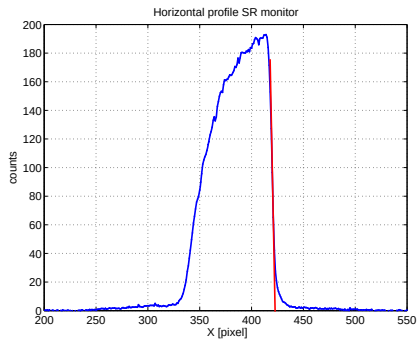

Figure 4: Horizontal beam profile from the synchrotron monitor in the first magnetic chicane.

electro-optical modulators (EOM) that actively phase lock the laser oscillator to the machine reference. To compensate for the potential laser phase slippage, a programmable fast phase shifter was installed. The results are shown in Fig. 3(a). The remaining repetitive phase error amounted to only 0.045°. For comparison, the RF feedbacks were switched off, resulting in a peak-to-peak phase drift of 8.5 ° from the first to the last bunch in the bunch train. This is caused by thermal heating of the gun body.

GRADIENT STABILITY OF ACC1

The beam exits the RF gun with an energy of 4.5 MeV and is accelerated in the ACC1 to 127 MeV before entering a chicane. The dispersion in the chicane is R_{16} =340 mm for 18° bending angle. Gradient variations of ACC1 cause horizontal position shifts of the beam which can be monitored parasitically using the synchrotron radiation (SR) emitted in the dipoles. A new vacuum chamber with a special SR port was installed behind the third dipole in October 2006 [3]. The SR is imaged by a telescope onto a gated, intensified CCD camera. The width and position of the gate is adjusted such that only one bunch per image is recorded.

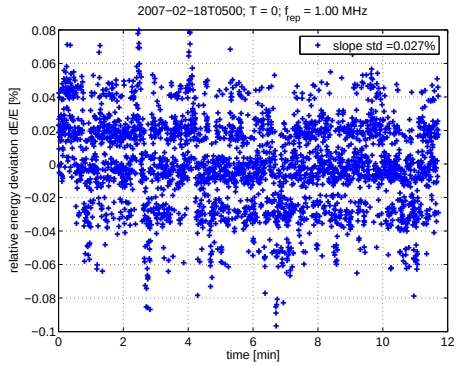

Figure 5: Energy stability of the first bunch in a pulse train.

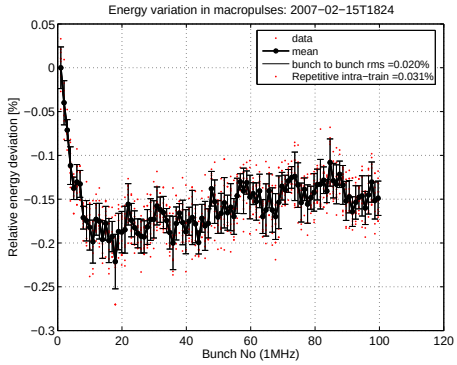

Figure 6: Energy deviation across macro-pulses.

Most of the beam energy stability measurements are carried out at 9° during FEL operation. The energy distribution of a 10 ps FWHM electron bunch with a residual energy spread of only a few keV is comprised of a steep rising edge at high energies with a low energy tail, as plotted in Fig. 4. Phase variation of the acceleration module changes the tail distribution, while gradient variations shift the entire profile. To determine the energy stability, the offset value of a linear fit on the rising edge is used. The monitor is calibrated by varying the dipole current while tracking the profile movement. The value for 18° bend angle is dE/E=2.5·10^{-4}/pixel.

Figure 5 shows the energy stability recorded for the first bunch in the pulse train over a period of 12 minutes. Typically, an energy stability of 2.7·10^{-4} is measured, where values as small as 1.5·10^{-4} have been recorded. This is an improvement of a factor of two compared to earlier measurements. The better stability was achieved after the removal of a faulty probe signal from the vector sum and optimal adjustment of the feedback gain.

The energy stability within macro-pulse trains of 100 bunches is shown in Fig. 6. Each individual bunch was recorded for 20 shots before the gate was shifted by 1μs. To compensate acceleration field variations caused by beam loading, charge measurements were incorporated into the low level RF regulation[4]. Besides transient effects during the first 10μs of the macro-pulse, which could not be corrected within one shift, a beam energy stability of 0.07% peak-to-peak (0.02% rms) has been achieved.

PHASE STABILITY OF ACC1

Off-crest acceleration provides an energy chirp that leads to a compression of the electron bunch in a magnetic chicane. Compression is monitored at FLASH using a diffraction radiator after the chicane and a pyro-electric sensor that records the Terahertz radiation power emitted at the radiator. When the phase of ACC1 is scanned from on-crest to about -20° the compression monitor detects, within a narrow phase range of about 4° FWHM, a large coherent signal. At $\phi_{ACC1} \approx -9°$ the monitor voltage varies strongly with the ACC1 phase and the slope of the linear

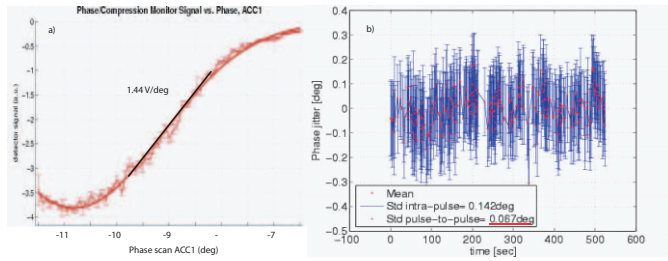

Figure 7: (a) Phase scan of first acceleration module. (b) Pulse-to-pulse phase jitter extracted signal variation of pyro-electric detector (1.44 V/deg).

fit, depicted in Fig. 7(a), provides a conversion factor for a phase measurement. The phase stability over 10 minutes is shown in Fig. 7(b) and amounts to 0.067°. Beam injection, however, is influenced by the laser and the RF gun phase, so the quoted value is an upper limit on the phase stability achieved by the low level RF regulation.

SUMMARY

We present techniques to measure the phase stability of the photo-injector RF gun and the first superconducting acceleration module. An upper limit for the phase stabilities is 0.06°, a value that is limited by laser arrival time stability. An amplitude stability of 2-3·10^{-4} was also measured for a single acceleration module which provides an energy gain of 120 MeV.

REFERENCES

[1] H. Schlarb *et al.*,"Precision RF Gun Phase Monitor System for FLASH", Proc. EPAC'06 conf., Edinburgh, UK, (2006)

[2] E. Vogel *et al.*,"FPGA-based RF Field Control", Proc. EPAC'06 conf., Edinburgh, UK, (2006)

[3] Ch. Gerth,"Synchrotron Radiation Monitor for Energy Spectrum measurements in the bunch compressor at FLASH", WEPC03, this conference.

[4] E. Vogel *et al.*,"Beam Loading Compensation using Real Time Bunch Charge Information from a Toroid Monitor at FLASH", to be publish PAC'07

DEVELOPMENTS AT ELETTRA OF THE ELECTRONICS FOR THE BUNCH-ARRIVAL MONITOR*

L. Pavlovic†, T. Korosec, M. Vidmar, University of Ljubljana, Ljubljana, Slovenia
M. Ferianis, F. Rossi, Sincrotrone Trieste, Trieste, Italy
K. Hacker, F. Loehl, H. Schlarb, DESY, Hamburg, Germany

Abstract

Within the framework of the EUROFEL project, a task has been started in 2006 for a joint development of a Bunch Arrival Monitor (BAM), based on the original idea from DESY. ELETTRA is responsible for the development of the VME-controlled clock-delay board of the BAM system. A variable clock-delay circuit (a phase shifter) is required to adjust the acquisition sampling point of the pick-up-modulated optical pulses of the master-laser oscillator. Since the optical pulses have a repetition rate of 40.625MHz (54MHz in the future) and the acquisition sampling frequency is double than this value, the clock-delay module operates in the 80-120MHz frequency range. The clock timing jitter of the acquisition system greatly affects the measurements: the output timing jitter from the clock-delay board should be less than 0.5ps-rms. Therefore, due to the very strict additive timing-jitter requirements, three phase shifter versions were designed, built and phase-noise evaluated. The low-pass-filter implementation achieved 563fs of total-system timing jitter (with source at 283fs), the integrated IQ multiplier 365fs (source jitter is 188fs) and the passive IQ modulator 265fs (source at 208fs).

INTRODUCTION

Bunch-arrival monitor (BAM) system designed at DESY, Hamburg, Germany, is based on the acquisiton of master-laser oscillator's (MLO) optical pulses, modulated by the electron-beam pick-up signal. Therefore amplitude changes of the acquisited signal corresponds to the beam (bunch) arrival time. Modulated laser pulses, converted to electrical signals using high-speed photodiodes, are sampled (acquisited) by a fast analog-to-digital converter (ADC), which requires suitable and phase-adjustable clock for adjusting the optimal sampling point. For this purpose clock-delay module was proposed in collaboration between DESY (Hamburg) and ELETTRA (Trieste) within EUROFEL DS3 design study. Block diagram of the test bench used at DESY for the bunch-arrival monitor is shown in figure 1.

Clock-delay module (CDM) is basically an electrically-adjustable phase shifter, with VersaModule Eurocard-bus (VME-bus) digital control and/or external analog control of the phase shifting. Input levels to the clock-delay module are from -30 to -10dBm. Since clock-delay module is used as a phase shifter for precise acquisition system, very strict output timing-jitter is required. For the DESY BAM test bench, the total output timing jitter from the CDM is defined as 500fs-rms.

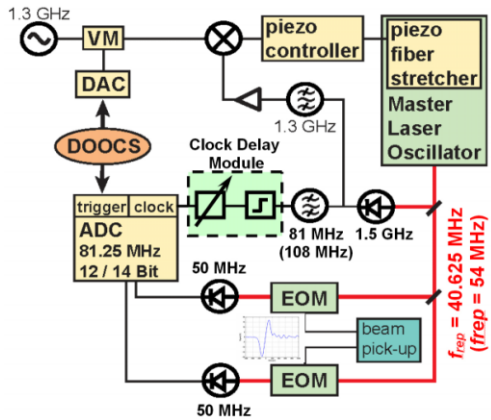

Figure 1: Block diagram of the bunch-arrival monitor test bench [1].

CLOCK-DELAY MODULE

The clock-delay module proposed is a VME-controlled phase shifter operating in the 80-120MHz frequency range. Beside digital control by VME bus, analog control is also possible by external inputs connected directly to the phase shifter using jumpers. The time step of the phase shifter is defined by digital-to-analog converter (DAC) resolution of 16-bits, which is sufficient to achieve the value of 500fs at 100MHz. For read-back and verification of the preset phase value, an analog-to-digital converter (ADC) is connected to the phase shifter control lines, again with 16-bit resolution. Output from the CDM is taken in a digital form with low-voltage positive emitter-coupled logic (LVPECL) and low-voltage differential signaling (LVDS) logic standard. Since both logic standards require DC coupling and 100Ω termination, proper connectors, interconnect cables and receiver front-ends must be used. An auxiliary output with 20dB gain from the input and sinewave waveform is added for test purposes. Block diagram of the clock-delay module is shown in figure 2.

* This work has been partially supported by the EU Commission in the Sixth Framework Program, Contract No. 011935 – EUROFEL.
† leon.pavlovic@fe.uni-lj.si

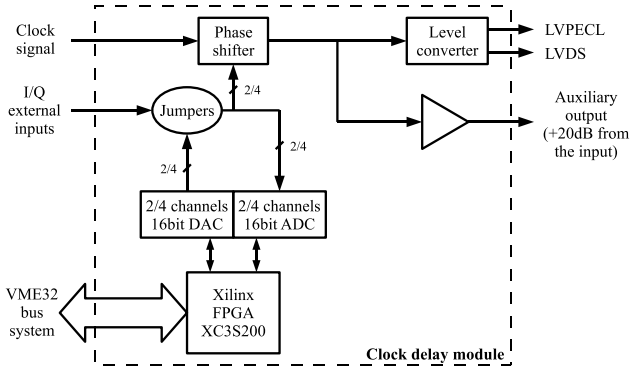

Figure 2: Block diagram of the clock-delay module.

CLOCK-DELAY MODULE PHASE-SHIFTER IMPLEMENTATIONS

Due to the fact that the BAM test bench requires stable and low-noise clock signal for precise acquisition system, three different phase-shifter variants have been designed, implemented and phase-noise evaluated.

Tunable low-pass filter as a phase shifter

First solution for the phase shifter is based on high-order tunable low-pass filter (LPF) with high cut-off frequency. Such filter has a variable amplitude and phase response resulting in phase shifting at the certain frequency. We have designed a 65^{th} order filter with high cut-off frequency assuring quite stable amplitude response (less than 3.5dB difference between the lowest and highest cut-off) and more than 360° phase shift in the range 80-120MHz. The designed filter is LC type built from fixed inductors and variable capacitors BB833. Varactors are biased with bias voltage from 0 to 9V to bring the desired performances.

The complete phase shifter design consists of a tunable low-pass filter itself, an input amplification stage and an output limiter as schematically shown in figure 3. For the final CDM implementation, a level converter at the output is also required, but it was omitted in this development stage.

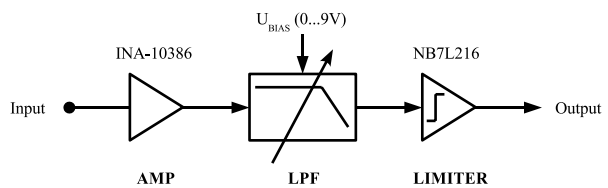

Figure 3: Block diagram of the low-pass filter as a phase shifter.

As the characteristic feature, phase noise and timing jitter of the overall phase shifter was measured at the input frequency of 100MHz. For comparison, the phase noise of signal oscillator and phase shifter output were measured. The obtained timing-jitter results are shown in table 1.

Table 1: Timing-jitter results of the low-pass filter as a phase shifter.

	Total timing jitter (10Hz-10MHz)
Anritsu MG3692B output	283 fs
Low-pass filter output	563 fs

Integrated IQ multiplier as a phase shifter

Using commercially available IQ multiplier ADL5390 from Analog Devices, IQ modulation is possible using an additional 90° splitter. Figure 4 shows a block diagram of the implementation of the phase shifter, operating in the frequency range from 80MHz to 120MHz, limited by the bandwidth of the power splitter. The DAC drives the IQ multiplier directly by differential I and Q signals for the best performance. The LVPECL and LVDS outputs are transformed to single-ended signals and AC-coupled for the direct connection to the phase-noise measurement equipment for the phase-noise evaluation.

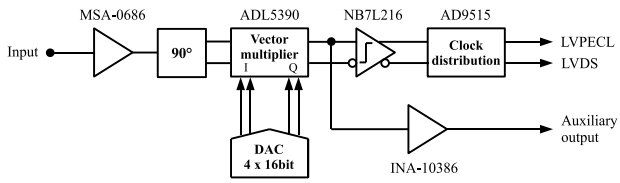

Figure 4: Block diagram of the integrated IQ multiplier as a phase shifter.

Total system timing-jitter results, computed from the phase-noise measurements, for the source and phase shifter output at 100MHz and -10dBm input power are shown in table 2.

Table 2: Timing-jitter results of the integrated IQ multiplier as a phase shifter.

	Total timing jitter (10Hz-10MHz)
Anritsu MG3692B output	188 fs
Integrated IQ multiplier output	365 fs

Passive IQ modulator as a phase shifter

Commercially available IQ modulator MIQC from Mini Circuits is used. Figure 5 shows a block diagram of the phase-shifter implementation, operating in the frequency range from 52MHz to 88MHz for the MIQC-88M partnumber, limited by the bandwidth of the MIQC device. The DAC drives the IQ modulator using a low-noise operational amplifier. The LVPECL and LVDS outputs are transformed to single-ended signals and AC-coupled for the direct con-

nection to the phase-noise measurement equipment for the phase-noise evaluation.

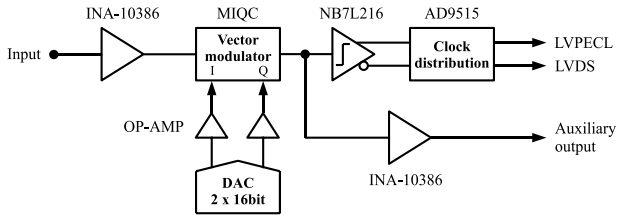

Figure 5: Block diagram of the passive IQ modulator as a phase shifter.

Total system timing-jitter results, computed from the phase-noise measurements, for the source and phase shifter output at 82MHz and -10dBm input power are shown in table 3.

Table 3: Timing-jitter results of the passive IQ modulator as a phase shifter.

	Total timing jitter (10Hz-10MHz)
Anritsu MG3692B output	208 fs
Passive IQ modulator output	265 fs

CLOCK-DELAY MODULE AS A STANDALONE VME-BUS CARD

The DESY control system used for the bunch-arrival-monitor set-up is based on a VME32 bus system. The module we are developing is a mixed signal board with an interface to this kind of bus system.

The analogue part of the board contains the circuits used to obtain the required phase shift values while the digital part has the interface to the bus system. The phase shifter can be driven by the VME bus or by external signals (jumpers located on the board). In this way the selection of the signal source for the phase shifter is manual: we have preferred this solution instead of another one (for example analogue multiplexers controlled by the VME bus) to reduce noise impairments on the phase shifter input signals.

The core of the board, which connects the two sections just described, is based on a programmable logic device, the XC3S200 chip from the Xilinx Spartan 3 family of FPGAs. The FPGA is programmed implementing a state machine for the interface to the VME bus (using the VME terminology, it's a slave module with A16 and D16 capabilities) and for the control of the 16-bits ADC/DAC chips. The ADC is used for monitoring operations while the DAC is actively used to drive the phase shifter section. The two interfaces to the analogue world are controlled by independent serial controllers.

CONCLUSIONS

Three different schemes of phase shifters were designed and phase-noise evaluated. Timing-jitter performance was found best with the passive IQ modulator version, where total system timing jitter measured was 265fs (the criteria for the BAM test bench is 500fs). The comparison of the phase noise profiles for the source and the output of the passive IQ modulator solution (measured with the Agilent E5052A) is shown in figure 6.

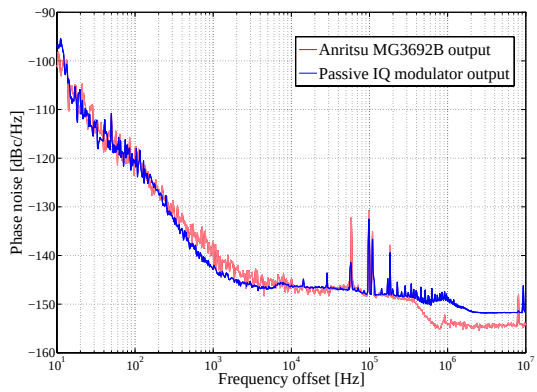

Figure 6: Phase noise profiles for the signal generator and the passive IQ modulator output.

However, additional phase-noise or timing-jitter improvement is possible with the optimization of the voltage levels between various stages in the analog section of the CDM (front-end amplifier, IQ modulator and level converter).

REFERENCES

[1] F. Loehl, K. Hacker, F. Ludwig, H. Schlarb, B. Schmidt, A. Winter, "A sub 100 fs electron bunch arrival-time monitor system for FLASH", Proceedings of EPAC 2006, Edinburgh, Scotland, 2006, pp. 2781–2783.

SECONDARY ELECTRON EMISSION BEAM LOSS MONITOR FOR LHC

D. Kramer*†, B. Dehning, E.B. Holzer, G. Ferioli, CERN, Geneva, Switzerland

Abstract

Beam Loss Monitoring (BLM) system is a vital part of the active protection of the LHC accelerators' elements. It should provide the number of particles lost from the primary hadron beam by measuring the radiation field induced by their interaction with matter surrounding the beam pipe. The LHC BLM system will use ionization chambers as standard detectors but in the areas where very high dose rates are expected, the Secondary Emission Monitor (SEM) chambers will be employed because of their high linearity, low sensitivity and fast response. The SEM needs a high vacuum for proper operation and has to be functional for up to 20 years, therefore all the components were designed according to the UHV requirements and a getter pump was included. The SEM electrodes are made of Ti because of its Secondary Emission Yield (SEY) stability. The sensitivity of the SEM was modeled in Geant4 via the Photo-Absorption Ionization module together with custom parameterization of the very low energy secondary electron production. The prototypes were calibrated by proton beams in CERN PS Booster dump line, SPS transfer line and in PSI Optis line. The results were compared to the simulations.

BLM SYSTEM

The Beam Loss Monitoring system [1] is a vital part of the active protection of the LHC. It has to detect dangerous beam losses which could quench superconductive magnets or even damage components of the accelerator. 3700 ionization chambers (BLMI) will be used in LHC as the main beam loss detectors.
Additional 280 SEM detectors (BLMS) are needed for the high radiation areas; mainly the collimation zones, injection points, interaction points, beam dump and at other critical aperture limits.

BLMS DETECTOR

The BLMS detector will usually be installed in pair with the BLMI to extend the dynamic range of the system towards higher dose rates without saturation of the detector or electronics. Considering a possible beam lifetime of 1 s during acceleration, the BLMI would have an output of 3 A if no saturation or limitation occurred. The maximum steady state input current for the electronics is 1 mA, therefore a 3×10^3 to a 10^4 times lower sensitivity is needed compared to the BLMI.

The ultimate transient loss event of 3×10^{13} p^+ lost in 20 μs in case of an injection kicker fault has to be measurable by the BLMS (i.e. a full injection from the SPS).
The lifetime of the detector should be 20 years as the exchange will be impossible in some locations due to high radiation levels. The expected radiation dose at some locations is several ten MGy per year.

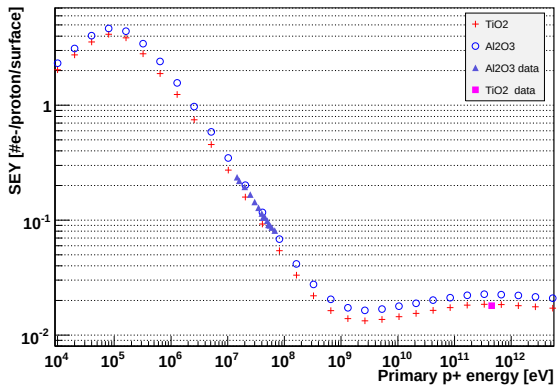

Figure 1: Modified Sternglass formula for true SEY of primary protons for different materials scaled by factor 0.8 to fit reference data[6, 7].

SEM working principle

The BLMS detector is based on the Secondary Electron (SE) emission from solids. When a charged particle passes through the signal electrode, it can excite conduction band or inner shell electrons. These so called "True Secondary Electrons" can diffuse only several nm as they usually have energies lower than 50 eV independent of the primary particle's energy and type [2] in contrary to the "knock-on" δ electrons. The material escaping SE come only from a thin surface layer of the traversed material and are subsequently drifted away by a bias electric field. The Secondary Electron Emission Yield (SEY) is proportional to the electronic energy loss of the particle in the surface layer of the signal electrode. The resulting current between the signal and bias electrodes (and also between the signal electrode and mass) is measured.
The high energy δ electrons leaving the Ti electrode do not produce a signal, because their contribution is canceled by the δ electrons arriving from the bias electrodes but only if they don't have enough energy to penetrate the electrode plates. The BLMS can detect neutral particles only indirectly, if they initiate a shower in the steel vessel.

* daniel.kramer@cern.ch
† Technical University of Liberec, Czech Rep.

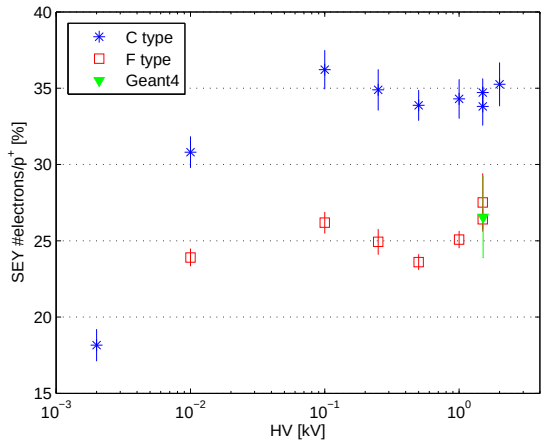

Figure 2: Variation of BLMS normalized response with bias voltage for two prototype detector versions (63 MeV cyclotron proton beam in PSI).

Prototype design

The signal electrode is made of 0.5mm thick Ti, because its SEY was found to be constant up to 10^{20} p^+/cm^2 integrated dose [5]. The bias electrodes are made of Al. The detector has to operate in high vacuum of at least 10^{-4} $mbar$, because the contribution of the gas ionization to the signal has to be kept below 1% of the secondary emission to prevent a nonlinear response. All the steel components undergo the standard CERN UHV cleaning procedure and are vacuum fired at $950°C$ for several hours. A careful insulation of the signal path outside of the detector was found to be very important to prevent a signal contribution from the ionization in air.
For the final version, all the electrodes will be made of 0.25mm thick Ti. It will also contain a NEG ST707 foil of 170 cm^2 active area inside the steel vessel which can adsorb a quantity of H_2 higher than the total surface capacity of the chamber.

MODELING OF BLMS RESPONSE

SEY estimation

It is not straightforward to simulate the SE in Geant4 [3] as it has no corresponding process defined. A modified semiempirical formula of Sternglass [4] (the contribution of δ electrons to the true SEY was not included) was used to calculate the SEY for TiO_2 surface.

$$SEY = 0.01 C_F L_S \frac{dE}{dx}|_{el} \quad L_S = (0.23 N \sigma_g)^{-1}. \quad (1)$$

Where $dE/dx|_{el}$ stands for electronic energy loss, L_S for effective penetration distance of SE, N for number of atoms per unit volume and $\sigma_g = 1.6 Z^{1/3} 10^{-16}\ cm^{-2}$. The calibration factor $C_F = 0.8$ was used in order to match the experimental data for Al_2O_3 [6] and TiO_2 [7]. The maximum measured SEY for the very low energy (i.e. 100 keV) protons hitting the Al target is 1.3 [8] (not plotted) compared to 2 from the parametrization, but particles with such energies have a negligible contribution to the signal as they don't penetrate the chamber walls or lie below the e^- production cut of the simulation. The resulting functional dependence for different materials can be found in Figure 1.

Geant4 simulations

The geometry of the BLMS prototype was implemented in Geant4 including a thin layer of TiO_2 on the signal electrodes.

When a charged particle passes through the TiO_2 to vacuum interface, the SEY is calculated in the G4UserSteppingAction using the Eq. and a SE is recorded with the corresponding probability. The $dE/dx|_{el}$ is calculated by the G4EmCalculator but in case of primary e^- or e^+, the dE/dx from Bremsstrahlung must be subtracted and for mu^- or mu^+ also the e^-/e^+ pair production, as these processes don't contribute directly to secondary emission. Nevertheless, their products are treated as other particles. The δ electrons are produced by the Photo-Absorption Ionization (PAI) module and are treated as other charged particles. The δ electrons are only recorded as signal if they are able to penetrate the electrodes (i.e. $E_k > 750\ keV$). The Geant4 QGSP_HP module was used for simulating the hadronic interactions. The simulations were performed using a round beam of 0.5 or 1cm radius. The cut value for electrons was found to influence the results and is the main reason for the 10% error bar of the simulation points.

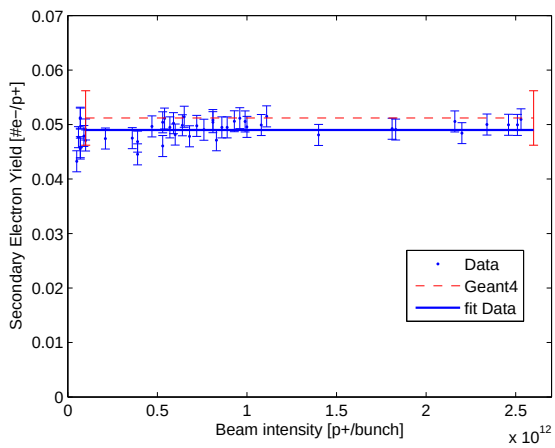

Figure 3: SEY of BLMS as function of proton beam intensity at 1.4 GeV. Simulation error was estimated to 10%.

MEASUREMENTS

The simulations are validated by measurements with particle beams of well known parameters. The prototypes were placed directly in the primary proton beams in the

Paul Scherrer Institute (PSI) and in CERN PSB and SPS transfer line.

Calibration with 63 MeV protons

Two prototype versions ("type C" and the newer "type F" which was simulated) were tested in the 62.9 MeV proton Optis line in PSI [9]. Protons were entering through the 5 mm thick steel bottom cover of the detector. The output current was measured by a Keithley electrometer 6517A. The bias high voltage was varied from 2 V to 1.5 kV and the resulting SEY was calculated by dividing the beam current by the detector output. Figure 2 shows a systematic pattern which seems to be caused by the low energy δ electrons coming from the HV electrodes. The corresponding simulations were performed with a 1.5 kV electric field and are in a surprising agreement with measurements for the "F type".

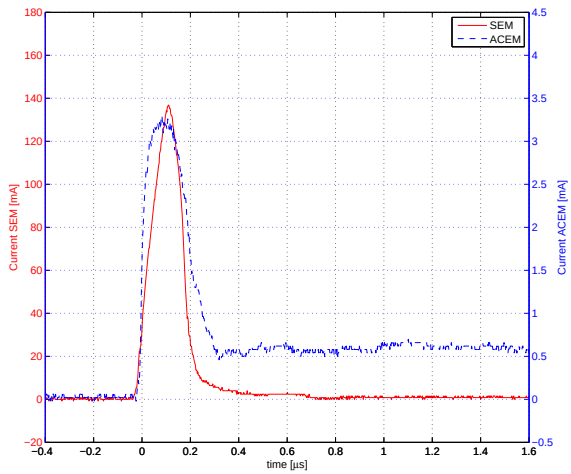

Figure 4: Time response to single bunch compared to reference ACEM detector (160 ns bunch of 2.16×10^{12} p^+ at 1.4 GeV).

Calibration with 1.4 and 400 GeV protons

The older "prototype C" was installed in the PS Booster dump line and tested with a bunched proton beam. Figure 3 shows a very good linearity of the BLMS and a reasonable agreement with the simulation, which lies within the statistical error. A reference ACEM (Aluminum Cathode Electron Multiplier tube) detector with fast response time was installed close to the BLMS outside of the beam. Figure 4 shows a very fast time response without any undershoot or tail in the signal for a bunch length of about 160ns. The chamber signals were measured with Tektronics oscilloscope and 50 Ω termination. The integration was done offline in Matlab code.

The preliminary calibration in the SPS TT2 transfer line at 400 GeV resulted to 0.134 electrons/proton, but the beam profile was not measured. Therefore the measurement will be repeated soon. The corresponding Geant4 simulations estimate the sensitivity to 0.116 electrons/proton with relatively high contribution of δ electrons.

CONCLUSIONS

The BLMS prototype showed no saturation effect and high linearity at the ultimate particle flux as foreseen in the design. Measurements at different energies seem to validate the chosen approach of Secondary Electron Emission simulation in Geant4, which can now be used for determination of thresholds of the LHC BLM system. The largest relative error between measurements and simulations is 14% for the case of 400 GeV protons. More understanding of the model is needed in order to set correctly the production cuts for electrons to find a better agreement at high energies. Further tests in a mixed radiation field on the SPS beam dump and SPS collimation area for proton and ion beams are foreseen or ongoing.

REFERENCES

[1] E.B. Holzer et al., Beam Loss Monitoring System for the LHC, IEEE NSS '05, Puerto Rico, CERN-AB-2006-009 BI.

[2] D. Hasselkamp et al., Particle Induced Electron Emission II, Springer-Verlag, (1992).

[3] GEANT4 simulation toolkit, http://www.cern.ch/geant4.

[4] E.J. Sternglass, Theory of Secondary Electron Emission by High-Speed Ions, Phys. Rev. 108(1957) 1.

[5] G. Ferioli and R. Jung, Evolution of the Secondary Emission Efficiencies of various materials measured in the CERN SPS secondary beam lines, CERN-SL-97-071-BI, (1997).

[6] C.M. Castaneda et al., Secondary electron yields from the bombardment of Al_2O_3 by protons, deuterons, alpha particles and positively charged hydrogen molecules at energies in the range of 10 to 80 MeV, Nuclear Instr. and Meth. B 129(1997) 199-202.

[7] K. Bernier et al., Calibration of secondary emission monitors of absolute proton beam intensity in the CERN SPS North Area, CERN-97-07, (1997).

[8] B. Svensson and G. Holmén, Electron Emission from aluminum and copper under molecular-hydrogen-ion bombardment, Phys. Rev. B 25(1982) 5.

[9] Paul Scherrer Institute, Villigen Switzerland, http://www.psi.ch.

TRANSVERSE FEEDBACK DEVELOPMENT AT SOLEIL

R. Nagaoka, L. Cassinari, J.C. Denard, J.M. Filhol, N. Hubert, M.P. Level, P. Marchand, C. Mariette, F. Ribeiro, R. Sreedharan, Synchrotron SOLEIL, St-Aubin, France
T. Nakamura, K. Kobayashi, SPring-8, Mikazuki-cho, Hyogo, Japan.

Abstract

The paper describes the bunch by bunch transverse feedback system developed and implemented at SOLEIL. In order to cope with diverse beam conditions involving multibunch and single bunch instabilities, a digital system has been developed. While a BPM, a RF frontend and a stripline developed in house are used in the feedback chain, the SPring-8 solution was chosen for the digital processor for its proven performance elsewhere. The commissioning of the system as well as attained feedback performance is presented.

INTRODUCTION

SOLEIL is a French third generation light source ring commissioned in 2006 and starting its user operation this year. Table 1 summarises the machine parameters related to the transverse feedback. The combination of the envisaged high current modes of operation both in terms of total and local intensity, along with small vertical vacuum chamber aperture adopted all around the machine to match low insertion device gaps, results in severe transverse collective beam instabilities, as anticipated from simulation studies. In particular, it has been observed that shifting of chromaticity to large positive values, a known remedy against these instabilities, is not effective at SOLEIL, due to excitation of higher order head-tail modes at high current, as predicted. Moreover, the electron beam is driven strongly unstable by ions existing in the chamber. Foreseeing this situation, it had been decided to install a digital bunch by bunch transverse feedback system, with an objective to keep the beam stable at zero chromaticity without spoiling the small emittance (Table 1), as well as to make it operational since the beginning of the user operation.

Table 1: SOLEIL machine parameters

Energy [GeV]	2.75
Nominal current [mA]	500, 8×10
Revolution frequency [kHz]	846.2
RF frequency f_{RF} [MHz]	352.2
Harmonic number	416
Fractional betatron tunes $\Delta Q_H/\Delta Q_V$	0.2/0.3
Synchrotron frequency [kHz]*	2.4
Betatron phase advance between detector and kicker**	0.0
Beta values at detector β_H/β_V [m] **	10/10
Horizontal emittance [nm·rad]	3.7
Vertical emittance [pm·rad]***	5.0

*At RF voltage of 2.0 MV
**In the present configuration
***Measured at low beam current

DEVELOPED SCHEME

Due to the imposed time constraint and the initially limited expertise in the concerned domain of technology at SOLEIL, the strategy adopted was to make use of already existing schemes and devices developed in other labs. We have followed particularly the systems developed at ELETTRA, the ESRF and SPring-8.

Bunch Position Detector

We have started from investigating whether our SOLEIL BPM had enough sensitivity to meet our requirement. Evaluating the signal level induced on an electrode with 500 mA beam current having rms bunch length of 20 ps as a function of frequency, the peak is found around 1.4 GHz, which is roughly four times f_{RF}, the RF frequency (Fig. 1). Signal levels at the end of a 22 m long 50 Ω coaxial cable of several different types are also shown in the figure. Taking the best case (CNT 600) and including the effect of a hybrid operation that creates a sum signal at the end of the cable, the peak difference signal is found to have the sensitivity of Δ_{peak} of 47 μV/mA/μm. The obtained sensitivity is used to evaluate the noise level at the exit of the RF frontend.

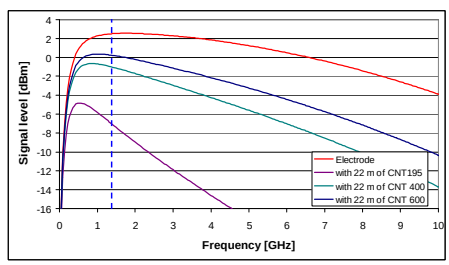

Figure 1: Sensitivity of a SOLEIL BPM against 500 mA beam (1.2 mA/bunch and bunch length of 20 ps).

RF Frontend

On the basis of the frequency dependence of the BPM sensitivity as found above, the ESRF scheme was followed to extract a band (f_{RF}/2) of beam signal at four times f_{RF} and down convert it to the baseband (Fig. 2). Fabrication of such RF frontend was made in house. The measurement precision was evaluated from the thermal noise generated in a 50 Ω cable transporting the 1.4 GHz band of signal, the noise amplification and the baseband conversion in the frontend. By comparing it with the above 47 μV/mA/μm, the resolution σ_δ at the entrance of the ADCs of the digital processor was deduced to be around 1 μm at 1 mA bunch current. On the other hand, Nakamura derived an equation that relates σ_δ to the rms

beam size σ_z arising from the feedback, due to its limited resolution, given by $\sigma_z \sim \sqrt{T_0 / \tau_{FB}} \cdot \sigma_\delta$, where T_0 is the revolution time and τ_{FB} is the feedback damping time [1]. Assuming τ_{FB} = 0.3 ms, a desired value, which was also confirmed achieved from the measurement (see below), we get σ_z = 0.06 μm at 1 mA. This means that the feedback induced beam size will not exceed one tenth of the vertical beam size (~10 μm) above the bunch current of 0.06 mA, or equivalently, the total current of 19 mA in the standard ¾ filling mode. We have thus concluded that the sensitivity of a SOLEIL BPM is sufficiently high.

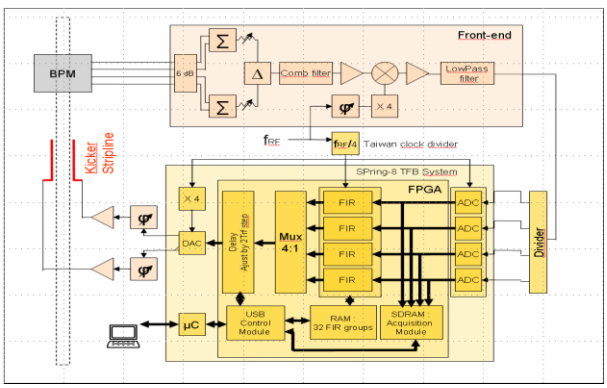

Figure 2: Layout of the SOLEIL feedback chain.

Digital Signal Processor

Among several solutions that were available, the digital signal processor developed at SPring-8 was chosen primarily for its proven performance in different machines. Details of its characteristics may be found elsewhere [2]. Here we merely note that it consists of 4 12-bit ADCs working at 88 MHz, 1/4th of f_{RF}, and having an analog bandwidth of 750 MHz. All FIR filters and multiplexers are integrated into one FPGA board, which allows achieving a latency of less than 1 turn (Fig. 2). The DAC has also 12-bit and works up to 1 GS/s. It must be mentioned that the willingness of TN and KK (the authors from SPring-8) to collaborate with the SOLEIL team, along with their expertise, was appreciable aid for the development of the present system.

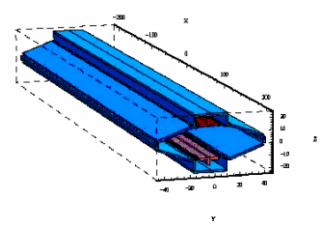

Figure 3: Vertical stripline with 2 electrodes.

Kicker

An extension of the already installed stripline, used for the tune measurement, was made to develop one that has higher shunt impedance, in view of generating a large beam deflection with a reasonable amount of power. In view of the strong vertical single bunch instability, a two-electrode structure (Fig. 3) was adopted for a vertical stripline for its much higher attainable shunt impedance as compared to a four-electrode structure, although the latter works in both transverse planes. The developed stripline achieves the shunt impedance of ~66 kΩ at 50 MHz and is planned to be installed during the forthcoming summer shutdown. Details are described in Ref. 3. The existing short-circuited stripline, the shunt impedance of which is estimated to be ~0.6 kΩ, is used for the feedback as a temporary solution.

RF Amplifiers

The necessary RF power was evaluated from the instability growth rate calculated with the impedance budget of the machine and the expected shunt impedance of 66 kΩ at 50 MHz attained for the developed vertical stripline. Estimating the maximum betatron amplitude damped by the system upon the condition $\tau_{FB} < \tau_G(I)$, where $\tau_G(I)$ denotes the current dependent instability growth time, we obtain the results as shown in Figs. 4, for the multibunch (left) and single bunch instabilities (right), respectively. A total RF power of 150 W (75 W per electrode) is well suited for the current-dependent resolution in position detection discussed above. Three units of 75 W (10 kHz-250 MHz) amplifiers were purchased.

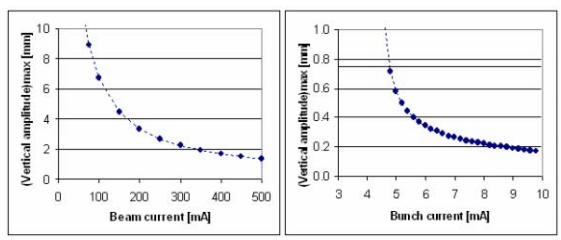

Figures 4: Estimated maximum current-dependent betatron amplitude damped by the feedback system.

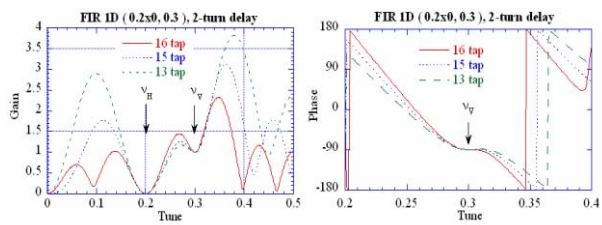

Figures 5: Phase and gain of the FIR filters.

COMMISSIONING OF THE SYSTEM

The entire feedback chain was commissioned with beam during two machine shifts in December 2006, in collaboration with TN and KK from SPring-8. As noted earlier, a shorted type 4-electrode stripline, dedicated to the tune measurement, was used as a provisional kicker, and a BPM in its vicinity as a detector (Table 1). The RF frontend was placed in a nearby rack. For easier operation, the digital processor and its dedicated pc were placed in the control room. The digital filtering was performed using a 16-tap FIR, according to the least-

square fit of the betatron oscillation scheme developed by Nakamura [2]. The optimised gain and phase of the filter are shown in Figs. 5 for the vertical case. Taking into account 1.12 μs of delay created due to the distance between the control room and the stripline, the FIR was shifted by 2 turns. Due to the number of RF amplifiers available, only two electrodes were used diagonally to deflect the beam. This, on the other hand, left us the possibility to try the feedback in the horizontal plane as well as in both transverse planes, by tuning the FIR filter. It turned out that the system managed to keep the beam stable up to the maximum allowed current of 300 mA at zero chromaticity in all three case.

CHARACTERISATION OF THE SYSTEM PERFORMANCE

We are currently at the stage of testing the system stability, reproducibility without retuning, as well as characterising its performance, prior to fully introducing it during the user operation. It has been verified that the feedback efficiency is not sensitive to tiny orbit changes. We neither observed noted degradation restarting the system after few weeks of machine shutdown.

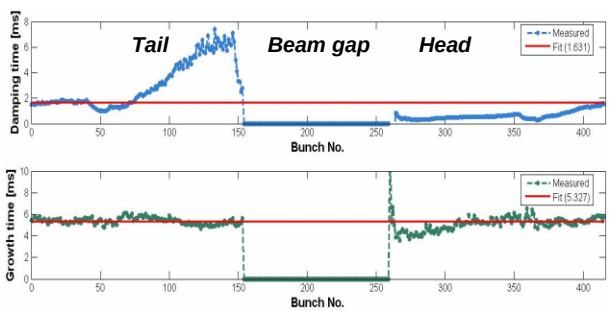

Figures 6: Observed bunch by bunch feedback damping and instability growth times at 50 mA in 3/4th filling.

Using the digital processor's capability to store bunch by bunch data over hundreds of milliseconds, damping and growth times have been pursued by triggering the data acquisition in switching off of the feedback over typically a few ms. The obtained data not only allow us to characterise the feedback performance, but also provide useful bunch by bunch information on the collective instability, particularly, on ion induced dynamics [4]. An example is shown in Figs. 6 where the feedback damping is found notably shorter at the head of the bunch train as compared to the tail, in the standard 3/4th filling. At the maximum allowed current of 250 mA, a growth time of $\tau_G(I)$ =0.93 ms and a damping time of $\tau(I)$ =0.49 ms were measured at zero chromaticity. The feedback damping time deduced from the former values is τ_{FB} = 0.32 ms.

Regarding the impact of the feedback on the vertical beam size, it has been observed that while the feedback manages to keep the beam size constant against beam current, the feedback generates a slight beam size increase at low current. A measurement performed with the lowest achievable emittance coupling of 0.125%, the vertical emittance increased by ~12%, namely the beam size by ~6% when switching on the feedback at low current. However, there was no further increase up to the maximum current of 200 mA followed [5]. A measurement comparing the beam size with and without feedback with a non-zero chromaticity is shown in Fig. 7.

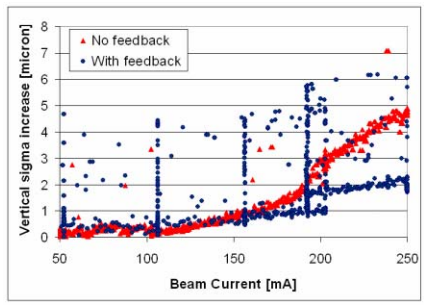

Figure 7: Vertical beam size versus current measured with a pinhole camera [5] at a non-zero chromaticity. Sharp peaks with feedback on are due to tune measurement.

CONCLUSION

By applying the schemes already developed in other machines, a bunch by bunch digital transverse feedback system was implemented and made operational in effectively a year time after the project was started. The system installed has proven to suppress impedance and ion induced beam instability up to 300 mA at zero chromaticity, in one or the other or both transverse planes simultaneously, with a single digital processor, developed by the SPring-8 group. The increase of the small vertical beam size due to the feedback observed so far appears to be within 10% of the original size at zero chromaticity. In future, further optimisation and extension are to be continued to reach the ultimate performance in both multibunch and single bunch modes of operation.

ACKNOWLEDGEMENT

Authors from SOLEIL thank E. Plouviez and G. Naylor at the ESRF, D. Bulfone and M. Lonza at ELETTRA for useful discussions and technical support, and K. Hsu at NSRRC (Taiwan) for kindly offering them a frequency divider for the digital processor. Thanks are also to the SOLEIL commissioning team and the operators for their active support in the control room.

REFERENCES

[1] T. Nakamura, "Residual Beam Motion Driven by the Noise at Transverse Feedback", Nanobeam2005, Kyoto University, Japan.
[2] T. Nakamura, K. Kobayashi, "FPGA Based Bunch-by-Bunch Feedback Signal Processor", ICALEPCA 2005, Geneva, Switzerland, and references therein.
[3] C. Mariette et al., "SOLEIL Vertical Stripline Development", this conference.
[4] R. Nagaoka and M.P. Level, "Beam Instability Observations and Analysis at SOLEIL", PAC07, in preparation.
[5] J.C. Denard et al., this conference.

SINGLE GAIN RADIATION TOLERANT LHC BEAM LOSS ACQUISITION CARD

E. Effinger, B. Dehning, J. Emery, G. Ferioli, C. Zamantzas, CERN, Geneva, Switzerland

Abstract

The beam loss monitoring system [1] is one of the most critical elements for the protection of the LHC. It must prevent the super conducting magnets from quenches and the machine components from damages, caused by beam losses. Ionization chambers and secondary emission based detectors are used at several locations around the ring. The sensors are producing a signal current, which is related to the losses. This current will be measured by a tunnel card, which acquires, digitizes and transmits the data via an optical link to the surface electronic. The usage of the system, for protection and tuning of the LHC and the scale of the LHC, imposed exceptional specifications of the dynamic range and radiation tolerance. The input dynamic allows measurements between 10pA and 1mA and its protected to high pulse of 1.5kV and its corresponding current. To cover this range, a current to frequency converter in combination with an ADC is used. The integrator output voltage is measured with an ADC to improve the resolution. The radiation tolerance required the adaption of conceptional design and a stringent selection of the components.

INTRODUCTION

There will be several systems installed for the protection of the LHC, but one of the most critical is the beam loss monitoring system. The system consists of around 4000 detectors, ionisation chambers and secondary emission monitors. A total of 650 data acquisition cards will be installed in the LHC arcs and side tunnels next to the straight sections of the ring. In the arc, the CFC card will be placed in small racks located below each quadrupole magnet. Due to the high radiation in the straight sections, the CFC cards are concentrated at two locations at each LHC interaction region. The CFC data will be transmitted via an optical link to the surface electronics. It consist of 340 TCs [2] with optical receiver mezzanine, situated in 25 VME creates, distributed in the surface buildings around the LHC. The VME creates will also host the PowerPC, a combiner card, and two timing-cards. The PowerPC collects the running sum values of the TC, and sends it to a database. The combiner card has a hardwired link to the BIC, which transmits the beam dump signal to kicker magnets.

SPECIFICATION OF THE DATA ACQUISITION CARD

The exposition to radiation leads to the requirement of a tolerance of a maximum of 400Gy integrated dose for 20 years LHC life-time. For the system and the performed tests a maximum value of 500Gy was chosen to ensure a safety margin.

The employment of the system for the LHC protection requires a high reliability of the CFC card. To achieve a reliability level SIL3 [3] (10^{-7} to 10^{-8} failure/h) of the system, several different test modes, status information, protection circuits and a redundant data transmission are implemented. For the verification, different tests have been performed, like irradiation, temperature and burn-in test. An additional test in magnetic field was included.

Table 1: Specifications requirements

Current measuring range	2.5pA	1mA
Error from 1nA to 1mA	-25%/+25%	
Error from 10pA to 10nA	-50%/+100%	
Maximal input current	561mA	
Input voltage peak	1500V @ 100us	
Radiation	500Gy in 20yr	
Digital supply	+ 2.5V	
Analogue supply	+/- 5V	
HV monitor input	0V	+5V

THE DATA ACQUISITION CARD

To measure a current over this high dynamic range, a CFC (figure 1) has been chosen, which is based on the balanced charge integrating techniques. In comparison with other switching techniques, the CFC advantage is given by no dead times and no losses of charges [4]. Since the output frequency depends on the input current (small current correspond to a very low frequency), an addition analogue to digital converter (ADC) is added to measure the output voltage of the integrator and to calculate partial counts in the TC. This measure decreases the response time and increases the dynamic range. The counting time window of the system is 40µs. The data including the counted CFC pulses and the integrator output voltage are transmitted every 40µs to the TC. The requirements of a small leakage current and a fast charge/discharge led to the choice of the OPA637 as the operational amplifier in the integration circuit. The radiation tests showed that the chosen amplifier OPA637 did resist the irradiation. But the input offset current increased from typically 2pA to a value between -50pA and -80pA with an integrated dose of 500Gy. Conversely, the amplifier maintained its functionality even with a dose of up to 1500Gy. The JFET J176 used for the switch discharge circuit was adding a positive leakage current of +150pA under radiation, but this current could be removed with the insertion of a diode BAV99 into the current path. The irradiation of the comparator NE521

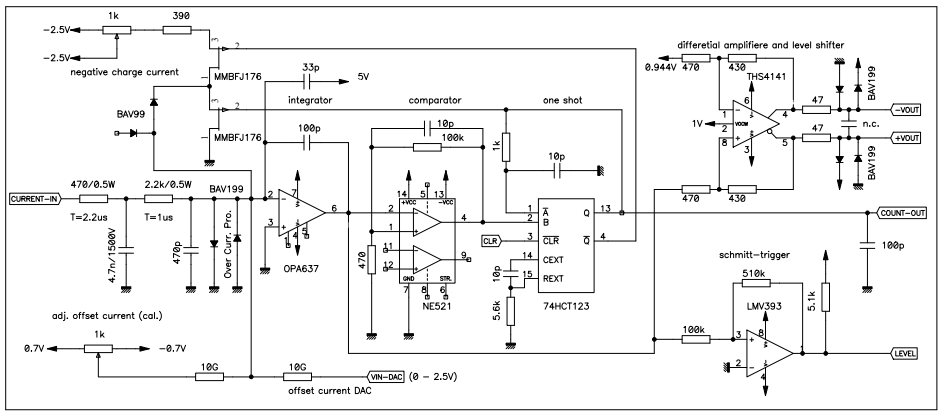

Figure 1: Example of a full-width figure showing the distribution of problems commonly encountered during paper processing.

and the one shot 74HCT123 produced an error of less than 0.5%. Standard ADCs have been irradiated and failed already with a small dose. The radiation tolerant ADC AD41240 produced by micro electronic group (MIC) showed no decrease in functionality under radiation. The AD41240 is used together with the deferential line-driver CRT933 (from MIC), which is needed as level shifter between the ADC and FPGA. To connect differential analogue input of the ADC to the single ended output of the integrator, a THS4141 is used.

For the data conditioning, a FPGA has been chosen. To achieve a higher radiation tolerance, an antifuse type is used instead of a flash based FPGA. Actel provides a standard type A54SX72A and a radiation hard type RT54SX72A, but the RT54SX72A are far too expensive for such a system, which requires 750 pieces. The FPGAs did withstand a total dose between 480Gy and 790Gy.

For the data transmission, an optical link is chosen instead of a copper based one, because the distance between the transmitter and the receiver, can be up to 2km. Several standard systems from the market have been tested but all of them failed while irradiation. Here again, the MIC provided the solution. For the CERN-CMS experiment, the MIC produced a gigabit optical link (GOL) [5], which is utilised in the gigabit optical hybrid (GOH). For the BLM system a special GOH with an E2000-APC optical connector and a different laser current was produced.

To survey the specified function of the CFC card several status bits are constantly checked and transmitted together with the data frame. All the voltage supplies, including the external high voltage, are monitored with a comparator circuit using a LMV393. Two independent monitoring systems are used for the CFC. A Schmitt trigger circuit, using a LMV393, monitors the integrator output level and sends a flag if it exceeds 2.4V. The second survey technique for the CFC introduces a constant input current of 10pA, which corresponds to one count every 20s. The counts are monitored, and in case of 120s without a count, an error flag is generated and transmitted. This input current has to be adjusted for each channel, therefore a potentiometer is implemented which sliding contact is connected with a 10G resistor to the CFC input.

Due to increasing negative leakage current of the OPA637 with the radiation dose, an active compensation has been added to ensure a constant 10pA input current. The compensation current is produced using an 8 bit digital to analogue converter AD5346 with a 10G resistor connected to the input of the CFC.

The complete CFC card has been irradiated up to a total dose of 500Gy. To detect SEU, the redundant CRCs had been verified and compared at the receiver part. No SEU was detected up to $1x10^{12}$ p/cm^2.

FUNCTIONAL DESCRIPTION OF THE FPGA

The functionality is shown in figure 2, more details can be found in paper [6]. All input signals are registered with 40MHz, due to some malfunctions of finite state machines (FSM) and other logical parts of the FPGA. Adding this register solved the malfunctioning of the input buffers.

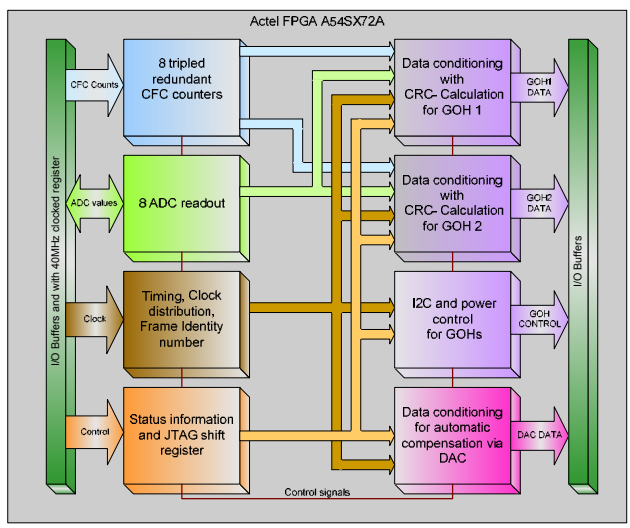

Figure 2: Block diagram for FPGA

Due to the limited FPGA size (an overall of 6036 cells), only the CFC counters, which are most critical, have been tripled. The ADC values are insignificant for the threshold value comparisons. Tripling will decrease the probability of a fault beam dump provoked by a SEU. The system reset is also tripled but all the remaining logic is not tripled. The two GOH interfaces are redundant blocks, which are connected to the GOHs. The GOH interface is calculating the CRC and sending the data to the GOH. The 40MHz system clock is connected to the hardwired HCLK and to the 4 quadrant QCLK. This opens the possibility to distribute the 40MHz internally in accordance to the importance of the blocks. The HCLK is used for the GOH interfaces, because of speed considerations, and for the counter block, because it is less sensitive to SEU.

TESTS, TEST-MODES AND ERROR DETECTION

To ensure the system is working properly and to increase the reliability, several tests, test modes and error detection system have been added.

Before the installation, a calibration and an initial test are performed using a BLECFT [7] USB card, which performs an automatically generated functional test pattern. This system will also be used for additional tests after tunnel installation.

The constantly performed test using 10pA offset current, provides a count every 20s. After absence of the count for more than 120s, an error bit is activated.

Table 2: Status bits (E =error, W=warning, I=information)

Status 1			Status 2		
DAC_over	W	255	CFC-ER8	E	>120s
DAC_155	W	>155	CFC-ER7	E	>120s
GOH2 ready	W	"0"	CFC-ER6	E	>120s
GOH1 ready	W	"0"	CFC-ER5	E	>120s
TEMP 2	W	>60ºC	CFC-ER4	E	>120s
TEMP 1	W	>35ºC	CFC-ER3	E	>120s
GOH_RST_R	I	(≥2000V)	CFC-ER2	E	>120s
RST_GOH	I	≥ 0.390V	CFC-ER1	E	>120s
DAC_RST_R	I	(≥1825V)	LEVEL 8	W	>2.4v
RST_DAC	I	≥ 4.006V	LEVEL 7	W	>2.4v
TEST_ON	I	(≥1655V)	LEVEL 6	W	>2.4v
TEST_CFC	I	≥ 3.633V	LEVEL 5	W	>2.4v
Status_HV	E	≥ 3.183V	LEVEL 4	W	>2.4v
Status_P2V5	E	<2.25V	LEVEL 3	W	>2.4v
Status_M5V	E	>-4.72V	LEVEL 2	W	>2.4v
Status_P5V	E	<4.73V	LEVEL 1	W	>2.4v

For the data transmission a CRC is added, which will be verified at the TC. Due to the redundant link, even if one transmission is corrupted, data are still available.

The card identity number (CID) is sent and checked every transmission to ensure the used threshold table belongs to the correct chamber. Lost data transmission will be detected by the check of the frame identity number (FID) at each data transmission.

With the CFC_TEST activated (HV ≥ 1655V for 240s), 100pA are added on the input of the CFC, to test the corresponding response of the acquisition chain. It is foreseen that this test will be carried out before each beam fill.

A HV modulation test uses capacitive current injection via chamber electrodes to detect the degradation of the complete acquisition chain. This test will be carried out before each beam fill.

There is also 32 status bit (table 2) which are sent and readout every transmission. Depending on the indicated malfunction a beam-dump is initiated.

CONCLUSION

An acquisition system to measure current in the range of 2.5pA to 1mA has been constructed and tested. An error smaller than the 6% from 1nA to 1mA and 25% from 10pA to 1nA has been measured with an accurate calibration. A radiation tolerance of 500Gy has been achieved for all components except two components. The one shot 74HCT123 showed some malfunction at 340Gy but it recovered after stopping the irradiation. The antifuse FPGA form Actel did withstand radiation between 480Gy to 790Gy, no SEU was detected up to $1x10^{12}$ p/cm^2. Several protection and supervision circuits are build in and were tested successfully. The optical link is radiation tolerant due to its design and in a test setup installed in HERA no CRC occurred for several months. The system passed a temperature test (0 to 70°C) which caused some CRC errors while data transmission. The complete system was also tested in a magnetic field up to 1000Gauss with a small offset current change.

REFERENCES

[1] B. Dehning, et al. "The Beam Loss Monitoring System", Chamonix 2004
[2] C. Zamantzas, et al. "The LHC Beam Loss Monitoring System's Surface Building Installation", Poster/Paper LECC 2006
[3] G. Gauglio, "Reliability of the Beam Loss Monitor System for the Large Hadron Collider at CERN", PhD at CERN AB/BI/BL 2005
[4] W. Friesenbichler, "Development of the Readout Electronics for the Beam Loss Monitors of the LHC", Diplom Thesis AB/BI/BL 2002
[5] P. Moreira, et al. "A Radiation Tolerant Gigabit Serializer for LHC Data Transmission", CCPM, Marseille
[6] E. Effinger, et al. "The LHC beam loss monitoring system's data acquisition card", Talk/Paper LECC 2006.
[7] J. Emery, et al. "Functional and linearity test system for the LHC beam loss data acquisition card", Poster/Paper LECC 2006.

INJECTION DIAGNOSTICS USING TRIGGERED BUNCH-BY-BUNCH DATA ACQUISITION *

D. Teytelman†, F.-J. Decker, SLAC, Stanford, USA

Abstract

Quality of injection is very important for reliable and successful operation of colliders and light sources. In this paper we present a technique for real-time monitoring of injection transients in storage rings. We also demonstrate how the data can be used for tuning the injection system. A novel data processing method, coupled with triggered bunch-by-bunch data acquisition system enables one to monitor the effect of adjustments nearly in real time. The acquisition and post-processing technique will be illustrated with the data from PEP-II, DAΦNE, and KEKB.

INTRODUCTION

Injection in a storage ring can excite significant transient processes in the injected bucket as well as perturb stored beam. In the recent years the question of injection quality became more important as colliders and light sources started to adopt top-up (top-off, trickle, continuous) injection mode [1, 2]. In this regime charge is injected into a storage ring during user operation and injection transients directly affect synchrotron light quality or luminosity.

Here we present a technique to characterize injection quality in the transverse plane using a triggered bunch-by-bunch recorder. By automatically extracting the first revolution after injection it serves as a fast diagnostic tool for optimizing kicker amplitudes, relative and absolute timings. This technique can be operated in real-time at 1 Hz update rate serving as an injection quality monitor.

MEASUREMENT TECHNIQUE

A number of high-speed digitizers with appropriate clocking and triggering can be used to capture the beam motion. We have used the data acquisition capabilities of the Gproto bunch-by-bunch feedback system [3].

Data analysis approach presented here makes several assumptions about the ring injection process and the data acquisition. These assumptions are:

- Data acquisition trigger precedes actual injection;
- Between injections the beam is transversely stable;
- Acquired data contains many (10+) betatron cycles;
- All filled buckets are closely matched in charge;
- Injection kicker pulse width is shorter than one turn.

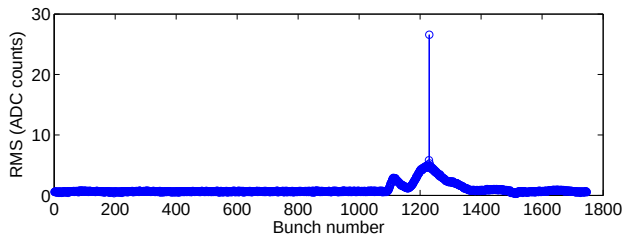

Figure 1: Bunch-by-bunch RMS of a data set from PEP-II HER.

Of these assumptions the last one is not absolutely required — the technique can be easily tailored to longer kicker pulses.

Once the data is acquired we post-process it using a Matlab script. This post-processing extracts what we call the first-turn orbit — transverse beam displacements from nominal positions during the revolution when the injection kicker fires. The first-turn orbit carries an imprint of injection kicker pulse shapes and allows one to extract information on relative and absolute kicker timing as well as amplitude balance (bump closure).

The first step in the post-processing is to perform bunch-by-bunch DC offset removal. This removes static orbit offsets as well as modulations due to uneven bunch currents[1]. In this step we generate data matrix with elements d_{mk} — DC-less signal of bunch m on turn k.

Next we compute the bunch-by-bunch RMS $\sigma_m = \sqrt{\sum_k d_{mk}^2/N}$ where N is the number of recorded revolutions. An example of such an RMS for PEP-II HER is shown in Fig. 1. Note that the RMS of the injected bunch is significantly higher than that of the rest of the beam. From the RMS vector we automatically determine the injected bucket and shift the data samples to place the injected bucket in the middle of the turn.

In the third step we automatically determine the injection turn (first-turn) by computing a turn-by-turn RMS vector $\sigma_k = \sqrt{\sum_m d_{mk}^2/M}$ where M is the number of bunches. For stable operation this RMS value is determined by the noise floor of the ADC and the receiver front-end and is typically below 0.5 counts. As shown in Fig. 2 the turn-by-turn RMS increases dramatically at the moment of the injection. Finding the first data point in this vector to rise above some predetermined threshold, typically taken as $3\min_k(\sigma_k)$, gives us the necessary first turn index (29 for Fig. 2).

* Work supported by U.S. Department of Energy contract DE-AC02-76SF00515 and by the US-Japan collaboration in High Energy Physics

† dim@slac.stanford.edu

[1] Recorded signal is typically a product of transverse coordinate and bunch current. If bunch-by-bunch current information is available it can be used to improve the measurement accuracy.

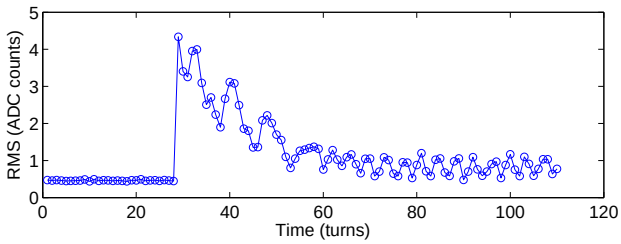

Figure 2: Turn-by-turn RMS of a data set from PEP-II HER.

In order to improve DC orbit rejection we redo offset removal using data only before the injection turn. Finally we plot the extracted first-turn orbit as well as the last turn before injection as shown in Fig. 3(a). Comparing the two vectors we clearly see the injection kicker firing including risetime wiggle due to pulse shape mismatches between kickers. Note that the absolute kicker timing is correct — maximum stored beam bump coincides with the injected bunch. We also observe significant ringing after the pulse. By adjusting relative kicker amplitudes we can improve bump closure as shown in Figure 3(b). In this case stored beam perturbation is reduced from 20 to 5 ADC counts.

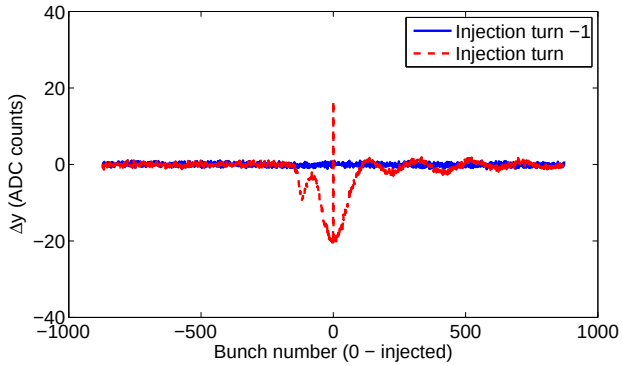

(a) Before kicker amplitude adjustment

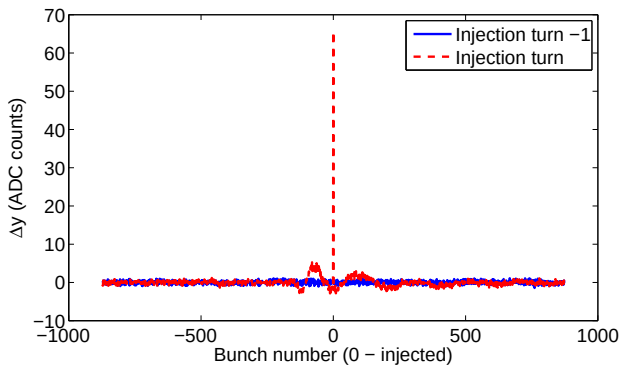

(b) After kicker amplitude adjustment

Figure 3: Extracted first-turn orbit for the PEP-II HER injection

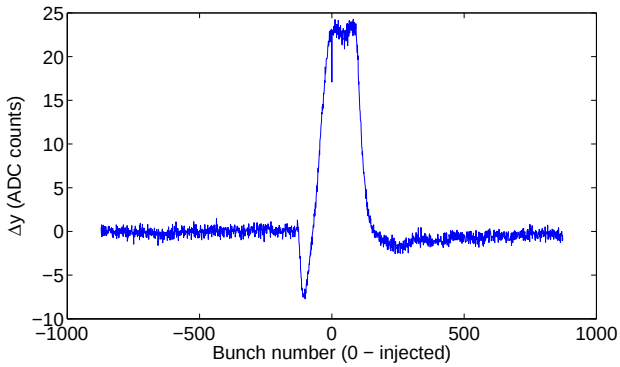

(a) Full one turn

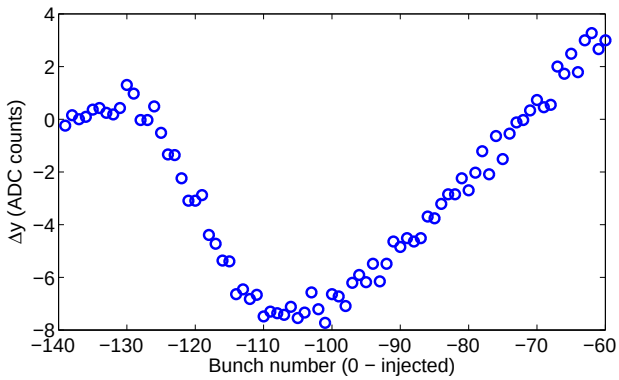

(b) Zoom around kicker rise

Figure 4: First-turn orbit in PEP-II LER before injection kicker tuning.

EXPERIMENTAL RESULTS

First we present analysis and tuning of injection into PEP-II LER. In this case the tuning procedure was performed parasitically while the collider was delivering luminosity and was limited to adjusting injection kicker timing and amplitudes. Figure 4(a) shows the initial first-turn orbit before any adjustment. From this plot we can draw several conclusions. First of all, there is a relative timing error between the two injection kickers, since the bunches from -130 to -70 are deflected in the negative direction while the main pulse shows positive deflection. By zooming in in that region as shown in Fig. 4(b) we can estimate the timing error. Around bunch -130 the first kicker starts rising. Around -110 the rising edge of the second kicker stops the deflection increase. Thus the error is around 20 bunches or 84 ns. In order to center the bump on the injected bunch we need to shift the second kicker earlier.

First-turn orbit taken after this adjustment is shown in Fig. 5(a). At this point the injection takes place very close to the peak of the injection kicker pulse. Next we can adjust the amplitude balance for better bump closure. Figure 5(b) shows the injection orbit after one of the adjustments. Clearly the amplitude has been overcompensated creating displacement with the opposite sign. Final adjustment of the kickers has to take into account not only stored

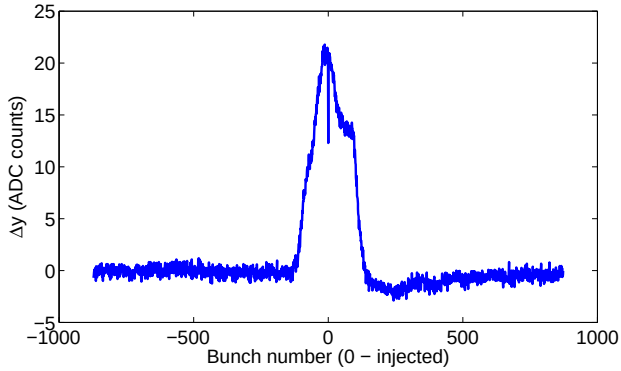

(a) After timing adjustment

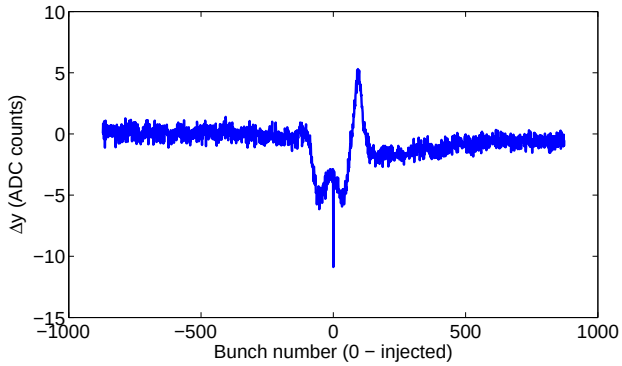

(b) After amplitude adjustment

Figure 5: First-turn orbits in PEP-II LER during injection kicker tuning.

beam perturbation but also the detector backgrounds generated by the injected bunch. Leaving in some amount of orbit bumping is typically used to find an injection "sweet" spot with respect to backgrounds.

The technique presented here has been tested in several accelerators in addition to PEP-II. In Fig. 6 the first-turn orbit after injection into KEKB LER is shown. In this machine two bunches with separation of 49 RF buckets are injected simultaneously [4]. On the plot these are placed in locations 0 and 49. KEKB injection kicker is specified to have 1 μs rise and fall times. In Fig. 6 the significant orbit

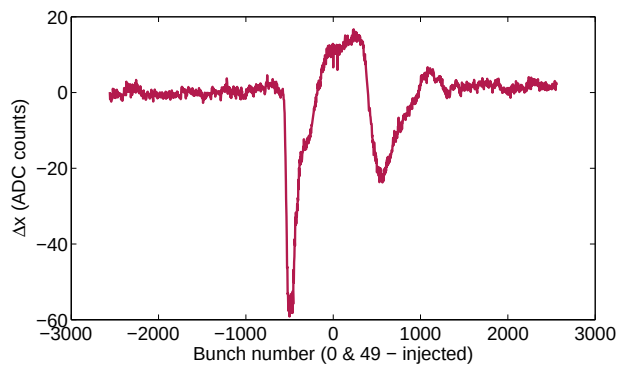

Figure 6: First-turn orbit in KEKB LER.

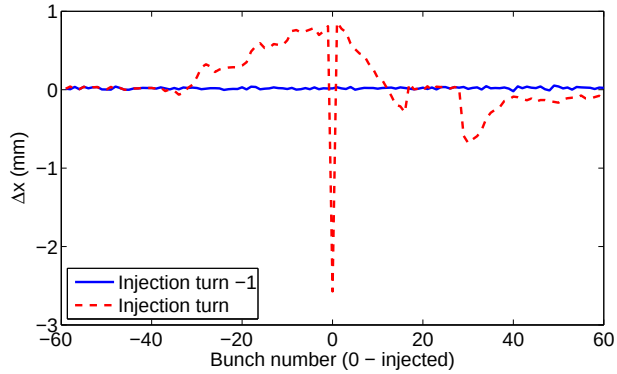

Figure 7: First-turn orbit in DAΦNE positron ring.

perturbations last for roughly 3 μs, suggesting both relative timing and pulse shape errors. At the same time beam perturbation at the center of the pulse is relatively small and suggests good amplitude balance.

It is possible to calibrate the front-end of the data acquisition system by creating an orbit bump at the proper BPM location. For measurements in DAΦNE such calibration has been performed. As a result one can present the first-turn orbit in physical millimeter units as shown in Fig. 7. Relative kicker timing error is evident in the negative deflection of bunches 11-40 (zero-signal region is the 12 bunch fill-pattern gap).

SUMMARY

Triggered bunch-by-bunch data acquisition provides a wealth of beam diagnostic information. Automated post-processing techniques allow one to quickly tune the injection system and to periodically verify the injection quality. Analysis of first-turn orbits provides information on several different types of injection system errors such as amplitude imbalance, relative and absolute timing, and phase advance. Future developments should include calibration to actual beam motion and automated kicker adjustment hinting.

REFERENCES

[1] J. Turner *et al.*, "Trickle-charge: A new operational mode for PEP-II," in *9th European Particle Accelerator Conference (EPAC 2004)*, pp. 881–883, European Physical Society Accelerator Group, 2004.

[2] A. Lüdeke and M. Muñoz, "Top-up operation experience at the Swiss Light Source," in *EPAC 2002: proceedings*, pp. 721–723, 2002.

[3] Teytelman *et al.*, "Design and testing of Gproto bunch-by-bunch signal processor," in *10th European Particle Accelerator Conference (EPAC 2006)*, pp. 3038–3040, European Physical Society Accelerator Group, 2006.

[4] A. Emonoto *et al.*, "Increase of positrons by a high-intensity two-bunch acceleration scheme at the KEKB linac," in *Proceeding of the 2001 Particle Accelerator Conference*, pp. 3284–3286, IEEE, 2001.

FIBEROPTICS-BASED INSTRUMENTATION FOR STORAGE RING BEAM DIAGNOSTICS*

J.M. Byrd, S. De Santis# LBNL, Berkeley, U.S.A.
Y. Yin, YYLabs, Fremont, CA 94537, U.S.A.

Abstract

In several cases, coupling synchrotron light into optical fibers can substantially facilitate the use of beam diagnostic instrumentation that measures longitudinal beam properties by detecting synchrotron radiation. It has been discussed in [1] with some detail, how fiberoptics can bring the light at relatively large distances from the accelerator, where a variety of devices can be used to measure beam properties and parameters. Light carried on a fiber can be easily switched between instruments so that each one of them has 100% of the photons available, rather than just a fraction, when simultaneous measurements are not indispensable. From a more general point of view, once synchrotron light is coupled into the fiber, the vast array of techniques and optoelectronic devices, developed by the telecommunication industry becomes available.

In this paper we present the results of our experiments at the Advanced Light Source, where we tried to assess the challenges and limitations of the coupling process and determine what level of efficiency one can typically expect to achieve.

INTRODUCTION

The main challenges in realizing a beam diagnostic system that makes use of synchrotron light carried on optical fibers are to be found in the coupling efficiency and in the dispersion introduced by propagation along the fiber. These two aspects are indeed strictly correlated when one is trying to design such a system: since there are minimum requirements on the signal-to-noise ratio, if the coupling efficiency is too low, one is forced to couple light on a larger bandwidth, which in turn makes the dispersion worse, for example.

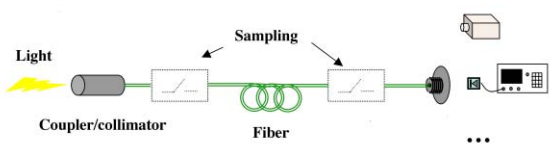

Figure 1. Scheme of principle of a fiberoptics-based system. A light sampling component can be present at the beginning of the fiber, after some distance, or not at all.

Figure 1 shows the typical elements a generic fiberoptics-based diagnostic system is composed of. Their choice depends of course on the characteristics (i.e. photon flux) of the synchrotron light source and on specific applications one may have in mind. Commercially available optical fiber can support transmission with low attenuation in a wide wavelength region from ~1600 nm to the visible spectrum. In practical applications one would have to transmit synchrotron light over distances of a few 100's of meters at most, so that fiber propagation attenuation is seldom an issue. In case of highly radioactive environments, radiation-hard fibers, usually Fluorine based, are available at the price of a slightly higher attenuation [2].

While for our applications optical fibers are inherently wide-band, as just said, other components one has to use (couplers, detectors, etc.) work instead on limited wavelength ranges. Commercially, three bands have seen the almost totality of technological developments and are readily available: 1550, 1310 and 850 nm.

A first choice the designer has to make is between single-mode and multimode fibers. This is another case where one has to find a compromise between coupling efficiency and dispersion:

- Multimode fibers allow for a substantially more efficient coupling into the fiber, up to a large fraction of the total available power. On the other end, they are dominated by intermodal dispersion. Fig.2a shows the classic bandwidth/distance curves for multimode fibers. Commercial graded-index fibers developed for LAN's can provide bandwidths around 30 GHz, for a 100 m long fiber, in the 850 nm range [3].
- Dispersion in single-mode fibers can in principle be cancelled out by using *dispersion compensated fibers*, even in the case of a wideband source. Fig. 2b shows the dispersion curves for several types of fibers. It can be seen that it is possible to obtain near-zero dispersion, if the bandwidth is kept small enough, once again underscoring the importance of obtaining the best possible coupling of synchrotron light into the fiber.

In general, best coupling is obtained through the use of telescopes, GRIN lenses, or collimators, depending on the specific characteristics of the light port and the source. It must be kept in mind that, in most cases, the source's modal spectrum cannot be transversally matched into a single-mode fiber propagating mode, so that the coupling efficiency is necessarily much lower than unity.

Another way of canceling the effects of dispersion, for both single and multimode fibers, is outlined in Fig.1: by sampling the signal immediately after the coupling elements. the effect of the fiber is taken out of the

*Work supported by the.U.S. Department of Energy under. Contract No. DE-AC0-05CH11231.
#sdesantis@lbl.gov

equation since each sample can be time-tagged and the time resolution is defined by the samples duration alone.

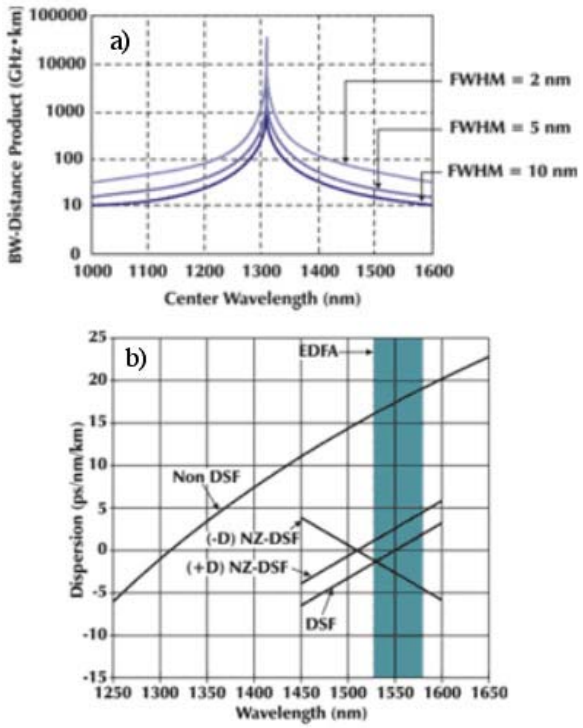

Figure 2 Bandwidth/distance curves for multimode fibers (a). Dispersion curves for single-mode fibers (b).

EXPERIMENTAL SETUP AT THE ALS

We performed experiment at the ALS, where a diagnostic beamline is available from time to time, using a variety of fibers, couplers and detectors.

Beamline 3.1 synchrotron radiation source is one of the ALS 1.3 T dipoles. The beamline, which is dedicated to an x-ray CCD camera during user operations, can be used for visible-IR wavelengths during dedicated shifts.

Figure 3 shows the photon flux out of an ALS dipole with 400 mA circulating in the machine.

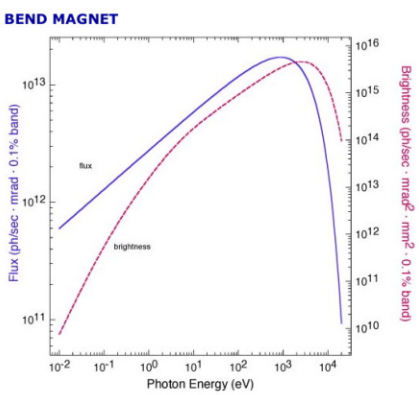

Figure 3. Photon flux for an ALS dipole.

The beamline optics have been described in [1].

Figure 4 shows our experimental setup, with the final three flat mirrors and the micrometric positioning stage with the telescope used with multimode fibers.

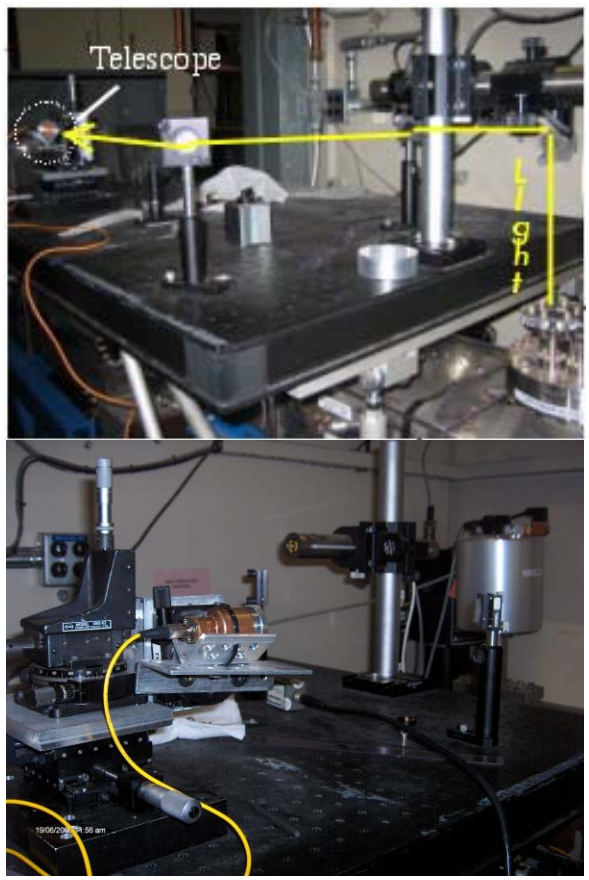

Figure 4. Experimental setup at Beamline 3.1, with coupling stage detail.

We use the visible component for a first order alignment and then we optimize coupling by maximizing the readout on an optical powermeter at the desired wavelength. The average available power at maximum current can be calculated from Fig.3 and in the 1000-1600 nm band is found to be around 110 μW. One has to take into account losses on the mirrors: we measured the losses on the three external mirrors and found them to be around 3 dB. There is another in-vacuum mirror and the two K-B mirrors that focus the synchrotron radiation. At this point we don't have a definite value for the losses introduced by these mirrors, but we guess we could have only a quarter of the theoretical power available at the coupling element.

For single-mode fibers we tried a variety of arrangements and finally we got our best results using a Thorlabs Long Working Distance Collimator, which has a 10% bandwidth around 1550 nm.

For signal detection we used several different photodiodes (Si and InGaAs) and a LeCroy 3 GHz oscilloscope, as well as an 86116A optical input module on a 53 GHz Agilent sampling scope. We eventually

obtained our best results using a Discovery Semiconductors DSC50S InGaAs PIN diode [4], which is limited to a 5 GHz band though.

EXPERIMENTAL RESULTS

At present we have concentrated our efforts on obtaining maximum coupling of synchrotron radiation into the optical fiber on a 10-20% band at either 1550 or 1310 nm, where we have most of our components available. Once one has achieved coupling a healthy signal into the fiber, then it is relatively easy to use longer fibers and study the effects of dispersion.

As coupling of average power is concerned, we have obtained up to 10 μW on multimode fibers. Based on what said in the previous section about the total available power, that means at least 20%, and up to 50% coupling efficiency. For single-mode fibers the result is substantially lower: not only is more difficult to deal with a 9 μm, rather than a 50 μm, core experimentally, but considering our source characteristic one cannot expect to mode match more than a few percent into the single-mode fiber [5]. In fact, we have obtained values 10 times lower with single-mode fiber, compared to multimode.

Nonetheless even this lower coupled power is sufficient to give a rather accurate longitudinal profile of the ALS beam.

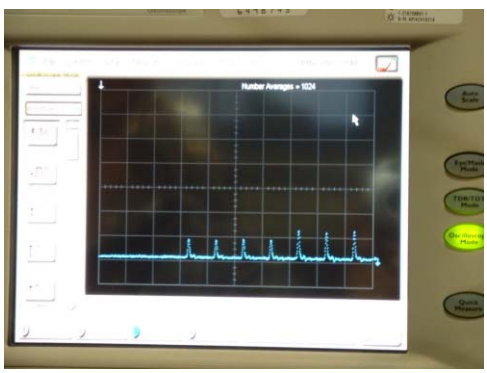

Figure 5 Beginning of the ALS bunch train (Corning SMF-28 fiber, Thorlabs collimator, Discovery Semiconductors PIN diode).

Figure 5 shows the screen of our Agilent 53 GHz digital sampling scope. We used a single-mode fiber, with the Thorlabs collimator and the DSC50S photodetector described above. The first 7 ALS bunches, following the ion-clearing gap in the fill are clearly visible, spaced by 2 ns.

Figure 6 (top) shows the postprocessed numerical data of a similar picture: this time the horizontal span is increased so that we see the first 14 bunches, the large bunch in the middle of the gap (a.k.a. *camshaft*) and, in between them, a small bunch generated by the injection process (*parasitic*, these are eliminated for user operations by a betatron resonant cleaning procedure). Fig.6. (bottom) shows a close-up of the camshaft. The measured FWHM is around 100 ps, which is higher than the expected ~60 ps. In this case (we where using just a few feet of fiber) this is not due to dispersion, but to the response time of our detector. Also, there is a 20 ps jitter in the storage ring orbit clock used for timing, which also contributes to the bunch widening, when using a sampling scope.

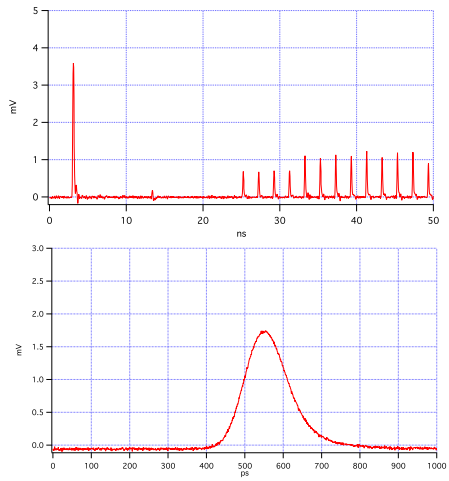

Figure 6. Postprocessed data. ALS train, camshaft bunch and parasitic bunch (top), detail of camshaft (bottom).

CONCLUSIONS AND FUTURE PLANS

Our experiments have shown that it is possible to obtain adequate coupling efficiency at the ALS using both multimode (~50%) and single-mode (~4%) fibers. Comparing with the available photon fluxes and most required measurements on other machines (LHC, for instance), we believe these are fairly representative results.

We are planning to further the investigation, as dispersion is concerned, after buying longer fiber spools and a new photodetector with a 10 ps response time, which we have already identified on the market.

ACKNOWLEDGMENTS

The authors wish to thank the ALS personnel who helped with the scheduling of the measurements and in setting up the machine.

REFERENCES

[1] S. De Santis, J.M. Byrd, *et al.*, "Fiberoptics-based Instrumentation for Storage Ring Longitudinal Diagnostics", EPAC'06, Edinburgh, June 2006, p. 1247.
[2] http;//www.thorlabs.com
[3] LaserWave 500™, http;//www.ofsoptics.com
[4] http;//www.chipsat.com
[5] M. Zolotorev, private communication.

CLASSIFICATION OF THE LHC BLM IONIZATION CHAMBER

Markus Stockner, Bernd Dehning, Christian Fabjan, Eva Barbara Holzer, CERN, Geneva
Daniel Kramer, CERN, Geneva and TUL, Liberec

Abstract

The LHC beam loss monitoring (BLM) system must prevent the super conducting magnets from quenching and protect the machine components from damage. The main monitor type is an ionization chamber. About 4000 of them will be installed around the ring. The lost beam particles initiate hadronic showers through the magnets and other machine components. These shower particles are measured by the monitors installed on the outside of the accelerator equipment. For the calibration of the BLM system the signal response of the ionization chamber is simulated in GEANT4 for all relevant particle types and energies (keV to TeV range). For validation, the simulations are compared to measurements using protons, neutrons, photons and mixed radiation fields at various energies and intensities. This paper will focus on the signal response of the ionization chamber to various particle types and energies including space charge effects at high ionization densities.

INTRODUCTION

Figure 1: The LHC beam loss monitors (yellow insulation, mounted on a red support) are mounted on the outside of the cryostats, horizontally aligned to the beam pipe.

An unprecedented amount of energy will be stored in the circulating beams of the LHC (up to 360 MJ per beam) and in the magnet system (10 GJ). The loss of even a very small fraction of this beam may induce a quench of the superconducting magnets or cause physical damage to machine components. The BLM system [1] detects and quantifies the amount of lost beam particles. It generates a beam abort trigger when the losses exceed predetermined threshold values. About 4000 detectors will be installed, mostly around the quadrupole magnets (Fig. 1). The detectors probe the transverse tails of the hadronic showers through the cryostats which are induced by lost beam particles. The start-up calibration of the BLM system is required to be within a factor of five in accuracy, and the final accuracy within a factor of two. For the calibration and threshold determination a number of simulations are combined: Beam particles are tracked to find the most probable loss locations. At these locations hadronic showers through the machine components are simulated to get the particle spectra at the detector locations. A further simulation yields the detector response. The quench levels of the superconducting magnets, according to loss duration and beam energy, are simulated separately. Whenever possible, crosschecks with measurements have been performed or are planned before the start-up of the LHC. This paper will focus on the detector response simulation, which is part of the system calibration, and on the uncertainty estimation of transverse hadronic shower tail simulations, which contributes to the system calibration error.

IONIZATION CHAMBER RESPONSE

Simulations

The main detector type is an ionization chamber with parallel aluminum electrodes separated by 0.5 cm (Fig. 2). The detectors are about 50 cm long with a diameter of 9 cm and a sensitive volume of 1.5 liter. The chambers are filled with N_2 at 100 mbar overpressure and operated at 1.5 kV.

Figure 2: Inside structure of the LHC BLM ionization chamber.

Depending on the loss location the detectors will be exposed to different radiation fields. The energy of the particles is spread over a large range from keV to TeV. GEANT4 (version 4.8.1.p01 QGSP BERT HP [2]) simulations of the ionization chambers were performed to determine the signal response for different particle types at various kinetic energies in the range of 10 keV to 10 TeV. The sensitive volume was determined by simulation of the electric field configuration. It is 4% bigger than the volume covered by the electrodes (2 mm larger diameter). The cut off value of the ionization chambers is below about 2 MeV for photons and electrons and below about 30 MeV for neutrons and protons. See Fig. 3 for the response function for transverse impacting particle direction.

Verification Measurements

Mixed Radiation Field Measurements: At CERF (CERN-EU High Energy Reference Field Facility) a copper target (length 50 cm, diameter 7 cm) was placed in a secondary beam of 120 GeV/c hadrons. The main beam particles were pions (60.7%), protons (34.8%) and kaons

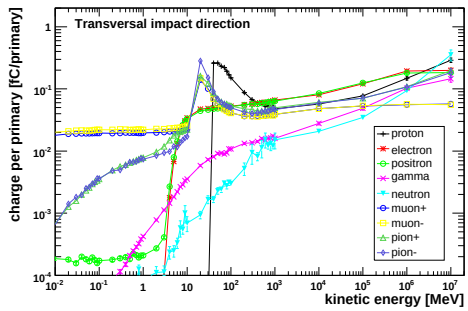

Figure 3: Response of the ionization chamber for particles impacting transversely to the detector axis.

(4.5%) with intensities up to $9.5 \cdot 10^7$ hadrons per 4.8 seconds. Five ionization chambers were positioned around the copper target so that they were exposed to different radiation fields (varying in particle composition and energy). FLUKA simulated spectra from [3] were used as input to simulate the detector response with GEANT4. A comparison of the GEANT4 simulation to the BLM detector measurement shows a relative difference of about 12%, except at detector position 1 (Table 1). There, a relative difference of 21% can be seen. The detector specific energy cut-off and the shift of the particle spectrum to lower energies (below 1 GeV) lead to low statistics in the number of particles that contribute to the detector signal. The error on the measurement includes the statistical error and a systematic error from uncertainties on the beam intensity measurement (10%) and from misalignment investigations on the detector positions [3]. The error on the simulation includes only the statistical error of the signal simulation, it does not include the uncertainties in the spectrum. All detectors showed a linear behavior at measurements over one order of magnitude in beam intensity.

Table 1: Result of GEANT4 simulations, beam measurements and their comparisons for mixed radiation fields, proton, gamma and neutron measurements.

	Simulation		Measurement		sim./meas.	
	BLM	err.	BLM	err.	ratio	err.
pos.	CERF experiment [pC per $9.2 \cdot 10^7$ hadrons]					
1	91.13	0.35	115.33	11.66	0.79	0.08
2	281	6	—	—	—	—
3	1656	18	1578	163	1.05	0.11
4	2387	22	2122	231	1.12	0.12
5	3944	23	3532	370	1.12	0.12
6	6496	18	7091	1097	0.92	0.14
	proton experiment [C/(p·cm)]					
	125	25	110	0.06	1.13	0.23
	gamma experiment [aC/γ]					
	0.27	0.02	0.42	0.01	0.64	0.05
	neutron experiment [aC/n]					
long.	12.94	0.16	15.23	0.09	0.85	0.01
trans.	6.74	0.09	9.57	0.06	0.70	0.01

Proton Measurements with 400 GeV/c protons at an SPS extraction line (T2) were compared to the simulation. The beam size was estimated to 1 cm horizontally and 0.5 cm vertically (4σ). The intensity was $(30.0 \pm 0.1) \cdot 10^{11}$ protons per 4.8 seconds. A vertical scan of the beam position was simulated and compared to the measurement. The unknown beam position (vertically) relative to the inner structure (parallel electrodes) led to a systematic uncertainty of 23%. Measurement and simulation agree within errors.

Gamma Ray Measurements: A further comparison between simulation and measurement was done with 662 keV gamma rays at the TIS-RP Calibration Laboratory for Radiation Protection Instruments (CERN) with Cs137 sources at various activities and distances. The detector showed once more a linear behavior over two orders of magnitude in dose rate (30 μSv/h to 3 mSv/h). The response simulation results for 600 keV and 700 keV gamma rays were interpolated and compared to the measured results. The measurement and the simulation agree within 64% with an error of 7%.

Neutron Measurements were performed at the Svedberg Laboratory, Uppsala University (Sweden) [4]. The neutrons had a peak energy of 174 MeV and an intensity from $0.7 \cdot 10^6$ to $4.6 \cdot 10^6$ per second. They were produced by an incident proton beam of 179 MeV and a maximum beam current of 0.4 μA on a 23.5 mm thick lithium target. The contribution of gamma rays to the measured signal was estimated to between 11.2% and 16%. The results are shown in Table 1, assuming an 11.2% gamma contribution, for longitudinal and transversal neutron impact direction on the chamber. For an 11.2% gamma contribution, the agreement is 85% and 70% for longitudianl and transversal impact respectively. For a 16% gamma contribution, the agreement is 90% and 74% for longitudinal and transversal impact.

SHOWER TAIL MEASUREMENTS AT HERA

The HERA internal proton beam dump served as a test bed for the LHC BLM system. The proton energy at collision is about twice the LHC injection energy. The particle spectrum outside the dump is comparable to the one outside of an LHC magnet. It is dominated by low energy (below 10-100 MeV) neutrons and photons. The HERA machine was running nearly continuously since the installation of the experiment in 2005, allowing for a long term test of the complete LHC BLM system. Six ionization chambers are placed on top of the dump, with a longitudinal spacing of about 1 m. They measure the tails of the hadronic showers induced by the impacting protons. The proton energy is 39 GeV at injection and 920 GeV at collision. The beam intensity is in the range of $1.3 \cdot 10^{11}$ to $1.3 \cdot 10^{13}$ protons per 21 μs. The measurements have been corrected for space charge effects according to a formula derived in [5]. Above a critical ionization density a dead zone of thickness $d - x_0$ (d being the electrode spacing) forms next to the cathode:

$$x_0 = \left[\frac{\epsilon_0}{q} \frac{4\mu V^2}{\phi} \right]^{1/4}$$

μ is the ion mobility, ϕ is the ionization per volume and time, V is the chamber voltage and q is the elementary charge. The magnitude of this correction is shown in Table 2. At the standard LHC operation range of the ionization chambers, the ionization density is lower and the dead zone will not form. It will only be reached at special beam tests. At HERA, on the contrary, it gives a correction of up to a factor of 8.7.

Table 2: Range of correction factors due to space charge for all detectors depending on proton beam energy and current.

Det.	39 GeV		920 GeV	
	I_{min} 1 mA	I_{max} 90 mA	I_{min} 1 mA	I_{max} 100 mA
1	1.	2.95	1.17	6.70
2	1.	3.80	2.00	8.71
3	1.	3.27	1.97	8.61
4	1.	2.60	1.71	7.95
5	1.	1.76	1.16	6.34
6	1.	1.35	1.	5.03

Fig. 4, left, shows the case of the highest correction, the signal of detector 2 (charge per proton) at 920 GeV as a function of beam current before and after space charge correction. On the right side all 6 detector signals at 920 GeV after correction are shown with a linear fit through zero. Most of the nonlinearity in the signals is corrected for by the simple model of space charge.

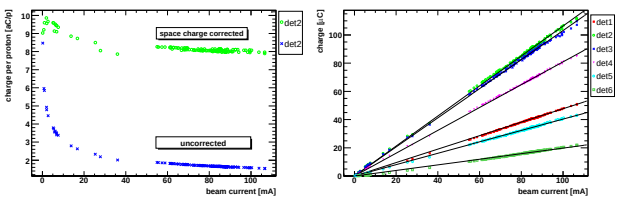

Figure 4: Signal as function of beam current at 920 GeV beam energy before (left) and after (right and left) space charge correction.

The showers through the beam dump have been simulated with GEANT 4.8.2 and two different physics models, QGSP BERT HP and FTFP. A FLUKA simulation of the dump was also done for comparison. Fig. 5 gives the preliminary results of the simulations and the measurements. The measurements have been corrected for space charge effects. The predicted signal strongly depends on the choice of simulation code and physics model. All models significantly underestimate the transverse shower tails. The GEANT4 QGSP BERT HP is closest to the data, within less than a factor of 2 in the detector 2, which is close to the shower peak. Longitudinally as well, the models underestimate the extent of the shower in both directions, backward (detector 1) and forward (detectors 4, 5 and 6).

CONCLUSION

The GEANT4 detector response simulations are part of the LHC BLM calibration. Various verification measurements were performed. Generally, the simulations and

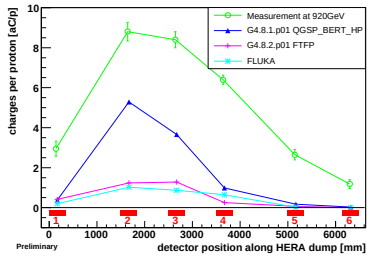

Figure 5: Preliminary simulated and measured signals versus detector position on the HERA proton beam dump. Detector positions (in scale) indicated at the bottom.

measurements agree very well. The highest deviation is 36% in the gamma source measurement.

A rather simple model of space charge can explain most nonlinearities encountered in the detector responses in the HERA measurements. However, this space charge regime will not be reached during normal LHC operation of the ionization chambers. A final verification of the HERA results is pending (including a completely independent simulation). If confirmed, the LHC threshold calibration will take into account the significant deviation of the measured shower tails from the simulated ones. The simulated threshold values will have to be corrected accordingly.

ACKNOWLEDGMENT

The authors would like to thank Michael Bieler, Philip Duval, Bernhard Holzer, Peter Schmid, Michael Schmitz, Rüdiger Schmitz, Josef Wilgen, Ferdinand Willeke and Kay Wittenburg from DESY for their kind support of the experiment during the past three years, Roderik Bruce, CERN, for the FLUKA simulations of the HERA beam dump and Helmut Vincke, CERN, for the FLUKA spectra for the CERF measurements.

REFERENCES

[1] E. B. Holzer et al., IEEE NSS-MIC '05, Puerto Rico, CERN-AB-2006-009 BI, 2005. W. Friesenbichler, CERN-THESIS-2002-028, Diplomarbeit, Fachhochschule Wr. Neustadt, 2002. C. Zamantzas et al., CERN-AB-2005-082, DIPAC 05, Lyon, France, 2005. C. Zamantzas, PhD Thesis, Brunel University, London, UK, 2006. C. Zamantzas et al., IEEE NSS-MIC '06, San Diego, IEEE Trans. Nucl. Sci. V2 p950, 2006. `http://www.cern.ch/blm`

[2] GEANT4 collaboration, `http://geant4.web.cern.ch/geant4`, viewed October 30, 2006.

[3] H. Vincke et al., CERN EDMS No.: 457013, (CERN-SC-2004-025-RP-TN).

[4] A. V. Prokofiev et al., International Workshop on Fast Neutron Detectors and Applications, University of Cape Town, South Africa, (FNDA2006 016), 2006.

[5] R. M. Zwaska, PhD thesis, University of Texas at Austin, December 2005.

TUNE, COUPLING, AND CHROMATICITY MEASUREMENT AND FEEDBACK DURING RHIC RUN 7*

P. Cameron, J. Cupolo, W.C. Dawson, C. Degen, A. DellaPenna, L.T. Hoff, Y. Luo, A. Marusic, R. Schroeder, C. Schultheiss and S. Tepikian BNL, Upton, NY 11973, U.S.A.

Abstract

Tune feedback was first implemented in RHIC in 2002, as a specialist activity. The transition to full operational status was impeded by dynamic range problems, as well as by overall loop instabilities driven by large coupling. The dynamic range problem was solved by the CERN development of the Direct Diode Detection Analog Front End[1]. Continuous measurement of all projections of the betatron eigenmodes made possible the world's first implementation of coupling feedback during beam acceleration, resolving the problem of overall loop instabilites[2,3]. Simultaneous tune and coupling feedbacks were utilized as specialist activities for ramp development during the 2006 RHIC run. At the beginning of the 2007 RHIC run there remained two obstacles to making these feedbacks fully operational in RHIC - chromaticity measurement and control, and the presence of strong harmonics of the power line frequency in the betatron spectrum. Preliminary investigations of power line harmonics were presented earlier[4]. We report here on progress in tune, coupling, and chromaticity measurement and feedback, and discuss the relevance of our results to the LHC commissioning effort.

INTRODUCTION

The abstract for this paper was written and submitted before the start of the present RHIC run. It asserted that there remained two obstacles to making the feedbacks operational, namely mains harmonics and chromaticity control. While the experience with gold beams during Run 7 has shown that this remains true, a variety of new phenomena have revealed themselves. The RHIC Tune Feedback system and results with proton beams from Run 6 are described in detail elsewhere [5]. The focus of this paper is on the unexpected difficulties encountered during the ongoing Run 7.

ANOMALOUS BEAM RESPONSE

When beam was first available at the start of Run 7, an anomalous beam response was observed, with many peaks at irregular intervals. This greatly complicated efforts to acquire a proper phase lock to the beam at injection. The underlying machine physics (or technology) of this beam response is not yet understood. Figure 1 is an FFT in the vicinity of the vertical betatron resonance in one of the two RHIC rings. It is typical of what is seen at injection in RHIC during Run 7, in both planes of both rings. *There was no deliberate beam excitation.* The tunes were decoupled and separated. The horizontal tune was at 18.1KHz when this image was captured, which is not within the 1.2KHz span of the image. The synchrotron frequency at injection is ~180Hz.

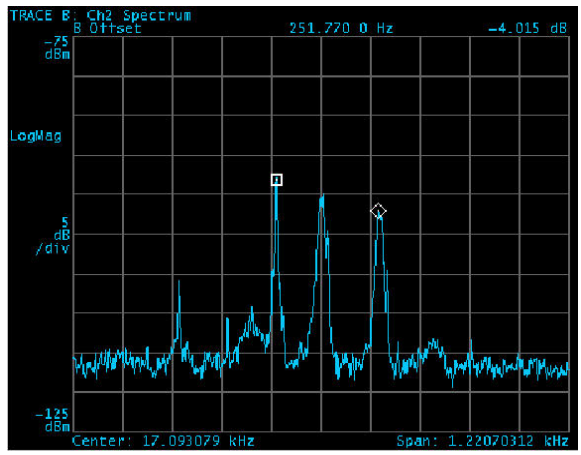

Figure 1. Unexcited betatron spectrum at injection

Four sharp peaks are visible in the image, as well as two smaller broad peaks. The spacing of the peaks is irregular, and cannot be correlated with either the synchrotron or power line frequencies. Chromaticity changes did not have a strong effect on the appearance. There was no significant effect resulting from changing the RF voltage. Over time there were minor variations in the appearance from plane-to-plane and from ring-to-ring. The tune tracker would lock to any of the lines. At times there was what seemed to be an unpredictable relation between which line was acquired and the phase of the coupling measurement relative to the skew quad correction families. Sometimes the coupling feedback loop would be unstable when closed at injection, and the beam would be lost. Upon refilling and reacquiring lock on a different line the coupling loop would be stable. The lines were closely spaced (~.001 units of tune) and quite sharp. The most central peak was generally the most favorable for locking. The tracker would auto-lock on the first peak it found, which inevitably was not the central peak, and would have to be manually and laboriously teased onto the proper line.

This behavior was not seen during Run 6 with polarized protons, or in earlier runs with ions. However, this was the first ion run in which the baseband tune track was used. Earlier ion runs used the 245MHz tune tracker, which is above the coherent spectrum at injection. This may explain why this beam response has not been previously seen.

There is some speculation that the observed anomalous beam response results from the low injection energy for ions. At injection many power supplies are close to minimum current, where regulation is poor. As the ramp

begins and currents increase the anomalous response diminishes.

Beyond the problem of the anomalous beam response, the difficulty of acquiring a proper lock was compounded by persistent current decay at injection, which caused large and fast drifts in tune, coupling, and chromaticity.

SENSITIVITY TO PID PARAMETERS

Efforts to tune the PID loop of the tune tracker at injection revealed a second surprise, namely a discontinuous behaviour of tune tracking with small changes in loop parameters. As proportional gain was increased there was a sudden and dramatic change in the amplitude and phase signals, and an improvement in tune tracking. This might be at least partially attributed to the anomalous beam response observed at injection, where the conjecture is that higher gains prevent jumping between the multiple peaks. However, while the preference for higher proportional gains is somewhat diminished at store, where the beam response is much more normal, the advantage of high proportional gains does persist.

EXCESSIVE NOISE WHEN CLOSING THE MAGNET LOOPS

The anomalous beam response at injection may have contributed to the excessive noise that appeared in tune tracking when the feedback loops were closed. In previous years, the additional noise and tune dither resulting from closing the loops was barely perceptible. In the present run the tune dither increased by roughly an order of magnitude when the loops were first closed. We have not yet been successful in finding a loop filter that permits closing the loops at injection without introducing substantial tune dither.

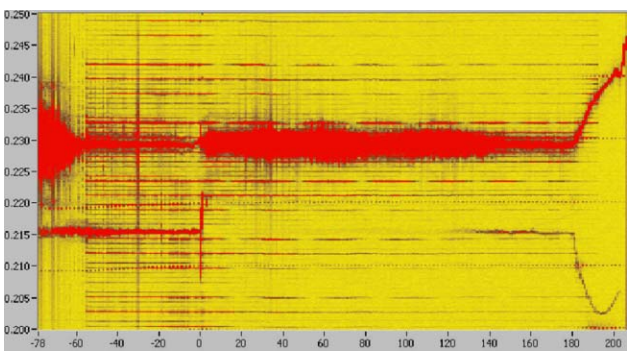

Figure 2. Beam spectrum in the vicinity of the betatron line during ramping

Figure 2 is an FFT of the signal from the horizontal plane of the tracker during a feedback ramp. The horizontal scale is time in seconds, and the vertical is tune, with the ramp starting at -78s and transition (it is necessary to cross transition with ions in RHIC, but not with protons) at 0s. Tune tracker loop gains and kicker excitations were constant throughout this ramp. It can be seen that early in the ramp there is 0.01 units of tune dither. This is a lot. As the magnet power supplies start to ramp the dither gradually diminishes to the more typical 0.001 range. The turn-on of the main dipole ramping supplies is clearly visible ~20s into the ramp. The ramp tune was defined to keep it between the strongest mains harmonics, which are spaced by 180Hz. This can be seen in the image. The revolution frequency in RHIC changes enough during ramp that without this adjustment the tune would have been dragged across a strong mains harmonic. The increased dither after transition results from chromaticity being too small.

'TUNE SCALLOPING'

The fourth surprise was quite interesting. Both during ramping and at store (but not at injection) we observed a phenomenon that we call 'tune scalloping'. This is new. We haven't seen it before, or at least we didn't recognize it if we did see it. Our speculation is that, with certain combinations of chromaticity, loop gains, and kicker excitation, the tracker drives a narrow slice of the tune/momentum distribution to high amplitude. The tune shifts as the amplitude of this slice increases, and the tracker follows the shift. The slice eventually de-populates, and the tracker falls back into the middle of the tune distribution, where it grabs another slice, drives it up and follows it out,…

Figure 3 shows (from the bottom) tunes, and the horizontal and vertical plane in-phase and quadrature signals from the tune tracker during a ramp with feedbacks. This was a development ramp with increased betatron phase advance, to reduce the effect of intra-beam scattering during store. With feedbacks on, beam was successfully delivered to full energy on the first attempt.

The blue vertical bars in the images are 'stepstones', places in the ramp where machine parameters like tune, coupling, and chromaticity can be adjusted. In this ramp tune and coupling were being continuously controlled by the feedback loops, but chromaticity was open-loop, being adjusted at the stepstones. In the upper pane, the amplitude of the vertical response takes off at a stepstone shortly before mid-ramp, then begins to oscillate as slices are driven up, depopulated, driven up,… The oscillations stopped when loop gains and kicker excitation were manually lowered. After ~30 sec they were restored to slightly less than their original values, and the oscillations took off again, stopping when gains and excitation were again lowered. The tune fluctuations, despite the effect of the feedback loop, are visible in the tune traces at the bottom of the image. The quality of the coupling feedback was also affected by this.

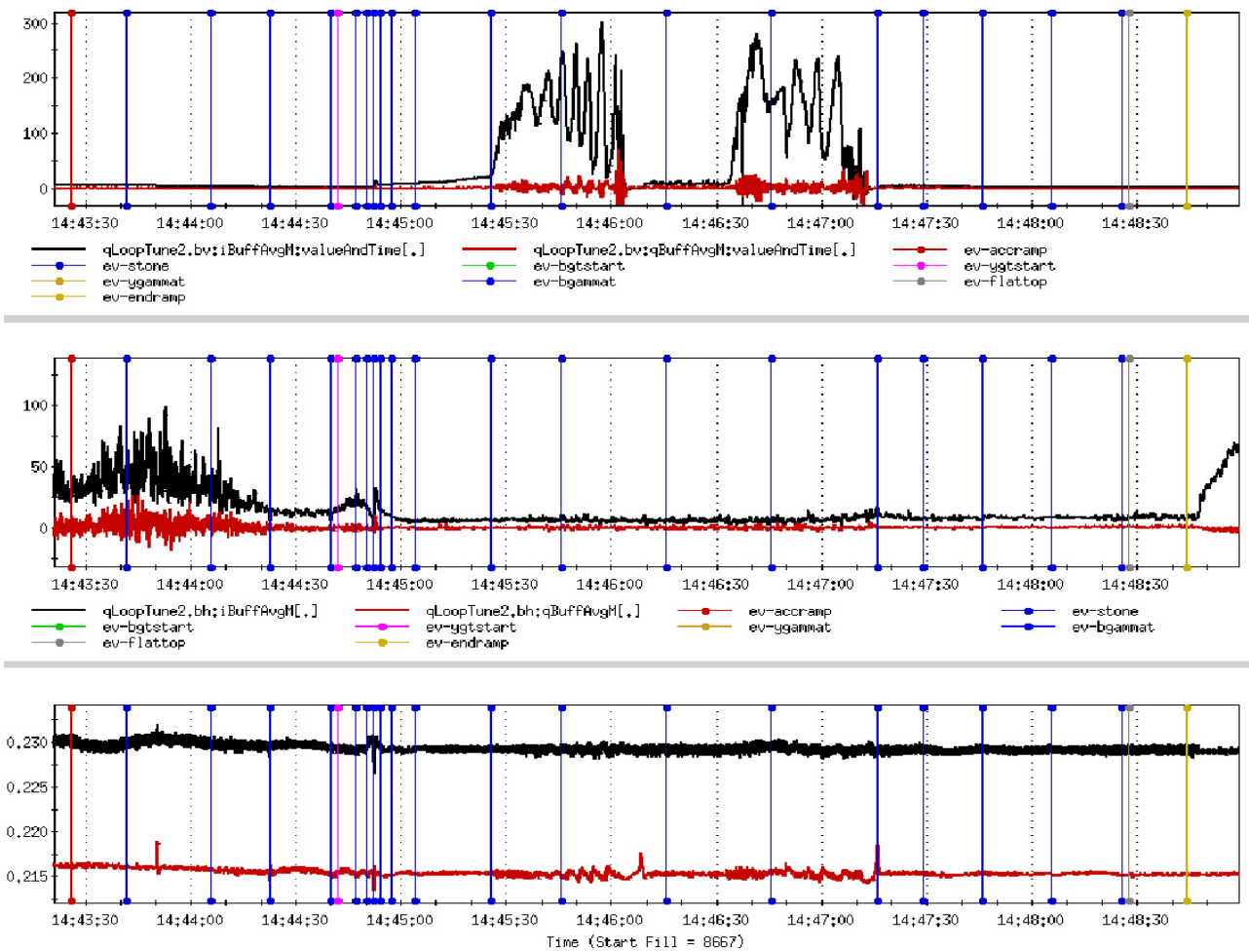

Figure 3. Tune Scalloping during ramping

This new behavior put the tune feedback effort in a pretty tight box. To maintain reliable lock in the presence of mains harmonics requires large kicker excitation. To have reliable and precise tune tracking requires proper loop gains. Chromaticity feedback is not operational. When chromaticity gets small scalloping sets in. The problems of mains harmonics and chromaticity control have found a particularly bothersome way to manifest themselves.

CONCLUSION

Despite the difficulties outlined here, the tune and coupling feedback effort made a useful contribution to Run 7 ramp development, and has also proven to be an essential tool for machine studies.

The presence in the betatron spectrum of strong harmonics of the power line frequency continues to be the primary obstacle to making tune and coupling feedbacks fully operational. During ramping these lines are some 60 to 70dB above the noise floor of the tune tracker, and the kicker excitation needed to track tune reliably in their presence causes significant emittance growth, as well as contributing to the problem of 'tune scalloping'. The origin of these power line harmonics is not understood, and is being actively investigated. Given the fact that this is not understood, the possibility that a similar problem might show up at the LHC cannot be ruled out.

Chromaticity control remains a second significant obstacle. The peak detection analog front end of the tune tracker is sensitive to instabilities. Several feedback ramps were lost due to poor chromaticity control. The infrastructure is in place to close the loop on chromaticity feedback. We hope to test this during the present RHIC run.

REFERENCES

[1] M. Gasior and R. Jones, CERN-LHC Project Report 853, 2005, available at http://documents.cern.ch/cgi-bin/setlink?base=preprint&categ=cern&id=lhcproj-2005-853

[2] Y. Luo et al, PRST-AB 9, 124001, Dec. 2006.

[3] R. Jones et al, "Towards a Robust Phase-Locked Loop Tune Feedback Sysem" DIPAC 2005, Lyon.

[4] P . Cameron et al, C-AD AP Note 253, available at http://www.agsrhichome.bnl.gov/AP/ap_notes/cad_ap_index.html

[5] P. Cameron et al, PRST-AB 9, 122801, Dec. 2006.

FERMI@ELETTRA TIMING SYSTEM: DESIGN AND RECENT SYNCHRONIZATION ACHIEVEMENTS

M. Ferianis, L. Banchi and F. Rossi Sincrotrone Trieste ScpA, Trieste, Italy
J. Byrd, R.Wilcox, J. Staples and L. Doolittle, LBNL Berkeley, CA U.S.A.
F. X. Kaertner, J. Kim and J. Chen, MIT Boston, MA U.S.A.
A. Winter, F. Loehl, F. Ludwig and H. Schlarb, DESY Hamburg, D

Abstract

FERMI@elettra is the fourth generation light source under construction at Sincrotrone Trieste. Being a seeded-FEL source, the requirements for the timing system are very tight as the final goal is a stable seeding process with sub-picosecond electron bunches and seeding laser pulses. Based on demonstrated results achieved in the main laboratories worldwide active in the field, like DESY, LBNL and MIT, an hybrid timing system scheme has been proposed which is currently under development. Both "pulsed" and "continuous wave (CW)" optical timing systems are being deployed, the choice being based on the differences among the different timing system clients; a Low Level Radio Frequency processor is a "quasi-CW" client whereas the lasers and some "longitudinal" diagnostics are "time discrete" clients. In this paper the FERMI@elettra timing system and the recent advances are presented. A pulsed optical clock has been locked to an ultra stable reference; its output pulses distributed over stabilized fiber optic links. As a benchmark client, a femto-second laser oscillator has been synchronized to the optical clock testing different possible schemes.

OVERVIEW OF THE FERMI TIMING SYSTEM

The FERMI timing and synchronization (T&S) scheme (see figure 1) is based on a hybrid system utilising both "pulsed" and continuous wave (CW) optical timing techniques. The optical "pulsed" technique has been originally developed at MIT [1], whereas the "CW" optical technique by LBNL at Berkeley [2].

Timing system clients

The optical pulses distributed over dispersion compensated fiber links (FO) give the time reference to all the "pulsed" timing clients, such as lasers and diagnostics systems. The "CW" optical timing, developed by LBNL at Berkeley, is based on a frequency stabilized CW laser, amplitude modulated by the radio frequency (RF) needed as a phase reference by the timing clients, such as low level RF systems. In this scheme, the FO links are stabilized using the optical mixing concept which fully exploits the ratio (10^5) between the optical carrier frequency and the RF signal to be distributed. The reference oscillator for the whole timing system is a microwave sinusoidal oscillator [3], operating at the European X-band frequency of 11.992GHZ, which provides the required, fs grade, ultra low phase noise and long term stability. The oscillator is housed in a temperature controlled "timing hutch" close to a set of ultra low phase noise dividers which generate the European S-band frequency (2,998.010MHz), the optical master oscillator (OMO) reference frequency, $f_{REF\ OMO}$), and the greatest common divisor frequency, f_{COIN}, output signals. The output signals are distributed to the OMO, to the CW timing and to the master time-base unit and finally, via dedicated stabilized optical channels, to the timing system end users.

The timing system is completely integrated into the FERMI control system, thus allowing for remote control and monitoring of the performance and reliability of all key sub-systems.

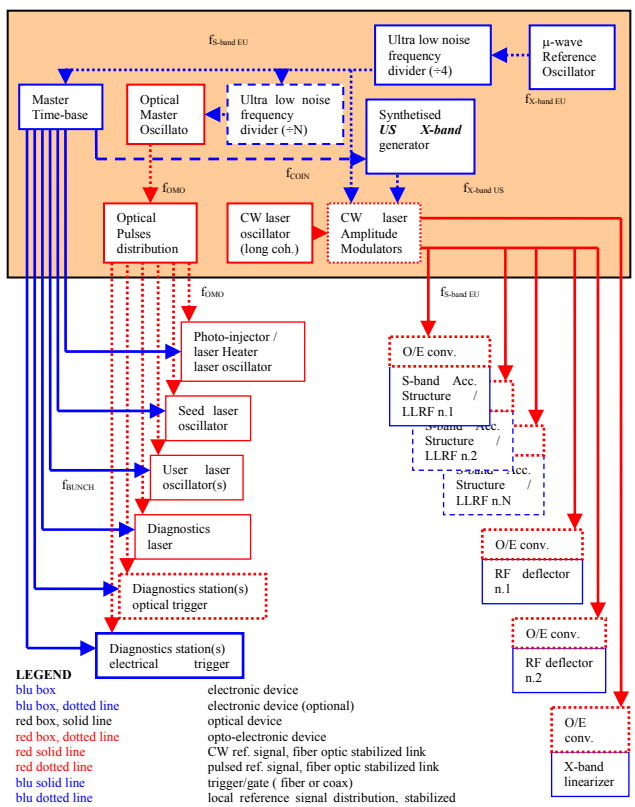

Figure 1: Block diagram of the FERMI timing system.

TIMING SYSTEM SPECIFICATIONS

The various timing system clients have different requirements in terms of maximum allowed jitter. These values have been computed by means of jitter sensitivities studies carried out for the FERMI accelerator [4].

Jitter budget

For each timing client, the net effect on the jitter of the bunch is computed as the quadratic sum of the timing line (phase reference) and the client (sub-system) contributions, since the two contributions are Gaussian and statistically independent. The resulting values for each timing reference line are listed in table 1, under the heading "Timing line jitter".

Table 1: Allowed jitter for each timing line.

Timing client	Client jitter [fs_{RMS}]	Timing line jitter [fs_{RMS}]	Bandwidth of interest
RF S-band	167	118	DC - 1kHz
RF X-band	69	49	DC - 1kHz
Photo-injector laser	200	141	DC - ≈1kHz*
seed laser	100	71	DC - ≈1kHz*
experimental laser	100	71	DC - ≈1kHz*
Streak Camera driver	500	354	DC - 1kHz
Streak Camera fiducial	100	71	DC - 50MHz
Bunch arrival monitor	100	71	DC - 50MHz
EO sampling station	100	71	DC - 50MHz

* synchronized by means of electrical timing stabilizer

In Table 1, under "Bandwidth of interest", the bandwidth within which each timing client is most sensitive to jitter has been indicated. The different sensitivities are explained by the intrinsic band characteristics of the sub-systems (RF accelerating structures) and the related stabilization loops (laser PLLs). This is an important issue that must be taken into consideration in the design of the timing lines to the different sub-systems.

Reference frequencies for FERMI

The FERMI timing system has to be compatible with both the European ($f_{S\text{-}band\text{-}EU}$=2.998010GHz) and U.S ($f_{S\text{-}band\text{-}US}$=2.856GHz) S-band frequencies (see Table 2). This is a necessary condition since the fourth harmonic (X-band) linearizer, that is part of the FEL design, will work at the US frequency. The greatest common divisor of these two frequencies is the coincidence frequency f_{COIN} (15.779MHz) used to generate the "bunch clock" at the FEL repetition rate frequency f_{bunch} of 10-50Hz.

Table 2: Reference frequencies for FERMI

Signal name	Symbol	Value	Notes
μ-wave master	f_{MASTER}	11.992040GHz	EU X-band
FERMI RF	f_{RF}	2.998010GHz	EU S-band
US RF	$f_{US\ REF}$	2.855998GHz	US S-band
US X-band	$f_{US\ X\text{-}band}$	11.423996GHz	US X-band
G.C.D.	f_{COIN}	15.779000MHz	EU S-band/190 US S-band/181

The ultra low phase noise μ-wave master oscillator [3] will provide the fs level phase reference to the OMO and its S-band output will be directly distributed to the Radio Frequency clients by amplitude modulating the CW laser.

TEST SET-UP AT ELETTRA

The block diagram of the test set up for the Optical timing system at ELETTRA is shown in figure 2. The reference electrical (RF) generator is located in the Klystron Gallery of the LINAC, close to the Optical master Oscillator. An harmonically Mode Locked fiber laser [5] has been phase locked to the RF generator. The repetition rate of the optical pulses is 3GHz, the same of the RF generator. A 300m long single mode fiber stabilized link, indicated in red, distributes the Optical reference signal to the Storage Ring where the timing clients are located. Different schemes for the locking of remote clients are shown in figure 2, both electrical and optical.

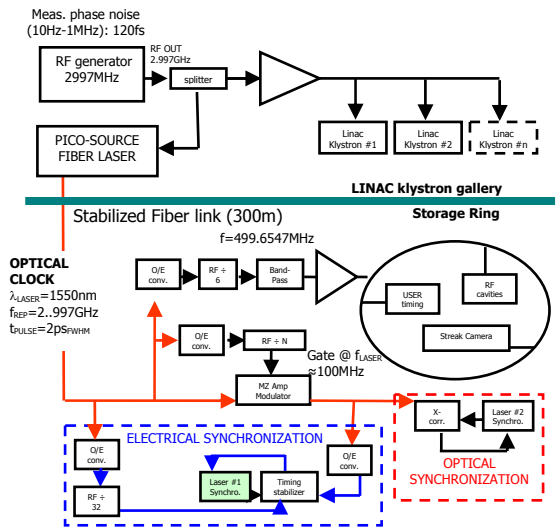

Figure 2: Optical Clock test bed at Elettra: red lines indicate optical signals, blu lines indicate electrical signals.

Extraction to an electrical timing reference

As shown in figure 2, to obtain an electrical timing signal from the optical reference pulse train at a remote station direct conversion to the electrical domain may be applied, followed by a division chain to obtain the required reference frequency to feed the timing stabilizer of the remote system (laser). In figure 3, the block diagram of the tested set-up is presented.

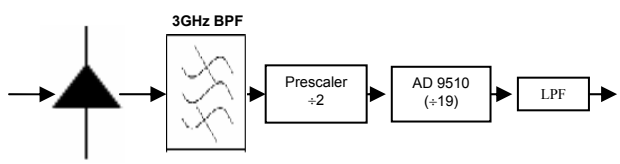

Figure 3: block diagram of the "direct conversion".

The optical pulses, generated by the stabilized harmonic Mode Locked fiber laser [5], are sent along an optical fiber link, laid down in the Klystron Gallery, with a length of 210m. The phase noise measurements have been performed using an Agilent 5052A Signal Source Analyzer (SSA) and are represented in figures 4a and 4b.

In figure 4a the phase noise of the electrical signal is reported, out of the Band Pass Filter downstream the photodiode. In figure 4b the phase noise of the low frequency reference after the dividers is shown. It's important to note that the SSB phase noise profiles can't be compared directly, as they refer to different carriers.

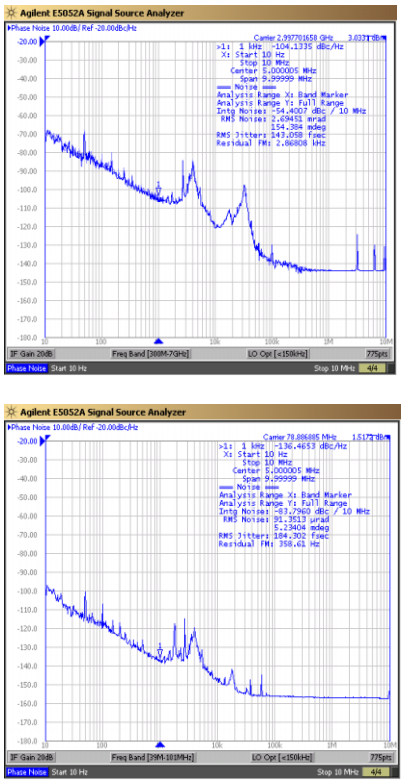

Figure 4: phase noise in the bandwidth 10Hz-10MHz of the extracted 3GHz reference, 143fs$_{RMS}$ (upper trace) and of the low frequency (78.86MHz) reference: 184fs$_{RMS}$ (lower trace).

Preliminary tests of a remote fs-laser oscillator synchronization

Some tests for the synchronization of a remote fs laser oscillator have been carried out using an available Cr:Lisaf laser oscillator.

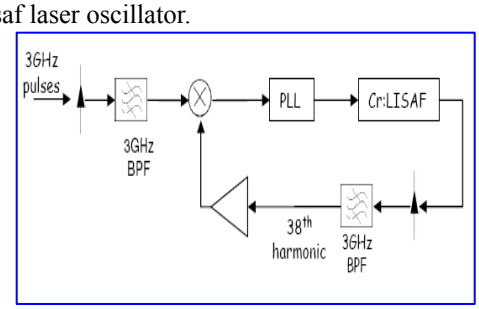

Figure 5: schematic of the remote laser synchronization to the 3GHz optical reference.

We installed standard telecom optical fibers (ITU-T G.652.A) and tested the links performance in terms of phase noise. After 210m of fiber optic link the timing jitter increases by about 15fs$_{RMS}$.

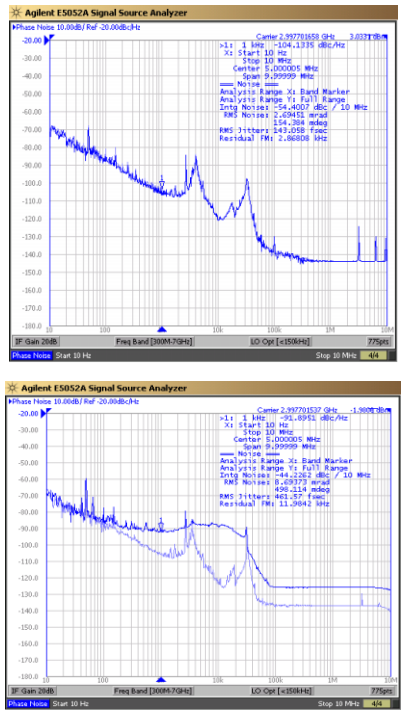

Figure 5, upper trace: phase noise of the Optical reference, 146fs$_{RMS}$. Lower trace: phase noise of the remote fs laser locked to it, 461fs$_{RMS}$.

By filtering an harmonic of the remote laser, it was possible to use this harmonic to lock the remote fs-laser with higher resolution. Tests need to be repeated in a quieter environment as remote laser set-up has not been optimized jet. The phase detection is performed at 3GHz, i.e. the 38th harmonic of the remote fs laser.

ACKNOWLEDGMENT

This work has been partially supported by the EU Commission in the Sixth Framework Program, Contract No. 011935 – EUROFEL.

REFERENCES

[1] A. Winter et al. "High precision laser master oscillators for optical timing distribution systems in future light sources"", Proceedings of EPAC 2006, Edinburgh, Scotland

[2] J. M. Byrd et al. "Timing distribution in acceleration via stabilized optical fiber links", Proceedings of LIANC 2006, Knoxville, Tennessee, USA

[3] Poseidon Scientific Instruments, Fremantle WA 6160 AUSTRALIA; http::\www.psi.com.au

[4] P. Craievich, S. Di Mitri, A. Zholents, "Jitter studies for the FERMI@ELETTRA Linac", Proceedings of EPAC 2006, Edinburgh, Scotland

[5] L. Banchi et al. "Synchronization of a 3GHz repetition rate harmonically mode locked fiber ring laser for optical timing application", Proceedings of DIPAC 2007, Venezia, Italy

JITTER REDUCED PUMP-PROBE EXPERIMENTS

A. Azima*, S. Duesterer, H. Redlin, P. Radcliffe, H. Schlarb, J. Feldhaus (DESY, Hamburg)
M. Meyer (LIXAM/CNRS, UMR 8624 Centre Universitaire Paris-Sud, France)

Abstract

For two-colour pump-probe experiments carried out at the free electron laser FLASH at DESY, the XUV FEL laser pulses must be synchronized with femtosecond precision to optical laser pulses (120 fs, 20 μJ Ti:Sapphire). An electro-optical (EO) sampling diagnostic measures the arrival time jitter of the infrared pump-probe laser pulse with respect to the electron bunch of the FEL. Here, the electron arrival time is spatially encoded into the laser pulse profile and read out by an intensified camera. In this paper we report about the improvement of the temporal resolution of pump-probe experiments on gaseous targets using the arrival time data acquired by the EO-diagnostic.

INTRODUCTION

Fast physical processes in the fs time domain can be observed using pump-probe experiments. Two ultrashort pulses are temporally and spatially overlapped in some target. The first pulse induces a reaction and the second pulse probes the changes of the target material induced by the first pulse. To scan the time evolution of the reaction, one introduces a variable time delay ΔT_{PP} between both pulses. The infrastructure to perform two-colour pump-probe experiments was built up at the FLASH facility. One pulse in the near infrared range is generated by an amplified Ti:Sa oscillator at a wavelength of 800 nm. The Ti:Sa pulse is amplified up to 20 μJ by an optical parametric amplifier . Its pulse duration at the experimental site is 120 fs FWHM. The focal intensity is in the range of a few TW·cm^{-2}. FLASH generates the second ultra-short pulse of high intense ($\approx 10^9$ W) XUV light in the spectral range from 13.8 nm to 40 nm. The XUV pulses have a pulse duration of about 30 fs. The pulse pattern of both sources consist of pulse trains with up to 30 pulses with a 1 MHz repetition rate within the burst and a burst repetition rate of 5 Hz.

Since the sources of the two laser pulses are independent from each other, they have to be synchronized. The synchronization is jitter afflicted. The temporal jitter worsens the temporal resolution of pump-probe experiments to about five times the resolution determined by the pulse duration of the optical laser. One source of this temporal jitter is the energy fluctuation of the electron bunch, which becomes an arrival-time fluctuation after the electron bunch compressors. The second source of timing jitter is due to the imperfect synchronization of the Ti:Sa laser oscillator with respect to the reference RF line. Both jitter add to about 250 fs RMS measured during one hour.

To increase the temporal resolution, one can precisely measure the jitter pulse-by-pulse and sort the experimental data according to the measured arrival-time. This is achieved by a diagnostic called Timing by Electro-Optical sampling (TEO). Utilizing this technique, the temporal resolution is no longer dominated by the jitter. It is dominated only by the precision of the timing measurement, which can be made substantially better than the width of the temporal jitter.

EXPERIMENTAL SETUP OF TEO

The TEO diagnostic was set up measure the precise relative arrival-time ΔT_{el} of the electron bunch and the IR laser pulse in the accelerator tunnel.

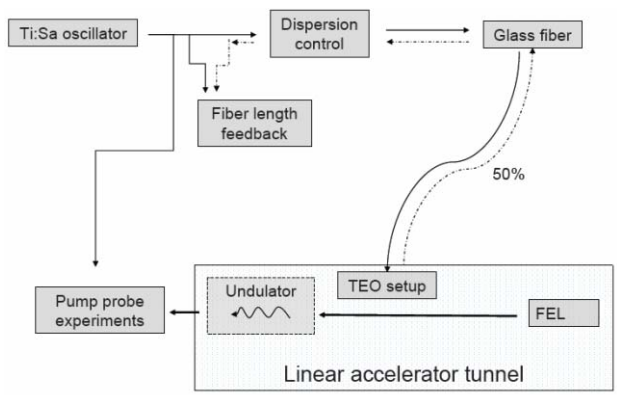

Figure 1: *Overview of the principle setup of the TEO experiment. The relative arrival time between FEL pulse and IR pulse is measured inside the accelerator tunnel using the electron bunches instead of the XUV pulses.*

It uses the electro-optical effect with the spatial encoding technique to map time into space and produces a signal, from which the relative arrival-time between laser pulse and electron bunch can be extracted (fig. 2). The electron bunch and the IR pulse are arriving simultaneously at an electro-optical GaAs crystal. Here, the longitudinal electron bunch profile is encoded inside the polarization of the transverse laser profile and transformed into an intensity modulation by a polarizer. The transversal position of the signal is depending on the relative arrival-time of electron bunch and optical laser pulse at the EO crystal because of an angle of incidence of 45° of the optical laser to the EO crystal surface. See [3] for more details. Since the used EO

* email: armin.azima@desy.de

technique detects primarily the arrival of the electron bunch peak, which produces the FEL SASE pulse, the measured electron bunch arrival-time is in good approximation equal to the relative arrival time of both photon pulses at the experiment. Thus, by measuring the electron arrival-time the photon arrival-time can be predicted within the error bars of the method ($\approx$ 90-120 fs RMS). A similar diagnostic on an incoherent light source at SLAC [2] has shown comparable experimental error bars of $\approx$ 60 fs RMS of the photon pulse arrival-time.

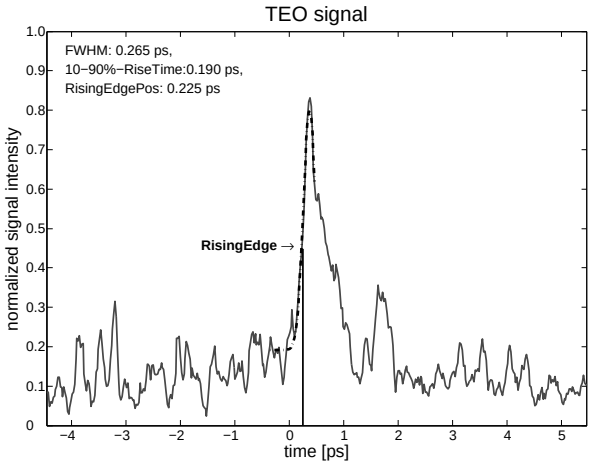

Figure 2: *TEO signal with GaP crystal, 180 μm thickness, non-wedged, crystal edge distance from e^--beam about 1.5 mm. The arrival-time of the electron bunch is indicated with highest precision by the rising edge, which has a 10%-90% rise time of 190 fs. The inflexion point on this edge is used to read off the arrival-time.*

The IR laser system is located in a laser laboratory at the end of the FEL linear accelerator in close vicinity to the pump-probe experiments. To transport the laser pulse Fourier limited to the location of TEO in the accelerator tunnel, which is located 160 m away from the laser laboratory (see fig. 1). The laser pulse transport system is the most complex part of the TEO experiment, because the dispersion of 160 m bulk glass fibre has to be recompressed accurately. Additionally the fibre length is modulated by thermal expansion and micro-phonics, which has to be compensated by active path length stabilization. A detailed description of the dispersion compensation can be found in [3] .
Currently the diagnostic can deliver the arrival time for one arbitrary bunch of each bunch train.

PUMP-PROBE EXPERIMENT

The performance of the TEO diagnostic can be tested utilizing sideband generation. [6]. For that, the FEL is focussed inside a low pressure Xe gas target of 10^{-6} mbar to ionize the gas atoms. The photo electrons are collected by a magnetic bottle type time of flight spectrometer [5]. The IR pulse from the amplified Ti:Sa laser is focussed into the gas collinearly with the XUV beam of the FEL. Once the two laser pulses overlap in space and time, the electric field of the IR laser pulse interacts with the photo electrons and modulates their kinetic energy by a multiple of $\hbar\omega_{IR} = \pm 1.55$ eV. Thus, additional sidebands appear in the photo electron spectrum. The intensity and number of sidebands depend on the strength of the modulating electric field of the IR laser pulse, which interacts with the photo electrons. The better the overlap, the more photons are absorbed from the IR field, thus, the sideband intensity increases and sidebands of higher order become visible (fig. 3). Without any spatial jitter (i.e. changing spatial overlap due to pointing fluctuations of the FEL) the sideband intensity is an indicator of the temporal overlap of both pulses with a precision of about 50 fs, according to [6].

Experimental parameters

During the experiment, the FEL was operating at 13.8 nm (89.9 eV) in single-bunch mode with a peak energy of up to 50μJ per pulse. The diameter of the XUV-FEL beam in the interaction volume was $100 \pm 10\,\mu$m. The IR laser was focussed down to $50 \pm 10\,\mu$m in diameter with about 5 μJ per pulse and a pulse duration of 120 fs FWHM. Some of the measured electron energy spectra are shown in fig. 3. The excited state $5p^{-1}$ of the Xe atoms has a binding energy of 12.13 eV [4]. Its photo-electron line was observed at about 78 eV inside the time-of-flight spectrum. It splits up into two lines of the spin 1/2- and 3/2-states.

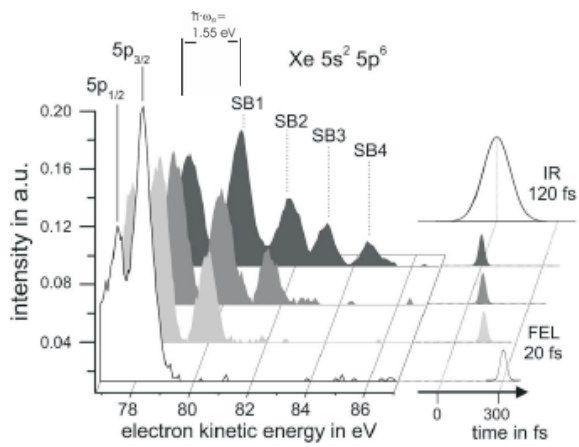

Figure 3: (Figure adapted from [6]) *Time of flight spectra of Xe photo electrons with varying temporal overlap between the optical and XUV laser pulse.*

Experimental results

In the following, only the first sideband of the photo electrons is used. The sideband amplitude is correlated with the time information set by a delay stage to scan a time interval of 3 ps around time zero point of best temporal overlap. For each 0.1 ps time step the sideband amplitude is averaged over 250 shots. The correlation is shown in fig. 4 by the outer graph. This trace is the scanned sideband correlation of the XUV and IR laser pulse.

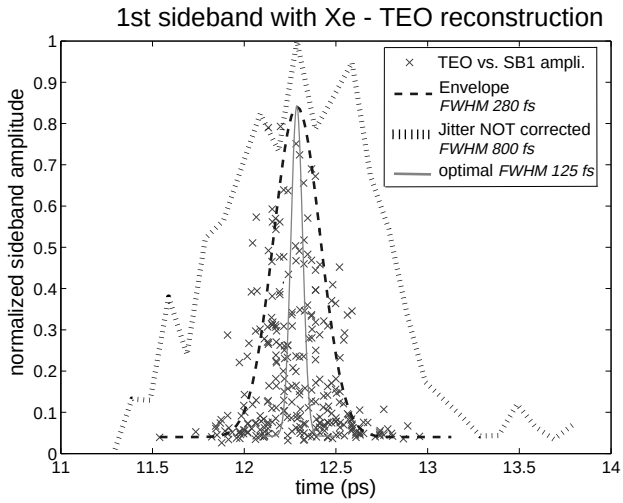

Figure 4: *Final result of the bunch by bunch correlation between the sideband amplitude and the arrival time measured by TEO. The envelope of the measured data points is the reconstructed temporal cross-correlation of both pulses (dashed line). The outer line (dotted) is the averaged cross-correlation from a pump-probe scan and the inner line (gray) is the theoretically expected cross-correlation.*

In a second experiment the delay stage was set to time zero. The arrival-time of each event is measured by TEO and correlated with the sideband amplitude normalized by the integral of the photo electron main line, which is proportional to the FEL energy per pulse. The spread of the time jitter of the FEL was large enough to cover the expected time interval of possible temporal overlap between both pulses. Therefore, a time scan over a large interval was not necessary. The result of the correlation is shown in fig. 4 by the data points.
The width of the scanned correlation ΔT_{scan} (outer line) is 800 fs FWHM ($\approx$ 350 fs RMS). This width is due to the influence of the temporal jitter much larger than the optimal width $\Delta T_{optimal} \approx 125$ fs FWHM for the cross-correlation of both laser pulses (inner line).
The envelope of the data points is the reconstructed sideband cross-correlation. The width of the envelope ($\Delta T_{corrected}$) is 280 ± 10 fs FWHM. It is two times smaller than the width of the averaged signal. Thus, the signal of the sideband correlation of XUV and IR laser pulse was measured with reduced temporal jitter utilizing the TEO timing information.
Compared with the duration of the theoretical signal, the remaining temporal jitter and drift was reduced from $\sqrt{{\Delta T_{scan}}^2 - {\Delta T_{optimal}}^2}/2.35 \approx 340$ fs RMS to $\sqrt{{\Delta T_{corrected}}^2 - {\Delta T_{optimal}}^2}/2.35 \approx 105$ fs RMS. (In general the variances of two independent Gaussian distributions are added quadratically.)
The data points below the envelope are a result of spatial jitter. That is, despite a good temporal overlap for several data points, the measured sideband amplitude was small, because the spatial overlap of these shots was imperfect.

CONCLUSION

We have shown in a pump-probe experiment, that the Electro-Optical Spatial Decoding technique provides the possibility of an online non-destructive single-shot measurement of the relative arrival time between a high intensity optical laser and the FEL-XUV pulse with a resolution of better than 110 fs. This opens the door for further precise pump-probe experiments at FLASH.

ACKNOWLEDGEMENTS

We are greatly indebted to the scientific and technical team at FLASH, in particular the machine operators and run coordinators, being the foundation of the successful operation and delivery of the SASE-FEL beam.

REFERENCES

[1] V. Ayvazyan, et al. First operation of a free-electron laser generating GW power radiation at 32 nm wavelength. Eur. Phys. J D 37, 297-303, (2006)

[2] A. Cavalieri et. al. Clocking Femtosecond X Rays. In *PRL 94, 114801 (2005)*, San Francisco, 2005.

[3] A. Azima et. al. Monitoring of the electron bunch. In *EPAC proceedings 2006*, Edinburgh, 2006.

[4] F. Brandi, I. Velchev, W. Horgervorst, and W. Ubachs Vacuum-ultraviolet spectroscopy of Xe: Hyperfine splittings, isotope shifts, and isotope-dependent ionization energies In *Phys. Rev. A 64, 032505 (2001)*.

[5] P.Radcliffe, et. al. Two-color photoionization setup for high intensity extreme-UV free electron and near IR laser pulse experiments. to be published in *NIM A*.

[6] P.Radcliffe, et. al. Single-shot characterization of independent femtosecond extreme ultraviolet free electron and infrared laser pulses. published in *Applied physics letters, 90, 131108, 2007*.

SEGMENTED BEAM DUMP FOR TIME RESOLVED SPECTROMETRY ON A HIGH CURRENT ELECTRON BEAM

T. Lefèvre, H. H. Braun, E. Bravin, C. Dutriat, C. P. Welsch
CERN, Geneva, Switzerland

Abstract

In the CLIC Test Facility 3 (CTF3), the strong coupling between the beam and the accelerating cavities induces transient effects such that the head of the pulse is accelerated twice as much as the rest of the pulse. Three spectrometer lines are installed along the linac with the aim of measuring energy spread versus time with a 20ns resolution. A major difficulty is due to the high power carried by the beam which imposes extreme constraints of thermal and radiation resistances on the detector. This paper presents the design and the performances of a simple and easy-to-maintain device, called 'segmented dump'. In this device, the particles are stopped inside metallic plates and the deposited charge is measured in the same way as in Faraday cups. Simulations were carried out with the Monte Carlo code 'FLUKA' to evaluate the problems arising from the energy deposition and to find ways to prevent or reduce them. The detector resolution was optimized by an adequate choice of material and thickness of the plates. The overall layout of the monitor is described with special emphasis on its mechanical assembly. Finally, limitations arising at higher beam energies are discussed.

INTRODUCTION

In CTF3 an electron pulse of 3.5A and 1.5µs is accelerated using fully loaded 3GHz accelerating structures [1]. The resulting energy spectrum shows a strong time dependency with higher energies in the first 10-50 nanoseconds of the pulse, followed by 1.35µs of steady behaviour. Time-resolved spectrometry is therefore an essential beam diagnostic to correctly set the phase of the accelerating structures. Several spectrometer lines are installed along the CTF3 linac for this purpose. They consist of a bending magnet, which provides horizontal deflection to the electrons, followed by a transverse profile monitor measuring the beam position and its transverse width. The beam lines are classically equipped with an optical transition radiation (OTR) screen [2] observed by a CCD camera for the setting up of the line, and a novel segmented beam dump for time resolved measurements.

The latter is a device composed of parallel metallic plates designed to stop the incident particles. By measuring the deposited charge in each segment, the beam profile can be reconstructed. The material and the dimension of the segments must be optimized depending on the beam parameters. In particular, they need to be long enough to stop the particles. On the other hand, the segment thickness must be chosen to optimize the spatial resolution which will tend to degrade due to multiple Coulomb scattering [3]. Moreover, because of the high power carried by the beam, thermal changes must be considered as a crucial issue as well as radiation effects that will influence the long term behavior the detector.

In 2004 a first version of the segmented dump was built and implemented in the machine [4]. The design consisted of 24 water-cooled 2mm thick tungsten plates spaced by a 1mm thick insulator. In this first design it was not possible to find an insulating material with an adequate radiation resistance, since ceramics are very difficult to braze directly on tungsten. Thus, the insulator had to be replaced after only one year of operation. The electrical connections were realized by directly converting the current in each segment into a voltage through a 1Ω resistance to ground and 50Ω in series. The presence of overshoot and undershoot effects at the beginning and the end of the pulses indicated a bandwidth limitation to 20MHz. This was interpreted as the signature of a beam inductive coupling because in this design 1/3 of the beam was not stopped in the plates and thus propagated through the device to the iron blocks located 20cm downstream.

Recently a new study was initiated to overcome the observed limitations. The final goal will be to maximize the spatial resolution of the segmented dump while optimizing its mechanical design in terms of long-term reliability and in particular radiation hardness.

FLUKA SIMULATION

In order to find out about the deposited energy on the dump, simulation studies with the Monte Carlo code FLUKA [5] were performed.

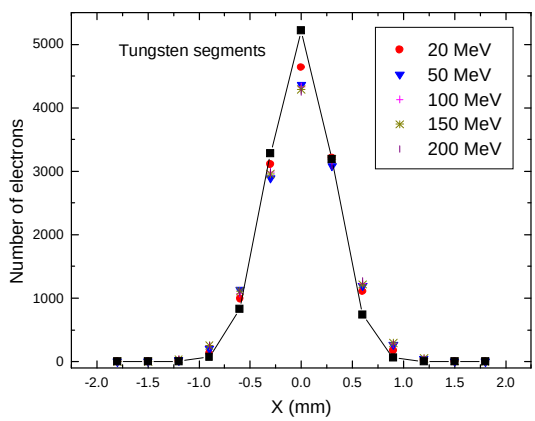

Figure 1: Simulated profile measurements on a tungsten segmented dump for different beam energies.

As a first step of the optimization process, the original geometry of the device built in 2004 was used, i.e. with

2mm thick plates spaced by 1mm. The deposited energy inside the device and the individual tracks of the particles are recorded for each simulation. In order to get a reasonable statistics, the simulation uses $2 \cdot 10^4$ electrons. Two different materials (tungsten and iron) were considered and simulations were performed for 20, 50, 100, 150 and 200 MeV electrons. The transverse size of the beam is assumed to be Gaussian with a typical width of σ=3mm. From the single particle tracks, the measured beam profile can then be reconstructed as shown in fig. 1. Each point represents the number of particles stopped in a given plate. The black curve represents the initial beam profile at the entrance of the beam dump, while the different points indicate the transverse profile measured for different beam energies. Gaussian profiles were then fitted through these points. The errors made in these profile measurements are summarized in table 1.

Table 1: Error made in the beam profile measurement for iron and tungsten plates at different beam energies

Beam energy (MeV)	20	50	100	150
Error (%) for tungsten plates	10	21	23.5	28
Error (%) for iron plates	61	78	82	82

Errors larger than 60% for iron plates illustrate the strong effects of multiple scattering. The spatial resolution is degrading rapidly for low Z and low density materials. For tungsten, the error remains relatively small for low energy electrons, but increases rapidly with beam energy. Therefore it needs to be subtracted in the data analysis.

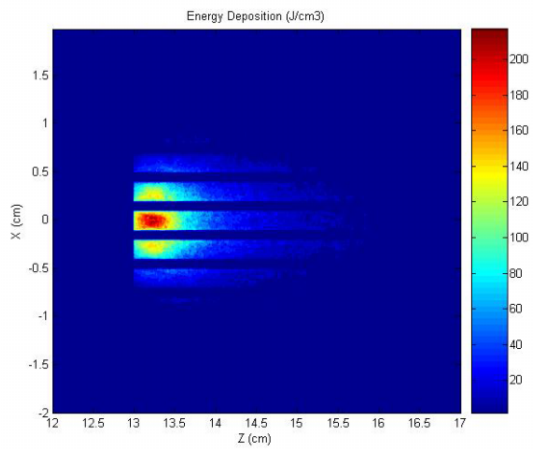

Figure 2: Energy deposition in tungsten plates for a 50MeV electron beam.

The energy deposition along the dump is presented in fig. 2 in form of an XZ surface plot. This example corresponds to 50MeV electrons stopped in tungsten. The maximum local temperature and the total power absorbed by the dump can be calculated using the deposited energy. The corresponding values are given in table 2. The maximum local temperature remains low enough to prevent any damage to the tungsten plates. However, the power deposited in the dump still needs to be dissipated, in particular to minimize the mechanical stress induced on the electrical connections.

Table 2: Temperature and power in the dump

Beam energy (MeV)	20	50	100	150	200
Maximum ΔT (K)	92	93	118	145	165
Total power (W)	88	219	434	639	847

The performance of the first option of direct water cooling of the dump segment turned out to degrade rapidly due to strong radiation effects. A second design was thus based on the use of a multi-slit collimator installed just upstream of the segmented dump. Its role is to capture as much beam power as necessary to ensure a good signal, but keep the deposited power low enough so that the segmented dump does not require direct water cooling anymore. In this scenario, radiation hard ceramics can be used as insulating material. The mechanical assembly of the multi-slit collimator and of the segmented dump are depicted in fig. 3.

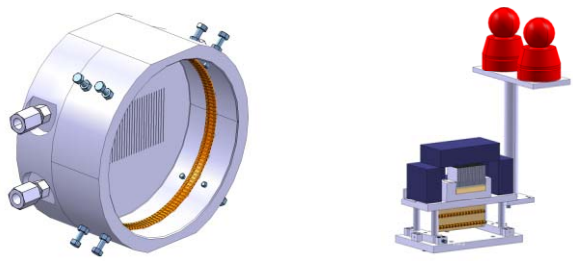

Figure 3: (a) Multi-slit collimator, (b) segmented dump.

From the construction point of view, thin slits have to be machined over few centimetres long distances precisely enough to guarantee good positioning, constant thickness and high parallelism between them.

Simulations were performed to study the impact of the slit width on the spatial resolution of the measurements. The difference is less than 5% for slit widths varying between 200µm and 1mm and this independently from the initial beam energy. A slit width of 400µm, stopping 75% of the incident electrons, was thus chosen as a good compromise between mechanical tolerance and collimation performance. In order to keep the costs reasonably low, an iron collimator was used.

The maximum temperature and power stopped in the collimator and the segmented dump are presented in table 3. In these simulations, we assumed a 4cm long collimator. These values must then be compared with the ones shown in table 2: At 20MeV the collimator is highly efficient, the temperature in the dump decreases by a factor 2 and the power by a factor 4. This is in perfect agreement with what one can await from the slit geometry. However, with increasing beam energies, showers induced by the particles stopped in the collimator start to contribute significantly to the deposited energy in the segmented dump. At 200MeV the efficiency of the collimator reduces to only 28%. A longer collimator, where the shower is better absorbed, might improve on this situation.

Table 5: Temperature and power collimator and dump

Beam energy (MeV)	20	50	100	150	200
Max ΔT_{Coll} (K)	22	22	22	28	31
Total $Power_{Coll}$ (W)	115	234	371	467	538
Max ΔT_{dump} (K)	51	60	68	86	116
Total $Power_{dump}$ (W)	21	74	217	404	614

From energy deposition simulations, one can extract the estimated radiation dose that will be received by the device. An example is shown in fig. 4 where the segmented dump is assumed to be used one hour per day, 10 days a year at a repetition frequency of 1Hz.

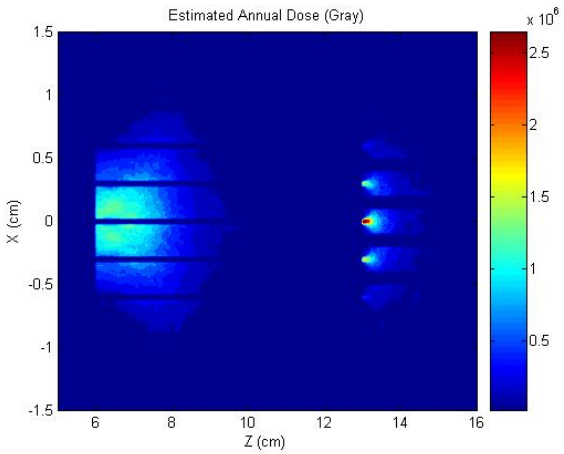

Figure 4: Energy deposition in the iron multi-slit collimator and the tungsten segments for 50MeV electrons.

It can be seen that the ceramics, located in between the metallic plates but shifted downwards by 2 cm from the beam position, receives an annual dose between 0.8 and 2MGy, depending on the initial electron energy. In radiation tests [6], it has been observed that alumina has not suffered any noticeable damage even if exposed to doses of 100MGy.

INSTALLATION AND MEASUREMENT

A test device was constructed in January 2006 and installed in a spectrometer line in April as shown in fig. 5. Typical beam energies at this spectrometer line range from 20-40MeV. In the meantime, the electronics was modified, and now the current of each segment is read directly with 50Ω impedance to ground.

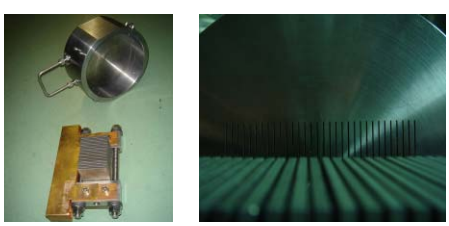

Figure 5: Photos of segmented dump and collimator in the lab (left) and installed in the beam line (right).

The first energy spectra measured recently are shown in fig. 6. The parasitic overshoot and undershoot have disappeared and the bandwidth is now limited only by the 100 MSa/s sampling rate of the ADC.

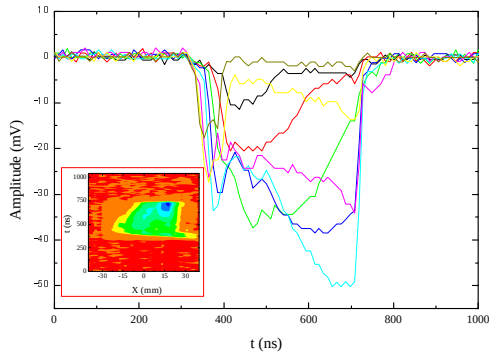

Figure 6: Time signals and time resolved spectra.

CONCLUSION

A radiation hard segmented dump was designed and commissioned successfully with beam. The output signal bandwidth, better than 50MHz, satisfied the requirements.

FLUKA simulations were carried out to estimate the spatial resolution of the device and deposited power on the different segments. Errors, which need to be subtracted, result from multiple Coulomb scattering and lead to increased profiles in the order of some percents.

The input collimator absorbs most of the beam power (~80%) and works very well for low-energy beams. However, its efficiency decreases with beam energy and other devices should be considered at energies above ~100 MeV [7].

REFERENCES

[1] R. Corsini et *al*, "First Full Beam Loading Operation with the CTF3 Linac", EPAC 2004, Lucerne, Switzerland, pp.39.

[2] C.P. Welsch, E. Bravin, T. Lefèvre, "Investigations of OTR Screen Surfaces and Shapes", EPAC 2006, Edinburgh, UK, pp.1220.

[3] J.W. Motz, H. Olsen and H.W. Koch, 'Electron scattering without Atomic or Nuclear Excitation', Review of Modern Physics **36,** (1964), 881.

[4] T.Lefèvre et *al*, "Time Resolved Energy Measurement at CTF3", DIPAC 2005, Lyon, France, pp.60.

[5] A.Fasso *et al.*, "FLUKA: Status and Prospective for Hadronic Applications", Monte Carlo 2000 Conference, Lisbon, pp.955.

[6] P. Beynel, P. Maier and H. Schönbacher, 'Compilation of radiation damage test data, Part III: Materials used around high-energy accelerators', CERN 82–10 (1982).

[7] T. Lefèvre et *al*, "Time Resolved Spectrometry at CTF3", EPAC 2006, Edinburgh, UK, pp.1205.

EXCITATION STRIPLINE FOR SOLEIL FAST TRANSVERSE FEEDBACK

C. Mariette, J-C. Denard, R. Nagaoka
Synchrotron Soleil, Gif-sur-Yvette, France

Abstract

SOLEIL, the new French third generation light source, is equipped with excitation striplines for a tune monitor and for the (bunch-by-bunch) Fast Transverse Feedback that has been recently implemented. A careful design of the striplines and their vacuum feedthroughs was aimed at maximizing the effectiveness of the excitation power via high shunt impedances, and minimizing the power taken from the beam via parasitic mode losses. Three stripline kickers have to be developed for these applications. We report on the design of the first two, using RADIA and GdfidL simulation codes.

INTRODUCTION

The first transverse feedback implementation has been done with an existing stripline kicker initially meant for a spare tune monitor. The system includes a BPM, an RF Front-End, a processor, two power amplifiers and a stripline kicker. The tune stripline is not optimized for this application. The SMA feedthroughs cannot really feed a large amount of power to the stripline. Its length and the short circuited design will not be efficient enough to damp the beam instabilities next year when the second cryomodule will allow the beam current to raise from 300 to 500mA. But it is efficient up to 300mA.

The main instabilities being in the vertical plane, we only address that plane at the moment. This paper compares the simulations between the TFB and the tune striplines.

The magnetic field simulations have been done using Radia code. The signal reflection, shunt impedance and beam impedance have been calculated using the Gdfidl code.

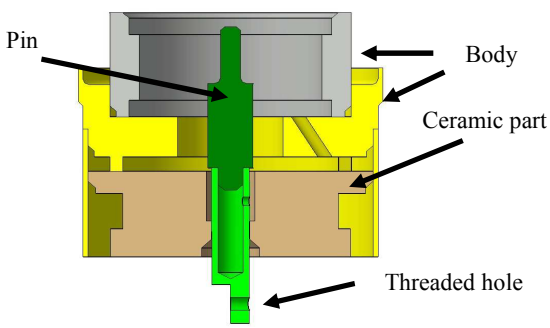

Figure 1: N-type feedthrough design

TFB STRIPLINE SIMULATIONS

The vertical stripline is matched to a 50Ω characteristic impedance with feedthroughs at both ends. The 426mm long electrode corresponds to λ/2 of RF frequency (352MHz). The stripline transverse geometry is strongly constrained by its 50Ω characteristic impedance. The first design guideline is to keep the electrode flush with the vacuum chamber wall, avoiding cross section changes from upstream and downstream.

Feedthrough Design

A new N-type feedthrough has been developed in order to allow a greater excitation power. There is a threaded hole on the feedthrough for the connection to the electrode (fig. 1).

The feedthrough ceramic geometry has been optimized for minimizing the reflection in time domain (Fig.2).

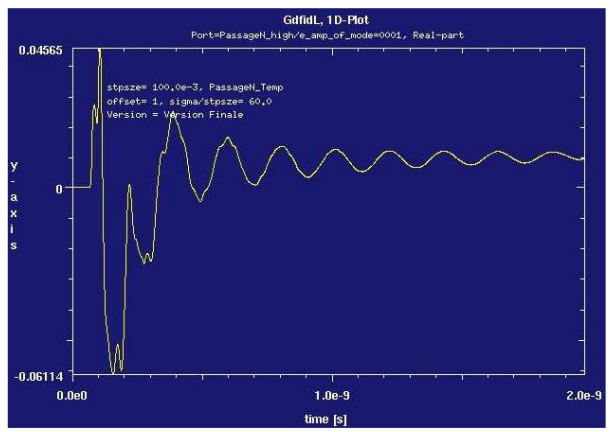

Figure 2 : N feedthrough reflection in time

The maximum reflection is about 5% during a very short time. The feedthrough is matched to 50Ω up to 10GHz.

Stripline Design

The capacitive gap at the end of the electrodes is kept as small as possible in order to suppress the parasitic mode losses. The feedthroughs are connected to the electrodes by a 0.2mm thick stainless steel foil. Each electrode stands on three quartz columns. The figure 3 presents the stripline inner.

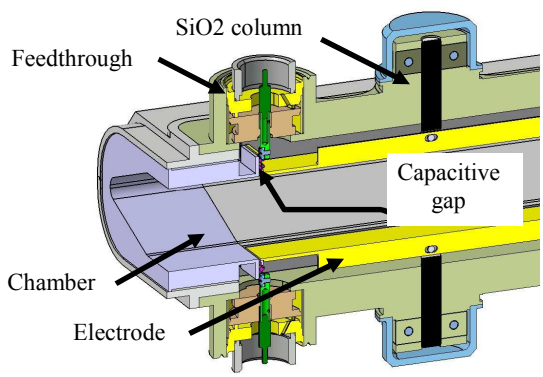

Figure 3 : TFB Stripline Geometry

Stripline Electric Field Simulations

The electric field has been estimated in 2D static regime. The field in the vertical plane has a maximum value of 6.9kV/m, with a driving power of 2 x 75W rms.

The figure 4 presents the electric field distribution of a quarter stripline transverse plane.

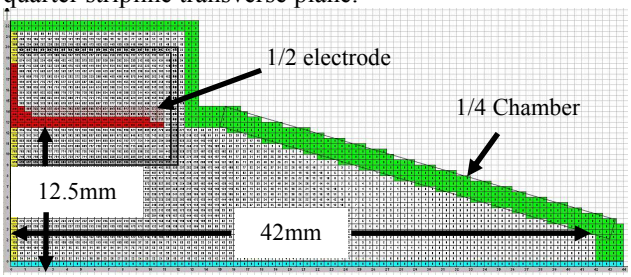

Figure 4: Electric field distribution in 1/4 of the stripline cross-section.

The electric field is computed with Microsoft Excel in one quarter of the vacuum chamber cross section, as shown in figure 4.

Stripline Magnetic Field Simulations.

The magnetic simulation corresponds to a current of 1.41A, from 50W amplifiers. The magnetic field on the beam path is shown in figure 5. The field stays above 35µT in ±5 mm from the orbit center.

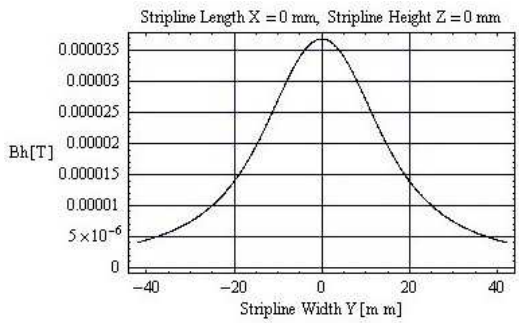

Figure 5: Magnetic field on the horizontal plane

Two 75W RF amplifiers will create a 45µT magnetic field on the beam path.

Stripline Time Domain Analysis

The S11 reflection parameter on the feedthrough is shown in figure 6 [1].

The -0.7 reflection peak corresponds to a capacitive gap added at each electrode end for reducing the parasitic mode losses. The capacity is made of two lips facing each other, one on the electrode, the other on the vacuum chamber wall (Fig.3). In this way, only the lower part of the beam spectrum power is trapped into the stripline structure. There is a reflection before this peak. It is due to the feedthrough-to-electrode connection.

After the peak, the plot corresponds to the electrode 50Ω impedance of the stripline.

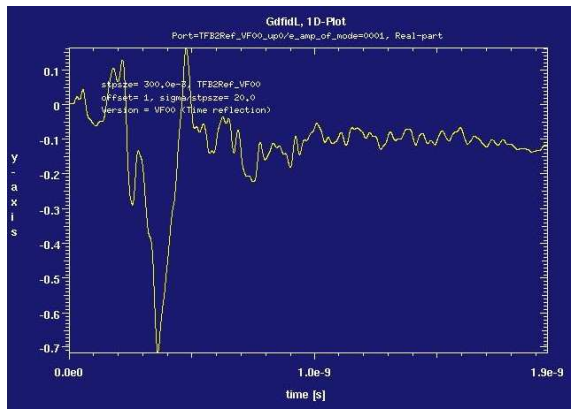

Figure 6: S11 parameter simulation with Gdfidl

Stripline Coupling Impedance

The longitudinal and vertical beam impedance, respectively ZL and ZV, versus frequency are shown in figures 7 and 8. They are small.

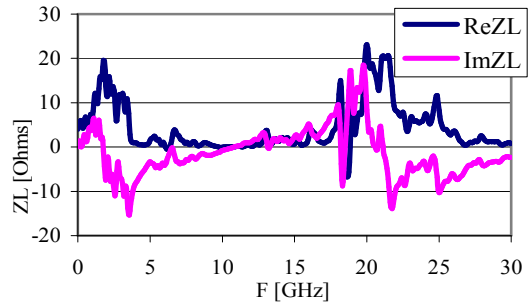

Figure 7: Calculated longitudinal impedance

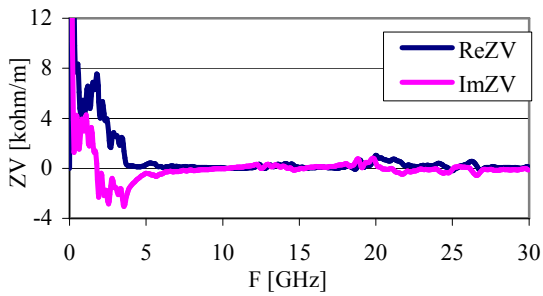

Figure 8: Calculated vertical impedance

The remainder is due to the beam proximity (12.5mm) and to the non negligible gap size. At the beginning of the study, the gap was 0.3mm wide. But, one expect significant lengthening expected during the baking to 180°C. The gap has been widened to 0.5 mm to avoid the risk of short circuit. Having the capacitive gaps at the end of the electrodes decreases the parasitic mode losses by a factor of two.

Stripline Shunt Impedance

The shunt impedance (Zsh) is representative of the stripline efficiency: the higher the better. Zsh has been estimated versus frequency.

The 2D (Poisson's law [3]) and 3D (Gdfidl [2]) simulations are shown in figure 9.

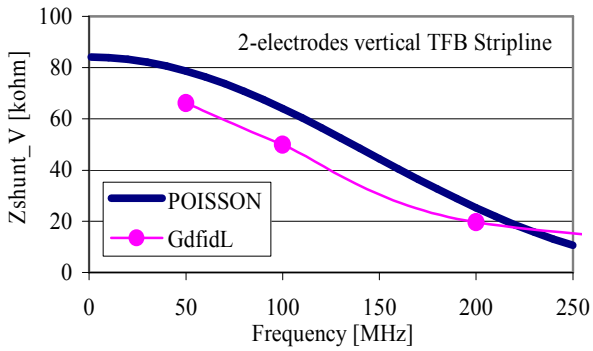

Figure 9: Calculated shunt impedance versus frequency

Both results predict a high shunt impedance value.

SIMULATION COMPARISON

The TFB stripline simulations are compared to that of the tune stripline.

Efficiency Difference

The Excel simulation indicates the new vertical stripline design will produce an electric field 6 times greater than that of the tune stripline, meaning a much higher shunt impedance. This is confirmed by Gdfidl. At 50MHz the TFB stripline shunt impedance is 66.2kΩ while that of the tune stripline is 590Ω. The longitudinal and vertical beam impedances of the TFB stripline and other Soleil equipments are shown in table 1 and 2. Compared to other Soleil equipments like the BPMs or the vertical scraper, the TFB stripline contribution to the vacuum chamber impedance is small.

Table 1: Longitudinal impedance comparison

	Loss V/pC	$\mathrm{Re}(ZL)_{eff}$ Ω	$\mathrm{Im}(ZL/n)_{eff}$ mΩ
TFB stripline	0.075	5.30	1.62
Tune stripline	0.007	0.48	0.27
120 BPMs	0.360	28.80	13.2
V scraper	0.453	32.13	7.03

Table 2: Vertical impedance comparison

	$\mathrm{Re}(ZV)_{eff}$ at $\xi = 0.3$ kΩ/m	$\mathrm{Im}(ZV)_{eff}$ kΩ/m
TFB stripline	0.46	0.88
Tune stripline	0.02	0.03
120 BPMs	2.4	4.8
V scraper	2.8	4.88

The main differences between TFB and tune striplines are due to the transverse geometry. In fact, the TFB stripline has its electrodes very close to the beam. It also has feedthroughs at both ends. The tune stripline has four electrodes at a further distance from the beam (two upper electrodes and two lower electrodes) and they are shorted.

CONCLUSION

We reported on the design of the vertical stripline of the bunch-by-bunch transverse feedback. The challenge is mainly to produce strong kicks with low parasitic mode losses. The tune excitation stripline served as a starting point. The deflecting force has been increased via the shunt impedance. The latter has been evaluated in time domain using GdfidL in a 3D study [3], as well as with a semi-analytical method in frequency domain [2]. Both approaches gave consistent results. Unlike the tune excitation stripline, a 2-electrode structure was adopted for a higher efficiency, despite losing the advantage of working in both transverse planes. The optimised solution in this configuration yields a 66 kΩ shunt impedance at 50 MHz, which is nearly two orders of magnitude larger than that of the tune stripline. It allowed relaxing the output power requirement of the RF amplifiers. However, compared to the tune stripline, its impedance seen by the beam is 10 times greater; this is not a real problem since it remains small compared to other vacuum component of the machine such as the BPMs and the vertical scraper.

AKNOWLEDGEMENT

The authors thank J-L. Marlats and D. Zerbib of the SOLEIL Designing and Engineering Service, as well as our diagnostics colleagues.

REFERENCES

[1] W. Bruns, "The Gdfidl Electromagnetic Field Simulator", http://www.gdfidl.de.

[2] D.A. Goldberg and G.R. Lambertson, “Dynamic Devices: A Primer on Pickup and Kickers”, Lawrence Berkeley Lab., California, Nov. 2001.

[3] A. Gallo, A. Ghigo, F. Marcellini, M. Serio, B. Spataro and M. Zobov "The Transverse Feedback Kicker", DAFNE, INFN, Italy, Dec. 1995.

[4] R. Nagaoka, L. Cassinari, J-C. Denard, J-M. Filhol, N. Hubert, M-P. Level, P. Marchand, C. Mariette, F. Ribeiro, R. Sreedharan (SOLEIL, Gif-sur-Yvette), T. Nakamura, K. Kobayashi (JASRI/SPring-8, Hyogo-ken), "Transverse Feedback Development at SOLEIL", DIPAC 07

FAST ORBIT FEEBACK SYSTEM UPGRADE WITH NEW DIGITAL BPM AND POWER SUPPLY IN THE TLS

C. H. Kuo#, P. C. Chiu, K. H. Hu, Jenny Chen, K. B. Liu, K.T. Hsu
NSRRC, Hsinchu 30076, Taiwan
A. Bardorfer, Instrumentation Technologies d.o.o., Solkan 5250, Slovenia

Abstract

Orbit feedback system of the Taiwan Light Source (TLS) has been deployed for a decade. The loop bandwidth was limited by existing hardware. The system cannot remove perturbation caused by fast source. Therefore, speed of gap and phase change of the conventional insertion devices is restricted to a relatively slow motion. To improve orbit feedback performance, BPM system and corrector power supply are planned to upgrade within a couple of years. The upgrade plan which replaces half of existing analogue type BPM by new digital BPM will be carried out stage by stage but due to limited resource, the BPM system will be a mixed type at this moment. The digital BPM electronics are commercial available by using direct RF sampling technology, FPGA, and embedded control environment running GNU/Linux. The programmable nature of new system is beneficial for multi-mode high precision beam diagnostics purposes. Sub-micron resolution is achieved for averaged beam position measurement with high update rate. The corrector power-supply is also replaced by high performance switching type power supply with wide bandwidth in the same time. The integration of old and new BPM, power supply control for fast orbit feedback will be summarized in this report.

STATUS OF THE EXISTING ORBIT FEEDBACK SYSTEM

Global orbit feedback system was deployed in ten years ago. The early system was composed of two VME crates. One was for BPM data acquisition; the other was corrector feedback control. A DSP module was installed at the corrector control VME crate to execute control rule. To achieve better functionality and ease the maintenance, the system had been modified slightly in 2002. The modified system was composed of three VME crates. The functions of DSP board were moved into a PowerPC CPU module located at the third VME crate which replaced original DSP module to simplify the programming environment.

The orbit feedback system will use measurement of the beam position to compare against a reference orbit and calculate the desired corrections by the error to be applied to the corrector magnets in the storage ring. This procedure must provide global communication that required higher bandwidth than is available in a commercial network. TLS has a control network for slow data acquisition in 10 Hz and a dedicated network for fast data acquisition in 1 kHz. Reflective memory is a solution to access distributed data without required extra processor time for the latter. Coefficients of PID controller which determines feedback loop performance will be assigned properly. SVD is used to obtain inversion of response matrix.

CORRECTOR POWER SUPPLY AND BPM UPGRADE

To satisfy the users' demand in orbit stability, upgrade the orbit feedback system is planned. Corrector power supplies and partial BPM electronics upgrade will be done before spring of 2008. Orbit feedback system will be improved during the course of upgrade.

Corrector Power Supply Upgrade

Corrector power supply of TLS was composed of linear type power supply oringinally. Despite its low efficiency, suffered from high frequency noise for infrared beamline, the power supply had been modified to reduce its loop bandwidth to less than 10 Hz. Nevertheless, loop bandwidth of the orbit feedback system was limited by the power supply bandwidth and the eddy current effect of vacuum chamber. This kind of power supply was also a burden from maintenance point of view due to its dimension and weight. To provide better performance, switching power supply with good performance was adopted. All power supplies for vertical correctors have been replaced by new power supply during shutdown period of early 2007. Figure 1 shows the better performance of switching power supply compared with that of the old type power supply in standard deviation of read back value. As a result, power supply for horizontal corrector will also be replaced in early 2008.

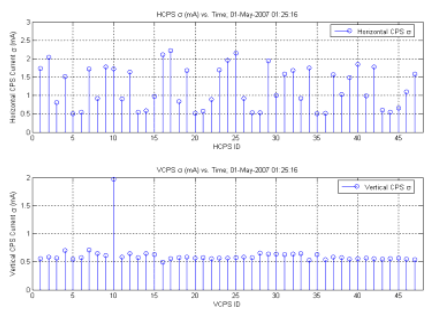

Figure 1: Comparison of steering magnet current read back for old and new corrector power supply.

#chkuo@nsrrc.org.tw

BPM Upgrade

To achieve stringent requirements of orbit stability, TLS has developed and improved orbit feedback system ceaselessly. Our recent efforts are primarily put on electronics upgrade for half of BPM of the storage ring, of which we expect better functionality and performance, to suppress vibration down to sub-micro level and up to 50 Hz. Libera Electron is chosen for this upgrade. Each Libera Electron will be connected to slow orbit acquisition server by means of a private Ethernet link. Another gigabit network switcher is used to access fast orbit and connect to VME CPU board. Fast orbit data is stored in the reflective memory and shared to orbit feedback related VME crates via dedicated fibre link. Testing of Libera Electron was performing during this year and it was planned to be integrated seamless into the existing Bergoz's BPM system [1]. The upgrade is scheduled to be completed no later than early 2008.

NEW ORBIT FEEDBACK INFRASTRUCTURE

The new infrastructure of orbit feedback system consists of several VME crates. Their functions include Bergoz's orbit server VME crate, corrector power supply analog setting and read back VME crate, one feedback computation VME crate. There is another node running PC/Linux served as Libera BPM server for slow data access and management independently of orbit feedback. The precision fast orbit data will be acquired by gigabit Ethernet to three CPU modules equipped with gigabit Ethernet ports. The parallel processing is employed to reduce accumulating latency caused by Libera and data transmission. The number of the CPU modules is therefore adjustable according to the results of latency testing. A group of eight to ten Liberas (one super-period) will send Ethernet packets at 10 kHz rate to a gigabit network switch [2] which serializes these packets and sends them to each CPU module. Fast orbit data is shared by all nodes by reflective memory. Figure 2 shows the hardware configuration of the new orbit feedback infrastructure.

Since precision orbit data from Libera Elecein is in 32 bit format with unit of nano-meter, it is not compatible with the existing system which uses 16 bits ADC to convert measured analog output of Bergoz's BPM. Truncation of 32 bit data into 16 bit format is a provisional solution to compatible with the existing system. It is possible to use the 32 bit data after all of BPMs replaced by Libera Electron in the future.

Fast orbit data from Libera Electron is updated into reflective memory in 10 kHz rate. To accompany with existing 1 kHz orbit feedback loop, the data will be re-sampling at a feedback computation engine. The corrector is updated at 1 kHz rate.

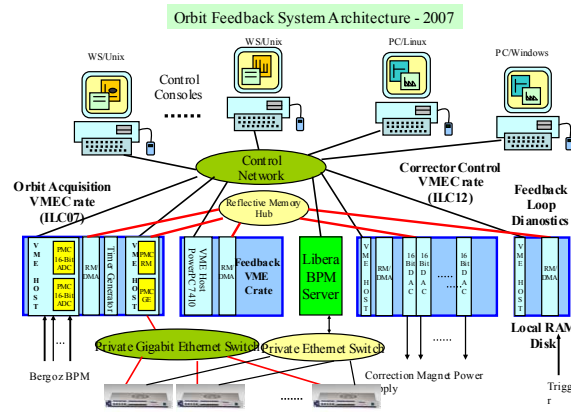

Figure 2. Infrastructure for the orbit feedback system.

PRELIMINARY TEST

To evaluate the performance of the new orbit feedback system, various tests are on-going. Several current efforts are summary in the following paragraphs. Figure 3 shows the set-up for this test.

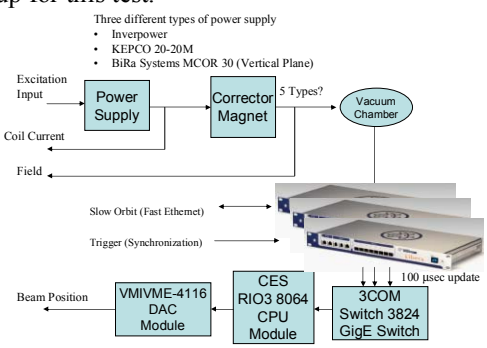

Figure 3. Setup for jitter and response measurement.

Jitter and Performance of GigE Interface

In the real-time system, timing problem is becoming critical in control design and its computer-based implementation as more complicated communication network and stringent speed requirement. It can be categorized three parts: latency delay, sampling jitter and transient errors. Latency delay is primary related to computation and communication delay; sampling jitter is due to assumed constant sampling period but actually time-variant sampling interval; transient errors can result data loss from disturbance in the communication medium.

Our observation implies that the sampling jitter is obvious and never vanishes as process goes on. Research shows that the jitter may degrade the system performance and even lead to instability in the system [3]. In Figure 4, we analyzed the jitter pattern and its distribution. Further research is expected to compensate its possible negative effect.

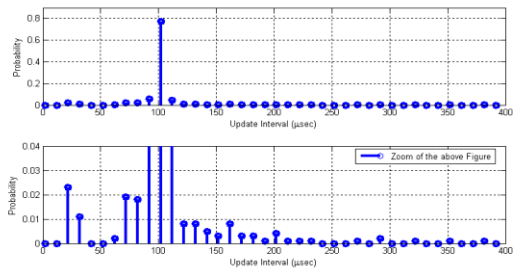

Figure 4. History of the sampling interval for one Libera Electron communicate with VME host.

Since there is one dedicated CPU module for one super-period BPM data acquisition, the GigE interface performance and jitter will vary and depend on how many Libera connected. Test for 10 sets of Libera can guaranteed updated abound 1 msec/update. To improve system efficiency in communication, group of several Libera Electron together and provide better timing of sampling is under way.

System Latency

Latency time of Libera Electron is about 350 μsec. Delay due to communication and computation is estimated around 150 μsec. These delays will not lead any stability problem of the feedback loop. Further simulation will be done soon.

Response Include Beam

To model the system for orbit feedback, except for laboratory measurement of various system components response, response including beam was performed recently. Adopting the similar configuration for jitter measurements, dynamic signal analyzer is employed to measure this response including the beam. Vacuum chamber of the TLS is an 80 mm x 38 mm in major and minor axis respectively. Chamber thickness is 4 mm. There are cooling channels on the major axis direction. Standard TLS vacuum chamber measured response is near to 80 Hz in vertical plane and 20 Hz in horizontal direction. Response including beam in vertical direction with new switching power supply is shown as Figure 5. The notch in magnitude and phase response nearby 1.7 kHz is due to the notch filter designed to remove the glitch of quasi-crossbar switch inside Libera Electron. The -3 dB bandwidth is about 100 Hz in vertical plane while the bandwidth is reduced to less than 20 Hz in horizontal plane with old power supply as shown in Figure 6.

System identification and modelling is still ongoing by means of applying pseudo-random binary sequence (PRBS) or another kind of excitation signals to excite the beam. The system model can be extracted by analysis of the data captured by the Libera Electron.

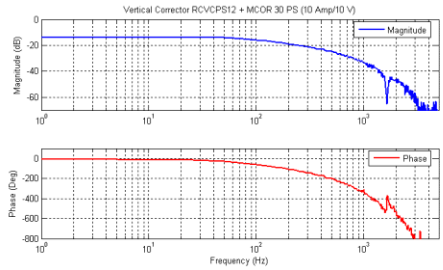

Figure 5. Measured response of the vertical plane with beam.

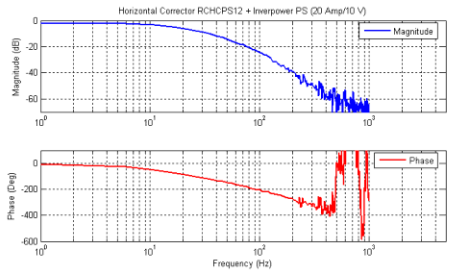

Figure 6: Measured horizontal plane transfer function include beam.

SUMMARY

To achieve a better orbit control and take advantage of latest development, upgrade of orbit feedback system for the TLS is on-going. All of vertical corrector power supplies have been replaced by switching power supplies in February 2007 and the horizontal ones are also planned to upgrade in early 2008. Libera Electron will be integrated into the existing system to enhance functionality and provide precision fast orbit information for orbit feedback purpose. Infrastructure of the orbit feedback system is scheduled and will be finished within 6 months. It is expected that feedback loop can be completed no later than December 2007. It is also expected that this upgrade will provide better orbit control and satisfy users' requirement.

REFERENCES

[1] C. H. Kuo, et al., "Design of a Fast Global Orbit Feedback System for the TLS Storage Ring", 10th ICALEPCS Int. Conf. on Accelerator & Large Expt. Physics Control Systems. Geneva, 10 - 14 Oct 2005.

[2] D. Bulfone, R. De Monte, V. Forchi', G. Gaio, M. Lonza, "Design of a Fast Global Orbit Feedback System for the ELETTRA Storage Ring", 10th ICALEPCS Int. Conf. on Accelerator & Large Expt. Physics Control Systems. Geneva, 10 - 14 Oct 2005.

[3] B. Wittenmark, et al., "Timing Problems in real-time Control System", Proceedings of the American Control Conference, Seattle, Washington, June 1995. p. 2000.

TOROID PROTECTION SYSTEM FOR FLASH

A. Hamdi, M. Luong, J. Novo, F. Ballester, CEA-Saclay, Gif sur Yvette, France
L. Froehlich, M. Goerler, M. Werner, S. Magnus, M. Staack DESY, Hamburg, Germany

Abstract

The FLASH fast machine protection includes a beam loss interlock using toroids to measure the beam charge. This system monitors the beam losses across the whole linac while other protection systems are specifically dedicated to critical components. Four protection modes are used to handle different scenarios of losses: charge validation, single bunch, slice and integration modes. This system is based on 4 ADC's to sample the top and bottom of upstream and downstream toroid signals. A microcontroller drives 2 programmable delay generators to adjust the top and bottom ADC trigger during the calibration phase. Then, the samples are collected by a 200Kgates FPGA to process the various protection modes. At first, a VHDL testbench was developed to generate test vectors at the FPGA design inputs. Then, an electronic testbench simulates the linac signals to validate the global hardware functions. Finally, the toroid protection was tested on FLASH with macropulses of up to 800 bunches and bunch repetition rates of up to 1 MHz.

INTRODUCTION

At FLASH (Free electron LASer in Hamburg), the high average beam power (up to 50 kW) and the small beam size (< 1 mm) require a very fast detection of beam losses in order to avoid any accelerator systems damages. The Toroid Protection System (TPS) is a part of the whole Machine Protection System (MPS [1]). Its principle is to compare across the linac the bunch charge difference to a threshold. The FLASH has two beam lines, FEL and bypass. The FEL beam line is the regular one to produce the SASE* FEL radiation with a wavelength down to 12 nm. The bypass was added to avoid using the undulator and seeding section and for both accelerator research or electron beam commissioning. Each beam line has 2 TPS, as illustrated in the Figure 1.

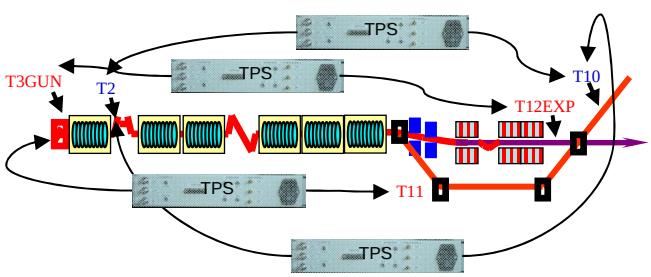

Figure 1: Layout of the TPS for FLASH

* Self Amplified Spontaneous Emission

To validate this system, three approaches were followed: software simulation, hardware simulation and hardware test with beam. First of all, the testbench in VHDL was written to validate the FPGA configuration [2]. A simulation box was designed by DESY-FEA to simulate the signals given by TTF2 (former name of FLASH). This simulation box was applied to the TPS to test the hardware at CEA-Saclay. The last step consists in the integration and the test of the TPS in the MPS at DESY.

HARDWARE DESCRIPTION

Beam charge measurement

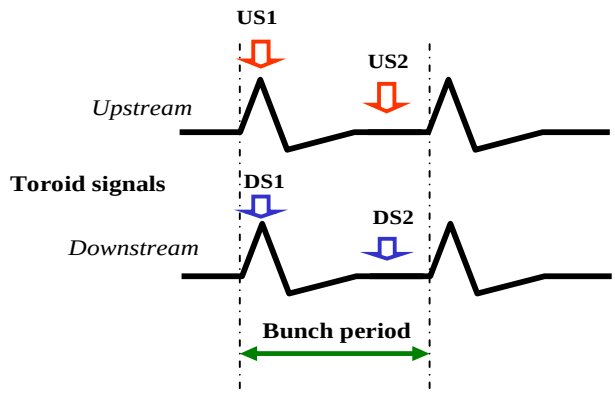

Figure 2: Principle of differential sampling

The top and bottom of upstream and downstream toroid signals (Figure 2) are sampled with four 14 bits AD9240 fast pipeline ADC's. The toroid electronics' sensitivity is 500 mV/nC and the input range of the ADC's is -2 V to +2 V or - 4 nC to +4 nC. This range was chosen to overcome the droops phenomenon due to the inductive response of the toroids. The absolute difference measured between upstream and downstream toroids makes it possible to know the beam losses precisely or if the beam deviates from his trajectory before the downstream toroid. If this case, there is a secondary emission of electrons superior to the number of transmitting electrons. Then, the amplitude of the signal measured by the downstream toroid is higher.

To adjust the top and bottom ADC clocks during the calibration phase, an ADUC812 microcontroller drives 2 programmable delay generators DS1023 by a serial transmission. The samples are collected by a Xilinx FPGA of the Spartan2 family. The FPGA synchronisation of the toroid signals is implemented with shift registers to take account of the ADC latency, the time of flight and

the cabling delay. Then the ADC's digitized values are frozen in a latch controlled by the delayed Bunch Gate signal (derived from the Pockel cells of the photoinjector) before the various protection modes are processed.

Simulation Box

The hardware simulation was done using the Simulation Box based on a design of 2 ALTERA ACEX PLD's. These PLD's are clocked by a 36 MHz internal oscillator. The 9 MHz main clock of the design is produced by this oscillator. Each PLD drives a 14 bits AD9754 DAC which can be run up to 125 MSPS to generate the simulated toroid signals. The remote loading of the design is done directly by the parallel port of a PC. The remote loading protocol is standard JTAG; it can be performed either towards a PROM or towards the PLD by using jumpers. The Simulation Box is able to generate 800 µs macropulses at a repetition rate of up to 10 Hz with amplitudes of the toroid signals (T1, T2) variable from 0 V to 3.5 V and an adjustable offset. Several bunch repetition rates are possible: 1 MHz, 2.25 MHz and 9 MHz. The CLK clock can also be delayed of 256 ns maximum with a 16 ns resolution. The Bunch Gate signal can be delayed by N multiple of 110.8 ns, as well as the delay between toroid signals.

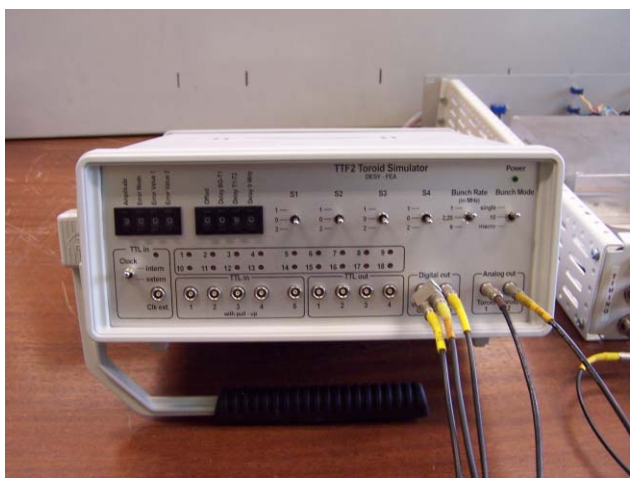

Figure 3: TTF2 Toroid Simulator – designed by Desy-Hamburg

But the major feature is the ability to simulate losses through 4 different modes:

- reduction of the amplitude of each channel individually around 0 to 50 % of the initial amplitude,
- modulation of the outputs by a pseudo random value adjustable of 0 to ±10 %,
- modulation of the output amplitude by a falling ramp; upward gradient within the range 0 to -34 mV/µs (macropulse mode only),
- modulation of the output amplitude by a rising ramp; upward gradient within the range 0 to +34 mV/µs (macropulse mode only).

This TTF2 Toroid Simulator allowed to test the FPGA configuration to set the shift registers to take the time of flight and the transit in the cables into account. Finally, each alarm could be tested in almost the same FLASH conditions saving beam time to other users.

TEST WITH BEAM

The TPS (Figure 4) was integrated to the FLASH MPS [1]. The four alarms for each TPS use an RS422 interface to the BIC (Beam Interlock Concentrator). The BIC is used to concentrate the interlock signals to one signal switching off the laser controlling the gun.

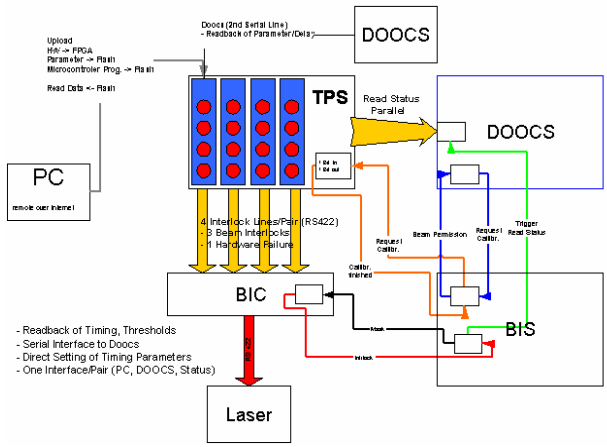

Figure 4: TPS environment at FLASH

The BIS (Beam Interlock System) controls the BIC to enable masking of the alarms or to initiate a calibration of the TPS. A more detailed description can be found in reference [3]. The DOOCS (Distributed Object Oriented Control System) enables to integrate and control all kinds of devices in the accelerator. We used the DOOCS to check the correlation between the alarm triggered by TPS and the amplitude of the toroids.

Test conditions and results

The thresholds were set as follow:

- Charge Validation mode: 0.3 nC,
- Single Bunch mode: 25 %,
- Slice mode: 3 %,
- Integration mode: ~24 nC (i.e 3 % for 1 nC nominal charge).

To measure the noise (toroid electronics', cabling, linac environment, etc…), we switched off the beam, and measured 1500 ADC samples: standard deviations on the toroids were around 2.1 mV. We can expect to get around 4.2 pC resolution with this system.

During those tests, one of the tricky problems we met was the synchronisation before the four channels 14 bits latch (Figure 5). Modifying the threshold values in the FPGA design often leads to a different post place and route design. A new design that couldn't synchronise the

ADC's samples. One way to overtake this error was to set the VHDL attribute value to FAST to the components before the latch and to move all the combinatorial modules after the 14 bits latch.

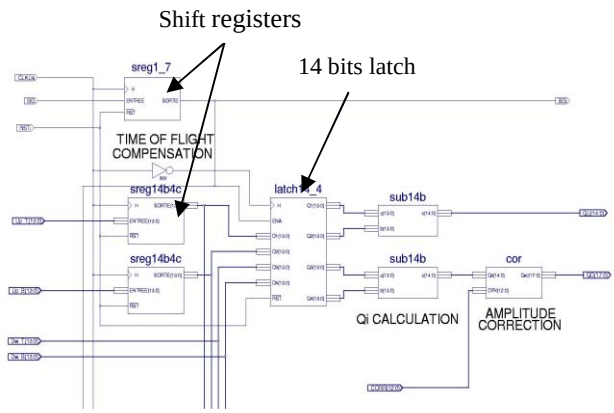

Figure 5 VHDL design for sample synchronisation

The position of a collimator was used to decrease the bunch charge measured at the downstream toroid, thus creating adjustable beam losses. To measure TPS reaction time, the principle was to kick one bunch out of the macropulse. This missing bunch triggers an alarm of the TPS single bunch mode, and we measure three more bunches leaving the gun, before the laser was switched off. Hence, the total reaction time in FEL mode is smaller than 4 µs.

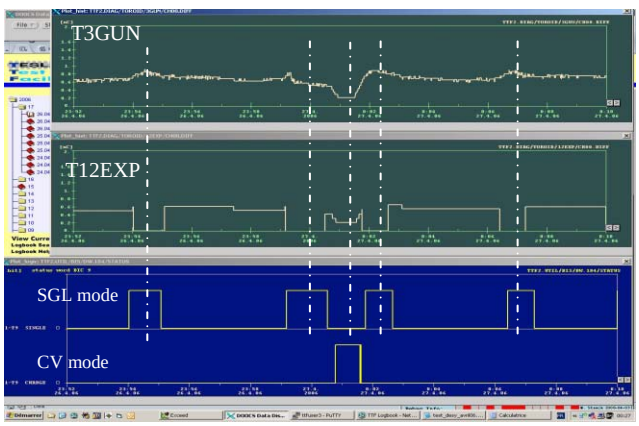

Figure 6 Charge transmission across FLASH linac

The Figure 6 shows the charge measured on the linac for T3GUN and T12EXP vs. time and the correlated alarms triggered on the TPS in blue background. At the bottom, there is a charge validation (CV) mode alarm caused by the weak charge < 0.3 nC on the gun toroid. Just above, the single bunch (SGL) mode alarm fired when the losses exceeded 25 %.

CONCLUSION

The hardware and software were tested with all machine protection modes on the FEL beam line with up to 800 bunches at 1 MHz bunch repetition rate during the FEL studies - KW7. The different steps followed to design and validate the TPS on the linac strongly helped to demonstrate all the functionalities of the system at 1 MHz bunch repetition rate. The design can even be pushed to 9 MHz bunch repetition rate, allowing 7200 bunches in the machine. Actually, the thresholds are set in the configuration program of the FPGA, this could be done using the microcontroller by UART transmission. The FPGA design robustness should be improved with specific timing constraints applied to the worst-case paths.

REFERENCES

[1] L. Froehlich, A. Hamdi, M. Luong, J. Novo, M. Goerler, P. Goettlicher, D. Noelle, D. Pugachov, H. Schlarb, S. Schreiber, M. Staack, M. Werner, "First operation of the flash machine protection system with long bunch trains". In Proceedings of LINAC'06, Knoxville, USA, 2006.

[2] A. Hamdi, M. Luong, and M. Werner, "VHDL design and simulation of a fast beam loss interlock for TTF2". In Proceedings of EPAC'04, pp. 2020–2022. Lucerne, Switzerland, 2004.

[3] D. Nölle, P. Göttlicher, R. Neumann, D. Pugachov, K. Wittenburg, M. Wendt, M. Werner, M. Staack, M. Desmons, A. Hamdi, M. Jablonka, M. Luong, H. Schlarb, "The Beam Inhibit System For TTF II". In Proceedings of DIPAC'03, Mainz, Germany, 2003.

A REAL-TIME BEAM MONITOR FOR HADRONTHERAPY APPLICATIONS BASED ON THIN FOIL SECONDARY ELECTRON EMISSION AND A BACK-THINNED MONOLITHIC PIXEL SENSOR*

L. Badano†, O. Ferrando‡, Fondazione TERA, Milano, Italy
M. Caccia, C. Cappellini, V. Chmill, M. Jastrzab, University of Insubria, Como, Italy
K. Abbas, U. Holzwarth, P. N. Gibson, Institute for Health and Consumer Protection, Joint Research Centre, European Commission, Ispra, Italy
G. Molinari, CERN, Geneva, Switzerland

Abstract

A novel, non-disruptive beam profile monitor for low intensity light-ion beams has been constructed and tested. The system is designed for use in medical hadrontherapy centers where real-time monitoring of the beam intensity profile is of great importance for optimization of the accelerator operation, patient safety and dose delivery. The beam monitor is based on the detection of secondary electrons emitted from a submicron thick Al_2O_3 foil placed in the beam at an angle of 45 degrees. The present paper reports the latest results achieved with a customized back-thinned monolithic active pixel array, which provides the beam intensity and position with a precision of better than 1 mm at a 10 kHz frame rate. The monitor performance has been tested with a patterned beam, produced with a multi-hole collimator, with the results indicating that the system performs according to its design specifications.

INTRODUCTION

Hadrontherapy is a radiotherapy technique using highly accelerated light ion beams (usually protons or carbon) to irradiate tumours. The intense end-of-track Bragg energy deposition peak, together with variations in beam profile and energy, are used to deliver an optimized dose to the tumour minimizing the damage to nearby healthy tissues [1]. Patient safety, accelerator operation, and dose delivery would all benefit if the beam intensity and profile could be continuously monitored in the extraction line during the treatment. An effective device for on-line beam monitoring must produce negligible effects on the few nA clinical beam, featuring a spatial resolution not exceeding 1 mm, a beam current measurement resolution of few percent and a frame rate of the order of 10 kHz [2].

Up to present this has not been possible, since existing interceptive monitors interfere with the beam, causing significant beam disruption for therapeutic kinetic energies (60 MeV to 250 MeV for protons and 120 MeV/nucleon to 400 MeV/nucleon for carbon ions). At the same time non-interceptive instrumentation is not sensitive enough to detect average beam intensities from a few pA to a few nA, with extracted beam durations of the order of 1 s. To overcome this limitation an innovative, non disruptive beam monitor, named SLIM (Secondary emission monitor for Low Interception Monitoring) [3, 4], capable of providing beam intensity and profile measurement during the treatment has been proposed, constructed and tested. The device has been developed in the framework of the SUCIMA (Silicon Ultra Fast Cameras for electrons and gamma sources In Medical Application) project [5] funded by the European Commission. In-beam testing has been carried out at the Cyclotron Laboratory of the European Commission (EC) Joint Research Centre, Ispra, Italy.

Previous attempts to use the secondary emission from thin foils as a mean to measure the main beam parameters can be found in [6, 7, 8, 9]. The devices illustrated in [6, 7] concern only beam intensity measurements, while the detectors described in [8, 9] do not fulfill the hadrontherapy requirements either in terms of beam acceptance (70 mm), or in terms of spatial (1 mm) and time resolution (100 μs).

BEAM MONITOR WORKING PRINCIPLES

The proposed monitor is based on the secondary electron emission from a thin Al foil intercepting the hadron beam path at 45° as shown in Figure 1. The Al foil has a diameter of 65 mm to 70 mm and consists of a support of 0.1 - 0.3 μm of Al_2O_3 coated on each side with 0.01 - 0.02 μm of Al. Ionization of the Al atoms by the hadron beam can result in electrons receiving energy and momentum sufficiently large to escape from the foil surface. Electrons with a kinetic energy below 50 eV are conventionally called secondary electrons (SE). These are the predominant component (85%) of the emission spectrum [10]. An electrostatic field accelerates the SE and focuses them onto an imaging device with a final electron energy in the 10 - 30 keV range and a flux in the 1 - 10^4 e^-/pixel/100 μs range[1]. The op-

*Work supported by the European Commission under the contract G1RD-CT2001-00561.

† laura.badano@elettra.trieste.it, at present with Sincrotrone Trieste, Trieste, Italy.
‡ at present with Ente Ospedaliero Ospedali Galliera, Genova, Italy.

[1]The number of electrons/pixel is independent on the pixel size that is fixed by the required resolution and optical system demagnifying factor; 100 μs corresponds to the required frame rate.

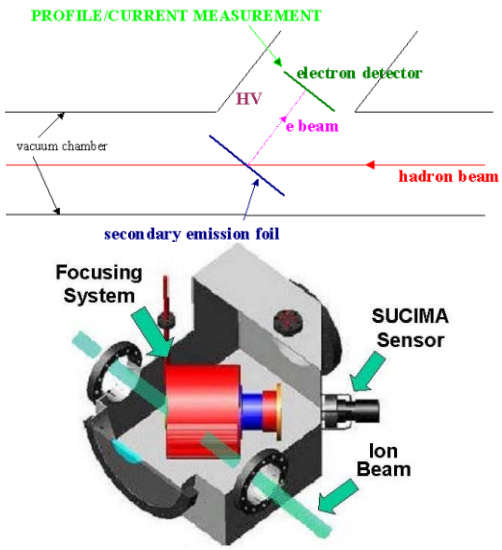

Figure 1: *(a) Schematic drawing of the SLIM (Secondary electron emission for Low Interception Monitoring) beam monitor working principle and (b) of the focusing system prototype inside the vacuum chamber; an arc of the cylindrical cage electrode is covered with 40 μm wires, 4 mm spacing for a 99% transparency to the hadron beam.*

tics for the collection of the SE, the type, the size and the pitch of the electron detector, the front-end electronics and the readout system have been designed to fulfil the beam monitor requirements [11].

The SUCIMA collaboration developed a dedicated CMOS silicon detector, named MIMOTERA (see Table 1) with an area of 17×17 mm^2 and a pixel pitch of ~ 200 μm assuming a focusing system demagnifying factor of about 5. Due to the short range (3 μm in silicon) of low energy electrons, their detection with a CMOS sensor is a challenging task that can be accomplished with a complete substrate removal. In addition to the MIMOTERA tests, a before commercially available system, that does not feature the required frame rate, has been used to measure the electrostatic lenses optical properties. It consists of a MCP (micro-channel plate) coupled to a phosphor screen and a CCD (charged coupled device) [3].

Table 1: *MIMOTERA main characteristics*

Size [pixels]	112×112
Pixel pitch	$153 \times 153\,\mu$m^2
Frame rate	10 kHz
Parallel analog output	4 channels
Technological process	$0.6\,\mu$m AMS CUA
Epitaxial (sensitive) layer	$\sim 14\,\mu$m
Dynamic range (20-keV e$^-$)	$1 - 10^4$e$^-$/pixel/100μs

Low energy electron detection in a silicon sensor has been demonstrated as follows:

- sensitivity to beam current variations has been measured with a hybrid, moderate granularity pad sensor [12] read out with a high dynamic range charge integrating ASIC [13];
- profiling capability has been investigated relying on the dedicated monolithic CMOS sensor.

This paper refers to the first results obtained with the MIMOTERA sensor mounted in the SLIM monitor on the Ispra cyclotron beam line, using a 17 MeV proton beam.

EXPERIMENTAL RESULTS

Preliminary tests of the electrostatic focusing system were first performed using thermionic emission from a hot tungsten wire as a source of electrons [14]. The experimental results confirm that the optical properties are in good agreement with the computer simulations and fulfill the SLIM beam monitor requirements [3, 11].

The full system testing is being carried out at the Scanditronix MC40 cyclotron of the EC Joint Research Centre located in Ispra (Italy). The cyclotron is capable of accelerating various light ions up to an energy of 39 MeV (for protons) with a beam intensity in 5 nA - 50 μA range. With no loss of generality and considerable cost saving, initial tests were performed with a standard Al sheet about 10 μm thick[2]. The SLIM was initially tested on beam with the commercial MCP, phosphor and CCD system. Following the commissioning, the pad sensor was integrated to assess the sensitivity to beam current fluctuations [3].

As a second stage spatial granularity and sensitivity of the system were studied integrating the backthinned MIMOSA CMOS sensor MIMOTERA. Images of 17 MeV proton beams with 10-nA intensity were acquired and analyzed. The beam energy was chosen for the most efficient use of the beam time slots in between commercial radioisotope production without the need of readjusting the accelerator parameters. The secondary emission efficiency with 17 MeV primary proton is expected to be at $\sim$10% [11].

The data acquisition was based on a custom developed DAQ system [15]. The response of the SLIM was studied by inserting in the beam path a 12 mm-thick Al collimator with six rows of 1 mm-diameter holes and pitches from 1.5 up to 6.5 mm as shown in Figure 2(a). During the test with the MIMOTERA, the secondary electrons were accelerated to 10 keV giving to a sharper image on the on-line display. The recorded image on the CMOS sensor is shown in Figure 2(b).

The image is the average of 500 frames (100 μs/frame readout time) after pedestal subtraction and the color scale represents the signal intensity for each pixel. The image appears tilted by about 210° in agreement with the mounting scheme of the sensor on the focusing system. Hot spots corresponding to the collimator holes are clearly visible.

[2]Since the secondary emission is a surface effect, the replacement of the Al foil will not modify the secondary emission yield and energy and angular spectra.

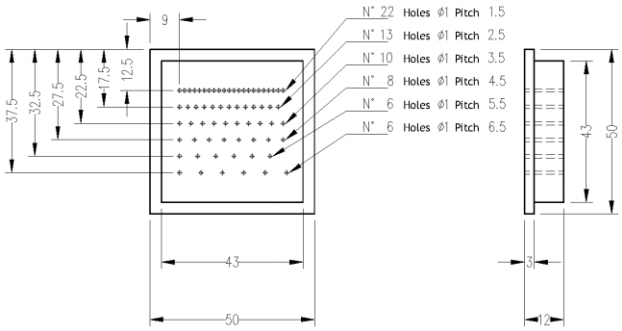

(a) Collimator

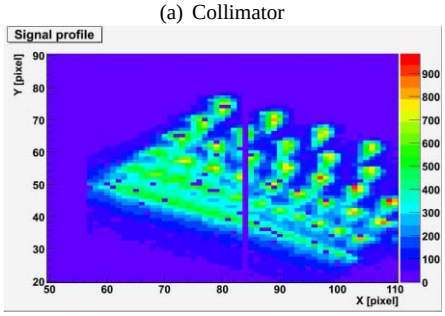

(b) Contour image

Figure 2: *(a) Schematic drawing of the collimator placed in the beam path, consisting of a 12 mm-thick aluminium block with 6 rows of holes of 1 mm diameter. The hole pitches range from 1.5 up to 6.5 mm. (b) An image of the beam profile on the SLIM monitor as detected by the CMOS sensor. According to the mounting scheme of the sensor on the focusing system the image appears tilted by* $210°$*. The gray scale on the right represents the mean analogue signal stored in each single pixel.*

The demagnifying factor was measured by comparing the peak separations on the sensor with the real pinhole separations - the resulting value was 4.3. The discrepancy with respect to the nominal value of 5 might be due to a shift in the detector position with respect to the simulated focal plane, due to mechanical constraints. It might be also due to aberration effect since the image is off-centered with respect to the sensor centre.

Different explanations for the high level of signal in between the adjacent hot spots have been envisaged, such as background ionizing radiation field in the extraction line beam pipe, divergence of the proton beam after passing through the collimator, together with forward scattering of the beam from the front edges (incident beam side) of the holes in the collimating block or thermionic electron emission from the Al foil caused by primary beam heating.

Tests and calculations demonstrate that none of the above effects can account for the observed signal. Since the blooming effect is certainly present, to exclude an electronics misbehaviour of the sensor due to an oversaturating secondary electron flux or a distortion of the electrostatic field due to charge-up of the insulating parts of the focusing system, beam tests with the collimated beam and the commercial detector are scheduled as well as further studies of the background signal origin.

CONCLUSIONS

A beam monitor, innovative in terms of beam acceptance, spatial and time resolution for real time diagnostics of charged particle beams in the extraction lines of a hadrontherapy centre has been designed, developed and tested. The laboratory tests with thermionic electrons have demonstrated that the focusing system optical properties fully satisfy the requirements in terms of linearity, demagnifying factor and resolution. The results of the first measurements on a cyclotron proton beam with both the phosphor screen viewed with a CCD camera and a pad sensor for the secondary electrons detection were successful. The latest experiment using as a detector the dedicated ultrathin back-illuminated CMOS sensor sensitive to 20 keV electrons has been performed with promising results. Further tests to identify the origin of the observed background signal are underway.

REFERENCES

[1] J. Castro, Hadrontherapy in Oncology (U. Amaldi and B. Larsson eds, Elsevier Science Pub. Co., Amsterdam, 1994).

[2] L. Badano et al., Nucl. Instrum. Meth. A430, 512 (1999).

[3] L. Badano et al., IEEE Trans. Nucl. Sci. 51, 133 (2004).

[4] L. Badano et al., IEEE Trans. Nucl. Sci. 52, 830 (2005).

[5] M. Caccia et al., Nucl. Phys. B (Proc. Suppl.) 125, 133 (2003).

[6] C. Fernandez-Figueroa and G. Molinari, 3rd European Particle Accelerator Conference (EPAC 92), Berlin, 1992.

[7] C. Chianelli et al., Nucl. Instr. Meth. A273, 245 (1988).

[8] E. P. Marsh, M. D. Strathman, D. A. Reed, and R. W. Odom, Proceedings Accelerator instrumentation, Batavia, 213 (1990).

[9] J. Bosser et al., CERN SPS/ABM/Note 1987-06 (Tech), Geneva, 1987.

[10] D. Hasselkamp et al., Particle Induced Electron Emission II (Springer-Verlag, Berlin, 1992), 60 - 62.

[11] L. Badano, Development of a Novel Beam Monitor for Real-time Measurements of Hadrontherapy Beams, PhD thesis, Strasbourg, 2005 (http://eprints-scd-ulp.u-strasbg.fr:8080/497/).

[12] A. Braem et al., Nucl. Instrum. Meth. A478, 400 (2002).

[13] VASCM2 data sheet V 0.9 (downloadable at: http://www.ideas.no).

[14] A. C. Melissinos, Experiments in Modern Physics (Academic Press, New York, 1966).

[15] A. Czermak et al., Astroparticle, particle and space physics, detectors and medical physics applications, 360 365, World Scientific, 2004.

DIAGNOSTICS OF THE WAVEFORM OF PICOSECOND ELECTRON BUNCHES USING THE ANGULAR DISTRIBUTION OF COHERENT SUB-MM TRANSITION AND DIFFRACTION RADIATION*

A.G. Shkvarunets+, R.B. Fiorito, University of Maryland, College Park, MD U.S.A.
F. Mueller, V. Schlott, PSI, Villigen, Switzerland

Abstract

The spectra of sub-mm wavelength coherent transition radiation (TR) and diffraction radiation (DR) have previously been used to measure the bunch length of picosecond electron beam pulses. However, both the spectral and angular distributions of the radiation from a finite target with dimension r, are strong functions of the wavelength, when $\lambda \approx 2\pi r/\gamma$ where γ is the relativistic factor of the beam. This dependence must be taken into account to determine the bunch form factor and bunch shape. Also the spectral density of the bunch is a strong function of wavelength when $\lambda \approx d$, the characteristic length of the bunch. When both the above conditions are fulfilled, i.e. $\lambda \approx 2\pi r/\gamma \approx d$, the angular distribution (AD) of the radiation is very sensitive to the longitudinal distribution of the bunch. We are investigating the use of the AD, rather than the spectrum of TR or DR, to diagnose the bunch length and shape. Here we present a comparison of measured and calculated angular distributions (projected on the plane of observation) from two targets: a solid rectangle and a rectangular slit, which we have used to determine the bunch length of PSI's SLS pre-injector LINAC for two different beam tunes.

THEORETICAL BACKGROUND

TR from a radiator whose dimensions are close to the radiation impact parameter $\gamma\lambda$ is closely related to DR via Babinet's principle [1]. We have calculated the spectral angular intensities of coherent TR from a finite size solid rectangular radiator and coherent DR from a rectangular radiator with a rectangular slit.

The TR and DR radiation fields can be calculated by assuming that, the source of these fields are the fields induced by the electron on the solid surface of the radiator. In cylindrical coordinates the longitudinal Fourier components of the electric field of a relativistic electron in free space can be written as:

$$E_r(r,\varphi,z,\omega) = E(r,\omega)\exp(i\omega z/V) \qquad (1)$$

where $E(r,\omega) = e\alpha K_1(\alpha r)/\pi V$, $K_1(\alpha r)$ is the first order MacDonald function, e is the charge of the electron $\alpha = \omega/V\gamma$ and the velocity of the electron V is parallel to the axes z [2].

We will assume that the induced surface fields radiate to the vacuum and that the field radiated into free space can be found using the Huygens-Fresnel principle. Thus, the components of the electric field parallel and perpendicular to the (x,z) or horizontal plane at the observation point p are given by:

$$E_{P,\perp}(p) = \frac{k}{2\pi i}\int_{S'}\frac{a_{P,\perp}\cos\nu\cdot\exp(ikR'))}{R'}dS' \qquad (2)$$

Where $a_P = E(r',\omega)\cdot\exp(ikz'/\beta)\cdot cos\varphi'$ and $a_\perp = E(r',\omega)\cdot\exp(ikz'/\beta)\cdot\sin\varphi'$ are the complex amplitudes of the components of the electron electric field on the tilted surface S', R' is the distance from surface element dS' to the observation point p and r',φ',z' are the coordinates of the surface element $dS' = r'dr'd\varphi'/\cos\nu$, ν is a tilt angle of the surface, $k=\omega/c$ is the modulus of the wave vector, ω is the frequency of the radiation and c is the speed of light in vacuum [3].

We assume that at moderate distance from the radiator where $R' >> \sqrt{S'}$ and $kR' >> 1$ the radiation does not differ from a spherical wave and the field can be found using Eq. (2). In this work we calculate the integral in Eq.(2) numerically. The spectral energy density at the point p on a flat observation plane, averaged over the period of oscillation is given by:

$$J_{P,\perp}(\omega,p) \propto \left|E_{P,\perp}(\omega,p)\right|^2\cos\vartheta \qquad (3)$$

where ϑ is the angle of incidence of the spherical wave on the observation plane. For each target the code calculates a set of 100 distributions in the relevant frequency band (25 - 2525 GHz), where coherent emission of radiation is expected from a short electron bunch. Some of these are shown in Fig. 1 for CDR.

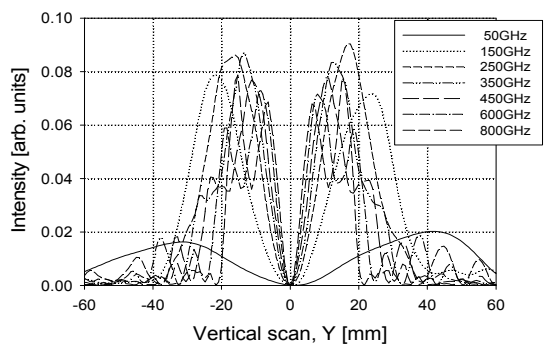

Figure 1: Spectral energy density (projected angular distribution) of CDR for various frequencies.

*Work supported by US Office of Naval Research
+ shkvar@umd.edu

Calculation of CDR intensity for a bunch

Assume that a longitudinally modulated electron beam hits the target and radiation of each particle has the same distribution of the Fourier component of the field $E(\omega, p)$ with the same initial phase at the moment of impact. In this case the total radiation field of the bunch of electrons is

$$E_\rho(\omega, p) = E(\omega, p)\int \rho(z)\exp(ikz/\beta)dz \qquad (4)$$

where $\rho(z)$ is longitudinal distribution of the bunch. The spectral density is then given by

$$J_\rho(\omega, p) = J(\omega, p)K(\omega) \qquad (5)$$

$$K(\omega) = \left|\int_{z1}^{z2} \rho(z)\exp(i\omega z/V)dz\right|^2 \qquad (6)$$

where $K(\omega)$ is the longitudinal form factor of the beam. The energy density in the spectral interval (ω_1, ω_2) is given by

$$W(p) = \int_{\omega 1}^{\omega 2} J(\omega, p)K(\omega)d\omega \qquad (7)$$

In the case of a "finite" target, and/or within the "near field" of the radiation [3], the intensity J is a function of frequency. As the result, the energy density Eq. (7) is a function of the form factor of the beam. By comparing the measured and calculated distributions one can determine how close the model predicts the real waveform of the beam. In this work we use a single Gaussian distribution to model the waveform of the bunch, i.e. $\rho(z) = \rho_0 \exp(-z^2/2\sigma^2)$, where $\sigma = 0.425L$ and L is the full width at half maximum; the pulse duration $T = LV$. For each L or T the code calculates the form factor and the energy density and compares the measured (7) and calculated energy distributions. Typical distributions for the CDR target integrated over the frequency band 25 – 2525 GHz are shown in Fig.2.

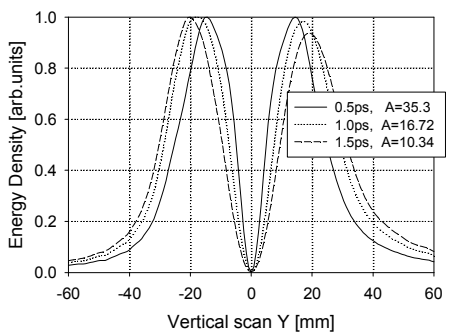

Figure 2: Energy density distribution of CDR for various pulse widths; A is the amplitude for each case.

One can see that the shorter is the pulse, the narrower and more intensive is the distribution.

EXPERIMENTAL METHOD

Measurements of the transverse emission distribution of CDR and CTR were performed at the ALIDI-SM-5 optical monitor station behind the 100 MeV pre-injector LINAC of the Swiss Light Source (SLS). While the LINAC is usually running in the top-up operation mode of the SLS, it was set-up to a "short bunch mode" for the CDR-CTR measurements. Single-shot electro-optical bunch length measurements at the same optical monitor station have resulted in bunch lengths between σ_{PBU-0} = 0.75 ps and σ_{PBU+3} = 1 ps, depending on the setting of the pre-buncher phase [4]. Here, PBU-0 corresponds to the optimum phase setting for shortest bunches and PBU+3 corresponds to a 3° phase offset from this optimum setting. Results of the CDR-CTR measurements shown in the final paragraph of this paper have been obtained with comparable LINAC settings.

Optical Monitor and Measurement Set-Up

A specific radiator has been designed for the measurements at the ALIDI-SM-5 optical monitor station providing well defined emission characteristics for CDR and CTR. At its upper position, the radiator houses a YAG:Ce scintillation screen, which is typically used for beam profile and emittance measurements. The CTR radiator is a plane and polished Al surface (λ/10 at 630 nm) and the CDR radiator consists of a 10 mm rectangular slit within the polished Al surface. All edges are chamfered to avoid diffraction. A mechanical drawing of the radiator is shown on the right side of Fig. 3.

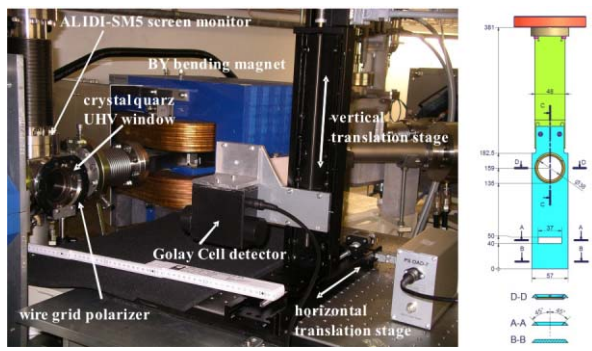

Figure 3: Experimental set-up at ALIDI-SM-5 optical monitor station (left), CTR-CDR radiator (right)

The radiator was mounted in the UHV chamber under 45° so that the backward CDR and CTR is reflected out of the UHV system through z-cut crystal quartz window, which provides good transmission above 100 μm (3 THz) wavelength. The 100 MeV electron beam has been focused on the radiator and the vertical radiator positions could be adjusted by a motorized linear vacuum feedthrough with a precision of better than 10 μm. At a distance of 430 mm from the radiator, a Golay cell detector was scanned horizontally and vertically by two motorized linear stages. The polarization of the radiation was selected by a wire grid polarizer, which was placed directly behind the UHV window. A photograph of the set-up is shown on the left side of Fig. 3.

DATA FITTING PROCEDURE

The goal of our fitting procedure is to achieve the best value of L which provides a 'best fit' of theory and experiment. The essence of this procedure is to scale the calculated scan $T(y)$ by a constant A until the best fit of the theoretical scan to the data scan $E(y)$ is obtained. To do this we have written a code to compare the similarity of the two functions $A \cdot T(y) > 0$ and $E(y) > 0$ in the interval (y_1, y_2) defined in terms of integral deviation defined as:

$$D(A) = \left[(y_2 - y_1)^{-1} \int_{y_1}^{y_2} \left(\frac{A \cdot T(y) - E(y)}{A \cdot T(y) + E(y)} \right)^2 dy \right]^{1/2} \qquad (8)$$

The closer the functions $A \cdot T(y)$ and $E(y)$ are to each other, the smaller is the value of D. We define the maximum similarity (RMS) of the two functions when $D(A)$ is at its minimum value, as $RMS = D(A_{\min})$. For each L the code calculates value of $RMS(L)$. Minimum value of $RMS(L)$ corresponds to the best fit of theoretical and experimental distributions and corresponding value of L is the best fit of the model to the width of the bunch.

RESULTS AND ANALYSIS

The result of our fitting procedure for the case of beam tune PBU-0 for CTR and CDR are shown in Fig. 4 and Fig. 5. Here the finite aperture of detector (~10mm in diameter) is taken into account. Fig. 4 shows the energy distributions for the best fit of theory to the experimental data. Calculations using Eq. 8 shows that the minimum RMS integral deviation (5% and 8.6%) occurs at a value of bunch widths T=0.69 and 0.78 ps for the CTR and CDR data respectively (Figs 4 and 5).

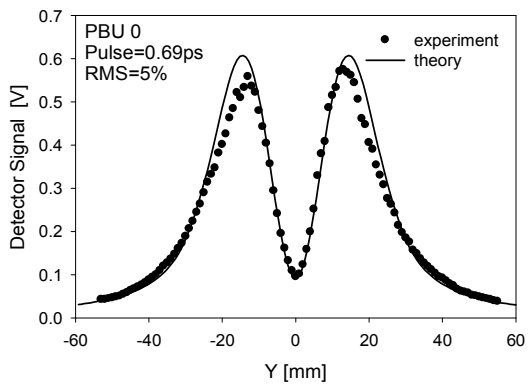

Figure.4: Energy distribution of CTR for tune PBU-0.

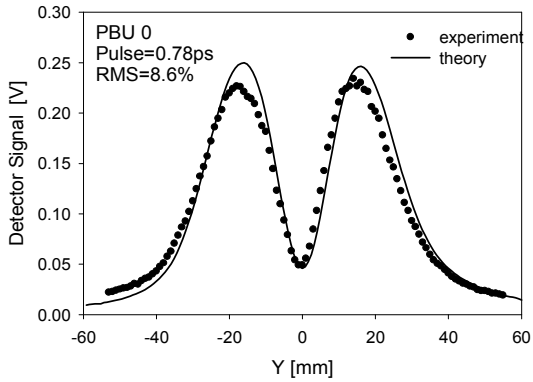

Figure 5: Energy distribution of CDR for tune PBU0.

Table I: Fitted Parameters

Target	Tune	T(ps)	RMS,%
CTR	PBU-0	0.69	5
CTR	PBU+3	1.1	9.1
CDR	PBU-0	0.78	8.6
CDR	PBU+3	1.07	10.7

Table I. shows the fitted bunch lengths T, for CTR and CDR targets for both beam tunes PBU-0 and PBU+3. There is excellent agreement for bunch sizes determined using the two radiation sources.

CONCLUSIONS

We have used the angular distributions of CTR from a finite rectangular solid and CDR from a rectangular slit to determine the beam bunch length of the SLS pre-injector LINAC for two different beam tunes. Both types of radiation produce the same results for each tune and show that the angular distribution alone can provide the bunch size without the need for spectral or interferometric measurements. If a linear or 2D array is used to obtain the data, a single shot determination of bunch size may be possible with this method providing the potential for an online diagnostics of bunch length and bunching along an X-FEL LINAC.

REFERENCES

[1] R.B. Fiorito and D. W. Rule, Nuc. Instrum. and Methods B, 173, 67 (2001).

[2] A.G.. Shkvarunets, R.B. Fiorito and P. G. O'Shea, Nuc. Instrum. and Methods B, 201, 153 (2003).

[3] R. B. Fiorito and A.G. Shkvarunets, T. Watanabe, V. Yakimenko and D. Snyder, Phys. Rev ST Accel and Beams, 9, 052802 (2006).

[4] D. Sütterlin, " Single Shot Electron Bunch Length Measurements with a Spatial Electro-Optical-Auto-Correlation Interferometer using Coherent Transition Radiation at the 100 MeV SLS Pre-Injector LINAC", PhD-thesis, Diss ETH Nr. 16668, ETH-Zürich 2006

SYNCHRONIZATION OF 3GHZ REPETITION RATE HARMONICALLY MODE-LOCKED FIBER LASER FOR OPTICAL TIMING APPLICATIONS*

L. Banchi#, F. Rossi and M. Ferianis, ELETTRA Sincrotrone, Trieste, Italy
A. Bogoni, L. Potì and P. Ghelfi, CNIT, Pisa, Italy.

Abstract

We have successfully stabilized a 3GHz Harmonically Mode-Locked fiber ring laser by a PLL feedback control of the cavity length to reduce the pulses RMS timing jitter. The laser cavity is composed of all PM fibers and components to eliminate polarization instabilities and to reduce the vibration sensitivity. The laser stability in terms of timing jitter was around 9ps in the range 10Hz-10MHz. Using a PLL scheme we synchronized the laser repetition rate to an ultra stable RF generator. The noise characteristics of the laser output were measured by observing the SSB noise spectra of the 1st harmonic, from 10Hz to the Nyquist frequency (1.5GHz). We have obtained a global reduction of fiber laser timing jitter value down to less than 100fs in the range 10Hz-10MHz; a complete overlapping between the laser and the RF generator spectral profiles in the loop bandwidth has been observed. An extended investigation has been performed to estimate the phase noise spectra and timing jitter up to 1.5GHz. By doing so, the contribution of the laser supermodes to the phase noise has been taken into account as well, to quantify the true value of the total RMS timing jitter of the optical pulses.

INTRODUCTION

FERMI is the fourth generation Light Source that is currently being designed at ELETTRA. The timing system will play a crucial role in achieving the expected performance in Linac based FELs due to the sub-ps electron bunch length and to the expanded use of fs-lasers as key components in future light sources. Optical timing systems currently seem to be the only technique to enable an RMS jitter at the 10fs level. A fundamental component of the system here analyzed is the optical reference oscillator.

Within EUROFEL DS3 design study, CNIT Pisa developed an "ad hoc" fiber ring laser source: this source works in regenerative Harmonic Mode-Locking (HML) at 3GHz. Currently it is the only one Optical Master Oscillator in the accelerator community working at 3GHz. At ELETTRA, a PLL system ha been developed to decrease the HML fiber laser Phase Noise and RMS Timing Jitter. An extended investigation has been performed to estimate the phase noise spectrum and timing jitter up to 1.5GHz.

HML FIBER LASER SETUP

The HML fiber laser setup is shown in fig. 1. The cavity is composed by an Optical Band Pass Filter (OBPF) that selects the wavelength, an Optical Isolator and an Erbium Doped Fiber Amplifier (EDFA). The laser cavity is composed of all PM fibers and components to eliminate polarization instabilities and to reduce the vibration sensitivity. The fiber laser under test is thermal stabilized. The cavity length is around 63m, that means a mode spacing about 3.18MHz (f_0).

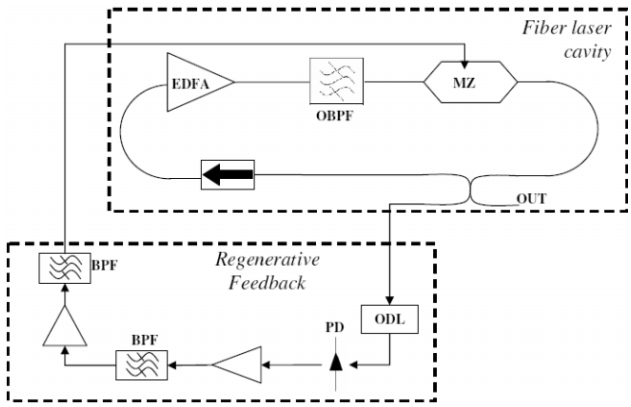

Figure 1: Fiber Laser cavity and Regenerative Feedback; Erbium Doped Fiber Amplifier (EDFA), Optical Band Pass Filter (OBPF), Electrical Band Pass Filter (BPF) Mach Zehnder modulator (MZ), Isolator, Optical Delay Line (ODL), Photodiode (PD).

The stable mode-locking condition is achieved using a Regenerative Feedback loop that selects the 942nd harmonic, this signal drives the Mach Zehnder modulator (MZ) imposing the laser repetition rate of 2.997GHz (f_c). With the Optical Delay Line (ODL) in the regenerative feedback it is possible to adjust the phase of the extracted harmonic respect to the phase of the cavity mode.

PHASE-LOCKED LOOP

A Phase Locked Loop (PLL) is a negative feedback system where an oscillator-generated signal is phase and frequency locked to a reference signal [1].

PLL is a powerful system that can provide elegant solution in many applications such as: skew suppression, frequency synthesis, clock recovery and jitter reduction [2].

The PLL scheme is shown in fig. 2. In these measurements we adopted as Master Oscillator (MO) a low phase noise RF generator (Anritsu MG3692), as Phase Detector a dual balanced mixer (ZX05-2-42). The role of the Voltage Controlled Oscillator (VCO) was covered by the HML fiber laser and the Piezo fiber stretcher (Optiphase PZ2-HE). The piezo fiber stretcher dynamically changes the cavity length to make the laser

* This work has been partially supported by the EU Commission in the Sixth Framework Program, Contract No. 011935 – EUROFEL.
# luca.banchi@elettra.trieste.it

repetition rate equal to the MO frequency. In particular the piezo fiber stretcher introduces a maximum delay of 10ps on the cavity round trip time, which means a fiber length increasing of 3.04mm. Using this piezo fiber stretcher it is possible to correct the fiber laser repetition rate of 130kHz around its nominal frequency (f_c). The *capture range* (Δf_{MAX}) of our system is 250kHz, this is the maximum frequency difference for which the loop locks. By varying the attenuation (LOSS) it is possible to change the phase detector gain (K_{PD}), thus the PLL gain changes to reach the locked state.

The two different frequencies, one taken from the MO and the other from the regenerative feedback, beat at the mixer and generated the Phase Error Signal. The phase error signal is amplified (Gain) and processed by the Proportional-Integrative (P-I) regulator. The gain factor of each arm of the P-I regulator has been adjusted to obtain a stable loop response. When the PLL is locked the I-arms compensates the phase drift. The DC-offset adds a DC voltage offset to the error signal to force the PZT fiber stretcher to work in the middle of the stretching range.

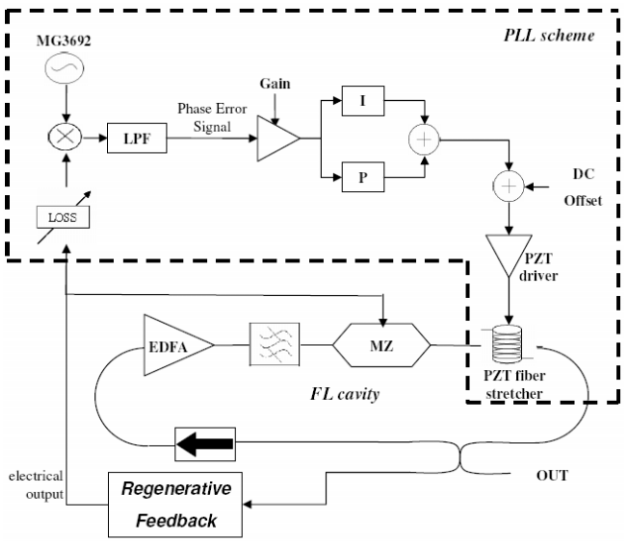

Figure 2: Phase Locked Loop scheme where the VCO is the fiber laser.

EXPERIMENTAL RESULTS

The usefulness of the Harmonically Mode-Locked (HML) laser is highly dependent on the output stability, which makes stabilization and noise characterization crucial for practical applications.

In HML lasers there are two kinds of phase noise contributions depending on the correlation between the pulses inside the cavity: *correlated noise* and *uncorrelated noise*. Correlation of noise on different pulses can arise from: gain dynamics, composite cavity HML lasers, RF oscillator noise [3, 4]. To characterize the correlated noise we photodetected the optical pulses with a photoreceiver (NewFocus 1544B) and we observed the photoreceiver output signal on the Agilent SSA E5052A performing an out-of-loop analysis. The SSB phase noise power spectral density ($L(f)$) has been integrated from 10Hz up to 1.6MHz ($f_0/2$) when the PLL was OFF giving an RMS timing jitter about 9ps. When the PLL was locked the RMS value of the timing jitter decreased to 98fs (J_{corr}). This value is perfectly in accordance with the specification for the narrow band timing application such as: S-band structure, Photoinjector laser, streak camera driver [5]. In fig. 3 the SSB phase noise spectral profile of the HML laser is compared, up to 40 MHz, with its RF reference: a complete overlapping between the two phase noise spectral profiles in the loop bandwidth (1kHz) has been observed.

A strong reduction of "low frequency" contributes of phase noise occurs when the HML fiber laser is stabilized with the PLL.

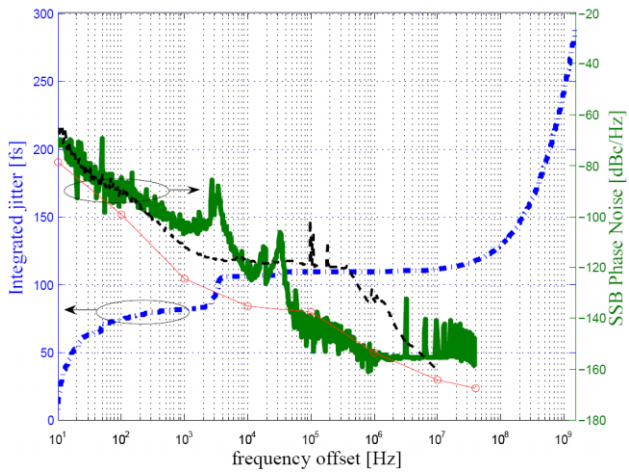

Figure 3: Left axes: integrated RMS timing jitter up to 1.5GHz (tick dashed line). Right axes: SSB phase noise of the HML laser (solid line) and the reference MO (dashed line). Interpolated SSA phase noise floor (circle).

The peak of phase noise at 3.5kHz is due to the PLL dump oscillation, the peak at 30kHz is the laser relaxation oscillation, the peaks beyond 3MHz are the supermodes.

In HML laser uncorrelated noise arises because spontaneous emission and vacuum fluctuation on different pulses are independent. The consequence of the uncorrelated noise is the formation of peaks in the HML laser spectrum at multiple of the f_0, called supermodes [3, 6, 7]. The supermode phase noise peaks contribution increases significantly timing jitter of the HML laser when they are used in wide band applications such as: cross-correlation, seeding, optical sampling. There are N-1 identical noise peaks in a bandwidth equal to the pulse repetition frequency (f_c), where $N=f_c/f_0$. The RMS value for the pulse timing fluctuations due to the supermodes can be obtained by the integration of phase noise PSD over a bandwidth equal to f_0 centred on the supermode, then multiplying the results by square root of N [3]. Experimentally we analyzed the 1st supermode measuring the residual phase noise respect the cavity feedback signal. The experimental setup is showed in fig. 4; where the phase shifter ($\Delta\varphi$) was used to maintain the quadrature between the two mixer (ZX05-2-42) inputs to reduce AM noise [8, 9]. The mixer output was amplified by a series

of two amplifiers (ZFL-1000LN, ZFL-1000) to increase the spectrum analyzer sensitivity.

The RMS value of the timing jitter of a single supermode is 12fs and the total contribution of the uncorrelated noise (J_{unc}) is 265fs up to 1.5GHz.

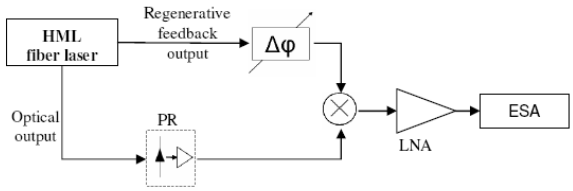

Figure 4: Residual phase noise measurement setup; phase shifter ($\Delta\varphi$), photoreceiver (PR), low noise amplifier (LNA), spectrum analyzer (ESA).

The global timing jitter (J_{RMS}) of the HML fiber laser RMS is 283fs, according with $J_{RMS}^2 = J_{corr}^2 + J_{unc}^2$ [3]. In fig. 3 we report the RMS timing jitter of the HML fiber laser as a function of the frequency offset from the carrier integrated up to 1.5GHz.

Moreover the long term stability of the locked system has been observed. The PLL remain locked for tens of hours and it has a good capacity to recover the locking as showed in fig. 5.

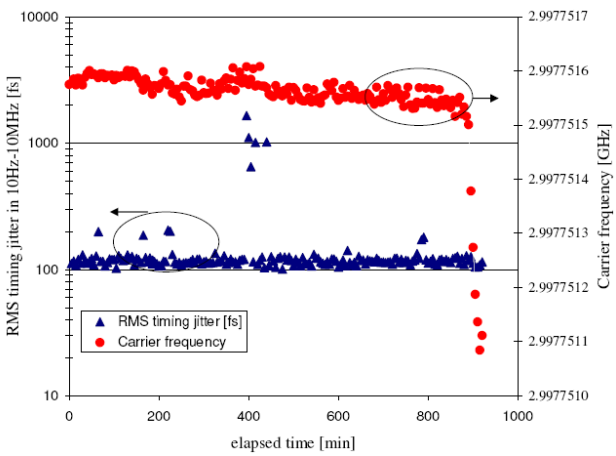

Figure 5: Long term stability of the locking: RMS timing jitter (triangle), carrier frequency drift (circle).

The RIN of the HML laser has been estimated by measuring the spectrum of the photocurrent at baseband a with network analyzer (Standford SR780). The network analyzer provided the AM noise spectrum with no PM noise present. We obtained a RIN of 0.35% integrating the RIN spectral profile, showed in fig. 6, in 10Hz-100kHz.

The PLL stabilization of the laser repetition rate does not have any effect on the amplitude noise of the laser in agreement with [8].

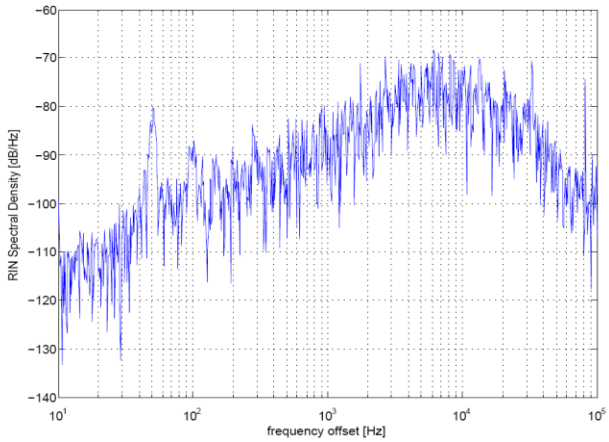

Figure 6: RIN of the HML fiber laser.

CONCLUSIONS

With this work we have performed a complete characterization of the phase noise of the HML fiber laser up to the Nyquist frequency (1.5GHz), and the characterization of the amplitude instability of the laser up to 100kHz

Using a PLL system we locked the 3GHz repetition rate HML fiber laser with a RF master oscillator. In this way we reduced the timing jitter of the laser down to 100fs. We reached the reference oscillator intrinsic RMS timing jitter limit in the PLL bandwidth. Moreover the PLL has showed strong long term stability and a good recovery capacity.

REFERENCES

[1] D. Fischette, "Practical Phase-Locked Loop Design", ISSCC Tutorial. (2004)

[2] B. Razavi, "Monolithic phase-locked loops and clock recovery circuits. Theory and Design", Wiley Interscience.

[3] F. Rana, *et al.*, "Characterization of the noise and correlation in harmonically mode-locked lasers", Journal Opt. Soc. Am., Vol. 19, pp.2609 (2002).

[4] D. von der Linde, "Characterization of the noise in continuously operating mode-locked Lasers", Appl. Phys. B 39, 201-217. (1986)

[5] M. Ferianis, "FERMI Timing and Synchronization", FERMI Conceptual Design Report, cap. 9.

[6] M. E. Grein, *et al.*, "Observation of quantum-limited timing jitter in an active, harmonically Mode-Locked Fiber Laser", Optics Letters, vol.27 pp.957.

[7] N. Onodera, "Supermode beat suppression in harmonically mode-locked erbium doped fibre ring lasers with composite cavity structure", Elect. Lett. Vol.33 pp.962-963, (1997).

[8] R. P. Scott, *et al.*, "High-dynamic-range laser amplitude and phase noise measurement techniques", IEEE Journal on Selec. Topics Quant. Electr., vol.7 pp.641-655, (2001).

[9] T. R. Clark, *et al.*, "Phase noise measurements of ultrastable 10GHz harmonically modelocked fibre laser", Elett. Lett. V.35 pp.720, (1999).

PROGRESS OF THE DIAGNOSTICS AT THE PROSCAN BEAM LINES

R. Dölling, PSI, Villigen, Switzerland

Abstract

Operation experience, improvements and new variants of the PROSCAN beam line diagnostics as well as an improved profile-evaluation technique are reported.

INTRODUCTION

PROSCAN, the dedicated new medical facility at PSI using proton beams for the treatment of deep seated tumours and eye melanoma, has restarted routine operation with Gantry 1. Further beam lines will be commissioned in this year. Air and N_2 filled ionisation chambers (IC) and secondary emission monitors (SEM) in several configurations are used as current, profile, halo, position and loss monitors (Fig. 1, [1, 2]). New variants of a multi-leaf Faraday cup (MLFC) and an IC position monitor will be used at the beam line to OPTIS 2.

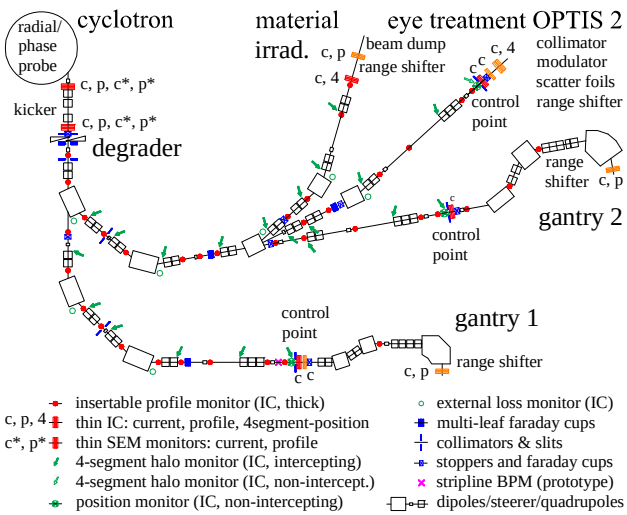

Figure 1: Overview of beam lines and diagnostics.

STATUS AND OPERATION EXPERIENCE

During commissioning and operation, the diagnostics performed as intended. It contributed only negligibly to the unscheduled down time of the facility. The sensitivity, accuracy and speed of the various IC monitors fully suit the requirements. Comprehensive online beam information as well as fast surveillance options are already available, but are not fully used in the present stadium of the project. The self-tests of the diagnostics are still unavailable, awaiting changes in the logarithmic amplifier modules and support by the control system.

The thin IC current and profile monitors in front of the degrader are, together with the thin current monitors at the "control points" and the stoppers, the most important diagnostics of the beam lines. The high chamber voltage gradient of 2 kV/2 mm is sustained reliably without arcing. Nevertheless, after months of operation, the high voltage at the detector decreased due to leakage currents caused by silver dendrites growing over the ceramic insulation gaps at the thick film plated foil carriers. This electrochemical migration caused by minimal remnants of hygroscopic solder flux and air humidity was remedied by improved cleaning and using a flow of dry nitrogen (1.5 litre/h) instead of ambient air as the chamber gas. The other thin IC current monitors based on FR4 carriers are not affected and are still operated in ambient air.

At low beam currents, microphonic noise significantly adds to the signal currents of the thin SEM in front of the degrader and averaging would be required for accurate current determination. This is not needed since the SEM is only used as backup to the thin IC monitors for the case of high current densities. Nevertheless, the saturation effects at the IC monitors are lower than expected [2] and hence the SEM can be viewed as solely redundant.

The possibility to adapt the strip configuration of the retractable thick multi-strip ionisation chamber (MSIC) profile monitors to the local beam width proved useful.

NEW COMPONENTS AND TECHNIQUES

Ionisation Chamber Position Monitors

Three variants of 4-segment IC position monitors (ICPM) will be operated at the PROSCAN beam lines: A conventional IC made from 12 µm thick aluminised Kapton foils with one of the measurement electrodes segmented to 4 quadrants, at the exit of the material irradiation beam line. Non-intercepting position monitors of only 9 mm diameter with intercepting circumferential 4-segment halo monitors, at the control points in front of the gantries [2]. A non-intercepting position and halo monitor at the control point in front of OPTIS 2 (Fig. 2). All are operated with a high voltage of 2 kV in ambient air.

Figure 2: 4-segment ICPM. The electrode configuration from outside to the centre is: ground/high voltage/halo-monitor/position-monitor (= centre electrode). The position monitor covers the full radius of 21 mm, while the halo monitor is fed only from the outer 8 mm. The separatrix splitting the active length of 58 mm between both results from the electric field configuration.

Since the ICPM output depends on the beam size, the absolute position can be estimated only roughly, while the beam centering still can be controlled accurately (Fig. 3).

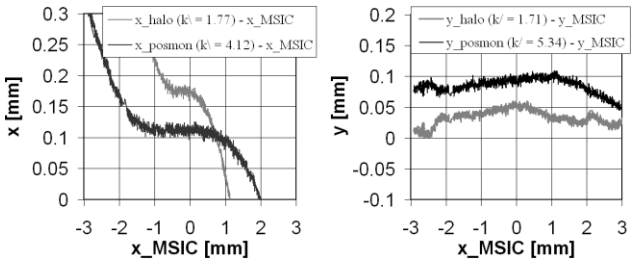

Figure 3: Horizontal and vertical beam position determined from a halo and position monitor of the gantry control point type, referenced to the position from a close-by MSIC. The beam is scanned horizontally. Integration time 20 ms/point. k-values are fitted for horizontal central slopes. (From [2], where erroneously all numbers were shown too large by a factor of 10.) The differences stem from misalignments or errors of the current readings: ±5% current error at the halo monitor or ±3% at the ICPM yields ~±0.1 mm position error in the worst case.

Multi-Leaf Faraday Cups

The beam energy can be determined by a MLFC [3]. After gaining experience with in-air prototypes [4, 5], two variants of in-vacuum MLFCs [6] were built. The latter consist of 64 copper sheets separated by 75 μm Kapton foils and are mounted on compressed-air actuators. The 64 currents are fed to the outside and processed as in the case of the MSIC. Since there is no active cooling, the beam power has to be limited to ~200 kJ/day. Using an electrode at the bottom of the detector head, a voltage pulse can be coupled capacitively to the copper sheets, allowing for a check of the whole system without beam.

The two variants use different sets of sheet thicknesses. Both cover the full energy range of the degrader (Gantry-MLFC: 68 - 252 MeV, Optis-MLFC: 65 - 255 MeV) but the Optis-MLFC uses the thinnest copper sheets of 0.1 and 0.2 mm to improve the resolution in the range of 65 - 85 MeV.

The layout evolved from the following concurrent aspects: The peak should distribute to only a few sheets, giving high enough signals (>>10 pA) even at low beam currents (~500 pA). The ratio of the fwhm peak width w_{peak} to the width of a single sheet w_{leaf} should be larger than 1 for an accurate evaluation (see next chapter). The number of sheets is limited to 64 for a simple realisation.

The total peak width can be estimated from the contributions σ_{stragg}[mm] = 0.0105 R of the straggling in copper and σ_{beam}[mm] = 3.2 dp/p R from the beam momentum spread dp/p as w_{peak}[mm] = 2.35 $\sqrt{\sigma_{stragg}^2 + \sigma_{beam}^2}$ (with Range R [mm]) [5]. The chosen layouts are depicted by Fig. 4. In the low energy range of the Optis-MLFC the peak-to-leaf width ratio is large enough for an accurate evaluation already at dp/p = 0. For the Gantry-MLFC a dp/p of 0.2 - 0.5% is needed to reach the crucial ratio of 1.

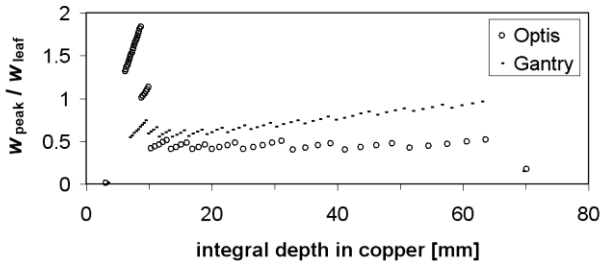

Figure 4: Peak-to-leaf width ratio of the 64 sheets for dp/p = 0. (Data points in copper sheet centres. 75 μm Kapton taken as 16.5 μm copper).

With an assumed overall position accuracy of 0.08 bins (see next chapter) and the given copper sheet thicknesses, the absolute position accuracy of the MLFCs can be estimated. The accuracy expressed in mm H_2O equals roughly the copper sheet thickness in mm at the peak location divided by 2 (Fig. 5). The results for the Optis-MLFC are: 0.05 mm H_2O in the range of 35.5 - 50.7 mm H_2O (65 - 79 MeV) and 0.1 mm H_2O in the range of 50.7 - 58.4 mm H_2O (79 - 86 MeV).

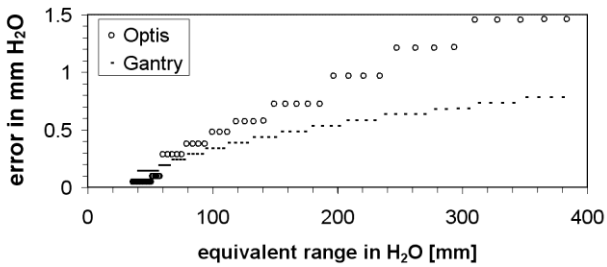

Figure 5: Estimated accuracy of evaluated peak position.

Evaluation of Histograms

Histograms resulting from the measurement of a beam profile with a MSIC or of an energy spectrum with a MLFC are routinely evaluated for beam centre and width. A step-shaped distribution is generated following the shape of the histogram except for the broader outer strips, where a special correction is required. For narrow beams, the beam width calculated from the second moment of the distribution is corrected by an empirical formula [1].

Nevertheless, from the MLFC energy spectra, the underground must be eliminated by ignoring the distribution if it is below a certain cut-off level. Here, the step-shape causes increased errors of position and width and hence a smoother distribution is needed. Nicely smooth area-true representations of histograms are delivered by shape-preserving histopolation algorithms as treated in [7]. On the other hand, the determination of the emittance by the varied-quadrupole method needs a more accurate evaluation of the width of very narrow beams. When this profile width decreases to or below the bin width of the histogram, a priori information on the profile shape is required. Since it is likely that the beam profile resembles a Gaussian, we propose here a "Gaussian histopolation" algorithm. It is based on the fact that for any three positive currents of three contiguous bins (not necessarily of the same width) of a histogram, an area true approxima-

tion by the function

$j(x) = j_0\, e^{-(x-x_0)^2/(2\tilde{s})}$ with $-\infty < \tilde{s}, x_0 < \infty$ and $j_0 \geq 0$

exists. This function is used as a representation for the central bin of the three. An iterative routine is used for each bin to find the parameters $j_0, \tilde{s}, x_0$. Since its present implementation is slow, only off-line evaluations could be done so far. The both outermost bins of the histogram are approximated by a straight line as shown in [1], since this is more reliable in giving a plausible shape than extending the functions of the second outermost bins. Since the algorithm needs non-zero positive bin currents, a minimum bin current is introduced, corresponding to the lower range limit of the logarithmic amplifiers of ~10 pA. In return, the corresponding line current density is subtracted from the resulting distribution.

The algorithm excels in the case of very narrow distributions of nearly Gaussian shape, but is also advantageous in the general case. The fact that the resulting curve is not strictly continuous is of minor importance as long as the beam parameters are derived from moments.

Fig. 6 depicts the evaluation of a simulated distribution (which resembles a MLFC energy spectrum) by the step-shaped distribution ("histogram") and by the Gaussian histopolation, both using a cut-off level of 25% of its peak value. Fig. 7 illustrates the advantage of the smoother distribution. Fig. 8 indicates a position accuracy of the order of ~0.05 bins and a width accuracy of ~20% if the fwhm width of the main peak equals or exceeds the bin width. Error-free current readings are assumed, with a signal sum of 2.5 nA (the beam current of Optis). At very low beam currents (~200 pA), when the 10 pA range limit is not negligible, the errors are larger by a factor of 2 - 3.

For longer integration times (~1s), the accuracy of the current readings of the logarithmic amplifiers depends only on the calibration and the long term stability. With the aspired current accuracy of ±2% [8] the position accuracy decreases to the order of 0.07 bins while the width accuracy is only moderately affected (Fig. 8).

For the MLFC, the individual copper sheet thicknesses have been determined by weighing. The errors introduced thereby are below those from the current measurements.

Similar results were obtained starting from other plausible simulated distributions. An overall accuracy of 0.06 - 0.1 bins can be expected, depending on the current errors.

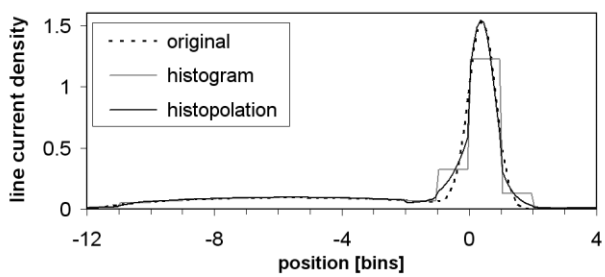

Figure 6: Gaussian histopolation to the histogram of an original distribution (dotted). The fwhm width of the main peak $w_{peak} = 2.35\ \sigma_{original}$ equals the bin width w_{bin}.

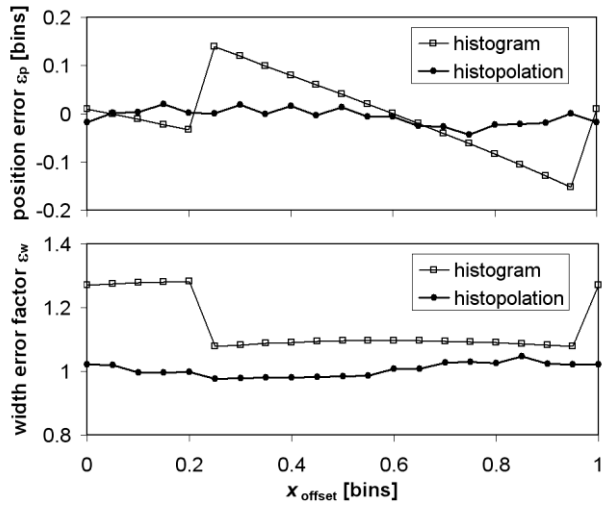

Figure 7a, b: Position error $\varepsilon_p = x_{evaluated} - x_{original}$ and width error $\varepsilon_w = \sigma_{evaluated} / \sigma_{original}$ in dependence on the relative position x_{offset} of the original function of Fig. 6 to the histogram grid.

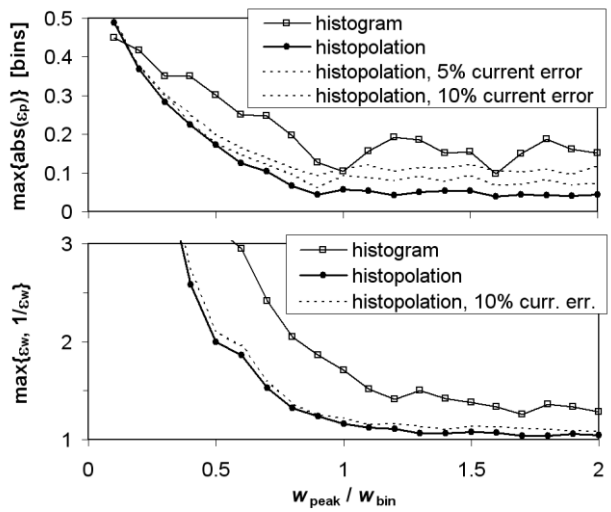

Figure 8 a, b: Maximum position and width errors as from Fig. 7 for a varied width of the main peak of the original distribution. The indicated errors of the histogram bin currents are placed such as to maximise their effect.

ACKNOWLEDGEMENT

I like to thank M. Rohrer for the thorough mechanical design and R. Erne, G. Gamma and B. Rippstein for mounting and wiring of the MLFCs and ICPMs.

REFERENCES

[1] R. Dölling, AIP Conf. Proc. 732 (2004) 244.
[2] R. Dölling, AIP Conf. Proc. 868 (2006) 271.
[3] B. Gottschalk et al., Med. Phys. 26 (1999) 2597.
[4] H. Berkhoff et al., PSI Sci. Rep. 2003, vol VI, p. 103.
[5] P. Wittendorp, PROSCAN Docum. P24/WP85-401.
[6] R. Dölling, PROSCAN Document P24/DR84-619.1.
[7] P. Costantini, F. Pelosi, Adv. Comput. Math. 26 (2007) 205.
[8] P. Duperrex et al., AIP Conf. Proc. 732 (2004) 268.

A SELF CALIBRATING REAL TIME MULTI-CHANNEL PROFILE MONITOR FOR THE ISIS PROTON SYNCHROTRON

S.J.Payne, P.G. Barnes, G.M. Cross, A. Pertica and S.A Whitehead.

ISIS Diagnostics Section, Rutherford Appleton Laboratory, Chilton, Didcot, Oxfordshire, OX11 0QX, UK

Abstract

A +ion 'multi-channel' (gas ionisation) profile monitor (MCPM) has been developed at the Rutherford Appleton Laboratory to capture 'real time' beam profile data within the accelerating ring of the 800MeV ISIS proton synchrotron. The MCPM uses an array of 40 electron multipliers (Channeltrons), operating at a gain of ~10^4, to measure transverse beam profile data in the horizontal plane. The data obtained is an average of two rotations of the beam bunch, a limitation due solely to the speed of the +ions. Fast electronics and a multi-channel PXI / LabVIEW data acquisition system are used to simultaneously process and display 40 channels of beam profile information. Variations in the channeltron's gain are dealt with using an independent motor driven +ion detector. The beam profiles obtained from this single detector are stored and used as a calibration file to correct data obtained from the new multi-channel profile monitor.

INTRODUCTION

At ISIS the accelerator ring (gas ionisation) profile monitors use a single electron multiplier, a Channeltron [1], to measure the +ion current from the proton beam / residual gas interactions. At ISIS this equates to a +ion flow of around 200pA per sq. cm into the electron multiplier at beam centre. The Channeltron is stepped across the top of the proton beam in 6mm increments and the +ions are swept into the monitor using a high voltage drift field (typ. 30kV). Real time profiles cannot be obtained because the mechanical system takes several minutes to complete each scan. A new multi-channel detector has now been developed which uses an array of 40 fixed Channeltrons, that span 240mm across the beam path, to simultaneously collect beam profile information over a single 10ms ISIS acceleration cycle. The new monitor is located in the same stainless steel vessel as one of the original motorised beam profile monitors. Calibration problems with the multi-detector array have been taken care of by using the single channel profile monitor as a calibration tool. This is possible since the gain of the single detector does not vary during a scan. Data acquisition is achieved using a fast sampling PXI system [2] which can simultaneously sample all 40 channels at 100µs intervals over the 10ms acceleration cycle. Performance of the electronics / PXI systems can be checked using a newly developed computer controlled MCPM simulator. The simulator also allows further development of the complete data acquisition system in the absence of a proton beam.

THE DETECTOR

The new profile monitor has been built using 40 miniature Channeltrons (figures 1 & 2). The Channeltrons are mounted in ceramic blocks, 10 to each block. Each block is powered by its own dedicated power supply. The Channeltron aperture is 15.75mm x 4.5mm and the centre to centre spacing of these electron multipliers is 6mm - giving a total span across the beam of 240mm. In front of the detectors is an earth shield (not shown) that has a slot cut into it and which allows the +ions through to the Channeltrons.

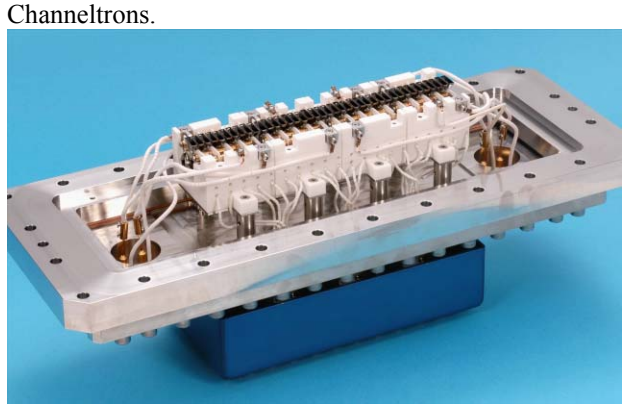

Figure 1. Multi-channel Profile monitor consisting of 40 miniature electron multipliers covering 240mm across the proton beam path.

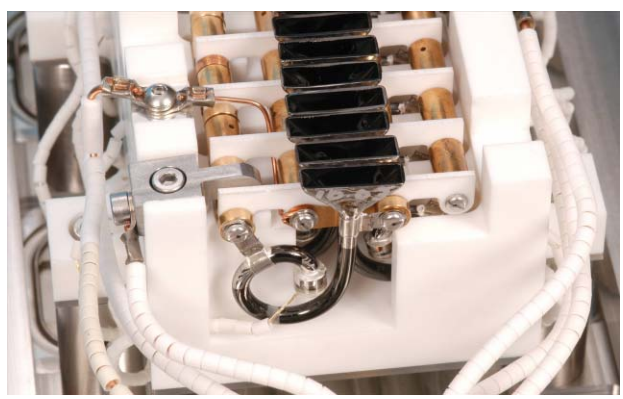

Figure 2 Close up the electron multipliers (Channeltrons)

Individual ceramic blocks were used in order to make construction of the MCPM simpler and provide a means of 'coarse' calibration. The middle two blocks (i.e. the middle 20 Channeltrons) will see more +ion current, since

they cover the centre of the beam, and so their gain will fall off more quickly than that of the outside 20 Channeltrons. This fall in gain over time can be compensated for by adjustments to the individual power supplies. Final calibration is carried out by the MCPM calibration system.

DATA ACQUISTION SYSTEM

The data acquisition system consists of the electronic hardware, a PXI (PC based DAQ system) running LabVIEW and a Vsystem Vista Control System [3]. The output current of the Channeltrons, under normal beam conditions, varies from tens of nA near the beam edge to 2.5µA at beam centre. The electronics front end of the MCPM system consists of a set of 40 pre-amplifiers which convert the Channeltron current into a voltage (0 – 10V dc). The output of the pre-amplifiers is sampled 100 times (at 100us intervals) over the 10ms ISIS acceleration cycle. Any of the 100 profile samples can be selected and sent to a multiplexer which will display the 'raw' profile on an oscilloscope. The complete set of 100 sampled profiles is sent to the PXI controller via a set of five, 8 channel, 14 bit analogue to digital PXI-6133 cards.

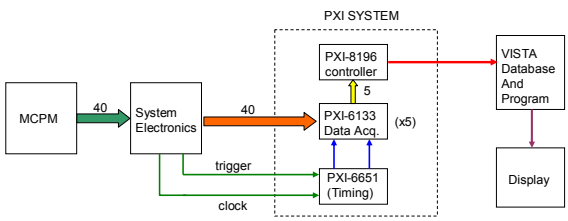

Figure 3 Layout of data acquisition system (see [2] for PXI module details)

The PXI system will display any selected profile and will also give the beam position and beam width numerically, for a single profile at a selected time, and graphically for data representing full 10ms acceleration cycle. The PXI places the results into a system database which can be accessed by the Vista Control System computer. This computer provides the main beam profile display.

When the operator presses the run button on the Vista Control screen (figure 4) the PXI reads the beam profile data, carries out the calibration, and stores the results in a database. The PXI also calculates the beam centre and 90% beam width of each profile and stores it in the database. In figure 4 the data is displayed as a single profile at a user selected time, 1ms in this case (top left); the whole 100 samples over the 10ms acceleration cycle (top right); the beam position, over 10ms (bottom left) and the beam width, over 10ms (bottom right). The Vista screen includes controls to manage the voltage of the Channeltron power supplies, the high voltage drift field, and provides a means of averaging the profile data over *n* beam pulses if required.

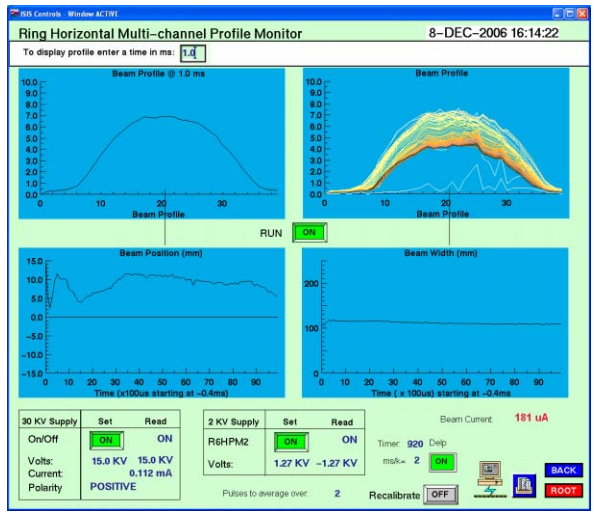

Figure 4. VISTA display

MCPM CALIBRATION

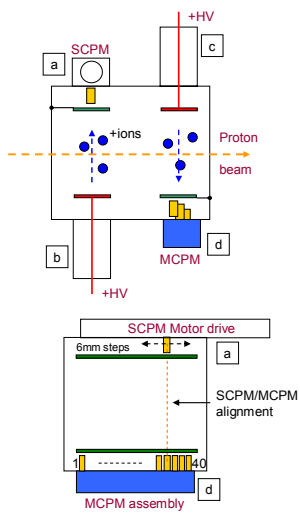

Figure 5. Calibration schematic

The motorised profile monitor, shown schematically in figure 5, produces a beam profile by moving a single Channeltron across the top of the beam in 40 equal steps of 6mm. Each stepping point is in exact alignment with one of the 40 fixed Channeltrons in the MCPM. The outputs from every fixed and moving Channeltron 'pair' are sampled and recorded. The ratio of these results is then stored as calibration data. All MCPM data can then be software corrected to produce an accurate beam profile.

Figures 6a and 6b show the effect of calibration. In figure 6a the raw data is displayed. It can be seen that

there is no real discernable profile. This is due to the relatively large variations in the Channeltron gains. In figure 6b the profile is recovered using the calibration file.

A second profile monitor has been built (for the vertical plane) using 40 Channeltron electron multipliers mounted in 10 blocks of 4 . Each set of 4 Channeltrons have been factory matched (BURLE Industries www.burle.com) so this problem with the raw data should be much reduced. This option of having the matched electron multipliers was not available first time around.

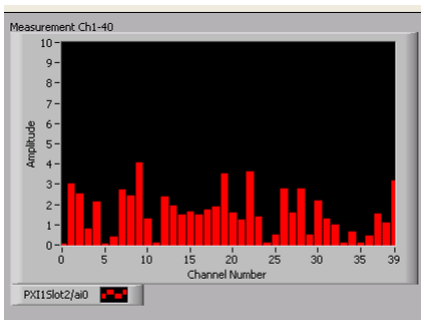

(6a)

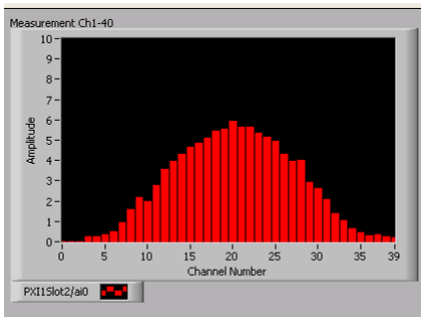

(6b)

Figure 6 – raw (a) and calibrated (b) beam profile data

MCPM SIMULATOR

The MCPM project involved developing, from the ground up, the detector and all electronics and computer hardware and software. Since no part of the system was proven, a MCPM simulator was constructed to produce exactly the current outputs (over the 40 channels) that would be expected from the real monitor. This meant that all electronics and computer hardware and software could be proven prior to the commissioning of the MCPM.

The simulator is a PIC based microprocessor that can provide authentic beam profiles of any width and beam position. It can be switched into circuit should a problem arise with the profile monitor system so as to ascertain whether the fault is with the MCPM or the electronics / PXI or computer systems. Development of the electronics and software can also be carried out during times when the synchrotron is shut down by switching in the MCPM simulator.

Creation of the beam profiles is achieved using a spreadsheet (Microsoft Excel). The user enters an initial (symmetrical) profile and then edits the width and position of the profile as required. The output profile data files are uploaded into the microcontroller. To generate the required output profile digital potentiometers have been used to adjust the output level of each channel as required (figure 7). The 40 potentiometers (one for each channel) have been daisy-chained together and are all programmed by the microcontroller.

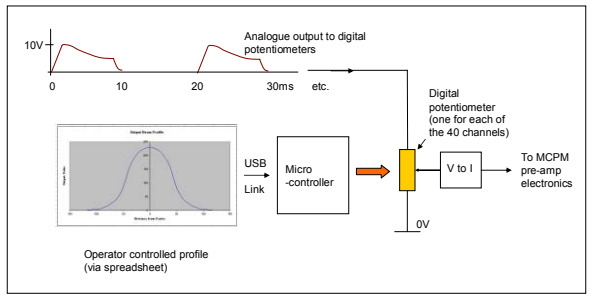

Figure 7 MCPM Simulator channel control

In order to simulate the real multi-channel profile monitor as much as possible an analogue input (from a programmable signal generator) is used to provide the source for the profile outputs. This means the simulator can mimic the +ion intensity fall off that occurs, with increasing beam energy, during the 10ms acceleration cycle. The voltages across the potentiometers are buffered before being passed through a V-I converter to provide an accurate simulated input to the MCPM electronics.

SUMMARY

The MCPM has shown the ability to capture real time beam profile data in the ISIS proton synchrotron. The use of a single channeltron profile monitor as a calibration tool means that the MCPM can easily be kept fully calibrated regardless of the aging of the channeltrons. Further multi-channel profile monitors are being constructed, the first being a vertical monitor a few meters downstream of the horizontal beam profile monitor reported here. A faster profile monitor measuring electrons is being considered for the future to capture turn by turn beam profile data. The detector will be essentially the same; the use of magnetic fields and shaping electrodes for the electric field would be the main differences.

REFERENCES

1) See ‘Channeltron Electron Multiplier handbook’, BURLE industries, www.burle.com
2) See National Instruments www.ni.com
3) Vista Control Systems, 176 Central Park Square, Los Alamos, NM 87544 USA www.vista-control.com

TRANSVERSE BUNCH-BY-BUNCH FEEDBACK FOR THE VEPP-4M ELECTRON-POSITRON COLLIDER

V. Cherepanov, E. Dementev, E. Levichev, A. Medvedko, V. Smaluk, D.Sukhanov,
Budker Institute of Nuclear Physics, Novosibirsk, Russia

Abstract

Transverse mode coupling instability (TMCI or fast head-tail) is the principal beam current limitation of the VEPP-4M electron-positron collider. For the high-energy physics experiments at the 5.5 GeV energy, the VEPP-4M bunch current should exceed much the TMCI threshold. To suppress transverse beam instabilities, a broadband bunch-by-bunch digital feedback system is developed. The feedback concept is described, the system layout and first beam measurements are presented.

HEAD-TAIL EFFECTS

For high-energy physics experiments in the 5.2-5.5 GeV energy range, design value of the VEPP-4M beam current is 40 mA per bunch in $2e^- \times 2e^+$-bunch operation mode. At the injection energy of $E = 1.8$ GeV, the beam current is limited by the vertical transverse mode coupling instability (TMCI or fast head-tail) [1]. There is an approximate formula for the TMCI threshold current derived using a two-particle model [2]:

$$I_{tmci} = \frac{\sigma_z}{\sqrt{2\pi}R}\frac{8\pi\frac{E}{e}\nu_s}{\sum_k \Im Z_{\perp k}\beta_k}, \qquad (1)$$

where σ_z is the r.m.s. bunch length, R is the average machine radius, ν_s is the synchrotron tune, and $\sum_k \Im Z_{\perp k}\beta_k$ is the beta-weighted broad-band reactive impedance of the ring. For the VEPP-4M at the injection energy, the threshold current is 10-12 mA.

If a machine chromaticity $\xi = \frac{\delta\nu_\beta}{\delta p/p}$ is non-zero, the chromatic head-tail effect appears, and some oscillation modes become unstable for any beam current, and the current threshold can result from radiation damping only. For the chromatic head-tail, an increment/decrement of the coherent oscillation mode ($1/\tau_+$) and incoherent one ($1/\tau_-$) is expressed as [2]:

$$\frac{1}{\tau_\pm} = \mp\frac{I_b c R}{16\pi\nu_\beta\frac{E}{e}\,\sigma_z}\Im\left[Z_\perp f(2\chi)\right], \qquad (2)$$

where ν_β is the betatron tune, $f(2\chi)$ is the complex function $f(u) = \int_0^\pi e^{iu\sin x}dx$ of the head-tail phase

$$\chi = \frac{\xi}{\alpha}\frac{\sigma_z}{R}, \qquad (3)$$

which is a betatron phase advance caused by the chromaticity during a half-period of synchrotron oscillation (from head to tail). The coherent mode (center of mass oscillation) is damped if $\xi > 0$ and anti-damped if $\xi < 0$ (for a positive momentum compaction α), whereas for the incoherent modes (beam size) the effect is vice versa.

FEEDBACK THEORY

As it follows from (2), positive chromaticity suppress the coherent oscillation mode, i.e. makes bunch center of mass stable, but other oscillation modes are unstable, negative chromaticity has the inverse effect.

A detailed analysis of a feedback applicability is given in [3]. The main idea is to suppress the coherent oscillation mode using a resistive feedback, while to keep other modes stable due to a negative chromaticity.

Because of the beam-environment interaction, each particle in a bunch is perturbed by electro-magnetic fields induced by all other particles. For the model bunch of N macro-particles uniformly distributed over synchrotron phases, a system of differential equations can be written:

$$\frac{dy_k}{dz} + \frac{1}{N}\frac{\omega_0 I_b\langle\beta\rangle}{4\pi\frac{E}{e}}\sum_{j=0}^{N-1}\left(y_j\sum_{m=0}^{\infty}W_{kjm}\right) = 0, \qquad (4)$$

where

$$W_{kjm} = Z_\perp\left[-i\omega_0(m-\nu_s)\right]\exp\left[i\omega_0(m-\xi)\frac{z_k - z_j}{c}\right],$$

y_k is the complex betatron oscillation amplitude of $k-$th particle, ω_0 is the revolution frequency, I_b is the bunch current, $\langle\beta\rangle$ is the average beta-function. $Z_\perp$ is the broad-band transverse coupling impedance, characterizing the short-range beam-environment interaction. The VEPP-4M vertical broad-band coupling impedance estimated from the coherent tune shift measurement [1] is about 2 MΩ/m.

It is not conveniently to analyze such complicated motion using the system (4), because the number of equations is equal to the number of particles N, which should be big enough to obtain reasonable results. Moreover, since the longitudinal coordinates of the particles z_k, z_j are explicitly time-dependent, the system (4) is a system of differential equations with variable coefficients.

As it is shown in [3], an analysis using symmetric mode expansion is much more efficient because only a few of lowest oscillation modes are significant. In addition, this approach allows us to avoid the variable coefficients. Using the continuous medium model and Vlasov equation, the problem of stability can be reduced to a system of algebraic equation:

$$(i\lambda + in)a_{nk} + \frac{I_b\langle\beta\rangle}{4\pi\nu_s\frac{E}{e}}\sum_{n'=-\infty}^{\infty}\sum_{k'=0}^{\infty}A_{nk}^{n'k'}a_{n'k'} = 0, \qquad (5)$$

where a_{nk} are the complex amplitudes of oscillation modes, n, n' are the indices of transverse modes, k, k' are the indices of longitudinal modes. The matrix elements $A_{nkn'k'}$ are functions of the broad-band coupling impedance $Z_\perp(\omega)$, and of the head-tail phase (3).

A feedback can be introduced in (5) as an equivalent transverse impedance Z_{FB}. In terms of oscillation modes, the system of equations with a feedback takes on form:

$$i\lambda a_{nk} + \sum_{n'=-\infty}^{\infty}\sum_{k'=0}^{\infty}[I(A_{nk}^{n'k'} + \delta_{n0}\delta_{n'0} f B_{nk}^{n'k'}) + in\delta_{nn'}\delta_{kk'}]a_{n'k'} = 0, \qquad (6)$$

where $B_{nk}^{n'k'}$ are the feedback matrix elements dependent on the feedback impedance Z_{FB}. A real feedback system including beam position monitors and kickers can effect on a beam center of mass only, this is expressed in (6) by the Kronecker delta product $\delta_{n0}\delta_{n'0}$. I is the dimensionless bunch current normalized in such a way that the factor before the sums in (6) is equal to unity:

$$I = \frac{I_b}{I_{b0}}, \qquad I_{b0} = \frac{4\pi\nu_s \frac{E}{e}}{Z_\perp\langle\beta\rangle}\frac{\sigma_z}{R}. \qquad (7)$$

The feedback parameter f is a complex normalization factor of the feedback matrix elements $B_{nk}^{n'k'}$. If only $B_{00}^{00} = 1$ and all other $B_{nk}^{n'k'} = 0$, the feedback contribution to the complex betatron frequency shift, related to the synchrotron frequency, is ifI. For a rigid bunch of the $I_b = I \cdot I_{b0}$ current, a decrement of the resistive feedback with the parameter f is $\tau_{FB}^{-1} = fI\omega_s$ s^{-1}.

Stability analysis is done in the following way: the system (5) is an algebraic system of equations with zero right-hand part, therefore it has nontrivial solutions only if $-i\lambda$ values coincide with eigenvalues of the matrix related to the a_{nk}. Because the system (5) is infinite-dimensional, it should be truncated to the required number of modes. For each oscillation mode, λ is the complex dimensionless frequency shift, $\Re\lambda = \frac{\Delta\omega_\beta}{\omega_s}$ is the relative betatron frequency shift, $\Im\lambda = \frac{2\pi}{\tau\omega_s}$ is the increment (if $\Im\lambda < 0$) or decrement (if $\Im\lambda > 0$), normalized by the synchrotron frequency. So, on the basis of the system (5) eigenvalues, it is possible to make a conclusion about stability of the motion: if $\Im\lambda < 0$ for at least one mode, the motion is unstable.

Numerical solutions of the eigenvalue problem (6) for 10 lower oscillation modes are shown in figure 1. There are $\Re\lambda$ (upper plots) and $\Im\lambda$ (lower plots) in dependence of the bunch current I_b. The left pair of plots corresponds to zero chromaticity $\xi = 0$ without a feedback $f = 0$, the right pair corresponds to a negative chromaticity $\xi = -8$ with a resistive feedback $f = 5$. For the $\xi = 0, f = 0$ case, when the bunch current exceeds the threshold (about 11 mA), one can see first two-mode coupling. At the same time a negative $\Im\lambda$ values corresponding to an increment appear. However for the $\xi = -8, f = 5$ case, a negative $\Im\lambda$ corresponding to an increment appears when the bunch current exceeds the TMCI threshold about 4 times ($I_b > 40$ mA).

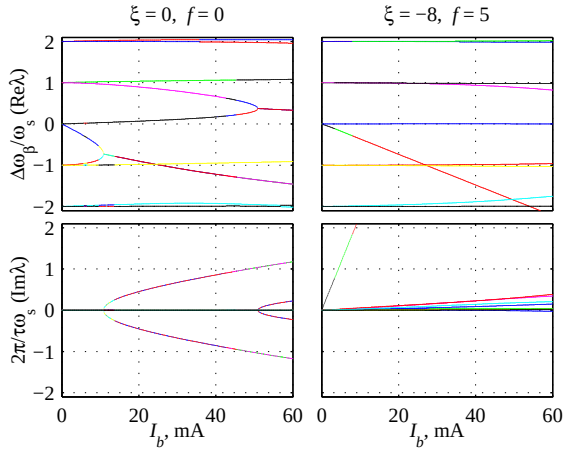

Figure 1: Eigenvalue problem solution.

Thus, using numerical solution of the eigenvalue problem (6) with various bunch current I, we can find a range of the feedback parameter where all the oscillation modes are stable. Figure 2 shows the maximum possible current I_{max} of a stable bunch in dependence of the complex feedback parameter f (presented as the module $|f|$ and argument $\arg f$) for the chromaticity of $\xi = -8$. One can see an area of f when the bunch of current exceeding 40 mA is stable, the black arrow indicates the maximal current of 42 mA achievable with $f = 2.65 + 0.38i$.

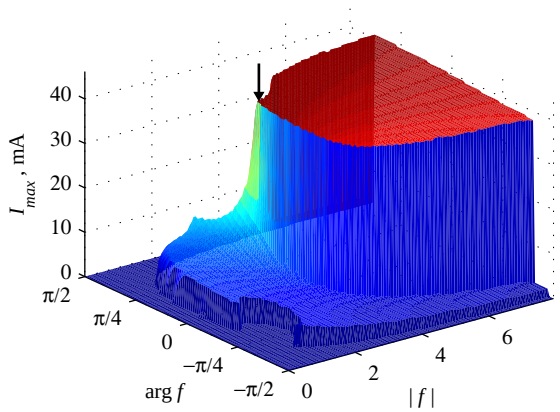

Figure 2: Feedback parameter optimization, $\xi = -8$.

Let's calculate the kicker voltage required. If the feedback works in the presence of coherent betatron oscillation, a beam is deflected turn-by-turn by the feedback kicker. The feedback kick $\Delta y'_{FB}$ is related to the beam position y and angle y' at the feedback beam position monitor (BPM) through the transition matrix dependent on the β and α lattice functions at the BPM and at the kicker, and on the betatron phase advance between the BPM and the kicker. To obtain the y' value which can not be measured directly, two BPMs are used. For rough estimation, we can assume $\Delta y'_{FB} \propto \frac{y}{\langle\beta_y\rangle}$, where $\langle\beta_y\rangle$ is the average beta-function.

As it was mentioned above, the feedback parameter f

is an ω_s-normalized decrement introduced by the feedback into a motion of a rigid bunch with a unit normalized current $I = 1$. Expressing the feedback kick $\Delta y'_{FB}$ through the feedback parameter f, we can write:

$$\Delta y'_{FB} = 4\pi\nu_s |f| I \frac{y}{\langle\beta_y\rangle}. \quad (8)$$

For the kicker formed by two matched strip-lines, the voltage amplitude required for the $\Delta y'_{FB}$ kick, is:

$$V_{FB} = \frac{E}{e}\frac{d}{L}\Delta y'_{FB}, \quad (9)$$

where L is the kicker length and d is the gap between the strip-lines.

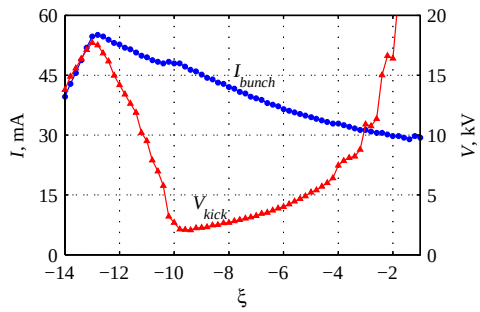

Figure 3: Maximal beam current and kicker voltage.

For the VEPP-4M, taking $L = 1.8$ m, $d = 25$ mm, $\nu_s = 0.02$, and $\langle\beta_y\rangle = 13.6$ m, the maximal achievable beam current together with the required kicker voltage have been calculated with various chromaticity and with initial betatron oscillation amplitude of $y = 1$ mm. The calculation result is presented in figure 3. As one can see, the optimal chromaticity is about -10, where the bunch current exceeds 40 mA with a reasonable kicker voltage of 1.8 kV. Since four kickers are planned to use, and the initial betatron oscillation amplitude can be reduced down to 0.5 mm by fine adjustment of the injection, the kicker voltage of 200-250 V seems to be enough.

FEEDBACK SYSTEM LAYOUT

Figure 4 shows a block diagram of the VEPP-4M transverse feedback system. Beam-induced signals of two 45 m-distanced strip-line BPMs pass through a sum-difference circuit to the pickup station, which forms an analogous signal of 30 MHz frequency band, proportional to the beam position. These signals come to the signal processing board to be digitized by the 12-bit 50 MHz ADC. Then the beam position data are processed by the digital signal processor (DSP) TMS320C6713, which calculates kick parameters required for the oscillation damping. The kick signals formed by the DSP are converted in the 12-bit digital-to-analog converter, and after amplification by the broad-band power amplifiers come to the kickers. The same BPMs and kickers are used both for the electron and positron bunches, but with separated signal processing electronics.

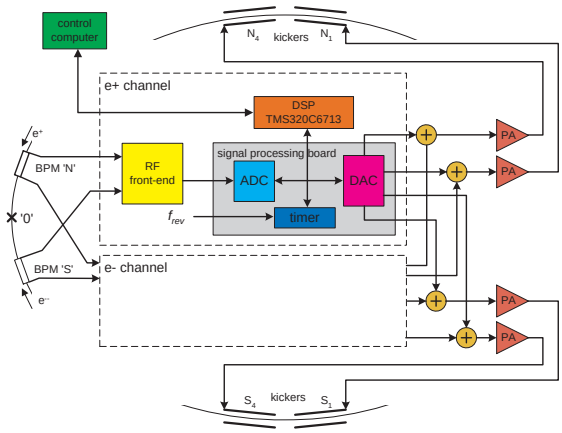

Figure 4: Feedback system block diagram.

BEAM MEASUREMENTS

At present, all the electronics for one feedback channel is designed, produced and installed at the VEPP-4M. A test beam measurements have been done to evaluate the system sensitivity and spatial resolution. Turn-by-turn r.m.s. resolution of the strip-line BPM, measured with a beam of 10^{10} particles, is about 80 μm.

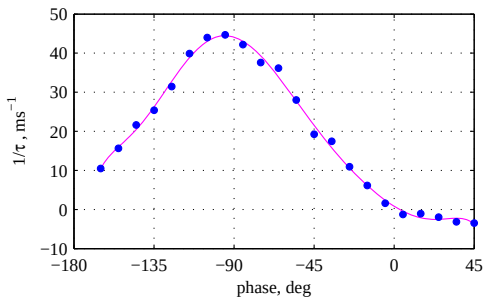

Figure 5: Feedback decrement vs phase.

One more set of beam measurements have been done to find an optimal range of the feedback phase. The feedback decrement in dependence of the phase is presented in figure 5. A range of the feedback phase where the decrement is higher than 35 ms^{-1} (i.e. $\tau_{FB} < 2\pi/\omega_s$) is about 45°. This suggests that the feedback will be able to work stably during the VEPP-4M energy ramp, when the betatron tune can vary with time.

REFERENCES

[1] V.Kiselev, V.Smaluk, Experimental Study of Impedances and Instabilities at the VEPP-4M Storage Ring, EPAC'98, Stockholm, 1998

[2] A. Chao, Physics of Collective Beam Instabilities, Wiley, New York, 1993

[3] M. Karliner, K. Popov, Theory of a feedback to cure transverse mode coupling instability, Nuclear Instruments and Methods in Physics Research A 537 (2005) 481-500

SEGMENTED FOIL SEM GRIDS FOR HIGH-INTENSITY PROTON BEAMS AT FERMILAB*

Sacha Kopp#, Bruce Baller, Sam Childress, Richard Ford, Deborah Harris, Dharma Indurthy, Cary Kendziora, Craig Moore, Žarko Pavlović, Marek Proga, Gianni Tassotto, Robert Zwaska.

Abstract

We present recent beam data from a new design of a profile monitor for proton beams at Fermilab. The monitors, consisting of grids of segmented Ti foils 5μm thick, are secondary-electron emission monitors (SEM's). We review data on the device's precision on beam centroid position, beam width, and on beam loss associated with the SEM material placed in the beam.

INTRODUCTION

The extracted beam transport lines and transfer lines between accelerators at Fermilab must operate at ever higher proton fluences to service the neutrino program and the production of antiprotons for the Tevatron collider program. Fig. 1 shows schematically a portion of the Fermilab accelerator complex. The 400 MeV linac supplies beam to the 8 GeV Booster accelerator and is also foreseen to service an extracted beam line to study muon ionization cooling. The Booster delivers beam to the Booster Neutrino Beam (BNB) servicing the MiniBooNE experiment [1]. The Booster is also used to fill the Main Injector with 7 and hopefully up to 11 batches of protons for acceleration to 120 GeV. These 120 GeV protons are split between antiproton production and "Neutrinos at the Main Injector (NuMI)" facility [2].

Design intensity for NuMI beamline is 4×10^{13} protons per spill, with repetition rate of 0.53Hz and transverse beam size of ~1mm.

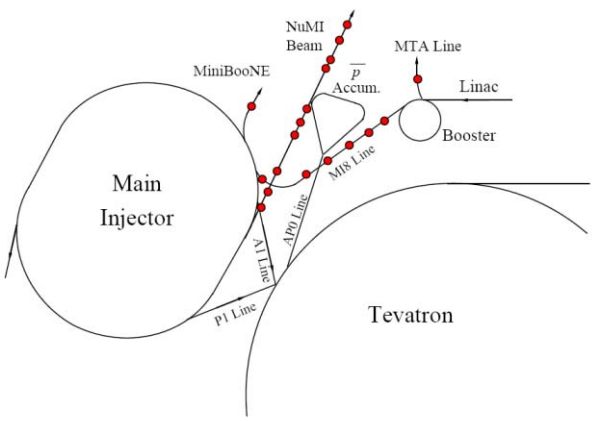

Figure 1: Schematic diagram of a portion of the Fermilab accelerator complex including the 400 MeV linac, 8 GeV Booster, 120 GeV Main Injector, and the extracted beam lines for the Neutrinos at the Main Injector (NuMI), MiniBooNE experiment, and the Muon-Cooling Test Area (MTA). Stations already or soon to be instrumented with foil SEM's are indicated by the circles.

*Work supported by U.S.DoE, contracts DE-FG03-93ER40757 and DE-AC02-76CH3000

#kopp@hep.utexas.edu

Such fluences place stringent criteria on invasive instrumentation to measure proton beam profiles. Currently at Fermilab, they are measured with Secondary-electron Emission Monitors (SEM's) made from grids of 75μm Ø Tungsten wires [3], which at 1 mm pitch place sufficient amount of material to cause significant fractional loss of beam particles into nearby magnets. The desirability of being able to perform diagnostic measurements while the beams are operated at their nominal intensities motivated lower-mass SEM design.

Based on a design from CERN [4] we have built SEM's consisting of Ti foils. The foil SEM's provide several features over the 75μm Ø Au-plated W-wire SEM's currently in use at FNAL: (1) a factor 50-60 lower fractional beam loss, which is important for reduced component activation or groundwater contamination; (2) greater longevity of Ti signal yield [5], as compared with W or Au-W, which degraded by 20% over the course of running the KTeV fixed-target experiment [3]; (3) a 'bayonnette'-style frame permitting insertion/retraction from the beam without interruption of operations; and (4) reduced calculated beam-heating from the high-intensity proton-pulses, which results in less sag [6].

SEM CHAMBER DESIGN

A view of the foil SEM paddle is shown in Figs. 2 and 3. Three planes of solid Ti foil, 2.5μm in thickness, are interleaved with segmented foils intended for X and Y profiles. The signal foils are 5μm thick. Over the 8cm diameter area of the SEM traversed by the beam, the signal foil strips are 0.15 mm in width. A total of 44 strips are etched into the foil, along with 1.5cm wide strips to measure beam halo out to 3.8cm radius.

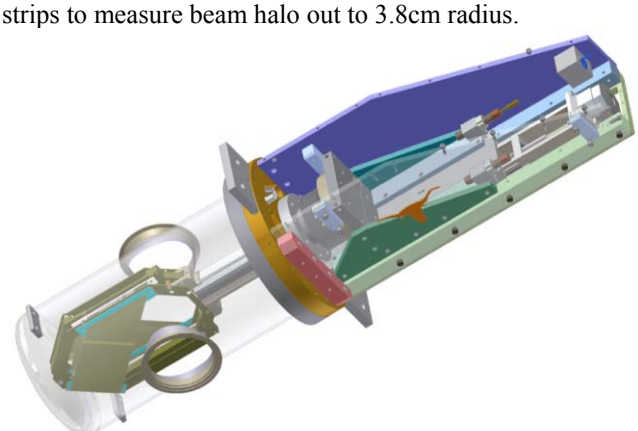

Figure. 2. Drawing of the SEM vacuum chamber. The evacuated portion of the chamber is shown with semi-transparent walls to illustrate the location of the internal foil paddle.

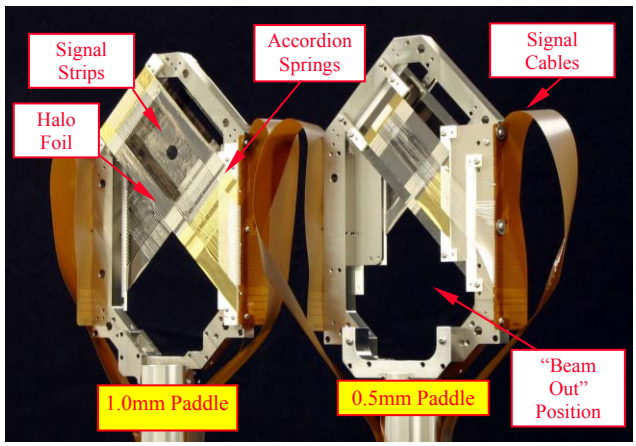

Figure.3: Photograph of a 1.0 mm pitch and a 0.5 mm pitch foil paddle. The paddles have two planes of strips for X and Y profile measurements.

The paddle completely surrounds the beam, so the foils may be inserted into the beam or retracted without the paddle frame traversing the beam. The foils are mounted on precise ceramic combs which define the strip pitch and the foil location on the paddle [7]. A "beam hole" of 12 mm diameter in the bias foil permits most of the 1 mm beam spot to pass through without beam loss, while still permitting adequate voltage bias to maintain signal yield.

Each signal strip has accordion springs pressed into its ends. The springs are elongated by approximately 4 mm prior to installation on the paddle. At this extension, our measurements indicate a tension of ~1g is attained on each strip. The mechanical sag was estimated to be δy=40μm.

The foil actuating mechanism and vacuum can are shown in Fig. 2. The foil paddle is cantilevered on a 5cm diameter hollow shaft, the other end of which is welded to a 12cm "conflat" flange. A linear motion stage and stepper motor actuate the assembly into or out of the beam. A 9cm outer diameter, 6.4cm inner diameter bellows forms the vacuum seal for the actuator. Ceramic-insulated limit switches halt the stepper travel at either end, while a linear variable differential transformer (LVDT) confirms the final beam "in" position of the foils with 1μm accuracy. Kapton-insulated signal cables are routed through the hollow shaft to feedthroughs at its end. The cables are bonded to the foil strips using a conducting epoxy appropriate for ultra-high vacuum, which is also how the strips are bonded to the ceramics. Brackets mount the linear stage to the large 25cm diameter conflat flange on the end of the SEM's vacuum chamber. Precise dowel holes in the 25cm flange and in the moving flange at the end of the bellows allow in situ optical survey of the foil position when installed in the beam line. The 16 liter vacuum chamber is 20cm diameter cylinder with 10cm diameter quick-disconnect flanges at the beam ports.

Each foil plane is measured after mounting on its paddle for mechanical accuracy. Measurements of strip-to-strip pitch are made by analysis of digital photographs suggesting better than 20μm pitch accuracy.

THERMAL SIMULATIONS

We have performed detailed finite element calculations of the temperature induced in the foil SEM's due to heating by the NuMI beam [6]. The heat input to the SEM comes from the energy lost by the beam, and the power dissipated by the SEM comes from blackbody radiation and from thermal conduction through the SEM material. We performed the calculations for several materials. We also compared the heating of wires and foils; wire SEM's cool less efficiently because blackbody radiation is proportional to the surface area of the emitter.

The temperature rise in the SEM material results from ionization energy loss by the 120GeV protons. We used "restricted energy loss" [9] to account for the fact that some δ rays escape out the back of the SEM, so do not deposit their energy in the SEM. The effect of restricted energy loss is greater for thin foils than for wire SEM's and tends to lower the predicted energy deposited in the foil SEM. Fig. 4 shows the results of the thermal model for a 5 μm thick Ti foil. The left plot shows the temperature profile along the center-most strip at several times during the 1.9sec beam cycle, after many transpired beam cycles. As seen in the graph, the beam causes a sharp rise in temperature at t=0 sec. The cooling between spills is predominantly due to blackbody radiation. The (small) effect of thermal conduction is evident by the broadening temperature profile over the course of the cooling cycle. The right graph shows the linear expansion of the foil strip, and compares to the elongation expected for a Ti wire 50 μm in diameter.

We compared various materials and looked at the temperature rise ΔT, maximum linear elongation ΔL, as well as dynamic stress. The dynamic stress may be compared to the "yield stress" for the material, the point at which the material may deform plastically. Beryllium, Carbon fiber and Titanium are preferable from the point of view of long term material damage, *ie*: have dynamic stress values below the yield stress.

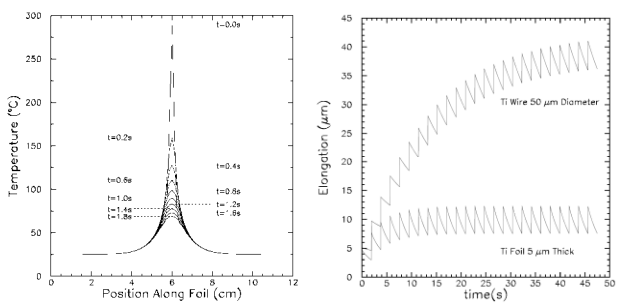

Figure 4: Results of the thermal model of 5μm Ti foil in the NuMI beam. (left) Temperature along the center most strip at several time increments through one beam cycle: at t=0sec the beam passes through the foil, and at then it cools down till next spill arrives 1.9sec later. (right) Net elongation of a 12cm long, 5μm thick, Ti foil strip as a function of time, showing the repeated heating and cooling of several beam cycles. The Ti foil's elongation is compared to that for a 50 μm diameter Ti wire.

The Ti foil SEM experiences 12μm elongation. Because of the 4 mm extension in the accordion springs, we note that this elongation results in <1% tension loss. Of note as well is the fact that a W-wire SEM, when strung on a frame at the maximum stress (the yield stress), stretches the wires by 160μm; thus, beam heating will drop the tension of such a wire SEM by nearly ⅓. Such loss motivates the accordion springs for the foil SEM or individual springs on wire SEM's as has been used by previous workers [11].

IN-BEAM PERFORMANCE

The resolution of the foil SEM grids has been studied previously using a prototype chamber installed in the 8 GeV transfer line to the MiniBooNE experiment [8]. The MiniBooNE beam has transverse size varying from 3mm to 8mm and intensity (4-5)×10^{12}ppp. The observed resolution on beam centroid and width measurements was compared to a model of the chamber's response which included electronics noise and uncertainties in the foil strips' placement.

More recently, data from the 120 GeV NuMI line has been available. The NuMI beam has ~1mm beam size, affording comparison to the model at a different transverse beam size and also different beam intensity from the data in [8]. Fig. 5 shows data from two adjacent foil SEM's in the NuMI line. The SEM's are approximately 14 m apart with no intervening magnets. The left plot, showing data over the period of a few weeks, shows some variation in the correlation between the two chambers, probably reflecting different beam angles. The right plot shows a 1-dimensional histogram of that data. Interpreting the scatter as arising purely from device resolution, we see that the SEM resolution on centroid is approximately 38μm/√2=27μm, consistent with the expectations of [8]. Comparing the beam width as measured by the two monitors suggests the beam width resolution of 20μm.

The primary motivation for the foil SEM's was the possibility to perform invasive beam measurements with

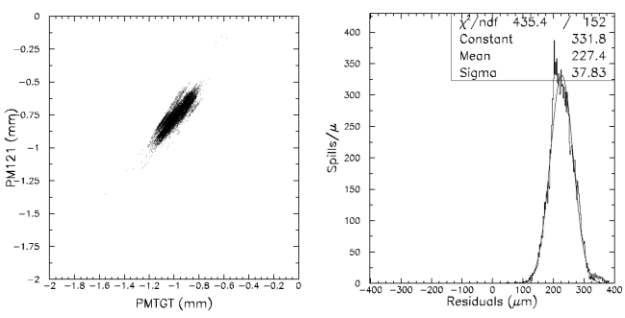

Figure 5: (left) Scatter plot of beam positions as detected by two adjacent foil SEM's in the NuMI beam line. Each point represents one beam spill at 5×10^{12} protons/pulse. The scatter arises in part from beam variations and in part from device resolution. (right) Residuals of the scatter plot on the left.

reduced fraction beam loss as compared to the previous available instrumentation at FNAL. We compared the beam loss as measured by two ionization chamber loss monitors downstream of a pair of SEM chambers. The two chambers, PM117 and PM118, were both removed and then sequentially re-inserted into the beam. PM118 is a Tungsten-wire SEM (25μmØ), while PM117 is a Ti foil SEM (both are 1.0mm pitch). The relative increase in observed loss at both stations indicates that that PM118 causes approximately 5.9 times more loss than PM117. These measurements indicate that the foil SEM's reduce the beam loss relative to the 75μmØ W wire SEM's [4] by a factor ~50-60. Such reduction will permit profile measurements to be peformed at full design intensity for the transfer lines. Such has proven to be important, as many diagnostics have heretofore been possible only at low intensity.

SUMMARY

Beam profile and halo detectors have been developed for transfer lines and external beam lines at Fermilab. The detectors, based on segmented 5μm Ti foils, have been shown to have sufficient beam centroid and width resolutions, and have enabled measurements to be performed at full beam instantaneous intensities with sufficiently low (~3×10^{-6}) fractional beam loss.

ACKNOWLEDGMENT

We thank J.D. Gilpatrick of LANL and G. Ferioli of CERN for valuable discussion and advice. We thank the members of the University of Texas at Austin's Physics Department mechanical shops for their efforts toward the chambers' construction, as well as the Fermilab Particle Physics, and Accelerator Divisions for their assistance in integration and installation of the devices. This work was supported by the U.S. Department of Energy and by the Fondren Family Foundation.

REFERENCES

[1] C.Moore et al, Proc. 2003 Part. Accel. Conf., pp1652-1654, Stanford, CA, May, 2003.
[2] See S. Kopp, "The NuMI Beam at Fermilab," Fermilab-Conf-05-093-AD, Proc. 2005 Part. Accel. Conf.
[3] R.Drucker, R.Ford, & G.Tassotto, FERMILAB-Conf-98/062, published Proc. Beam Diag. and Instr. for Part. Acc. (DIPAC), Frascati (Rome), Italy, (1997).
[4] G.Ferioli, private communication.
[5] G.Ferioli and R.Jung, CERN-SL-97-71(BI), published in Proc. Beam Diag. and Instr. for Part. Acc. (DIPAC), Frascati (Rome), Italy, (1997).
[6] Ž.Pavlović et al., Fermilab-TM-2312-AD (2005).
[7] D. Indurthy et al., Fermilab-Conf-04-520, AIP Conf. Proc. 732:341-349 (2004), Proc. 11th Beam Instr. Wkshp (BIW04).
[8] S.Kopp et al, "Beam Test of a Segmented Foil SEM Grid,", Nucl.Instr.Meth.A554(2005)138.
[9] Particle Data Group, http://pdg.lbl.gov.
[10] National Institutes of Standards and Technologies, "Stopping Powers of Electrons, Protons, and Alpha Particles," data available at the URL: http://physics.nist.gov/PhysRefData.
[11] J. Krider and C. Hojvat, Nucl. Instr. Meth. A247, 304 (1986).

TIMING AND SYNCHRONIZATION AT THE LCLS*

P. Krejcik#, R. Akre, S. Allison, M. Browne, L. Dalesio, J. Dusatko, J. Frisch, R. Fuller, A. Gromme, K. Kotturi, S. Norum, D. Rogind, W. White, M. Zelazny

SLAC, Menlo Park, CA, 94025, U.S.A.

Abstract

Timing and synchronization in the LCLS is a three tier process: At level 1 an event generator broadcasts timing fiducials to event receivers over a fiber network. Hardware and software triggers are created in the event receiver according to the digital pattern broadcast at 360 Hz by the event generator. Beam synchronous data acquisition driven by these triggers allows time-stamped acquisition of all diagnostic devices simultaneously on every pulse. Timing fiducials are phase synchronized to the low level RF reference system with 10 ps precision. Level 2 synchronization ensures that individual klystrons powering gun and accelerating sections remain within a few tenths of a degree S-band to the phase reference distribution scheme. The gun laser system is also phase locked to this reference to within 0.5 ps. Level 3 provides synchronization at the 10 fs level between the electron beam and pump-probe laser systems in the end station experiments. This will be achieved with electro-optic sampling of the electron bunch and by synchronizing the laser systems over a stabilized fiber distribution system. A fiber stabilization scheme is currently under test at Lawrence Berkeley Laboratory.

INTRODUCTION

The Linac Coherent Light Source project, LCLS, is a 4th generation X-ray light source using the SLAC linac to deliver 14 GeV single bunch electrons to an undulator FEL operating at 1.5 Å. Linac based FELs are single pass machines where each pulse uses a fresh electron bunch from the gun. Stability of operation requires tight tolerances on the timing and synchronization of the production and acceleration of these bunches. Ultrafast science can be done with the femtosecond bunches from the LCLS and requires femtosecond clocking of the bunches.

Timing and synchronization incorporates several levels of the accelerator control system. It includes the programmable triggers that drive hardware functions. A synchronous data acquisition scheme to record data from devices on a single beam pulse throughout the machine is coupled with the broadcasting of event triggers. The timing triggers and synchronous acquisition systems have been programmed onto Micro-Research™ event generator and event receiver modules.

Synchronization with the beam also requires that the RF system be phase locked the beam. The low level RF (LLRF) distribution is based on a low noise master oscillator and a temperature stabilized copper coaxial cable phase reference distribution system.

Both the LCLS timing system and the LLRF are constrained by the requirement to be compatible with the existing SLAC systems and remain in synchronism with other beams in the SLAC linac. The LCLS system is built on top of the existing SLAC systems and to provide greater precision and stability for LCLS beams.

A new requirement for the LCLS is the need to synchronize laser systems at the femtosecond level. Many experiments at the LCLS rely on pump-probe systems where femtosecond phenomena are only revealed if the pump laser synchronization is known with this precision.

THE TIMING EVENT SYSTEM

A feature of the SLAC timing system is that the triggers are phase locked to the LLRF distribution system. A main drive line (MDL) running the length of the 3 km linac carries a 476 MHz reference signal. Superimposed on the RF are 360 Hz fiducials in the form of double amplitude pulses. A receiver attached to the MDL detects these fiducials and outputs both a 119 MHz reference RF signal plus a 360 Hz clock signal, as shown in Figure 1.

The clock signal and the reference RF are fed into an event generator (EVG), supplied by MicroResearch™[1]. The EVG has been programmed at SLAC to broadcast event codes at 360 Hz out to each of the event receivers (EVRs). The EVRs, also manufactured by Micro-Research™, are linked to the EVG over optical fiber through a fanout module. The EVG must pay heed to the pattern broadcast by the existing SLAC master pattern generator (MPG) which sets up beam codes in a 360 Hz pattern for the other accelerator systems. Eventually the EVG will take over the role of the MPG for all SLAC timing systems, but for now it receives the digital pattern broadcast over a pattern network (PNET). This allows the existing SLC timing network infrastructure to be used for the klystron modulator triggers and remain in synchronism with the new LCLS timing system.

The event codes are setup through an EPICS input output controller (IOC) interface. The EVR IOC has a user interface for setting up individual trigger characteristics (delay, width, polarity) and assigning them to an event code from the EVG.

The stability of the timing triggers has been measured by comparing them with triggers from the standard timing buffer (STB) in Figure 1. For the VME based EVR we measured a RMS timing jitter of less that 10 ps over a 30 minute period.

*Work supported by DOE contract number DE-AC02-76SF00515
#pkr@slac.stanford.edu

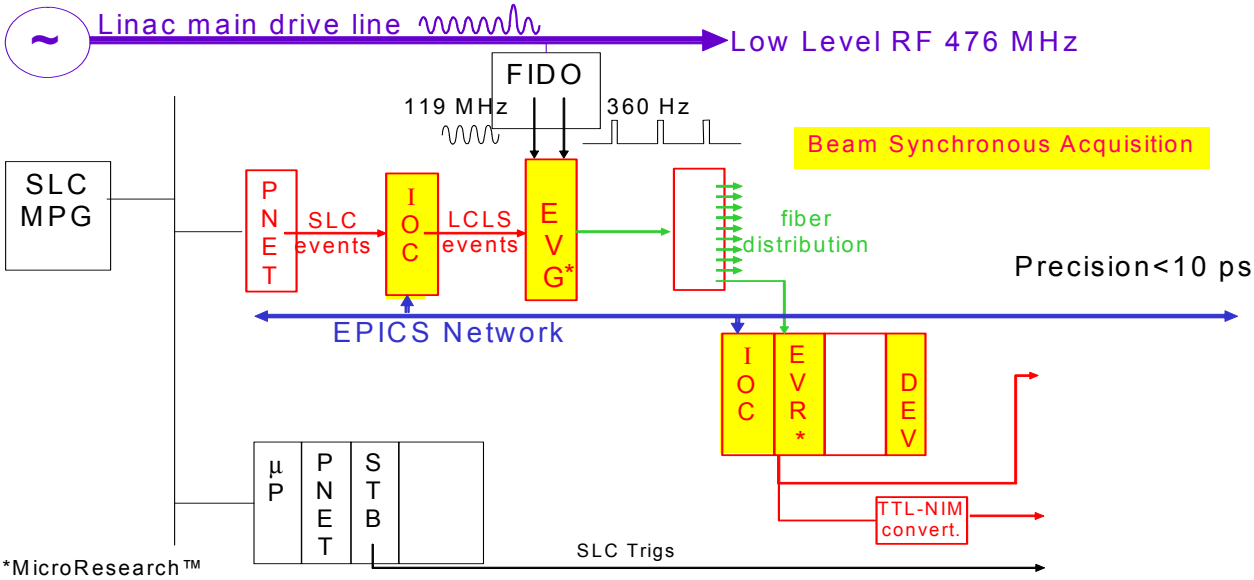

Figure 1: Block diagram of the major timing system components synchronized to the low level RF.

Beam Synchronous Acquisition

The EVR supplies triggers to the measurement devices such as beam position monitors (BPMs) as well as supplying time stamp data to the IOC for the data acquisition. Every measurement record taken on a single beam pulse through out the machine can be correlated by this common time stamp. Further more, each IOC connected with an EVR has a number of data buffers set up to receive data from beam synchronous acquisition devices. These buffers can be programmed to accept beam data in unison across the machine with any prescribed pulse pattern, which we call an event definition. Buffered data for all devices can be recorded up to the full machine rate of 120 Hz for as many as 2800 pulses. Thus all devices in the machine can be correlated on a single beam pulse measurement and all devices can be read for up to 2800 consecutive pulses.

LOW LEVEL RF SYNCHRONIZATION

A low-noise microwave oscillator is phase locked to the MDL at a pick off point near the LCLS injector, as shown in Figure 2. We therefore remain synchronous with the other accelerator users but we use its output as the new phase reference for LCLS LLRF and for locking the photoinjector laser. Copper coaxial cable provides the phase reference distribution. Critical components are housed in a temperature stabilized room and the reference line passes through the accelerator tunnel which maintains a temperature stability of a few tenths of a degree during normal operation.

Experience was gained at the Sub-Picosecond Pulsed Source (SPPS) project[2] at SLAC in locking a Ti:Sapphire laser to a low noise oscillator. The new oscillators have a measured noise floor of -157dBc/Hz at 476MHz, corresponding to 11fS RMS Jitter in 5MHz BW or 31fS RMS Jitter in 40MHz BW.

Each klystron in the LCLS injector is driven by a solid state sub-booster stage (SSSB) so that the phase and amplitude can be individually controlled by an electronic I&Q modulator. The output of the accelerating structures is coupled to a phase and amplitude detector so that the phase of the RF as seen by the beam can be compared to the reference RF.

Low Level RF Control

Digital I&Q control of the LLRF uses LCLS phase and amplitude control (PAC) modules and phase and amplitude detector (PAD) modules throughout. A local oscillator (LO) signal operating at 2830.5 MHz is derived from the reference 2856 MHz and is mixed with the RF detected in the PAD. This gives an IF of 25.5 MHz which is digitized in the PAD ADC. The ADC clock signal of 104 MHz is also derived from the LO module.

Software feedback loops between the PAD and the PAC compensate for slow drifts in the klystron and laser systems. In figure 2 only the laser feedback is shown. An optical diode detects part of the light output from the laser and the feedback maintains the laser phase with respect to the RF reference.

Performance requirements for the low level RF

The longitudinal beam dynamics requirements for the bunch compression in the LCLS dictate that the phase stability of the RF is within very tight tolerances. The laser phase stability is to be better than 0.8 ps. The S-band phase stability is given as 0.10° S-band and the higher harmonic cavity has a stability requirement of 0.50° X-band. A beam based feedback using the measured energy and bunch length of the electron beam will provide final control of the injector LLRF settings.

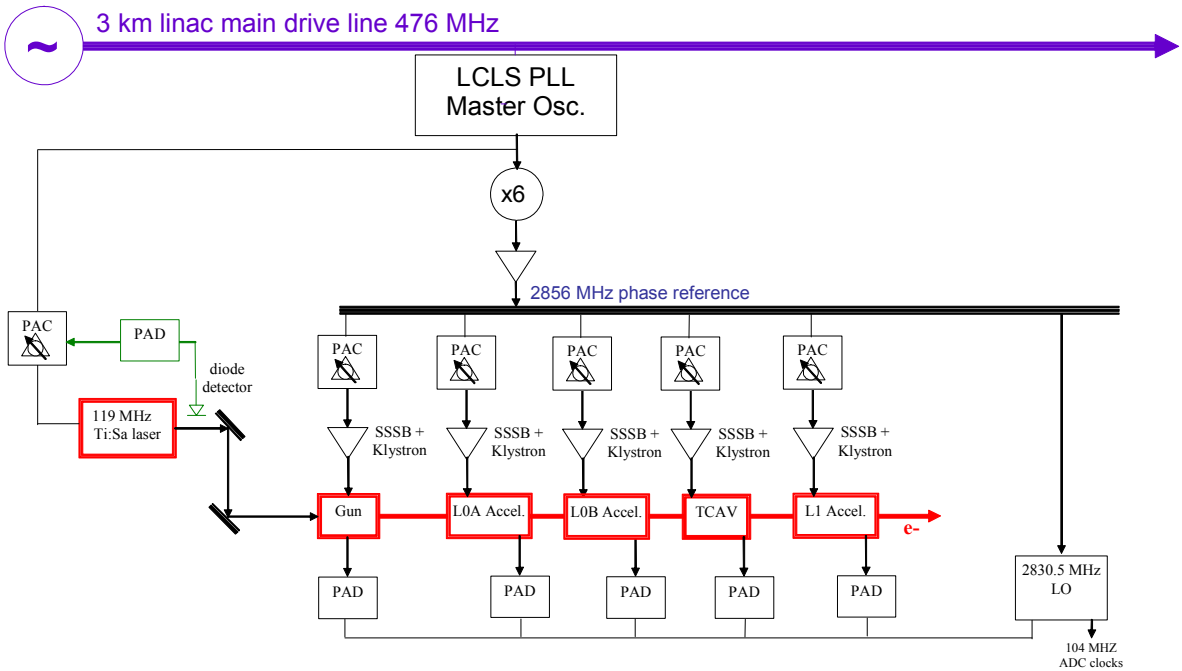

Figure 2: Low level RF for the LCLS photoinjector.

OPTICAL SYNCHRONIZATION

The stability of a state-of-the-art microwave phase reference scheme is of the order of hundreds of femto seconds. To move beyond this level requires different technologies. Two schemes are pursued at the LCLS. One is distribute a lower noise reference signal to the laser and klystron system via an optical distribution scheme. The other is to accept a certain amount of jitter in the electron beam arrival time, but to measure it with respect to a reference laser in conjunction with a pump-probe experiment. Both schemes rely on sending signals down a stabilized optical fiber.

Two optical fiber schemes are being studied. In one scheme a CW laser allows the optical length of a fiber to be regulated at one wavelength using a heterodyne detection method[3]. This technique offers great precision since the fiber length can be maintained to within one optical wavelength. However, difficulties arise when the optical carrier is modulated in order to transmit the RF signal. The modulation sidebands have a group velocity deviation because of the dispersion in the fiber so that the stabilization at the carrier frequency is no longer as precise.

A second scheme uses a pulsed laser to measure and stabilize the fiber[4]. The fiber is stabilized at the wavelength of the modulation envelope of the pulsed signal, so it cannot approach the precision of the optical wavelength stabilization scheme described above. However, it is simpler to implement because the LLRF signal is already carried by the fiber. For this reason it is an attractive solution for a staged approach to providing femtosecond synchronization.

The final challenge is to synchronize two remote lasers with femtosecond precision. It is desirable to lock a pump-probe laser to the master laser of the photoinjector. Even greater precision is called for to lock the pump-probe laser to a diagnostic laser for measuring the electron bunch arrival time. At the SPPS an electro optic (EO) detection scheme was used to clock the electron bunch arrival time with respect to the laser[5]. This method relies on the EO laser being synchronized to the pump-probe laser at the femtosecond level.

While many parts of optical synchronization have been demonstrated it still remains to put them together in a workable system for use at a facility like the LCLS.

REFERENCES

[1] MicroResearch, http://www.micro-researchfinland.fi/
[2] P. Krejcik et al, Commissioning of the SPPS linac bunch compressor**,** Proc. Particle Accelerator Conference, Portland, Oregon, 12-16 May 2003, pp. 423-425.
[3] J. W. Staples and R. Wilcox, Fiber Transmission Stabilization By Optical Heterodyning Techniques And Synchronization Of Mode-Locked Lasers Using Two Spectral Lines, Proc. of the 27th International Free Electron Laser Conference, Stanford, California, August 2005, pp. 686-689.
[4] A. Winter et al, High-Precision Optical Synchronization Systems For X-Ray Free Electron Lasers, Proc. of the 27th International Free Electron Laser Conference, Stanford, California, August 2005, pp. 677-681.
[5] A. Cavalieri et al, Clocking Femtosecond X Rays, Phys. Rev. Lett. **94**, 114801 (2005).

LOW-LATENCY HIGH-RESOLUTION SINGLE-SHOT BEAM POSITION MONITORS

D. M. Treyer, Paul Scherrer Institute, CH-5232 Villigen, Switzerland*

Abstract

In this paper design aspects of fast high-resolution, single-shot transverse beam position monitors (BPMs) are discussed. The focus is on BPMs which can provide (sub-) micrometer position resolution within measurement speeds of less than one hundred nanoseconds. Different pickups and analog signal conditioning electronics are reviewed. Their characteristics and limitations with respect to application in high-resolution, fast BPMs are pointed out. Exemplary implementations of pickups and electronics are reviewed. A BPM based on a resonant stripline pickup, developed for a fast transverse feedback system for the European X-FEL, is also presented.

INTRODUCTION

Next generation machines like the European X-Ray Free Electron Laser (E-XFEL) or the International Linear Collider (ILC) require extremely stable beams throughout their Linacs, in order to meet the transverse position stability requirements inside the undulators or at the interaction point, respectively. Table 1 lists the specified beam parameters [1][2].

Table 1: *Beam parameters of next generation machines.*

Parameter	E-XFEL	ILC
Energy	20 GeV	1 TeV
Bunch charge	1 nC	3.2 nC
Bunch spacing	200 ns	307 ns
Pulse length	3250	2820
Pulse rate	10 Hz	5 Hz
Bunch length σ_z	0.02 mm	0.3 mm
Bunch size σ_x	30 µm	554 nm
Bunch size σ_y	30 µm	3.5 nm

To stabilize the beam in the E-XFEL within 10 % of the ~30 µm beam size inside the undulators, a feedback system as shown in Figure 1 is currently under development at PSI and DESY [1]. In contrast to other proposed linac-based FELs that use single bunches with repetition rates in the order of 100 Hz, the E-XFEL will have bunch trains of up to 3250 bunches with 200 ns bunch spacing and 10 Hz repetition rate.

To damp harmful transversal beam position perturbations of these bunch trains up to hundreds of kilohertz (which originate from various noise sources and wakefields), the feedback system must act on a bunch-by-bunch basis. This requires beam position monitors (BPMs) having a position resolution in the micrometer region and very low latency.

*Work supported by Swiss State Secretariat for Education and Research SER

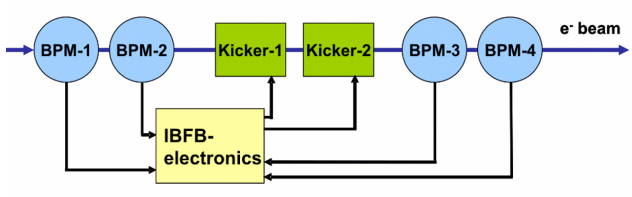

Figure 1: *Proposed topology of the E-XFEL intra-bunch-train feedback system [1].*

This paper focuses on fast BPMs for application in fast transversal intra-bunch-train feedback or interaction point feedback systems. Characteristic for such systems are the following parameters:

- Measurement rate: Equal to the bunch rate
- Bunch spacing: In the order of a few 100 ns
- Transversal resolution: ~1 µm
- Transversal measurement range: ~ ±1 mm
- Latency: <100 ns
- Bunch charge: 0.1 to 5 nC

Latency is the delay between the instant where the electron bunch passes through the pickup until the BPM outputs valid position data. Reasons for low latency are a) support of short bunch spacing, b) fast feedback.

Note that BPM systems for machines with longer bunch spacing (e.g. single-bunch Linacs) allow for much higher latency and therefore have relaxed requirements on noise, bandwidth, and processing speed. The construction of a such slow BPM may be entirely different from that of a fast BPM and therefore is not considered herein.

COMPONENTS OF A HIGH-RESOLUTION BPM

The building blocks of a BPM system are depicted in Figure 2. The pickup provides electrical signals that contain information about the beam position, usually in the signal amplitude. The most widely used pickup types include the button, matched stripline, resonant stripline, and cavity pickups.

Considering that, except for cavity pickups, the signal amplitudes from opposing pickup electrodes change by roughly 2 dB/mm when the beam moves in the respective plane, achieving micrometer resolution requires very careful signal handling: A change in cable attenuation of just 0.01 dB, which easily occurs when bending a cable, may lead to a measurement error of ~5 µm. Phase changes have similarly strong effects, depending on the processing scheme. Analog preprocessing close to the pickup is therefore necessary to transform the signals such that they can be transmitted over longer cables

without the degrading effect on stability just described. This is done typically by some kind of normalization circuit or 180° hybrids (see below). In the case of a cavity pickup, the intensity or monopole mode signal may be rejected by special couplers or a 180° hybrid.

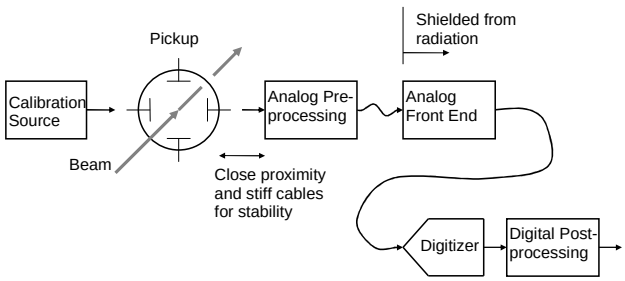

Figure 2: *Components of a BPM system.*

The analog front end may be favorably placed further away from the pickup in a radiation free location. However, cable length should be limited for low latency (1 m of standard cable makes a delay of 5 ns) and to reduce interference. Functions of the analog front end may include filtering, amplification, frequency conversion, normalization and detection. Afterwards the signal can be digitized for digital postprocessing, which may include offset and gain correction, linearization, normalization and filtering.

To compensate for drift and aging, the whole signal chain needs to be calibrated periodically. As a test signal either the beam (beam based alignment) or an electrical calibration signal source is used. It is possible to calibrate the BPM electrically between bunch trains.

PICKUP SELECTION

General Considerations

The type of pickup not only affects the achievable beam position resolution, but also many other characteristics of a BPM system, as well as the required signal processing. Some criteria for pickup selection are:

- Sensitivity of pickup signals to bunch charge and beam position (V/nC/mm)
- Operating frequency and bandwidth
- Separation of intensity and position signals
- Accuracy and stability
- Sensitivity to secondary beam parameters such as bunch length, beam angle, temperature
- Wakefields
- Size
- Manufacturability (complexity, tolerances, alignment)

The sensitivity of the pickup signals to beam position increases as the beam pipe diameter is made smaller. However, reasons for maintaining a large beam pipe diameter are a) vacuum pumping restrictions, b) reduced wakefield excitation and their effects on the beam, and c) easier initial machine alignment.

For achieving high resolution, we want high signal level and sensitivity. For low latency, we want high bandwidth. Both can be achieved with a resonant type of pickup operating in the gigahertz range, such as a short resonant stripline or a cavity pickup. A resonant stripline operating in the 1 to 3 GHz range or a cavity somewhere between 4 to 12 GHz will also be very compact.

To avoid overlap of signals produced by consecutive bunches, the quality factor (Q) of resonant pickups must be limited (i.e. to reduce ringing decay time).

Frequency and Bandwidth Selection

- The minimum signal bandwidth depends on the required latency and decay time
- Relative bandwidth decreases for higher operating frequencies (better for analog preprocessing)
- Electronics is more challenging to construct for higher operating frequencies
- Stay away from the machine RF and harmonics thereof
- Avoid widely used communication frequencies (e.g. GSM, DECT, WLAN)
- Measure other interferers in situ. Interference can enter the BPM system at the pickup and through long cables.
- Stay below beam pipe cutoff

PICKUP TYPES

Only commonly known pickups that provide signals strong enough for high-resolution BPMs are discussed. The signals produced by the widely used button pickups are too weak to obtain micrometer resolution for single-shot operation. There are also other special types of pickups recently developed, such as the perpendicularly mounted stripline pickup [3] or the inductive pickup [4], which are not considered here. Higher order modes (HOMs) of accelerating cavities have too large Q-factors and poorly defined dipole mode polarizations.

Matched Stripline Pickup

This pickup provides just sufficiently high signal level. Theoretical analysis shows that in the thermal noise limited case, it can provide submicrometer resolution. However, no practical implementation could be found which achieves this. A special feature of this pickup is its inherent directivity, allowing to separate counterpropagating beams. The electrical center depends on electrode alignment, and thus is rather poorely defined.

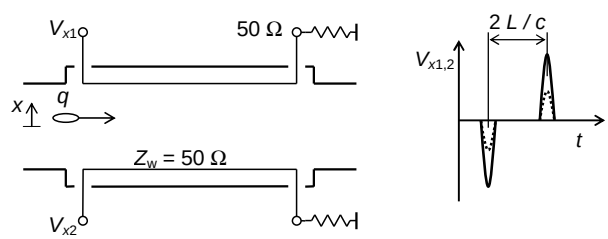

Figure 3: *Matched stripline pickup and waveform.*

A schematic sketch of the matched stripline pickup, along with its output voltage waveform, is shown in Figure 3. In the typical case the dielectric of the striplines is vacuum, the stripline characteristic wave impedance is

chosen equal to the load impedance (i.e. 50 Ω), and coupling between stripline electrodes is weak. Under these conditions, each stripline electrode produces two pulses of opposite sign, separated by twice the propagation delay along the stripline. The ratio of the signal voltages $V_{x1,2}$ from opposing electrodes depends on the transversal beam position x. An estimate for the beam position is:

$$x \sim \frac{\Delta}{\Sigma} \quad \text{with} \quad \Delta = \left(V_{x2} - V_{x1}\right) \quad \text{and} \quad \Sigma = \left(V_{x2} + V_{x1}\right)$$

Around the center position, the difference signal is proportional to the beam charge and position ($\Delta \sim q\,x$), and the sum signal is proportional to the charge only ($\Sigma \sim q$). Alternatively, the log ratio of the levels of signals from opposing electrodes may be used as a position estimate, i.e. $x \sim \log(V_{x2} / V_{x1})$.

A BPM system utilizing a matched stripline pickup in a 34 mm diameter beam pipe has been presented in [5]. Using electronics based on the wide band time normalizer principle, a single-shot resolution of ~7 µm over ±5 mm range has been demonstrated at a bunch charge of 1 nC.

Resonant Stripline Pickup

Larger signal level within reduced bandwidth compared to matched striplines is obtained with resonant striplines [1][6]. As the signal level increases by the loaded quality factor Q_L, and the processing bandwidth is reduced by the same factor to match the pickups bandwidth, an improvement in resolution δx in the order of $\sim 1/Q_L$ can be achieved.

A schematic sketch of a resonant stripline pickup is shown in Figure 4. The 1.6 GHz pickup presented in [1] employs a simple and compact construction. All four electrodes (two per plane) are milled out of the same piece. The pickup exhibits a Q_L of 32, resulting in a time constant of 7 ns. Figure 4 shows its signal waveform, after low pass filtering to remove higher order harmonics.

Due to the strong coupling between stripline electrodes, the Δ-signal (dipole mode) and the Σ-signal (monopole mode) have slightly different resonance frequencies. For the pickup described above, the separation is 25 MHz.

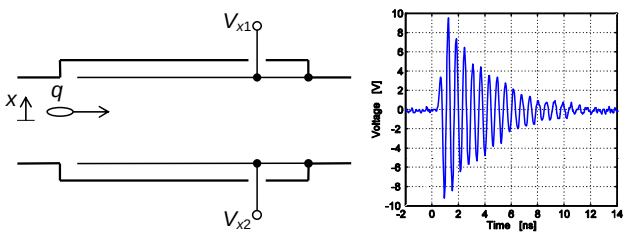

Figure 4: *Resonant stripline pickup and waveform.*

Pillbox Cavity Pickup

A cavity is a step discontinuity in the beam pipe diameter. It supports an infinite number of electro-magnetic modes. For BPMs the two lowest order modes are employed: The monopole mode TM_{010} providing a signal proportional to the bunch charge, and the dipole mode TM_{110} providing a signal proportional to the bunch charge times beam position.

An example of a high resolution single-shot cavity has beem presented in [7], and is sketched on the left side of Figure 5. It operates at 5.7 GHz, with a Q_L of 130, and provides a resolution of 25 nm at 1 nC. The beam pipe diameter is 20 mm. This example illustrates nicely that cavities can provide very high position sensitivity, while still being easy to manufacture.

Loaded Q values may range from 100 to 6'000. The mechanical and electrical center is defined accurately because of rotational symmetry. A reference pickup may be required for detection and normalization. The reentrant cavity [8] is a space saving variant.

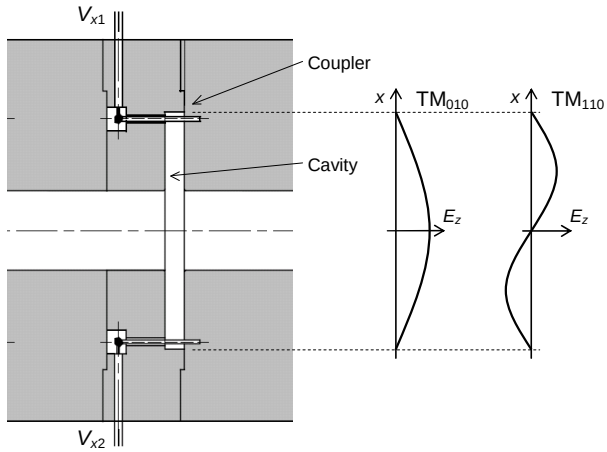

Figure 5: *Cavity pickup [7], and E_z field distributions.*

Signal Spectra of Pickup Candidates

The spectra of the three pickup types discussed are shown in Figure 6. Means to separate the difference or dipole mode signal (D) from the sum or monopole mode signal (M) depend on their spectral overlap. For striplines, only modal separation by a 180° hybrid is feasible. For the cavity, separation by frequency filtering and synchronous detection is also possible. Further, specially designed couplers may be used which inherently reject the monopole mode [9].

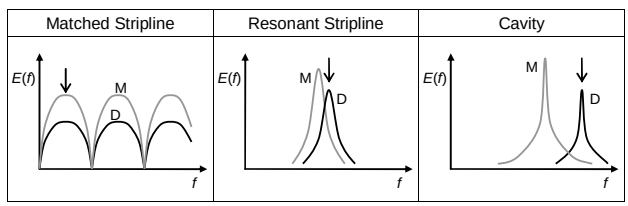

Figure 6: *Pickup signal spectra. Higher order modes of resonant stripline and cavity are not shown.*

ANALOG FRONT END ELECTRONICS

To handle the microwave signals produced by resonant pickups, analog front end electronics are required. Direct sampling of the pickup signals is not yet feasible due to dynamic range and jitter limitations of current digitizers. Analog processing schemes have been described in [10].

Log Ratio Method

A position estimate $x \sim \log(V_{x2} / V_{x1})$ can be obtained by passing the pickup signals through logarithmic amplifiers, and subtracting their outputs. However, the linearity error of practical logarithmic amplifiers of ~0.3 dB would lead to a charge dependent position error of ~150 μm.

AM/PM Method

Converting the amplitude differences of pickups signals from opposing electrodes to phase difference by a 90° hybrid and using a phase detector results in a position estimate of $x \sim \text{atan}(V_{x2} / V_{x1}) - \pi/2$. The problem of this method with respect to high resolution is the phase detector: Limited sensitivity and additional nonlinearity when using a mixer, or the limited operating frequency and increased noise when using an XOR logic gate.

Wide Band Time Normalizer

This method converts the amplitude difference of impulse signals into a time difference. The requirement on the input signal of having a single zero crossing limits this method to button or matched stripline pickups. It provides, like the log ratio and the AM/PM methods, intrinsic charge normalization and is insensitive to beam phase. However, position resolution better than 5 μm and operation beyond 500 MHz have not been demonstrated yet. Estimation of resolution is complicated by the non-ideal effects of the fast comparator circuits involved. This method can be viewed as a baseband realization of the AM/PM method, thus it cannot handle ringing signals.

Δ and Σ Preprocessing and Synchronous Detection

High linearity and low noise can be obtained by first separating the difference and sum signals (Δ and Σ) using a 180° hybrid, followed by synchronous detection and digitization. The normalization $x \sim \Delta / \Sigma$ is done digitally. A fast look-up table based division algorithm may be used (Σ fluctuates only by ~15 %). The method is highly suited for cavity pickups having monopole-mode rejecting couplers, saving the 180° hybrid. For the resonant stripline, the resolution limit is given by the finite common-mode rejection of the 180° hybrid.

Instead of synchronous detection, downconversion to a low IF, with single ended or I/Q mixing, and subsequent digitization, is an alternative. The price for the resulting increase in flexibility is analog hardware, complex digital postprocessing, and latency.

Analog front ends for cavity pickups are presented in [7][8][9]. A front end for a resonant stripline is discussed below.

ELECTRONICS FOR RESONANT STRIPLINE PICKUP

An analog front end based on processing of Δ and Σ signals is presented for a 1.6 GHz resonant stripline pickup. See Figure 7 for a block diagram. The processed Δ and Σ baseband signals are subsequently digitized for postprocessing.

The main difficulty lies in the separation of the Δ and Σ signals. To achive a crosstalk of better than -40 dB, total amplitude and phase imbalances in the pickup, cables and 180° hybrid must not exceed 0.12 dB and 0.8° simultaneously. A phase error of 0.8° at 1.6 GHz corresponds to a cable length mismatch of 0.27 mm ($\varepsilon_r = 2.3$). This indicates that crosstalk in the order of -60 dB can only be obtained by applying amplitude and phase tuning.

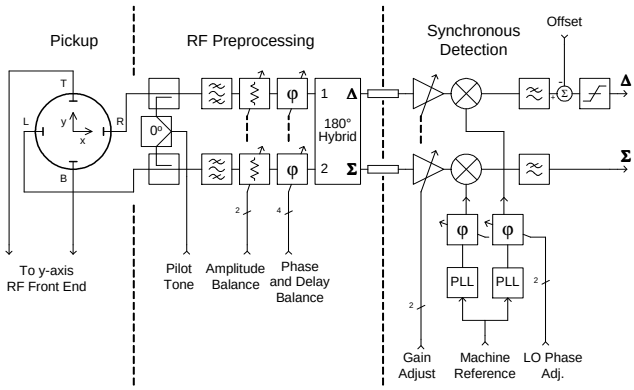

Figure 7: *Analog front end for resonant stripline [1].*

When exciting the pickup monopole mode by injecting a pilot tone from the y-axis path, electronically variable differential attenuators and phase shifters are tuned to cancel the Σ signal leaking into the Δ output of the hybrid. This procedure is repeated periodically between bunch trains. Due to the frequency difference between the monopole and dipole modes, imperfect cancelation of the Σ signal on the Δ output leads to a time-varying offset which is difficult to remove in postprocessing.

The intention of the ringing bandpass filters at the front end input is to stretch the pickup signals and flatten their peaks. This has the benefical effects of a) reducing the peak amplitude to avoid nonlinear distortions in the electronic tuning elements and mixer, b) reducing the signal envelope variation to minimize dynamic range (digitizer bits) and sampling jitter requirements, and c) creating the possibility of averaging over more samples. Stripline technology is used to obtain filters with closely matched frequency responses.

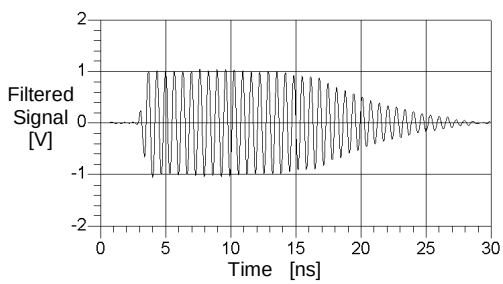

Figure 8: *Signal from resonant stripline pickup after microwave FIR ringing filter matched to the pickup Q.*

A simple form of a ringing filter is a Gaussian bandpass filter. Greater flexibility for shaping the pulse envelope is

possible with microwave FIR techniques. The effect of a 21-tap microwave FIR ringing filter on the pickup waveform from Figure 4 is depicted in Figure 8. After synchronous detection, the envelope of the ringing signal is obtained.

The reference signals for synchronous detection are derived from the highly stable machine clock. Because the monopole and dipole mode signals from the resonant stripline pickup have unequal frequencies, independent LO sources and phase shifters are required.

SUMMARY

Design considerations for fast beam position monitors delivering high resolution on a bunch-by-bunch basis have been discussed. Both the resonant stripline and cavity pickups have been discussed because of their potential of providing large output signals and high sensitivity. Analog signal processing by first separating the Δ and Σ signals using a 180° hybrid, and subsequent synchronous detection was found to be advantageous with respect to linearity and noise. Analog front end electronics for a stripline pickup has been presented. Compensation of the finite crosstalk of a 180° hybrid by electronic tuning, and ringing filters for easier signal handling have been discussed.

REFERENCES

[1] B. Keil, et al., “Design of an Intra-Bunch-Train Feedback System for the European X-Ray FEL”, this conference.
[2] T. Raubenheimer, “Suggested ILC Beam Parameter Range”, Rev. 2/28/05.
[3] K.E. Hacker, et al., “BPM with Large Horizontal Aperture for Use in Dispersive Sections of Magnetic Chicanes”, this conference.
[4] L. Soby, “Precision Beam Position Monitor for EUROTeV”, this conference.
[5] D. Nölle, M. Wendt, “TTF2 Beam Monitors for Beam Position, Bunch Charge and Phase Measurements”, Proc. LINAC'04.
[6] M. Dehler, “Resonant Stripline BPM for Ultra Low Current Measurement”, Proc. DIPAC'05.
[7] T. Shintake, “Development of Nanometer Resolution RF-BPMs”, Proc. HEAC'99.
[8] C. Simon, et al., “Beam Position Monitors Using a Reentrant Cavity”, this conference.
[9] A. Lunin, et al., “Design of Submicron Resolution Cavity BPM for ILC Main Linac”, this conference.
[10] G. Vismara, “The Comparison of Signal Processing Systems for Beam Position Monitors”, Proc. DIPAC'99.

DIAGNOSTIC INSTRUMENTATION FOR MEDICAL ACCELERATOR FACILITIES

M. Schwickert, GSI, Darmstadt, Germany
A. Peters, Hit GmbH, Heidelberg, Germany

Abstract

A number of accelerator facilities are presently emerging for the medical treatment of tumor patients using proton and light ion-beams. Both, the development of relatively compact accelerators and extensive studies on ion-therapy carried out at various accelerator laboratories were prerequisites for the layout of dedicated medical accelerator facilities.

This paper focuses on the special demands for beam diagnostic devices during the commissioning and routine operation of a medical accelerator. The proton-therapy project PROSCAN at the Paul-Scherrer-Institute in Villigen/Switzerland exemplifies medical treatment in the frame of a research institute. As examples for dedicated ion-therapy projects the beam diagnostic layout is presented for the CNAO project (Centro Nazionale Adroterapia Oncologica) located in Pave/Italy and the HIT facility (Heidelberg Ion Therapy) in Heidelberg/ Germany. Beam diagnostic devices of HIT are illustrated and the underlying concept for the type and precision of the devices is explained. Additionally, measurement results of the HIT linac and synchrotron commissioning are presented.

MEDICAL ACCELERATOR FACILITIES

The basic physical concept of hadrontherapy is that charged hadrons deposit the maximum energy density at the very end of their range (Bragg peak). The penetration depth in matter, i.e. the position where the ion beam is applied, is determined by the kinetic energy of the particles. In order to penetrate 30 cm in the human body an ion energy of 250 MeV for protons is needed, and 430 MeV/u for carbon ions, respectively [1]. The reason for the use of carbon ions instead of protons is the increased energy deposition per unit track length (Linear Energy Transfer, LET) therefore resulting in increased radiation efficacy.The radio-biological motivation for hadron-therapy is that the ion energy is applied to destroy the DNA inside the tumor-cell nucleus. Single or double strand breaks of the DNA can be restored, but not for very high local doses producing clustered lesions [2]. Since 1997 the so-called rasterscan method has been successfully applied in the GSI pilot project [3]. By this method the tumor volume is painted with a pencil-ion beam using an active variation of the beam properties, i.e. energy, intensity and position. The beam energy is given by the synchrotron extraction energy. The beam intensity is monitored with ionization chambers, and the beam width is measured using fast multiwire proportional chambers, both placed in front of the patient.

Hospital based facilities for radiotherapy with carbon ions are up to now in operation only in Japan (HIMAC, HIBMC). Two European carbon facilities, CNAO in Pave (Italy) and HIT in Heidelberg (Germany) are presently under construction and are presented in more detail in the next paragraphs.

Protontherapy for deep-seated tumors is at the moment performed or in the planning phase at hospital based facilities in Switzerland, France, Italy, Germany, USA (5), Japan (2), China and Korea [5].

Whereas the PROSCAN project at the Paul-Scherrer-Institut represents a development of a medical treatment facility on the site of a research institute, HIT and CNAO are examples, where the know-how of a research institute has been successfully deployed to construct a medical accelerator facility as part of a hospital complex. From the European point of view the activities are now concentrated in the European Network for Light Ion Therapy (ENLIGHT++) [4].

GENERAL CONSIDERATIONS FOR BEAM DIAGNOSTICS

Beam diagnostics (BD) plays an important role especially in medical accelerator facilities, due to the fact, that in this case reliable beam production is a prerequisite for the availability of medical treatments. The layout of the beam diagnostics has to obey important characteristics, concerning the precision of the devices, their usability, as well as their operational availability.

The precision of the detectors has to fit the needs for troubleshooting and/or upgrades. In many cases an order of magnitude in precision resolves error states otherwise not detectable, like long-term drifts of power supplies, or 50Hz-noise on the beam transport system etc. Another important task that is more unique to beam production facilities is to put high priority on the usability of BD devices (e.g. the user interface has to be self-explanatory). Thirdly all specifications for the BD devices have to comply with every defined beam parameter and possibly beyond, in order to ensure their operational availability to the user.

Additional requirements, more related to the routine operation of the facility, are the reliability, maintainability, modularity and/or standardization of the BD components. Reliability of the devices is constituted by taking into account the error tolerance of the devices, redundant layouts (where possible) and intrinsically safe devices with interlock generation. In order to optimize the BD maintainability, e.g. offline test functions are important, as well as the availability of commercial parts on the hardware side. Additionally a modular hardware

structure using standardized equipment allows for a fast substitution of erroneous components. In this context medical accelerator facilities have to be regarded as beam production machines with a well-defined parameter space in contrast to research institutes with a continuous upgrade situation.

THE PROSCAN PROJECT

The Paul-Scherrer Institute (PSI) in Villigen (Switzerland) is one of Europe's centres for proton-therapy research and has recently begun work with a new superconducting proton cyclotron COMET [5]. In 1984 the OPTIS proton therapy programme started in collaboration with the Lausanne University Eye clinic. PSI has experiences in the use of beam scanning techniques for the treatment of very large tumors. In 1996 Gantry 1 started, where the beam scanning technique has been adopted to perform radiation therapy with a scanned proton beam on a gantry [6]. Before the Proscan project Gantry 1 had used the proton beam from the large 590 MeV proton cyclotron for the treatment of deep-seated tumors with intensity modulated proton therapy (IMPT). In the past one of the main disadvantages has been that the cyclotron has shut down periods of about four months per year for service and upgrades. Therefore, in 2000 PSI decided to expand its radiotherapy activities into the PROSCAN project, a dedicated accelerator facility at PSI for proton therapy with a new Gantry 2 (cf. Figure 1).

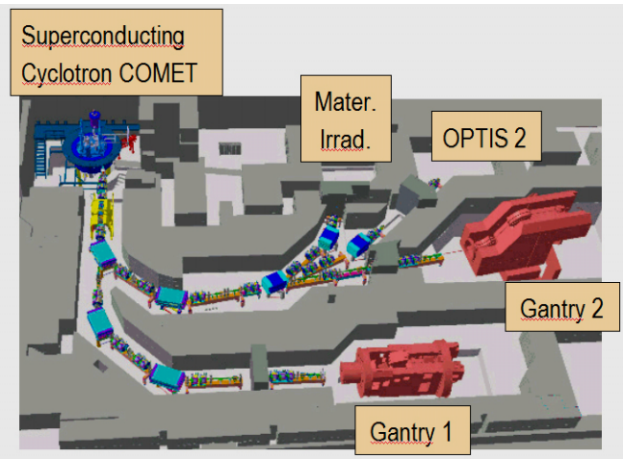

Figure 1 Beam line layout of PROSCAN (PSI)

The new cyclotron COMET was manufactured by ACCEL Instruments GmbH in close collaboration with PSI. Whereas Gantry 2 is still under construction, the superconducting cyclotron has been installed and the commissioning took place from 2005-2006. The first beam of the new cyclotron has been extracted in April 2005. The extraction efficiency has reached the design value of 80% in October 2005 and the first patient treatment using a proton beam from the new cyclotron took place in February 2007.

Proscan Beam Diagnostics

At the PROSCAN beam lines 37 "thick" (beam destructive) multi strip ionization chamber (MSIC) profile monitors can be inserted on demand for machine tuning purposes. In addition, 5 of 8 stoppers serve as Faraday cups. Continuous online measurements are provided by 6 „thin" current monitors (4 with added multi strip profile monitors), 4 beam position monitors, 22 halo monitors and 7 external loss monitors. Nearly all detectors are based on ionization chambers (IC) [7].

The "thick" MSICs consist of three successive metalized ceramic boards, divided by 4 mm wide air gaps. Whereas the outer boards provide the HV electrodes, the inner board has a thick-film coating of metalized strips in horizontal (front side, seen in beam direction) and vertical direction (other side). A high voltage of +0.6 kV is sufficient to suppress ion recombination to less than 10%. If a thick monitor is placed erroneously in the beam, the beam energy is degraded strongly and the beam is lost in the next dipole magnet.

The "thin" current monitors in front of the degrader and of the gantries are mounted fixed in the beam path as safety devices. Due to their small thickness excessive beam scattering is prevented. The devices in front of the degrader also include profile monitors (Figure 2). They consist of a stack of alternating high-voltage and measurement planes made from 6 µm titanium foils. The beam current is measured by a full foil, while two foils with 32 etched strips with 1mm pitch deliver the horizontal and vertical beam profiles. The IC monitor is immersed in nitrogen inside a box with 50 µm titanium entrance and exit windows. It is operated at a bias voltage of 2 kV in order to prevent recombination and to reduce the charge collection time.

In addition the same mechanical setup is placed directly in vacuum (without the detector box) and serves as a secondary emission monitor with a linear response even at the highest beam current densities.

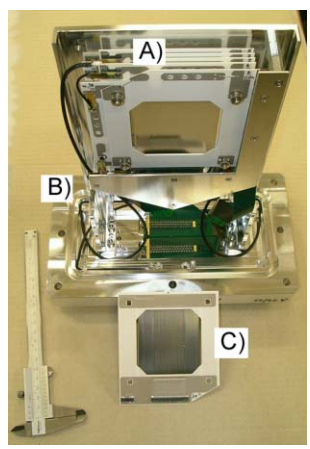

Figure 2 Thin current and profile monitor in front of the degrader A) stack of titanium foils for HV supply and measurements, B) flange and C) ceramic frame with multi-strip foil.

THE CNAO FACILITY

In 2001 the Italian Ministry of Health has created the CNAO Foundation (Centro Nazionale Adroterapia

Oncologica), consisting of five hospitals situated in Milan and Pave and the former TERA foundation [8]. Additionally the Italian National Institute of Nuclear Physics (INFN), the University and Polytechnic of Milan, and the University and Town of Pave now participate in CNAO. In 2002 the final design of the CNAO accelerator facility was settled [9].

The CNAO facillity will use light ion beams (proton, carbon) for tumor treatment and radiobiological research. The treatment will be performed in the end-stage of CNAO using 5 treatment rooms, 3 rooms with fixed beam and 2 rooms with gantries. In the first stage of CNAO 3 treatment rooms will be equipped with 3 horizontal and 1 vertical fixed beam setups (see Figure 3). The CNAO cancer therapy facility is presently under construction in Pave, 30 km south of Milan. The facility is located in close proximity to the San Matteo hospital, which offers a well-suited medical infrastructure for the new treamtent facility. The underground level of the building hosts the accelerator and the treatment rooms.

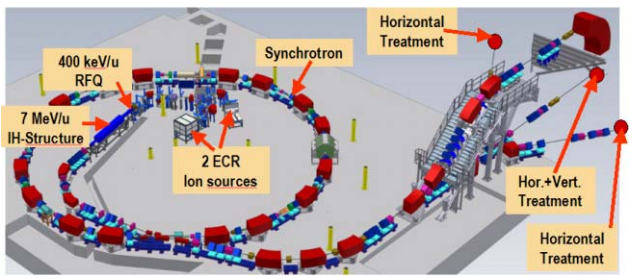

Figure 3 Layout of the CNAO facility

The accelerator part follows partly the concept of the Proton Ion Medical Machine Study (PIMMS) hosted at CERN [10]. In the frame of the collaboration with CNAO GSI is responsible for the layout, construction and delivery of the CNAO Linac. The Linac is composed of an RFQ and an IH-structure identical to the one designed for the HIT facility [11]. The RFQ accelerates particles from 8 keV/u to 400 keV/u and the IH further accelerates the ion beam 7 MeV/u. The CNAO synchrotron consists of two symmetric achromatic arcs connected by two dispersion free straights and has a circumference of approximately 78 m. The maximum energy of the ions is 400 MeV/u at a repition rate of 0.4 Hz. The synchrotron and high-energy part of the machine are engineered by CERN, INFN and LPSC/IN2P3. At present it is foreseen to begin the commissioning of the machine in fall 2007.

To facilitate the commissioning and integration of the Linac system into the CNAO facility an autonomous control system and all necessary BD devices were included into the GSI delivery. The GSI BD group manufactures, delivers and commissions diagnostic components for the Linac and MEBT (Medium Energy Beam Transfer) sections. For monitoring the beam profile at the entrance of the Linac and in the MEBT in total 7 profile grids will be installed. The ion current will be detected with 2 AC-transformers and 5 Faraday-Cups. Here GSI supplies the electronics for the Faraday-cups. In order to detect the beam energy using the time-of-flight method 4 phase probes are included in the delivery. A detailed description of the detectors is given in the next section since they are identical to the BD components produced for HIT. Also the foil stripper mounted on a stepping motor vacuum feed-through and a modular DAQ system is supplied in the frame of the GSI BD delivery.

Part of the BD equipment produced for CNAO was used in the test measurements at the RFQ-Testbench installed at GSI during October/November 2006.

HIT – HEIDELBERG ION THERAPY

Since 1997 more than 350 patients have been successfully treated in the GSI experimental cancer treatment program using the intensity controlled rasterscan method with carbon ions [3]. Based on the GSI pilot project it was decided to build a dedicated facility at the university hospital of Heidelberg for the treatment of about 1000 patients/year [12].

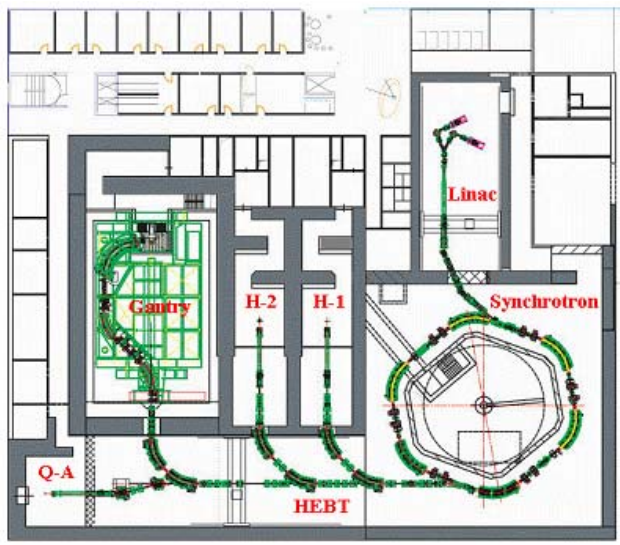

Figure 4 Layout of the HIT facility

All key parameters of the HIT facility are defined by the demands for radiotherapy. Two ECR ion sources allow for a relatively fast change of the ion species (p, He, C and O ions). Patient treatment is performed in 3 treatment areas, including the first heavy ion isocentric gantry.
The ion energy of 50-430 MeV/u is chosen such that the ion range in water is 20-300 mm. The synchrotron has an extraction time of 1-10s with 1E6 to 4E10 ions per spill and the beam diameter can be chosen from 4-10 mm FWHM. Figure 4 presents the layout of the first underground floor of the HIT facility housing the accelerator complex.

The two parallel ECR ion sources produce dc-beam currents of up to 1.2 mA for protons at 8 keV/u. The injector linac consists of an RFQ accelerating the ions to 400 keV/u in close connection to an IH-structure that accelerates the beam to the synchrotron injection energy of 7 MeV/u. A compact synchrotron with a circumference of 65 m further accelerates the ion beam. The beam is distributed to four target stations. Two stations have a

fixed horizontal beam and the third treatment place is equipped with the isocentric gantry allowing 3D irradiations from all directions [13]. The gantry beam transport system (3 dipoles, 8 quadrupoles) has a weight of 140t and the total weight of the gantry adds up to 570t. The construction of the gantry structure and the integration of the components were performed by MT Aerospace. All treatment places are equipped with a magnetic scanner system for 3D volume conformal irradiations using the rasterscan method.

Commissioning of the HIT accelerator

In winter 2005/2006 the low energy beam transport system (LEBT) has been assembled in the new Linac hall and the commissioning of the ion sources started in April 2006. The LEBT, Linac and MEBT (medium energy beam transport) sections were mounted and commissioned successively in the period May-December 2006.
The commissioning of the LEBT and Linac sections was performed in three steps: 1) ion sources and LEBT, 2) 400 keV/u RFQ and 3) 7 MeV/u IH-structure. The measurements of all relevant beam parameters (beam intensity, profile, energy etc.) were performed using the HIT BD components [14, 15].

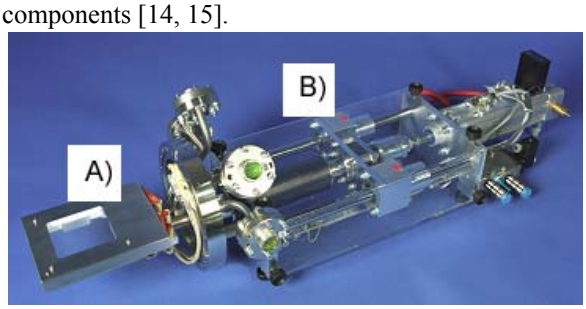

Figure 5 Profile grid (A) with pneumatic actuator (B)

During the commissioning of the LEBT section (May-June 2006) the dc beam of the two ion sources was measured using Faraday-cups and profile grids. The BD components in the two ion sources branches were especially designed to withstand the relatively high dc-beam power of up to 360 W at a very small penetration depth of approx. 100 nm. Water-cooled Faraday-cups were used for the detection of the beam current in the two source branches. The intersecting part of the device is made of a W/Cu sandwich structure with a circular shaped suppression electrode operated at 1 kV.

In each source branch a combination of horizontal slits and a Faraday-cup is installed at the exit of the spectrometer magnet for the acquisition of mass spectra. Profile grids were used for the alignment of the ion beam with the geometrical axis of the transport system and to tune the focussing elements. Figure 5 shows a standard profile grid with 64 wires per plane, both horizontal and vertical, and a spacing of the grid wires of 1.2 mm.

The main task of the Linac commissioning (Sept.-Dec. 2006) was to tune the RFQ to the design energy of 400 keV/u. For precise energy measurements a temporary setup at the RFQ exit was equipped with 3 phase probes for energy detection using the time-of-flight (TOF) method. The signals of the capacitive pickups are amplified by low-noise 60dB pre-amps and fed into fast 4 GSa/s digitizer boards for online display in the accelerator control system.

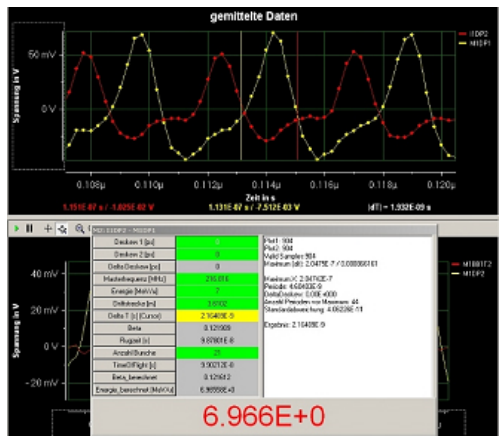

Figure 6 TOF-Energy measurement at the exit of the IH-DTL, top: signals of 2 successive phase probes, bottom: energy calculation using the cross-correlation of the phase probe signals (E=6.996 MeV/u)

Figure 6 shows an example measurement of two successive phase probes at the exit of the RFQ. The visible phase shift of the signals reflects the time-of-flight between the two probe positions. The graphical user interface allows displaying the beam energy online by calculating the cross-correlation of the two phase probe signals. To control the beam intensity in the linac section 3 AC-Transformers are installed and an online display of all 3 ACTs allows monitoring the beam transmission during routine operation of the Linac. By the end of 2006, the installation of the synchrotron and HEBT sections was finished and in February 2007 the first beam was injected into the HIT synchrotron. The synchrotron ring is equipped with two viewing screens, one screen is installed in period 1 (just before the re-entry into the injection septum) and a second viewing screen is installed in the extraction channel.
Figure 7 displays the image of the very first turn of a 7 MeV/u carbon ion beam in the HIT synchrotron.

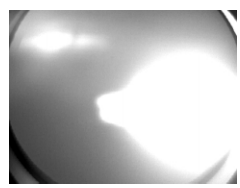

Figure 7 First circulating beam in the HIT synchrotron, detected with a viewing screen

The target of the viewing screens is coated with P43, a scintillating material optimized concerning low beam intensities and small optical decay times (1 ms), in order to preserve the time structure of the beam. To monitor the position of the circulating beam each of the 6 synchrotron periods is equipped with a shoe-box type beam position

monitor (BPM). The pick-ups have been especially designed for the relatively low revolution frequency of 0.5-3 MHz of the HIT synchrotron. nd the plate signals are converted to position data using commercial log-ratio BPM electronics [16].

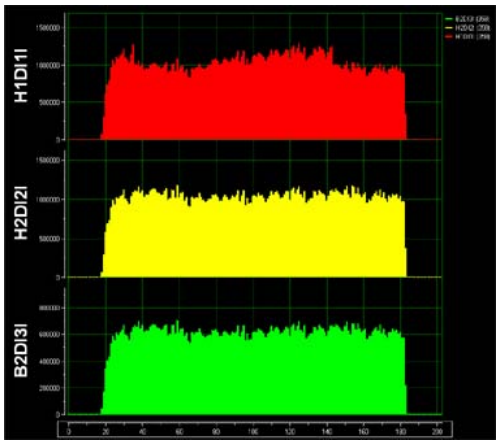

Figure 8 Spillstructure measured with 3 successive ionization chambers

As an example of HEBT diagnostics Figure 8 shows the signals of 3 successive ionization chambers for a 250 MeV/u carbon beam with an optimized flat spill structure The ionization chamber is part of a combined detector head consisting of a multi-wire proportional chamber (MWPC) on the front and the IC on the backside, both operated with Ar/CO_2 gas.

Figure 9 First beam at the Isocenter, measured with the isocenter-diagnostics device (beam diam.: 10 mm)

At the treatment places special viewing screens are used to verify the beam position and profile at the so-called iso-center, i.e. the point where the ion beam is applied to the patient. These isocenter-diagnostic devices consist of a 20x30mm viewing screen (P43), that is monitored using a double peltier-cooled high-resolution CCD camera [17]. The whole setup is mounted on air inside a metal housing to prevent the camera from outside stray light. The isocenter-diagnostics is fixed to the patient robot for the positioning of the scintillating screen.
In March 2007 the first beam was successfully transmitted to the target, represented by the isocenter diagnostics. Figure 9 shows the isocenter screen hit by a 430 MeV/u carbon ion beam.

SUMMARY AND OUTLOOK

It was shown, that hadrontherapy has developed from a research-center based niche medical application to a potentially standard technique. Three examples for medical treatment facilities have been presented, all in different project states. The PSI PROSCAN project has recently started patient treatment but is still located inside a research center. The CNAO facility is under construct-ion and will serve as the major centre for hadrontherapy in Italy. Various examples of the HIT beam diagnostic measurements underlined the importance of BD during the commissioning phase. The facilities presented in this report open up the scenery for far more standardized hospital-based medical accelerators of the future.

ACKNOWLEDGEMENTS

I'm greatly indebted to my former colleague and present collaboration partner Andreas Peters, who has been responsible for the BD layout of HIT at the GSI therapy project, for his introduction to beam diagnostics and so many fruitful discussions. Rudolf Dölling is acknow-ledged for kindly providing information about the PROSCAN diagnostics. For the CNAO project I thank Sandro Rossi for the supplied data and Bernhard Schlitt and Andreas Reiter of the GSI-CNAO collaboration. Udo Weinrich and Dieter Wilms are thanked for the joint effort of the HIT commissioning team.

REFERENCES

[1] H. Stelzer, Nuclear Physics B Proc. Suppl. 61(3), 1998, 650.
[2] Y. Schweinfurth et al., GSI Scientific Report 2004, 2004, 274.
[3] G. Kraft et al. , Conf. Proc. EPAC1998, 1998, 212.
[4] http://ptcog.web.psi.ch/
[5] J.M. Schippers et al., Conf. Proc. Cyclotrons2004, 2004, 188.
[6] J.M. Schippers et al., Journal of Physics: Conference Series 41 (2006) 61.
[7] R. Dölling, this Conf. Proceedings.
[8] U. Amaldi and M. Silari, "The TERA Project and the Centre for Oncological Hadrontherapy", Laboratori Nazionali dell'INFN, Frascati, 1995.
[9] S. Rossi, Conf. Proc. EPAC2006, 2006, 3631.
[10] L. Badano, S. Rossi et al., "Proton-Ion Medical Machine Study (PIMMS), Part I and II, CERN/PS 1999-010 DI and CERN/PS 2000-007 DR, Geneva.
[11] B. Schlitt et al., Conf. Proc. LINAC2006, 2006, 148.
[12] H.Eickhoff et al., Conf. Proc. EPAC2004, 2004, 290.
[13] U. Weinrich, Conf. Proc. EPAC2006, 2006, 963.
[14] A. Reiter et al., Conf. Proc. EPAC 2006, 2006, 1028.
[15] A. Peters and P. Forck, Conf. Proc. BIW 2000, 2000, 519.
[16] www.bergoz.com
[17] www.hamamatsu.com

List of Authors

Italic papercodes indicate primary authors

— A —

Abbas, K. WEPC20
Abbott, M. G. MOD1A01
Abiven, Y.-M. *WEPB24*
Agari, A. MOO3A01
Akre, R. WEPC28
Alesini, D. TUPB32, TUPC10, WEO1A03, WEO2A03
Allison, S. WEPC28
Andersson, Å. *TUPB27*, TUPC25
Andre, C. A. MOO3A02
Andre, T. A. WEPB31
Arutunian, S. G. MOO3A03, *WEPB26*
Aryshev, A. S. WEPB13
Asova, G. *TUPB23*, TUPC02
Ausset, P. WEPB31
Azima, A. *WEPC13*

— B —

Baboi, N. TUPB12, TUPB15, TUPC26
Bacci, A. WEO2A03
Badano, L. *TUPC11*, *WEPC20*, *WEPC20*
Baehr, J. W. TUPB13, TUPB29, TUPC02, TUPC05, TUPC07, *WEPB20*
Bal, C. B. TUPB24, TUPB28
Baller, B. B. WEPC27
Ballester, F. WEPC19
Banchi, L. *WEPC22*
Barabin, S. V. TUPB14
Bardorfer, A. WEPC17
Barnes, P. G. WEPC24
Battistello, L. TUPB04
Becker, F. *MOO3A02*
Behrmann, G. J. WEPB02
Beijers, J. P.M. TUPC24
Bellaveglia, M. WEO2A03
Belleman, J. M. TUPB09
Belohrad, D. B. *WEPB09*
Berden, G. WEO2A02
Böge, M. TUPB26
Biscari, C. WEO1A03
Blaskiewicz, M. TUO1A01
Blind, B. TUPB10
Bocci, A. *WEPB29*
Bogard, D. TUPB17
Bogey, T. *TUPB31*
Bogoni, A. WEPC22
Boni, R. WEO2A03
Bontoiu, C. TUPC09
Boogert, S. T. WEPB13
Boscolo, M. WEO2A03
Brabant, A. TUPB17
Brandenburg, S. TUPC24
Braun, H.-H. WEO1A03, WEPC14
Bravin, E. *MOO1A02*, TUPB28, WEO1A03, WEPC14
Brennan, J. M. *TUO1A01*
Browne, J. WEPC28
Bulfone, D. TUPB04
Buonomo, B. *TUPB05*, WEO1A03
Burger, S. TUPB28, WEO1A03
Byrd, J. M. *WEO1A02*, WEPC08

— C —

Caccia, M. WEPC20
Cameron, P. *TUPC08*, *WEPC10*
Cappellini, C. WEPC20
Carlson, K. WEPB18
Cassinari, L. TUPC16, TUPC20, WEPB05, WEPC04
Castellano, M. WEO2A03
Catani, L. WEO2A03
Cestelli Guidi, M. C.G. WEPB29
Chel, S. TUPB15
Chen, J. WEPB16, TUPB30, WEPC17
Cherepanov, V. P. *WEPC26*
Chiadroni, E. WEO2A03
Childress, S. C. WEPC27
Chiu, P. C. TUPB30, WEPC17
Chmill, V. WEPC20
Chrin, J. T.M. TUPB26
Chubar, O. V. TUPB27, TUPC16
Cialdi, S. WEO2A03
Cianchi, A. *WEO2A03*
Clozza, A. WEPB29, WEO2A03
Coiro, O. WEO1A03
Contrepois, P. TUPB15
Cook, A. M. WEO2A03
Corsini, R. WEO1A03
Couprie, M.-E. WEPB05
Craievich, P. *TUPC09*, *TUPC10*, WEO1A03
Cross, G. M. WEPC24
Cultrera, L. WEO2A03
Cupolo, J. WEPC10
Curtoni, A. TUPB17

— D —

Dabrowski, A. E. WEO1A03
Dach, M. TUPC25
Dalesio, L. R. WEPC28
Dawson, W. C. WEPC10
De Monte, R. TUPB04, *TUPC13*
De Santis, S. *WEPC08*
Decker, F.-J. WEPC07

Decker, G. *MOO3A03*, WEPB26
Degen, C. WEPC10
Dehler, M. WEPB02
Dehning, B. WEPC03, WEPC06, WEPC09
Della Penna, A. J. WEPC10
Dementyev, E. N. WEPC26
Denard, J.-C. TUPC16, TUPC20, WEPC04, WEPC16
Di Mitri, S. TUPC06, TUPC10
Di Pirro, G. WEO2A03
Dölling, R. *WEPC23*
Doebert, S. WEO1A03
Dohou, F. WEPB24
Doutresssoulles, C. WEPB31
Drago, A. WEPB29, WEO2A03
Düsterer, S. WEPC13
Ducoudret, B. WEPB31
Dunning, M. P. WEO2A03
Duperrex, P.-A. *WEPB19*
Dusatko, J. E. WEPC28
Dutriat, C. WEPC14

— E —

Effinger, E. *WEPC06*
Emanuele, E. P. WEPB29
Emery, J. E. WEPC06
Epaud, F. TUO1A03
Esposito, A. WEO2A03
Evtushenko, P. WEPB01

— F —

Fabjan, C. WEPC09
Fadil, H. WEPB23
Faircloth, D. C. WEO2A01
Farabolini, W. *TUPB17*
Feldhaus, J. WEPC13
Ferianis, M. *MOO2A03*, TUPC06, TUPC09, TUPC10, TUPC11, WEPC02, WEO1A03, *WEPC11*, WEPC22
Ferioli, G. WEPC03, WEPC06
Ferrando, O. WEPC20
Ferrari, A. WEO1A03
Ferrario, M. WEO2A03
Ficcadenti, L. TUPB32
Filhol, J.-M. WEPC04
Filippetto, D. WEO2A03
Fiorito, R. B. WEPC21
Floettmann, K. TUPB23
Foggetta, L. G. TUPB05
Fontanini, S. TUPB04
Forchi', V. TUPB04
Forck, P. MOO3A02, TUPB06, TUPB14
Ford, R. D. WEPC27
Fox, J. D. *TUPB02*
Frigola, P. WEO2A03
Frisch, J. C. WEPC28
Froehlich, L. WEPC19
Fuersch, J. TUPB21, WEPB21
Fujita, T. TUPB22
Fuller, R. WEPC28
Fusco, V. WEO2A03

— G —

Gabor, C. TUPB11, WEO2A01
Gaio, G. TUPB04
Galatis, A. A. *TUPB06*
Gallo, A. WEO2A03
Gamma, G. G. WEPB19
Garvey, T. TUPC07
Gasior, M. TUPC08
Gatti, G. WEO2A03
Gerth, C. *MOO2A02*, *TUPC03*, WEPC01
Ghelfi, P. WEPC22
Ghigo, A. WEO1A03, WEO2A03
Giacomini, T. TUPB14
Giacuzzo, F. TUPB04
Giannessi, L. WEO2A03
Gibson, P. N. WEPC20
Gillespie, W. A. WEO2A02
Gilpatrick, J. D. *TUPB10*
Girardot, P. TUPB15, TUPB17
Gluhov, S. I. WEPB04
Gobin, F. TUPB17
Goddard, B. TUPB28
Goettmann, W. *TUPB25*
Gorlov, T. V. TUPC18
Granelli, R. TUPB17
Grieser, M. WEPB23
Grilli, A. G. WEPB29
Görler, M. WEPC19
Gromme, A. E. WEPC28
Gurko, V. F. WEPB04

— H —

Hacker, K. E. *TUPB20*, WEPB15, WEPC02
Hamdi, A. *WEPC19*
Harrault, F. TUPB17
Harris, D. WEPC27
Hartmann, P. *TUPB21*, *WEPB21*
Hasan, S. TUPB05
Hirose, E. MOO3A01
Hänel, M. TUPB29
Hoff, L. T. WEPC10
Hoffmann, D. MOO3A02
Holder, D. J. TUPB23
Holzer, E. B. WEPC03, WEPC09
Holzwarth, U. WEPC20
Hori, Y. WEPB22
Hosaka, M. WEPB22
Hsu, K. T. TUPB30, WEPC17
Hsu, S. Y. TUPB30
Hu, K. H. WEPC17

Hubert, N. *TUPC20*, WEPC04
Hutchins, S. C. TUPB28

— I —

Ieiri, M. MOO3A01
Ilday, F. O. WEPB03
Incurvati, M. WEO2A03
Indurthy, D. WEPC27
Iriso, U. *MOD1A03*
Ivanisenko, Ye. *TUPC02*

— J —

Jamet, C. *WEPB31*
Jamison, S. P. WEO2A02
Jansson, A. TUPC08
Jastrzab, M. WEPC20
Jolly, S. *WEO2A01*
Joly, B. TUPB18
Jones, O. R. TUPB31
Justus, M. *WEPB01*

— K —

Kaertner, F. X. WEPB16
Kalekin, O. TUPC02
Karataev, V. WEPB13
Kasprowicz, G. *TUPB09*
Katoh, M. WEPB22
Katoh, Y. MOO3A01
Kaufmann, W. TUPB16
Kazakevich, G. M. WEPB18
Keil, B. *WEPB02*, WEPB19
Kendziora, C. L.K. WEPC27
Khilchenko, A. D. WEPB04
Khodyachykh, S. TUPB13, TUPB23, TUPC05, *TUPC07*
Kim, J. WEPB16
Kiselev, V. A. WEPB04, WEPB06
Knaack, K. TUPB12, *WEPB30*
Knabbe, E.-A. WEO2A02
Kobayashi, K. WEPC04
Koch, J. M. *TUO1A03*
Koerfer, M. TUPB25
Kopp, S. E. WEPC27
Koprek, W. WEPC01
Korepanov, S. A. TUPB13, *TUPB32*, TUPC02
Korosec, T. WEPC02
Kotturi, K. D. WEPC28
Kowina, P. *TUPB16*
Kramer, D. K. *WEPC03*, WEPC09
Kramert, R. WEPB02
Krasilnikov, M. *TUPB29*, TUPB13, TUPB23, TUPB32, TUPC02, TUPC07
Krejcik, P. *WEPC28*
Kremers, H. R. *TUPC24*
Krempasky, J. TUPB26
Krouptchenkov, I. *TUPC12*
Kube, G. *MOO1A03*, *TUPB19*
Kuo, C. H. *TUPB30*, *WEPC17*
Kurennoy, S. S. TUPB10
Kvashnin, A. N. WEPB04

— L —

Labat, M. *WEPB05*
Lahonde-Hamdoun,C.L.H. TUPB17
Lang, K. TUPB06
Laxdal, R. E. WEPB07
Le Coz, W. LC. WEPB31
Leclercq, N. L. TUPC20
Lee, D. TUPB30
Lee, D. A. *TUPB11*, WEO2A01
Leemann, S. C. TUPC25
Lefevre, T. *TUPB28*, *WEO1A03*, *WEPC14*
Lehnert, U. WEPB01
Lerch, T. TUPB17
Level, M.-P. WEPC04
Levichev, E. B. WEPB04, WEPC26
Liakin, D. A. *TUPB14*
Ligi, C. WEO2A03
Lipka, D. TUPB12
Liu, K.-B. WEPC17
Loehl, F. TUPB20, WEPB08, *WEPB15*, *WEPB16*, WEPC01, WEPC02
Longo, S. WEPB09
Lonza, M. *TUPB04*
Lorbeer, B. *WEPB08*, *WEPB08*
Ludwig, F. WEPB08
Luedecke, H. L. WEPB20
Luedeke, A. TUPB27
Lund-Nielsen, J. TUPB12, *TUPC26*, WEPB02
Lunin, A. *TUPC23*
Luo, Y. WEPC10
Luong, M. TUPB15, TUPB17, WEPC19

— M —

MacLeod, A. WEO2A02
Magnus, S. WEPC19
Mailian, M. R. MOO3A03, WEPB26
Malka, V. *MOO2A01*
Marcelli, A. WEPB29
Marcellini, F. WEO1A03
Marchand, P. WEPC04
Marchetto, M. WEPB07
Mariette, C. WEPC04, *WEPC16*
Marinkovic, G. WEPB02
Marizza, R. TUPB04
Marusic, A. WEPC10
Mastorides, T. TUPB02
Mazzitelli, G. TUPB05
McCrady, R. C. TUPB10
Medvedko, A. S. WEPC26
Meshkov, O. I. WEPB04, *WEPB06*

Meyer, M. WEPC13
Michel, P. WEPB01
Migliorati, M. WEO2A03
Mildner, N. TUPB12
Minakawa, M. MOO3A01
Mitsuhashi, T. WEPB12
Müller, M. U. WEPB19
Mochihashi, A. *WEPB22*
Molinari, G. WEPC20
Moore, C. D. WEPC27
Morgan, A. F.D. *WEPB28*
Mosnier, A. TUPB17
Mostacci, A. WEO2A03
Mozzanica, A. TUPB05
Muchnoi, N. Yu. WEPB06
Mueller, F. WEPC21
Mueller, J. M. WEPB08
Muratori, B. D. TUPB23
Murtas, F. TUPB05
Musumeci, P. WEO2A03

— N —

Nadji, A. TUPC20
Nadolski, L. S. TUPC20
Nagaoka, R. WEPB05, *WEPC04*, WEPC16
Nakamura, T. WEPC04
Naumenko, G. A. WEPB13
Naylor, G. A. TUO1A03, *TUPB18*
Neubert, R. WEPB30
Neumann, R. TUPB12
Nguyen, H. TUPB01
Nietzsche, S. WEPB30
Noelle, D. *TUPB12*, WEPB02
Norum, S. N. WEPC28
Noumi, H. MOO3A01
Novo, J. WEPC19

— O —

Obina, T. *WEPB12*
Odier, OP. WEPB09
O'Hara, J. F. TUPB10
Olivetto, C. O. WEPB31
Olmos, A. MOD1A03, *TUPC19*
Oppelt, A. TUPC07
Orlov, A. Y. TUPB14
Orsini, F. TUPB17

— P —

Pace, E. WEO2A03
Palumbo, L. WEO2A03
Passuello, R. TUPB04
Patrick, R. P. WEPB24
Pavlovic, L. *WEPC02*
Pavlovic, Z. *WEPC27*
Payne, S. J. *WEPC24*
Peauger, F. TUPB17
Pedeau, D. TUPC16, TUPC20, WEPB05
Pellegrino, L. WEO2A03
Pertica, A. WEPC24
Peters, A. TUPB06, WEPB30, WEO3A02
Petrarca, M. WEO2A03
Petronio, M. TUPC10
Petrosyan, B. TUPC02
Phillips, P. J. *WEO2A02*
Piccinini, M. P. WEPB29
Pillai, C. TUPB10
Piminov, P. A. WEPB04
Piotrowski, J. P. WEPB29
Pivetta, L. TUPB04
Plouviez, E. TUO1A03
Podadera Aliseda, I. *TUPB03*
Poggi, M. TUPC09
Pollet, P. WEPB02
Poti', L. WEPC22
Pottin, B. TUPC16
Potylitsyn, A. WEPB13
Power, J. F. TUPB10
Pozimski, J. K. TUPB11, WEO2A01
Preger, B. WEO1A03
Prest, M. TUPB05
Pérez, F. TUPC19
Prieto, V. TUPB24
Proga, M. WEPC27
Prost, L. R. WEPB18

— Q —

Quattromini, M. WEO2A03
Quintieri, L. TUPB05

— R —

Raco, A. R. WEPB29
Radcliffe, P. WEPC13
Raich, U. TUPB09
Rawnsley, W. R. WEPB07
Redlin, H. WEPC13
Rehm, G. *MOD1A01*, TUPC19, WEPB25, WEPB28
Renaglia, T. TUPB28
Ribeiro, F. WEPC04
Ricci, R. WEO2A03
Riesch, W. TUPC26
Rimjaem, S. TUPB13
Roensch, J. *TUPB13*, TUPC07, WEPB20
Roggli, M. WEPB02
Rogind, D. WEPC28
Rohrer, M. TUPB27, TUPC25, WEPB02
Romanov, G. TUPC23
Ronsivalle, C. WEO2A03
Rosenbaum, G. MOO3A03, WEPB26
Rosenzweig, J. B. WEO2A03
Rossbach, J. TUPB13

Rossi, A. R. WE02A03
Rossi, F. WEPC02, WEPC22
Rouvière, N. TUPB15
Rowland, J. MOD1A01
Rybarcyk, L. TUPB10

— S —

Sanelli, C. WE02A03
Sasaki, S. *TUPB22*
Sato, Y. MO03A01
Sautier, R. S. TUPB24
Savage, P. TUPB11, WE02A01
Scafuri, C. TUPB04
Scheidt, K. B. *TUPB07*, *TUPB08*
Schilcher, T. WEPB02
Schiller, F. WEPB30
Schirmer, D. TUPB21
Schlarb, H. TUPB20, WEPB08, WEPB15, WEPB16, *WEPC01*, WEPC02, WEPC13
Schlott, V. TUPB26, TUPB27, *TUPC25*, WEPB02, WEPC21
Schmidt, B. WE02A02
Schmidt, T. TUPB26
Schmidt-Foehre, F. TUPB12
Schmüser, P. WE02A02
Schoelles, J. TUPB16
Schoo, D. P. TUPB01
Schroeder, R. WEPC10
Schultheiss, C. WEPC10
Schwickert, M. *WE03A02*
Sellberg, G. W. TUPB01
Serafini, L. WE02A03
Serio, M. WE02A03
Severino, F. TU01A01
Sgamma, F. WE02A03
Shimada, M. WEPB22
Shkvarunets, A. G. *WEPC21*
Shoji, M. TUPB22
Sieber, T. *WEPB23*
Siemens, M. TUPB12, WEPB02
Simon, C. *TUPB15*, TUPB17
Sinyatkin, S. V. WEPB06
Smaluk, V. V. TUPC09, WEPB04, WEPB06, WEPC26
Soby, L. TUPB03, WE01A03
Solyak, N. TUPC23
Sorchetti, R. S. WEPB29
Spataro, B. WE02A03
Spesyvtsev, R. *TUPC05*
Sreedharan, R. WEPC04
Staack, M. WEPC19
Staykov, L. TUPB13, TUPC05, TUPC07
Steffen, B. WE02A02, WEPB03
Steinhagen, R. J. *TU01A02*
Stephan, F. TUPB13, TUPB23, TUPB29, TUPB32 TUPC02 TUPC07
Stockner, M. *WEPC09*, ,
Streun, A. TUPB26, TUPB27, TUPC25
Sukhanov, D. P. WEPC26
Sukhikh, L. G. *WEPB13*
Sutherland, M. WEPB18
Suzuki, Y. MO03A01

— T —

Takahashi, H. MO03A01
Takasaki, M. MO03A01
Takashima, T. TUPB22
Takashima, Y. WEPB22
Tan, C.-Y. TUPC08
Tanaka, K. H. MO03A01
Tassotto, G. R. *TUPB01*, WEPC27
Tazzioli, F. WE02A03
Tecker, F. WE01A03
Tepikian, S. WEPC10
Teytelman, D. *WEPC07*
Thomas, C. A. *WEPB25*
Thoulet, S. WEPB09
Tomassini, S. WE02A03
Tordeux, M.-A. *TUPC16*
Toyoda, A. *MO03A01*
Traber, T. TUPB12
Tranquille, G. *TUPB24*
Treyer, D. M. WEPB02, *WE03A01*
Tron, A. M. *TUPC18*
Trovato, G. TUPC09
Trovo, M. TUPC11

— U —

Urakawa, J. WEPB13
Urschütz, P. WE01A03
Uzun, I. MOD1A01, WEPB28

— V —

Vaccarezza, C. WE02A03
Valente, P. TUPB05
Vallazza, E. TUPB05
van der Meer, A. F.G. WE02A02
van Garderen, E. D. *TUPB26*
Velasco, M. WE01A03
Veronese, M. *TUPC06*, TUPC10, TUPC11, WE01A03
Verzilov, V. A. *WEPB07*
Vescovi, M. WE02A03
Vicario, C. WE02A03
Vidmar, M. WEPC02
Vignet, J. L. WEPB31
Vilcins, S. TUPB12, WEPB02
Vodel, W. WEPB30
Vogel, E. WEPC01
von Hahn, R. WEPB23

— W —

Wagner, R. WEPB21
Warner, A. *WEPB18*
Watanabe, H. MOO3A01
Weis, T. TUPB21, WEPB21
Welsch, C. P. WE01A03, WEPC14
Wendt, M. TUPC23
Werner, M. TUPB19, WEPC19
White, W. E. WEPC28
Whitehead, S. A. WEPC24
Will, I. TUPB29
Wille, K. TUPB21, WEPB21
Winter, A. *WE01A01*, *WEPB03*, WEPB08
Wittenburg, K. TUPC12, WEPB30
Wolf, A. WEPB23
Wu, C. Y. TUPB30
Wulf, F. TUPB25

— Y —

Yamanoi, Y. MOO3A01
Yin, Y. WEPC08

— Z —

Zamantzas, C. WEPC06
Zelazny, S. WEPC28
Zhilich, V. N. WEPB06
Zhuravlev, A. N. *WEPB04*, WEPB06
Zubarev, P. V. WEPB04
Zwaska, R. M. WEPC27

Institutes List

ALBA
Bellaterra
- Iriso, U.
- Olmos, A.
- Pérez, F.

ANL
Argonne, Illinois
- Decker, G.

BINP SB RAS
Novosibirsk
- Cherepanov, V. P.
- Dementyev, E. N.
- Gluhov, S. I.
- Gurko, V. F.
- Khilchenko, A. D.
- Kiselev, V. A.
- Kvashnin, A. N.
- Levichev, E. B.
- Medvedko, A. S.
- Meshkov, O. I.
- Muchnoi, N. Yu.
- Piminov, P. A.
- Sinyatkin, S. V.
- Smaluk, V. V.
- Sukhanov, D. P.
- Zhilich, V. N.
- Zhuravlev, A. N.
- Zubarev, P. V.

BNL
Upton, Long Island, New York
- Blaskiewicz, M.
- Brennan, J. M.
- Cameron, P.
- Cupolo, J.
- Dawson, W. C.
- Degen, C.
- Della Penna, A. J.
- Hoff, L. T.
- Luo, Y.
- Marusic, A.
- Schroeder, R.
- Schultheiss, C.
- Severino, F.
- Tepikian, S.

Bergische Universität Wuppertal
Wuppertal
- Wagner, R.

Bilkent University
Bilkent, Ankara
- Ilday, F. O.

CEA
Gif-sur-Yvette
- Ballester, F.
- Bogard, D.
- Brabant, A.
- Chel, S.
- Contrepois, P.
- Curtoni, A.
- Farabolini, W.
- Girardot, P.
- Gobin, F.
- Granelli, R.
- Hamdi, A.
- Harrault, F.
- Lahonde-Hamdoun, C. L.H.
- Lerch, T.
- Luong, M.
- Mosnier, A.
- Novo, J.
- Orsini, F.
- Peauger, F.
- Simon, C.

CERN
Geneva
- Bal, C. B.
- Belleman, J. M.
- Belohrad, D. B.
- Bogey, T.
- Braun, H.-H.
- Bravin, E.
- Burger, S.
- Corsini, R.
- Dehning, B.
- Doebert, S.
- Dutriat, C.
- Effinger, E.
- Emery, J. E.
- Fabjan, C.
- Ferioli, G.
- Gasior, M.
- Goddard, B.
- Holzer, E. B.
- Hutchins, S. C.
- Jones, O. R.
- Kasprowicz, G.
- Kramer, D. K.
- Lefevre, T.
- Longo, S.
- Molinari, G.
- Odier, OP.
- Podadera Aliseda, I.
- Prieto, V.
- Raich, U.
- Renaglia, T.
- Sautier, R. S.
- Soby, L.
- Steinhagen, R. J.

- Stockner, M.
- Tecker, F.
- Thoulet, S.
- Tranquille, G.
- Urschütz, P.
- Welsch, C. P.
- Zamantzas, C.

CNIT
Pisa
- Bogoni, A.
- Ghelfi, P.
- Poti', L.

DEEI
Trieste
- Petronio, M.

DELTA
Dortmund
- Fuersch, J.
- Hartmann, P.
- Schirmer, D.
- Weis, T.
- Wille, K.

DESY Zeuthen
Zeuthen
- Asova, G.
- Baehr, J. W.
- Hänel, M.
- Ivanisenko, Ye.
- Khodyachykh, S.
- Korepanov, S. A.
- Krasilnikov, M.
- Luedecke, H. L.
- Oppelt, A.
- Petrosyan, B.
- Riesch, W.
- Rimjaem, S.
- Spesyvtsev, R.
- Staykov, L.
- Stephan, F.

DESY
Hamburg
- Asova, G.
- Azima, A.
- Baboi, N.
- Düsterer, S.
- Feldhaus, J.
- Floettmann, K.
- Froehlich, L.
- Gerth, C.
- Görler, M.
- Hacker, K. E.
- Knaack, K.
- Knabbe, E.-A.
- Koerfer, M.
- Koprek, W.
- Krasilnikov, M.
- Krouptchenkov, I.
- Kube, G.
- Lipka, D.
- Loehl, F.
- Ludwig, F.
- Lund-Nielsen, J.
- Magnus, S.
- Mildner, N.
- Mueller, J. M.
- Neumann, R.
- Noelle, D.
- Radcliffe, P.
- Redlin, H.
- Schlarb, H.
- Schmidt, B.
- Schmidt-Foehre, F.
- Schmüser, P.
- Siemens, M.
- Staack, M.
- Steffen, B.
- Traber, T.
- Vilcins, S.
- Vogel, E.
- Werner, M.
- Winter, A.
- Wittenburg, K.

Diamond
Oxfordshire
- Abbott, M. G.
- Morgan, A. F.D.
- Rehm, G.
- Rowland, J.
- Thomas, C. A.
- Uzun, I.

ELETTRA
Basovizza, Trieste
- Badano, L.
- Banchi, L.
- Battistello, L.
- Bontoiu, C.
- Bulfone, D.
- Craievich, P.
- De Monte, R.
- Di Mitri, S.
- Ferianis, M.
- Fontanini, S.
- Forchi', V.
- Gaio, G.
- Giacuzzo, F.
- Lonza, M.
- Marizza, R.
- Passuello, R.
- Pivetta, L.
- Rossi, F.

- Scafuri, C.
- Trovato, G.
- Trovo, M.
- Veronese, M.

ENEA C. R. Frascati
Frascati (Roma)
- Giannessi, L.
- Quattromini, M.

ESRF
Grenoble
- Epaud, F.
- Joly, B.
- Koch, J. M.
- Naylor, G. A.
- Plouviez, E.
- Scheidt, K. B.

Ente Ospedaliero Ospedali Galliera
Genova
- Ferrando, O.

Erlangen University
Erlangen
- Kalekin, O.

FOM Rijnhuizen
Nieuwegein
- Berden, G.
- van der Meer, A. F.G.

FSU Jena
Jena
- Neubert, R.
- Nietzsche, S.
- Schiller, F.
- Vodel, W.

FZD
Dresden
- Justus, M.
- Lehnert, U.
- Michel, P.

Fermilab
Batavia, Illinois
- Baller, B. B.
- Carlson, K.
- Childress, S. C.
- Ford, R. D.
- Harris, D.
- Jansson, A.
- Kazakevich, G. M.
- Kendziora, C. L.K.
- Lunin, A.
- Moore, C. D.
- Nguyen, H.
- Prost, L. R.
- Romanov, G.
- Schoo, D. P.
- Sellberg, G. W.
- Solyak, N.
- Sutherland, M.
- Tan, C.-Y.
- Tassotto, G. R.
- Warner, A.
- Wendt, M.

GANIL
Caen
- Andre, T. A.
- Doutresssoulles, C.
- Ducoudret, B.
- Jamet, C.
- Le Coz, W. LC.
- Vignet, J. L.

GSI
Darmstadt
- Andre, C. A.
- Becker, F.
- Forck, P.
- Galatis, A. A.
- Giacomini, T.
- Kaufmann, W.
- Kowina, P.
- Lang, K.
- Peters, A.
- Schoelles, J.
- Schwickert, M.

HIT
Heidelberg
- Peters, A.

HMI
Berlin
- Goettmann, W.
- Wulf, F.

INFN-Milano
Milano
- Bacci, A.
- Cialdi, S.
- Rossi, A. R.
- Serafini, L.

INFN-Roma II
Roma
- Catani, L.
- Cianchi, A.

INFN-Roma
Roma
- Petrarca, M.
- Valente, P.

INFN-Trieste
Trieste
- Vallazza, E.

INFN/LNF
Frascati (Roma)
- Alesini, D.
- Bellaveglia, M.
- Biscari, C.
- Bocci, A.
- Boni, R.
- Boscolo, M.
- Buonomo, B.
- Castellano, M.
- Cestelli Guidi, M. C.G.
- Chiadroni, E.
- Clozza, A.
- Coiro, O.
- Cultrera, L.
- Di Pirro, G.
- Drago, A.
- Esposito, A.
- Ferrario, M.
- Filippetto, D.
- Fusco, V.
- Gallo, A.
- Gatti, G.
- Ghigo, A.
- Grilli, A. G.
- Incurvati, M.
- Ligi, C.
- Marcelli, A.
- Marcellini, F.
- Mazzitelli, G.
- Murtas, F.
- Pace, E.
- Pellegrino, L.
- Preger, B.
- Quintieri, L.
- Raco, A. R.
- Ricci, R.
- Ronsivalle, C.
- Sanelli, C.
- Serio, M.
- Sgamma, F.
- Sorchetti, R. S.
- Spataro, B.
- Tazzioli, F.
- Tomassini, S.
- Vaccarezza, C.
- Vescovi, M.
- Vicario, C.

INFN/LNL
Legnaro, Padova
- Poggi, M.

IPHC
Strasbourg Cedex 2
- Olivetto, C. O.

IPN
Orsay
- Ausset, P.
- Rouvière, N.

ITEP
Moscow
- Barabin, S. V.
- Liakin, D. A.
- Orlov, A. Y.

Imperial College of Science and Technology, Department of Physics
London
- Jolly, S.
- Lee, D. A.
- Savage, P.

Instrumentation Technologies
Solkan
- Bardorfer, A.

JAI
Egham, Surrey
- Boogert, S. T.
- Karataev, V.

JASRI/SPring-8
Hyogo-ken
- Fujita, T.
- Kobayashi, K.
- Nakamura, T.
- Sasaki, S.
- Shoji, M.
- Takashima, T.

JRC
Ispra
- Abbas, K.
- Gibson, P. N.
- Holzwarth, U.

Jefferson Lab
Newport News, Virginia
- Evtushenko, P.

KEK
Ibaraki
- Aryshev, A. S.
- Hori, Y.
- Mitsuhashi, T.
- Obina, T.
- Takasaki, M.
- Tanaka, K. H.
- Urakawa, J.
- Agari, A.
- Hirose, E.
- Ieiri, M.
- Katoh, Y.
- Minakawa, M.
- Noumi, H.
- Sato, Y.
- Suzuki, Y.
- Takahashi, H.
- Toyoda, A.
- Watanabe, H.
- Yamanoi, Y.

KVI
Groningen
- Beijers, J. P.M.
- Brandenburg, S.
- Kremers, H. R.

LAL
Orsay
- Garvey, T.

LANL
Los Alamos, New Mexico
- Blind, B.
- Gilpatrick, J. D.
- Kurennoy, S. S.
- McCrady, R. C.
- O'Hara, J. F.
- Pillai, C.
- Power, J. F.
- Rybarcyk, L.

LBNL
Berkeley, California
- Byrd, J. M.
- De Santis, S.

LIXAM
Orsay
- Meyer, M.

LOA
Palaiseau
- Malka, V.

LPI
Moscow
- Tron, A. M.

MAX-lab
Lund
- Andersson, Å.

MBI
Berlin
- Will, I.

MEPhI
Moscow
- Gorlov, T. V.

MIT
Cambridge, Massachusetts
- Chen, J.
- Kaertner, F. X.
- Kim, J.

MPI-K
Heidelberg
- Fadil, H.
- Grieser, M.
- Sieber, T.
- Wolf, A.
- von Hahn, R.

NSRRC
Hsinchu
- Chen, J.
- Chiu, P. C.
- Hsu, K. T.
- Hsu, S. Y.
- Hu, K. H.
- Kuo, C. H.
- Lee, D.
- Liu, K.-B.
- Wu, C. Y.

NU
Evanston
- Dabrowski, A. E.
- Velasco, M.

Nagoya University
Nagoya
- Hosaka, M.
- Takashima, Y.

PSI
Villigen
- Andersson, Å.
- Behrmann, G. J.
- Böge, M.
- Chrin, J. T.M.
- Dach, M.
- Dehler, M.
- Duperrex, P.-A.
- Dölling, R.
- Gamma, G. G.
- Keil, B.
- Kramert, R.
- Krempasky, J.
- Leemann, S. C.
- Luedeke, A.
- Marinkovic, G.
- Mueller, F.
- Müller, M. U.
- Pollet, P.
- Roggli, M.
- Rohrer, M.
- Schilcher, T.
- Schlott, V.
- Schmidt, T.
- Streun, A.
- Treyer, D. M.
- van Garderen, E. D.

Rome University La Sapienza
Roma
- Ficcadenti, L.
- Migliorati, M.
- Mostacci, A.
- Palumbo, L.

SLAC
Menlo Park, California
- Akre, R.
- Allison, S.
- Browne, J.
- Dalesio, L. R.
- Decker, F.-J.
- Dusatko, J. E.
- Fox, J. D.
- Frisch, J. C.
- Fuller, R.
- Gromme, A. E.
- Kotturi, K. D.
- Krejcik, P.
- Mastorides, T.
- Norum, S. N.
- Rogind, D.
- Teytelman, D.
- White, W. E.
- Zelazny, S.

SOLEIL
Gif-sur-Yvette
- Abiven, Y.-M.
- Cassinari, L.
- Chubar, O. V.
- Couprie, M.-E.
- Denard, J.-C.
- Dohou, F.
- Filhol, J.-M.
- Hubert, N.
- Labat, M.
- Leclercq, N. L.
- Level, M.-P.
- Marchand, P.
- Mariette, C.
- Nadji, A.
- Nadolski, L. S.
- Nagaoka, R.
- Patrick, R. P.
- Pedeau, D.
- Pottin, B.
- Ribeiro, F.
- Sreedharan, R.
- Tordeux, M.-A.

STFC/DL/ASTeC
Daresbury, Warrington, Cheshire
- Holder, D. J.
- Jamison, S. P.
- Muratori, B. D.

STFC/RAL
Chilton, Didcot, Oxon
- Faircloth, D. C.
- Pozimski, J. K.

STFC/RAL/ASTeC
Chilton, Didcot, Oxon
- Gabor, C.

STFC/RAL/ISIS
Chilton, Didcot, Oxon
- Barnes, P. G.
- Cross, G. M.
- Payne, S. J.
- Pertica, A.
- Whitehead, S. A.

TPU
Tomsk
- Naumenko, G. A.
- Potylitsyn, A.
- Sukhikh, L. G.

TRIUMF
Vancouver
- Laxdal, R. E.
- Marchetto, M.
- Rawnsley, W. R.
- Verzilov, V. A.

TU Darmstadt
Darmstadt
- Hoffmann, D.

TUHH
Hamburg
- Lorbeer, B.

TUL
Liberec
- Kramer, D. K.

The University of Texas at Austin
Austin, Texas
- Indurthy, D.
- Kopp, S. E.
- Pavlovic, Z.
- Proga, M.
- Zwaska, R. M.

UAD
Dundee
- MacLeod, A.
- Phillips, P. J.

UCLA
Los Angeles, California
- Cook, A. M.
- Dunning, M. P.
- Frigola, P.
- Musumeci, P.
- Rosenzweig, J. B.

UGA
Athens, Georgia
- Rosenbaum, G.

UMD
College Park, Maryland
- Fiorito, R. B.
- Shkvarunets, A. G.

UU/ISV
Uppsala
- Ferrari, A.

UVSOR
Okazaki
- Katoh, M.
- Mochihashi, A.
- Shimada, M.

Uni HH
Hamburg
- Roensch, J.
- Rossbach, J.

Uni LJ
Ljubljana
- Korosec, T.
- Pavlovic, L.
- Vidmar, M.

Univ. Insubria and INFN Milano
Como
- Caccia, M.
- Cappellini, C.
- Chmill, V.
- Foggetta, L. G.
- Hasan, S.
- Jastrzab, M.
- Mozzanica, A.
- Prest, M.

University of Dundee
Nethergate, Dundee, Scotland
- Gillespie, W. A.

Università Roma Tre
Roma
- Piccinini, M. P.

Università degli Studi di Firenze
Firenze
- Emanuele, E. P.

Vigo System Sa
Warsaw
- Piotrowski, J. P.

Y. Y. Labs, Inc.
Fremont, California
- Yin, Y.

YerPhI
Yerevan
- Arutunian, S. G.
- Mailian, M. R.

Participants List

— A —

Yves-Marie **Abiven**
SOLEIL
Gif-sur-Yvette
France

Christiane **Andre**
GSI
Darmstadt
Germany

Ivan **Andrian**
ELETTRA
Basovizza, Trieste
Italy

Pascal **Anger**
GANIL
Caen
France

Galina **Asova**
DESY
Hamburg
Germany

Armin **Azima**
DESY
Hamburg
Germany

— B —

Laura **Badano**
TERA
Novara
Italy

Jürgen **Bähr**
DESY-Zeuthen
Zeuthen
Germany

Cathelijne **Bal**
CERN
Geneva
Switzerland

Luca **Banchi**
ELETTRA
Basovizza, Trieste
Italy

Borut **Baricevic**
Instrumentation Technologies
Solkan
Slovenia

Peter **Barnes**
STFC/RAL/ISIS
Chilton, Didcot, Oxon
United Kingdom

Silvano **Bassanese**
ELETTRA
Basovizza, Trieste
Italy

Giorgio **Bassato**
INFN/LNL
Legnaro, Padova
Italy

Andrea **Battistella**
INFN/LNL
Legnaro, Padova
Italy

Frank **Becker**
GSI
Darmstadt
Germany

David **Belohrad**
CERN
Geneva
Switzerland

Julien **Bergoz**
BERGOZ Instrumentation
Saint Genis Pouilly
France

Michel **Bernard**
LAL
Orsay
France

Sandra **Biedron**
ANL
Argonne, IL
United States of America

Carlo **Bocchetta**
Instrumentation Technologies
Solkan
Slovenia

Thierry **Bogey**
CERN
Geneva
Switzerland

Mark **Boland**
ASP
Clayton, Victoria
Australia

Enrico **Bravin**
CERN
Geneva
Switzerland

Joseph **Brennan**
BNL
Upton, Long Island, NY
United States of America

Marlen **Bugmann**
PSI
Villigen
Switzerland

Stephane **Burger**
CERN
Geneva
Switzerland

John **Byrd**
LBNL
Berkeley, CA
United States of America

— C —

Luciano **Calabretta**
INFN/LNS
Catania
Italy

Peter **Cameron**
BNL
Upton, Long Island, NY
United States of America

Stefania **Canella**
INFN/LNL
Legnaro, Padova
Italy

Lodovico **Cassinari**
SOLEIL
Gif-sur-Yvette
France

Alessandro **Cianchi**
INFN-Roma II
Roma
Italy

Giulia **Ciani**
ELETTRA
Basovizza, Trieste
Italy

Paolo **Craievich**
ELETTRA
Basovizza, Trieste
Italy

Gillian **Cross**
STFC/RAL/ISIS
Chilton, Didcot, Oxon
United Kingdom

— D —

Raffaele **De Monte**
ELETTRA
Basovizza, Trieste
Italy

Stefano **De Santis**
LBNL
Berkeley, CA
United States of America

Glenn **Decker**
ANL
Argonne, IL
United States of America

Joze **Dedic**
Cosylab
Ljubljana
Slovenia

Bernd **Dehning**
CERN
Geneva,
Switzerland

Jean-Claude **Denard**
SOLEIL
Gif-sur-Yvette
France

Simone **Di Mitri**
ELETTRA
Basovizza, Trieste
Italy

Jürgen **Dietrich**
FZJ
Jülich
Germany

Francis **Dohou**
SOLEIL
Gif-sur-Yvette
France

Rudolf **Dölling**
PSI
Villigen
Switzerland

Clement **Doutresssoulles**
GANIL
Caen
France

Alessandro **Drago**
INFN/LNF
Frascati (Roma)
Italy

Pierre-Andre **Duperrex**
PSI
Villigen
Switzerland

— E —

Ewald **Effinger**
CERN
Geneva
Switzerland

Jonathan **Emery**
CERN
Geneva
Switzerland

— F —

Enrico **Fagotti**
INFN/LNL
Legnaro, Padova
Italy

Wilfrid **Farabolini**
CEA
Gif-sur-Yvette
France

Mario **Ferianis**
ELETTRA
Basovizza, Trieste
Italy

Peter **Forck**
GSI
Darmstadt
Germany

Richard **Ford**
FNAL
Batavia, IL
United States of America

John **Fox**
SLAC
Menlo Park, CA
United States of America

Jonathan **Fürsch**
DELTA
Dortmund
Germany

— G —

Christoph **Gabor**
STFC/RAL/ASTeC
Chilton, Didcot, Oxon
United Kingdom

Andreas **Galatis**
GSI
Darmstadt
Germany

Roland **Garoby**
CERN
Geneva
Switzerland

Marek **Gasior**
CERN
Geneva
Switzerland

Christopher **Gerth**
PSI
Villigen
Switzerland

Tino **Giacomini**
GSI
Darmstadt
Germany

J. **Gilpatrick**
LANL
Los Alamos, NM
United States of America

Walter **Göttmann**
HMI
Berlin
Germany

Alexis **Gogolev**
TPU
Tomsk
Russia

Timofey **Gorlov**
MEPhI
Moscow
Russia

Hans-Jürgen **Grabosch**
DESY-Zeuthen
Zeuthen
Germany

Jean-Jacques **Gras**
CERN
Geneva
Switzerland

Ana **Guerrero Ollacarizqueta**
CERN
Geneva
Switzerland

— H —

Kirsten **Hacker**
DESY
Hamburg
Germany

Abdallah **Hamdi**
CEA
Gif-sur-Yvette
France

Peter **Hartmann**
DELTA
Dortmund
Germany

Tobias **Hoffmann**
GSI
Darmstadt
Germany

Andre **Hofmann**
DESY-Zeuthen
Zeuthen
Germany

Eva **Holzer**
CERN
Geneva
Switzerland

Kuo-Tung **Hsu**
NSRRC
Hsinchu
Taiwan

Nicolas **Hubert**
SOLEIL
Gif-sur-Yvette
France

— I —

Fatih **Ilday**
Bilkent University
Bilkent, Ankara
Turkey

Ubaldo **Iriso**
ALBA
Bellaterra
Spain

Vadym **Ivashchenko**
NSC/KIPT
Kharkov
Ukraine

— J —

Christophe **Jamet**
GANIL
Caen
France

Simon **Jolly**
Imperial College of Science
and Technology
London
United Kingdom

Benoit **Joly**
ESRF
Grenoble
France

Matthias **Justus**
FZD
Dresden
Germany

— K —

Alexander **Kalinin**
STFC/DL/ASTeC
Daresbury, Warrington, Cheshire
United Kingdom

Anders **Källberg**
MSL
Stockholm
Sweden

Thorsten **Kamps**
BESSY
Berlin
Germany

Grzegorz **Kasprowicz**
CERN
Geneva
Switzerland

Boris **Keil**
PSI
Villigen
Switzerland

Anthony **Kershaw**
STFC/RAL/ISIS
Chilton, Didcot, Oxon
United Kingdom

Sergiy **Khodyachykh**
DESY-Zeuthen
Zeuthen
Germany

Janko **Kolar**
Instrumentation Technologies
Solkan
Slovenia

Sergey **Korepanov**
DESY-Zeuthen
Zeuthen
Germany

Tomaz **Korosec**
UniversityLjubljana
Ljubljana
Slovenia

Piotr **Kowina**
GSI
Darmstadt
Germany

Mikhail **Krasilnikov**
DESY
Hamburg
Germany

Patrick **Krejcik**
SLAC
Menlo Park, CA
United States of America

Herman **Kremers**
KVI
Groningen
The Netherlands

Igor **Krouptchenkov**
DESY
Hamburg
Germany

Gero **Kube**
DESY
Hamburg
Germany

Peter **Kuske**
BESSY
Berlin
Germany

— L —

Marie **Labat**
SOLEIL
Gif-sur-Yvette
France

David **Lee**
Imperial College of Science
and Technology
London
United Kingdom

Thibaut **Lefevre**
CERN
Geneva
Switzerland

Dimitry **Liakin**
ITEP
Moscow
Russia

Florian **Löhl**
DESY
Hamburg
Germany

Bastian **Lorbeer**
DESY
Hamburg
Germany

Michael **Ludwig**
CERN
Geneva
Switzerland

Jorgen **Lund-Nielsen**
DESY
Hamburg
Germany

Andrei **Lunin**
FNAL
Batavia, IL
United States of America

— M —

Victor **Malka**
LOA
Palaiseau
France

Christophe **Mariette**
SOLEIL
Gif-sur-Yvette
France

Oleg **Meshkov**
BINP SB RAS
Novosibirsk
Russia

Toshiyuki **Mitsuhashi**
KEK
Ibaraki
Japan

Akira **Mochihashi**
UVSOR
Okazaki
Japan

Alun **Morgan**
Diamond
Oxfordshire
United Kingdom

Hendrik **Mostert**
—
—

Jost **Müller**
DESY
Hamburg
Germany

— N —

Graham **Naylor**
ESRF
Grenoble
France

Jörgen **Nielsen**
ISA
Aarhus
Denmark

Dirk **Nölle**
DESY
Hamburg
Germany

— O —

Takashi **Obina**
KEK
Ibaraki
Japan

Matej **Oblak**
Instrumentation Technologies
Solkan
Slovenia

Angel **Olmos**
ALBA
Bellaterra
Spain

— P —

Leon **Pavlovic**
University Ljubljana
Ljubljana
Slovenia

Zarko **Pavlovic**
The University of Texas at Austin
Austin, TX
United States of America

Stephen **Payne**
STFC/RAL/ISIS
Chilton, Didcot, Oxon
United Kingdom

Dominique **Pedeau**
SOLEIL
Gif-sur-Yvette
France

Francisco **Pérez**
ALBA
Bellaterra
Spain

Alex **Pertica**
STFC/RAL/ISIS
Chilton, Didcot, Oxon
United Kingdom

Andreas **Peters**
HIT-GSI
Heidelberg
Germany

Paul **Phillips**
UAD
Dundee
United Kingdom

Igor **Pinayev**
BNL
Upton, NY
United States of America

Marco **Poggi**
INFN/LNL
Legnaro, Padova
Italy

— R —

Uli **Raich**
CERN
Geneva
Switzerland

Udo **Rauch**
GSI
Darmstadt
Germany

Günther **Rehm**
Diamond
Oxfordshire
United Kingdom

Hue **Robert**
GANIL
Caen
France

Cristiana **Roberti**
ELETTRA
Basovizza, Trieste
Italy

Juliane **Rönsch**
University HH
Hamburg
Germany

Fabio **Rossi**
ELETTRA
Basovizza, Trieste
Italy

— S —

Martin **Sachwitz**
DESY Zeuthen
Zeuthen
Germany

Shigeki **Sasaki**
JASRI/SPring-8
Hyogo-ken
Japan

Kees **Scheidt**
ESRF
Grenoble
France

Holger **Schlarb**
DESY
Hamburg
Germany

Volker **Schlott**
PSI
Villigen
Switzerland

Bernhard **Schmidt**
DESY
Hamburg
Germany

Rico **Schurig**
FZD
Dresden
Germany

Marcus **Schwickert**
GSI
Darmstadt
Germany

Mario **Serio**
INFN/LNF
Frascati (Roma)
Italy

Thomas **Shea**
ORNL
Oak Ridge, TN
United States of America

Thomas **Sieber**
MPI-K
Heidelberg
Germany

Claire **Simon**
CEA
Gif-sur-Yvette
France

Om **Singh**
BNL
Upton, NY
United States of America

Victor **Smaluk**
BINP SB RAS
Novosibirsk
Russia

Lars **Søby**
CERN
Geneva
Switzerland

Jens **Spanggaard**
CERN
Geneva
Switzerland

Bruno **Spataro**
INFN/LNF
Frascati (Roma)
Italy

Ralph **Steinhagen**
CERN
Geneva
Switzerland

Angelo **Stella**
INFN/LNF
Frascati (Roma)
Italy

Leonid **Sukhikh**
TPU
Tomsk
Russia

— T —

Caterina **Tabacco**
ELETTRA
Basovizza, Trieste
Italy

Gianni **Tassotto**
FNAL
Batavia, IL
United States of America

Dmitry **Teytelman**
SLAC
Menlo Park, CA
United States of America

Dejan **Tinta**
Instrumentation Technologies
Solkan
Slovenia

Marie-Agnès **Tordeux**
SOLEIL
Gif-sur-Yvette
France

Akihisa **Toyoda**
KEK
Tsukuba
Japan

Daniel **Treyer**
PSI
Villigen
Switzerland

Giuseppe **Trovato**
ELETTRA
Basovizza, Trieste
Italy

— U —

Klaus **Unser**
Private Address
Prevessin
France

Rok **Uršič**
Instrumentation Technologies
Solkan
Slovenia

Vyacheslav **Uvarov**
NSC/KIPT
Kharkov
Ukraine

— V —

Paolo **Valente**
INFN-Roma
Roma
Italy

Elsa **van Garderen**
PSI
Villigen
Switzerland

Marco **Veronese**
ELETTRA
Basovizza, Trieste
Italy

Victor **Verzilov**
TRIUMF
Vancouver
Canada

Jean-Luc **Vignet**
GANIL
Caen
France

Wolfgang **Vodel**
FSU Jena
Jena
Germany

— W —

Arden **Warner**
FNAL
Batavia, IL
United States of America

Ilde **Weffort**
ELETTRA
Basovizza, Trieste
Italy

Matthias **Werner**
DESY
Hamburg
Germany

Sarah **Whitehead**
STFC/RAL/ISIS
Chilton, Didcot, Oxon
United Kingdom

Axel **Winter**
DESY
Hamburg
Germany

Kay **Wittenburg**
DESY
Hamburg
Germany

Diana **Wright**
STFC/RAL/ISIS
Chilton, Didcot, Oxon
United Kingdom

— Z —

Christos **Zamantzas**
CERN
Geneva
Switzerland

Andrey **Zhuravlev**
BINP SB RAS
Novosibirsk
Russia

MAQbox

The Alternative to Conventional Oscilloscopes for Multichannel Data Acquisition

Maximum Channel Density and Flexibility

- A turnkey solution for measurements of up to 28 channels
- Up to 8 GS/s sampling rate, 3 GHz bandwidth and 1 Gpoints of memory
- Allows combination of different digitizers for 8-, 10-, and 12-bit recording
- Multichannel synchronization capability
- High data throughput for automatic storage to disk in HDF5 format, compatible with MATLAB or IDL
- Autosetup mode to quickly find unknown signals
- Multi-waveform display on a large high resolution screen
- Clear identification of each trace

acqiris

For more information, call us at +41 22 884 32 90
or visit our website at **www.acqiris.com**

Agilent Technologies

Gli oscilloscopi che catturano tutti i segnali

Analizzate con Agilent tutti i segnali analogici, digitali e seriali

Serie Agilent 6000

Serie Agilent 8000

Oscilloscopi Agilent a Segnali Misti

	serie Agilent 6000	serie Agilent 8000
Segnali analogici	2-4ch, 100 MHz – Ampiezza di banda: 1GHz	4ch, 600 MHz – Ampiezza di banda: 1GHz
	Display XGA di tipo analogico con 256 livelli di intensità	
	Fino a 100 k forme d'onda/sec	Analisi estesa anche del jitter
Segnali digitali	16 canali logici di temporizzazione in ordine cronologico	
	Attivazione di modelli e di segnali misti	
	Applicazione della sonda dinamica FPGA	
Segnali seriali	Attivazione USB, I²C, SPI, **CAN/LIN** e opzioni di decodifica hardware	Opzioni di decodifica MegaZoom I²C, SPI, **CAN**, applicazioni seriali Ethernet GBit
	Fino a 8 Mpts di memoria profonda	Fino a 128 Mpts di memoria MegaZoom profonda

Gli oscilloscopi della serie Agilent 6000 e 8000 a segnali misti catturano tutti i segnali e li esaminano in profondità.

Oggi è possibile catturare in tempo reale segnali seriali, analogici e digitali in una sola acquisizione, scegliendo una qualsiasi combinazione tra i canali di ingresso. Gli oscilloscopi Agilent serie 6000 e 8000 visualizzano forme d'onda analogiche e digitali e flussi di dati seriali sul display, correlati nel tempo.

La veloce memoria MegaZoom ad alte prestazioni (fino a 128 Mpts) cattura le forme d'onda in un'altissima risoluzione, in periodi di tempo prolungati, conservando e visualizzando tutti i vostri dati.

Scoprite come migliorare l'analisi dei segnali misti, scaricando l'ultima nota applicativa dedicata agli oscilloscopi Agilent serie 6000 e 8000 dal sito www.agilent.com/find/scopes2

Per ulteriori informazioni, o per richiedere una dimostrazione dei prodotti, chiamate lo 02 9260 8484

www.agilent.com/find/scopes2

©Agilent Technologies, Inc. 2006

Agilent Technologies

Bergoz Instrumentation
Espace Allondon Ouest
01630 St-Genis-Pouilly France

New Products!

New UHV Parametric Current Transformer

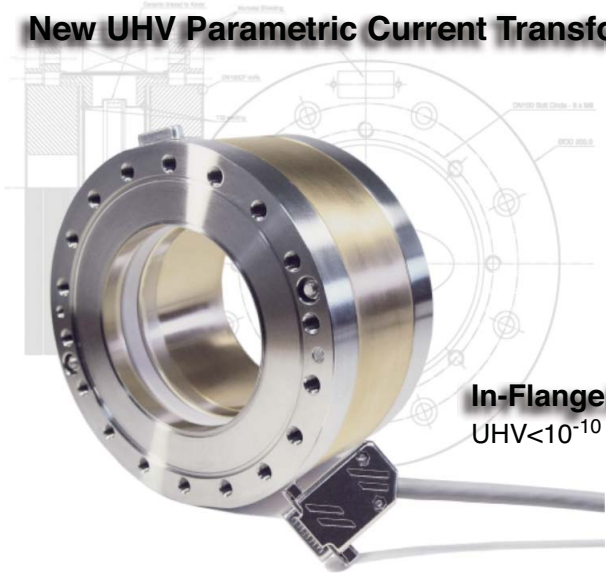

In-Flange.NPCT
UHV<10^{-10} mbar

Up to 500 MHz bandwidth
Higher sensitivity

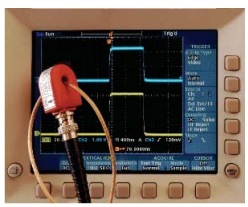

CT
Current Transformer

UHV FCT, ICT, ACCT & TCT

In-Flange.CT
UHV<10^{-10} mbar

E-Mail:info@bergoz.com www.bergoz.com

Hamamatsu technology provides a full line of optoelectronics components (Photomultiplier Tubes, MCP, X-ray Image intensifiers , Light Sources , Photodiodes, Silicon Strip Detector ,Infrared Detectors , CCD and IR Cameras , Streak Cameras , Image Analysis Systems).
Our products cover a wide range of applications running from Spectroscopy , High Energy Physics , Medical Imaging , Biotechnology, Environmental and Radiation Monitoring.

Femtosecond Streak Camera

The FESCA-200 is an ultra fast streak camera with a temporal resolution of 200 fs (typ.). It is designed for use with single-shot or slow-repetitive phenomena, as in Research of the dynamics of chemical reactions in the femtosecond region or Diagnosis of femtosecond lasers.

Features
- Single Shot 200 fs (typ.) Temporal Resolution
- Ultra-high sensitivity (detection of single photons)
- IEEE-488 (GP-IB) control

X-ray Camera

Hamamatsu X-ray Camera Series are designed for Synchrotron Radiation Facilities.
- X-ray Camera with Fiber Optics Window which enable high optical coupling efficiency. The fiber optics is directly couplet to CCD without using conventional lenses. Various type of Scintillator are available.
- High Resolution X-ray Imaging system enables to combine various type of CCD cameras for real time X-ray beam alignment. Beryllium input window realized wide range of X-ray energy.
-**Direct X-ray Imaging System** without using scintillator. User may choose from 3 type of CCD depends of the X-ray energy level they can detect.

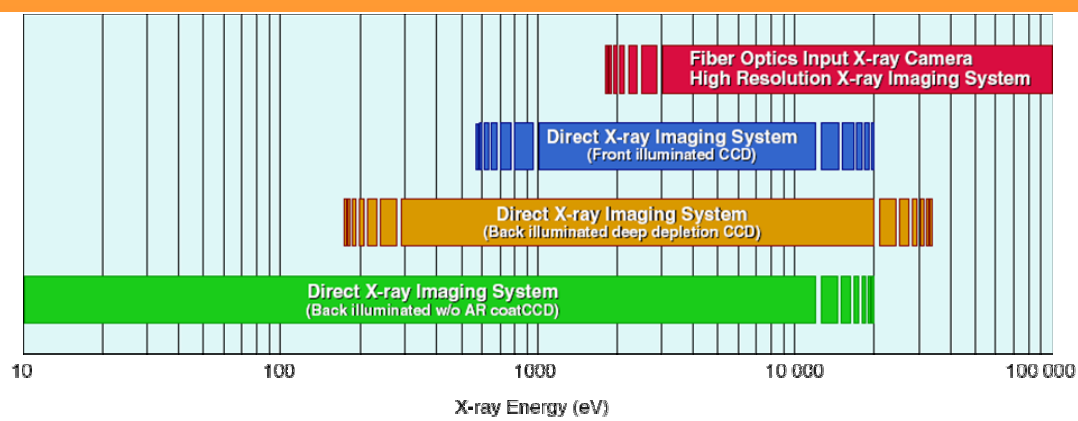

Loop Closed !

- More than a thousand Libera units worldwide
- 5 latest machines completely equipped with Libera: ALBA, Australian Synchrotron, DIAMOND Light Source, SSRF, Synchrotron SOLEIL
- 2 machines upgraded with Libera: Elettra and GSI-SIS18
- 18 further machines deploying Libera: ANL-APS, BNL, CLS, CERN, DELTA, DESY, ESRF, ANKA, IHEP, INFN – LNF, ISSP, SPring-8, KEK, NSRL, NSRRC, PAL, SLAC, SLS
- Global orbit stability at Elettra with closure of orbit feedback loop.

- After the proven accomplishments of Libera we are launching the new "Libera Brilliance" with even greater performance (RMS, current dependence, coupling) ready to meet the next generation of objectives while maintaining the same control system interface.

Join the growing Libera community – exchange your ideas and experience in the forum, participate in the Libera Workshop and subscribe to the I-Tech newsletter!

Instrumentation Technologies

www.i-tech.si
Instrumentation Technologies, Velika pot 22, SI-5250 Solkan, Slovenia
T : +386 5 33 52 600
F : +386 5 33 52 601
info@i-tech.si

When your users demand a stable orbit

You and Varian: the Winning Team.

Get the benefits of a global supplier of Vacuum Technology:

- A pioneer in the vacuum industry for over 50 years
- 24 hours Service Support available worldwide
- Innovative Turbomolecular pump line with controllers on board
- Full range of Diffusion, Rotary Vane and Scroll pumps
- World leader in Ion Pumps and Leak Detection technologies
- On-line ordering now available

Interactive catalog on CD

Varian, Inc.
Vacuum Technologies
Via F.lli Varian 54, 10040 Leini, (Torino), Italy
Tel: (39) 011 997 9 111, Fax: (39) 011 997 9 350
Toll Free Number: 00 800 234 234 00

www.varianinc.com/vacuum

Inspiring Excellence™

VARIAN

SOLUTIONS &
PRODUCT OVERVIEW

TEST & MEASUREMENT

QUALITY ■ INNOVATION ■ FORESIGHT

YOKOGAWA

More than 1000 units reference in SPring-8.

ISP-90

ISP-250B

ISP-500B

Oil-free Scroll Vacuum Pump

ECO : air cooled and saving power comsumption.

Dry : free daily maintenance of lubricating oil and oil filter.

After Service

: easy maintenance, maintenance service network world wide.

Easy Installation

: light weight – compact design.
No water/ N_2 piping installation.

ANEST IWATA was the first in the world to develop the air-cooled dry scroll vacuum pumps.

ANEST IWATA Corporation

3176, Shinyoshida-cho, Kohoku-ku,
Yokohama 223-8501 Japan
Telephone +81-(0)45-591-1112
Fac
simile +81-(0)45-593-1539
http://www.anest-iwata.co.jp/
ispinfo@anest-iwata.co.jp

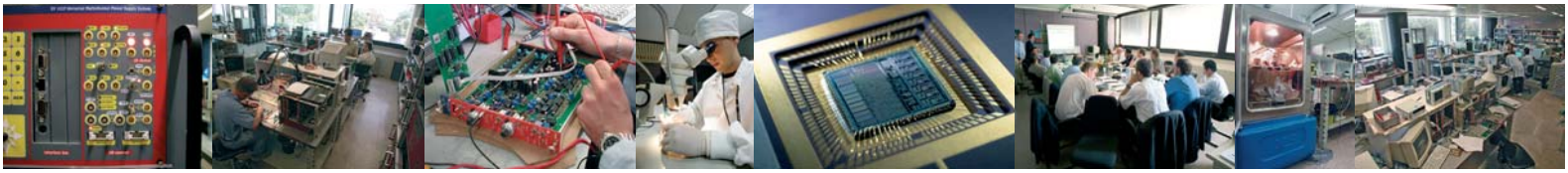

CAEN
Tools for Discovery

www.caen.it

CAEN spa is one of the most important industrial spin off of the Italian Nuclear Physics Research. The company was founded in Viareggio (Italy) in 1979 by a group of senior engineers from the Istituto Nazionale di Fisica Nucleare (INFN).
Today CAEN, is acknowledged as the only company in the world providing a complete range of High/Low Voltage Power Supply systems, powerful Crates and Front-End/DAQ modules which meet IEEE Standards for Nuclear and Particle Physics (NIM, CAMAC and VME).
Extensive Research and Development capabilities have allowed CAEN to play an important, long term role in this field. Our activities have always been at the forefront of technology, thanks to years of intensive collaborations with the most important Research Centres of the world.

Our products appeal to a wide range of customers including engineers, scientists and technical professionals who all trust them to help achieve their goals faster and more effectively.
Our catalog includes more than 250 products, however, this list is not exhaustive: almost 40% of CAEN production is Custom designed and does not appear in the catalog. CAEN has always been and would like to continue to be the experimenters' partner.

In order to strengthen its presence in the North American territory, CAEN opened its new branch company in the United States, **CAEN Technologies Inc.**, based in New York.
With the same aim and in order to provide its customers with a better assistance and services, CAEN established another sister company in Germany, **CAEN GmbH**, based in Solingen.

Our Mission:

- To provide our customers with better solutions to measure, research and test the world around them.
- To proceed along this path with continuous energy to live the new electronics reality and offer the best technical support to the researchers of the new century.
- To provide innovative products allowing our customers access to improved scientific results.
- To offer effective sales and after-sales support.
- To represent a real added value to our products and services with our on-line Customer care.

Our Vision:

To realize our customer's dream: developing the most useful "Tools for Discovery".

CAEN S.p.A.
Via Vetraia, 11
55049 - Viareggio - Italy
Phone +39.0584.388.398
Fax +39.0584.388.959
info@caen.it
www.caen.it

CAEN Technologies, Inc.
1140 Bay Street - 2C
Staten Island, NY 10305
USA
Phone +1.718.981.0401
Fax +1.718.556.9185
info@caentechnologies.com
www.caentechnologies.com

CAEN GmbH
Eckehardweg 10
42653 - Solingen
Germany
Phone +49.212.2544077
Fax +49.212.2544079
info@caen-de.com
www.caen-de.com

CAEN Headquarters, Viareggio - Italy

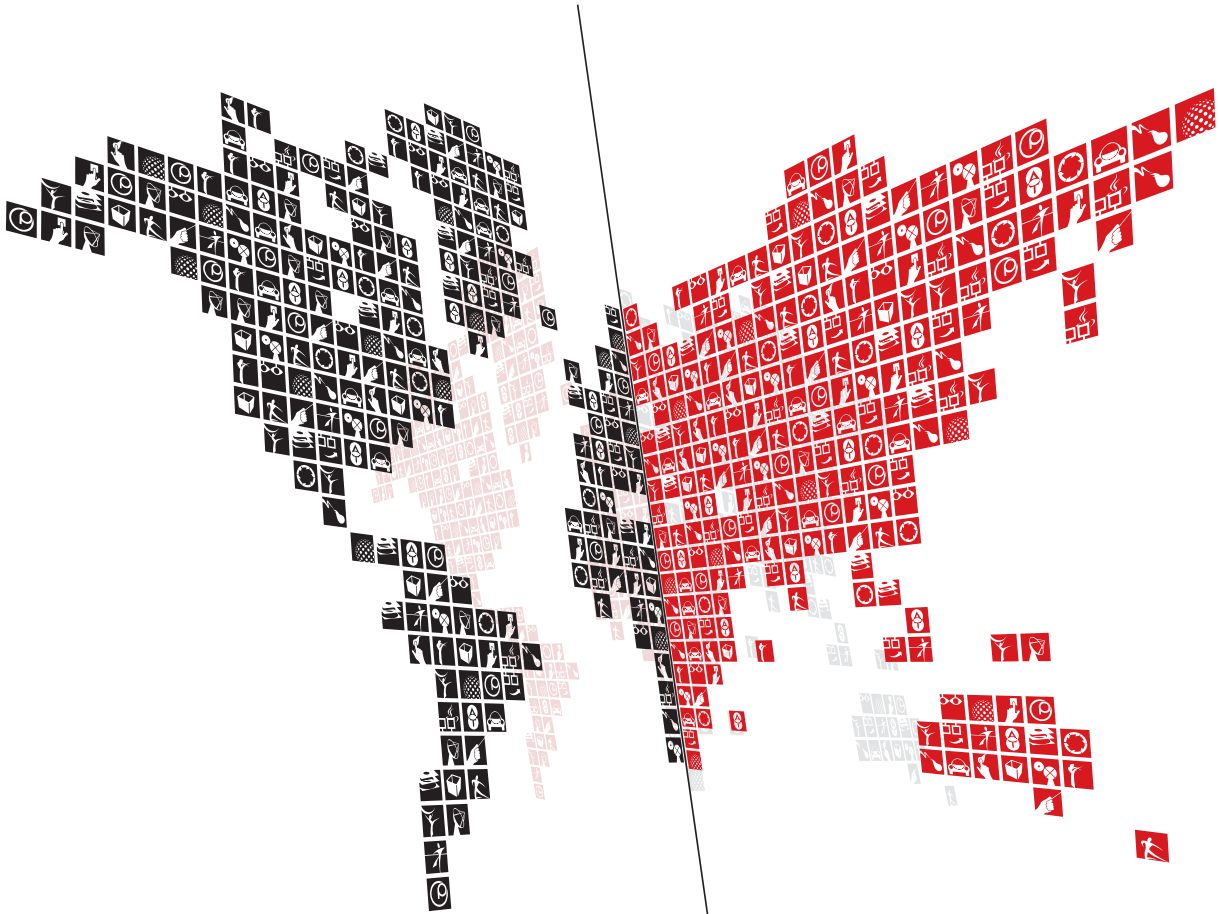

cosylab
CONTROL SYSTEM LABORATORY

www.cosylab.com

Cosylab is the world leading company in the field of control systems for particle accelerators, synchrotron radiation beamlines and radio telescopes. We provide professional solutions from system engineering and project management, custom development to complete turnkey control systems. We serve over 50 major accelerator facilities in Europe, USA, Japan, Australia and their main suppliers.

Based on our experience we designed our own set of instruments - microIOC family. With integration of microIOC family into your facility, you get:

- plug & play integration of devices into control system; software is part of the package
- standardized solution based on experience and expertise in accelerators
- high reliability; no moving parts, reliable building blocks, each unit tested
- flexible installation and access

Instrumentation, Software and Systems

Stepper Motor Control & Power Drive Solutions

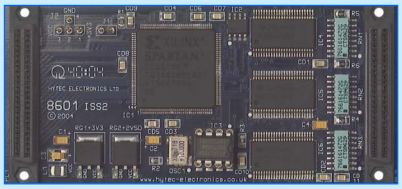

CONTROL The 8601 Industry Pack (IP) Card is a 4 channel controller with step, position, ramp and direction registers, encoder and limit switches.

CONTROL 24 AXES Self contained IOC with 6 industry pack (IP) slots each with a signal conditioning card, PMC slot, PC104+ processor, Ethernet, USB, RAM. It will run Linux, Windows XP or RTEMS. With 6off 8601 IP cards fitted, 24 motors can be controlled from one 1U 9010.

DRIVE Compact 8909U DIN Rail Driver for 5, 6 or 8-lead hybrid stepper motors. FPGA controls the excitation of 4 motors up to 1 amp per phase.

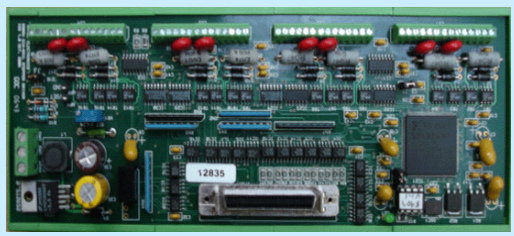

DRIVE SMDS system available as unipolar (L/R) or bipolar driver with current limit by PWM in groups of 4 stepper motors, up to 5 amps per phase. Internal or external power supply.

Full range includes ADCs, DACs, Digitisers, RS232/485 and Scalers

CAMAC, VME, PCI, VME64x, Industry Packs

Hytec Electronics Ltd, 5 Cradock Road, Reading, Berkshire, RG2 0JT, England

Tel: +44 (0)118 9757770 Fax : +44 (0)118 9757566
Email: **sales@hytec-electronics.co.uk** Web: **www.hytec-electronics.co.uk**

INCAA COMPUTERS

DESIGN AND MANUFACTURING of computer systems for:

Science	Industry	Automotive	Vending systems	OEM

Scalable data acquisition systems; Alarm systems; Test systems; Board computers; Electronic modules; GPS applications; GPRS applications; VME modules; CompactPCI modules; POS; Custom design.....

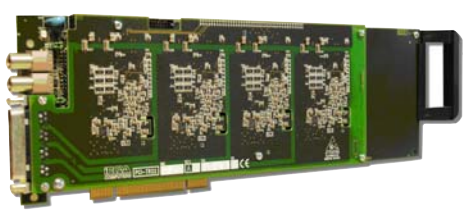

INCAA Computers B.V. P.O. Box 722 7300 AS APELDOORN The Netherlands Tel: +31-55-542 50 01 sales@incaacomputers.com www.incaacomputers.com

PXI The Test Platform of Choice for Thousands of Companies Worldwide

Microsoft
BAE Systems
Lockheed Martin
United States Air Force
Honeywell
Saab
Johns Hopkins University
Pyrex
DePuy, a Johnson & Johnson Company
Samsung

Stanford University
National Institute of Ocean Technology
Lund Institute of Technology
Sandia National Laboratories
Lexmark
Magneti Marelli, a Fiat company
Renault
Summitek Instruments
United States Navy
United States Army

Toshiba
Flextronics
Fiat
Niksar Australia Pty Ltd.
NEC Aerospace Systems
Siemens
SELEX Sistemi Integrati
Huari Telecom
Soliton Technologies
Active Signal Technologies

PC-Based Controller | Modular Instruments DC to 6.6 GHz | Rack Mount or Portable Chassis

PXI is a modular, software-defined platform for measurement and automation systems.

- Open industry standard supported by more than 70 vendors and 1,200 products
- Highest-accuracy instruments, including the highest-resolution digitizer with -120 dBc typical SFDR
- Industrial-grade, cost-effective system based on standard PC technologies
- Direct connectivity to existing instruments using GPIB, Ethernet/LAN, USB, CompactPCI, PCI, and PCI Express
- Software-defined configuration and automation with National Instruments LabVIEW and LabWindows™/CVI, C/C++, NI TestStand, and Microsoft .NET

Choose from a complete set of PXI chassis, controllers, and modular instruments from NI.

PXI Chassis	3U, 6U, rack-mount, 4 to 18 slots
PXI Controllers	Remote or embedded
Digitizers/Oscilloscopes	Up to 24 bits, 2 GS/s
Signal Generators	Up to 16 bits, 200 MS/s
High-Speed Digital I/O	Up to 400 Mb/s
RF	Up to 6.6 GHz, 20 MHz RTB
Digital Multimeters	Up to 7½ digits, LCR, 1,000 V
Programmable Power Supplies	Up to 20 W, 16 bits
Audio Analyzers	Up to 24 bits, 500 kS/s
Switches	Multiplexers, matrices, RF, relays
Multifunction I/O	Analog I/O, digital I/O, counters

To learn why each of these customers chose PXI, visit **ni.com/pxi**

02 41 309 277

© 2007 National Instruments Corporation. All rights reserved. CVI, LabVIEW, National Instruments, NI, ni.com, and NI TestStand are trademarks of National Instruments. Other product and company names listed are trademarks or trade names of their respective companies. 2007-8693-501-122

NATIONAL INSTRUMENTS™

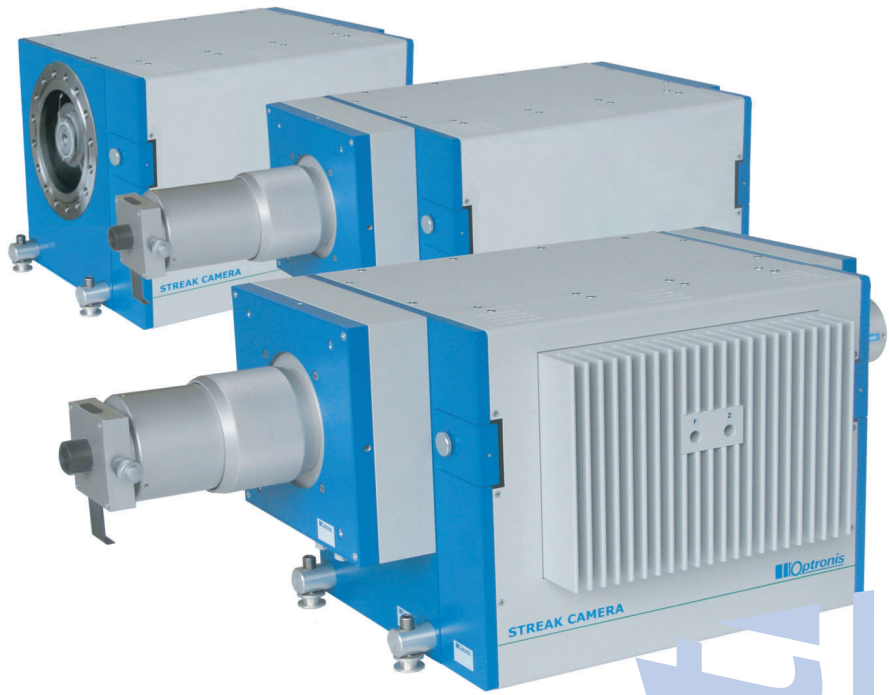

Optronis develops and distributes Streak Cameras and Fast Video Cameras for scientific and industrial applications.

It is the goal of Optronis to provide solutions for demanding applications. Optronis is today in a position to offer standard products as well as being a competent partner for particular system requirements.

Streak Cameras

- Down to 2 ps resolution
- Trigger sweep up to 4 MHz
- Synchroscan up to 250 MHz
- Ethernet interface
- Complete software control

Optronis GmbH
Honsellstr. 8 D-77694 Kehl
Internet: www.optronis.com

Tel.: +49 (0) 7851/9126- 0
Fax: +49 (0) 7851/9126-10
e-mail: info@optronis.com

PhoTrix

PhoTrix is specialized in producing modules, instruments, and subsystems, for processing wide-bandwidth optical signals: from generation and transmission, to elaboration and measurement.
The long expertise of PhoTrix staff in ultra-fast optical signal processing, can supply you with products for optical applications requiring bandwidth in excess of 200 GHz.

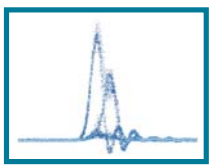

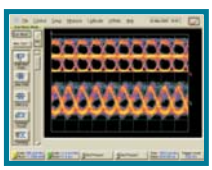

Products

Ultra-short pulse generation and measurement

- Optical high repetition-rate ultra-short pulse sources
- Optical low repetition-rate ultra-short pulse sources
- Optical pulse compressors
- Optical pulsed comb generators
- Optical time-division multiplexers
- High resolution optical sampling oscilloscope

Optical signal processing

- Optical amplifiers
- Optical 2R regenerators
- Optical 3R regenerators

Applications

- Optical communications
- Synchronization - clock distribution
- Optical sampling
- Optical sensing
- BioPhotonics
- Spectroscopy

Visit us at www.photrix.it

PhoTrix S.r.l. is a spin-off company of CNIT and Scuola Superiore Sant'Anna within IRCPhoNeT (Integrated Research Center for Photonics Networks and Technologies) in Pisa, Italy.

Completely Customized Production

Pico Source

Optical Clock
developed for
Elettra - Sincrotrone Trieste

Features

- High-quality pulses
- Excellent long-term stability
- Optical VCO functionality
- User-friendly

Characteristics

Nominal Repetition Rate	2.997 GHz
Central Wavelength	1549.7 nm
Pulsewidth	10 ps
Average Optical Power	8 dBm
Polarization State	linear
Phase Noise [10Hz-10MHz]	63 fs
Optical VCO Bandwidth	2 kHz

PhoTrix S.r.l.
via Moruzzi 1, 56100 Pisa - Italy
tel. +39 (0)50 5492217/21/37, fax. +39 (0)50 5492220, e.mail: info@photrix.it, sales@photrix.it
www.photrix.it

RIAL VACUUM S.P.A.
Via Tito ed Ettore Manzini, 7/A 43100 - Parma - Italy
Tel. +39 0521 949311 Fax. +39 0521 949300
www.rialvacuum.com - sales@rialvacuum.com

RIAL VACUUM
FINBER GROUP

digigraphparma.it

Saint-Gobain Solcera

Nos produits

Notre savoir-faire

SAINT-GOBAIN

MATERIAUX HAUTE PERFORMANCE

Tektronix®

Enabling Innovation

Tektronix è un fornitore leader di prodotti di verifica, misurazione e monitoraggio, di soluzioni e servizi per i settori delle comunicazioni, dell'informatica e dei semiconduttori, nonché per i settori militare/aerospaziale, elettronica consumer, istruzione e una vasta gamma di altri settori in tutto il mondo. Grazie a 60 anni di esperienza Tektronix consente ai propri clienti di progettare, costruire, distribuire e gestire reti di comunicazione globali di nuova generazione, utilizzando tecnologie avanzate e notevolmente diffuse. Con sede a Beaverton, in Oregon, Tektronix è presente in 19 paesi nel mondo. L'indirizzo Web di Tektronix è www.tektronix.com.

PRODUCTS

- **Test & Measurement**
- Oscilloscopes
- Real-Time Spectrum Analyzers
- Logic Analyzers
- Signal Generators
- Probes & Accessories

- **Communications** - Solutions for:
- Equipment Manufacturers
- Network Operators

- **Video Test**
- Signal Analyzers, Generators & Monitors
- MPEG Analyzers, Generators & Monitors
- Content Verification

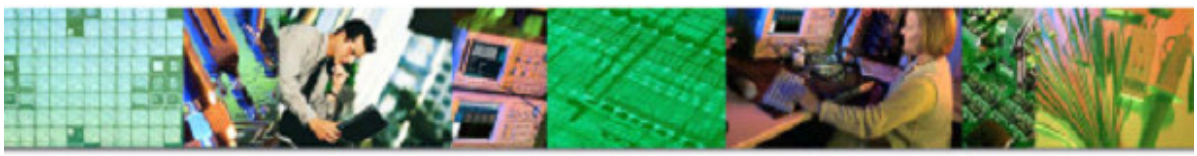

Image courtesy HESS Collaboration

Modules

NIM, VME and Camac Modules

New!

New!

Nembox

Universal Programmable NIM Module with USB port

- Multichannel LE Discriminator
- 4 ch. ADC / DAC
- Coincidence, Fan In / Fan Out, AND, OR, Logic, Gate Generator
- Timer, Pulser, TDC

CAMAC and VME Controllers

- USB, PCI and VME-CAMAC interfaces
- NIM I/O Programmable Ports

New!

Preamplifiers and Shapers

For PMTs, Si and Ge Detectors

- No high current requirements on the 12 V line
- With CF Discriminators
- With Multiplicity Trigger
- USB Programmable

Neutron/Gamma Discriminator

For Liquid Scintillators

- 4 Channel Pulse Analyzer
- USB Programmable
- Real Time

And much more...
www.wiener-d.com

Wiener Plein & Baus GmbH
Muellersbaum 20, 51399 Burscheid (Germany)
Tel. +49 2174 678 0

wiener
Plein & Baus Elektronik
Werk für Industrie-elektronik Nuklear-elektronik Regelungs-technik